R. E. Kaiser

ANL-7410

ANL-7410

Argonne National Laboratory

REACTOR PHYSICS DIVISION

ANNUAL REPORT

July 1, 1967 to June 30, 1968

The facilities of Argonne National Laboratory are owned by the United States Government. Under the terms of a contract (W-31-109-Eng-38) between the U. S. Atomic Energy Commission, Argonne Universities Association and The University of Chicago, the University employs the staff and operates the Laboratory in accordance with policies and programs formulated, approved and reviewed by the Association.

MEMBERS OF ARGONNE UNIVERSITIES ASSOCIATION

The University of Arizona
Carnegie Institute of Technology
Case Institute of Technology
The University of Chicago
University of Cincinnati
Illinois Institute of Technology
University of Illinois
Indiana University
Iowa State University
The University of Iowa
Kansas State University
The University of Kansas
Loyola University
Marquette University
Michigan State University
The University of Michigan
University of Minnesota
University of Missouri
Northwestern University
University of Notre Dame
The Ohio State University
Purdue University
Saint Louis University
Washington University
Wayne State University
The University of Wisconsin

LEGAL NOTICE

This report was prepared as an account of Government sponsored work. Neither the United States, nor the Commission, nor any person acting on behalf of the Commission:

A. Makes any warranty or representation, expressed or implied, with respect to the accuracy, completeness, or usefulness of the information contained in this report, or that the use of any information, apparatus, method, or process disclosed in this report may not infringe privately owned rights; or

B. Assumes any liabilities with respect to the use of, or for damages resulting from the use of any information, apparatus, method, or process disclosed in this report.

As used in the above, "person acting on behalf of the Commission" includes any employee or contractor of the Commission, or employee of such contractor, to the extent that such employee or contractor of the Commission, or employee of such contractor prepares, disseminates, or provides access to, any information pursuant to his employment or contract with the Commission, or his employment with such contractor.

Printed in the United States of America
Available from
Clearinghouse for Federal Scientific and Technical Information
National Bureau of Standards, U. S. Department of Commerce
Springfield, Virginia 22151
Price: Printed Copy $3.00; Microfiche $0.65

ANL-7410
Reactor Technology

Argonne National Laboratory

9700 South Cass Avenue
Argonne, Illinois 60439

REACTOR PHYSICS DIVISION ANNUAL REPORT

July 1, 1967 to June 30, 1968

Robert Avery, Division Director
Harry H. Hummel, Associate Division Director
W. C. Redman, Associate Division Director
William J. Sturm, Assistant Division Director
Lyman J. Templin, Assistant Division Director

January 1969

Foreword

This is the fifth successive issue of the Reactor Physics Division Annual Report and, in format, it simulates the preceding report, ANL-7310. As in previous reports, it emphasizes work performed by members of the Division, rather than integrated programmatic accomplishments. Nevertheless, when reasonable and possible, papers related to a given subject are grouped together within a Section.

In order to assist those who may wish to pursue a given subject more extensively, a list of pertinent references is included in each article. A catalog of open-literature and report publications and of abstracts prepared by staff of the Reactor Physics Division during the reporting period are appended in Section VII to further aid those who may be interested in having additional information concerning work done in this Division.

Table of Contents

SECTION I

FISSION PROPERTIES AND CROSS SECTION DATA

I-1. Introduction 3
A. B. Smith

I-2. Polarization in the Elastic Scattering of Neutrons from Intermediate Weight Nuclei .. 3
S. A. Cox and E. E. Dowling Whiting

I-3. Elastic and Inelastic Scattering from Spherical Nuclei—Introduction 7
A. B. Smith

I-4. Elastic and Inelastic Scattering from Spherical Nuclei—Germanium 7
D. Lister and A. B. Smith

I-5. Elastic and Inelastic Scattering from Spherical Nuclei—Titanium 8
A. B. Smith, J. Whalen and P. Guenther

I-6. Elastic and Inelastic Scattering from Spherical Nuclei—Iron 8
E. Barnard, J. A. M. De Villiers, C. A. Engelbrecht, D. Reitmann and A. B. Smith

I-7. Elastic and Inelastic Scattering from Spherical Nuclei—Bismuth 10
A. B. Smith, J. Whalen, E. Barnard, J. A. M. De Villiers, C. A. Engelbrecht and D. Reitmann

I-8. Elastic and Inelastic Scattering from Spherical Nuclei—Palladium 10
A. B. Smith

I-9. Neutron Scattering from Heavy Deformed Nuclei 11
A. B. Smith and G. Sherwood

I-10. Fast Neutron Processes in Vanadium and Intermediate Structure 14
A. B. Smith and J. F. Whalen

I-11. Fast Neutron Cross Sections 17
J. F. Whalen

I-12. The Total Cross Section of Li-7 from 100 to 650 keV 19
J. W. Meadows and J. F. Whalen

I-13. Extension of Automated Neutron Cross Section Measurements to Higher Energies .. 21
J. F. Whalen and J. W. Meadows

I-14. Activation Methods for Actinide Isotope Capture Rate Measurements 21
R. J. Hall, W. C. Redman and M. L. Pool

I-15. Correlation of Mass, Energy and Angle in 1.5 and 5.6 MeV Neutron Fission of U-238 .. 26
J. W. Meadows

I-16. Energy Dependence of the Delayed Neutron Yield from Neutron Induced Fission of Th-232, U-235, and U-238 27
S. A. Cox and E. E. Dowling Whiting

I-17. Spontaneous Fission Decay Constant of U-238 30
J. H. Roberts, R. Gold and R. J. Armani

I-18. T-Violation Effects in Direct Reactions 31
P. A. Moldauer

I-19. Statistics of Resonance Widths and Spacings 31
P. A. Moldauer

I-20. Shell Model R-Matrix Theory 32
K. Takeuchi

I-21. Fine Structure of Doorway States 33
K. Takeuchi

I-22. Phenomenological Doorway State Theory 34
K. Takeuchi
I-23. Monte Carlo Interpretation of a U-238 Spherical Shell Transmission Experiment at 23 keV 34
L. B. Miller and W. P. Poenitz
I-24. Multilevel Analysis of the Pu-239 Fission Cross Section from 40 to 150 eV 36
P. Lambropoulos, T. Hill and C. N. Kelber
I-25. Multilevel Effects on Infinite Dilution Resonance Integrals 38
E. M. Pennington and D. A. Sargis
I-26. Compilation of Neutron Cross Section Data for Natural Helium 40
E. M. Pennington
I-27. Developments Relating to the Evaluated Nuclear Data File/B (ENDF/B) Project .. 41
E. M. Pennington and J. C. Gajniak

SECTION II

THERMAL REACTOR PHYSICS

II-1. Revised Conversion Ratio Results for 3% and 5% Enriched UO_2-Fueled H_2O-Moderated Cores 49
K. E. Plumlee
II-2. Activation Measurements in the Plutonium Recycle Core of the Experimental Boiling Water Reactor (EBWR) 51
K. E. Plumlee, R. E. Grajek and K. E. Freese
II-3. Argonne Advanced Research Reactor Critical Experiments—Summary of Report .. 56
K. E. Plumlee, G. S. Stanford, J. W. Daughtry, W. R. Robinson, T. W. Johnson and R. A. Schultz
II-4. Argonne Advanced Research Reactor Calculations—Preface 57
D. H. Shaftman, A. E. McArthy, R. P. Savio and L. K. Volodka
II-5. Argonne Advanced Research Reactor Calculations—General Reactor Physics Analysis. 58
D. H. Shaftman, R. P. Savio and L. K. Volodka
II-6. Argonne Advanced Research Reactor Calculations—General Shield Design Analysis... 62
D. H. Shaftman and A. E. McArthy
II-7. Argonne Advanced Research Reactor Calculations—Summary Remarks on Interactions of Reactor Core Design and Levels of Thermal Neutron Flux in the Internal Thermal Column 65
D. H. Shaftman

SECTION III

FAST REACTOR PHYSICS

III-1. A 4000-Liter Uranium Oxide Fast Core, Assembly 6 of ZPR-6 75
R. A. Karam, L. R. Dates, W. Y. Kato, J. E. Marshall, T. Nakamura and G. K. Rusch
III-2. ZPR-9 Assemblies 19, 21, 22 and 24 80
L. G. LeSage and W. R. Robinson
III-3. Analysis of Doppler Effect Measurements in CH_2-Softened Spectra, ZPR-9 Assemblies 13–17 87
R. B. Pond and C. E. Till
III-4. Sensitivity of Small-Sample Doppler-Effect Measurements to Environment 96
R. A. Lewis and T. W. Johnson
III-5. Doppler Effect Measurements to 2000°K in ZPR-9 103
J. W. Daughtry, E. F. Groh and C. E. Till

III-6. Application of Statistical Theory and Multilevel Formalism to Doppler Effect Analysis 108
R. N. Hwang
III-7. Variance in the Doppler Coefficient Due to Statistical Selection of Resonance Parameters 109
L. B. Miller and R. N. Hwang
III-8. Monte Carlo Calculation of Multi-Region Hot-Cold Interference Effects 110
R. N. Hwang and L. Miller
III-9. Collision Density in the Doppler Region 113
M. Segev
III-10. Influence of Resonances of Moderating Elements on the Collision Density 116
M. Segev
III-11. Self-Shielding Factors by the Ladder Method 121
M. Segev
III-12. The Variable Temperature Rodded Zone Project 124
R. A. Lewis, F. H. Martens and C. E. Till
III-13. Sodium Void Effects in a Large UO_2 Core, Assembly 6 of ZPR-6 125
R. A. Karam, J. E. Marshall, L. R. Dates and G. K. Rusch
III-14. Gap Worths of Large Critical Assemblies 129
G. K. Rusch
III-15. Heterogeneity Effects in a Large UO_2 Core, Assembly 6 of ZPR-6 133
R. A. Karam, K. D. Dance, L. R. Dates, W. Y. Kato, J. E. Marshall, T. Nakamura and G. K. Rusch
III-16. Heterogeneity Calculations for Plate-Type Heterogeneous Reactors 140
K. Dance, R. A. Karam and J. E. Marshall
III-17. An Investigation of the Properties of Zoned Systems 145
L. G. LeSage, E. F. Groh and W. R. Robinson
III-18. Neutron Spectroscopy in ZPR-6 Assembly Using Proton-Recoil Counters 151
E. F. Bennett and R. A. Karam
III-19. Fine-Spectral Interface Effects of Resonance Scattering Upon Multigroup Cross-Section Averaging 156
D. Meneghetti and K. E. Phillips
III-20. Calculated Spatially-Dependent Fine-Energy Neutron Spectrum for ZPR-3 Assembly 51 164
D. A. Meneghetti and K. E. Phillips
III-21. Analysis of Central Reactivity Worths Incorporating Self-Shielding 165
T. Nakamura, R. A. Karam and K. D. Dance
III-22. Measurement of the Capture-to-Fission Ratio of U-235 and Pu-239 in the Kilovolt Region Using Critical Assembly Null-Reactivity Techniques 169
C. E. Till, L. G. LeSage, G. S. Stanford, E. F. Groh and W. R. Robinson
III-23. Pu-239 and U-235 Capture-to-Fission Ratio Measurements by the Reactivity-Reaction Rate Method in Assembly 24 of ZPR-9 172
M. M. Bretscher and W. C. Redman
III-24. Li-6 as a Reference Absorber for Capture-to-Fission Ratio Measurements in Zero Power Fast Critical Assemblies 178
M. M. Bretscher
III-25. Preliminary Measurements of the Fission Yield of Mo-99 and Ba-140 from Pu-239 in Fast Spectra 182
R. J. Armani, R. Gold, R. P. Larsen and J. H. Roberts
III-26. Reactor Neutron Noise Studies 183
N. Pacilio
III-27. Studies of Reactivity Coefficients in Large Fast Reactors 189
H. H. Hummel and L. K. Volodka
III-28. Fast Reactor Calculations with Consistent Sets for Some Important Neutron Cross Sections 191
J. M. Kallfelz and W. P. Poenitz

III-29. The Effective Delayed Neutron Fraction in Fast Reactors 198
D. A. Meneley
III-30. The Effect of U-238 Resonance Shielding on the Rate of Production of Np-237 from U-236 200
L. B. Miller
III-31. EBR-II Power Coefficient Variations During Operational Run 26 201
P. J. Persiani, J. Kallfelz, F. Kirn, J. K. Long and R. Smith
III-32. Analysis of the Variation in the EBR-II Power Coefficient Due to Blanket Change 203
P. J. Persiani, T. R. Bump, R. A. Cushman, J. Long and D. Kucera
III-33. Further Investigation of the Linear Components of the Power Coefficient of EBR-II 204
R. E. Jarka and J. T. Madell
III-34. EBR-II Control-Rod-Bank Dynamic Reactivity Feedback 208
J. A. Deshong, Jr.
III-35. Analysis and Development of Neutron Cross Sections for EBR-II Studies 209
D. A. Kucera and J. T. Madell
III-36. Analysis of Experimental Subassemblies in EBR-II 214
J. T. Madell and R. E. Jarka
III-37. Investigation of Regional Representations of the Core of EBR-II 217
R. E. Jarka and J. T. Madell
III-38. The Experimental Breeder Reactor II (EBR-II) Shield Design and Performance 219
A. E. McArthy and F. S. Kirn
III-39. Calculational Studies in Support of the Fast Flux Test Facility (FFTF) Critical Experiments on ZPR-3 221
D. Meneghetti, A. J. Ulrich, P. J. Persiani and J. C. Beitel

SECTION IV

FAST REACTOR SAFETY

IV-1. High Power Level Transient Reactor Test (TREAT) Facility Sodium Loop Meltdown Experiment on an Unbonded EBR-II Mark I Fuel Pin 231
C. E. Dickerman, F. L. Willis, R. R. Smith, P. B. Henault, R. Purviance, J. F. Boland, A. Devolpi and R. A. Noland
IV-2. Experiments on "High-Swelling" Fuel of Experimental Breeder Reactor-II (EBR-II) Mark-1A Type 233
A. B. Rothman, C. J. Renken, R. R. Stewart, N. R. Tucker and C. E. Dickerman
IV-3. Digital Photographic Readout System for Fast Neutron Hodoscope in the Transient Reactor Test (TREAT) Facility 240
A. Devolpi, R. Pecina, E. Rolnicki, D. Travis and G. Larsen
IV-4. Apparatus for High Speed Photographic Safety Experiments on Irradiated Fast Reactor Fuel Specimens 245
L. E. Robinson and C. August
IV-5. Standards, Quality Control, Fabrication and Assembly of Mark II Integral Sodium TREAT Loops 255
L. E. Robinson
IV-6. Design of Advanced Shipping Cask for Transient Reactor Test (TREAT) Facility Experiments 260
C. E. Dickerman, A. P. Gavin, R. Robertson, F. L. Willis and J. Cizek
IV-7. Low Level Activity Plutonium Handling Facility for Transient Reactor Test (TREAT) Facility Experimental Apparatus 261
C. E. Dickerman, C. August, N. R. Tucker and W. B. Doe
IV-8. Conversion of the Transient Reactor Test (TREAT) Facility for Testing Fast Reactor Subassemblies 263
H. P. Iskenderian

IV-9. Analytical Studies of Experiments on Transient Sodium Vaporization and Expulsion in Fast Reactor Coolant Channels 267
N. W. Hough, C. E. Dickerman and D. A. Daavettila
IV-10. Modifications of the Transient Heat Transfer Code ARGUS 269
J. P. Regis
IV-11. Sodium Boiling Transients in Carbide-Fueled Fast Reactors 270
D. R. MacFarlane, N. A. McNeal, D. A. Meneley and C. K. Sanathanan
IV-12. Theoretical-Experimental Collaboration on Fast Reactor Sodium Void Safety Problems 276
N. A. McNeal
IV-13. SASIA Computer Code as a Tool for Fast Power Breeder Reactor Safety Analysis 278
J. C. Carter, G. J. Fischer, T. J. Heames, D. R. MacFarlane, N. A. McNeal, P. M. Margel, C. K. Sanathanan, W. T. Sha and C. K. Youngdahl
IV-14. Stability in the Large of Reactor Systems 282
W. T. Sha
IV-15. Maximum Accident of Zoned Fast Reactors 286
W. T. Sha and R. B. Nicholson
IV-16. The Phenomenology of Fast Reactor Accidents 290
J. C. Carter
IV-17. Phenomena Leading to Fuel Casing Rupture During Transients 293
C. K. Sanathanan and J. C. Carter
IV-18. Accelerated Creep in Fuel Cladding 302
J. C. Carter
IV-19. Equation of State Studies 304
D. Miller
IV-20. Calculation of Expansion of Super-Critical Sodium Vapor Released in an Experimental-Loop Accident 306
D. Miller
IV-21. Preliminary Report on the Equation of State of Iron and Steel 308
D. Miller
IV-22. Surface Tension and Critical Points of Alkali Metals 312
D. Miller
IV-23. Fast Reactor Fuel Testing in a Thermal Reactor 313
J. C. Carter
IV-24. Proposal on "Vented" Containment for a Liquid Metal Fast Breeder Reactor (LMFBR) 316
R. O. Brittan
IV-25. Contribution to Formulation of Fuel Failure Propagation Program 323
R. O. Brittan
IV-26. Temperature Sensor Distribution Required for Gas Mass Determination in Leakage Tests 331
R. O. Brittan
IV-27. Coherence Effects in Super-Prompt Critical Excursions 334
C. N. Kelber
IV-28. Design Basis Accident Calculation for ZPR-6 and -9 Plutonium Safety Analysis Report 336
G. K. Rusch

SECTION V

EXPERIMENTAL TECHNIQUES AND FACILITIES

V-1. Basic Measurements Underlying Nuclear Reactor Data 341
A. DeVolpi and K. G. Porges

V-2. Absolute Fission Rate Measurements with Solid-State Track Recorders 342
R. Gold, R. J. Armani and J. H. Roberts
V-3. Fission Rate Measurements in Low Power Fast Critical Assemblies with Solid-State Track Recorders 342
J. H. Roberts, Song-Teh Huang, R. J. Armani and R. Gold
V-4. A Shared Peripheral Computer System 346
J. F. Whalen and C. E. Cohn
V-5. Reliability Improvements for the DDP-24 Computer 347
C. E. Cohn
V-6. Digital-Computer Processing of Sampling-Oscilloscope Data 349
C. E. Cohn
V-7. Time-Optimal Direct Digital Control of Zero Power Nuclear Reactors 353
T. J. Marciniak
V-8. Use of a Small Computer for Proton-Recoil Proportional Counting 358
T. J. Yule and E. F. Bennett
V-9. Evaluation of Photomultipliers for Optimum Noise and Timing Characteristics 360
W. Corwin, K. Porges and R. Gold
V-10. Instrumentation for Processing Nuclear Detector 367
A. DeVolpi, S. Rudnick, R. Daly, J. English and R. Pecina
V-11. Single and Coincidence Counts of Multiply Emitting Sources 371
K. Porges and A. DeVolpi
V-12. Compton Recoil Continuum Measurements for In-Core Gamma-Ray Spectroscopy 373
R. Gold
V-13. Analysis and Reduction of Proton-Recoil Data 377
R. Gold, E. F. Bennett and I. K. Olson
V-14. Automatic Dead-Time Correction in Precision Counting Experiments 378
K. G. Porges and S. J. Rudnick
V-15. Note on the S^2/B Criterion of Quality for Counting Equipment 381
K. G. Porges
V-16. Noise Studies on a Digital Reactor Control System 382
C. E. Cohn
V-17. Problems and Precautions in Spectral-Index Measurements 384
G. S. Stanford
V-18. Time Invariance of the Elementary Charge 385
R. Gold

SECTION VI

REACTOR COMPUTATION METHODS AND THEORY

VI-1. The Argonne Reactor Computation (ARC) System 389
B. J. Toppel and L. Just
VI-2. Accuracy of Factorizing Methods in Spatial Kinetics 391
K. O. Ott, D. A. Meneley and E. S. Wiener
VI-3. Further Developments of the Quasistatic Neutron Kinetics Model 398
D. A. Meneley, K. O. Ott and E. S. Wiener
VI-4. Variational Flux Synthesis With Discontinuous Trial Functions 400
V. Luco and G. K. Leaf
VI-5. A New Formulation of Multigroup Microscopic Cross Sections 413
A. Travelli
VI-6. Ultrafine Adjoint Neutron Fluxes in Fast Breeder Reactors 421
A. Travelli and J. D. Eckard
VI-7. A Modification of the Bell Approximation for Slab Geometries 424
A. Travelli

VI-8. Multigroup Transport Analysis of Neutron Wave Propagation in Fast Multiplying Media 426
A. Travelli
VI-9. Extension of Monte Carlo Methods of Reactor Analysis 432
L. B. Miller
VI-10. Comparison of Reaction Rates in Uniform and Non-Uniform Lattices 433
L. B. Miller
VI-11. An Equivalence Theory Capture Cross Section Code for Plate-Type Cells 434
K. D. Dance
VI-12. Use of Group-Space-Dependent Bucklings to Simulate a Transformation of the Coordinate System in Neutron Diffusion Calculations 435
A. J. Ulrich
VI-13. Efficient Programming in FORTRAN 438
C. E. Cohn
VI-14. Error Analysis of Linked Difference Equations 439
N. F. Morehouse and J. C. Carter

SECTION VII

PUBLICATIONS, REACTOR PHYSICS DIVISION

(July 1, 1967 to June 30, 1968)

Open Literature 443
Reports 444
Abstracts 444

Section I

Fisson Properties and Cross Section Data

In close support of the reactor program, experimental and theoretical studies of neutron interactions with those nuclei found in the structural and fuel components of reactor systems continue to be carried out. This work is performed principally to provide information necessary for optimal reactor physics design. The major portion of the effort is devoted to studies of fast neutron induced processes, especially those which are important in fast reactors. The studies are directed toward neutron elastic and inelastic scattering, neutron induced reactions including capture, and to characteristics of the fission processes.

I-1. Introduction

A. B. Smith

The experimental and theoretical program of microscopic neutron cross section studies has the objective of providing knowledge of nuclear data and properties to meet the present needs of the reactor development program and of establishing the broad understanding of neutron processes requisite to the long range success of the applied nuclear energy effort. The work is inclusive of studies of: a) fast neutron scattering, capture, fission, and total cross sections; b) properties of the fission process; c) requisite instrument development; d) neutron activation of applied interest; e) compilation and evaluation of neutron data; and f) the theory of nuclear reactions. Examples of accomplishment in each of these areas are cited in this report. They should not be construed as comprehensive or inclusive but are illustrative of the varied facets of the endeavor.

I-2. Polarization in the Elastic Scattering of Neutrons from Intermediate Weight Nuclei

S. A. Cox and E. E. Dowling Whiting

A systematic study of polarization produced by the elastic scattering of low energy neutrons from nuclei of intermediate weight has been in progress for the past year. One of the objectives of the program is to supply accurate polarization data for a large number of nuclei from vanadium to uranium. In this way it is hoped that systematic trends which are amenable to theoretical interpretation will be established. A second program objective is to use the polarization measurements as an additional constraint on the possible choice of optical model parameters which give a good fit to the differential scattering data.

A schematic diagram of the experimental facility is shown in Fig. I-2-1. Additional details are given in Ref. 1. Partially polarized neutrons emitted at 51 deg from the Li(p,n) reaction traverse a solenoid magnet which is capable of precessing the neutron spin 180 deg. Data taken with the solenoid field alternately on and off corresponds to the usual left-right asymmetry measurement. The collimated neutron beam is scattered by a 1 in. high by 1 in. diam. scattering sample. The scattered neutrons are detected simultaneously by a set of four neutron detectors. Pulse-shape discrimination techniques are used for γ-ray rejection. The set of four detectors can be placed in either of two angular orientations by operation of the air cylinder depicted in the figure. In the forward position, the detectors are at the nominal angles 20, 60, 100, and 140 deg. In the backward position, the detector angles are 35, 75, 115, and 155 deg. All data were corrected for effects due to angular resolution, flux attenuation, and multiple scattering. Cross section measurements were made relative to the 20 and 35 deg scattering cross sections of carbon as reported by R. Lane et al.[2] It should be noted that the measured polarization in each case is equal to the product of $P1$, the polarization of neutrons from the $Li^7(p,n)$ reaction, and $P2$, the analyzing power of the scattering sample. In order to calculate $P2$ it was necessary to know $P1$, and this was obtained by interpolation between the results of A. Elwyn and R. Lane[3] at $E_n \approx 500$ keV and that of R. Walter[4] at 1 MeV for the polarization of neutrons emitted at 51 deg from the $Li^7(p,n)$ reaction.

As pointed out some time ago by R. Lane,[5] a correction to the polarization data is also necessary at the forward angles because of distortion of the polarization due to Schwinger scattering.[6] The effect of interference between Schwinger and nuclear scattering is to make the measured polarization at angles near zero degrees more negative than that which would result from nuclear scattering alone. We have corrected our data at 20 and 35 deg, using a method developed by A. Elwyn and J. Monahan.[7]

The twelve elements reported here were chosen to provide more complete information on the behavior

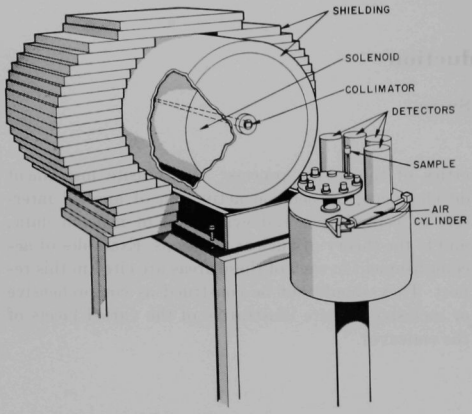

FIG. I-2-1. Diagram of Experimental Arrangement for Polarization Measurements. *ANL Neg. No. 112-8411 Rev. 1.*

of the polarization from $A \sim 50$ to 120.[8] The data were averaged over a 200 keV interval with an average neutron energy of about 870 keV. The theoretical fits to the data were made with ABACUS II.[9] Five parameters were varied: the depths of the real, imaginary, and spin-orbit potential wells, and the radii $R1$ and $R2$ of the real and imaginary wells, respectively. For most of the calculations the radius of the spin-orbit potential was set equal to that of the real potential. In a few cases, the spin-orbit radius, $RR1$, was varied independently of $R1$, and for these cases the best results were obtained for values of $RR1$ smaller than $R1$. A Saxon-Woods real potential, a pure surface imaginary potential, and a Thomas spin-orbit potential were used in all calculations. Final parameters chosen for the twelve elements are listed in Table I-2-I.

During the optical model parameter scans it was observed that while the amplitude of the polarization depended upon the depth of the spin-orbit potential, the shape of the polarization angular distribution was much more sensitive to changes in the real and imaginary potentials. Therefore, as these parameters were varied to change the shapes of the differential cross sections, they also produced wide variations in the polarizations, and this has been a valuable aid in removing some of the ambiguities of the optical

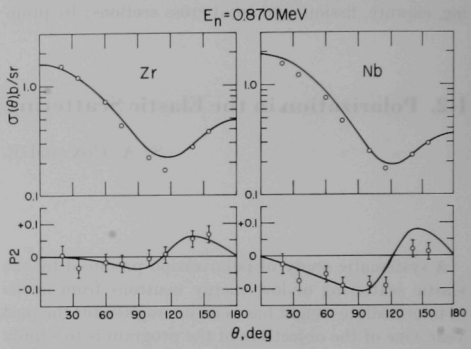

FIG. I-2-2. Optical Model Fit to Differential Scattering Cross Section and Polarization Data for Zr and Nb. The Solid Curves are Calculated from the Parameters Given in Table I-2-I. *ANL Neg. No. 112-9947 Rev. 1.*

TABLE I-2-I. PARAMETERS FOUND FROM OPTICAL MODEL FIT

(Additional parameters used for all cases: $A_1 = 0.62$ F; $A_2 = 0.50$ F; $C_1 = 15$ F; VSI = 0)

Element	A	Energy, MeV	VR, MeV	VI, MeV	VSO, MeV	F			
						R_1	R_2	$R_2 - R_1$	R_{R1}
Ti	48	0.900	34.75	12.0	6.0	4.615	4.865	0.25	—
Ti[a]		0.870	50.0	20.0	14.0	4.615	4.615	0	—
Fe	56	0.870	43.0	12.0	6.0	4.738	4.938	0.20	—
Fe[a]		0.867	50.0	16.0	6.0	4.638	4.838	0.20	—
Ni	58	0.800	46.0	18.0	6.0	4.790	4.790	0	—
Cu	63	0.800	44.0	18.0	6.0	5.015	5.115	0.10	—
Se	80	0.800	51.4	17.0	2.0	5.400	5.400	0	3.800
Y	89	0.800	49.3	14.0	4.0	5.620	5.620	0	—
Zr	90	0.870	51.0	8.0	4.0	5.500	5.900	0.40	—
Nb	93	0.870	51.0	12.0	4.0	5.656	5.656	0	—
Mo	96	0.800	52.0	16.0	6.0	5.835	5.835	0	—
Cd	112	0.870	47.0	10.0	4.0	6.091	6.091	0	—
Sn	120	0.800	46.0	10.0	6.0	6.320	6.320	0	—
Sb	123	0.870	48.0	8.0	5.0	6.300	6.800	0.50	5.300

[a] For these elements the parameter set was obtained by first demanding a fit to the polarization data. In all other cases, the differential scattering cross section was fitted first.

model. It often happens in practice that two or more sets of parameters can be found which give good fits to the cross section for a particular element, but that the corresponding curves for the polarization angular distributions are quite different from one another. By demanding a simultaneous fit to both the cross section and the polarization, then, it is often possible to determine the parameters uniquely.

Figure I-2-2 shows our results for zirconium and niobium. The differential scattering cross sections of elastically scattered neutrons are at the top of the figure and the polarization angular distributions are at the bottom. The error bars for *P2* represent estimates of systematic errors. Counting statistical errors are much smaller. The maximum polarization measured is approximately 10% and the errors assigned to the data points are only 2.5%. It is just because of the small magnitude of the polarization that the correction for Schwinger scattering is significant at the first two angles. For zirconium for example, the data point at 20 deg has been corrected upward by a value of 0.03 which is half the maximum polarization for that element. At angles greater than 45 deg the correction is

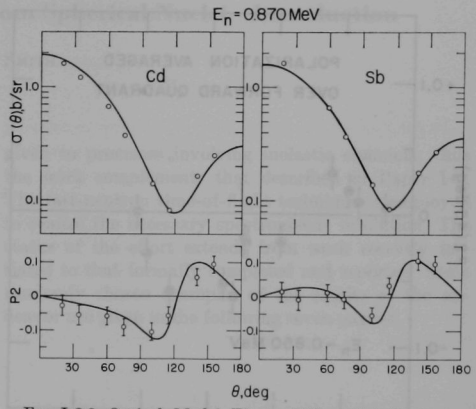

FIG. I-2-3. Optical Model Fit to Differential Scattering Cross Section and Polarization Data for Cd and Sb. The Curves are Calculated from the Parameters Given in Table I-2-I. The significance of the Solid and Dashed Curves is Explained in the Text. *ANL Neg. No. 112-9946.*

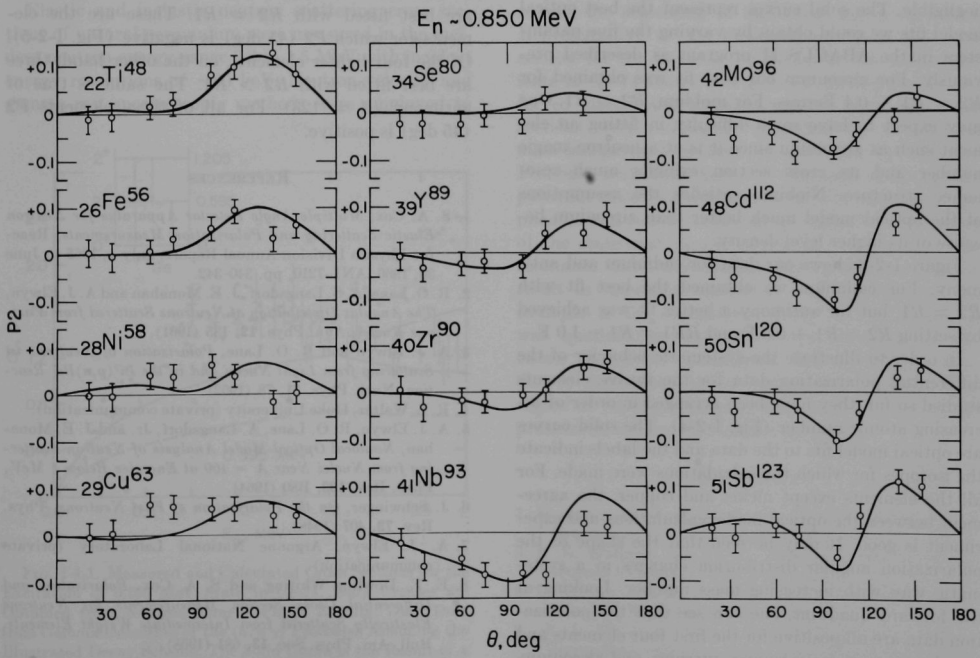

FIG. I-2-4. Comparison Between Optical Model Calculations are Polarization Data for all Elements Studied. The Solid Curves are the Polarization Calculations Corresponding to the Best Fit to the Differential Scattering Cross Section. *ANL Neg. No. 112-9949 Rev. 1.*

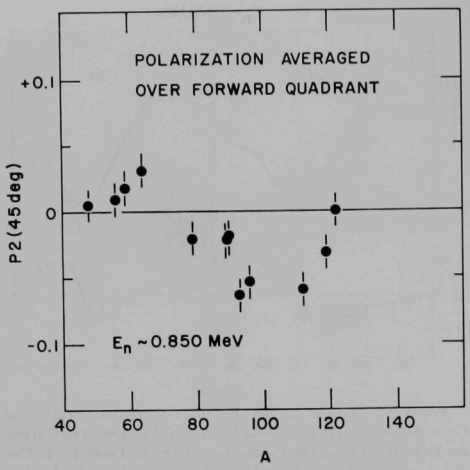

FIG. I-2-5. Dependence on Mass Number for Polarization Data Averaged Over Forward Quadrant. *ANL Neg. No. 112-9950 Rev. 1.*

negligible. The solid curves represent the best optical model fits we could obtain by varying the five parameters in the ABACUS II program as described previously. For zirconium our best fit was obtained for $R2 = R1 + 0.4$ Fermis. For niobium, $R2 = R1$. One may expect to have some difficulty in fitting an element such as zirconium since it is at a neutron magic number and its cross section exhibits much resonance structure. Niobium satisfies the assumptions of the optical model much better than zirconium because of its higher level density.

Figure I-2-3 shows our data for cadmium and antimony. For cadmium we obtained the best fit with $R2 = R1$, but for antimony a better fit was achieved by setting $R2 = R1 + 0.5$ F and $RR1 = R1 - 1.0$ F.

In order to illustrate the systematic behavior of the differential polarization data for the twelve elements studied so far, they have been arranged in order of increasing atomic number (Fig. I-2-4). The solid curves are optical model fits to the data and the labels indicate the isotopes for which the calculations were made. For all the elements except nickel and copper, the agreement between the optical model calculations and experiment is good. It may be seen that the shape of the polarization angular distribution changes in a systematic way with increasing mass number. Looking at the forward quadrant, one can see that the polarization data are all positive for the first four elements and are close to zero for selenium, yttrium, and zirconium. Then, in the region from niobium to tin, the polarization is negative, and the negative portions of the curves are becoming more sharply peaked. For the last element, antimony, the polarization in the forward quadrant is again positive, but there is still a strong negative peak at 100 deg.

To better illustrate this point the data have been averaged for the first four angles for each element and plotted against mass number. The results are given in Fig. I-2-5. The polarization at an average angle of ~45 deg is positive for low mass numbers and becomes negative in the vicinity of the P-wave strength function maximum at $A \sim 90$. It should also be mentioned that four of the elements shown in Fig. I-2-5 have odd Z, but no odd-even Z effect is observed.

In conclusion, we can now make one generalization concerning our data for these twelve elements in relation to the "fringe absorption model." In this model the radius ($R2$) of the surface imaginary potential is set equal to 0.5 F greater than the radius ($R1$) of the real potential. We found that while we could usually obtain a good fit to the differential cross section with this model, the polarization data were often not fitted very well. With the single exception of zirconium, all of the elements from selenium ($A = 80$) to tin ($A = 120$) are best fitted with $R2 = R1$. These are the elements for which $P2$ (45 deg) is negative (Fig. I-2-5). Of the four lighter elements, on the other hand, three are best fitted with $R2 > R1$. The same is true of antimony ($A = 123$). For all of these elements $P2$ (45 deg) is positive.

REFERENCES

1. S. A. Cox, *Multiple Angle Detector Apparatus for Neutron Elastic Scattering and Polarization Measurements*, Reactor Physics Division Annual Report, July 1, 1965 to June 30, 1966, ANL-7210, pp. 340–342.
2. R. O. Lane, A. S. Langsdorf, J. E. Monahan and A. J. Elwyn, *The Angular Distribution of Neutrons Scattered from Various Nuclei*, Ann. Phys. **12**, 135 (1961).
3. A. J. Elwyn and R. O. Lane, *Polarization of Neutrons in Scattering from Light Nuclei and in the $Li^7(p,n)Be^7$ Reaction*, Nucl. Phys. **31**, 78 (1962).
4. R. L. Walter, Duke University (private communication).
5. A. J. Elwyn, R. O. Lane, A. Langsdorf, Jr. and J. E. Monahan, *Nonlocal Optical-Model Analysis of Neutron Scattering from Nuclei Near A = 100 at Energies Below 1 MeV*, Phys. Rev. **133**, B80 (1964).
6. J. Schwinger, *On the Polarization of Fast Neutrons*, Phys. Rev. **73**, 407 (1948).
7. A. J. Elwyn, Argonne National Laboratory (private communication).
8. E. E. Dowling Whiting and S. A. Cox, *Polarization and Differential Cross Section Measurements for Neutrons Elastically Scattered from Intermediate Weight Elements*, Bull. Am. Phys. Soc. **13**, 681 (1968).
9. E. H. Auerbach, *ABACUS II (Revised Version). Program Operation and Input Description.* (Preliminary Edition, 1962); BNL-6562, (to be published).

I-3. Elastic and Inelastic Scattering from Spherical Nuclei—Introduction

A. B. Smith

A continuing program of experimental studies of elastic and inelastic neutron scattering from spherical nuclei was pursued throughout the past year. The work is undertaken in direct response to Atomic Energy Commission requests for nuclear data and in an effort to establish an understanding of the neutron scattering process. The measurements extend from the very light nuclei to the heavy masses near the doubly closed shell at $A = 208$. Primary attention is given to processes involving inelastic channels; thus the work complements that described in Paper I-2. The fast-neutron time-of-flight technique is employed to realize the necessary spectrometric resolution. The status of the effort extends from work recently initiated to that formally completed and reported. Some randomly chosen examples of the results of the endeavor are given in the following seven papers.

I-4. Elastic and Inelastic Scattering From Spherical Nuclei—Germanium

D. Lister and A. B. Smith

Elastic and inelastic neutron scattering cross sections of natural germanium were measured in the incident neutron energy range 0.3 to 1.5 MeV with incident energy resolutions of ~20 keV. Neutron-velocity and gamma-ray spectroscopic methods were employed to resolve the scattering to individual low-lying states. Representative of the measured results is the cross section for the inelastic excitation of the 0.595 MeV state in Ge-74 shown in Fig. I-4-1. Generally, the observed elastic and inelastic neutron scattering cross sections were reasonably described by a spherical mass-independent optical potential and the Hauser-Feshbach statistical theory.[2, 3] The form of the optical potential employed was consistent with that found applicable in a similar mass-energy region.[4] Modification of the statistical theory to provide "corrections" for resonance width fluctuations and correlations did not result in improved agreement with experiment.[5] An example is the comparison shown in the figure. It was qualitatively suggested that discrepancies between "corrected" calculation and experiment were due to deficiencies in the model and potential in a region of rapidly changing shell structure and in the presence of strong vibrational excitations.

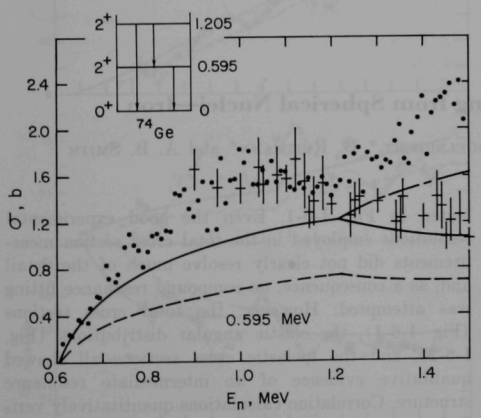

Fig. I-4-1. Measured and Calculated Cross Sections for the Excitation of 0.595 MeV State in Ge-74. Data Crosses are Obtained from Neutron Time-of-Flight Results, Data Dots from Gamma Detection of the $(n:n'\gamma)$ Processes Assuming the Illustrated Decay Scheme. The Solid Curve is the Result of a Statistical Model Calculation While the Dashed Curve Represents a Calculation Inclusive of Width Fluctuation Corrections. *ANL Neg. No. 113-478.*

References

1. D. Lister and A. B. Smith, *Fast Neutron Scattering from Germanium*, to be submitted to Phys. Rev.
2. P. E. Hodgson, *The Optical Model of Elastic Scattering*, (Oxford University Press, London 1963).
3. W. Hauser and H. Feshbach, *The Inelastic Scattering of Neutrons*, Phys. Rev. **87**, 366 (1952).
4. P. A. Moldauer, *Optical Model of Low Energy Neutron Interactions with Spherical Nuclei*, Nucl. Phys. **47**, 65 (1963).
5. P. A. Moldauer, *Average Compound-Nucleus Cross Sections*, Rev. Mod. Phys. **36**, 1079 (1964).

I-5. Elastic and Inelastic Scattering from Spherical Nuclei—Titanium

A. B. Smith, J. Whalen and P. Guenther

Experimental study of elastic neutron scattering from titanium has been completed for incident energies of 0.3 to 1.5 MeV with experimental resolutions of ~20 keV. Complementary total cross section measurements have been made from 0.1 to 1.0 MeV (resolution $\lesssim$1 keV) and inelastic scattering results have been obtained. Representative measured values are shown in Fig. I-5-1. The total cross section and inelastic measurements are being extended to a maximum energy of 1.5 MeV. The interpretation of the data is being pursued in the framework of the "intermediate" optical model (see Paper I-10) and by detailed fitting of the compound nucleus resonances. The latter procedure should result in resonance parameters at incident energies below about 500 keV. Concurrently, the results are being compared with the contents of the evaluated nuclear data file, ENDF-B, in an effort to improve the basic quantities employed in the physical design of reactors.

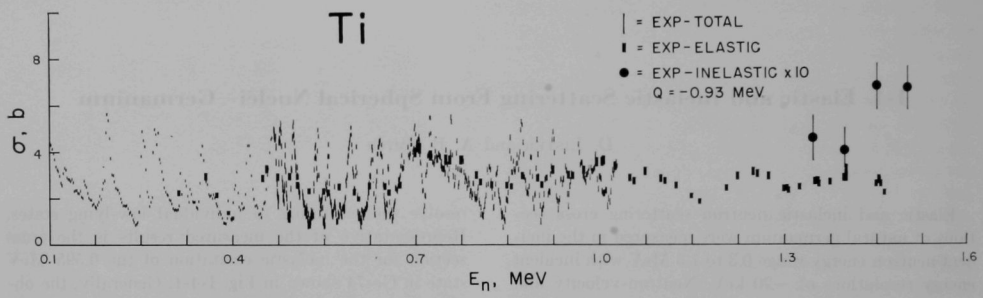

Fig. I-5-1. Observed Total Cross Sections and Elastic and Inelastic Scattering Cross Sections of Natural Titanium. *ANL Neg. No. 113-947.*

I-6. Elastic and Inelastic Scattering from Spherical Nuclei—Iron

E. Barnard,* J. A. M. De Villiers,* C. A. Engelbrecht,* D. Reitmann* and A. B. Smith

The experimental study of total neutron cross sections and of elastic and inelastic neutron scattering cross sections of natural iron has been completed and a formal journal report accepted for publication.[1] The total cross sections were determined from 0.1 to 1.5 MeV with resolutions ranging from 2.5 to less than 1 keV. Elastic scattering cross sections were measured with resolutions of ~20 keV from 0.3 to 1.5 MeV. The inelastic excitation of the 850 keV state was directly determined with resolutions of $\gtrsim$ 5 keV. All of the experimental results indicated a great deal of compound nuclear resonance structure of the type illustrated in Fig. I-6-1. Even the good experimental resolutions employed in the total cross section measurements did not clearly resolve much of the detail and, as a consequence, no compound resonance fitting was attempted. However, the total cross sections (Fig. I-6-1), the elastic angular distributions (Fig. I-6-2), and the inelastic cross sections all showed qualitative evidence of an intermediate resonance structure. Correlation calculations quantitatively verified this evidence but indicated no correlation between differing exit channels, i.e., elastic-inelastic. The observed intermediate structure has been interpreted by J. Monahan and A. Elwyn[2] in terms of "doorway state resonances."

Particularly, the measured elastic and inelastic scattering values were examined in the context of the

* Atomic Energy Board, Pelindaba, Transvaal, Republic of South Africa. This work was performed as a joint research effort by staff members of Argonne National Laboratory and Pelindaba Laboratory.

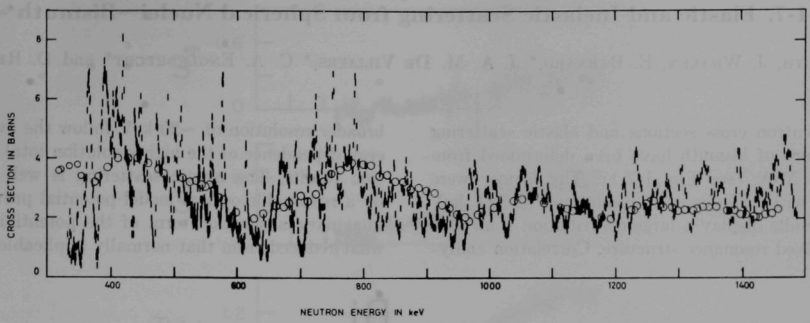

FIG. I-6-1. High-resolution Total Cross Sections (bars) Compared with Broad-resolution Elastic Scattering Cross Sections (circles). *ANL Neg. No. 113-1483.*

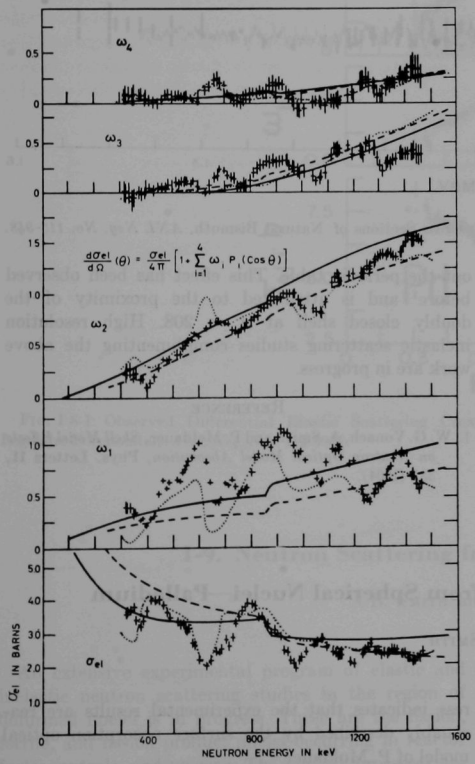

FIG. I-6-2. Differential Elastic Scattering Cross Sections of Fe. Average Incident Energy Resolution is 50 keV. The Dashed Curves Represent HF Calculations Using V_c = 46 MeV, W_c = 14 MeV, While the Solid Lines Were Calculated Using V_c = 41 MeV, W_c = 12 MeV. The Dotted Lines are Based on Continuously Varying Values of V_c and W_c. *ANL Neg. No. 113-1484.*

optical model[3] and statistical theory.[4] Consideration was given to the detailed variation of the optical potential with energy as derived from a fitting to the measured elastic scattering data and to the effect of resonance width fluctuations and correlations.[5] Some of these calculated results are compared with experiment in Fig. I-6-2. Generally, it was found necessary to rapidly vary both the real and imaginary portions of the optical potential in order to obtain a reasonable fit to the basic experimental results. Such variation is consistent with "doorway" state concepts.[6] The average energy dependence ($\Delta E \sim 100$ keV) was rather well described by a more conventional local and energy independent optical potential inclusive of reaction cross sections corrected for fluctuation effects. The latter corrections were particularly important in obtaining agreement with measured inelastic scattering values.

A comparison of the measured results with the pertinent portions of the Evaluated Nuclear Data File-B (ENDF-B) indicated that the latter failed to describe much of the detailed resonance structure, but rather tended to provide a smooth averaging characteristic of the intermediate resonances.

REFERENCES

1. E. Barnard, J. A. M. De Villiers, C. A. Engelbrecht, D. Reitmann and A. B. Smith, *Fast Neutron Cross Sections of Fe*, Nucl. Phys. (to be published).
2. J. Monahan and A. Elwyn, *Relation Between Fine and Intermediate Structures in the Scattering of Neutrons by Fe*, Phys. Rev. Letters **20**, 1119 (1968).
3. P. Hodgson, *Optical Model of Elastic Scattering* (Oxford Press, London, 1960).
4. W. Hauser and H. Feshbach, *The Inelastic Scattering of Neutrons*, Phys. Rev., **87**, 366 (1952).
5. P. Moldauer, *Average Compound-Nucleus Cross Sections*, Rev. Mod. Phys. **36**, 1079 (1964).
6. H. Feshbach, et al., *Intermediate Structure and Doorway States in Nuclear Reactions*, Annals Phys. **41**, 230 (1967).

I-7. Elastic and Inelastic Scattering from Spherical Nuclei—Bismuth*

A. B. Smith, J. Whalen, E. Barnard,* J. A. M. De Villiers,* C. A. Englebrecht* and D. Reitmann*

Total neutron cross sections and elastic scattering cross sections of bismuth have been determined from 0.2 to 1.5 MeV (see Fig. I-7-1). The former were measured with experimental resolutions of $\gtrsim 1$ keV and the results display a large contribution from partially resolved resonance structure. Correlation analysis indicates that this structure is consistent with that expected from known distributions of compound nucleus resonance widths and spacings. There was no clear indication of any intermediate resonance structure. The elastic scattering results obtained with a broader resolution of ~20 keV follow the average energy dependence of the high-resolution total cross section results. The elastic scattering is well described by a reasonable optical model potential providing the imaginary absorption term of the potential is somewhat reduced from that normally applicable throughout the periodic table. This effect has been observed before[1] and is attributed to the proximity of the doubly closed shell at $A = 208$. High resolution inelastic scattering studies complimenting the above work are in progress.

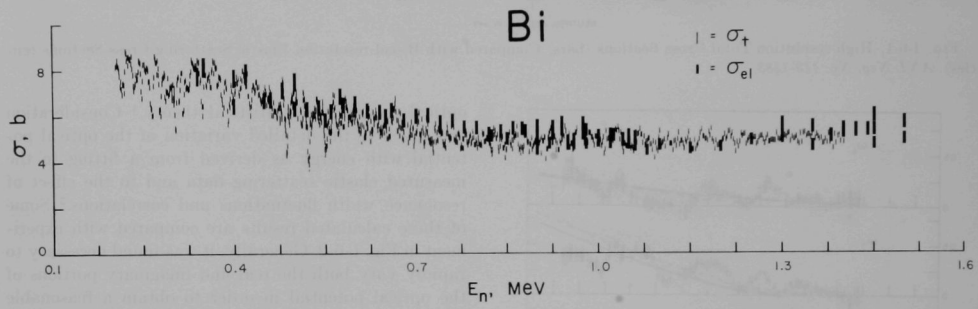

Fig. I-7-1. Observed Total (bars) and Elastic Scattering (boxes) Cross Sections of Natural Bismuth. *ANL Neg. No. 113-948.*

* Atomic Energy Board, Pelindaba, Transvaal, Republic of South Africa. This work was performed as a joint research effort by staff members of Argonne National Laboratory and Pelindaba Laboratory.

Reference

1. W. G. Vonach, A. Smith and P. Moldauer, *Shell Model Effects on Neutron Optical Model Absorption*, Phys. Letters **11**, 331 (1964).

I-8. Elastic and Inelastic Scattering from Spherical Nuclei—Palladium

A. B. Smith

Representative of the study of the scattering from nuclei in the region of $A \approx 100$ is the measurement of elastic and inelastic neutron scattering from palladium. The differential elastic scattering results are indicated in Fig. I-8-1 and are complemented by determinations of inelastic excitation cross sections and total neutron cross sections. Analysis now in progress indicates that the experimental results are reasonably described by the surface absorption optical model of P. Moldauer.[1]

Reference

1. P. A. Moldauer, *Optical Model of Low Energy Neutron Interactions with Spherical Nuclei*, Nucl. Phys. **47**, 65 (1963).

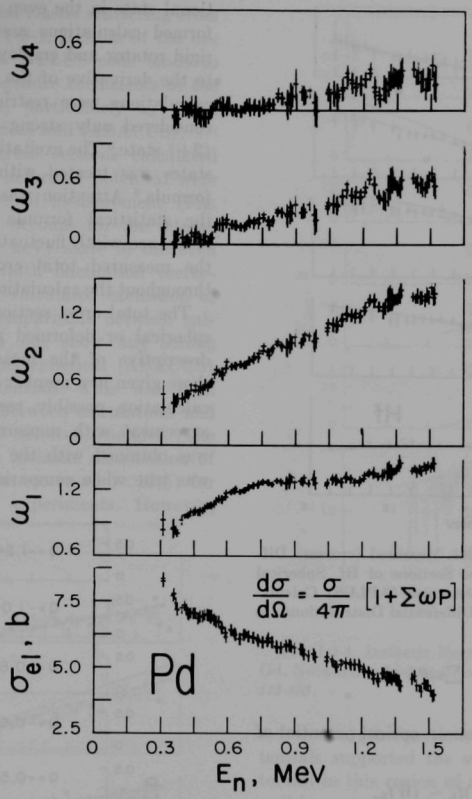

FIG. I-8-1. Observed Differential Elastic Scattering Cross Sections of Pd Expressed in the Form of an Expansion of Legendre Polynomials. *ANL Neg. No.* 112-*9095*.

I-9. Neutron Scattering from Heavy Deformed Nuclei

A.B. SMITH and G. SHERWOOD*

An extensive experimental program of elastic and inelastic neutron scattering studies in the region of deformed nuclei is in progress. These are the fission, fertile, and fission product nuclei occurring in reactor fuels, controls, and poisons. The nuclear processes are of physical interest since direct excitation of collective nuclear configurations has an appreciable effect on neutron cross sections, even at relatively low incident neutron energies. Studies of fast neutron scattering from hafnium, gadolinium, and samarium have been completed over the energy range 0.3 to 1.5 MeV. The results are illustrated in the following paragraphs.

HAFNIUM

The measured differential elastic scattering cross sections are summarized in Fig. I-9-1. These results have been extensively compared with theoretical cal-

* Student, Northwestern University, Evanston, Illinois.

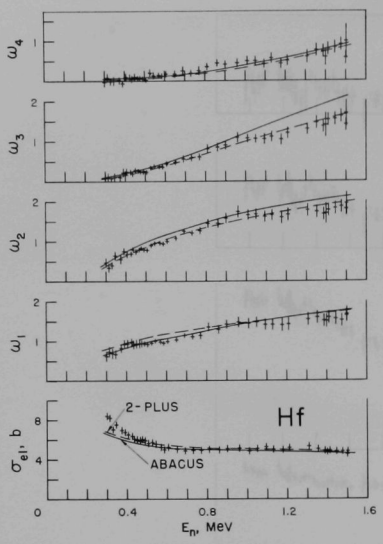

FIG. I-9-1. *ANL Neg. No. 113-801.* Measured (crosses) Differential Elastic Scattering Cross Sections of Hf. Spherical Optical Model (ABACUS) and Deformed (2-PLUS) Calculations are Indicated with Curves. Differential Distributions are Expressed in the Form

$$\frac{d\sigma}{d\Omega} = \frac{\sigma}{4\pi}[1 + \sum \omega_i P_i].$$

culations[1] which were based on an optical potential of the form

$$V_c = (V + iU)f_1 - iWf_2,$$

where

$$V = V_0 - 0.25E \text{ (MeV)}$$

$$W = W_0 - 0.2E \text{ (MeV)}$$

$$U = 0.125E - 0.0004E^2.$$

The well-shape of f_1 of the Saxon-Wood form with a mean radius R_1 and a diffuseness a_1 was assumed. The absorption, f_2, was assumed to have a Gaussian form with mean radius R_2 and width a_2. The cross sections for elastic scattering were calculated from this spherical potential using the NEARREX-ABACUS computational program.[2] These spherically symmetric calculations did not take cognizance of the direct excitation of the collective rotational states of the deformed nucleus.[3] A second, and more physically proper, set of calculations, employing 2-PLUS,[(4)] was carried out using a deformed potential and considering direct excitation of the first excited (2+) rotational state in the even isotopes of hafnium. The deformed calculations assumed that the nucleus is a rigid rotator and employed a direct well proportional to the derivative of the real potential. The deformed calculations were restricted to the even nuclei and considered only strong coupling to the first-excited (2+) state.[5] The excitation of other and higher energy states was treated with the conventional statistical formula.[6] Attention was also given to corrections to the statistical formula involving considerations of resonance width fluctuations.[7] A good agreement with the measured total cross section[8] was maintained throughout the calculations.

The total cross sections calculated from either the spherical or deformed potential were quantitatively descriptive of the measured values and similar to those given in a number of evaluations.[9] The spherical calculation possibly resulted in a somewhat better agreement with measured total cross sections than was obtained with the deformed well. The converse was true when comparison was made between calcu-

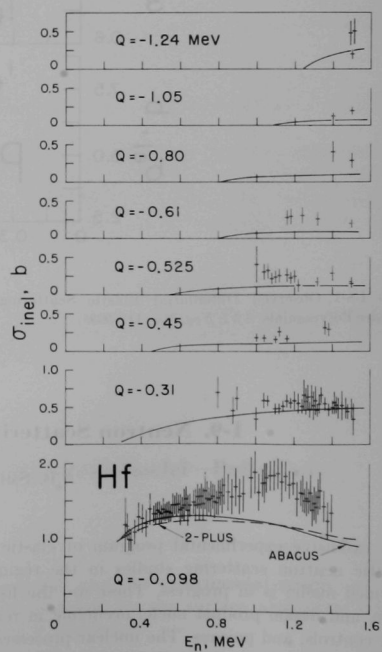

FIG. I-9-2. Inelastic Scattering Excitation Cross Sections of Hf. Measurements are Indicated by Crosses, Calculations by Curves. Observed Reaction Q Values are Indicated in MeV. *ANL Neg. No. 133-819 Rev. 1.*

lated and measured differential elastic scattering cross sections as indicated in Fig. I-9-1. Results of the deformed calculation using the 2-PLUS code tends to better describe the higher Legendre coefficients of the elastic angular distributions, particularly ω_3, than those obtained from the spherical well (ABACUS).

The inelastic excitation cross sections calculated with either the spherical or deformed potential were only qualitatively descriptive of measurement (Fig. I-9-2), both failing to fully account for the intense excitation of the 2+ (~100 keV) state in the even isotopes. Consideration of width fluctuation corrections led to an even smaller calculated excitation of the 2+ state. The above comparisons between calculation and experiment do not show any strong perference for the use of either spherical (ABACUS) or deformed (2-PLUS) potentials. This was born out by detailed comparisons between calculations and experiment at a number of selected energies. The calculated asymmetry of the inelastic distribution of the 2+ state about 90 deg was too small (<10%) for observation in the present experiments. However,

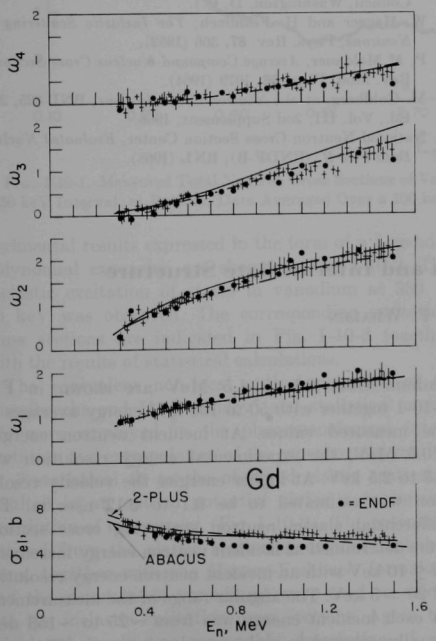

Fig. I-9-3. Differential Elastic Scattering Cross Sections of Gd. The Format and Notation is the Same as that of Fig. I-9-1 With the Addition of the Respective Evaluated Quantities Given in ENDF-B[9]. *ANL Neg. No. 113-851.*

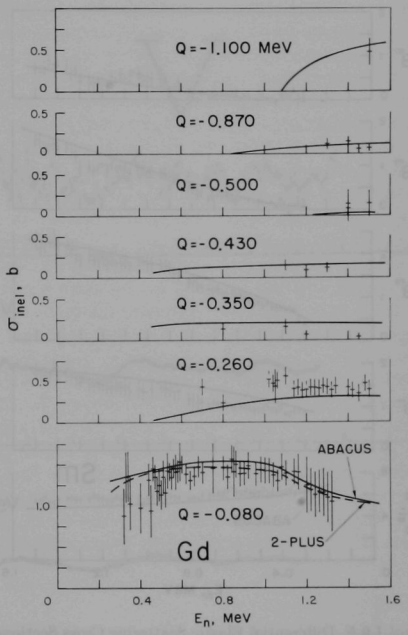

Fig. I-9-4. Inelastic Neutron Scattering Cross Sections of Gd. Notation is Identical to that of Fig. I-9-2. *ANL Neg. No. 113-853.*

$\ell = 0$ strength functions calculated with the two potentials supported the validity of the deformed potential in this region of strong deformation. This is a well known effect of the deformation, causing a splitting of the single strength function maximum at $A \sim 160$ into a doublet. Unfortunately, the available experimental strength functions in the region vary appreciably, and quantitative comparison between experiment and calculation is difficult.

Generally, the results of the hafnium studies fulfill the reactor needs for scattering data to incident energies of 1.5 MeV. They are consistent with a physical interpretation based upon a deformed optical potential and statistical theory. However, the latter potential did not give good detailed and quantitative agreement with measured inelastic scattering cross sections, and thus the use of the potential for precise extrapolation of measured values is questionable.

Gadolinium and Samarium

The measurements and calculations outlined above for the element hafnium were extended to the elements gadolinium and samarium with representative results

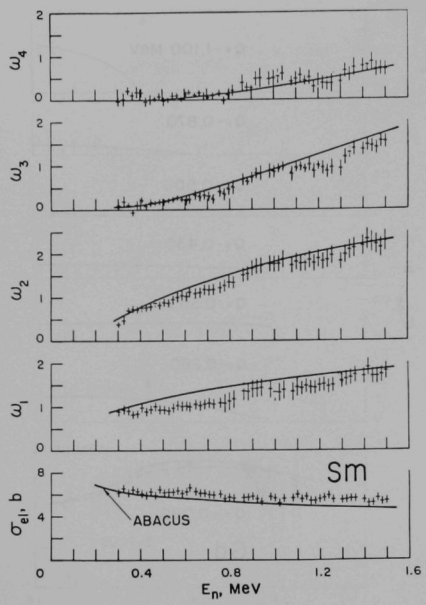

FIG. I-9-5. Differential Elastic Scattering Cross Sections of Sm. The Format is the Same as that of Fig. I-9-1. *ANL Neg. No. 113-1531.*

shown in Figs. I-9-3 through I-9-5. As for hafnium, the measured results well-defined the differential elastic and inelastic scattering cross sections of gadolinium and samarium for incident neutron energies of 0.3 to 1.5 MeV. These experimental values were reasonably described by calculations of the same type employed in the study of hafnium. As was true for the case of hafnium, the deformed-well calculation tends to give a slightly better agreement with experiment than one based on the spherical potential.

References

1. P. Hodgson, *Optical Model of Elastic Scattering*, (Oxford Press, London, 1960).
2. P. Moldauer, C. A. Engelbrecht and G. J. Duffy, *NEARREX, A Computer Code for Nuclear Reaction Calculations*, ANL-6978; also, E. Auerbach, *Program Operation and Input Description*, BNL-6562.
3. B. Mottelson and S. Nilsson, *The Intrinsic States of Odd-A Nuclei Having Ellipsoidal Equilibrium Shape*, Kgl. Danske Videnskab. Selskab, Mat. Fys, Skrifter **1**, No. 8 (1959).
4. C. L. Dunford, 2 *PLUS*, NAA-SR-11706 (unpublished) (1966).
5. Nuclear Data Sheets, (U. S. Government Printing Office, National Academy of Sciences, National Research Council, Washington, D. C.).
6. W. Hauser and H. Feshbach, *The Inelastic Scattering of Neutrons*, Phys. Rev. **87**, 366 (1952).
7. P. A. Moldauer, *Average Compound-Nucleus Cross Sections*, Rev. Mod. Phys. **36**, 1079 (1964).
8. M. Goldberg, et al., *Neutron Cross Sections*, BNL-325, 2nd Ed., Vol. III, 2nd Supplement, 1966.
9. National Neutron Cross Section Center, *Evaluated Nuclear Data File-B*, (ENDF-B), BNL (1968).

I-10. Fast Neutron Processes in Vanadium and Intermediate Structure

A. B. SMITH and J. F. WHALEN

Total neutron cross sections and elastic and inelastic neutron scattering cross sections have been experimentally studied. Total neutron cross sections were determined with good resolution from 0.1 to 1.5 MeV. Differential elastic and inelastic scattering angular distributions were measured at incident neutron energies from 0.3 to 1.5 MeV. The experimental results have been interpreted in terms of the optical model and statistical concepts inclusive of resonance width fluctuations and correlations.[1-3] The observed intermediate structure was examined in the context of strongly overlapping resonances,[4] distributions in resonance widths and spacings,[5] and in terms of an intermediate optical model.[6]

The measured total neutron cross sections of vanadium from 0.1 to 1.5 MeV are shown in Fig. I-10-1 together with 50 to 100 keV energy averages of the measured values. At incident neutron energies <0.5 MeV, the experimental energy resolution was 1.5 to 2.5 keV. At higher energies the velocity resolution was estimated to be 0.1 to 0.12 nsec/m. The differential elastic neutron scattering cross sections were determined at incident neutron energy increments of $\lesssim$ 10 keV with an incident neutron energy resolution of 20 ± 5 keV. The angular range of the measurements at each incident energy was from ~25 to ~155 deg., usually covered in eight angular intervals. The scattered neutron velocity resolution of 1.5–2.0 nsec/m was sufficient to resolve the elastically scattered neutrons from inelastically scattered components. Ex-

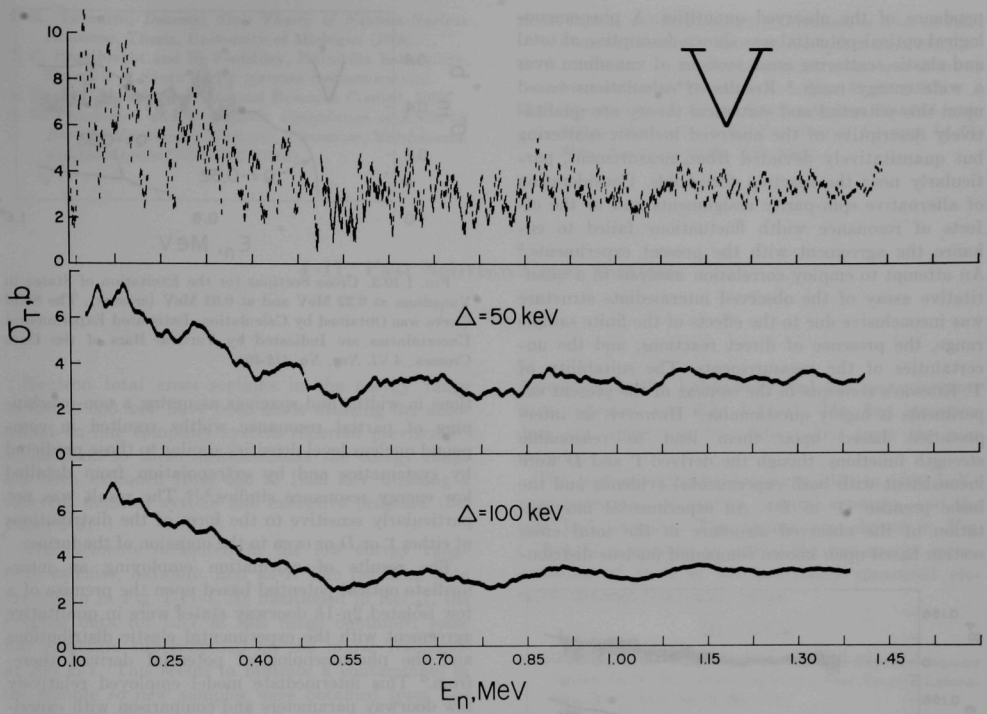

FIG. I-10-1. Measured Total Neutron Cross Sections of Vanadium; a) Top, Basic Measured Data, b) Center, Data Averaged Over a 50 keV Interval, c) Bottom, Data Averaged Over a 100 keV Interval. *ANL Neg. 112-9505.*

perimental results expressed in the form of a Legendre polynomial expansion are shown in Fig. I-10-2. The inelastic excitation of states in vanadium at 330 ± 10 keV was observed. The corresponding excitation cross sections are indicated in Fig. I-10-3 together with the results of statistical calculations.

The equivalent non-local optical potential of C. Engelbrecht and H. Fiedeldey[7] and statistical methods were employed in the phenomenological interpretation and extrapolation of the experimental results. A χ^2 statistical fit to the observed elastic scattering resulted in an optical potential giving a reasonable description of experiment (Fig. I-10-2). The potentials derived from the elastic scattering angular distributions, together with the Hauser-Feshbach formalism and the structure of vanadium[8] were used to calculate the inelastic excitation cross sections. Again the calculated result was reasonably descriptive of experiment (Fig. I-10-3).

Since a motivation of the present work was the provision of fast neutron data for reactor design it is instructive to compare the present results with the pertinent contents of the Evaluated Nuclear Data File-B (ENDF-B).[(9)] Generally, the ENDF-B file gives a reasonable description of the results of the present experiments, though the latter show more detailed resonance structure and result in somewhat larger inelastic cross sections. Whether or not these are critical matters may well depend upon what use is to be made of the information in designing reactor systems. The ENDF-B values at energies >1.5 MeV closely correspond to other reported measurements of total and scattering cross sections and to the predictions of the optical model and statistical calculations outlined above.

The observed total, elastic, and inelastic scattering cross sections were characterized by both a fine and intermediate energy dependent structure. Though of good resolution the results did not provide a definition commensurate with compound nucleus resonance analysis and the interpretation was confined to the intermediate structure and the average energy de-

pendence of the observed quantities. A phenomenological optical-potential was shown descriptive of total and elastic scattering cross sections of vanadium over a wide energy range.[7] Results of calculations based upon this potential and statistical theory are qualitatively descriptive of the observed inelastic scattering but quantitatively deviated from measurement, particularly near the reaction thresholds. Consideration of alternative spin-parity assignments and/or the effects of resonance width fluctuations failed to enhance the agreement with the present experiments.[3] An attempt to employ correlation analysis in a quantitative assay of the observed intermediate structure was inconclusive due to the effects of the finite sample range, the presence of direct reactions, and the uncertainties of the measurements. The suitability of T. Ericson's concepts in the context of the present experiments is highly questionable.[4] However, an interpretation based upon them lead to reasonable strength functions, though the derived Γ and D were inconsistent with both experimental evidence and the basic premise ($\Gamma \gg D$). An experimental interpretation of the observed structure in the total cross section based upon known compound nucleus distributions in widths and spacings assuming a non-overlapping of partial resonance widths resulted in compound nucleus level densities similar to those predicted by systematics and by extrapolation from detailed low energy resonance studies.[5,10] The result was not particularly sensitive to the form of the distributions of either Γ or D or even to the omission of the former.

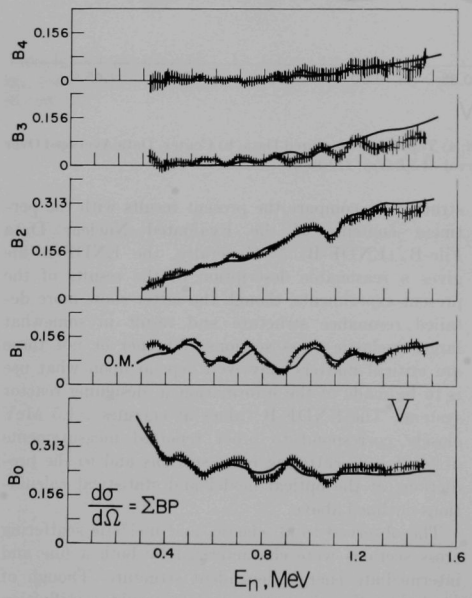

FIG. I-10-2. Differential Elastic Scattering Cross Sections of Vanadium. A 50 keV Average of the Measurements is Indicated by the Data Points. The Solid Curve is the Result of Optical Model Calculation. *ANL Neg. No. 112-9471.*

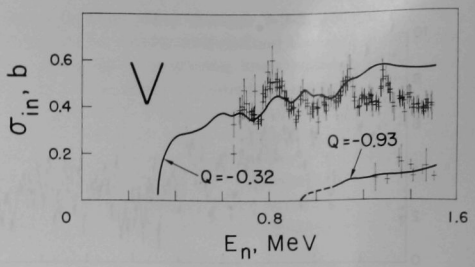

FIG. I-10-3. Cross Sections for the Excitation of States in Vanadium at 0.32 MeV and at 0.93 MeV (crosses). The Solid Curve was Obtained by Calculation. Estimated Experimental Uncertainties are Indicated by Vertical Bars of the Data Crosses. *ANL Neg. No. 113-501.*

The results of calculation employing an intermediate optical potential based upon the premise of a few isolated $2p$-$1h$ doorway states were in qualitative agreement with the experimental elastic distributions and the phenomenological potential derived therefrom.[6] This intermediate model employed relatively few doorway parameters and comparison with experiment lead to parameter values of the magnitude expected from theoretical estimates.[11] A wider application of the method may assist in determining some of the statistical properties of door states.

Apparent intermediate structure is present in the measured cross sections. The latter two of the above interpretations appear both physically applicable and to result in qualitative agreement with experiment. They are not unique and other interpretations have led to similar qualitative successes.[12] The interpretations are not necessarily mutually exclusive and may each contribute appreciably to the physical reality.

References

1. P. Hodgson, *Optical Model of Elastic Scattering*, (Oxford University Press, London, 1963).
2. W. Hauser and H. Feshbach, *The Inelastic Scattering of Neutrons*, Phys. Rev. **87**, 366 (1952).
3. P. Moldauer, *Average Compound-Nucleus Cross Sections*, Rev. Mod. Phys. **36**, 1079 (1964).
4. T. Ericson, *A Theory of Fluctuations in Nuclear Cross Sections*, Ann. Phys. **23**, 390 (1963).
5. A. Agodi and G. Pappalardo, *Statistical Fluctuations of Compound Nucleus Level Density and Nuclear Cross Sections*, Nucl. Phys. **47**, 129 (1963).

6. K. Takeuchi, *Doorway State Theory of Neutron-Nucleus Reactions*, Thesis, University of Michigan (1968).
7. C. Engelbrecht and H. Fiedeldey, Pelindaba Laboratory, Republic of South Africa (private communication).
8. Nuclear Data Sheets, National Research Council, 1963.
9. E. Pennington and S. Gajniak, *Compilation of ENDF-B Data for Magnesium, Titanium, Vanadium, Molybdenum, and Gadolinium*, ANL-7387 (1968).
10. A. Carlson and H. Barschall, *Fluctuations in Neutron Total Cross Sections*, Phys. Rev. **158**, No. 4, 1142 (June 1967).
11. H. Feshbach et al., *Intermediate Structure and Doorway States in Nuclear Reactions*, Ann. Phys. **41**, 230 (1967).
12. J. Monahan and A. Elwyn, *Relation Between Fine and Intermediate Structures in the Scattering of Neutrons by Fe*, Phys. Rev. Letters **20**, 1119 (1968).

I-11. Fast Neutron Cross Sections

J. F. Whalen

Neutron total cross sections in the energy range of 100 to 650 keV have been made utilizing the automated on-line computer system reported previously.[1] In addition to these measurements the energy range has been extended from 650 to 1500 keV utilizing a different detector system and executive program (see Paper I-9).

The elements measured in the low energy range were calcium, hafnium, and Li-7. The resulting data are shown in Fig. I-11-1. As mentioned in Ref. 1, the original data for Li-7 in this range contained some fine structure superimposed on the major resonance at 260 keV. This seems to indicate a contaminate in the sample so new samples were obtained from Los Alamos Scientific Laboratory and the measurements were repeated (see Fig. I-11-1). The fine structure does not appear in the data taken from the new samples.

The high energy measurements (650 to 1500 keV) were performed on carbon, natural uranium, and the new Li-7 samples. The results are shown in Fig. I-11-2. It is planned to extend the low energy measurements of most of the previously measured elements through this higher range.

Reference

1. J. F. Whalen, R. Roge and A. B. Smith, *A Digital Computer System for the Executive Control of a Fast Neutron Laboratory*, Nucl. Inst. Meth. **39**, 1966.

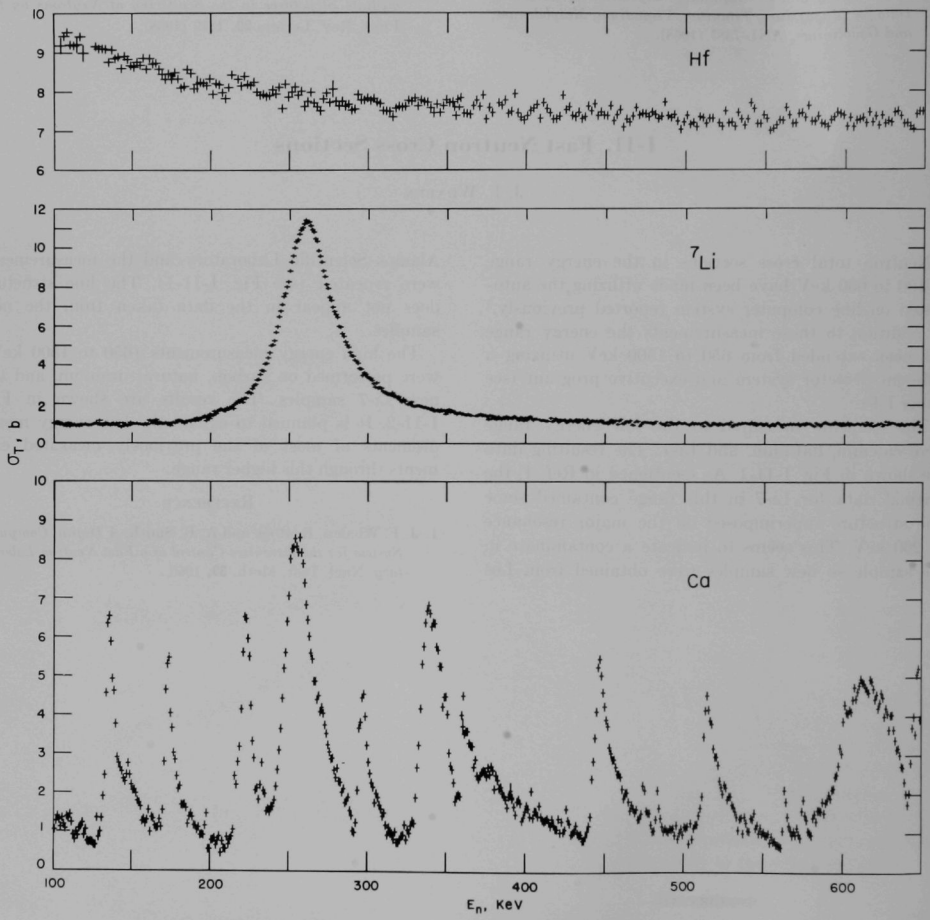

FIG. I-11-1. Total Cross Sections in Low Energy Range. *ANL Neg. No. 113-1447.*

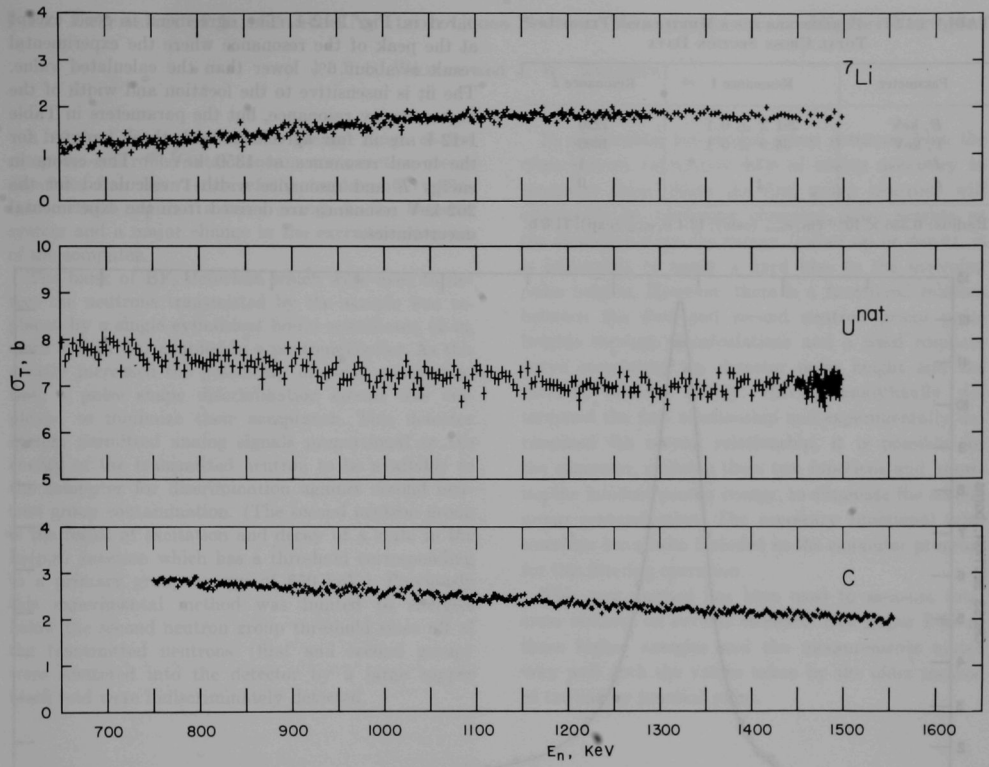

FIG. I-11-2. Total Cross Sections in High Energy Range. *ANL Neg. No. 113-1448.*

I-12. The Total Cross Section of Li-7 from 100 to 650 keV

J. W. MEADOWS and J. F. WHALEN

The sample transmissions and total cross sections of Li-7 have been measured from 100 to 650 keV utilizing the on-line computer system.[1]

Neutrons were produced by the $Li^7(p,n)Be^7$ reaction. The energy resolution of 2.5 to 3.0 keV was determined primarily by the lithium metal target thickness. Measurements were made at 1 keV intervals thoughout the measured interval. The hydrogen ion beam from the accelerator was magnetically analyzed and the H_2^+ component passed an electrostatic analyzer which controlled the accelerator potential. The energy calibration was based on a $Li^7(p,n)Be^7$ threshold of 1881.0 keV. There was a systematic uncertainty of ±2 keV due to the changing optical properties of the ion source. The samples were 1 in. diam. cylinders of Li-7 encased in steel cans with 0.005 in. thick end pieces. An empty can was used for "sample out" measurements. Sample thicknesses of 0.1431×10^{24}, 0.1152×10^{24}, and 0.0693×10^{24} atoms/cm^2 were used. The principal contaminants were ~0.2% sodium and ~0.05% potassium.

An attempt was made to fit the data with the single level Breit-Wigner formula and assigning the 260 keV resonance to a $J = 3^+$ state excited by $\ell =$

TABLE I-12-I. PARAMETERS FOR A MULTI-LEVEL FIT OF Li-7 TOTAL CROSS SECTION DATA

Parameter	Resonance 1	Resonance 2
E, keV	261.2 ± 0.1	1220
Γ, keV	35.9 ± 0.1	1000
J^π	3+	1−
ℓ	1	0

Radius: 0.336×10^{-12} cm, σ_{max} (calc): 12.4 b, σ_{max} (exp): 11.6 b.

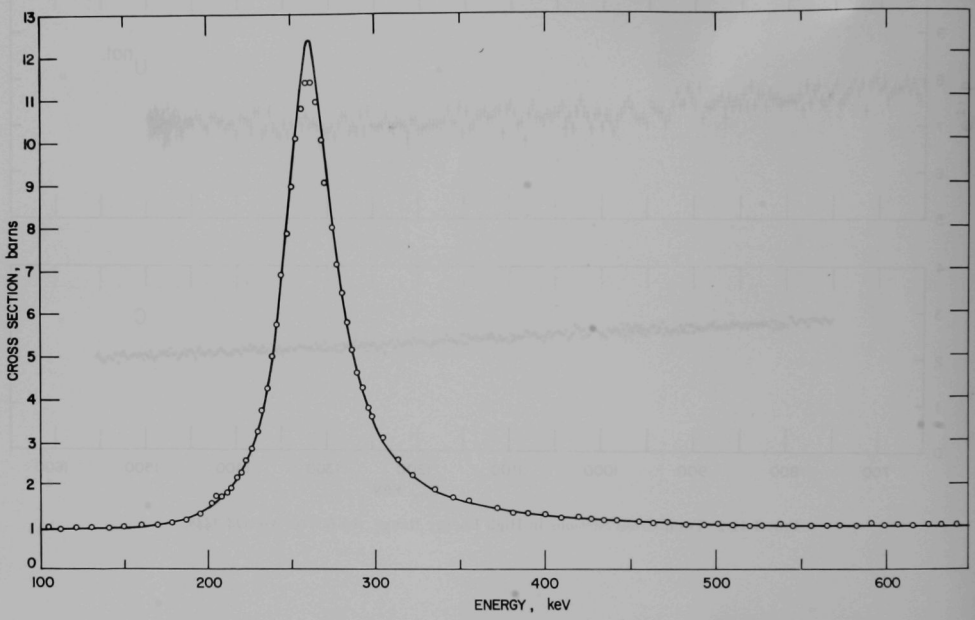

FIG. I-12-1. The Total Cross Section of Li-7 from 100 to 650 keV. The Data was Taken at 1 keV Intervals but for This Figure They Have Been Averaged in Groups of Three Over the Resonance and in Groups of Nine Elsewhere. The Solid Curve is the Result of the Multi-Level Fit. *ANL Neg. No. 113-794.*

1 neutrons. A reasonably good fit was obtained in the region of the resonance but the discrepancy was relatively large near 600 keV. Better results were obtained using a multi-level fit and two resonances. The parameters are listed in Table I-12-I and the calculated and experimental cross sections are compared in Fig. I-12-1. The agreement is good except at the peak of the resonance where the experimental result is about 6% lower than the calculated value. The fit is insensitive to the location and width of the higher energy resonance, but the parameters in Table I-12-I are in fair agreement with those reported for the broad resonance at 1350 keV.[2] The errors in energy E and resonance width Γ calculated for the 262 keV resonance are derived from the experimental uncertainties.

REFERENCES

1. J. F. Whalen, R. Roge and A. B. Smith, *A Digital Computer System for the Executive Control of a Fast Neutron Laboratory*, Nucl. Inst. Methods **39**, 185 (1966).
2. T. Lauritsen and F. Ajzenberg-Selove, *Energy Levels of Light Nuclei*, Nucl. Phys. **78**, 1 (1966).

I-13. Extension of Automated Neutron Cross Section Measurements to Higher Energies

J. F. Whalen and J. W. Meadows

A method for extending the energy range of the computer-controlled total neutron cross section measurements has been successfully implemented. This new method required a basic change in the detector system and a major change in the executive program of the computer.

The bank of BF_3 detectors which were used to detect the neutrons transmitted by the sample was replaced by a single cylindrical liquid scintillator (2 in. diam × 2 in. ht) coupled to a photomultiplier. As this greatly increased the possibility of γ-ray contamination, a pulse shape discrimination circuit was employed to minimize their acceptance. This detector system permitted analog signals proportional to the energy of the transmitted neutron to be available to the computer for discrimination against second neutron group contamination. (The second neutron group is the result of excitation and decay of a state in the Li(p,n) reaction which has a threshold corresponding to a primary group energy of 650 keV.) Previously this experimental method was limited to energies below the second neutron group threshold since all of the transmitted neutrons (first and second group) were scattered into the detector by a large copper block and were indiscriminately detected.

In eliminating the second group neturons from the cross section calculation it is of course necessary to recognize them. Since the first group neutrons will constantly be producing changing pulse heights as the computer steps the energy (either up or down), it is impossible to apply a fixed bias to the incoming pulse heights. However, there is a functional relation between the first and second neutron group pulse heights through Q calculations and a fixed response curve correlating the detector pulse height and the incident neutron energy. Having analytically determined the first relationship and experimentally determined the second relationship, it is possible for the computer, utilizing these two functions and knowing the incident proton energy, to eliminate the second group contamination. The necessary functional relationships have been included in the computer program for this filtering operation.

This new method has been used to measure total cross sections on several elements (see Paper I-9) at these higher energies and the measurements match very well with the values taken by the older method at the energy junction point.

I-14. Activation Methods for Actinide Isotope Capture Rate Measurements

R. J. Hall,* W. C. Redman and M. L. Pool†

Introduction

High burnup in breeder reactors enhances the importance of the reaction rates for isotopes other than the principal fissile and fertile materials. A combination of radiochemical and mass spectrometric techniques is now used to determine reaction rates for isotopes subjected to extended irradiation in existing power reactors. A study was undertaken to determine the feasibility of such determinations by activation techniques for samples irradiated in fast critical assemblies. The feasibility of such methods as an alternate to the usual techniques now employed in high fluence irradiations was also of interest, as a means to confirm such results.

Each isotope of significance in breeder reactor fuel cycles presents a different problem. Techniques that have been used, principally for both fission and capture rates for Th-232, U-233, U-235, U-238, and Pu-239, include: (1) singles counting with[1] and without[2] prior radiochemical separation; (2) coincidence counting with[3] and without[4] prior radiochemical separation; and (3) mass spectrographic analysis.[5] The counting techniques for capture rate measurements involved detecting either the decay of the neutron capture product or its radioactive daughter.

* Student, Ohio State University, Columbus, Ohio.
† Ohio State University, Columbus, Ohio.

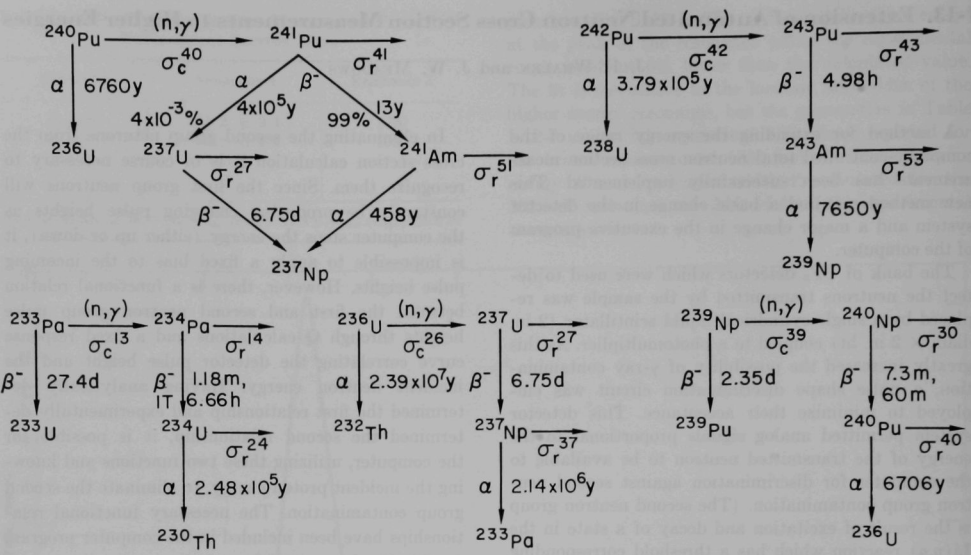

FIG. I-14-1. Neutron Capture and Subsequent Decay Chains. *ANL Neg. No. 113-857.*

TABLE I-14-I. ACTIVITY OF (n,γ) PRODUCT PER GRAM OF TARGET

Target	(n,γ) Product	$\frac{(n,\gamma)\text{ Product Activity}}{\text{Gram of Target}}$, dis/h	
		$\tau = 1$ h	$\tau = 24$ h
U-236	U-237	1.83×10^7	1.65×10^7
Pu-240	Pu-241	3.30×10^4	3.30×10^4
Pu-242	Pu-243	2.35×10^8	9.45×10^6
Pa-233	Pa-234	2.66×10^8	2.43×10^7
Np-239	Np-240	1.99×10^8	2.46×10^1

Significant isotopes for which no fast spectra capture rate measurements have been reported include U-236, Pu-240, Pu-242, Np-239, and Pa-233. The fast spectra neutron capture rates of these isotopes have been evaluated and are reported in what follows. The applicability of the previously mentioned techniques as methods for capture rate measurements in both zero and high power reactors was considered, and proposed procedures are reported. The method suggested for the measurement of the capture rate of U-236 has been tested and verified by a measurement in the fast zero power critical facility ZPR-9.

CALCULATED ACTIVITIES

To evaluate the target and equipment requirements for capture rate measurements of the isotopes of interest, the expected decay rates of the neutron capture product and its daughter were calculated. The primary reaction chains involved are shown in Fig. I-14-1. H. Bateman[6] has formulated equations which describe the production and loss of iostopes in such chains. These were used in calculating the activities of the neutron capture product and its daughter. For Pa-233 and Np-239, beta decay of the target isotope followed by neutron capture produces U-234 and Pu-240 respectively. This production mechanism was not included in the calculations.

In all calculations, the assumption was made that the neutron capture product and its daughter were initially absent. An irradiation time of 10 h at a flux of 10^8 n/cm^2-sec with a typical fast reactor neutron spectrum was used. The effective capture cross sections used were: U-236, $\sigma_c = 0.5$ b; Pu-240, $\sigma_c = 0.6$ b; Pu-242, $\sigma_c = 0.4$ b; Pa-233, $\sigma_c = 0.5$ b; and Np-239, $\sigma_c = 0.5$ b.

The calculated activity of the neutron capture product per gram of target at $\tau = 1$ h and $\tau = 24$ h after irradiation is presented in Table I-14-I. Table I-14-II gives the calculated activity of the neutron capture product's daughter per gram of target at various times τ after irradiation. The calculated ratio of the target activity to the neutron capture product activity at $\tau = 1$ h after the postulated irradiation is given in Table I-14-III.

If the flux restriction were relaxed, as would be

the case for an irradiation in a power reactor, it is found that at an integral flux of 10^{12} n/cm^2-sec, the relationships given in Tables I-14-I and I-14-II are still linear functions of the flux to within 20%. Hence, for rough calculations the numbers given in these tables can be multiplied by 10^4 to give the activities that would be produced by an irradiation at a flux of 10^{12} n/cm^2-sec; however the time of maximum activity of the (n,γ) capture product's daughter would occur later. The ratios given in Table I-14-III can be divided by 10^4 to give the corresponding values for a flux of 10^{12} n/cm^2-sec.

Evaluation

The possibility of a capture rate determination for a specific actinide isotope by counting techniques following a low flux irradiation depends on many factors. These include the half-life and decay scheme of the isotope, the capabilities of various counting devices, the minimum sample size required, the time lag between irradiation and data collection, the maximum practical target size, and the activities and activity ratios such as presented in Tables I-14-I, I-14-II and I-14-III. An evaluation of the specific situation for each of the five isotopes considered indicated that a low-flux-counting procedure was practical at present only for U-236 and Pu-242. A high flux irradiation would be required for a Pu-240 capture rate measurement. Even with a high flux irradiation, a counting technique did not appear feasible for either Pa-233 or Np-239 capture rate determinations. A description of the verified method for U-236 capture and the proposals for Pu-242 and Pu-240 follow.

U-236 Capture Rate Measurement

The method selected for the low-flux U-236 capture-rate determination uses the decay of U-237 as the indicator of U-236 neutron capture. From Table I-14-II it is seen that the daughter, Np-237, of the neutron capture product undergoes only 0.169 dis/h-g of target 1000 h (approximately 42 days) after irradiation. Therefore, a low-flux capture rate measurement from observation of the daughter's decay is impractical. On the other hand, the information given in Tables I-14-I and I-14-III shows that the activity of U-237 per gram of U-236 is high and that the ratio of U-236 activity to U-237 activity is reasonably low. The U-237 (6.75 day half-life) activity 24 h after irradiation is 1.65×10^7 dis/h-g of target and the ratio of the U-236 activity to the U-237 activity is 4.6×10^2 one hour after irradiation.

The decay of U-236 is by alpha emission, and only one gamma ray has been observed originating from the decay.[7] It has an energy of 163 keV and an abundance of approximately 0.5%. From consideration of the U-237 decay scheme,[8, 9] shown in abridged form in Fig. I-14-2, it was found that both (β,γ) coincidence counting and (γ,γ) coincidence counting are possible means for detecting the U-237 decay. (Singles counting is also possible but coincidence counting is preferable because of its higher background supression capabilities.) The decision on which type of coincidence counting to use was based on the desire to count the target directly, i.e., without fission product removal, or altering its physical form. (γ,γ)

TABLE I-14-II. Activity of (n,γ) Product's Daughter per Gram of Target

Target	(n,γ) Product's Daughter	(n,γ) Product's Daughter Activity / Gram of Target dis/h, $\tau = \tau_{max}$	$\tau = 1000$ h	$\tau^{(a)}_{max}$
U-236	Np-237	1.73×10^{-1}	1.69×10^{-1}	181 d
Pu-240	Am-241	8.51×10^2	5.69	68.5 y
Pu-242	Am-243	3.50×10^1		114 h
Pa-233	U-234	1.47		184 h
Np-239	Pu-240	4.90×10^1		23 h

[a] $\tau_{max} \equiv$ time at which the activity of the (n,γ) product's daughter reaches a maximum.

TABLE I-14-III. Ratio of Target Activity to (n,γ) Product Activity at $\tau = 1$ h

Target	(n,γ) Product	Target Activity / (n,γ) Product Activity
U-236	U-237	4.6×10^2
Pu-240	Pu-241	9.2×10^9
Pu-242	Pu-243	2.2×10^3
Pa-233	Pa-234	1.0×10^{10}
Np-239	Np-240	1.4×10^{11}

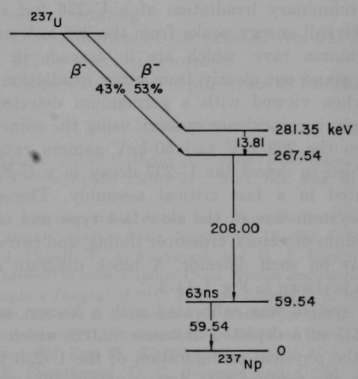

Fig. I-14-2. ^{237}U Decay Scheme (Abridged). *ANL Neg. No. 113-864.*

I-15. Correlation of Mass, Energy and Angle in 1.5 and 5.6 MeV Neutron Fission of U-238

J. W. Meadows

It is still not clear whether the mass division in fission is determined at the saddle point or at some later stage in the fission process. In an attempt to obtain some insight into this problem, studies of the mass-energy-angle distribution of fragments from the U^{238} (n,f) reaction have been carried out at incident neutron energies of 1.8 and 5.6 MeV. As these energies are below the $(n,n'f)$ threshold the study is not complicated by neutron emission prior to fission.

TABLE I-15-I. The Average Values of the Mass and Energy, the Variances of Their Distributions, and the Yield at Symmetry (Y_s) for 1.5 and 5.6 MeV Neutron Fission of U-238 and for Thermal Neutron-induced Fission of U-235

Angle	U-238, 1.5 MeV			U-238, 5.6 MeV			U-235, Thermal		
	7	45	90	7	45	90	7	45	90
$\langle M_L \rangle$	100.2		99.9	99.9	99.6	99.6	97.2	97.2	97.4
$\langle M_H \rangle$	139.0		138.9	139.5	139.0	139.2	139.1	139.1	139.1
$\sigma^2(M)$	37.0		37.0	43.4	42.4	42.8	34.7	33.5	34.9
$\langle E_L \rangle$	99.0		99.2	97.7	97.8	97.2	100.2	100.2	100.2
$\langle E_H \rangle$	71.2		71.6	70.2	70.3	69.9	70.3	70.2	70.4
$\langle E_{kT} \rangle$	170.2		170.8	167.9	168.1	167.0	170.5	170.4	170.6
$\sigma^2(E_{kT})$	112.1		110.8	120.2	115.9	118.6	112.6	112.7	111.7
Y_s	0.015 ±0.007		0.021 ±0.007	0.10 ±0.01	0.09 ±0.01	0.12 ±0.01	0.020 ±0.002	0.020 ±0.002	0.020 ±0.002

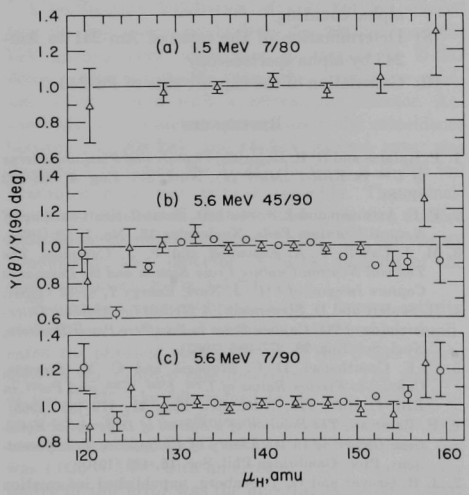

Fig. I-15-1. The Mass Dependence of the Ratio of the Yields at 7 and 45 Degrees to the Yield at 90 Degrees for Neutron Induced Fission of U-238. The Data Represented by △ are at the Indicated Energies While the ○ Give the Results of the Corresponding U-235 Calibration Measurements. Each Point Represents an Interval 6.1 amu Wide in the 1.5 MeV Data and 3.6 amu Wide in the 5.6 MeV Data. The Apparent Mass-angle Correlation of the 45 to 90 Degree Ratio is Caused by a Systematic Effect. *ANL Neg. No. 113-105.*

The experimental apparatus, techniques, and method of analysis have been described previously.[1] Measurements of the mass-energy distribution of neutron induced fission of U-238 were made at three angles: 7, 45 and 90 deg. Concurrent measurements of thermal neutron induced fission of U-235 were made for detector calibration and to test for systematic errors.

The results are summarized in Table I-15-I. The data show no angular dependence outside experimental error. The value of $\sigma^2(M)$ is consistently less at 45 deg than at the other angles but this occurs in both the thermal and fast neutron fission data and is caused by a systematic effect that has been discussed elsewhere.[1] The mass dependence of the yield ratios, $Y(M,\theta)/Y(M,90)$, is shown in Fig. I-15-1. The 45 deg data shows an apparent mass dependence but this is caused by the systematic effect mentioned above. This is illustrated by the agreement with the U-235 thermal fission data plotted on the same graphs. $Y(M,7)/Y(M,90)$ does not show any significant departure from 1.0 in either measurement. This is particularly evident at 5.6 MeV where fair statistical accuracy extends into the region of symmetric fission.

The experimental data presented here does not provide any evidence that saddle point states determine the mass distribution.

REFERENCE

1. J. W. Meadows, *Correlation of Mass, Energy and Angle in Thermal and 6-MeV Neutron Fission of U-235*, Reactor Physics Division Annual Report, July 1, 1966 to June 30, 1967, ANL-7310, pp. 13–16.

I-16. Energy Dependence of the Delayed Neutron Yield from Neutron Induced Fission of Th-232, U-235, and U-238

S. A. COX and E. E. DOWLING WHITING

A knowledge of the energy dependence of the delayed neutron yield from fissile and fertile elements is important to the fields of reactor kinetics and reactor control. While there have been extensive measurements of delayed neutron yields and periods for thermal neutron-induced fission and for fission induced by fast fission spectrum neutrons, there have been only isolated measurements reported at other energies.[1] B. Maksiutenko[2] has reported measurements for several nuclides using monoenergetic neutrons with energies of 2.4, 3.3, and 15. MeV. There has been no adequate investigation of the region between thermal energy and 2.4 MeV. This report describes such an investigation for U-235 at several energies from 0.25 to 1.5 MeV and for U-238 and Th-232 from the onset of the fission threshold to 2.4 MeV.

Two different aspects of the delayed neutron process were investigated. One series of measurements was made at a number of different incident neutron energies to determine if there were any change in the time dependence of the decay of the delayed neutron activity. A second series of measurements was made to determine if there were any dependence of the total yield on the delayed neutron activity as a function of incident neutron energy.

Because the requirements of the two types of measurements were so different, two separate experimental arrangements were necessary. For the time dependent measurements, it was important to have the highest possible yield. Thus the cylindrical sample (0.5 in. dia. by 0.75 in. long) of U-235, U-238, and Th-232 were positioned as close as possible to the neutron source for irradiation. For all measurements the neutrons were obtained from the Li(p,n) reaction using a Van de Graaff accelerator. After irradiation for a preset time (usually ~4 min) the sample was "fired" from a distance of ~6 ft into a shielded counting assembly consisting of ten BF_3 counters moderated by paraffin. The transit time was ~0.2 sec. The data were collected using a 400 channel analyzer with scaling time ranging from 0.075 to 2. sec per channel. The longest scaling times were used for background determination. Because of the high yield requirement which necessitated "poor" geometry the experimental arrangement was not suitable for monitoring of the neutron flux from the lithium target. Thus the yields at different energies could not be directly compared. Examples of the decay curves for Th-232, U-235, and U-238 are given in Fig. I-16-1. The horizontal and vertical bars represent the data. The solid curve is a multi-exponential fit obtained by using a variable metric minimization program.[3] The data were analyzed in terms of five exponential components. It was assumed that the six-component representation used by G. R. Keepin[1] would be a rough approximation to the present data. This is supported by Keepin's measurements at thermal and fission spectrum energies which yielded similar half-lives for the decay. The half-lives obtained by Keepin were approximately 0.2, 0.5, 2., 6., 22., and 54. sec. The shortest half-life, 0.2 sec, could not be extracted from our data because of the transit time of 0.2 sec. Based on this assumption the data were then analyzed in pairs of components. First, all the data beyond 200 sec were analyzed for a background component and a long half-life component. The cut-off time of 200. sec was chosen to be approximately ten half-lives away from the 22. sec component. Thus the data used should be represented very accurately by a single long half-life (~54. sec) plus background. This criterion was used throughout the analysis; i.e. the second stage in analysis used data from 60. sec upward, the third stage data from 20. sec upward, and the fourth stage data from 2. sec upward. In the first stage there were three free parameters: the background, the amplitude, and the half-life of the exponential component. In the second stage the background was held at the value determined in the first stage and the amplitudes and half-lives of two exponential components were treated as free parameters. In the third stage the background and the

energies from 0.25 to 1.5 MeV. For Th-232 and U-238 measurements were made from the vicinity of the fission threshold to 2.4 MeV. The data for all elements were normalized at 1450 keV to Keepin's fast neutron determinations. Our results for U-235 are given in Fig. I-16-3 together with Keepin's[1] values for thermal and fast neutron irradiations. The errors in the individual points are estimated to be ±5%, based on both the counting statistics and the reproducibility of the measurements. Within the estimated error of 5% there is no significant change in the delayed neutron yield over the energy range from thermal energy to 1.5 MeV, although there appears to be some slight indication of an increase. Our data for U-238 and Th-232 are not yet completely analyzed. The much more pronounced angular distribution in the fission fragments, especially near threshold, and the very sharp rise at the fission threshold necessitate more detailed corrections than are required for U-235. Nevertheless at this stage it can still be stated that there is no change in excess of 20% in the delayed neutron yield below 2.4 MeV for either U-238 or Th-232.

We conclude that within 3 to 5% there is no significant change in the ratio of our delayed neutron activity to that of Keepin's for U-235 from 150 to 1300 keV. Similarly, our measurements for Th-232 at 1450, 1500, and 1640 keV and for U-238 at 1400, 1500, and 1750 keV yield ratios which agree at all decay times with Keepin's measurements to within 5%. We also conclude that the total delayed neutron yield is constant to within 5% from thermal irradiation to 1.5 MeV irradiation for U-235, although there is a slight indication of an increase.

References

1. G. Robert Keepin, *The Physics of Nuclear Kinetics*, (Addison-Wesley, Reading, Massachusetts, 1965) Chapter 4, p. 73.
2. B. P Maksiutenko, *Relative Yields of Delayed Neutrons in Fission of U-235, U-238, and Th-232*, J. Exptl. Theoret. Phys. (USSR) **35**, 565L (1959).
3. Burton S. Garbow, *Variable Metric Minimization*, ANL-2013 (1965).

I-17. Spontaneous Fission Decay Constant of U-238

J. H. Roberts,* R. Gold and R. J. Armani

Precise measurement (approximately 1.6% relative error) of the spontaneous fission decay constant of U-238 has been carried out with solid-state track recorders (SSTR) of pre-etched mica.[1] (See Paper V-2 for further details on the SSTR method.) Table I-17-I compares the present experimental result with earlier measurements.

TABLE I-17-I. Measurements of the Spontaneous Fission Decay Constant of U-238

Investigators	Year	Method	λ_F[a]
Perfilov[2]	1947	Fission chamber	5.3 ± 0.9
Segrè[3]	1952	Fission chamber	8.7 ± 0.3
Fleischer and Price[4]	1964	SSTR	6.6 ± 0.8
		K-40 and Rb-87 dating	6.9
		Weighted average	6.85 ± 0.20
Rao and Kuroda[5]	1966	Radiochemical	7.8 ± 0.9
Roberts, Gold and Armani	1968	SSTR	7.03 ± 0.11

[a] Units of 10^{-17}/y.

References

1. J. H. Roberts, R. Gold and R. J. Armani, *Spontaneous Fission Decay Constant of ^{238}U*, Phys. Rev. (in press).
2. N. A. Perfilov, *Half-Life Periods of the Spontaneous Fission of Uranium and Thorium*, Zh. Elesperim. i. Teor. Fiz. **17**, 746 (1947).
3. E. Segrè, *Spontaneous Fission*, Phys. Rev. **86**, 21 (1952).
4. R. L. Fleischer and P. B. Price, *Decay Constant for Spontaneous Fission of U^{238}*, Phys. Rev. **133**, B63 (1964).
5. M. N. Rao and P. K. Kuroda, *Decay Constant and Mass-Yield Curve for the Spontaneous Fission of Uranium-238*, Phys. Rev. **147**, 884 (1966).

* Northwestern University, Evanston, Illinois.

I-18. T-Violation Effects in Direct Reactions

P. A. Moldauer

A general study of the effects of time reversal invariance violating forces in nuclear reactions[1] has been reported on previously. This work has now been extended and specialized to the case of direct nuclear reactions.[2] Using the methods of the Distorted Wave Born approximation the results of Ref. 1 were confirmed and applied to the analysis of published data.[3]

A time reversal violating nuclear force results in a violation of the detailed balance relation connecting the value of the cross section for a certain reaction with that of the inverse reaction. This violation is due to an antisymmetric part of the T-matrix. The principal result obtained is that this antisymmetric part of the T-matrix is equal to the commutator of the symmetric (or T-conserving) part of the T-matrix and the matrix elements of the T-violating part of the nuclear Hamiltonian.

This result was used to obtain estimates on the possible magnitudes of the T-violating parts of the Hamiltonian H' from experimentally obtained limits on detailed balance violation. The results of W. Weitkamp et al.[3] imply a limit of about 25 keV on the matrix elements of H'. The contrast experiments with fluctuating cross sections[4,5] are able to set an upper limit of about 50 eV.

References

1. P. A. Moldauer. *Effects of T-Violation in Nuclear Reactions*, Phys. Rev. **165**, 1136 (1968).
2. P. A. Moldauer, *T-Violation and Detailed Balance in Direct Reactions*, Phys. Letters **26B**, 713 (1968).
3. W. G. Weitkamp, D. W. Storm, D. C. Shreve, W. J. Braithwaite and D. Bodansky, *Test of Time-Reversal Invariance in the Reactions* $Mg^{24} + d \leftrightarrows Mg^{25} + p$, Phys. Rev. **165**, 1233 (1968).
4. W. von Witsch, A. Richter and P. von Brentano, *Upper Limit of T Nonconservation in the Reactions* $^{24}Mg + \alpha \leftrightarrows Al + p$, Phys. Rev. Letters **19**, 524 (1967).
5. S. T. Thornton, C. M. Jones, J. K. Bair, M. D. Mancusi and H. B. Willard, *Test of Time-Reversal Invariance in the Reaction* $^{16}O(d,\alpha)^{14}N$ *and Its Inverse*, Phys. Rev. Letters **21**, 447 (1968).

I-19. Statistics of Resonance Widths and Spacings

P. A. Moldauer

Both the energy averages and fluctuations of neutron cross sections depend on the detailed properties of resonance parameters, their averages, their fluctuations, and their correlations. For well separated resonances, with widths much less than spacings, these statistical properties of resonance parameters are well understood. The mean spacings D can be calculated from the thermal properties of a Fermi gas. The resonance energy correlations are dominated by the Wigner repulsion effect. The partial widths have the Porter-Thomas distribution and the average width $\bar{\Gamma}$ determines the absorption rate through its relation with the optical model transmission coefficient $T = 2\pi\bar{\Gamma}/D$.

However, at neutron energies of typically several hundred keV in medium and heavy nuclei the resonances begin to overlap and interfere. The very meaning of resonance then becomes ambiguous and so do the resonance parameters and their statistical properties. One possible definition of a resonance is that it is an R-matrix state. The statistical properties of these states are well understood, but the connections between their parameters and the properties of cross sections are very indirect and the calculation of cross sections in terms of R-matrix parameters is very laborious.

A more direct definition of resonances is in terms of the poles of the reaction amplitude. The pole positions in the complex energy plane are specified by resonance energies E_μ and widths Γ_μ, and the residues of these poles are specified by residue amplitudes $g_{\mu c}$. In terms of these parameters the reaction amplitudes for transitions from channel c to channel c' is written as

$$S_{cc'} = S^0_{cc'} - i\Sigma_\mu \frac{g_{\mu c} g_{\mu c'}}{E - E_\mu + \frac{1}{2} i\Gamma_\mu}, \qquad (1)$$

where $S^0_{cc'}$ is a smooth function of the energy.

The relationships between the average values of these resonance parameters and their connections with the channel transmission coefficients $T_c = 1 - |S_{cc}|^2$ had previously been discussed by means of special

models of the reaction amplitude,[1] yielding the relations

$$2\pi\bar{\Gamma}_c/D = -\ln(1 - T_c) \tag{2}$$

and

$$2\pi\,|\overline{g_c^2}|/D = T_c/\sqrt{1 - T_c}\,, \tag{3}$$

where $\bar{\Gamma}_c$ and $\overline{g_c^2}$ are averages over the resonance index μ and $\Gamma_\mu = \Sigma_c\Gamma_{\mu c}$. Equation (3) has now been confirmed by direct proof[2] and both Eqs. (2) and (3) have been found to agree with the results of extensive statistical model calculations.[3]

These same statistical model calculations, which were based on R-matrix models of the reaction process, provided insight into the distributions of resonance parameters.[3] The most striking result is the very broad distributions of values of the $\Gamma_{\mu c}$ and of the $g_{\mu c}$, particularly when T_c is large. This phenomenon gives rise to structure in the observed cross sections that is not predicted by the conventional fluctuation theory and is more akin to what has been called "intermediate" structure. The occurrence of such "intermediate" structure is then predictable on the basis of optical model transmission coefficients.

A succinct summary of these considerations has been prepared.[4]

References

1. P. A. Moldauer, *Unitary Models of Nuclear Resonance Reactions*, Phys. Rev. **157**, 907 (1967).
2. P. A. Moldauer, *Sum Rule for Resonance Reactions*, Phys. Rev. Letters **19**, 1047 (1967).
3. P. A. Moldauer, *Resonance Widths and Spacings; Their Averages and Distributions*, Phys. Rev. **171**, 1164 (1968)
4. P. A. Moldauer, *Interfering Resonances*, ANL-7467 (1968).

I-20. Shell Model R-Matrix Theory

K. Takeuchi*

Success in calculating the elastic scattering cross section of N-15 by R. Lemmer and C. Shakin[1] has stimulated interest in the dynamical theory of nuclear reactions. Cross sections of lead isotopes, C-12, F-19 and Ni-58 were calculated by C. Shakin,[2] I. Lovas,[3] I. Afnan,[4] and K. Takeuchi,[5] respectively. In Feshbach's unified theory,[6] used in these calculations, it is difficult to take into account the identity of particles. To avoid this difficulty, H. Weidenmüller[7] proposed a model of the restricted function space in the continuum written in the second quantization formalism by W. MacDonald and A. Mekjian.[8] The diagonalization of the model Hamiltonian is another difficulty. In general, the Hamiltonian diagonalization problem becomes more difficult with an increasing number of particles and levels. There are many intermediate states of continuum even if the number of particles in the continuum is restricted to one. Moreover, this calculation must be repeated at every total energy.

The R-matrix concept is an efficient theory to deal with the continuum. M. Haglund and D. Robson[9] proposed use of R-matrix theory and the work was extended by P. Buttle.[10] In their theory, there are two sources of difficulty in the correct treatment of identity of particles. One is that identity of particles has not been treated in the R-matrix theory. The other is that the R-matrix theory was applied to a single particle state obtained after Feshbach's expansion; i.e., one particle state is represented on a basis different from that for the remaining particles. The first problem is treated in the present work by correcting the R-matrix theory. It is found that one may use conventional R- and S-matrix relations but reduced widths must be corrected by a factor $\sqrt{N}$, where N is the number of particles which are active in the reaction. In this manner, conventional R-matrix theory may be applied to the statistical theory. In the present development of a dynamic theory, this factor is a serious correction.

The second difficulty of Haglund and Robson is solved by choosing multiples of single particle R-matrix states as the basis for R-matrix states of a many-particle system. It is found that the boundary condition imposed on a single particle state is equal to that for the R-matrix states on the surface.

Calculations based upon the above theory were programmed for computer computation. It was found that a new kind of intermediate state exists, differing from the usual doorway states. The magnitudes of reduced widths were in the order of those of the single particle states, those of the new intermediate

* Post-doctor, University of Michigan, Ann Arbor, Michigan.

states, and those of doorway states. The lowest energy intermediate resonances of V-51 measured by A. Smith[11] was found to be due to such an intermediate state. Further systematic study using the program is in progress.

References

1. R. H. Lemmer and C. M. Shakin, *Resonance Reactions and the Nuclear Shell Model I*, Ann. of Phys. **27**, 13 (1964).
2. C. M. Shakin, *On Model Calculations of Neutron Widths and Strength Functions*, Ann. of Phys. **21**, 373 (1963)
3. I. Lovas, *Elastic Neutron Scattering on C^{12}*, Nucl. Phys. **81**, 353 (1966).
4. I. R. Afnan, *Shell-Model Theory of Nuclear Reactions in Deformed Nuclei*, Phys. Rev. **163**, 1016 (1967).
5. K. Takeuchi, *The Doorway State Theory of Neutron-Nuclear Reactions*, Thesis, University of Michigan (1967).
6. H. Feshbach, *A Unified Theory of Nuclear Reactions II*, Ann. of Phys. **19**, 287 (1962).
7. H. A. Weidenmüller, *On the Theory of Nuclear Reactions*, Nucl. Phys. **75**, 189 (1966).
8. W. MacDonald and A. Mekjian, *Fine Structure in Nuclear Resonances*, Phys. Rev. **160**, 730 (1967).
9. M. E. Haglund and D. Robson, *Intermediate Structure and Channel Coupling Theory*, Phys. Letters **14**, 225 (1965).
10. P. J. A. Buttle, *Solution of Coupled Equations by R-Matrix Techniques*, Phys. Rev. **160**, 719 (1967).
11. A. B. Smith, Argonne National Laboratory (private communication).

I-21. Fine Structure of Doorway States

K. Takeuchi*

The intermediate structure of cross sections has been interpreted in terms of the doorway states.[1,2] Effects of the doorway states on the analytic structure of the S-matrix, or resonance widths and resonance energies, have been studied by C. Mahaux and H. Weidenmüller.[3] Information on the doorway state, e.g. identification of a doorway state and its constants, along with their resulting characteristic distribution of resonance widths versus resonance energies, have been obtained for the nuclides Ni-58 and Ni-60.[(4)] Correcting the Mahaux and Weidenmüller's study, A. Lejeune and C. Mahaux[5] also determined the doorway state constants of Pb-207. However, in the above determination of the doorway state constants there were ambiguities in the choice of coupling strength relations of a doorway state to the continuum, $\Gamma^{\uparrow}$, and to the compound states, $\Gamma^{\downarrow}$ [weak coupling, $\Gamma^{\downarrow}/\Gamma^{\uparrow} \gtrsim 1$; intermediate coupling, $\Gamma^{\downarrow}/\Gamma^{\uparrow} \approx 1$; and strong coupling $\Gamma^{\downarrow}/\Gamma^{\uparrow} \gtrsim 1$]. Moreover, the choice of the coupling strength relations affected the determination of the values of the doorway state constants.

In order to avoid such ambiguities, the analytic properties of the S-matrix and effects of the doorway states on the total cross section have been thoroughly studied.[6] In particular, fine resonance shape, background cross section, and average cross sections around a doorway state were examined in detail. It was found that the variation of these quantities across the doorway state were useful for choosing the coupling strength relations and the determination of the doorway state constants. In the case of the weak coupling, the fine resonance shapes around the doorway state systematically varied and deviated from the conventional Breit-Wigner shape. It was found that given the potential phase shift, the resonance width distribution, the quantitative background cross section and the average cross section could be related in terms of the doorway state constants and that identified doorway states of Ni-58 and Ni-60 had quite similar properties. The doorway state constants for Ni-58 and Ni-60 determined from the calculations, are listed in Table I-21-I.

TABLE I-21-I. The Doorway State Constants of Ni-58 and Ni-60

	E_d,[(a)] keV	$\Gamma^{\uparrow}$,[(b)] keV	$\Gamma^{\downarrow}$,[(c)] keV
Ni-58	205	42	113
	410	144	61
	580	137	72
Ni-60	195	32	109
	320	146	75
	500	123	60

[a] Doorway state energy.
[b] Coupling strengths of a doorway state to the continuum.
[c] Coupling strengths of a doorway state to the compound states.

References

1. A. K. Kerman, L. S. Rodberg and J. E. Young, *Intermediate*

* Post-doctor, University of Michigan, Ann Arbor, Michigan.

Structure in the Energy Dependence of Nuclear Cross Sections, Phys. Rev. Letters **11**, 422 (1963).
2. H. Feshbach, A. K. Kerman and R. H. Lemmer, *Intermediate Structure and Doorway States in Nuclear Reactions*, Ann. of Phys. **41**, 230 (1967).
3. C. Mahaux and H. A. Weidenmüller, *The Fine Structure of a Doorway State*, Nucl. Phys. **A91**, 241 (1967).
4. K. Takeuchi, *Fine Structure of Doorway States*, Bull. Am. Phys. Soc. II, 12 (1966).
5. A. Lejeune and C. Mahaux, *Fine Structure of a Doorway State in Pb^{207}*, Nucl. Phys. **207**, 35 (1967).
6. K. Takeuchi, *The Doorway State Theory of Neutron-Nuclear Reactions*, Thesis, University of Michigan (1967).

I-22. Phenomenological Doorway State Theory

K. Takeuchi*

It was found that real and imaginary parts of the optical model potential vary greatly around a doorway state.[1-3] This property has been applied to doorway state analysis of measured total, inelastic, elastic, and elastic differential cross sections of V-51 by A. Smith.[4] In the above theory and analysis of experiment, it is assumed that the form factor of a doorway state is given by the one dimensional function with radial dependence of the imaginary part of the optical model potential. Based upon Smith's success and upon systematic characteristics of the doorway states (see Paper I-21) a phenomenological doorway state theory was proposed where the above form factor is extensively applied to the fine structure study of doorway states. Of course, the form factor of an individual doorway state can be obtained for a given configuration of the doorway state and the two-body interaction potential. Discarding such details, one may perform with certain reliance systematic study of the intermediate structure over different isotopes and energies.

It was learned that the shift function can be expressed by $\Gamma^{\uparrow}$ (see Paper I-21). Therefore, interference effects of doorway states can be studied without increasing the number of parameters which are necessary for the doorway state analysis based on the single doorway state assumption. Computer programming suitable for applying these theoretical concepts was partially developed.

* Post-doctor, University of Michigan, Ann Arbor, Michigan.

References

1. R. H. Davis, *Mechanisms for Alpha Particle Scattering*, Proc. Symposium on Recent Progress in Nuclear Physics with Tandems, University of Heidelberg, 1966, Heidelberg, Germany.
2. H. Feshbach, A. K. Kerman and R. H. Lemmer, *Intermediate Structure and Doorway States in Nuclear Reactions*, Ann. of Phys. **41**, 230 (1967).
3. K. Takeuchi, *The Doorway State Theory of Neutron-Nuclear Reactions*, Thesis, University of Michigan (1967).
4. A. B. Smith, Argonne National Laboratory (private communication).

I-23. Monte Carlo Interpretation of a U-238 Spherical Shell Transmission Experiment at 23 keV

L. B. Miller and W. P. Poenitz

Precise values for the cross sections of the primary fissile and fertile materials are required for optimization of fast reactor designs and evaluation of the relative merits of various design concepts. Of particular importance are accurate determinations of absolute cross sections which can be used to normalize existing curves of $\sigma_a(E)$ in the keV region. Spherical shell transmission experiments should yield accurate absolute cross sections, since the method does not require a measurement of the source strength, absolute fluxes, or reaction rates, but depends only on the relative values of the neutron flux with and without a spherical shell of the sample materials surrounding the source.

Measurements of neutron transmission through

spherical shells of U-238 were performed by T. Belanova et al.,[1] using 23 keV neutrons from an Sb-Be source. Their interpretation of the results, however, was based on the assumption that resonance self-shielding was negligible. Similar experiments with materials of less interest to reactor design have been analyzed with resonance self shielding taken into account by H. Schmitt and C. Cook,[2] D. Bogart and T. Semler,[3-5] and F. Froehner.[6] Significant self-shielding correction factors were computed for some isotopes; e.g., 0.68 ± 0.10 for cadmium.[2]

Therefore, Belanova's experimental results have been reinterpreted using the Monte Carlo code AMC[(7)] to take into account the resonance structure of the cross sections as well as the geometry of the experiments. Values for the average total cross section, level spacing, and strength functions for s-wave and p-wave interactions were taken from various sources in the literature.[8-13] The values used were $S_0 = 0.90 \times 10^{-4}$, $S_1 = 1.8 \times 10^{-4}$, $\bar{D}_0 = 20.8$ eV and $\sigma_T = 13.4$ b. Resonance structure was generated using the Porter-Thomas distribution for Γ_n and the Wigner distribution for D. The average capture width and the potential scattering cross section were determined by fitting the total cross section and the measured transmission probabilities of 0.919 and 0.736 for U-238 shells of thicknesses 2 and 5 cm, respectively. The average capture width was found to be $\bar{\Gamma}_\gamma = 24$ meV with $\sigma_p = 10.0$ b.

The transmission probabilities reported by Belanova included corrections for the neutrons emitted by the Sb-Be source at 380 keV and for the finite size of the detector. Considering also the moderation of neutrons in the beryllium and fissions in the natural uranium sample, the above value of $\bar{\Gamma}_\gamma$ corresponds to an average capture cross section $\sigma_\gamma = 493$ mb for U-238 at 23 keV.

The AMC code was also used to obtain the smooth 1/v cross section which would fit each transmission value. The ratio of the smooth cross section to the average resonance cross section is the resonance self-shielding factor. The computed values were 0.835 and 0.723 for the 2 and 5 cm-thick shells, respectively. Applying these corrections to the cross sections computed by Belanova from the same experiments yields $\sigma_\gamma = 498$ mb, in good agreement with the value 493 mb from the detailed AMC calculation.

This reinterpretation of Belanova's experimental results yields a cross section in better agreement with the values reported by Moxon and Chaffey,[13] H. Menlove and W. Poenitz,[14] Mackling and Gibbons,[13] and H. Miessner and E. Arai,[15] as shown in Fig. I-23-1. U-238 capture cross sections which have been normalized to the value given by Belanova, e.g., V. Tolstikov et al.,[16] should be renormalized to the present value of 495 at 23 keV.

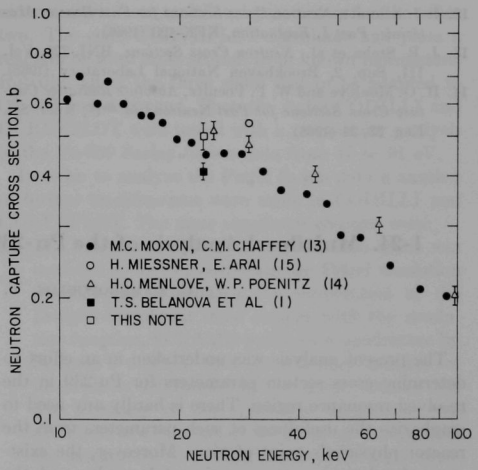

FIG. I-23-1. Capture Cross Sections of U-238 in the Energy Range 10–100 keV. *ANL Neg. No. 113-407 Rev. 1.*

REFERENCES

1. T. S. Belanova et al., *Absolute Measurements of the Absorption Cross Sections of 24 KeV Neutrons*, J. Nucl. Energy **20**, 411 (1966).
2. H. W. Schmitt and C. W. Cook, *Absolute Neutron Cross Sections for Sb-Be Photoneutrons*, Nucl. Phys. **20**, 202 (1960).
3. D. Bogart and T. T. Semler, *Monte Carlo Interpretation of Sphere Transmission Experiments for Average Capture Cross Sections of 24 keV*, Conference on Neutron Cross Section Technology, Washington, March, 1966, Conf-660303, Book 1, 502.
4. D. Bogart, *Monte Carlo Interpretation of Sphere Transmission Experiments for Average Capture Cross Sections at 24 keV*, Proc. Conference on Nuclear Data for Reactors, Paris, October 17–21, 1966, Vol. I, p. 455, International Atomic Energy Agency, Vienna.
5. T. T. Semler, *A Monte Carlo Analysis of Gold Shell Transmission Experiments at 24 keV Using Spin-Dependent Statistical Data*, Trans. Am. Nucl. Soc. **11**, 162 (1968).
6. F. H. Froehner, *Monte Carlo Reinterpretation of Gold Sphere Transmission Data at 24 keV Neutron Energy*, GA-8072 (1967).
7. L. B. Miller, *Monte Carlo Analysis of Reactivity Coefficients in Fast Reactors; General Theory and Applications*, ANL 7307 (1967).
8. J. B. Garg et al., *Neutron Resonance Spectroscopy III Th^{232} and U^{238}*, Phys. Rev. **134**, B985 (1964).
9. M. Asghar et al., *Low-Energy Neutron Resonance Parameters of U^{238}*, Nucl. Phys. **85**, 305 (1966).
10. N. W. Glass et al., *^{238}U Neutron Capture Results from Bomb Source Neutrons*, Second Washington Conference on Neutron Cross Sections and Technology, D-13 (1968).
11. K. K. Seth et al., *s-, p- and d-wave Neutron Strength Functions*, Phys. Letters **13**, 70 (1964).

12. J. J. Schmitt, *Neutron Cross Sections for Fast Reactor Materials, Part I, Evaluation*, KFK-120 (1966).
13. J. R. Stehn et al., *Neutron Cross Sections*, BNL-325, Vol. III, Sup. 2, Brookhaven National Laboratory (1965).
14. H. O. Menlove and W. P. Poenitz, *Absolute Radiative Capture Cross Sections for Fast Neutrons in* ^{238}U, Nucl. Sci. Eng. **33**, 24 (1968).
15. H. Miessner and E. Arai, *Zur Absolutmessung von Effektiven Neutronenwirkungsquerschnitten im keV Gebiet mit einer schnellen gepulsten Anordnung*, Nukleonik **8**, 428 (1966).
16. V. A. Tolstikov et al., *A Measurement of the Capture Cross Sections of* ^{238}U *and* ^{232}Th *for 5-200 keV Neutrons*, J. Nucl. Energy **18**, 599 (1964).

I-24. Multilevel Analysis of the Pu-239 Fission Cross Section from 40 to 150 eV

P. Lambropoulos, T. Hill* and C. N. Kelber

The present analysis was undertaken in an effort to determine cross section parameters for Pu-239 in the resolved resonance region. There is hardly any need to emphasize the usefulness of such parameters from the reactor physicist's point of view. Moreover, the existence of relatively new experimental results and the need to account for level–level interference effects makes a multilevel analysis particularly relevant at the present time.

The data used were those taken by E. Shunk, W. Brown and R. LaBauve[1] using the nuclear explosion Petrel as a neutron source. The advantage of these data compared with data obtained from other experiments is the low background. As a consequence, the valleys of the cross section are cleaner and more reliable, and one should be able to see more clearly interference effects at the wings. The measurements were taken using a flight path of 185 m with a time resolution of approximately 3 μsec in the energy region between 20 and 320 eV. The time resolution function is a compound of an LRC smoother circuit and a 3 μsec exponential decay.[2] A very good analytical approximation of the resolution function is given by[3]

$$F(t) = c[e^{\gamma t} - e^{\alpha t}(B \sin wt + \cos wt)] \qquad (1)$$

where

$$\gamma = -\tfrac{1}{3}\ \mu\text{sec}^{-1}, \qquad \alpha = -\tfrac{5}{3}\ \mu\text{sec}^{-1}$$

$$w = 0.958\ \mu\text{sec}^{-1}, \qquad B \equiv \frac{\gamma - \alpha}{w}$$

and

$$c \equiv -\gamma \frac{w^2 + \alpha^2}{w^2 + (\gamma - \alpha)^2}$$

is a normalization constant such that

$$\int_0^\infty F(t)\, dt = 1.$$

The analysis was terminated at 150 eV for two reasons: the energy resolution was bad after 150 eV and the experimental points started becoming too rare for the least squares analysis to be meaningful. The full width at half maximum of the resolution function is given by

$$\Delta E = 0.543 \times 10^{-3}\, E^{3/2}, \qquad (2)$$

where E is the neutron energy in eV. Since the Pu-239 sample was at room temperature,[4] one can easily verify that after about 39 eV the resolution width is larger than the Doppler width. For example, at 100 eV the former is already twice the latter. Also, in view of the fact that the resolution function is not a Gaussian but has a long tail on the low energy side, the broadening is resolution-dominated over the whole energy range under consideration.

The approach used in the present analysis was a least squares fit to the data using a multilevel Kapur-Peierls formula. This as well as the associated computer code CODILLI have been developed by F. Adler and D. Adler.[5] The theory of the approach is discussed in Ref. 5 and will not be elaborated upon here. The general expression for the cross section for the process X can be written as

$$\sigma^{(X)}(E) = \frac{C}{E} 2\,(1 - \cos\omega) + \frac{C}{\sqrt{E}} \sum_{k=1}^{N} \frac{\nu_k(G_k^{(X)} \cos\omega + H_k^{(X)} \sin\omega) + (\mu_k - E)(H_k^{(X)} \cos\omega - G_k^{(X)} \sin\omega)}{(\mu_k - E)^2 + \nu_k^2}$$
$$+ \frac{C}{\sqrt{E}} (A_1^{(X)} + A_2^{(X)} E^{-1} + A_3^{(X)} E^{-2} + \ldots + B_1^{(X)} E + B_2^{(X)} E^2 + \ldots), \qquad (3)$$

where $C = 6.52 \times 10^5$ b-eV and ω is set equal to zero for reaction cross sections. For total cross sections,

* Student, Kansas State University, Manhattan, Kansas.

$\omega = 2ka$, where k is the incident neutron wave number and a is the appropriate channel radius. The summation extends, in principle, over all levels of the compound system but in practice is limited by the number of levels that can be handled by the computing machine in the least squares fitting as well as by other numerical considerations.

The contribution of each level to the cross section is determined by four parameters; i.e., μ_k, ν_k, $G_k^{(X)}$, $H_k^{(X)}$. The first two represent the position and width of the kth level respectively. One should note the difference between μ_k and the corresponding level E_k of R-matrix theory; μ_k includes the shift of E_k due to level–level interference. In fact, all four parameters include the effects of level–level interference and are in general complicated functions of R-matrix parameters. The quantities μ_k and ν_k depend only on the level under consideration while, as the superscript X suggests, the parameters $G_k^{(X)}$ and $H_k^{(X)}$ depend also on the process X. Thus in an analysis of cross sections for different processes of the same nucleus one should obtain compatible values for all μ_k and ν_k. Although all four parameters are somewhat energy dependent, for practical purposes they can be assumed to be constant over an appropriately small energy range. If it is justified to assume that $H_k^{(X)} = 0$, the resulting expression is essentially a sum of single-level Breit-Wigner resonances.

The expression containing powers of E is added in order to take into account background contributions. Such contributions, slowly varying with energy, appear on the basis of the theoretical derivation of Eq. (3) as well as on the basis of experimental considerations.

In analyzing experimental data for reaction cross sections, one calculates the convolution of Eq. (3) with the Doppler kernel and then the convolution of the resulting cross section with the resolution kernel appropriate to the experimental data under consideration. For total cross sections this procedure is somewhat different because the fit is usually made to transmission data (see the relevant discussion in Ref. 5). The Doppler- and Resolution-broadened cross section is then fitted to the experimental data using the method of least squares. In performing the fit, one guesses values for μ_k and ν_k and the least squares analysis yields values for G_k and H_k. One then changes the values of μ_k and ν_k and the process is repeated until a satisfactory fit is obtained. This will be referred to as "linear fit". After a number of linear fits, one can consider all four parameters μ_k, ν_k, G_k and H_k as unknown and determine them by the least squares analysis. This will be referred to as "non-linear" fit.

The code CODILLI is accompanied by two other codes, namely SIGMA and CURVEPLOT. The code SIGMA calculates one of the fission, total or capture cross sections from multilevel parameters for the other two. The code CURVEPLOT calculates and plots a reaction or total cross section from known parameters. Initially, all of the three codes had to be adapted to OS-360 and debugged. Then the codes CODILLI and CURVEPLOT were tested with a preliminary analysis of the Pu-239 Saclay fission data from 47 to 91 eV.

In order to analyze the Petrel fission data a number of further modifications were made in CODILLI and CURVEPLOT. The more significant changes were:

(a) The subroutine SCRAMB used in both codes was modified so as to incorporate the Petrel resolution function. In calculating the convolution of the Doppler-broadened cross section with the resolution function, SCRAMB performs a quadrature by Simpson's method with an arbitrary number of intervals as determined by the input variable NI. The accuracy of this numerical integration was examined as a function of the integration range and the integration step. Finally, the resolution function was truncated (on the low energy side) at the point where its value is 1% of the maximum. On the high energy side the function has a theoretical zero at a finite energy and the integration extends up to that point. It was found that 100 integration steps gave sufficient accuracy.

(b) The ability to CALCOMP-plot the calculated results was incorporated into CODILLI by a call to the GRAPH subroutine from the SIGWE subroutine. Unless the input variable NOPLOT = 1, this plot is automatically produced, resulting in a large saving of time over the former two-step CODILLI-CURVEPLOT procedure.

(c) All of the dimensioned variables in CODILLI were increased in size to allow analysis of a broader energy range. The code now permits the analysis of up to 80 resonance levels and 4000 data points.

(d) A call to subroutine OMASK was placed at the beginning of CODILLI. This routine supresses the printing of program interrupt messages for any exponential overflows or underflows that occur during the computation.

(e) A few minor changes were also made in the input variables and formats.

(f) Both CODILLI and CURVEPLOT have been compiled and link-edited under OS Release 14.1 and exist as load modules by the above names in the data set THOMAS.HILL on Disk 22. They may be executed directly from disk in the standard procedure for load module execution.

Some time was also devoted to further numerical experimentation with the codes. The effect of the size of the determinant of the error matrix on the accuracy of the parameters was investigated. The subroutine

QUICKW was examined as an alternative technique to that presently used for calculating the Doppler-broadened line-shape functions ψ and χ in the CODILLI code. Both procedures were found to be equivalent as far as accuracy and run time are concerned.

The actual analysis of the Petrel fission data from 40 to 150 eV has reached the final stages. A preliminary set of parameters has been arrived at but some further study is needed before they can be finalized. Generally the results are compatible with J. Farrell's[7] analysis of a smaller portion of the same data using the Reich-Moore formalism. Questions such as the existence of Lynn[8] doublets, spin assignments to the levels, etc., are being investigated.

References

1. E. R. Shunk, W. K. Brown and R. LaBauve, *Fission Cross Sections from Petrel*, LA-3586 (September 1966), pp. 45–58 and 155–172.
2. P. A. Seeger, A. Hemmendinger and B. C. Diven, *Fission Cross Sections of Am-241 and Am-242m*, Nucl. Phys. **A96**, 605 (1967).
3. D. W. Bergen, Los Alamos Scientific Laboratory (private communication).
4. W. K. Brown, Los Alamos Scientific Laboratory (private communication).
5. F. T. Adler and D. B. Adler, *Neutron Cross Sections in Fissible Elements*, Proc. Conference on Breeding, Economics and Safety in Large Fast Power Reactors, October 7–10, 1963, ANL-6792, pp. 695–708; also *Analysis of Neutron Resonances in Fissible Elements; Programs CODILLI, CURVEPLOT and SIGMA*, *COO*-1546-3 (September 1966).
6. A. M. Lane and R. G. Thomas, *R-Matrix Theory of Nuclear Reactions*, Revs. Mod. Phys., **30**, 257 (1958).
7. J. A. Farrell, *Multilevel Analysis of Pu-239 Fission Cross Section from 14 to 90 eV*, Phys. Rev., **165**, 1371 (1968).
8. J. E. Lynn, *Analysis and Interpretation of the Slow Neutron Cross Sections of the Fissionable Nuclei*, Phys. Rev. Letters **13**, 412 (1964).

I-25. Multilevel Effects on Infinite Dilution Resonance Integrals

E. M. Pennington and D. A. Sargis

A comparison was made for Pu-239 of the effect of using either single-level or multilevel formulae in calculating infinite dilution capture and fission resonance integrals. Resonance parameters were generated according to the appropriate statistical distributions and used in both the Reich-Moore multilevel[1] and Breit-Wigner single-level formulae to calculate capture and fission cross sections. The capture and fission resonance integrals were then computed by numerical integration.

In order to illustrate the effects involved, we first consider the case of two neighboring resonances with the same partial widths, Γ_n, Γ_γ, and Γ_f, and with $\Gamma_n \ll \Gamma_\gamma$ or Γ_f. One fission channel is considered. The relations between the infinite dilution multilevel (ML) capture and fission resonance integrals and the corresponding single-level (SL) values are given in Eqs. (1) and (2):

$$\bar{I}^{ML}_{\gamma\infty} = I^{SL}_{\gamma\infty}\left[1 + \frac{\Gamma_f^2}{D^2 + \Gamma_\gamma(\Gamma_\gamma + 2\Gamma_f)}\right], \quad (1)$$

$$\bar{I}^{ML}_{f\infty} = I^{SL}_{f\infty}\left[1 - \frac{\Gamma_\gamma\Gamma_f}{D^2 + \Gamma_\gamma(\Gamma_\gamma + 2\Gamma_f)}\right]. \quad (2)$$

Here D is the separation of the two interfering levels. Other notation is obvious, except that the bars on $\bar{I}^{ML}_{\gamma\infty}$ and $\bar{I}^{ML}_{f\infty}$ indicate an average over the angle between the fission vectors in the formulation of E. Vogt.[2] For one fission channel, this angle is either 0 deg or 180 deg. Equation (1) shows that on the average the multilevel capture resonance integral is higher than the corresponding single-level value, while Eq. (2) shows the reverse to be true for the fission resonance integrals. Thus the multilevel capture-to-fission ratio, $\bar{\alpha}$, is expected to be higher than the single-level $\bar{\alpha}$, as in Eq. (3),

$$\frac{\bar{\alpha}^{ML}}{\bar{\alpha}^{SL}} = \frac{\bar{I}^{ML}_{\gamma\infty}}{\bar{I}^{ML}_{f\infty}} \Big/ \frac{I^{SL}_{\gamma\infty}}{I^{SL}_{f\infty}} = 1 + \frac{\Gamma_f(\Gamma_\gamma + \Gamma_f)}{D^2 + \Gamma_\gamma(\Gamma_\gamma + \Gamma_f)} \approx 1 + \frac{\Gamma_f(\Gamma_\gamma + \Gamma_f)}{D^2}. \quad (3)$$

Although such a simple model is not expected to be quantitatively correct for the general case of many resonances generated from statistical parameters, the results given below are in qualitative agreement with Eqs. (1), (2), and (3).

Resonances were generated for Pu-239 using the average s-wave parameters in Table I-25-I. The $J = 0$ resonances are quite wide, while the $J = 1$ resonances are narrow. This corresponds to two fission channels being fully open for $J = 0$ and one channel being partly open for $J = 1$. Multilevel effects are expected to be more important for $J = 0$ than for $J = 1$, as is indicated by the parameter in the last line of Table I-25-I.

The resonance energies were generated by assuming

that the level spacing for each J is given by a Wigner distribution.[3] The reduced neutron widths follow a chi-squared distribution of one degree of freedom (Porter-Thomas distribution), since the corresponding amplitudes satisfy a Gaussian distribution.[3] The amplitudes in each fission channel also follow a Gaussian distribution. Capture widths were assumed to be constant since there are many capture channels. The computer calculations were carried out on the Argonne CDC-3600 using a Fortran code based on the COMBCO program,[4] which calculates cross sections using the Reich-Moore formulae.[1]

TABLE I-25-I. AVERAGE RESONANCE PARAMETERS FOR Pu-239

	$J = 0$	$J = 1$
D, eV	8.67	3.12
Γ_n^0, eV$^{1/2}$	8.67×10^{-4}	3.12×10^{-4}
Γ_δ, eV	0.040	0.040
Γ_f, eV	2.8	0.055
ν_f [a]	2	1
$\Gamma_f(\Gamma_\gamma + \Gamma_f)/D^2$	0.106	0.00054

[a] ν_f is the number of degrees of freedom for the fission width.

TABLE I-25-II. MULTILEVEL AND SINGLE-LEVEL RESONANCE INTEGRALS FOR Pu-239 FROM 100 TO 300 eV

Case		$\bar{I}_{\gamma\infty}$, b	$\bar{I}_{f\infty}$, b	$\bar{\alpha}$	$\overline{(I_{\gamma\infty}^{ML}/I_{\gamma\infty}^{SL})}$	$\overline{(I_{f\infty}^{ML}/I_{f\infty}^{SL})}$	$\overline{(\alpha^{ML}/\alpha^{SL})}$
$J = 0$	*SL*	0.34673	8.2713	0.045895	1.2218 ± 0.1391	0.9841 ± 0.0243	1.2485 ± 0.1794
	ML	0.42181	8.1072	0.055390			
$J = 1$	*SL*	13.789	9.2075	1.5400	1.0016 ± 0.0015	0.9958 ± 0.0033	1.0058 ± 0.0048
	ML	13.809	9.1706	1.5488			
Total	*SL*	14.136	17.479	0.84417	1.0072 ± 0.0052	0.9894 ± 0.0124	1.0185 ± 0.0179
	ML	14.231	17.278	0.85779			

Results of the calculations are listed in Table I-25-II, where the averages of 43 runs covering the energy range from 100 to 300 eV are presented. For the wide $J = 0$ resonances the multilevel capture resonance integral is over 20% larger on the average than the corresponding single-level value, while the multilevel fission resonance integral is a little smaller than the single-level value. Also the computer output showed that the multilevel capture cross section for $J = 0$ was often quite different as a function of energy from the single-level cross section. For the narrow $J = 1$ resonances, the average multilevel capture resonance integral is only slightly larger and the fission integral slightly smaller than the single-level values. Since almost all of the capture involves the $J = 1$ resonances, the total multilevel $\bar{\alpha}$ is only around 2% higher than the single-level value.

Some calculations were also performed for U-235, using average resonance parameters which were not especially good because they yielded too high a value of $\bar{\alpha}$. These calculations gave $(\overline{\alpha^{ML}/\alpha^{SL}}) = 1.07$.

J. Garrison[5] has studied (numerically) interference effects of two neighboring resonances having equal Γ_γ and various Γ_n, Γ_f, and D. He concluded that the average capture cross section is enhanced at the expense of the fission cross section.

The results of the calculations using statistical parameters are in qualitative agreement with expectations based on the simple model of two neighboring levels with equal partial widths. The multilevel effects on resonance integrals are not very large in general, although the capture resonance integral for Pu-239 for $J = 0$ is considerably different from the single-level value. An effect which has not been considered here is the $(n,\gamma f)$ reaction.[6] This reaction should be counted as a fission rather than as a capture and so would reduce the value of $\bar{\alpha}$. Thus the $(n,\gamma f)$ reaction would tend to cancel the effects produced by using multilevel rather than single-level formulae.

It does not appear that multilevel effects on resonance integrals in the unresolved resonance region are sufficiently large to justify the use of multilevel formulae in place of the simpler single-level formula in reactor physics cross section codes.

REFERENCES

1. C. W. Reich and M. S. Moore, *Multilevel Formula for the Fission Process*, Phys. Rev. **111**, 929 (1958).
2. E. Vogt, *Resonance Theory of Neutron Cross Sections of Fissionable Nuclei*, Phys. Rev. **112**, 203 (1958).
3. C. E. Porter, *Statistical Theories of Spectra: Fluctuations*, (Academic Press, New York, 1965).
4. M. K. Butler, N. Hollister, M. Legan and L. Ranzini, *Argonne Code Center: Compilation of Program Abstracts*, ANL-7411 (1968), pp. 258–259.
5. J. D. Garrison, *Reactor Physics in the Resonance and Thermal Regions. Volume II. Resonance Absorption*, A. J. Goodjohn and G. C. Pomraning, Eds. (M.I.T. Press, Cambridge, Massachusetts, 1966), pp. 3–35.
6. J. E. Lynn, *On the Slow Neutron, Gamma Fission Reaction*, Phys. Letters **18**, 31 (1965).

I-26 Compilation of Neutron Cross Section Data for Natural Helium

E. M. Pennington

Since natural helium is a possible coolant for fast breeder reactors, the present compilation of helium cross section data was carried out. The data will be distributed with ENDF/B identification number, MAT = 1088.

The composition of natural helium is 99.99987 % He-4 and 0.00013 % He-3. Because of the low abundance of He-3, only its (n,p) cross section, which is large at low energies, need be considered. Elastic scattering is the only possible reaction for neutrons incident on He-4 at energies below 15 MeV. Thus the elastic scattering cross section and values of $\bar{\mu}_L$, ξ, and γ are included in the compilation, as well as elastic scattering Legendre coefficients. Here $\bar{\mu}_L$ is the average cosine of the angle of elastic scattering in the laboratory system, ξ is the average logarithmic energy decrement in an elastic collision, and γ is the average of the square of the logarithmic energy decrement divided by twice the average logarithmic energy decrement.

Data Sources

The elastic scattering cross section and Legendre expansion coefficients were calculated from s-, p-, and d-wave phase shifts using a Fortran program written for the purpose. The phase shifts were read from smooth curves based on Table I of Ref. 1. At energies below the 300 keV lower limit of Table I, each of the two p-wave phase shifts was obtained by assuming a functional form based on the low-energy limit for a single p-wave resonance, with parameters determined from fitting the low-energy phase shifts of the table. The

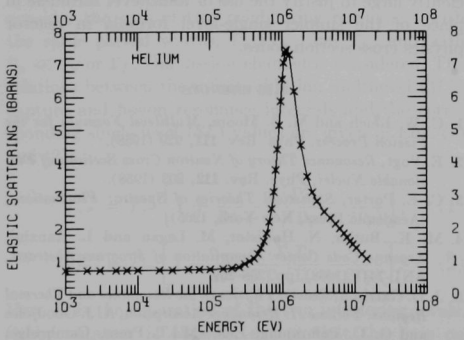

Fig. I-26-1. Elastic Scattering Cross Section for Helium. *ANL Neg. No. 113-681.*

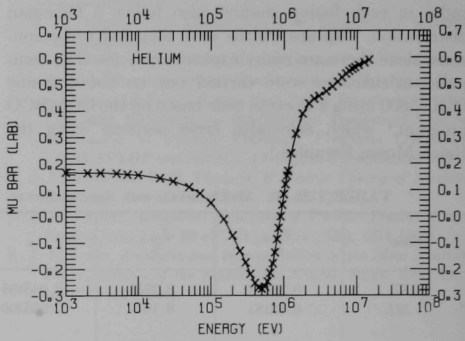

Fig. I-26-2. $\bar{\mu}_L$ for Helium. *ANL Neg. No. 113-696.*

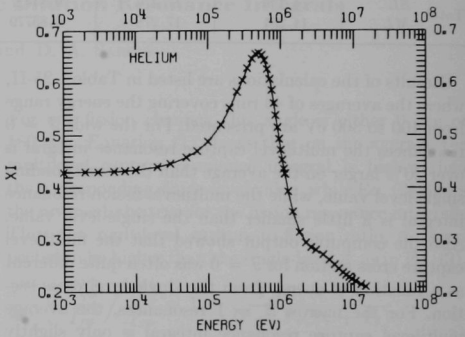

Fig. I-26-3. ξ for Helium. *ANL Neg. No. 113-698.*

s-wave phase shift below 300 keV was calculated using hard sphere scattering and a nuclear radius, a = 2.4 F. This yields the thermal scattering cross section of $4\pi a^2$ = 0.7238 b in agreement with the experimental value[2] of 0.73 ± 0.05 b. The low-energy s-wave phase shifts of Ref. 1 are consistent with a nuclear radius of about 2.48 F and so would yield a somewhat high thermal cross section.

Values of $\bar{\mu}_L$, ξ, and γ were calculated from the Legendre coefficients using a Fortran program, MUXIGA. This program is based on the equations of Refs. 3–5.

An elastic scattering transformation matrix from the center-of-mass system to the laboratory system was computed using CHAD.[6]

The (n,p) cross section for He-3 is that recommended in the He-3 evaluation by J. Als-Nielsen.[7] Extension from 10 to 15 MeV was made using linear extrapolation on a $\log \sigma - \log E$ scale.

The total cross section is the sum of the elastic scattering and (n,p) cross sections.

Figures I-26-1, I-26-2, and I-26-3 show the elastic scattering cross section, $\bar{\mu}_L$ and ξ. Data at energies below 1 keV are not shown because the values of the quantities are so close to those at zero energy. Not all points are plotted at high energies in order to avoid clutter on the graphs.

Discussion

The phase shifts of Ref. 1 are optical model phase shifts chosen to fit both angular distribution and polarization data at many energies. The total cross section is also fit within the scatter of the experimental points. Another recent set of phase shifts[8] is not very different from that used here and could also have been used in the present work. There should be no serious errors in the He-4 data calculated from the phase shifts.

As discussed in Ref. 7, the He-3 (n,p) cross section is rather well known. Probably more error is introduced into the (n,p) cross section for natural helium by the uncertainty in the He-3 isotopic abundance than by the uncertainty in the He-3 (n,p) cross section itself.

Previous evaluations of natural helium for reactor calculations include those of J. J. Schmidt[9] and B. R. S. Buckingham et al.[10] Schmidt's evaluation includes the (n,p) cross section for He-3 and σ_s, $\bar{\mu}_L$, and a set of phase shifts for He-4. Buckingham et al. give separate compilations for He-3 and He-4. For He-3, elastic, (n,p), (n,d), and $(n,2n)$ cross sections are given, as well as elastic angular distributions. The He-4 evaluation gives σ_s and angular distributions.

The present compilation is described in detail in Ref. 11.

References

1. G. R. Satchler et al., *An Optical Model for the Scattering of Nucleons from ^{4}He at Energies below 20 MeV*, Nucl. Phys. **A112**, 1 (1968).
2. R. Genin et al., *Détermination des Sections Efficaces d'Absorption et de Diffusion des Gaz Rares pour les Neutrons Thermiques*, J. Phys. Radium **24**, 21 (1963).
3. H. Amster, *Evaluation of the Cross-Section Transformation Matrices of Zweifel and Hurwitz*, J. Appl. Phys. **27**, 307 (1956).
4. H. Amster, *Errata: Evaluation of the Cross-Section Transformation Matrices of Zweifel and Hurwitz*, J. Appl. Phys. **27**, 663 (1956).
5. H. Amster, *Heavy Moderator Approximations in Neutron Transport Theory*, J. Appl. Phys. **29**, 623 (1958).
6. R. F. Berland, CHAD, Code to Handle Angular Data NAA-SR-11231 (1965).
7. E.N.E.A. Neutron Data Compilation Centre Newsletter No. 6 (1967).
8. B. Hoop, Jr., and H. H. Barschall, *Scattering of Neutrons by α-Particles*, Nucl. Phys. **83**, 65 (1966).
9. J. J. Schmidt, *Neutron Cross Sections for Fast Reactor Materials*, KFK-120. Part II: Tables. Part III: Graphs (1962). Part I: Evaluation (1966).
10. B. R. S. Buckingham et al., *Neutron Cross Sections of Selected Elements and Isotopes for Use in Neutronics Calculations in the Energy Range 0.025 eV–15 MeV*, AWRE O-28/60 (1961).
11. E. M. Pennington, *ENDF/B Neutron Cross Section Data for Natural Helium*, ANL-7462 (to be published).

I-27. Developments Relating to the Evaluated Nuclear Data File/B (ENDF/B) Project

E. M. Pennington and J. C. Gajniak

Introduction

The ENDF/B system of neutron cross section data and processing codes is the main source for production of library tapes for use with the multigroup cross section code MC^2.[(1)] Brief descriptions of the ENDF/B codes CHECKER, CRECT, DAMMET, ETØE and MERMC2 and of their adaption to the CDC-3600, are given in Ref. 2. Also the compilation of data for magnesium, titanium, vanadium, molybdenum and gadolinium was outlined therein.[3] Reference 4 describes this compilation and gives listings of the data in the ENDF/B format as well as graphs of much of the data.

Additional work has been done on codes relating to ENDF/B on the CDC-3600; also, most of the codes have been converted to the IBM system 360. Many of the materials on the ENDF/B category 1 data tapes, which were received near the end of 1967, have been processed to produce MC^2 library tapes for both computers. Category 1 refers to data which have been approved for release by the committee responsible for the ENDF/B study. New evaluation work includes the determination of unresolved resonance parameters for U-235 and the compilation of cross section data for natural helium. A brief description of the helium compilation is given in Paper I-26.

TABLE I-27-I. ENDF/B MATERIALS ON AN MC² LIBRARY TAPE

MAT	MC²ID	Legendre Data	MAT	MC²ID	Legendre Data	MAT	MC²ID	Legendre Data
1010	C 12	Yes	1061	W 183	No	1054	PU241	No
1052	PUFP1	No	1062	W 184	No	1007	BE 9	Yes
1053	PU240	No	1063	W 186	No	1024	NB	No
1070	PUFP2	No	1013	Ø 16	Yes	1044	U 235	No
1071	PUFP3	No	1020	FE	Yes	1055	PU242	No
1009	B 10	Yes	1026	XE135	No	1041	U 233	No
1012	N 14	Yes	1027	SM149	No	1015	AL 27	Yes
1016	TI	Yes	1043	U 234	No	1005	LI 6	No
1017	V	Yes	1046	U 236	No	1006	LI 7	No
1025	MØ	Yes	1047	U 238	No	1037	AU197	Yes
1035	TA181	No	1051	PU239	No	1019	MN	No
1059	NA 23	Yes	1018	CR	Yes	1038	TH232	No
1060	W 182	No	1021	NI	Yes			

FORTRAN CODES ON THE CDC-3600

EDIT

The ENDF/B program EDIT, which was written by D. Irving of Oak Ridge National Laboratory, has been made operational on the CDC-3600. This program prints selected portions of an ENDF/B tape with sufficient identifying information to make the data understandable to a person not familiar with ENDF/B formats.

ETØE

A revised version of ETØE[2,5] has been received and run successfully on the CDC-3600. The revised version contains corrections of errors present in the original program and a new option which allows calculation of elastic scattering from resonance parameters using a multilevel formula instead of the Breit-Wigner single-level formula.

MUXIGA

A Fortran program, MUXIGA, was written to calculate the parameters $\bar{\mu}_L$, ξ, and γ from the Legendre expansion coefficients for elastic scattering angular distributions. Here $\bar{\mu}_L$ is the average elastic scattering cosine in the laboratory system, ξ is the average logarithmic energy decrement, and γ is the Greuling-Goertzel parameter. The series given by H. Amster[7,8] were used in the program. It was found that, even for highly peaked angular distributions, the first four or five coefficients yield quite accurate values for these parameters. However, many more coefficients may be required in order to give positive angular distributions over the complete range of the scattering angle.

CODE CONVERSION TO THE SYSTEM 360

The five codes CHECKER, CRECT, DAMMET, ETØE and MERMC2, which are required for conversion from ENDF/B binary coded data (BCD) to an MC² library tape, have all been converted to the IBM system 360 50/75 computer system. These codes exist as load modules on a disk. It is possible to use the flexibility of the system 360 job control language to run several of these codes in succession in a single job, thereby avoiding the waiting periods between jobs.

Most of the work involved in the Fortran conversion was fairly straightforward, although care had to be taken with subtle differences in the CDC-3600 and system 360 Fortran languages. For example, the BACKSPACE statement operates differently on the two computers, as does the treatment of a DØ loop which may have the second index equal to zero in certain runs. The ETØE and MERMC2 codes had to be changed to work with double precision quantities, since the system 360 version of MC² expects to read a double precision library tape. More difficulty was encountered in determining the appropriate job control language than in converting the Fortran codes themselves.

PROCESSING OF CATEGORY 1 ENDF/B DATA

An MC² library tape was prepared on the CDC-3600 including thirty-eight ENDF/B materials. Table I-27-I lists the ENDF/B identification numbers (MAT), the MC² identifications (MC² ID), and whether or not the materials have elastic scattering Legendre coefficient data on the tape. Legendre coefficients are not included for materials lighter than beryllium, since MC² cannot perform the Legendre treatment option for such materials. Also Legendre coefficients are not usually included for heavy materials, since energy loss by inelastic scattering is considerably more important for these materials than that by elastic scattering, and the time-consuming Legendre treatment is not necessary.

All data for the materials in Table I-27-I are category 1 data, except for U-233 and Th-232, for which only preliminary data have been issued.

In some cases changes were made in the original ENDF/B data using CRECT in order to obtain compatibility with MC^2 formats. These changes involved the inelastic scattering secondary energy distributions for chromium, nickel and carbon, and the $(n,2n)$ secondary energy distributions for Pu-241 and beryllium.

Most of the data for materials in Table I-27-I have also been processed to form a library for the system 360 version of MC^2.

Unresolved Resonance Parameters for U-235

EQUATIONS FOR AVERAGE CROSS SECTIONS IN THE UNRESOLVED REGION

The average infinite dilution capture, fission, and elastic scattering cross sections in the unresolved resonance region are given by the equations

$$\langle\sigma_\gamma\rangle = \sum_{\ell J} \frac{\pi}{2}\left(\frac{4\pi g_J}{k^2}\right)\frac{1}{\bar{D}_{\ell J}}\left\langle\frac{\Gamma_n\Gamma_\gamma}{\Gamma}\right\rangle_{\ell J} \tag{1}$$

$$\langle\sigma_f\rangle = \sum_{\ell J} \frac{\pi}{2}\left(\frac{4\pi g_J}{k^2}\right)\frac{1}{\bar{D}_{\ell J}}\left\langle\frac{\Gamma_n\Gamma_f}{\Gamma}\right\rangle_{\ell J} \tag{2}$$

and

$$\langle\sigma_n\rangle = \sum_{\ell J}\left(\frac{4\pi g_J}{k^2}\right)\mu_{\ell J}\sin^2\phi_\ell + \sum_{\ell J}\frac{\pi}{2}\left(\frac{4\pi g_J}{k^2}\right)\frac{1}{\bar{D}_{\ell J}}\left[\left\langle\frac{\Gamma_n\Gamma_n}{\Gamma}\right\rangle_{\ell J} - 2\bar{\Gamma}_{n\ell J}\sin^2\phi_\ell\right] \tag{3}$$

respectively. The notation relating to Eqs. (1)–(3) is as follows:

$\langle\sigma_\gamma\rangle, \langle\sigma_f\rangle, \langle\sigma_n\rangle \equiv$ average capture, fission, and elastic cross sections, respectively

$k \equiv 0.00219685\ E^{1/2}A/(1 + A)$ barn$^{-1/2}$

$E \equiv$ laboratory energy in eV at which cross sections are calculated

$A \equiv$ mass of target/neutron mass

$\ell, I, J \equiv$ orbital angular momentum, target spin, and total spin, respectively

$$g_J \equiv \frac{2J+1}{2(2I+1)}$$

$\bar{D}_{\ell J} \equiv$ average level spacing

$\Gamma_{n\ell J}, \Gamma_{\gamma\ell J}, \Gamma_{f\ell J} \equiv$ neutron width, capture width, fission width, respectively

$\Gamma_{\ell J} \equiv$ total width, $\Gamma_{\ell J} = \Gamma_{n\ell J} + \Gamma_{\gamma\ell J} + \Gamma_{f\ell J}$

$\bar{\Gamma}_{n\ell J}, \bar{\Gamma}_{\gamma\ell J}, \bar{\Gamma}_{f\ell J}, \bar{\Gamma}_{\ell J} \equiv$ average neutron, capture, fission and total widths, respectively

$\bar{\Gamma}^0_{n0J} \equiv$ average reduced neutron width for $\ell = 0$, $\bar{\Gamma}_{n0J} = \bar{\Gamma}^0_{n0J}E^{1/2}$

$\bar{\Gamma}^0_{n1J} \equiv$ average reduced neutron width for $\ell = 1$, $\bar{\Gamma}_{n1J} = \bar{\Gamma}^0_{n1J}E^{1/2}\mu_{1J}\rho^2/(1 + \rho^2)$

$\mu_{\ell J} \equiv$ number of degrees of freedom for $\Gamma_{n\ell J}$

$\phi_\ell \equiv$ phase shift, $\phi_0 = \rho$, $\phi_1 = \rho - \tan^{-1}\rho$

$\rho \equiv ka$

$a \equiv$ (nuclear radius in barns)$^{1/2}$

$$\left\langle\frac{\Gamma_n\Gamma_\gamma}{\Gamma}\right\rangle_{\ell J} = \left(\frac{\bar{\Gamma}_{n\ell J}\bar{\Gamma}_{\gamma\ell J}}{\bar{\Gamma}_{\ell J}}\right)R_{\gamma\ell J}$$

$$\left\langle\frac{\Gamma_n\Gamma_f}{\Gamma}\right\rangle_{\ell J} = \left(\frac{\bar{\Gamma}_{n\ell J}\bar{\Gamma}_{f\ell J}}{\bar{\Gamma}_{\ell J}}\right)R_{f\ell J}$$

$$\left\langle\frac{\Gamma_n\Gamma_n}{\Gamma}\right\rangle_{\ell J} = \left(\frac{\bar{\Gamma}_{n\ell J}\bar{\Gamma}_{n\ell J}}{\bar{\Gamma}_{\ell J}}\right)R_{n\ell J}\,.$$

The quantities $R_{\gamma\ell J}$, $R_{f\ell J}$, and $R_{n\ell J}$ are fluctuation integrals for capture, fission, and elastic scattering, respectively. They involve averaging the quantities in the $\langle\ \rangle$ brackets over the chi-squared distributions of the appropriate number of degrees of freedom for scattering, capture, and fission widths. It is assumed that an infinite number of degrees of freedom is associated with the capture width so that averaging is actually over only the scattering and fission width distributions. L. Dresner[9] has shown that the multiple integrals may be reduced to a single integral, which may be evaluated by numerical integration.

METHOD FOR DETERMINATION OF UNRESOLVED PARAMETERS FOR ENDF/B

The resolved resonance range in the original ENDF/B version of U-235 extends up to 64.504 eV. The energy range from 64.504 eV to 50 keV was broken up into 23 intervals. The capture, scattering, and fission cross sections of the original evaluation were averaged over these intervals, and the average values were associated with the midpoint energy. A Fortran program, UR, was written which calculates $\langle\sigma_\gamma\rangle$, $\langle\sigma_f\rangle$, and $\langle\sigma_n\rangle$ from Eq. (1)–(3) using parameters for $\ell = 0$ and $\ell = 1$ resonances. This gives six (ℓ,J) pairs since $J = 3$ or 4 for $\ell = 0$ and $J = 2, 3, 4$ or 5 for $\ell = 1$. Higher ℓ values would make negligible contributions in the energy range considered. Program UR calculates $\langle\sigma_\gamma\rangle$ and $\langle\sigma_f\rangle$ using the input parameters and then varies $\bar{\Gamma}_{f0J}$ and $\bar{\Gamma}_{n0J}$ until $\langle\sigma_\gamma\rangle$, $\langle\sigma_f\rangle$ and $\langle\alpha\rangle = \langle\sigma_\gamma\rangle/\langle\sigma_f\rangle$, as calculated with the new parameters, agree with the input average values within a convergence criterion. This criterion was taken to be 0.5% in this work. The variations in $\bar{\Gamma}_{f0J}$ were carried out such that $\Delta\bar{\Gamma}_{f03}/$

$\bar{\Gamma}_{f03} = \Delta\bar{\Gamma}_{f04}/\bar{\Gamma}_{f04}$. The neutron widths $\bar{\Gamma}_{n0J}$ were varied in a similar manner. Since only constant values of $\bar{\Gamma}^0_{n\ell J}$ are allowed under the present ENDF/B formats, the calculations were repeated using constant values of $\bar{\Gamma}^0_{n0J}$ with the converged values of $\bar{\Gamma}_{f0J}$ and a large convergence criterion in order to get smooth background cross sections for capture and fission. Smooth background cross sections for elastic scattering were determined by subtracting the average values calculated from resonance parameters and constant $\bar{\Gamma}^0_{n0J}$ from the average smooth values of the original evaluation. Parameters were specified at 64.504 eV and 50 keV which yield the same cross sections as those at the midpoints of the first and last intervals. This is true because the MC^2 code would otherwise assume zero cross sections in the unresolved range below the first midpoint and above the last midpoint. Thus there is a total of 25 energies given in the unresolved region.

NUMERICAL VALUES OF UNRESOLVED PARAMETERS

The level spacings were determined from the relation

$$\bar{D}_{\ell J} = \bar{D}_J = \frac{\text{constant}}{2J+1} \exp\left(\frac{J(J+1)}{2\sigma^2}\right),$$

where $\sigma = 4$ as suggested by J. Schmidt.[10] The constant was determined by assuming an average spacing of 0.5 eV for s-wave resonances. A constant capture width of $\bar{\Gamma}_{\gamma\ell J} = 0.035$ eV was used for all (ℓ,J) pairs. The strength functions $\bar{\Gamma}^0_{n0J}/\bar{D}_{0J}$ and $\bar{\Gamma}^0_{n1J}/\bar{D}_{1J}$ were taken to be 1.0×10^{-4} eV$^{-1/2}$ and 2.0×10^{-4} eV$^{-1/2}$, respectively. There is one degree of freedom associated with each of the two reduced neutron widths for $\ell = 0$. For $\ell = 1$, the $J = 2$ and $J = 5$ reduced neutron widths have one degree of freedom, while those for $J = 3$ and 4 have two degrees of freedom. This is so because the target spin, $I = 7/2$, can combine with both channel spins $S = 1/2$ and $3/2$ to give $J = 3$ and 4.

All of the above parameters are roughly the same as those used in a number of versions of U-235 unresolved parameters. The most controversial parameters described below, are the fission widths and the associated number of degrees of freedom.

The channel theory of fission[11] relates the average fission width to the average level spacing for a given spin state by the equation

$$2\pi\frac{\bar{\Gamma}_f}{\bar{D}} = \sum_f P_f = \sum_f \frac{1}{1 + \exp[-2\pi(E - E_f)/\hbar\omega_f]}, \quad (4)$$

where E_f is the energy associated with the transition state f, and ω_f is the frequency of an inverted harmonic oscillator potential representing the fission barrier. Based on considerations in Ref. 12, two channels were assumed fully open for $\ell = 0$ and $J = 3$, and one channel was assumed fully open for $\ell = 0$ and $J = 4$. Thus we have $\Gamma_f = D/\pi$ for $J = 3$ and $\Gamma_f = D/2\pi$ for $J = 4$ as the initial values which were varied to fit the average cross sections. For $\ell = 1$, it was assumed that one channel was fully open and another had $P_f = 0.8$ for $J = 2$ and 4, and that one channel had $P_f = 0.8$ for $J = 3$ and 5. Thus we have $\Gamma_f = 1.8D/2\pi$ and $\nu_f = 2$ for $J = 2$ and 4, and $\Gamma_f = 0.8D/2\pi$ and $\nu_f = 1$ for $J = 3$ and 5, where ν_f is the number of degrees of freedom associated with the fission width. These considerations yield Γ_f values of 0.332, 0.127, 0.286 and 0.143 for $\ell = 1$ and $J = 2, 3, 4, 5$, respectively.

The nuclear radius, a, used in the calculations is 0.83668 barn$^{1/2}$ which is consistent with the C value of 0.0018302 eV$^{-1/2}$ of the resolved region of the original evaluation. Here $\rho = ka = CE^{1/2}$, where $C = 0.00219685\, aA/(1 + A)$ for a in barn$^{1/2}$ and E in eV. The value of a is significant in calculating the capture and fission cross sections at energies where $\ell = 1$ events are important. This is because of the factor $\rho^2/(1 + \rho^2)$ which is involved in the relationship of $\bar{\Gamma}_{n1J}$ to $\bar{\Gamma}^0_{n1J}$.

The unresolved resonance parameters for U-235 are summarized in Tables I-27-II and I-27-III. Table I-27-IV gives energy-dependent values of $\bar{\Gamma}^0_n$ for $\ell = 0$ which could be used in place of the constant $\bar{\Gamma}^0_n$ in Table I-27-II to avoid the necessity of having smooth capture and fission background cross sections in the unresolved region. If it is desired to use the energy-dependent $\bar{\Gamma}^0_n$ in MC^2, the smooth capture and fission cross sections could be replaced by zeroes on the BCD ENDF/B tape using CRECT, and the constant $\bar{\Gamma}^0_n$

TABLE I-27-II. UNRESOLVED RESONANCE PARAMETERS

Parameter	$\ell = 0$		$\ell = 1$			
	$J = 3$	$J = 4$	$J = 2$	$J = 3$	$J = 4$	$J = 5$
$\bar{D}$, eV	1.00	1.00	1.16	1.00	1.00	1.12
$\bar{\Gamma}^0_n$, eV$^{1/2}$	1.0×10^{-4}	1.0×10^{-4}	2.32×10^{-4}	2.00×10^{-4}	2.00×10^{-4}	2.24×10^{-4}
$\bar{\Gamma}_\gamma$, eV	0.035	0.035	0.035	0.035	0.035	0.035
$\bar{\Gamma}_f$, eV	Table I-27-III		0.332	0.127	0.286	0.143
ν_f	2	1	2	1	2	1
μ	1	1	1	2	2	1

TABLE I-27-III. ENERGY-DEPENDENT FISSION WIDTHS FOR $\ell = 0$

E, eV	$\bar{\Gamma}_{f03}$, eV	$\bar{\Gamma}_{f04}$, eV	E, keV	$\bar{\Gamma}_{f03}$, eV	$\bar{\Gamma}_{f04}$, eV	E, keV	$\bar{\Gamma}_{f03}$, eV	$\bar{\Gamma}_{f04}$, eV
64.504	0.29474	0.14737	0.85	0.23327	0.11663	12.5	0.43837	0.21918
82.0	0.29264	0.14632	1.25	0.30220	0.15110	17.5	0.43870	0.21935
125.0	0.24623	0.12311	1.75	0.35300	0.17650	22.5	0.45035	0.22517
175.0	0.24258	0.12129	2.50	0.42449	0.21225	27.5	0.47280	0.23640
225.0	0.26413	0.13207	3.50	0.32358	0.16179	35.0	0.52078	0.26039
275.0	0.49705	0.24852	4.50	0.32196	0.16098	45.0	0.59992	0.29996
350.0	0.27310	0.13655	5.50	0.32284	0.16142	50.0	0.57033	0.28517
450.0	0.45109	0.22554	7.00	0.33009	0.16505			
600.0	0.44004	0.22002	9.00	0.33291	0.16646			

could be replaced with the variable $\bar{\Gamma}_n^0$ in processing the data through ETØE.

DISCUSSION OF UNRESOLVED RESONANCE PARAMETERS

The U-235 unresolved resonance parameters described here are by no means unique. They should do an adequate job of predicting criticality since they were chosen to yield average values of the infinite dilution capture and fission cross sections of the original evaluation. Since U-235 is not normally strongly self-shielded in reactors, little error in criticality should be possible. The fact that background capture and fission cross sections are necessary because of the constant $\bar{\Gamma}_n^0$ restriction does introduce some error in self-shielding.

As mentioned above, the fission widths and associated numbers of degrees of freedom are the most controversial of the unresolved resonance parameters. The values recommended here are based on the channel theory of fission. This results in fission widths which are larger than averages of experimental fission widths for resolved resonances. A possible explanation is the assumption that wide resonances may be missed experimentally because of the associated small peak height. Also it is possible, as pointed out by J. Lynn,[13] for two wide resonances to interfere in such a way as to yield what appears to be a single narrow resonance. Another point of view is to accept average fission widths more in line with averages of resolved widths, and to choose higher numbers of degrees of freedom (approximately 4) in order to decrease the ratio R_γ/R_f. This can yield about the same $\langle\alpha\rangle$ as larger fission widths and smaller numbers of degrees of freedom.

The present fitting technique varied $\bar{\Gamma}_n^0$ and $\bar{\Gamma}_f$ for the s-wave resonances to agree with the capture and fission data. Other parameters could have been varied, or the s-wave $\bar{\Gamma}_n^0$ and $\bar{\Gamma}_f$ could have been varied in a different manner. It might have been better at high energies to vary some of the $\ell = 1$ parameters since p-wave contributions become increasingly important as the energy increases. The values of the average capture width, the p-wave strength function, the nuclear radius,

TABLE I-27-IV. ENERGY-DEPENDENT $\bar{\Gamma}_n^0$ FOR $\ell = 0$ TO AVOID SMOOTH CAPTURE AND FISSION BACKGROUND

E, eV	$\bar{\Gamma}_n^{0\,(a)}$, eV$^{1/2} \times 10^{-4}$	E, keV	$\bar{\Gamma}_n^{0\,(a)}$, eV$^{1/2} \times 10^{-4}$	E, keV	$\bar{\Gamma}_n^{0\,(a)}$, eV$^{1/2} \times 10^{-4}$
64.504	0.73528	0.85	1.0712	12.5	1.0641
82.0	0.83252	1.25	1.1125	17.5	1.0775
125.0	0.97151	1.75	1.0351	22.5	1.0665
175.0	1.0129	2.50	0.99587	27.5	1.0499
225.0	1.2508	3.50	1.0654	35.0	1.0179
275.0	1.1250	4.50	1.1134	45.0	0.94713
350.0	0.94534	5.50	1.1618	50.0	1.0026
450.0	1.0079	7.00	1.0974		
600.0	1.1528	9.00	1.1569		

[a] The $\bar{\Gamma}_n^0$ values apply to both $J = 3$ and $J = 4$.

and the average s-wave level spacing are all somewhat uncertain, although the values used here should be reasonable. Also the method of calculation of level spacings for various J values is open to question, and the results are considerably different from the often used $1/(2J + 1)$ dependence. In conclusion, it is felt that the present set of unresolved parameters for U-235 is adequate for exploratory calculations, but is certainly not a definitive set.

REFERENCES

1. B. J. Toppel, A. L. Rago and D. M. O'Shea, *MC²*, *A Code to Calculate Multigroup Cross Sections*, ANL-7318 (1967).
2. E. M. Pennington, J. C. Gajniak and W. Bohl, *Fortran Codes for Processing Neutron Cross Section Data*, Reactor Physics Division Annual Report, July 1, 1966 to June 30, 1967, ANL-7310, pp. 442–444.
3. E. M. Pennington, *Compilation of ENDF/B Cross Sections for Magnesium, Titanium, Vanadium, Molybdenum and Gadolinium*, Reactor Physics Division Annual Report, July 1, 1966 to June 30, 1967, ANL-7310, pp. 22–30.
4. E. M. Pennington and J. C. Gajniak, *Compilation of ENDF/B Data for Magnesium, Titanium, Vanadium, Molybdenum and Gadolinium*, ANL-7387 (1968).
5. D. M. Green and T. A. Pitterle, "*ETØE, A Program for*

ENDF/B to MC² Data Conversion, APDA Technical Memorandum No. 44 (1967).
6. D. M. Green, Atomic Power Development Associates (private communication).
7. H. Amster, *Evaluation of the Cross Section Transformation Matrices of Zweifel and Hurwitz*, J. Appl. Phys. **27**, 307 (1956).
8. H. Amster, *Heavy Moderator Approximations in Neutron Transport Theory*, J. Appl. Phys. **29**, 623 (1958).
9. L. Dresner, *Resonance Absorption of Neutrons in Nuclear Reactors*, ORNL-2659, (1959).
10. J. J. Schmidt, *Neutron Cross Sections for Fast Reactor Materials*, KFK-120, Part I: Evaluation, (1966) pp. E25, E26, D101.
11. D. L. Hill and J. A. Wheeler, *Nuclear Constitution and the Interpretation of Fission Phenomena*, Phys. Rev. **89**, 1102 (1953).
12. J. E. Lynn, *Interpretation of Neutron-Induced Fission Cross Sections and Related Data*, Proc. Conference on Nuclear Data for Reactors, Paris, October 17–21, 1966; IAEA, Vienna (1967), Vol. II.
13. J. E. Lynn, *Quasi-Resonances and the Channel Theory of Neutron-Induced Fission*, Nuclear Structure Study with Neutrons, Proc. International Conference on the Study of Nuclear Structure with Neutrons, Antwerp, July 19–23, 1965 (North Holland Publishing Company, Amsterdam, 1966).

Section II

Thermal Reactor Physics

During the past several years, the thermal reactor projects (High Conversion Experiments, Experimental Boiling Water Reactor Plutonium Measurements, and the Argonne Advanced Research Reactor) and related studies were being completed or were otherwise terminated. Concurrently, the Liquid Metal Fast Breeder Reactor (LMFBR) program, which has been well established in the Reactor Physics Division for a number of years, was increasingly emphasized. The result of these events accounts for the relatively limited description of thermal reactor work in this report.

II-1. Revised Conversion Ratio Results for 3% and 5% Enriched UO_2-Fueled H_2O-Moderated Cores

K. E. Plumlee

Introduction

Revised results have been issued for the conversion ratio measurements reported[1] for 3% and 5% enriched UO_2 fueled cores. All the results have been revised downward, by net relative reductions of ~4% to 15%. The revision resulted from a more appropriate method of data analysis than originally used. The improved analysis adjusts accurately for the epicadmium flux component present in the graphite thermal columns, which affected the reference irradiations used for normalization of these measurements.

The revised results for initial conversion ratios range from 0.44 ± 0.01 to 1.25 ± 0.04 for H:U-238 atom ratios of 4.16 down to 0.50 (which is a subcritical composition), using 3.04 w/o enrichment UO_2 fuel and H_2O moderator and reflector. The UO_2 pellet diameter was 0.935 cm and an average of 853.3 g was contained as a 121.9 cm length column in each fuel element. The cladding was 1.06 cm o.d. stainless steel, with 0.05 cm wall thickness.

It was suspected that the conversion ratios originally reported for the last core of the series assembled for these measurements were too high, and that the reason for this might have affected other results as well.[2] A remeasurement had been made, but the additional data did not change the results. Since then, the original data have been reevaluated.

Original Methods of Data Treatment

The modified conversion ratio (MCR) and initial conversion ratio (ICR) were measured according to Eqs. (1) and (2). The measured capture and fission rates in the cores were compared with those of similar materials irradiated simultaneously in the thermal, or reference, flux of a graphite thermal column for which thermal cross sections apply.

$$\mathrm{MCR} = \left[\frac{N^{28}}{N^{25}}\right]\left[\frac{P}{R}\right]\left[\frac{\sigma_c^{28}}{\sigma_f^{25}}\right]_{\mathrm{TC}} \tag{1}$$

$$\mathrm{ICR} = [\mathrm{MCR}]\left[\frac{1}{1+\alpha^{25}}\right] \tag{2}$$

N^{28} and N^{25} are the atom number densities of U-238 and U-235, respectively, in the core. P is the measured ratio of neutron capture by U-238 in a thin slice of UO_2 across a fuel pellet, to capture by U-238 in an identical UO_2 disc during a simultaneous irradiation in a thermal flux (i.e. a reference irradiation in a thermal column). R is the ratio of fissions in U-235 in the same two samples. The cross sections (σ) are for the thermal column (reference) flux only, and it is necessary to adjust those values quite accurately for self-shielding, as for example, to avoid errors in the estimates of capture-to-fission ratios in the reference irradiations. The term α^{25} is the calculated capture-to-fission ratio for U-235 in the core.

Difficulty was encountered because of a significant epithermal flux component present in the thermal column regions used for reference irradiations, some of which were made fairly close to the source plane. Because U-238 has a low energy resonance, epicadmium capture by U-238 in the thermal columns varied significantly with surface area. For the first two reference irradiations, the 0.03 mm thick gold cadmium ratios (CdR) were 50 and 90, respectively. Following these, reference irradiations were made in a semi-permanent graphite thermal column at locations where the CdR of the gold ranged from 105 to 115. For the last two core loadings the usual location was not available, and the reference measurements were made in thermal column locations for which the CdR's were 32 and 35 for gold and 7.9 and 8.7 for U-238. From the observed ratio of $(\mathrm{CdR\text{-}1})_{\mathrm{U\text{-}238}}/(\mathrm{CdR\text{-}1})_{\mathrm{Au}} = 0.22 \pm 0.01$, it was concluded that CdR's of U-238 equal to ~12 and ~21 corresponded with CdR's of gold of 50 and 90 respectively.

The thermal column (TC) flux had been too low for accurate measurement of the CdR of U-238 initially, and it was decided to use the formula for C. Westcott's (two-group) cross sections[3] to account for the epicadmium flux component present, as in Eq. (3); where g, r, and S are Westcott's tabulated factors:

$$\sigma_{eff} = \sigma_{2200}\sqrt{\frac{\Pi T_0}{4T_n}}\,[g(T) + rS(T)]. \tag{3}$$

Substitution of these terms into Eq. (1) results in

$$\mathrm{MCR} = \left[\frac{N^{28}}{N^{25}}\right]\left[\frac{P}{R}\right]\left[\frac{\sigma_c^{28}}{\sigma_f^{25}}\right]_{2200} \cdot \left[\frac{g_c^{28}(T) + rS_c^{28}(T)}{g_f^{25}(T) + rS_f^{25}(T)}\right]_{\mathrm{TC}}. \tag{4}$$

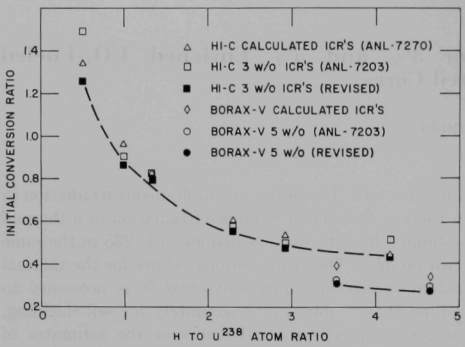

FIG. II-1-1. Conversion Ratios in UO_2 Fueled, H_2O Moderated Cores. *ANL Neg. No. 113-790.*

Since the ratio $(\sigma_c^{28}/\sigma_f^{25})$ is used, the explicit temperature terms of Eq. (3) cancel in Eq. (4). (It can be shown that the implicit temperature dependence is small by substitution of typical approximations for $g(T)$ and $S(T)$ for which the temperature dependence cancels.) The neutron temperature in a graphite thermal column is close to room temperature, and any reasonable estimate of neutron temperature should be adequate for use with Eq. (4), since only the ratios of capture-to-fission in the thermal columns are obtained from calculated cross sections.

Equations (3) and (4) apply only to infinite dilution conditions, and adjustments must be made for both thermal and resonance self-shielding in the discs irradiated for reference use if these equations are used with accuracy.

Some preliminary results were obtained using Eq. (4), effectively, but in subsequent reference irradiations it was found that the calculated cross sections for U-238, using Eq. (3), were not very consistent with the measured specific activities. A wide variety of compositions and dimensions of metallic uranium foils and UO_2 discs and pellets had been irradiated in the graphite thermal column in testing the calculated cross sections. Although $[rS_c^{28}(T)]$ varied significantly, the quantity $[rS_f^{25}(T)]$ proved to be negligible in the reference irradiations.

The measured subcadmium U-238 capture rates and U-235 fission rates were quite consistent with the calculated (self-shielded) cross sections, and as a consequence the subcadmium U-238 capture rates were used for the original MCR and ICR results.[2] Effectively, each value of P used in Eq. (4) had been revised by multiplication by the quantity [CdR/(CdR-1)] measured, or estimated, for U-238 capture in the corresponding reference irradiation.

The use of these subcadmium thermal column activities required the removal of the $[rS(T)]$ terms from Eq. (4) as in the revised Eq. (9). During the recent review of the Hi-C data it was found that this had not been done originally. The original results had been obtained by substitution of terms resembling P^* and R^*, as defined for use with Eq. (9), in place of P and R in Eq. (4).

Modified Equations for Subcadmium or for Thermal Activation Ratios

The modification of Eq. (4) to use subcadmium or thermal activations for normalization required the following terms, including Westcott's expression[3] for infinite dilution cadmium ratio, shown as Eq. (6).

$$\frac{\text{Subcadmium Activation}}{\text{Bare Foil Activation}} = \frac{\text{CdR-1}}{\text{CdR}}, \tag{5}$$

$$\text{CdR} = \frac{g(T) + rS(T)}{rS(T) + rP_{cd}(T)}, \tag{6}$$

$$P^* = \frac{\text{Bare Capture Rate in Core}}{\text{Subcadmium Capture Rate in TC}} = P\left[\frac{g_c^{28}(T) + rS_c^{28}(T)}{g_c^{28}(T) - rP_{cd}(T)}\right], \tag{7}$$

$$R^* = \frac{\text{Bare U-235 Fission Rate in Core}}{\text{Subcadmium U-235 Fission Rate in TC}} = R\left[\frac{g_{fiss}^{25}(T) + rS_{fiss}^{25}(T)}{g_{fiss}^{25}(T) - rP_{cd}(T)}\right], \tag{8}$$

$$\text{MCR} = \left[\frac{N^{28}}{N^{25}}\right]\left[\frac{P^*}{R^*}\right]\left[\frac{\sigma_c^{28}}{\sigma_f^{25}}\right]_{2200} \cdot \left[\frac{g_c^{28}(T) - rP_{cd}(T)}{g_{fiss}^{25}(T) - rP_{cd}(T)}\right]. \tag{9}$$

Use of thermal activations rather than subcadmium activations made no significant difference in these results; however, the definitions of P^* and R^* would be slightly different from that shown above, and the quantity $P_{cd}(T)$ would not appear explicitly in Eq. (9) if derived for thermal activations. Since $rP_{cd}(T)$ is shown to be negligible, the equations for subcadmium rates in the thermal column are equally precise and somewhat simpler than for thermal activations.

The value of $rP_{cd}(T)$ is indicated by substitution of an infinite dilution CdR of gold into Eq. (6) and solving for $rP_{cd}(T)$, which is negligible. Since the thermal column flux is very close to thermal neutron temperature the 25°C values for $g(T)$ and $S(T)$ were used. Using data from Ref. 4 to extrapolate data from these foils to infinite dilution gives: $(\text{CdR})_{inf.\ dil.} = 1 + 0.39\,(\text{CdR-1})_{meas}$. The infinite dilution CdR's of gold of 13.1, 14.3, 20.1, 35.7, 41.6 and 45.5 correspond to measured CdR's of gold of 32, 35, 50, 90, 105 and 115 respectively. Using the tabulated[3] values of $g = 1.006$ and $S \approx 17.5$ for gold indicated that $0.0005 < rP_{cd}(T) <$

0.0025 for the various thermal column locations. (The value[3] of $P_{cd}(T)$ is approximately 0.5.)

The revised ICR's are plotted versus H:U-238 atom ratio in Fig. II-1-1 along with calculated ICR's from Ref. 5 and the original values from Ref. 1. A slightly different set of cross sections and α^{25} values were used in the calculations. The use of those cross sections in the experimental data analysis would reduce the revised MCR's and ICR's by about 1.6%, and thus would increase the differences significantly. The use of the same values of α^{25} would slightly increase most of the experimental points, but a change of no more than ±0.5% would result. The net effect would be to slightly decrease the average difference. The BORAX-V results involved reference runs in which the CdR's of gold were 50 and 90, and the extreme left and right Hi-C results, as plotted, involved reference conditions where CdR's of gold were 32 and 35.

Effect of Use of Currently Recommended Cross Sections

Recommended cross sections obtained from Ref. 6 were used for the revised conversion ratios reported herein. These include $\sigma_f^{25} = 577.1$ and $\sigma_c^{28} = 2.73$ b for 0.0253 eV energy neutrons. The values used for the results given originally were listed as $\sigma_f^{25} = 581.95$ and $\sigma_c^{28} = 2.72$ b. Use of the currently recommended cross sections increased the results by 1.2% relatively, compared with the use of the older cross section.

References

1. K. E. Plumlee, *Addendum to the Report on the High Conversion Critical Experiments*, ANL-7203 (Addendum).
2. A. R. Boynton, Q. L. Baird, K. E. Plumlee, W. C. Redman, W. R. Robinson and G. S. Stanford, *High Conversion Critical Experiments*, ANL-7203 (1967).
3. C. H. Westcott, *Effective Cross Section Values for Well-Moderated Thermal Reactor Spectra*, AECL-1101 (CRRP-960) (November 1960).
4. N. P. Baumann, *Resonance Integrals and Self-Shielding Factors for Detector Foils*, DP-817 (January 1963).
5. E. M. Pennington, *Analysis of High Conversion Critical Experiments*, ANL-7270 (March 1967).
6. Neutron Cross Sections, BNL-325, Second Edition, Supplement No. 2.

II-2. Activation Measurements in the Plutonium Recycle Core of the Experimental Boiling Water Reactor (EBWR)

K. E. Plumlee, R. E. Grajek and K. E. Freese

Introduction

Activation measurements were made in the Plutonium Recycle Core[1] of the Experimental Boiling Water Reactor (EBWR) to obtain data relevant to the thermal and epithermal neutron energy distributions; to indicate the spatial distribution of the neutron flux; and to permit a comparison with data already available for uranium-fueled systems. Activations were obtained during critical operation at a few hundred watts of fission power with the core at room temperature, and also during power operation at levels of 37, 40, 61, and 70 MW with production of 600 psig (~490°F) steam. Insofar as was feasible, experiments which had been performed before power operation commenced were repeated near the end of the recycle operation. The limited availability of personnel for such experiments and the early termination of the program, followed by prompt unloading of the Plutonium Recycle Core, prevented duplication of measurements. In a few instances it would have been helpful to confirm the results by remeasurements.

Core Description

The plutonium fuel region where the measurements were made was loaded with vibration-compacted rods consisting of 1.5 w/o PuO_2 blended with depleted UO_2 (0.22 w/o U-235 in U), and contained by 0.025 in. wall thickness × 0.372 in. i.d. Zircalloy-2 tubing. The isotopic composition of the plutonium was 91.4 w/o Pu-239, 7.8 w/o Pu-240, and 0.73 w/o Pu-241. The oxide fuel content averaged 827 g, 88% being uranium and plutonium. The length of the oxide portion was 48 in. The fuel rods were positioned by grids in a 0.569 in. pitch square lattice, and 36 rods filled a 3.75 in. square assembly. As indicated by Fig. II-2-1, there were nine such assemblies in the square formed by four control blades. The central plutonium region was bounded by rows of 6 w/o enriched UO_2 (Eu, 1st, and 2nd shim zones). The outermost or blanket region was loaded with natural uranium oxide filled rods (designated U). Some of the access positions for irradiation experiments are also indicated.

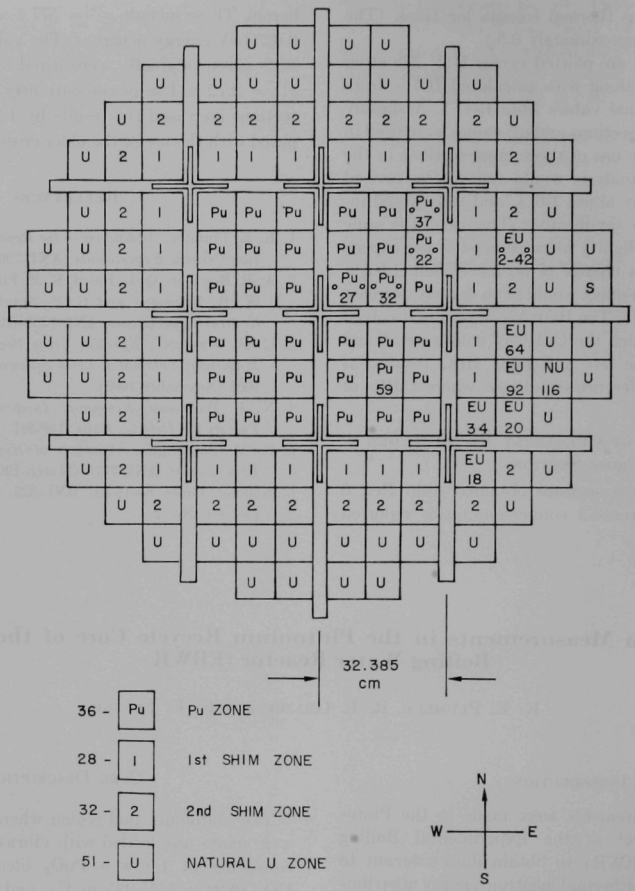

FIG. II-2-1. EBWR Fuel-loading Diagram Showing Locations of Foil Irradiation Facilities. *ANL Neg. No. 113-325.*

Irradiation Positions

The room temperature irradiations were obtained by insertion of foils to a point 2 cm above the center grid. There were various fixtures, one for pressing foil holders against fuel rods, for reproducibility, and another for measuring the distribution of flux between rods by means of five parallel wires.

The measurements during 35 MW to 70 MW power were made inside miniature "rabbit tubes" of $^3/_{16}$ in. o.d. Inconel tubing. The chains were inserted and withdrawn pneumatically at positions shown by Fig. II-2-1 as Pu-22, 27, 32, 37, and Eu 2-42.

Cadmium Ratios during Critical Operation

Activations of 0.32 cm diam foils in 0.051 cm thick aluminum or cadmium pill boxes were obtained at the beginning and the end of the 3,000 MWD/Tonne fuel cycle. The boxes were pressed against the fuel rods, but positioning errors may have caused some bad data. The positioning errors resulted from twisting of the 20 ft long insertion tools.

Cadmium ratios (CdR) are listed in Table II-2-I for the plutonium-fueled region. The results for several materials, including U-235 fission CdR, are in good agreement with a linear relation between the

TABLE II-2-I. CADMIUM RATIOS MEASURED DURING CRITICAL OPERATION

Material	Core Exposure		Expected for Uranium Oxide Cores[2]	
	Zero	~3,000 MWD/Tonne	Zero Exposure	~3,000 MWD
Au (0.03 mm)	1.89	1.93	2.0	2.1
Cu	4.7 to 5.8	5.1	5.7	6.0
In (0.03 mm)	1.63	2.42	2.0	2.1
Ir-192	2.62	1.4 to 2.0	—	—
Ir-194	1.23	1.1 to 1.9	—	—
Lu-176	1.13	1.19	—	—
Lu-177	12.9	12.0 to 23.0	—	—
Mn	6.4	6.4	6.0	6.4
U-235 fission	9.5 ± 0.06	10.4 ± 0.1	9.9	10.5
Pu-239 fission	8.3 ± 0.1	7.6 to 11.2	—	—

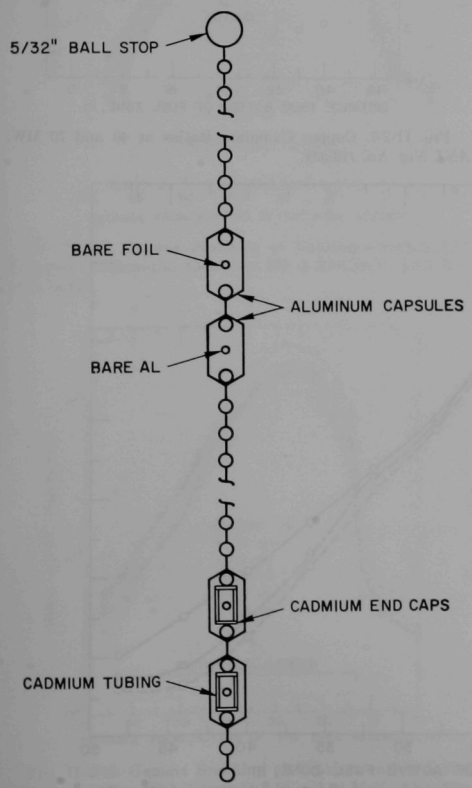

FIG. II-2-2. Bead Chain Assemblies with Alternating Bare and Cadmium-covered Foils. *ANL Neg. No. 113-317.*

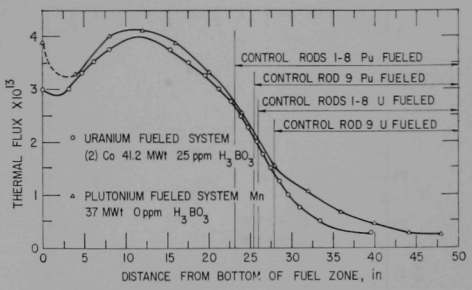

FIG. II-2-3. Comparison of Activation Distributions in Plutonium-Fueled and Uranium-Fueled Cores. *ANL Neg. No. 113-324.*

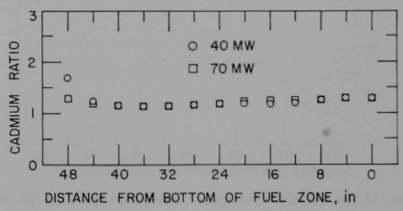

FIG. II-2-4. Gold Cadmium Ratios at 40 and 70 MW. *ANL Neg. No. 113-316.*

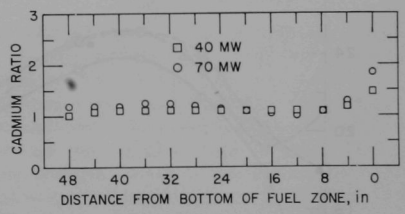

FIG. II-2-5. Lu-176 Cadmium Ratios at 40 and 70 MW. *ANL Neg. No. 113-315.*

quantities (CdR-1) and moderating ratio (MR) of enriched uranium-fueled cores.[2] These results indicate that the CdR's of manganese and U-235 are only slightly affected by the presence of up to 1.5 w/o plutonium in oxide-fueled cores and that the calculation of moderating ratio for a core is sufficient for accurate prediction of these CdR's.

On the other hand, the CdR of gold was depressed slightly below the linear plots for uranium cores. This difference was attributed to resonance absorption by the plutonium isotopes, which depleted the epithermal flux and thereby reduced the number of neutrons thermalized. Because gold has a resonance at a higher energy than some of the plutonium resonances, the

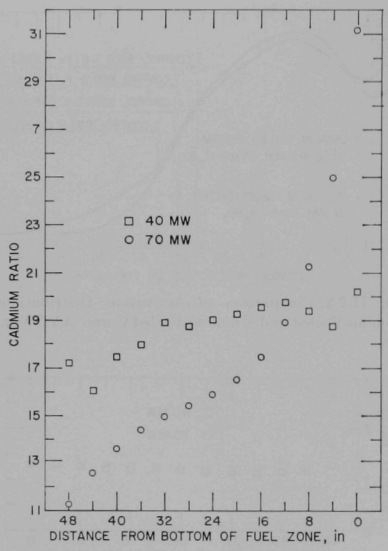

FIG. II-2-6. Lu-177 Cadmium Ratios at 40 and 70 MW. *ANL Neg. No. 113-319.*

epicadmium activation of gold may not have been reduced proportionally with the subcadmium activations. Thus the presence of 1.5 w/o plutonium reduced the CdR of gold by about 5% compared with that expected in uranium oxide fueled cores.

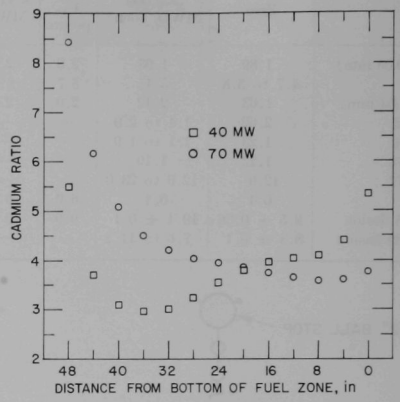

FIG. II-2-7. Copper Cadmium Ratios at 40 and 70 MW. *ANL Neg. No. 113-328.*

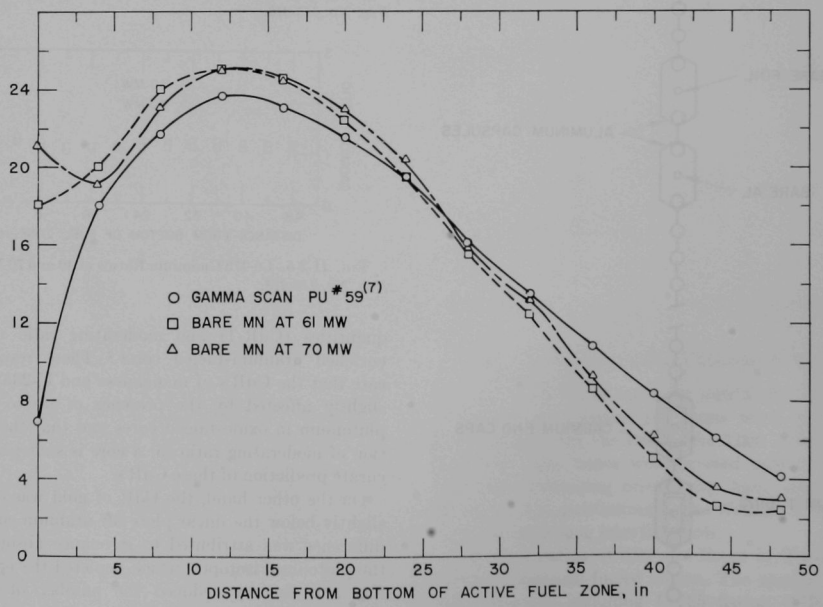

FIG. II-2-8. Power-distribution Comparison Using Manganese Subcadmium Activation and Element-gamma Scanning. *ANL Neg. No. 113-308.*

Activity Distributions and Cadmium Ratios during Operation at 37 MW to 70 MW Power Levels

A brief summary of in-core irradiations is given for power levels of 37, 40, 61, and 70 MW in Ref. 3. The analysis of these data to obtain measured activation ratios between various isotopes is still pending.

The spherical foils used were 0.0625 ± 0.002 in.

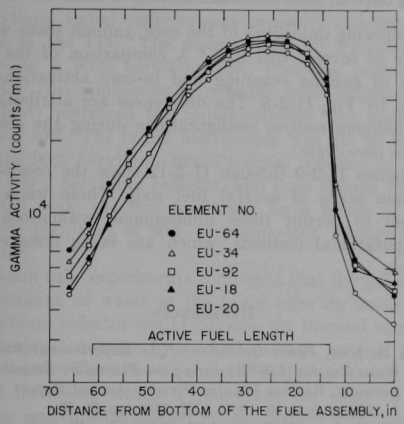

Fig. II-2-9. Gamma Scanning of Uranium-enriched Fuel Elements; Differential Counts at 165 ± 0.02 MeV. *ANL Neg. No. 113-327.*

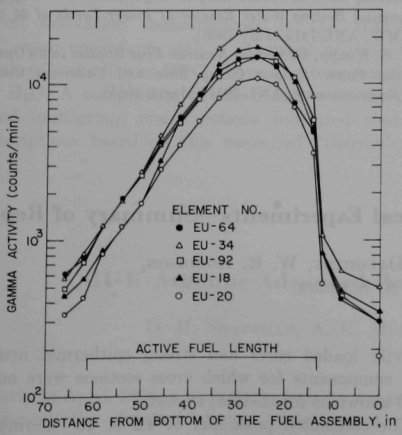

Fig. II-2-10. Gamma Scanning of Uranium-enriched Fuel Elements; Differential Counts at 2.55 ± 1.04 MeV. *ANL Neg. No. 113-309.*

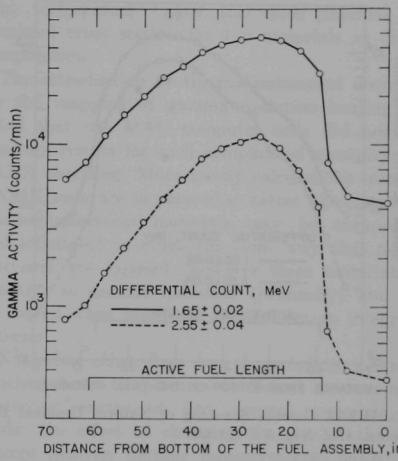

Fig. II-2-11. Gamma Scanning of Plutonium Fuel Elements. *ANL Neg. No. 113-311.*

diam high purity aluminum alloy containing one of the following:

Gold	0.065%	Manganese	1.0%
Copper	1.00%	Lutetium	6.0%
Indium	0.035%	Iridium	0.25%

High-purity aluminum

Bare and cadmium-covered foils were encapsulated in ⅜ in. long, 0.116 in. o.d., 0.100 in. i.d. aluminum tubing by forming the ends over the 3/32 in. o.d. aluminum bead chain. Cadmium covers used were fashioned from tubing with a 15 mil thickness, and the end caps were punched from a 15 mil sheet. Each chain assembly contained bare and cadmium-covered spheres in alternate positions, as shown in Fig. II-2-2.

During the early stages of the experiment, interference was found from Na-24 activity resulting from the Al-27 (n,α) reaction, which has an effective threshold above 6 MeV. This problem was overcome by accompanying each activation capsule with one capsule containing a high-purity aluminum sphere to be used for background subtraction. The chain used to transport the spheres is designed to position the top sample at the top of the fuel zone. The samples are spaced at 4 in. intervals, to give a total of 13 positions throughout the fuel zone. Chains are positioned by attaching a ball-stop at a premeasured distance above the first sample.

Lutetium and iridium, each of which contained two active isotopes, required special counting considerations. These foils were initially counted shortly after irradiation, which yielded the total activation

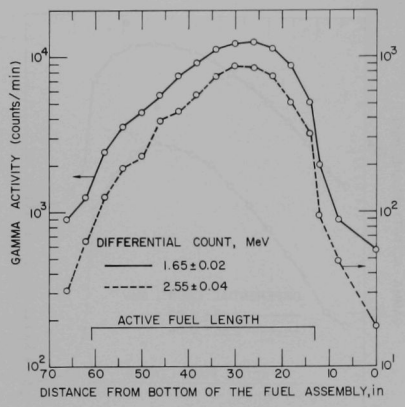

FIG. II-2-12. Gamma Scanning of Natural Uranium Fuel Elements. *ANL Neg. No. 113-322.*

of both isotopes. The individual activity of each isotope was determined by recounting the foils at the same discriminator bias after the short half-lived isotope had decayed. To reproduce the discriminator level setting, a standard americium source was used for the calibration of each isotope. For lutetium, the bias was set just below the Am-241 0.06 MeV energy peak; for iridium, the Am-243 0.106 MeV energy peak was used. Identical foils were irradiated simultaneously in the Argonne Thermal Source Reactor (ATSR) graphite pile for calibration.

The resulting traverses were compared with one another and with data available from uranium-fueled cores,[4] as shown by Fig. II-2-3. The differences shown are mostly attributable to differences in operating configurations.

The cadmium ratios of activities such as gold and Lu-176 were close to unity and were only slightly affected by changes in power level, as shown by Figs. II-2-4 and II-2-5, but those of Lu-177 and copper were strongly affected as shown by Figs. II-2-6 and II-2-7.

Information of the nature reported is useful in evaluation of the effects of temperature and of steam void fraction on activation ratios and on neutron energy distributions.

Post-Shutdown Gamma Scans of Fuel Rods

Following unloading of the core, gamma scans were made of several fuel rods.[3] A comparison of the results of gamma scanning and in-core activations is given by Fig. II-2-8. The differences are attributable to changing control configurations during the course of the core cycle.

Figures II-2-9 through II-2-12 show the results of gamma scans of several fuel rods. These were obtained to permit three dimensional evaluations of computational methods, which are being done elsewhere.

References

1. P. H. Kier, *Power Operation of the Experimental Boiling Water Reactor (EBWR) during the Plutonium Recycle Experiment*, Reactor Physics Division Annual Report, July 1, 1966 to June 30, 1967, ANL-7310, pp. 38–39.
2. A. R. Boynton, Q. L. Baird, K. E. Plumlee, W. C. Redman, W. R. Robinson and G. S. Stanford, *High Conversion Critical Experiments*, ANL-7203 (January 1967).
3. R. E. Grajek and K. E. Freese, *In-Core Activation Traverses during the Plutonium Recycle Experiment in the Experimental Boiling Water Reactor at Power Levels of 35 to 70 MW*, ANL-7414 (July 1968).
4. W. G. Knapp, *Method for Neutron-Flux Studies in an Operating Power Reactor Using Bare and Cadmium Covered Radioactivants*, ANL-7011 (March 1965).

II-3. Argonne Advanced Research Reactor Critical Experiments—Summary of Report

K. E. Plumlee, G. S. Stanford, J. W. Daughtry, W. R. Robinson, T. W. Johnson and R. A. Schultz

A report[1] has been prepared describing critical experiments with stainless steel clad highly enriched uranium cores which were studied during the design of the Argonne Advanced Research Reactor[2] (AARR). Excellent agreement has been reported[3] between the experimental data and reactor calculations, over a wide range of fuel loading densities. The heavily loaded cores had strong epithermal neutron flux components for which cross sections were not as well known as for thermal systems.

The calculated peak flux of 4.2×10^7 thermal n/cm^2-sec in the internal thermal column (ITC) per watt of total power in the critical experiment (see Paper II-5) was confirmed within the limits of ex-

perimental errors. The AARR stainless steel core reference design is not expected to provide quite as high a peak flux per unit power as did the critical experiment, because of differences in structure, composition and dimensions of the reflector. Installation of a detailed reflector mockup had been planned but critical experimentation was terminated before it could be prepared. The experimental results reported are for fairly simple radial reflector structures which crudely simulated the reference design.

The maximum thermal neutron flux in the 100% beryllium radial reflector was typically one-third of that in the ITC. The incorporation of Plexiglas to provide a 90% beryllium-10% Plexiglas radial reflector (i.e. simulating a reflector with hydrogenous coolant) increased the radial reflector flux peak by about 10%. The radial distribution was not as broad in the 90% beryllium-10% Plexiglas reflector as with the 100% beryllium reflector, and even though higher at the peak, the flux was lower by a factor of two at the periphery of 90% beryllium-10% Plexiglas reflector.

Beam tube experiments confirmed that the judicious positioning of water at the beam tube tip inside the beryllium reflector would increase the thermal neutron (emergent) current by several percent, as had been predicted.[4] The ratio of thermal to fast neutrons was also increased, which is important for some of the beam experiments desired in conjunction with AARR. Again, these were somewhat preliminary experiments and it may be profitable to investigate further into the geometry required for optimization of beam tube yields.

Foil activation measurements in the H_2O-filled ITC were consistent with a "thermal neutron temperature" which was 30°C above the temperature of the H_2O. A comparison of this result with the computed multigroup cross sections indicated that the prescriptions based on this measured "thermal neutron temperature" gave the same thermal flux-averaged cross section for 1/v materials as did the computation.

The introduction of thermoluminescent dosimetry[5] for the mapping of gamma radiation heating indicated that the MAC computer code did not yield accurate results for such complicated geometry as in AARR shielding. More recent calculations using the ANISN code are in somewhat better agreement. The thermoluminescent materials may be encapsulated and irradiated in much the same way that neutron activants are exposed; however these materials are sensitive to gamma radiation (primarily) and must be heated when ready for readout by an integrating detector.

Numerous other data are presented in the report which includes temperature coefficient measurements; reactivity worths of fuel, control materials, and voids; the effect of changing the size of the ITC; prompt neutron lifetime measurements; pulsed neutron measurements; and fast neutron yield (from beam tubes) measurements.

References

1. K. E. Plumlee, J. W. Daughtry, T. W. Johnson, W. R. Robinson, R. A. Schultz and G. S. Stanford, *Argonne Advanced Research Reactor Critical Experiments*, ANL-7483, (to be published).
2. L. W. Fromm, J. F. Matousek, R. R. Rhode, D. H. Shaftman and J. H. Tessier, *Preliminary Safety Analysis Report on the Argonne Advanced Research Reactor*, ANL-7448 (1968).
3. R. P. Savio and D. H. Shaftman, *Argonne Advanced Research Reactor Calculations—Analysis of the Critical Experiments with the Intermediate Spectrum Core*, Reactor Physics Division Annual Report, July 1, 1967 to June 30, 1968, ANL-7310, pp. 94–99.
4. C. N. Kelber, *Enhancement of Experimenter's Fluxes in the Argonne Advanced Research Reactor*, Trans. Am. Nucl. Soc. **6**, 5 (1963).
5. G. S. Stanford and T. W. Johnson, *Determination of Gamma-Ray Heating in a Critical Facility by Thermoluminescent Dosimetry*, ANL-7373 (1968).

II-4. Argonne Advanced Research Reactor Calculations—Preface

D. H. Shaftman, A. E. McArthy, R. P. Savio* and L. K. Volodka

Early in April, 1968, a budgetary decision was made to cancel the detailed design, procurement, and fabrication efforts on the Argonne Advanced Research Reactor (AARR). In the time period beyond the preceding Annual Reports on the project physics work for the AARR,[1] the needs of the project for detailed design information dominated the reactor physics studies, and many abbreviated, specialized

* Reactor Operations Division, Argonne National Laboratory.

calculations were made to resolve these needs. Some of the detailed results are summarized in Papers II-5 through II-7, but, in general, results of broader interest have been selected for presentation.

Paper No. II-5, on general reactor physics analyses of the AARR, includes discussions, formulas, and data which are of more general interest for an understanding of the reactor physics of this type of high-flux research reactor. Also in this paper are results of some of the more specialized studies referred to above, including, for example, calculations relating to the reactivity shutdown margins of new fuel elements of the HFIR type in water. These calculations were performed to determine the importance of reactivity monitoring of fuel assemblies while in transit.

Paper II-5 also is concerned with one of the important problems of the earlier analyses, namely, the spatial variation of the thermal neutron flux in the reflectors and especially farther out in the external radial beryllium reflector. In the earlier 16-group statics calculations of neutron flux, a model of a net neutron downscattering from (thermal) group No. 15 [0.1–0.4 eV] to group No. 16 was used. Paper II-5 summarizes comparisons of thermal neutron flux spectra and total thermal neutron flux for various multigroup models.

Paper II-6 summarizes the status of the shield design and shield-design analyses for the AARR at the time of Project cancellation.

In Paper II-7, a theoretical correlation is suggested for the efficiencies of internal flux traps in intermediate-spectrum and thermal-spectrum reactors of the AARR/HFIR type. These results and other remarks in Paper II-7 stem from a composite of the analyses on the earlier AARR systems, with heavily loaded annular reactor cores, and on the more recent AARR with the more lightly loaded HFIR-type reactor core.[2]

These papers represent the final detailed Annual Reports on the AARR Project physics work.

References

1. D. H. Shaftman, A. E. McArthy and R. P. Savio, *Argonne Advanced Research Reactor Calculations—Preface*, Reactor Physics Division Annual Report, July 1, 1966 to June 30, 1967, ANL-7310, pp. 92–94.
2. F. T. Binford, T. E. Cole and E. N. Cramer, Eds., *The High Flux Isotope Reactor, A Functional Description, Volume 1A*, ORNL-3572, Rev. 2 (May 1968).

II-5. Argonne Advanced Research Reactor Calculations—General Reactor Physics Analysis

D. H. Shaftman, R. P. Savio* and L. K. Volodka

Introduction

In FY-1968, most of the effort of general reactor physics analysis was closely tied to the demands of the developing detailed design of the reactor. Indeed, there were many highly specialized calculations of little general interest. A selection of topics of somewhat more general interest has been made for this final Annual Report on the general reactor physics analysis of the AARR, except for two topics that might be of some special interest in connection with the High Flux Isotope Reactor (HFIR) at Oak Ridge National Laboratory. These items are analyses of the reactivity perturbation and flux perturbation effects of increasing the coolant-hole size in the permanent beryllium reflector of the AARR, and analyses of shutdown margins for fresh HFIR-type fuel elements in water or in position in the reactor pressure vessel.

Other subjects discussed on the present paper are: (a) simplified formulas for reactivity loss due to xenon buildup upon power setback; (b) analyses of neutron inventories; and (c) the spatial variation of the thermal neutron flux in the radial beryllium reflector.

Reactor Physics Effects of Enlarged Coolant Holes in the Permanent Beryllium Reflector

Multigroup diffusion theory calculations were made to study reactor physics perturbations that would result if the diameter of the cooling holes in the permanent beryllium reflector were increased by 50%, from $\frac{1}{8}$ to $\frac{3}{16}$ inches. The purpose of this coolant-hole enlargement is to provide a greater margin of safety against transient voiding of coolant in the beryllium, e.g., in the event of an electrical outage which would result in a reduction of coolant flow, and to ease the problem of fabricating the permanent beryllium reflector.

* Reactor Operations Division, Argonne National Laboratory.

Most of the water volume in the various azimuthal sectors of the permanent beryllium reflector is directly associated with experimenters' facilities. Thus, an increase of as much as 50% in coolant-hole diameter would mean a 125% increase in coolant-hole volume but less than a 20% increase in the local average water content in each macroscopic sector of the permanent beryllium reflector. In some zones of the permanent beryllium reflector, the increase in water volume is only ~5% of the present design water volume.

For such an increase in coolant-hole diameter, it is calculated that there would be an insignificant reduction (~0.04%) in the available excess reactivity. The calculated thermal neutron flux at the tip of the blind beam tubes is reduced by less than 1%, and it is expected that correspondingly the Users' fluxes would be reduced very slightly. The thermal neutron flux in the center of each through-tube is reduced by less than 5%—possibly by only ~3%. Two cases have been analyzed for the perturbation of the thermal neutron flux in the principal sector of the beryllium reflector containing vertical irradiation facilities. In one case, the target volume was assumed to be filled with aluminum. In the second case, additional neutron poisoning, corresponding to actual target material, was included. In each case, an increase in coolant-hole diameter, in the permanent beryllium, from 1/8-in. to 3/16-in., caused small reductions in the calculated thermal neutron flux, with a maximum reduction of ~4%.

Reactivity Shutdown Margins for Fresh HFIR-Type Fuel Elements

One-dimensional diffusion theory computations were made, using the standard 16-group set of neutron cross sections developed for the AARR/HFIR analyses, to examine safety margins of handling fuel elements. The question at issue was whether it would be strongly advisable to use a reactivity monitoring device that would travel with the fuel element as it would be moved about during loading and unloading operations.

For the case of a full fresh core in water, the calculated k_{eff} was low by approximately 3.3% as compared with measurements performed at Oak Ridge National Laboratory for purposes of HFIR operation.[1] In the tabulation below, the *ad hoc* assumption was made that the calculated reactivities for all other cases also were low by 3.3%, and a correction of this type has been applied.

The actual storage cells for fuel elements are planned to permit the assemblage of an inner and an outer fuel element in their normal relative positions as a full reactor core. However, each cell includes solid neutron absorbers in the internal reflector and near the outer boundary of the outer fuel element. The calculations summarized in Table II-5-I, wherein the storage-cell absorbers are ignored, therefore provide overestimates of k_{eff} for fuel elements in storage cells. All results are rounded-off high. Also in Table II-5-I are calculated k_{eff}'s for fuel elements in their normal spatial locations in the core with the fresh beryllium reflector present and control plates inserted fully.

TABLE II-5-I. Effective Multiplication Factors (k_{eff}) for Fresh HFIR-Type Fuel Elements

Description of Loading of Fuel Elements in Water	k_{eff}	Description of Loading of Fuel Elements in Core Locations	k_{eff}
Outer fuel element	0.75	Outer fuel element	0.90
Inner fuel element	0.65	Inner fuel element	0.66
Inner fuel element (no boron)	0.74	Inner fuel element (no boron)	0.76
Reactor core (no boron)	1.04	—	—
Reactor core	0.98	—	—

Buildup of Xenon after Setback of Reactor Power from Equilibrium Operation

In a thermal reactor operating at high power densities, such as the HFIR and the AARR, a large relative setback in reactor power from the equilibrium level would cause a rapid buildup of Xe-135 in the fuel and a corresponding rapid reduction in available excess reactivity. Therefore, if it becomes necessary to reduce reactor power to a level low by comparison with the normal operating level (100 MWt), there is a limited period of time during which the reactor may be returned to power before xenon shuts it down. The following analysis reveals the characteristic times available as a function of time in the core cycle and as a function of the setback level of power.

At space-point **r**, assume that the pre-setback destruction rate of xenon by neutron capture is $\phi_0(\mathbf{r})\sigma_a^{Xe}$, that the setback rate is $\phi_1(\mathbf{r})\sigma_a^{Xe}$, and that $\frac{\phi_1(\mathbf{r})}{\phi_0(\mathbf{r})}$ is a constant and is much smaller than unity. The times of interest will be seen to be 1/2 hour or less, which is a short time by comparison with the decay half-lives of Xe-135 (9.2 hr) and the precursor nuclide, I-135 (6.7 hr). Therefore, it is a good approximation to ignore the reduction in I-135 inventory due to decay following setback. Since $\frac{\phi_1(\mathbf{r})}{\phi_0(\mathbf{r})} \ll 1$, it is also a good approximation to ignore the contribution to the iodine inventory arising from continuing power operation at the setback level.

The resulting approximate equation for the time-dependent concentration of Xe-135 following a power

setback at time zero is

$$\frac{d\mathrm{Xe}}{dt} = [\lambda^I I_0 + \phi_1 \Sigma_f \gamma(\mathrm{Xe})] - [\lambda^{\mathrm{Xe}} + \phi_1 \sigma_a^{\mathrm{Xe}}]\,\mathrm{Xe}. \quad (1)$$

In Eq. (1),

$\mathrm{Xe} \equiv \mathrm{Xe}(\mathbf{r},t)$ is the concentration of Xe-135, atoms/cm³

$\phi_1 \Sigma_f \gamma(\mathrm{Xe}) \equiv$ direct source rate of Xe-135 from fission, atoms/cm³-sec

$\lambda^I, \lambda^{\mathrm{Xe}} \equiv$ decay constant for I-135, Xe-135, respectively, sec⁻¹

$t \equiv$ time after setback, sec.

Solving Eq. (1), expanding the solution to terms of second order, and taking the ratio of the change in xenon concentration (ΔXe) to the pre-setback concentration:

$$\frac{\Delta\mathrm{Xe}(\mathbf{r},t)}{\mathrm{Xe}(\mathbf{r},0)} \approx \left[1 - \frac{\phi_1\sigma_a^{\mathrm{Xe}}}{\phi_0\sigma_a^{\mathrm{Xe}}}\right]\left[1 - \frac{\lambda^{\mathrm{Xe}} + \phi_1\sigma_a^{\mathrm{Xe}}}{2}\,t\right]\phi_0\sigma_a^{\mathrm{Xe}}t.$$

Using a point-reactor model and taking the volume-averaged rates $\phi_0\sigma_a^{\mathrm{Xe}}$ and $\phi_1\sigma_a^{\mathrm{Xe}}$, the change in available excess reactivity may be written:

$$\Delta\left(\frac{\Delta k}{k}\right) \approx \frac{\Delta k}{k}(\mathrm{Xe}^{(0)})\left[1 - \frac{P_1}{P_0}\right] \cdot \left[1 - \frac{\lambda^{\mathrm{Xe}} + \phi_1\sigma_a^{\mathrm{Xe}}}{2}\,t\right]\phi_0\sigma_a^{\mathrm{Xe}}t, \quad (2)$$

where

$\Delta\left(\frac{\Delta k}{k}\right)$ is the time-dependent change in available excess reactivity due to Xe-135 buildup

$\frac{\Delta k}{k}(\mathrm{Xe}^{(0)})$ is the reactivity controlled by Xe-135 at the pre-setback quasi-equilibrium level

$\frac{P_1}{P_0}$ is the ratio of setback reactor power to pre-setback reactor power.

Thus, to first order, if the pre-setback available excess reactivity is $R \times \frac{\Delta k}{k}(\mathrm{Xe}^{(0)})$, the time available before the reactor power level must be raised to the vicinity of P_0 to prevent shutdown by xenon is

$$t_{max}(\mathrm{sec}) \approx \frac{R}{\left[1 - \frac{P_1}{P_0}\right]\phi_0\sigma_a^{\mathrm{Xe}}}. \quad (3)$$

In the AARR, the available excess reactivity at the beginning of the fuel cycle will be approximately 3%, with the exact value depending upon the specific neutron poisonings of the ITC and the beryllium reflector by target materials. Approximately 4½% in reactivity is tied up in equilibrium xenon, according to data from the operating HFIR, with the same core and removable-beryllium reflector. Thus, $R \approx \frac{2}{3}$ early in core life. In Eq. (3), $\phi_0\sigma_a^{\mathrm{Xe}} \approx 7.5 \times 10^{-4}$ events/sec and $t_{max} \approx \frac{0.9}{\left[1 - \frac{P_1}{P_0}\right]} \cdot 1000$ sec. If power is set back to one-tenth of the pre-setback level, $t_{max} \sim 17$ min. Actually, since it takes some time to return the power to level P_0, t_{max} is smaller.

Later in the core life, R is reduced and $\phi_0\sigma_a^{\mathrm{Xe}}$ is increased, both effects acting in the same direction, namely, to reduce t_{max}.

Neutron Inventories

Analyses of neutron inventories have been made to investigate further certain reactor physics characteristics of the AARR reactor. The results summarized in the following paragraphs cannot be correlated simply with reactivity losses and gains, since average "importance" weightings for fission events, net neutron leakage, and neutron capture must be applied on an energy-group-by-energy-group basis. Nevertheless, the energy-integrated summaries are aids to a deeper insight into the physics behavior of the system.

The analyses constitute interpretations of the printout of a one-dimensional (cylinder) 16-group k_{eff} calculation with the diffusion theory program MACH-1. The reactor state is an idealized system: the (super critical) fresh hot reactor, without fission products and with control rods fully withdrawn. The Internal Thermal Column (ITC) is assumed to be fully loaded with aluminum capsules, with a total additional neutron poisoning of the ITC equivalent to 0.5 g natural boron representing the total neutron capture cross section of the actual target materials. With a normal HFIR loading of boron as a burnable neutron poison for this system, the calculated $k_{eff} = 1.076$.

In the following summaries, the fuel zone is defined to be the volume made up of a 20-in. active core height and radial dimensions from the inner surfaces to the outer surfaces of the active fuel plates in the inner and outer fuel elements. Table II-5-II displays the input group-averaged η's in the fuel, and the inferred fractional distributions of fission events in various radial locations and the average over the entire fuel zone.

Table II-5-III summarizes the fractional distribution of neutron losses to absorption and leakage. In Table II-5-III, the losses are sums over all 16 groups, for each of the two fuel elements. There are other small neutron losses to capture by other materials, including impurities in the aluminum and oxygen; this has been ignored, in compiling Table II-5-III.

In the idealized case represented for Table II-5-III, the control rods are withdrawn fully, leaving the aluminum control-rod followers in place at the outer radial

TABLE II-5-II. GROUP-AVERAGED η'S AND ENERGY DISTRIBUTIONS OF FISSION EVENTS IN THE AARR FUEL ZONE USING THE HFIR-TYPE CORE

Group Number	Energy Range	Group-Averaged η	Local Fractional Distributions of Fission Events				
			Inner Fuel Element		Outer Fuel Element		Average Over Fuel Zone
			Near Inner Boundary	Central Region	Central Region	Near Outer Boundary	
1	3–∞ MeV	2.819	0.0007	0.0017	0.0018	0.0006	0.0016
2	1.4–3 MeV	2.453	0.0015	0.0036	0.0042	0.0015	0.0036
3	0.9–1.4 MeV	2.308	0.0007	0.0018	0.0022	0.0008	0.0018
4	0.4–0.9 MeV	2.196	0.0010	0.0027	0.0032	0.0012	0.0027
5	0.1–0.4 MeV	2.104	0.0013	0.0033	0.0039	0.0015	0.0033
6	17–100 keV	1.924	0.0017	0.0041	0.0048	0.0019	0.0041
7	3–17 keV	1.853	0.0022	0.0053	0.0063	0.0025	0.0053
8	0.55–3 keV	1.722	0.0038	0.0089	0.0106	0.0043	0.0090
9	100–550 eV	1.637	0.0087	0.0203	0.0238	0.0098	0.0203
10	30–100 eV	1.517	0.0119	0.0271	0.0313	0.0132	0.0268
11	10–30 eV	1.452	0.0109	0.0244	0.0279	0.0120	0.0241
12	3–10 eV	1.167	0.0107	0.0236	0.0267	0.0117	0.0231
13	1–3 eV	1.867	0.0078	0.0172	0.0196	0.0085	0.0168
14	0.4–1 eV	2.143	0.0147	0.0317	0.0359	0.0159	0.0311
15	0.1–0.4 eV	2.007	0.1440	0.1897	0.1983	0.1351	0.1894
16	0–0.1 eV	2.075	0.7784	0.6346	0.5993	0.7794	0.6370

1. The group-averaged parameter, η_i, is the assigned average number of fission neutrons produced per neutron absorbed in the uranium-fuel.

2. The local fractional distribution is normalized to a total fission rate of unity locally. Four decimal places are included to avoid too much roundoff at high energies; these are the calculated values, and they bear no stamp of certitude to four decimals.

3. At the inner and outer boundaries of the fuel zone, more than 90% of the fissions are caused by neutrons of "thermal" energies, say groups Nos. 15 and 16 (0–0.4 eV). Averaging over the fresh fuel zone, more than 80% of the fissions occur in this energy range.

boundary of the outer fuel element. More realistically, control rods are partially inserted, and there is a radial shift in power toward the ITC and hence a greater radial leakage of high-energy neutrons into the ITC. There would be also a larger net "leakage" out of the outer fuel element, for the control rods would absorb some neutrons that otherwise would enter the fuel zone from last collisions in the outer radial reflector zones. Moreover, xenon builds up early in the reactor operation and compensates a large fraction of the initial available excess reactivity. Consequently, the overall effects of the control rods on the inventory of neutron losses in the fuel zone should be small. Of course, since the values in Table II-5-III are normalized to unit total loss in the fuel zone, all values then must be adjusted to account for the reactivity losses to xenon and to control-rod absorptions.

TABLE II-5-III. FRACTIONAL DISTRIBUTIONS OF NEUTRON LOSSES IN THE AARR FUEL ZONE (SUMMED OVER NEUTRON ENERGY)

Type of Loss	Inner Fuel Element	Outer Fuel Element	Fuel Zone
Net axial leakage	0.024	0.042	0.066
Net radial leakage out, inner boundary	0.047	−0.010	0.037
Net radial leakage out, outer boundary	0.036	0.253	0.289
Captures by aluminum (in fuel zone)	0.0055	0.0082	0.014
Captures by hydrogen	0.0075	0.0121	0.020
Captures by boron	0.027	—	0.027
Absorptions by U-238	0.0010	0.0026	0.004
Captures by U-235	0.033	0.070	0.103
Fissions of U-235	0.142	0.297	0.439
Total fractional loss	0.32	0.68	1.00

Notes: There are slight inconsistencies between individual and total losses; they are caused by roundoff.

A net negative leakage out, at a boundary, is equivalent to a net source of neutrons into the zone at that boundary, summed over all neutron energies.

SPATIAL VARIATION OF THERMAL NEUTRON FLUX

In most of the earlier analyses in multigroup diffusion theory, the thermal neutron energy range from 0 to 0.4 eV has been partitioned into two groups: group No. 15 [0.1–0.4 eV]; and group No. 16 [0–0.1 eV]. The particular computer program used, the MACH-1[1] code, does not provide for neutron upscattering. Consequently, a cross section for a net neutron dowscatter has been calculated, using the program THERMOS[2] in calculating the detailed thermal neutron spectrum. This model fails when the

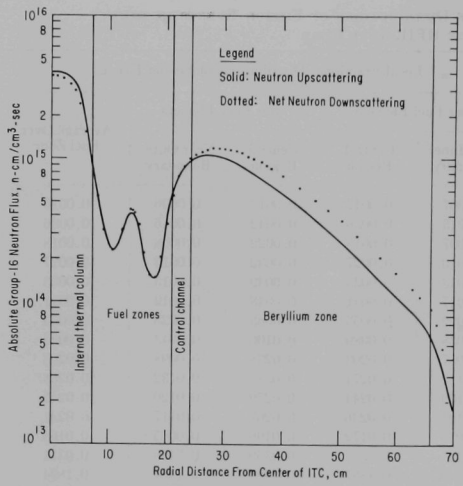

FIG. II-5-1. Radial Distribution of Group-16 Neutron Flux at Core Midheight (Reactor Power: 100 MW; Control Rods Withdrawn; Blind-Beam-Tube Sector). *ANL Neg. No. 113-1485.*

ratio of the group-16 flux to the group-15 flux begins to deviate from the assumed equilibrium case. Far out in the radial beryllium reflector of the AARR, this ratio of group fluxes increases rapidly and the model is invalidated. The explanation for this divergence is that in a weakly absorbing moderator like beryllium (or D_2O or graphite), when the thermal migration area exceeds the neutron age, eventually the thermal neutron flux is determined by diffusion of these thermal neutrons, and not by the source from higher energies.

The effects of collapsing the two thermal groups to one group, or of specifically assigning upscatter cross sections as well, instead of net downscatter, have been studied using a computer program of multigroup diffusion theory that permits neutron upscattering (DIF-1D)[3]. Figure II-5-1 gives a comparison of the group-16 fluxes at core midheight for two of the multigroup models: downscatter and upscatter of neutrons; and net neutron downscatter. The important conclusion with regard to the spatial distributions is that the *total* thermal neutron flux (0–0.4 eV) as calculated with two thermal groups and neutron upscattering agrees very closely with that obtained from a calculation wherein a single group characterizes that energy range. This agreement applies throughout the entire radial beryllium reflector (1-*D* calculation, radially). Surprisingly, even for the case of two thermal groups and a net downscatter, the *total* thermal neutron flux does match the one-thermal-group flux quite closely. However, there are differences in reactivity (~1%) among the various calculations and differences in the spatial distribution of power. In these respects, the model of a single thermal neutron group is much less accurate.

REFERENCES

1. D. A. Meneley, L. C. Kvitek and D. M. O'Shea, *MACH 1, A One-Dimensional Diffusion-Theory Package* ANL-7223 (1966).
2. B. J. Toppel and I. Baksys, *The Argonne-Revised THERMOS Code*, ANL-7023 (1965).
3. B. J. Toppel, Ed., *The Argonne Reactor Computation (ARC) System*, ANL-7332 (1967), pp. 74 ff.

II-6. Argonne Advanced Research Reactor Calculations—General Shield Design Analysis

D. H. SHAFTMAN and A. E. MCARTHY

INTRODUCTION

The general shield-design analyses for the AARR in FY-1968, to the time of Project cancellation, included the following categories of activities:

1. Collaboration with the Architect-Engineer in establishing the design of plant radiation shielding beyond the reactor pressure vessel
2. Collaboration with the Architect-Engineer in the evaluation of the methods of shielding-design analysis used by the Architect-Engineer for the design work
3. Analyses concerned with the detailed design of reactor components within the reactor pressure vessel.

The intent of this paper is to summarize the status of the first two categories of activities at the time of the cancellation of the Project, which was also the time when the shielding-design work of the Architect-

Engineer on the AARR ceased. The analyses of category No. 3 were based on the use of the Argonne-MAC code, where such analyses required conservative data of heating rates; they are not reported here.[1]

Status of the Plant Shield Design at the Time of Project Cancellation

As indicated in the corresponding report for FY-1967,[1] preliminary Title-II dose-rate analyses were prepared by the Architect-Engineer in FY-1967 for gamma-ray radiations from the water purification system and from pools and canals with spent fuel in transit or in storage. Also, except for radiation dose rates due to radiation penetrating the bulk reactor biological shields, detailed calculations were made for radiation dose rates at selected dose points on the Service Floor and the Experiment Floor in the Reactor Containment Building. As the detailed design proceeded, in FY-1968, these analyses were reviewed by the Architect-Engineer and revised as necessary. At the time of Project cancellation, the continuing detailed Title-III design had introduced penetrations for instrumentation, etcetera, which required additional analysis of shielding against radiations from active materials in the pools and canals. The analyses for radiation dose rates due to gamma-ray radiation from the water purification system were completed.

The calculations of dose rates due to radiation penetrating the bulk reactor biological shield still had not been performed because of the continuing problems faced by the Architect-Engineer in getting the NRN[2] computer program in operation on the digital computer then commercially available to them. At the time of work stoppage, the sytem debugging was in its last phase. Ray paths had been chosen jointly by Argonne National Laboratory and the Architect-Engineer for calculations of neutron and/or gamma-ray dose rates at various points, and preliminary calculations were completed for the required subsidiary geometry input. These problems involve calculations of deep penetration of radiation, with the usual questions of the degree of conservatism. From preliminary calculations with the Argonne-MAC code, it appeared that the shielding would be adequate. It was expected that this would be confirmed by the computations of neutron fluxes, using NRN, and of gamma-ray dose rates, using the code QAD.[3]

For the most part, the design provided adequate shielding to satisfy the criteria of design dose rates to personnel without additional close monitoring of radiation dose rates (see Ref. 1, Table II-21-I). At certain locations, it was conceivable that high dose rates would result unless certain operations were carefully controlled, and it would have been extremely difficult to provide additional radiation shielding to eliminate this potential radiation hazard. The most prominent example is that during transfer of a spent fuel element it was important to keep the fuel element from getting close to the pool wall, at the vertical elevation of certain horizontal penetrations. When not in use, these Users' penetrations would be plugged, normally. The calculations indicated local dose rates of the order of 1R/hr on the outside of the pool wall at that level, if the spent fuel element were kept to its optimum lateral distance and the penetrations were filled only with water. If the fuel element were erroneously moved up to the pool wall, near one of those penetrations, the corresponding dose rate would be increased to roughly 1000 R/hr there. This potential problem would have been minimized by special procedures and by radiation monitoring during such a transfer of spent fuel.

With the exception of the computations for the bulk reactor biological shield, the major shield-design analyses for normal operating conditions were complete or almost complete, with careful review by the Architect-Engineer. Upon completion of the NRN/QAD computations, the corresponding shield-design effort by the Architect-Engineer would have been reduced subtantially, but with staffing adequate for the continuing review of drawings to search for potential shielding problems and to determine the magnitudes of the corresponding dose rates.

One phase of shield-design analysis that was nearing completion at that time was the revision of the calculations of direct gamma-ray dose rates to personnel in the Laboratory and Office Building in the event of a postulated Maximum Credible Accident (MCA) in the Reactor Containment Building. These analyses were required to confirm that there would be adequate shielding to protect these personnel for a conservatively long period of time to permit their evacuation. Calculations were made for each of several dose points. The revised results reported by the Architect-Engineer are that the integrated dose for the first 15 min after the postulated MCA began would be less than 10 R. In the Reactor Control Room, the integrated dose in the first 15 min would be less than 10 mR. In each case, pessimistic conditions of accumulation of fission products were assumed. These results imply that the plant design would also provide adequate shielding for personnel in the Laboratory and Office Building against direct gamma-ray radiation from the Reactor Containment Building in the postulated case.

Remarks on Methods of Shielding-Design Analysis

In the detailed shield-design work by the Architect-Engineer, wherever corresponding data were available from dose-rate measurements at the High Flux Isotope Reactor (HFIR), reliance was placed on measurement, with computational extrapolation to account for small differences in actual shielding thickness. Check calculations were made to verify that the computational methods were adequate. One such computation was the dose rate at the top of the pool water above spent fuel, at the HFIR, for which measured data were obtained from Oak Ridge National Laboratory. The computed absolute gamma-ray dose rate and the computed change of dose rate with change of shielding-water thickness were in very good agreement with measurement, even allowing for the inevitable uncertainty in the association of measured and computed dose rates.

In general, scoping analyses were performed to determine whether a given radiation source would offer a real problem at a given dose point, relative to an assigned criterion dose rate. If the scoping calculations implied a possibly sizeable contribution, detailed calculations were made. These detailed calculations were based upon standard formulas[4,5] for calculations of gamma-ray dose rate. For the most part, "hand" calculations were made.

In preparing to use NRN, each subroutine of NRN which is used to fit or average neutron cross sections was checked independently. The cross section library of NRN was reviewed, and the point-by-point cross section library was checked against the most recent ENDF/B data and other recent evaluated-data sources, and also comparisons were made with the 05R[6] library. Subsequently, the NRN library was modified by the joint efforts of the Architect-Engineer and Argonne National Laboratory staff personnel.

The code QAD, for analysis of gamma-ray dose rates, has been applied by the Architect-Engineer to calculations of the gamma-ray heating rate at the outer boundary of the reactor core, due to neutron absorptions (fissions and captures) by the U-235 fuel in the reactor core. A number of cases were studied, with the reactor power distribution input as: (a) radially flat, axially peaked; (b) radially peaked, axially flat; (c) peaked in both directions; (d) flat in both directions; and various other assigned spatial power distributions. Comparisons have been made with gamma-ray heating rates as computed with the code ANISN[7] at Oak Ridge National Laboratory, through the cooperation of H. C. Claiborne and F. R. Mynatt (ORNL). For the same input gamma-ray source, the heating rate predicted by ANISN at the inner edge of the beryllium reflector, due to core gamma-rays, is approximately 20% higher than the corresponding QAD result.

In all such comparisons of computer output using the various shielding-analysis codes, it should be noted that each code typically is used with its associated cross section set. Not only are the methods of analysis different, but the cross sections are different and usually even source distributions are different.

It is interesting to note also the QAD results with regard to the effects of the assumed spatial distributions of reactor core power on the gamma-ray heating rate at the inside surface of the beryllium reflector at core midheight. With a flat axial power shape, the cases studied of flat and peaked radial power distributions yielded almost identical heating rates. Peaking the axial power distributions, with a 1.3 maximum-to-average axial power ratio, increased this heating rate by only 13%.

Remarks on Computations of Thermal Neutron Flux

A number of the shielding-analysis codes, among them the MAC code,[8,9] do not provide for upscattering of neutrons in the thermal energy range. A basic cross-section library associated with MAC employs 31 neutron energy groups, of which the last 3 or 4 may be identified as "thermal". As a result, strange behavior of neutron fluxes may be expected in such environments as the beryllium reflector of the AARR. This difficulty is analogous to the problem discussed in Paper II-5, and it has been observed in MAC calculations of the AARR. In the absence of a provision for neutron upscattering in the calculation, it would seem to be preferable to use only one thermal neutron group, with averaged cross sections. It is expected that anomalous flux distributions would be observed in calculations of reactors with thick graphite reflectors when a model such as the 31-group MAC model is used. There has been no attempt at Argonne National Laboratory to examine more closely the consequences of such changes in model. Indeed, it might prove to be unimportant in dose-rate calculations. In Paper II-5, it is observed that the total thermal neutron flux near the outer boundary of the radial beryllium reflector is not particularly sensitive to the model used, whether upscattering is included, or net-downscattering is assumed, or the two thermal neutron groups are combined into one.

REFERENCES

1. A. E. McArthy, D. H. Shaftman and I. Charak, *Argonne Advanced Research Reactor Calculations—General Shield-Design Analysis*, Reactor Physics Division Annual Report, July 1, 1966 to June 30, 1967, ANL-7310, pp. 113–119.
2. L. Hjärne et al., *A Users' Manual for the NRN Shield Design Method*, AE-145 (June 1964).
3. R. E. Malenfant, *QAD—A Series of Point-Kernel General-Purpose Shielding Programs*, LA-3573 (April 1967).
4. T. Rockwell III, Ed., *Reactor Shielding Design Manual*, (D. Van Nostrand Company, Inc., Princeton, New Jersey, 1956).
5. E. P. Blizard, Ed., *Reactor Handbook, Volume III, Part B, Shielding*, Second Edition (Interscience Publishers, New York, N. Y., 1962).
6. R. R. Coveyou et al., *O5R, A General-Purpose Monte Carlo Neutron Transport Code*, ORNL-3622 (February 1965).
7. W. W. Engle, Jr., *A Users' Manual for ANISN—A One Dimensional Discrete Ordinates Transport Code with Anisotropic Scattering*, K-1693 (March 1967).
8. E. G. Peterson, *MAC—A Bulk Shielding Code*, HW-73381 (April 1962).
9. A. E. McArthy and H. Yamanouchi, *Revision of the Bulk Shielding Code MAC for the CDC-3600 Computer*, Reactor Physics Division Annual Report, July 1, 1965 to June 30, 1966, ANL-7210, pp. 396–399.

II-7. Argonne Advanced Research Reactor Calculations—Summary Remarks on Interactions of Reactor Core Design and Levels of Thermal Neutron Flux in the Internal Thermal Column

D. H. SHAFTMAN

INTRODUCTION

In the course of design of the AARR, two principal reference design cores, fueled with highly-enriched U-235, were studied. One reference reactor core was a heavily-loaded, low-intermediate-spectrum core with an anticipated reactivity core life of ~10,000 MWd. Later, in Fiscal Year 1967, a budgetary decision was made to use the more lightly loaded, thinner, High Flux Isotope Reactor (HFIR)-type reactor core, and studies on this system have been performed. Moreover, in the supporting program of zero-power criticality experiments for the earlier system, a wide range of fuel loadings were investigated experimentally and theoretically. Certain basic, common characteristics of interactions of the reactor core design and levels of the thermal neutron fluxes in the Internal Thermal Column (ITC) are evident, and a principal purpose of the present report is to summarize these characteristics.

Among the topics discussed in the present report are: (1) the influence of fuel-zone thickness on the peak thermal neutron flux in the ITC, for fixed maximum power density or for fixed total reactor power; and the reactivity effects of such a change in fuel-zone thickness from a designated reference value; (2) the effect of the fuel-loading density, in the reactor core, on the peak thermal neutron flux in the ITC, for a fuel zone of fixed dimensions; and (3) composition of these effects to explain the differences between the levels of peak thermal neutron flux in the ITC of the two reference AARR's.

Some of these results have been reported before, in connection with publications about the earlier reference AARR design. Much of the data is new, however, and the present unification of results should be of value.

Reference 1 is devoted to a discussion of factors which influenced the design optimization of experimenters' thermal neutron flux in the earlier design reference AARR. This provides details which will not be repeated in the present paper, and it should be viewed as an essential companion paper. In particular, Fig. II-20-3 and the associated remarks on pp. 96–98 of Ref. 1 clarify the relationships between reactor core size and peak thermal neutron fluxes in the flux-trap zones of the earlier AARR system. For this reason, only a brief summary is given in the present report, and topics Nos. 1–3 enumerated above are combined.

Other topics treated in the present paper are: the efficient utilization of reactor power, to raise the levels of thermal neutron flux in the flux-trap per unit reactor power; and the effect of reactor purposes on the possible merits of using other types of fuel (e.g., Pu-239), other fuel-zone spectra, or other reactor types.

The detailed calculations were performed in collaboration with R. P. Savio (Reactor Operations Division) and L. K. Volodka (Reactor Physics Division).

Design Constraints Affecting the Levels of Thermal Neutron Flux in the Internal Thermal Column of the AARR

In designing an advanced high-flux research reactor with flux-trap zones outside the reactor core, typically one important constraint is the designated limit of peak power density in the fuel zone. In the earlier reference AARR, a power level of 100 MWt was assigned and a peak power density was chosen which was conservatively below burnout level and for which it was expected that the reactivity life would determine core life. Other constraints specific to the AARR were: (1) maximization of the peak thermal neutron flux in the ITC at a total reactor power of 100 MWt; and (2) the establishment of a sufficiently long core life to keep the monetary costs of reactor operation to an acceptable range.

In other flux-trap reactors, the constraint might be to maximize the value of the peak thermal neutron flux in the ITC per unit reactor power, or perhaps to maximize the total rate of capture of thermal neutrons in the targets in the ITC. In other flux-trap reactors, these constraints might indeed be different and they might lead to different reactor designs.

The AARR was intended to be a multipurpose reactor, with flux-trap zones at both radial boundaries of the cylindrical annular fuel zone. This introduced another constraint, namely, the attainment of high thermal neutron fluxes in the radial beryllium reflector. This constraint is not independent of the other constraints, insofar as the design of the reactor fuel zone is concerned.

Levels of Thermal Neutron Flux in the Internal Thermal Column of the AARR as Functions of Size and Fuel Loadings of the Reactor Core

Values of peak thermal neutron flux at the center of a 7-cm-radius ITC have been estimated for a variety of cylindrical annular reactor cores. The fuel zones ranged from the thin, lightly-loaded HFIR-type core to the heavily-loaded intermediate-spectrum core of the earlier AARR design.[1,2] In each case the fissionable material was uranium highly enriched in U-235.

For the limiting case of an all-H_2O ITC, without irradiation tubes, calculated peak thermal neutron fluxes at 100 MWt were: $\sim 3.7 \times 10^{15}$ n-cm/cm^3-sec, for the earlier design AARR, and $\sim 5.1 \times 10^{15}$ for the modified AARR with the HFIR-type reactor core and the gray portions of the central plates inserted. The most important contributions to the difference in peak ITC flux are: (1) the higher average power density of the thinner HFIR-type core; and (2) the smaller fuel loading of the HFIR-type core.

The actual volume of the fueled portion of the HFIR-type fuel zone is $\sim$50 liters, which is 20% smaller than the corresponding volume of the fuel zone of the heavily loaded AARR system. Therefore, at the fixed reactor power level of 100 MWt, the average power density in the HFIR-type fuel zone is 25% higher, and this translates approximately to a correspondingly higher rate of production of source neutrons.

The effects of the smaller fuel loading are to increase the peak thermal neutron flux in the ITC. The direction of this change and its approximate magnitude have been discussed in reports on calculations and experiments for criticality facility loadings for the earlier AARR.[1,3] It is estimated that this results in an increase of $\sim$15% in the peak ITC flux for the HFIR-type core.

Therefore, for fixed average power density in the fuel zone, the peak thermal neutron flux in the ITC is approximately 15% higher in the case of the HFIR-type reactor core. And this increase occurs even though the resulting total reactor power would be 20% lower at the fixed average power density.

In these analyses, the converged calculated thermal neutron fluxes were normalized to a fission-spectrum-neutron source rate corresponding to the correct preassigned reactor power. The calculations were idealized in one sense, however, in that final "criticality" was achieved by varying the values of ν (number of fission neutrons produced per fission) rather than attempt to perform the realistic 3-dimensional analysis for the actual configuration with criticality controlled by moving the solid control rods.

Figure II-7-1, obtained for the earlier reference design AARR with a radially-graded, intermediate-spectrum reactor core, shows the relative contribution of fission-spectrum neutron sources to the peak group-16 (0–0.1 eV) neutron flux in the ITC. The curve is normalized to unity at the beginning of the actual fuel at the ITC boundary. It is also normalized to constant total cylindrical shell source at each radial position r.[3]

A similar figure (Fig. II-7-2) has been determined for a simplified model of the HFIR-type fuel zone in the AARR. In these calculations, a spatially uniform fuel loading was used corresponding to the fuel loading in the middle of the outer fuel element and without boron. This approximation was made to simplify interpretation of a series of calculations with other energy ranges of neutron sources, as discussed in a later section on efficiency of utilization of reactor power.

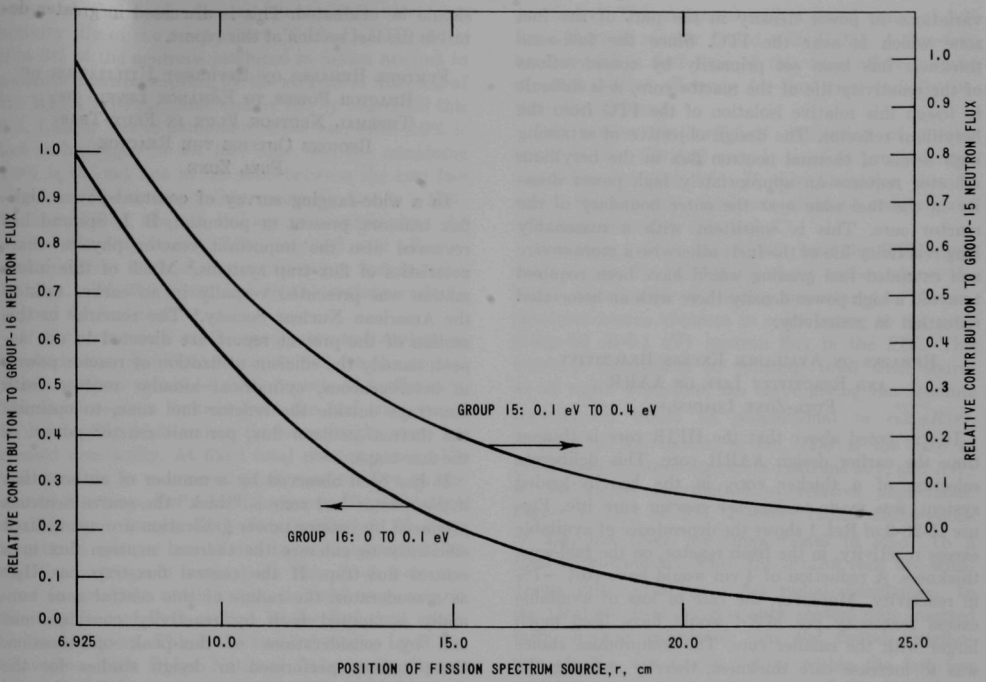

FIG. II-7-1. Relative Contribution by Fission Spectrum Sources in the Core to the Thermal Neutron Flux at the Center of th AARR Internal Thermal Column (Normalized to Unit Contribution by Source at Inner Boundary of Reactor Core). *ANL Neg. No 112-7595.*

From Figs. II-7-1 and II-7-2, note that the relative contribution drops off somewhat less rapidly with distance from the ITC in the case of the HFIR-type core. This is a composite of effects of different fuel loading and different structural material (aluminum, for the HFIR; stainless steel, for the earlier core); the water volume fraction is 0.5 in both types of reactor fuel zones.

As noted in Ref. 1, the function $A \exp(-0.18\, r)$ is an excellent fit to the curve in Fig. II-7-1 in the vicinity of the ITC, where r is the distance from the ITC, in units of centimeters. Similarly, the function $B \exp(-0.15\, r)$ provides a good fit to the curve of Fig. II-7-2 near the ITC. In these fittings, A and B are constants of normalization.

A very important and obvious implication of Figs. II-7-1 and II-7-2 is that the source neutrons produced by fissions near the outer boundary of the reactor core contribute little to the peak thermal neutron flux in the ITC. Similarly, the thermal neutron flux in the beryllium reflector is relatively insensitive to local

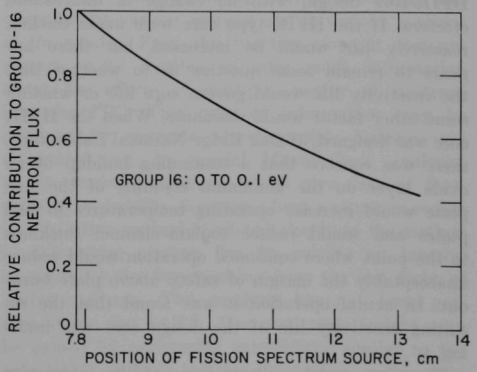

FIG. II-7-2. Relative Contribution by Fission Spectrum Sources in A Simplified Model of the HFIR-Type Core to the Group-16 Neutron Flux at the Center of the AARR Internal Thermal Column (Normalized to Unit Contribution by Source at Inner Boundary of Reactor Fuel). *ANL Neg. No. 113-1545.*

variations in power density in the part of the fuel zone which is near the ITC. Since the fuel-zone thickness has been set primarily by considerations of the reactivity life of the reactor core, it is difficult to lessen this relative isolation of the ITC from the beryllium reflector. The design objective of attaining high levels of thermal neutron flux in the beryllium reflector requires an appropriately high power density in the fuel zone near the outer boundary of the reactor core. This is consistent with a reasonably long reactivity life of the fuel; otherwise a more severe and extended fuel grading would have been required to avoid a high power density there with an associated reduction in reactivity.

Remarks on Available Excess Reactivity and Reactivity Life of AARR Fuel-Zone Loadings

It was noted above that the HFIR core is thinner than the earlier design AARR core. This deliberate selection of a thicker core, in the heavily-loaded system, was made to increase reactor core life. Figure II-20-3 of Ref. 1 shows the dependence of available excess reactivity, in the fresh reactor, on the fuel-zone thickness. A reduction of 4 cm would have cost ~7% in reactivity. Moreover, the rate of loss of available excess reactivity per MWd would have been much larger with the smaller core. The compromise choice was to increase core thickness, thereby reducing the peak ITC flux per unit reactor power but greatly increasing the reactivity life of the core.

The adoption of the HFIR-type reactor core for the AARR meant the use of the actual reference HFIR-core design, with no change in dimensions, etcetera. If the HFIR-type core were made thicker, reactivity life would be increased, but there appears to remain some question as to whether then the reactivity life would govern core life or whether some other factor would dominate. When the HFIR core was designed, at Oak Ridge National Laboratory, there was concern that a continuing buildup of an oxide layer on the aluminum cladding of the fuel plate would increase operating temperatures in fuel plates and would reduce coolant-channel thickness to the point where continued operation would reduce unacceptably the margin of safety above plate burnout. In actual operation it was found that the resulting reactivity life of the design core was limiting.

These are graphic illustrations of the interaction of reactor physics characteristics and practical reactor design of flux-trap reactors. In comparing the effectiveness of various reactor fuels and core loadings, all important constraints on the design of the reactor should be evaluated. This is discussed in greater detail in the last section of this report.

Further Remarks on Efficient Utilization of Reactor Power to Enhance Levels of Thermal Neutron Flux in Flux-Trap Regions Outside the Reactor Fuel Zone

In a wide-ranging survey of constant-power high-flux reactors, present or potential, B. I. Spinrad has reviewed also the important reactor physics characteristics of flux-trap systems.[7] Much of this information was presented verbally in an earlier talk to the American Nuclear Society.[8] The remarks in this section of the present report are directed to one aspect, namely the efficient utilization of reactor power, in heterogeneous, cylindrical annular reactors with flux-traps outside the reactor fuel zone, to optimize the thermal neutron flux, per unit reactor power, in the flux-traps.

It has been observed by a number of authors that if the reactor fuel zone is "thick" the source neutrons produced by reactor power generation are not utilized efficiently to enhance the thermal neutron flux in a central flux-trap. If the central flux-trap has H_2O as a moderator, the radius of this central zone normally is limited both by reactivity considerations and by considerations of flux-peak optimization. Computations performed in design studies for the AARR indicated that optimization of peak thermal neutron flux was achieved when the radius of the H_2O central flux-trap was in the range of 6 to 8 cm. For smaller radii, the peak thermal flux rapidly dropped, and for larger radii not only was the peak flux lower but also the loss of reactivity became intolerable. If the central flux-trap were to be loaded more heavily with targets and target diluents, for maximization of average thermal neutron flux in the targets a larger central flux-trap zone would have been required.

When the central flux-trap is small, there are two aspects of inefficiency of "thick" fuel zones. If the fuel zone is "thick" in units of mean free paths for neutrons of important source energies, the source neutrons produced at distances of one or more mean free paths contribute little to the thermal neutron flux in the central flux-trap. Secondly, there is the inefficiency resulting from the small solid angle presented by the central flux-trap to neutrons produced at larger distances, where distance is measured in centimeters.

Both the AARR and the HFIR designs force degrees of inefficiency of the utilization of source neutrons produced by fissions in the fuel zone, be-

cause of the needs for an economically long reactivity life of the reactor core. Table II-5-III shows that 6% of the neutrons produced in fission are lost to parasitic neutron capture by the structural material of the HFIR-type fuel zone and by the hydrogen. Of this 6%, 1.4% is lost to aluminum in the fuel zone, 2.0% is lost to hydrogen in the fuel zone, and the remaining 2.6% is the net loss in the zone between the two fuel elements. The corresponding reactivity loss is ~13%. By comparison, the net leakage of neutrons into the central flux-trap is only 3.7%, summed over all neutron energies; 6.6% of the neutrons are lost to axial leakage; and 28.9% are lost to the regions radially beyond the fuel zone.

If D_2O were used as the moderator and coolant in the fuel zone, and H_2O were retained for the central flux-trap, there would be other aspects of inefficiency. The axial neutron leakage from the fuel zone would be intolerably high unless the core height were increased drastically. At fixed total reactor power, this would result in a lowered peak neutron flux in the central flux-trap. For AARR purposes, the advantage of having a longer ITC, for irradiation of more targets, in general would not have compensated for the disadvantage of lower peak flux. If it were desired to irradiate much target material in a central flux-trap, use of D_2O coolant in the fuel zone might be less inefficient. This is the basis of studies by R. D. Cheverton, Oak Ridge National Laboratory, for an enlarged HFIR-type reactor operating at high power densities, with a central H_2O flux-trap and a D_2O-cooled fuel zone.[4]

If the interest principally is in providing high thermal neutron fluxes for beam-tube facilities, D_2O moderation and cooling comes to the fore. The High Flux Beam Reactor (HFBR) of Brookhaven National Laboratory is cooled and reflected with D_2O.[(9)] The Franco-German high-flux reactor, for beam-tube experiments, will have a thin annular fuel zone with D_2O as coolant and reflector.[10] These two reactors have their experimental facilities in the outer radial reflector. The peak thermal neutron fluxes per unit reactor power at the tips of blind beam tubes in these reactors are $\sim 1.7 \times 10^{13}$ n-cm/cm^3-sec/MWt, which compares with calculated values in the range 1.2 to 1.5×10^{13} n-cm/cm^3-sec/MWt for the AARR with the HFIR-type core.

It has been suggested that other fissionable isotopes (e.g. Pu-239) might offer substantial improvements of efficiency of power utilization for flux-trap reactors. The following section includes some discussion along this line. According to Ref. 7, a fast-spectrum fuel zone with Pu-239 fuel has an idealized maximum value of 1.9 neutrons available for leakage, per fission. This compares with a listed value of 1.26 for a thermal reactor fueled with U-235. A flux-trap reactor with a fuel zone of this type offers promise of much higher efficiency for flux-traps radially beyond the fuel zone.

One reason for inefficient utilization of reactor power is that the fuel zone is sized to provide extra reactivity for core life. If this limitation can be eased, the fuel-zone thickness could be reduced and efficiency enhanced. (See Ref. 7.)

Returning now to the AARR with the HFIR-type reactor core, Fig. II-7-2, discussed earlier, shows the radial distribution of relative importance of fission-spectrum source neutrons in contributing to the peak group-16 (0–0.1 eV) neutron flux in the ITC. This curve is normalized to constant total shell source at all radii. Therefore, the curve giving the absolute contribution would be proportional to $r\overline{\nu\Sigma_f\phi}R(r)$, where r is the radius, in cm, $\overline{\nu\Sigma_f\phi}$ is the rate of production of fission-spectrum neutrons at r, and $R(r)$ is the radial distribution of relative importance. Figure II-19-3 of Ref. 2 shows radial distributions of $\overline{\Sigma_f\phi}$, but these are proportional to $\overline{\nu\Sigma_f\phi}$. To a good approximation, when the control rods are withdrawn fully, $\overline{\nu\Sigma_f\phi}$ has a flat radial distribution. In the idealized fresh reactor with control rods inserted fully, it was calculated that the radial distribution of $\overline{\nu\Sigma_f\phi}$ was nearly flat to within the last few centimeters from the outer edges of the fuel plates in the outer fuel element (see Fig. II-19-3(a) of Ref. 2).

The function $R(r)$ represents complicated sequences of events, including neutron scattering and migration at various energies and in various portions of the reactor. From this function alone, it does not appear to be feasible to infer much information about the effects of multiple reentry of neutrons into the ITC. This type of information may be obtained by methods where particle histories are elaborated, e.g., by special Monte Carlo analyses, or by computer programs which give data of first-collision probability in region j from a source in region k. The latter method is related closely to the method of calculating neutron flux by solving an integral equation for the flux resulting from the last flight of source neutrons. This analysis has not been performed for the AARR. However, some insight may be gained by performing calculations similar to the calculation of $R(r)$ but for cases where only source neutrons of a given energy group (groups 1–16) are introduced. The results, shown in Figs. II-7-3a and II-7-3b, give relative contributions of importance to the peak group-16 flux in the ITC for each of

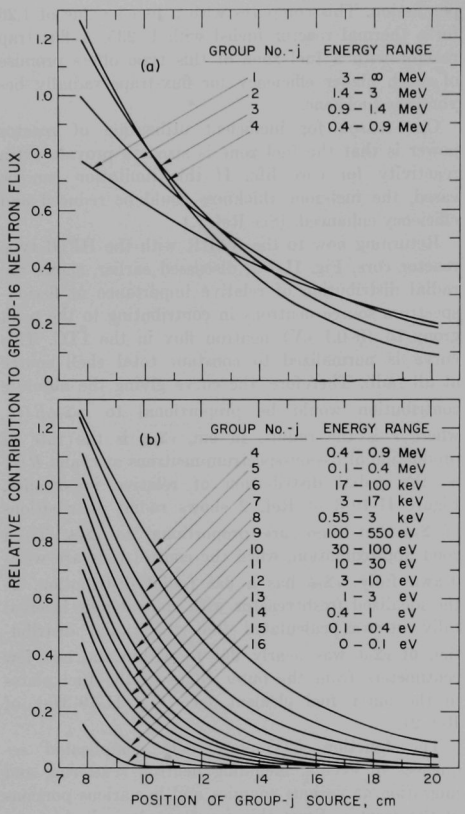

FIG. II-7-3. Relative Contribution by Group-j Neutron Sources in a Simplified Model of the HFIR-Type Core to the Group-16 Neutron Flux at the Center of the AARR Internal Thermal Column (Normalized to Unit Contribution by Group-2 Source at Inner Boundary of Reactor Fuel). *ANL Neg. No. 113-1544.*

the 16 energy groups. Not only are these distributions normalized to constant total shell source at r, but also they are renormalized relative to the curve for group No. 2 (1.4–3 MeV). Group No. 2 encompasses 34% of the total fission spectrum, and its energy span includes also the mean energy of fission neutrons.

Note that the importances of high-energy neutrons are high and that these importances drop off much less rapidly with distance from the ITC than the importances of low-energy neutrons. In particular, neutrons reentering the reactor core at low energy after suffering their last elastic collision in the ITC would have little effect on the thermal neutron flux in the ITC unless the next collision was close to the ITC. As noted earlier in this section, however, the total net leakage fraction of neutrons into the ITC of the AARR with the HFIR-type core is only 3.7%, summed over all neutron energies, and improvements in reentry contribution should be explored.

Remarks on Figures of Merit in Comparing Fuel Materials and Core Spectra for Optimizations of Levels of Thermal Neutron Flux in Flux-Traps

One parameter that has been suggested as an indicator of relative merits of different fuels and core spectra for flux-trap reactors is the maximum number of neutrons, per fission, that can be made available in the absence of parasitic neutron capture by the other materials in the fuel zone. The flux-trap reactors at issue here are systems of the general AARR/HFIR-type, namely, reactors with flux-trap regions outside the reactor fuel zone. This maximum excess number of neutrons per fission is $\nu-(1 + \alpha)$, where ν is an average value of the number of fission-spectrum neutrons produced per fission and $(1 + \alpha)$ is the associated average value of the number of neutrons absorbed by the fuel per fission. In part, these excess neutrons are available for leakage to flux-trap regions. However, the available excess reactivity must compensate actually for other neutron absorption in the fuel zone, and for unused leakage, e.g. axial leakage. And reactivity must be provided for the operation of the reactor and for core life.

For some flux-trap reactors it would be desirable to utilize some of the excess neutrons per fission by modifying the core design to increase the probability of neutron leakage. With thermal-spectrum or low-intermediate-spectrum cores of the AARR types, typically this would be accomplished by reducing the outer radius of the fuel zone. In these reactors there is a small contribution of power production at the inner (outer) boundary of the fuel zone to the thermal neutron flux in the flux-trap region near the outer (inner) boundary. Assuming that the amplitude and spatial distribution of power density are unchanged, the reduction in core thickness alone would have little effect on the levels of the thermal neutron flux in the flux-trap regions. (See Figs. II-7-1 and II-7-2.) However, there would be a more efficient utilization of the fission events in the fuel zone, i.e., the flux-trap levels of thermal neutron flux per unit reactor power would be raised. It is only in reactors where source neutrons from all radial regions of the reactor core contribute significantly

to the flux levels in the flux-traps that the reduced core thickness would significantly affect the flux levels; then the effect would be to reduce those flux levels, in the absence of changes in amplitude and spatial distribution of power density in the thinned core.

If the design constraint is the total reactor power, and if it is feasible to increase the power density in the fuel near the flux-trap zone, such a reduction in core thickness indeed would lead to an increase in experimenters' flux levels in the flux-trap. This benefit would be achieved at the cost of reactivity life of the core, but this might not be a significant disadvantage for some systems where reactivity life would not determine operating core life. Normally, however, the present interest in advanced constant-power flux-trap reactors is to operate at maximum power levels which are safely below burnout levels but are not very conservatively below. Therefore, for a well-designed reactor of this type, with a water-cooled reactor core, it would be the peak thermal neutron flux per unit reactor power that would be improved by a reduction in fuel-zone thickness, i.e., the efficiency of power utilization would be increased and not the absolute values of the thermal neutron flux in the flux-trap zones.

Another way to utilize available excess reactivity is to make the central flux-trap actually more heavily absorbing for thermal neutrons.[11] For reactors where it may be desired to increase the total capture rate in that flux-trap region, this might result in impressively large increases in total capture rate. But then the capture rate per atom of target material would be reduced drastically; for some experiments, this flux depression might be quite undesirable. An example of this is the AARR, for which it was intended that typically the parasitic macroscopic capture cross section of target material in the ITC would be kept small so as to minimize depression of the thermal neutron flux in the ITC.

For a given type of fuel zone (thermal, intermediate, fast) the average ν of the fissionable material influences the levels of Users' flux. If only the fission-spectrum-neutron source distributions were important to Users' flux, then, for fixed reactor power densities, the Users' flux would be proprotional to ν.

In view of the purposes of the AARR, and for a thermal or near-thermal reactor core, perhaps the most important improvement in peak Users' fluxes that would result from using a fissionable isotope like Pu-239 would be due to the higher values of ν. Preliminary calculations have been made for Pu-239 fuel and U-235 fuel in HFIR-type cores in the AARR. Pu-239 replaced U-235 on an atom-for-atom basis. For fixed reactor size and fixed reactor power, the calculational results are that the higher ν of Pu-239 provides a correspondingly higher peak thermal neutron flux in the radial beryllium reflector. However, the percentage increase in the peak thermal neutron flux in the ITC was only half as great. At least part of this difference may be explained by the increased blackness of the reactor fuel zone when Pu-239 is used on this basis.

These particular comparisons of Pu-239 and U-235 loadings were not sufficiently definitive to permit quantitative conclusions, but there was no clear indication, however, of a significant difference in the available excess reactivities of the two loadings when the boron burnable poison was deleted. Therefore the principal effects on thermal neutron flux levels outside the fuel zone were the difference in ν and probably the effect of Pu-239 in inhibiting repeated entry of near-thermal neutrons into the ITC.

Thus the choice of figures of merit for comparison of usefulness of reactor fuels and reactor types might be determined principally by the objectives and design constraints of the particular flux-trap reactor. For some flux-trap reactors, the parameter $\nu - (1 + \alpha)$, the maximum number of excess neutrons per fission, might be a useful figure of merit. For other flux-trap reactors, perhaps the average value of ν itself is of principal interest.

References

1. D. H. Shaftman, *Argonne Advanced Research Reactor Calculations—Factors in Optimization of Experimenters' Flux*, Reactor Physics Division Annual Report, July 1, 1965 to June 30, 1966, ANL-7210, pp. 95–99.
2. D. H. Shaftman and R. P. Savio, *Argonne Advanced Research Reactor Calculations—General Reactor Physics Design Analysis*, Reactor Physics Division Annual Report, July 1, 1966 to June 30, 1967, ANL-7310, pp. 99–107.
3. R. P. Savio and D. H. Shaftman, *Argonne Advanced Research Reactor Calculations—Analysis of Critical Experiments with the Intermediate-Spectrum Core*, Reactor Physics Division Annual Report, July 1, 1966 to June 30, 1967, ANL-7310, pp. 94–99.
4. T. E. Cole, *The Oak Ridge High Flux Isotope Reactor; Design and Initial Operation*, Seminar on Intense Neutron Sources, Santa Fe, New Mexico, September 19–23, 1966, CONF-660925 Physics, pp. 183–213.
5. F. T. Binford, T. E. Cole and E. N. Cramer, Eds., *The High-Flux Isotope Reactor; A Functional Description:* Volume 1, ORNL 3572 (Rev. 2), (May 1968).
6. H. A. McLain, *HFIR Fuel Element Steady State Heat Transfer Analysis (Revised Version)*, ORNL-TM-1904 (December 1967).
7. B. I. Spinrad, *Limitations of Steady State, High Flux Reactors, Current and Future*, Seminar on Intense Neutron Sources, Santa Fe, New Mexico, September 19–23, 1966, CONF-660925 Physics, pp. 319–359.
8. C. N. Kelber, B. I. Spinrad and L. J. Templin, *Advanced*

High-Flux Research Reactor Technology, Trans. Am. Nucl. Soc. **5**, 425 (1962).

9. K. H. Beckurts and R. Dautray, *Project Studies for the Franco-German High Flux Reactor*, Seminar on Intense Neutron Sources, Santa Fe, New Mexico, September 19–23, 1966, CONF-660925 Physics, pp. 281–310.
10. J. M. Hendrie and H. J. C. Kouts, *HFBR: A Source Reactor for Neutron Beams*, Seminar on Intense Neutron Sources, Santa Fe, New Mexico, September 19–23, 1966, CONF-660925 Physics, pp. 157–182.
11. C. N. Kelber, *Physics of Plutonium Fueled Thermal Research and Test Reactors*, Reactor Physics Division Annual Report, July, 1, 1966 to June 30, 1967, ANL-7310, pp. 42–45.

Section III

Fast Reactor Physics

Intensive work on liquid metal fast breeder reactor physics continued in the Reactor Physics Division during Fiscal year 1968 and much of the analytical and experimental effort is reported in this section. The first two papers describe various assemblies in ZPR-6 and -9, and report results of measurements of these assemblies. The next six papers are concerned with problems related to Doppler phenomena and the next several papers treat neutron resonance studies. Two papers consider heterogeneity effects and several papers discuss neutron spectral problems. A number of papers report on a miscellany of studies pertinent to fast reactors, eight papers present analyses of various EBR-II problems, and one paper describes calculations made in support of the Fast Flux Test Facility (FFTF).

III-1. A 4000-Liter Uranium Oxide Fast Core, Assembly 6 of ZPR-6

R. A. Karam, L. R. Dates, W. Y. Kato, J. E. Marshall, T. Nakamura*
and G. K. Rusch

A 4000-liter UO_2 fast core, Assembly 6 of ZPR-6, was built for the purpose of obtaining experimental parameters characteristic of large fast reactors. Such parameters are used to verify data sets and analytical methods.

Assembly 6 was cylindrical in geometry with L/D, the length to diameter ratio, of 0.84. The core was reflected with 30 cm of depleted uranium (0.2% enrichment) in both the radial and axial directions. The height of the core was 152.4 cm and the total height (core and reflector) was 212.4 cm. The radial dimensions as well as the material concentrations in each region are given in Table III-1-I. (The non-uniformity of the concentrations of the materials in the core regions is due to differences in the weight per unit length of the various plates used.) The core was loaded with plates which in effect formed planes interrupted only by the stainless steel in the square matrix unit cell of the ZPR-6 facility.[1] The unit cell in the core regions comprised a single drawer loading pattern in which the plates were arranged in the manner shown in Fig. III-1-1. This pattern, as well as the material composition, is similar to those of the proposed ZPPR Assembly 3. ZPPR Assembly 3, however, will be fueled with plutonium instead of the uranium in Assembly 6. Figure III-1-2 shows a cross sectional view of Assembly 6.

TABLE III-1-I. Material Concentrations in Assembly 6 of ZPR-6

Region	Outer Radius, cm	Atoms per cc, $\times 10^{24}$						
		U-235	U-238	Na	O	Fe	Ni	Cr
1	77.17	0.001150	0.005796	0.009142	0.01465	0.01410	0.001365	0.002788
2	85.53	0.00107	0.005790	0.007790	0.01465	0.1572	0.001582	0.003254
3	90.87	0.00156	0.005780	0.008310	0.01465	0.01524	0.001518	0.003115
Blanket	120.63	0.0000827	0.04008	—	—	0.0042282	0.0005665	0.001215

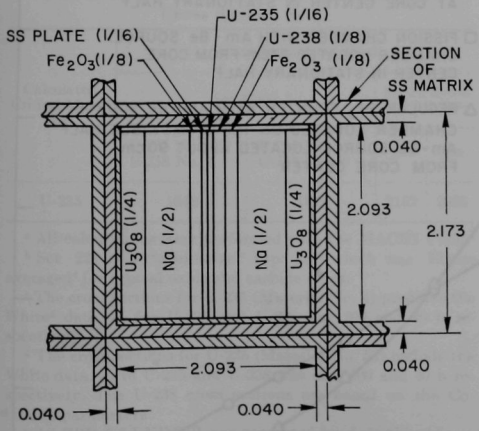

Fig. III-1-1. Normal Drawer Loading Pattern. *ANL Neg. No. 113-1386 A.*

Multiplication

The usual two BF_3 proportional counters located on top of the square matrix of ZPR-6, when used for multiplication purposes in conjunction with the Am-Be sources located in each half at the core-reflector interface, yield multiplication curves that predict too large a critical mass at the beginning of the multiplication process. The slope of the curves changes as the multiplication process continues and a prediction of too small a critical mass, shifting toward the true critical mass as the critical size is approached, become apparent. Placing additional counters such as fission chambers in or around the core center never eliminated the non-linearity of reciprocal multiplication versus fuel mass. The reason for the non-linearity is tied to the change in the spatial distribution of the neutrons as the size of the core is increased. The variation in the spatial

* Resident Associate, Japan Atomic Energy Research Institute, Tokai-mura, Japan.

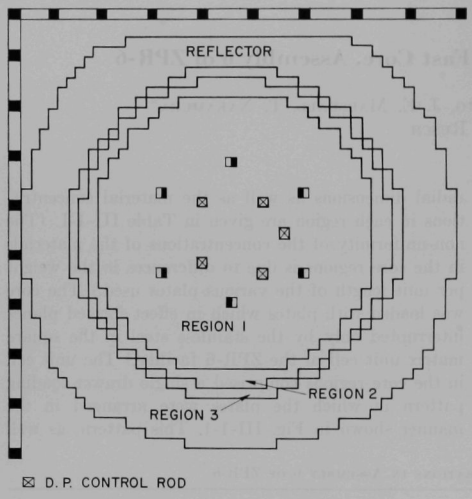

FIG. III-1-2. Cross Sectional View of Assembly 6.

distribution can be minimized provided the neutron source and the neutron monitor are placed at the core center. The flux gradient of the asymptotic mode at the core center is zero when the system is critical. When the sytem contains no fuel, the flux distribution may be approximated by an exponential.

$$\phi(x) = \phi_0 e^{-\alpha x},$$

and

$$\left.\frac{d\phi(x)}{dx}\right|_{x=0} = -\alpha\phi_0,$$

where ϕ is the neutron flux, ϕ_0 is the neutron source strength and α is the removal cross section of the diluent materials. Thus, if the value of α is small, as is the case in fast reactors, then the spatial variations in the flux at the center of the core is minimized.

Such a technique was applied to Assembly 6. A BF_3 proportional counter was placed along with a Cf-252 source at the core center. The source strength was about 5×10^5 neutrons per sec. The results obtained with this method are compared with the previously used methods illustrated in Fig. III-1-3. It is seen that a very nearly straight line is obtained

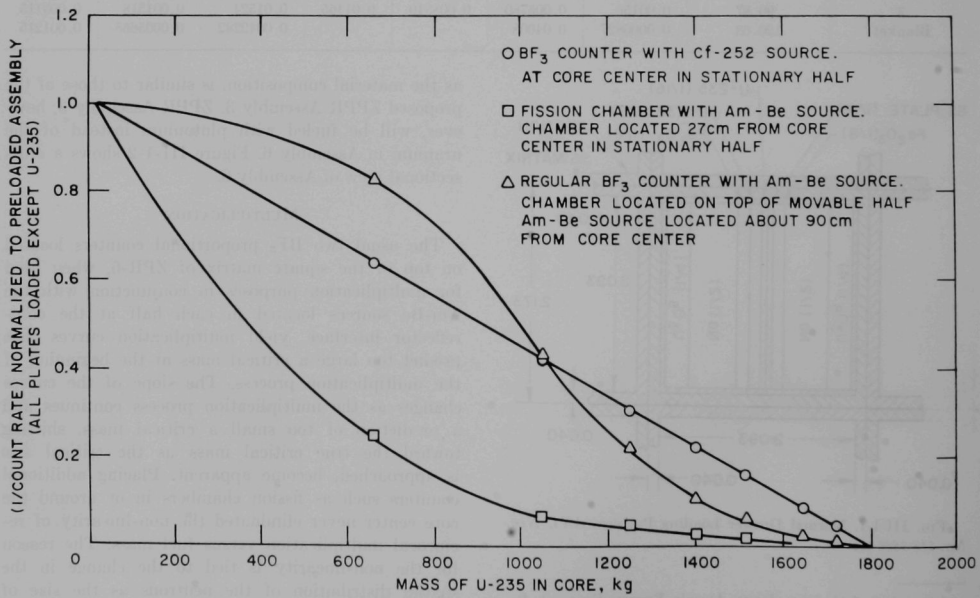

FIG. III-1-3. Critical-loading History of Assembly 6 of ZPR-6. *ANL Neg. No. 113-1462.*

when the counter and source are at the center of the core.

Fatman Effect

The effect of introducing hydrogenous material between the separated halves on the k_{eff} of one half was investigated for the purpose of determining the hazard associated with a man walking between the halves. This investigation comprised measuring the increase in multiplication associated with the stationary half when a slab of benelex (fatman), 20 cm thick, was slowly inserted to cover its face. The locations of the neutron source and the detector were at the center of the stationary half. The measurements were

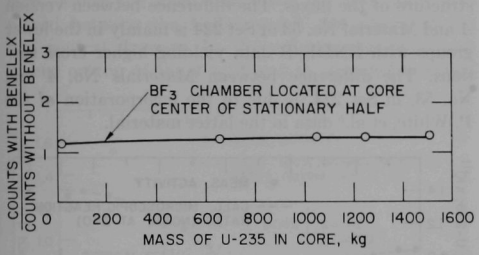

Fig. III-1-4. Measurement of Fatman Effect for Assembly 6 of ZPR-6. *ANL Neg. No. 113-1463.*

TABLE III-1-II. Critical Mass Dependence on Cross Section Sets

Calculated Critical Mass,[a] kg	Cross Section Set Used			
	Set 224[b]		Set ZPR-6-6 ENDF/B[e]	
	U-235 No. 4 [c] U-238 No. 1	U-235 No. 53[d] U-238 No. 58	A[f]	B[g]
U-235	1648	1729	2152	2088

[a] All calculations were performed with the MACH1 Code.[2]

[b] Set 224 is a "workhorse" type set[3] which was Elmoe averaged[4] for typical oxide and carbide cores.

[c] The cross sections for U-235 (Material No. 4) predates the White[5] data. σ_p for U-235 and U-238 was 200 and 40 b respectively.

[d] The cross sections for U-235 (Material No. 53) include the White data. σ_p of U-235 and U-238 was also 200 and 40 b respectively. The U-238 cross sections are based on the Columbia parameters.

[e] Set ZPR-6-6 ENDF/B was generated for Assembly 6 from the ENDF/B data with the MC^2 Code.[6] Self-shielding in U-238 was included via group dependent σ_p.

[f] Version A of Set ZPR-6-6 ENDF/B did not include the spatial averaging of the cross sections with the fine structure of the fluxes in a unit cell.[7]

[g] Version B of this set did include the averaging referred to in footnote f.

TABLE III-1-III. Comparison of Absorption Cross Sections of U-238 Used in Sets

Group	Lower Energy Boundary, keV	Set 224		Set ZPR-6-6 ENDF/B	
		Material No. 4, σ_p = 40 b	Material No. 58, σ_p = 40 b	A	B
1	3.6788×10^3	0.6386	0.6387	0.7594	0.7873
2	2.2313×10^3	0.5960	0.5860	0.5872	0.5980
3	1.3534×10^3	0.4841	0.4841	0.4893	0.4920
4	8.2085×10^2	0.1552	0.1551	0.1722	0.1745
5	4.9787×10^2	0.1317	0.1316	0.1412	0.1421
6	3.0197×10^2	0.1158	0.1158	0.1349	0.1357
7	1.8316×10^2	0.1398	0.1398	0.1511	0.1512
8	1.1199×10^2	0.1914	0.1914	0.1818	0.1815
9	6.7379×10^1	0.2588	0.2588	0.2359	0.2357
10	4.0868×10^1	0.3366	0.3394	0.3321	0.3317
11	2.4787×10^1	0.4172	0.4068	0.4401	0.4390
12	1.5034×10^1	0.5011	0.5034	0.5559	0.5524
13	9.1188×10^0	0.6177	0.6085	0.6731	0.6681
14	4.3074×10^0	0.6600	0.7142	0.8049	0.7989
15	2.6126×10^0	0.7526	0.5653	0.9655	1.0003
16	2.0347×10^0	0.8200	0.5875	1.008	0.9308
17	1.2341×10^0	0.8910	0.5943	0.9152	0.8810
18	9.6112×10^{-1}	0.9425	0.8158	1.082	1.053
19	5.8295×10^{-1}	0.9290	0.9472	1.120	1.093
20	2.7536×15^{-1}	0.9067	0.7762	0.9794	0.9527
21	1.0130×10^{-1}	1.174	1.364	1.317	1.263
22	2.9023×10^{-1}	1.827	1.808	1.499	1.456

TABLE III-1-IV. Comparison of Absorption Cross Sections of U-235 Used in Sets

Group	Set 224		Set ZPR-6-6 ENDF/B	
	Material No. 4	Material No. 53	A	B
1	1.279	1.279	1.372	1.970
2	1.333	1.333	1.339	1.730
3	1.383	1.383	1.346	1.645
4	1.365	1.365	1.342	1.552
5	1.310	1.311	1.335	1.397
6	1.438	1.437	1.453	1.498
7	1.620	1.636	1.616	1.615
8	1.895	1.905	1.888	1.867
9	2.288	2.218	2.215	2.182
10	2.771	2.607	2.617	2.560
11	3.365	3.076	3.060	2.979
12	4.111	3.653	3.545	3.411
13	4.904	4.075	4.211	4.018
14	6.309	4.972	5.535	5.200
15	8.116	6.476	6.820	6.385
16	9.108	7.750	8.217	7.224
17	9.973	9.218	10.03	8.967
18	11.27	11.24	13.24	11.57
19	12.75	13.14	15.26	13.20
20	15.94	16.81	19.70	16.48
21	22.55	24.21	32.89	25.23
22	32.18	34.40	36.17	27.75

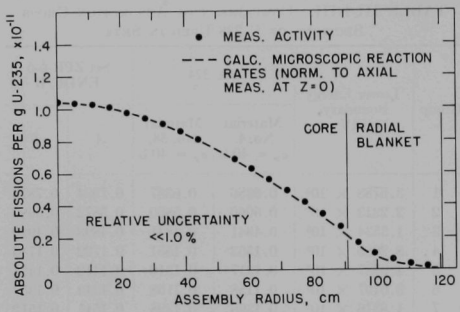

FIG. III-1-5. U-235 Fission Distribution as a Function of the Radial Dimension in Assembly 6, ZPR-6. *ANL Neg. No. 113-1493.*

made as a function of the amount of U-235 in the system when the two halves were opened. Figure III-1-4 shows the results. It is seen that the increase in the multiplication associated with the fatman was negligible.

Control Rods

The measured reactivity worth of a B-10 safety blade at an equivalent radius of 38.7 cm from the center of the core was 82.5 Ih (1% $\Delta k/k$ = 458 Ih). The B-10 blade contained 365.28 g of 90% enriched boron. The B-10 material was enclosed in a stainless steel shell with inside dimensions of 75 × 4.72 × 71.12 cm. The wall of the stainless steel shell was 0.081 cm thick.

The measured reactivity worth of a control drawer was 14 Ih at an equivalent radius of 27.62 cm. A control drawer was the same as any other drawer, except that the $\frac{1}{16}$ in. plate of stainless steel shown in the loading pattern of Fig. III-1-1 was removed and compensated for with thicker walls of the control drawer.

Critical Mass

The measured critical mass of Assembly 6 for the loading pattern shown in Fig. III-1-1 was 1817 kg of U-235. This value of critical mass is corrected for excess reactivity only.

The value of the calculated critical mass varied with the cross section set used. The calculations are summarized in Table III-1-II. Descriptions of the cross section sets are given in the footnotes to Table III-1-II. The reason for the wide variation in the calculated critical mass is primarily due to the large variations in the group cross sections of U-238 and U-235. Table III-1-III shows the absorption cross sections of U-238 used in the four sets. It is seen from Table III-1-III that the U-238 absorption cross section obtained with the Columbia parameters (Material No. 58) are considerably lower in groups 11–20 than those obtained from ENDF/B. In fact the discrepancy in some groups is as high as 75%. Further investigations of the origin of those discrepancies is required before definitive conclusions can be made.

Table III-1-IV compares the absorption (capture and fission) cross sections of U-235 in the various sets. The difference in values between versions *A* and *B* of the ZPR 6-6 ENDF/B cross section set is due to spatial averaging of the cross sections with the fine structure of the fluxes. The difference between version *A* and Material No. 53 of Set 224 is mainly in the lower groups with ENDF/B data yielding higher cross sections. The difference between Materials No. 4 and No. 53, in Set 224, is due to the incorporation of the P. White, et al.[5] data in the latter material.

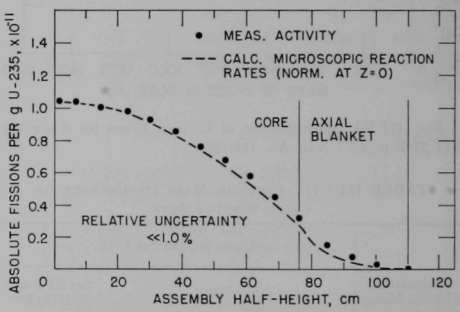

FIG. III-1-6. U-235 Fission Distribution as a Function of the Axial Dimension of Assembly 6, ZPR-6. *ANL Neg. No. 113-1492.*

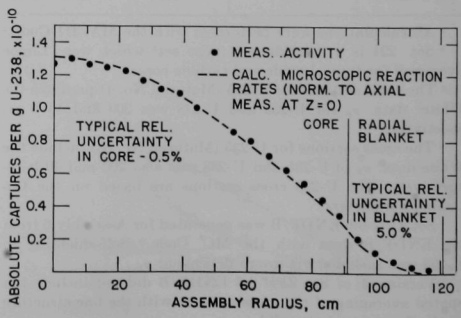

FIG. III-1-7. U-238 Capture Distribution as a Function of Radius in Assembly 6, ZPR-6 *ANL Neg. No. 113-1491.*

Spatial Distribution of Fission and Capture Rates

The fission rates in U-235 and U-238 and capture rates in U-238 were measured with foils as functions of the axial and radial dimensions in Assembly 6. Depleted uranium foils (0.2% enrichment, 5 mils thick by ⅝ in. diam) and U-235 foils (93% enrichment, 4.5 mils thick by ⅜ in. diam) were respectively placed in the stationary and movable halves at corresponding locations about the center of the core. For the radial traverses the foils were placed in every drawer, between the 1/16 in. U-235 plate and the ⅛ in. U-238 plate (see Fig. III-1-1) at a distance of 2 in. from the mid-section of the core. Along the axial dimension the foils were also placed between the U-235 and U-238 plates in the two central drawers. In the reflector the foils were placed on top of the 2 × 2 × 5 in. depleted uranium blocks. The foils were counted and converted to absolute numbers by the method described in Paper III.15. The results are plotted in Figs. III-1-5 through III-1-10.

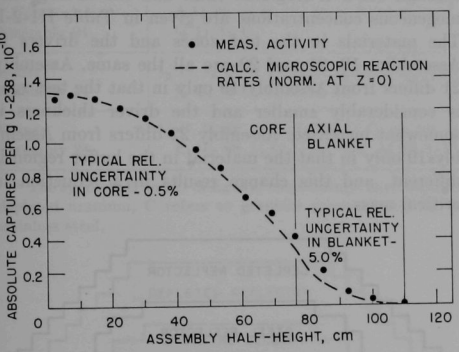

Fig. III-1-8. U-238 Capture Distribution as a Function of Z in Assembly 6, ZPR-6. *ANL Neg. No. 113-1515.*

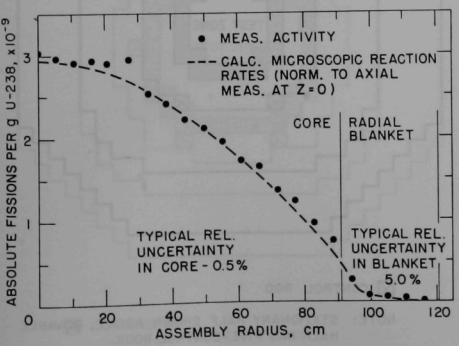

Fig. III-1-9. U-238 Fission Distribution as a Function of Radius in Assembly 6, ZPR-6. *ANL Neg. No. 113-1494.*

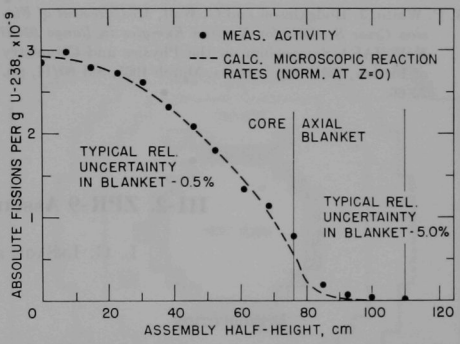

Fig. III-1-10. U-238 Fission Distribution as a Function of Height in Assembly 6, ZPR-6. *ANL Neg. No. 113-1490.*

The reaction rates, shown in Figs. III-1-5 through III-1-10, were also calculated with the ZPR 6-6 ENDF/B-B cross section set and the MACH1 code.[2] Since this cross section set overpredicted the critical mass, it was necessary to do a concentration search, increasing the U-235 concentrations uniformly in the core at the expense of the U-238 concentrations, and holding the measured critical dimensions constant. This procedure was necessary in order to have the measured and calculated boundaries and interfaces coincide. In Fig. III-1-9 the seemingly bad measured points are due to systematic errors associated with the reactor because this measurement was repeated twice with reasonably good reproducibility.

Other Parameters

Measurements of such parameters as heterogeneity effects, sodium void effects, central reactivity worths of various samples and neutron spectrum are reported elsewhere (see Papers III-13, III-15, III-18 and III-21).

References

1. W. Y. Kato, G. J. Fischer and L. R. Dates, *Safety Analysis Report—Argonne Fast Critical Facility ZPR-6*, ANL-6271 (1963).
2. D. A. Meneley, L. Kvitek and D. O'Shea, *MACH 1, A One-Dimensional Diffusion-Theory Package*, ANL-7223 (1966).
3. D. M. O'Shea, H. H. Hummel, W. B. Loewenstein and D. Okrent, *Twenty-Six Group Cross Sections*, Trans. Am. Nucl. Soc. **7**, 242 (1964).
4. A. L. Rago and H. H. Hummel, *ELMOE, An IBM 704 Program Treating Elastic Scattering Resonances in Fast Reactors*, ANL-6805 (1964).

5. P. White, J. Hodgkinson and G. Wall, *Measurement of Fission Cross Sections for Neutron Energies in Range 40–50 KeV*, IAEA Symposium on the Physics and Chemistry of Fission, Salzburg, Austria, March 1965, SM 60/14, pp. 22–66.
6. B. J. Toppel, A. L. Rago and D. M. O'Shea, *MC²—A Code to Calculate Multigroup Cross Sections*, ANL-7318 (1967).
7. D. Meneghetti, *Calculation Studies of Sodium Void Reactivity Variations Due to Thin Slab Heterogeneities in Fast Criticals*, ANL-7320 (1966).

III-2. ZPR-9 Assemblies 19, 21, 22 and 24

L. G. LeSage and W. R. Robinson

Introduction

During the period from July 1967 to June 1968, four different small-zoned critical assemblies were constructed on ZPR-9. These were designated Assemblies 19, 21, 22 and 24. An assembly designated as number 20 was planned, but later dropped from the experimental program. Assembly 23 was also constructed, but it was identical to Assembly 19. A description of each of the assemblies is contained in this paper. Both calculated and measured data are included. The measurements which were a part of the experimental programs carried out on the assemblies are reported in Paper III-17.

General Description of Assemblies

All the assemblies were basically cylindrical and contained a central test zone surrounded by concentric buffer, driver, inner reflector and outer reflector regions. Steel was used in the inner reflector regions to reduce the critical mass. The loading arrangement patterns for the assemblies are given in Figs. III-2-1 through III-2-4. Regional radii and the average homogeneous concentrations are given in Table III-2-I. The materials in the test zones and the drivers in Assemblies 19, 21 and 22 are all the same. Assembly 21 differs from Assembly 19 only in that the test zone is considerably smaller and the driver thickness is somewhat increased. Assembly 22 differs from Assembly 19 only in that the material in the buffer region is different, and this change results in a reduction in critical mass.

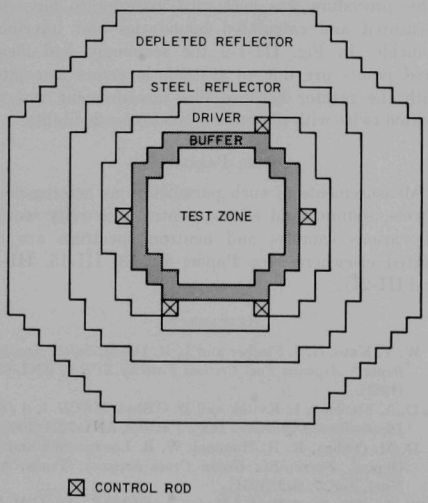

Fig. III-2-1. Assembly Loading Pattern ZPR-9, Assembly 19. *ANL Neg. No. 113-1404.*

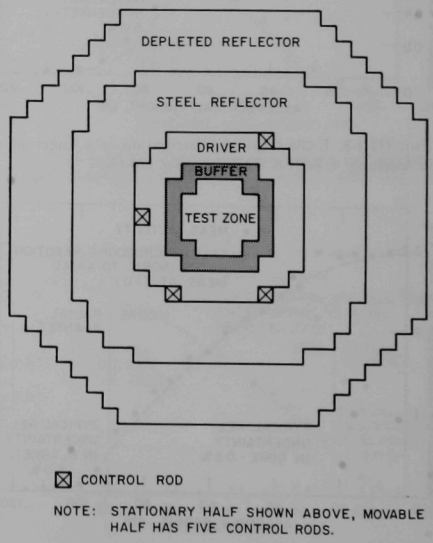

Fig. III-2-2. Assembly Loading Pattern ZPR-9, Assembly 21. *ANL Neg. No. 113-1409.*

The specific drawer loading patterns for each assembly in the test zone, buffer, and driver regions are as follows, with plate thicknesses given in inches; e.g., ¼ U_3O_8 implies ¼ in. thick U_3O_8 plate:

Test Zone Assemblies 19, 21 and 22	¼ U_3O_8, ½ Na, ⅛ Fe_2O_3, 1/16 SS,[a] 1/16 E,[a] ⅛ D,[a] ⅛ Fe_2O_3, ½ Na, ¼ U_3O_8.
Buffer Assemblies 19 and 21	¼ U_3O_8, ¼ Al, ¼ U_3O_8, ⅛ Al, ¼ U_3O_8, ⅛ Al, ¼ U_3O_8, ¼ Al, ¼ U_3O_8.
Buffer Assembly 22	2 Al (full drawer of aluminum)
Driver Assemblies 19, 21 and 22	⅛ C,[a] ⅛ SS, ⅛ C, ⅛ E, ⅛ SS, ⅛ C, ⅛ SS, 1/16 SS, ⅛ C, 1/16 SS, ⅛ SS, ⅛ C, ⅛ SS, ⅛ E, ⅛ C, ⅛ SS, ⅛ C.
Test Zone (Null Composition) Assembly 24	⅛ C, ⅛ D, ¼ C, ⅛ D, [1/16 Row: ⅔ C & ⅓ D], ¼ C, 1/16 E, ¼ C, ¼ D, ¼ C, ⅛ D, ⅛ C.
Buffer Assembly 24	⅛ D, ¼ C, ⅛ D, ¼ C, ⅛ D, ¼ C, ⅛ D, ¼ C, ⅛ D, ¼ C, ⅛ D.
Driver Assembly 24	⅛ C, ⅛ SS, ¼ C, ⅛ SS, ¼ C, 1/16 SS, ⅛ E, 1/16 SS, ¼ C, ⅛ SS, ¼ C, ⅛ SS, ⅛ C.

[a] The symbols E and D designate respectively, enriched and depleted uranium, C refers to graphite (carbon) and SS to stainless steel.

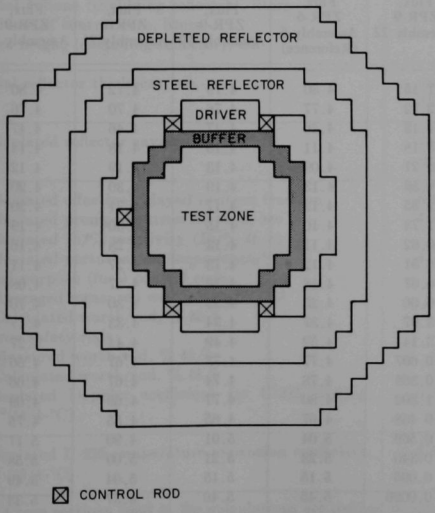

FIG. III-2-3. Assembly Loading Pattern ZPR-9, Assembly 22. *ANL Neg. No. 113-1403.*

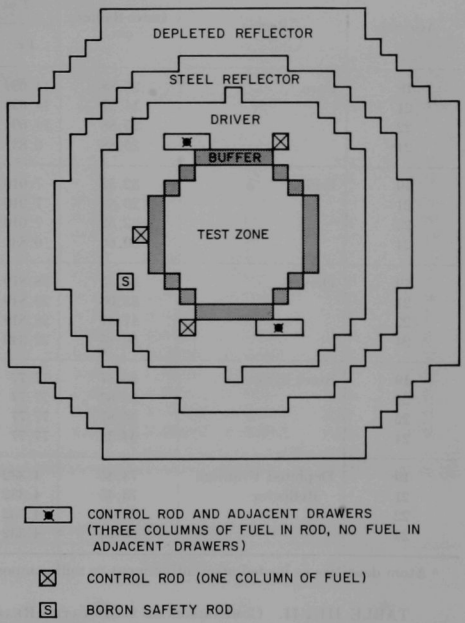

FIG. III-2-4. Assembly Loading Pattern ZPR-9, Assembly 24. *ANL Neg. No. 113-1411.*

The calculated real and adjoint centerline fluxes are included in Tables III-2-II and III-2-III. The appropriate reference spectra for each of the zoned assemblies is also included for comparison. The calculations were made with the one-dimensional diffusion code, MACH-1,[1] in cylindrical geometry. The cross section sets used for the calculation of the fluxes and other parameters are identified in the appropriate tables. Generally, the cross section sets were generated by the MC^2 code;[2] however, some of the analysis was completed before the ENDF/B cross sections were available. No heterogeneity corrections have been included in the calculations.

Calculated and measured parameters for the assemblies are included in Table III-2-IV. As before, most of the calculations were performed using the Mach-1 code. The control rod calculations were made using the first-order perturbation subroutine to the MACH-1 code, DEL, by perturbing the control rod material throughout the region. Good agreement between the calculated and measured rod worths has been obtained for the dual-purpose fuel rods. The calculations generally overpredict the worth of the boron rods because of self-shielding in the boron.

TABLE III-2-I. ZPR-9 ASSEMBLIES 19, 21, 22, AND 24

Assembly	Region	Outer Radius, cm	Atom Densities × 10^{-21}								
			Fe	Ni	Cr	Na	C	O	Al	U-238	U-235
19	Core	25.88	14.694	1.202	3.035	9.323	—	14.563	—	5.813	1.156
21		14.27	14.694	1.202	3.035	9.323	—	14.563	—	5.813	1.156
22		25.88	14.694	1.202	3.035	9.323	—	14.563	—	5.813	1.156
24[a]		25.88	6.831	0.864	1.950	—	44.736	—	—	12.624	1.171
19	Buffer	32.52	7.010	0.793	2.00	—	—	21.732	18.708	8.259	0.017
21		20.89	7.010	0.793	2.00	—	—	21.732	—	8.259	0.017
22		32.52	7.010	0.793	2.00	—	—	—	49.927	—	—
24		30.66	6.831	0.864	1.950	—	43.330	—	—	14.560	0.0311
19	Driver	43.35	28.819	3.536	8.196	—	30.331	—	—	0.325	4.553
21		32.06	28.819	3.536	8.196	—	30.331	—	—	0.325	4.553
22		41.31	28.819	3.536	8.196	—	30.331	—	—	0.325	4.553
24		50.85	22.349	2.825	6.379	—	43.330	—	—	0.162	2.277
19	Steel Reflector	56.87	77.77	0.891	2.036	—	—	—	—	—	—
21		56.87	77.77	0.891	2.036	—	—	—	—	—	—
22		56.87	77.77	0.891	2.036	—	—	—	—	—	—
24		64.38	77.77	0.891	2.036	—	—	—	—	—	—
19	Depleted Uranium Reflector	73.45	4.332	0.540	1.140	—	—	—	—	39.93	0.081
21		73.45	4.332	0.540	1.140	—	—	—	—	39.93	0.081
22		73.45	4.332	0.540	1.140	—	—	—	—	39.93	0.081
24		80.95	4.332	0.540	1.140	—	—	—	—	—	—

[a] Atom densities as loaded after adjustment to null composition.

TABLE III-2-II. COMPARISON OF CALCULATED REAL AND ADJOINT CENTERLINE FLUXES FOR ZPR-6 ASSEMBLY 6 AND ZPR-9 ASSEMBLIES 19, 21, AND 22[(a)]

Group	Group Lower Energy Limit, keV	Centerline Flux, ZPR-6 Assembly 6 (Reference)	Centerline Flux, ZPR-9 Assembly 19	Centerline Flux, ZPR-9 Assembly 21	Centerline Flux, ZPR-9 Assembly 22	Centerline Adjoint Flux, ZPR-6 Assembly 6 (Reference)	Centerline Adjoint Flux, ZPR-9 Assembly 19	Centerline Adjoint Flux, ZPR-9 Assembly 21	Centerline Adjoint Flux, ZPR-9 Assembly 22
1	3679	1.20	1.19	1.16	1.15	4.80	4.79	4.72	4.80
2	2231	2.74	2.72	2.68	2.72	4.77	4.76	4.70	4.76
3	1353	4.45	4.41	4.41	4.13	4.46	4.47	4.46	4.47
4	821	5.69	5.68	5.81	5.18	4.11	4.15	4.18	4.14
5	500	10.23	10.25	10.50	10.21	4.09	4.13	4.19	4.12
6	302	9.40	9.45	9.71	9.59	4.13	4.19	4.30	4.20
7	183	11.89	11.98	12.21	12.55	4.12	4.17	4.31	4.20
8	111	12.05	12.11	12.08	11.73	4.10	4.15	4.30	4.19
9	67.4	10.22	10.22	10.10	10.62	4.11	4.13	4.28	4.16
10	40.9	8.60	8.58	8.40	8.51	4.12	4.13	4.27	4.11
11	24.8	6.44	6.41	6.32	6.67	4.18	4.16	4.27	4.08
12	15.0	6.12	6.09	5.94	6.06	4.25	4.22	4.30	4.10
13	9.12	3.96	3.93	3.82	3.97	4.37	4.34	4.33	4.17
14	4.31	2.89	2.87	2.83	3.14	4.52	4.49	4.44	4.27
15	2.61	0.622	0.619	0.616	0.607	4.77	4.73	4.67	4.56
16	2.03	0.779	0.777	0.795	0.369	4.78	4.74	4.67	4.66
17	1.23	1.400	1.402	1.379	1.302	4.80	4.77	4.69	4.69
18	0.961	0.427	0.428	0.408	0.458	4.67	4.65	4.55	4.75
19	0.583	0.507	0.505	0.462	0.569	5.04	5.01	4.90	5.17
20	0.275	0.307	0.303	0.271	0.346	5.23	5.21	5.09	5.58
21	0.101	0.084	0.083	0.075	0.095	5.15	5.15	5.04	5.49
22	0.0290	0.0081	0.0079	0.0076	0.0096	5.45	5.46	5.37	5.33

[a] The spectra were computed in cylindrical geometry by the MACH-1 code[1] using the cross section sets generated by the MC[2] code[2]. ENDF/B cross sections were not used.

TABLE III-2-III. COMPARISON OF CALCULATED REAL AND ADJOINT CENTERLINE FLUXES FOR THE REFERENCE CASE (INFINITE MEDIUM) AND FOR ZPR-9 ASSEMBLY 24[a]

Group	Group Lower Energy Limit, keV	Centerline Flux (Reference)	Centerline Flux ZPR-9 Assembly 24	Centerline Adjoint Flux, (Reference)	Centerline Adjoint Flux, ZPR-9 Assembly 24	Group	Group Lower Energy Limit, keV	Centerline Flux (Reference)	Centerline Flux, ZPR-9 Assembly 24	Centerline Adjoint Flux (Reference)	Centerline Adjoint Flux, ZPR-9 Assembly 24
1	3679	1.33	1.30	4.12	4.18	16	2.03	1.37	1.39	3.32	3.30
2	2231	2.66	2.59	3.84	3.93	17	1.23	2.19	2.24	3.40	3.38
3	1353	4.14	4.04	3.45	3.54	18	0.961	0.861	0.879	3.51	3.49
4	821	5.65	5.55	3.04	3.14	19	0.583	1.30	1.33	3.66	3.64
5	500	7.73	7.63	2.99	3.07	20	0.275	1.19	1.22	3.85	3.83
6	302	8.97	8.88	2.95	2.99	21	0.101	0.650	0.666	3.80	3.78
7	183	9.15	9.09	2.90	2.92	22	0.0373	0.221	0.227	3.70	3.68
8	111	8.69	8.67	2.86	2.86	23	0.0290	0.0114	0.0118	2.98	2.96
9	67.4	8.32	8.33	2.82	2.82	24	0.0226	0.0130	0.0133	3.38	3.36
10	40.9	7.82	7.86	2.80	2.79	25	0.0137	0.00827	0.00852	2.42	2.40
11	24.8	6.95	7.01	2.79	2.78	26	0.00831	0.00380	0.00393	3.19	3.16
12	15.0	6.13	6.20	2.82	2.81	27	0.00306	0.00120	0.00125	1.36	1.35
13	9.12	5.34	5.41	2.88	2.87	28	0.00113	0.00041	0.00043	4.69	4.66
14	4.31	6.05	6.14	2.97	2.95	29	0.000414	0.000086	0.000091	5.96	5.91
15	2.61	3.26	3.31	3.18	3.15	30	0.000025	0.000011	0.000011	4.36	4.32

[a] The MACH-1 one-dimensional diffusion code[1] (cylindrical geometry) and a cross section set generated by the MC[2] code[2] from ENDF/B data were used in the calculations.

TABLE III-2-IV. LIST OF MEASURED AND CALCULATED PARAMETERS FOR ASSEMBLIES 19, 21, 22, AND 24

	Assembly[a]			
	19	21	22	24
Measured critical mass, kg	480.3	340	439.3	505
Calculated critical mass, kg	506	329	418	508
Mass of U-235 in central core, kg	87	26	87	87
Total volume (excluding reflector), liters	540	295	490	743
Volume of central core, liters	192	58	192	192
Core height (excluding reflector), cm	91.4	91.4	91.4	91.4
Axial reflector thickness, cm	15.2 Steel 15.2 U	15.2 Steel 15.2 U	15.2 Steel 15.2 U	15.2 Steel 15.2 U
Calculated reflector savings, cm	core 18.2 driver 8.2	core 18.2 driver 8.2	core 18.2 driver 8.2	—
Calculated effective delayed neutron fraction	6.89×10^{-3}	6.89×10^{-3}	6.76×10^{-3}	7.04×10^{-3}
Calculated prompt neutron lifetime, sec	4.07×10^{-7}	4.66×10^{-7}	4.41×10^{-7}	5.57×10^{-7}
Calculated Ih/% reactivity (Ih/% $\delta k/k$)	435.5	429.5	435.2	422.4
Calculated perturbation denominator[b]	4.72×10^{5}	2.99×10^{5}	4.36×10^{5}	7.23×10^{5}
Dual purpose (fuel) control rods:				
Averaged measured worth/rod, % $\delta k/k$	0.243	0.300	0.255	0.135[c]
Calculated worth/rod, % $\delta k/k$	0.220	0.370	0.238	0.117
Boron safety rods:				
Measured worth/rod, % $\delta k/k$	−0.180	—	—	−0.36
Calculated worth/rod, % $\delta k/k$	−0.335	−0.570	—	−0.51
Calculated Doppler coefficient for U-235 heating, ($\delta k/k$-°C)	$+0.96 \times 10^{-6}$	$+0.79 \times 10^{-6}$	—[d]	$+2.88 \times 10^{-6}$
Calculated U-235 temperature expansion coefficient, ($\delta k/k$-°C)	-4.86×10^{-6}	-5.19×10^{-6}	—[d]	-3.3×10^{-6}

[a] Cross sections used in the calculations are defined in the footnote of Tables III-2-II and III-2-III.

[b] The values are normalized such that $\sum_i (\nu\Sigma_f)_i \phi_i = 1$ and $\sum_i \chi_i \phi_i^* = 1$ at the center of the core.

[c] Control rod drawers with triple columns of fuel measured 0.327% $\delta k/k$.

[d] Some of the calculations for Assembly 22 are omitted since it varied only slightly from Assembly 19.

TABLE III-2-V. CENTRAL REACTIVITY WORTHS IN ASSEMBLY 19; COMPARISON WITH ASSEMBLY 6

Sample Material	Weight of Sample, g	Can Type	Can Weights, g	Gross Sample Worth, Ih	Net Sample Worth, Ih	Specific Sample Worth, Ih/kg	Worth Assy 19, ZPR-9 / Worth Assy 6, ZPR6
$(CH_2)_n$	58.986	bare	—	17.513 ± 0.009	17.513 ± 0.009	296.9 ± 0.2	1.421
Be	114.308	bare	—	1.801 ± 0.007	1.801 ± 0.007	15.76 ± 0.06	1.381
B^{10}	29.29	SS	55.73	−39.312 ± 0.070	−39.195 ± 0.071	−1338.2 ± 2.4	1.689
C	102.0	bare	—	0.459 ± 0.007	0.459 ± 0.007	4.50 ± 0.07	1.254
Na	51.38	SS	56.42	−0.095 ± 0.005	0.020 ± 0.007	0.39 ± 0.14	1.538
Al	165.33	bare	—	−0.091 ± 0.007	−0.091 ± 0.007	−1.15 ± 0.04	1.566
Fe	488.0	bare	—	−0.720 ± 0.007	−0.720 ± 0.007	−1.475 ± 0.014	1.600
SS Can	72.39	bare	—	−0.153 ± 0.005	−0.153 ± 0.005	−2.11 ± 0.07	—
SS Block	480.9	bare	—	−0.871 ± 0.007	−0.871 ± 0.007	−1.81 ± 0.02	1.643
Ni	546.0	bare	—	−1.435 ± 0.007	−1.435 ± 0.007	−2.63 ± 0.02	1.725
Zr	406.0	bare	—	−0.748 ± 0.007	−0.748 ± 0.007	−1.84 ± 0.02	1.688
Nb	481.2	SS	30.10	−5.983 ± 0.007	−5.920 ± 0.009	−12.30 ± 0.02	1.679
Mo	599.0	bare	—	−5.115 ± 0.075	−5.115 ± 0.075	−8.539 ± 0.125	1.642
Ta	924.7	bare	—	−19.724 ± 0.007	−19.724 ± 0.007	−21.269 ± 0.008	—
W	1108.0	bare	—	−8.945 ± 0.007	−8.945 ± 0.007	−8.074 ± 0.007	1.756
Enriched	18.17 U 16.93 U-235	SS	72.603	1.100 ± 0.007	1.254 ± 0.009	69.01 ± 0.50	—
Depleted	1153.8	bare	—	−6.317 ± 0.007	−6.317 ± 0.007	−5.475 ± 0.006	1.678

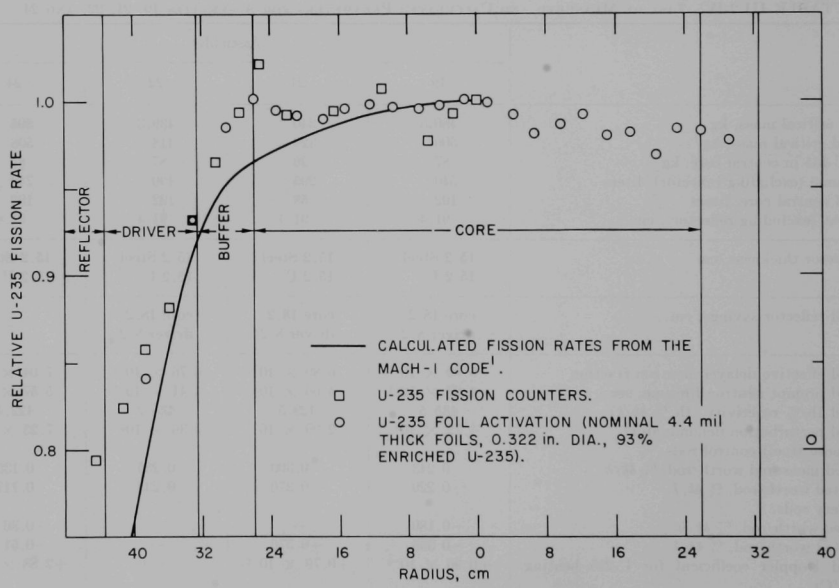

FIG. III-2-5. Radial U-235 Fission Rate Measurement ZPR-9, Assembly 19. *ANL Neg. No. 113-1443.*

Doppler difference cross sections as a function of equivalent σ_p for the different Doppler isotopes have been generated at Argonne and are described in Ref. 3. The Doppler cross sections with the appropriate equivalent σ_p values were used with the DEL subroutine to calculate the Doppler coefficients. Only the Doppler effect in the fissionable isotope was considered. For example, the U-238 Doppler effect was

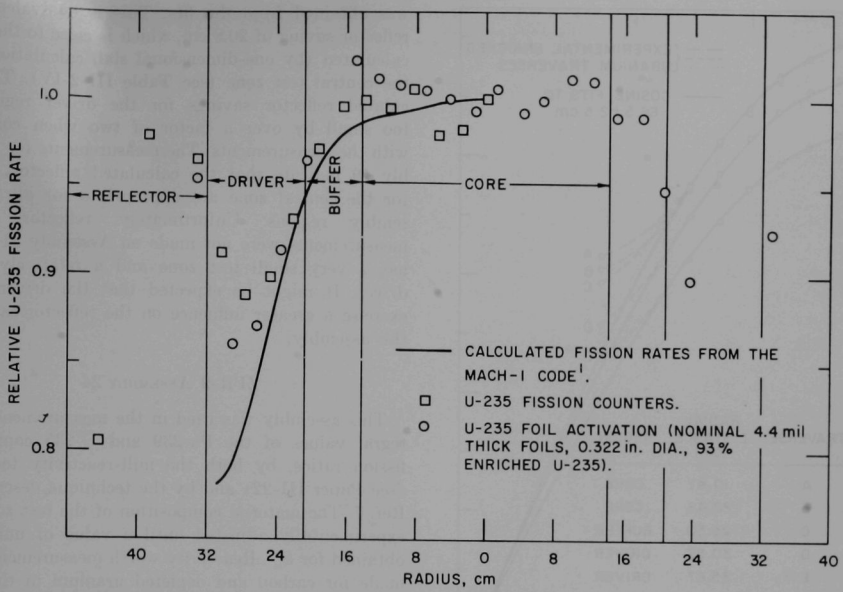

FIG. III-2-6. Radial U-235 Fission Rate Measurement ZPR-9, Assembly 21. *ANL Neg. No. 113-1441.*

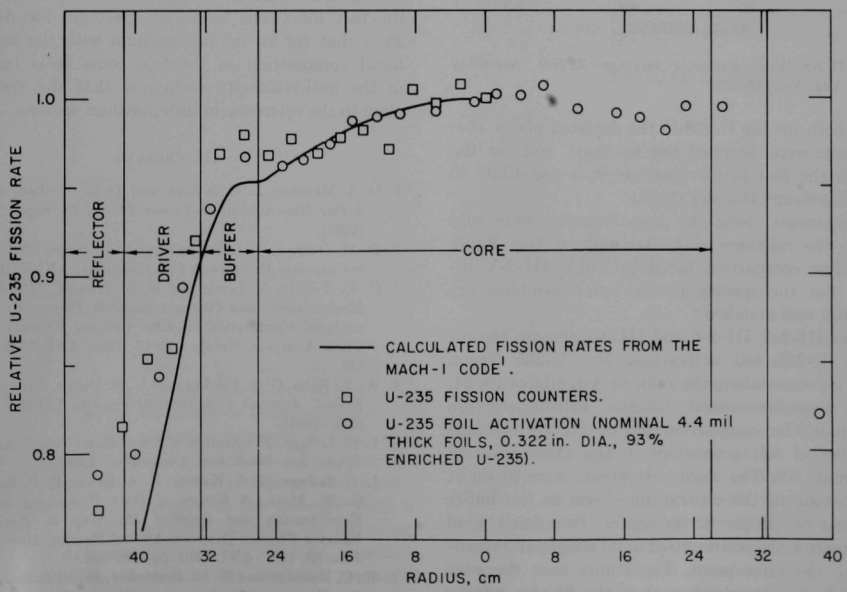

FIG. III-2-7. Radial U-235 Fission Rate Measurement ZPR-9, Assembly 22. *ANL Neg. No. 113-1445.*

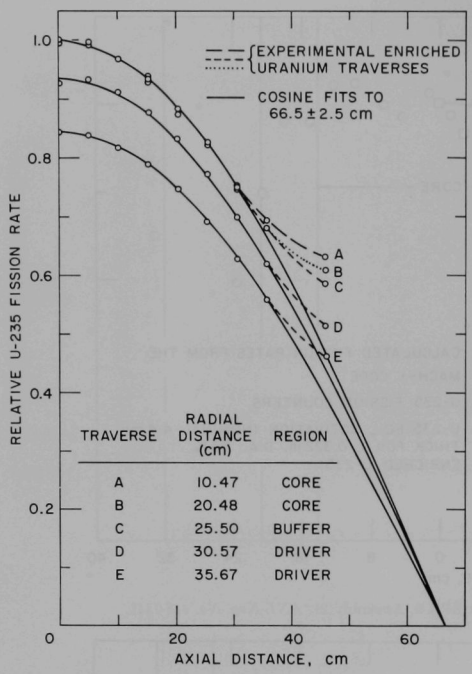

FIG. III-2-8. Axial Reflector Savings—ZPR-9, Assembly 19. *ANL Neg. No. 113-1410.*

ignored both for the U-238 in the depleted plates (because they were assumed not to heat) and for the U-238 in the fuel plates (because it is too dilute to have a significant Doppler effect).

Measurements using the same samples were also made in the reference core, Assembly 6 (see Paper III-1). The comparison listed in Table III-2-V indicates that the spectra in the two assemblies are reasonably well matched.[6]

Figures III-2-5, III-2-6 and III-2-7 contain the results of U-235 foil activations and U-235 fission counter traverses along the radii of Assemblies 19, 21, and 22. One-dimensional diffusion calculations are also included for comparison. Figure III-2-8 contains the results of foil activations in the axial direction in Assembly 19. The axial activations were made at two locations in the central zone, one in the buffer region and two in the driver region. To a fairly good approximation the cosine-fitted axial shapes all extrapolated to the same point. The points near the edge of the reflector, were not used in the fit. An extrapolated half-height of approximately 66.5 ± 2.5 cm was obtained from the fits. This is equivalent to a reflector saving of 20.8 cm, which is close to the value calculated (by one-dimensional slab calculations) for the central test zone (see Table III-2-IV). The calculated reflector savings for the driver region are too small by over a factor of two when compared with the measurements. The measurements for Assembly 19 indicate that the calculated reflector savings for the central zone are appropriate for all the assembly regions. Unfortunately, reflector savings measurements were not made on Assembly 21, which has a very small test zone and a relatively larger driver. It might be expected that the driver would exercise a greater influence on the reflector saving in this assembly.

ZPR-9 Assembly 24

This assembly was used in the measurement of integral values of the Pu-239 and U-235 capture-to-fission ratios, by both the null-reactivity technique (see Paper III-22) and by the technique described in Ref. 7. The material composition of the test zone was experimentally adjusted until a value of unity was obtained for k_∞. Reactivity worth measurements were made for carbon and depleted uranium in the zone. The adjustment was then accomplished by varying the ratio of carbon to depleted uranium throughout the test zone. The reference spectrum for Assembly 24 is that for an infinite medium with the same material composition as the test zone. It is important in the null-reactivity technique that the spectra be close to the reference infinite medium spectra.

References

1. D. A. Meneley, L. C. Kvitek and D. M. O'Shea, *MACH-1, A One-Dimensional Diffusion Theory Package*, ANL-7223 (1966).
2. D. M. O'Shea, B. J. Toppel and A. L. Rago, *MCC—A Code to Calculate Multigroup Cross Sections*, ANL-7318 (1967).
3. C. E. Till, R. A. Lewis and R. N. Hwang, *ZPR-6 Doppler Measurements and Comparisons with Theory*, Proc. International Conference on Fast Critical Experiments and Their Analysis, October 10–13, 1966, ANL-7320, pp. 319–333.
4. W. Y. Kato, G. J. Fischer and L. R. Dates, *Safety Analysis Report, Argonne Fast Critical Facility (ZPR-VI)*, ANL-6271 (1963).
5. L. G. LeSage, *Verification of Zoned Fast Critical Assemblies*, Trans. Am. Nucl. Soc. (November 1968).
6. L. G. LeSage, R. A. Karam, R. A. Lewis, E. F. Bennet and G. W. Main, *A Review of Data Pertaining to Spectral Equilibration and Spectral Matching in Zoned Cores*, Reactor Physics Division Annual Report, July 1, 1966 to June 30, 1967, ANL-7310, pp. 199–204.
7. W. C. Redman and M. M. Bretscher, *Direct Determination of the Uranium-235 Capture-to-Fission Ratio in a Zero-Power Reactor*, Nucl. Sci. Eng. **27**, 34–44 (1967).

III-3. Analysis of Doppler Effect Measurements in CH_2-Softened Spectra, ZPR-9 Assemblies 13–17

R. B. Pond* and C. E. Till

Introduction

A consistent analysis of U-235 and U-238 Doppler effect and central reactivity worth measurements in four polyethylene moderated reactor spectra is presented in this paper. The reactor compositions in increasing order of spectrum softness were designated Assemblies 13, 14, 16 and 17, and were constructed in the ZPR-9 reactor facility. These assemblies were intended to investigate reactivity systematics of reactor spectra softer than previously had been considered at ANL, with particular emphasis on the U-235 Doppler effect. The experimental results, measurement procedures and description of the reactor compositions are given in Ref. 1.

Previous comparisons of this kind in more usual fast reactor spectra have shown large discrepancies between measurements and calculations of the U-235 Doppler effect. Those comparisons were based upon statistical calculations because the extent of resolved resonance data and the Doppler effect magnitude in the resolved region is minimal in typical fast spectra. Variation of the unresolved resonance parameters within their recommended ranges can significantly affect the Doppler effect calculations.[2] This variation, compounded with uncertainty about statistical averaging itself and resonance overlap effects, which also have been found to be significant,[3] leads to large uncertainties and typically the calculations overestimate measurements by 100–200%. Similar comparisons of the U-238 Doppler effect are usually much better—discrepancies of the order of 10–20% are usual. In this case, the resonances in the energy region of importance are mostly resolved and do not overlap each other. The present work represents an attempt to specifically investigate the systematics of the U-235 Doppler effect.

Also, agreement between calculated and measured central reactivity worths has generally not been good. First-order perturbation theory is usually used to calculate these worths; however, because of the size of the experimental samples and the reactivity measurement procedures, sample size effects generally enter.

The intent in the analysis of the measurements in these softer spectra, therefore has been the following: (1) by focusing attention on the resolved resonance region of U-235, to check the resolved resonance calculational procedure and resonance parameters for the U-235 Doppler effect; (2) in general, to check the entire Doppler energy range to determine how well the balance of component fission and absorption Doppler effects are calculated in soft reactor spectra. The magnitude and sign of the fissile element Doppler effect is very sensitive to this balance and therefore, as a function of spectral weighting of the component effects, a sensitive test of the averaging procedures and the assumed resonance parameters; (3) to attempt to identify the source of discrepancy between U-235 Doppler effect measurements and calculations; (4) to calculate the U-238 Doppler effect in enough detail to indicate general agreement with measurements; (5) to assess the effects of sample size in central reactivity worth measurements; (6) to test fast reactor calculational procedures as applied to softer reactor spectra.

For comparison with the analysis of Assemblies 13–17 measurements, the analysis of fast spectrum Assembly 12 (which was the assembly from which Assemblies 13–17 were derived[1]) Doppler and central worth measurements are also included in this paper.

Calculational Procedure

Cross Sections

Reactor cross sections for each test zone composition were calculated with the MC[2] code[4] using ENDF/B nuclear data. Additionally, an MC[2] calculation was made for the driver zone composition. Cross sections for the buffer and reflector region compositions were selected from those generated for the test and driver region compositions.

Doppler sample cross sections were generated at room temperature, 293, 500, and 1100°K. The effective potential scattering cross section σ_p^{eff} was 43 b for sample N1 (natural uranium, 99.3 wt% U-238), 53 b for sample HE-8 (highly enriched uranium, 97.7 wt% U-235) and 58 b for both samples HE-9 and HE-10. The latter two samples were of the constrained expansion (NNE) type while the other samples were freely expanding (FE). U-238 Doppler broadened cross sections for sample N1 (FE) were calculated using the ERIC 2 code[5] and ENDF/B resonance parameters. For the U-235 samples, Doppler broadened cross sections were calculated only for HE-8 (FE) using the RP-270 code[6] in the unresolved resonance

* Student, Ohio State University, Columbus, Ohio.

TABLE III-3-I. THIRTY GROUP STRUCTURE

Group	Lower Lethargy Bound	Lower Energy Bound
1	1.0	3.679 MeV
2	1.5	2.231
3	2.0	1.353
4	2.5	820.8 keV
5	3.0	497.9
6	3.5	302.0
7	4.0	183.2
8	4.5	111.1
9	5.0	67.38
10	5.5	40.87
11	6.0	24.79
12	6.5	15.03
13	7.0	9.119
14	7.75	4.307
15	8.25	2.613
16	8.5	2.035
17	9.0	1.234
18	9.25	961.1 eV
19	9.75	582.9
20	10.5	275.4
21	11.5	101.3
22	12.5	37.27
23	12.75	29.02
24	13.0	22.60
25	13.5	13.71
26	14.0	8.315
27	15.0	3.059
28	16.0	1.125
29	17.0	0.414
30	19.8	0.0253

region and the RABBLE code[7] in the resolved region. Unresolved U-235 parameters were those given by J. Schmidt[8] and resolved parameters were from the ENDF/B library. The RP-270 calculated cross sections were modified, when appropriate, to include estimates of same- and inter-sequence resonance interference effects using an extrapolation of the procedure given by R. Hwang.[3]

EXPANSION AND SAMPLE SIZE EFFECTS

The method of calculating the reactivity expansion effect in Doppler samples[9] also has been used here to calculate sample size effects in the central reactivity worth measurements. This method calculates groupwise fluxes in the sample from a consideration of the neutron balance equation between the sample and the reactor. These perturbed sample fluxes are then used in first-order perturbation theory in place of the usually assumed unperturbed reactor fluxes.

REACTOR CALCULATIONS

One-dimensional diffusion theory, using the MACH 1 code,[10] has been used to calculate the critical parameters of these assemblies. The DEL subroutine (first-order perturbation theory) of MACH 1 was used, in combination with the Doppler induced changes in Doppler sample cross sections, to calculate the Doppler effects and also to calculate central reactivity worths when sample size effects were not considered. All calculations have been made using a thirty group energy structure covering the energy range between 10 MeV and thermal. Listed in Table III-3-I are the group lower lethargy and energy bounds.

COMPARISON OF EXPERIMENTAL RESULTS WITH CALCULATIONS

REACTOR PARAMETERS

Listed in Table III-3-II are several assembly-dependent reactor parameters calculated with MACH 1 using MC^2 cross sections. The critical masses can be compared to the experimental masses of 579.6, 402.8, 374.1, 333.1 and 126.7 kg for Assemblies 12, 13, 14, 16 and 17, respectively. (Heterogeneity effects have been accounted for in the resonance region only. It would be expected that inclusion of high-energy heterogeneity effects would decrease the calculated critical mass somewhat, although in these assemblies this is not expected to be a large effect.) These results show that the calculated critical masses are higher than the experimental values in Assemblies 12 and 17 by 4 and 7%, respectively, and in Assemblies 13, 14 and 16 lower by 7–12%.

CENTRAL WORTHS

Table III-3-III shows the calculated sample worths, with and without sample size effects, that correspond to the experimental worths of Table III-3-IV. When size effects are considered in the absorbing materials, molybdenum, tungsten, tantalum, boron, B_4C, depleted and enriched uranium, and plutonium, the calculated worths are generally in better agreement with the experimental worths than are the comparable calculations using usual first-order perturbation theory. The effects of flux self-shielding in these absorbers are readily apparent. The particularly large change noted for plutonium is due to the very large capture resonance at 1.1 eV for Pu-240. In order to show this effect, the calculated plutonium sample worths are also shown without the Pu-240 component.

Depending upon whether size effects are considered, percentage overestimates of the experimental central worths are generally reduced for the non-fissile absorbers. This reduction for boron samples is from several hundred percent to typically 60% or less; for tungsten and tantalum, by ½ to ⅓; and for molyb-

TABLE III-3-II. Reactor Parameters in Assemblies 12, 13, 14, 16 and 17

	Assembly 12	Assembly 13	Assembly 14	Assembly 16	Assembly 17
Critical mass, kg U-235	601.2	374.9	349.7	294.4	136.1
1% $\Delta k/k$, Ih	445.76	428.71	425.41	417.53	385.02
Core material reflector savings,[a] cm	11.26	9.77	9.86	10.07	11.18
Critical search region radius, cm	41.15	37.37	36.93	35.93	28.22
Mean Energy					
Source	121 keV	817 eV	726 eV	567 eV	287 eV
Absorption	58 keV	743 eV	651 eV	494 eV	243 eV
Flux	172 keV	188 keV	189 keV	192 keV	215 keV
Prompt neutron lifetime, μsec	0.234	1.160	1.239	1.420	1.957
Delayed neutron fraction, $\times 10^3$	7.295	7.435	7.456	7.505	7.758
Perturbation denominator, arbitrary scale	6.498	8.444	8.740	9.463	12.90

[a] Driver material reflector savings = 11.15 cm.

TABLE III-3-III. Calculated Central Worths with and without Sample Size Effect, Ih/kg

Sample	Assembly 12		Assembly 13		Assembly 14		Assembly 16		Assembly 17	
	Without Size Effect	With Size Effect	Without Size Effect	With Size Effect	Without Size Effect	With Size Effect	Without Size Effect	With Size Effect	Without Size Effect	With Size Effect
Mo	−9.543	−9.080	−29.52	−27.56	−30.81	−28.82	−33.25	−31.25	−32.97	−31.80
Ni	−2.585	−2.364	−9.177	−8.221	−9.336	−8.396	−9.422	−8.560	−5.964	−5.868
Fe	−2.478	−2.309	−5.209	−4.895	−5.083	−4.799	−4.557	−4.365	+0.506	+0.130
Be	+7.237	+10.20	+63.87	+61.44	+71.56	+68.63	+89.92	+85.81	+157.4	+148.7
C	−1.318	−0.615	+19.97	+20.37	+22.98	+23.33	+30.36	+30.58	+59.82	+59.39
Al	−2.818	−2.682	+0.418	+0.603	+1.297	+1.458	+3.639	+3.728	+15.99	+15.64
Na	−0.535	−0.526	+4.089	+3.746	+4.995	+4.662	+7.365	+7.062	+19.22	+19.10
W	−8.785	−8.161	−52.45	−36.87	−56.04	−39.20	−63.91	−44.21	−82.70	−54.54
Ta	−24.45	−20.36	−124.3	−82.95	−132.8	−88.39	−151.5	−100.2	−196.4	−126.5
B	−273.4	−244.9	−4541.	−1154.	−4956.	−1239.	−5909.	−1428.	−8937.	−1930.
Poly (CH_2) 1	+314.7	+532.7	+652.2	+854.1	+710.2	+904.0	+845.9	+1013.	+1193.	+1175.
Poly (CH_2) 2	+314.7	+409.5	+652.2	+710.9	+710.2	+766.7	+845.9	+895.0	+1193.	+1189.
SS (304)	−2.609	−2.399	−6.677	−6.261	−6.631	−6.247	−6.267	−5.982	−1.397	−1.774
B_4C	−214.2	−200.3	−3549.	−1103.	−3873.	−1187.	−4618.	−1374.	−6981.	−1889.
Depleted Uranium	−5.679	−5.725	−15.41	−13.81	−16.10	−14.37	−17.46	−15.44	−18.11	−15.17
Enriched Uranium	+64.84	+65.92	+135.4	+130.8	+138.0	+134.0	+140.6	+138.5	+103.3	+113.7
Pu	+88.40	+96.11	+125.5	+205.4	+120.9	+212.9	+104.6	+226.4	−30.63	+207.5
Pu[(a)]	+87.87	+95.26	+251.9	+220.8	+259.9	+229.6	+272.6	+246.2	+231.2	+245.6

[a] Pu sample worth without the Pu-240 component.

denum, by a modest amount. Differences for depleted uranium, enriched uranium, and plutonium, vary depending upon the particular reactor assembly. For these three materials in Assembly 12, negligible size effect is evident, and likewise, for enriched uranium in Assemblies 13, 14 and 16. In the latter assemblies, the overestimate of the depleted uranium worth is reduced from approximately 85 to 65%. In Assembly 17, the overestimate of depleted uranium by 52%, and the underestimate of enriched uranium by 23% are reduced to 28 and 16%, respectively. Plutonium in Assemblies 16 and 17, depending upon whether the Pu-240 component is included, shows varying degrees of consistency. However, probably neither calculation is truly representative of the experimental worth since unshielded cross sections were used in the calculations.

The predominantly scattering materials also show varying degrees of consistency. As expected, however, where the sample fluxes would be most strongly perturbed from the reactor spectrum, most of the calculated worths are improved by the sample size effect calculation.

DOPPLER EFFECTS

Description of Presentation of Results

Table III-3-V shows the calculated and experimental Doppler results per kilogram of the predominate uranium isotope for each Doppler element in Assem-

TABLE III-3-IV. REACTIVITY WORTH MEASUREMENTS

Sample[a]	Weight, g	Can Weight, g	Assembly 12,[b] Net Ih/kg	Assembly 13,[c] Net Ih/kg	Assembly 14,[d] Net Ih/kg	Assembly 16,[e] Net Ih/kg	Assembly 17,[f] Net Ih/kg
Mo	598.8	—	−8.059 ± 0.017	−19.41 ± 0.05	−20.28 ± 0.00	−21.43 ± 0.01	−24.87 ± 0.12
Ni	546.1	—	−2.992 ± 0.018	−11.60 ± 0.03	−11.99 ± 0.02	−12.79 ± 0.00	−14.44 ± 0.01
Fe	484.3	—	−2.110 ± 0.021	−6.186 ± 0.03	−6.084 ± 0.015	−6.040 ± 0.002	−3.494 ± 0.008
Be	114.3	—	+12.20 ± 0.09	+39.20 ± 0.06	+46.13 ± 0.11	+56.89 ± 0.03	+128.69 ± 0.03
C	102.0	—	+1.578 ± 0.109	+10.52 ± 0.04	+13.66 ± 0.08	+17.74 ± 0.01	+48.81 ± 0.31
Al	167.1	—	−2.561 ± 0.060	−1.143 ± 0.150	−0.325 ± 0.006	+0.993 ± 0.000	+10.64 ± 0.04
Na	51.39	56.42 (SS)	−1.376 ± 0.200	−1.323 ± 0.720	+0.108 ± 0.049	+1.693 ± 0.078	+13.90 ± 0.33
W	1108.	—	−7.340 ± 0.009	−23.07 ± 0.32	−27.53 ± 0.32	−30.01 ± 0.32	−42.19 ± 0.32
Ta	924.7	27.54 (SS)	−17.982 ± 0.016	−49.04 ± 0.38	−57.58 ± 0.38	−62.16 ± 0.38	−89.23 ± 0.38
B	75.2	20.6 (SS)	—	−824. ± 6.	−975. ± 3.	−1090 ± 5	−1660 ± 5
Poly (CH_2) 1	58.988	—	+443.40 ± 0.25	+436.65 ± 0.08	+487.39 ± 5.93	+488.2 ± 3.9	+707.8 ± 4.2
Poly (CH_2) 2	13.70	72.32 (SS)	—	+469.0 ± 3.1	+512.2 ± 3.1	+550.1 ± 0.9	+905.7 ± 1.3
SS-304	481.0	—	−2.364 ± 0.021	−7.958 ± 0.029	−8.059 ± 0.004	−8.281 ± 0.019	−7.029 ± 0.023
SS can	72.38	—	−2.542 ± 0.138	−8.994 ± 0.041	−9.600 ± 0.034	−9.837 ± 0.111	−8.635 ± 0.290
B_4C	59.62	64.70 (SS)	—	−713.2 ± 5.9	−757.0 ± 5.9	−837.1 ± 5.9	−1295. ± 6.
Depleted uranium	1155.	—	−4.674 ± 0.009	−8.510 ± 0.005	−8.911 ± 0.012	−9.191 ± 0.001	−11.88 ± 0.04
Al can	26.36	—	—	—	—	+1.328 ± 0.076	+10.85 ± 0.27
Enriched uranium	18.11[g]	72.38 (SS)	+70.12 ± 0.88[h]	—	—	—	—
Enriched uranium	18.24[g]	72.34 (SS)	—	+134.5 ± 0.5[h]	—	—	—
Enriched uranium	18.17[g]	72.34 (SS)	—	—	+137.4 ± 0.3[h]	+143.6 ± 0.0[h]	+135.0 ± 0.7[h]
Pu	119.24[i]	22.27 (SS) 6.85 (Al)	+93.05 ± 1.68[j]	—	—	—	—
Pu	121.55[i]	19.77 (SS) 7.05 (Al)	—	—	—	+199.0 ± 2.0[j]	+228.1 ± 2.2[j]

[a] All samples are nominal 1 x 2 x 2 in. except the enriched uranium $\frac{1}{16}$ x $\frac{1}{2}$ x 2 in. and the plutonium $\frac{1}{4}$ x 2 x 2 in.
[b] Assembly 12: 1% $\Delta k/k$ = 451.2 Ih.
[c] Assembly 13: 1% $\Delta k/k$ = 438.86 Ih.
[d] Assembly 14: 1% $\Delta k/k$ = 435.69 Ih.
[e] Assembly 16: 1% $\Delta k/k$ = 428.07 Ih.
[f] Assembly 17: 1% $\Delta k/k$ = 391.78 Ih.
[g] 93.2 wt% U-235.
[h] U mixture.
[i] 0.01 wt% Pu-238; 95.05 wt% Pu-239; 4.48 wt% Pu-240; 0.45 wt% Pu-241; 0.01 wt% Pu-242.
[j] Pu mixture.

blies 12, 13, 14, 16 and 17 between room temperature and 500 and 1100°K. (The experimental data for Assemblies 13–17 are from Ref. 1. Assembly 12 experimental data were obtained by multiplying Assembly 5 Doppler measurements[11] by the conversion factor 1.4. This factor represents the ratio of the perturbation denominators of Assemblies 5 and 12 and was obtained from the average of experimental ratios of selected sample material central worths.[12]) The effect of the diluent uranium isotope U-238 or U-235 has been subtracted from each of the experimental values, prorated on the basis of mass from the experimental results given by either the N1 (FE) or HE-8 (FE) Doppler element, as appropriate.

To show how sample flux-depression and resonance interference effects influence the calculated U-235 Doppler effects, the energy region corresponding to Groups 11–22 was investigated under various assumptions. The Doppler broadened cross sections were calculated in four ways:

Assumption 1—no sample flux-depression and no resonance interference effects

Assumption 2—no sample flux-depression but with estimated resonance interference effects

Assumption 3—with sample flux-depression but no resonance interference effects

Assumption 4—with sample flux-depression and with the estimated resonance interference effects.

In Groups 23–30 (the resolved resonance region of the ENDF/B data for U-235) the Doppler broadened RABBLE calculated cross sections were held constant as each of the four assumptions was applied in cal-

TABLE III-3-V. CALCULATED AND EXPERIMENTAL[a] DOPPLER EFFECTS IN ASSEMBLIES 12, 13, 14, 16 AND 17 BETWEEN 293°K AND THE INDICATED TEMPERATURE, Ih/kg

Element/Groups/Assumption	Assembly 12		Assembly 13		Assembly 14		Assembly 16		Assembly 17	
	500°K	1100°K	500°K	1100°K	500°K	1100°K	500°K	1100°K	500°K	1100°K
U-235 (FE)/11-30/1	+0.109	+0.248	+0.718	+1.818	+0.662	+1.660	+0.481	+1.153	−0.789	−2.386
U-235 (FE)/11-30/2	+0.087	+0.196	+0.503	+1.266	+0.460	+1.146	+0.324	+0.764	−0.637	−1.919
U-235 (FE)/11-30/3	+0.111	+0.252	+0.626	+1.525	+0.589	+1.424	+0.472	+1.102	−0.331	−1.058
U-235 (FE)/11-30/4	+0.089	+0.202	+0.427	+1.023	+0.398	+0.945	+0.307	+0.700	−0.300	−0.918
U-235 (FE)/Experimental	+0.042	+0.075	+0.235	+0.812	+0.228	+0.714	+0.162	+0.517	−0.275	−0.694
U-235 (NNE)/Experimental	+0.050	+0.094	+0.207	+0.672	+0.218	+0.644	—	—	−0.335	−0.784
U-238 (FE)/11-30/1	−0.101	−0.246	−0.914	−2.592	−0.981	−2.788	−1.131	−3.226	−1.527	−4.411
U-238 (FE)/Experimental	−0.158	−0.422	−0.602	−1.956	−0.717	−2.155	−0.801	−2.354	−1.323	−4.045

[a] Diluent uranium isotope U-238 or U-235 subtracted based on N1 (FE) or HE-8 (FE), as appropriate.

TABLE III-3-VI. SOURCE AND SINK, U-235 (FE) DOPPLER EFFECT COMPONENTS IN ASSEMBLIES 12, 13, 14, 16, AND 17 BETWEEN 293 AND 1100°K, Ih/kg OF U-235

	Assembly 12			Assembly 13			Assembly 14			Assembly 16			Assembly 17		
	$\delta\nu\Sigma_f$ (+)	$\delta\Sigma_a$ (−)	Net	$\delta\nu\Sigma_f$ (+)	$\delta\Sigma_a$ (−)	Net	$\delta\nu\Sigma_f$ (+)	$\delta\Sigma_a$ (−)	Net	$\delta\nu\Sigma_f$ (+)	$\delta\Sigma_a$ (−)	Net	$\delta\nu\Sigma_f$ (+)	$\delta\Sigma_a$ (−)	Net
Above 37 eV	0.696	0.494	+0.202	10.573	9.515	+1.057	11.109	10.102	+1.008	12.126	11.284	+0.841	15.024	15.295	−0.272
Below 37 eV	0	0	0	2.146	2.180	−0.034	2.300	2.363	−0.063	2.620	2.761	−0.141	3.856	4.502	−0.646
Above 100 eV	0.693	0.490	+0.202	8.020	6.895	+1.125	8.417	7.312	+1.106	9.162	8.146	+1.017	11.214	10.909	+0.305
Below 100 eV	0.003	0.003	0	4.698	4.800	−0.102	4.992	5.153	−0.165	5.583	5.900	−0.317	7.666	8.888	−1.222

culating the total U-235 (FE) Doppler effect over the entire Doppler energy range (Groups 11–30).

In Table III-3-VI, the calculated component source term, $\delta\nu\Sigma_f$, and sink term, $\delta\Sigma_a$, of the U-235 (FE) Doppler effect have been listed. These components represent the change from 293 to 1100°K and for the U-235 Doppler effect calculated with Assumption 4 cross sections. This table shows the balance in these terms and the net contributions above and below arbitrary energy levels, 37 and 100 eV.

Because of the particular energy group structure chosen for these calculations, Groups 23–30 cover the energy region below 37 eV and these groups therefore include most of the U-235 resolved resonance energy region of the ENDF/B data. (ENDF/B resolved resonance data for U-235 exists up to 60 eV.) The component Doppler effects in the energy region above and below 100 eV have also been listed since there is resolved resonance data, from other sources, which cover this energy region. (Particularly, Schmidt data exists up to 150 eV and could have been used to investigate the energy region below 100 eV. However, for consistency in using entirely ENDF/B nuclear data, where available, these Schmidt data were not used.)

Assembly 12

Comparison of the U-235 (FE) experimental and calculated Doppler effects in Assembly 12 shows that the calculations are overestimated by 112–169% when either Assumption 2 or 4 cross sections are used, and from 160–236% with either Assumption 1 or 3. The effect of the experimentally observed, negative U-235 expansion effect (see Table III-3-V and the experimental results for FE and NNE elements) would tend to decrease these overestimates if expansion corrections were applied to the data. The U-238 Doppler results show the calculations underestimate of the measured Doppler effects by approximately 40%.

These U-235 results show that the Doppler effect is relatively insensitive to flux-depression in the sample; however, it is very sensitive to the estimate of the resonance interference effects. As the interference effects, particularly in the unresolved region, can only be estimated with very limited confidence, the calculation of the U-235 Doppler effect in assemblies with spectra similar to Assembly 12 must have large uncertainties attached to it.

The experimental Doppler effects for U-235 and U-238 in this particular assembly may be overesti-

mated somewhat due to the fact that the 1.4 conversion factor is derived from central worth ratios. No account, for example, is taken of the difference in axial flux profile over a sample of finite length, which in this case is 12 in. for the Doppler samples. The physical axial height of the core material in Assemblies 12 and 5 was 36 and 56 in., respectively. This is not a large effect, and is not significant compared to other uncertainties, but would tend to lower the ratio. Of more importance is the uncertainty which exists in the match of central reactor spectra of Assemblies 12 and 5. Assembly 12 was designed to match the calculated central fluxes of Assembly 5; however, any mismatch in the spectrum could be reflected differently for Doppler worths than for central reactivity worths. Because of the rather inconclusive Assembly 12 experimental Doppler measurements, compared to the very definitive Assembly 5 measurements, these comparisons were nevertheless based on the Assembly 5 results using the conversion factor 1.4 as a reasonable upper limit. The actual Doppler data from Assembly 12 indicates that the conversion factor could be as low as 1.2.[12]

Within the uncertainties of the experimental Doppler effects and the uncertainties inherent in the resonance interference calculations, the calculated U-235 Doppler effect is generally consistent with previous comparisons of this kind.[2] However, the 40% underestimate of the U-238 Doppler effect is about twice the 10–20% underestimate usually found.

Possible explanations for the discrepancy in the U-238 Doppler effect are: (1) the conversion of the experimental data from Assembly 5 to Assembly 12; (2) the effects of flux-depression in the sample cross sections; (3) resonance interference effects; and (4) ENDF/B data—that is, the correctness of Doppler-region U-238 reactor cross sections and in turn the Doppler-region fluxes. The first effect would cause an obvious improvement if a smaller conversion factor were applied. The flux-depression effect, however, would be expected to be a small effect in the Doppler-region of importance in this assembly. Resonance interference effects, particularly sample-reactor interaction, might be large due to the concentration of U-238 present in Assembly 12 (approximately 7/1 ratio of U-238/U-235). Finally, since the U-238 Doppler effect magnitude is directly proportional to the Doppler-region fluxes, the uncertainty in accounting for U-238 reactor cell heterogeneity and in turn, effective homogeneous U-238 capture cross section, would cause this uncertainty to be reflected in the Doppler-region fluxes.

Estimation of these effects in Assembly 4Z,[13] for example, showed a 20% enhancement in the U-238 Doppler effect when flux-depression and sample-reactor interaction effects were accounted for, and this factor would be expected to apply almost verbatim to the present results. Similarly, reactor heterogeneity effects caused an 8% deviation in the calculated U-238 Doppler effect. Considering these uncertainties and the magnitude of the correction effects, the indicated 40% discrepancy in the U-238 Doppler effect may not be unreasonable. However, it does indicate the need for further investigation, and in particular, re-examination of the ENDF/B data is suggested.

Assemblies 13–16

Assemblies 13, 14 and 16 can be considered as a group since they represent soft spectrum assemblies with U-238/U-235 ratios in the range of 4/1.

In these assemblies, considerable variations exist between calculated and experimental U-235 (FE) Doppler effects. The magnitudes of the differences depend strongly upon the particular cross section assumptions used. The calculated Doppler effects are larger than the measured effects and vary from 123–206% with Assumption 1, from 48–114% with Assumption 2, from 88–191% with Assumption 3 and from 26–90% with Assumption 4. The effect of the experimentally observed, positive U-235 expansion effect (see Table III-3-V) would tend to increase this overestimate if expansion corrections were applied to the data. The U-238 Doppler results show that calculation overestimates the measured Doppler effects from 29–52%.

These U-235 Doppler results show that the spectral shift to lower energies has increased the calculated Doppler effect sensitivity to the cross section Assumptions 1, 2, 3 or 4, as would be expected. Sample flux-depression and resonance interference effects, individually and in combination, strongly affect the Doppler results and therefore both effects should be accounted for in these softer spectrum assemblies.

The influence of spectral softening on the U-235 Doppler effect is evident from the component Doppler effects listed in Table III-3-VI. The influence has shifted the relative contributions of the resolved and unresolved resonance regions and even the net balance within any given region. (Of note in these assemblies is the substantial increase in magnitude of the components and the smaller percentage difference between components as compared with Assembly 12.) The large, net positive Doppler effect in the unresolved region predominates and effectively cancels the relatively small net negative Doppler effect in the resolved region.

The agreement with theory must be considered in

light of the inherent inaccurracies of the statistical calculations necessary for the unresolved resonance region. Because of the near balance between the source and sink terms, the net mangitude (and sign) would be extremely sensitive to an error in either component.

In the resolved resonance region, where one has a reasonably good chance to estimate the Doppler effect on the basis of isolated, single-level resonance formalism, the relatively small, net negative Doppler contribution subtracts little from the unresolved region. As indicated by the component contributions above and below 100 eV, it would be desirable to use as much resolved resonance data as possible. Based upon these calculations, one could increase the resolved resonance region contribution by at least 100%, and thereby decrease the unresolved resonance region contribution and sensitivity to the overall calculation.

The U-238 Doppler effect in these assemblies are overestimated by approximately 40%. However, the approximations in the calculational procedures used for U-238 generally become less valid as the spectrum softens. Flux-depression effects in the U-238 cross sections, which become increasingly important in these soft spectrum assemblies, would be expected to reduce the magnitude of the calculated Doppler effect due to the reduction in Doppler-region fluxes. Sample reactor interactions and reactor geometry heterogeneity effects would be expected to become less of an effect in these assemblies because of the amount of U-238 in a unit cell (approximately 4/1 ratio of U-238/U-235). However, accounting for the heterogeneity effect in the resonance energy region would be subject to increased uncertainty due to the assumptions inherent in MC^2. Nevertheless, the 40% overestimate of the measurements still seems high.

Assembly 17

Assembly 17 is the softest spectrum reactor constructed in this series since all depleted uranium plates were removed from the test zone composition. The only U-238 present was the 7% contained in the enriched uranium plates.

In this assembly, the effects of sample flux-depression and resonance interference substantially affect the calculational estimates of the experimental U-235 (FE) Doppler effect. With these various cross section assumptions, the overestimates range from 187–243% for Assumption 1, from 132–177% for Assumption 2, from 20–52% for Assumption 3 and from 9–32% for Assumption 4. The effect of the experimentally observed, positive U-235 expansion effect (see Table III-3-V) would tend to decrease these overestimates if expansion corrections were applied to the data. The U-238 Doppler calculation overestimates the experimental measurements from 9–15%.

The effect of spectral softening in this assembly, as shown by the U-235 Doppler effect components of Table III-3-VI, has been to substantially shift the relative contributions from the unresolved resonance region to the resolved region, and the balance between the positive and negative components in the unresolved region has taken on added significance. Therefore, the previous discussions of the effects of the balance between components in the resolved and unresolved resonance region, also apply here. However, the added importance given to the resolved resonance region and its predominant effect on the overall U-235 Doppler effect calculation, does show a trend towards better agreement of the calculation with experiment.

Similar arguments concerning the U-238 Doppler effect which applied in Assemblies 13–16 should also apply here. Particularly, the flux-depression effects should account for some of the overestimate in the calculation. The reduction from a 40% overestimate in Assemblies 13–16 to a 10% overestimate in Assembly 17 may be some indication of the magnitude of a reactor cell geometry heterogeneity effect. Within the limits of MC^2 the somewhat simpler cell geometry of this assembly should be more amenable to cross section calculations. The fact that the agreement is considerably better in this assembly, which contains little U-238, would tend to support the premise that the major problem in Assemblies 13–16 was caused by inaccuracies in the reactor U-238 cross section, whether due to heterogeneity uncertainties or simply inaccuracies in the basic data.

Expansion Corrections

Because of the lack of consistent U-235 expansion calculations, (discussed in the following) none of the calculated Doppler effects in Table III-3-V reflect expansion effects. Shown in Table III-3-VII are the expansion corrections for each Doppler element in Assemblies 12–17, calculated using the perturbed-flux perturbation formalization.

U-235—Assembly 12

With calculated FE and NNE sample expansion corrections applied to Assembly 12 data, the measured U-235 Doppler effect between 293 and 500°K and between 293 and 1100°K are approximately +0.049 and +0.107 Ih/kg, respectively. These expansion-corrected Doppler results are in agreement with the similarly corrected Assembly 5 results when

TABLE III-3-VII. Doppler Element Expansion Calculations in Assemblies 12–17

Assembly	HE-9 or HE-10,[a] Ih/kg U-235		HE-8, Ih/kg U-235		N1, Ih/kg U-238	
	500°K	1100°K	500°K	1100°K	500°K	1100°K
12	−0.000	−0.015	−0.006	−0.030	+0.000	+0.001
13	+0.000	+0.007	+0.001	+0.006	−0.001	−0.006
14	−0.000	−0.001	−0.002	−0.008	−0.001	−0.006
16	−0.001	−0.022	−0.010	−0.046	−0.001	−0.007
17	−0.004	−0.138	−0.053	−0.250	−0.002	−0.009

[a] Assemblies 12 and 17 were calculated for HE-10 and Assemblies 13, 14 and 16 were calculated for HE-9.

multiplied by the conversion factor 1.4.[14] Therefore, in these two assemblies the enriched NNE and FE samples are brought into agreement (neglecting the slight difference in σ_p^{eff}) to within the experimental precision of the measured Doppler effects in Assembly 5. The calculated U-235 Doppler effect in Assembly 12, however, still represents an overestimate of the expansion-corrected experimental data from 82–89% over the temperature range from 293 to 1100°K.

U-235—Assemblies 13–17

In the softer spectra of Assemblies 13–17, the expansion effect is a positive reactivity effect as is evident from a comparison of the two U-235 Doppler element types within the same assembly (see Table III-3-V). However, the calculated expansion effects shown in Table III-3-VII indicate this positive effect is substantially underestimated in Assembly 13 and predicts negative expansion in Assemblies 14–17. The FE and NNE samples are therefore not brought into agreement as they were in the fast spectrum assemblies.

The obvious conclusion here is that the expansion effects in the resonance energy region are not well calculated, as might be expected from the broad-group treatment of rapidly varying cross sections in these soft spectrum assemblies. Therefore, when this region dominates in the expansion calculation, the calculational procedure is clearly inadequate to predict the expansion effects.

U-238—Assemblies 12–17

U-238 expansion calculations in Assemblies 12–17 show that there is a negligible expansion effect (see Table III-3-VII). Compared with the observed U-238 Doppler effect, the expansion correction is approximately ¼% of the Doppler signal at any given temperature, and has therefore been ignored.

Discussion of Results

Reactor Parameters

The experimental critical masses have been overestimated in the calculations by approximately 5% in Assemblies 12 and 17, and underestimated by approximately 10% in Assemblies 13, 14 and 16.

The somewhat larger differences between the calculated and measured critical masses of Assemblies 13, 14 and 16 may be due to a number of things. First, the small driver regions involved in these particular assemblies may result in configuration effects that are not accounted for in the calculations. Homogenization of the driver region into an equivalent cylindrical shell may not be adequate to describe the actual experimental situation. Second, the basic nuclear data, ENDF/B, may not be adequate over the full nuclear energy range and for the particular nuclear materials of the present investigations. The relatively small discrepancies between the calculated and measured critical masses, however, argue against the presence of large errors in the data of the major constituent isotopes. And third, the macroscopic properties of these assemblies may be sensitive to the MC^2 approximations assumed for material heterogeneity and resonance interference effects.

Central Worths

Use of a modified version of first-order perturbation theory, wherein perturbed sample fluxes are calculated, provides increased accuracy in calculating, in particular, absorber material central reactivity worths. The improved agreement in these calculations with respect to the experimental worths, however, is not as good as one would like in some of these assemblies. In particular, the reduction in the overestimate from 85 to 65% for depleted uranium in Assemblies 13, 14 and 16 is much less than it should be for this very important reactor constituent. This lack of significant improvement may be an indication of a systematic error in the calculation. In support of such a systematic error is also the consistent underestimate of the critical masses and overestimates of the U-238 Doppler effects in these assemblies. The central worth calculations are dependent on the correctness of the homogeneous real and adjoint fluxes which approximate the fluxes of the actual heterogeneous reactor configuration. The limitations and approximations made for material heterogeneity and resonance effects in the MC^2 cross section code, therefore, could have a substantial effect in the resonance energy region of these soft spectrum assemblies.

Also inherent in these perturbation theories is the assumption that the sample cross sections are characteristic of the sample and therefore are appropriately self-shielded. In the central worth measurements of these investigations, for those isotopes which were in a particular assembly composition, in general, the same cross sections were also used as the sample cross sections. The molybdenum, tungsten, tantalum and boron cross sections were estimated in part from ANL cross section set 224 and interpolations from I. Bondarenko[15] self-shielded cross sections. The beryllium, aluminum, Pu-239, Pu-240 and Pu-241 cross sections were infinitely dilute and were generated with the MC^2 code and ENDF/B nuclear data.

Scattering material worths are less sensitive to the modified method and are generally comparable in magnitude to the worths predicted by usual perturbation theory. Since both methods are more sensitive to the adjoint flux than to the real flux as such, the indicated agreement of calculations with experiment is about the same. The inability to even predict the sign of the observed reactivity in some samples indicates the inherent difficulties in calculating scattering material worths. Therefore, it would seem that this relatively broad energy group structure is not sufficient to specify the adjoint fine structure in the detail necessary to describe scattering reactivity effects.

In general, for all materials in which the sample fluxes are likely to be substantially perturbed compared with the unperturbed reactor fluxes, the perturbed flux formalization provides better accuracy. It should also be noted that there is a tendency, at least, to predict the direction of improvement, even for many of the scattering materials.

Summary and Conclusions

1. This series of polyethylene moderated reactor assemblies has provided an opportunity to systematically investigate static and Doppler reactivity measurements and to compare these measurements with calculations. In each of these soft spectrum reactors the measured critical masses and the material reactivities measured in the central reactor spectra have been predicted with an accuracy comparable with that generally found in similar calculations of this kind in more usual fast reactor spectra.

2. The U-235 Doppler effect is positive in reactor spectra characterized by reactor U-238/U-235 ratios in the range of 5/1 to 3/1, and is negative in a softer spectrum when the only predominant reactor absorber is U-235.

The calculated U-235 Doppler effect is extremely sensitive to the balance between changes in the fission and absorption rates. In the unresolved resonance region particularly, where one is confronted with having to use a statistical averaging technique to calculate this balance, the inherent inaccuracies of this type of procedure are compounded by resonance interference effects. Since only estimates of these interference effects are presently available, the identification of the particular problem causing the usually large discrepancy between measured and calculated U-235 Doppler effects is masked in the overall calculational procedure. However, within the statistical procedure, estimated corrections to account for resonance interference effects do tend to reduce the differences between measurements and calculations by as much as 50–100%. This indicates therefore a substantial part of this discrepancy is probably due to such interference effects. Clearly, further work in this area is indicated in order to better understand Doppler broadening effects in U-235 and in fissile materials in general. It was further found that when the resolved resonance calculation predominates and correspondingly the exact calculated balance in the unresolved resonance region is less sensitive in the net Doppler effect, the calculated U-235 Doppler effects agreed much better with the measurements. Indeed, where current theory and methods can be used with much more confidence to specify resonance structure and interference effects, calculations are in line with experiment. The importance of resolved resonance data is clear in calculations of this kind.

3. Comparison of the measured and calculated U-238 Doppler effects in these investigations show somewhat greater discrepancies than previous work has shown. It is believed that the problem areas are sufficiently understood that current theory and methods could be used to account fairly accurately for the differences caused solely by inadequacies in the calculational model. As these investigations were centered on the U-235 Doppler effect, the additional labor necessary to apply the more detailed method to the U-238 calculations was not felt to be warranted. However, the discrepancy observed may well be outside that attributable to the calculational model.

4. An alteration to first-order perturbation theory to include perturbed fluxes has demonstrated that improved estimates of experimental reactivity worths are generally obtained by even relatively simple procedures of this kind. However, this by no means is always the case. In particular, the U-235 expansion

effects in these soft spectra were not adequately handled by this calculational technique.

References

1. R. B. Pond and C. E. Till, *Doppler Effect Measurements in CH_2-Softened Spectra, ZPR-9 Assemblies 13–17*, Reactor Physics Division Annual Report, July 1, 1966 to June 30, 1967, ANL-7310, pp. 159–163.
2. C. E. Till and R. A. Lewis, *Fissile Doppler Effect Measurement Data and Techniques*, Proc. Conference on Neutron Cross Sections and Technology, Washington, D. C., March 4–7, 1968, NBS Special Publication **299**, 1, pp. 323–336.
3. R. N. Hwang, *Doppler Effect Calculations With Interference Corrections*, Nucl. Sci. Eng. **21**, 523–535 (April 1965).
4. B. J. Toppel, A. L. Rago and D. M. O'Shea, *MC^2, A Code to Calculate Multigroup Cross Sections*, ANL-7318 (1967).
5. H. M. Sumner, *ERIC 2, A FORTRAN Program to Calculate Resonance Integrals and from Them Effective Capture and Fission Cross Sections*, AEEW-R323 (1964).
6. A. Rago, *Resonance Integral*, Applied Mathematics Division Library Program B387/RP270, Argonne National Laboratory (September 23, 1964).
7. P. H. Kier and A. A. Robba, *RABBLE, A Program for Computation of Resonance Absorption in Multiregion Reactor Cells*, ANL-7326 (1967).
8. J. J. Schmidt, *Neutron Cross Sections for Fast Reactor Materials, Part I: Evaluation*, KFK 120 (EANDC-E-35U) (February 1966).
9. C. E. Till, *Fissile Doppler Effect Measurements and the Effects of Thermal Expansion*, Reactor Physics Division Annual Report, July 1, 1966 to June 30, 1967, ANL-7310, pp. 143–151.
10. D. A. Meneley, L. C. Kvitek and D. M. O'Shea, *MACH 1, A One-Dimensional Diffusion-Theory Package*, ANL-7223 (1966).
11. R. A. Karam, L. R. Dates, E. F. Groh, W. Y. Kato, R. A. Lewis, G. W. Main, J. E. Marshall, G. K. Rusch and C. E. Till, *Measured Physics Parameters in a Large Uranium Carbide Fast Core, Assembly 5 ZPR-6*, Reactor Physics Division Annual Report, July 1, 1966 to June 30, 1967, ANL-7310, pp. 167–189.
12. L. G. LeSage, R. A. Karam, R. A. Lewis, E. F. Bennett and G. W. Main, *A Review of Data Pertaining to Spectral Equilibration and Spectral Matching in Zoned Cores*, Reactor Physics Division Annual Report, July 1, 1966 to June 30, 1967, ANL-7310, pp. 199–204.
13. R. A. Lewis and C. E. Till, *Analysis of Small-Sample Doppler-Effect Measurements*, Reactor Physics Division Annual Report, July 1, 1966 to June 30, 1967, ANL-7310, pp. 139–143.
14. C. E. Till, R. A. Lewis and E. F. Groh, *U-235 Doppler Effect Measurement Data and Techniques*, Reactor Physics Division Annual Report, July 1, 1966 to June 30, 1967, ANL-7310, pp. 151–158.
15. I. I. Bondarenko (Ed.), *Group Constants for Nuclear Reactor Calculations* (Consultants Bureau, New York, 1964).

III-4. Sensitivity of Small-Sample Doppler-Effect Measurements to Environment

R. A. Lewis and T. W. Johnson

Doppler effect measurements in fast reactor critical assemblies performed at Argonne[1] over the past several years have utilized a reactivity technique in which a small heated sample of fertile or fissile material is oscillated in and out of the center of an unheated (20°C) core. The fast critical assemblies in which these measurements have been made, the Argonne ZPR facilities, are constructed of small plates of fertile, fissile and diluent materials arranged in 2 in. square cross section stainless steel drawers. Because of this construction, significant unavoidable heterogeneities occur in the immediate environment of the small Doppler measurement samples as a result of local configuration of plate material, size, and orientation. These heterogeneities are significant in that they affect the gross flux and adjoint spectra at the samples and, when the resonant material of the sample is present, unheated, in the surrounding core, the heterogeneities affect the microstructure of the flux incident on the sample.

Analyses have been completed of a series of experiments in which the environment of the Doppler sample was extensively varied in order to study the sensitivity of the measured Doppler results to the environment configuration. The experiments were performed with a 1 in. diam × 12 in. long natural UO_2 Doppler sample. This sample was chosen because of the high concentration of U-238 in the fast assemblies of interest, which emphasizes any heterogeneity effect, and because of the extensive measurements made on this sample in the past.

Experimental Results

The measurements reported here were performed in a zoned fast critical assembly (ZPR-9 Assembly 18) which had an average central core composition typical of a dilute sodium-cooled uranium-carbide fueled (U-238/U-235 = 7/1) fast power reactor. This composition was identical to that used for previously reported ZPR-6 and -9 Doppler measurements. The loading pattern of Assembly 18 is shown schematically in Fig. III-4-1. The drawer patterns for the

various core regions are summarized in Table III-4-I. Equivalent outer radii and homogenized regional atomic densities are given in Table III-4-II.

Figure III-4-2 shows the standard environment which has been used routinely in the experiments up to this time. The figure shows a section view normal to the core axis at the reactor midplane with the sample in place. Oscillation occurs normal to the plane of the figure. The drawer pattern shown is repeated vertically. The sample cans, oscillator drawer, and adjacent reactor matrix constitute a built-in stainless steel filter approximately ¼ in. thick which is always present interposed between the core and the sample.

The first variation of the standard configuration

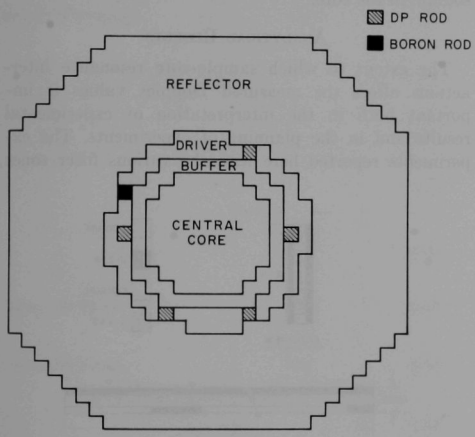

FIG. III-4-1. ZPR-9, Assembly 18 Loading Pattern. *ANL Neg. No. 113-112.*

TABLE III-4-I. ZPR-9 ASSEMBLY 18 REGIONAL DRAWER LOADING PATTERNS

Core[a] (see Fig. III-4-2)	
Type 1:	⅛ D, ½ Na, ⅛ D, 1/16 E, ⅛ C, ⅛ D, ⅛ C, 1/16 D, ½ Na, ⅛ D, ⅛ C
Type 2:	⅛ D, ⅛ C, 1/16 E, ⅛ C, 1/16 D, ½ Na, ⅛ D, ½ Na, ⅛ D, 1/16 E, ⅛ C, 1/16 D
Type 3:	⅛ D, ⅛ C, ⅛ D, ½ Na, ⅛ D, ⅛ C, ⅛ D, 1/16 E, ⅛ C, 1/16 D, ½ Na
Buffer[a]	⅛ C, ⅛ D, ⅛ C, ¼ Na, ⅛ C, ⅛ D, ⅛ C, ⅛ C, ⅛ D, ⅛ C, ¼ Na, ⅛ C, ⅛ D, ⅛ C
Driver[a]	⅛ D, ¼ Na, ⅛ E, ⅛ C, ¼ Na, ⅛ E, ⅛ D, ¼ Na, ⅛ C, ⅛ E, ¼ Na, ⅛ C

[a] ⅛ D = ⅛-in. thick depleted uranium plate; Na, E, C ≡ sodium, enriched uranium, and graphite plates.

of Fig. III-4-2 is shown schematically in Fig. III-4-3 and will be referred to as the Revised Standard configuration. Details of the sample can and oscillator drawer have been suppressed in the figure. The configuration change consisted of turning all of the plates in the adjacent four drawers so that their flat sides rather than their edges (as in the Standard case) face the sample. The plates were then subdivided and rearranged in the adjacent eight drawers so that each adjacent drawer contained four identical ½-in. thick sections, each containing approximately core-average composition. The arrangement is detailed in Fig. III-4-4.

The second variation consisted of rotating through 90° the adjacent four drawers in the Revised Standard configuration so that the plate edges face the sample; this will be called the 90°-Rotated Revised Standard Configuration.

TABLE III-4-II. ZPR-9 ASSEMBLY NO. 18

Region	Outer Radius, cm	Atom Densities $\times 10^{-24}$						
		Fe	Ni	Cr	Na	C	U-238	U-235
Core	25.883	0.009086	0.001148	0.002593	0.009028	0.012986	0.010633	0.001547
Buffer	32.525	0.008825	0.001116	0.002520	0.003917	0.034635	0.009708	0.000020
Driver	40.750	0.010638	0.001345	0.003038	0.007833	0.012986	0.005381	0.006876
Reflector I	54.520	0.004322	0.00054	0.00114	—	—	0.03990	0.000081
Reflector II	80.750	0.077772	0.000891	0.02036	—	—	—	—

Calculated critical mass: 581.8 kg U-235
Measured critical mass: 579 kg U-235
Mass of U-235 in central core: 116.2 kg
Core height: 91.44 cm (36 in.)
Estimated axial reflector savings: 16.1 cm
Total assembly volume (excluding reflector): 477.0 liters
Volume of central core: 192.4 liters

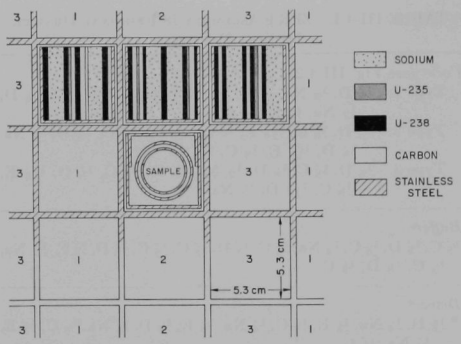

FIG. III-4-2. Standard Doppler Sample Environment. *ANL Neg. No. 112-8354.*

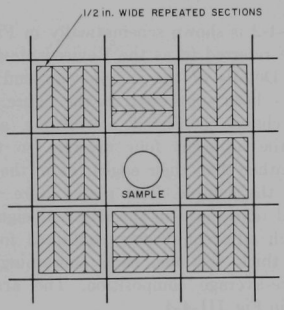

FIG. III-4-3. Revised Standard Configuration. *ANL Neg. No. 113-115.*

Environment variations three through six consisted of introducing filter zones around the sample by replacing portions of the Revised Standard configuration adjacent to the sample. Filters consisting of ¼ in., ½ in. and 1 in. thick stainless steel and ¼ in., ½ in. and 1 in. thick depleted uranium were investigated. The configuration is illustrated schematically in Fig. III-4-5 for the ½ in. stainless steel filter. Note that the built-in ¼ in. stainless-steel-equivalent filter zone is present in all cases.

Five additional variations were considered consisting of the Standard, Revised Standard, 90°-Rotated Revised Standard, ½ in. Stainless Steel Filter and the 1 in. Stainless Steel Filter cases, all with sodium removed from the core.

The experimental results for the various configurations are listed in Table III-4-III. Previous measurements[1] have indicated that this 1 in. natural UO_2 sample has a negligibly small expansion effect so that the numbers in the table represent Doppler changes. The details of the technique by which the data were obtained and reduced is discussed in Ref. 1. The data are summarized in Table III-4-IV where the estimated Doppler reactivity effect between room temperature and 1100°K is normalized to the results of the Revised Standard Configuration measurement.

Examination of the results shown in Table III-4-IV for the measurement variations in which the orientation of the U-238 plates in the drawers adjacent to the sample was changed with respect to the sample—viz., the Standard, Revised Standard and 90°-Rotated Revised Standard cases—indicate that reasonable plate reorientation does not affect the results more than about 5% either with or without sodium in the core.

Analytical Results

The extent to which sample-core resonance interactions affect the measured Doppler values is important both in the interpretation of experimental results and in the planning of experiments. The experiments reported here with the various filter zones

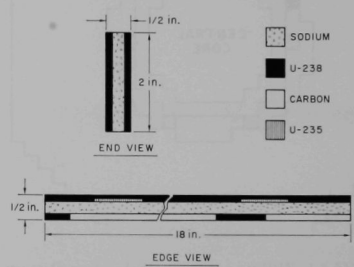

FIG. III-4-4. Detail of Repeated 1/2-in. Thick Section of Revised Standard Configuration. *ANL Neg. No. 113-116.*

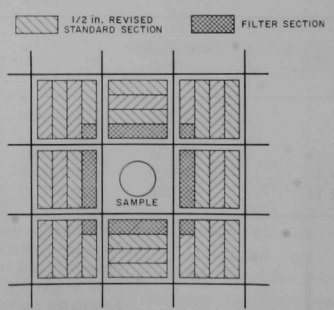

FIG. III-4-5. 1/2-in. Stainless Steel Filter Configuration. *ANL Neg. No. 113-108.*

TABLE III-4-III. EXPERIMENTAL RESULTS FOR 1 in. NATURAL UO_2 SAMPLE, ZPR-9 ASSEMBLY 18

[*Sample mass = 1.116 kg uranium (1.266 kg UO_2)*]

Sample Environment	Sodium in Core	Date (1967)	Standard Deviation Each Point, Ih/kg-U	Sample Temperature, °K[a] / Reactivity Change, Ih/kg-Uranium			
Standard	Yes	6/23	0.002	293	510	773	1058
				0.000	−0.155	−0.289	−0.394
		7/13	0.002	293	762		
				0.000	−0.289		
		8/25	0.002	293	756	1044	
				0.000	−0.278	−0.388	
		8/28	0.003	293	776		
				0.000	−0.284		
Revised Standard	Yes	6/28	0.002	293	499	782	1059
				0.000	−0.157	−0.303	−0.418
		8/8	0.002	293	768		
				0.000	−0.301		
		8/21	0.002	293	749	1044	
				0.000	−0.291	−0.408	
		8/23	0.001	293	748	1043	
				0.000	−0.291	−0.404	
		8/23	0.002	293	748	1043	
				0.000	−0.292	−0.406	
¼-in. SS Filter	Yes	8/17	0.001	293	479	758	1051
				0.000	−0.151	−0.299	−0.408
½-in. SS Filter	Yes	7/11	0.001	293	771		
				0.000	−0.316		
		7/11	0.001	293	771		
				0.000	−0.318		
		8/11	0.001	293	505	775	
				0.000	−0.160	−0.320	
		8/16	0.001	293	760	1064	
				0.000	−0.320	−0.444	
1-in. SS Filter	Yes	7/5	0.002	293	505	786	1075
				0.000	−0.181	−0.353	−0.477
90 deg-Rotated Rev. Stan.	Yes	8/22	0.001	293	751	1045	
				0.000	−0.289	−0.393	
		8/22	0.001	293	748		
				0.000	−0.281		
		8/24	0.002	293	752	1046	
				0.000	−0.283	−0.394	
¼-in. Depl. U Filter	Yes	8/18	0.002	293	749	1043	
				0.000	−0.263	−0.356	

TABLE III-4-III. *(Continued)*

Sample Environment	Sodium in Core	Date (1967)	Standard Deviation Each Point, Ih/kg-U	Sample Temperature, °K[a] / Reactivity Change, Ih/kg-Uranium			
½-in. Depl. U Filter	Yes	7/10	0.002	293	511	796	1047
				0.000	−0.128	−0.239	−0.318
1-in. Depl. U Filter	Yes	7/6	0.002	293	512	796	1057
				0.000	−0.089	−0.173	−0.233
Standard	No	9/5	0.002	293	772	1043	
				0.000	−0.199	−0.270	
Rev. Stan.	No	9/6	0.001	293	766	1043	
				0.000	−0.205	−0.279	
90 deg-Rot. Rev. Stan.	No	9/6	0.001	293	1043		
				0.000	−0.269		
½-in. SS Filter	No	9/8	0.001	293	768	1043	
				0.000	−0.215	−0.296	
1-in. SS Filter	No	9/11	0.002	293	770	1043	
				0.000	−0.242	−0.320	

[a] Data normalized to 0.00 at 293°K.

TABLE III-4-IV. SUMMARY OF EXPERIMENTAL RESULTS FOR 1-in. NATURAL UO_2 SAMPLE, 293–1100°K

Configuration	Na in Core	Normalized to Rev. Stan. with Na	Normalized to Rev. Stan. without Na
Revised Standard	Yes	1.000	
90 deg Rotated Rev. Stan.	Yes	0.958 ± 0.010	
Standard	Yes	0.948 ± 0.010	
¼-in. Extra SS Filter	Yes	0.995 ± 0.010	
½-in. Extra SS Filter	Yes	1.068 ± 0.010	
1-in. Extra SS Filter	Yes	1.138 ± 0.016	
¼-in. Depl. U Filter	Yes	0.869 ± 0.010	
½-in. Depl. U Filter	Yes	0.779 ± 0.011	
1-in. Depl. U Filter	Yes	0.566 ± 0.010	
Revised Standard	No	0.683 ± 0.009	1.000
90 deg Rotated Rev. Stan.	No		0.962 ± 0.010
Standard	No		0.969 ± 0.010
½-in. Extra SS Filter	No		1.062 ± 0.015
1-in. Extra SS Filter	No		1.144 ± 0.018

surrounding the samples were undertaken primarily as an aid in the determination of the magnitude of this sample-core interaction effect. Thus, in conjunction with the measurements a detailed analysis has been made of the Revised Standard, ¼ in. Stainless Steel Filter, ½ in. Stainless Steel Filter and ¼ in. Depleted Uranium Filter cases, and for a hypothetical reference case in which the core is brought up to the sample surface (i.e., the built-in ¼ in. stainless-steel-equivalent filter is removed). Qualitatively, interposing stainless steel reduces the resonance-interaction effect between sample and core (an effect which increases the Doppler effect) and increases the Doppler range flux at the sample. Thus a balancing effect is to be expected as is seen in Table III-4-IV where the ¼ in. Stainless Steel filter case gives essentially the same result as the Revised Standard Case.

The basic analytical tool used was the RABBLE code[2] which performs a detailed resonance absorption calculation in the cylindrical multiregion configuration of the measurement. The code solves the integral slowing-down equation by dividing the energy range into many very small (compared to the Doppler width) energy groups and applying collision-probability theory (flat-source) on a series of small annular regions. RABBLE allows arbitrary combinations of resonant and non-resonant materials in the various regions of the problem and region-dependent temperatures. The code provides regional coarse-group flux-collapsed cross sections as output. The equivalent cylindrical configuration used for the analysis is shown in Fig. III-4-6 for the ½ in. Stainless Steel Filter Case.

Code limitations make it necessary to approximate the core region as a homogeneous region. This approximation is not too bad, as was shown in Ref. 3. Further, it is possible to mitigate the error introduced by manipulating the input data to adjust the broad-group macroscopic absorption cross section to

an appropriate value in the core region. This preserves the gross source reduction rate.

RABBLE calculations were perfromed over the energy range 111 keV to 29 eV with the sample at 293 and 1100°K and with the rest of the reactor at 293°K. The sample-region Doppler cross section changes and the induced core-region cross section. changes were calculated both with U-238 resonances outside of the sample region explicitly included and with these resonances suppressed and replaced by a uniform background absorption cross section. ENDF/B (Category 1, zero iteration) resonance parameters were used with appropriately distributed resonances generated at energy points throughout the unresolved range. Only s-wave Doppler effects were considered on the assumption that the p-wave resonances are so small and strongly-overlapped, where they are important, as to have no Doppler effect.

Core region coarse group cross section sets were generated with the MC² code[4] on the basis of the ENDF/B (Category 1, zero iteration) microscopic cross section set. These cross sections together with the RABBLE-generated sample-region cross sections were used in SNARG-1D S_8 calculations to determine the sample-core coarse-group flux and adjoint flux distributions; the flux was calculated with the sample at 1100°K and the adjoint flux and the sample at 293°K.

The results of the SNARG flux and adjoint calculations are summarized in Table III-4-V. The expected sample-region coarse-group flux variation is seen. The No-Filter case in the table refers to the

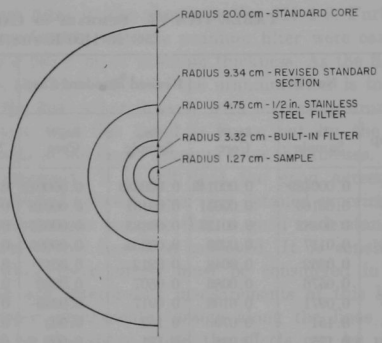

FIG. III-4-6. Equivalent Cell Used for RABBLE Analysis 1/2-in. Stainless Steel Filter Configuration. *ANL Neg. No. 113-111.*

hypothetical case in which the core begins at the sample surface. Table III-4-VI summarizes the calculated RABBLE sample-region Doppler changes (293 to 1100°K) and the induced core region changes in U-238 cross sections listed per U-238 atom in the sample. For reference, sample cross section values calculated with the U-238 resonances outside of the sample region suppressed are shown at the right-hand edge of the table.

The calculated sample and core-region Doppler cross section changes and the calculated flux and adjoint distributions were used in the usual multigroup perturbation formulation to obtain calculated values for the relative Doppler effect to be expected

TABLE III-4-V. SUMMARY OF CALCULATED FLUX AND ADJOINT RATIOS (SAMPLE/CORE) AND CALCULATED CORE FLUX AND ADJOINT SPECTRUM

Group	Lower Energy Limit, eV	No Filter		Revised Standard Case		¼-in. SS Filter		½-in. SS Filter		¼-in. Depl. Uranium Filter		Core Flux	Core Adjoint Flux
		Flux Ratio	Adjoint Ratio	Flux Ratio	Adjoint Ratio	Flux Ratio	Adjoint Ratio	Flux Ratio	Adjoint Ratio	Flux Ratio	Adjoint Ratio		
8	111,100												
9	67,380	1.011	0.989	1.010	0.983	1.015	0.978	1.020	0.973	1.014	0.947	10.22	3.37
10	40,870	1.012	0.985	1.016	0.979	1.017	0.974	1.018	0.968	1.018	0.933	8.54	3.29
11	24,790	1.007	0.981	1.029	0.972	1.056	0.964	1.093	0.956	1.022	0.965	6.85	3.26
12	15,030	0.988	0.976	0.898	0.972	0.865	0.956	0.833	0.960	0.858	0.903	5.48	3.29
13	9,119	0.985	0.970	1.094	0.962	1.123	0.953	1.153	0.943	1.049	0.881	3.84	3.37
14	4,307	1.002	0.964	1.094	0.951	1.163	0.933	1.250	0.914	1.023	0.956	3.01	3.51
15	2,613	1.147	0.956	1.604	0.942	2.013	0.927	2.613	0.910	1.529	0.845	0.534	3.85
16	2,035	0.934	0.967	0.897	0.958	0.896	0.947	0.920	0.932	0.797	0.886	0.354	3.98
17	1,234	0.900	0.973	0.928	0.959	0.941	0.944	0.961	0.926	0.841	0.895	0.995	4.06
18	961	0.921	0.975	0.980	0.952	1.011	0.930	1.054	0.907	0.886	0.879	0.318	4.18
19	583	0.964	0.972	1.081	0.965	1.172	0.955	1.298	0.943	0.994	0.895	0.370	4.49
20	275	0.985	0.974	1.173	0.956	1.358	0.939	1.641	0.918	1.097	0.894	0.196	4.75
21	101.3	0.996	0.980	1.321	0.961	1.717	0.941	2.416	0.918	1.233	0.892	0.0385	4.82
22	29.02	1.137	0.979	1.178	0.955	1.610	0.931	2.356	0.902	1.248	0.884	0.00303	4.62

TABLE III-4-VI. SUMMARY OF CALCULATED *s*-WAVE DOPPLER CROSS SECTION CHANGES, 293 TO 1100°K FOR 1 in. NATURAL UO_2 DOPPLER SAMPLES

	No Filter		Revised Standard Case		¼-in. SS Filter		½-in. SS Filter		¼-in. Depl. Uranium Filter		No. Res. Core
Group	$\delta\sigma_a$ Sample	$\delta\sigma_a^{(a)}$ Core	$\delta\sigma_a$ Sample	$\delta\sigma_a^{(a)}$ Core	$\delta\sigma_a$ Sample	$\delta\sigma_a^{(a)}$ Core	$\delta\sigma_a$ Sample	$\delta\sigma_a^{(a)}$ Core	$\delta\sigma_a$ Sample	$\delta\sigma_a^{(a,b)}$	$\delta\sigma_a$ Sample
9	0.000489	0.000143	0.000383	0.000042	0.000355	0.000040	0.000343	0.000012	0.000408	0.000052	0.000333
10	0.00169	0.00051	0.00131	0.00018	0.00122	0.00008	0.00117	0.00002	0.00140	0.00020	0.00114
11	0.00482	0.00127	0.00385	0.00057	0.00360	0.00027	0.00349	0.00000	0.00407	0.00052	0.00340
12	0.0117	0.0029	0.00955	0.00099	0.00901	0.00040	0.00878	0.00012	0.00999	0.00110	0.00858
13	0.0252	0.0048	0.0212	0.0017	0.0202	0.0009	0.0198	0.0004	0.0220	0.0021	0.0194
14	0.0576	0.0086	0.0507	0.0030	0.0489	0.0013	0.0481	0.0006	0.0521	0.0037	0.0476
15	0.0971	0.0108	0.0917	0.0045	0.0903	0.0021	0.0897	0.0009	0.0940	0.0055	0.0894
16	0.151	0.070	0.142	0.003	0.141	0.002	0.140	0.000	0.146	0.003	0.139
17	0.175	0.038	0.171	0.002	0.170	0.001	0.170	0.000	0.170	0.002	0.167
18	0.255	−0.010	0.245	0.001	0.243	0.002	0.242	0.000	0.251	0.001	0.249
19	0.356	−0.007	0.354	−0.003	0.353	0.000	0.352	0.000	0.354	−0.003	0.352
20	0.357	−0.014	0.357	−0.001	0.355	0.000	0.354	0.000	0.358	−0.007	0.354
21	0.407	−0.032	0.426	−0.020	0.429	−0.021	0.428	−0.010	0.426	−0.035	0.430
22	0.285	−0.073	0.342	−0.023	0.350	−0.005	0.345	−0.002	0.341	−0.041	0.345

[a] Per U-238 atom in sample.
[b] ¼-in. depleted uranium filter zone.

TABLE III-4-VII. CALCULATED FLUX AND ADJOINT-WEIGHTED RELATIVE DOPPLER EFFECTS: 1 in. NATURAL UO_2 SAMPLE

Environment[a]	With Core Resonances	Without Core Resonances
No-Filter	1.000	1.000
Revised Standard	0.973	1.087
¼-in. Extra SS	0.996	1.157
½-in. Extra SS	1.064	1.252
¼-in. Depleted U	0.857	0.931

Ratios	With Resonances Core / Without Resonances Core
No-Filter	1.187
Revised Standard	1.063
¼-in. Extra SS	1.023
½-in. Extra SS	1.008
¼-in. Depleted U[(b)]	1.086

[a] All cases except No-Filter include built-in ¼-in. SS filter.
[b] Without-Resonance case has U-238 resonances in the ¼-in. depleted uranium filter also suppressed.

in the various configurations. These values are listed in Table III-4-VII, normalized to the No-Filter case.

The calculated extent of sample-core resonance interaction is also shown in Table III-4-VII where the calculated Doppler changes with core resonances are normalized to the case with these resonances suppressed.

These analytical results indicate that, while an approximately 19% resonance interaction effect is present with no filter between the sample and the core, this effect is reduced to approximately 6% in the usual measurement configuration and to about 3% with an additional ¼ in. stainless steel filter.

Figures III-4-7 and III-4-8 demonstrate the agreement between calculation and experiment. Figure III-4-7 demonstrates the way the two effects—flux perturbation and hot-cold resonance interaction—combine to make up the total effect. The figure is normalized such that the ideal case with no flux perturbation or resonance interaction has a Doppler effect of unity. As the figure shows, the hot-cold resonance interaction effect decreases rather rapidly with increasing filter thickness, and the flux perturbation effect increases in a regular manner with increasing filter thickness. The three experimental points relevant

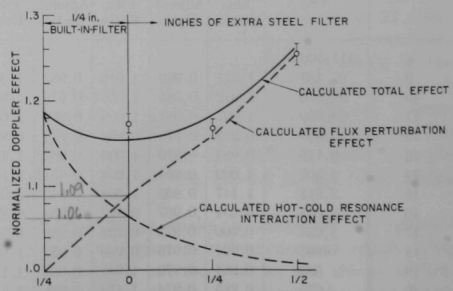

FIG. III-4-7. Effect on the Doppler Effect of Steel Filter Extrapolated Back to Zero Steel Thickness—Comparison of Calculation and Experiment. *ANL Neg. No. 113-483.*

to this comparison show good agreement with the predicted trend of the total effect.

Figure III-4-8 shows the effects both of steel and uranium filters. The right-hand side of Fig. III-4-8 essentially repeats the information given in Fig. III-4-7, except that the calculations are not extrapolated back to zero-filter thickness. The left-hand side of Fig. III-4-8 shows the effect of increasing uranium filter thickness, but this differs somewhat from the steel filter case, in that a combination of steel and uranium is always present in the uranium filter experiments because of the presence of the ¼ in. built-in steel filter. In addition to the calculations shown in Fig. III-4-7, the calculation of the effect of ¼ in. of uranium filter is also shown in Fig. III-4-8. Further, the experiments with the uranium filter were carried out to a full 1 in. of uranium thickness. As the figure shows, the main effect of the uranium filter is to depress the flux rather linearly with increasing uranium thickness, and this trend is borne out by the experiments at the larger uranium filter thicknesses.

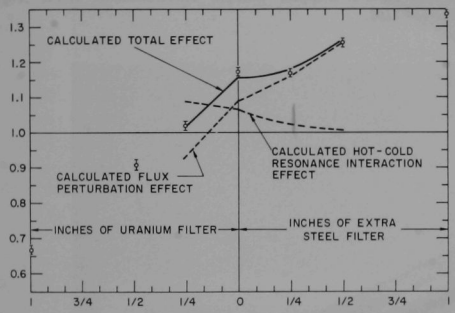

Fig. III-4-8. Effect on the Doppler Effect of Steel and Uranium Filters, 1/4-in. Built-In Steel Filter Always in Place—Comparison of Calculation and Experiment. *ANL Neg. No. 113-486.*

In summary, it is felt that the good agreement demonstrated between these very detailed experiments and calculations indicate that a good understanding of these effects has been achieved. It is concluded that while these effects must be considered in designing and interpreting measurements of this kind, by proper experimental design along the lines suggested by the above work, the effects can be made rather small and of known magnitude. Specifically, the hot-cold interaction effects, which require very detailed calculations, can be made small; in fact they are normally rather small in the usual experimental environments of reactivity Doppler measurements done to date.

References

1. C. E. Till, R. A. Lewis and R. N. Hwang, *ZPR-6 Doppler Measurements and Comparisons with Theory*, Proc. International Conference on Fast Critical Experiments and their Analysis, 1966, ANL-7320, p. 319.
2. P. H. Kier and A. A. Robba, *RABBLE, A Program for Computation of Resonance Absorption in Multiregion Reactor Cells*, ANL-7326 (1967).
3. R. A. Lewis and C. E. Till, *Analysis of Small-Sample Doppler Effect Measurements*, Trans. Am. Nucl. Soc. **10**, No. 1, 274 (1967).
4. B. J. Toppel, A. L. Rago and D. M. O'Shea, *MC²—A Code to Calculate Multigroup Cross Sections*, ANL-7318 (1967).

III-5. Doppler Effect Measurements to 2000° K in ZPR-9

J. W. Daughtry, E. F. Groh and C. E. Till

Introduction

Most Doppler effect measurements performed at Argonne in recent years have employed the small sample-reactivity measurement technique, in which a heated sample is oscillated in and out of a critical facility. This method has been used successfully in studying the systematics of the Doppler effect in fast reactor spectra over the temperature range 293 to 1100°K.

In calculating the energy release in fast power reactors under accident conditions one needs to know the Doppler effect at temperatures up to and beyond the melting point of the fuel. There is, therefore, considerable interest in extending the temperature range of the Doppler measurements to higher temperatures to reduce the error inherent in the extrapolation of data beyond the range of experimental results. Thus, one area in which development work is being carried on is in the design of equipment for making very high temperature Doppler measurements. Progress in this area has lead to a series of Doppler measurements in which average sample temperatures exceeded 2000°K. This report describes, briefly, the main features of the new equipment and presents the results of experi-

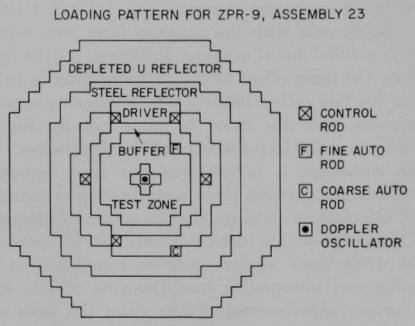

FIG. III-5-1. Loading Pattern for ZPR-9, Assembly 23. *ANL Neg. No. 113-1516 T-1.*

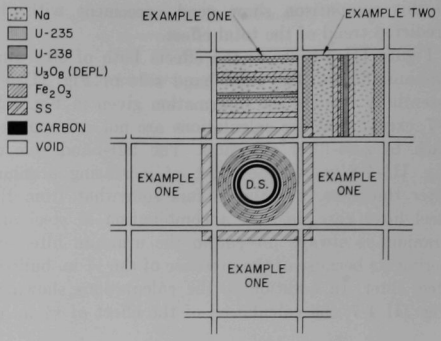

FIG. III-5-2. Doppler Sample Environment. *ANL Neg. No. 113-1496.*

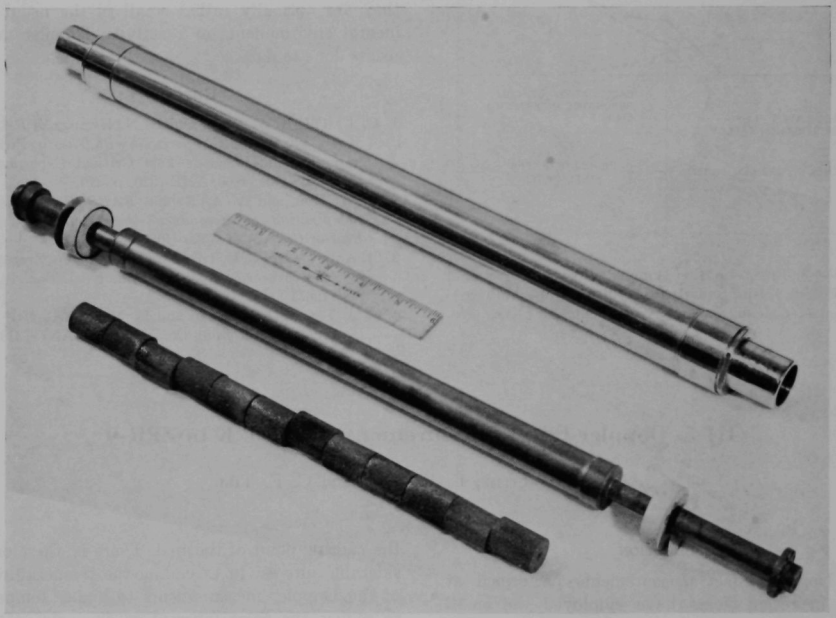

FIG. III-5-3. Graphite Sample Holder and UO_2 Pellets. *ANL Neg. No. 113-944.*

ments in which the Doppler effects of UO_2 and four refractory metals were measured over the extended temperature range.

Experimental Facilities and Equipment

The experiments were performed in ZPR-9 Assembly 23, one of a series of zoned cores designed to have central real and adjoint spectra typical of a sodium cooled fast breeder reactor with a large dilute U-235 fueled oxide core. The loading pattern for Assembly 23, as shown in Fig. III-5-1, approximated a set of concentric cylinders with an outer radius of 73.45 cm. The composition of each zone was the same as Assembly 19 which is described in

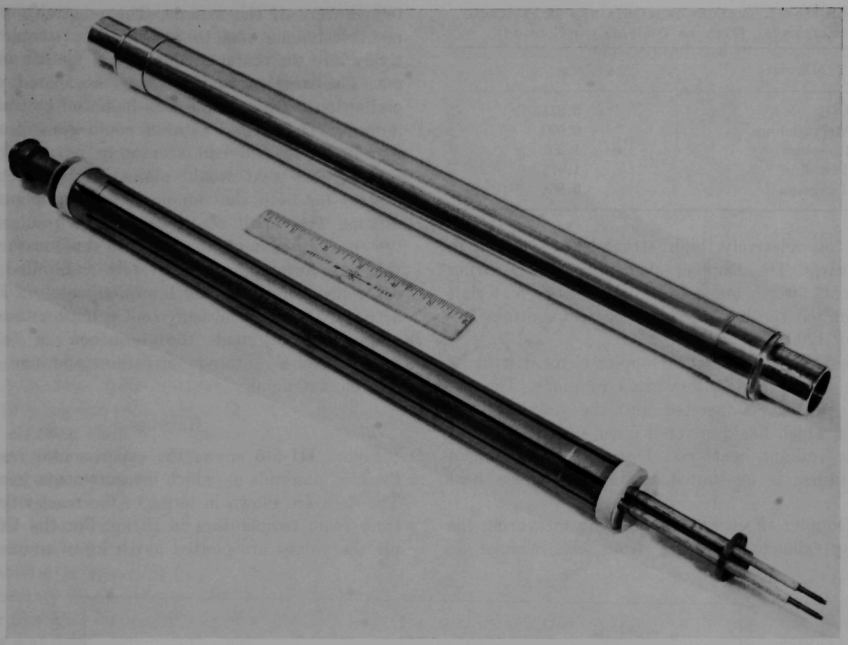

FIG. III-5-4. Assembled Doppler Element With Graphite Heater. *ANL Neg. No. 113-942.*

Paper III-2. The center of the test zone is shown in Fig. III-5-2. Each matrix position is approximately 5.3 cm square, not including the matrix structure. The central position was occupied by the Doppler oscillator shown semi-schematically with the Doppler sample in a graphite container, which in turn was surrounded by a graphite heater. This was enclosed in an evacuated stainless steel tube. Two additional stainless steel tubes are shown; these are for the counter-flow cooling system necessary to remove heat escaping from the Doppler capsule to prevent a rise in the temperature of the adjacent materials. A stainless steel filter surrounded the central matrix tube. The matrix material is also stainless steel. The filter is approximately ¼ in. thick; the stainless steel in the Doppler oscillator and the matrix structure adds an equal amount giving a total thickness of approximately ½ in. The two layers of carbon, representing the sample holder and heater, have a total thickness of less than 0.16 in.

The plate arrangement indicated in the drawer labeled "Example two" is (except for the stainless steel corner) the arrangement in the drawers of the central test zone. The drawers labeled "Example One" have a modified plate arrangement that retains, outside of the void region, the same composition of materials as the remainder of the test zone. Each of the drawers labeled "Example One" is loaded the same, going radially outward from the Doppler oscillator.

The purpose of this modified configuration is explained in detail in Paper III-4.

A typical high temperature Doppler element is shown in Fig. III-5-3. The one shown will accept samples 1.9 cm diam and up to 30 cm long. The samples have axial holes to permit the insertion of thermocouples. During the experiments, five thermocouples were equally spaced along the axis of the sample. The element is all graphite except for the beryllium oxide insulators for supporting the heater and the 2-mil thick molybdenum heat shields at each end. For some materials, UO_2 in particular, the chemical reaction rate with graphite at high temperatures required the use of a liner between the sample and sample holder. One mil thick tantalum foil was used. It is advantageous to minimize the amount of refractory metal present so that the Doppler effect for the empty capsule will be small. Graphite is not a resonance absorber and has the additional ad-

TABLE III-5-I. VALUES OF n OBTAINED BY FITTING EXPERIMENTAL DATA TO $T^n(dk/dT)$ = Constant

Material	n
UO_2	0.871
Molybdenum	0.900
Rhenium	1.207
Tantalum	1.076
Tungsten	0.808

vantage of relatively high strength at very high temperatures. The Doppler elements used in earlier experiments were made of nickel-alloy materials which limited the measurements to temperatures below about 1200°K.

Figure III-5-4 shows the Doppler element with its graphite heater and power leads in place. The assembled element is inserted into the stainless steel container which has a silvered inner surface to minimize the radiant heat loss. During the experiment the container is evacuated to further reduce heat losses.

The Doppler effect was obtained by measuring the reactivity change resulting from the change in temperature of the sample. The reactivity measurement technique was to oscillate the sample repetitively into the center of the critical facility and back out. The large reactivity change associated with the oscillation of the sample was balanced by the coarse autorod. The coarse autorod could control approximately 50 Ih and had accurately reproducible preset positions that would maintain the reactor near critical for both the sample-in and sample-out conditions. The small reactivity change resulting from the change in sample temperature was measured with the fine autorod, an accurately calibrated, servo-controlled boron rod, worth approximately 2 Ih in reactivity. During a measurement a master timer automatically controlled the sequence of oscillator motion, coarse autorod activation, and fine autorod position averaging.

RESULTS

Figure III-5-5 shows the experimental results for the five materials on which measurements were made. The data are shown in terms of the reactivity change from room temperature in Ih/kg. For the UO_2 sample the values are plotted as Ih/kg of uranium. The

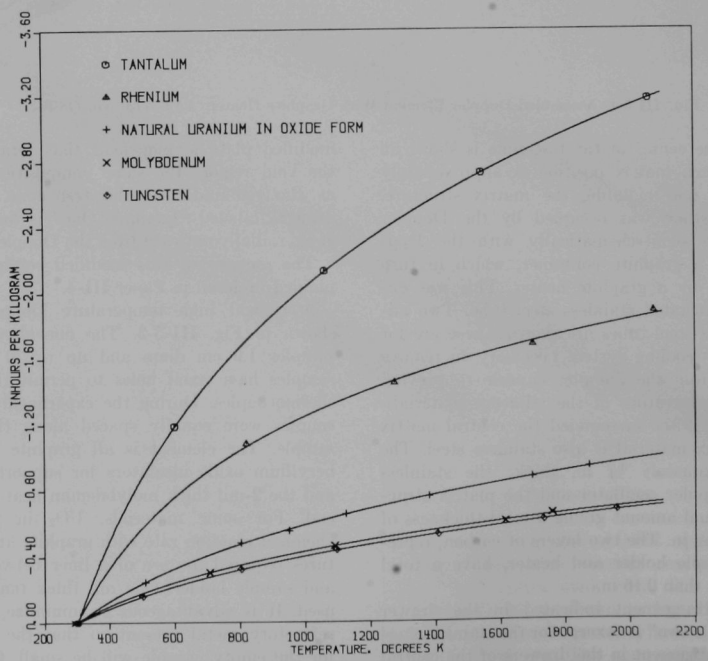

FIG. III-5-5. Measured Doppler Effect—No Expansion Corrections. *ANL Neg. No. 113-1502.*

experimental points as shown have been corrected for the effect of the empty capsule, so that the indicated reactivity change is due to the Doppler effect and sample expansion, both of which are negative. Calculations indicate that the expansion effect is small, amounting to no more than 3 to 4% of the total reactivity change for tantalum and molybdenum, less than 1% for tungsten, and negligible for UO_2 relative to the experimental accuracy. Subtracting the calculated expansion effect from the molybdenum and tungsten data leads to the interesting result that the measured Doppler effect for these two refractory metals is the same within experimental accuracy, in this spectrum.

For UO_2 the measurements made in Assembly 23 with the new high temperature equipment can be compared directly with measurements made in Assembly 19 using the standard ANL freely expanding Doppler element. Such a comparison shows excellent agreement over the temperature range common to both sets of measurements.

The curves shown in Fig. III-5-5 were obtained by fitting the experimental points to the expression $T^n\, dk/dT$ = constant. The value of n obtained for each material is shown in Table III-5-I. For UO_2 the uncertainty in n is estimated to be ± 0.028. Fitting only the five UO_2 data points below 1200°K yields a value for n at 0.89.

Comparisons with Calculations and Other Experiments

Some calculational effort has been made to investigate the degree of agreement that one can obtain using available cross section data and calculational methods. In all calculations only ENDF/B cross sections were used. Multigroup cross section sets were generated by the MC² code and used in the DEL subroutine of MACH 1 for the calculation of the Doppler reactivity changes.

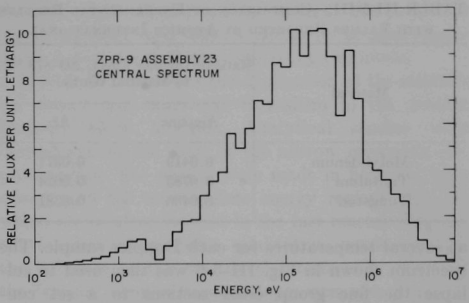

FIG. III-5-6. ZPR-9, Assembly 23 Central Spectrum as Computed by MCC From ENDF/B Cross Sections. *ANL Neg. No. 113-1501.*

Specifically, a multigroup set of fluxes was calculated for the central zone of Assembly 23 using the P_1 fundamental-mode option of MC². The cell structure was specified to insure the correct potential scattering cross section for U-238. The calculation was performed with ultrafine groups (lethargy width: 1/120). The neutron fluxes in ultrafine group form were then reduced to a fine group set consisting of 66 groups with a lethargy width of 0.25 as shown in Fig. III-5-6.

Fine group cross sections were generated by MC²

TABLE III-5-II. COMPARISON OF MEASURED AND CALCULATED RESULTS

Material	*A* Reactivity Worth at ~25°C, Ih/kg		*B* Reactivity Change 293 to 2000°K, Ih/kg		Calculated Expansion Correction 2000–293°K, Ih/kg	*B/A*	
	Measured	Calculated	Measured	Calculated		Measured	Calculated
UO_2	−5.876 ±0.025	−7.001	−0.983 ±0.014	−0.692	+0.000	0.167	0.099
Molybdenum	−8.870 ±0.017	−16.095	−0.696 ±0.009	−0.162	−0.026	0.078	0.010
Rhenium	−31.375 ±0.011	—	−1.8484 ±0.018	—	—	0.059	—
Tantalum	−23.333 ±0.014	−22.894	−3.171 ±0.028	−3.306	−0.050	0.136	0.144
Tungsten	−8.134 ±0.010	−9.780	−0.682 ±0.008	−0.675	−0.006	0.084	0.069

TABLE III-5-III. COMPARISON OF EXPERIMENTAL RESULTS WITH VALUES REPORTED BY ATOMICS INTERNATIONAL

Material	Ratio of Doppler Effect, 293–873 °K, to Material Worth	
	Argonne	AI
Molybdenum	0.0419	0.0371
Tantalum	0.0785	0.0624
Tungsten	0.0436	0.0381

at several temperatures for each Doppler sample. The spectrum shown in Fig. III-5-6 was then used to collapse the fine group cross sections to a set consisting of 25 broad groups. Reactor calculations were made with MACH 1 in 25 groups and cylindrical geometry. The Doppler sample and its environment were included in a criticality calculation, which was followed by perturbation calculations to determine the worth of the sample at each temperature for which cross section data had been generated.

A comparison of measured and calculated results is given in Table III-5-II. The values quoted for UO_2 are in Ih/kg of uranium. No ENDF/B data are available for rhenium, which is the reason for the absence of calculations for that material. The columns under *A* are the central reactivity worths of the materials in Assembly 23. The agreement between measured and calculated worth is poorest for molybdenum, where the calculations overpredict the worth by more than 80%. It is known, however, that the ENDF/B library does not include the latest cross section data for molybdenum; and the difference between the data used in ENDF/B and the newer data is significant.

The columns under *B* include the combined effect of Doppler broadening and sample expansion; thus the calculated values under *B* include the calculated expansion effect shown in the adjacent column. Again the agreement is quite poor for molybdenum; however, here the calculated value is too low. A check of ENDF/B shows that this is due to the absence of unresolved resonance parameters for molybdenum. For UO_2 the agreement between experiment and calculations is not as good as has been obtained when other cross section sets were used, prior to the availability of ENDF/B. This suggests the possibility of errors in the U-238 cross sections in the ENDF/B library.

The ratio of *B* to *A* is of interest since it cancels out the effect of errors that may exist in the calculated perturbation denominator. It is clear that the best agreement is obtained for tantalum.

Table III-5-III shows a comparison of our results with those reported by Atomics International (AI).[1] This comparison is over the temperature range of the Atomics International measurements. Here again the quantity being compared is the ratio of the Doppler effect to the material worth. The Argonne values are higher by 13% for molybdenum, 14% for tungsten, and 26% for tantalum. The use of the stainless steel filter around the oscillator drawer causes a flux perturbation effect that could account for some of this difference.

REFERENCE

1. S. G. Carpenter, L. A. Mountford, T. H. Springer and R. J. Tuttle, *Dependence of the Doppler Coefficient of Reactivity for Heavy Elements on Chemical Form, Surface-to-Mass Ratio, and Neutron Spectrum*, Proc. International Conference on Fast Critical Experiments and Their Analysis, October 10–13, 1966, ANL-7320, pp. 334–340.

III-6. Application of Statistical Theory and Multilevel Formalism to Doppler Effect Analysis

R. N. HWANG

The influence of the multilevel multichannel interference effect on the Doppler effect of fissile isotopes has been of considerable practical interest in recent fast reactor studies. As a part of a series of studies now under way, the main purpose of the present paper is to improve the understanding of the theory and application of the multilevel, multichannel formalism to Doppler effect studies in the unresolved region. In particular, the emphasis of this work is on the analytical aspects of the problem. The detailed description will appear in Refs. 1 and 2.

In the present work, the concept of the "statistical collision matrix" introduced by P. A. Moldauer[3] was used. Reference 1 describes the formulation of the Doppler broadened cross sections in terms of *S*-matrix parameters and the statistical considerations pertinent to the fissile isotopes. It is shown that, in the *S*-matrix formulation, the Doppler broadened

cross sections, in general, can be expressed in terms of the usual ψ and χ function if the ideal gas model is assumed. The disadvantage of the S-matrix formulation is the apparent lack of knowledge of the precise statistical behavior of the S-matrix parameters. The distribution functions, in principle, can be determined from the given R-matrix distribution functions. In order to improve understanding of the S-matrix statistics, a simple example using two interfering levels was carried out analytically. With the distribution functions expressed in the explicit functional form, it is possible to study the characteristics of these functions in great detail. It was found that the S-matrix levels no longer exhibit the Wigner repulsion. The degree of distortion in the distribution function for the S-matrix level spacing depends on the ratio of the average total width to the average spacing. The distribution function for the S-matrix total width was found to be wider than the corresponding R-matrix distribution function. Realistic examples for fissile isotopes including many levels and channels were also given on the basis of the statistical collision matrix concept. The results in the many-level case were found to be in good qualitative agreement with the cases using two levels.

Reference 2 describes the application of the statistical theory and multilevel formalism to the reactor Doppler effect analysis. Analytical studies were carried out on the basis of the narrow resonance approximation. The studies were made in both the high energy and the intermediate energy regions, both of which are of great interest in the fast reactor Doppler effect calculations. Some qualitative conclusions on the influence of the multilevel interference effect on the Doppler effect of fissile isotopes were also given.

References

1. R. N. Hwang, *Application of Statistical Theory and Multilevel Formalism to Doppler Effect Analysis*—Part I, Nucl. Sci. Eng. (to be published).
2. R. N. Hwang, *Application of Statistical Theory and Multilevel Formalism to Doppler Effect Analysis*—Part II, Nucl. Sci. Eng. (to be published).
3. P. A. Moldauer, *Statistical Theory of Nuclear Collisions Cross Sections*, Phys. Rev. **135**, No. 3B, 642–659 (1964).

III-7. Variance in the Doppler Coefficient Due to Statistical Selection of Resonance Parameters

L. B. Miller and R. N. Hwang

Method of Analysis

Letting

$F \equiv$ number of fissions per source neutron
$C \equiv$ number of captures per source neutron,

the multiplication constant for an infinite system with repeated cells is

$$k = \frac{\nu F}{F + C} \tag{1}$$

Differentiating with respect to temperature, T,

$$\frac{1}{k}\frac{dk}{dT} = \frac{1}{\nu F}\frac{d(\nu F)}{dT} - \frac{1}{F + C}\left(\frac{dF}{dT} + \frac{dC}{dT}\right). \tag{2}$$

Since all neutrons are eventually absorbed, the total number of fissions and captures per source neutron is unity. Therefore the second term on the right is zero.

It may be of interest to determine the Doppler coefficient of reactivity due to resonances in a small energy region or due to all the resonances in the Doppler region. The following analysis applies to both cases.

If we let the subscript d denote the resonance region of interest, ℓ denote the lower energy region, and h denote the higher energy region, then

$$\frac{1}{k}\frac{dk}{dT} = \frac{1}{\nu F}\left(\frac{d(\nu F)}{dT}\right)_d + \frac{1}{\nu F}\left(\frac{d(\nu F)}{dT}\right)_\ell + \frac{1}{\nu F}\left(\frac{d(\nu F)}{dT}\right)_h. \tag{3}$$

The changes with temperature in the fission and capture rates in the lower energy region are due to the depletion of the flux in the lower energy region, caused by increased absorption in the resonance region of interest. This affects the fission and capture rates in the same way, so the fractional change in the fission rate is equal to the fractional change in the capture rate in the lower energy region; that is

$$\left(\frac{1}{\nu F}\frac{d(\nu F)}{dT}\right)_\ell = \left(\frac{1}{F + C}\frac{d(F + C)}{dT}\right)_\ell. \tag{4}$$

Therefore the second term in Eq. (3) is

$$\frac{1}{\nu F}\left(\frac{d(\nu F)}{dT}\right)_\ell = \frac{1}{\nu F}\left(\frac{dC}{dT} + \frac{dF}{dT}\right)_d\left(\frac{F}{F + C}\right)_\ell. \tag{5}$$

Using Eq. (6) in Eq. (4),

$$\frac{1}{k}\frac{dk}{dT} = \frac{(\nu F)_d}{\nu F}\left(\frac{1}{\nu F}\frac{d(\nu F)}{dT}\right)_d - \frac{(\nu F)_\ell}{\nu F}\frac{(F+C)_d}{(F+C)_\ell}\frac{1}{(F+C)_d}\left(\frac{dF}{dT}+\frac{dC}{dT}\right)_d. \quad (6)$$

The logarithmic derivatives in the Doppler region can be computed accurately using the AMC code,[1] and the reaction rate ratios are given with sufficient accuracy by a fundamental mode calculation using the MC^2 code.[2]

System Studied

A sodium-cooled, stainless-steel clad, UO_2-PuO_2 system was considered, with 0.658 cm fuel rods in a 2.57 cm pitch hexagonal lattice. The U-238-to-Pu-239 ratio was 7 to 1. The energy region from 300 to 4000 eV was considered in the AMC calculation.

To determine the variance in the Doppler coefficient due to the statistical selection of resonance parameters, sixteen calculations were performed with different sets of Pu-239 resonance parameters. The resolved resonance parameters for U-238 were used in all cases. For each case different sets of resonance parameters and level spacings for Pu-239 were selected from the appropriate statistical distributions using average values suggested by J. Schmidt.[3] The $J = 0$ and $J = 1$ resonances of Pu-239 were considered to be statistically independent.

Results

The Doppler coefficient for the system was found to be -0.164×10^{-4} with a standard deviation of 0.012×10^{-4}.

To determine the separate contributions of U-238 and Pu-239 to the Doppler coefficients, the same problem was repeated with the temperature derivatives of the Pu-239 cross sections set equal to zero. In this case the Doppler coefficient was found to be -0.194×10^{-4}. This represents the U-238 contribution to the Doppler coefficient. The difference between the total Doppler coefficient and the U-238 contribution, $+0.030 \times 10^{-4}$, is the Doppler coefficient due to Pu-239. All the variance in the total coefficient is due to Pu-239 since only the resolved resonances were considered for U-238.

The Pu-239 contribution is 18% of the net Doppler coefficient, while the probable error in the calculated Doppler coefficient is only 5%. Therefore, the variance in the Doppler coefficient due to statistical selection of Pu-239 resonance parameters, although it is significant, is certainly tolerable.

References

1. L. B. Miller, *Monte Carlo Analysis of Reactivity Coefficients in Fast Reactors, General Theory and Applications*, ANL-7307 (1967).
2. B. J. Toppel, A. L. Rago and D. M. O'Shea, *MC^2, A Code to Calculate Multigroup Cross Sections*, ANL-7318 (1967).
3. J. J. Schmidt, *Neutron Cross Sections for Fast Reactor Materials, Part I, Evaluation*, KFK-120 (1966).

III-8. Monte Carlo Calculation of Multi-Region Hot-Cold Interference Effects

R. N. Hwang and L. Miller

Introduction

The influence of the unheated material surrounding the heated element in a Doppler coefficient measurement has been investigated and discussed by theoretical and experimental reactor physicists for several years. The Argonne Monte Carlo program AMC[(1)] is convenient for treating the rapid fluctuations of the neutron flux in space and energy which results from the heterogeneous arrangement of resonance absorbers in these experiments.

The AMC code was used to compute the space and energy dependent reaction rates and their derivatives with respect to the temperature of the Doppler sample for several exemplary cases. Five cases of practical significance were investigated. The phenomena considered were:

1. The effect of "cold" resonances on the heated sample, with the cold material containing resonance absorbers different from the sample
2. The effect of "cold" resonances on the heated sample, with the cold material containing the same resonance absorber as the sample
3. The effect of separating the interacting resonance materials with non-resonant structural materials
4. The effect of surrounding the Doppler element with a thin blanket in a core containing the same resonance absorber as the Doppler element
5. The effect of varying the thickness of the blanket surrounding the Doppler element.

The first three cases were intended to determine whether the presence of "cold" resonances in the surroundings influence the resonance integral and its temperature derivative of the "hot" sample under various conditions. The problems in Case 4 were run with a more complex geometry to provide a theoretical interpretation of the experimental results of S. Carpenter et al.[2] The energy region from 1.0 to 1.4 keV was considered. The resonance parameters of F. Firk et al.[3] were used for U-238 and the resonance parameters for thorium were taken from BNL-325.

AMC CALCULATIONS

Case 1: Doppler Element Surrounded by Different Resonance Materials

To isolate the effect of the interaction of the broadened resonances in the Doppler element and the unbroadened resonances in the surrounding medium, four two-region problems were run. The Doppler region was a circular cylinder, 1.125 cm diam. This was surrounded by a cylinder of hexagonal cross section 3 cm on a side. In all four problems the outer region contained a reference core material of 15 v/o U-238, 15 v/o U-235, 15 v/o Fe, and 55 v/o Na.

In the first two problems the Doppler element was thorium metal; therefore, the resonances in the two regions were at different energies. To determine the effect of the interference of these resonances, the first problem was run with resonances in both regions, and the second was run with the resonance cross sections in the outer region set equal to zero. As shown in Table III-8-I, the effect was very small. The fractional increase in the absorption rate of the Doppler element, per degree K, was 6% higher with the interacting resonances present.

Case: 2 Doppler Element Surrounded by the Same Resonance Absorber

In the third and fourth problems the Doppler element was uranium metal; therefore, the resonances in the two regions were at the same energies. The resulting interaction was found to be significant. The resonances in the outer region increased the Doppler effect in the uranium Doppler element by 43% at room temperature.

Case 3: Interacting Materials Separated by Iron

Additional problems were run to determine the effect of the heater and the structural material separating the sample from the unheated core region. It was found that the interaction effect was significantly reduced when the interacting resonance materials were separated by iron. The amount of iron considered was equivalent to 1/16, 1/8, and 1/4 in., respectively. The presence of these iron cans reduced the interaction effect from 43% to 29%, 8%, and 5%, respectively, as shown in Table III-8-II. The amount of iron present in the Argonne experiments[4] was probably sufficient to prevent the detection of any interaction effect.

TABLE III-8-I. DOPPLER ELEMENT SURROUNDED BY DIFFERENT RESONANCE MATERIAL

Region 1	Region 2	$\frac{1}{A_1}\frac{\partial A_1}{\partial T} \times 10^4$,[a] Region 1
Thorium (Res.)	U-Na-Fe (Res.)	4.55 ± 0.09
Thorium (Res.)	U-Na-Fe (No Res.)	4.20 ± 0.09
Uranium (Res.)	U-Na-Fe (Res.)	3.44 ± 0.10
Uranium (Res.)	U-Na-Fe (No Res.)	2.41 ± 0.04

[a] $A_1 \equiv$ absorption rate at room temperature.
$T \equiv$ temperature, °K.

TABLE III-8-II. EFFECT OF STRUCTURAL MATERIAL SEPARATING DOPPLER ELEMENT AND SURROUNDING MATERIAL WITH THE SAME RESONANCES

Composition			$\frac{1}{A_1}\frac{\partial A_1}{\partial T} \times 10^4$, Region 1	Relative Values
Region 1	Region 2	Region 3		
U-238 (Res.)	VOID	U-Na-Fe (No Res.)	2.41 ± 0.04	1.00
U-238 (Res.)	VOID	U-Na-Fe (Res.)	3.44 ± 0.10	1.42
U-238 (Res.)	1/16 in. Fe	U-Na-Fe (Res.)	3.12 ± 0.10	1.29
U-238 (Res.)	1/8 in. Fe	U-Na-Fe (Res.)	2.60 ± 0.10	1.08
U-238 (Res.)	1/4 in. Fe	U-Na-Fe (Res.)	2.52 ± 0.10	1.05

Case 4: Thorium Resonances Surrounding Doppler Elements

To more closely represent the experiments,[2] additional problems were run with the geometry and compositions shown in Fig. III-8-1. The thorium Doppler element was surrounded by a 1/4 in. annulus of 25% iron, 75% void, to represent the heater and heat shields. This was surrounded by a blanket region of different composition in each of the four problems considered. The outer region was again the reference core composition. The results shown in Table III-8-III indicate that the effect of the thorium blanket is to increase the Doppler effect of the thorium Doppler element by 41%.

Table III-8-IV shows the relative values of the computed fractional change in absorption rate and the corresponding measured Doppler coefficients.[2] Results

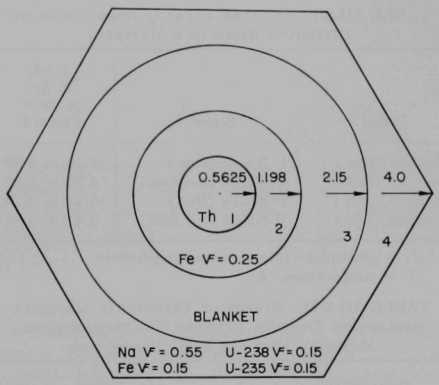

FIG. III-8-1. Geometry and Composition of Four-region Problems. *ANL Neg. No. 113-1290.*

TABLE III-8-III. EFFECT OF THORIUM RESONANCES IN BLANKET SURROUNDING THORIUM DOPPLER ELEMENT

Blanket Material	$\frac{1}{A_1}\frac{\partial A_1}{\partial T} \times 10^4$, Region 1
Thorium with resonances	6.2 ± 0.1
Thorium without resonances	4.4 ± 0.1

TABLE III-8-IV. RELATIVE DOPPLER COEFFICIENT OF THORIUM DOPPLER ELEMENT IN IRON CONTAINER, 1/16 IN. THICK SURROUNDED BY VARIOUS BLANKETS, 3/8 IN. THICK, IN CORE OF 55% Na, 15% U-235, 15% U-238, 15% Fe

Blanket	Relative Value of $\frac{1}{A_1}\frac{\partial A_1}{\partial T}$ Computed	Relative Doppler Coefficient Measured
Void	1.00	1.00
Thorium	1.13	1.01
Uranium	0.77	0.83

TABLE III-8-V. VARIATION OF INTERFERENCE EFFECT WITH BLANKET THICKNESS

Region 1: Th Doppler element
Region 2: 1/16 in. Fe
Region 3: Th blanket
Region 4: U-Na-Fe core

Blanket Thickness, in.	$\frac{1}{A_1}\frac{\partial A_1}{\partial T} \times 10^4$, Region 1
0	−5.4
3/16	−5.9
3/8	−6.2
3/4	−4.4

are shown for the cases of a blanket of the same composition as the Doppler element and a blanket of different composition. The exact geometry of the experiment was not available for the calculations, and the results of the calculations are not directly comparable to the measured reactivity changes; nevertheless, qualitative agreement is shown.

Case 5: Variation of Interference Effect with Blanket Thickness

Additional problems were run to determine the optimum thickness of the blanket to produce the maximum interference effect. As shown by Table III-8-V, the optimum thickness is about 3/8 in. of thorium metal.

DISCUSSION AND CONCLUSION

From the results given in Table III-8-I through Table III-8-V, one is led to the following conclusions:

(1) The presence of the unbroadened resonances in the "cold" surrounding material significantly increase the Doppler effect of the heated sample when the Doppler element and surroundings contain the same resonance absorber.

(2) The Doppler effect of the heated sample is relatively insensitive to the presence of unbroadened resonances in those surroundings which are different from those of the sample.

(3) The cold-hot-interaction effect which is closely analogous to the usual Dancoff effect is extremely sensitive to the presence of the non-resonant scatterers surrounding the sample. The presence of a large amount of these non-resonant scatterers, such as stainless steel tubing and structural materials which exist in almost all Doppler measurements, may substantially decrease the interaction effect discussed above.

A theoretical interpretation of the question of the cold-hot-interaction effect is given as follows:

The absorption probability of the sample is

$$A_1 \approx \iint \sigma_{\gamma_1}(u)\phi_1(u,\mathbf{r})\, d\mathbf{r}\, du,$$

where $\sigma_{\gamma_1}(E)$ and $\phi_1(E,\mathbf{r})$ are the capture cross section and neutron flux in Region 1, respectively. In the energy region of interest, the "effective" flux $\phi_1(u)$ in the sample can be pictured as a superposition of two terms

$$\Sigma_{t_1}(u)\phi_1(u) = (1 - P_1)\sum_{n=1}^{N}\int_{u-\epsilon_n}^{u}\frac{e^{(u'-u)}}{1-\alpha_n}\Sigma_{s_1}(u')\phi_1(u')\, du'' + P_2\Sigma_2(u)\phi_2(u), \quad (1)$$

where P_1 and P_2 are the resonance escape probabilities of Regions 1 and 2, respectively. The presence of resonances in Region 2 will, in general, reduce the second

term in Eq. (1), so that the absorption probability A_1 is reduced accordingly. The quantity of interest is

$$\frac{1}{A_1}\frac{\partial A_1}{\partial T} \propto \int \bar{\phi}_1(u)\,\frac{\partial \sigma_\gamma(u)}{\partial T}\,du + \int \sigma_\gamma(u)\,\frac{\partial \bar{\phi}_1(u)}{\partial T}\,du. \tag{2}$$

For the case where the cell size is much larger than the sample, the temperature derivative $\partial\bar{\phi}_1(u)/\partial T$ is nearly independent of the presence of resonances in Region 2 as long as Region 2 is unheated. The first term in Eq. (2), however, is sensitive to the unbroadened resonances in the surroundings. The reason for this can be explained quite readily by referring to the simplified model given in Fig. III-8-2. The figure shows the variation $\bar{\phi}_1(u)\partial\sigma_\gamma(u)/\partial T$ near a resonance for the case

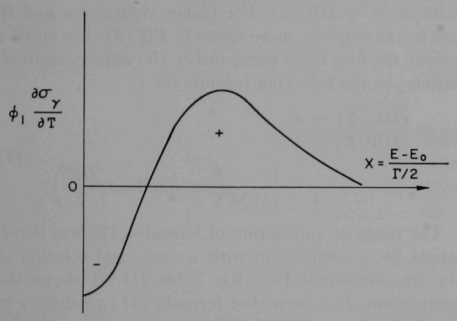

FIG. III-8-2. Variation of $\phi_1 \frac{\partial\sigma_\gamma}{\partial T}$. *ANL Neg. No. 113-1289.*

where there is no resonance in Region 2. The contribution of the first integral in Eq. (2) depends entirely on the relative magnitudes of the positive and negative areas enclosed by the curve. It is quite clear that the presence of resonances in Region 2 will change the relative contribution of the positive and negative areas by the flux depression. If the resonances in Region 2 are the same as those in Region 1, the effect is to increase the relative magnitude of the positive contribution due to the more significant flux dip near the peak of the resonance. As a result, the presence of resonances of the same kind in Region 2 tends to increase the Doppler effect. On the other hand, if the resonances in Region 2 are different from those in the sample, the effect may increase or decrease the Doppler effect of the sample depending on the relative locations of the resonances in Region 2 with respect to those in Region 1. The net effect is believed to be unimportant for two completely uncorrelated resonance sequences.

References

1. L. B. Miller, *Monte Carlo Analysis of Reactivity Coefficients in Fast Reactors: General Theory and Applications*, ANL-7307 (1967).
2. S. G. Carpenter, L. A. Montford, T. H. Springer and R. J. Tuttle, *Variation of Doppler Coefficient with Change in Surrounding Materials*, Proc. Conference on Fast Critical Experiment and Their Analysis, October 10–12, 1966, ANL-7320, p. 334.
3. F. W. K. Firk, J. E. Lynn and M. C. Moxon, *Resonance Parameters of the Neutron Cross Section of U-238*, Nucl. Phys., **41**, 614 (1963).
4. C. E. Till, R. A. Lewis and E. F. Groh, *Doppler Effect Measurements on a Dilute Fast-Carbide Assembly, ZPR-6 Assembly 4Z*, Trans. Am. Nucl. Soc., **8**, 454 (1965).

III-9. Collision Density in the Doppler Region

M. Segev*

In a search for analytic-approximate descriptions of the collision density in fast reactor mixtures we consider here elastic slowing down in the Doppler region, i.e., below some 40 keV. Ignoring inelastic scattering from the 8 keV level of Pu-239 and neglecting the fission spectrum in the range, the P_1 equations, with which we start, are source free. We further simplify the discussion by considering a finite homogeneous medium consisting of one isotope.

Constant Cross Sections

To learn about average trends in the collision density we start with the assumption of constant cross sections. The P_1 equations, in lethargy units, are

$$\operatorname{div} \mathbf{j}(\mathbf{r},u)e^u = \frac{s}{\alpha}\int_{u+\ln(1-\alpha)}^{u} du' F(\mathbf{r},u')e^{u'} - F(\mathbf{r},u)e^u, \tag{1}$$

$$\mathbf{j}(\mathbf{r},u)e^u = \frac{s}{\alpha}\int_{u+\ln(1-\alpha)}^{u} du' \mu_L(u',u)\mathbf{j}(\mathbf{r},u')e^{u'} - \frac{1}{3\Sigma^2}\,\mathbf{grad}\,F(\mathbf{r},u)e^u, \tag{2}$$

where F is the collision density, $\mathbf{j}$ is the current, Σ is the total cross section, s is the ratio of the scattering to the total cross section, $\mu_L(u',u)$ is the scattering

* Visiting Scientist, Israel Atomic Energy Commission, Soreq Research Center, Yavne, Israel.

cosine for $u' \to u$ lethargy change, in laboratory coordinates, α is the maximum lethargy gain in a scattering event.

Equations (1) and (2) are combined into

$$\frac{1}{3\Sigma^2}\nabla^2 F(\mathbf{r},u)e^u = \int_u^{u+\ln(1-\alpha)} du'\left[\delta(u'-u) - \frac{s}{\alpha}\mu_L(u',u)\right] \times \frac{s}{\alpha}\int_{u'}^{u'+\ln(1-\alpha)} du'' F(\mathbf{r},u'')e^{u''} + F(\mathbf{r},u')e^{u'}. \tag{3}$$

We assume a solution of the form

$$F(\mathbf{r},u) = \psi(\mathbf{r})e^{-\nu u}, \tag{4}$$

where $\psi(\mathbf{r})$ satisfies the buckling equation

$$\nabla^2\psi(\mathbf{r}) + B^2\psi(\mathbf{r}) = 0. \tag{5}$$

Substitution of Eqs. (4) and (5) into Eq. (3) leads to a transcendental equation for ν:

$$\frac{1}{3}\left(\frac{B}{\Sigma}\right)^2 T(s,\alpha,\nu) + \frac{1}{s} - \xi(\alpha,\nu) = 0, \tag{6}$$

where

$$-\xi(\alpha,\nu) \equiv \frac{1}{\alpha}\frac{1}{1-\nu}[(1-\alpha)^{1-\nu} - 1] \tag{7}$$

$$T(s,\alpha,\nu) \equiv \frac{1}{s}\Big/\left\{1 + \frac{s}{2\alpha}\left[\left(\frac{A-1}{1.5-\nu} - \frac{A+1}{0.5-\nu}\right)(1-\alpha)^{1-\nu} + \left(\frac{A-1}{0.5-\nu} - \frac{A+1}{1.5-\nu}\right)\right]\right\}. \tag{8}$$

Note that for an infinite medium ($B = 0$), Eq. (6) reduces to the equation given by G. Placzek.[1] Also, the transport approximation to Eqs. (1) and (2) leads to a transcendental equation similar to Eq. (6) but with $T(s,\alpha,\nu)$ approximated by $T(s,\alpha,0)$.

By expanding Eq. (6) in powers of ν and by inverting the series, an expansion series for ν is obtained.

$$\nu = \left(\frac{a'/s}{\chi_1}\right)\left[1 - \frac{\chi_2}{\chi_1}(a'/s) + \left(\frac{2\chi_2^2}{\chi_1^4} - \frac{\chi_3}{\chi_1^3}\right)(a'/s)^2 + \ldots\right], \tag{9}$$

where

$$a' \equiv a + \frac{DB^2}{\Sigma} \tag{10}$$

$$a \equiv 1 - s \tag{11}$$

$$D \equiv 1\Big/\left[3\Sigma\left(1 - \frac{2}{3A}s\right)\right] \tag{12}$$

$$\chi_n \equiv \xi_n - \frac{1}{3}\left(\frac{B}{\Sigma}\right)^2 T_n \tag{13}$$

$$\xi_n \equiv \frac{1}{n!}\left[\frac{\partial^n}{\partial\nu^n}\xi(\alpha,0)\right] \tag{14}$$

$$T_n \equiv \frac{1}{n!}\left[\frac{\partial^n}{\partial\nu^n}T(s,\alpha,0)\right]. \tag{15}$$

For very small a and $\frac{1}{3}(B/\Sigma)^2$ values Eq. (9) yields

$$\xi_1\nu \equiv \left(1 + \frac{1-\alpha}{\alpha}\ln(1-\alpha)\right)\nu \approx a + \frac{DB^2}{\Sigma} \quad \text{for} \quad [a + \tfrac{1}{3}(B/\Sigma)^2] \ll 1. \tag{16}$$

Thus, the spectrum of a finite system with a buckling B^2 and absorption ratio a is, for very small a and B^2, the spectrum of an infinite system having an absorption ratio of $(a + DB^2/\Sigma)$. For higher values of a and B^2 one has to consider more terms in *EQ* (9). For small a values, the first three terms in Eq. (9) reduce, approximately, to the following formula for ν:

$$\xi_1\nu \approx \frac{(DB^2/\Sigma) + a}{(DB^2/\Sigma) + 1} \cdot \frac{1}{1 - (\frac{1}{3})a}\left(\text{for small } \alpha, a, \frac{DB^2}{\Sigma}\right). \tag{17}$$

The range of application of formula (17) was determined by a comparison with a numerical solution of the transcendental Eq. (6). Table III-9-I shows the comparison. It is seen that formula (17) predicts ν to better than some 5% of error for a large range of mass numbers, absorption ratios and system dimensions.

A preliminary analysis indicates that the use of $e^{-\nu u}$, (ν given by Eq. (17)) as collision density in calculating self-shielding factors for energy intervals of 0.5 lethargy units results in values which are 4 to 5 percent higher than those obtained in a calculation based on a constant collision density.

Resonant Cross Sections

Although the cross sections in the Doppler region are resonant, we can expect the collision density to show a long range variation as given by Eqs. (4) and (17), where D/Σ and a in Eq. (17) stand for some average values of $D/\Sigma(u)$ and $a(u)$. To determine the kind of average involved, we turn to the simpler problem of an infinite medium. The equation is

$$F(u)e^u = \frac{1}{\alpha}\int_{u-\epsilon}^{u} s(u')F(u')e^u, \tag{18}$$

where

$$\epsilon \equiv -\ln(1-\alpha). \tag{19}$$

In most of the Doppler region the interval ϵ contains many resonances. We therefore assume

$$\epsilon \gg S, \tag{20}$$

where S is the average level spacing. Assuming for a moment that the resonant $s(u')$ in Eq. (18) is a periodic function, the solution $F(u)$ must contain a periodic part. Denoting the average level width by Γ, if $S \gg \Gamma$ then $\epsilon \gg \Gamma$ and only a small fraction of the scattered neutrons will fall into the resonances. If $S \approx \Gamma$ the overlap is strong and the periodic structure of $s(u')$ is of small amplitude. In both cases the periodic part of $F(u)$ will have a small amplitude.

We try a solution of the form

$$F(u) = e^{-\nu u} f(u), \tag{21}$$

where $f(u)$ is periodic with the period S. Substituting Eq. (4) into Eq. (1) and differentiating with respect to u, we obtain

$$(1 - \nu)f(u) + f'(u) = \frac{1}{\alpha}[s(u)f(u) + (1 - \alpha)^{1-\nu}s(u - \epsilon)f(u - \epsilon)]. \tag{22}$$

We are interested in the collision density for weighting purposes in an energy range of a typical coarse group. Such a range contains many periods. Therefore we may adjust the group limits so that $f(u_{g-1}) = f(u_g)$. For the same reason also

$$\int_{group} du\, f(u)s(u) = \int_{group} du\, f(u - \epsilon)s(u - \epsilon).$$

Moreover, the above is true even if the assumption of strict periodicity is replaced by resonance parameter distributions. The average resonance parameter must, however, remain constant within the coarse group.

Integrating Eq. (22) over an energy group we obtain the infinite medium transcendental equation

$$\frac{1}{\langle s \rangle} - \xi(\alpha,\nu) = 0 \tag{23}$$

$$\langle s \rangle \equiv \int_{group} du\, s(u)f(u) \Big/ \int_{group} du\, f(u), \tag{24}$$

or, due to the small amplitudes of $f(u)$,

$$\langle s \rangle \approx \int_{group} du \frac{\Sigma_s(u)}{\Sigma(u)} \Big/ \int_{group} du. \tag{25}$$

The average absorption ratio that goes into formula (17) is thus temperature dependent. With it the spectrum $e^{-\nu u}$ is temperature dependent.

A Remark Concerning Mixtures

A mixture of two heavy absorbers, such as uranium and plutonium, is described by one integral term in Eqs. (1) and (2) or in Eq. (18), due to the close α values of the isotopes.

TABLE III-9-I. A Comparison of ν Values

Mass Number	Absorption Ratio	Dimension of the Medium In Units of Mean Free Path	$\epsilon_1\nu$	
			Numerical Solution of Eq. (6)	Values by Eq. (17)
200	0.0	100	0.000329	0.000329
		10	0.0319	0.0319
		3	0.271	0.276
	0.15	100	0.159	0.158
		10	0.187	0.186
		3	0.407	0.397
	0.45	100	0.548	0.530
		10	0.571	0.550
		3	0.752	0.703
10	0.0	100	0.000329	0.000329
		10	0.0331	0.0319
		3	0.274	0.268
	0.15	100	0.158	0.158
		10	0.188	0.186
		3	0.415	0.397
	0.45	100	0.542	0.530
		10	0.565	0.550
		3	0.748	0.703
4	0.0	100	0.000329	0.000329
		10	0.0360	0.0319
		3	0.288	0.268
	0.15	100	0.158	0.158
		10	0.190	0.186
		3	0.430	0.397
	0.45	100	0.532	0.530
		10	0.556	0.550
		3	0.741	0.703

In a mixture of plutonium with a medium-weight background scatterer, say sodium, the situation is of double narrow resonance,[2] as evident from inequality (20). In this case the collision density is constant over a single resonance, the constant being $1/\xi_1$, where ξ_1 is a weighted average of the isotopic ξ_1's:[2]

$$\xi_1 = \frac{\xi_1(\mathrm{Pu})\Sigma(\mathrm{Pu}) + \xi_1(\mathrm{Na})\Sigma(\mathrm{Na})}{\Sigma(\mathrm{Pu}) + \Sigma(\mathrm{Na})}. \tag{26}$$

Therefore, in applying Eq. (17) to a mixture in the Doppler region, ξ_1 is a weighted average as indicated in Eq. (26).

References

1. G. Placzek, *On the Theory of the Slowing Down of Neutrons in Heavy Substances*, Phys. Rev. **69**, 423–438 (1946).
2. R. Goldstein and E. R. Cohen, *Theory of Resonance Absorption of Neutrons*, Nucl. Sci. Eng., **13**, 132–140 (1962).

III-10. Influence of Resonances of Moderating Elements on the Collision Density

M. Segev*

Introduction

In a search for analytic-approximate descriptions of the collision density in fast reactor mixtures, we consider here the energy spectrum of neutrons during elastic moderation in a uniform medium with a spatially flat source at high energies.

Analytic solutions have been presented for certain simple cases:

(a) A single isotope with isotropic scattering and weak absorption.[1,2]

(b) A single-isotope with energy-independent anisotropy of the scattering.[3]

(c) A mixture of isotopes with constant cross sections and isotropic scattering.[1]

(d) A mixture consisting of a light isotope with a constant scattering cross section and a heavy isotope with a resonant cross section such that either the "narrow resonance" (N.R.) or the "wide resonance" (W.R.) approximation applies.[4]

Semi-analytic methods have been developed for more complex cases. R. Goldstein[4] reduced the solution for mixture (d) above, with a resonance of any width, to the solution of a transcendental equation. L. Finkelstein[5] reduced the solution for the general problem of neutron moderation by elastic-isotropic scattering to the solution of recursion and transcendental equations.

The typical "fast" mixture, namely of a background heavy absorber with a resonant moderator is outside the range of application of the above solutions, with the possible exception of an extension of Finkelstein's method. However, this latter method is relatively complicated and implicit.

In the following we derive a simple analytic approximation to the collision density which applies to a variety of mixtures and, in particular, to typical fast mixtures. The main feature of the approximation is that the collision density is about proportional to the inverse of the lethargy gain per scattering in the mixture. This solution contains cases (a) through (d) above as a particular instance where the average lethargy gain is a constant.

Expansion of the Slowing Down Equation in Slowing Down Moments

The collision density resulting from a monoenergetic source in an infinite medium shows Placzek-type oscillations[1] under the most general laws of absorption and elastic scattering.[6] Hence the asymptotic range is reached approximately below a few scattering intervals from the source, and we apply the asymptotic slowing down equation to the energy region below the fission source and the inelastic scattering.

The number of isotopes in the mixture is denoted by I; the isotopic scattering probability from lethargy u' to lethargy u'' by $P_i(u',u'')$; the ratio of the isotopic scattering cross section to the total cross section of the mixture by $s_i(u)$; $\frac{4A_i}{(A_i+1)^2}$ by α_i, where A_i is the isotopic mass; the isotopic maximum lethargy gain per scattering by $\epsilon_i = |\ln(1-\alpha_i)|$; the collision density by $F(u)$; the slowing down number by $q(u)$; then $F(u)$ and $q(u)$ are related by Eqs. (1) and (2):

$$q(u) = \sum_{i=1}^{I} \int_{u-\epsilon_i}^{u} du'\, s_i(u')F(u') \cdot \int_{u}^{u'+\epsilon_i} du''\, P_i(u',u'') \tag{1}$$

and

$$\frac{\partial q(u)}{\partial u} = [s(u) - 1]F(u), \tag{2}$$

where

$$s(u) \equiv \sum_{i=1}^{I} s_i(u). \tag{3}$$

By a change of variables and a Taylor expansion about u, Eq. (1) can be brought to the following form:

$$q(u) = \sum_{\ell=1}^{\infty} (-1)^{\ell-1} \frac{\partial^{\ell-1}}{\partial u^{\ell-1}} [s(u)\xi^{(\ell)}(u)F(u)], \tag{4}$$

where

$$\xi^{(\ell)}(u) \equiv \sum_{i=1}^{I} s_i(u)\xi_i^{(\ell)}(u)/s(u) \tag{5}$$

and

$$\xi_i^{(\ell)}(u) \equiv \frac{1}{\ell!}\int_{-1}^{1} d\mu\, |\ln^{\ell}\left(1 - \frac{\alpha_i}{2} + \frac{\alpha_i}{2}\mu\right)| P_i(u,\mu). \tag{6}$$

$P_i(u,\mu)$ is the isotopic normalized angular distribution curve at lethargy u.

The homogeneous mixture and its Eq. (4) are defined in terms of $\xi^{(\ell)}(u)$, the slowing down moments of the mixture. The ℓth moment of the mixture is, by Eq. (5),

* Visiting Scientist, Israel Atomic Energy Commission, Soreq Research Center, Yavne, Israel.

an average over $\xi_i^{(\ell)}(u)$, the isotopic ℓth moments. The isotopic ℓth moment is, by Eq. (6), the average of the ℓth power of the lethargy gain per collision, divided by $\ell!$.

In the past, some of the effects of absorption and scattering anisotropy on the neutron spectrum have been investigated by a moment expansion of the integral equation for a medium consisting of a single isotope.[1,3,7] In the following, Eq. (4) is used to study the mixing effect on the collision density.

Limiting Cases of a Smooth Collision Density

In the limit of constant scattering ratio and constant slowing down moments, namely

$$\begin{aligned} &\text{I.} \quad s(u) = s \\ &\text{II.} \quad \xi^{(\ell)}(u) = \xi^{(\ell)}, \end{aligned} \tag{7}$$

the right hand side of Eq. (2), when equated to the lethargy derivative of the right hand side of Eq. (4), yields the following equation for the collision density:

$$\frac{s-1}{s} F(u) = \sum_{\ell=1}^{\infty} (-1)^{\ell-1} \xi^{\ell} \frac{\partial^{\ell}}{\partial u^{\ell}} F(u). \tag{8}$$

We assume a solution of the form

$$F(u) = Ce^{-\nu u} \tag{9}$$

and substitute it into Eq. (8) to obtain an equation for

$$\frac{1-s}{s} = \sum_{\ell}^{\infty} \xi^{(\ell)} \nu^{\ell}. \tag{10}$$

For isotropic scattering in a medium consisting of a single isotope, Eq. (10) will be recognized as Placzek's expansion of the corresponding transcendental equation for ν.[4] An inversion of the expansion then expresses ν as a power series in $(1 - s)/s$, and as shown by Dresner,[2] different truncations of the series correspond to the different expressions for the resonance escape probability as given by Wigner, Goertzel-Grueling, and Weinberg-Wigner.

In a mixture, or for anisotropic scattering, Eq. (10) converges rapidly for $s \neq 0$ after a certain number of terms, since by Eqs. (5) and (6), $\xi^{(\ell)} < 1/\ell!$. For weak absorption the series, Eq. (10), may be inverted to express ν as a highly convergent power series in $(1 - s)/s$.

The collision density is thus a smooth function if the conditions of Eq. (7) are satisfied. The influence of resonant cross sections is studied now to a first approximation, namely by regarding a resonance, or resonances, of a single element as mixed with a constant background. The constant background is defined by the total scattering cross section $\Sigma_{r,b}$ of the non-resonant isotopes and by effective slowing down moments $\xi_b^{(\ell)}$ for these isotopes. Defining $\tau^{(\ell)}(u)$ as the ratio of the ℓth scattering power of the resonant element to the ℓth scattering power of the background,

$$\tau^{(\ell)}(u) \equiv \frac{\Sigma_{s,r}(u)\xi_r^{\ell}(u)}{\Sigma_{s,b}\xi_b^{(\ell)}}, \qquad (\ell \geq 0), \qquad (\xi_i^0 \equiv 1). \tag{11}$$

The conditions of Eq. (7) are approximately satisfied by

$$\left.\begin{aligned} &\text{I. Small resonance structure, or} \\ &\text{II. Weak absorbtion, where} \\ &\quad \text{a. } [\xi_r^{(\ell)}(u)/\xi_b^{(l)}] \approx 1 \quad \text{for} \quad \ell \geq 1 \\ &\quad \text{b. } \tau^{(\ell)}(u) \ll 1 \quad \text{for} \quad \ell \geq 1. \end{aligned}\right\} \tag{12}$$

The conditions of Eq. (12) may be simplified if the isotopic angular distributions are equal, namely if $P_i(u,\mu) = P(u,\mu)$ for $i = 1, 2, \cdots I$ (in the range of isotropic scattering this is strictly the case; approximately, though, it is the case in a considerable part of the anisotropic range of interest, where the anisotropy is weak). By the non-negativity of the integrals in Eq. (6) and of the terms in Eq. (5) it is sufficient then to satisfy the conditions for $\ell = 1$. Thus IIa of Eq. (12) is the case of nearly equal scattering ranges for the resonance and the background; and IIb is the case of an infinitely low scattering power of the resonance, relative to the scattering power of the background.

The asymptotic flux is, by Eq. (9), proportional to $e^{-\nu u}$, where ν is the solution of Eq. (10). Eqs. (2), (8), and (9) determine the value of C [(Eq. (9)] as $1/\xi$.[1] Normalizing the flux outside the resonance range to $e^{-\nu u}$, the flux inside the resonance range is given as,

for IIa:

$$\phi(u) = e^{-\nu u} \frac{\Sigma_b + \Sigma_p}{\Sigma_b + \Sigma_r(u)} \tag{13}$$

and

for IIb:

$$\phi(u) = e^{-\nu u} \frac{\Sigma_b + \Sigma_{s,r}(u)}{\Sigma_b + \Sigma_r(u)}, \tag{14}$$

where Σ_p is the potential scattering cross section of the resonant element.

We note again that Eqs. (13) and (14) are valid only for weakly absorbing systems. Compared with the usual N.R.-N.R. and N.R.-W.R. approximations,[4] however, the expressions have two favorable features: one—the exponential factor in Eqs. (13) and (14) provides for a flux drop as the lethargy changes from above to below the resonance range; secondly, the application of Eqs. (13) and (14) does not involve the somewhat ambiguous notion of the practical width of the resonances.

The Collision Density in the Vicinity of Wide Scattering Resonances

Turning upon a general case, we inquire as to whether the series (4) may be truncated as in the following:

$$q(u) \approx s(u)\, \xi^{(1)}(u)\, F(u). \tag{15}$$

Substituting Eq. (5) in Eqs. (2) and (4) we obtain

$$q(u) = \exp\left[-\int_{u_0}^{u} du' \frac{1 - s(u')}{s(u')} \frac{1}{\xi^{(1)}(u')}\right] \tag{16}$$

$$\left|\sum_{\ell=2}^{\infty} (-1)^{\ell-1} \frac{\partial^{\ell-1}}{\partial u^{\ell-1}} [\beta^{(\ell)}(u) q(u)]\right| \ll 1, \tag{17}$$

where

$$\beta^{(\ell)}(u) \equiv \xi^{(\ell)}(u)/\xi^{(1)}(u). \tag{18}$$

For a resonance of lethargy width $\Gamma_u = \Gamma/E_s$ (where E_s is the resonant energy) and for weak absorption the condition (17) can be reduced to the following condition:

$$\frac{\Gamma_u}{2} \gg \beta_b^{(2)} \frac{|\tau_0^{(2)} - \tau_0^{(1)}|}{(1 + \tau_0^{(1)})^{3/2}}, \tag{19}$$

where τ_0 is the value of τ (see Eq. (11)) at the resonance peak.

A few conclusions of a practical nature are drawn from the condition of Eq. (19).

1. Increasing the energy decreases Γ_u so that for given $\tau_0^{(1)}$, $\tau_0^{(2)}$ and $\beta_b^{(2)}$ the inequality, Eq. (19), is less often satisfied. Generally, the inequality is violated for a resonance of a heavy element (where Γ is small to begin with) mixed with a light moderator (such that $|\tau_0^{(2)} - \tau_0^{(1)}|$ is not very small) so that Eq. (15) cannot be applied as a solution. However, increasing the energy decreases the peak height and with it the scattering power of the resonance and the fluctuations in the collision density; the latter follows the discussion of limiting cases of a smooth collision density, in a previous section.

2. In a mixture of elements such as uranium, iron, sodium and oxygen, the scattering range of any of the light elements is often close to the scattering range of the corresponding background; then the difference $|\tau_0^{(2)} - \tau_0^{(1)}|$ is small and the inequality, Eq. (19), is satisfied. If the difference $|\tau_0^{(2)} - \tau_0^{(1)}|$ is not sufficiently small, then for powerful resonances, the factor $1/(1 + \tau_0^{(1)})^{3/2}$ substantially reduces the right hand side of Eq. (19), and Eq. (15) can be applied as a solution. If, on the other hand, the resonance is weak, then by a previous discussion, the fluctuations in the collision density are small.

3. In deriving the condition, Eq. (19), it was assumed that the distance from the resonance energy, measured in half-width units, was less than $(1 + \tau_0^{(1)})^{1/2}$. The practical meaning of the assumption is that the larger the relative scattering power of the resonance, the larger is the lethargy range in the vicinity of the resonance to which the solution, Eq. (15), applies. This is a favorable situation since the fluctuations in the collision density are expected to be of an increasing range as the resonance gains in scattering power.

Since we have assumed that the tail of the series, Eq. (4), is small starting with $\ell = 2$, we may improve the solution by considering two terms of the series:

$$q(u) = s(u)\xi^{(1)}(u)F(u) + \frac{\partial}{\partial u}[\beta^{(2)}(u)s(u)\xi^{(1)}(u)F(u)]. \tag{20}$$

For the derivative of $q(u)$ one term will suffice:

$$\frac{\partial q(u)}{\partial u} = \frac{\partial}{\partial u}[s(u)\xi^{(1)}(u)F(u)]. \tag{21}$$

Defining $a \equiv 1 - s$, we obtain by Eqs. (2), (20), and (21)

$$q(u) = \exp\left[-\int_{u_0}^{u} du' \frac{a(u')}{s(u')\xi^{(1)}(u')\left[1 + \frac{\partial}{\partial u}\beta^{(2)}(u')\right] - a(u')\beta^{(2)}(u')}\right], \tag{22}$$

$$F(u) = \frac{q(u)}{s(u')\xi^{(1)}(u)\left[1 + \frac{\partial}{\partial u}\beta^{(2)}(u)\right] - a(u)\beta^{(2)}(u)}. \tag{23}$$

In the limit of moderation by a single element with mass $\gg 1$, low absorption, and constant cross sections, the solution, Eq. (23), reduces to

$$F(u) \propto \exp\left[-\left(\frac{a/\xi^{(1)}}{1 - (1/3)a}\right)u\right]. \tag{24}$$

The comparison of Eq. (24) with a numerical solution of Eq. (10) shows that, for $A \geq 4$ and $a \leq 0.5$, the value of ν is approximated by the coefficient of u in Eq. (24) to an error less than 4 %.

In the limit of pure scattering the solution reduces to

$$F(u) = \frac{1}{\xi^{(1)}(u)\left[1 + \frac{\partial}{\partial u}\beta^{(2)}(u)\right]}. \tag{25}$$

In a mixture of scatterers, where Eq. (25) applies, the fluctuations in the collision density are mainly the inverse of the fluctuations in the average lethargy gain

per scattering in the mixture. However, as expected from the slowing down nature of the scattering, the changes in $\xi^{(1)}(u)$ are not immediately followed by inverse changes in $F(u)$. The departure from immediate response is estimated by the inverse of $\left[1 + \frac{\partial}{\partial u}\beta^{(2)}(u)\right]$. Thus, in a binary mixture, depending on whether ξ_r is greater or less than ξ_b, the collision density is respectively dipped or peaked in the vicinity of a resonant maximum (and vice versa for a resonant minimum) and the dip or peak are shifted to higher lethargies. These features are illustrated in Fig. III-10-1.

The combined effect of scattering and absorption on the collision density is seen in the following expression:

$$F(u) = \frac{\exp\left[-\int_{u_0}^{u} du' \frac{a(u')}{\xi^{(1)}(u')}\right]}{\xi^{(1)}(u)\left[1 + \frac{\partial}{\partial u}\beta^{(2)}(u)\right]}, \qquad (26)$$

which approximates Eq. (23). In the vicinity of a resonance, if $F(u)$ is peaked and shifted by the denominator, the accumulative effect of the absorption in the numerator will compete in shifting the peak back to, and below, the resonance lethargy. This competition has been investigated by R. Goldstein[1] in a mixture of uranium with a light moderator. However, in the vicinity of a resonance of a light element or a structural element in a fast mixture, $F(u)$ is often dipped and shifted by the denominator and the effect of the absorption will be to enhance the shifting.

A Comparison Between the Approximate-Analytic and the Exact-Numerical Solutions of the Slowing Down Equation in Scattering Mixtures

With the restriction of small absorption, the main simplification offered by the theory here is the approximate analytic description of the mixing effect on the collision density in the vicinity of scattering resonances of light and medium elements. In a scattering mixture, Eqs. (1) and (2) reduce to

$$F(u)e^{u} = \sum_{i=1}^{I} \frac{1}{\alpha_i} \int_{u-\epsilon_i}^{u} du' s_i(u')F(u')e^{u'}. \qquad (27)$$

The approximate solution of Eq. (27), namely Eq. (25), was compared with its numerical solution, as coded on the IBM-360/75. Two resonances were studied, each in four mixtures as described in Tables III-10-I and III-10-II, respectively.

Figure III-10-1 shows a comparison between the numerical solution of Eq. (27) and the analytic solution, Eq. (25), in two truly binary mixtures of the iron resonance (Table III-10-I) with fictitious isotopes. In Fig. III-10-1, mixture A, the fictitious isotope is given by mass 90 and cross section 12.5 b (per iron atom); in mixture B by mass 190 and cross section 10.2 b (per iron atom). These fictitious elements represent, respectively, the backgrounds for the iron resonance in mixtures 1 and 2 (Table III-10-II). The collision density in mixtures 1 and 2 will, of course, differ to some extent from curves A and B in Fig. III-10-1, but a binary mixture is more illustrative in bringing out the mixing effect on the collision density.

The relative scattering power of the iron is greater in mixture B than it is in mixture A; therefore, the

TABLE III-10-I. Resonances Studied in the Comparison of Eq. (25) with the Numerical Solution of Eq. (27)

Isotope	Resonance Energy, keV	Resonance Width, keV	Potential Scattering, b	Resonance Peak, b
Na	2.85	0.38	3	600
Fe	28.3	1.6	5	80

TABLE III-10-II. Mixutres Studied in the Comparison of Eq. (25) with the Numerical Solution of Eq. (27)

1	EBR-II core (U, Fe, Na) with the full content of Na
2	EBR-II core (U, Fe, Na) with the Na voided by 90%
3	Westinghouse 1000 MWe core (U, Fe, Na, C) with the full content of Na
4	Westinghouse 1000 MWe core (U, Fe, Na, C) with the Na voided by 90%

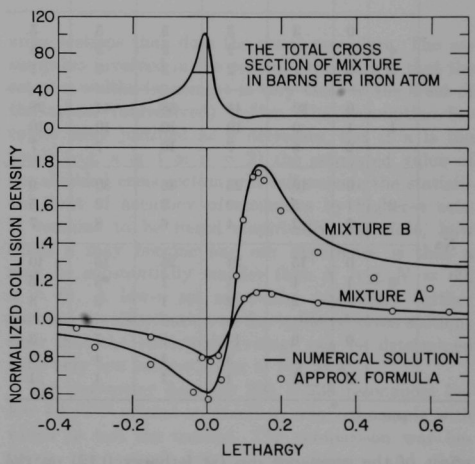

Fig. III-10-1. The Collision Density in Binary Mixtures in the Vicinity of the 28.3 keV Fe Resonance. *ANL Neg. No. 113-647.*

TABLE III-10-III. A Comparison Between Exact and Approximate Flux Integrals

Resonance	Mixture	$j^{(a)}$	$\lvert(\phi^{(j)}/\phi) - 1\rvert \times 100^{(a)}$ Group limits (lethargy) −0.75–−(0.25)	−0.5–0.0	−0.25–0.25	0.0–0.5	0.25–0.75
Fe	1	0	4	7	7	11	3
		1	1	1	4	3	2
		2	1	1	2	1	1
	2	0	8	15	32	44	28
		1	5	6	7	7	7
		2	5	6	8	7	7
	3	0	3	5	9	10	7
		1	1	4	3	3	4
		2	1	1	7	8	4
	4	0	3	3	5	5	5
		1	2	2	3	3	3
		2	1	2	3	3	1
Na	1	0	30	44	58	44	28
		1	9	10	10	10	10
		2	6	7	10	7	7
	2	0	10	25	46	30	9
		1	5	9	7	3	5
		2	2	4	6	8	7
	3	0	15	21	25	16	10
		1	1	1	1	5	5
		2	2	2	1	2	3
	4	0	6	14	9	7	3
		1	1	3	1	4	2
		2	1	1	1	1	1

(a) j—see text.

effect of the resonance dip (at lethargy 0.12) on the collision density is greater in mixture B than it is in mixture A. Also, the shifting effects, discussed previously, are visible about the resonance peak and dip (lethargies −0.01 and 0.12, respectively).

The approximate solution, Eq. (25), compares in Fig. III-10-1 quite well with the exact curve and few other figures could illustrate both better and worse agreements with exact curves. However, since we are not interested in the collision density per se, but rather in reaction rates, we chose to compare the group removal cross section $\Sigma(k \to k + 1)$ which is most sensitive to the weighting spectrum. For groups of 0.5 lehargy in width none of the elements in Tables III-10-I and III-10-II will scatter from group k to group $k + 2$. Therefore, $\Sigma(k \to k + 1)$ is given by the ratio of $q(u_k)$ (u_k being the high lethargy limit of group k) to the flux integral in group k. Since $q(u_k) = 1$ in a scattering mixture, we have

$$1/\Sigma(k \to k + 1) = \int_{group\ k} \frac{F(u)}{\Sigma(u)}\, du \equiv \phi_k. \quad (28)$$

The flux integral was compared for five groups. Table III-10-III presents values of $\lvert[\phi/\phi^{(j)}] - 1\rvert$ for $j = 0, 1, 2$, where

$$\left.\begin{aligned} \phi^{(0)} &\equiv \int \frac{du}{\Sigma(u)} \frac{1}{\xi^{(1)}} \\ \phi^{(1)} &\equiv \int \frac{du}{\Sigma(u)} \frac{1}{\xi^{(1)}(u)} \\ \phi^{(2)} &\equiv \int \frac{du}{\Sigma(u)} \frac{1}{\xi^{(1)}(u)} \frac{1}{1 + \frac{\partial}{\partial u}\beta^{(2)}(u)} \end{aligned}\right\} \quad (29)$$

and where the scriptless ϕ is the exact flux integral.

The figures in Table III-10-III indicate that the estimates $\phi^{(1)}$ and $\phi^{(2)}$ of the flux integral are usually much better than $\phi^{(0)}$ which is the estimate based on a constant collision density. Despite the fact that the shifting effects are estimated only if the term $\frac{\partial}{\partial u}\beta^{(2)}(u)$ is included in Eq. (25), the integrals $\phi^{(1)}$ and $\phi^{(2)}$ are both within a few percent of the exact integral. Therefore, the use of $\phi^{(1)}$ rather than $\phi^{(2)}$ can simplify the evaluation of group cross sections.

Conclusions

The theory, as presented in the previous sections, provides us with a rational approach to the description of the collision density in the vicinity of a resonance in weakly absorbing mixtures: in the limit of a very high scattering power (relative to the background) the collision density is approximated by Eq. (23); in the limit of a very low scattering power (relative to the background) the collision density is practically smooth. In intermediate cases, Eq. (23) will apply if the resonance is wide in the sense of Eq. (19). Although narrow resonances do occur in light and structural elements, their mutual overlap broadens the structure in the cross section and renders the use of Eq. (23) reasonable in a variety of cases. In particular, the mixture cross section is always of a wider structure than each of two overlapping resonances that belong to two elements; therefore, Eq. (23) is applicable in ranges where resonances of several elements occur simultaneously.

Finally, we note that the application of the theory is confined to the energy region below inelastic scattering. Therefore, at this stage, the treatment of inelastic moderation still calls for numerical tools, e.g. the ELMOE code.[8]

REFERENCES

1. G. Placzek, *On the Theory of the Slowing Down of Neutrons in Heavy Substances*, Phys. Rev. **69**, 423–438 (1946).
2. L. Dresner, *Resonance Absorption in Nuclear Reactors*, (Pergamon Press, New York, 1960).
3. A. Kean, *Slowing Down from an Energy Distributed Neutron Source*, Nucl. Sci. Eng. **10**, 117–119 (1961).
4. R. Goldstein, *Spectral Distribution of Neutrons in the Vicinity of a Resonance*, Nucl. Sci. Eng. **19**, 359–362 (1964).
5. L. Finkelstein, *Formal Solution to the Neutron Moderation Problem in Nonhydrogenous Infinite Homogeneous Media*, Nucl. Sci. Eng. **32**, 241–248 (1968).
6. M. Segev and S. Yiftah, *Placzek-Type Oscillations in General Neutron Slowing Down*, Nucl. Sci. Eng. **33**, 147–150 (1968).
7. G. Rakavy and J. J. Wagschal, *Generalization of the Fermi Age Theory and its Application to the Calculation of Resonance Escape Probability*, Proc. 1964 Geneva Conference **2**, Paper No. 827, pp. 149–152.
8. A. L. Rago and H. H. Hummel, *ELMOE: An IBM-704 Program Treating Elastic Scattering Resonances in Fast Reactors*, ANL-6805 (1964).

III-11. Self-Shielding Factors by the Ladder Method

M. SEGEV*

It has been proposed that effective group cross sections in the unresolved region be estimated by statistical averages.[1,2] The unresolved ladder of resonances in the group was assumed to be one of infinitely many that can be derived from given average parameters and given distribution functions. The efficiency of the method has been doubtful because there are not as many resonances in a group as needed to obtain a narrow distribution of effective cross sections. The earlier approach is improved by estimating self-shielding factors rather than effective cross sections.

The improvement is due to the fact that the self-shielding factor is less ladder-dependent than the effective cross section. Since the infinitely dilute cross section is, by measurement, statistically accurate, the percentage inaccuracy in the estimated effective cross section is equal to the (low) percentage inaccuracy in the ladder-averaged self-shielding factor.

The method may be further improved by the following procedure for ladder construction: each ladder consist of N resonances; the width (spacing) distribution be divided into n ($\leqslant N$) ranges of equal probability; the average widths (spacings) in these ranges constitute a predetermined set of n values; a ladder be generated by a random sampling of widths (spacings) for the $1st$, $2nd$ $\cdots$ Nth resonance from the predetermined set of n values. All such ladders are different distributions of a single set of numbers, whereas the usual sampling procedure[1,2] generates ladders which are different distributions of different sets of numbers. Consequently, the present sampling procedure yields a narrower distribution of shielded cross sections than does the usual procedure. The assumption involved in the present procedure is that the set of n widths (spacings) is very close to the n-set of the actual (unresolved) ladder. The assumption becomes more justified as n decreases, but if n is too small (e.g. $n = 1$ or $n = 2$) the estimated value of the shielded cross section will fall outside the statistical limit of accuracy of estimates by higher-n sets. It remains to be found empirically, therefore, how small n may become and our experience is that n may be substantially smaller than N (e.g. $N = 60$, $n = 6$). A low-n set of widths (spacings) further narrows the distribution of the laddered cross sections such that the statistical average can be determined from very few ladders, often as few as 3.

The parameter data for 200 U-238 resonances below 4 keV[3] offered an excellent resolved sample with which to test the method. The comparison was between the actual self-shielding factors and their temperature derivatives for two groups of 60 resonances each, and the corresponding estimated values by a set of 6 widths (spacings). The figures are shown in Table III-11-I.

Table III-11-I shows the average resonance parameters for the two groups, evaluated from the resolved data. These average values were kept unchanged during runs so that the testing is concerned with purely statistical questions.

To estimate a group average and its standard deviation a number of ladders were constructed. At the construction of each new ladder the average and standard deviation were reestimated from the total of ladders. The process was terminated when the estimated values reached a fairly constant value. Table III-11-II is an example of the estimation process.

* Visiting Scientist, Israel Atomic Energy Commission, Soreq Research Center, Yavne, Israel.

TABLE III-11-I. Average Resonance Parameters for Groups 1 and 2

Group	Center Energy, keV	Strength Function, 10^{-4}	Level Spacing, eV	Capture Width, eV	Potential Scattering, b
1	2.1	0.995	22.2	0.0248	10.6
2	3.2	0.773	21.3	0.0248	10.6

Table III-11-III illustrates the fact that the distribution of the self-shielding factors is narrower than the distribution of the cross sections.

Table III-11-IV compares the self-shielding factors of groups 1 and 2 and their temperature derivatives with the corresponding estimations obtained by ladders built from the actual 60 spacings and widths and with estimates obtained by ladders built from the contracted set of six parameters. As expected, the 60-set estimations fall largely within one standard deviation (see Table III-11-III) of the actual values. The figures indicate also that the 6-set estimates are generally no worse than the 60-set estimates and many other examples, not shown here, amplify this indication.

Table III-11-V shows, in fact, that for the 6-value distributions, few ladders suffice to determine the average. If, for practical reasons, the values of f and

TABLE III-11-II. Estimation of Capture Self-Shielding Factors of Group 1 by Ladders Built from 60-Value Distributions

	Number of Ladders									
	5	10	15	20	25	30	35	40	45	50
Average value	0.711	0.719	0.724	0.723	0.723	0.726	0.728	0.729	0.728	0.728
Relative standard deviation	0.032	0.037	0.036	0.036	0.035	0.034	0.033	0.033	0.033	0.033

TABLE III-11-III. Relative Standard Deviations for the Population of σ's, f's and Their Temperature Derivatives Resulting from Ladders Built on 60-Value Distributions

	Temperature, °K							
	Group 1				Group 2			
	300	900	1500	2100	300	900	1500	2100
σ_γ (100 b, T)	0.107	0.109	0.110	0.110	0.073	0.076	0.078	0.078
f_γ (100 b, T)	0.045	0.037	0.033	0.030	0.030	0.023	0.020	0.018
$\frac{\partial}{\partial T}$ [σ_γ (100 b, T)]	0.151	0.158	0.195	0.262	0.129	0.150	0.177	0.234
$\frac{\partial}{\partial T}$ [f_γ (100 b, T)]	0.063	0.077	0.135	0.216	0.054	0.086	0.131	0.208

TABLE III-11-IV. The Self-Shielding Factors of Groups 1 and 2 and Their Temperature Derivatives Compared with Estimations by the Ladder Method

	Temperature, °K							
	Group 1				Group 2			
	300	900	1500	2100	300	900	1500	2100
f_γ (100 b, T)	0.650	0.734	0.773	0.797	0.783	0.853	0.882	0.899
Estimated by a 60-set	0.642	0.724	0.761	0.785	0.769	0.838	0.867	0.884
Estimated by a 6-set	0.654	0.741	0.780	0.805	0.772	0.845	0.876	0.894
$\left[\frac{\partial}{\partial T} f_\gamma(100\text{ b}, T)\right] \times 10^4$	2.52	0.80	0.42	0.25	2.24	0.64	0.32	0.18
Estimated by a 60-set	2.47	0.78	0.41	0.24	2.21	0.62	0.30	0.17
Estimated by a 6-set	2.51	0.83	0.44	0.26	2.34	0.71	0.36	0.20

TABLE III-11-V. ESTIMATION OF f_γ(100 b, 900°K) AND $\frac{\partial}{\partial T} f_\gamma$ (100 b, 900°K) OF GROUP 1 BY LADDERS BUILT FROM 6-VALUE DISTRIBUTIONS

	Number of Ladders											
	2	4	6	8	10	12	14	16	18	20	22	24
Average of f_γ (100 b, 900°K) $\times 10^4$	7418	7425	7409	7412	7416	7423	7422	7425	7430	7428	7424	7421
Average of $\left[\frac{\partial}{\partial T} f_\gamma \text{ (100 b, 900°K)}\right] \times 10^8$	918	915	914	905	906	904	905	906	906	907	908	907

TABLE III-11-VI. COMPARISON BETWEEN ACTUAL VALUES OF f AND $\frac{\partial}{\partial T} f$ AND THEIR ESTIMATION BY THE LADDER METHOD FROM THE ACTUAL AVERAGE RESONANCE PARAMETERS WITH ASSUMED WIGNER AND PORTER-THOMAS DISTRIBUTIONS

	Temperature, °K							
	Group 1				Group 2			
	300	900	1500	2100	300	900	1500	2100
f_γ (100 b, T)	0.650	0.734	0.773	0.797	0.783	0.853	0.882	0.899
Estimated value	0.649	0.742	0.784	0.808	0.770	0.846	0.876	0.894
$\left[\frac{\partial}{\partial T} f_\gamma \text{ (100 b, } T)\right] \times 10^4$	2.52	0.80	0.42	0.25	2.24	0.64	0.32	0.18
Estimated value	2.74	0.91	0.47	0.30	2.45	0.61	0.25	0.13

$\frac{\partial f}{\partial T}$ need be known to only two figures, the table indicates that they may be estimated by as few as two ladders.

So far the tests have shown that, given the resonance parameters of a group but not the actual ladder, the ladder-generation method is efficient in producing a good estimate of the group self-shielding factors and their temperature derivatives. Perhaps the figures in Table III-11-VI are even more significant in showing that, given the average resonance parameters of a group, but not the actual distribution about the average, the ladder method produces good estimates of the above group quantities by assuming a Wigner distribution law for the level spacings and a Porter-Thomas distribution law for the neutron widths.

CONCLUSION

It is felt that the presented method enables a reliable estimation of group self-shielding factors and their temperature derivatives. Since few ladders are needed for the estimation process, the method is not time consuming. The computer code with which the method was tested is mainly numerical, therefore its extension to include mixtures of isotopes and of resonance sequences is straightforward.

REFERENCES

1. C. N. Kelber and P. H. Kier, *The Effect of Randomness on Group Cross Sections*, Nucl. Sci. Eng. **26**, 67–72 (1966).
2. M. W. Dyos and C. A. Stevens, *On the Utility of the Statistical Treatment of Resonance Absorption in the Unresolved Resonance Region*, Nucl. Sci. Eng. **25**, 294–295 (1966).
3. J. J. Schmidt, *Neutron Cross Sections for Fast Reactor Materials, Part I—Evaluation*, KFK 120/I (1966).

III-12. The Variable Temperature Rodded Zone Project

R. A. Lewis, F. H. Martens and C. E. Till

The Variable Temperature Rodded Zone (VTRZ) is a facility that will allow integral measurements to be done in environments that closely simulate power reactor conditions. Measurements in this facility are expected to provide the necessary confirmation of the adequacy of calculational techniques currently in use for extrapolation of measurements done in cold plate-type criticals to hot rodded geometries typical of power reactors.

Design Summary

The VTRZ, which will be installed in ZPR-9, is currently under construction. The equipment will consist of a large in-core section, heated electrically and capable of maintaining any temperature up to 550°C. The in-core section is composed of two octagon-cross-section cylinders, one along the axis of each half of the reactor, arranged so that when the halves are together they form an 18 in. diam by 6 ft long cylindrical zone. The interior of each half is made up of standard ZPR matrix tubes that receive sodium-filled calandrias of the same cross section as standard fuel drawers. Fuel in the form of small-diameter rods is to be loaded into tubes running through each calandria. The shell of the in-core section that holds the matrix tubes is surrounded in turn by insulating material, a cooling-air guard ring, and an outer shell. The matrix around the outer shell will contain drawers of the normal ZPR type, and will form the necessary buffer and driver regions for spectral matching and criticality.

Access to the center of the zone for equipment to oscillate samples of various reactor materials as well as Doppler samples is to be provided. The basic idea is that the zone will provide an environment in which measurements similar to those carried out in the cold plate-type environments can be done in geometries and under conditions which simulate those of a power reactor.

The initial inventory of calandrias and fuel will be the following: Three types of calandrias will be available, differing only in their sodium content. The calandrias are 2 x 2 in. in cross section by 12 in. long and penetrated by sixteen ⅜ in. tubes to provide fuel sites. One calandria type will be totally filled with sodium; a second type will contain a lesser amount of sodium corresponding to reduced sodium density at reactor operating temperatures; and a third type will contain no sodium at all. Sufficient calandrias of each type will be available to fill the nominal 18 in. diam zone over a combined core and reflector height totalling 6 ft. PuO_2-UO_2 fuel rods corresponding to the Zero Power Plutonium Reactor (ZPPR) Core 3 fertile-to-fissile ratio in an amount sufficient to fill the zone to a total height of 6 ft will be available. Additionally, sufficient PuO_2-UO_2 rods of the same fertile-to-fissile ratio as the basic Pu-U-Mo plate-type fuel inventory will be acquired to allow the zone to be filled with a mixture of these rods and depleted UO_2 rods, again with an average fertile-to-fissile ratio equivalent to that of ZPPR Core 3. Comparison of the two loading types, each having the same average composition, will allow examination of the effects of pin-mixing. Analogous quantities of U-235 enriched fuel, based on the composition of ZPR-6 Assembly 6, are also to be acquired, and the initial measurements will be done using the U-235 fuel. Finally, sufficient depleted UO_2 in rod form will be available for mixing with the plutonium or U-235-containing fuel to give mixed pin fertile-to-fissile ratios over the full range of interesting compositions, as well as for use in blanket mockups.

Program Emphasis

The experimental program utilizing the VTRZ will aim at confirmation of the reliability of the analytical techniques used for extrapolation of measurements of the Doppler and sodium voiding coefficients in plate-type criticals to the operating conditions of fast power reactors. It will concentrate on the effects of heterogeneity and elevated temperature.

The basic idea is to make measurements of the Doppler and sodium coefficients in a succession of environments, in which only one significant variable will change from environment to environment so that the various effects can be separated and evaluated. The succession of zones will be the following, with the volume fraction of materials in each zone remaining as closely as possible the same throughout: a) The first zone will be a cold plate-type zone, fueled with U-235, of the same composition as the core of ZPR 6 Assembly 6—a full-scale large dilute oxide core. Measurements of various kinds will be done to establish the normalization between the zone and the full-scale equivalent. b) The next zone will be one in which the local structure of a power reactor is faithfully mocked up using subassemblies of fuel pins in the sodium-filled calandrias. The measurements will

be done unheated and comparison of the results from this and the previous zone will show up the effects of the differences in heterogeneity between rodded and plate configurations. c) The third zone will be one in which the calandria and pin subassembly can be heated. The major difference between this and the previous zone will be a lower sodium density, corresponding to the density change upon heating the sodium. Measurements will first be done cold to evaluate the difference between the two arrangements as the result of the change in sodium density. The measurements will then be done at progressively higher temperatures to evaluate the effects of temperature. d) A series of zones analogous to the above, but based on the ZPPR Core 3 composition, using plutonium fuel, will then be done.

The basic measurement technique will be the small-sample oscillation reactivity measurement technique which is capable of very high precision. Following these measurements, it is anticipated that measurements of the Doppler and sodium voiding effects in a small (approximately 4 in. diam) zone at the center of the large heated zone will be done. The small zone will have the same composition as the larger but will be heated and cooled independently. It will be oscillated physically in the same manner as the existing Doppler samples to take advantage of the attendant reactivity measurement precision. These measurements should allow a direct link between the small sample Doppler and sodium coefficients and the analogous coefficients of the zone itself.

The total reactivity effect of heating the zone itself can also be measured. Considerably more difficulty in analyzing this measurement is to be expected, however. In particular, the separation of the Doppler and expansion effects is a known problem. However, the information given by the small sample and small zone measurements may be expected to assist considerably in this task.

The zone is designed so that local areas or the total volume can be voided of sodium. Measurements will also be done to evaluate the interaction between the Doppler effect and sodium voiding in pin-type environments and at elevated temperatures.

It is expected that these measurements will provide definitive information on the effects of heterogeneity on sodium voiding coefficients and the effects of environmental temperature on the Doppler coefficients.

III-13. Sodium Void Effects in a Large UO_2 Core, Assembly 6 of ZPR-6

R. A. Karam, J. E. Marshall, L. R. Dates and G. K. Rusch

The sodium void coefficient was mapped as a function of position along the radial and axial dimensions in a 4000 liter UO_2 Core, Assembly 6 of ZPR-6 (see Paper III-1). Additionally, the void coefficient was measured in different loading patterns: in rodded, plate, and homogeneous samples, and also as a function of the enrichment of UO_2. These measurements provide reference checks with which data sets and analytical methods are verified.

Mapping of Sodium Void Coefficient

The sodium void coefficient was measured as a function of position along the axial and radial dimensions in Assembly 6 with the normal loading pattern of the plates in the unit cell (Fig. III-13-1a). The measurements along the axial direction consisted of determining the reactivity worth of sodium filled cans in sections 4 in. long in each half of the reactor relative to empty cans which were identical to the sodium containers. The sodium-void effect was measured in the nine central drawers per half (equivalent outer radius of 9.35 cm). The results are given in Table III-13-I. The physical location of each section referred to in Table III-13-I is defined in Fig. III-13-2. The uncertainty in the values listed in Table III-13-I is typically 0.1 Ih (1% $\Delta k/k$ = 459 Ih).

Radial sodium void coefficient measurements were made by voiding the entire amount of sodium from the specific drawers along the radial dimension. The sodium was removed from four drawers, two to the left and two to the right of the center of the core, in each measurement. At the core center only two drawers were voided. In each case the opposing drawers in each half of the ZPR-6 machine were voided. Table III-13-II lists the results. Again the uncertainty in the values listed is typically 0.1 Ih.

It is seen from Table III-13-I that the sodium void coefficient is practically zero at the center of Assembly 6 and decreases as a function of axial dimension. The decrease is due to the leakage component which

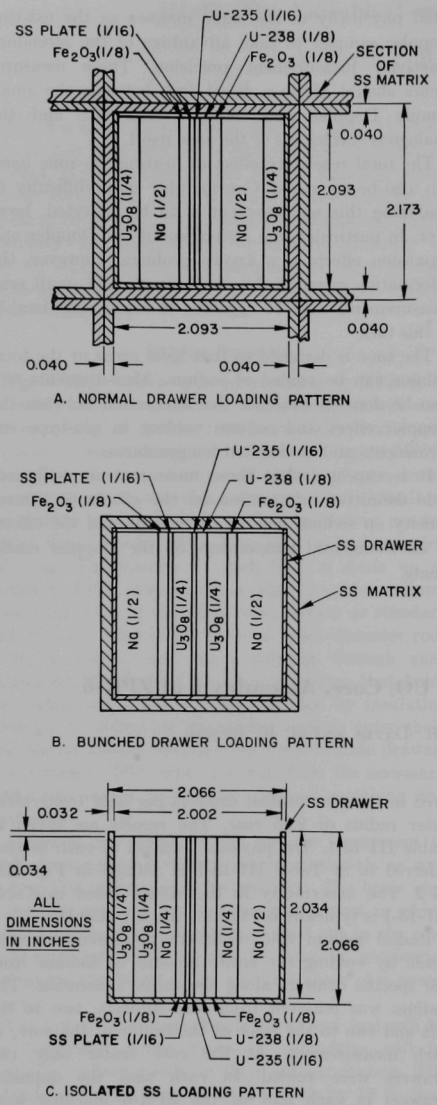

FIG. III-13-1. Cell Dimensions and Three Drawer Loading Patterns Used in Assembly 6 of ZPR-6. *ANL Neg. No. 113-1386 T-1.*

is zero at the center and maximum at the core reflector boundary. In Table III-13-II the void coefficient is seen to increase as a function of radius. The reason for this is that the transverse leakage, the scattering, and the capture components of the void coefficient all decrease faster than the increase in the radial leakage component along the radial dimension.

Loading Pattern Effect on the Sodium Void Coefficient

The sodium void coefficient was also measured in the 18 central drawers with the loading patterns shown in Fig. III-13-1b and Fig. III-13-1c. All loading patterns extended from the center of the core to a radius of 27.4 cm, some 19 cm beyond the region where the actual voiding took place. The consequence of the changes in loading patterns is that the self-shielding in the U-238 cross sections increases. The σ_p^{238} for the bunched loading pattern, Fig. III-13-1b, is about 15–20% lower than that in the normal loading pattern, Fig. III-13-1a (see Paper III-15, Table III-15-I). The σ_p^{238} for the isolated stainless steel case Fig. III-13-1c is only 5–10% lower than that of the normal case. In each case the measurement comprised removal of the sodium from the front 6 in. and from the entire axial length (30 in.) in each half of the reactor. The results are given in Table III-13-III and the uncertainty in these results is typically 0.1 Ih.

It is seen from Table III-13-III that the sodium void coefficient is most negative when the self-shielding in the U-238 plates is the largest (bunched case). These results confirm previous conclusions[1] that the positiveness of the sodium void coefficient is in a large measure tied to the concentrations, hence

TABLE III-13-I. Sodium-Void Coefficient as a Function of Axial Height in Normal Loading of Assembly 6 of ZPR-6

Sections Voided	ΔZ,[a] cm	Sodium Weight, kg	Sodium-Void Coefficient[b] Normal Loading	
			Ih/section	Ih/kg Na
A	0.0–5.08	0.8806	−0.082	−0.093
B	5.08–15.2	1.955	−0.088	−0.045
C	15.2–25.4	1.955	−0.415	−0.212
D	25.4–35.6	1.955	−0.825	−0.422
E	35.6–45.7	1.955	−1.643	−0.840
F	45.7–55.9	1.955	−2.477	−1.267
G	55.9–66.0	1.955	−2.941	−1.504
H	66.0–76.2	1.955	−3.203	−1.639
All sections (measured)	0.0–76.2	14.401	−13.464	−0.861
All sections (summed)	0.0–76.2	14.401	−11.271	−0.783

[a] ΔZ is the length of each section in each half.
[b] 1% $\Delta k/k$ = 459 Ih.

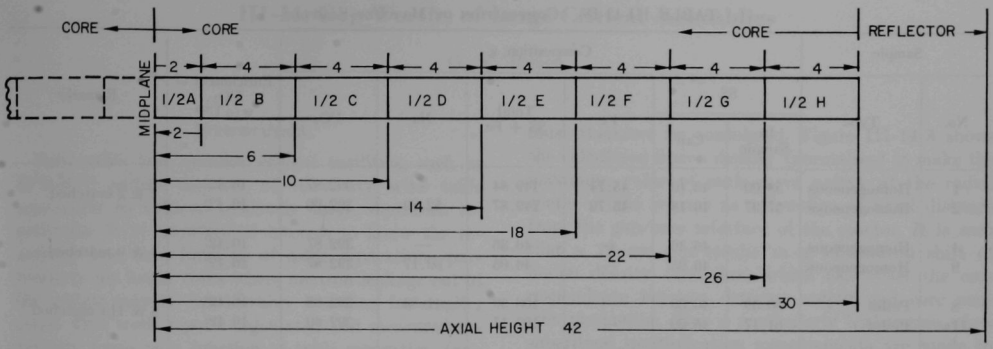

FIG. III-13-2. Sections Where Sodium Was Removed at Center of Assembly 6. *ANL Neg. No. 113-1406.*

capture rates, of U-238. The underlying reason for this is that upon removal of the sodium the neutron spectrum hardens and consequently the captures in U-238 decrease.

Sodium Void Coefficient in Homogeneous, Rodded, and Plate Heterogeneous Samples

The sodium void coefficient was measured also in homogeneous, rodded, and plate samples at the center of the core. The measurements consisted of oscillating "matched" samples, one with and one without sodium, relative to each other. The matched samples were very nearly identical in composition except for the sodium. Table III-13-IV lists the matched samples and their compositions. The samples were nominally 2 in.[3]; for more details about these samples see Paper III-15.

TABLE III-13-II. Sodium-Void Coefficient as a Function of Radius in Normal Loading Pattern of Assembly 6 of ZPR-6

Drawers Voided	Equivalent Radius, cm	Sodium Removed, kg	Sodium-Void Coefficient[b]	
			Ih/section	Ih/kg Na
S/M 2323[a]	0	1.604	−1.610	−1.004
S/M 2321 + 2325	11.0	3.248	−2.980	−0.918
S/M 2319 + 2327	22.1	3.248	−3.078	−0.948
S/M 2316 + 2330	38.7	3.248	−2.681	−0.825
S/M 2313 + 2333	55.3	3.267	−2.700	−0.826
S/M 2310 + 2336	71.9	3.254	−2.449	−0.753
S/M 2307 + 2339	88.5	2.767	−1.532	−0.554

[a] The letters S/M represent the stationary/movable halves of ZPR-6 and the numbers 2323, for example, designate the drawers occupying matrix position 2323, the location of the center of the core.

[b] 1% $\Delta k/k$ = 459 Ih.

TABLE III-13-III. Sodium-Void Coefficient Dependence on Loading Patterns

Section Voided	Amount of Sodium, kg	Loading Pattern	Na-Void Coefficient, Ih/kg[(a)]
Front 6 in.	2.835	Normal loading pattern (Fig. III-13-1a)	−0.060
Front 6 in.	2.835	Bunched case (Fig. III-13-1b)	−0.736
Front 6 in.	2.648	Isolated SS case (Fig. III-13-1c)	−0.116
30 in.	14.401	Normal case (Fig. III-13-1a)	−0.861
30 in.	14.401	Bunched case (Fig. III-13-1b)	−1.473
30 in.	13.424	Isolated SS case (Fig. III-13-1c)	−1.101

[a] 1% $\Delta k/k$ = 459 Ih.

The reactivity worth of the sodium in the three types of samples was measured in the plate environment (normal loading pattern Fig. III-13-1a) and in a rodded zone comprising 26 (2.00 x 2.00 x 3.17 in.) calandria cans built around the samples at the center of the core. All the results are given in Table III-13-V.

It is seen from Table III-13-V that the void coefficient is strongly affected by whether or not the homogeneous samples contained stainless steel powder. Furthermore, the environment has a noticeable effect on the measured values.

Sodium Void Coefficient as a Function of the Enrichment of UO_2

The sodium void coefficient was also measured by the oscillation technique with nominally 2 in.[3] rodded

TABLE III-13-IV. Composition of Matched Samples

Sample		Composition, g						Enrichment of UO_2, w/o U^{235}	Remarks
No.	Type	SS		Fe	Total SS + Fe	Na	UO_2		
		In-Sample	Can						
1	Homogeneous	58.00	46.10	45.74	149.84	—	392.87	16.42	1 & 2 matched
2	Homogeneous	57.97	46.18	45.72	149.87	52.89	392.66	16.42	
4	Homogeneous	—	46.36	—	46.36	—	392.87	16.42	4 & 9 matched
9	Homogeneous	—	46.05	—	46.05	69.17	392.87	16.42	
8	Pellet	60.39	46.00	—	106.39	41.33	392.65	16.42	8 & 11a matched
11a	Pellet	61.17	46.00	—	107.17	—	392.60	16.42	
11b	Pellet	61.17	46.00	32.31	139.48	—	392.60	16.42	
11a	Plate	45.18	46.08	46.28	137.54	42.94	399.29	16.41	11a & 11b matched
11b	Plate	45.18	46.08	46.28	137.54	—	399.29	16.41	
20a	Plate	45.35	34.25	46.88	126.29	—	403.36	16.40	20a & 20b matched
20b	Plate	45.35	34.25	46.88	126.29	42.94	403.36	16.40	

TABLE III-13-V. Heterogeneity Effects on Na Void Coefficient in Assembly 6 of ZPR-6 (*16.42% Enrichment*)

Sample Type	Na Void Coefficient, Ih/kg	
	Plate Environment	Pellet Environment
Plate heterogeneous (normal loading pattern, Fig. III-13-1a)	+0.147 ± 0.079	−0.014 ± 0.070
Bunched plate heterogeneous (Fig. III-13-1b)	+0.047 ± 0.040	—
Pellet heterogeneous	+0.189 ± 0.027	+0.302 ± 0.039
Homogeneous without SS powder	+0.821 ± 0.020	+0.888 ± 0.020
Homogeneous with SS powder[a]	+0.199 ± 0.025	+0.221 ± 0.017

[a] Stainless steel powder (304L) was added to mock up the SS in the tubes housing the pellets.

TABLE III-13-VI. Sodium-Void Coefficients in Rodded Samples as a Function of UO_2 Enrichment

Sample Description	Sodium Weight, g	Coefficient, $Ih^{(a)}$	Specific Coefficient, Ih/kg Na
0.22% enriched pellet type	40.748	+0.0182 ± 0.0024	+0.448 ± 0.059
11.94% enriched pellet type	40.803	+0.0052 ± 0.0021	+0.128 ± 0.052
15.86% enriched pellet type	40.712	0.0000 ± 0.0020	0.000 ± 0.050
19.95% enriched pellet type	40.909	−0.0027 ± 0.0026	−0.066 ± 0.064

[a] 1% $\Delta k/k$ = 459 Ih.

samples as a function of the enrichment of UO_2. The following enrichments of ¼ in. diam by ½ in. long pellets were used: 0.22, 11.94, 15.86 and 19.95%. The results are given in Table III-13-VI. It is seen that the void coefficient is positive in depleted uranium oxide and it decreases and becomes negative as the enrichment is increased.

Finally the sodium void coefficient in 20 (2.00 x 2.00 x 3.17 in.) calandria cans filled with pellets that have the same average enrichment as the rest of the core, and placed along the entire axial dimension at the center of the core, was measured. The measured value was −0.677 ± 0.05 Ih/kg sodium. For comparison, the void coefficient of two plate-loaded drawers (normal pattern and 60 in. long) measured at the same position, was −1.004 ± 0.100 Ih/kg.

Reference

1. R. A. Karam, L. R. Dates, W. Y. Kato, J. E. Marshall and G. K. Rusch, *Sodium Void Effects in a Large UC Fast Reactor*, Trans. Am. Nucl. Soc. **11**, 244 (1968).

III-14. Gap Worths of Large Critical Assemblies

G. K. Rusch

Introduction

Split table fast neutron critical facilities, such as ZPR-6,[1] utilize the loss of reactivity with table separation to achieve relatively large shutdown reactivities. It is therefore of interest to know the reactivity loss as a function of table separation—particularly for larger cores where neutron leakage out of the system may be considerably less than for smaller cores. This work reports calculated and measured reactivity losses as a function of table separation (gap worths) for a 2600 liter carbide core—Assembly 5[2] of ZPR-6—and measured gap worths for a 4000 liter oxide core—Assembly 6 (see Paper III-1) of ZPR-6.

Although the measurements were done prior to the calculations, the calculated results are presented first since they are useful when discussing the measured results.

Calculations

Calculations were performed using Argonne National Laboratory's two dimensional neutron transport code SNARG.[3] A quadrant of the reactor calculated is shown in Fig. III-14-1. The reactor was divided into 20 radial mesh intervals and 24 axial mesh intervals after test computations indicated the calculated reactivity to be essentially constant for larger and somewhat smaller numbers of mesh intervals. A 22 group cross section set,[4] which closely predicted the critical mass for Assembly 5, was collapsed to two groups using a one dimensional diffusion theory code[5] for use in the SNARG calculations. An S_6 approximation was chosen as a suitable compromise between accuracy and problem running time.

Assembly 5 reactivity was calculated for table separations of 0.04, 1, 2, 4, 6, 8, 10 and 12 cm. The 0.04 cm gap is used as a reference point. Results are shown in Fig. III-14-2. The maximum slope of the calculated gap worth curve is about 240 Ih cm^{-1} and a 12 cm gap is worth about 2500 Ih ($7.3).

Measurement Considerations

Of interest when considering gap worth measurements is the "flux tilt" which occurs when the tables are separated.* Any such change in flux profile can limit the accuracy of reactivity measurements and must therefore be considered. Figure III-14-3 shows the calculated fission density (normalized to make the maximum value of each curve unity) at the radial center of the reactor as a function of axial distance from the gap/core interface of the reactor. It is seen that a 12 cm gap results in a substantial shift of fission density (and flux) which can offset the correspondence between detector output and core neutron production. This is particularly bothersome when subcritical multiplication measurements are made to determine the effective multiplication factor. Smaller gaps would of course result in smaller flux changes but perhaps not necessarily in smaller percentage measured-reactivity errors.

In addition to the axial flux tilt shown in Fig. III-14-3, one gets a radial flux tilt as indicated by Fig. III-14-4. Neutrons tend to stream to outer portions of the core, resulting in relatively greater fission densities in outer regions as the gap increases. Whereas the effects of an axial flux shift on detector sensitivity can be ameliorated to some extent by extending the detector length through the entire half height of the core, radial compensation may not be achieved as readily without preliminary calculations to determine optimum detector locations. The change in neutron importance with position further complicates detector compensation.

Gap Worth Measurement Techniques

Establishing Criticality

With large reactors such as Assembly 5, it is usually impractical to measure gap worths by establishing criticality at various table separations. To do so requires changing either the core composition or the core size (which results in a different reactor) at each separation of interest. In addition the relatively large quantity of fuel required to establish criticality was not available. Thus subcritical measurements were made.

Subcritical Multiplication Measurements

A set of gap worth measurements using the subcritical multiplication technique was made on Assembly 5. A neutron detector was located near the center of the reactor core and a neutron source was introduced in each half of the reactor at the radial core/blanket interface about 8 cm axially back from the core/gap interfaces. The source locations were

* Additional flux tilts are introduced by placing neutron sources in the core, as is done when subcritical multiplication measurements are made.

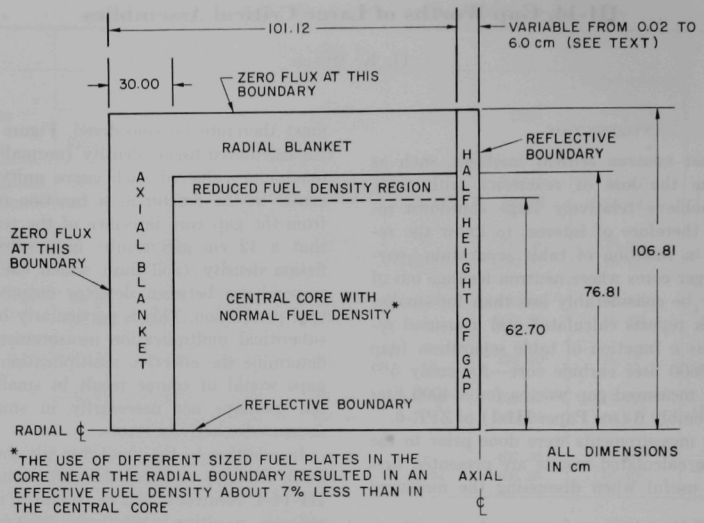

FIG. III-14-1. Quadrant of Assembly 5 of ZPR-6 Used In SNARG 2D Calculations. *ANL Neg. No. 113-835.*

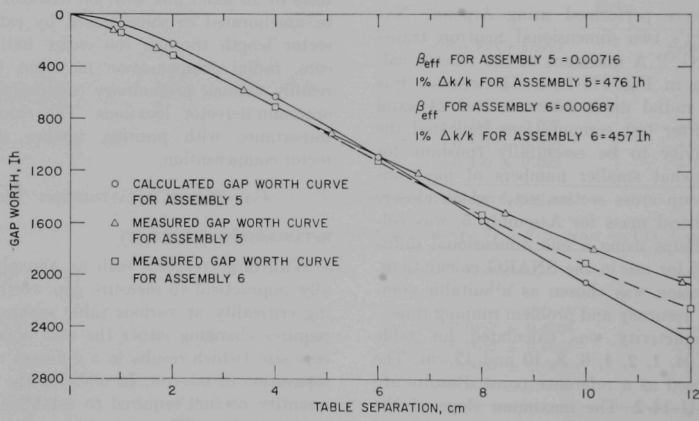

FIG. III-14-2. Reactivity Worth of Gap. *ANL Neg. No. 113-833.*

chosen to emphasize radial flux tilts to provide a comparison of indicated gap worth results with those obtained from measurements which did not have such radial flux tilts. The magnitude of the effect due to radial flux tilts can thus be inferred.

Measurements were obtained from gaps of 0.5, 1.0, 2.0, 4.0, 6.0 and 8.0 cm. Larger gap worths could not be measured accurately due to lack of detector sensitivity.

DYNAMIC REACTIVITY MEASUREMENTS

The gap worths of Assembly 5 and Assembly 6 were measured using a "dynamic measurement" technique. The measurement was preceded by taking the reactor to critical at a suitably high power level to assure that the influence of spontaneous fissioning effects in the core and blanket were negligible and subsequently allowing the delayed neutron precursor population to stabilize. The tables were then sepa-

rated at a speed of about 25 cm/min and an average in-core neutron flux and table position as a function of time were fed into an on-line computer which used an inverse kinetics algorithm[6] to determine reactivity as a function of time. No auxilliary neutron sources were used during the measurements and the detector was located near the center of the reactor as for the multiplication measurement. Thus radial flux tilt due to extraneous sources was purposely suppressed. This method is convenient as it can be performed during a reactor shutdown and an entire gap worth curve can be obtained from the computer in plotted form within a few minutes.

MEASUREMENT RESULTS

The gap worth obtained for Assembly 5 using the multiplication technique and the dynamic measurement technique were in reasonably good agreement, indicating only a nominal influence of the source-induced flux tilt. From the comparison between measured and calculated gap worths in Fig. III-14-2, it is noted that the measured gap worths are larger for small table separations than the calculations indicate. Changing axial and radial flux tilts could account for some of this descrepancy. It is also noted that, contrary to what might be expected, the smaller core (Assembly 5) had the smaller gap worths for larger table separations. This may be attributed, at least in part, to the initial power level which was about a factor of 10 higher for the Assembly 6 measurement than it was for the Assembly 5 measurement. The resultant relatively low neutron flux levels existing with the larger gaps and the influence of spontaneous fission neutrons may have affected the accuracy of the Assembly 5 measurement for larger gaps. Incorrect effective delayed neutron fractions could also affect the results.

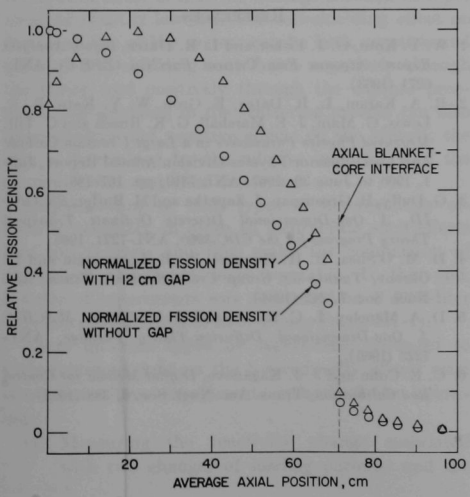

FIG. III-14-3. Effect of 12 cm Air Gap on Axial Fission Density. *ANL Neg. No. 113-798.*

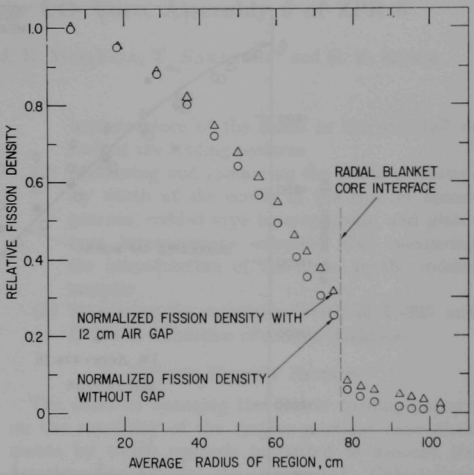

FIG. III-14-4. Effect of 12 cm Air Gap on Radial Fission Density. *ANL Neg. No. 113-838.*

DETECTOR LOCATIONS

A number of measurements were made, using the dynamic reactivity technique, with the neutron detector in various locations. The locations chosen were (1) near the radial center of the core with one end of the detector at the core/gap interface and extending about 20 cm into the core, (2) near the radial center of the core with 30 cm of core material between the gap/core interface and the end of the detector, (3) behind the axial blanket of the core, and (4) on top of the matrix assembly near the core/gap interface plane. The resulting data and the curve obtained using the subcritical multiplication technique are shown in Fig. III-14-5. It is apparent that flux tilts and neutron streaming to the vicinity of the detector location significantly affect the indicated results.

CONCLUSIONS

As seen in Fig. III-14-2, SNARG 2D calculations using an S_6 approximation results in smaller than measured gap worths for separations to about 6 cm

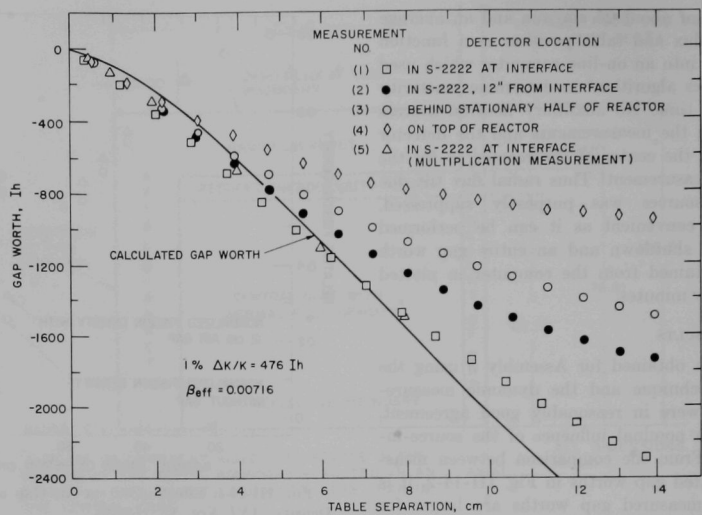

FIG. III-14-5. Indicated Gap Worth as a Function of Detector Location. *ANL Neg. No. 113-836.*

and larger than measured gap worths for larger separations for Assembly 5 of ZPR-6.

The small gap descrepancies are attributed primarily to flux tilts occurring with table separation. Discrepancies at the larger table separations are attributed to changing flux tilts, spontaneous fission neutrons which induce non-linearities at lower flux levels and multiplications, and possibly accumulated errors in the delayed neutron precursor inventory due to non-exact delayed neutron fractions used by the kinetics code. The absolute accuracy associated with the SNARG calculations is not known.

Calculated fission densities clearly show that substantial flux tilts occur during table separation and indicate that efforts should be made to minimize the effects of these flux tilts during gap worth measurements. It is also clear that flux tilts can ultimately limit the accuracy of gap worth measurements in spite of such efforts.

Measurements performed with neutron detectors located in various positions are shown to give different results and point out the need for careful detector location selection for gap worth measurements. It is apparent that both flux tilts and direct streaming of neutrons to the detector are important considerations. Both can change as a function of table separation.

Finally, it is shown that at least moderately accurate gap worth measurements can be obtained with a minimum of effort and reactor operating time by using the dynamic reactivity measuring technique.

REFERENCES

1. W. Y. Kato, G. J. Fisher and L. R. Dates, *Safety Analysis Report—Argonne Fast Critical Facility (ZPR-6)*, ANL-6271 (1963).
2. R. A. Karam, L. R. Dates, E. Groh, W. Y. Kato, R. A. Lewis, G. Main, J. E. Marshall, G. K. Rusch and C. Till, *Measured Physics Parameters in a Large Uranium Carbide Fast Core*, Reactor Physics Division Annual Report, July 1, 1966 to June 30, 1967. ANL-7310, pp. 167–188.
3. G. Duffy, H. Greenspan, J. Zapatka and M. Butler, *SNARG-ID, A One-Dimensional Discrete Ordinate Transport Theory Program for the CDC-3600*, ANL-7221, 1966.
4. D. M. O'Shea, H. H. Hummel, W. B. Lowenstein and D. Okrent, *Twenty-six Group Cross Sections*, Trans. Am. Nucl. Soc. **7**, 242 (1964).
5. D. A. Meneley, L. C. Kvitek and D. M. O'Shea, *MACH 1, A One-Dimensional Diffusion-Theory Package*, ANL-7223 (1966).
6. C. E. Cohn and J. J. Kaganove, *Digital Method for Control Rod Calibration*, Trans. Am. Nucl. Soc. **5**, 388 (1962).

III-15. Heterogeneity Effects in a Large UO_2 Core, Assembly 6 of ZPR-6

R. A. Karam, K. D. Dance, L. R. Dates, W. Y. Kato, J. E. Marshall, T. Nakamura* and G. K. Rusch

There are two main types of heterogeneity effects associated with fast criticals loaded with plate-type geometries: (1) fast effect, and (2) resonance effect. The fast effect depends on (a) the physical shape of the fissile materials, i.e. thickness and length of column, and (b) the physical separation between the fissile and fertile plates. The thickness of the plate of fissile materials contributes positively to the reactivity of the system through an increase in the yield of neutrons per fission due to fission neutrons that never leave the plate before causing another fission, and to neutrons that leave the plate and return to cause fissions before reaching the equilibrium spectrum. The length of the plate affects the reactivity in a similar manner and contributes to the peaking of the fluxes in and around the plate. The fast heterogeneity effect is also affected by the increase or decrease in the total fissions of U-238 in the heterogeneous system relative to the homogeneous system. The nearness of the U-238 atoms to the fissile atoms bears importantly on the total number of fissions in U-238.

The resonance heterogeneity effect is a self-shielding effect. Resonance neutrons are readily absorbed at the surface of the plate. This process allows fewer such neutrons to reach the interior of the plate and the overall effect is that the average reaction rate per atom of plate is lowered. The self-shielding effect on the reactivity of the system can be both negative and positive. Self-shielding contributes negatively through the fission and positively through the capture processes. Self-shielding in the scattering process can also have positive and negative effects on the system; the sign is determined by the relative importance of the neutron before and after scattering.

Understanding of both types of heterogeneity effects is necessary in order to incorporate such effects into the analysis and thus make the comparison of experiment and theory more equitable. To that end, a series of experiments was performed on a 4000-liter UO_2 core, Assembly 6 of ZPR-6 (see Paper III-1).

Three different types of experiments designed to yield pertinent data on the heterogeneity effects were conducted. These experiments comprised the following:

(1) Measuring the reactivity change associated with two changes of loading patterns and the intrastructure of the fluxes in the unit cell of each of the loading patterns

(2) Measuring and comparing the relative reactivity worth at the center of the core of homogeneous, rodded-type heterogeneous, and plate-type heterogeneous samples; also, measuring the intrastructure of the fluxes in the rodded samples

(3) Measuring the reactivity worth of U-235 and U-238 as a function of sample thickness.

Loading Pattern Effects

The effect of changing the drawer loading pattern on the reactivity of the system provides convenient means by which methods purported to account for heterogeneity effects can be tested. Calculations showed that a considerable change in σ_p^{238} takes place when the normal loading pattern shown in Fig. III-15-1a is rearranged to the bunched loading pattern of Fig. III-15-1b. Calculations also showed that when the appropriate amount of stainless steel in the matrix and drawer is homogenized with the two $U_3^{238}O_8$ plates in two adjacent cells, σ_p^{238} is increased by 5–10%. For this reason a loading pattern in which the stainless steel was isolated, Fig. III-15-1c, was used. Table III-15-I shows the calculated average σ_p^{238} and the corresponding capture cross sections for the three loading patterns and for the homogeneous case.

The measured reactivity change associated with the change in loading pattern shown in Fig. III-15-1a to that shown in Fig. III-15-1b, in a central region of the core comprising 76 drawers per half (Fig. III-15-2), was 93.06 Ih (0.203% $\Delta k/k$). The same measurement performed on 9 central drawers per half gave 11.53 Ih. The reactivity change associated with such change in loading pattern was also calculated by the procedure discussed elsewhere (see Paper III-16). The calculated values were 63.81 and 8.07 Ih for the change in the 76 and in the 9 drawers per half respectively.

The measured change in reactivity corresponding to the change in loading pattern from Fig. III-15-1a to Fig. III-15-1c, in a square region comprising the 25 central drawers per half, was 4.47 Ih. The calculated value for such change was 2.99 Ih.

In addition to the measurements of loading pattern effects on the reactivity of the system, an independent series of experiments measuring the fission

* Visiting Scientist, Japan Atomic Energy Research Institute, Tokai-mura, Japan.

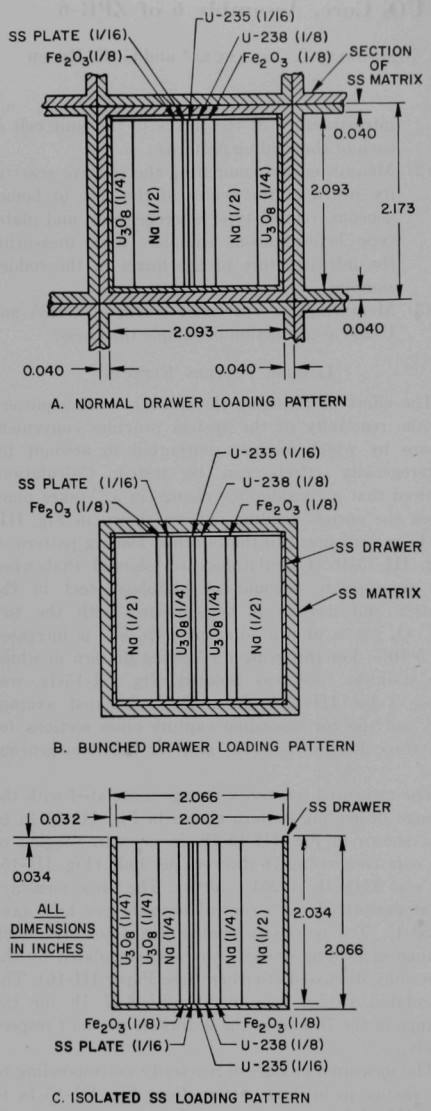

FIG. III-15-1. Cell Dimensions and Three Drawer Loading Patterns Used in Assembly 6 of ZPR-6. *ANL Neg. No. 113-1386 T-1.*

rates in U-235 and U-238 as well as the capture rates in U-238, were made as a function of position in the unit cell. Such integral measurements provided tests to verify the adequacy of the theoretical methods for predicting the spatial intrastructure of the fluxes in the unit cell. It should be noted that the detailed shapes of the fluxes have significant influence on the spatially averaged cross sections (see Paper III-16).

Depleted uranium foils (0.2% enrichment, 5 mil thick by ⅝ in. diam) and U-235 foils (93% enrichment, 4.5 mil thick by ⅜ in. diam) were placed at corresponding locations about the center of the core in the two halves of the ZPR-6 machine.[1] The foils were placed among the adjoining surfaces of all the plates in the unit cell. All foils were irradiated for one hour at a power level of about 50 watts. Five hours after irradiation, the activities of the U-238 foils were counted for fission fragments (counting gammas with energies above 0.41 MeV) and for capture by counting the 106 keV gammas from excited Pu-239 in coincidence with x-rays produced by internal K conversion electrons. The five-hour waiting period was necessary to allow sufficient time for the buildup of Np-239 from U-239. The U-235 foils were counted for fission fragments in a manner similar to that for counting the U-238 foils. A few foils were radiochemically analyzed for the absolute number of fissions in U-235 and absolute number of fissions and captures in U-238. The radiochemical results were used to obtain efficiency factors to convert the rest of the data to absolute numbers. Irradiations of the U-235 and U-238 foils were performed in each of the loading patterns shown in Figs. III-15-1a, III-15-1b, and III-15-1c.

In another experiment, a 2 x 2 x 1/16 in. plate of 93% enriched uranium and a 2 x 2 x ⅛ in. plate of depleted uranium (0.2% enriched) that were normally in the core were replaced by packets of foils equivalent in weight and enrichment to the two plates. This arrangement provided means by which the spatial distribution of the fluxes within the fissile and fertile plates can be verified by measuring the capture and fission rates. The packets were irradiated in the manner described earlier. For each of the 2 x 2 x 0.005 in. foils comprising the packets, a ⅝ in. diam foil was punched out from the center and counted. This procedure eliminated any requirement for edge effect corrections.

The results are shown in Figs. III-15-3 through III-15-6. Figure III-15-3 shows, across the normal loading pattern cell, the measured and calculated fission rates in U-235 and U-238, the capture rates in U-238, the fission in U-238 to fission in U-235 ratio, and the capture in U-238 to fission in U-235 ratio. The calculated fission rates in U-235 and U-238 were obtained using the cell fluxes from the SNARG-1D code,[2] with S_{32} and modified Gaussian quadratures,[3] and the cross sections in Set ZPR-6-6 ENDF/B-A (see Paper III-1). The capture rates in U-238 were

TABLE III-15-I. HOMOGENOUS AND CELL-AVERAGED σ_p AND CORRESPONDING σ_c OF U-238 FOR THE THREE LOADING PATTERNS OF ASSEMBLY 6 OF ZPR-6

Energy Group	Homogenous[a]		Normal[b]		Bunched[c]		Isolated SS[(d)]	
	σ_p, b	σ_c, b	σ_p, b	σ_c, b	σ_p, b	σ_c, b	σ_p, b	σ_c, b
11	48.69	0.4357	38.63	0.4223	32.41	0.4011	36.43	0.4201
12	40.75	0.5502	34.37	0.5313	30.48	0.5052	32.95	0.5286
13	51.97	0.6721	40.37	0.6426	33.37	0.6021	37.70	0.6375
14	69.53	0.8206	47.38	0.7690	36.02	0.7030	42.64	0.7579
15	107.3	1.048	53.58	0.9121	37.29	0.8134	46.46	0.8884
16	91.13	1.097	49.69	0.9467	36.69	0.8394	44.36	0.9199
17	58.62	0.9724	42.40	0.8702	34.91	0.7867	39.37	0.8513
18	56.30	1.117	42.10	0.9874	35.22	0.8885	39.38	0.9649
19	57.27	1.203	42.56	1.035	35.66	0.9174	39.80	1.006
20	60.09	1.147	43.72	0.9810	36.59	0.8768	40.76	0.9534
21	64.50	1.676	45.09	1.339	38.44	1.181	42.03	1.288
22	67.04	2.129	45.71	1.701	39.57	1.526	42.68	1.642

[a] All materials homogenized; calculated with σ_p code (Paper III-16).
[b] Loading pattern of Fig. III-15-1a.
[c] Loading pattern of Fig. III-15-1b.
[d] Loading pattern of Fig. III-15-1c.

calculated in a similar manner except that the cross sections used outside the slabs containing U-238 were infinite dilution cross sections. The cross sections for the slabs containing U-238 were those of Set ZPR-6-6 ENDF/B-A in which the self-shielding was accounted

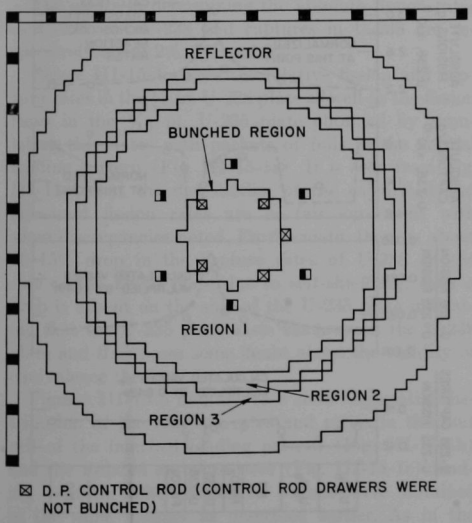

FIG. III-15-2. Regions in Assembly 6 of ZPR-6. D.P. Control Rod Drawers Were Not Bunched. *ANL Neg. No. 113-1385.*

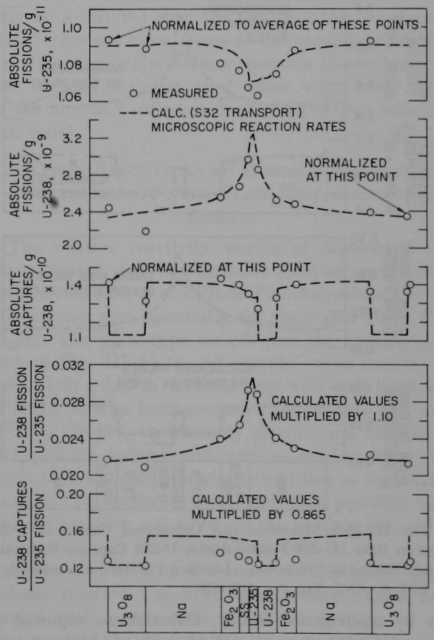

FIG. III-15-3. Measured and Calculated Values of U-235 Fission Rate, U-238 Fission Rate, U-238 Capture Rate and Their Ratios in "Normal" Loading of Assembly 6 of ZPR-6. *ANL Neg. No. 113-1294.*

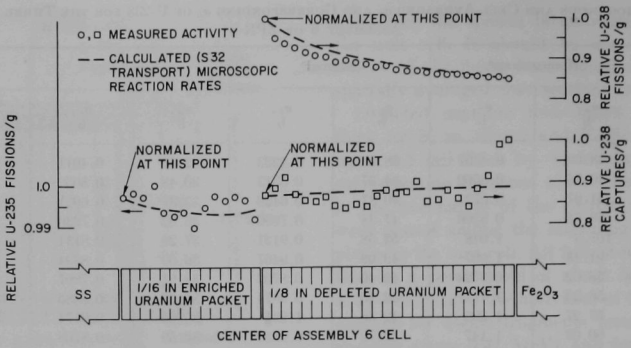

FIG. III-15-4. Relative Fissions in U-235 and U-238 Packets and Relative Capture in U-238 Packet Simulating the U-235 and U-238 Plates in Assembly 6 of ZPR-6. *ANL Neg. No. 113-1235.*

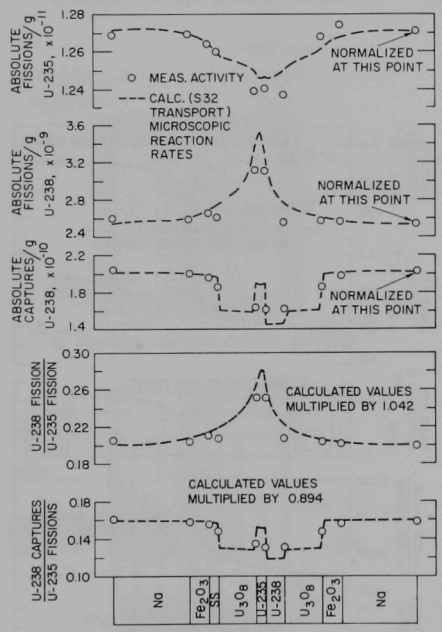

FIG. III-15-5. Measured and Calculated Values of U-235 Fission Rate, U-238 Fission Rate, U-238 Capture Rate and Their Ratios in "Bunched" Loading Patterns of Assembly 6 of ZPR-6. *ANL Neg. No. 113-1296.*

for by equivalence theory. Calculations reported in Figs. III-15-4 through III-15-6 were obtained in a similar manner.

It is seen from Fig. III-15-3 that the transport calculations underpredict the decrease in the U-235 fissions about the 1/16 in. plate of U-235. The calculated spatial distribution of the U-238 fission rates is in fair agreement with the measurements. The measured and calculated capture rates in U-238 are in apparent

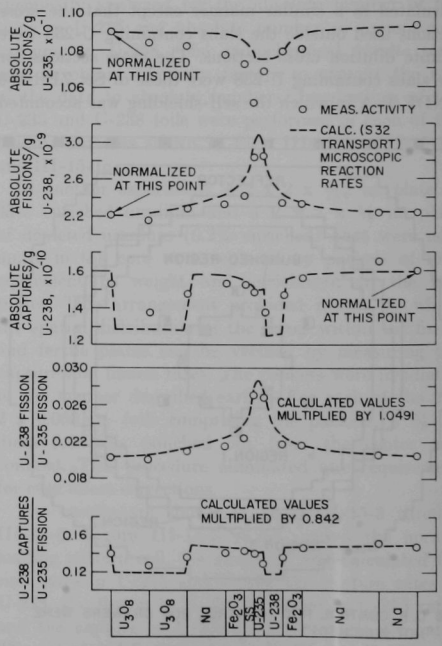

FIG. III-15-6. Measured and Calculated Values of U-235 Fission Rate, U-238 Fission Rate, U-238 Capture Rate and Their Ratios in an "Isolated Stainless Steel" Loading Pattern of Assembly 6 of ZPR-6. *ANL Neg. No. 113-1295 Rev. 2.*

TABLE III-15-II. SAMPLES USED IN HETEROGENEITY EFFECTS STUDY

Sample		Composition, g						Enrichment of UO_2, w/o U-235
No.	Type	Stainless Steel		Fe	Total SS + Fe	Na	UO_2	
		In-Sample	Can					
1	Homogeneous	58.00	46.10	45.74	149.84	—	392.87	16.42
2	"	57.97	46.18	45.72	149.87	52.89	392.66	16.42
3	"	—	46.36	—	46.36	—	452.00	16.42
4	"	—	46.36	—	46.36	—	392.87	16.42
9	"	—	46.05	—	46.05	69.17	392.87	16.42
8	Pellet	60.39	46.00	—	106.39	41.33	392.65	16.42
11a	"	61.17	46.00	—	107.17	—	392.60	16.42
11b	"	61.17	46.00	32.31	139.48	—	392.60	16.42
11a	Plate	45.18	46.08	46.28	137.54	42.94	399.29	16.41
11b	"	45.18	46.08	46.28	137.54	—	399.29	16.41
20a	"	45.35	34.25	46.88	126.29	—	403.36	16.40
20b	"	45.35	34.25	46.88	126.29	42.94	403.36	16.40

agreement, although the step function description of the U-238 capture cross sections would not reflect flux depression in the vicinity of the U-238 plates. (Note that the point of normalization is arbitrary.) The calculated ratio of fission in U-238 to fission in U-235 is about 10% lower than the measured value. The discrepancy is uniform as a function of position in the unit cell. The calculated capture in U-238 to fission in U-235 ratio is overestimated by about 15%.

The errors in determining the absolute fission rates in U-235 and U-238 and captures in U-238 are respectively about 2%, 5% and 5%.

Figure III-15-4 shows the relative fission and capture rates in the ⅛ in. U-238 plate as well as the fission rates in the 1/16 in. U-235 plate obtained by simulating the plates with packets of foils in the normal loading pattern (Fig. III-15-1a). It is seen from Fig. III-15-4 that the distribution of the calculated and measured fission rates are in fair agreement with some discrepancies noted. Furthermore, there is about 10–15% drop in the capture rates of U-238 on the side of the Fe_2O_3 plate due to self-shielding; such a drop is absent on the side of the U-235 plate indicating that the U-235 plate casts shadows on the U-238 plate and thus poses some doubt about the validity of equivalence theory.

Figures III-15-5 and III-15-6 show the spatial distribution of the reaction rates and ratios in the unit cell of the bunched loading pattern (Fig. III-15-1b) and the isolated stainless steel (Fig. III-15-1c) loading pattern. The calculated values were obtained in the same manner as described earlier. As in the case of the normal loading pattern, the calculated ratios of fission in U-238 to fission in U-235 and capture in U-238 to fission in U-235 were respectively lower and higher than the measured values. Furthermore, the calculated fission-to-fission ratios for these cases were only 5% lower than measurements to be compared with 10% for the normal loading case. This may be associated with the fact that the one dimensional transport calculations do not accurately account for streaming. (The sodium channels in the bunched and isolated stainless steel cases were wider than in the normal case when one considers two adjacent unit cells).

RELATIVE REACTIVITIES OF HOMOGENEOUS, PELLET-HETEROGENEOUS, AND PLATE-HETEROGENEOUS SAMPLES

The relative reactivity worths of nominal 2 in.^{3} plate, rodded, and homogeneous samples were measured in Assembly 6 of ZPR-6. The compositions of all the samples were essentially the same (see Table III-15-II). The plate-type sample had the loading pattern of Fig. III-15-1a. All samples were encased in 1.90 x 1.90 x 2.00 in. SS(304) cans with wall thickness of 0.015 in. The homogeneous samples were mixtures of UO_2 (16.43% enrichment) powder and sodium or UO_2 powder, sodium, and stainless steel powder—the latter to mockup the stainless steel tubes in the rodded samples. The stainless steel and UO_2 powders were blended together and sintered; the particle size of the blend was such that only about 53% of the volume would be used when packed under vibration. The empty volume fraction was filled with sodium. Tests conducted with x-rays, and an actual opening of one can, revealed that the mixture was quite homogeneous. The rodded samples consisted of 0.25 in. diam by ½–⅝ in. long pellets inserted in 36-tube calandria cans. The pellets consisted of two enrichments, 19.947%

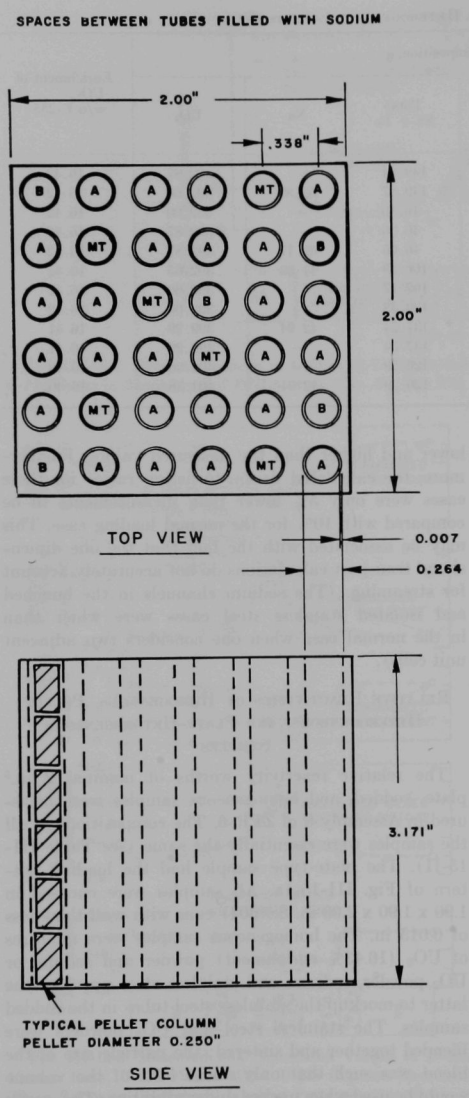

FIG. III-15-7. Square Calandria Can for Rodded Zone. *ANL Neg. No. 113-1383.*

and 15.861%, prorated to give an average enrichment of 16.43%. A test of the reactivity worth of UO_2 with each enrichment and the two combined showed that the assumption of linear dependence was adequate.

The measurements were conducted as follows: the reactivity of a sample was measured relative to void by the period method (at least 5 times); the relative worth of that sample was then measured relative to other samples using an oscillator in conjunction with an autorod. The autorod was calibrated differentially and integrally "online" with the aid of a recently developed code.[4]

In addition to the rodded samples that were oscillated, there were 26 (2.00 x 2.00 x 3.17 in.) calandria cans (Fig. III-15-7) with which a rodded zone was built around the sample being oscillated at the center of the core. This rodded zone comprised the first 3 in. of 13 drawers in each half of Assembly 6. The relative reactivity worths of the plate, rodded, and homogeneous samples were measured in the rodded zone environment as well.

The results are given in Table III-15-III. All samples were measured relative to homogeneous Sample №3 which was measured relative to void by the period method. The errors listed reflect the relative errors associated with the oscillation method and not the period method. The values listed for samples without sodium contain minor corrections accounting for small differences in composition between homogeneous Sample №1 and the rest. The values for the samples with sodium have been normalized to the composition of homogeneous Sample №2. The corrections were prorated linearly according to the worth of the material in its particular geometry. For example, the worth of stainless steel powder was obtained from the relative worth of homogeneous Samples №1 and №4.

TABLE III-15-III. MEASURED REACTIVITY WORTHS AT CENTER OF ASSEMBLY 6 OF ZPR-6

($1\%\ \Delta k/k = 458\ Ih$)

Sample No.	Sample Type	Sample Worth Relative to Void, Ih	
		Normal Plate Environment	Pellet Environment
1	Homogeneous with SS, no Na	1.364 ± 0.003	1.379 ± 0.002
11b	Pellet, no Na	1.351 ± 0.004	1.345 ± 0.003
11b	Plate, no Na	1.369 ± 0.005	—
20a	Plate, no Na	—	1.367 ± 0.003
2	Homogeneous with Na and SS	1.361 ± 0.002	1.375 ± 0.003
20b	Plate, with Na	1.359 ± 0.003	1.367 ± 0.003
8	Pellet, with Na	1.347 ± 0.003	1.359 ± 0.003

It is seen from Table III-15-III that the relative reactivities of the plate, rodded, and homogeneous samples are essentially the same. It appears that cancellation effects such as the increase in capture in U-238 and fission in U-235 in the homogeneous sample relative to the heterogeneous samples do take place.

In a separate experiment, the first 3 in. plate-loaded segments in 26 drawers were replaced with 26 (3 in.) pellet cans at the core center. The relative reactivity difference for all 26 cans was only 1.61 Ih.

The fission rates in U-235 and fission and capture rates in U-238 were measured in the 3 in. calandria cans. Depleted and 93% enriched uranium foils (0.25 in. diam) were placed between the last two pellets in tubes along the diagonal line of the calandria. In one tube there were no pellets and therefore the foil was placed at the bottom (Fig. III-15-8). The foils were irradiated and analyzed in the manner described earlier. The results are shown in Fig. III-15-8.

It is seen from Fig. III-15-8 that the spectrum in the empty tube is significantly softer in the high energy groups (fission in U-238) than that in the pellet-filled tubes. Furthermore, the captures in the U-238 foil in the empty tube are also higher than the average captures in a foil "sandwiched" between two pellets. This indicates that there are heterogeneity effects in the rodded samples; yet these effects combine in such a way that the reactivities of the rodded, plate, and homogeneous samples are all the same.

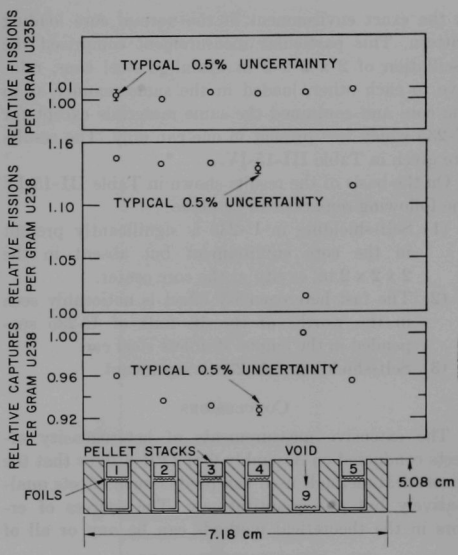

FIG. III-15-8. Cross Section of Pellet Can Diagonal. *ANL Neg. No. 113-1384.*

REACTIVITY WORTHS OF U-235 AND U-238 AS A FUNCTION OF THICKNESS

The calibrated autorod[4] was used in the measurement of the reactivity worth of U-235 and U-238 as a function of sample thickness. The samples comprised 0.005 in. thick foils with nominal area of 4 in.^{2} stacked together, and placed in a 2 x 2 x 2 in. stainless steel can on a $\frac{1}{32}$ in. wire rack that supported the samples at 1 in. from the bottom of the can. The samples were oscillated relative to an empty SS can with wire racks. In the case of U-235, the reactivity worth as a function of sample thickness was also measured

TABLE III-15-IV. REACTIVITY WORTH OF U-235, U-238, IRON, AND NICKEL AS A FUNCTION OF SAMPLE THICKNESS

Material and Environment	No. of Foils	Total Foil Wt, g	Worth, Ih	Specific Worth, Ih/kg Material
93% enriched uranium foils suspended in a 2- x 2- x 2-in. empty stainless steel can	1	4.638	+0.1857 ± 0.0019	+40.04 ± 0.41
	2	9.002	+0.3619 ± 0.0018	+40.20 ± 0.20
	5	23.059	+0.9266 ± 0.0016	+40.18 ± 0.07
	16	73.634	+3.039 ± 0.010	+41.14 ± 0.14
93% enriched uranium foils in plate-type heterogeneous cans identical to core-loading pattern	—	—	—	—
	1	4.511	+0.2110 ± 0.002	+46.66 ± 0.44
	2	9.221	+0.406 ± 0.002	+44.06 ± 0.22
	5	22.950	+0.969 ± 0.020	+42.22 ± 0.87
	8	36.851	+1.544 ± 0.020	+42.17 ± 0.54
	14	64.349	+2.682 ± 0.020	+41.68 ± 0.31
$\frac{1}{16}$-in. plate		61.491	+2.567 ± 0.020	+41.75 ± 0.31
Depleted uranium foils suspended in a 2- x 2- x 2-in. empty stainless steel can	1	5.913	−0.0252 ± 0.0017	−4.262 ± 0.288
	2	11.739	−0.0429 ± 0.0021	−3.654 ± 0.179
	5	28.977	−0.1034 ± 0.0016	−3.568 ± 0.055
	10	60.227	−0.2202 ± 0.0015	−3.656 ± 0.025
	25	147.123	−0.5136 ± 0.0018	−3.491 ± 0.009
2- x 2- x 1-in. block		1153.58	−3.764 ± 0.01	−3.263 ± 0.009

in the exact environment of the normal core loading pattern. This particular measurement comprised the oscillation of 2 x 2 x 2 in. stainless steel cans, relative to each other, loaded in the same manner as in the core and contained the same materials except for U-235 which was present in one can only. The results are given in Table III-15-IV.

On the basis of the results shown in Table III-15-IV the following remarks can be made:

(1) Self-shielding in U-235 is significantly present in the core environment but absent in the 2 x 2 x 2 in. cavity at the core center.

(2) The fast heterogeneity effect is noticeably seen in the worths of the 16 foils of U-235 suspended in the empty stainless steel can.

(3) Self-shielding in U-238 is significant.

Conclusions

The extensive measurements of heterogeneity effects conducted on Assembly 6 of ZPR-6 show that the theoretical methods used can predict such effects qualitatively but not quantitatively. The sources of errors in the theoretical methods can be any or all of the following: (1) basic data (ENDF/B file), (2) non-applicability of equivalence theory, and (3) use of a few (22) groups to obtain the spatial distribution of the fluxes with which the cross sections are averaged in the unit cell. Before the blame can be put on the basic data as being the main culprit for much of the discrepancies, a considerable amount of refining and validating of the methods for treating such data are required. An alternative is to eliminate the complexities of the heterogeneity effects by simply studying a few select homogeneous cores.

References

1. W. Y. Kato, G. J. Fischer and L. R. Dates, *Safety Analysis Report—Argonne Fast Critical Facility ZPR-6*, ANL-6271 (1963).
2. G. J. Duffy, H. Greenspan, S. D. Sparck, J. V. Zapatka and M. K. Butler, *SNARG-1D A One Dimensional Discrete-Ordinate Transport Theory Program for the CDC-3600* ANL-7221 (1966).
3. D. Meneghetti, *Discrete Ordinate Quadratures for Thin Slab Cells*, Nucl. Sci. Eng. **11**, 295–303 (November 1968).
4. C. E. Cohn, R. A. Karam, J. E. Marshall and J. M. van Doorninck, *Computer Aided Calibration of a Fine Autorod*, Trans. Am. Nucl. Soc., **11**, 2 (November 1968).

III-16. Heterogeneity Calculations for Plate-Type Heterogeneous Reactors

K. Dance, R. A. Karam and J. E. Marshall

Several measurements of heterogeneity effects in Assembly 5 of ZPR-6 have been made and reported earlier.[1] The generation of cross sections appropriate for analyzing heterogeneity effects has been carried out and is reported herein, along with a comparison of the measured results. In particular, cell averaged cross sections for overall-core calculations and in-plate cross sections for cell reaction rate calculations have been generated.

Present reactor codes do not have the capability of making overall core computations which treat in detail the fine plate structure of the ZPR cores. Thus cell heterogeneity effects are calculated separately and used to construct multigroup cross sections. The broad group cross sections $\overline{\Sigma}_j$ could, in principle, be found from an ultrafine group, transport theory cell calculation in which the spatial and energy dependent flux $\phi(\mathbf{r},E)$ is used to weight the broad group cross sections:

$$\overline{\Sigma}_j = \frac{\int_{cell} d\mathbf{r} \int_{E_j}^{E_{j+1}} \Sigma(\mathbf{r}, E)\phi(\mathbf{r}, E)\, dE}{\int_{cell} d\mathbf{r} \int_{E_j}^{E_{j+1}} \phi(\mathbf{r}, E)\, dE} . \qquad (1)$$

For a complicated cell such as that of Assembly 5, however, a full ultrafine group, transport calculation would not be feasible. An alternate method in which the cross sections were flux-weighted using the ultrafine group structure of $MC^{2(2)}$ while conserving the reaction rate via equivalence theory,[3] was used. The MC^2 calculation for a homogeneous composition of Assembly 5 was made using ENDF/B data. The U-238 resonance range cross sections were then corrected for the difference in σ_p between the actual heterogeneous configuration and the homogeneous mixture used in the MC^2 calculation. The resonance range equivalence theory corrections were made using the SIGP code, described in Paper VI-11, to ratio the capture cross sections according to the change in the potential scattering cross section.

The σ_p-corrected MC^2 broad group cross sections were then used in a transport calculation (SNARG-1D)[(4)] to determine the broad group flux shapes. These calculations were made using the modified single Gaussian angular points of D. Meneghetti[5] with order $N = 16$. The broad group fluxes were then used to weight the cross sections to preserve reaction rates in the cell. The diffusion coefficient was also flux

weighted to preserve the fundamental mode transverse leakage. (In the transport cell calculation, the transverse dimensions were chosen to preserve the full three-dimensional leakage of the overall core). However, a diffusion tensor is really needed to properly describe the highly anisotropic nature of the plate type ZPR cores.

Bilinear (adjoint) weighting, following the formulation of D. Shaftman and H. Greenspan,[6] was also used to obtain cell averaged cross sections for use in overall core reactivity calculations. The broad group real and adjoint fluxes were used in the calculations. The cell-averaged total removal cross section for any broad group $\overline{\Sigma_{Rj}}$ was calculated from the relation

$$\overline{\Sigma_{Rj}} = \frac{\int \Sigma_{Rj}(\mathbf{r})\phi_j(\mathbf{r})\phi_j^*(\mathbf{r})\, d\mathbf{r}}{\int \phi_j(\mathbf{r})\phi_j(\mathbf{r})\, d\mathbf{r}}, \qquad (2)$$

whereas the scattering matrix terms were calculated from the expression

$$\overline{\Sigma_{i\to j}} = \frac{\int \Sigma_{i\to j}(\mathbf{r})\phi_i(\mathbf{r})\phi_j^*(\mathbf{r})\, d\mathbf{r}}{\int \phi_i(\mathbf{r})\phi_j^*(\mathbf{r})\, d\mathbf{r}}. \qquad (3)$$

The fission source terms were weighted as in Eq. (3), and the diffusion coefficients were weighted as in Eq. (2). The bilinear weighted cross sections do not preserve reaction rates, but for fundamental mode calculations it can be shown that bilinear weighting preserves reactivity. The cell averaged cross sections can thus be used in overall core, criticality calculations. A. Henry[7] has shown, however, that if bilinear weighted cross sections are used, then in order to maintain a consistent variational approach the usual flux and current continuity boundary conditions at interfaces must be replaced with special boundary conditions involving discontinuities in the fluxes and currents. In the calculations of ZPR-6 Assembly 5, however, the boundary conditions used at the reflector-core interface were assumed to have a small effect on the overall reactivity and the bilinear weighted cross sections were used in a standard diffusion code with standard current and flux continuity boundary conditions at the core-reflector interface.

The criticality calculations for the reference and bunched loading patterns, shown in Figs. III-16-1 and III-16-2, were also carried out as outlined for the normal loading pattern (Fig. III-16-3). The potential scattering cross section σ_p of the normal and reference loadings was about 25 b whereas the σ_p of the bunched loading pattern was about 20 b in comparison to a σ_p of about 35 b for a homogeneous mixture of the same composition. The results of the measurements and the calculations are shown in Table III-16-I. The results show fair agreement between the calculated and measured changes in critical mass due to a change in loading pattern even though the absolute calculated critical mass values are far too high.

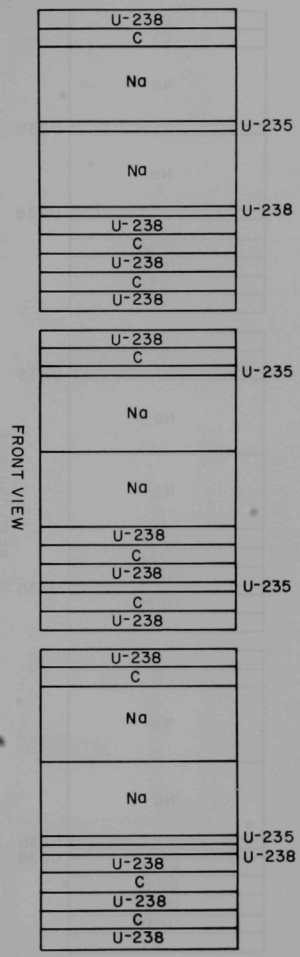

Fig. III-16-1. Reference Loading Patterns of Three-drawer Cell for Bunching U-238 in Assembly 5 of ZPR-6. *ANL Neg. No. 112-9223.*

The reactivity worths of plate type, rodded type

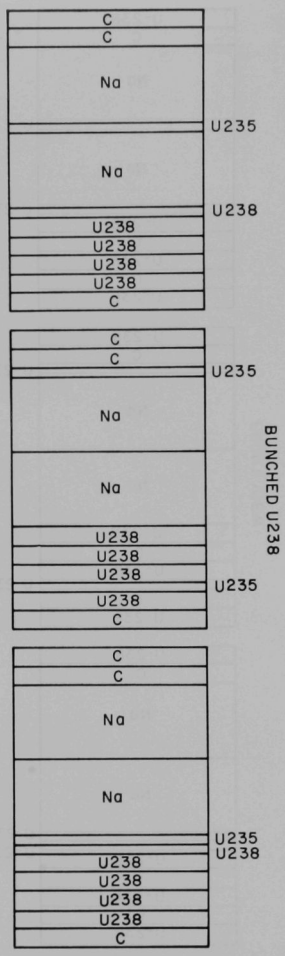

FIG. III-16-2. Bunched U-238 Loading Patterns in Three-drawer Cell of Assembly 5 of ZPR-6. *ANL Neg No. 112-9278.*

and homogeneous 2 x 2 x 2 in. sample cans were measured at the core center, and calculations were then made for the rodded type samples using the same technique as used for the generation of cross sections in plate type assemblies. In order to determine the proper broad group flux shape it was found necessary to use the "white" boundary condition option available in the SNARG-1D code to eliminate the Newmarch effect[8] (unreal flux peaking due to the cylindrical cell approximation). It was also found that while fast convergence could be obtained using a quadrature set constructed by K. Lathrop and B. Carlson,[9] the quadrature set contained internally in the SNARG code gave adequate convergence with S_n order 8 or 16. This is in contrast to the plate type heterogeneity problem in which adequate convergence cannot be obtained using the quadrature points contained in the SNARG code. The calculations showed that the σ_p of the homogeneous sample cans and the rodded sample cans were essentially the same and

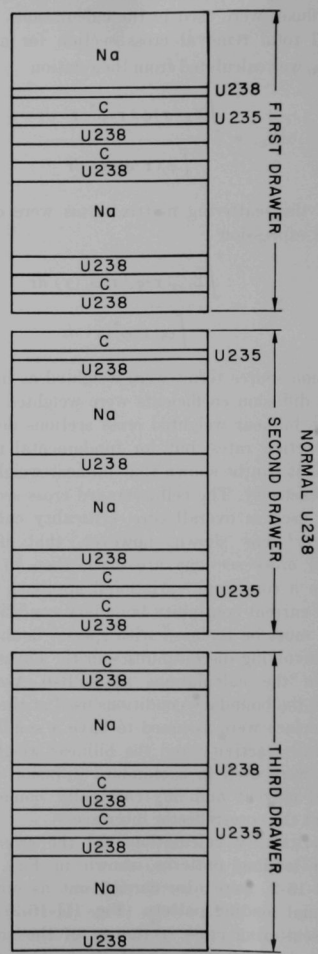

FIG. III-16-3. Normal Loading Patterns of Three-drawer Cell in Assembly 5 of ZPR-6. *ANL Neg. No. 112-9277.*

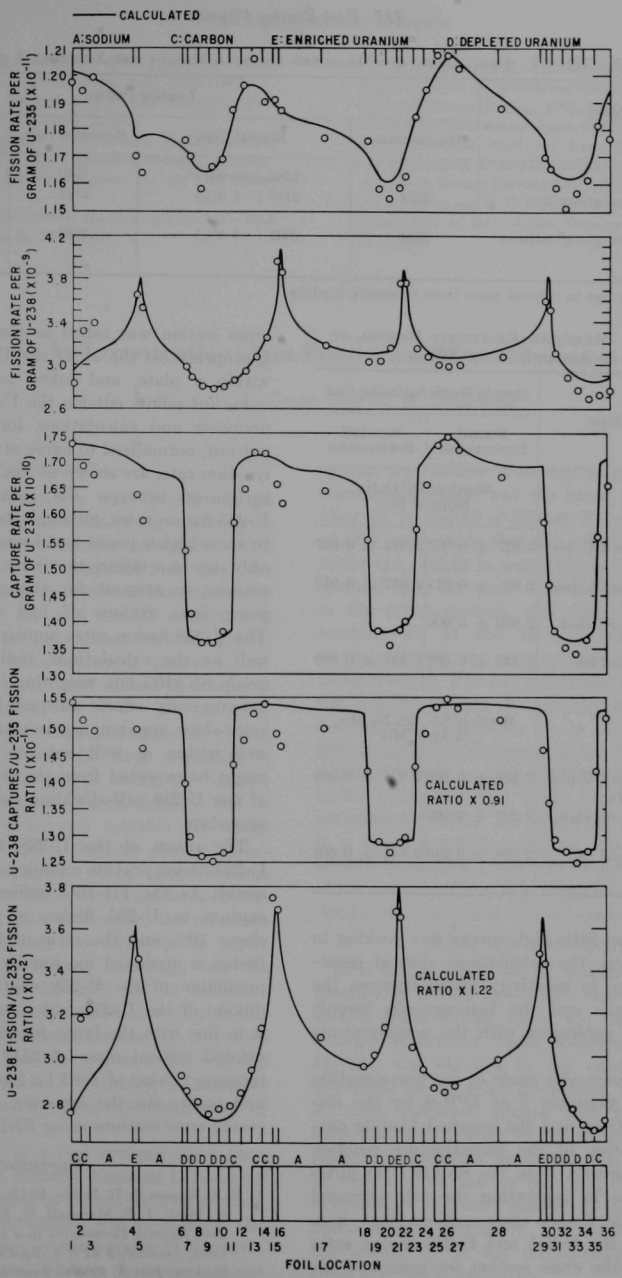

FIG. III-16-4. Measured and Calculated Values of U-235 Fission Rate, U-238 Fission Rate, U-238 Capture Rate, and Their Ratios in a Bunched Configuration of U-238 in Assembly 5 of ZPR-6. *ANL Neg. No. 113-1053.*

TABLE III-16-I. CALCULATED AND MEASURED CRITICAL MASSES FOR ASSEMBLY 5 OF ZPR-6

Critical Mass, kg of U-235	Loading Pattern			
	Homogeneous	Normal Core	Reference Core	Bunched Core
Measured		1583 (−0.6%)[a]	1592	1505 (−5.6%)
Calculated using broad group flux weighting	2554	2113 (−1.3%)	2141	2005 (−6.3%)
Calculated using broad group adjoint weighting	2554	2001 (−1.8%)	2038	1818 (−7.3%)

[a] ( ) ≡ Percent change in critical mass from reference loading.

TABLE III-16-II. MEASURED REACTIVITY WORTHS AT CENTER OF ASSEMBLY 5 OF ZPR-6

Sample No.	Sample Type	Sample Worth Excluding Can	
		Normal Environment	Bunched Environment
		Worth of UC Only, Ih/kg of UC	
3	Homogeneous UC, no Na	3.027 ± 0.007	2.982 ± 0.007
5	Homogeneous UC plus SS, no Na	2.991 ± 0.011	2.932 ± 0.012
7	Rodded UC, SS clad, no Na	2.970 ± 0.009	—
1	Plate U, C and SS, no Na	3.436 ± 0.007	3.391 ± 0.009
		Worth of UC, SS, Na Mix, Ih/kg of Mix	
6	Homogeneous UC plus SS, with Na	2.224 ± 0.006	2.221 ± 0.008
8	Rodded UC, SS clad, with Na	2.227 ± 0.007	—
2	Plate U, C and SS, with Na	2.698 ± 0.010	2.644 ± 0.008

that there was very little high energy flux peaking in the fuel pins. Thus, the calculations showed essentially no difference in reactivity worth between the rodded sample cans and the homogeneous sample cans, which is in agreement with the measurements (Table III-16-II).

Measurements were also made of the fine-structure reaction rates in Assembly 5 of ZPR-6 for the reference loading pattern and the bunched loading pattern. The calculation of the fine-structure reaction rates was made directly from the SNARG-1D fluxes calculated for use in generating the cell averaged cross sections. The fission cross sections that were used to calculate the U-235 and U-238 fission rates were taken from the cross section set generated for Assembly 5 by the MC² code. The U-238 capture cross section was taken as the capture cross section appropriate to the σ_p of the U-238 plates for points within a plate, and taken as the infinite dilution value for points outside the U-238 plates. The measurements and calculations for the bunched loading pattern, normalized to agree at the point of maximum reaction rate, are shown in Fig. III-16-4. There is fair agreement between the measured and calculated U-235 fission rates, although the measured values tend to show higher peaks and lower valleys. This is probably due to a failure to correct the U-235 fission cross sections to account for changes in self-shielding in going from regions of fuel to regions of diluent. The U-238 fission rates appear to be described rather well by the calculations, indicating that the broad group SNARG flux weighting handles the high energy heterogeneity effects adequately. The U-238 capture rates show apparent agreement only for points either well within or well outside the U-238 regions, as might be expected from the step function description of the U-238 self-shielding used in the calculational procedure.

The ratios of the U-238 fission and capture to U-235 fission provide an index of the cross section adequacy. As Fig. III-16-4 indicates, the ratio of U-238 capture to U-235 fission is predicted too high by about 10% and the ratio of U-238 fission to U-235 fission is predicted too low by about 20%. The overprediction of the U-238 capture and the underprediction of the U-238 fission relative to U-235 fission is in line with the large discrepancy between the calculated critical mass of 2112 kg of U-235 and the measured value of 1583 kg for Aseembly 5 of ZPR-6, and points out the apparent error in the MC² generated cross sections using ENDF/B data.

REFERENCES

1. R. A. Karam, L. R. Dates, E. Groh, W. Y. Kato, R. A. Lewis, G. Main, J. E. Marshall, G. K. Rusch and C. Till, *Measured Physics Parameters in a Large Uranium Carbide Fast Core, Assembly 5 ZPR-6*, Reactor Physics Division Annual Report, July 1, 1966 to June 30, 1967, ANL-7310, pp. 167–189.

2. B. J. Toppel, A. L. Rago and D. M. O'Shea, *MC²*, *A Code to Calculate Multigroup Cross Sections*, ANL-7318 (1967).
3. L. Dresner, *Resonance Absorption in Nuclear Reactors*, (Pergamon Press, New York, 1960), p. 63.
4. G. J. Duffy, H. Greenspan, S. D. Sparck, J. V. Zapatka and M. K. Butler, *SNARG-1D, A One-Dimensional, Discrete-Ordinate, Transport-Theory Program for the CDC-3600*, ANL-7221 (1966).
5. D. Meneghetti, *Discrete Ordinate Quadratures for Thin Slab Cells*, Nucl. Sci. Eng., **4**, 295 (1962).
6. D. H. Shaftman and H. Greenspan, *An Importance-Weighting Procedure for Averaging Group Parameters in Multigroup Diffusion Theory*, ANL-7010, 246 (1964).
7. A. F. Henry, *Few-Group Approximations Based on a Variational Principle*, Nucl. Sci. Eng., **27**, 493 (1967).
8. D. A. Newmarch, *Errors Due to the Cylindrical Cell Approximation in Lattice Calculations*, AEEW-R34 (1960).
9. K. D. Lathrop and B. G. Carlson, *Discrete Ordinates Angular Quadrature of the Neutron Transport Equation*, LA-3186, 31 (1965).

III-17. An Investigation of the Properties of Zoned Systems

L. G. LeSage, E. F. Groh and W. R. Robinson

Introduction

A program of measurements was carried out on ZPR-9 in order to better understand the systematics of small, cylindrical, zoned critical assemblies. Four different assemblies were investigated and these are described in Paper III-2. In three of the assemblies (ZPR-9 Assemblies 19, 21, and 22) the central test zone plate arrangement simulated uranium oxide material. The fourth zone contained plates of enriched and depleted uranium and carbon in combination such that k_∞ was unity.

The primary advantage of a zoned assembly over a full-size critical assembly is the large reduction in critical mass. The incentives for using the smaller zoned assemblies are discussed in more detail in Ref. 1.

Zoned critical assemblies are suitable for many types of primarily spectral dependent physics measurements, such as Doppler effect measurements or fission ratios, provided the correct neutron spectrum is achieved in the test zone. Generally, the reference system (which may or may not actually be built) is defined as a full-size critical assembly, and the central spectrum for this assembly is the reference spectrum. The test zone in the zoned assembly should have the same material composition as the reference system, and the buffer and the driver regions in the zoned systems are designed to minimize, as much as possible, the spectral mismatch at the boundaries of the test zone.

Experimental studies of zoned systems have been carried out previously at Argonne National Laboratory and the results are reported in Refs. 1–3. The primary emphasis in these measurements was to confirm the spectrum in zoned systems by comparison of measurements made in the zoned system to measurements made in a full-size reference system. The reference system was ZPR-6 Assembly 5, a large, dilute uranium-carbide core, and the zoned cores were Assemblies 4Z, 11 and 12 of ZPR-9. The general conclusions of this work were that the central reactivity worth ratios (i.e., worth in zoned system/worth in reference system) were the most sensitive test of the spectrum in the zoned systems, and that the spectra in Assemblies 4Z, 11 and 12 were adequately matched to the reference for most types of spectral dependent measurements. The one important exception was that the adjoint spectra in Assemblies 11 and 12 were not matched adequately to do accurate sodium void measurements, as discussed in Ref. 1.

The primary purposes of the zoned core measurements reported herein were: (1) to develop an experimental method for checking spectral matching in a zoned assembly when no full-size reference assembly is available; and (2) to better evaluate some of the analytical methods normally used in zoned core design, by comparison with a variety of measurements.

Procedure and Equipment

ZPR-9 Assemblies 19, 21 and 22 were constructed specifically for the zoned core experimental program. ZPR-9 Assembly 24, which was used in the null-reactivity plutonium alpha measurement (see Paper III-22), was checked by the experimental methods developed on the other assemblies. Assemblies 19 and 24 were optimized designs with regard to spectral matching. The spectra in Assemblies 21 and 22 were purposely perturbed, by making the central zone small in Assembly 21 and by changing the buffer material in Assembly 22 from a mixture of U_3O_8 and aluminum plates to pure aluminum. The latter was done to test the sensitivity of the measurements to reasonable cases of spectral mismatch.

The measurements made on the assemblies were

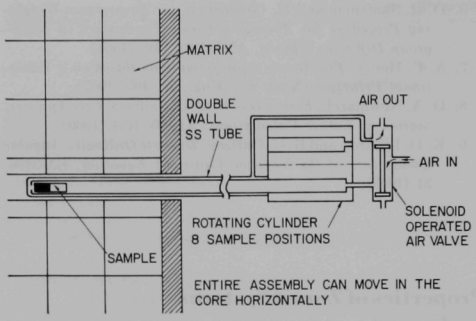

FIG. III-17-1. Sketch Showing Important Features of Radial Sample Changer. *ANL Neg. No. 113-880.*

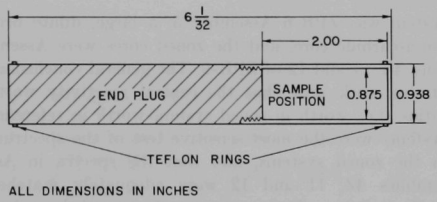

FIG. III-17-2. Out Drawing of Reactivity Sample and Sample Holder. *ANL Neg. No. 113-1444.*

central and radial reactivity worth, radial fission counter and BF_3 counter ratios, radial and axial U-235 foil activations and central U-238 Doppler effect. A special pneumatic sample changer was constructed for the reactivity measurements. Cylindrical samples approximately ⅞ in. in diameter and 2 in. long were oscillated into and out of the assembly, and the reactivity was determined by a calibrated autorod, which held the flux level constant. The autorod was calibrated from period measurements. Figure III-17-1 is a rough outline drawing showing some of the important features in the operation of the sample changer. The entire sample changer could be moved horizontally so that the samples could be oscillated to any point along the radius. The rotating cylinder has eight sample positions which can be adjusted to accept samples up to 6 in. long. The samples are enclosed in stainless steel sample holders, and the double wall tube which extends into the matrix is also made of stainless steel. A detailed drawing of a sample and sample holder is shown in Fig. III-17-2. The sample holder diameter was somewhat smaller than the inner tube diameter, and small teflon rings were used to seal the air flow and provide the bearing surface. The transit times for the samples were slightly over 1 sec, and the sample impact at the ends was cushioned by an orifice arrangement which controlled the rate of air escape from in front of the samples. End caps for the sample holders with thicknesses of 1/32, 2 and 4 in. were provided in order to stop neutron streaming in the sample changer tube. This effect is discussed below. In addition, an alternate inner sample changer tube was provided which contained a 4 in. stainless steel plug to stop neutron streaming in the inward direction.

The U-235, U-238, sodium, and boron reactivity samples were sealed inside thin wall (0.010 in.) stainless steel cans for safety. The geometry of the samples was either hollow or solid cylinder, 0.87 in. in outer diameter, depending upon the amount of material required. The one exception was the natural boron powder sample, which was contained in a stainless steel tube approximately ⅛ in. in diameter and 2 in. long. The samples were sized to give reactivity signals ranging from 0.050–0.250 Ih in Assembly 19, and the accuracy of the measurements was about ±0.002 Ih.

The same radial hole and drive mechanism was used for the U-235 and U-238 fission counters and the BF_3 counter. The double wall stainless steel tube was replaced by a stainless steel probe with the counter attached to the end.

Measurements were made to check the effect on the reactivity results of neutron streaming in the sample changer tube and also the effect due to the stainless steel in the thick sample holder end cap plugs. Since it was not possible to separate the two effects in the pneumatic sample changer, a measurement was made in an axial oscillator drawer in Assembly 24. The oscillator drawer was loaded solid with material so that no streaming was possible. Measurements were made of carbon, a material very sensitive

TABLE III-17-I. COMPARISON OF REACTIVITY WORTHS WITH AND WITHOUT STAINLESS STEEL STREAMING PLUG

Assembly	Material	Reactivity Worth, Ih[a]			
		Center of Zone		Radius 22.1 cm	
		Sample with Thin End Closure	Sample with 4 in. SS Plug	Sample with Thin End Closure	Sample with 4 in. SS Plug
19	U-235	0.2095	0.2105	—	—
	B	−0.2293	−0.2331	—	—
	Al	−0.0629	−0.0619	−0.0103	−0.0123
	C	0.1284	0.1266	0.1683	0.1519
21	Al	−0.0328	−0.0329	—	—
22	Al	−0.0293	−0.0356	—	—

[a] Approximate uncertainty ±0.002 Ih.

TABLE III-17-II. Reactivity Worths, Ih/kg

Assembly	Sample Material	Sample Weight, g	Radial Position, cm							Average Uncertainty
			0	5.52	10.04	16.56	22.08	27.60	30.36	
19	Enriched U	3.084	68.26	69.55	68.06	66.44	65.86	65.01	59.40	0.75
	Depleted U	25.988	−6.503	−6.364	−6.565	—	−6.399	−5.991	—	0.080
	B (Nat.)	0.553	−421.5	−415.0	−414.5	−413.9	−427.1	−409.6	−415.6	—
	Al	53.014	−1.185	−1.168	−1.147	−1.028	−0.866	−0.232	−0.232	0.040
	C	33.441	3.786	—	3.765	—	4.542	6.046	—	0.070
	Na	16.564	−0.097	—	0.115	—	−0.054	1.539	—	0.130
	SS 304	34.511	—	—	—	—	—	—	—	—
21	Enriched U	3.084	101.82	101.30	100.16	93.71	—	—	—	0.50
	B (Nat.)	0.553	−622.6	−626.2	−629.8	−609.6	−592.6	—	—	3.5
	Al	53.014	−0.621	−0.262	0.315	0.272	—	—	—	0.030
	C	33.441	6.043	—	7.578	—	—	—	—	0.035
22	Enriched U	3.084	73.74	—	72.31	—	61.96	53.92	—	0.70
	B (Nat.)	0.553	−475.6	—	−452.1	—	−452.1	−472.3	—	4.2
	Al	53.014	−0.672	−0.506	−0.121	—	1.111	1.422	—	0.035
	C	33.441	5.499	—	6.854	—	13.67	21.22	—	0.065
24	Enriched U	3.084	60.18	—	61.28	—	68.48	—	—	1.50
	Al	53.014	−2.346	—	−2.246	—	−2.327	—	—	0.115

TABLE III-17-III. Reactivity Worth Ratios, Ih/kg

Assembly	Worth Ratio	Radial Position, cm							Average Uncertainty
		0	5.52	11.04	16.56	22.08	27.60	30.36	
19	ρ(Al)/ρ(U-235)	−0.01736	−0.01679	−0.01685	−0.01547	−0.01315	−0.00357	−0.00391	0.0005
	ρ(C)/ρ(U-235)	0.05521	—	0.0553	—	0.0690	0.0930	—	0.001
	ρ(Nat. B)/ρ(U-235)	−6.17	−5.97	−6.16	−6.23	−6.48	−6.30	−7.00	0.10
	ρ(U-238)/ρ(U-235)	−0.0953	−0.0915	−0.0965	—	−0.0972	−0.0922	—	0.002
21	ρ(Al)/ρ(U-235)	−0.00610	−0.00259	0.00314	0.00290	—	—	—	0.0004
	ρ(C)/ρ(U-235)	0.0593	—	0.0757	—	—	—	—	0.0006
	ρ(Nat. B)/ρ(U-235)	−6.11	−6.18	−6.29	−6.51	—	—	—	0.10
22	ρ(Al)/ρ(U-235)	−0.00911	—	−0.00167	—	0.01793	0.02637	—	0.0006
	ρ(C)/ρ(U-235)	0.0746	—	0.0948	—	0.2206	0.3935	—	0.001
	ρ(Nat. B)/ρ(U-235)	−6.45	—	−6.25	—	−7.30	−8.76	—	0.10
24	ρ(Al)/ρ(U-235)	−0.390	—	−0.367	—	−0.340	—	—	0.0025

to small spectral changes, both with a void next to the carbon and with approximately 300 g of stainless steel next to the carbon. The stainless steel simulated the stainless steel end plugs on the sample holder. The measured carbon worths were, respectively, −0.282 ± 0.002 and −0.277 ± 0.002 Ih. These values are very nearly in agreement, which is an indication that the effect of the stainless steel end plugs on the measured worths was small.

Measured reactivity worths, using the pneumatic sample changer, with and without the stainless end plugs at both the zone center and near the edge of the zone, are listed in Table III-17-I. Except for the carbon value at 22.1 cm radius, all the measured worths with and without the stainless steel end plugs are either in agreement or very nearly so. The good agreement for the primarily absorbing materials boron and U-235 is further indication that the spectrum perturbation effect of the stainless steel is not large. The carbon measurements, however, seemed to indicate the possibility that a small, but not insignificant, streaming effect does exist. Therefore, most of the

TABLE III-17-IV. NORMALIZED COUNT RATES FOR U-235 AND U-238 FISSION COUNTERS AND A BF_3 COUNTER[a]

Radial Position, cm	Assembly 19			Assembly 21			Assembly 22		
	U-235	U-238	BF_3	U-235	U-238	BF_3	U-235	U-238	BF_3
0	1.000	1.000	1.000	1.000	1.000	1.000	1.000	1.000	1.000
2.76	0.993	0.998	—	0.983	1.006	0.987	1.008	1.030	1.038
5.52	0.977	1.004	1.015	0.980	0.986	1.005	0.996	0.972	0.977
8.28	—	—	—	1.005	1.001	0.980	1.005	1.006	0.987
11.05	1.007	1.001	1.005	0.995	1.009	1.009	0.971	0.975	0.973
13.80	—	—	—	0.999	0.990	1.006	0.982	1.003	1.001
16.56	0.994	1.000	1.017	0.996	1.043	0.982	0.978	0.959	1.033
19.32	—	—	—	0.971	—	0.938	0.970	0.962	1.063
22.10	0.992	0.995	1.012	0.932	1.415	0.886	0.978	1.006	1.059
24.84	1.021	0.984	1.029	0.899	—	0.892	0.968	0.995	1.006
27.60	0.994	1.052	1.007	0.880	1.153	0.940	0.980	1.085	1.006
30.36	0.965	1.237	—	0.912	—	1.172	0.969	1.238	0.973
33.12	0.932	1.380	0.915	0.965	0.616	1.333	0.920	1.378	0.922
35.88	0.882	—	—	—	—	—	0.859	1.322	0.895
38.63	0.858	1.137	0.883	0.979	0.301	1.670	0.853	1.147	0.893
41.39	0.824	—	—	—	—	—	0.815	—	0.938
44.16	0.794	0.578	0.943	0.805	0.158	1.396	0.768	0.589	0.961
49.67	0.617	0.257	0.763	0.545	—	0.865	0.606	0.233	0.780
55.19	0.339	0.121	0.373	0.253	—	0.347	0.317	—	0.411
60.71	0.178	0.052	—	0.122	—	0.149	0.173	—	0.256
66.23	0.101	—	—	—	—	—	—	—	—

[a] All counts were normalized to 1.0 at assembly center. Statistical uncertainties were less than 1% for the U-235 and BF_3 counters and about 1.5% for the U-238 counter.

TABLE III-17-V. NORMALIZED COUNT RATE RATIOS FOR U-235, U-238 FISSION COUNTERS AND A BF_3 COUNTER[a]

Radial Position, cm	Assembly 19			Assembly 21			Assembly 22		
	BF_3/U-235	U-238/ U-235	U-238/BF_3	BF_3/ U-235	U-238/ U-235	U-238/BF_3	BF_3/U-235	U-238/ U-235	U-238/BF_3
0	1.000	1.000	1.000	1.000	1.000	1.000	1.000	1.000	1.000
2.76	—	1.005	—	1.004	1.023	1.019	1.030	0.998	0.992
5.52	1.038	1.028	0.989	1.026	1.006	0.981	0.981	0.976	0.995
8.28	—	—	—	0.975	0.996	1.021	0.982	1.001	1.019
11.05	0.998	0.994	0.996	1.014	1.014	1.000	1.002	1.004	1.002
13.80	—	—	—	1.007	0.991	9.84	1.019	1.021	1.002
16.56	1.023	1.006	0.983	0.986	1.047	1.062	1.056	0.981	0.928
19.32	—	—	—	0.966	—	—	1.095	0.992	0.905
22.10	1.020	1.003	0.983	0.951	1.518	1.597	1.082	1.029	0.950
24.84	1.008	0.964	0.956	0.992	—	—	1.040	1.028	0.989
27.60	1.013	1.058	1.045	1.068	1.310	1.227	1.027	1.107	1.078
30.36	—	1.282	—	1.285	—	—	1.004	1.278	1.272
33.12	0.981	1.481	1.508	1.381	0.638	0.462	1.002	1.498	1.495
35.88	—	—	—	—	—	—	1.042	1.539	1.477
38.63	1.029	1.301	1.288	1.706	0.307	0.180	1.047	1.345	1.284
41.39	—	—	—	—	—	—	1.151	—	—
44.16	1.188	0.728	0.613	1.733	0.196	0.113	1.251	0.767	0.613
49.67	1.236	0.417	0.337	1.587	—	—	1.287	0.384	0.299
55.19	1.100	0.357	0.324	1.372	—	—	1.297	—	—
60.71	—	—	—	—	—	—	1.479	—	—

[a] All ratios are normalized to 1.0 at assembly center. Statistical uncertainties are less than 2% for all ratios.

TABLE III-17-VI. CENTRAL REACTIVITY WORTHS IN ASSEMBLY 19; COMPARISON WITH ASSEMBLY 6

Sample Material	Weight of Sample, g	Can Type	Can Weights, g	Gross Sample Worth, Ih	Net Sample Worth, Ih	Specific Sample Worth, Ih/kg	Worth Assy 19, ZPR-9 / Worth Assy 6, ZPR-6
$(CH_2)_n$	58.986	bare	—	17.513 ± 0.009	17.513 ± 0.009	296.9 ± 0.2	1.421
Be	114.308	bare	—	1.801 ± 0.007	1.801 ± 0.007	15.76 ± 0.06	1.381
B-10	29.29	SS	55.73	−39.312 ± 0.070	−39.195 ± 0.071	−1338.2 ± 2.4	1.689
C	102.0	bare	—	0.459 ± 0.007	0.459 ± 0.007	4.50 ± 0.07	1.254
Na	51.38	SS	56.42	−0.095 ± 0.005	0.020 ± 0.007	0.39 ± 0.14	1.538
Al	165.33	bare	—	−0.091 ± 0.007	−0.091 ± 0.007	−1.15 ± 0.04	1.566
Fe	488.0	bare	—	−0.720 ± 0.007	−0.720 ± 0.007	−1.475 ± 0.014	1.600
SS can	72.39	bare	—	−0.153 ± 0.005	−0.153 ± 0.005	−2.11 ± 0.07	—
SS block	480.9	bare	—	−0.871 ± 0.007	−0.871 ± 0.007	−1.81 ± 0.02	1.643
Ni	546.0	bare	—	−1.435 ± 0.007	−1.435 ± 0.007	−2.63 ± 0.02	1.725
Zr	406.0	bare	—	−0.748 ± 0.007	−0.748 ± 0.007	−1.84 ± 0.02	1.688
Nb	481.2	SS	30.10	−5.983 ± 0.007	−5.920 ± 0.009	−12.30 ± 0.02	1.679
Mo	599.0	bare	—	−5.115 ± 0.075	−5.115 ± 0.075	−8.539 ± 0.125	1.642
Ta	924.7	bare	—	−19.724 ± 0.007	−19.724 ± 0.007	−21.269 ± 0.008	—
W	1108.0	bare	—	−8.945 ± 0.007	−8.945 ± 0.007	−8.074 ± 0.007	1.756
Enriched U	18.17 U 16.93 U-235	SS	72.603	1.100 ± 0.007	1.254 ± 0.009	69.01 ± 0.50	—
Depleted U	1153.8	bare	—	−6.317 ± 0.007	−6.317 ± 0.007	−5.475 ± 0.006	1.678

measurements were made with the thick (4 in.) stainless steel end plug on the sample holder (as shown in Figure III-17-2).

DISCUSSION

Since the test zone in a zoned assembly usually has the same material composition as the reference assembly, the problem of spectral matching is primarily one of designing the buffer and driver regions so that the spectrum in the zone converges rapidly to the asymptotic spectrum characteristic of the reference material. The radial measurements were made primarily to obtain information on spectral change along the radius. If the measurements indicate a stable, unchanging spectrum over a large area at the center of the test zone, then the spectrum must have converged to the stable spectrum characteristic of the reference material, and the spectrum can be considered as reasonably well-matched.

Consider the ratio of the reactivity worths of two materials as a function of radius. This ratio will change if the spectrum changes or if the relative leakage effects of the two samples change. A change in the magnitude of the flux will not affect the worth ratios. Calculations indicate that, along the horizontal midplane in the test zones of the assemblies considered, the leakage worths of the samples were very small compared to the total worth (i.e., less than 2% for all samples in all assemblies). Therefore, the change in the worth ratios with radius was primarily due to spectrum change. Calculated leakage connections were generally not made, since they were smaller than the uncertainties in the measured ratios. In the case of the fission counter and BF_3 counter ratios, the change in these values with radius is entirely due to spectrum change.

RESULTS

The important reactivity worth and fission and BF_3 counter results are contained in Tables III-17-II through III-17-VI. Some of the more interesting comparisons are shown in Figs. III-17-3 through III-17-6. All four assemblies are compared in Fig. III-17-3 which shows the ratio of aluminum worth to U-235 worth for each assembly. The nearly constant value for this ratio over a large section of the central zone for Assemblies 19 and 24 indicates a reasonably stable spectrum in the central test zone, is predicted by the calculations. The rapidly changing value for this ratio in Assemblies 21 and 22 indicates a changing spectrum throughout most of the central zone. This ratio is clearly sensitive to the difference between the well-matched spectra of Assemblies 19 and 24 and the perturbed spectra of Assemblies 21 and 22. Figure

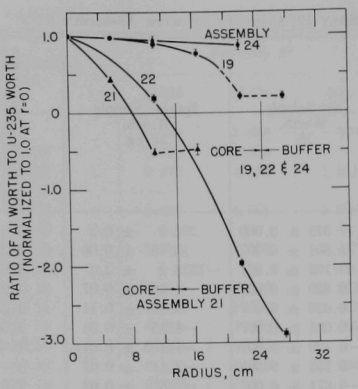

FIG. III-17-3. Normalized Radial Reactivity Worth Ratios for Aluminum and U-235 in ZPR-9 Assemblies 19, 21, 22 and 24. *ANL Neg. No. 113-879.*

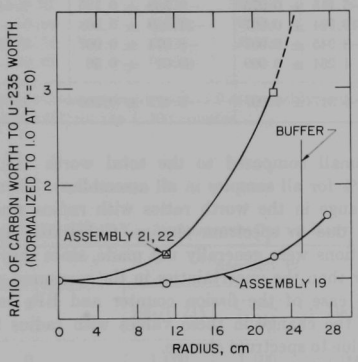

FIG. III-17-4. Normalized Radial Reactivity Worth Ratios for Carbon and U-235 in ZPR-9 Assemblies 19, 21 and 22. *ANL Neg. No. 113-875.*

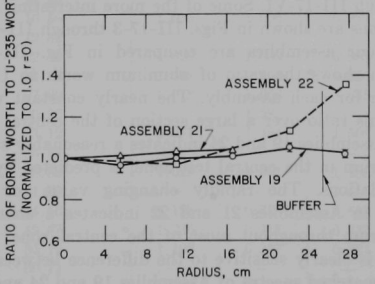

FIG. III-17-5. Normalized Radial Reactivity Worth Ratios for Boron and U-235 in ZPR-9 Assemblies 19, 21 and 22. *ANL Neg. No. 113-878.*

III-17-4 shows the carbon-to-U-235 worth ratio for Assemblies 19, 21 and 22, and the differences between Assembly 19 and Assemblies 21 and 22 are again clearly indicated. Figure III-17-5 shows the boron-to-U-235 worth ratios for Assemblies 19, 21 and 22. Differences among the assemblies are not clearly indicated in this figure, although the softening of the spectrum near the aluminum buffer in Assembly 22 is apparent. Two conclusions from the comparison of these figures are: (1) Since boron and U-235 are absorbing materials, more or less directly proportional to the spectrum, it appears that the magnitude of the spectrum perturbations in Assemblies 21 and 22 are not exceptionally large. This conclusion is further substantiated by fission and BF_3 counter ratios and

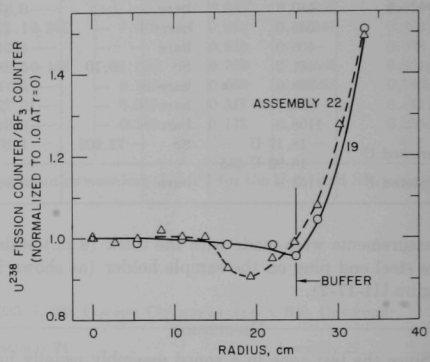

FIG. III-17-6. Normalized Radial Count Ratios for U-238 Fission Counter and BF_3 Counter in ZPR-9 Assemblies 19 and 22. *ANL Neg. No. 113-873 Rev. 1.*

TABLE III-17-VII. CENTRAL WORTH RATIOS IN ASSEMBLIES 19, 21 AND 22

Material	Sample Weight, g	Worth Ratios, Ih	
		Assembly 21 / Assembly 19	Assembly 22 / Assembly 19
B	0.553	1.48	1.13
C	33.441	1.60	1.45
Al	53.014	0.53	0.57
SS 304	34.511	1.37	1.05
Ta	5.772	1.47	1.15
Enriched U (93%)	3.084	1.49	1.08
	2.868 U-235		
Depleted U	25.988	1.43	1.12
Absorber Avg.[a]		1.47	1.12

[a] Average uncertainty ±1–2%, except for Al which was ±8%.

by the multigroup calculations. (2) The ratio of a scattering material, such as aluminum or carbon, and an absorbing material is a sensitive index of spectral change. The sensitivity of the ratio is due to the sensitivity of the scattering material worths to small changes in the adjoint spectrum. This is discussed in more detail in Ref. 1. The radial worth ratios, therefore, afford a fairly good test of spectral convergence in a zoned assembly.

The ratio of the U-238 fission counter to the BF_3 counter is shown in Fig. III-17-6 for Assemblies 19 and 22. The Assembly 21 ratio was not significantly different from Assembly 19 throughout the central region of Assembly 21. This ratio should be a sensitive index of the high energy to low energy real flux ratio. Although the effect of the aluminum buffer in Assembly 22 is indicated, the difference between the assemblies is not nearly as apparent as that indicated by the worth ratios.

It was possible to confirm the spectral matching in Assembly 19, by a method independent of the radial worth measurements, since the materials in the test zones in Assemblies 19, 21 and 22 were selected to be the same as those of ZPR-6 Assembly 6 (see Paper III-1), so that Assembly 6 could serve as a full-size reference assembly. The central worth measurements in Assemblies 19 and 6 are compared in Table III-17-VI. The same reactivity samples were used in both assemblies. The relatively constant worth ratios between the assemblies indicates fairly good spectral matching as discussed in Ref. 1. The values indicate that the matching of Assembly 19 to Assembly 6 was at least as good as the matching of ZPR-9 Assembly 12 to ZPR-6 Assembly 5.

The U-235 activation results are given in Paper III-2 and the results are discussed therein. The good agreement between the radial U-235 fission counter and activation results indicates that neutron streaming in the radial sample changer hole did not significantly affect the fission counter results. The activations were made along the same radius but about 2 in. removed from the radial hole.

Central natural UO_2 Doppler measurements were made only in Assemblies 19 and 21. The final Doppler results are not yet available; however, the preliminary results indicate that the Doppler effect in Assembly 21 was about 25% larger than in Assembly 19. Table III-17-VII gives the central reactivity worth ratios between Assemblies 21 and 19 and between 22 and 19. The Assembly 21-to-19 ratio predicts that the Doppler effect in Assembly 21 should be about 45-50% greater than in Assembly 19 for good spectral matching between the two assemblies. The Doppler results indicate that the Doppler energy flux in Assembly 21 is, therefore, somewhat deficient. This is undoubtedly due to the small size of the test zone and the fact that the driver spectrum is considerably harder than the test zone spectrum. The indication is then that this particular zone is too small to do meaningful Doppler measurements.

The evaluation of the zoned core analytical techniques, by comparison with measurements, is not yet complete and will not be reported in this paper.

References

1. L. G. LeSage, R. A. Karam, R. A. Lewis, E. F. Bennett and G. W. Main, *A Review of Data Pertaining to Spectral Equilibration and Spectral Matching in Zoned Cores*, Reactor Physics Division Annual Report, July 1, 1966 to June 30, 1967, ANL-7310, pp. 199–204.
2. R. A. Karam and L. G. LeSage, *Zoned-Core Concepts*, Trans. Am. Nucl. Soc. **10**, 270 (1967).
3. R. A. Lewis, C. E. Till, E. F. Groh, L. G. LeSage and J. E. Marshall, *Verification of Doppler Measurements in Zoned Fast Critical Assemblies*, Trans. Am. Nucl. Soc. **10**, 273 (1967).

III-18. Neutron Spectroscopy in ZPR-6 Assembly 6 Using Proton-Recoil Counters

E. F. Bennett and R. A. Karam

Introduction

In-core measurements of the neutron spectrum in various of the ZPR-6 assemblies have been made using proton-recoil proportional counters. The method has been discussed elsewhere.[1,2] The measurements described here were the last to be made on a series of fast critical assemblies fueled with U-235 and include central spectra (also with sodium voiding) as well as spatially dependent spectra.

Intercomparison of measured spectra with calculated values are also included and a discussion of possible systematic errors both in the measurement and in the intercomparison with calculation is made.

Experimental Results

The proton-recoil detectors used for these measurements are described in Refs. 1 and 2 and the preamplifier is described in Ref. 3. Each spectrum contains

TABLE III-18-I. As-Loaded Material Concentrations in Assembly 6 of ZPR-6

Region	Outer Radius, cm	Atoms ($\times 10^{-24}$) per cc						
		U-235	U-238	Na	O	Fe	Ni	Cr
1 (core)	77.17	0.001150	0.00579	0.00914	0.01465	0.01410	0.001365	0.002788
2 (core)	85.53	0.001070	0.00579	0.00579	0.00779	0.01465	0.01572	0.003253
3 (core)	90.87	0.001560	0.00579	0.00831	0.01465	0.01524	0.001518	0.003115
4 (blanket)	120.63	0.000083	0.04008	—	—	0.00423	0.000567	0.001215

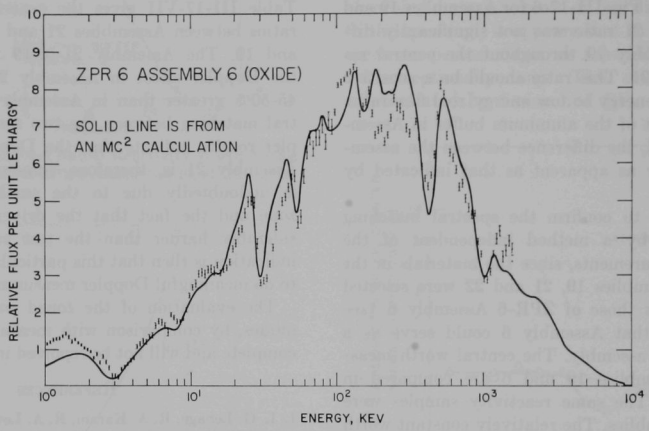

Fig. III-18-1. Central Neutron Spectrum in ZPR-6, Assembly 6 Together with an MC² Calculation. *ANL Neg. No. 112-9998 T-1.*

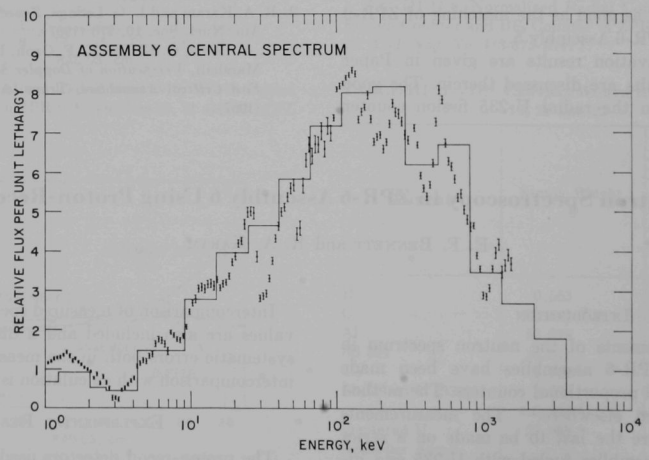

Fig. III-18-2. Central Neutron Spectrum in ZPR-6, Assembly 6 Together with a 22-group Diffusion Theory Calculation. *ANL Neg. No. 113-850.*

the results of several runs (at the same reactor flux level) with the electronics set to view consecutive regions of the proton-recoil energy distribution. In addition, two detectors were used: one, filled with a predominantly hydrogen gas mixture, covered the energy region below 100 keV while the other, containing methane, was used for energies above 100 keV. At the higher energies wall-and-end events were significant and an appropriate correction described in Ref. 4 was made to the measured distributions.

The detectors were placed in the core in substitution for a drawer (5 x 5 cm) containing representative core material. The mean composition of Assembly No. 6 core is shown in Table III-18-I. Measurements were made at several radial locations with the center of the detectors axially displaced from the reactor midplane by about 12 cm.

Figures III-18-1 through III-18-4 are for spectra measured at the reactor midplane and with the center of the counters located at a radial distance of 88 cm

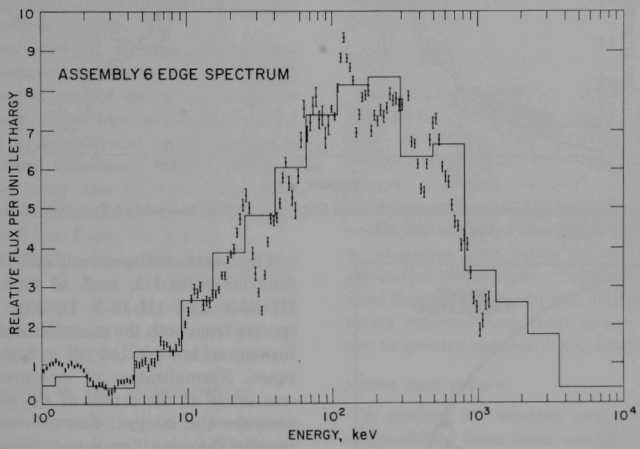

FIG. III-18-3. Edge Spectrum (γ = 88.0 cm) in ZPR-6, Assembly 6 Together with a 22-group Diffusion Theory Calculation. *ANL Neg. No. 113-846.*

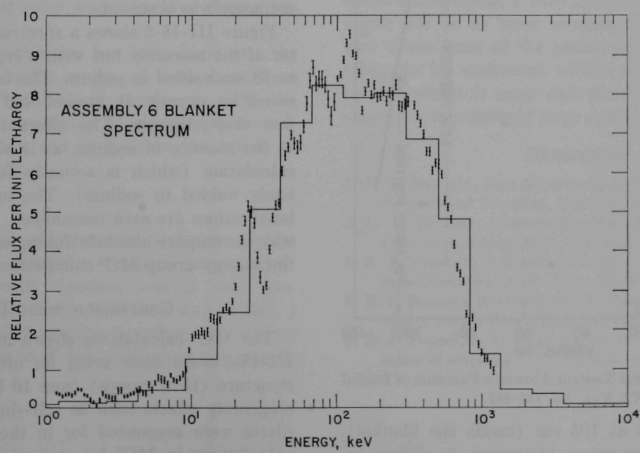

FIG. III-18-4. Blanket Spectrum (r = 108.0 cm) in ZPR-6, Assembly 6 Together with a 22-group Diffusion Theory Calculation. *ANL Neg. No. 113-847.*

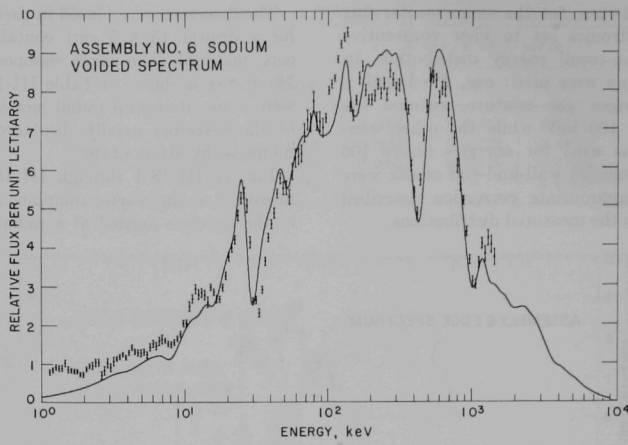

FIG. III-18-5. Central Neutron Spectrum in a Sodium-Voided Region of ZPR-6, Assembly 6 Together with an MC² Calculation for an Infinite Sodium-voided Region. *ANL Neg. No. 113-843.*

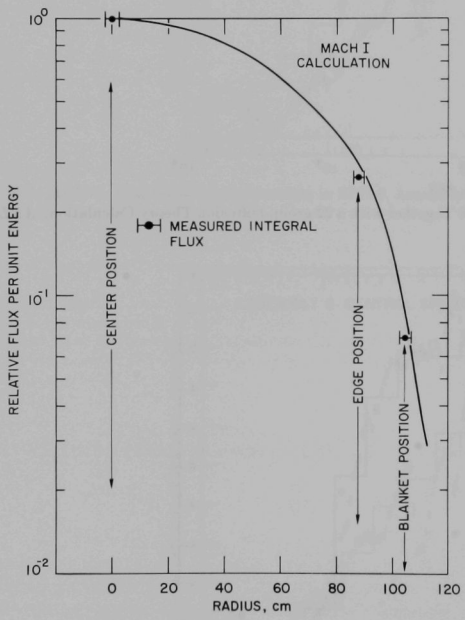

FIG. III-18-6. Integral Neutron Flux as a Function of Radial Detector Location. *ANL Neg. No. 113-891.*

(edge of core) and at 105 cm (inside the blanket). A calculated energy-group histogram is shown together with the measurements; the calculation will be discussed in the next section.

The calculated spectrum and the measurement are area normalized in each of Figs. III-18-1, III-18-2, III-18-3, and III-18-5. In Fig. III-18-6 integrated spectra from both the measurement and from the group histogram are plotted as a function of radial distance. Normalization of measurement to calculation was made at the center of the core only in order to compare the integral flux decrease with radius. The rapidly changing flux across distances equal to a fuel drawer size tends to complicate the interpretation of this intercomparison. Generally, no significant discrepancy was observed.

Figure III-18-5 shows a spectrum taken at the center of the assembly but with a region of radius equal to 18 cm voided in sodium. The large scattering resonance in oxygen at around 450 keV depresses the flux very strongly. The effect is more pronounced in the absence of sodium, as is also indicated by the calculation (which is actually for an assembly entirely voided in sodium). The measured and calculated values are area normalized. There is no obvious way to compare absolute fluxes, as measured, with the fine energy-group MC² calculations.[5]

Comparison with Theory

The MC² calculations shown in Figs. III-18-1 and III-18-5 were done using an ultrafine energy-group structure (1510 groups) from 10 MeV to 29 eV. Heterogeneity effects such as self-shielding in the U-238 plates were accounted for in the fundamental mode calculations in MC² by equivalence theory. The resulting ultrafine group fluxes from MC² are appropriate for an equivalent homogeneous core and thus do not

incorporate any spatial effects inherent in the criticals loaded with plate geometry. The resolution of measurements was never sufficient to reveal all of the resonance detail present in the calculated spectrum. Experimental resolution was known, however, and a smoothing of the MC^2 calculation over a Gaussian function with an energy-dependent width representing experimental resolution was made before plotting. Insofar as the overall experimental resolution function cannot be approximated by a Gaussian (generally this is so), any comparison of calculation and experiment will be subject to error.

Perhaps the most striking discrepancy between calculation and experiment occurs at low energies in Fig. III-18-1. Known sources of systematic error (in particular, pulse pileup distortion) probably occurred during the counting and additional errors (discussed below) may also have influenced results. Furthermore the discrepancy may also be due to the nonapplicability of equivalence theory to the complex unit cell of Aseembly 6 (see Paper No. III-1).

The calculated spatially dependent broad group neutron spectra shown in Figs. III-18-2, III-18-3, and III-18-4 were obtained with a one-dimensional diffusion theory calculation using cross-section set ZPR-6-6 ENDF/B-B (see Paper No. III-15).

Systematic Errors in the Measurements

These measurements were the last to be made with the spectrometer described in Refs. 1 and 2. The original instrument was used in several of the ZPR-3, ZPR-6, and ZPR-9 assemblies and a variety of sources of systematic error were identified during the period of its use.

An improved spectrometer has been built and the more apparent systematic errors, at least, have been reduced substantially although results on ZPR assemblies are not yet available. It is appropriate here to discuss these errors and to indicate the extent of their effect upon result.

CALIBRATION

An accurate relationship between ionization (pulse height) and proton energy is required for spectroscopy. Calibration with standard sources may provide this relationship; the method described in Ref. 1 (using the $N^{14}(n,p)C^{14}$ reaction together with a very simple assumption as to W behavior) does not provide good agreement as to the location of resonance detail, especially at low energies. The location of a resonance depression can be ascertained with considerable accuracy and a correspondingly precise calibration is required if agreement with theory is expected. One may question the significance of any detail measured within a large scattering-resonance as compared with an MC^2 calculation. The heterogeneous core arrangement, especially as obtained during measurements with a probe, may effect details within strong resonances in ways not allowed for by the calculations.

HEAVY PARTICLE RECOILS

Gas mixtures used for spectroscopy contain nuclei other than hydrogen (in particular carbon and nitrogen). Scattering from these nuclei will introduce a sizeable systematic error into the results of certain spectra, especially at lower energies. A correction has been made to allow for this effect but the correction is not reliable, due primarily to the lack of data on ionization from heavy particles stopping in hydrogen gas at low energies. The amount of contamination from these heavy nuclei was excessive for the measurements reported here. This source of systematic error can be greatly reduced in the future.

FINITE SIZE EFFECT

A method for treating numerically the systematic errors arising from finite size effects is given in Ref. 4. This method has been applied to the data shown here. The correction is expected to be generally adequate below about 1 MeV; residual systematic errors ought not be as large as statistics. At higher energies where most of the proton tracks are too long in range to be contained within the effective counter, the correction is large and the corrected spectrum is subject to increasingly large errors.

References

1. E. F. Bennett, *Fast Neutron Spectroscopy by Proton-Recoil Proportional Counting*, Nucl. Sci. Eng. **27**, 16 (1967).
2. E. F. Bennett, *Neutron Spectrum Measurement in a Fast Critical Assembly*, Nucl. Sci. Eng. **27**, 28 (1967).
3. E. F. Bennett, *A Modified Cascade Preamplifier for Proportional Counters*, Nucl. Instr. Methods **48**, 170 (1967).
4. E. F. Bennett, R. Gold and I. K. Olson, *Analysis and Reduction of Proton-Recoil Data*, ANL-7394 (1968).
5. B. J. Toppel, A. L. Rago and D. M. O'Shea, *A Code to Calculate Multigroup Cross Sections*, ANL-7318 (1967).

III-19. Fine-Spectral Interface Effects of Resonance Scattering Upon Multigroup Cross-Section Averaging

D. Meneghetti and K. E. Phillips

Introduction

Detailed neutron spectra and fine-flux-weighted coarse group cross sections for fundamental mode systems containing resonance scattering materials may be calculated by methods such as that used in the Argonne program ELMOE.[1] For the central region of a core wherein the flux spectrum is closely similar to that of an equivalent bare core, this space-independent approach suffices. In regions near interfaces or in reflector regions the fundamental mode solutions do not apply. Application of a method of iteration between spatial-dependent coarse group solutions and ELMOE calculations has been described.[2,3] The approximate method did not consider effects of fine-energy flux-detail across an interface.

More recently, however, a method of calculating fine-energy-detailed fluxes across an interface between media of differing resonance-scattering characteristics has been described.[4] This used a combination of the ELMOE library of angular scattering data in conjunction with the Argonne discrete-S_n code 2D-SNARG.[5] The two-dimensional program was used for these one-dimensional cases because the ordering of the calculation, proceeding group by group, keeping only those group constants for the current group in memory at any point in time, enabled a problem with a very large number of energy groups to be carried out. Furthermore, if the only projected usage for this ELMOE-SNARG linkage was for S_2 solutions a more efficient approach would be a more direct (non-discrete-ordinate) P_1 or consistent P_1 method.

The present study describes use of collapsed cross sections obtained by direct calculation of spatially-dependent fine-group solutions as energy and also spatial weighting factors.[6]

A sensitive measure of the effect of employing pointwise or subregionally-dependent cross sections for interface cases is the comparison of the calculated coarse-group leakages across an interface compared with the sum of the corresponding directly calculated fine-group leakages.

Method

Spatially-dependent fine-energy detailed fluxes through interfaces between various scattering media were directly calculated in the energy range of interest for resonance scattering effects. The fine-energy-group scattering cross sections used were those of the ELMOE library of angular scattering data. The fine equal-lethargy intervals had 0.982666 as the ratio of successive fine-energy-group boundaries. Since only the fine detail cross section data for the elastic scattering process are given in the ELMOE library, only the elastic transfer matrix and the scattering portion of the total (or transport) cross section are normally in fine cross section detail. In the usual usage of the ELMOE library other cross section processes are obtained from a much coarser cross section set and the assumption of cross section constancy over the fine groups encompassed within a coarse group is employed. The present studies also use coarse group cross sections for these processes. The choice of fine-group cross sections within the coarse group intervals, however, were instead smoothed by parabolic fitting. This circumvented the otherwise abrupt changes in cross section at the coarse energy group boundaries from effecting the smoothness of fine-group solutions in cases where the elastic scattering process is not the predominant process in the energy range of interest.

The cross section data were entered into a modified[4] version of the discrete S_n code 2D-SNARG. Only a limited range of energies were fine-group subdivided. In these studies the corresponding coarse groups were generally 0.5 lethargy units wide and the fine-energy structure consisted of about 28 to 30 equal lethargy subdivisions for each coarse interval.

The fine-solutions used for collapsing the fine-group cross sections to effective coarse group cross sections are applied fission source (inhomogeneous solution) anisotropic S_2 results. For simplicity of presentation, the one-dimensional slab geometry, consistent-P_1 equations rather than the linearly anisotropic S_2 equations are used in the following description of the spatially-dependent fine-solution-weighted cross section collapse. For fine-energy group j for a homogeneous region, the consistent P_1 equations

$$\frac{d\phi_j^1(z)}{dz} + \Sigma_j\phi_j^0(z) = \sum_{j'=1}^{j} \Sigma^0_{s_{j'\to j}}\phi_{j'}^0(z) + S_j(z) \quad (1)$$

and

$$\frac{1}{3}\frac{d\phi_j^0(z)}{dz} + \Sigma_j\phi_j^1(z) = \sum_{j'=1}^{j} \Sigma^1_{s_{j'\to j}}\phi_{j'}^1(z) \quad (2)$$

may be rewritten in terms of the fine-group diagonal transport cross section, $\Sigma^d_{tr_j} \equiv \Sigma_j - \Sigma^1_{s_{j'\to j}}$, and group removal cross section, Σ_{re_j}, as

$$\frac{d\phi_j^1(z)}{dz} + \Sigma_{re_j}\phi_j^0(z) = \sum_{j'=1}^{j-1} \Sigma^0_{s_{j'\to j}}\phi_{j'}^0(z) + S_j(z) \quad (3)$$

$$\frac{1}{3}\frac{d\phi_j^0(z)}{dz} + \Sigma^d_{tr_j}\phi_j^1(z) = \sum_{j'=1}^{j-1} \Sigma^1_{s_{j'\to j}}\phi_{j'}^1(z). \quad (4)$$

Since the energy-collapsed effective coarse-group cross sections were subsequently used in diffusion theory calculations, the coarse transport cross section at a given spatial position for a coarse group J was obtained by

$$\Sigma_{tr_J} = \frac{\sum_{j \text{ in } J} \Sigma^d_{tr_j}\phi_j^1 - \sum_{j \text{ in } J} \sum_{j'=1}^{j'=j-1} \Sigma^1_{j'\to j}\phi_{j'}^1}{\sum_{j \text{ in } J} \phi_j^1} \quad (5)$$

since from Eq. (4) both $\Sigma^d_{tr_j}$ and $\Sigma^1_{s_{j'\to j}}$ are current weighted. Coarse removal and coarse transfer cross sections were obtained by flux weighting taking account of transfers over coarse group boundaries.

Effective coarse group cross sections energy-collapsed over a subregion consisting of many mesh points used analogous formulae except that spatially-integrated fine-group fluxes and fine-group currents were used for the weightings.

Cases Studied

Four slab-geometry cases simulating core-reflector systems representing interface situations with differing abutting media have been studied. The geometrical dimensions in all four cases are identical and are shown in Fig. III-19-1.

The interface is at 30 cm from the core center. The applied source is a spatially-flat fission-energy-distribution source in the core region. The broken lines in Fig. III-19-1 show the possible subregions into which the core and reflector regions were subdivided for purposes of obtaining six subregional collapsed cross section sets for comparison with a separ-

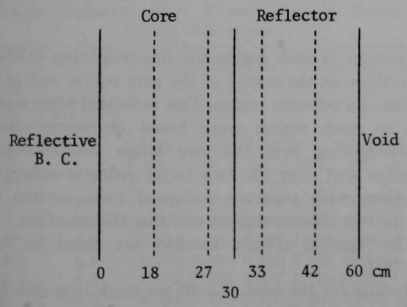

Fig. III-19-1. Slab-geometry Arrangement and Dimensions Used for Core-reflector Interface Studies. *ANL Neg. No. 113-1532.*

TABLE III-19-I. Regional Atomic Densities, 10^{24} atoms per cm^3

Case	Core		Reflector	
A	Al U-235	0.0603 0.004[a]	Fe	0.0847
B	C U-235	0.054 0.004[a]	Ni	0.0913
C	U-238 U-235	0.035[a] 0.004[a]	Al	0.0603
D	Pu-239 U-238 O Fe Ni Cr	0.00092[a] 0.00644[a] 0.01472 0.01044 0.001305 0.01472	Na	0.022

[a] Only the absorption property of fission and not the source property is used. Also these elements are not treated by the detailed Legendre polynomial expansion coefficients.

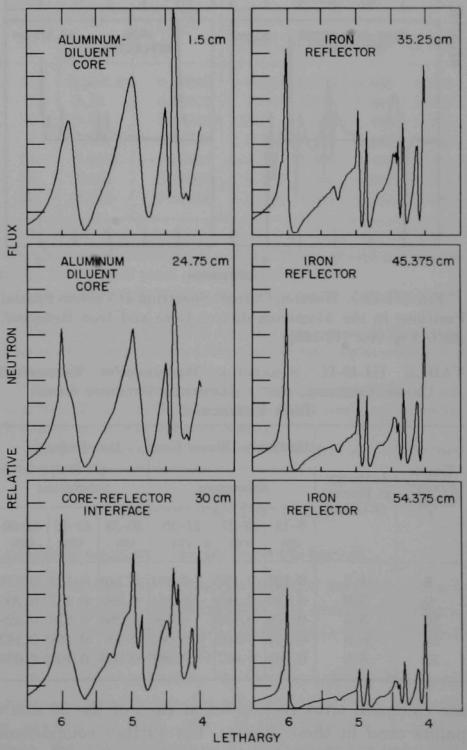

Fig. III-19-2. Neutron Flux Spectrum at Various Spatial Positions in the Aluminum-diluent Core and Iron Reflector. *ANL Neg. No. 113-1529.*

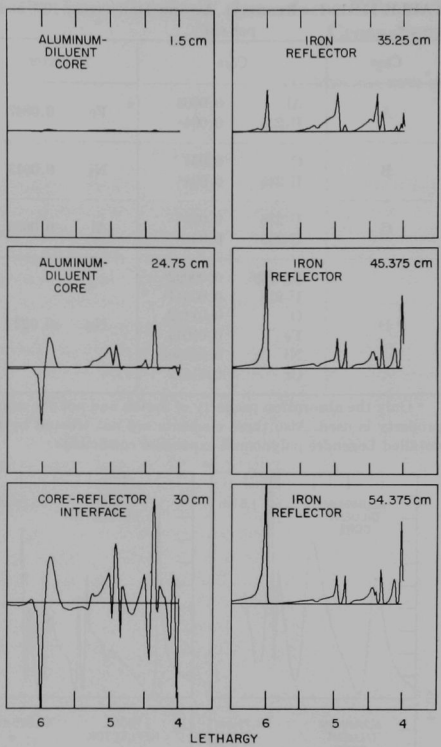

FIG. III-19-3. Neutron Current Spectrum at Various Spatial Positions in the Aluminum-diluent Core and Iron Reflector. *ANL Neg. No. 113-1534.*

TABLE III-19-II. SUBREGION MACROSCOPIC TRANSPORT CROSS SECTIONS, cm^{-1}: ALUMINUM-DILUENT CORE, IRON REFLECTOR

Coarse Energy Group, J	Lethargy at Bottom of Group	Aluminum-Diluent Core			Iron Reflector		
		Subregions			Subregions		
		0–18 cm	18–27 cm	27–30 cm	30–33 cm	33–42 cm	42–60 cm
8	4.5	0.197	0.112	−0.464	1.240	0.172	0.131
9	5.0	0.193	0.165	0.055	0.387	0.197	0.200
10	5.5	0.169	0.162	0.150	0.286	0.318	0.328
11	6.0	0.112	0.106	−0.002	2.15	0.168	0.182
12	6.5	0.086	0.087	0.087	0.005	0.104	0.096

ate collapsed cross section set at each of the 50 mesh points used in these studies. For further comparison one and two collapsed cross section sets were also obtained for each region. In the case of one collapsed cross section set in each region the fine-weighting solutions were those at the center of the core region and at the center of a reflector region. Two collapsed cross section sets in each region were based on energy-spatial fine-weighting over the two larger core-subregions together and over the two larger reflector-subregions together, with separate collapsed cross section sets for the two thinner regions abutting the interface.

The regional atomic densities are listed in Table III-19-I.

Results for the case of a 30 cm thick iron slab having an applied fission at one face will also be given later.

TABLE III-19-III. SUBREGION MACROSCOPIC ELASTIC TRANSFER ($J \rightarrow J + 1$) CROSS SECTIONS, cm^{-1}: ALUMINUM-DILUENT CORE, IRON REFLECTOR

Coarse Energy Group, J	Lethargy at Bottom of Group	Aluminum-Diluent Core			Iron Reflector		
		Subregions			Subregions		
		0–18 cm	18–27 cm	27–30 cm	30–33 cm	33–42 cm	42–60 cm
8	4.5	0.0329	0.0331	0.03871	0.0160	0.0159	0.0141
9	5.0	0.0274	0.0272	0.0261	0.0238	0.0220	0.0215
10	5.5	0.0154	0.0161	0.0186	0.0180	0.0223	0.0231
11	6.0	0.0097	0.0106	0.0117	0.0553	0.0395	0.0399
12	6.5	0.0029	0.0029	0.0028	0.0077	0.0086	0.0081

TABLE III-19-IV. CORE LEAKAGE: ALUMINUM-DILUENT CORE, IRON REFLECTOR

Coarse Energy Group, J	E_{lower}, MeV	Fine Group Calc.[a]	Coarse Group Calc./Fine Group Calc.			
			2 Sets[b]	4 Sets[c]	6 Sets[d]	50 sets[e]
8	0.11–0.18	0.000556	5.89	1.025	1.890	0.990
9	0.067	0.0165	0.840	0.974	0.982	1.000
10	0.0407	0.00926	1.463	1.053	1.014	1.000
11	0.025	0.00776	1.520	1.118	1.115	1.000
12	0.015	−0.0159	1.152	1.097	1.069	1.000

[a] Summed from directly calculated fine-group spatially dependent solution employing about 29 fine groups per coarse group. Based upon total applied source of unity.

[b] One coarse cross-section set in each region. Interface at 30 cm.

[c] Two coarse cross-section sets in each region. Subregional outer boundaries are 27 and 30 cm in the core region and 42 and 60 cm in the reflector region.

[d] Three coarse cross-section sets in each region. Subregional outer boundaries are 18, 27, and 30 cm in the core region and 33, 42, and 60 cm in the reflector region.

[e] Using 50 coarse cross-section sets at each of the 50 mesh intervals of the calculation.

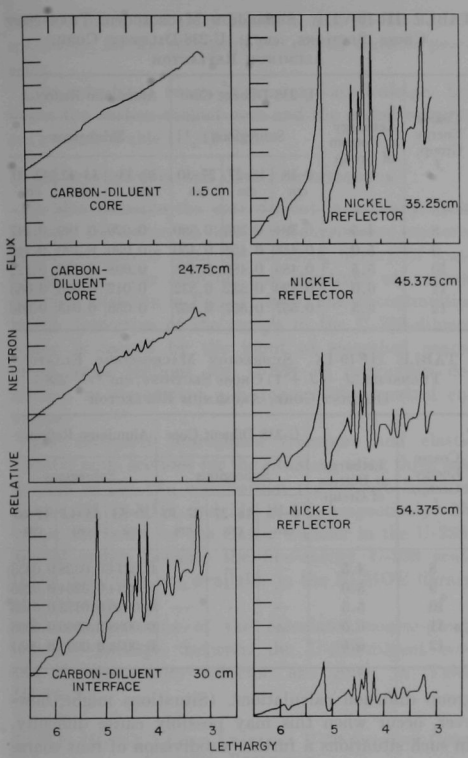

FIG. III-19-4. Neutron Flux Spectrum at Various Spatial Positions in the Carbon-diluent Core and Nickel Reflector. *ANL Neg. No. 113-1536.*

TABLE III-19-V. SUBREGION MACROSCOPIC TRANSPORT CROSS SECTIONS, cm^{-1}: CARBON-DILUENT CORE, NICKEL REFLECTOR

Coarse Energy Group, J	Lethargy at Bottom of Group	Carbon-Diluent Core			Nickel Reflector		
		Subregions			Subregions		
		0–18 cm	18–27 cm	27–30 cm	30–33 cm	33–42 cm	42–60 cm
6	3.5	0.210	0.214	0.213	0.426	0.326	0.317
7	4.0	0.241	0.234	0.229	0.511	0.457	0.455
8	4.5	0.264	0.276	0.409	1.469	0.403	0.381
9	5.0	0.276	0.263	0.237	0.686	0.531	0.518
10	5.5	0.283	.0.306	0.073	6.714	0.385	0.378
11	6.0	0.294	0.276	0.276	1.065	1.005	1.006
12	6.5	0.299	0.293	0.289	2.376	1.877	1.871

TABLE III-19-VI. SUBREGION MACROSCOPIC ELASTIC TRANSFER ($J \rightarrow J + 1$) CROSS SECTIONS, cm^{-1}: CARBON-DILUENT CORE, NICKEL REFLECTOR

Coarse Energy Group, J	Lethargy at Borrom of Group	Carbon-Diluent Core			Nickel Reflector		
		Subregions			Subregions		
		0–18 cm	18–27 cm	27–30 cm	30–33 cm	33–42 cm	42–60 cm
6	3.5	0.0604	0.0605	0.0597	0.0248	0.0234	0.0245
7	4.0	0.0675	0.0675	0.0677	0.0326	0.0333	0.0329
8	4.5	0.0748	0.0751	0.0757	0.0313	0.0308	0.0327
9	5.0	0.0733	0.0728	0.0698	0.0477	0.0392	0.0384
10	5.5	0.0728	0.0730	0.0707	0.0379	0.0333	0.0339
11	6.0	0.0773	0.0769	0.0768	0.0775	0.0737	0.0719
12	6.5	0.0747	0.0737	0.0702	0.1876	0.1512	0.1501

TABLE III-19-VII. CORE LEAKAGE: CARBON-DILUENT IN CORE, NICKEL REFLECTOR

Coarse Energy Group, J	E_{lower}, MeV	Fine Group Calc.[a]	Coarse Group Calc./Fine Group Calc.			
			2 Sets[b]	4 Sets[c]	6 Sets[d]	50 Sets[e]
6	0.3–0.5	0.00309	0.312	0.930	0.946	1.000
7	0.18	0.00521	1.016	0.978	1.016	1.000
8	0.11	0.000217	10.7	1.595	1.220	0.992
9	0.067	0.00856	0.591	0.937	0.952	1.000
10	0.0407	−0.00221	−4.37	0.495	0.498	1.005
11	0.025	0.00669	0.985	0.940	0.947	1.001
12	0.015	0.00906	0.740	0.841	0.845	1.000

[a] Summed from directly calculated fine-group spatially dependent solution employing about 29 fine groups per coarse group. Based upon total applied source of unity.

[b] One coarse cross-section set in each region. Interface at 30 cm.

[c] Two coarse cross-section sets in each region. Subregional outer boundaries are 27 and 30 cm in the core region and 42 and 60 cm in the reflector region.

[d] Three coarse cross-section sets in each region. Subregional outer boundaries are 18, 27, and 30 cm in the core region and 33, 42, and 60 cm in the reflector region.

[e] Using 50 coarse cross-section sets at each of the 50 mesh intervals of the calculation.

RESULTS AND DISCUSSION

ALUMINUM-DILUENT CORE AND IRON REFLECTOR

The neutron flux spectrum and the neutron current spectrum at various positions in the aluminum-diluent core and iron reflector case are shown in Figs. III-19-2 and III-19-3, respectively.

The penetration across the interface of the flux spectrum characteristic of the adjacent resonance scatterer is evident on both sides of the interface. Furthermore, the rapid variations in sign and magnitude with respect to energy and space, of the current indicates

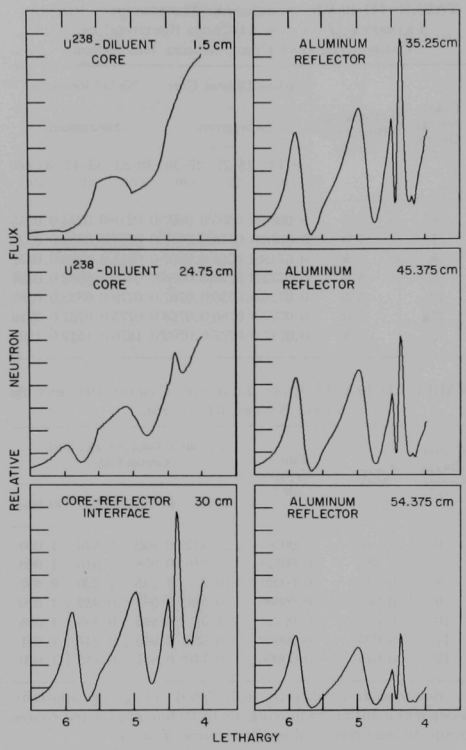

FIG. III-19-5. Neutron Flux Spectrum at Various Spatial Positions in the U-238 Core and Aluminum Reflector. *ANL Neg. No. 113-1530.*

the possible care required in collapsing transport cross sections in the locale of interfaces.

The collapsed cross sections for transport and elastic transfer for the approximation utilizing six cross section sets—three sets for the three core subregions and three sets for the three reflector subregions—are listed in Tables III-19-II and III-19-III, respectively. The transport values include both the light atom and heavy atom contributions. The elastic transfer values do not include the heavy atom contribution.

The collapsed transport cross sections are seen to vary considerably and in some instances be negative near interfaces. Negative values and small positive values occur from the combination of negative currents in some fine energy intervals with large values of fine group cross sections. In this series of studies the negative transport values did not appear to give rise to difficulties in their usage in the coarse group diffusion calculations. (Situations might, however, occur when this may possibly cause difficulty. In such situations a further subdivision of that coarse group into, for example, two coarse groups may circumvent the difficulty.)

TABLE III-19-VIII. SUBREGION MACROSCOPIC TRANSPORT CROSS SECTIONS, cm^{-1}: U-238-DILUENT CORE, ALUMINUM REFLECTOR

Coarse Energy Group, J	Lethargy at Bottom of Group	U-238-Diluent Core			Aluminum Reflector		
		Subregions			Subregions		
		0–18 cm	18–27 cm	27–30 cm	30–33 cm	33–42 cm	42–60 cm
8	4.5	0.394	0.393	0.390	0.620	0.189	0.147
9	5.0	0.448	0.454	0.450	−0.030	0.190	0.140
10	5.5	0.489	0.486	0.486	0.098	0.134	0.122
11	6.0	0.529	0.532	0.532	0.012	0.095	0.053
12	6.5	0.557	0.557	0.557	0.056	0.043	0.046

TABLE III-19-IX. SUBREGION MACROSCOPIC ELASTIC TRANSFER ($J \rightarrow J + 1$) CROSS SECTIONS, cm^{-1}: U-238-DILUENT CORE, ALUMINUM REFLECTOR

Coarse Energy Group, J	Lethargy at Bottom of Group	U-238-Diluent Core			Aluminum Reflector		
		Subregions			Subregions		
		0–18 cm	18–27 cm	27–30 cm	30–33 cm	33–42 cm	42–60 cm
8	4.5	—	—	—	0.0314	0.0328	0.0353
9	5.0	—	—	—	0.0244	0.0264	0.0295
10	5.5	—	—	—	0.0190	0.0175	0.0165
11	6.0	—	—	—	0.0088	0.0090	0.0098
12	6.5	—	—	—	0.0034	0.0033	0.0031

It is noted that utilization of a separate cross section for each mesh point results in interface leakage values essentially as in the reference fine-group calculation. The use of 2 or 3 subregional sets in each region is seen to give considerably better results than the simple use of one set for a given composition region. These coarse group calculations were carried out using the diffusion theory option of SNARG-1D.[6]

CARBON-DILUENT CORE AND NICKEL REFLECTOR

The neutron flux spectrum at various positions in the carbon-diluent core and nickel reflector case is shown in Fig. III-19-4. In this case the core diluent is a nonresonance scatterer and the reflector a resonance scatterer.

The collapsed subregional cross sections for the approximation utilizing three sets in each composi-

tion are listed in Tables III-19-V and III-19-VI, respectively, for the transport and elastic transfer processes.

The calculated coarse-group interface-leakages between the carbon-diluent core and the nickel reflector are given in Table III-19-VII.

U-238-DILUENT CORE AND ALUMINUM REFLECTOR

In this example the core diluent is a heavy atom and only the scattering data for the resonance scatterer of the reflector is from the ELMOE library of scattering data. The neutron flux spectrum at various positions is shown in Fig. III-19-5. The discontinuities in the derivative of the curves in the U-238-diluent region is caused by the input of smoothed coarse group cross sections for U-238 as previously described, to circumvent a histogram-like spectral envelope.

The collapsed subregional transport and elastic transfer cross sections for the situation using three sets in each of the two composition regions are listed in Tables III-19-VIII and III-19-IX, respectively. No values are listed for the elastic transfer in the U-238-diluent region because the fine-energy U-238 scattering data were not available in the ELMOE library of scattering data.

The comparisons of the calculated coarse-group interface leakages between the U-238-diluent core and the aluminum reflector are given in Table III-19-X.

TABLE III-19-X. CORE LEAKAGE: U-238-DILUENT CORE, ALUMINUM REFLECTOR

Coarse Energy Group, J	E_{lower}, MeV	Fine Group Calc.[a]	Coarse Group Calc./Fine Group Calc.			
			2 Sets[b]	4 Sets[c]	6 Sets[d]	50 Sets[e]
8	0.11–0.18	0.00164	2.64	1.274	1.083	0.999
9	0.067	−0.00824	0.856	0.953	0.992	1.000
10	0.0407	−0.00287	2.26	1.350	1.126	1.001
11	0.025	−0.0102	0.750	0.960	0.983	1.001
12	0.015	−0.00247	1.963	1.196	1.070	1.001

[a] Summed from directly calculated fine-group spatially dependent solution employing about 29 fine groups per coarse group. Based upon total applied source of unity.

[b] One coarse cross-section set in each region. Interface at 30 cm.

[c] Two coarse cross-section sets in each region. Subregional outer boundaries are 27 and 30 cm in the core region and 42 and 60 cm in the reflector region.

[d] Three coarse cross-section sets in each region. Subregional outer boundaries are 18, 27, and 30 cm in the core region and 33, 42, and 60 cm in the reflector region.

[e] Using 50 coarse cross-section sets at each of the 50 mesh intervals of the calculation.

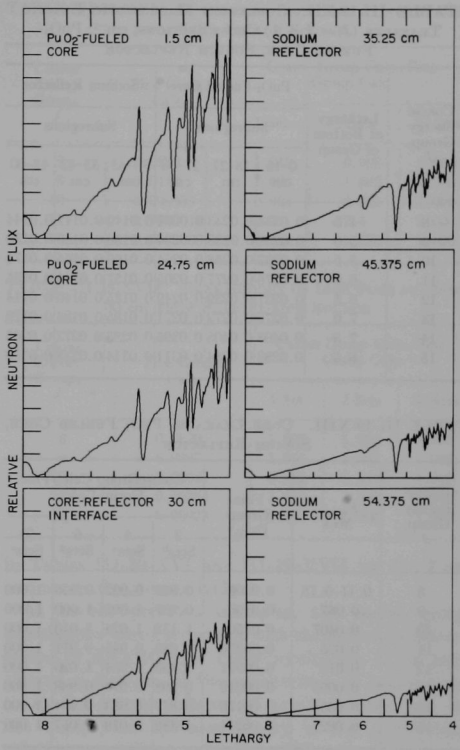

FIG. III-19-6. Neutron Flux Spectrum at Various Spatial Positions in the PuO_2 Fueled Core and Sodium Reflector. *ANL Neg. No. 113-1533.*

TABLE III-19-XI. SUBREGION MACROSCOPIC TRANSPORT CROSS SECTIONS, cm^{-1}: PuO_2-FUELED CORE, SODIUM REFLECTOR

Coarse Energy Group, J	Lethargy at Bottom of Group	PuO_2-Fueled Core			Sodium Reflector		
		Subregions			Subregions		
		0–18 cm	18–27 cm	27–30 cm	30–33 cm	33–42 cm	42–60 cm
8	4.5	0.221	0.220	0.215	0.0827	0.0804	0.0793
9	5.0	0.253	0.252	0.243	0.0980	0.0920	0.0894
10	5.5	0.258	0.260	0.268	0.1159	0.0930	0.0899
11	6.0	0.311	0.305	0.197	0.0900	0.0904	0.0882
12	6.5	0.265	0.263	0.261	0.0914	0.0901	0.0908
13	7.0	0.331	0.330	0.326	0.1079	0.1106	0.1118
14	7.5	0.471	0.470	0.462	0.1735	0.1644	0.1616
15	8.5	0.472	0.478	0.559	0.3866	0.2515	0.2427

TABLE III-19-XII. SUBREGION MACROSCOPIC ELASTIC TRANSFER ($J \rightarrow J + 1$) CROSS SECTIONS, cm^{-1}: PuO_2-FUELED CORE, SODIUM REFLECTOR

Coarse Energy Group, J	Lethargy at Bottom of Group	PuO_2-Fueled Core			Sodium Reflector		
		Subregions			Subregions		
		0–18 cm	18–27 cm	27–30 cm	30–33 cm	33–42 cm	42–60 cm
8	4.5	0.0234	0.0233	0.0231	0.0149	0.0147	0.0144
9	5.0	0.0238	0.0238	0.0234	0.0158	0.0153	0.0150
10	5.5	0.0257	0.0258	0.0264	0.0160	0.0165	0.0171
11	6.0	0.0276	0.0277	0.0265	0.0157	0.0144	0.0131
12	6.5	0.0237	0.0239	0.0249	0.0135	0.0140	0.0144
13	7.0	0.0272	0.0272	0.0271	0.0185	0.0184	0.0179
14	7.5	0.0408	0.0408	0.0395	0.0285	0.0273	0.0265
15	8.5	0.0283	0.0284	0.0311	0.0314	0.0338	0.0338

TABLE III-19-XIII. CORE LEAKAGE: PuO_2 FUELED CORE, SODIUM REFLECTOR

Coarse Energy Group, J	E_{lower}, MeV	Fine Group Calc.[a]	CoarseGroup Calc./Fine Gorup Calc.			
			2 Sets[b]	4 Sets[c]	6 Sets[d]	50 Sets[e]
8	0.11–0.18	0.0308	0.962	0.992	0.996	1.000
9	0.067	0.0196	0.997	1.002	1.000	1.000
10	0.0407	0.0150	1.132	1.024	1.010	1.000
11	0.025	0.00876	0.686	0.945	0.971	1.000
12	0.015	0.00971	1.195	1.034	1.020	1.000
13	0.0091	0.00619	0.898	0.970	0.988	1.000
14	0.0055	0.00170	0.877	0.983	0.994	1.000
15	0.0021	0.00214	1.482	1.070	1.057	1.000

[a] Summed from directly calculated fine-group spatially dependent solution employing about 29 fine groups per coarse group. Based upon total applied source of unity.

[b] One coarse cross-section set in each region. Interface at 30 cm.

[c] Two coarse cross-section sets in each region. Subregional outer boundaries are 27 and 30 cm in the core region and 42 and 60 cm in the reflector region.

[d] Three coarse cross-section sets in each region. Subregional outer boundaries are 18, 27, and 30 cm in the core region and 33, 42 and 60 cm in the reflector region.

[e] Using 50 coarse cross-section sets at each of the 50 mesh intervals of the calculation.

PuO_2-FUELED CORE AND SODIUM REFLECTOR

In this example the composition of the core region simulates a PuO_2-fueled core containing sodium coolant and steel structural materials. The sodium reflector region can represent a plenum. Details of neutron flux spectrum at various spatial positions are shown in Fig. III-19-6. For this example a larger number of coarse energy groups was subdivided into fine groups in order to insure that the lower groups containing the large resonance of sodium would be included.

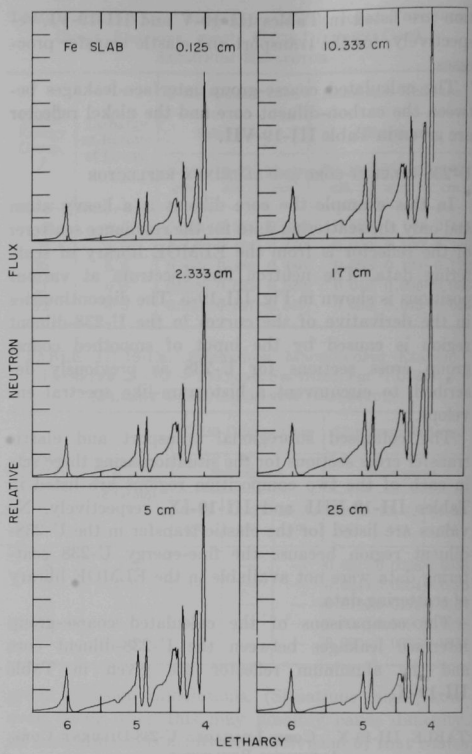

FIG. III-19-7. Neutron Flux Spectrum at Various Spatial Positions in the Iron Slab. *ANL Neg. No. 113-1528.*

The spectrum variations due to the sodium scattering resonance structure are only those caused by the sodium resonances having widths which are close to the fine-energy group intervals. The many narrower sodium resonances thus do not show explicitly their effects upon the spectrum fine structure.

The collapsed cross sections corresponding to the situation having each composition region described by three subregional sets are shown in Tables III-19-XI and III-19-XII, respectively, for the transport process and for the light-materials elastic transfer process.

Comparisons of calculated coarse interface-leakages between the representative PuO_2-fueled core and the sodium plenum are given in Table III-19-XIII.

IRON SLAB WITH APPLIED SOURCE AT A SURFACE

In this example a 30 cm thick iron slab was assumed to have an applied fission-spectrum source at one surface. The detailed spectrum at various positions, over an energy range of interest for studying resonance scattering effects, is shown in Fig. III-19-7. For this case, in addition to collapse of a separate coarse cross section set at each of 50 mesh intervals, a one-set and a two-set collapse were also obtained. The one-set collapsed cross sections used the fine flux and current solutions corresponding to the midpoint of the slab. The two-set coarse cross sections used the spatial-averaged fluxes and the spatial-averaged currents corresponding to the subregions from 0 to 2 cm from the source and from 2 to 30 cm from the source. The collapsed cross sections for the latter subregional division are listed in Tables III-19-XIV and III-19-XV, respectively, for the transport and elastic transfer processes.

In this case the calculated coarse currents at the 2 cm position and the leakage out of the slab at the 30 cm position, using one, two, and 50 cross section sets, are compared with the corresponding values by the direct fine-group solution. These results are given in Tables III-19-XVI and III-19-XVII for the 2 cm and outer edge, respectively.

As in the previous examples, the coarse group calculations were carried out with the diffusion-theory-option of SNARG-1D. These results are to be considered a measure of the sensitivities of calculations to spatial-energy collapse of cross sections and do not imply that diffusion theory is the appropriate solution approximation for the problems.

TABLE III-19-XIV. SUBREGION MACROSCOPIC TRANSPORT CROSS SECTIONS, cm^{-1}: IRON SLAB

Coarse Energy Group, J	Lethargy at Bottom of Group	Iron Slab	
		Subregions	
		0–2 cm	2–30 cm
8	4.5	0.138	0.138
9	5.0	0.211	0.221
10	5.5	0.318	0.336
11	6.0	0.282	0.260
12	6.5	0.098	0.093

TABLE III-19-XV. SUBREGION MACROSCOPIC ELASTIC TRANSFER ($J \rightarrow J + 1$) CROSS SECTIONS, cm^{-1}: IRON SLAB

Coarse Energy Group, J	Lethargy at Bottom of Group	Iron Slab	
		Subregions	
		0–2 cm	2–30 cm
8	4.5	0.0108	0.0121
9	5.0	0.0173	0.0179
10	5.5	0.0151	0.0192
11	6.0	0.0412	0.0366
12	6.5	0.0037	0.0060

TABLE III-19-XVI. CURRENT IN IRON SLAB AT ABOUT 2 cm FROM SLAB FISSION SOURCE

Coarse Energy Group, J	Fine Group Calc.	Coarse Group Calc./Fine Group Calc.		
		1 Set	2 Sets	50 Sets
8	0.0230	1.010	0.996	1.000
9	0.0118	1.020	1.002	1.000
10	0.000953	0.924	0.994	1.000
11	0.0000044	35.0	−2.4	1.000
12	0.000326	0.740	1.035	1.000

TABLE III-19-XVII. LEAKAGE OUT OF IRON SLAB AT ABOUT 30 cm FROM SLAB FISSION SOURCE

Coarse Energy Group, J	Fine Group Calc.	Coarse Group Calc./Fine Group Calc.		
		1 Set	2 Sets	50 Sets
8	0.0629	1.007	1.000	1.000
9	0.0267	1.026	1.007	1.000
10	0.00921	0.952	0.982	1.000
11	0.00364	1.012	1.030	1.000
12	0.00973	1.053	1.028	1.000

REFERENCES

1. A. L. Rago and H. H. Hummel, *An IBM-704 Program Treating Elastic Scattering Resonances in Fast Reactors*, ANL-6805 (1964).
2. D. Meneghetti, *Evaluation of Group Cross Sections for Light Reflectors*, Trans. Am. Nucl. Soc. **8**, 247 (1965).
3. D. Meneghetti, *Effects of Leakage Upon Evaluation of Fast Reactor Multigroup Cross Sections for Reflectors*, ANL-7170 (1966).
4. D. Meneghetti, A. L. Rago and K. E. Phillips, *Use of the ELMOE-SNARG Programs to Study Details of Neutron Spectra Through Regions of Resonance Scattering Media*, Resumenes de los Articulos Presentados en la Conferencia Internacional sobre Utilization de Reactores de Investigacion y Computo y Mathematicas de Reactores, Mexico City, 1967.
5. G. J. Duffy, H. Greenspan, S. D. Sparck, J. V. Zapatka and M. K. Butler, *SNARG-2D, A Two-Dimensional, Discrete-Ordinate Transport Theory Program for the CDC-3600*, ANL-7426 (1968).
6. D. Meneghetti and K. E. Phillips, *Fine-Spectral Interface Effects of Resonance Scattering Upon Multigroup Cross-Section Averaging*, Trans. Am. Nucl. Soc. **11**, 205 (1968).

III-20. Calculated Spatially-Dependent Fine-Energy Neutron Spectrum for ZPR-3 Assembly 51

D. Meneghetti and K. E. Phillips

Results of neutron spectrum measurements in core and reflector regions of ZPR-3 Assembly 51, the first of a series of critical assemblies in support of the Fast Flux Test Facility (FFTF), using a proton-recoil neutron spectrometer have been reported by J. Powell.[1]

A spatially-dependent fine-energy-detailed neutron flux spectrum using 371 equal-lethargy energy groups

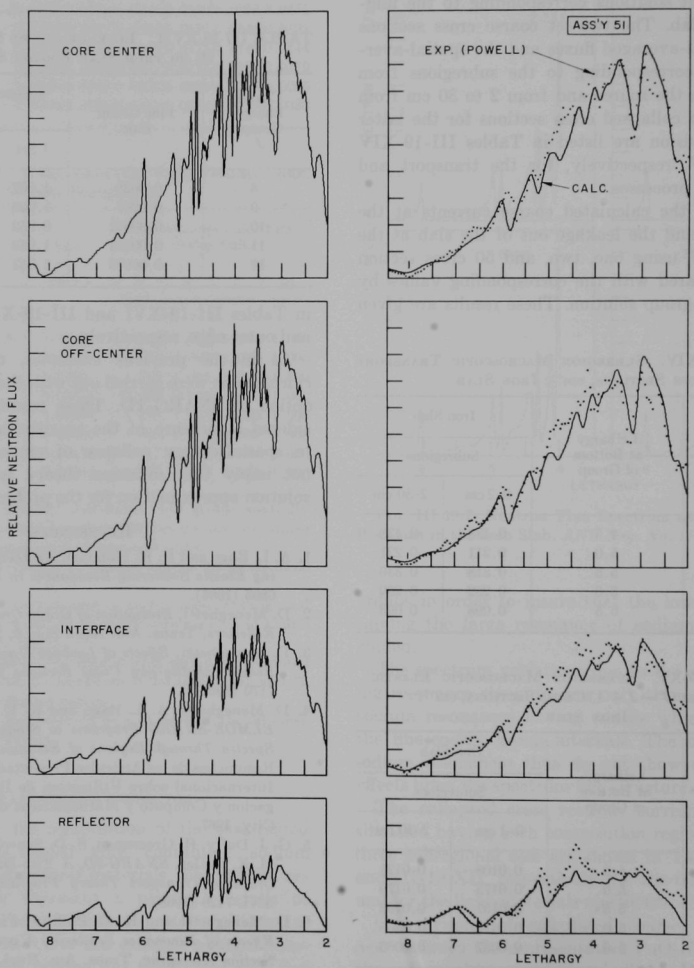

Fig. III-20-1. Calculated Position-dependent Fine-spectrum Compared with Experiment. *ANL Neg. No. 113-558.*

in the energy range 2.1 keV to 1.35 MeV has been calculated by use of a composite[2] of the ELMOE library of angular scattering data and the Argonne discrete S_n transport code. Cross sections other than those for transport and elastic transfer properties were derived by smoothing the coarse cross sections in the Yiftah, Okrent and Moldauer compilation.[3] Cross section smoothing was done to prevent cross section discontinuities at the coarse group boundaries from distorting local spectral variations. The one-dimensional cylindrical geometry S_2 analysis was an inhomogeneous calculation and used the transport approximation. The inhomogeneous calculation utilized an estimated spatially distributed fission source in the core to circumvent the need for source iteration. Axial leakage effects were included by using fine-energy leakage-absorptions.

The assembly had a plutonium-fueled core and a two-zone radial reflector. The inner and outer radial reflectors consisted of nickel, sodium, and steel-matrix and iron and steel-matrix, respectively, The cylindricalized core radius used in the analysis was 28.1 cm. The outer radii of the radial reflectors were 47.6 and 64.0 cm respectively. The radial dimensions of Assembly 51 are smaller than the normal dimensions since a larger degree of subcriticality had been necessary in the reported spectral measurements in order to reduce the spontaneous neutron background due to plutonium.

Both high resolution calculated spectra and calculated spectra through a 15% resolution Gaussian energy-window at positions approximately corresponding to the four experimental positions reported by Powell are shown in Fig. III-20-1. The calculated positions are at the core center, at 11.2 cm, at 25.2 cm (near the core-reflector interface), and at 36.2 cm (near the center of the nickel-sodium reflector). For comparison, the experimental data[1, 4] are also shown. The calculated and experimental values have been normalized at the core center for best fit over the energy range of interest. Since a coarse energy structure was used above 1.35 MeV (2.0 lethargy) the lethargy region corresponding to the energy just below 1.35 MeV contains distortion of the envelope of the flux-shape which tends to make the calculated flux too low near that energy interface. Structures in the spectra are primarily due to iron, oxygen, chromium, nickel and sodium in the core and to nickel, sodium and iron in the reflector.

References

1. J. E. Powell, *Fast-Neutron Spectrum Measurements in the Core and Reflector of ZPR-3 Assembly 51*, Trans. Am. Nucl. Soc. **11**, 217 (1968).
2. D. Meneghetti, A. L. Rago and K. E. Phillips, *Use of the ELMOE-SNARG Programs to Study Details of Neutron Spectra Through Regions of Resonance-Scattering Media*, Proc. International Conference on Research Reactor Utilization and Reactor Mathematics, Mexico City (May 1967).
3. S. Yiftah, D. Okrent and P. A. Moldauer, *Fast Reactor Cross Sections*, (Pergamon Press, New York, 1960).
4. J. E. Powell, Argonne National Laboratory (private communication).

III-21. Analysis of Central Reactivity Worths Incorporating Self-Shielding

T. Nakamura,* R. A. Karam and D. K. Dance

The central reactivity worth of a material provides a convenient means of verifying material cross section data sets in a particular neutron spectrum if sample size effects are accounted for correctly. In this work, corrections to first order perturbation theory incorporating self-shielding effects both inside and outside the sample, as well as scattering, fission, and edge effect perturbations were made in each energy group.

Theory

The basic concept used was the calculation of the ratio of the actual average flux in the sample to the unperturbed flux for each energy group. This ratio was then used to multiply the components of $\delta k/k$, i.e. absorption, fission, scattering and leakage in each group, obtained from first order perturbation (FOP) calculations. The perturbed-to-unperturbed flux ratio R_i in group i can be expressed as

$$R_i = \frac{\overline{C_i}}{(\Sigma_a)_i T \phi_i^0} \tag{1}$$

where $\overline{C_i}$ is the absorption rate in group i per unit surface area of a finite sample of thickness T, Σ_{ai} is the absorption cross section in group i, and ϕ_i^0 is the unperturbed flux prior to the insertion of the sample.

The formulation for $\overline{C_i}$ is based in part on the single

* Visiting Scientist, Japan Atomic Energy Research Institute, Tokai-mura, Japan.

scattering treatment given by K. Beckhurt and K. Wirtz.[1] We consider first the infinite slab problem. For such a case the number of neutrons in group i which suffer their first collision in dx about x is[1]

$$P_{1i}(x)\,dx = (\phi_i^0/2)\{E_2[\Sigma_{ti}(T-x)] + E_2(\Sigma_{ti}x)\}\Sigma_{ti}\,dx, \tag{2}$$

where

ϕ_i^0 is the unperturbed flux
$E_2(\ )$ is the exponential function of order 2
Σ_{ti} is the total cross section in group i
T is the thickness of the slab.

The fraction of the total collisions which lead to absorption in group i is given by $(\Sigma_{ai}/\Sigma_{ti})$, whereas the number of neutrons born into any group j due to a collision in group i is given by

$$A_{i\to j} = \frac{\Sigma_{si\to j} + \chi_j(\nu\Sigma_f)_i}{\Sigma_{ti}}. \tag{3}$$

The probability that a neutron isotropically scattered in dx about x in the sample escapes without making another collision is

$$\tfrac{1}{2}\{E_2[\Sigma_{ti}(T-x)] + E_2(\Sigma_{ti}x)\};$$

therefore the nonescape probability is

$$B_j(x) = 1 - \tfrac{1}{2}\{E_2[\Sigma_{tj}(T-x)] + E_2(\Sigma_{tj}x)\} \tag{4}$$

and the number of neutrons which suffer a second collision in group j is

$$P_{2j} = \sum_{i=1}^{NG} A_{i\to j}\int_0^T P_{1i}(x)B_j(x)\,dx. \tag{5}$$

The symbol NG designates the number of groups. Note that the summation over $i = 1$ to NG is done to allow for fission neutrons contributed to the various groups when the collision ends in a fission. Now, given that a second collision takes place and assuming that P_{2j}, an integral quantity over the sample, has a flat distribution, the number of neutrons that suffer three collisions is

$$P_{3j} = \sum_{i=1}^{NG} A_{i\to j}\int_0^T (P_{2i}/T)B_j(x)\,dx, \tag{6}$$

which may be written as

$$P_{3j} = \sum_{i=1} A_{i\to j}P_{2i}\overline{B}_j, \tag{7}$$

where

$$\overline{B}_j = \int_0^T B_j(x)\,dx \Big/ \int_0^T dx.$$

In a similar manner the number of neutrons that undergo k collisions are

$$P_{kj} = \sum_{i=1}^{NG} A_{i\to j}P_{k-1,i}\overline{B}_j. \tag{8}$$

The total number of neutrons absorbed in the infinite slab of thickness T in group j after k collisions can now be written as

$$\begin{aligned} C_j = (\Sigma_{aj}/\Sigma_{tj})\Bigg\{&\int_0^T P_{1j}(x)\,dx \\ &+ \sum_{i=1}^{NG} A_{i\to j}\int_0^T P_{1i}(x)B_j(x)\,dx \\ &+ \overline{B}_j\sum_{i=1}^{NG} A_{i\to j}\left(\sum_{n=1}^{NG} A_{n\to i}\int_0^T P_{1n}(x)B_i(x)\,dx\right) \\ &+ \ldots + \left[\overline{B}_j\sum_{i=1}^{NG} A_{iTj}P_{k-1,i}\right]\Bigg\}. \end{aligned} \tag{9}$$

The foregoing development is rigorous within the broad group approximation of the neutron spectrum for infinite slabs only. Considerations of neutrons that make collisions through the edge of a disc-shaped sample was treated by G. Hanna.[2] The increase in the number of collisions due to the finiteness of the sample can be represented as

$$P'_{kj} = P_{kj}(1 + \epsilon_j), \tag{10}$$

where P'_{kj} is the number of neutrons that suffer k collisions in the finite sample and ϵ is given by the expression

$$\epsilon_j = \{2\Sigma_{tj}T/[1-2E_3(\Sigma_{tj}T)]\}[2/(\pi n)]\{I[\Sigma_{tj}T - \Delta(n\Sigma_{tj}T)]\}, \tag{11}$$

where

$$n = 2(R/T) \equiv \text{the radius-to-thickness ratio},$$

$$\begin{aligned} I(\Sigma_{tj}T) = (2/\Sigma_{tj}T)\int_0^{\pi/2}\{1 + e^{-\Sigma_{tj}T\sec\theta} \\ - [2/(\Sigma_{tj}\sec\theta)](1 - e^{-\Sigma_{tj}T\sec\theta})\}\sin^2\theta\,d\theta, \end{aligned} \tag{12}$$

and

$$\Delta(n\Sigma_{tj}T) = \int_0^1 E_2(n\Sigma_{tj}T\sin\phi)\,d(\cos\phi). \tag{13}$$

As the collision density increases because of the finite size of the sample so does the escape probability. The decrease in the nonescape probability due to the finiteness of sample is taken into account by multiplying the quantities B_j of Eq. (4) by the ratio of the nonescape probabilities of the finite to the infinite samples as obtained from the rational approximation. Specifically this ratio can be written as:

$$K_i = \frac{\left(1 - \dfrac{1}{1 + \dfrac{4V}{S}\Sigma_{tj}}\right)_{finite}}{\left(1 - \dfrac{1}{1 + \dfrac{4V}{S}\Sigma_{tj}}\right)_{infinite}} = \frac{1 - \dfrac{1}{1 + \dfrac{2\Sigma_{tj}T}{1 + \dfrac{T}{R}}}}{1 - \dfrac{1}{1 + 2\Sigma_{tj}T}}, \tag{14}$$

where V and S are the volume and surface area of the sample.

Finally the effect of the sample on the flux outside the sample must be considered. The outer flux perturbation may be defined as the ratio of the flux at the surface of the sample to the flux at the same point prior to the introduction of the sample. This perturbation factor, according to R. Ritchie and H. Eldridge,[3] can be expressed as

$$F_i = (1 + \{\tfrac{1}{2} - E_3[\Sigma_{ti}T]\}g_i)^{-1}, \tag{15}$$

where the g factor can be approximated according to Ref. 4 by the relation

$$g_i = 1.05\, R/\lambda_{ti}\,. \tag{16}$$

where λ_{ti} is the total mean free path in group i of the core material.

The final relationship governing the number of neutrons absorbed per unit area in a circular disk of radius R and thickness T in group j after k collisions can be written as

$$\begin{aligned}\overline{C}_j = (F_j\Sigma_{aj}/\Sigma_{tj}) \Bigg\{ & \int_0^T P'_{1j}(x)\,dx \\ & + \sum_{i=1} K_j A_{i\to j} \int_0^T P'_{1i}(x) B_j(x)\,dx \\ & \cdot \overline{B}_j \left(\sum_{i=1}^{NG} K_j A_{i\to j}\right) \left[\sum_{n=1}^{NG} K_i A_{n\to i}\right. \\ & \left. \cdot \int_0^T P_{1n}(x) B_i(x)\,dx\right] + \ldots \\ & + \overline{B}_j \sum_{i=1}^{NG} K_j A_{i\to j} P_{k-1,i} \Bigg\}.\end{aligned} \tag{17}$$

Equation (17) was used in conjunction with Eq. (1) to obtain the appropriate correction factors to first order perturbation calculations.[5]

Comparison of Theory and Measurements

The foregoing theoretical treatment of self-shielding was applied to calculate the central reactivity worths of various samples whose worths have been measured in a large oxide core, Assembly 6 of ZPR-6. Assembly 6 was a 4000 liter cylindrical core reflected with 30 cm of depleted uranium (0.2% enrichment). Complete details of this assembly were reported elsewhere (see Paper III-1).

The reactivity worth of a sample was measured by either of two methods: (1) If the reactivity of a sample was one inhour or more, its worth was determined by the period method, i.e. measuring repetitively the period of a slightly above critical system (~10 Ih) with and without (void) the sample at the center of the core. The accuracy of this procedure is typically 0.005 Ih. (2) The reactivity of small samples was determined by oscillating the sample relative to void and using a calibrated autorod. The accuracy inherent in this technique can be as low as 0.001 Ih provided the autorod is accurately calibrated. The samples used were 2 in. square (nominally) by various thicknessess.

The calculated and measured values for the central worths in Assembly 6 are compared in Table I. The third column in Table III-21-I lists the calculated values obtained using first order perturbation[4] (FOP) theory and Cross Section Set 224.[6] Values in parentheses were obtained with Set ZPR-6-6 ENDF/B-A generated specifically for Assembly 6 (see Paper III-1). The FOP values were corrected for self-shielding according to Eq. (17) with the number of consecutive scatterings terminated after 5, and the results are listed in the fourth column of Table III-21-I. The measured values are listed in the last column.

It is seen from Table III-21-I that a significant improvement in the agreement between the calculated and measured values results as a consequence of the self-shielding corrections. Note that for B-10, where the cross sections are smooth with energy, the agreement between the calculated and measured value is very good. For U-238, which has many resonances, the agreement with measurements is good for the thinnest and thickest samples. This may be due to negligible self-shielding in the thinnest sample and to a small contribution from resonance neutrons to the total worth of the large sample. The calculated values of iron, chromium, niobium, aluminum and molybdenum are somewhat higher than the measured values. This discrepancy could very well be due to the inadquacy of the multigroup approximation to the neutron spectrum in the resonance energy range rather than to inaccuracies in basic data. In the case of nickel, ENDF/B data seem to result in low values for the cross sections. For molybdenum, the ENDF/B values are significantly different from those of Cross Section Set 224. The calculated and measured values of U-235 are in good agreement.

TABLE III-21-I. MEASURED AND CALCULATED CENTRAL REACTIVITY WORTHS IN ASSEMBLY 6 OF ZPR-6

Material	Sample Weight, g	Calculated Worth,[a] Ih[(b)]				Measured Worth, Ih
		First Order Perturbation (FOP)		FOP Corrected for Self-Shielding		
Fe	488.0	−0.745[d]	(−0.658)[e]	−0.646	(−0.561)	−0.450 ± 0.004
Ni	546.0	−1.069	(−0.721)	−0.929	(−0.748)	−0.833 ± 0.008
Cr	220.73	−0.363	(−0.403)	−0.352	(−0.369)	−0.222 ± 0.008
Na	51.38	−0.023	(+0.002)	−0.033	(−0.004)	+0.013 ± 0.008
B-10	29.29	−33.015	(−32.842)	−21.945	(−22.145)	−23.209 ± 0.010
Ti	90.42	−0.045	—	−0.061	—	+0.026 ± 0.013
Zr	406.0	−0.464	—	−0.425	—	−0.443 ± 0.007
Nb	481.2	−5.259	—	−4.290	—	−3.525 ± 0.007
Mo	599.0	−3.888	(−6.211)	−3.165	(−4.371)	−3.115 ± 0.021
Al	165.33	−0.279	(−0.204)	−0.263	(−0.192)	−0.122 ± 0.010
C	103.0	+0.036	)+0.060)	+0.042	(+0.066)	+0.366 ± 0.002
Be	114.31	—	(−0.4711)	—	(−0.352)	+1.304 ± 0.003
U-238	5.913	−0.0211	(−0.0248)	−0.0211	(−0.0248)	−0.0252 ± 0.002
U-238	11.739	−0.0420	(−0.0493)	—	(−0.0494)	−0.0429 ± 0.002
U-238	28.977	−0.1037	(−0.1216)	—	(−0.122)	−0.103 ± 0.002
U-238	60.227	−0.215	(−0.253(	—	((−0.255)	−0.220 ± 0.002
U-238	147.123	−0.526	(−0.617)	—	(−0.623)	−0.514 ± 0.002
U-238	1153.580	−4.132	(−4.838)	—	(−3.710)	−3.764 ± 0.003
U-235	4.511	—	(+0.191)	—	(+0.190)	+0.186 ± 0.002
U-235	22.950	—	(+0.969)	—	(+0.986)	+0.947 ± 0.002
U-235	61.491	—	(+2.596)	—	(+2.665)	+2.567 ± 0.020

[a] Calculated with one-dimension diffusion theory.[4]
[b] 1% $\Delta k/k$ = 458 Ih.
[c] The number of consecutive scatterings in sample was terminated after 5.
[d] Values obtained from Cross Section Set 224.[(6)]
[e] Values in parenthesis obtained from ENDF/B parameters.

TABLE III-21-II. CALCULATED CENTRAL REACTIVITY WORTHS AS A FUNCTION OF THE NUMBER OF CONSECUTIVE SCATTERINGS IN SAMPLE, ZPR-6

Material	Sample Size, in.	Worth, Ih[(a)]				
		Measurement	FOP[(b)] Values	No. of Consecutive Scatterings in Sample		
				1	3	5
Na	2 x 2 x 1	+0.013 ± 0.008	−0.00230	−0.00989	−0.00503	−0.00434
Fe	2 x 2 x 1	−0.450 ± 0.004	−0.6581	−0.4856	−0.5448	−0.5607
Ni	2 x 2 x 1	−0.832 ± 0.008	−0.7204	−0.7184	−0.7514	−0.7477
Cr	2 x 2 x 1	−0.222 ± 0.008	−0.4034	−0.3375	−0.3622	−0.3692
B-10	2 x 2 x 1	−23.208 ± 0.012	−32.842	−21.812	−22.139	−22.145
Mo	2 x 2 x 1	−3.115 ± 0.021	−6.2113	−3.5795	−4.2362	−4.3713
Al	2 x 2 x 1	−0.122 ± 0.010	−0.2042	−0.1803	−0.1906	−0.1920
Mn	2 x 2 x 1	−0.481 ± 0.006	−1.1963	−0.5028	−0.5702	−0.5939
Be-9	2 x 2 x 1	−1.304 ± 0.003	−0.4711	−0.5686	−0.4325	−0.3525
C	2 x 2 x 1	−0.366 ± 0.001	0.06037	0.00991	0.05527	0.06644

[a] 1% $\Delta k/k$ = 458 Ih.
[b] First order perturbation theory calculations with ENDF/B data.

The disagreement between the calculated and measured values of scattering materials such as carbon and beryllium may be associated with inaccuracies in the calculated adjoint fluxes rather than with errors in basic data.

The calculated worth as a function of the number of consecutive scatterings in the sample for a few materials is shown in Table III-21-II. It is seen that convergence has been achieved with five scatterings for practically all the materials except sodium, beryllium, and carbon.

REFERENCES

1. K. H. Beckurts and K. Wirtz, *Neutron Physics*, translated by L. Dresner, (Springer-Verlag, New York, Inc. 1964, pp. 239–246.
2. G. C. Hanna, *The Neutron Flux Perturbation Due to an Absorbing Foil; A Comparison of Theories and Experiments*, Nucl. Sci. Eng. **15**, 325 (1963).
3. R. H. Ritchie and H. B. Eldridge, *Thermal Neutron Flux Depression by Absorbing Foils*, Nucl. Sci. Eng. **8**, 300 (1960).
4. Reactor Physics Constants, Section 9, ANL-5800 (1963).
5. D. A. Meneley, L. C. Kvitek and D. M. O'Shea, *MACH-1, A One-Dimensional Diffusion-Theory Package*, ANL-7223 (1966).
6. D. M. O'Shea, H. H. Hummel, W. S. Lowenstein and D. Okrent, *Twenty-Six Group Cross Sections*, Trans. Am. Nucl. Soc. **7**, 242, (1964).

III-22. Measurement of the Capture-to-Fission Ratio of U-235 and Pu-239 in the Kilovolt Region Using Critical Assembly Null-Reactivity Techniques

C. E. TILL, L. G. LESAGE, G. S. STANFORD, E. F. GROH and W. R. ROBINSON

Spectrum averaged values for the capture-to-fission ratio for U-235 and Pu-239, in spectra designed to maximize the number of reactions in the kilovolt region, have been measured using the null-reactivity technique. The measurements were made in a zoned fast critical assembly, ZPR-9 Assembly 24. The composition of the test zone in Assembly 24 was experimentally adjusted to establish a k_∞ of unity, so that the total fission source rate equalled the total absorption rate in a central region. The fission rates and the important capture rates, except for the fissile element capture, were measured directly.

The following section contains a brief discussion of the theory of this experiment, and the final section describes the conduct of the experiment. The final results are not available at the time of this writing.

DISCUSSION

In order for the fission sources to equal the absorptions, it is necessary both that the measured reactivity worth of the test zone material be equal to zero and also that the spectrum in the test region be the infinite-medium spectrum characteristic of the test zone composition. If the spectrum is not correct, it is possible for the fission sources and the absorption not to be equal, and to still have an indicated null reactivity. The following equations for the capture-to-fission ratios for U-235 and Pu-239 are obtained by equating the fission sources and the absorptions.

$$\alpha^{25} = (\nu^{25} - 1) + (1/F^{25})[\nu^{28} - 1)F^{28} - C^{28} - C^{ss}] \quad (1)$$

and

$$\begin{aligned}\alpha^{49} = (\nu^{49} - 1) + (1/F^{49})[(\nu^{25} - 1)F^{25} \\ + (\nu^{28} - 1)F^{28} + (\nu^{40} - 1)F^{40} \\ + (\nu^{41} - 1)F^{41} - (C^{25} + C^{28} + C^{40} + C^{41} \\ + C^{ss})],\end{aligned} \quad (2)$$

where α is the capture-to-fission ratio, C and F are the average radiative capture and fission rates in the test region, respectively, and the superscripts refer to the isotopes, with "*ss*" referring to stainless steel. In order to determine the alpha values, the important terms on the right-hand sides of Eqs. (1) and (2) are measured individually. The exceptions are the ν values, for which the literature values must be used, and the absorption in the stainless steel, which is calculated. The fraction of the absorptions in the stainless steel is small however. Minor corrections are also necessary in the plutonium case for the higher isotope content.

DESCRIPTION OF EXPERIMENT

The measurements were made in ZPR-9 Assembly 24 which is described in detail in another paper in this annual report (see Paper III-2). Assembly 24 was a zoned core, with a central region about 26 cm in radius, which was made up of enriched and depleted uranium and carbon plates in addition to the stainless steel in the matrix. For the Pu-239 measurement, a small plutonium null zone, composed of plates of depleted uranium, carbon and stainless steel clad plutonium, was substituted at the center of the U-235 zone. The plutonium zone was designed both for null reactivity and to have a characteristic infinite medium spectrum for the uranium zone. The calculated infinite medium spectra for the plutonium and uranium zones were in good agreement. The size and the average atomic concentrations for the plutonium zone are given in Table III-22-I.

The null-zone compositions were selected to sensitize the measurements to the alpha values between 100 eV and 25 keV. As indicated in Fig. III-22-1, approximately one-half of the total fissions were in

TABLE III-22-I. ZPR-9 ASSEMBLY 24, PLUTONIUM ZONE[a]

Material	Atom Densities $\times 10^{-21}$
Pu-239	1.008
Pu-240	0.047
Pu-241	0.005
Aluminum	0.519
U-235	0.029
U-238	13.346
Iron	7.309
Nickel	0.924
Chromium	2.086
Carbon (Graphite)	41.129

[a] Equivalent radius of zone: 9.34 cm; height of zone: 7.62 cm.

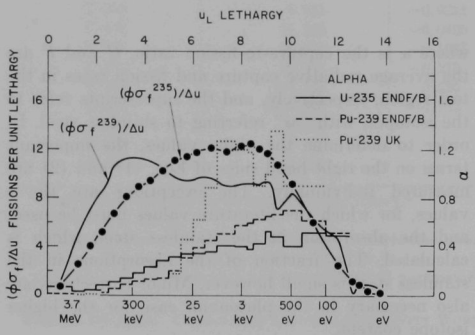

FIG. III-22-1. Capture-to-Fission Ratio and Fissions Per Unit Lethargy vs. Neutron Energy. *ANL Neg. No. 113-484.*

this range, and the fissions were distributed fairly uniformly in energy over this region as well.

Calculated differential alpha values for U-235 and Pu-239 using MC² averaged ENDF/B data and for Pu-239 using the higher reported measurements[1] are also included in Fig. III-22-1. Spectrum averaged alphas for Pu-239 of 0.33 and 0.58 are predicted for this measurement by the ENDF/B data and the higher measurements, respectively.

An 11 ft axial oscillator drawer, installed at the test zone center matrix position, and a sample changer, capable of inserting or removing from the oscillator drawer two 2 x 2 x 2 in. SS sample boxes, were constructed for the reactivity measurements. Figure III-22-2 shows the important features of the oscillator as installed in the assembly. The oscillator drawer was loaded identically to the other drawers in the test zone, except for the two sample positions, and the drawer was long enough so that during oscillation very little reactivity change was observed.

The sample boxes were loaded with plates of enriched and depleted uranium and carbon and the ratios of materials were varied slightly in the reactivity measurements in order to determine the null composition precisely. When this was completed, the central region was reloaded to the experimentally determined null composition and the null re-checked by further reactivity measurements.

The size of the test zone was chosen to be the same as that of two other zoned assemblies, ZPR-9 Assemblies 12 and 19. The central spectra in both of these assemblies have been checked experimentally

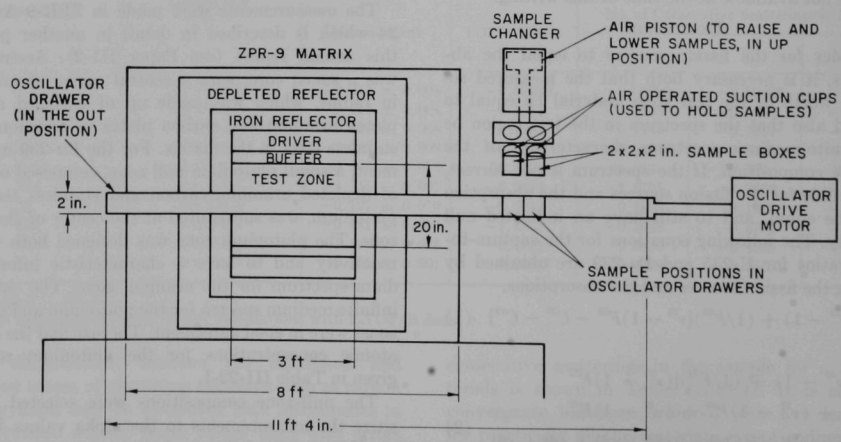

FIG. III-22-2. Axial Sample Changer Installed in Assembly. *ANL Neg. No. 113-1480.*

and found to be well converged. Because of the heavy loading of depleted uranium in the test zone, the size of Assembly 24 was effectively greater than either of the other assemblies in terms of mean free paths. Another favorable factor was that the enrichment of the driver region was considerably less in Assembly 24 than in either of the other assemblies so that the spectrum entering the test zone was more nearly matched to the test zone spectrum. In order to experimentally check the spectral convergence in the test zone, radial and axial foil activations and radial reactivity worth measurements were made. The foil activations indicated a spatially flat spectrum in the central part of the test zone, and the radial reactivity worth measurements indicated a stable, converged spectrum throughout most of the test zone. The radial reactivity measurements are discussed in detail in another paper in this annual report (see Paper III-17).

In order to determine the alpha values, the individual fission and capture rates indicated in Eqs. (1) and (2) were measured, and a considerable redundancy in the measurements was achieved for the important terms. In some cases the ratios were measured directly and in other cases absolute measurements on the individual rates were performed. In Eq. (1) the important terms were C-28, F-25 and F-28. The ratio F-28/F-25 was measured by in-core fission counters and the ratio C-28/F-25 was determined using simultaneous thermal irradiations. The terms C-28, F-25 and F-28 were determined by radiochemistry. The radiochemical determinations were performed by R. J. Armani. For the fission rates the separated Mo-99 activity was counted and for C-28 the separated Np-239 activity was counted. The U-238 capture rate was also determined by counting irradiated U-238 foils in a calibrated counter. An absolutely calibrated Am-243 source was used to calibrate the counters for the U-238 capture rate measurements. The fission rates at the surfaces of the plates were also determined by fission track counting in mica foils. The fission track counting was performed by J. Roberts of Northwestern University. In order to properly average the fission and absorption rates over the test zone composition, detailed mappings were made using thin irradiation foils of the relative fission and absorption rates throughout the sample boxes, as indicated in Fig. III-22-3.

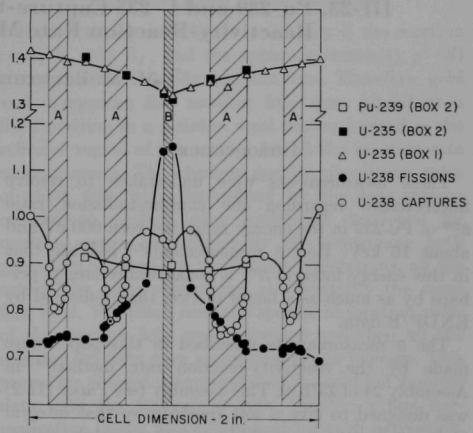

FIG. III-22-3. Measured Fission and Capture Rates in Sample Boxes. *ANL Neg. No. 113-487.*

For the plutonium-alpha measurement, the fission rate in Pu-239 was measured by the same techniques used for the other fission rate measurements. Calculated corrections were made for the Pu-240 and Pu-241 terms; however, these contributed a very small uncertainty to the final result, since the plutonium plate in the test box contained only 1.0% Pu-240 and a nearly negligible amount of Pu-241.

REFERENCE

1. M. G. Schomberg, M. G. Sowerby and F. W. Evans, *A New Method of Measuring Alpha for Pu-239*, Symposium on Fast Reactor Physics and Related Safety Problems, Karlsruhe, October 1967, Paper SM-101/41.

III-23. Pu-239 and U-235 Capture-to-Fission Ratio Measurements by the Reactivity-Reaction Rate Method in Assembly 24 of ZPR-9

M. M. Bretscher and W. C. Redman

Introduction

These measurements were undertaken to resolve uncertainties regarding the capture-to-fission ratio $\bar{\alpha}^{239}$ of Pu-239 in the energy range between 600 eV and about 10 keV. Recent measurements[1,2] indicate that in this energy interval $\bar{\alpha}^{239}$ is considerably larger, perhaps by as much as a factor of two, than indicated by ENDF/B data.

The $\bar{\alpha}$ measurements described in this paper were made by the reactivity-reaction rate method[3,4] in Assembly 24 of ZPR-9. This assembly (see Paper III-2) was designed to give a soft spectrum so that integral alpha measurements would be sensitive to alpha values in the energy range of 1 to 10 keV. For this core, the calculated median fission energy was 13 keV.

Method

The reactivity-reaction rate technique for determining capture-to-fission ratios in low flux critical assemblies is described in Paper III-24. For convenience, however, the fundamental equations, derived from first-order perturbation theory, are repeated below. They apply to a sample located at the center of the reactor where there are no flux gradients.

$$(1 + \bar{\alpha}) = \frac{R_a(A)F\ W_a(A)/W_a}{\rho(A)[1 - \{\rho_s(A)/\rho(A)\}]} \quad (1)$$

$$= (1 + \bar{\alpha}^{238})[F/F(U^{238})]W_a(U^{238})/W_a, \quad (2)$$

where

$$F = \{\rho[1 - (\rho_s/\rho)]/R_f\} - \bar{\nu}\rho'(S)[W_f/W_f(S)]/S. \quad (3)$$

Here

$\rho_s/\rho \equiv$ the fraction of the total reactivity contributed by scattering

$R_f, R_c \equiv$ the specific fission and capture rates in the sample, respectively

$\bar{\alpha} = R_c/R_f \equiv$ the effective capture-to-fission ratio

$\bar{\nu} \equiv$ the effective number of neutrons emitted per fission

$S \equiv$ the neutron emission rate from the Cf-252 spontaneous fission source

$W_f \equiv$ the average neutron importance, weighted according to the sample's virgin fission neutron distribution

$W_a \equiv$ the average neutron importance, weighted according to the sample's absorption rate

$\rho \equiv$ the specific reactivity of the sample

$\rho'(S) \equiv$ the apparent reactivity associated with the emission of spontaneous fission neutrons, normalized to the flux level corresponding to the reaction rate measurements.

The symbol A refers to a reference absorber or substitute material which in these measurements was usually Li-6. Manganese, used successfully in earlier $\bar{\alpha}^{235}$ measurements in thermal criticals, was also used here as a second reference absorber. However, manganese is not an ideal reference absorber in fast spectra because scattering contributes a sizeable fraction of the total reactivity.

It will be noted that in Eqs. (1) through (3), the quantity $(1 + \bar{\alpha})$ results from a combination of the measured absolute reaction rates, relative reactivities, and other quantities such as $\bar{\nu}$ and S. Hence, for a meaningful determination of $\bar{\alpha}$ by this reactivity-reaction rate method, the experimentally determined quantities and related correction factors must be established precisely. For this reason the discussion which follows emphasizes the thoroughness of the measurements and related evaluations involved in the determination of the various quantities on which the resulting values for $\bar{\alpha}$ are based.

TABLE III-23-I. Isotopic Composition of Samples

Sample	Isotopic Composition, Isotope- Wt %			
Pu	239-98.938964	240-1.011915	241-0.049125	242-0.000000
Enriched U	234-0.65730	235-93.098349	236-0.322750	238-5.921597
Depleted U		235-0.231485	236-0.002301	238-99.766215
Enriched Li		6-94.939655	7-5.060345	
Depleted Li		6-0.006001	7-99.993999	

Description of Samples

Samples of identical dimensions were used for both reactivity and reaction rate measurements. Table III-23-I summarizes the isotopic composition of the plutonium, uranium, and lithium samples.

All of the samples were contained in stainless steel cans having an outer diameter of 0.865 in. and a length of 1.995 in., for use in the ZPR-9 radial sample changer. The plutonium was alloyed with 1.2 w/o aluminum and rolled into three foil thicknesses: 0.005 in., 0.015 in., and 0.030 in. Annular samples of these thicknesses, each having a diameter of 0.825 in. and a length of 1.250 in. were enclosed in welded stainless steel cans. The uranium samples were prepared by wrapping foil around the inner walls of the stainless steel sample cans. All of the enriched uranium samples had a length of 1.750 in., with thicknesses of 0.005 in., 0.020 in., and 0.040 in. The depleted uranium sample was of similar dimensions, except that the wall was 0.035 in. thick.

Cylindrical samples, both enriched and depleted in Li-6, were prepared by extruding lithium in an argon atmosphere to a diameter of 0.623 in. and cutting it into 0.850 in. lengths. After weighing, the samples were sealed by electron beam welding in aluminum cans having a wall thickness of 0.020 in. Two of these samples were placed end to end and positioned at the center of the stainless steel sample cans for subsequent reactivity and reaction rate measurements. The samples contained 99.8703 w/o lithium, 0.0007 w/o chlorine, 0.0448 w/o carbon, and 0.0291 w/o nitrogen.

At the start of these measurements it was known that manganese might not be a very useful reference absorber (see Paper III-24). Nevertheless, manganese was used as a second reference absorber because beta-gamma coincidence counting equipment was available for measuring absolute manganese absorption rates. To prepare foils suitable for irradiation and absolute counting, manganese was alloyed with copper and nickel. The composition of this alloy was 95.160 w/o manganese, 2.864 w/o copper, 1.459 w/o nickel, 0.377 w/o nitrogen, 0.073 w/o oxygen, 0.064 w/o carbon, and 0.003 w/o hydrogen. Reactivity and absorption rate measurements were performed with cylindrical samples of this alloy. These samples were composed of 0.825 in. diameter pellets stacked to a height of 1.750 in., to fill the stainless steel can. Manganese foils, 0.001 in. thick, were positioned at the ends of the cylinder and between these were solid 0.247 in. thick manganese pellets to average the absolute absorption rate over the sample dimensions.

Cylindrical samples of copper, nickel, aluminum, and stainless steel were also used for reactivity measurements, to permit corrections for the presence of these materials in the primary samples.

Reaction Rate Measurements

Equations (1) and (2) are valid only if the reaction rates, R_a and R_f, and the apparent reactivity ρ' (S) are normalized to a common flux level. Therefore, gold and manganese flux monitor foils were placed at a fixed position in a stainless steel drawer located in the reflector region of the reactor for all the reaction rate measurements. The absolute specific absorption rates of these foils were determined by the beta-gamma coincidence method using equipment developed for neutron source calibrations by the manganese bath procedure.[5] Except for the lithium irradiations, all the activations were carried out at essentially the same flux level. For these runs the specific absorption rates of the monitor foils were averaged and then all the monitor foil data were normalized to the average. This procedure allowed a comparison of the gold foil monitor data with the manganese data. Finally, a flux normalization factor was determined for each activation, by taking the weighted mean of the gold and manganese data.

Fission rates for Pu-239, U-235, and U-238 were determined radiochemically by a procedure[6] involving the recovery of the fission product Mo-99 from the irradiated sample and absolute beta counting. Prior to the chemical analysis, each irradiated sample was cut into several pieces and each piece analyzed separately. The end result was based on the average of these individual determinations.

The Pu-239 specific fission rate R_f^{239} was calculated from the following equation:

$$R_f^{239} = \frac{R_f(\text{Pu-Al})}{a_{230}(1 - a_{\text{Al}})[1 + (a_{240}R_f^{240} + a_{241}R_f^{241})/a_{239}R_f^{239}]},$$

where R_f(Pu-Al) is the measured fission rate per gram of the plutonium-aluminum alloy, normalized to the common flux level. A value of 5.9 %[7] was used for the yield of Mo-99 for fast fission of Pu-239. The a_i's are the isotopic weight fractions given in Table III-23-I and a_{Al} is the weight fraction of aluminum in the sample. Thirty-group cross sections generated by the MC^2 code[8] from ENDF/B data and MACH-I central fluxes[9] were used to calculate the term in square brackets, equal to 1.00233.

Isotopic uranium fission rates were evaluated from the following equations:

$$R_f^e = a_{235}^e R_f^{235}[1 + (a_{234}^e R_f^{234} + a_{236}^e R_f^{236})/a_{235}^e R_f^{235}] + a_{238}^e R_f^{238}$$

$$R_f^d = a_{235}^d R_f^{235} + a_{238}^d R_f^{238}[1 + \{a_{236}^d R_f^{236}/a_{238}^d R_f^{238}\}].$$

R_f^e and R_f^d are the flux normalized fission rates per gram of the enriched and depleted samples, respectively. Again, the a_i's are the isotopic weight fractions given

TABLE III-23-II. Pu-239, U-235, AND U-238 ABSOLUTE SPECIFIC FISSION RATES[a]

Isotope	Wall Thickness, in.	R_f, fissions/g-sec
Pu-239	0.005	(3.40284 ± 0.01956) 10^6
Pu-239	0.005	(3.45314 ± 0.02311) 10^6
Weighted Mean:		(3.42383 ± 0.02480) 10^6
Pu-239	0.015	(3.34659 ± 0.03444) 10^6
Pu-239	0.030	(3.28635 ± 0.02267) 10^6
U-235	0.005	(3.81607 ± 0.02038) 10^6
U-235	0.005	(3.76855 ± 0.01810) 10^6
Weighted Mean:		(3.78950 ± 0.02360) 10^6
U-235	0.020	(3.66117 ± 0.03732) 10^6
U-235	0.040	(3.53793 ± 0.02420) 10^6
U-238	0.035	(6.13739 ± 0.04525) 10^4

[a] R_c^{238} = (4.92232 ± 0.05911) 10^5 captures/g-sec
$\bar{\alpha}^{238} = R_c^{238}/R_f^{238}$ = 8.02022 ± 0.10134

in Table III-23-I. As before, the bracketed terms were calculated using the MC^2 and MACH-I codes. These equations were solved simultaneously to determine the isotopic fission rates R_f^{235} and R_f^{238}. Two separate irradiations were made for the 0.005 in. thick uranium and plutonium samples. A summary of the isotopic specific fission rates for samples of different thicknesses, based on several values per sample, is given in Table III-23-II.

The U-238 capture rate was measured by a radiochemical technique[6] which allows U-239 to decay to Np-239 which is then extracted by an ion exchange process. Absolute beta counting was used to determine the Np-239 activity. The errors quoted in Table III-23-II represent the precision of the measurement and do not include uncertainties associated with the fission yield of Mo-99.

The method for determining the absorption rate in the lithium samples has been described previously (see Paper III-24). For these samples, enriched and depleted in Li-6, the normalized tritium production rate per gram of sample may be expressed as

$$R^e_{n,t} = a^e_{\mathrm{Li}}(a^e_6 R^6_{n,t} + a^e_7 R^7_{n,t})$$

and

$$R^d_{n,t} = a^d_{\mathrm{Li}}(a^d_6 R^6_{n,t} + a^d_7 R^7_{n,t}),$$

where the a_i's are the isotopic weight fractions (Table III-23-I) and where a_{Li} is the fraction of lithium in the sample. These equations were solved simultaneously to determine $R^6_{n,t}$, the specific tritium production rate in Li-6. The absorption rate, R_a(Li-6), is nearly equal to $R^6_{n,t}$:

$$R_a(\mathrm{Li\text{-}6}) = R^6_{n,t}[1 + (R^6_{n,\gamma} + R^6_{n,p})/R^6_{n,t}]$$
$$= 1.000198\, R^6_{n,t}\,.$$

MACH-I fluxes and MC^2 cross sections generated from the ENDF/B data for lithium were used to calculate the term in brackets. To correct for decay, a tritium half-life of 12.346 ± 0.002 yr[10] was used.

Manganese capture rates were measured by the same beta-gamma coincidence method used in our previous $\bar{\alpha}$ determinations. Manganese foils, 0.001 in. thick, were irradiated at various positions along the axis of the cylindrical manganese absorber with the plane of the foils parallel to the cylinder base. Cylinder and foil diameters were equal. These foils were counted at two different times so that a correction could be made for the small amount of the Cu-64 activity produced in the foils. The capture rate of the manganese sample was then evaluated from the equation

$$R_{n,\gamma} = \int_0^M r_{n,\gamma}(m)dm/M = \int_0^1 r_{n,\gamma}(x)\,dx,$$

where M is the total mass of the manganese sample and x is the fraction of the sample mass between one end of the cylinder and the position of the foil whose normalized specific capture rate is $r_{n,\gamma}(x)$. Gaussian quadrature methods were used to perform the numerical integration.

From this capture rate one may evaluate the specific manganese absorption rate, R_a(Mn), as follows:

TABLE III-23-III. Li-6 AND MANGANESE ABSOLUTE SPECIFIC ABSORPTION RATES

Sample	R_a(Li-6) abs/g-sec	Sample	R_a(Mn), abs/g-sec
Li^6-27	(7.15740 ± 0.06920) 10^7	Mn-2	(2.94339 ± 0.017026) 10^5
Li^6-25	(7.26508 ± 0.04269) 10^7	Mn-3	(3.03406 ± 0.018928) 10^5
Li^6-29	(7.24747 ± 0.12653) 10^7	Mn-4	(2.96225 ± 0.018347) 10^5
Li^6-33	(7.27355 ± 0.14613) 10^7	Mn-5	(3.02240 ± 0.013912) 10^5
Li^6-19	(7.28337 ± 0.08587) 10^7		
Li^6-32	(7.43519 ± 0.17289) 10^7		

Weighted Mean: R_a(Li-6) = (7.27701 ± 0.04097) 10^7 abs/g-sec
R_a(Mn) = (2.99328 ± 0.02178) 10^5 abs/g-sec

$$R_a(\mathrm{Mn}) = R_{n,\gamma}[1 + (R_{n,\alpha} + R_{n,p})/R_{n,\gamma}]/a_{\mathrm{Mn}}$$
$$= 1.053466\, R_{n,\gamma}\,.$$

The fraction of manganese in the sample is a_{Mn} and the term in brackets was also evaluated from ENDF/B data. In Table III-23-III we list the measured absorption rates, normalized to the reference flux level, for both Li-6 and manganese.

Reactivity Measurements

Reactivities were measured using the fine autorod mechanism and radial sample changer available in the ZPR-9 facility. Equations similar to those used to evaluate isotopic fission and absorption rates are needed to extract the required reactivities from the measurements. Thus, for the plutonium samples,

$$\rho^{239} = \frac{(\rho_{\mathrm{Pu-Al}} - a_{\mathrm{Al}}\rho_{\mathrm{Al}})}{(1 - a_{\mathrm{Al}})a_{239}[1 + (a_{240}\rho^{240} + a_{241}\rho^{241})/a_{239}\rho^{239}]}\,,$$

where the a's have already been defined and the ρ's refer to specific reactivities. Again, the MACH-I program was used to evaluate the term in brackets. Similar equations apply to the enriched and depleted uranium samples.

$$\rho^{e}(\mathrm{U}) = a^{e}_{235}\rho^{235}[1 + (a^{e}_{234}\rho^{234} + a^{e}_{236}\rho^{236})/a^{e}_{235}\rho^{235}] + a^{e}_{238}\rho^{238}$$

$$\rho^{d}(\mathrm{U}) = a^{d}_{235}\rho^{235} + a^{d}_{238}\rho^{238}[1 + (a^{d}_{236}\rho^{236}/a^{d}_{238}\rho^{238})].$$

For the case of lithium,

$$\rho^{e}(\mathrm{Li}) = a_{\mathrm{Li}}a^{e}_{6}\rho^{6}[1 + (a_{\mathrm{Cl}}\rho_{\mathrm{Cl}} + a_{\mathrm{C}}\rho_{\mathrm{C}} + a_{\mathrm{N}}\rho_{\mathrm{N}})/a_{\mathrm{Li}}a^{e}_{6}\rho^{6}] + a_{\mathrm{Li}}a^{e}_{7}\rho^{7}$$

$$\rho^{d}(\mathrm{Li}) = a_{\mathrm{Li}}a^{6}_{d}\rho^{6} + a_{\mathrm{Li}}a^{d}_{7}\rho^{7}[1 + (a_{\mathrm{Cl}}\rho_{\mathrm{Cl}} + a_{\mathrm{C}}\rho_{\mathrm{C}} + a_{\mathrm{N}}\rho_{\mathrm{N}})/a_{\mathrm{Li}}a^{d}_{7}\rho^{7}].$$

Finally, for the manganese sample,

$$\rho_{\mathrm{Mn}} = \frac{(\rho_{\mathrm{alloy}} - a_{\mathrm{Cu}}\rho_{\mathrm{Cu}} - a_{\mathrm{Ni}}\rho_{\mathrm{Ni}})}{a_{\mathrm{Mn}}[1 + (a_{\mathrm{C}}\rho_{\mathrm{C}} + a_{\mathrm{N}}\rho_{\mathrm{N}} + a_{\mathrm{O}}\rho_{\mathrm{O}} + a_{\mathrm{H}}\rho_{\mathrm{H}})/a_{\mathrm{Mn}}\rho_{\mathrm{Mn}}]}\,.$$

The terms in the numerator were determined from experimental data while the terms in the brackets were evaluated from ENDF/B data and MACH-I calculations. Specific reactivities, measured at the center of the reactor, are listed in Table III-23-IV.

TABLE III-23-IV. Specific Reactivities

Sample	Wall Thickness, in.	Specific Reactivity, Ih/g
Pu-239	0.005	$(7.23013 \pm 0.03985)\ 10^{-2}$
Pu-239	0.015	$(7.20374 \pm 0.02353)\ 10^{-2}$
Pu-239	0.030	$(7.19045 \pm 0.01063)\ 10^{-2}$
U-235	0.005	$(6.31267 \pm 0.03375)\ 10^{-2}$
U-235	0.020	$(6.16492 \pm 0.01012)\ 10^{-2}$
U-235	0.040	$(6.03137 \pm 0.02283)\ 10^{-2}$
U-238	0.035	$-(5.03893 \pm 0.03512)\ 10^{-3}$
Li-6		$-(8.85939 \pm 0.01055)\ 10^{-1}$
Li-7		$-(9.78881 \pm 0.27936)\ 10^{-3}$
Mn		$-(5.04177 \pm 0.01317)\ 10^{-3}$
Al		$-(2.38821 \pm 0.03141)\ 10^{-3}$
Cu		$-(4.23687 \pm 0.01850)\ 10^{-3}$
Ni		$-(2.72312 \pm 0.01005)\ 10^{-3}$

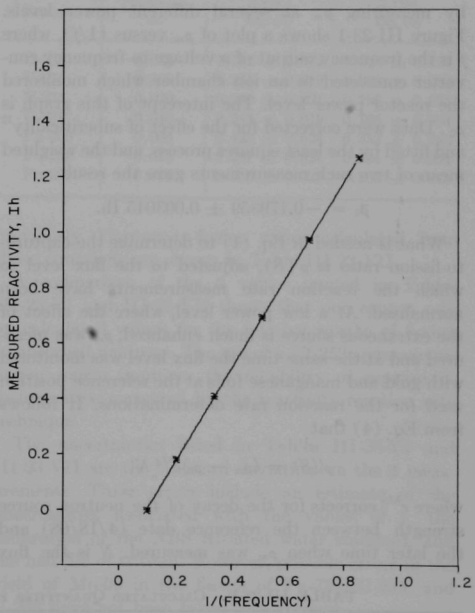

Fig. III-23-1. Reactor Response to Cf-252 Spontaneous Fission Neutrons. *ANL Neg. No. 113-1407.*

Response to Extraneous Cf-252 Neutron Source

Two Cf-252 spontaneous fission neutron sources were prepared and sealed by welding in double-walled aluminum containers. Both capsules are of identical dimensions, $^{15}/_{16}$ in. long and 0.665 in. diameter. The strength of each source was measured by the manganese bath technique.[11] For these $\bar{\alpha}$ measurements, the two sources were placed end to end and used as a composite source. April 18, 1968 was chosen as a reference date and the combined strength of these sources at this time was found to be

$$S(4/18/68) = (7.54784 \pm 0.03032)\ 10^6 + (4.95932 \pm 0.02137)\ 10^6 = (1.25072 \pm 0.00371)\ 10^7 \text{ n/sec.}$$

The measured reactivity of an extraneous neutron source consists of two parts. One part is the reactivity of the source container as well as the reactivity associated with neutron-induced reactions in Cf-252. We shall denote this reactivity contribution by ρ_0. The second part is the apparent reactivity associated with the emission of spontaneous fission neutrons. Call this contribution $\rho'(S)$. Then

$$\rho_m = \rho_0 + \rho'(S), \tag{4}$$

where ρ_m is the measured reactivity. Now $\rho'(S)$ varies directly as the neutron source strength S and inversely as the reactor power level. Thus, ρ_0 may be determined by measuring ρ_m at several different power levels. Figure III-23-1 shows a plot of ρ_m versus $(1/f)$, where f is the frequency output of a voltage-to-frequency converter connected to an ion chamber which monitored the reactor power level. The intercept of this graph is ρ_0. Data were corrected for the effect of subcriticality[12] and fitted by the least-squares process, and the weighted mean of two such measurements gave the result

$$\bar{\rho}_0 = -0.179359 \pm 0.003045 \text{ Ih.}$$

What is needed in Eq. (1) to determine the capture-to-fission ratio is $\rho'(S)$, adjusted to the flux level to which the reaction rate measurements have been normalized. At a low power level, where the effect of the extraneous source is much enhanced, ρ_m was measured and at the same time the flux level was monitored with gold and manganese foils at the reference position used for the reaction rate determinations. It follows from Eq. (4) that

$$\rho'(S) = (\rho_m - \rho_0)e^{\lambda t_d} N,$$

where $e^{\lambda t_d}$ corrects for the decay of the neutron source strength between the reference date (4/18/68) and the later time when ρ_m was measured. N is the flux normalization ratio, the flux level for the ρ_m measurement divided by the flux level to which all the reaction rate measurements have been normalized. The weighted mean of two such measurements is

$$\bar{\rho}'(S) = 0.173506 \pm 0.000964 \text{ Ih.}$$

Calculated Quantities

Several quantities appearing in Eqs. (1) through (3) must be obtained by calculation. These are $W_a(A)/W_a$, $W_f/W_f(S)$, $\bar{\nu}$, and $[1 - (\rho_s/\rho)]$, where

$$W_a = \sum_i \phi_i^*(\sigma_c + \sigma_f)_i\phi_i / \sum_i (\sigma_c + \sigma_f)_i\phi_i$$

$$W_f = \sum_j \phi_j^* \chi_j$$

$$\bar{\nu} = \sum_i (\nu\sigma_f)_i\phi_i / \sum_i \sigma_{fi}\phi_i .$$

These quantities have been calculated using MC² cross sections obtained from the ENDF/B data and fluxes and adjoints from the MACH-I code. For Li-6, manganese and Pu-239 perturbed fluxes, obtained from a self-shielding calculation,[13] were used. The U-235 and U-238 samples were heavily shielded by the surrounding core materials and therefore fluxes characteristic of the center of the core were used for these calculations. These results are summarized in Table III-23-V.

Results

With the quantities found in Tables III-23-II through III-23-V together with the californium data, the capture-to-fission ratios may be evaluated from Eqs. (1) through (3). The $\bar{\alpha}$ values determined in this manner are shown in Table III-23-VI. Values listed under the column headings $\bar{\alpha}$-Mn and $\bar{\alpha}$-Li^6 are calculated from Eq. (1) with manganese and Li-6 as the reference absorbers, respectively. Under the $\bar{\alpha}$-U^{238} heading are the values calculated from Eq. (2) using the radiochemical result for $\bar{\alpha}^{238}$. Note that the first entry in this column is the radiochemical value of $\bar{\alpha}^{238}$.

At the start it was recognized that manganese was not an ideal reference absorber for $\bar{\alpha}$ determinations in

TABLE III-23-V. Calculated Quantities for $(1 + \bar{\alpha})$ Measurements in ZPR-9, Assembly 24

Isotope	Thickness, in.	$1 - (\rho_s/\rho)$	W_f/W_f(Cf)	W_a(Li-6)/W_a	W_a(Mn)/W_a	W_a(U-238)/W_a	$\bar{\nu}$
Pu-239	0.005	1.00591	0.98950	0.96551	1.07489	0.96661	2.91578
Pu-239	0.015	1.00700	0.98958	0.96625	1.07572	0.96735	2.92183
Pu-239	0.030	1.00842	0.98967	0.96719	1.07676	0.96829	2.92982
U-235	0.005	1.00893	0.98053	0.97328	1.08354	0.97439	2.44952
U-238	0.035	0.84054	0.98643	0.99886	1.11202	1.00000	2.80292
Li-6	—	0.99116					
Mn-55	—	0.99497					

TABLE III-23-VI. MEASURED CAPTURE-TO-FISSION RATIOS

Sample	Thickness, in.	$\bar{\alpha}$-Mn, Eq. (1)	$\bar{\alpha}$-Li^6, Eq. (1)	$\bar{\alpha}$-U^{238}, Eq. (2)	$\bar{\alpha}$ Calculated from ENDF/B Data
U-238	0.000				9.183
U-238	0.035	6.124 ± 0.076	7.855 ± 0.085	8.020 ± 0.101	
U-235	0.000				0.346
U-235	0.005	0.068 ± 0.021	0.327 ± 0.026	0.352 ± 0.031	
U-235	0.020	0.061 ± 0.022	0.318 ± 0.027	0.343 ± 0.032	
U-235	0.040	0.052 ± 0.021	0.307 ± 0.026	0.331 ± 0.031	
Pu-239	0.000				0.352
Pu-239	0.005	0.205 ± 0.025	0.497 ± 0.031	0.525 ± 0.037	
Pu-239	0.015	0.183 ± 0.026	0.471 ± 0.033	0.498 ± 0.038	
Pu-239	0.030	0.167 ± 0.024	0.450 ± 0.030	0.477 ± 0.035	

fast spectra because its scattering cross section is very large relative to the capture cross section and the cross sections are not known precisely. For this case the correction factor $[1 - \{\rho_s(\mathrm{Mn})/\rho(\mathrm{Mn})\}]$ is large and uncertain because it depends very sensitively on the shape of the adjoint flux. The results in Table III-23-VI certainly support this prediction. However, the very wide disagreement between $\bar{\alpha}$ values based on the manganese data from those obtained from the Li-6 and U-238 data is not completely understood and is still under investigation.

It is seen from Table III-23-VI that the reactivity-reaction rate method using Li-6 as the standard absorber gives an $\bar{\alpha}$ value for U-238 which is in agreement, within experimental errors, with the independent result based on radiochemical techniques. This provides a direct check on the self-consistency of this reactivity-reaction rate technique for measuring capture-to-fission ratios in low flux systems.

T. L. Andersson et al.,[14] and W. N. Fox et al.,[15] used the reactivity-reaction rate method to determine $\bar{\alpha}^{239}$ and $\bar{\alpha}^{235}$ in different fast reactor spectra. Since they did not have a calibrated Cf-252 fission source, they relied on a calculated value for W_f/W_a, the worth of virgin fission neutrons relative to that for neutrons absorbed in the sample. For purposes of comparison, we too have evaluated our data omitting the information provided by the californium source. From first-order perturbation theory we obtain the result

$$(1 + \bar{\alpha}) = \bar{\nu} W_f/W_a + \frac{\rho[1 - (\rho_s/\rho)]R_a(A)W_a(A)}{\rho(A)[1 - \{\rho_s(A)/\rho(A)\}]R_f W_a}. \quad (5)$$

Using the U-238 data,

$$(1 + \bar{\alpha}) = \bar{\nu} W_f/W_a + \frac{\rho[1 - (\rho_s/\rho)]R_f^{238}W_a^{238}[1 + \bar{\alpha}^{238} - (\bar{\nu}^{238}W_f^{238}/W_a^{238})]}{\rho^{238}[1 - (\rho_s^{238}/\rho^{238})]R_f W_a} \quad (6)$$

All the symbols in these equations have been defined

TABLE III-23-VII. MEASURED CAPTURE-TO-FISSION RATIOS BASED ON A CALCULATED VALUE FOR THE RELATIVE WORTH OF VIRGIN FISSION TO ABSORBED NEUTRONS

Sample	Thickness, in.	$\bar{\alpha}$-Li^6, Eq. (5)	$\bar{\alpha}$-U^{238}, Eq. (6)
U-238	0.035	7.782 ± 0.072	8.020 ± 0.101
U-235	0.005	0.265 ± 0.019	0.208 ± 0.033
U-235	0.020	0.256 ± 0.021	0.198 ± 0.035
U-235	0.040	0.244 ± 0.019	0.186 ± 0.034
Pu-239	0.005	0.423 ± 0.024	0.352 ± 0.042
Pu-239	0.015	0.397 ± 0.027	0.324 ± 0.044
Pu-239	0.030	0.376 ± 0.023	0.302 ± 0.042

previously. Capture-to-fission ratios calculated from these equations are shown in Table III-23-VII.

A comparison of the $\bar{\alpha}$ values quoted in Tables III-23-VI and III-23-VII shows that one cannot rely on calculated values for the relative worths of fission to absorbed neutrons. The use of a Cf-252 spontaneous fission source improves the reliability of capture-to-fission ratios measured by the reactivity-reaction rate technique.

The uncertainties listed in Tables III-23-VI and III-23-VII are the standard deviations in the $\bar{\alpha}$ measurements. These errors include an estimate of the uncertainties associated with the values of $\bar{\nu}$, the calibration of the NBS tritiated water standard, and the half-life of tritium. However, possible errors in the yield of Mo-99 in the fission of Pu-239, U-235, and U-238 have not been taken into account.

The measured capture-to-fission ratios for Pu-239 obtained here are considerably larger than the value calculated for an infinitely thin sample using the ENDF/B data. Thus, the ENDF/B data apparently underestimates the amount of capture or overestimates the amount of fission in Pu-239.

REFERENCES

1. M. G. Schomberg, M. G. Sowerby and F. W. Evans, *New Method of Measuring Alpha (E) for Pu^{239}*, Symposium on

Fast Reactor Physics and Related Safety Problems, Karlsruhe, Germany (IAEA, Vienna, 1968), Vol. 1, CONF-671043, pp. 289–301.
2. R. Gwin, L. W. Weston, G. de Saussure, R. W. Ingle, J. H. Todd and F. E. Gillespie (ORNL), and R. W. Hockenbury and R. C. Block (RPI), *Measurement of the Neutron Fission and Absorption Cross Sections of Pu^{239} Over the Energy Range 0.01 eV to 30 keV*, Neutron Physics Division Annual Progress Report for Period Engind May 31, 1968, ORNL-4280, pp. 13–16.
3. W. C. Redman and M. M. Bretscher, *Direct Determination of Uranium-235 Capture-to-Fission Ratio in a Zero Power Reactor*, Nucl. Sci. Eng. **27**, 34 (1967).
4. W. C. Redman and M. M. Bretscher, *Low Flux Measurement of U-235 Epi-Cadmium Capture-to-Fission Ratio*, Nucl. Sci. Eng. **31**, 247 (1968).
5. A. De Volpi, K. G. A. Porges and R. N. Larsen, *Mn^{56} Coincidence Counting Facility*, ANL-6760 (1963).
6. R. J. Armani, *Absolute Determination of Fission Rates in U-235 and U-238 and Capture Rates in U-238 by Radiochemical Techniques*, Reactor Physics Division Annual Report, July 1, 1965 to June 30, 1966, ANL-7210, p. 304.
7. I. F. Croall, *Yields from Neutron Induced Fission*, AERE-R-5086 (1967).
8. B. J. Toppel, A. L. Rago and D. M. O'Shea, *MC^2, A Code to Calculate Multigroup Cross Sections*, ANL-7318 (1967).
9. D. A. Meneley, L. C. Kvitek and D. M. O'Shea, *MACH-I, A One-Dimensional Diffusion Theory Package*, ANL-7223 (1966).
10. K. C. Jordon, B. C. Blanke and W. A. Dudley, *Half-Life of Tritium*, J. Inorg. Nucl. Chem. **29**, 2129 (1967).
11. A. De Volpi, K. G. Porges and R. J. Armani, *Absolute Calibration of Fission Neutron Source Strength Relying Upon an Improved Manganese Bath Technique and Absolute Beta-Gamma Coincidence Counting*, Symposium on Standardization of Radionuclides, Vienna, October 10–14, 1966 (IAEA, Vienna, 1967), pp. 717–727.
12. W. C. Redman, *Reactor Response to an Oscillating Neutron Source*, Reactor Physics Division Annual Report, July 1, 1965 to June 30, 1966, ANL-7210, pp. 319–321.
13. C. E. Till, *Fissile Doppler Effect Measurements and the Effects of Thermal Expansion*, Reactor Physics Division Annual Report, July 1, 1966 to June 30, 1967, ANL-7310, pp. 143–151.
14. T. L. Andersson, E. Hellstrand, R. Hakansson and Z. Bajbor, *Measurement of the Effective Capture-to-Fission Ratio in Pu-239 and U-235 in Two Different Fast Reactor Spectra*, Symposium on Fast Reactor Physics and Related Safety Problems, Karlsruhe, Germany (IAEA, Vienna, 1968), Vol. 2, CONF-671043, pp. 171–185.
15. W. N. Fox, R. Richmond, D. J. Skillings and R. C. Wheeler *The Measurement of Pu^{239} Capture-to-Fission Ratios in Fast Reactor Lattices*, J. Brit. Nucl. Energy Soc. **6**, 63 (1967).

III-24. Li-6 as a Reference Absorber for Capture-to-Fission Ratio Measurements in Zero Power Fast Critical Assemblies

M. M. Bretscher

Introduction

Low flux capture-to-fission ratio measurements, described in Refs. 1 and 2, use a reactor oscillator method in combination with absolute counting. As tests of this direct low-flux method, the effective capture-to-fission ratio $\bar{\alpha}$ was measured for U-235 in both the thermal[3] and epithermal[4] portions of the flux in the Argonne ZPR-7 facility, Hi-C Core 10. Having demonstrated that capture-to-fission ratios can be measured in zero power thermal systems by this technique, a study[5] was undertaken to determine what modifications, if any, were needed to apply this method to $\bar{\alpha}$ measurements in low-power fast critical assemblies.

For $\bar{\alpha}$ measurements corresponding to nearly thermal energies, manganese proved to be a very useful substitute material, or reference absorber. However, in a fast flux the manganese (n,γ) cross section is very small and a large fraction of the total cross section comes from scattering. It will be shown that Li-6 is a nearly ideal absorber and more appropriate than manganese for use in $\bar{\alpha}$ measurements by the oscillator method in zero power fast reactors. A technique for determining the absolute absorption rate in a Li-6 sample is also described.

The Oscillator Method

According to first-order perturbation theory, the reactivity associated with a fissile material located at the center of a reactor may be written as[6]

$$\rho = \rho_{source} + \rho_{absorption} + \rho_{scatter}$$

$$= \frac{N}{D}\int_{sample}\Big[\sum_j \phi_j^* \chi_j \sum_i (\nu\sigma_f)_i\phi_i - \sum_i \phi_i^*(\sigma_c + \sigma_f)_i\phi_i - \sum_j\sum_k (\phi_j^* - \phi_k^*)\sigma_{j\to k}\phi_j\Big]\,dV,$$

where N is the number density of nuclei in the sample; σ_f, σ_c, and $\sigma_{j\to k}$ are microscopic fission, capture, and transfer (from the jth to the kth group) cross sections, respectively; ϕ_i and ϕ_i^* are the real and adjoint fluxes belonging to the ith group; ν is the average number of neutrons per fission; and χ_j is the fraction of fission neutrons born into the jth group. The perturbation

denominator is denoted by D. For small samples the unperturbed flux is essentially constant over the dimensions of the sample and the above equation may then be written in the form

$$\rho(1 - \rho_s/\rho) = [W_f\bar{\nu}R_f - W_aR_f(1 + \bar{\alpha})]/D, \quad (1)$$

where

$\rho_s/\rho \equiv$ fraction of the total reactivity resulting from scattering

R_f, $R_c \equiv$ fission and capture rates in the sample, respectively

$\bar{\nu} = \sum_i (\nu\sigma_f)_i\phi_i / \sum_i \sigma_{fi}\phi_i$

$\equiv$ average number of neutrons emitted per fission

$\bar{\alpha} = R_c/R_f \equiv$ effective capture-to-fission ratio

$W_f = \sum_i \phi_i^* \chi_i \equiv$ average neutron importance weighted according to the sample's virgin fission neutron distribution

$W_a = \sum_i \phi_i^*(\sigma_c + \sigma_f)_i\phi_i / \sum_i (\sigma_c + \sigma_f)_i\phi_i$

$\equiv$ average neutron importance weighted according to the sample's absorption rate.

For a nonfissionable absorber,

$$\rho(A)[1 - \rho_s(A)/\rho(A)] = -R_a(A)W_a(A)/D_A, \quad (2)$$

where $\rho(A)$ and $R_a(A)$ are the reactivity and absorption rate of absorber A, respectively. Similarly, an extraneous neutron source has an apparent reactivity

$$\rho'(S) = SW_f(S)/D_S, \quad (3)$$

where S is the neutron emission rate. The perturbation denominators in the reactivity expressions for the absorber and extraneous source are denoted by D_A and D_S, respectively.

Now if the reaction rates R_f and $R_a(A)$ and the apparent reactivity $\rho'(S)$ are all normalized to the same flux level $D = D_A = D_S$, Eqs. (1), (2), and (3) combine to give

$$(1 + \bar{\alpha}) = \frac{R_a(A)W_a(A)/W_a}{\rho(A)[1 - \rho_s(A)/\rho(A)]} \cdot \left[\frac{\rho(1 - \rho_s/\rho)}{R_f} - \frac{\bar{\nu}\rho'(S)W_f/W_f(S)}{S}\right]. \quad (4)$$

W. C. Redman has suggested[7] that capture-to-fission ratios could be measured in zero power reactors through the use of Eq. (4). The quantities $R_a(A)$, R_f, S, ρ, $\rho(A)$ and $\rho'(S)$ appearing in this equation are measured experimentally while the other terms must be calculated. Reactivities may be measured with a pile oscillator while absolute counting methods are needed to determine the reaction rates and the neutron source strength.

TABLE III-24-I. Calculated Quantities for $(1 + \bar{\alpha})$ Measurements in ZPR-9 Assembly 24

Quantity	Pu-239	U-235	U-238	Li-6	B-10	Mn-55
$1 - (\rho_s/\rho)$	1.00478	1.00730	0.84449	0.99386	0.99936	1.13909
$W_f/W_f(\mathrm{Cf})$	0.99496	0.98171	0.98932			
$W_a(\mathrm{Mn}^{55})/W_a$	1.15706	1.16546	1.20791			
$W_a(\mathrm{Li}^6)/W_a$	0.97451	0.98159	1.01734			
$W_a(\mathrm{B}^{10})/W_a$	1.01433	1.02170	1.05891			
$W_a(\mathrm{U}^{238})/W_a$	0.95790	0.96486	1.00000			
$\bar{\nu}$	2.91332	2.44795	2.80230			

Choice of a Reference Absorber

In order that the quantity $(1 + \bar{\alpha})$ be relatively insensitive to calculated corrections, materials must be chosen such that $W_f/W_f(S)$, $W_a(A)/W_a$ and $[1 - \rho_s(A)/\rho(A)]$ are all very close to unity for the neutron spectrum of interest. Also, the reference absorber must lend itself to an absolute determination of the absorption rate $R_a(A)$.

A Cf-252 spontaneous fission source is a very adequate choice for the extraneous neutron emitter. As seen in Table III-24-I, $W_f/W_f(\mathrm{Cf})$ differs from unity by less than 2% for both U-235 and Pu-239.

Three materials, Mn-55, Li-6, and B-10, have been considered as references for Pu-239 and U-235 $\bar{\alpha}$ measurements in fast spectra. For ZPR-9 Assembly 24,[8] $W_a(A)/W_a$ and $[1 - \rho_s(A)/\rho(A)]$ have been calculated for these materials located at the center of the core. The results are summarized in Table III-24-1. These quantities were calculated from MACH-I[6] fluxes and thirty-group cross sections generated by the MC^2 code.[9] No self-shielding corrections have been made.

Table III-24-I shows that manganese is not very suitable as a reference absorber because the value obtained for $(1 + \bar{\alpha})$ depends strongly on the calculated corrections $[1 - \rho_s(\mathrm{Mn})/\rho(\mathrm{Mn})]$ and $W_a(\mathrm{Mn})/W_a$. On the other hand, Li-6 and B-10 appear to be equally suitable for use as standards since these corrections amount to only a few percent at most.

Radiochemical methods[10] may be used to measure fission and capture rates in U-238. Thus, $(1 + \bar{\alpha})$ measurements may be made relative to an experimental value of $(1 + \bar{\alpha})$ for U-238. For this case, Eq. (4) takes the form

$$1 + \bar{\alpha} = (1 + \bar{\alpha}^{238}) \cdot \frac{\left[\dfrac{\rho(1 - \rho_s/\rho)}{R_f} - \dfrac{\bar{\nu}\rho'(S)W_f/W_f(S)}{S}\right]}{\left[\dfrac{\rho(1 - \rho_s/\rho)}{R_f} - \dfrac{\bar{\nu}\rho'(S)W_f/W_f(S)}{S}\right]_{\mathrm{U}^{238}}} \frac{W(\mathrm{U}^{238})}{W_a}. \quad (5)$$

Unfortunately, as Table III-24-I shows, scattering contributes about 15.5% to the total measured reac-

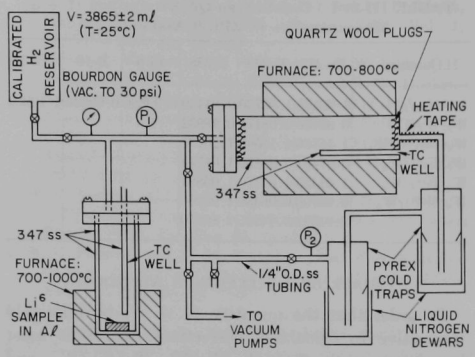

FIG. III-24-1. Tritium Extraction System for Irradiated $Li^6(n,\alpha)H^3$ Samples. *ANL Neg. No. 113-1052.*

tivity of U-238, necessitating a relatively large calculated correction. Nevertheless, the use of U-238 offers a direct check on the self-consistency of this technique for measuring the capture-to-fission ratio. One can compare the $(1 + \bar{\alpha})$ value for U-238 as obtained through the use of a reference absorber [Eq. (4)] with the direct radiochemical determination.

Capture-to-fission ratio measurements in fast spectra using this technique have been reported recently;[11,12] however, W_f was calculated rather than determined experimentally with a californium source. In both of these measurements, B-10 was chosen as the standard with BF_3 counters used to determine the absorption rates. Reactivity measurements were made with annular samples of B-10. Consequently, the sample used for reaction rate measurements had a self-shielding factor different from that used for the reactivity determinations.

For the recent measurements of $\bar{\alpha}$ for Pu-239 and U-235 in ZPR-9 Assembly 24 (see Paper III-23) Li-6 was chosen as the reference. Cylindrical lithium samples, enriched to 95.6% in Li-6, were extruded in an argon atmosphere to a diameter of 0.623 in. and cut into lengths of 0.850 in. The samples were weighed and sealed by electron beam welding in aluminum cans having a wall thickness of 0.020 in. These samples were used for both reactivity measurements and absolute absorption rate determinations.

Absolute Li-6 Absorption Rate

The absorption rate in Li-6 may be written as

$$R_a(Li^6) = R_{n,\alpha} + R_{n,\gamma} + R_{n,p} = R_{n,\alpha}[1 + (R_{n,\gamma} + R_{n,p})/R_{n,\alpha}] = 1.000198\, R_{n,\alpha}\,,$$

where $(R_{n,\gamma} + R_{n,p})/R_{n,\alpha}$ is calculated from MACH-1 fluxes and MC^2 30-group cross sections using ENDF/B data for Li-6.[13] Thus, the absorption rate is dominated by the reaction $Li^6 + n \rightarrow He^4 + H^3$.

This reaction rate can be determined by measuring the tritium activity induced in the irradiated sample. Following the irradiation, tritium may be removed from the lithium sample by an isotopic dilution method using hydrogen as the carrier gas. This technique was used by a number of investigators[14-16] who measured the $Li^7(n,t)$ cross section.

Briefly, the procedure consists of placing the irradiated sample in a stainless steel oven, evacuating the system, and then adding a known amount of hydrogen from a calibrated reservoir. The oven is then heated to about 750°C. In the hydrogen environment the lithium at this temperature is readily converted to molten lithium hydride and additional hydrogen is added to maintain a pressure of about one atmosphere. Once the hydrogen pressure reaches an equilibrium value, the oven temperature is raised to about 900°C where the LiH readily decomposes with the liberation of a mixture of hydrogen and tritium gas. Following a technique used by E. N. Sloth, et al.,[17] this hydrogen-tritium mixture is passed over a hot (750°C) bed of CuO. The hydrogen reduces the CuO with the subsequent formation of water vapor which is then collected in a liquid nitrogen cold trap. The activity of this tritiated water is determined by dissolving a portion of the sample in a dioxane base liquid scintillator and counting the tritium decays. Calibration of the counting system is accomplished by the use of a tritiated water sample obtained from the National Bureau of Standards. The absolute activity of this NBS standard was measured by two independent laboratories[18,19] with results that agree within 0.25%.[20]

Apparatus for extracting tritium from neutron-irradiated lithium samples has been built and tested. A sketch of this system is shown in Fig. III-24-1, where P_1 and P_2 represent thermocouple pressure gauges. Oven walls and thermocouple wells are made of Type 347 stainless steel in order to minimize hydrogen losses by diffusion through the hot surfaces.[21] Also, Type 347 stainless steel is more corrosion resistant to molten lithium and lithium hydride than most materials. The oven for heating the lithium sample is fitted with a Type 347 stainless steel liner which is replaced at the beginning of each extraction. This prevents cross contamination from one sample to the next.

Before each tritium extraction a freshly activated bed of CuO is prepared. Hydrogen is passed over commercial grade CuO (in wire form) at a temperature of about 350°C. After reducing all the CuO to copper the hydrogen flow is stopped and the excess gas is pumped

out of the system. Oxygen is then passed over the bed at a temperature of 425°C. With the formation of a fresh supply of CuO the oxygen supply is turned off and the entire system is outgassed. A greater fraction of the initial hydrogen is converted to water if freshly activated CuO is used in place of a commercial grade of CuO.

With the oven at room temperature, the aluminum-jacketed lithium sample is placed in position and the reservoir is filled with ultra pure hydrogen (99.999%). The reservoir pressure is read with a fused quartz precision pressure gauge and the temperature is also measured. Typically, the initial pressure is 30.00 psi at room temperature.

After evacuating the system, the oven containing the lithium sample is valved off from the fore pump and about one atmosphere of hydrogen is added to it. The oven is now turned on and the temperature set at 750°C while additional hydrogen is added so as to maintain a pressure of about one atmosphere. Complete formation of LiH is signaled when the pressure reaches an equilibrium value. The oven temperature is now raised to 900°C where lithium hydride readily dissociates[22] and the gas is allowed to slowly flow from the lithium oven over the hot (750°C) CuO bed to the liquid nitrogen cold traps which have been isolated from the vacuum pump. After all the hydrogen in the reservoir has been used, the tritiated water is vacuum distilled into the second trap and then carefully weighed. About 6 h are required for the extraction and the amount of water collected shows that about 1% of the initial hydrogen supply is lost during this time.

A small fraction of tritium probably remains in the lithium-aluminum residue following the primary extraction. To investigate this possibility, the system was allowed to cool and then a second extraction was performed on the sample. The activity of this second water sample was only 0.05% of that of the first. Following this second extraction, the residue was again allowed to cool and was then dissolved in ethyl alcohol. The hydrogen released in this process was passed through a series of liquid nitrogen cold traps designed to freeze out any alcohol vapor that might be present. Again the hydrogen was passed over the hot CuO bed with the water vapor collected in the final traps. The activity of this water sample was about 0.06% of that of the first sample.

The aluminum jacket surrounding the lithium sample does not disturb the results. During the initial heating process the aluminum melts and lithium aluminum hydride may be formed:

$$\mathrm{Li} + \mathrm{Al} + 2\mathrm{H}_2 \rightarrow \mathrm{LiAlH}_4 .$$

However, this compound readily dissociates at temperatures above 200°C:[21]

$$\mathrm{LiAlH}_4 \xrightarrow{200^\circ\mathrm{C}} \mathrm{LiH} + \mathrm{Al} + \tfrac{3}{2}\mathrm{H}_2 .$$

F. Brown, et al.,[14] have shown that no detectable amounts of tritium result from neutron interactions on aluminum.

The lithium samples contain 4.4% Li-7 and so a small correction must be made for the tritium activity resulting from the $\mathrm{Li}^7(n,n'\alpha)\mathrm{H}^3$ reaction. Lithium samples containing 99.993% Li-7 were irradiated and the induced tritium activity was measured by the methods just described. The tritium produced in the Li-7 reaction requires a correction of only 0.005%.

With the methods just described the R_a(Li-6) reaction rate can be measured with an accuracy of about 1% for samples irradiated in zero power fast reactors. The oscillator method was recently employed using Li-6 as the standard absorber to measure $\bar{\alpha}$ for Pu-239 and U-235 in ZPR-9 Assembly 24 (see Paper III-23).

References

1. W. C. Redman and M. M. Bretscher, *Direct Measurement of Effective Capture-to-Fission Ratio at Low Flux*, Reactor Physics Division Annual Report, July 1, 1964 to June 30, 1965, ANL-7110, pp. 261–266.
2. W. C. Redman and M. M. Bretscher, *Low Flux Measurement of U-235 Epicadmium Capture-to-Fission Ratio*, Reactor Physics Division Annual Report, July 1, 1965 to June 30, 1966, ANL-7210, pp. 315–318.
3. W. C. Redman and M. M. Bretscher, *Direct Determination of Uranium-235 Capture-to-Fission Ratio in a Zero-Power Reactor*, Nucl. Sci. Eng. **27**, 34 (1967); *Reactor Oscillator Determination of Capture-to-Fission Ratio in an Under-moderated Critical Assembly*, ANL-7143 (1966).
4. W. C. Redman and M. M. Bretscher, *Low Flux Measurement of U-235 Epicadmium Capture-to-Fission Ratio*, Nucl. Sci. Eng. **31**, 247 (1968).
5. T. G. Hersum, *Adaptation of a Low-Flux Capture-to-Fission Ratio Measurement Technique to Fast Critical Assemblies*, Unpublished M.S. Thesis, Michigan Technological University (1966).
6. D. A. Meneley, L. C. Kvitek and D. M. O'Shea, *MACH 1, A One-Dimensional Diffusion Theory Package*, ANL-7223 (1966).
7. W. C. Redman, *Pile Oscillator Determination of Capture-to-Fission Ratio*, TID-17738 (1962).
8. L. G. LeSage, W. R. Robinson and C. E. Till, Argonne National Laboratory (private communication).
9. B. J. Toppel, A. L. Rago and D. M. O'Shea, *MC²*, *A Code to Calculate Multigroup Cross Sections*, ANL-7318 (1967).
10. R. J. Armani, *Absolute Determination of Fission Rates in U-235 and U-238 and Capture Rates in U-238 by Radiochemical Techniques*, Reactor Physics Division Annual Report, July 1, 1965 to June 30, 1966, ANL-7210, p. 304.
11. T. L. Andersson, E. Hellstrand, R. Hakansson and Z. Bajbor, *Measurement of the Effective Capture-to-Fission Ratio in Pu-239 and U-235 in Two Different Fast Reactor Spectra*, Symposium on Fast Reactor Physics and Re-

lated Safety Problems, Karlsruhe, Germany (IAEA, Vienna, 1968), pp. 171–185. See STI/Pub-165 (Vol. 2); CONF-671043 (Vol. 2).
12. J. Adamson, R. M. Absalom, A. R. Baker, G. Ingram, S. K. I. Pattenden and J. M. Stevenson, *Zebra 6: A Dilute Plutonium-Fuelled Assembly*, ANL-7320, pp. 216–230.
13. M. E. Battat, D. J. Dudziak and R. J. LaBauve, *Li-6 and Li-7 Data in the ENDF/B Format*, LA-3695-MS (1967).
14. F. Brown, R. H. James, J. L. Perkin and J. Barry, *The Cross Section of the $Li^7(n,t)$ Reaction for Neutron Energies Between 3.5 and 15 MeV*, J. Nucl. Energy **17**, 137 (1963).
15. M. E. Wyman and M. M. Thorpe, *A Measurement of the $Li^7(n,n'\alpha)$ T Cross Section for Several Neutron Energies from 4 to 15 MeV by Absolute Counting Techniques*, LA-2235 (1963).
16. L. A. Currie, W. F. Libby and R. L. Wolfgang, *Tritium Production by High-Energy Protons*, Phys. Rev. **101**, 1557 (1956).
17. E. N. Sloth, D. L. Horrocks, E. J. Boyce and M. H. Studier, *Tritium in the Thermal Neutron Fission of Uranium-235*, J. Inorg. Nucl. Chem. **24**, 337 (1962).
18. A. Spernol and B. Denecke, *Absolute Tritium Counting in Internal Gas Counter*, Intern. J. Appl. Rad. Isotopes **15**, 241 (1964).
19. W. B. Mann, R. W. Medlock and O. Yura, *A Recalibration of the National Bureau of Standards Tritiated Water Standards by Gas Counting*, Intern. J. Appl. Rad. Isotopes **15**, 351 (1964).
20. W. B. Mann and A. Spernol, *The National Bureau of Standards Tritiated Water Standards*, Intern. J. Appl. Rad. Isotopes **15**, 628 (1964).
21. P. S. Flint, *The Diffusion of Hydrogen Through Materials of Construction*, KAPL-659 (1961); D. Randall and O. N. Salmon, *The Permeability of Type 347 Stainless Steel to Hydrogen and Tritium*, KAPL-904 (1953); N. J. Hawkins, *Solubility of Hydrogen Isotopes in Nickel and Type 347 Stainless Steel*, KAPL-868 (1953); R. R. Heinrich, C. E. Johnson and C. E. Crouthamel, *Hydrogen Permeation Studies*, J. Electrochem. Soc. **112**, 1067 (1965).
22. C. E. Messer, *A Survey Report on Lithium Hydride*, NYO-9470 (1960).

III-25. Preliminary Measurements of the Fission Yield of Mo-99 and Ba-140 from Pu-239 in Fast Spectra

R. J. Armani, R. Gold, R. P. Larsen* and J. H. Roberts†

Absolute radiochemical yields from fast neutron induced fission in Pu-239 have not been accurately measured to date, as may be inferred by an examination of the appropriate literature.[1-3] The need for these yields has and will continue to increase with the increased use of Pu-239 fuel in fast reactors. Several yields are extremely useful for radiochemical determinations of fuel burn-up, such as Mo-99, Ba-140 and Cs-137. Consequently, accurate yield data for any of these isotopes is highly desirable.

Fission yield measurements for Pu-239 in fast neutron spectra have been planned. These measurements will be made in environments where the neutron spectrum has been well calculated and, wherever possible, experimentally measured (either by time-of-flight or with proportional counters). The spectra that have been chosen are similar to those expected in fast breeder reactors. Initial measurements will be made of the fission yields of Mo-99 and Ba-140. Subsequent measurements will include other isotopes of interest.

The initial measurements of Mo-99 and Ba-140 will be carried out by using radiochemical techniques to determine the amount of Mo-99 and Ba-140 produced in irradiated Pu-239 foils. The measurement of the total number of fissions which occur in the foil will be accomplished by using the solid-state track recorder technique.[4] Irradiations will be carried out with nanogram quantities (10^{-9} g) of Pu-239 plated on platinum planchets. These electroplated samples will serve as fission sources for the solid-state track recorders. In addition, such small quantities of Pu-239 will be accurately determined by alpha counting, since the Pu-239 half life has been accurately reported. Milligram quantities of Pu-239 in the form of metal foils will be included in the sample capsules for the radiochemical determination of Mo-99 and Ba-140. The arrangement of track recorders and metal foils in the capsule will be such that symmetry, flux gradients, and flux depression will be taken into account.

The fission yield can then be calculated from the fission rate equation

$$Y = \frac{A}{F(1 - e^{-\lambda t})}, \qquad (1)$$

where

Y ≡ fission yield
F ≡ fission rate
A ≡ activity of the isotope of interest

* Chemical Engineering Division, Argonne National Laboratory.
† Northwestern University, Evanston, Illinois.

λ ≡ decay constant of the isotope of interest
t ≡ irradiation time at constant flux level.

It is expected that with these techniques, it will eventually be possible to attain accuracies of 2% for Mo-99 and Ba-140.

Preliminary measurements have been planned for the Gulf General Atomics Assembly, ZPR-3, and the Argonne Thermal Source Reactor (ATSR) Snell Block. The fast neutron spectum is either well calculated or measured for all these environments.

References

1. S. Katcoff, *Fission Product Yields from Neutron-Induced Fission*, *Nucleonics*, **18**, 201–208 (November 1960).
2. I. F. Croall, *Yields from Neutron Induced Fission*, AERE-R 5086 (1967).
3. M. E. Meek and B. F. Rider, *Summary of Fission Product Yields for U-235, U-238, Pu-239, and Pu-241 at Thermal, Fission Spectrum and 14 MeV Neutron Energies*, APED-5398 (March 1968).
4. R. Gold, R. J. Armani and J. H. Roberts, *Absolute Fission Rate Measurements with Solid-State Track Recorders*, Nucl. Sci. Eng., **34**, 13–32 (October 1968).

III-26. Reactor Neutron Noise Studies

N. Pacilio*

An extensive and detailed study has been made concerning advanced methods of reactor-neutron-noise time analysis. These methods can yield accurate information on reactor kinetic parameters and will therefore become more important in both basic and applied aspects of nuclear reactor science and technology.

The presentation is divided into five sections representing independent areas of reactor neutron noise studies. This summary, which is essentially theoretical, is dedicated to a better understanding of the phenomenology involved in the various experimental procedures. Those subjects which have been more completely covered in the literature are cited in the general reference list.

The Role of the Polarity Correlation Function in Reactor-Noise Analysis

The most recent trend of noise analysis is oriented to the consideration of a discrete noise field to be sampled in the time domain. This return to the study of individual pulses must be essentially intended as an extension of the original approach, motivated by new theoretical and technological opportunities, which now allow a profitable application of noise techniques to any type of reactor. Among the main elements of this approach is the development of new techniques[1] in which only the sign of the signal (with respect to the mean value) is needed to determine the time-correlation function and, therefore, the kinetic parameters.

The work has been limited to considering the techniques involving polarity correlation; this function and its dependence on the probability distribution of pulses are introduced and described. Several types of amplitude distributions are considered in order to take into account the possible characteristics of the detected pulses, viz. their limited number, the mutual degree of correlation and some other non-Gaussian properties.

The polarity correlation function is expressed as a function of the numerical correlation function of counts, under the hypothesis that the signal from a neutron detector placed inside a reactor follows a Gauss or an Edgeworth amplitude distribution. Since the correlation function of the power level signal in a steady-state operating reactor has been extensively treated by many authors, the polarity algorithm and its experimental applications find, in this way, the link to reactor kinetic analysis.

The well-known sinusoidal[2,3] relation between the polarity correlation and the numerical correlation function—valid under the Gaussian and standard-measure assumption—needs to be modified[4] when the previous conditions are not satisfied, i.e. for non-zero mean, skew and non-mesokurtic distributions. The corrections have been calculated for the conditions of small or an unrestricted degree of correlation between the two variables. Some questions arising from the experimental realization of the technique have been treated. It has been noted that the first-order corrections are proportional to the correlation or constant; they do not affect the obtainable results since the required correlation function is a linear combination of exponentials whose decay constants give

* Resident Associate, Comitato Nazionale Per L'Energia Nucleare, Rome, Italy.

the wanted information. If a higher degree of correlation is achieved, the sensitivity of the method is improved but higher-order corrections are not negligible anymore and the interpretation of the experimental data is less immediately feasible.

Reactor-Noise Analysis from the Sign of the Fluctuations around a Steady-State Power Level

The method described[5] has its point of departure essentially in the Feynman variance procedure, which is the common ancestor of the whole ensemble of neutron statistics techniques applied at the present time.

Until now, no results have been obtained by measuring the covariance between samplings from two counters, as suggested by C. E. Cohn,[6] who emphasizes some advantages of this technique not obtainable by using a single detector and the computation of the variance. In fact, the adoption of two counters relieves the stringent necessity of a high detection-efficiency and allows these techniques to be applied to fast systems also.

The theory concerning this experiment can be easily extracted from some of the previous works on the subject merely by taking into account the presence of two differently effective detectors and the consequent modifications. In this way a relation can be obtained between the covariance of the neutron counts from both detectors and the kinetic parameters of the system. This relation also depends on the time interval adopted to record the counting events. Although this covariance method seems to offer good experimental prospects, its realization may benefit from further improvement if the meaning and the role of the covariance of a certain joint distribution of variables is recalled and appropriately used in order to optimize the data collection process. In fact it can be shown that no numerical information about the two signals is indispensable for the calculation of the covariance, since merely knowing the sign of the two variables with respect to their mean values and employing some properties of the probability distribution function allows the covariance to be determined by a simpler and faster procedure.

The experiment may be conceived on the following basis:

Assume that a certain population is sampled in a time interval t by two simultaneously operating counters and that some polarity information is collected from both of them, e.g. the sign of the difference between the number of pulses occurring in that interval t and the mean number of events expected in the same interval t, or any other equivalent information about the mean level of the fluctuation signal (higher or lower with respect to the long-time-averaged level) in the given interval t. This measurement is repeated N times.

Four types of results are clearly possible; let $N1$, $N2$, $N3$, and $N4$ be the number of pairs featuring the following combination of signs ($++$, $-+$, $--$, $+-$), respectively. Their sum is equal to N.

If the outputs of the two counters are positively (negatively) correlated, $N1$ and $N3$ ($N2$ and $N4$) are expected to be greater than $N2$ and $N4$ ($N1$ and $N3$) according to the amount of coherence involved. This is obviously given by the covariance of the two variables for the adopted gate-width t. If standard-measure conditions hold for both the variables, the covariance is also called the correlation coefficient.

If calculated for the neutron population in a steady-state operating reactor, the covariance is a function of the reactor static and dynamic conditions, viz. reactivity, flux shape, and fuel, as well as of the time interval t. In particular, $[\mathrm{cov}(t)/\mathrm{mean}]$ is monotonically increasing with respect to t from a zero value toward an asymptotic value depending essentially on the detector efficiency and the reactivity. Thus, $N1$ and $N3$ are expected to be as probable as $N2$ and $N4$ in the case of short time intervals t, since the two detectors are actually independent; however, in the case of longer intervals, a trend appears in both detectors toward a similar behavior of their characteristic counting fluctuations. Then, $N1$ and $N3$ become more probable than $N2$ and $N4$; the excess of $N1$ and $N3$ and the defect of $N2$ and $N4$ can be quantitatively interpreted in terms of the increasing degree of coherence between the two detectors. In this way experimental observation of the quantities $N1$, $N2$, $N3$, and $N4$ leads to the determination of $\mathrm{cov}(t)$, whose magnitude for various values of t can be analyzed and interpreted in terms of reactor parameters.

In the first part of the work, the formation of $\mathrm{cov}(t)$ is given in the case of the described experiment of two detectors placed inside or near a multiplying assembly. In the second part, the role of the covariance in the probability distribution of two correlated variables is outlined under the assumption of Gauss and Edgeworth frequency surfaces and the possibility of its determination from only the sign of the variables with respect to their mean values is presented.

Some geometric and numerical properties of the quantities involved, viz. the probability distribution functions, are also taken into account to allow a better and more direct understanding of some of the physical phenomena treated on the way to the final formulae.

Remarks on Methods Based on the Expected Number of Correlated Neutron Pairs and Triplets for Kinetic Parameter Determination

An interesting alternative to the variance experiment is based on the determination of the ratio of the expected number of correlated neutron pairs to the expected number of random neutron pairs in a given time interval. This parameter, Z, is strictly related to the instantaneous and mean counting rates and it is found to be quite close to the correlated relative variance Y. It can also profitably replace Y in some experimental circumstances where the variance approach proves unfruitful, i.e. for subcritical measurements. The procedure is unsuitable for non-zero power and fast reactor systems.

The new method[7,8] has its point of departure from an analysis of some of the inconvenient aspects of the correlated relative variance method. In addition it possesses independent physical meaning and phenomenology. Actually this procedure represents a new method of data treatment, since the measuring apparatus and the data collection can be essentially identical to those adopted for the conventional variance experiment.

In order to understand the advantages of the procedure, some comments concerning the theoretical formulation of the prompt variance analysis are necessary. In the prompt variance method, the main role is played by the quantity Y which suffers from the following shortcomings:

1. Y is not a real reactor parameter since its magnitude depends on detector sensitivity and location inside the reactor, i.e. it depends on the flux profile.
2. The value of Y is small in the time region where the maximum of correlated neutron pairs is expected, i.e. its value is small in the range of time intervals α where its dependence on the prompt-neutron decay eigenvalue is strong and, conversely, becomes large where the dependence is no longer sensitive.
3. The value of Y is small if detector count rates are small with respect to the overall fission rate, i.e. a location far away from the flux peak and/or small detector sensitivity.
4. The dependence of Y on reactivity is such that Y decreases with respect to reactivity more rapidly than $(1 - \$)^{-1}$, since increasing values of α demand shorter intervals to be accurately determined. Thus the Feynman-variance method cannot be applied to strongly subcritical systems, a small Y being prohibitive for any analysis.
5. In some assemblies such as natural uranium and light water lattices even the asymptotic and maximum values of Y are on the order of 0.01 and hence then practically useless for any significant interpretation.

The new term Z is equal to the ratio of the expected number of correlated neutron pairs to the expected number of random neutron pairs. The physical meaning and the basic characteristics of the parameter Z, partially in contrast with the quantity Y, can be summarized as follows:

1. The value of Z vanishes for a Poisson process, as does Y, according to the absence of any correlated pair. This is also equivalent to the fact that Z vanishes if no multiplication exists.
2. Contrary to Y, Z is large in the range of short time intervals and has a strong dependence on the value of α.
3. For very short time intervals Z does not vanish, contrary to Y, since no correlation is detectable for vanishing sampling intervals. Conversely, Z remains finite and tends to a maximum since the chances of correlated pairs increase with respect to those of random pairs. The limit value $Z(0)$ coincides with correlated-to-uncorrelated ratio of the Rossi-alpha experiment and therefore offers a significant theoretical basis and the possibility of comparison between the two techniques.
4. For very long time intervals, but still in the prompt-neutron approximation, Z tends to vanish, since the number of correlated pairs saturates and practically all random pairs are detected.
5. Z is a characteristic physical parameter of the reactor, since it does not depend on detector location and sensitivity but only on reactivity and power (source) level as well as on the sampling interval Δt.
6. The dependence of Z on reactivity appears to be a direct function of α, i.e. the slope of the behavior, since the initial value $Z(0)$ is approximately constant for decreasing reactivities.

Further and recent investigations[9] on the neutron fluctuation phenomena have considered the possibility of reaching additional information via a third-order moment analysis of the distribution counts, and via the determination of the ratio of the expected number of correlation neutron triplets to the expected number of random neutron triplets. Both procedures may be regarded as extensions of the second-order moments previously discussed.

For instance, the mathematical formulation shows that, from a strictly theoretical point of view, experi-

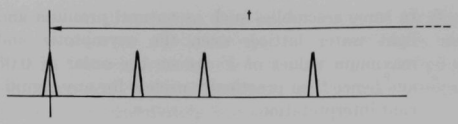

FIG. III-26-1. Phenomenology of the Rossi-Alpha Experiment. *ANL Neg. No. 112-9330.*

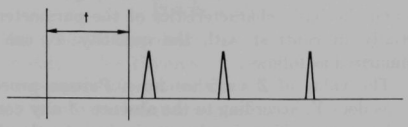

FIG. III-26-2. Phenomenology of the Zero Count Probability Experiment. *ANL Neg. No. 112-9330.*

ments of this type yield the effective total fraction β of delayed neutrons and the prompt-neutron generation time Λ separately without any need of static measurements. This would really be novel in reactor parameter measurements.

Several types of analyses have been proposed according to the several combinations of third-order moments which can be adopted in manipulating the collected data. The only experiment performed for those purposes has shown that, at the present time, the horizon of those procedures is not larger than that offered by the second-order methods. Furthermore, it has shown that a separate determination of β and Λ is based on the detection of events (a triplet of neutrons originated from the same fission event) which is too rare and infrequent to make it possible, at least in thermal reactors. Thus, at the present time, the third-order experiment is just another type of analysis which can be performed on the same set of data useful for the second-order experiments, and in some cases—e.g. those in which a very high efficiency is available—can allow a more adequate precision to be reached in comparison with the various variance procedures.

Comments on Some Probability Methods used in Reactor-Noise Time Analysis

Several methods based on analysis of the time probability distribution of neutron counts in a detector have been developed for the study of correlations among reactor neutrons. Four of them have interesting interrelationships and cover a wide range of possibilities in reactor measurements. The first is as old as reactor technology itself or at least as old as the idea of a correlation experiment; the second was developed in the early 1960's while the remaining two have quite recently appeared in the literature. The four methods are (see Figs. III-26-1 through III-26-4, respectively):

1. *the Rossi-alpha method,*[10] based on the determination of the time distribution of *all* pulses following a certain triggering pulse from the neutron detector;
2. *the zero count probability method,*[11] based on the determination of the probability of no counts as a function of the time interval t during which the neutron detector output is observed;
3. *the time interval from a random origin method,*[12] based on the determination of the time distribution of the pulse immediately following a random start of the time analysis; and
4. *the pulse-to-pulse time interval method,*[13] based on the determination of the time distribution of the pulse successive to the pulse which triggered the time analysis.

The described methods lead to the determination of some fundamental reactor kinetic parameters, which follow from the value of the prompt neutron decay eigenvalue α, measured at critical and subcritical. They are the ratio of the effective delayed neutron fraction to the prompt neutron lifetime, the reactivity, and all the kinetic and dynamic coefficients usually expressed in terms of reactivity. Determination of the detector efficiency and, therefore, of the absolute power level are also possible.

The four methods are complementary in their applicability and effectiveness. In fact, Method 1 is widely used in fast experiments but is too time-consuming for thermal experiments; furthermore it is power sensitive, that is to say, the smaller the power (source) level, the larger the correlation term, which contains the required information. Methods 2 and 3 are efficiency limited, that is to say, the larger the

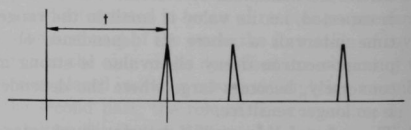

FIG. III-26-3. Phenomenology of the Time Interval from a Random Origin Experiment. *ANL Neg. No. 112-9330.*

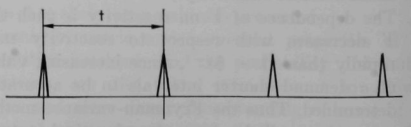

FIG. III-26-4. Phenomenology of the Pulse to Pulse Time Interval Experiment. *ANL Neg. No. 112-9330.*

detection efficiency, the larger the correlation term to measure. Thus, they are applicable only to thermal reactors. Method 4 suffers fewer limitations from power (source) and/or efficiency problems; it is rather equivalent to Method 1 in fast experiments; much faster than Method 1, more flexible than Method 2, and as effective as Method 3 in thermal experiments.

All the procedures imply the use of pulse counters and are thus limited to zero power reactors.

There is another new technique (*even- or odd-count probability method*) recently added to the long list of reactor-noise time-analysis procedures.[14] It is based on the determination of the parity of the number of pulses which occur in given time intervals.

Each technique has been applied to both random and correlated processes. Thus, the Poisson distribution has been adopted to describe uncorrelated events. The Pal-Mogilner-Zolotukhin distribution[11,15] (it represents the distribution of neutron counts in the one-point monokinetic model) and the Polya distribution[16] (often used instead of the more mathematically elaborate Pal-Mogilner-Zolotukhin distribution) have been chosen as distributions of events of a correlated nature. An extensive computational study of all the methods for each of the three considered distributions has been performed.

Reactor-Noise Analysis in the Time Domain: Current State of the Art

The author has written a book[17] as a partial and synthetic description of the state of the art of neutron fluctuation observations at the present time.

One of the most impressive facts concerning reactor-noise analysis methods is in the multiple differentiation and branching from one or two pioneering procedures into several special techniques from the viewpoint of methodology, data collection, and interpretation of results.

Today a unique reference list on reactor-noise analysis is no longer acceptable, since such a list would be extremely confusing for a neophyte. In order to avoid partially this inconvenience, the presentation has been limited to techniques related and/or applied to spontaneous fluctuations in the time domain and have dropped the Fourier-conjugated methods which imply the observation and analysis of the same phenomena in the frequency domain. The growth of published material requires this separation from the noise analysis via analog method as well as from all other non-neutronic noise techniques. Thus, the present work is essentially the description of the evolution of the art treated in Ref. 18.

Reference 17 has been directed to experimentalists: the reference list on reactor noise is full of extremely elegant theoretical treatments but is often short of practical indications of how experiments could be performed or which is the focal formula with which to work. For this purpose, we have divided the most frequently used techniques into four categories: each of these feature substantial differences concerning either the measuring apparatus or the treatment of data and the extraction of information on reactor parameters. The final formulae of each procedure are not derived but simply described and interpreted according to an experimental perspective, since the main emphasis is given to the methodology, the efficiency, and the more or less difficult realization of the techniques.

An extensive chronological reference list is also reported for each group in order to allow a sufficiently complete documentation of the theoretical background of the methods and of the most widely known results obtained in kinetic and reactive parameter measurements.

Outline

The analysis of the methods is divided into four groups:

1. Time Correlation Analysis Among Neutron Pulses
   a. Rossi-alpha method
   b. Inherent "pulsed-source" method
   c. Auto- and cross-correlation method of the neutron detector output
   d. Pulse-to-pulse time interval method
   e. Time interval from a random origin method
2. Analysis of the Moments of Neutron Distribution
   a. Feynman-variance method
   b. Expected number of correlated neutron pairs method
   c. Bennett-variance method
   d. Third-order moment method
   e. Covariance method
3. Analysis of the Probability of Neutron Distribution
   a. Zero probability method
   b. Even or odd-count probability method
   c. Polya model method
   d. Other intermediate methods
4. Analysis of the Signs of Fluctuations
   a. Polarity auto- and cross-correlation method
   b. Covariance method via polarity detection

Every method is treated in the following format:

1. presentation
2. mathematical formulation
3. experimental methodology
4. interpretation of data.

All the described techniques provide the determination of the values of time behavior parameters (e.g. prompt-neutron decay constant α) as well as those of

static parameters (e.g. reactivity, power) replacing and extending original reactor physics procedures used in earlier experiments. In fact, for a nuclear system, the prompt period at criticality, viz, the ratio of the prompt-neutron lifetime to the effective total fraction of delayed neutrons, is one of the most important parameters for comparison between theory and experiments. It is important because it allows basic data concerning cross-section libraries, spectral distributions and discretization into groups, importance function, etc., to be checked directly with the results of measurements. A homogeneous comparison between calculated and observed values of α offers valid additional information that can be obtained from even subcritical assemblies. For subcritical systems, the parameter α is observable while reactivity is not. This suggests a new approach to all the reactivity-related coefficient measurements, that is fuel, control rods, temperature, and moderator level, which is extendible to highly subcritical systems unlike all other reactivity-based procedures.

All mathematical developments are generally based on a bare monoenergetic diffusion-theory model; often the prompt-neutron kinetics approximation is adopted. Such a simplified treatment does not imply any unawareness of and/or disregard for reactor-noise theoreticians and their more complex and sophisticated models. Obviously the validity of the methods, as practical tools, remains intact and effective. Problems of a more subtle interpretation of the results come after and beyond the verified possibility of measuring reactor parameters.

Presently, reactor-noise time-analysis methods are a challenging but insufficiently applied tool of measuring reactor physics and engineering data. These techniques are fast, accurate, and inexpensive. In addition, they do not interfere with reactor operation. In all probability they will become routine procedures for research in low power critical (and subcritical) facilities as well as for control in high-power reactors. This is why Ref. 17 is a step, but only an intermediate step, toward the more extended message that still has to be communicated.

References

1. B. P. Th. Veltman and H. Kwakernaak, *Theorie und Technik der Polärätätskorrelation für die Dynamische Analyse Niederfrequenter Signale und Systeme*, Regelungstechnik **9**, No. 9, 357 (1961).
2. H. Cramèr, *Mathematical Methods of Statistics*, Chap. 21, 290 (Princeton University Press, 1946).
3. T. J. Stieltjes, *Extrait d'une Lettre Adressée a M. Hermite*, Bull. Soc. Math., Series 2, **13**, 170 (1889).
4. W. Heins, et al., *On the Polarity Correlation of Non-Zero Mean Gaussian Variables*, Report No. 65-2, Technological University of Delft, Netherlands (1965).
5. N. Pacilio, *Reactor-Noise Analysis: The Covariance Method via Polarity Detection*, Nucl. Sci. Eng. (to be published).
6. C. E. Cohn, Remark on the paper by H. Christensten, et al., *Neutron Noise, Waves and Pulse Propagation*, AEC Symposium Series **9**, 530 (1967).
7. A. Furuhashi and S. Izumi, *A Proposal on Data Treatment in the Feynman-α Experiment*, J. Nucl. Sci. Tech. Tokyo **4**, 101 (1967).
8. A. Furuhashi and S. Izumi, *The Third-Order Moment of the Number of Neutrons Detected in Short Time Intervals*, J. Nucl. Sci. Tech. Tokyo **5**, 48 (1968).
9. J. B. Dragt, *Three-Fold Correlation and Third-Order Moments in Reactor Noise*, Nukleonik **10**, 7 (1967).
10. J. D. Orndoff, *Prompt Neutron Periods of Metal Critical Assemblies*, Nucl. Sci. Eng. **2**, 450 (1957).
11. V. G. Zolotukhin and A. I. Mogilner, *The Distribution of Neutron Counts from a Detector Placed in a Reactor*, Atomic Energy (USSR) **15**, 11 (1963).
12. D. Babala, *Interval Distributions in Neutron Counting Statistics*, Nucl. Sci. Eng. **29**, 367 (1967).
13. D. Babala and R. Ogrin, *Measurement of the Prompt Neutron Decay Constant of the NORA Reactor by the Interval Distribution Technique*, Nucl. Sci. Eng. **29**, 367 (1967).
14. J. B. Dragt and E. Türkan, *Some Remarks on the Practical Use of the p-Method in Reactor Noise Analysis*, Nuckleonik **10**, 67 (1967).
15. L. I. Pal, *Determination of the Prompt Period from the Fluctuation of the Number of Neutrons in a Reactor*, J. Nucl. Energy: Pts. A & B **17**, 395 (1963).
16. N. Pacilio, *The Polya Model and the Distribution of Neutrons in a Steady-State Reactor*, Nucl. Sci. Eng. **26**, 565 (1966).
17. N. Pacilio, *Reactor-Noise Analysis in the Time Domain: Current State of the Art*, (USAEC), Critical Review Series (in press).
18. J. A. Thie, *Reactor Noise*, ANS Monograph (Rowman & Littlefield, New York, New York).

III-27. Studies of Reactivity Coefficients in Large Fast Reactors

H. H. Hummel and L. K. Volodka

Part A. Applicability of First-Order Perturbation Theory in Sodium Voiding Calculations

The reactivity change that occurs when sodium is voided from a reactor can be resolved by first-order perturbation theory into spectral (moderation), capture, and leakage components.[1-3] The approximation is made in the first-order theory that the unperturbed flux and adjoint are used in calculating reactivity changes; otherwise a k calculation is required for each perturbed configuration. Perturbation theory can be made to give the exact result for total reactivity change by using the unperturbed flux and perturbed adjoint, or vice versa. The resolution into components no longer has a precise physical meaning, however, since the components are slightly different by the two methods.

A question that arises in first-order perturbation theory in the diffusion theory approximation is what to use for δD, the change in diffusion coefficient. If $\Sigma_{tr_{1j}}$ and $\Sigma_{tr_{2j}}$ are the unperturbed and perturbed reactor transport cross sections respectively for group j, the exact expression for δD_j is $1/3\Sigma_{tr_{2j}} - 1/3\Sigma_{tr_{1j}} = (\Sigma_{tr_{1j}} - \Sigma_{tr_{2j}})/3\Sigma_{tr_{1j}}\ \Sigma_{tr_{2j}}$. If the perturbation is assumed small and $\Sigma_{tr_{2j}}$ is approximated in the denominator by $\Sigma_{tr_{1j}}$, δD_j becomes $(\Sigma_{tr_{1j}} - \Sigma_{tr_{2j}})/3\Sigma^2_{tr_{1j}}$. This expression and the exact one will be referred to as Option A and Option B respectively. (For exact perturbation theory only Option B is used.) For sodium voiding Option A will yield a smaller leakage component than the more correct Option B, since $\Sigma_{tr_2} < \Sigma_{tr_1}$. On the other hand, the neglect in flux (or adjoint) changes in calculation of the leakage component introduces an error which tends to oppose that of Option A, so that in some cases the use of Option A will roughly compensate the error from neglect of the flux perturbation.

A possible interpretation of the error from neglect of the flux perturbation in the core region is that the increase in reflector savings occurring on sodium voiding is not taken into account. The associated decrease in the gradient of the flux (or adjoint) is therefore not taken into account either, resulting in an overestimate of the leakage component.

First-order and exact perturbation calculations for sodium voiding are compared in Table III-27-I for a spherical and an infinite slab reactor. The exact solution given here is for the perturbed flux and unperturbed adjoint. Note that the perturbed eigenvalue k' occurs in the denominator of the tabulated reactivity values for the exact theory, while for the first-order theory results the unperturbed value k occurs. This slight inconsistency is not important for the present comparison. The compositions used in these calculations were those of the inner core region and axial blanket of a 1000 MWe reactor with PuC-UC fuel.[4] The fertile-to-fissile ratio in the core was 6.61, and approximate volume percentages of fuel, stainless steel, and sodium in both core and blanket were 26, 8, and 66 respectively. This sodium content is 1.5 to 2 times the range of current design interest, so that conclusions about the magnitudes of non-linearities on sodium voiding and of other properties dependent on sodium content should be interpreted accordingly.

Results are given in Table III-27-I for voiding the core alone, for voiding core plus blanket, and for voiding from full to half sodium, half to no sodium, and full to no sodium. Failure of the components for full-to-half and half-to-no sodium voiding to add up to those for the full-to-no sodium voiding case is a consequence of the ambiguity in the definition of these components mentioned above (and also because of a slight inconsistency in the denominator).

It is observed from Table III-27-I that, for voiding of the core alone, use of Option A usually gives better results because of the compensation of errors mentioned previously. Use of this option introduces large errors for blanket voiding, however. The errors indicated for the first order theory are so large that it should not be used for complete reactor voiding, although it is acceptable for voiding of small regions or for calculating the effect of small sodium density changes. Non-linearities with sodium content are large enough that extrapolation of the total voiding effect or of the leakage component from partial to total voiding is unsafe. (The large non-linearity in the leakage component arises from the fact that the δD corresponding to a given change in sodium content varies with sodium content.) For the spectral and capture components the non-linearity is small enough that extrapolation is a reasonable procedure.

While the effect of flux perturbations on the sodium voiding reactivity change by a perturbation calculation is significant (Exact versus Option B in Table III-27-I), it is much larger in a direct k calculation, in which there is no adjoint function weighting. In Table III-27-II the δk for sodium voiding for the cases of Table III-27-I is given along with similar results for a bare

TABLE III-27-I. EXACT VERSUS FIRST-ORDER PERTURBATION THEORY FOR SPHERICAL[a] AND INFINITE SLAB[b] REACTORS

Change in Sodium Content	Regions	k'	$\frac{\%\delta k}{k'}$, Exact[c] (Perturbed Flux)			$\frac{\%\delta k}{k}$, First Order $\delta D = \frac{\delta\Sigma_{tr}}{3\Sigma^2_{tr_1}}$ Option A			$\frac{\%\delta k}{k}$, First Order $\delta D = \frac{\delta\Sigma_{tr}}{3\Sigma_{tr_1}\Sigma_{tr_2}}$ Option B		
			Spectral + Capture	Leakage	Total	Spectral + Capture	Leakage	Total	Spectral + Capture	Leakage	Total
Sphere, Blanket Not Voided											
Full-Half		1.0063	3.05	−2.42	0.63	2.94	−2.22	0.72	2.94	−2.66	0.28
Half-No		1.0095	3.45	−3.12	0.32	3.33	−2.84	0.49	3.33	−3.60	−0.27
Full-No		1.0095	6.27	−5.33	0.94	5.88	−4.49	1.44	5.88	−6.71	−0.83
Sphere, Blanket Voided											
Full-Half	Core		3.00	−2.52	0.48	2.94	−2.22	0.72	2.94	−2.66	−0.28
	Blanket		0.42	−1.18	−0.76	0.37	−0.95	−0.58	0.37	−1.14	−0.77
	Total	0.9974	3.42	−3.70	−0.28	3.31	−3.17	0.14	3.31	−3.80	−0.51
Half-No	Core		3.21	−3.61	−0.40	3.29	−3.05	0.24	3.29	−3.85	−0.56
	Blanket		0.59	−2.14	−1.55	0.53	−1.61	−1.08	0.53	−2.05	−1.52
	Total	0.9785	3.80	−5.75	−1.95	3.82	−4.66	−0.84	3.82	−5.90	−2.08
Full-No	Core		5.87	−5.95	−0.08	5.88	−4.44	1.44	5.88	−6.71	−0.83
	Blanket		0.96	−3.09	−2.33	0.74	−1.90	−1.16	0.73	−2.90	−2.16
	Total	0.9785	6.83	−9.04	−2.21	6.62	−6.34	0.28	0.61	−9.61	−2.99
Infinite Slab, Blanket Not Voided											
Full-Half		1.0190	3.16	−1.30	1.86	2.98	−1.24	1.74	2.98	−1.49	1.49
Half-No		1.0416	3.72	−1.54	2.18	3.50	−1.46	2.04	3.50	−1.85	1.64
Full-No		1.0416	6.74	−2.74	4.00	5.96	−2.48	3.48	5.95	−3.75	2.20
Infinite Slab, Blanket Voided											
Full-Half	Core		3.12	−1.34	1.78	2.98	−1.24	1.74	2.98	−1.49	1.49
	Blanket		0.84	−1.59	0.75	0.75	−1.33	−0.58	0.75	−1.60	−0.85
	Total	1.0106	3.96	−2.93	1.03	3.73	−2.57	1.16	3.73	−3.09	0.64
Half-No	Core		3.53	−1.74	1.79	3.45	−1.55	1.90	3.45	−1.96	1.49
	Blanket		1.17	−2.69	−1.53	1.04	−2.11	−1.07	1.04	−2.69	−1.65
	Total	1.0134	4.70	−4.43	0.27	4.49	−3.66	0.83	4.49	−4.65	−0.16
Full-No	Core		6.41	−3.02	3.39	5.96	−2.48	3.48	5.95	−3.75	2.20
	Blanket		1.89	−3.98	−2.05	1.50	−2.66	−1.16	1.51	−4.06	−2.55
	Total	1.0134	8.30	−7.00	1.30	7.46	−5.14	2.32	7.46	−7.81	−0.35

[a] Core radius 83.2 cm; blanket extrapolation outer radius 128.2 cm.

[b] Half height: core 31.8 cm; core and blanket 76.8 cm.

[c] The unperturbed eigenvalue (before voiding) is denoted by k and the perturbed eigenvalue by k'. In each case $k = 1$ for full sodium, while k for half to no sodium equals k' for full to half. The first column was obtained by direct eigenvalue calculation, the others by perturbation theory.

core of the same composition, in which no change in reflector savings occurs on sodium voiding, so that the geometrical buckling remains constant. The effect of the change in reflector savings is seen to be very large in this case. A perturbation calculation was also made in which a "chopped" (sin Br)/Br flux was used over the spherical core, and the effect of a reflector savings change was obtained by varying the buckling. In this instance the effect of flux perturbation was much smaller and was of the same order as for the corresponding case in Table III-27-I, again showing the effect of adjoint function weighting.

Part B. Applicability of Simple Flux Approximations in Doppler Effect Calculations

A comparison is given in Table III-27-III of one- and two-dimensional calculations of the Doppler effect for the 1000 MWe reactor mentioned in Part A. The core of this reactor has two enrichment zones, as indicated, and the axial and radial blankets have different compositions. It was considered of interest to see how well the Doppler effect in this typical power reactor geometry could be predicted by the use of the simplest flux approximations.

The Doppler effect is primarily a spectral phenomenon and is not expected to be sensitive to geometrical details; for a large uniform core uniformly heated it is well predicted from a fundamental mode flux. In the present work, given in Table III-27-III, the results of two-dimensional and one-dimensional radial calculations for uniform heating of the core are compared. For the one-dimensional calculations the (group-independent) transverse buckling, assumed the same in all regions, was adjusted to obtain criticality. For the central region a "chopped" Bessel function fundamental mode calculation was also performed. Agreement among the three calculations is good, indicating that for this reactor the simplest flux approximations are adequate for Doppler effect calculations. More sophisticated techniques are undoubtedly required when moderating reflectors are present to augment the low-energy flux in the outer part of the core.

TABLE III-27-II. Reflector Savings and Bare Core Reactivity Effects for Cases in Table III-27-I

	λ_1, cm	$\delta\lambda$, cm	δk (Reflected), %	δk (Const. B^2), %
Sphere				
Blanket Not Voided				
Full-Half	19.2	4.3	0.63	−1.6
Half-No	23.5	6.4	0.32	−3.5
Sphere				
Blanket Voided				
Full-Half	19.2	2.6	−0.26	−1.6
Half-No	21.8	2.7	−1.89	−3.6
Slab				
Blanket Not Voided				
Full-Half	19.4	3.4	1.90	−1.6
Half-No	22.8	4.9	2.26	−3.2
Slab				
Blanket Voided				
Full-Half	19.4	2.6	1.06	−1.6
Half-No	22.0	3.1	0.28	−3.5

TABLE III-27-III. Doppler Effect[a] in Core of Combustion Engineering 1000 MWe Reactor, 1500 → 1100°K

(Core height 76 cm)

Radii, cm	0–78.0[b]	78.0–110.0[c]	Total
$\%\delta k$, 2D	0.0886	0.0311	0.1197
$\%\delta k$, 1D Radial	0.0849	0.0300	0.1149
$\%\delta k$,[d] Fund. Mode	0.0866	—	—

[a] By first-order perturbation theory.
[b] Fertile to fissile ratio 6.61.
[c] Fertile to fissile ratio 5.07.
[d] J_0^2 weighting for bare radius of 176 cm.

References

1. A. M. Weinberg and E. P. Wigner, *The Physical Theory of Neutron Chain Reactors*, (University of Chicago Press 1958) p. 540.
2. H. Soodak, ed. *Reactor Handbook*, Second Edition, Vol. III; Part A, *Physics*, (Interscience Publishers, New York, 1962).
3. G. K. Leaf and A. S. Kennedy, *PERC, A Two-Dimensional Perturbation Code Based on Diffusion Theory*, ANL-7304 (1967).
4. *Liquid Metal Fast Breeder Reactor Design Study*, CEND-200, Combustion Engineering Company (January 1964).

III-28. Fast Reactor Calculations with Consistent Sets for Some Important Neutron Cross Sections

J. M. Kallfelz and W. P. Poenitz

Introduction

In studies made in the past of the influence of various cross section changes on reactor calculations, it appears that proper consideration has often not been taken of the fact that a change in one cross section may require a correlated change in other cross sections. The study reported here was originally prompted by the question of how the lower capture cross sections for U-238 measured by M. Moxon and C. Chaffey[1] and H. Menlove and W. Poenitz[2] would influence fast reactor calculations. One question of interest was how much the lower σ_c for U-238 would compensate the

effect on k_{eff} of the higher values of $\alpha = \sigma_c/\sigma_f$ for Pu-239 recently measured by M. Schomberg et al.[3]

In considering these questions, three "consistent sets" for σ_c (U-238) and σ_f (U-235) were determined, for which a maximum effort was made to take into account the interrelation of various cross section measurements. We concluded that two different types of changes in cross sections should be studied.

(a) Changes due to correlated discrepancies between both capture and fission cross section values of several sets which were measured by different experimental methods, or with the use of different standards. For such discrepancies, a change in one cross section requires an associated change in other cross sections in the same direction.

(b) Changes due to uncorrelated discrepancies between data for the same cross section from different measurements using the same experimental method or standard. Such discrepancies allow uncorrelated changes of various capture and fission cross sections in different directions.

To determine the appropriate values for Pu-239 to use with each of the sets, a compiled ratio of $\sigma_f^{29}/\sigma_f^{25}$ was used; for this ratio, changes of type (b) were also considered.

Calculations of various integral parameters for a fast critical assembly have been made to determine the influence on the parameters of the above correlated and uncorrelated changes. The base set of cross section data, on which the alterations were performed, was that of the Evaluated Nuclear Data File (ENDF/B).

Cross Section Selection

Recently, there have been many measurements of fast neutron cross sections reported. A comparison of the data obtained by different experimental methods and different groups of experimenters allows some conclusions about the accuracy of these cross sections. The data available up to now are not sufficient to designate one set of fission and capture cross sections as the most accurate, but allows the determination of three different sets for σ_c and σ_f, shown in Figs. III-28-1 and III-28-2, which are consistent within themselves, but exclude one another.

(a) For Set 1, it is assumed that the fission cross section of U-235 as measured by P. White[4] and the capture cross section of U-238 measured by J. Barry et al.[5] are right. This would be supported by measurements by B. Diven for U-235 fission.[6]

(b) Set 2, whose values in the higher keV range are much lower than Set 1, is based on new capture cross section measurements performed with the associated activity method as well as with integral methods. The σ_c(U-238) curve for Set 2 is from the measurements of Menlove and Poenitz.[2] From σ_c(Au)/σ_c(U-235) measurements[8] and σ_c(Au) measurements of K. Harris et al.[9] and W. Poenitz et al.[10] the Set 2 values of σ_f (U-235) were computed; these values deviate from those of Set 1 in the same way as the σ_c(U-238) values.

(c) Set 3, which is generally in agreement with Set 2, is based on capture cross section measurements relative to the $B^{10}(n,\alpha)$ cross section which were performed for many materials.[1,11-16] They show generally

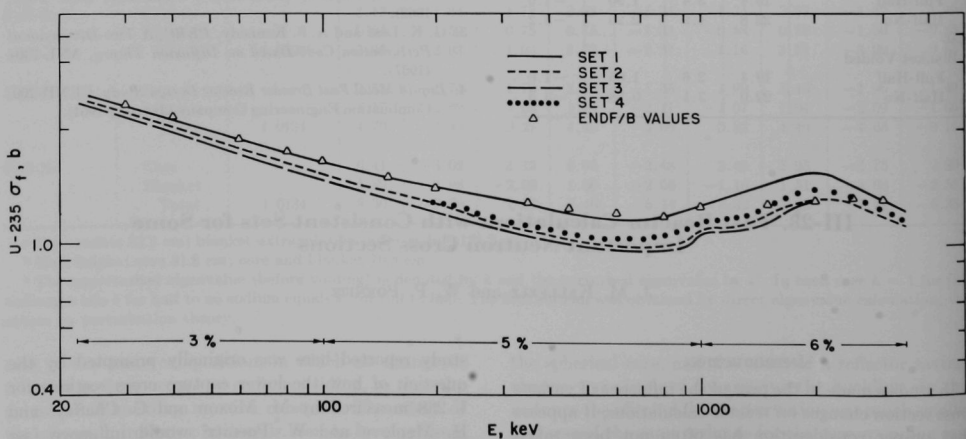

Fig. III-28-1. Fission Cross Section for U-235 for Various Sets. Below 200 keV, Set 4 Coincides with Set 2. The Percentages at the Bottom of the Figure are the Estimated Uncorrelated Uncertainties for Set 4. *ANL Neg. No. 113-1256 Rev. 1.*

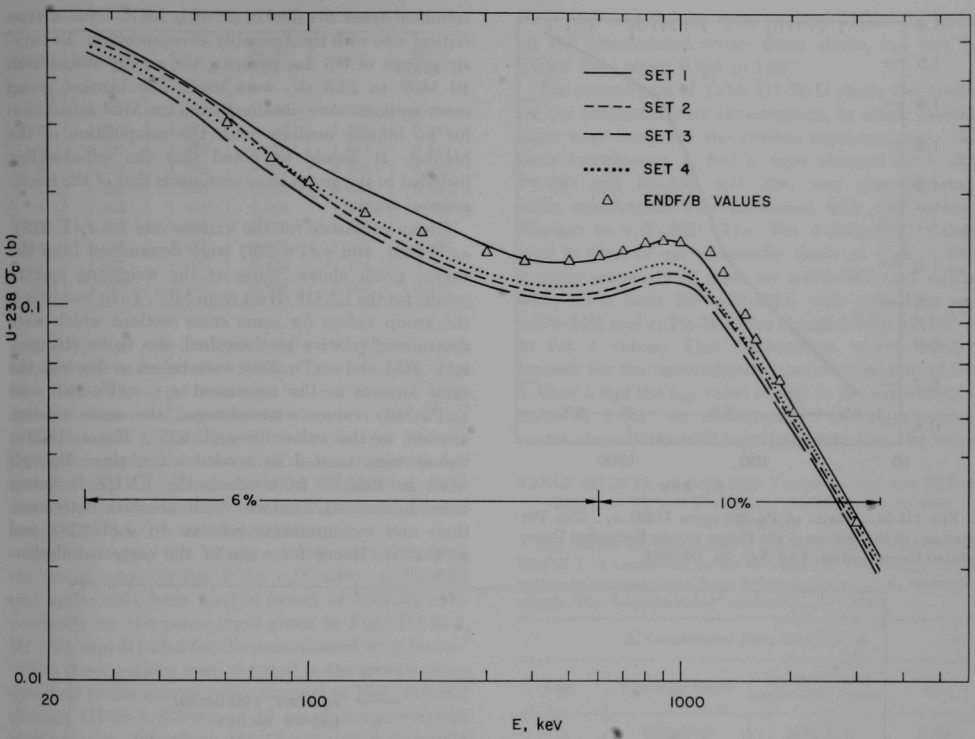

FIG. III-28-2. Capture Cross Section for U-238 for Various Sets. The Percentages at the Bottom of the Figure are the Estimated Uncorrelated Uncertainties for Set 4. *ANL Neg. No. 113-1255 Rev. 1.*

somewhat lower results in the lower keV energy range[11-13] and a somewhat steeper downward slope with increasing energy in the higher keV region[14-16] compared with the σ_c values used for Set 2. For Set 3 it was assumed that the ratio between σ_f(U-235) and σ_c (U-238) is the same as in Sets 1 and 2.

(d) Set 4 gives the cross sections which are the best estimate of the authors, based on the available data included in Sets 1–3. The estimated uncorrelated uncertainties, shown in Figs. III-28-1 and III-28-2, are for this set.

(e) The ratio of the fission cross sections of Pu-239 and U-235, given in Fig. III-28-3, is essentially that of W. Davey[17] except that it has been reduced slightly in the low energy range to include some new experimental data.

(f) Although the fissile element cross sections were the primary subject of the present considerations, some adjustments to the capture cross section for molybdenum were considered desirable, because several newer measurements deviate by as much as a factor of two from the ENDF/B data which were taken from J. Schmidt 1962.[18] To derive the σ_c(Mo) curve shown in Fig. III-28-4, data of H. Weigmann et al.,[13] D. Kompe,[15] and W. Poenitz[19] were taken into account.

Method of Reactor Calculations

Reactor calculations were performed for ZPR-3 Assembly 48, which was designed to provide core neutron spectra similar to those expected in large fast power reactors. The simplified model of Assembly 48 suggested by P. Greebler[20] for the testing of the ENDF/B file was used. This is a homogeneous spherical core containing the critical mass of 272 kg Pu-239, plus an additional 21.3 kg Pu-239 to account for the 0.0125 disadvantage in k_{eff} due to the assumption of homogeneity. The equivalent experimental k_{eff} of this sphere would be 1.011.

The ENDF/B core group cross sections were de-

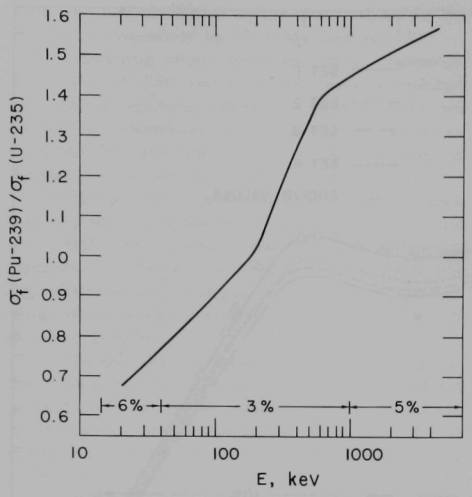

FIG. III-28-3. Ratio of Pu-239 σ_f to U-235 σ_f. The Percentages at the Bottom of the Figure are the Estimated Uncorrelated Uncertainties. *ANL Neg. No. 113-1254.*

termined from a calculation with MC$^{2(21)}$ for a bare critical core with the Assembly 48 composition. Twenty-six groups of 0.5 Δu, covering the energy range from 10 MeV to 22.5 eV, were used. The blanket group cross sections were obtained from an MC^2 calculation for an infinite medium with the composition of the blanket. It should be noted that the self-shielding included in the group cross sections is that of the homogeneous region.

Group constants for the various sets for σ_f(U-235), σ_c(U-238), and σ_f(Pu-239) were determined from the curves given above, using as the weighting spectra results for the ENDF/B set from MC^2. To be consistent, the group values for some cross sections which were determined relative to these had also to be changed. σ_c(U-235) and σ_c(Pu-239) were raised or lowered the same amount as the associated σ_f. σ_f(Pu-240) and σ_c(Pu-240) values were changed the same relative amount as the value for σ_f(U-235). The σ_f(U-238) values were treated in several ways, since Davey's work in 1966,[22] from which the ENDF/B values were determined, contains both absolute determinations and measurements relative to σ_f(U-233) and σ_f(U-235). Hence for some of the early calculations

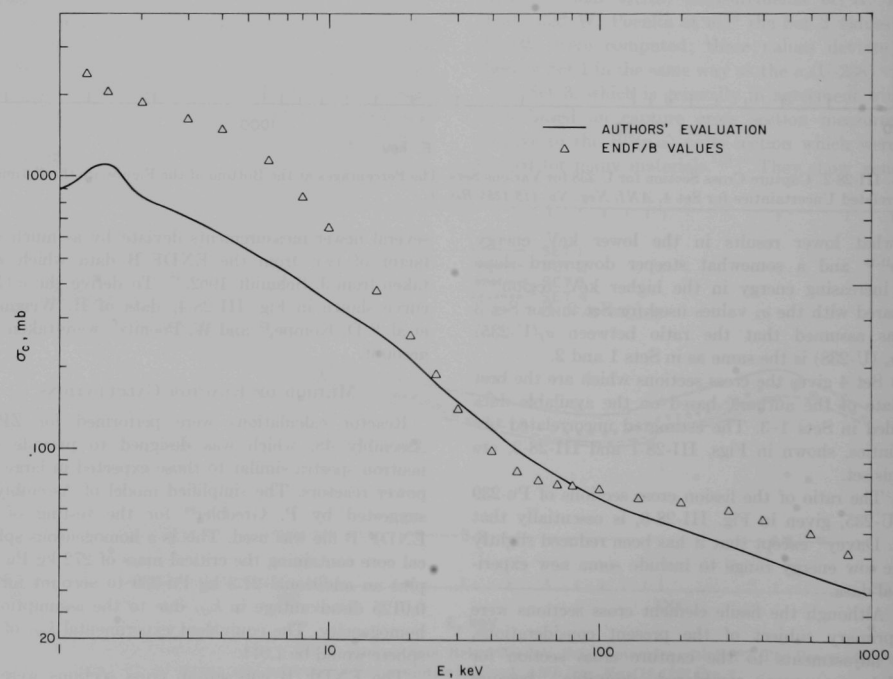

FIG. III-28-4. Capture Cross Section for Molybdenum. *ANL Neg. No. 113-1253.*

TABLE III-28-I. σ_f(U-235) VALUES FOR SEVERAL SETS

Group	ENDF/B	Set 1	Set 1/ ENDF-B	Set 3	Set 3/ ENDF-B
3	1.301	1.357	1.043	1.222	0.939
4	1.286	1.481	1.151	1.219	0.948
5	1.238	1.273	1.028	1.044	0.843
6	1.195	1.162	0.972	0.974	0.815
7	1.265	1.240	0.980	1.030	0.814
8	1.363	1.363	1.000	1.162	0.853
9	1.519	1.503	0.989	1.327	0.874
10	1.716	1.677	0.977	1.529	0.891
11	1.977	1.929	0.976	1.778	0.899
12	2.279	2.243	0.984	2.082	0.914

σ_f(U-238) was not changed, while for others it was changed the same relative amount as σ_f(U-235). Due to a reevaluation of some of the earlier σ_f(U-238) determinations, and some recent very accurate $\sigma_f^{28}/\sigma_f^{25}$ measurements, a more recent work (Davey 1968)[17] puts more emphasis on the relative measurements and uses the ratio $\sigma_f^{28}/\sigma_f^{25}$ as a basis for determining σ_f(U-238). For the later calculations, σ_f(U-238) was treated as based on relative measurements.

To investigate the effects of uncorrelated errors, the group values of Set 4 for σ_c(U-238), σ_c(Pu-239) and σ_f(Pu-239) were further raised or lowered independently by the percentages given in Figs. III-28-1, III-28-2, and III-28-3 for the uncorrelated error limits.*

The cross sections were changed in the groups corresponding to the energy range covered in Figs. III-28-1 through III-28-4. (Groups 3–12 for all isotopes except molybdenum, for which the changes were in groups 6–18.) Table III-28-I gives the group values for several of the sets compared to the ENDF/B values.

After changing the group values for the various cross sections, one dimension diffusion theory calculations of Assembly 48 were performed with MACH-1.[23] Besides k_{eff}, central reaction ratios and first-order perturbation theory central worths were calculated to compare with experiment. S_N transport theory calculations of the same assembly were also performed with SNARG-1D[24] for the basic ENDF/B values. The diffusion theory to S_4 correction factor of +0.008 in k_{eff} determined for this case was added to all MACH-1 k_{eff} results. The difference in k_{eff} between an S_4 and an S_{16} calculation was negligible.

CALCULATIONAL RESULTS

The first results shown in Table III-28-II are for the investigation of the uncorrelated errors. For these calculations only σ_f(Pu-239), σ_c(Pu-239) and σ_c(U-238) were changed from the ENDF/B values. It is interesting to note that simply by independently changing the U-238 and Pu-239 cross sections within the limits on the uncorrelated errors given above, k_{eff} can be varied from about 0.955 to 1.02.

The second part of Table III-28-II shows the results for the correlated error investigation, in which calculations were made for the various consistent sets. For these calculations, σ_c and σ_f were changed for U-235, Pu-239 and Pu-240. σ_c(U-238) was also adjusted, while calculations were performed with and without changes to σ_f(U-238). The "Set 4-Adjusted" values used in Case 17 are essentially those of Case 5 [Set 4 upper uncorrelated limit for σ_f(Pu-239) and σ_c(Pu-239), lower limit for σ_c(U-238)] with σ_f(U-238) and σ_c(Pu-240) and σ_f(Pu-240) also changed from ENDF/B to Set 4 values. This combination was calculated because for the uncorrelated error investigation of Set 4, Case 5 had the k_{eff} value closest to the experimental value of 1.011. As mentioned in the introduction, recent measurements[3,25] have indicated that the value

TABLE III-28-II. CALCULATED VALUES OF k_{eff} FOR ZPR-3, ASSEMBLY 48, FOR DIFFERENT ALTERATIONS TO THE ENDF/B SET

(All values are calculated in the spherical 1-D case, with MACH-1. A correction factor of 0.008 has been added to all values to convert them from diffusion theory to S_4 transport theory. The "experimental" value of k_{eff} is 1.011.)

A. Uncorrelated Error Investigation

Case	σ_c(U-238) Value	σ_f(Pu-239) and σ_c(Pu-239) Values	k_{eff}
1	ENDF/B	ENDF/B	1.000
2	Set 4	Set 4	0.984
3	Set 4 Lower Limit	Set 4	0.993
4	Set 4 Lower Limit	Set 4 Lower Limit	0.970
5	Set 4 Lower Limit	Set 4 Upper Limit	1.017
6	Set 4 Upper Limit	Set 4	0.976
7	Set 4 Upper Limit	Set 4 Upper Limit	1.000
8	Set 4 Upper Limit	Set 4 Lower Limit	0.954

B. Correlated Effort Investigation

Case	Consistent Set No.	σ_f(U-238) Changed	k_{eff}
9	1	No	1.004
10	2	No	0.973
11	3	No	0.971
12	4	No	0.984
13	1	Yes	1.010
14	2	Yes	0.969
15	3	Yes	0.966
16	4	Yes	0.984
17	4-Adjusted	Yes	1.016

* The uncorrelated error for Pu-239 was the square root of the sum of the squares of the errors for σ_f(U-235) and $\sigma_f^{49}/\sigma_f^{25}$.

TABLE III-28-III. CENTRAL REACTION RATES (PER ATOM) RELATIVE TO U-235 FISSION, IN ZPR-3, ASSEMBLY 48

Reaction	Measured	ENDF/B	Set 1	Set 2	Set 3	Set 4	Set 4-Adjusted
Pu^{239}-f	0.976 ± 0.010	0.928	0.945	0.922	0.917	0.928	0.968
U^{238}-c	0.138 ± 0.007	0.142	0.147	0.147	0.143	0.145	0.139
U^{238}-f	0.0307 ± 0.0003	0.0303	0.0306[a] / 0.0329	0.0312[a] / 0.0300	0.0311[a] / 0.0297	0.0309[a] / 0.0310	—[a] / 0.0309

[a] For U^{238}-f calculated values, the top and bottom numbers are for σ_f(U-238) unchanged and changed, respectively (see the discussion in the text). For the other reactions, the values are for σ_f(U-238) changed, and were practically identical with those for σ_f(U-238) unchanged.

TABLE III-28-IV. CENTRAL WORTH [Ih/kg] IN ZPR-3 ASSEMBLY 48
(Calculations are with MACH-1 perturbation theory option)

Element	Measured Worth	Calculated Worth[a, b, c]						
		ENDF/B	Set 1	Set 2	Set 3	Set 4	Set 4-Adjusted	
							ENDF/B Mo	Fig. 4 Mo
C[d]	−4.6 ± 1.2	+6.0	+4.2	+22.2	+25.7	+16.9	+3.9	+5.2
Na[d]	−6.3 ± 0.3	+1.2	−0.9	+5.8	+7.0	+3.9	+0.3	+0.5
Mo	−43.4 ± 0.4	−98.5	−98.0	−103.3	−105.7	−102.3	−99.2	−74.5
U-235	+339.0 ± 4.0	+397.2	+392.6	+396.5	+393.4	+392.9	+370.8	+369.8
U-238	−24.8 ± 0.5	−32.3	−33.5	−32.7	−31.8	−32.3	−30.9	−31.0
Pu-239	+445.0 ± 4.0	+523.4	+531.1	+519.3	+512.7	+518.9	+515.7	+514.7

[a] All set values are for case in which σ_f(U-238) was changed the same relative amount as σ_f(U-235).
[b] Calculated value of Ih/(%$\Delta k/k$) ranged from 986. to 993. For all values in this table, 990. Ih/(%$\Delta k/k$) was used.
[c] The self-shielding included in the group cross sections is that of the homogeneous core.
[d] Calculations are for C-12 and Na-23.

of $\alpha = \sigma_c/\sigma_f$ for Pu-239 may be much higher in the low-energy range than the values in the ENDF/B file. In anticipation of the expected drop in k_{eff} caused by raising this value,* the fact that the Set 4-Adjusted value of k_{eff} was greater than the experimental value was another argument for this combination.

Table III-28-III shows the value of the central reaction ratios for the important isotopes, compared to the experimental values. Only for Set 4-Adjusted do all calculated values fall within experimental limits.

For elements for which the scattering component is an important portion of the total central worth (e.g., carbon, sodium), it can be seen from Table III-28-IV that the calculated total central worth is fairly sensitive to the changes made in the various sets.† This is because the scattering component is a sum of positive and negative components which add up to nearly zero for this case, and the result is a sensitive function of the adjoint flux shape. While the overall agreement with experiment is slightly better for Set 4-Adjusted than for the other sets, most values are considerably outside the experimental error limits. This is probably due in part to self-shielding effects in the experimental samples which are not completely corrected for in the group cross sections, and to the fact that the fairly flat adjoint flux energy form in Assembly 48 decreases the accuracy of calculations of the scattering component of the central worth. At any rate, the simple homogeneous sphere model and diffusion theory used for the calculations should not be expected to give particularly accurate central worths; the influence of such effects as transport and heterogeneity on the central worths is difficult to calculate even with a more sophisticated model.

The poor agreement between calculated and measured molybdenum worths, which depends primarily on capture, probably is significant. The ENDF/B values give a worth more than 100% higher than experiment. The value with cross sections derived from the curve in Fig. III-28-4 or this curve lowered to

* A calculation for Assembly 48 using the Pu-α values of R. Gwin et al.,[25] assuming the ENDF/B σ_f values were correct and altering σ_c, gave a k_{eff} value 1.4% lower than for the ENDF/B Pu-α values.

† These calculations were all for a fixed core radius, so that k was different for the various sets (see Part B of Table III-28-II). For calculations in which the radius was varied to obtain $k = 1.0$, the differences in the worths for the different sets were only about half as large.

what the authors consider to be the lowest reasonable limit (15% lower over the entire energy range) are still about 70% and 60% higher than experiment, respectively. While alterations to the cross section values below 1 keV would improve the agreement somewhat, this poor agreement is not understood. This case seems indicative of limitations in the central worth calculational methods used and/or experimental accuracy.

Observations

The integral parameter calculations, which were all for one assembly, are obviously insufficient to give really strong evidence as to which cross section set is the most accurate. However, there are several interesting observations which result from this study.

(a) Considering the results for k_{eff} and the central reaction ratios, the fact that "Set 4-Adjusted" gave better comparison with experimental values than the other cross section sets is an indication that the ratio $\sigma_f(Pu^{239})/\sigma_c(U^{238})$ should be higher than is presently the case in the ENDF/B set.

(b) As a check for differential cross sections, the inherent difficulties involved in calculating accurate central worths (particularly for the light elements) make them appropriate only for identifying gross errors. It is the authors' opinion that for locating regions of possible moderate error in important cross sections, the integral parameters compared should be restricted to such significant and accurate parameters as k_{eff} and central reaction ratios of the important elements.

(c) The rather large uncertainty in k_{eff} which can be obtained just by adjusting the various cross sections within the uncorrelated error limits illustrates the danger of adjusting a particular differential cross section to fit integral data. The authors feel that comparisons of calculated and experimental integral data should be used primarily to help choose between two or more differing measured cross sections, or to indicate further areas of necessary experimental investigations of differential cross sections.

References

1. M. C. Moxon and C. M. Chaffey, *Neutron Cross Sections*, BNL-325, 2d Edition, Supplement No. 2, Vol. III, 1965, p. 92-238-24.
2. H. O. Menlove and W. P. Poenitz, *Absolute Radioactive Capture Cross Section for Fast Neutrons in ^{238}U*, Nucl. Sci. Eng. **33**, 24 (1968).
3. M. G. Schomberg, M. G. Sowerby and F. W. Evans, *A New Method of Measuring Alpha (E) for ^{239}Pu*, Proc. Symposium on Fast Reactor Physics and Related Safety Problems, Karlsruhe, Oct. 30–Nov. 3, 1967, IAEA, Vol. I, pp. 289–305.
4. P. H. White, *Measurements of the U^{235} Neutron Fission Cross Section in the Energy Range 0.04–14 MeV*, J. Nucl. Energy A/B **19**, 325 (1965).
5. J. F. Barry et al., *Cross Section for the Reaction ^{238}U (n,γ) ^{239}U in the Energy Range 0.12–7.6 MeV*, J. Nucl. Energy A/B **18**, 481 (1964).
6. B. C. Diven et al., *Fission Cross Section of U^{235} for Fast Neutrons*, Phys. Rev. **105**, 1350 (1957).
7. B. C. Diven et al., *Radiative Capture Cross Sections for Fast Neutrons*, Phys. Rev. **120**, 556 (1960).
8. See references cited in Ref. 10.
9. K. K. Harris et al., *The ^{197}Au (n,γ) ^{198}Au Cross Section from 13 keV to 638 keV*, Nucl. Phys. **69**, 37 (1965).
10. W. P. Poenitz et al., *The Neutron Capture Cross Section of Gold in the keV Energy Region*, J. Nucl. Energy A/B **22**, 505 (1968).
11. M. C. Moxon and E. R. Rae, *A Gamma-Ray Detector for Neutron Capture Cross Section Measurements*, Nucl. Inst. Meth., **24**, 445 (1963).
12. Y. P. Popov, Trudy Fiz. Inst. Nauk. XXIV (1964).
13. H. Weigmann et al., *A New Detector for Neutron Capture Cross Section Measurements*, Nucl. Inst. Meth. **50**, 265 (1967).
14. J. H. Gibbons et al., *Average Radiative Capture Cross Sections for 7-170 keV Neutrons*, Phys. Rev. **122**, 182 (1961).
15. D. Kompe; see W. P. Poenitz et al., *Some New Measurements and Renormalization of Neutron Capture Cross Section Data in the keV Energy Range*, KFK 635, 1967.
16. R. L. Macklin and J. H. Gibbons, *Capture Cross Section Studies for 30 to 220 keV Neutrons Using a New Technique*, Phys. Rev. **159**, 1007 (1967).
17. W. G. Davey, *Selected Fission Cross Sections for ^{232}Th, ^{233}U, ^{234}U, ^{235}U, ^{236}U, ^{237}Np, ^{238}U, ^{239}Pu, ^{240}Pu, ^{241}Pu and ^{242}Pu*, Nucl. Sci. Eng. **32**, 35–45 (1968).
18. J. J. Schmidt, *Neutron Cross Sections for Fast Reactor Materials*, KFK 120, Part II: Tables. Part III: Graphs. (1962).
19. W. P. Poenitz, *An Absolute (n,γ) Cross-Section Measurement for Gold at 30 keV and Its Application in the Normalization of Other Data*, Proc. Conference on Nuclear Data for Reactors, Paris, October 17–21, 1966, IAEA, Vol. 1, p. 277.
20. P. Greebler, *Testing of ENDF/B Cross-Section Data—Information on Simplified Model of ZPR-III Critical Assembly #48*, CSEWG Newsletter 7, Cross Section Evaluation Working Group, March 6, 1967.
21. B. J. Toppel, A. L. Rago and D. M. O'Shea, *MC^2, A Code to Calculate Multigroup Cross Sections*, ANL-7318 (1967).
22. W. G. Davey, *An Analysis of the Fission Cross Sections of ^{232}Th, ^{233}U, ^{234}U, ^{235}U, ^{236}U, ^{237}Np, ^{238}U, ^{239}Pu, ^{240}Pu, ^{241}Pu and ^{242}Pu from 1 keV to 10 MeV*, Nucl. Sci. Eng. **26**, 149 (1966).
23. D. A. Meneley, L. C. Kvitek and D. M. O'Shea, *MACH 1, A One-Dimensional Diffusion-Theory Package*, ANL-7223 (1966).
24. G. J. Duffy, H. Greenspan, S. D. Sparck, J. V. Zapatka and M. K. Butler, *SNARG-1D, A One-Dimensional, Discrete-Ordinate, Transport-Theory Program for the CDC-3600*, ANL-7221 (1966).
25. R. Gwin et al., *Measurement of the Neutron Fission and Absorption Cross Sections of ^{239}Pu Over the Energy Region 0.01 eV to 30 keV*, Neutron Physics Division Annual Progress Report, 1967–1968, ORNL-4280, par. 1.6.

III-29. The Effective Delayed Neutron Fraction in Fast Reactors

D. A. Meneley

Introduction

The commonly used expression for the effective delayed neutron fraction in reactor kinetics (e.g., Ref. 1) contains a parameter β representing the fraction of total fission neutrons from each fissioning isotope which are delayed. This parameter is usually assumed to be independent of the reactor system, at least for fast reactor calculations. Recommended β-values are commonly taken from Ref. 2. These β values are, in fact, derived quantities which depend on the reactor spectrum and on ν, the total fission neutron yield, as is shown below.

Given the inaccuracies in the basic delayed neutron data at the present time, it would probably be sufficient to redefine β values appropriate to each typical reactor spectrum. This would not require a change in definition of the effective β. It is possible, however, to reformulate the equation in a more general form with no increase in complexity. The changes remove the implicit dependence of delayed data on reactor spectrum and on prompt yield data, and clarify the physical meanings of basic data used in reactor calculations.

Basic Data

GROUP YIELDS AND DECAY CONSTANTS

Ideally, the group yields and decay constants would be the measured number of individual delayed neutron precursors produced per fission in each fissioning nuclide, and associated decay constants. The yields would be incident neutron energy-dependent due to the shift in mass-yield curves with energy. The decay constants would depend only on the precursor nuclide.

Currently available data[2] consists of measured total yields in neutrons per fission, with yield fractions and decay constants for characteristic delayed groups. These yield fractions are obtained by fitting emission decay curves to a sum of exponentials. G. Keepin[2] recommends the use of six groups of delayed neutron precursors, even though more than six actual precursors have been identified. He bases his choice on the observation that six groups give the statistical "best fit" of individual decay curves, and that identification of every precursor would lead to an unmanageably large number of delayed groups ($\sim$30). Unfortunately six-group fitting of individual decay curves results in fissioning-isotope-dependent decay constants. When there are five or six different fissioning isotopes, such as in fast breeders, one must treat each isotope separately. Thus in effect 30 or 36 delayed groups are required.

An alternate possibility is a simultaneous fit of the decay curve data from all isotopes and all measuring energies. The decay constants would be independent of fissioning isotope and incident energy; however the group yields would depend on both of these. The number of delayed groups could then be varied as required up to the total number of known precursors. Decay constants which are known from radiochemical analysis could be inserted directly into the equations. Fewer groups could be fitted for specific, lower accuracy applications.

There are two advantages to this treatment of basic data. The first is that the quantities presented are physically meaningful. The second is that the data storage requirements are simplified, since the total number of delayed groups is reduced and the delayed neutron yield cross sections ($\nu^d\Sigma_f$) can be stored on a "composition" level (a "composition" is defined as a homogeneous mixture of isotopes, more than one of which may be fissionable) in a manner completely analogous to the prompt neutron yield cross-sections ($\nu^p\Sigma_f$). A potential weakness of the approach lies in the difficulty of accomplishing a least squares fit with the large number of unknowns implied by the above arguments. The second question, common to all decay-curve analyses, is whether there are any significant precursor-parent isotopes which may introduce growth-decay behavior into individual precursor emission curves. There is some indication that this is not a serious problem.[3]

The processed data therefore would consist of a decay constant λ_i for each delayed precursor group i and an absolute yield $\nu^d_{i,j}(E)$ in neutrons per fission as a function of incident neutron energy E from fission in each isotope j.

EMISSION SPECTRA

In the ideal case these data would consist of the delayed neutron emission spectrum measured for decay from each neutron emitter. In Ref. 4 Keepin develops an empirical argument showing mutually exclusive conditions for isomerism and delayed neutron emission. Therefore the neutron precursors must undergo β-delay from ground state, resulting in emission spectra independent of the fissioning isotope and of the energy of the neutron causing fission.

The best emission spectra available were measured by R. Batchelor and H. McK. Hyder[5] for thermal fission in U-235. The individual delayed group spectra for four groups were obtained by use of characteristic-group half-lives and abundances from Ref. 6. Aside from the fact that the current recommended values of these quantities are quite different from those of Ref. 6, there is another factor that may make these spectra dependent on the fissioning isotope and incident energy of the neutron causing fission. Suppose that a typical characteristic group consists of one bromine and one iodine precursor. Their respective krypton and xenon emitters may have different emission spectra due to different β-decay energy excess over the neutron binding energy in the emitter. Therefore, as the relative quantities of bromine and iodine isotopes assigned to the group vary as a function of the fissioning nucleus and its excitation energy, the group emission spectrum will vary.

Provided that only one precursor is assigned to each delayed group, and provided that all precursors do in fact decay only from ground state, the delayed neutron spectra $\chi_i^d(E)$ for group i will be independent of incident neutron energy and of the isotope undergoing fission.

Effective Delayed Neutron Fraction

Using the basic data as defined in the previous section, the delayed neutron source cross section for group i at space point $(\mathbf{r},E)$ is given by

$$\nu_i^d\Sigma_f(\mathbf{r},E) = \sum_j n_j(\mathbf{r})\nu_{i,j}^d(E)\,\sigma_{f,j}(E), \tag{1}$$

where n_j is the density of isotope j at point $\mathbf{r}$, $\nu_{i,j}^d(E)$ is the yield into delayed group i per fission in isotope j at energy E, and $\sigma_{f,j}(E)$ is the fission cross section of isotope j at energy E. Following the development by A. Henry,[1] the effective delayed neutron fraction is then given by

$$\overline{\beta_i} = \frac{1}{F}\int_{\mathbf{r}}\int_{E'} \phi^*(\mathbf{r},E')\chi_i^d(E') \cdot \int_E \nu_i^d\Sigma_f(\mathbf{r},E)\phi(\mathbf{r},E)\,dE\,dE'\,d\mathbf{r}. \tag{2}$$

$\phi(\mathbf{r},E)$ and $\phi^*(\mathbf{r},E')$ are the real and adjoint flux in the system, respectively, and E and E' are the energies of the incident and emitted neutron, respectively. The value of F is unimportant except for the requirement that the same F be used in definition of the reactivity and neutron generation time. Common practice identifies F as the denominator of the perturbation theory expression for $\delta k/k$.

If the delayed neutron yield is assumed to be independent of incident energy E, Eq. (2) may be rewritten as

$$\overline{\beta_i} = \frac{1}{F}\int_{\mathbf{r}}\int_{E'} \phi^*(\mathbf{r},E')\chi_i^d(E') \cdot\left\{\sum_j \nu_{i,j}^d n_j(\mathbf{r}) \int_E \sigma_{f,j}(E)\phi(\mathbf{r},E)\,dE\right\} dE'\,d\mathbf{r}. \tag{3}$$

Note that Eq. (3) has roughly the same form as the usual expression for β-effective, except that the yield per fission in isotope j is assumed constant instead of the fraction of the total fission neutrons produced from isotope j. This latter assumption can be true only if the ratio $\nu_{i,j}^d(E)/\nu_j^p(E)$ is independent of E. There are theoretical arguments and recent experimental results[7,8] indicating that $\nu_{i,j}^d(E)$ generally decreases as a function of E, while $\nu_j^p(E)$ increases.

In order to see more clearly the main approximation introduced by the current formalism, recast the term inside the braces in Eq. (3) as

$$\left\{\sum_j \frac{\nu_{i,j}^d}{\bar{\nu}_j^{d+p}}\, n_j(\mathbf{r}) \int_E\left[\nu_j^p(E) + \sum_i \nu_{i,j}^d(E)\right] \cdot\sigma_{f,j}(E)\phi(\mathbf{r},E)\,dE\right\}, \tag{4}$$

where

$$\bar{\nu}_j^{d+p} = \frac{\int_E \left[\nu_j^p(E) + \sum_i \nu_{i,j}^d(E)\right]\sigma_{f,j}(E)\phi(\mathbf{r},E)\,dE}{\int_E \sigma_{f,j}(E)\phi(\mathbf{r},E)\,dE}, \tag{5}$$

$\nu_j^p(E)$ is prompt neutron yield per fission in isotope j at energy E, and the i summation extends over all delayed neutron groups.

The ratios $\nu_{i,j}^d/\bar{\nu}_j^{d+p}$ in Eq. (4) is recognized as the definition of the delayed neutron fraction $\beta_{i,j}$ given in Ref. 2, and the whole expression as the delayed neutron production term which appears in the usual $\bar{\beta}_i$ equation. The difference is the fact that in the usual formalism the $\phi(\mathbf{r},E)$ function in Eq. (5) is replaced by the flux spectrum in which the measurement is carried out. Also, unless $\bar{\nu}_j^{d+p}$ is measured directly, the fission cross section and the total yield per fission are replaced by values accepted at the time of the measurement. This error can probably be reduced by use of a $\bar{\nu}_j^{d+p}$ value which is more appropriate to the system under study.

Secondary approximations may arise due to the difference between the $\chi_i^d(E')$ as defined in Eq. (3) and the delayed spectra resulting from separation into characteristic delayed groups each representing more than one precursor. In any case the more precise Eq.

(2) must be used to account for the actual energy dependence of the $\nu_{i,j}^{d}(E)$ term, if it is important.

Summary

The effective delayed neutron fraction equation has been recast into a form consistent with the actual physical behavior of the delayed neutron precursors. Given the present state of the basic data, this reformulation probably does not change the β-effective computed in typical fast reactors outside the range of uncertainty in the basic data. Application of Eq. (3) in place of the older formulation using the delayed neutron fractions of Ref. 2 to a plutonium fueled fast breeder with median fission energy of $\sim$0.2 MeV gives an increase of approximately 3 percent in the contributions to $\bar{\beta}_i$ from thermally fissionable nuclides.

Two advantages may justify the formulation of Eq. (2). First, the basic data are included in a physically meaningful form, independent of artificial functional dependences (such as delayed yield dependence on prompt yield data). Secondly, the accuracy of Eq. (2) is governed only by the accuracy of basic data. It is not affected by the mismatch between actual conditions in the reactor and those assumed to apply during derivation of the delayed data (e.g., the dependence of fractional yields on measuring spectrum).

References

1. A. F. Henry, *The Application of Reactor Kinetics to the Analysis of Experiments*, Nucl. Sci. Eng. **3**, 52 (1958).
2. G. R. Keepin, *Physics of Nuclear Kinetics*, (Addison-Wesley Publishing Co., Inc., Reading, Mass. 1965) Chap. 4.
3. G. R. Keepin, *Discussion of Session VII*, Proc. IAEA Symposium on Physics and Chemistry of Fission, March 22–26, 1965, p. 222.
4. G. R. Keepin, *Interpretation of Delayed Neutron Phenomena*, J. Nuclear Energy **7**, 13 (1958).
5. R. Batchelor and H. R. McK. Hyder, *The Energy of Delayed Neutrons from Fission*, J. Nuclear Energy **3**, 7 (1956).
6. G. R. Keepin, *Progress in Nuclear Energy I*, (McGraw-Hill Book Co., Inc., New York 1956) Chap. 7.
7. G. Herman, J. Fiedler, G. Benedict, W. Eckhardt, G. Luthardt, P. Patzelt and H. D. Schüssler, *Comparison of Observed Delayed-Neutron Abundances with Calculated Fission Yields of Neutron Precursors*, Proc. IAEA Symposium on Physics and Chemistry of Fission, March 22–26, 1965, p. 197.
8. C. F. Masters, M. M. Thorpe and D. B. Smith, *Measurement of Absolute Delayed-Neutron Yields from 14-MeV Fission*, Trans. Am. Nucl. Soc. **11**, 179 (1968).

III-30. The Effect of U-238 Resonance Shielding on the Rate of Production of Np-237 from U-236

L. B. Miller

Neptunium can be produced by the irradiation of U-236 with neutrons. The reaction sequence involves neutron capture and subsequent β-decay:

$$_{92}U^{236} + {}_{1}n^{0} \rightarrow {}_{92}U^{237} \xrightarrow{6.75\ d} \beta^{-} + {}_{93}Np^{237}. \quad (1)$$

In one production method the U-236 to be irradiated in the neutron flux of a thermal reactor is contained in U-238 at a concentration of 500 ppm. The large amount of U-238 present reduces the reaction rate in the U-236. In particular, the 6.68 eV resonance of U-238 shields the 5.49 eV resonance of U-236 in which about one-half of the absorptions occur.

To determine the magnitude of this shielding effect, the Argonne Monte Carlo code[1] (AMC) was utilized to represent exactly the fourteen-region cell used in the irradiation. The dimensions of the regions are given in Table III-30-I. The energy range from 10.67 to 5.04 eV was divided into 10 equal lethargy intervals and the average fluxes, cross sections, and reaction rates in each lethargy interval were tabulated for each spacial region. The temperature of the uranium was taken as 600°K.

TABLE III-30-I. Composition of Cell used for Irradiation of U-236

Outer Radius, cm	Composition
0.551	Water
0.612	Zircaloy-2
1.483	Uranium
1.593	Zircaloy-2
2.242	Water
2.306	Zircaloy-2
2.987	Uranium
3.056	Zircaloy-2
3.439	Water
4.166	Zircaloy-2
4.242	Void
8.598	Graphite
10.206	Void
(Side of square = 21.495)	Graphite

TABLE III-30-II. U-236 Resonance Absorption Probability

	Without U-238 Resonance, $\times 10^{-3}$	With U-238 Resonance, $\times 10^{-3}$	Difference, $\times 10^{-3}$	Calculated Differential, $\times 10^{-3}$	Fractional Reduction in Reaction Rate
Inner fuel ring	0.567 ± 0.10	0.443 ± 0.08	0.124 ± 0.13	0.130 ± 0.019	0.229 ± 0.037
Outer fuel ring	0.947 ± 0.17	0.746 ± 0.09	0.201 ± 0.19	0.242 ± 0.027	0.256 ± 0.037
Total	1.514 ± 0.20	1.189 ± 0.12	0.325 ± 0.23	0.372 ± 0.033	0.245 ± 0.027

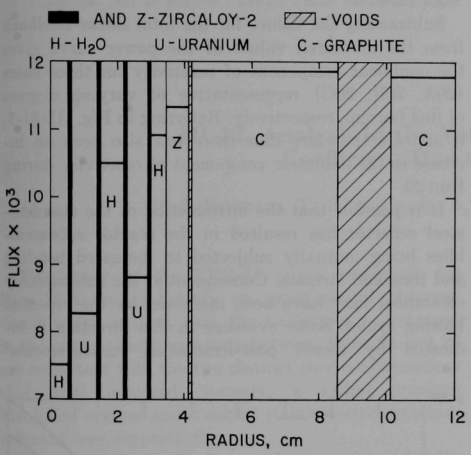

Fig. III-30-1. Flux Distribution in 14 Region Cell. *ANL Neg. No. 113-1209.*

Two cases were considered. In the first case the U-238 was assumed to have a potential scattering cross section of 8.3 barns and no resonance cross sections. In the second case the 6.68 eV resonance of U-238 was included. For these two cases the absorption rate in U-236 per neutron slowing down past 10.67 eV is shown in the first two columns of Table III-30-II. The difference is shown in the third column.

The difference was also calculated by a Monte Carlo perturbation technique similar to the technique previously used to compute temperature derivatives of reaction rates.[2] This technique yields a much more accurate value for the difference, with essentially no increase in computer time. The results of the computations are shown in column four of Table III-30-II. Based on this value, the reduction in the capture rate in the 5.49 eV U-236 resonance caused by U-238 shielding was determined to be approximately 25%, as is shown in column five of Table III-30-II.

The flux per unit area per lethargy interval, normalized to a slowing down density of one neutron per second in the cell, is plotted as a function of space in Fig. III-30-1.

References

1. L. B. Miller, *Monte Carlo Analysis of Reactivity Coefficients in Fast Reactors: General Theory and Applications*, ANL-7307 (1967).
2. L. B. Miller, *Stochastic Techniques for Reactor Analysis*, Reactor Physics Division Annual Report, July 1, 1964 to June 30, 1965, ANL-7110, pp. 357–359.

III-31. EBR-II Power Coefficient Variations During Operational Run 26[1]

P. J. Persiani, J. Kallfelz, F. Kirn,* J. K. Long* and R. Smith*

The purpose of this paper is to present a preliminary analysis of the reactivity versus power and partial flow experiments in EBR-II during Run 26. The experimental results for the power reactivity measurements made during this run appear to indicate that the reactivity curves at the end of the run differed in behavior from the curves determined in the early stages of operation.

In an attempt to identify the mechanisms that may contribute to these variations, the components of the power curves were analyzed separately.

The fuel temperature feedback was determined experimentally by measuring the change in reactivity between 41.5 MW-full flow and 22.5 MW-54% flow.

* Idaho Division, Argonne National Laboratory.

TABLE III-31-I. MEASURED CHANGE IN REACTIVITY BETWEEN 41.5 MW-FULL FLOW AND 22.5 MW-54% FLOW

Experiments	Reactivity in Inhours	Run	Burnup, MWd
1	8.8	26A-start	0
2	11.3	26B-start	114
3	11.6	26B-end	1056
4	9.5	26C-start	
5	14.8	26C-end	1750

The power-to-flow ratio for these two cases is constant, and one can assume that the only temperature differences for the two power conditions are those for the fuel.[2] A series of such measurements made at several stages of core burnup is included in Table III-31-I.

Of the data in Table III-31-I, values of experiments 2 and 4 should have associated with them large uncertainty factors. For experiment 3, the power was actually 24.2 MW rather than 22.5 MW so that an estimated correction to the experimental data was necessary. In experiment 5, the data were taken in the descending power mode as contrasted with the other runs, so that "hysteresis effects" are involved.

While the data are probably accurate to only several inhours, the trend of the measurements seems to indicate an increase in the power coefficient ranging from −0.95 to −1.25 Ih/MW in the fuel temperature feedback during Run 26. The value of −1.25 Ih/MW is used as the average for Run 26C, based on a weighted average feedback of 13.5 Ih for the last two measurements listed in Table III-31-I.

A possible explanation for such an effect would be that the fuel thermal conductivity and the thermal conductivity of the fuel-cladding bond decrease with burnup. This behavior is consistent with recent measurements[3] of the fuel thermal conductivity as a function of swelling and a/o burnup. The reported results[4] seem to indicate that a loss in thermal conductivity greater than 10% can be expected for EBR-II, Mark-IA driver fuels which have undergone a 4% swelling, at a burnup of 0.8 a/o and at an irradiation temperature of 484°C. As a result, fuel temperatures and associated fuel expansion would be greater at the end of the run than at the beginning, for the same power.

The uncertainties in the fuel pin temperature changes allow the possibility that some of the fuel pellets may undergo a phase transition. The heating of the U-5 w/o Fs fuel alloy to temperatures of 552°C or slightly higher results in the partial formation of a low density gamma uranium phase.[5] Associated with the gamma phase is a marked increase in the linear expansion coefficient. The change in the expansion coefficient as a function of burnup could in part account for the increase in the fuel temperature reactivity effect.

Assuming that the sodium temperature coefficient and, in turn, the sodium power coefficient of −0.85 Ih/MW remains constant throughout the run, the linear reactivity feedback increases from −1.8 to −2.1 Ih/MW.

Subtracting the values for the total linear feedback from the measured values of the power curve gives the nonlinear component of reactivity for three cases (26A, 26B, 26C) representative of varying degrees of fuel burnup, respectively. Referring to Fig. III-31-1, it appears therefore that there has also been an increase in the nonlinear component of reactivity during Run 26.

It is possible that the introduction of the stainless-steel reflector has resulted in the reactor subassemblies being mutually subjected to increased bending and torsional stresses. Consequently, the subassembly clearances may have been increased by the repeated bowing cycles. Some evidence in this direction is indicated by recent post-irradiation measurements[6]

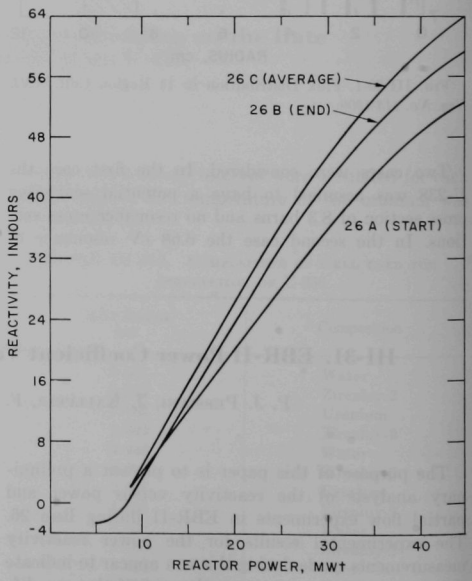

FIG. III-31-1. Nonlinear Component of Reactivity for Operational Power Run 26. *ANL Neg. No. 112-9480.*

made across the subassembly flats. This less-tight core configuration would result in an increase in the positive nonlinear feedback.

REFERENCES

1. P. J. Persiani, J. Kallfelz, F. Kirn, J. K. Long and R. Smith, *EBR-II Power Coefficient Variations During Operational Run 26*, Trans. Am. Nucl. Soc. **11**, 281 (1968).
2. P. J. Persiani, T. R. Bump, R. A. Cushman, J. K. Long and D. Kucera, *Analysis of the Variation in the EBR-II Power Coefficient Due to Blanket Change*, Trans Am. Nucl. Soc. **11**, 282 (1968).
3. R. di Novi, *Postirradiation Thermal Properties of a Uranium-Fission Alloy as a Function of Burnup*, Trans. Am. Nucl. Soc. **10**, 476 (1967).
4. Reactor Development Program Progress Report for January 1968, ANL-7419, p. 56.
5. S. T. Zegler and M. V. Nevitt, *Structures and Properties of Uranium-Fission Alloys*, ANL-6116 (1961); see also *Transformation Temperatures and Structures in Uranium-Fissium Alloys*, J. Nucl. Materials **1**(1), 6–12 (1959); see also, *Some Properties of Uranium-Fissium Alloys*, Nucl. Sci. Eng. **6**, 222–228 (September 1969).
6. Reactor Development Program Progress Report for January 1968, ANL-8419, p. 36.

III-32. Analysis of the Variation in the EBR-II Power Coefficient Due to Blanket Change[1]

P. J. PERSIANI, T. R. BUMP, R. A. CUSHMAN,* J. LONG* and D. KUCERA

This study of the EBR-II power coefficient for Run 25 is based mainly on experimental observations[2] which suggest that the variations experienced in the power reactivity curve between Runs 24 and 25 are consistent with the two distinct core configurations that were involved; namely, a radial uranium blanketed system and a mixed stainless-steel-uranium reflected core, respectively.

The reactivity feedback as a function of power for the two operational runs are presented in Fig. III-32-1. The experimental data have been adjusted and normalized for reactivity effects resulting from the variation in initial power, inlet coolant temperature, burnup during measuring intervals, and control rod expansion effects.

The significant differences are the marked reduction in the slope of the power curve for Run 25 in the 15 to 30 MWt power range, and the reduction of about 25 inhours in the at-power 45 MWt reactivity decrement between Runs 24 and 25.

The total power reactivity feedback as given in Fig. III-32-1, can be primarily resolved into linear and nonlinear components. The linear component is that reactivity feedback resulting from the density change of the sodium, and the density change and axial expansion of the fuel with temperature. The reactivity feedback resulting from the radial movement of the core grid structure, and the core and blanket subassemblies, are included in the nonlinear bowing effect component.

The axial fuel expansion coefficient for Run 25 was obtained from the partial flow experiments performed at two power levels at the start of Run 25. The experiments yielded a value of −0.75 Ih/MW as the fuel expansion contribution to the linear component of the power coefficient. Assuming that the linear component is comprised mainly of the fuel-expansion

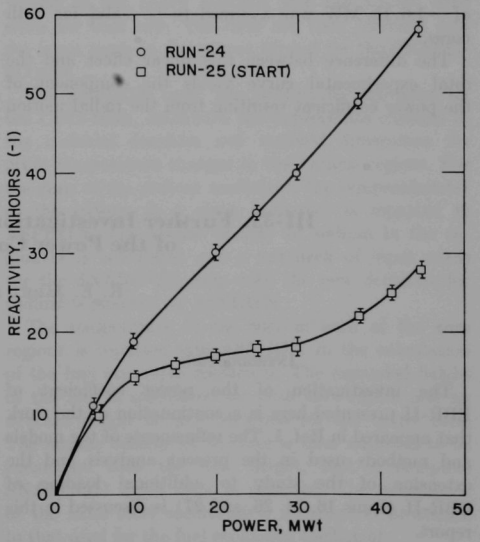

FIG. III-32-1. Measured Total Reactivity. *ANL Neg. No. 112-8751*. Rev. 1.

* Idaho Division, Argonne National Laboratory.

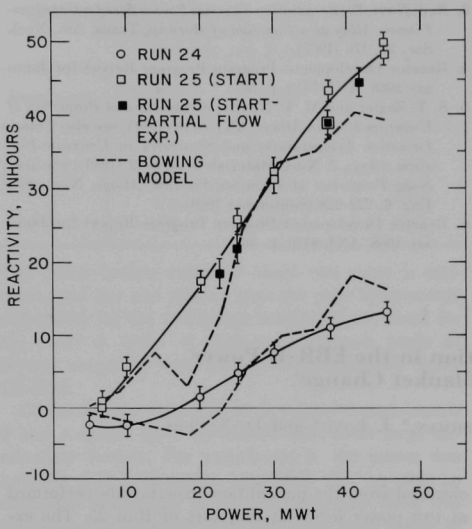

FIG. III-32-2. Nonlinear Component of Reactivity for Operational Power Runs 24 and 25. *ANL Neg. No. 112-9483.*

effect and the overall sodium-expansion effect (computed as −0.85 Ih/MW), the total linear component of −1.6 Ih/MW was assumed to be valid for both cores.

The difference between this linear effect and the total experimental curve yields the component of the power coefficient resulting from the radial motion of the core and blanket subassemblies, including the bowing effects. The results of separating the linear component from the total measured reactivity response with reactor power for Runs 24 and 25, are presented in Fig. III-32-2.

One of the more significant experiments performed in the study of the Run 25 power coefficient was a series of partial coolant flow measurements at several power levels. This series of measurements allowed a check on the consistency of deriving the nonlinear effect, i.e., bowing effect, from the full flow case. Referring to Fig. III-32-2, the magnitudes of the bowing reactivity effect between the full flow experiments are found to agree within the experimental error.

The general shape and the magnitude of the nonlinear component curves are used to check the adequacy of models being developed[3, 4] to describe the collective interactions of the radial deflections of the core and blanket subassemblies. The comparison of a preliminary model is also included in Fig. III-32-2.

References

1. P. J. Persiani, T. R. Bump, R. A. Cushman, J. Long and D. Kucera, *Analysis of the Variation in the EBR-II Power Coefficient Due to Blanket Change*, Trans. Am. Nucl. Soc. **11**, 282 (1968).
2. F. S. Kirn, J. K. Long and R. R. Smith, *Effect of Stainless-Steel Reflector on the Power Coefficient of EBR-II*, Trans. Am. Nucl. Soc. **10**, 648 (1967).
3. T. R. Bump, *Effect of Reactor Temperatures on Bowing of EBR-II Subassemblies*, Trans. Am. Nucl. Soc. **10**, 661 (1967).
4. R. A. Cushman, *The Effect of Radial Heat Transfer on the Temperature Distribution in EBR-II Stainless-Steel Reflector Subassemblies*, Trans. Am. Nucl. Soc. **10**, 661 (1967).

III-33. Further Investigation of the Constant Components of the Power Coefficient of EBR-II

R. E. JARKA and J. T. MADELL

Introduction

The investigation of the power coefficient of EBR-II presented here is a continuation of the work that appeared in Ref. 1. The refinements of the models and methods used in the present analysis and the extension of the study to additional loading of EBR-II (Runs 16, 24, 26, and 27) is discussed in this report.

The total power coefficient was obtained for EBR-II, as well as reactivity effects associated with the individual material components (fuel, sodium, and steel). A two dimensional transport code, SNARG-2D,[2] with a new six-group cross section set was used in the analysis (see Paper III-35). The reactivity effects due to changes in temperature and dimension from 0 to 45 MW operation were obtained by comparing the value of k_{eff} for EBR-II with specified changes to k_{eff} for a base case. EBR-II at a uniform 700°F was taken as the base case. The components which were investigated include: sodium in the core, in the upper blanket, in the inner blanket (reflector), and in the entire reactor; the expansion of

the fuel in the core; the radial and axial expansion of the steel structure.

CALCULATIONAL METHODS AND MODELS

More detailed temperature data were available for this study, resulting in a different representation of EBR-II for the two-dimensional calculations shown in Fig. III-33-1. The temperatures of the materials in each region are given in Table III-33-I for the cases of a steel reflector and a depleted uranium blanket surrounding the core. The temperatures were based on detailed heat transfer calculations.[3] The reactor dimensions, volume fractions, expansion coefficients, and the atom densities of iron and sodium are the same as those used in the previous study.

A systematic way of preparing the data for calculating the components of the power coefficient was developed. Two codes, HVYISO and ASPIRIN, were written to facilitate rapid and accurate preparation of the input cards for the calculation of the components. The HVYISO code programmed for the CDC-160A calculates the atomic densities of the heavy isotopes in the EBR-II fuel; that is, U-235, U-238, Pu-239, and fission product pairs. Printed computer output provides the weight of each nuclide for each subassembly in a loading. HVYISO combines the subassemblies into the proper row and converts the weight of the heavy nuclides into the atomic densities for that row. The data are then punched into the input cards in the proper format for the SNARG-2D code.

TABLE III-33-I. TEMPERATURE DATA BY MATERIAL AND REGION IN RUNS 16, 24, 25, 26, 27, AND 27′ OF EBR-II, °F

Region	Run 16, 24, 27′			Run 25, 26, 27		
	Fuel	Steel	Sodium	Fuel	Steel	Sodium
1	720	720	720	720	720	720
2, 3, 4	—	700	700	—	700	700
5	926	822	776	914	813	773
6	918	820	775	911	814	772
7	917	821	778	912	817	778
8	921	832	792	922	833	793
9	911	835	798	919	837	802
10	874	811	782	896	826	793
11	800	772	770	—	730	730
12, 18	—	853	853	—	846	846
13, 19	—	849	849	—	844	844
14, 20	—	858	858	—	856	856
15, 21	—	885	885	—	886	886
16, 22	—	896	896	—	904	904
17, 23	—	865	865	—	886	886
24	850	850	850	—	760	760

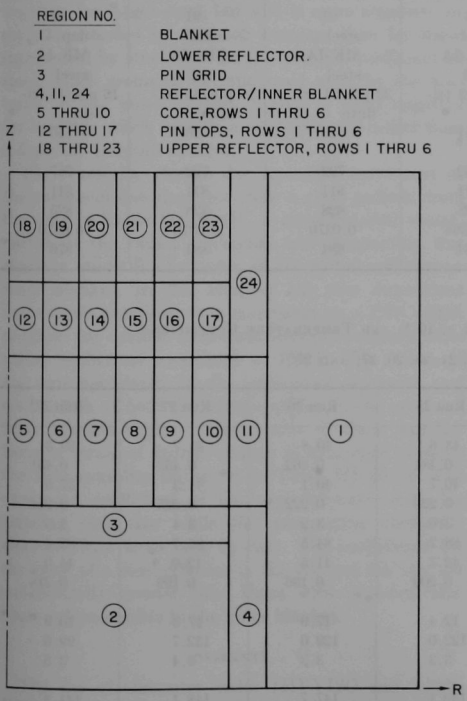

FIG. III-33-1. Representation of EBR-II for Two Dimensional Calculations with Region Number and Identification. *ANL Neg. No. 113-1511* Rev. 1.

The ASPIRIN code, also written for operation on the CDC-160A, calculates the appropriate changes in the material densities and regional dimensions for given temperature changes in the various regions. For the case of the sodium coefficient, the temperature(s) of the sodium in a given region(s) is inputted to ASPIRIN. The atomic density of sodium in the region(s) is calculated and a full deck of input cards for the SNARG-2D code with the new densities for sodium is punched by ASPIRIN.

The temperature of the fuel in each of the core regions is inputted into ASPIRIN in the calculation of the fuel expansion coefficient. The expanded height of the fuel is calculated for each core region and an average height is then obtained for the entire core. The atomic density of the fuel is then adjusted to be consistent with the new height, and a complete SNARG-2D input deck is punched. The calculation of the axial steel coefficient is identical in procedure to that used for the fuel expansion coefficient.

The radial expansion coefficient for steel is obtained by first assuming that the subassemblies in the core

are tightly packed at 700°F. Using the appropriate input values of the temperatures for each region the new radial dimensions are calculated by the following equation:

$$r_1 = r_0(1 - \alpha\Delta T)$$

where

$\alpha \equiv$ linear expansion coefficient

r_0, $r_1 \equiv$ initial and final radii

$\Delta T \equiv$ temperature rise above 700°F.

Again the atomic density of the material is corrected for the change in the dimensions and the input deck is prepared by the ASPIRIN code. The use of ASPIRIN has proved to be effective as a timesaver and also effective in reducing the number of errors in the input data to the SNARG calculations.

RESULTS

A brief description of the loadings for Runs 16, 24, 25, 26, 27, and 27′ is given in Table III-33-II. Run 27′ is a fictitious loading in which four half-loaded subassemblies in Run 27 were replaced by fully loaded subassemblies and the steel reflector subassemblies were replaced by depleted uranium subassemblies. The results of the k_{eff} calculations for the various components of the power coefficient are presented in Table III-33-III. Two sets of values are presented: reactivity defect from 0 to 45 MW in units of $\Delta k \times 10^{-5}$ and the temperature coefficient of reactivity in units of $\Delta k/\Delta T \times 10^{-5}$.

DISCUSSION OF THE RESULTS

The total reactivity defect for the six cases considered in this study differ by 2½% or less from the

TABLE III-33-II. DESCRIPTION OF THE CORE LOADING LOADINGS FOR RUN 16, 24, 25, 26, 27 AND 27′

Item	Run 16	Run 24	Run 25	Run 26	Run 27	Run 27′
Number of S/A in core[a]	75	81	88	91	91	91
Rows 7, 8	dep. U.	dep. U.	steel	steel	steel	dep. U.
Fuel type	MK-I	MK-IA	MK-IA	MK-IA	MK-IA	MK-IA
Axial blkt. material	dep. U.	steel	steel	steel	steel	steel
Axial blkt. design	pin	pin	50 pin/13 tri-flute	33 pin/31 tri-flute	16 pin/45 tri-flute	16 pin/45 tri-flute
Number of experiments	5	9	11	13	16	16
Ave. core Na temp, °F	791	787	792	792	792	787
Ave. fuel temp, °F	811	811	811	811	811	811
Ave. core steel temp, °F	830	825	828	828	828	825
Expansion core radius, cm	0.0347	0.0349	0.0364	0.0370	0.0370	0.0370
Ave. upper refl. Na temp, °F	881	876	884	884	884	876

[a] S/A ≡ subassembly.

TABLE III-33-III. REACTIVITY DEFECTS ($-\Delta k \times 10^{-5}$) AND TEMPERATURE COEFFICIENT $\left(\frac{-\Delta k}{\Delta°\mathrm{F}} \times 10^{-5}\right)$ FOR RUNS 16, 24, 25, 26, 27, AND 27′

	Run 16	Run 24	Run 25	Run 26	Run 27	Run 27′
Na core, Δk	44.7	40.7	43.6	40.8	41.7	39.3
Na core, $\Delta k/\Delta°$F	0.494	0.465	0.481	0.462	0.453	0.451
Na upper refl., Δk	29.6	30.9	40.7	40.1	41.3	37.5
Na upper refl., $\Delta k/\Delta°$F	0.16	0.189	0.223	0.222	0.225	0.214
Na inner refl., Δk	5.9	7.2	3.6	3.2	3.4	5.6
Na total, Δk	80.4	79.0	88.2	84.5	86.7	82.4
Fuel, Δk	44.6	43.6	42.3	41.5	42.0	44.0
Fuel, $\Delta k/\Delta°$F	0.211	0.206	0.200	0.196	0.199	0.218
Steel expansion						
axial, Δk	8.7	9.1	12.4	17.9	17.3	10.9
axial and radial, Δk	119.6	118.2	122.0	129.0	132.7	99.6
radial, Ih/mil	2.4	3.4	3.3	3.3	3.4	3.5
45 MW						
no radial exp., Δk	135.2	138.1	152.1	147.7	148.1	141.3
radial exp., Δk	255.3	250.3	255.7	253.9	265.9	244.0

mean value. Such deviation is considered to be within the accuracy of the calculations. There are, however, some larger variations in the individual components of the power coefficient for these cases (Table III-33-III), but there is difficulty in determining the cause for the variations from the results of this study. As may be seen from the loading description in Table III-33-II, several changes were made between each run and, therefore, a change in a coefficient cannot be attributed to one change in the loading. Furthermore, the analysis is hampered by a lack of reaction summaries for each material in the regions.

The sodium temperature coefficient of the core becomes less negative while that in the upper reflector becomes more negative as the size of the core increases. The sodium coefficient in the inner reflector region depends on whether a depleted uranium or stainless steel reflector is employed there. The fuel expansion coefficient does not seem to show any trend with just one parameter. The fuel coefficient is less negative for larger cores but also is more negative for cores surrounded by depleted uranium than for those surrounded by steel. The axial expansion coefficient of steel, which seems to be influenced most by the material in the inner blanket region, is most negative for loadings which include a steel reflector rather than a depleted uranium blanket.

The reactivity change due to radial movement of the subassemblies does not show a clear pattern from the data in Table III-33-III. A more detailed examination of the radial expansion and compaction was made to study the influence of the radial reflector or inner blanket. In this analysis the new dimensions and volume fractions were calculated on a CDC-160A program for various clearances between subassemblies under isothermal conditions at 700°F. The values of k_{eff} were calculated for the isothermal expansion and contraction of both the subassemblies in the core and inner blanket regions. The results of these calculations in terms of Ih/mil change in clearance between the subassemblies are given in Table III-33-IV. The expansion coefficient of the core increases with increasing core size while the compaction coefficient changes little from case to case. The coefficients for the cases of a steel reflector in the 7th and 8th row are substantially greater than those with depleted uranium subassemblies in the inner blanket.

TABLE III-33-IV. EXPANSION AND COMPACTION COEFFICIENTS OF THE CORE REFLECTOR AND BLANKET FOR RUN 16, 24, 25, AND 26

Run	Expansion, −Ih/mil		Compaction, −Ih/mil	
	Core	Blanket/Reflector	Core	Blanket/Reflector
16	3.13	0.10/N.A.[a]	2.73	0.11/N.A.[a]
24	2.73	0.11/N.A.[a]	2.61	0.11/N.A.[a]
25	2.60	N.C.(1)/0.39[b]	2.53	0.04/N.C.(2)[c]
26	2.50	N.C.(1)/0.40[b]	2.55	0.03/N.C.(2)[c]

[a] N.A.—not applicable; no reflector region present.

[b] N.C.(1)—not calculated, approximately equal to compaction coefficient −0.04 Ih/mil.

[c] N.C.(2)—not calculated, approximately equal to expansion coefficient −0.4 Ih/mil.

SUMMARY

The use of computer codes (HVYISO and ASPIRIN) to prepare the input cards for the reactivity calculations removes many of the errors that had previously occurred in the preparation of the SNARG-2D deck. This improvement can be seen in the internal consistency of the values calculated for the components of the reactivity coefficients and the total reactivity coefficients. The calculated values of the temperature coefficients for each component can be used to calculate an isothermal coefficient. Making this calculation results in a calculated value of −1.01 Ih/°F for the isothermal coefficient, which is in excellent agreement with experimental values. Where applicable the values of the temperature coefficients appearing in Ref. 4 have compared well with the values calculated in this study. It should be noted, however, that there are different assumptions and different divisions of the individual components of the temperature coefficients given in Ref. 4 and those presented here.

Even with this good agreement in the calculated values of the reactivity and temperature coefficients, the power reactor decrement for some of the recent runs of EBR-II has not been completely explained. The difficulty arises in understanding the non-linear components of the reactivity coefficients, most particularly the bowing effect. Work is continuing in analyzing the recent experimental data on the reactor power decrement and a new approach is being examined which employs the use of the isothermal expansion and compaction reactivity effects. These data will be employed to determine whether the reactivity effect of the bowing can be translated into a reasonable model of movement for the subassemblies in the core and blanket/reflector regions.

REFERENCES

1. J. T. Madell, *Investigation of the Temperature Coefficient of EBR-II, Run 25*, Reactor Physics Division Annual Report, July 1, 1966 to June 30, 1967, ANL-7310, pp. 228-230.

2. G. T. Duffy, H. Greenspan, S. D. Sparck, J. V. Zapatka and M. Butler, *SNARG, A Two-Dimensional Discrete-Ordinate, Transport-Theory Program for the CDC-3600*, ANL-7426 (1968).
3. R. A. Cushman, Argonne National Laboratory (private communication).
4. L. J. Koch, W. B. Loewenstein and H. O. Monson, *Addendum to Hazard Summary Report, Experimental Breeder Reactor-II (EBR-II)*, ANL-5719 (Addendum), (1962).

III-34. EBR-II Control-Rod-Bank Dynamic Reactivity Feedback

J. A. DeShong, Jr.

A theoretical model of the dynamics of the EBR-II control-rod-bank reactivity feedback has been developed as shown in Fig. III-34-1.[1] The coefficients C_1 through C_4 are associated with various lengths of the rod along its axis, each of which possess different dynamic characteristics.[2] The time constants shown for each section were calculated based on the dynamic heat-transfer characteristics of that section. The values d_1 through d_4 are the dynamic changes in length of various rod portions, and W converts these to reactivity feedback. The total expansion, d_{TOTAL}, at 45 MW is 153 mils, corresponding to 3.42×10^{-4} $\delta k/k$ or 14.7 Ih. The average coolant temperature rise in the control subassembly is represented by θ_c and the coolant temperature rise in the inner plenum by θ_p. ΔP represents a power increment, P_0 is the initial power, and s is the LaPlace transform variable. $\Delta\theta_{TC}$ is the effective temperature rise (for a power increment ΔP) of the coolant in contact with that portion of the control rod which passes through the top cover of the plenum.

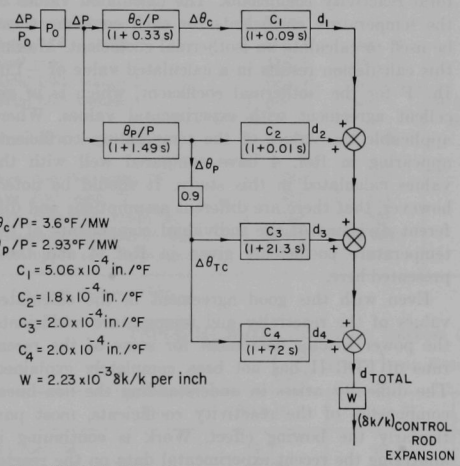

Fig. III-34-1. EBR-II Control-Rod-Bank Dynamic Reactivity Feedback. *ANL Neg. No. 113-648.*

The dynamic rod-bank reactivity effects are being used in an effort to understand the other feedback effects, including the positive structural effect. The dynamic reactivity of the rods has been subtracted from the measured reactor response to develop a model for the remaining reactivity effects.

References

1. L. J. Koch, W. B. Loewenstein and H. O. Monson, *Addendum to Hazard Summary Report Experimental Breeder Reactor-II (EBR-II)*, ANL-5719 (1964), p. 68.
2. M. H. Shackelford, Ed., *EBR-II Run 25 and 26A Interim Report, Appendix 5, Argonne National Laboratory* (November 10, 1967).

III-35. Analysis and Development of Neutron Cross Sections for EBR-II Studies

D. A. Kucera and J. T. Madell

Introduction

As mentioned in Ref. 1, the value of reactivity of EBR-II, Run 25, was calculated to be 1.05715. The measured value was between 1.003 and 1.005 at the start of Run 25. A discrepancy of over 5% in the value of the reactivity is unacceptable in calculations of an absolute nature, such as determining the enrichment or number of subassemblies required for criticality. A study was conducted to determine the cause of the discrepancy.

Areas of Investigation

Five general areas were considered to be possible sources of a discrepancy in the value of reactivity. A discussion of the investigation of these areas is given in sections 1–4.

1. Neutronic Model

One possible source of the discrepancy is the accuracy with which the neutronic model represents the physical system. The accuracy can be affected by the selection of the model to describe the neutron transport and by the selection of the number of energy groups to represent the neutron reactions. A series of diffusion and transport calculations was performed using a simple model of EBR-II. For these calculations EBR-II was represented as a three region (core, reflector, and blanket) sphere whose compositions are given in Table III-35-I. Using cross section Set 236(2) the MACH 1 code[3] calculated the critical radius of the core. For these critical dimensions and compositions a number of different types of diffusion and transport calculations were run to determine values of reactivity with the 22 and 6 group cross section sets. The results are presented in Table III-35-II.

The conclusions drawn at this point were: (1) the use of the 6-group set for the reflected EBR-II produced a reactivity which was 0.924% higher than that yielded by the 22-group set, and (2) the value of k calculated using MACH 1 was 2.7% lower and using the S_2 approximation was 2.6% higher than the value of k calculated using the S_{16} approximation. The comparisons between the reactivities calculated by the S_2, S_{16}, and diffusion approximations were in agreement with the comparisons presented in Ref. 4. Making corrections for the use of a 6 group set and the S_2 approximation, the new value of reactivity for EBR-II, Run 25, was determined to be 1.0191.

TABLE III-35-I. Composition for Simplified (Three Region, Spherical Geometry) Model of EBR-II

Material	Concentration, atoms/cm³ × 10²⁴		
	25.2 cm Radius Core	10.0 cm Thick Reflector	35 cm Thick Blanket
U-235	6.3×10^{-3}	—	6.0×10^{-5}
U-238	6.0×10^{-3}	—	2.9×10^{-2}
Pu-239	1.0×10^{-5}	—	3.0×10^{-5}
Fe	1.2×10^{-2}	4.5×10^{-2}	1.2×10^{-2}
Ni	1.5×10^{-3}	6.1×10^{-3}	1.5×10^{-3}
Cr	3.0×10^{-3}	1.4×10^{-2}	3.0×10^{-3}
Na	1.1×10^{-2}	4.0×10^{-3}	4.0×10^{-3}
Fission Prod.	1.0×10^{-4}	—	—
Mo	7.0×10^{-4}	—	—
Nb	3.0×10^{-6}	—	—
Zr	6.0×10^{-4}	—	—

TABLE III-35-II. Reactivity of EBR-II using Different Types of Neutronic Codes and Energy Groups

Type	Six Groups	Twenty-Two Groups
Diffusion	1.00924	1.00[a]
S_2	1.06287	1.05298
S_4	1.04021	
S_8	1.03803	
S_{16}	1.03711	

[a] Core radius varied to obtain $k = 1.00$.

2. Library Tapes of Cross Sections

Another source through which errors may be introduced is the neutron cross section library tapes. There have been experiences in which cross section data were either improperly punched on cards or improperly written onto the tape. This is a malfunction of the computer equipment rather than the computer programs. Investigation of the cross section data was carried out in two parts. In the first part the cross sections generated for the XLIBIT format were compared with those of the same nuclides produced in the MACHLIB format. No errors were found in the examination of these two cross section formats.

TABLE III-35-III. ATOM DENSITIES OF NUCLIDES USED IN GENERATING THE WEIGHTING SPECTRA FOR MC², atoms/cm³ × 10²⁴

Nuclide	Core	Blanket	Reflector
U-235	6.1238×10^{-3}	6.6036×10^{-5}	—
U-238	5.5760×10^{-3}	2.8658×10^{-3}	—
Pu-239	—	3.5940×10^{-5}	—
Fe	1.3718×10^{-2}	1.1960×10^{-2}	4.8535×10^{-2}
Ni	1.7365×10^{-3}	1.5141×10^{-3}	6.1460×10^{-3}
Cr	3.9194×10^{-3}	3.4173×10^{-3}	1.3868×10^{-2}
Na	1.1176×10^{-2}	4.3234×10^{-3}	4.3225×10^{-3}

Perturbation analysis was used to investigate any errors in the cross section library. The worths of several nuclides were evaluated in an EBR-II spectrum and were compared with similar data reported in Ref. 5 and found to be in general agreement. Although neither method of determining errors in the cross section data is foolproof, experience has shown that errors of the types being investigated here are large in magnitude and would usually be uncovered by one of these two lines of investigation.

3. NUCLIDE COMPOSITIONS IN EBR-II

The uncertainty in the fuel composition for Run 25 could explain some of the discrepancy in the reactivity. To eliminate this factor the reactivity of the wet critical experiment was calculated with an S_2 calculation using the 6-group cross section set.

The amount of fuel in the wet critical experiment was reported in detail and criticality was accurately measured at zero power. A value of 1.0597 was calculated for k_{eff}. The value corrected for the 6 groups and S_2 approximation is 1.02256. The discrepancy of over 2% k in calculating the well described and well controlled wet critical experiment suggests that the source of the trouble lies in the calculation of the broad group cross sections.

4. CALCULATION OF BROAD GROUP CROSS SECTIONS

Two remaining areas left for investigation were the MC² code[6] itself and the selection of the weighting spectrum used in the MC² code. An error in the MC² code was detected in the treatment of inelastic scattering. Calculations showed that the value of k_{eff} was reduced by 0.5% for a large oxide system when proper treatment of inelastic scattering was introduced. This information led to the development of a new cross section set from which the influences of the errors in the MC² code and the selection of the weighting spectrum were determined.

The MC² program generated 22-group cross sections weighted with typical EBR-II core, blanket, and reflector spectra. The compositions used in generating the spectra are given in Table III-35-III and the energy structure of the 22-group set is presented in Table III-35-IVa. The MC² program generating the core-average cross sections employed a buckling search to criticality and considered the heterogeneity of the EBR-II core. The other two programs used a homogeneous mixture of reflector and blanket materials with a buckling equal to zero. In addition to the nuclides on the MC² library tape, the 22-group cross sections of seven additional nuclides (molybdenum, niobium, zirconium, natural boron, B-10, tungsten, tantalum) from Set 224[7] were included. The cross sections for all these nuclides were converted from the MC² format to both MACHLIB and XLIBIT formats. A description of the nuclides —their weighting spectrum and their designation— is given in Table III-35-V.

TABLE III-35-IVa. GROUP STRUCTURE OF CROSS SECTION SET 238

Energy Group	Lower Energy Limit, eV	Upper Lethargy Limit
1	3.68×10^6	1.0
2	2.23×10^6	1.5
3	1.35×10^6	2.0
4	8.21×10^5	2.5
5	4.98×10^5	3.0
6	3.02×10^5	3.5
7	1.83×10^5	4.0
8	1.11×10^5	4.5
9	6.74×10^4	5.0
10	4.09×10^4	5.5
11	2.48×10^4	6.0
12	1.50×10^4	6.5
13	9.12×10^3	7.0
14	4.31×10^3	7.75
15	2.62×10^3	8.25
16	2.03×10^3	8.50
17	1.23×10^3	9.0
18	9.61×10^2	9.25
19	5.83×10^2	9.75
20	2.75×10^2	10.5
21	1.01×10^2	11.5
22	2.90×10^1	12.75

TABLE III-35-IVb. GROUP STRUCTURE OF CROSS SECTION SET 23806

Energy Group	Corresponding Set 238 Groups	Lower Energy Limit, eV	Upper Lethargy Limit
1	1, 2	2.35×10^6	1.5
2	3, 4	8.21×10^5	2.5
3	5, 6	3.02×10^5	3.5
4	7, 8	1.11×10^5	4.5
5	9, 10	4.09×10^4	5.5
6	11 through 22	2.90×10^1	12.75

TABLE III-35-V. THE LIST OF NUCLIDES, WEIGHTING SPECTRA, AND DESIGNATION ON CROSS SECTION TAPES FOR SETS 238 AND 23806

		Nuclide Designation on Cross Section Tapes			
		MACHLIB		XLIBIT	
		238	23806	238	23806
U-235	C(ore)	1	1	U235–C	R_1N_1
	R(eflector)	23	21	" R	R_2N23
	B(lanket)	12	41	" B	R_3N12
Pu-239	C	2	2	Pu239C	R_1N_2
	R	24	22	" R	R_2N24
	B	13	42	" B	R_3N13
U-238	C	3	3	U-238_C	R_1N_3
	R	25	23	" R	R_2N25
	B	14	43	" B	R_3N14
Pu-240	C	4	4	PU240C	R_1N_4
	R	26	24	" R	R_2N26
	B	15	44	" B	R_3N14
Fe	C	5	5	FE_ _ _C	R_1N_5
	R	27	25	" R	R_2N27
	B	16	45	" B	R_3N16
Ni	C	6	6	NI_ _ _C	R_1N_6
	R	28	26	" R	R_2N28
	B	17	46	" B	R_3N17
Cr	C	7	7	CR_ _ _C	R_1N_7
	R	29	27	" R	R_2N29
	B	18	47	" B	R_3N18
Na	C	8	8	NA_ _ _C	R_1N_8
	R	30	28	" R	R_2N30
	B	19	48	" B	R_3N19
FPAIR	C	9	9	FPAIR C	R_1N_9
	R	31	29	" R	R_2N31
	B	20	49	" B	R_3N20
Oxygen	C	10	10	OXY_ _C	R_1N10
	R	32	30	" R	R_2N32
	B	21	50	" B	R_3N21
Carbon	C	11	11	CAR_ _C	R_1N11
	R	33	31	" R	R_2N33
	B	22	51	" B	R_3N22

		Nuclide Designation on Cross Section Tapes			
		MACHLIB		XLIBIT	
		238	23806	238	23806
Mo	C(ore)		12		R_1N34
	R(eflector)		32		R_2N34
	B(lanket)		52		R_3N34
	Set 224	34		MO_ _ _ _	
Nb	C		13		R_1N35
	R		33		R_2N35
	B		53		R_3N35
	Set 224	35		NB_ _ _ _	
Zr	C		14		R_1N36
	R		34		R_2N36
	B		54		R_3N36
	Set 224	36		ZR_ _ _ _	
B_{nat}	C		15		R_1N37
	R		35		R_2N37
	B		55		R_3N37
	Set 224	37		BNAT_ _	
W	C		16		R_1N38
	R		36		R_2N38
	B		56		R_3N38
	Set 224	38		W_ _ _ _ _	
Ta	C		17		R_1N39
	B		47		R_2N39
	B		57		R_3N39
	Set 224	39		TA_ _ _ _	
B_10	C		18		R_1N40
	R		38		R_2N40
	B		58		R_3N40
	Set 224	40		B10_ _ _	
Stainless Steel	C	41	19		R_1N41
	R	43	39		R_2N43
	B	42	59		R_3N42
	Set 224				
Fissium	C		20		R_1N44
	R		40		R_2N44
	B		60		R_3N44
	Set 224	44			

The group collapsing routine of the MACH code was used to produce the 6-group sets (Set 23806) in both MACH and XLIBIT format. In this group-collapsing routine the groups are weighted linearly with the real flux, which was generated from the reactor system described in Table III-35-III. The energy structure of the six group set, which is given in Table III-35-IVb, is the same as that used in Set 23606. The basis for selecting the energy structure used in Set 23606 is described in Ref. 1.

COMPARISONS OF SETS 238 AND 23806 WITH SETS 236 AND 23606

A series of calculations was performed to compare the reactivity calculated with the new and the old cross section sets and with different weighting spectra

TABLE III-35-VI. VALUE OF k_{eff} FOR SPHERICAL REPRESENTATION OF EBR-II FOR VARIOUS CROSS SECTION SETS, WEIGHTING SPECTRA, AND NEUTRONIC MODELS

Case	Cross-Section Set	Weighting Spectrum for Cross Sections in Reflector Region	Diffusion	S_2	S_4	S_8
1	238	Reflector	0.9747	1.0231	1.0019	1.0000
2	238	Blanket	0.9848	1.0331	1.0122	1.0102
3	236	Blanket	0.9858	1.0276	1.0069	1.0050
4	236	Core	0.9855	1.0274	1.0066	1.0047
5	23806	Reflector	0.9758	1.0250	1.0035	1.0016
6	23806	Blanket	0.9866	1.0351	1.0138	1.0119
7	23606	Blanket	0.9894	1.0374	1.0164	1.0144
8	23606	Core	0.9886	1.0367	1.0155	1.0135

for nuclides in the reflector. The system used for comparison was a spherical representation of EBR-II with a core, reflector, and blanket region. The compositions of these regions are similar to those given in Table III-35-I. The values of the multiplication were calculated using diffusion theory and three orders of the transport approximation and were normalized in Table III-35-VI so that a value of 1.0 was obtained for the S_8 calculation in case 1.

The following observations are made from the data in Table III-35-VI.

1. The relationships between the various neutronic representations are the same as those reported earlier in this paper. That is, diffusion theory predicts a k_{eff} of about 2½% below the measured value whereas the S_2 approximation predicts a k_{eff} about 2½% larger than the measured value. Thus, the corrected values of k_{eff} for the wet critical and Run 25 remain about the same; that is, about 1.02.

2. The selection of a weighting spectrum in the reflector region has a significant effect on the value of k_{eff}. This can be seen by comparing the values of k_{eff} for all neutronic representations for case No. 1 with 2 and case No. 5 with 6. The only difference among these cases is the weighting spectrum used for the cross sections of the nuclides in the reflector regions. The use of a spectrum characteristic of reflector material produces a value of k_{eff} of about 1% less than blanket weighted cross sections do.

3. There appears to be little difference in the use of core or blanket-weighted cross sections in the reflector region. This can be seen by comparing case No. 3 with 4 and case No. 7 with 8.

4. The improved treatment of inelastic scattering incorporated within the latest MC² code appears to have little effect on the value of k_{eff} for these cases. The basis for this conclusion can be seen by comparing cases No. 2 and 3 and cases No. 6 and 7. In these cases the identical weighting spectra for the cross section were used in each region so the only difference in these cases is in the treatment of inelastic scattering by MC².

INVESTIGATING THE IMPORTANCE OF THE WEIGHTING SPECTRUM

A perturbation analysis was conducted to determine the cause of the difference in the k_{eff} calculated with a different weighting spectrum in the reflector region. The reactivity effect produced by exchanging blanket-weighted and reflector-weighted cross sections in the reflector region were calculated for the individual and total components of $\Delta k/k$. The results of the calculations given in Table III-35-VII revealed that the leakage component makes the largest contribution to the reactivity. The exchange

TABLE III-35-VII. COMPONENT AND TOTAL VALUES OF $\Delta k/k$ FOR THE EXCHANGE OF REFLECTOR WEIGHTED SPECTRUM CROSS SECTIONS IN THE REFLECTOR REGION

Nuclide	Capture	Radial Leakage	Elastic Scattering	Inelastic Scattering	Total $\Delta k/k$
Substituting Blanket for Reflector-Weighted Cross Sections in Case 1 MACH Calculation					
Fe	-3.19×10^{-4}	8.37×10^{-3}	1.44×10^{-4}	-1.61×10^{-6}	8.20×10^{-3}
Ni	-2.61×10^{-5}	-4.20×10^{-6}	-5.09×10^{-5}	-8.70×10^{-7}	-8.21×10^{-5}
Cr	5.48×10^{-6}	1.19×10^{-3}	3.14×10^{-5}	-2.77×10^{-6}	1.23×10^{-3}
Na	3.25×10^{-6}	5.85×10^{-5}	8.00×10^{-6}	$+2.59 \times 10^{-7}$	7.00×10^{-5}
Total for mixture	-3.36×10^{-4}	9.62×10^{-3}	1.32×10^{-4}	-4.99×10^{-6}	9.41×10^{-3}
Substituting Blanket for Reflector-Weighted Cross Sections in Case 2 MACH Calculation					
Fe	2.24×10^{-4}	-1.00×10^{-2}	-2.36×10^{-4}	$+6.70 \times 10^{-7}$	-1.00×10^{-2}
Ni	2.84×10^{-5}	-1.11×10^{-5}	$+2.98 \times 10^{-5}$	7.87×10^{-7}	4.79×10^{-5}
Cr	-6.69×10^{-6}	-1.18×10^{-3}	-3.32×10^{-5}	2.19×10^{-6}	-1.22×10^{-3}
Na	-3.08×10^{-6}	-5.06×10^{-5}	-1.06×10^{-5}	-3.32×10^{-7}	-6.46×10^{-5}
Total for mixture	2.43×10^{-4}	-1.13×10^{-2}	-2.50×10^{-4}	-3.32×10^{-6}	-1.13×10^{-2}

of reflector and blanket-weighted cross sections for iron accounts, in turn, for 89% of the total difference in the leakage. It is noted that the values of reactivity for the two substitutions have different absolute values due to the first order nature of the perturbation analysis. The sensitivity of the leakage component is related to the discrepancies in the transport cross section. The transport cross section of iron, for example, is very sensitive to the weighting spectrum in energy regions containing large resonances. For example, an 80% difference in the 11*th* broad group transport cross section of iron is seen between the cross sections weighted with reflector and blanket spectrum.

In generating broad group transport cross sections the MC² code weights the ultrafine group cross section data with the flux and the inverse of the homogenized transport cross section. If the weighting spectrum does not take into account the depressed flux and large homogenized transport cross section in a resonance region, the broad group cross section will be in error. Discrepancies in the transport cross sections in resonance regions of iron are expected because the spectrum characteristic of the blanket does not represent the spectrum in a region of high iron content. However, the sensitivity of the reactivity to the changes in the cross sections was not expected because (1) the iron resonances occur at the tail-end of EBR-II's spectrum; (2) the reflector is thin and not in a region of great importance; (3) to be significant, all of the errors must be in the same direction. An investigation showed that the effect of the weighting spectrum is important in this case because the gradients of the flux and adjoint flux in the resonance regions are large, even though the flux and adjoint are not, as may be seen from the equation

$$\delta k = \Sigma \delta k_j = \sum_j \nabla \phi_j \cdot \nabla \phi_j^{+} \delta \left(\frac{1}{3\Sigma_{tr_j}} \right), \qquad (1)$$

where

$j \equiv$ energy group.

Further, the value of δk_j has the same sign for all energies where the perturbation in the transport cross section is large. It should be noted that some other cross sections were more sensitive to the weighting spectrum than the transport cross section of iron, but had a small effect on the reactivity.

In analyzing many-region reactors, consideration must be given to the choice of the weighting spectrum, even for small regions of low importance. Some conditions for which one would expect the reactivity to be sensitive to the weighting spectrum of the cross section are: (1) an abundant nuclide has a nuclear property which varies significantly with energy (usually these are resonances), (2) the abundant nuclide occurs in substantially different amounts in the reactor than it did in the composition from which the weighting spectrum was generated, and (3) the nuclear property makes a significant contribution to the reactivity of the reactor in the energy regions where the variations exist.

References

1. J. T. Madell, *Investigation of the Temperature Coefficient of EBR-II, Run 25*, Reactor Physics Division Annual Report, July 1966 to June 1967, ANL-7310, pp. 228–230.
2. J. T. Madell, *Multigroup Cross Section Sets for Neutronic Calculations of EBR-II*, Reactor Physics Division Annual Report, July 1966 to June 1967, ANL-7310, pp. 223–228.
3. D. A. Meneley, L. C. Kvitek and D. M. O'Shea, *Mach 1, One-Dimensional Diffusion-Theory Package*, ANL-7223 (1966).
4. L. J. Templin, Ed., *Reactor Physics Constants*, ANL-5800, 2nd Edition, (July 1963) pp. 623–624.
5. L. J. Koch, H. O. Monson, D. Okrent, M. Levenson, W. R. Simmons, J. R. Humphreys, J. Haugsnes, V. C. Jankus and W. B. Loewenstein, *Hazard Summary Report, Experimental Breeding Reactor-II (EBR-II)*, ANL-5719 (1957).
6. D. M. O'Shea, B. J. Toppel and A. L. Rago, *MC², A Code to Calculate Multigroup Cross Sections*, ANL-7318 (1967).
7. D. M. O'Shea, H. H. Hummel, W. B. Loewenstein and D. Okrent, *Twenty-Six Group Cross Sections*, Trans Am. Nucl. Soc. **7**, (November 1964) pp. 242.

III-36. Analysis of Experimental Subassemblies in EBR-II

J. T. Madell and R. E. Jarka

The role of EBR-II is now defined as an irradiation facility for the Liquid Metal Fast Breeder Reactor (LMFBR) Program. To meet this role some of the standard fuel and blanket subassemblies have been replaced with subassemblies containing experiments for irradiation. There are approximately 25 experimental subassemblies now in EBR-II and their compositions and design vary widely. Calculations were performed to investigate (1) the effect of the experimental subassemblies upon the operation of EBR-II and (2) the performance of the experimental subassembly itself, the purpose of which was to determine the design features necessary to achieve the desired performance of the experimental subassemblies. Calculations are presented here dealing with two types of unencapsulated experimental subassemblies. The first subassembly contains Mark-II fuel and the second, a mixed oxide fuel.

Experimental Subassembly with a Mark-II Fuel

A new driver fuel for EBR-II, designated as Mark-II,[1] is being developed to provide increased burn-up capabilities. The Mark-II design has the same fuel (uranium-5 w/o fissium) but different dimensions for the jacket, fuel pin, and gas space than those of the Mark-IA design. The enrichment of the Mark-II fuel was calculated for two situations: first, for a loading of EBR-II with all driver fuel of the Mark-II design and second, for an experimental subassembly of the Mark-II design being irradiated in a core of Mark-IA fuel subassemblies.

Enrichment for Mark-II Core Loading

The enrichment calculations were carried out in a series of SNARG-2D[2] calculations (S_2) in the R-Z directions using the six group cross-section Set 23806.[3] The loading for EBR-II with Mark-II driver fuel used in these calculations is given in Table III-36-I. It should be noted that stainless steel reflector subassemblies occupy the *7th* and *8th* rows in these calculations. The material compositions and dimensions for the loading were obtained from various EBR-II reports.[4] For this loading, a 60 a/o enrichment of the uranium was calculated to achieve criticality at 45 MW. In addition, the relation between enrichment and reactivity was found to be $\Delta k/k = 0.0063\ \Delta$ (enrichment). Thus an increase of 1% above the calculated value of 60 a/o results in a 0.63% increase in reactivity. The calculated value of the enrichment was later altered to take into account changes in the basic core loading and differences in the operating characteristics of the fuel which were related to the initial reactivity requirements. The changes considered were:

1. Depeleted uranium blanket instead of a steel reflector
2. Change in the control rod design (replace sodium with natural boron followers)
3. Additional initial reactivity to compensate for higher burn-up
4. Additional reactivity for greater fuel expansion.

The predicted values of reactivity for each of these items are given in Table III-36-II. Taking into account all of these factors, an enrichment of 64.6 a/o is calculated for Mark-II core loading at 45 MW.

Enrichment of the Mark-II Experimental Subassembly in a Mark-IA Core

The enrichment of the experimental subassembly is based on the requirement that the experimental subassembly produces the same amount of power in a Mark-IA core loading at 50 MW as a Mark-II subassembly would produce in a Mark-II core loading at 62.5 MW. The enrichment has been calculated by using two approaches.

In the first approach, the power production in a subassembly is assumed to be proportional to the U-235 loading. Experience with other experimental subassemblies has determined this to be a reasonable assumption. A fully loaded Mark-IA fuel subassembly contains about 2880 g of U-235. To achieve the simulated power of 62.5 MW in a core producing 50 MW, the U-235 loading must be increased by a ratio of 62.5/50. Multiplying by this ratio yields a U-235 loading of 3600 g, which is equivalent to a 76 a/o enrichment in a Mark-II subassembly.

The second approach is based on an approximation that the flux levels in Mark-II loading are close to that in a Mark-IA loading for the same power production. Thus a Mark-II subassembly enriched to achieve criticality for a loading in Table III-36-I would produce the same power as a Mark-IA subassembly enriched to achieve criticality for the same loading. For a reactor loading described in Table III-36-I operating at 50 MW, a Mark-II experi-

mental subassembly would require a 75 a/o enrichment (60 a/o × 62.5/50) to simulate 62.5 MW operation. The change of subassemblies in the *7th* and *8th* rows from steel to depleted uranium would require an additional 2% enrichment of the Mark-II experimental fuel, or a total enrichment of 77 a/o.

Experimental Subassemblies with a Mixed Oxide Fuel

A study was conducted of some aspects of the performance of "typical" FFTF test subassemblies in EBR-II and of their effect on EBR-II's performance. Two "typical" mixed oxide experimental subassemblies were considered during the study—one designated as the ANL-GE type and the other as the PNL type. The ANL-GE type was studied

TABLE III-36-I. Description of the Mark II Loading for EBR-II

Type of Subassembly[a]	Number in Core
Total Core S/A's	91
Mark II Driver S/A's	61
Mark IA Control/Safety	12
Oscillator and Steel Dummy	2
Experiments (same as Run 27)	16

[a] S/A ≡ subassembly.

TABLE III-36-II. Reactivity Effect of Changes in the EBR-II Loading with Mark II Fuel

	$-\Delta k/k$, %
1. Change of steel reflector to depleted uranium blanket	1.0
2. Change of sodium to natural boron control followers	0.3
3. Excess reactivity for 2.0 a/o burnup	1.2
4. Excess reactivity for additional fuel expansion in Mk-II design	0.4
Total	2.9

TABLE III-36-IV. Percent Reactivity Change and Power Density Ratio for ANL-GE Subassemblies Versus Driver Fuel

U-235 Enrichment, %	Percent Reactivity Change					Power Density Ratio, Oxide/Driver
	Row #2	Row #3	Row #4	Row #5	Row #6	
93	+0.52	+0.42	+0.32	+0.24	+0.16	1.163
43	−0.07	−0.07	−0.05	−0.02	−0.003	0.708
0	−0.64	−0.53	−0.40	−0.30	−0.21	0.377

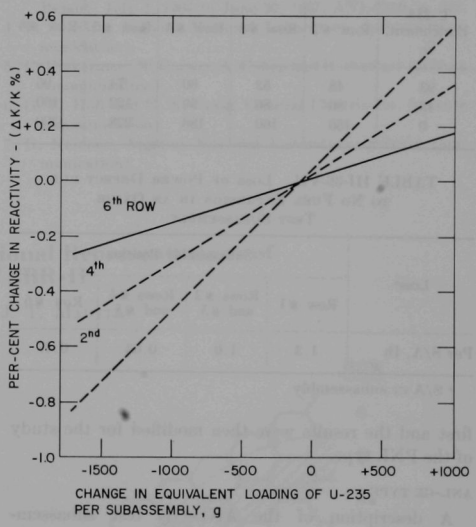

Fig. III-36-1. Reactivity Change Produced by Changing the U-235 (Equivalent) Loading in a Subassembly for Various Row Positions in EBR-II. *ANL Neg. No. 113-1497.*

TABLE III-36-III. Description of ANL, GE, and PNL Types of Oxide Test Subassemblies

	ANL	GE	PNL
Composition	UO_2-20 w/o PuO_2	UO_2-25 w/o PuO_2	UO_2-25 w/o PuO_2
Pellet diam., in.	0.245	0.243	0.210
Clad o.d., in.	0.290	0.290	0.250
Clad thick., in.	0.020	0.020	0.015
Theoretical density, %	~84	~85	83
Height, in.	11.0	13.5	13.5
Linear power, kW/ft	~17	~20	5–17
U enrichment, a/o	93	93	0, 43, 93
Pu enrichment, a/o	91	91	91

TABLE III-36-V. LINEAR POWER GENERATION OF ANL-GE OXIDE TEST SUBASSEMBLIES IN kW/ft (average)

U-235 Enrichment, %	Row #2	Row #3	Row #4	Row #5	Row #6
93	22.8	21.1	18.5	14.8	11.4
43	13.8	12.8	11.3	9.0	6.9
0	7.3	6.8	6.0	4.7	3.6

TABLE III-36-VI. NUMBER OF DAYS OF 45 MW OPERATION TO ATTAIN 1% BURNUP IN ANL-GE OXIDE TEST SUBASSEMBLY

U-235 Enrichment, %	Row #2	Row #3	Row #4	Row #5	Row #6
93	48	52	60	74	96
43	80	86	99	122	160
0	150	160	186	228	300

TABLE III-36-VII. LOSS OF POWER DEFECT DUE TO NO FUEL EXPANSION IN AN OXIDE TEST SUBASSEMBLY

Loss[a]	Subassembly Position			
	Row #1	Rows #2 and #3	Rows #4 and #5	Row #6
Per S/A, Ih	1.3	1.0	0.63	0.47

[a] S/A ≡ subassembly.

first and the results were then modified for the study of the PNL type.

ANL-GE TYPE

A description of the ANL-GE test subassembly[5, 6] is given in Table III-36-III. The reactivity worth of replacing an EBR-II driver with a test subassembly was obtained with *X-Y* SNARG calculations along with the resulting changes in power density. The reactivity worths of the experiments for various uranium enrichment and subassembly positions are given in Table III-36-IV. The ratio of the power density in the test subassembly to the driver that was replaced is also given in Table III-36-IV. The reactivity worth of the replacement is presented as a function of change in the loading of U-235 (equivalent) in Fig. III-36-1, where Pu-239 is assumed to be twice as reactive as U-235.

The power generation of a driver subassembly in the center of EBR-II is 1140 kW or 8.0 kW/ft at a reactor power of 62.5 MW.[7] The linear power generation in ANL-GE oxide was calculated (Table III-36-V) by correcting for the difference in power density and the length of fuel pins between the test and driver subassemblies. The number of days to achieve 1% burn-up for the mixed oxide fuel (Table III-36-VI) is obtained by correcting the driver fuel's value of 2735 MWD/1% burnup in the center position.

Two dimensional calculations were performed to determine the worth of fuel expansion (or the lack of it) by position in EBR-II. In considering the safety aspect of the oxide fuel loading, a conservative position of a zero fuel expansion coefficient was taken. The loss of the reactivity decrement at 45 MW due to a zero expansion coefficient of an oxide subassembly is given in Table III-36-VII as a function of core position.

PNL TYPE

A description of the PNL test subassembly[7] is given in Table III-36-III. The performance of a PNL type subassembly was based on the results for the ANL-GE type. The reactivity worth, power density ratio in Table III-36-VIII, the linear power

TABLE III-36-VIII. PERCENT REACTIVITY CHANGE AND POWER DENSITY RATIO FOR PNL SUBASSEMBLY VERSUS DRIVER FUEL

U-235 Enrichment, %	Percent Reactivity Change					Power Density Ratio, Oxide/Driver
	Row #1	Row #3	Row #4	Row #5	Row #6	
93	+0.12	+0.095	+0.065	+0.050	+0.030	0.92
43	−0.40	−0.33	−0.25	−0.20	−0.14	0.56
0	−0.80	−0.66	−0.52	−0.38	−0.25	0.30

TABLE III-36-IX. LINEAR POWER GENERATION IN PNL OXIDE PINS

U-235 Enrichment, %	Power Density, kW/ft (average)				
	Ring #2	Ring #3	Ring #4	Ring #5	Ring #6
93	18.0	16.7	14.6	11.7	9.0
43	10.5	9.9	8.8	6.9	5.3
0	5.8	5.4	4.7	3.8	2.9

TABLE III-36-X. NUMBER OF DAYS OF 45 MW OPERATION TO ATTAIN 1% BURNUP IN PNL OXIDE FUEL

U-235 Enrichment, %	Days for 1% Burnup				
	Row #2	Row #3	Row #4	Row #5	Row #6
93	60	65	75	92	120
43	100	107	124	152	200
0	188	200	232	285	375

generation in Table III-36-IX, and burn-up rates in Table III-36-X are based on the relative U-235 (equivalent) loadings of the PNL and ANL-GE types. The loss of the reactivity defect is the same in both types because both are assumed to have a zero fuel expansion coefficient.

Summary

There are other aspects of performance of the oxide test subassemblies which have been recognized as significant but which have not been determined quantitatively. The entire facet of the dynamic response of the oxide pins has not yet been analyzed, although it is obviously different from that of the metal pins. Another area for further attention is that of neutron streaming through the void space above or below the fuel.

A preliminary study has been made to determine the maximum number of oxide test subassemblies which can be loaded into EBR-II. The determination has been based on a maximum allowable loss of 10 Ih in the power decrement. Based on the data in Table III-36-VII the maximum number of test subassemblies ranges between 10 (for all test subassemblies in Rows 2 and 3) and 20 (for all test subassemblies in Row 6).

References

1. E. Hutter and O. S. Seim, Argonne National Laboratory (private communication).
2. G. J. Duffy, H. Greenspan, S. D. Sparck, J. V. Zapatka and M. Butler, *SNARG-2D, A Two-Dimensional Discrete-Ordinate, Transport Theory Program for the CDC-3600*, ANL-7426 (1968).
3. J. T. Madell, *Multigroup Cross Section Sets for Neutronic Calculations of EBR-II*, Reactor Physics Division Annual Report, July 1, 1966 to June 30, 1967, ANL-7310, p. 223.
4. F. S. Kirn, Argonne National Laboratory, (private communication).
5. C. Dickerman, N. Carson, A. Cohen and R. Stewart (private communication).
6. G. R. Hull and C. N. Craig, General Electric Co. (private communication).
7. R. Neidner, Argonne National Laboratory (private communication).

III-37. Investigation of Regional Representations of the Core of EBR-II

R. E. Jarka and J. T. Madell

The core of EBR-II is heterogeneous in two respects. First, within each subassembly there is a hetrogeneous array of steel-clad fuel pins surrounded by sodium coolant. Secondly, there are several types of subassemblies in the core which differ significantly in composition. For example, there are fully or partially loaded fuel subassemblies in the core region. Interest exists in examining the methods of representing EBR-II, with its various types of subassemblies, by a number of homogeneous regions in one-dimensional calculations.

The DENSE[1] code, developed at Argonne's Idaho Division, calculates the atomic densities for annular core regions of EBR-II. The code divides the core into 15 annular regions and assigns the exact fraction of each subassembly to the proper region. In a more commonly used method, each of the six hexagonally shaped rows of the core is assumed to constitute an annular region composed of the subassemblies in that ring (Fig. III-37-1).

One can see from Fig. III-37-1 that there is not a one-to-one correspondence between the hexagonal rows and annular regions. For example, some subassemblies in the sixth hexagonal row are partially in the fifth annular regions, and vice versa.

One-dimensional diffusion calculations in cylindrical geometry were performed with a 6-region and 15-region (from DENSE) representation of the EBR-II, Run 25,

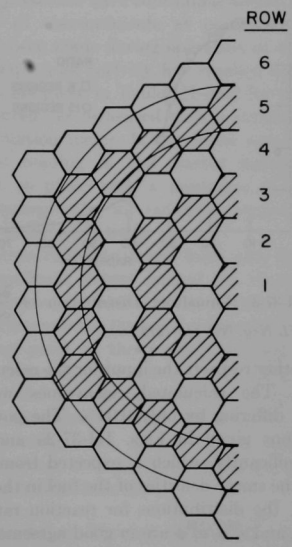

Fig. III-37-1. Representation of the Core of EBR-II by Hexagonal Rows and by Annular Regions. *ANL Neg. No. 113-1486.*

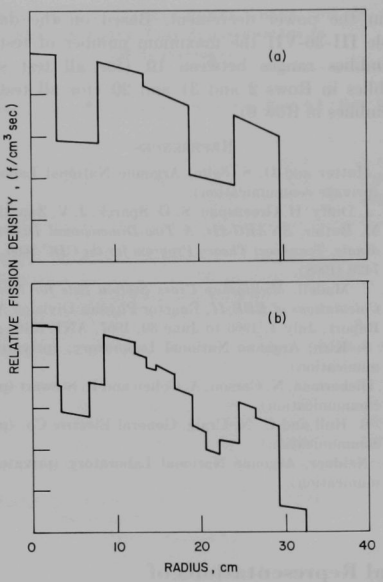

FIG. III-37-2. Fission Density Distribution for (a) 6-Region Core and (b) 15-Region Core. *ANL Neg. No. 113-1477.*

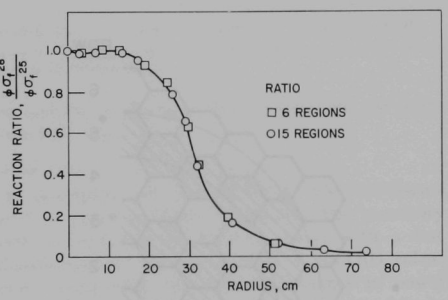

FIG. III-37-3. Normalized Distribution of $\frac{\phi\sigma_f^{28}}{\phi\sigma_f^{25}}$ Reaction Ratio. *ANL Neg. No. 113-1476.*

core. In other respects the input for the calculations was identical. The calculated eigenvalues were almost identical, differing by only 0.04%. The power density distributions given in Figs. III-37-2a and III-37-2b differ significantly, which is expected from the differences in the smear densities of the fuel in the two cases. However, the distributions for reaction rates of $\sigma_f^{25}\phi$, $\sigma_c^{25}\phi$, $\sigma_f^{28}\phi$, and $\sigma_f^{28}\phi/\sigma_f^{25}\phi$ are in good agreement for both cases, as may be seen in Figs. III-37-3 through III-37-6.

For Run 25 loading the simple 6-region representation

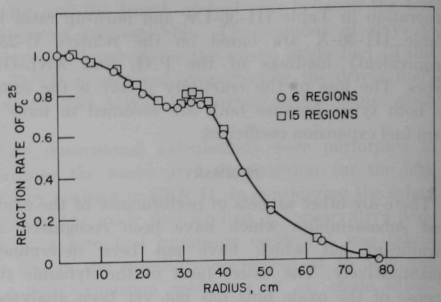

FIG. III-37-4. Normalized Distribution of σ_c^{25} Reaction Rate. *ANL Neg. No. 113-1500.*

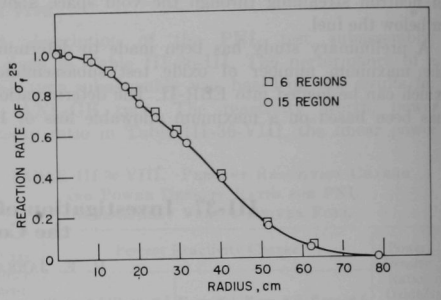

FIG. III-37-5. Normalized Distribution of σ_f^{25} Reaction Rate. *ANL Neg. No. 113-1510.*

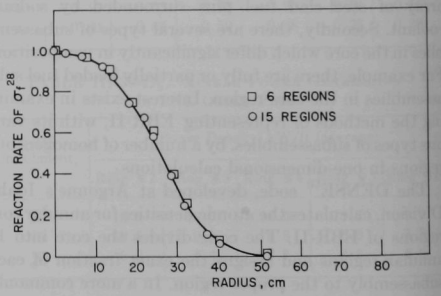

FIG. III-37-6. Normalized Distribution of σ_f^{28} Reaction Rate. *ANL Neg. No. 113-1509.*

of the core is sufficient for obtaining the eigenvalue and properties dependent only on the flux spectrum and distribution, such as reaction rate.

REFERENCE

1. Eric Dean, Argonne National Laboratory (private communication).

III-38. The Experimental Breeder Reactor II (EBR-II) Shield Design and Performance[1]

A. E. McArthy and F. S. Kirn*

The shielding and physics analyses for EBR-II are presented in Refs. 2–5; however, the more important parts of the shield design work are given in Ref. 1. Results of more recent radiation level measurements at several locations in the reactor are reported in this paper to indicate the performance of the shield.

The following is a summary of the work reported in Ref. 1.

In the radial cross section the EBR-II shielding consists of uranium blankets, graphite and borated-graphite neutron shield, sodium tank, and a final concrete biological shield. Magnetite concrete was used above the reactor to conserve space while all other concrete was ordinary. Boron in steel and borated graphite were used to reduce the activation of components and the sodium of the secondary coolant system.

Main shield design problems involved the following: (1) determination of multigroup neutron and gamma-ray flux distributions, (2) calculation of primary sodium activity, (3) prediction and reduction of the secondary sodium activity, and (4) calculation and control of the possible radiation through the many penetrations of the top shield.

The following are highlights of the design considerations discussed in Ref. 1:

1. Neutron flux distributions were based on twenty-group and ten-group diffusion theory calculations. The highest energy groups were ∞–1.35 MeV and 10–1.32 MeV, and the lowest energy groups were 0–0.085 eV and 0–0.27 eV, respectively. Gamma-ray calculations were based on point kernel integration with linear buildup based on H. Goldstein and J. Wilkins data.[6]

2. Fluxes from multigroup diffusion analyses were used to estimate the primary and secondary sodium coolant activities. Calculations of the relative neutron absorptions by neutron energy and by reactor region showed that essentially all neutron energies from thermal to over 1 MeV had to be considered. These calculations indicated that the secondary sodium activity was decreased by a factor of two by placing boron in the neutron shield. Another factor of three was realized by placing boron steel around the heat exchanger.

3. Several twenty-group diffusion theory calculations were made to account for the fact that the heat exchanger is not on the reactor radial centerline but significantly above it. Each calculation used the sodium thickness between the neutron shield and the heat exchanger specified by the angular path being considered.

4. Gamma-ray calculations showed that the sodium decay gamma-rays were the strongest source at the outside of the sodium tank. The more penetrating 8 MeV capture gamma-rays from the structural steel in the neutron shield dominated at the outside of the concrete.

Experimental Measurements of Shielding

During the initial operation of EBR-II and subsequent routine operation, careful radiation level measurements were made. It is almost impossible to make an unqualified measurement from which one can determine the accuracy of the calculations. Nevertheless, the shielding appears to be properly designed for both neutrons and gamma-rays at every critical position where personnel have continuous access.

A series of measurements at points of most interest have been made during operation at 45MW and after the sodium-24 activity has reached equilibrium. The results are given in Table III-38-I for the gamma radiation levels, as measured with a standard Geiger counter radiation meter. It should be noted that the background reading in the reactor building varies from place to place with a minimum of about 0.1 mR/hr. Consequently, all radiation levels should be considered as an upper limit.

The neutron radiation levels have also been measured at significant points around the reactor shield. Using a tissue-equivalent neutron dosimeter, no neutron dose rate greater than 0.1 mRem/hr was measured at any point in the reactor building with one exception. A maximum reading of 0.5 mRem/hr was obtained in the reactor basement in a region where there are penetrations through the concrete shield for the shield cooling ducts. Surveys taken with thermal neutron detectors indicate no thermal flux dose rate greater than 0.02 mRem/hr.

Activity of Primary Sodium Coolant

The activity of the primary sodium is routinely monitored. Samples are taken from the sodium puri-

* Idaho Division, Argonne National Laboratory.

TABLE III-38-I. GAMMA RADIATION LEVELS IN EBR-II

Pt.	Location	Level, mR/h	Note
1	Outside reactor radial shield	0.4	Minimum radial reading on horizontal reactor center line.
2		3.0	Directly across from Na purification room.
3		0.6	—
4	Top of reactor on top of shield plug	0.3	—
5		0.2	—
6	Control rod area at top of shield plug	0.2	—
7		0.2	—
8	Transfer arm at floor level	0.6	Affected by scattering from vertical pentrations.
9	At top of reactor above the Na-Na heat exchanger	12.0	—
10	Secondary sodium line outside building	6.0	—
11	Na cold trap room	$>10^6$	Primary sodium purification cold trap
12	Over west NaK lines to the shutdown coolers	135	This is a very localized radiation source which was unanticipated but now has been adequately shielded.

fication line, which by virtue of its sampling position should give a uniformly mixed sample. The sodium-24 equilibrium activity at 45MW has been measured repeatedly and found to be 6.4×10^2 μCi/gram (8.9×10^2 μCi/gram at 62.5 MW). This compares with the calculated value of 12×10^2 μCi/gram at 62.5 MW.

The sodium-22 formed by the $(n,2n)$ reaction on sodium-23 is also present in measurable amounts. As of December 1966, with 12,245 MWd accumulated by the reactor, the sodium-22 concentration was 3×10^{-2} μCi/gram.

Secondary Sodium Activity

The secondary sodium circulates through the neutron flux field when it passes through the Na-Na heat exchanger located inside the reactor tank. The equilibrium activity of the sodium during 45 MW operation has been determined to be 6.2×10^{-3} μCi/gram. As shown in Table III-38-I, the radiation level on the secondary piping at a radial level of 8 in. from the pipe center is 6 mR/hr which is less than the conservative prediction of a maximum of 50 mR/hr.

Cover Gas Activity

The reactor sodium in EBR-II is blanketed with argon as the cover gas. The activity of this gas has been measured using standard pulse height analysis techniques. The equilibrium argon-41 activity formed from the Ar^{40} (n,γ) reaction is 2.5 μCi/liter of gas at STP. There are about 2.2×10^4 liters of cover gas. In addition to the argon-41, the cover gas contains 7.5 μCi/liter of xenon-137 and 7.0 μCi/liter of xenon-135. These are fission product gases which come about from the fission of "tramp" uranium in the sodium. From a radiation hazards point of view, this fission product activity is more significant than the argon-41 activity.

References

1. A. E. McArthy and F. S. Kirn, *The Experimental Breeder Reactor II Shield Design and Performance*, Proc. International Conference on the Physics Problems of Reactor Shielding, Harwell, September 26–29, 1967. AERE-R5773, **5**, 1968, pp. 1373–1399.
2. M. Grotenhuis, A. E. McArthy and A. D. Rossin, *Experimental Breeder Reactor-II (EBR-II) Shield Design*, ANL-6614 (1962).
3. W. B. Loewenstein, *The Physics Design of the EBR-II*, ANL-6383 (1961).
4. L. J. Koch, H. O. Monson, D. Okrent, M. Levenson, W. R. Simmons, J. R. Humphreys, J. Haugsnes, V. Z. Jankus and W. B. Loewenstein, *Hazard Summary Report, Experimental Breeder Reactor II (EBR II)*, ANL-5719 (1957).
5. L. J. Koch, W. B. Loewenstein and H. O. Monson, *Addendum to Hazard Summary Report Experimental Breeder Reactor-II (EBR-II)*, ANL-5719 (Add.) (1964).
6. H. Goldstein and J. E. Wilkins, Jr., *Calculations of the Penetration of Gamma Rays*, NYO-3075 (1954).

III-39. Calculational Studies in Support of the Fast Flux Test Facility (FFTF) Critical Experiments on ZPR-3

D. Meneghetti, A. J. Ulrich, P. J. Persiani and J. C. Beitel

I. Introduction

The effort of the Reactor Physics Division in support of the FFTF critical experiment program on ZPR-3 is that of planning and calculational studies of the critical experiment needs of the Pacific Northwest Laboratory (PNL) reactor designs. Long range planning, as well as detailed planning, are carried out jointly with personnel of Argonne's Idaho Division and of the Pacific Northwest Laboratory. The joint planning effort during this reporting period was to prepare general plans and detailed descriptions of required experimental work plans. These have been directed principally toward the PNL axially-split conical-core design concept.[1] More recently the program of experimental studies has been directed toward the PNL concept of a central axial test zone region surrounded by an annular core.

Calculational studies have been conducted in support of experiments on ZPR-3 Assembly 51[(2)] and on the subsequent series of criticals denoted as Assemblies 52a through 52f.[(3-5)] Assembly 51 was a plutonium-fueled cylindrical core with a nickel-rich reflector. The core composition approximated the driver-core regions of the split-core FFTF concept if the dilutions due to controls, safety rods, and shims of the reactor design concept are disregarded. Construction of a critical assembly incorporating the dilutions representative of the average driver composition of the concept would lower the average fuel density and would require a plutonium mass above the 430 kg total-plutonium loading-maximum currently specified. The series of criticals 52a through 52f were scoping experiments with annular or axially-split cores having central or gap sodium zone regions, respectively.

These criticals are all part of phase B of the FFTF critical experiment program. Phase A critical experiments and calculations have been described previously;[(6-8)] it consisted of experiments on a modified ZPR-3 Assembly 48 primarily for poison control rod studies at central and at core-reflector interface positions. The modified assembly is referred to as Assembly 48a. Phase C is to consist of engineering mock-up experiments which will be planned toward finalizing important design parameters.

Calculational studies in support of these critical experiments have largely been scoping estimates to assist direction of the critical experiments. More recently detailed post-experimental analyses of some experiments have been initiated.

II. Multigroup Cross Sections

A 29-group cross section set, designated 29001, has been prepared. Except for the lowest energy group, the set was generated using the MC^2 code[9] with compositions approximating the core and reflector corresponding to ZPR-3 Assembly 51. (Not all nuclides needed to generate the cross section set were available in the library tapes which could be used with the MC^2 code. The composition was therefore modified by representing aluminum as sodium and by replacing manganese, silicon, and molybdenum by iron.) The sources of the basic cross section data are listed in Table III-39-I. The energy and lethargy structure of the 29-group set are listed in Table III-39-II. The core fine-flux-averaged cross sections were obtained using the heterogeneous fundamental mode option. The reflector cross sections were obtained using a homogeneous medium fine-flux calculation with zero buckling. For Doppler calculations, core cross sections for 1000°K, in addition to those for 300°K, were also prepared. Group-29 cross sections were generated using the THERMOS code[10] with compositions of core and reflectors. These were averaged over energies below 0.532 eV.

The heterogeneous option of the MC^2 code was used to approximate the effects of resonance self-shielding due to the slab-geometry thin-plate-structure configurations within the assembly core drawers. Since this option is only directly applicable for binary cells the more complicated intradrawer structures were approximated as binary cells.

The regionally-dependent six-group cross sections, designated as Set 29601, have also been derived by regional flux-weighted collapse using 29-group solutions. These are largely employed in two-dimensional analysis. The energy structure is given in Table III-39-III.

III. ZPR-3 Assembly 51

ZPR-3 Assembly 51 was a cylindrical core of radius ~33.5 cm and height 86.5 cm. The average regional atomic densities used in these calculations are listed in Table III-39-IV. The experimental compositions[7] differed slightly from these values. Axial re-

TABLE III-39-I. Cross Section Source

Material	Library[a]
Pu-239	ENDF/B
Pu-240	ENDF/B
Pu-241	ENDF/B
U-238	ENDF/B
U-235	ENDF/B
O	MC^2
C	MC^2
Fe	MC^2
Cr	MC^2
Ni	MC^2
Na	ENDF/B
B-10	ENDF/B

[a] Preliminary ENDF/B data (1967) was used; Status I data were not available at the time the cross sections were calculated.

TABLE III-39-II. Multigroup Cross Section Energy Structure

Group	Energy Lower Limit	Lethargy Lower Limit
1	3.68 MeV	1.0
2	2.23	1.5
3	1.35	2.0
4	0.821	2.5
5	0.498	3.0
6	0.302	3.5
7	0.183	4.0
8	0.11	4.5
9	67.4 keV	5.0
10	41.0	5.5
11	24.8	6.0
12	15.0	6.5
13	9.12	7.0
14	4.31	7.75
15	2.61	8.25
16	2.03	8.5
17	1.23	9.0
18	0.961	9.25
19	0.583	9.75
20	0.275	10.5
21	0.101	11.5
22	29.0 ev	12.75
23	17.6	13.25
24	6.48	14.25
25	3.93	14.75
26	1.44	15.75
27	0.876	16.25
28	0.532	16.75
29	thermal group	

flectors were 30.48 cm thick. The inner and outer radial reflectors, which also surround the axial reflector regions, were 17.8 cm and 15.5 cm thick, respectively.

Criticality Studies

Criticality studies were made not only for comparison with experimental results but to determine the sensitivity of the calculated criticality to methods of calculation and to the plutonium alpha value in the region of alpha uncertainty. Both 29-group and 6-group one-dimensional diffusion theory calculations using the MACH 1 program[11] were made. Axial buckling values of 0.000717 and 0.000711 cm^{-2}, respectively, derived from axial reflector savings obtained by auxiliary slab-geometry calculations, were used. These resulted in calculated critical mass (Pu-239 + Pu-241 + U-235) values of 209.5 and 211.0 kg, respectively, compared with the experimental value[12] of 212.08 kg. The calculated values include approximately the thin slab heterogeneity correction effects upon resonance self-shielding through the heterogeneous MC^2 generation of cross sections. However, these calculations do not include the reactivity effects of spatial flux variations across the drawer-cells due to heterogeneities.

To determine two-dimensional effects directly and to determine transport effects, the 6-group cross section set was utilized for a study to compare calculated $k_{effective}$ values derived from the one-dimensional cylindrical geometry diffusion theory with two-dimensional *RZ*-geometry diffusion and transport solutions. In two-dimensional calculations the 2D CANDID[13] diffusion program and the discrete-ordinate transport program SNARG-2D[14] were used.

TABLE III-39-III. Description of Energy Structure for Set 29601

Group	Lower Energy Limit
1	1.35 MeV
2	183. keV
3	24.8 keV
4	4.31 keV
5	275. eV
6	10^{-5} eV

TABLE III-39-IV. Average Regional Composition of ZPR-3 Assembly 51, atoms/b-cm

Material	Core	Axial Reflector	Radial Reflector I	Radial Reflector II
Pu-239	0.001731			
Pu-240	0.0001706			
U-235	0.0000150			
U-238	0.007018			
C	0.003113			
O	0.01279			
Fe	0.0162594	0.01076	0.007925	0.07547
Cr	0.003657	0.00259	0.001870	0.00115
Ni	0.001600	0.02893	0.05640	0.00049
Na	0.0043113	0.01037	0.00416	

Two-dimensional diffusion theory resulted in a reactivity increase of $+0.008\ \Delta k/k$, and two-dimensional S_4 (and S_6) calculations resulted in an increase of $+0.018\ \Delta k/k$ relative to one-dimensional cylindrical geometry diffusion theory. Since the previous one-dimensional 6-group and 29-group values of critical mass were similar, the latter 6-group two-dimensional *RZ* results indicate that a corresponding 29-group calculation should also be over-reactive by about the same amount.

Relative Reactivity Variations with S_N for ZPR-3 Assembly 51 Type Systems in Different Geometries

To determine the S_n approximation required for studying slab, cylinder, sphere, and finite cylinder reactivity aspects of Assembly 51 type systems, one-dimensional slab, cylinder, and sphere calculations in six energy groups using the one-dimensional discrete-ordinate transport code, SNARG-1D,[15] were made with S_2, S_4, and S_6 approximations. The cores had the composition of Assembly 51. The slab case had the axial reflector of Assembly 51 and the cylindrical case had the radial reflector composition of Assembly 51. The spherical cases were carried out successively with the radial reflector composition and thickness and axial reflector composition and thickness, respectively. Diffusion theory and S_2, S_4, and S_6 analyses using the *RZ* geometry of the two-dimensional diffusion theory program, CANDID-2D, and the transport theory program, SNARG-2D, were also made. The comparisons are shown in Table III-39-V.

Results show that the slab geometry aspects of the axial-direction would be adequately calculated by either diffusion theory or S_2 (which are essentially equivalent) in slab geometry. The cylindrical geometry aspects of the radial-direction requires S_4. The two-dimensional spherical results and also the two-dimensional cylinder results indicate that S_4 is needed. The simulative spherical cases show that the correction from S_2 to S_4 is about $-1.0\%\ \Delta k/k$ whereas the cylinder correction by 2-dimensional calculation is about $-0.7\%\ \Delta k/k$. Thus, if the k_{eff} ratio of S_4 to S_2 from simulative spherical geometry calculations are employed to correct a two-dimensional S_2 finite cylinder result to S_4 the correction will be of the order of 40% in error.

Effect of Pu-239 Alpha-Values upon Reactivity of ZPR-3 Assembly 51

Recent concern about the value of alpha of Plutonium-239 led to a calculational estimate on the reactivity effect upon Assembly 51 of increased alpha-values in the energy range 0.1 to about 25 keV. The increased alpha-values for the multigroup cross-section groups in this range were roughly based upon the provisional data reported by M. Schomberg, M. Sowerby and F. Evans.[16] The increased alpha-values were assumed to affect the group cross sections through increase in the group capture cross sections for Pu-239. The ratios of the group alpha-values based on the Schomberg data to those of cross-section Set 29001 are compared in Table III-39-VI. The calculations resulted in a reactivity decrease of about -3.4% upon use of the capture cross sections corresponding to the larger alpha values.

TABLE III-39-V. Comparative Variations of k for ZPR-3 Assembly 51 with S_N Approximations in Various Geometries

k_{eff} Ratios	2-Dim. Calc.	1-Dimensional Calculations			
		Sphere		Cylinder	Slab
	Cyl.	Rad. Refl.	Axial Refl.	Rad. Refl.	Axial Refl.
$k(DT)/k(S_6)$	0.991	0.990	0.987	0.993	0.999
$k(S_2)/k(S_6)$	1.007	1.010	1.013	1.006	0.999
$k(S_4)/k(S_6)$	1.000	1.001	1.001	1.001	1.000

TABLE III-39-VI. Ratios of Plutonium α-Values

Group J	E_J^{min}, keV	$\alpha_J^{SSE}/\alpha_J^{29001\,(a)}$	Group J	E_J^{min}, keV	$\alpha_J^{SSE}/\alpha_J^{29001}$
12	15.03[b]	1.85	17	1.23	1.89
13	9.11	2.24	18	0.96	1.66
14	4.31	2.27	19	0.58	2.82
15	2.61	2.12	20	0.28	1.93
16	2.03	2.06	21	0.10	2.11

[a] α_J^{SSE}: group-value of α roughly based upon provisional $\alpha(E)$ data of Ref. 16.

α_J^{29001}: group-value of α corresponding to group capture and fission cross sections in Set 29001.

[b] E_{12} upper energy is 24.8 keV.

Spatial-Variations of Pu-239 and U-238 Fission Detector Responses

The spatial variations of Pu-239 and U-238 fission detector responses for ZPR-3 Assembly 51 have been calculated. The analysis used the 6-energy-group cross section set in two-dimensional *RZ* diffusion theory. The 6-group detector cross sections used in the core region were obtained from the 29-group core-flux averaging. In the reflector region corresponding reflector-averaged detector values were used.

The calculated results are compared with the experimental values[17] (Figs. III-39-1 and III-39-2) obtained by the ZPR-3 experimental group.

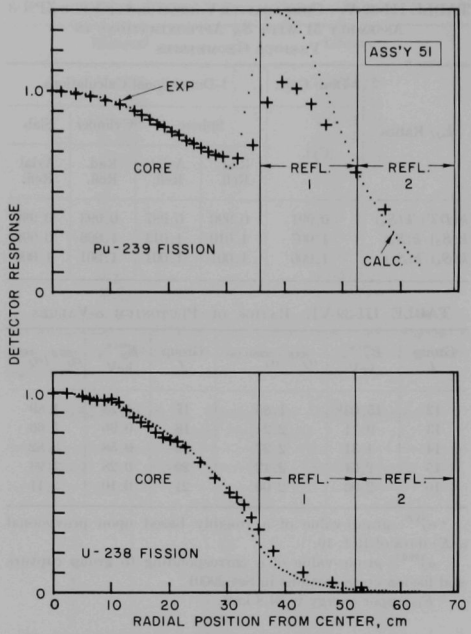

FIG. III-39-1. Calculated Radial Detector-responses Compared with Experiment. *ANL Neg. No. 113-1292.*

Spatially-Dependent Fine-Energy Neutron Spectra

Spatially-dependent fine-energy-detailed neutron flux spectra in the core and reflector regions have been calculated. The calculational results are described and compared with the experimental[18, 19] results in Paper III-20.

Safety Rod Worths

Calculations of the worths of the spiked safety rods used in Assembly 51 and of the initially unspiked safety rod have been made for a 10-in. removal position. Composition of the drawers, detailed geometrical configuration of the system, and the experimental values are reported in Ref. 2. The fissile and fertile atomic densities N in the spiked safety drawers are

$$N^{\text{Pu-239+241}} = 0.002990,\ N^{\text{Pu-240}} = 0.000329, \text{ and}$$

$$N^{\text{U-238}} = 0.014635.$$

The six-group cross section set was used in the two-dimensional, RZ geometry, discrete-ordinate transport code SNARG-2D in the S_2 approximation. Results are given in Table III-39-VII. The sensitivity of the calculated values to the composition surrounding the rod was estimated for the spike-rod case. Results of calculations using these neighboring-drawer composition values are also given in Table III-39-VII for comparison with the values obtained by use of overall-core-average composition surrounding the rod.

Distributed Sodium Worth

The reactivity change due to removal from Assembly 51 of approximately ten percent of the sodium throughout the core has been calculated using the two-dimensional SNARG transport code in S_2 approximation. The six-group cross section set was used.

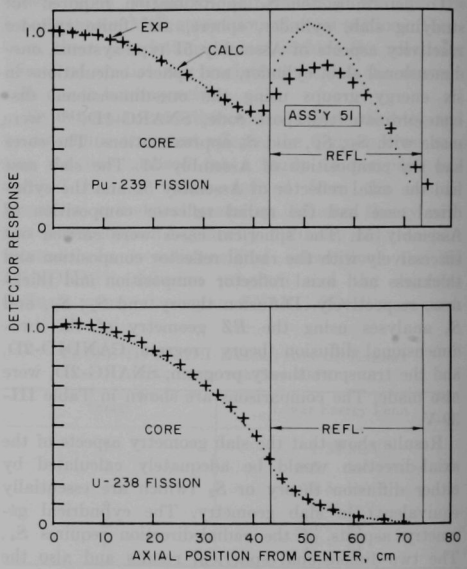

FIG. III-39-2. Calculated Axial Detector-responses Compared with Experiment. *ANL Neg. No. 113-1293.*

TABLE III-39-VII. CALCULATED % $\Delta k/k$ FOR 10 in. REMOVAL OF A SAFETY ROD FOR ZPR-3 ASSEMBLY 51

Safety Rod Type	Calculated % $\Delta k/k$		Experimental % $\Delta k/k$[a]
	Composition Surrounding the Rod		
	Overall Core Average	Neighboring Drawers	
Unspiked	−0.13		−0.115
Spiked	−0.26	−0.27	−0.238

[a] Estimated from data given in Ref. 2.

The quantity of sodium removed was 11.54 kg which is also the total quantity removed in the 112 A-type drawer experiment[20] which resulted in −201.6 Ih. The calculation gave −182 Ih using a conversion factor of 1036 Ih per percent $\Delta k/k$.

Substitution of Sodium Cans for Axially-Central Core Materials

The reactivity change due to substitution of sodium contained in stainless steel plate-shaped cans in place of the core material of the two axially central drawers and associated axial reflector materials was calculated. The MACH 1 diffusion theory code and the 29-group cross section set were used in the analysis. The calculated value was −789 Ih compared with the experimental value[20] of −763.08 Ih.

Estimate of Effect of Spontaneous Plutonium Fission Upon Subcritical Measurements

Previously reported studies[6] of the subcritical measurement of k_{eff} were concerned with the dependence of the inverse of multiplication on k_{eff} when poison was added to produce the subcriticality. When the subcriticality is caused by the removal of part of the plutonium fuel, the plutonium spontaneous fission source is also removed. Then the change in multiplication must be corrected for the change in the value of the source.

The size of this correction was investigated by comparing two computations for Assembly 51, using the MACH-1 code. In both computations a subcritical $\Delta k = -0.0072$ was produced by substituting canned sodium for core material throughout a central axial region representing the 2 × 2 in. cross section of the P-16 central drawers. In this comparison the subcritical multiplication was taken to be proportional to the computed B-10 reaction rate at the outer edge of the radial reflector. First, with the spontaneous fission source strength used in the MACH 1 calculation, the B-10 reaction rate was 4950, with the source still present in the sodium in the central drawers. In the second computation the spontaneous fission source was removed from the sodium to give a reaction rate of 4890. The corresponding multiplication is analogous to that which was experimentally measured. In this case a correction factor of about 1.012 must be applied to the Δk obtained from the second multiplication to obtain the desired Δk of −0.0072 which corresponds to the first multiplication.

Estimated Doppler Coefficient

The core drawer cells of ZPR-3 Assembly 51 contained three types[21] of fuel pieces; plutonium metal, designated type 1; ZPPR, type 2; and SEFOR, type 3. In the computation of the Doppler coefficient it was assumed that the heat produced by fissions in each type of fuel does not flow out of the fuel piece. Because the three types of fuel heat up at three different rates, a reference temperature rise was needed, and the Doppler coefficient, dk/dT_1, was computed per degree rise of plutonium metal fuel. Concomitantly, dT_2/dT_1 and dT_3/dT_1 had to be evaluated. It was also assumed that the temperature rise of each type of fuel is not a function of position in the reactor. Thus the coefficient is based on a spatial "average" temperature rise.

The reactivity effect of a temperature change was evaluated for each type of fuel separately by computing k_{eff} with the MACH 1 code, using the 29-group cross section set, when the temperature of each type of fuel was separately increased to 1000°K while other materials and other fuel types were held at 300°K.

The overall Doppler coefficient was found from

$$\frac{dk}{dT_1} = \left(\frac{dk}{dT}\right)_1 + \left(\frac{dk}{dT}\right)_2 \left(\frac{dT_2}{dT_1}\right) + \left(\frac{dk}{dT}\right)_3 \left(\frac{dT_3}{dT_1}\right)$$

to be $dk/dT_1 = -4.33 \times 10^{-6}/°\text{K}$ rise in the plutonium metal temperature. The Doppler effect was assumed to have a $1/T$ dependence.

IV. ZPR-3 Assemblies 52a Through 52f

The originally planned critical assembly program to follow Assembly 51 was to have consisted of a series of experiments carried out in an axially-split version of the ZPR-3 Assembly 51. Since annular cores with central test zones were subsequently also being considered by PNL, the critical experiments which followed those performed on ZPR-3 Assembly 51 consisted instead of a limited number of experiments upon a series of cores representative of both of these geometries. Basically, the experiments were intended to provide data for experiment-theory correlation for test-zone flux to core power ratios. The following is a description of the ZPR-3 Assembly 52 series of critical assemblies:

52a: Same as Assembly 51 except that the total nominal 30 cm thick radial reflector is nickel-containing, that the depleted drawers next to the spiked safety rods are normal drawers, and that the control rods are repositioned so as not to fall into the gap-position in subsequent assemblies of this series.

52b: Same as Assembly 52a except that is has a 3 x 3 sodium column region located along the central axis throughout the entire assembly.

52c: Same as Assembly 52b except that it has a 5 x 5 sodium column with the corners of core material

TABLE III-39-VIII. CALCULATED ESTIMATES OF CRITICAL MASSES AND OF FLUX LEVELS IN THE SODIUM REGIONS OF THE ZPR-3 ASSEMBLY 52 SERIES

ZPR-3 Assembly No.	Estimated Critical Mass (Pu-239 + Pu-241 + U-235), kg		Estimated Neutron Flux at Center per Unit Source in the System
	With Assembly 51 Safety Rods	With Additional Safety Rod Spiking	
52a	206 (200.7)[a]		5.1×10^{-4}
	210[b]		5.1×10^{-4}[(b)]
52b	250 (235.8)[a]		3.7×10^{-4}
52c	298 (280.0)[a]	287	3.0×10^{-4}
52e	348[c]	338 (282.0)[a]	2.7×10^{-4}
52f	347	338 (309.2)[a]	2.4×10^{-4}

[a] Experimental values in parentheses from Refs. 3, 4, and 5.
[b] 33 cm thick radial reflector. Others have been calculated with 30 cm thick radial reflectors.
[c] Assuming a circular periphery for core-drivers plus test zone.

retained; i.e., a 5 x 5 column minus the 4 corner columns.

52d: Same as Assembly 52a except that it has a 3 x 11 drawer rectangular sodium gap located axially throughout the entire assembly. The core contains additional safety spiking to insure sufficient rod worths.

52e: Same as Assembly 52d except that the rectangular sodium gap is now 3 x 15 drawers; i.e., up to the radial reflector.

52f: Same as Assembly 52c except that it has a 7 x 7 drawer sodium region having the 3 corner drawer-columns at each of the four corners of the sodium region retained as core columns. The core contains additional safety rod spiking (as in 52d and 52e).

Detailed descriptions of the experimental arrangements may be found in Refs. 3, 4, and 5.

Criticality and Flux Level Studies

Scoping studies of the critical masses for Assemblies 52a, b, c, and f were calculated by means of the one-dimensional MACH 1 diffusion code in cylindrical geometry using the 29 energy group cross-section set. The test regions were 80 v/o sodium and 20 v/o steel. The axial buckling previously used for Assembly 51 was employed. The results, normalized to the Assembly 51 experimental critical mass of 212.08 kg of Pu-239 + 241 and U-235 are given in Table III-39-VIII. Effects on critical mass caused by additional spiking of safety rods are also listed for Assemblies 52c, e, and f. The critical mass of Assembly 52e was obtained by the SNARG code in the S_2 approximation, using XY geometry with the six energy group cross-section set. It too was normalized to the experimental critical mass of Assembly 51. The reported experimental values[3-5] are given in parentheses. The additional safety-rod spiking corresponds to 2.15 kg of fissile material per rod instead of the normal spiking of 1.59 kg per rod. There are eight rods, four in each half of the assemblies.

The neutron flux at the center of each assembly per unit neutron source in the assembly also appears in Table III-39-VIII. For Assemblies 52a, b, c, and f the flux was obtained by the SNARG code in the S_2 approximation, using RZ geometry and six neutron energy groups. For Assembly 52e, the flux was based upon a SNARG XY computation and normalized to one neutron produced in the assembly.

The analogous flux levels per unit fission can be estimated by multiplying the per unit source values by 2.9.

Deviations of critical masses from experiment with the large central sodium regions are largely due to the use of the identical axial buckling for all the cores in this series. For the sodium-gap case, Assembly 52e, it has not been determined to what extent the use of the constant axial buckling is responsible for the deviation.

Estimates of the Safety Rod Worths for the ZPR-3 Assembly 52 Series of Annular Cores

Estimates of the safety rod worths for Assemblies 52a, b, c, and f were calculated by means of the one-dimensional MACH 1 diffusion code in cylindrical geometry using the 29 energy group cross-section set. Initially, rod spiking, rod locations, and average core compositions were assumed to be the same as in Assembly 51, except where otherwise indicated. Simulation of rod regions was effected by homogenization into an annular ring. The axial buckling previously used for Assembly 51 was employed. The

TABLE III-39-IX. CALCULATED ESTIMATES OF WORTHS OF EIGHT SAFETY RODS WITHDRAWN 9.5 in. FOR THE ANNULAR CORES OF THE ZPR-3 ASSEMBLY 52 SERIES

ZPR-3 Assembly No.	Worth of Eight Safety Rods, % $\Delta k/k$	
	With Assembly 51 Safety Rod Spiking	With Additional Safety Rod Spiking
51 & 52a	−1.8 (−1.85)[a]	
52b	−1.6 (−1.72)[a]	
52c	−1.4 (−1.37)[a]	−2.0
52f	−1.1	−1.6 (−1.72)[a]
52f (rods relocated)	−1.1	

[a] Experimental values from Ref. 5 using 1036 Ih per percent $\Delta k/k$.

results, normalized to eight times the Assembly 51 experimental worth of one safety rod withdrawn 9.5 in. (Ref. 5) are given in Table III-39-IX. For the purpose of these estimates the Assembly 52a rod worths were assumed to be the same as those for Assembly 51.

Calculations indicated that the larger cylindrical test zone cases required additional spiking to insure a reactivity of at least $-1.5\%\ \Delta k/k$. A calculation of the 52f core, which has the largest cylindrical test zone, was also made for safety rods positioned one drawer farther out radially so as not to abut the test zone. The worth did not change substantially. Other calculations using the additional safety rod spiking employed in Assembly 52d were also made to estimate safety rod worths for the 52f core. The fissile and fertile atomic densities in the rod drawer, corresponding to this additional spiking, were:

$$N^{\text{Pu-239+241}} = 0.004061,$$

$$N^{\text{Pu-240+242}} = 0.000380, N^{\text{U-238}} = 0.014635.$$

Approximate Method for Calculation of Axially-Split Cores

A possible method of approximating solutions for axially-split cylindrical cores has been studied. For a cylindrical reactor with an axial-gap and having non-uniform axial composition it would be convenient if the two calculational directions of a two-dimensional code could be utilized for the radial direction perpendicular to the split and for the axial direction. An approximation to account for the leakages in the radial direction parallel to the gap is made by substituting an approximate buckling in that direction; this is a function of the perpendicular distance from the gap and from the center of the axial position. The method is described in Paper VI-12.

References

1. E. R. Astley, *The Conceptual Evaluation of a Fast Flux Test Facility*, Proc. Fast Reactors National Topical Meeting, San Francisco, April 10–12, 1967, ANS-101 Supplement; see also BNWL-SA-978; see also Conf. 670413, USAEC.
2. Reactor Development Program Progress Report, ANL-7419 (1968), pp. 10–14.
3. Reactor Development Program Progress Report, ANL-7460 (1968), pp. 15–22.
4. Reactor Development Program Progress Report, ANL-7478 (1968), pp. 9–15.
5. Reactor Development Program Progress Report, ANL-7487 (1968), pp. 13–26.
6. P. J. Persiani, J. K. Long, A. J. Ulrich and D. A. Kucera, *Development of the Critical Experiment Program for the Fast Fuels Test Facility*, Reactor Physics Division Annual Report, July 1, 1966 to June 30, 1967, ANL-7310, pp. 232–238.
7. A. J. Ulrich, P. J. Persiani and J. C. Beitel, *Theoretical Study of the ZPR-3 Critical Experiments in Support of the Fast Fuels Test Reactor Concept*, Reactor Physics Division Annual Report, July 1, 1966 to June 30, 1967, ANL-7310, pp. 238–241.
8. J. K. Long, A. L. Hess, R. L. McVean, P. J. Persiani, A. J. Ulrich (ANL), Q. L. Baird, R. A. Bennett and S. L. Engstrom (BNW), *FFTF Critical Experiments-Control Rod Studies on ZPR-3*, Trans. Am. Nucl. Soc. **10**, 269 (1967).
9. B. J. Toppel, A. L. Rago and D. M. O'Shea, *MC²—A Code to Calculate Multigroup Cross Sections*, ANL-7318 (1967).
10. B. J. Toppel and I. Baksys, *The Argonne-Revised THERMOS Code*, ANL-7023 (1965).
11. D. A. Meneley, L. C. Kvitek and D. M. O'Shea, *MACH 1, A One-Dimensional Diffusion-Theory Package*, ANL-7223 (1966).
12. Reactor Development Program Progress Report, ANL-7445, 11–15 (1968).
13. G. K. Leaf, A. S. Kennedy and G. C. Jensen, *ANL-CANDID, A Two-Dimensional, Diffusion-Theory Code Based on CANDID 2D*, ANL-7305 (1967).
14. G. J. Duffy, H. Greenspan, S. D. Sparck, J. V. Zapatka and M. K. Butler, *SNARG-2D, A Two-Dimensional, Discrete-Ordinate, Transport Theory Program for the CDC-3600*, ANL-7426 (1968).
15. G. J. Duffy, H. Greenspan, S. D. Sparck, J. V. Zapatka and M. K. Butler, *SNARG-1D, A One-Dimensional, Discrete-Ordinate, Transport Theory Program for the CDC-3600*, ANL-7221 (1966).
16. M. G. Schomberg, M. G. Sowerby and F. W. Evans, *A New Method of Measuring Alpha (E) for Pu^{239}*, Symposium on the Physics and Safety Problems of Fast Reactors, Karlsruhe, German Federal Republic, 1967, Paper SM-101/41.
17. Reactor Development Program Progress Report, ANL-7457 (1968), pp. 20–27.
18. J. E. Powell, *Fast-Neutron Spectrum Measurements in the Core and Reflector of ZPR-3 Assembly 51*, Trans. Am. Nucl. Soc. **11**, 217 (1968).
19. J. E. Powell, Argonne National Laboratory (private communication).
20. Reactor Development Program Progress Report, ANL-7438 (1968), pp. 12–16.
21. Reactor Development Program Progress Report, ANL-7391 (1967), pp. 37–41.

Section IV

Fast Reactor Safety

Analysis of the course of accidents in fast power breeder reactor cores requires a broad range of reactor physics information. It is necessary to know damage and failure thresholds of the fuel; the types of fuel and coolant motion that can result, including acceleration and rate data; reactivity changes brought about by the motions, temperature changes, changes in neutron flux distributions throughout the core, etc.; and, finally, data sufficient to analyze the accident under study to its termination. Such matters are discussed in the papers of this section and, furthermore, the devices and means for acquiring and processing this kind of information are also treated.

IV-1. High Power Level Transient Reactor Test (TREAT) Facility Sodium Loop Meltdown Experiment on an Unbonded EBR-II Mark I Fuel Pin[1,2]

C. E. Dickerman, F. L. Willis, R. R. Smith,* P. B. Henault,* R. Purviance, J. F. Boland,* A. Devolpi and R. A. Noland†

The fact that more than 30,000 Experimental Breeder Reactor II (EBR-II) metallic driver fuel pins have been irradiated in the EBR-II core without a single identifiable or proven failure has demonstrated the conservatism of fuel design and reactor operation limits and the reliability of fuel fabrication and inspection. However, this experience does not relieve safety evaluations from the need to consider the possible consequences of a defective driver fuel pin being loaded into the core. Accordingly, sodium loop experiments are being performed in TREAT specifically to provide guidance for analyses of the behavior of a pin which either has no sodium thermal bond between fuel and cladding or which loses the bond upon reactor startup due to some unspecified defect. Two such experiments have been performed, ID-RP-1 and ID-RP-2, respectively. (A preliminary account of ID-RP-1 has been made.[3])

Each experimental sample consisted of a 6% enriched EBR-II fuel pin surrounded by a ring of six dummy pins on an EBR-II lattice pitch. Each fuel pin contained one atm of argon at room temperature, with no sodium bond, thus providing a limiting case simulation of complete expulsion of bond sodium. The samples were contained in a standard TREAT Mark I integral sodium loop.[4,5] Because the effective flow area per gram of fuel is approximately twice that in a true cluster, the flow rate was set at 4 m/sec through the test section.

ID-RP-1 was planned to correspond, with a modest degree of conservatism, to normal EBR-II operation. ID-RP-2 was deliberately run to appreciably more severe levels of coolant inlet temperature and fuel alloy power level. Experimental coolant temperature rises were not severe, but the coolant temperature levels were comparable to or in excess of reactor temperatures.

A summary of experimental conditions is given in Table IV-1-I. For comparison, the table includes ID-RP-1 conditions and EBR-II operating parameters for the central (i.e., highest power position) pin under Run 27A conditions. Each sample was subjected to a "flattop" TREAT transient[6] in which reactor power is sustained, after reaching the temperature limit corresponding to the initial reactivity insertion, by a pre-programmed withdrawal of a control rod. "Flattop duration" given in the table is the interval between the time of the temperature-limited peak to the reactor scram. In the case of TREAT, "reactor power" is the time-averaged power over this duration. The pin average power is the axial average, whether in TREAT or in EBR-II, per cc of fuel using ambient 17.5 grams/cc density. Two inlet coolant temperatures are given for each experiment, since the loops are package loops with no heat exchange capability.

No anomalies were found on the transient instrument record, which included inlet flow, inlet pressure, inlet coolant temperature, and outlet coolant temperature.

Post-experiment neutron radiographs and neutron hodoscope scans indicated that the pin was intact after ID-RP-2 but that some fuel slumping had occurred.

Post-transient examinations showed that the fuel had melted down but had been safely quenched in place by the sodium-cooled cladding. No indications of failure propagation or incipient propagation were found. Both pins survived exposure without a cladding failure. Figure IV-1-1 is a post-transient neutron radiograph of the ID-RP-2 pin *in situ* in its loop, showing the fuel slumped inside the cladding, with internal voids.

TABLE IV-1-I. Experimental Conditions

Parameter	ID-RP-1	ID-RP-2	Central Pin EBR-II, Run 27A
Flattop duration, sec	6.9	6.2	—
Power			
Reactor average, MW	57	90	45
Pin, W/cc	3100	4900	2680
Coolant			
Inlet initial temp., °C	390	435	374
Inlet final temp., °C	430	511	—
Temperature rise, °C	100[a]	116[a]	123

[a] Maximum.

* Idaho Division, Argonne National Laboratory.
† Metallurgy Division, Argonne National Laboratory.

a STEPPED TANTALUM RINGS FOR AXIAL SHAPING OF SAMPLE NEUTRON FLUX

b TOP END PLUG FUEL MOTION RESTRAINER

c POST-TRANSIENT LOCATION OF TOP OF FUEL

d POST-TRANSIENT LOCATION OF FUEL VOID

e LOOP WALL

f FUEL SAMPLE

g DUMMY PINS IN RING SURROUNDING SAMPLE

h FLANGE FOR INLET PRESSURE TRANSDUCER

i WIRE PIN HOLDING BOTTOM END PLUG SPADE EXTENSION OF THE PINS

j "SPADE" EXTENSION OF BOTTOM END PLUG OF PINS

k TYPICAL TEST SECTION ELECTRICAL PRE-HEATER WIRE

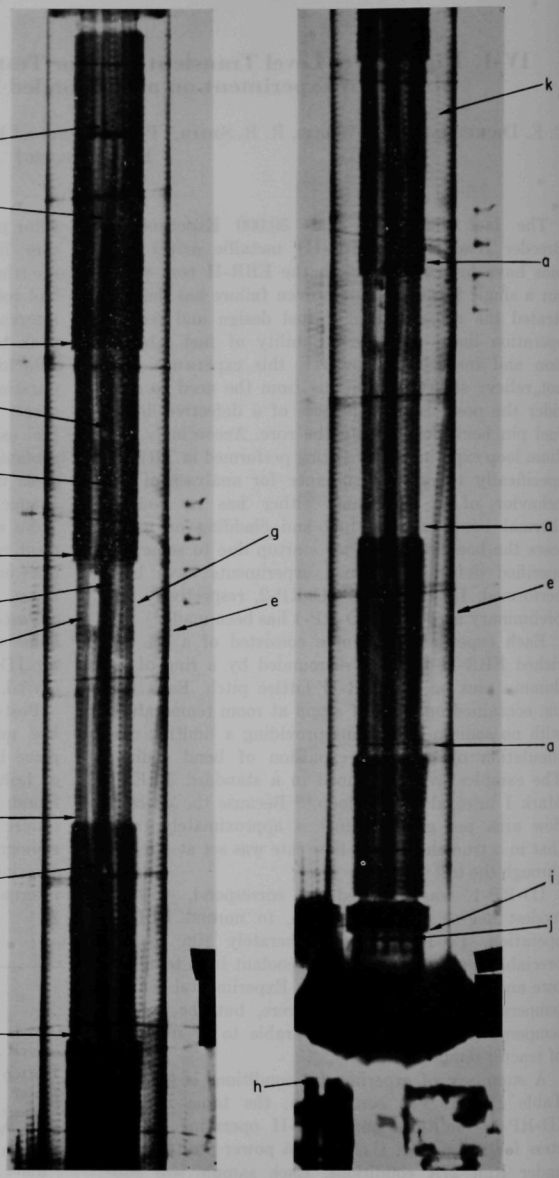

FIG. IV-1-1. Post-Transient Neutron Radiograph of the ID-RP-2 Pin. *ANL Neg. No. 113-598 Rev. 1.*

Metallographic examination of fuel from the relatively low power ID-RP-1 experiment disclosed a fine-grained (about 25 microns) matrix characteristic of molten alloy rapidly cooled through the solidification range. Shrinkage voids and irregular surfaces gave additional evidence of fuel melting and rapid solidification.

Calculations utilized an idealized model of meltdown in which fuel slumping against the cladding was assumed to occur abruptly and instantaneously along the length of the pin when the fuel surface at the axial midplane reached 1050°C. Transient heat transfer calculations[7] indicated that the fuel-cladding interface cooled too rapidly after contact to permit significant penetration of the cladding by eutectic formation, even for the high penetration rate of approximately 0.025 cm/sec, typical of attack by molten fuel.[8,9] Because the specific early stages of the hypothetical loss-of-bond incident are not well defined, they were replaced by an assumed case of complete gas bonding.

To provide additional information relevant to the mechanisms and consequences of bond-loss failures, flat-topped transient experiments are being considered for the following driver fuel failure simulations: a gas-bonded element which has been "soaked" under 800°F sodium, gas-bonded element which has been irradiated to 1.2 a/o (maximum) burnup, and an element which is partially sodium bonded.

References

1. F. L. Willis, C. E. Dickerman, P. Henault, R. Purviance, J. F. Boland and R. Noland, *TREAT Experimental Study of Survival of EBR-II Pin in a Loss-of-Bond Incident*, Trans. Am. Nucl. Soc. **11**, (November 1968).
2. C. E. Dickerman, R. R. Smith, F. L. Willis, A. B. Cohen and J. Regis, *Analysis of Transient Behavior of Unbonded EBR-II Fuel Pin Incident*, Trans. Am. Nucl. Soc. **11**, (November 1968).
3. C. E. Dickerman, F. L. Willis, R. R. Smith and A. B. Cohen, *Fast Reactor Safety Integral Loop Experiment on an Argon-Bonded EBR-II Pin*, Reactor Physics Division Annual Report, July 1, 1966 to June 30, 1967, ANL-7310, pp. 258–260.
4. E. S. Sowa and J. C. Heap, *The Development of a Small Integral Loop for In-Pile Fuel Failure Studies in the Presence of Flowing Sodium*, Trans. Am. Nucl. Soc. **8**, 559 (1965).
5. L. E. Robinson, R. T. Purviance and F. L. Willis, *Modification of the TREAT Integral Sodium Loops*, Reactor Physics Division Annual Report, July 1, 1964 to June 30, 1965, ANL-7110, pp. 268–274.
6. C. E. Dickerman, R. D. Johnson and J. Gasidlo, *Kinetics of TREAT Used as a Test Reactor*, ANL-6458 (1962).
7. J. Heestand, D. F. Schoeberle and L. B. Miller, *A Method of Calculating Transient Temperatures in a Multiregion, Axisymmetric Cylindrical Configuration, The ARGUS Program, 1089/RE 248, written in Fortran II*, ANL-6654 (1963).
8. C. M. Walter and L. R. Kelman, *Penetration Rate Studies of Stainless Steel by Molten Uranium and Uranium-Fissium Alloy*, J. Nucl. Mat. **6**, 281 (1962).
9. C. M. Walter and C. E. Dickerman, *TREAT Study of the Penetration of Molten Uranium and U-5 w/o fs Alloy Through Type 304 Stainless Steel*, Nucl. Sci. Eng. **18**, 518 (1964).

IV-2. Experiments on "High-Swelling" Fuel of Experimental Breeder Reactor-II (EBR-II) Mark-IA Type

A. B. Rothman, C. J. Renken*, R. R. Stewart, N. R. Tucker and C. E. Dickerman

Introduction

The initial application of EBR-II was to test the feasibility of a high performance central fast breeder power plant with a fast and economical fuel processing system.[1] Since that time the facility has served also to achieve high burnup in fast reactor fuels as a part of the Atomic Energy Commission's program for the development of power reactors. It is therefore of interest to run the EBR-II for extensive periods of time. However, due to its unique role in the Liquid Metal Fast Breeder Reactor Program, the safety of EBR-II must not be compromised in achieving high burnup.

Extensive analysis was employed initially to provide for the safe operation of EBR-II.[(1)] These early considerations have been updated by supporting experimental and operational data.[2] Two major categories of nuclear events may be considered, namely: (1) reactivity insertions or loss of coolant flow resulting from operational abnormalities, or (2) propagative failures resulting from loss of integrity of one fuel element or subassembly which might affect its neighbors and ultimately the prompt multiplication of the entire reactor system.

The EBR-II hazards studies[1,2] have considered the operational abnormalities in detail. With given modes of initiation, fuel element behavior and the degree of credibility and severity of such accidents have been

* Metallurgy Division, Argonne National Laboratory.

considered. The complete spectrum of fuel element failure propagation studies, however, is quite complex and outside the scope of the EBR-II hazards studies. Information on failure thresholds together with further studies on movement in failed or failing fuel elements is needed to assess the degree of credibility and severity of accidents resulting from the propagation of fuel element failure.

It was found from TREAT experiments[2,3] that a gross malfunction would be necessary in order to attain temperatures serious enough to cause damage to EBR-II fuel elements. However, reactivity insertions resulting from loss of integrity become a more serious consideration for EBR-II elements which have been fabricated from the so-called "high-swelling" fuel, i.e., fuel containing impurities responsible for high radiation-induced swelling. Extensive swelling from radiation exposure of these elements would be expected to cause failure for less severe operational malfunctions. For this reason an experimental program has been initiated to study the dimensional stability, failure thresholds and the internal movements of "high-swelling" EBR-II Mark IA driver fuel elements which have been irradiated to high burnup in EBR-II.

Experimental Program

The TREAT experiments on EBR-II Mark IA elements will have a twofold purpose. Dry transparent studies will be performed in TREAT to determine failure thresholds and dimensional changes of both "high-swelling" and "low-swelling" elements which have been pre-irradiated to the design limit of 1.2 a/o maximum burnup. An attempt will be made to instrument axial fuel motion as supplementary information in the understanding of fuel element integrity. Loop experiments will be carried out also in order to determine possible internal fuel movements and the integrity of the pin under mild accident conditions. For this purpose, single EBR-II Mark-IA pins, pre-irradiated to 1.2 a/o maximum burnup, will be tested in TREAT within a ring of six hollow dummy pins on an EBR-II pitch.

The peak temperatures for the series of tests which have been planned for the dry transparent series bracket the temperature range from the nominal operating temperature of EBR-II fuel to temperatures at the upper limit of fuel integrity. If necessary the pre-irradiated "high-swelling" fuel will be carried to a temperature required to cause failure in previous tests on fuel pre-irradiated in the MTR.[(3)] The upper limits of fuel temperature and temperature-rise rates for the dry transparent series are considerably greater than those which would be expected for operational abnormalities in EBR-II. Such latitude is needed, however, in order to study failure thresholds as well as such relevant phenomena as fuel slumping and cladding penetration by molten uranium.

Failure may be attained with sufficient time at temperature for more modest temperatures reasonably in excess of the operating fuel temperature in EBR-II. Such failure tests will be carried out in the loop experiments, which are more clearly a mock-up of failure and failure propagation in EBR-II. It is the intent that information from the dry transparent series of tests be used with or as a guide to the loop tests, as an aid to understanding the propagation of fuel element failure.

Dry Transparent Studies

Experiments for this series will be performed in the transparent photographic meltdown facility used for previous studies.[4] Briefly, the assembly consists of a fuel pin mounted inside a capsule contained in an atmosphere of flowing helium within a TREAT slot liner suitable for high-speed color photography. The sample load frame, test capsule, and slot liner have been modified to accomodate instrumentation and control leads to the sample. In order to eliminate severe power gradients in the 52% enriched 95% U-5% Fs Mark-IA pin, the capsule will be lined with a 5 mil cadmium foil sandwiched between layers of fiberglass cloth as in past TREAT studies of enriched Th-20 wt% U EBR-II type pins.[5] The ratio of sample to reactor power is also more favorable for TREAT operation with such a partial thermal neutron filter.

The schematic diagram for the instrumentation and pre-heating of the fuel element is given in Fig. IV-2-1. Leads are run behind the load frame and meltdown tray components, in order to provide protection for possible attack by molten sample fuel. The sodium in the fuel sample is maintained molten prior to each transient by the pre-heater. For operation with TREAT the output from the beaded thermocouple at the bottom of the fuel pin will be used, in conjunction with a controller and solenoid actuated relays, for temperature control by interruption of the current to the pre-heater. A nominal current of 60 amps at 2 to 3 V has been found adequate to heat the sample in flowing helium. The current is supplied through copper connectors to the fuel pin which is supported axially at the base electrode on the bottom of the load frame by a female adaptor to its bayonet fitting. The bottom electrode is grounded by a fine stainless steel wire. The current to the heater is interrupted with initiation of the TREAT transient.

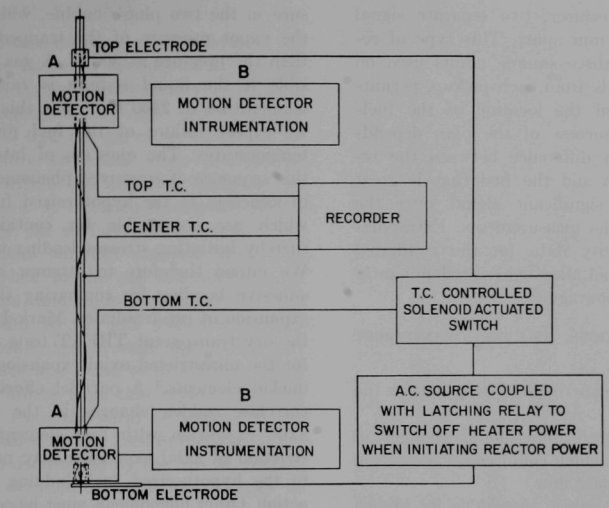

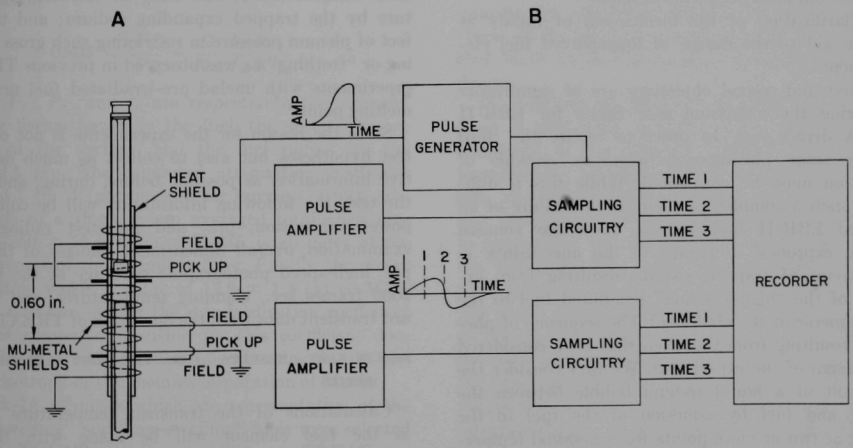

FIG. IV-2-1. Schematic Diagram for Instrumentation and Pre-Heating of EBR-II Mark IA Fuel Element. *ANL Neg. No. 113-950 Rev. 1.*

Two fast-response chromel-alumel thermocouples are welded to the cladding at the fuel midplane and top for fast response measurement of the cladding temperature during the transient.

Electromagnetic transducers have been developed[6] which are provided at the top and bottom of the fuel in order to measure fuel motion in the Mark-IA element during the course of the transient. The end of the fuel moves through a pulsed induction field generated and detected by transducers that consist of two pickup coils interspersed with three field coils, all located coaxially. The coils are fabricated from silicate-insulated 40 gauge copper wire, with a Mu metal magnetic shield, held on zirconium forms. A 2-mil stainless steel heat shield is provided also to protect the coils from radiation heating by the fuel sample. The three field coils are driven in series by the current pulse. As the fuel-sodium interface

moves through the transducer, two separate signal peaks are produced 4.3 mm apart. This type of response, as well as the three sample points used on each of the pulsed signals from each pickup, permits a useful measurement of the location of the fuel-sodium interface. The success of the plan depends upon the existence of a difference between the resistivities of the sodium and the fuel that is great enough to produce a significant signal over the temperature range for the measurements. Extrapolation of existing resistivity data for the irradiated elements, in which the fuel alloy exists predominantly as the alpha phase, is encouraging.

EXPERIMENTAL OBSERVATIONS IN THE TRANSPARENT SERIES

The objectives of the experimental program for the transparent series are:

(1) Detection of overall dimensional changes in EBR-II elements which could cause restriction or blockage of coolant flow
(2) Determination of failure thresholds for known thermal behavior of the element
(3) Clarification of the mechanism of failure as an aid to the design of longer-lived fuel elements.

The first and second objectives are of significance in realizing the maximum safe limits for EBR-II Mark-IA driver fuel. In order to realize the third objective some phenomenon which is capable of observation must be considered. While this is difficult for such a complex problem as the failure of an irradiated EBR-II fuel element, particular concern has been expressed in regard to the uncertainty in the behavior of trapped sodium resulting from expansion of the "high-swelling" irradiated fuel to the inner diameter of the cladding.[7] The sequence of phenomena resulting from this event has been considered in the design of the experiment. We first consider the entrapment of a liquid sodium bubble between the cladding and fuel by adhesion of the fuel to the cladding at two or more points for a nominal temperature of 500°C. The adhesion of the fuel to the cladding may be physical at the surface or of deeper penetration as may be possible with alloy formation. Provided that this adhesive force is strong enough to contain the sodium and there is no leakage of sodium through a crack in the cladding, considerable stress can be built up in the fuel element from restricted expansion of the liquid sodium at temperatures in excess of the trapping temperature. Under these conditions the cladding is in tension. As the bubble is cooled below 500°C, a gas pocket forms from the contraction of the liquid. The internal pressure in the two phase bubble, which is governed by the vapor pressure of the trapped sodium, is lower than the pressure at 500°C. A gas phase is also possible if the liquid sodium is raised to its critical temperature of 2460°C.[8] But this is academic since we expect failure of the fuel pin at much lower temperatures. The question of interest in regard to this sequence of conceived phenomena is the strength of adhesion at the hypothesized fuel-cladding bonds which are responsible for containing the sodium, thereby initiating stresses leading to cladding failure. We intend therefore to attempt a measure of this adhesive bonding by comparing the measured axial expansion of pre-irradiated Mark-IA fuel elements in the dry transparent TREAT tests with existing data for the unrestricted axial expansion of pre-irradiated unclad elements.[3] A parallel effort will be made to correlate sudden changes in the measured rate of axial expansion with fuel element failure. The restriction of axial expansion may not be related only to the hypothesized fuel-cladding mechanical interaction. Other phenomena must be considered, such as: local compression of fuel alloy at elevated temperature by the trapped expanding sodium; and the effect of plenum pressure in restricting such gross swelling or "frothing" as was observed in previous TREAT experiments with unclad pre-irradiated fuel near the melting point.[3]

Since the reason for the experiments is not only to test hypotheses but also to collect as much descriptive information as possible before, during, and after the test, the following information will be collected: power calibration, pre- and post-test radiographic examination, overall dimensional changes of the fuel pin, high-speed photographic coverage of the test at 2000 frames/sec., cladding temperatures, and standard transient data from the operation of TREAT.

PRELIMINARY RESULTS FOR THE DRY TRANSPARENT SERIES

Calculations of the transient temperature profile in the fuel element will be made with RE-248 ARGUS[9] using the methods described in Ref. 10. ARGUS computes the transient power input per unit volume of fuel, $P(r,z,t)$, at radius r, axial position z, and time t, given by

$$P(r,z,t) = \theta_0 \mu(r) \eta(z) n(t),$$

where μ, η, and n are arbitrary numerical functions given pointwise for r, z, and t respectively. The standardization coefficient θ_0, together with $\eta(z)$ and $\mu(r)$, may be determined from the power calibration reported previously for this series,[11] assuming a radial power distribution of the form

$$\mu(r) = I_0(Kr).$$

Radiochemical determinations of the fissions, by the La^{140} method, in fuel alloy sections of a Mark-IA pin exposed to an integrated power history in TREAT of 25 MW-sec yielded an average power density calibration of 0.98 ± 0.02 cal/gm of fuel-MW-sec for this test series. Since no axial power distribution could be detected within the precision limits of the measurements, $\eta(z) \equiv 1$. Detailed description of the neutron flux at the pin surface was obtained from the activation of 93% enriched uranium foils, 1 to 2 mils thick, attached to the pin circumference at the fuel top, bottom, and midplane. Despite a 10% power anisotropy due to the flux distortion by the cadmium-lined capsule, the average flux in the fuel to that at the surface was found to be 0.805 ± 0.055. This value, which differs from that reported in Ref. 11, was computed from the ratio of fissions in the fuel section, determined by the La-140 method, to fissions at the surface determined by the Mo-99 method. The value of the attenuation coefficient K may be computed for the distribution $\mu(r) = I_0(Kr)$ from the relation[12]

$$0.805 = \frac{\langle P_f \rangle}{P_s} = \frac{2}{Kr_0} \frac{I_1(Kr_0)}{I_0(Kr_0)},$$

where $\langle P_f \rangle$, P_s, and r_0 are respectively the average specific fission power in the fuel, the specific fission power at the surface, and the fuel radius for the Mark-IA pin. The computed attenuation coefficient 7.9 ± 1.7 cm^{-1} (uncorrected for burnup), which corresponds to a single group averaged total cross section of 350 ± 75 b/atom of U-235, is an index of the effectiveness of the cadmium filter. Finally the power calibration yields a value of 12.9 ± 1.3 cal/cc-MW-sec, at zero burnup, for the standardization coefficient θ_0. The computed precision for this coefficient does not take into consideration uncertainties due to the flux anisotropy or the chemical separation of Mo-99.

Mark-IA elements which are representative of the "high-swelling" and "low-swelling" fuels were selected for the TREAT experiments. The pre-TREAT examinations of these fuel elements have been completed. These examinations are:

1. Juggernaut neutron radiography (mainly for internal conditions)
2. X-ray photography (mainly for bond height and bond region)
3. Gross axial gamma scan (to check power distribution)
4. Full length macroscopic photographs of fuel elements
5. Diameter and density determinations.

Neutron radiographs of the "low-swelling" and "high-swelling" elements are shown in Figs. IV-2-2 and IV-2-3, respectively. The extent of axial growth is greater than had been anticipated previously. In the case of the "low-swelling" fuel the gap separation between the fuel and the restrainer is of the order of 0.2 in. This should be adequate to study the expansion of the fuel which is anticipated for the temperature range of the measurements. The "high-swelling" fuel of the 4015 series in Fig. IV-2-3 has gap separations of the order of 20 to 50 mils both at the top and bottom of the fuel. This is also the case for pin 14 of the SL-38 series. Pins 11 and 13 for the SL-38 series do not appear to be typical of the more interesting high axial growth "high-swelling" pins. They appear to be more typical of the "low-swelling" series. It is felt therefore that a mistake may have been made in the inventory of these particular pins.[13]

Dry transparent TREAT tests have been performed on the two unirradiated Mark-IA fuel pins, which were fabricated from "high-swelling" fuel. These particular runs provided metallurgical control samples for this series of tests as well as an in-pile check on the instrumentation of axial fuel motion in clad Mark-IA fuel using eddy current motion transducers.

The first pin, SL-33-3, was irradiated to integrated doses of 1597, 2431, and 2917 J/cc in three successive transients in the TREAT facility. Peak cladding temperatures for the center thermocouple were 503, 630, and 657°C, respectively. In each case the pin was pre-heated electrically to approximately 200°C to ensure that the sodium bond was molten prior to the transient. Two eddy current motion detectors were provided in the dry transparent test capsule. The center planes of these transducers were positioned at the top and bottom fuel surfaces of the pin, with the sodium bond molten, preliminary to insertion into the test capsule. The second pin, SL-33-6, was irradiated in another series of transients to successive integrated doses of 2917, 2986, and 3820 J/cc. Peak cladding temperatures for these transients were 668, 714, and 918°C, respectively.

The motion detectors were operative for all transients. Extreme bowing and separation of the fuel spacer-wire were observed at the termination of the third transient on the first pin, due to mechanical constraint of the pin by the upper coil support frame lavite insulator. This was corrected after removal and replacement of that pin. Bowing was observed after the third transient on the second pin. Since there was no detectable separation of the spacer wire, it appears that this was from normal sample behavior at

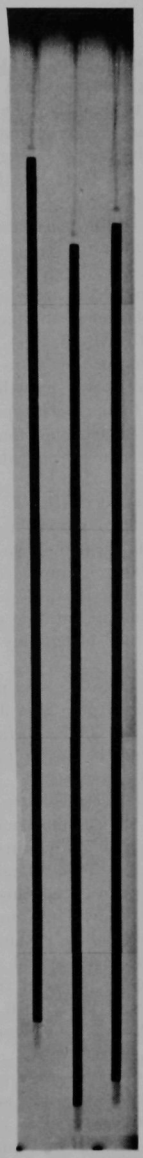

Pin No.	5	7	8
Element No.	81	80	79
Subassembly	B - 343		
Series	SL-40 Low Swelling		

FIG. IV-2-2. Pre-TREAT Neutron Radiographs of EBR-II Irradiated "Low-Swelling" Mark-IA Pins. *ANL Neg. No. 113-788.*

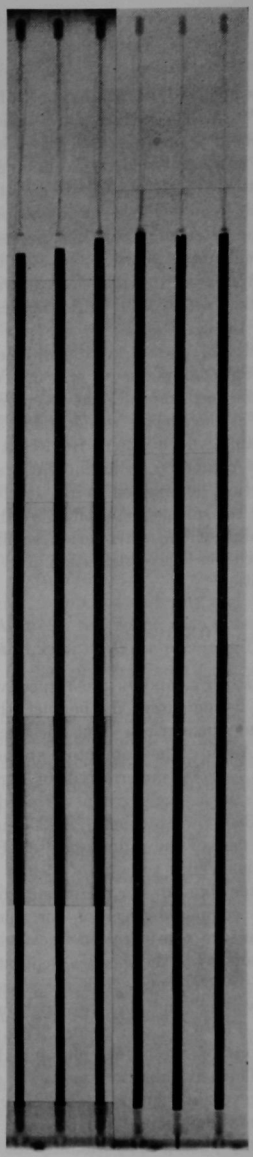

Pin No.	11	13	14	43	44	45
Element No.	11	10	9	12	11	10
Subassembly	B - 343			B - 342		
Series	SL-38 High Swelling			4015 High Swelling		

FIG. IV-2-3. Pre-TREAT Neutron Radiographs of EBR-II Irradiated "High-Swelling" Mark-IA Pins. *ANL Neg. No. 113-789.*

elevated temperatures rather than from mechanical constraint.

A post-mortem of the two test pins and analysis of data from the motion detectors will be performed in Fiscal 1969. The measured axial expansion for these tests may be compared with out-of-pile dilatometric data on U-5% Fs alloys[14] for temperatures up to 730°C. It should be possible to extend the data in Ref. 14 to temperatures in the range 900–950°C by the in-pile motion detector measurements.

Test Series

The dry capsule experiments on the pre-irradiated elements will be started in the first quarter of Fiscal 1969. The initial experiments will include the Mark-IA "high-swelling" and "low-swelling" fuel elements at the specific test conditions outlined in Table IV-2-I. Since the pre-irradiated pins were selected preliminary to the pre-test physical examination, it may be necessary to select alternate "high-swelling" pins as an upper limit of behavior for the test series, based upon the results of the neutron radiography discussed previously.

The program for tests on the single EBR-II Mark-IA pins in a Mark-I loop is given in Table IV-2-II. These studies are concerned with the behavior of irradiated Mark-IA pins under mild over-temperature conditions including (1) possible internal fuel movements, (2) possible localized damage due to fuel burnup and (3) loss of integrity under mild accident conditions. For this series single EBR-II Mark-IA pins will be tested inside a ring of six hollow dummy elements. The peak power level for each irradiation will correspond to the power level in the central pin in EBR-II at 80 MWt operation.

TABLE IV-2-I. Dry Transparent Test Series

Test No.	Sample No.	Burnup, a/o	Max Clad Temp., °C	Sample Energy, J/cc	Comments
1	3	1.2	500	1580	HS (high-swelling") irradiated pins
2	3	1.2	700	2770	
3	3	1.2	800	3380	
4	4	1.2	800	3380	
5	4	1.2	950[a]	4250	
6	5	1.2	800	3380	LS ("low-swelling") irradiated pins
7	5	1.2	950[a]	4250	
8	6	1.2	800	3380	
9	6	1.2	950[a]	4250	
10	7	1.2	800	3380	
11	7	1.2	950[a]	4250	

[a] Tentative specification: It is intended that these pins reach or exceed the failure threshold.

TABLE IV-2-II. Tests on Single EBR-II Mark-IA Pins in Mark-I Loop

Test No.	Sample No.	Flow,[a] m/sec	Sample Power, W/cc	Sample Energy, J/cc	Comments
1	1	4	4800	3,000[b]	Power level corresponds to central pin in EBR-II at 80 MWt operation
2	1	4	4800	~40,000	
3	2	4	4800	3,000[b]	Simulates flow decay with scram from initial conditions
4	2	4	4800	~10,000	

[a] Simulates 8m/sec for a pin inside a ring of fueled pins.
[b] Preliminary transient clipped to avoid fuel damage.

Summary

A test program has been planned to investigate the integrity of "high-swelling" EBR-II Mark-IA driver fuel in TREAT for over-temperatures from operational abnormalities of the EBR-II. Pre-test examination of the test elements has been completed. Initial TREAT tests have been performed on unirradiated fuel in order to (1) provide metallurgical control specimens and (2) proof-test the instrumental capsule with pre-heating and detection of axial fuel motion in the EBR-II fuel pin.

References

1. L. J. Koch, H. O. Monson, D. Okrent, M. Levenson, W. R. Simmons, J. R. Humphreys, J. Haugsnes, V. Z. Jankus and W. B. Loewenstein, *Hazards Summary Report Experimental Breeder Reactor II (EBR-II)*, ANL-5719 (1957), p. 1, pp. 105–114, pp. 195–226, pp. 281–360.
2. L. J. Koch, W. B. Loewenstein and H. O. Monson, *Addendum to Hazards Summary Report Experimental Breeder Reactor II (EBR-II)*, ANL-5719 Addendum (1964), pp. 98–104, pp. 225–269.
3. C. E. Dickerman, L. E. Robinson, E. S. Sowa, J. H. Monaweck and C. August, *TREAT Meltdown of Irradiated Metallic Fast-Reactor Fuel in an Inert Atmosphere*, Nuclear Appl. **3**, 461 (1967)
4. G. H. Golden, C. E. Dickerman and L. E. Robinson, *Facility for Photographing In-Pile Meltdown Experiments in TREAT*, ANL-6457 (1962).
5. C. E. Dickerman, L. E. Robinson, B. Blumenthal and R. Stewart, *Behavior of Th-20 w/o U Fast-Reactor Fuel Under Transient Heating to Failure*, Nuclear Appl. **3**, 10 (1967).
6. C. J. Renken, *Fuel-motion Studies with Mark-IA Fuel Elements*, Reactor Development Program Progress Report, May, 1968, ANL-7457, p. 62.
7. P. J. Persiani, R. K. Winkleblack, D. Okrent and S. Lawroski, Argonne National Laboratory (private communication).
8. D. Miller, A. B. Cohen and C. E. Dickerman, *Properties of Alkali Metals*, Reactor Physics Division Annual Report, July 1, 1966 to June 30, 1967, ANL-7310, p. 334.

9. D. T. Schoeberle, J. Heestand and L. B. Miller, *A Method of Calculating Transient Temperatures in a Multiregion, Axisymmetric, Cylindrical Configuration, The ARGUS Program, 1089/RE-248, Written in FORTRAN-II*, ANL-6654 (1963).
10. C. E. Dickerman, L. E. Robinson, E. S. Sowa and S. B. Skladzien, *Studies of Fast Reactor Fuel Element Behavior Under Transient Heating to Failure, II. In-Pile Experiments on UO_2 in the Absence of Coolant*, ANL-6845 (1965), pp. 31–39.
11. C. J. Renkin, *Fuel-motion Studies with Mark-IA Fuel Elements*, Reactor Development Progress Report, June, 1968, ANL-7460, pp. 53–54.
12. S. H. Paine, P. J. Persiani and W. F. Murphy, *Irradiation of Prototype CP-4 (EBR-I) Reactor Fuel Slugs in the CP-3′ Goat Hole*, ANL-5855 (1958), p. 19.
13. F. G. Foote, Argonne National Laboratory (private communication).
14. S. T. Zegler and M. V. Nevitt, *Structures and Properties of Uranium-Fission Alloys*, ANL-6116 (1961), p. 41.

IV-3. Digital Photographic Readout System for Fast Neutron Hodoscope in the Transient Reactor Test (TREAT) Facility

A. De Volpi, R. Pecina,* E. Rolnicki,* D. Travis* and G. Larsen†

The fast neutron hodoscope is a 334-detector device[1] which has been set up to detect the movement of fuel samples by observing fission neutrons emanating from fuel pins undergoing tests in TREAT. A previous limitation of the hodoscope instrumentation was the readout and recording system, which, in the analog form,[2] was unable to match the input data rates or to provide quantitative data. A new digital data photographic readout system has been completed, and in addition, the hodoscope has been brought up to a full complement of detectors. One further improvement is the relocation of all linear processing circuits in a rf-shielded mobile cage.

The digital photographic system is now undergoing final tests. This method of recording enables data to be accumulated at a peak instantaneous rate of nearly one billion counts per second while retaining all spatial and temporal information derived from the transient. The novel methods of data compression and recording which have been devised to satisfy these

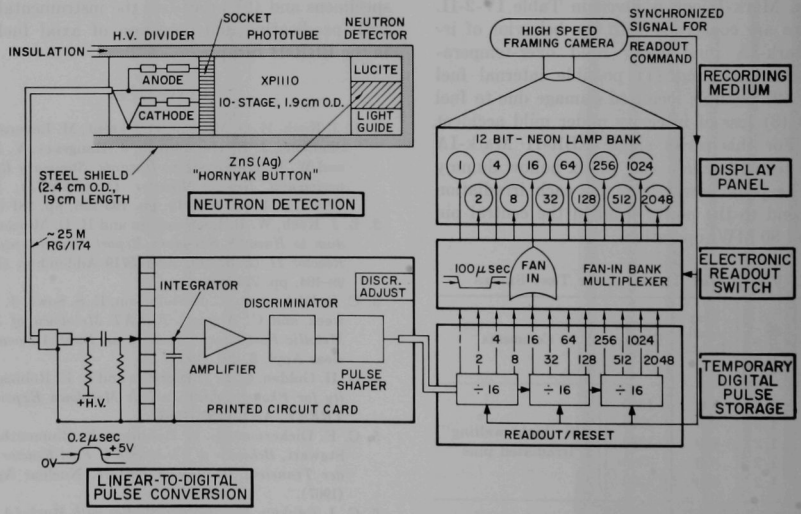

Fig. IV-3-1. Block Diagram Indicating Linear and Digital Pulse Processing Path. *ANL Neg. No. 112-8836.*

* Electronics Division, Argonne National Laboratory.
† Idaho Division, Argonne National Laboratory.

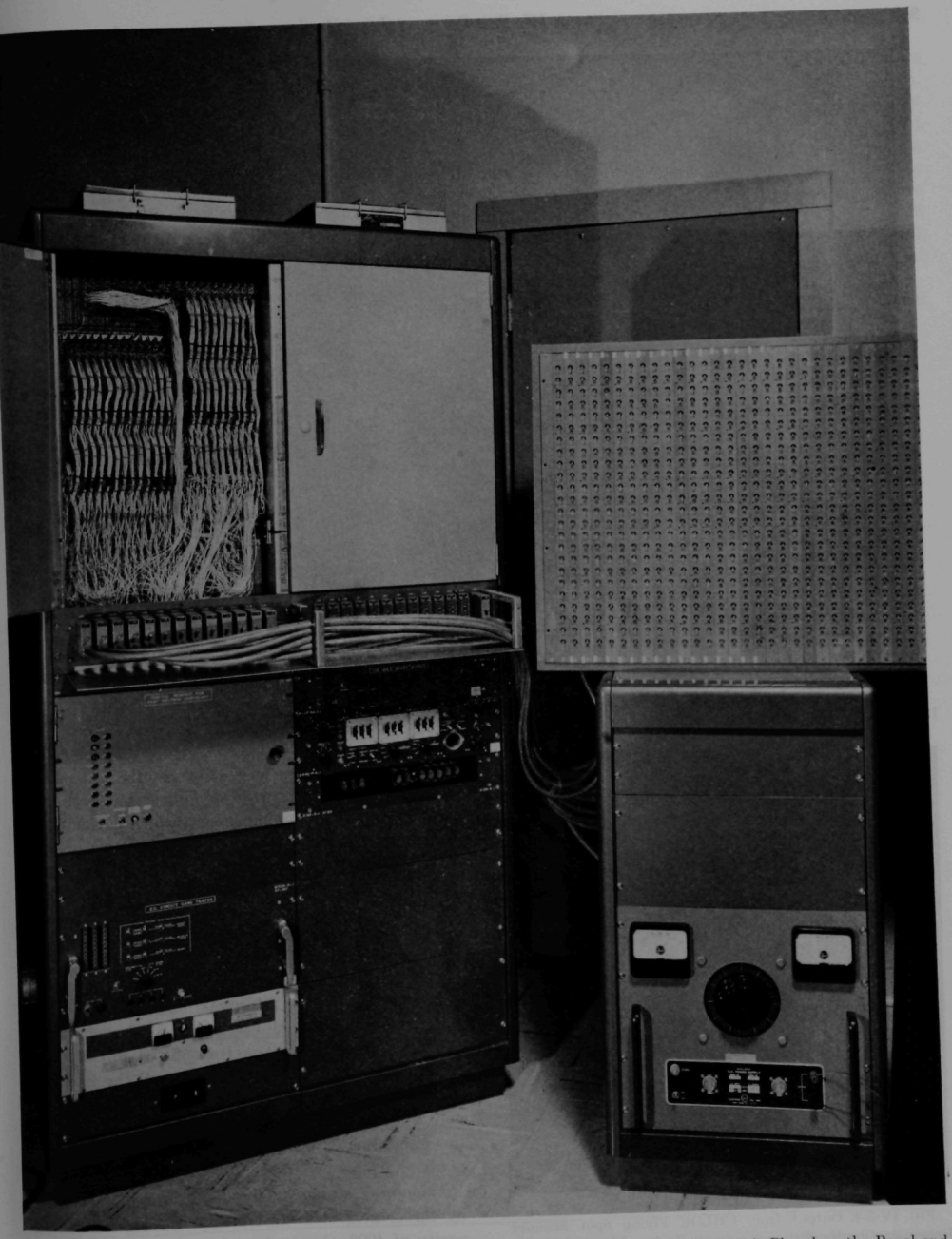

Fig. IV-3-2. 720 Lamp Display Panel and Associated Electronic Racks; During Use a Black Mask is Placed on the Panel and the Framing Camera is Placed in a Dark Room With the Panel. *ANL Neg. No. 143-2609.*

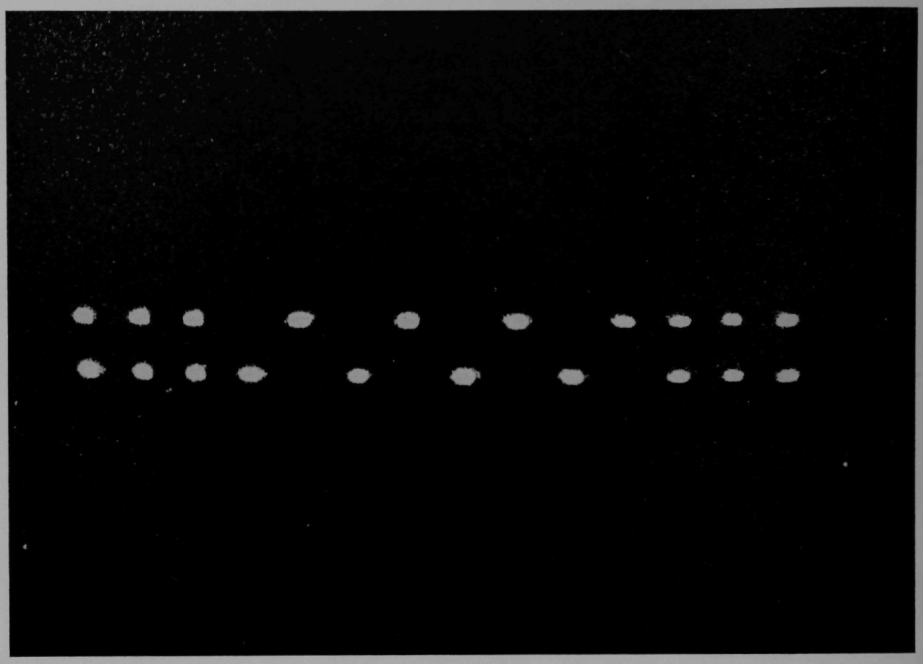

FIG. IV-3-3. An Example of One Frame of Digital Data Taken with HYCAM Camera Operating at 5000 Pictures/Sec; up to 720 Lamps can be Lit in One Frame. *ANL Neg. No. 113-831.*

FIG. IV-3-4. Output from CHLOE Flying Spot Scanner Demonstrating Rendition of a Single Frame of Digital Photographic Data.

objectives are based primarily on the commercial availability of integrated circuitry binary scalers and a high speed framing camera which has an 840 m film length capacity.

With 1-msec time resolution as an objective, it has been possible to temporarily store all data from each channel in integrated circuitry binary scalers—334 of them. The processing path which leads to this storage stage is outlined in Fig. IV-3-1.

Neutron detection is accomplished by a mixture of ZnS (Ag) in plastic (Hornyak button[3]) which produces scintillations observed by a photomultiplier tube. The linear signal is transmitted directly to a printed circuit card which contains all the linear-to-digital pulse conversion functions. After integration and amplification, those linear signals which exceed the discriminator level are shaped into digital pulses of about 200 μsec width.

Temporary storage of the digital pulse is performed by three integrated circuit chips having a total capacity of 4096. One such scale of 4096 is assigned to each detector channel. Since twelve readout lines are

required to sense the contents of each scaler, a data compression factor of 34 has been obtained. At this point, then, it is necessary to record an *ordered* twelve data bits every millisecond for each of 334 channels, or a total of 4×10^6 bits/sec. A data rate of this magnitude still exceeds the capacity of existing magnetic recording media, except for the rather expensive solution of placing a number of specialized units in parallel.

The data which have been accumulated in 1-msec intervals can be stored in digital fashion on photographic film. This is executed by displaying the data in a panel of lamps which are photographed in single flashes continuously by a high-speed framing camera.

The contents of each scaler can be released by activating an "AND" gate connected to every output line.[4] The electronic readout switch consists of a device which chooses a set of 56 out of 336 scalers to be read out simultaneously. The two extra scalers are associated with a timer. A cycle of six banks of 56 scalers completes the readout; it requires only 0.1 msec to disgorge a bank of 56 scalers, so the total cycle time is 1.2 msec.

As mentioned, 12 data lines are required for each

```
FRAME NUMBER        4
THRESHOLD FACTOR    0.5000

* * * * * * * * 0 0 0 0 0 0 0 0 0 0 * * * 0 0 0 0 0 0 0 * *
* 0 0 0 0 0 0 0 0 0 0 0 0 0 0 0 0 0 0 0 0 0 * 0 0 0 0 0 0 0 *
* * * * * * * * 0 0 0 0 0 0 0 0 0 0 * * * * 0 0 0 0 0 * * *
* 0 * * * * * * 0 0 0 0 0 0 0 0 0 0 * * * * 0 0 0 0 0 * * *
* * * * * * * * 0 0 0 0 0 0 0 0 0 0 * * * * 0 0 0 0 0 * * *
* * * * * * * * 0 0 0 0 0 0 0 0 0 0 * * * * 0 0 0 0 0 * * *
* 0 0 0 0 0 0 0 0 0 0 0 0 0 0 0 0 0 0 0 0 0 0 0 0 0 0 0 0 *
* * * * * * * * 0 0 0 0 0 0 0 0 0 0 * * * * 0 0 0 0 0 * * *
* 0 0 0 0 0 0 0 0 0 0 0 0 0 0 0 0 0 0 0 0 0 0 0 0 0 0 0 0 *
* * * * * * * * 0 0 0 0 0 0 0 0 0 0 * * * * 0 0 0 0 0 * * 0
* 0 0 0 0 0 0 0 0 0 0 0 0 0 0 0 0 0 0 0 0 0 0 0 0 0 0 0 0 0
* 0 0 0 0 0 0 0 0 0 0 0 0 0 0 0 0 0 0 0 0 0 0 0 0 0 0 0 0 0
* * * * * * * * 0 0 0 0 0 0 0 0 0 0 * * * * 0 0 0 0 0 * * *
* 0 0 0 0 0 0 0 0 0 0 0 0 0 0 0 0 0 0 0 0 0 0 0 0 0 0 0 0 *
* * * * * * * * 0 0 0 0 0 0 0 0 0 0 * * * * 0 0 0 0 0 * * *
* * * * * * * * 0 0 0 0 0 0 0 0 0 0 * * * * 0 0 0 0 0 * * *
* * * * * * * * 0 0 0 0 0 0 0 0 0 0 * * * * 0 0 0 0 0 * * *
* * * * * * * * 0 0 0 0 0 0 0 0 0 0 * * * * 0 0 0 0 0 * * *
* 0 0 0 0 0 0 0 0 0 0 0 0 0 0 0 0 0 0 0 0 0 0 0 0 0 0 0 0 *
* * * * * * * * 0 0 0 0 0 0 0 0 0 0 * * * * 0 0 0 0 0 * * *
* 0 0 0 0 0 0 0 0 0 0 0 0 0 0 0 0 0 0 0 0 0 0 0 0 0 0 0 0 *
* 0 0 0 0 0 0 0 0 0 0 0 0 0 0 0 0 0 0 0 0 0 0 0 0 0 0 0 0 *

THERE ARE 231 POINTS
```

Fig. IV-3-5. Resulting Compter Output Derived from Fig. IV-3-4. Demonstrating Final Recognition of Binary Condition of Each Lamp. *ANL Neg. No. 113-839.*

scaler. With 56 scalers being evaluated in any one phase of the readout cycle, at least 672 lamps are required to display their contents. Actually a 720-lamp array is used (Fig. IV-3-2) which includes lamps reserved for fiducial and phase indication purposes.

The digital pulses from the scalers are transferred to the lamp display in unison; at this instant the high-speed camera shutter opens to photograph the display. Proper timing is secured by deriving the synchronization signal from the position of the camera shutter. This "sync" pulse initiates the readout sequence, causing the neon lamp display to be ignited at the proper time. The lamps, of course, are ignited only when a pulse is applied. The combination of lamps "on" and "off" reflects the binary code of the scaler. A 0.1-msec flash is sufficient to expose adequately the high sensitivity film.

In order to follow a 1.2-msec schedule, the camera must operate at about 5000 frames/sec. We use a rotating-prism framing camera which has 1% electronic regulation. This camera can reach full speed in 3 sec with a loading of 840 m of 0.1-mm thick, 16-mm format high-speed film—enough to last over 20 sec. An example of data taken at this speed is provided in Fig. IV-3-3.

The effect of this procedure is that each scaler is interrogated every 1.2 msec; it is immediately reset to zero, and after the 0.1-msec readout period, it again commences storage. The entire binary-coded rate data which had been accumulated for 1.1 msec is stored on film, as single flashes, in groups of six frames.

Decoding of Data

With a camera operating at 5000 pictures/sec, up to 100,000 frames can be developed. Most of this film is removed in editing, and only those portions pertinent to the transient are retained. Calibration pulses are applied to the input for a number of frames prior to the meltdown. Even with this selection of film, a large amount of data remains for analysis. At least several hundred thousand coded bits are involved, out of the total film capacity of 100 million bits.

The film is translated by an existing automatic-flying spot scanning station (known as CHLOE) into computer-compatible data stored on magnetic tape. Figure IV-3-4 shows the impression gained by CHLOE from a single frame, and Fig. IV-3-5 displays the program output which has interpreted the magnetic tape data. The number and position of asterisks correspond to a visual examination of lamp exposures on the input frame. The data may now be correlated with the appropriate scaler, leading to an evaluation of the channel count rates for any given frame which was exposed at a registered time. A visual display of the decoded data is now being prepared.

Comparison with Magnetic Media

The method of photographic digital recording described above has certain merits in comparison with magnetic digital recording. Taking as a point of departure the output of the multiplexor—common to either method of recording—it can be seen that the remaining expense for photo-recording consists of a bank of neon lamps with associated driving circuitry and a high quality framing camera. This expense is at least an order of magnitude less than any conceivable magnetic medium.

It has already been mentioned that no single existing magnetic storage technique can accommodate the bit rates generated in this experiment. Even specialized units which approach 10^6 bits/sec require custom-made read stations to translate the data back to computer-compatible format. Furthermore, serious limitations caused by slewing (for magnetic tapes) and bit dropout must be considered.

It is true that a special film interpretation station is required for photographic digital readout, but such a station is already in existence at Argonne and at many other laboratories around the world.

One further observation is appropriate: the existing technique described in this paper does not exhaust the data density limits of digital photographic recording. At least an order of magnitude greater density is allowable under present film grain, fog, and scanning conditions. At slower camera speeds, corresponding to longer intervals between readout, better quality film can be utilized. In addition, the various time and spatial parameters can be varied to provide an inexpensive means of recording vast amounts of data; for example, photographic digital recording can be easily adapted to repetitive experiments conducted with large detector arrays.

References

1. A. De Volpi and C. H. Freese, *Fast Neutron Transient Detection Hodoscope for Reactor Fuel Meltdown Studies*, IEEE Trans. Nucl. Sci. **NS-13** (1), 623 (1965).
2. A. De Volpi, *High-Speed, Multi-Channel Data Recording for Nuclear Physics Experiments Using Fast-Framing Cameras*, Proc. 7th Intern. Conf. High Speed Photography, Zurich, Switzerland, September, 1965, (Verlag Dr. Othmar Helwich, Darmstadt, Germany), pp. 516–521.
3. W. F. Hornyak, *A Fast Neutron Detector*, Rev. Sci. Instr. **23**, 264 (1952).
4. A. De Volpi, R. Pecina, C. H. Freese, E. Rolnicki, D. Travis and G. Larsen, *Extended Capability for Fast Neutron Hodoscope Used at TREAT*, IEEE Trans. Nucl. Sci. **NS-15** (1), 77 (1968).

IV-4. Apparatus for High Speed Photographic Safety Experiments on Irradiated Fast Reactor Fuel Specimens

L. E. Robinson and C. August

Introduction

Direct observation of the course of meltdown experiments in the Transient Reactor Test Facility (TREAT) by means of high-speed photography has proved to be a very useful method of obtaining confirmations of post mortem reconstruction of fuel sample failure mechanisms. The extension of this technique to the study of the behavior of pre-irradiated specimens was accomplished through the design and fabrication of equipment to permit exposure of test samples previously irradiated to levels of appreciable fission product inventories.

In general, photographic experiments on pre-irradiated elements combine salient features of two types of experiments which had been performed previously: photographic tests on unirradiated samples and opaque tests on pre-irradiated specimens. The design of the in-pile apparatus for use with pre-irradiated fuel was based on the previous equipment for photographic meltdown experiments on unirradiated samples,[1] although the requirements of remote assembly, remote handling, and shipment to TREAT required extensive redesign of the components.

Description of the TREAT Transparent Facility

Test Capsules

Figure IV-4-1 shows the basic layout of the TREAT transparent in-pile facilities, both for unirradiated and irradiated samples. The sample fuel pin is contained in a double-walled zircaloy test capsule approximately 4.5 cm wide by 48 cm high by 42 cm long, having a total wall thickness of 0.125 cm. The front of the capsule has a 0.625 cm thick fused silica window (the "inner window" of the entire sub-assembly) attached, but not sealed, to the capsule. Behind the sample, there are a front-surfaced mirror and a 0.75 cm thick graphite slab which provide extra containment for the walls closest to the test element. Capsule walls are coated with a special paint mixture consisting of powdered alumina or titania in silicone paint in order to supply a diffuse high-reflectance background for photography. Figure IV-4-2 shows a disassembled test capsule. The window (made from UV grade artificial fused silica) slides down two tracks in the front of the capsule. One lower corner of the window is cut off to permit free circulation of the inert cover gas from the capsule to the remainder of the entire slot liner assembly. The cover gas inlet is attached to the white rubber tube connected to the rear of the capsule top. In front of the window in Fig. IV-4-2 is the test sample load frame, which is designed to hold the sample and any special instrumentation such as fuel motion detectors, and support instrumentation and thermocouple lead wires. The load frame slides into the capsule and is latched in place by tabs in the closed end of the capsule.

For special experiments in which additional heat

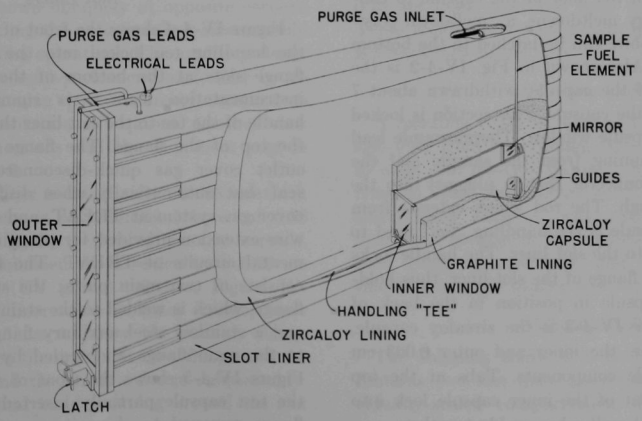

Fig. IV-4-1. Cutaway View of TREAT Transparent In-Pile Facility. *ANL Neg. No. 112-1223.*

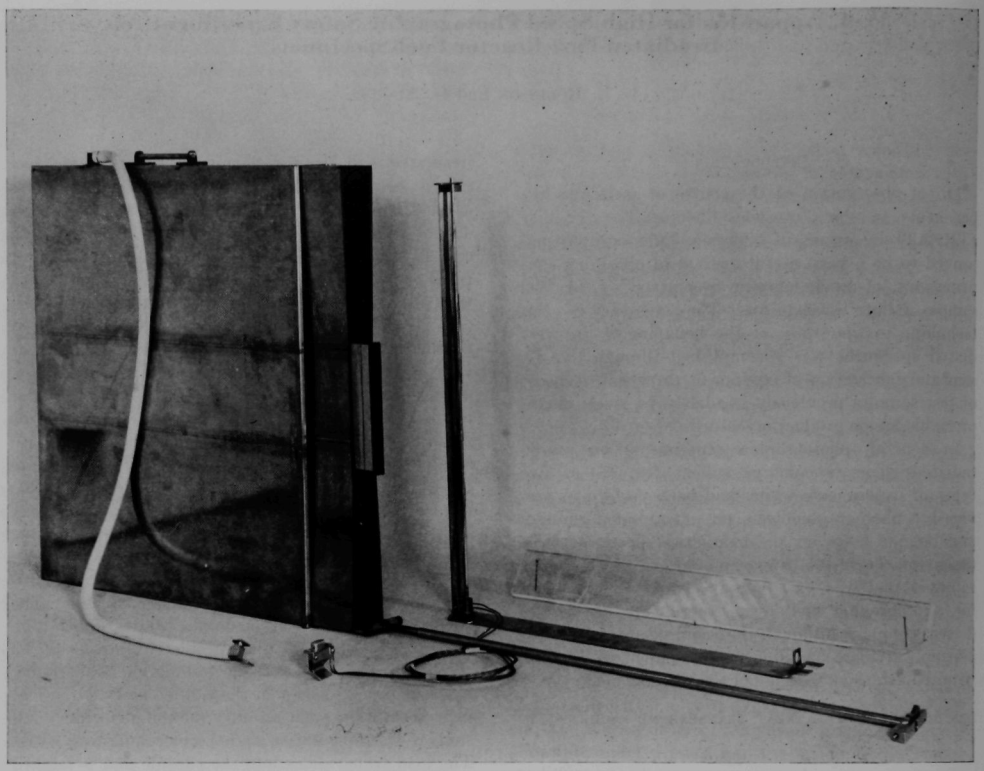

FIG. IV-4-2. Disassembled Test Capsule. *ANL Neg. No. 112-2981.*

capacity is needed in the floor of the capsule to contain very high energy meltdowns, a "meltdown tray" of zircaloy and graphite can be latched to the bottom of the load frame. Also shown in Fig. IV-4-2 is the inner-wall section of the capsule, withdrawn about 7 cm from the rest of the capsule. This section is locked into place by the capsule window. Thermocouple lead wires are shown running from the sample and the load frame to the connector that is plugged into the slot liner lead-through. The rod which extends from the front of the capsule is the handling "tee" used to insert the capsule into the slot liner. The handle locks into place inside the flange of the slot liner, thus holding the zircaloy capsule in position in the back of the assembly. Figure IV-4-3 is the zircaloy capsule, disassembled to show the inner and outer 0.063 cm wall zircaloy capsule components. Tabs at the top and bottom and front of the inner capsule lock into place to hold the dual-wall subassembly together.

Slot Liners

Figure IV-4-4 shows the front of the slot liner, with the handling tee locked into the slot liner window flange slots at the bottom of the window, and the instrumentation lead wires running up from the handle of the tee to the slot liner through-connector at the top of the flange. The flange top has inlet and outlet cover gas quick-disconnect connections that seal shut automatically when disconnected from the cover gas system at TREAT, and also the short lead wire extension provided for plugging into the experimental circuits at TREAT. The flange subassembly consists of two main parts: the stainless steel main flange, which is welded to the stainless steel slot liner, and a stainless steel auxiliary flange, which is bolted to the main flange and sealed by a silicone gasket. Figure IV-4-5 shows the front of the slot liner, with the test capsule partially inserted and the auxiliary flange removed to show its connections and gasket

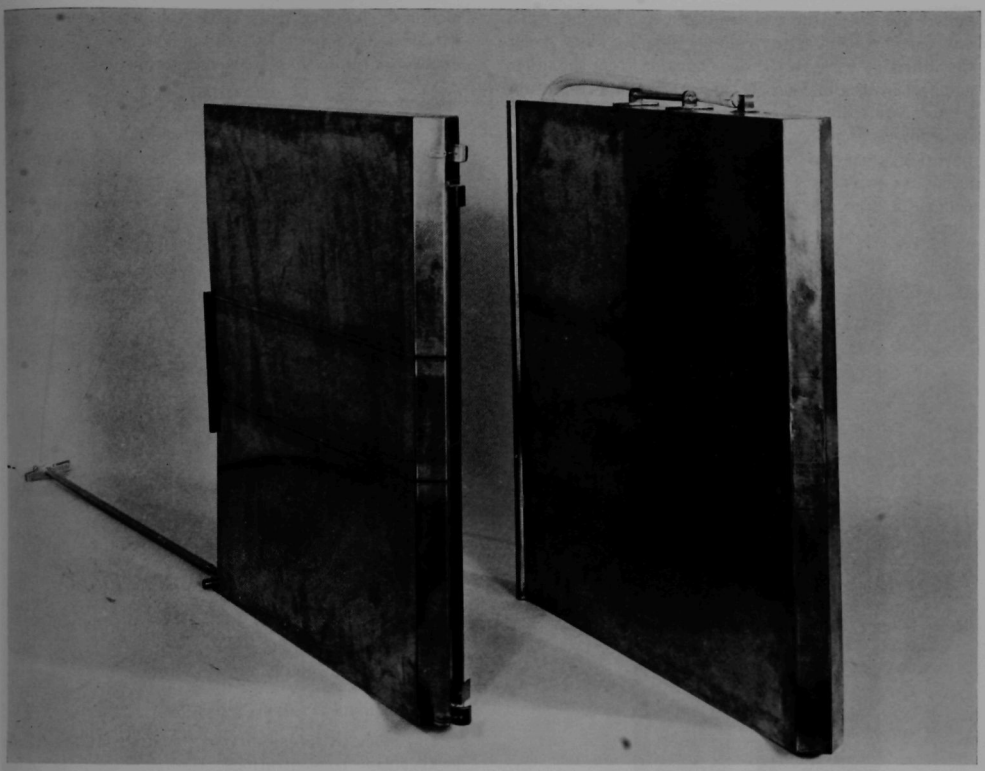

FIG. IV-4-3. Back View of Inner (left) and Outer (right) Zircaloy Capsule Components. *ANL Neg. No. 112-2979.*

from the rear. The two steel pegs on the front of the auxiliary flange, shown obliquely at opposite corners, are for use in aligning the outer window subassembly during remote loading operations. The auxiliary flange was designed as a semi-permanent part, and is removed only for changing the lead-through components when new instrumentation is required. Another view of the upper connections and the alignment pegs is shown in Fig. IV-4-6.

Inside, the slot liner is lined with a 0.063 cm thick zircaloy shell. There is an additional layer of 0.53 cm thick graphite in the region of the test capsule. The front of the subassembly is sealed by a 0.27 cm thick fused silica (UV grade) window. Figure IV-4-7 shows the slot liner with the inner zircaloy liner withdrawn about 5 cm to show the zircaloy flange that is held between the main slot liner flange and the auxiliary flange, and the window flange subassembly. The raised horizontal bands running around the slot liner are offsets, formed directly by rolling, in the 0.20 cm thick steel slot liner walls to stiffen them. These bands are shown clearly in Fig. IV-4-8, which is a back view of the liner.

Handling Coffin

A handling coffin is used at TREAT to transfer a slot liner from its shipping coffin to the reactor, and to align and position the liner for insertion into and removal from the reactor core. The coffin used for unirradiated samples[1] was modified for previously irradiated specimens by replacing the original lead shot filling by cast lead, and by adding auxiliary shielding near the sample position.

Shipping Coffin

The shipping coffin is a lead-shielded box which contains two slot liner assemblies in separate, individually-sealed compartments. Internal shielding is

included between the two compartments so that, with one compartment empty and its shielded door open, the radiation through the door opening from the other compartment would not be higher than the radiation levels outside the coffin walls. Each slot liner assembly is locked into its compartment by closing the compartment doors to prevent liner rattling inside the cask and window breakage during shipping. The coffin, in turn, is secured by cables to a shock-mounted shipping pad. With this arrangement, no windows have been lost throughout the use of the apparatus (more than a dozen experiments).

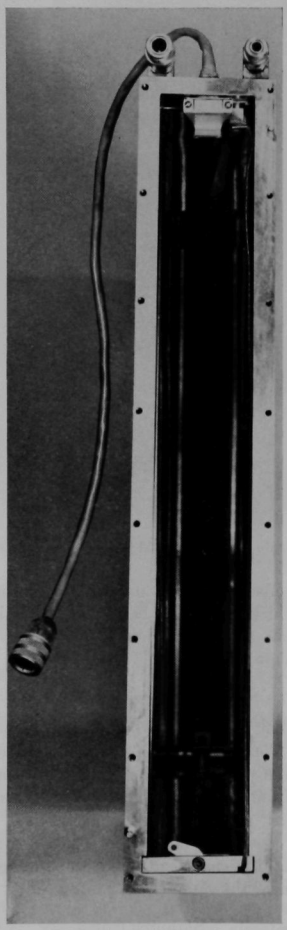

Fig. IV-4-4. Front View of Slot Liner with Capsule in Place, without Outer Window. *ANL Neg. No. 112-2976.*

REMOTE OPERATIONS

Figure IV-4-9 shows the remote loading apparatus, in place, through a cave window. In the front, on the table, are the welding clamps used for attaching thermocouples to the surface of the test sample. The sample proper is in its load frame, while the load frame and zircaloy capsule are fastened to the remote assembly jigs. In the foreground are two manipulators. A close up of the remote welding of a bare wire thermocouple to the pre-irradiated sample is shown in Fig. IV-4-10. After capsule assembly, the capsule is slid into its slot liner assembly (Fig. IV-4-4), the gas and instrumentation leads are plugged into the inside of the auxiliary flange (Fig. IV-4-5), and the window flange subassembly is bolted into place (Figs. IV-4-6 and IV-4-7). The slot liner flanges and connections are then checked for leaks using a helium mass spectrometer leak detector with a "sniffer" attachment to sense helium escaping from the liner. During the loading of the capsule, the slot liner is positioned, partly extended, in its shipping coffin compartment. After successful remote checking of the assembly, the liner is slid completely into its compartment, the shielded compartment door is lowered and sealed, and the coffin is removed from the cave.

SAFETY CONSIDERATIONS

To reduce the possibility of slot liner failure due to local stress concentrations, the slot liner is made from a single piece of 0.20 cm thick stainless steel. (The previous liners for unirradiated samples had top and bottom plates welded to the sides, and the stiffening ribs were separate bands spot welded to the liner sides proper[1]). The spot welds were eliminated by the integral stiffener design (Fig. IV-4-8). One weld at each top and bottom was eliminated by replacing separate top and bottom plates by forming the top and bottom into halves from the same steel sheet as the side. Top and bottom welds were thus restricted to the flange end, the round sample end, and a middle seam running the length of the slot liner.

Because of the stiffening bands and the round back end it was possible to design the unit for a routine proof test of 0.6 atm gage, prior to each experiment. Proof tests were performed originally using a mockup[1] of the TREAT viewing slot mechanical side restraints (essentially a succession of vertical line contacts at 10 cm intervals). Post-loading proof tests

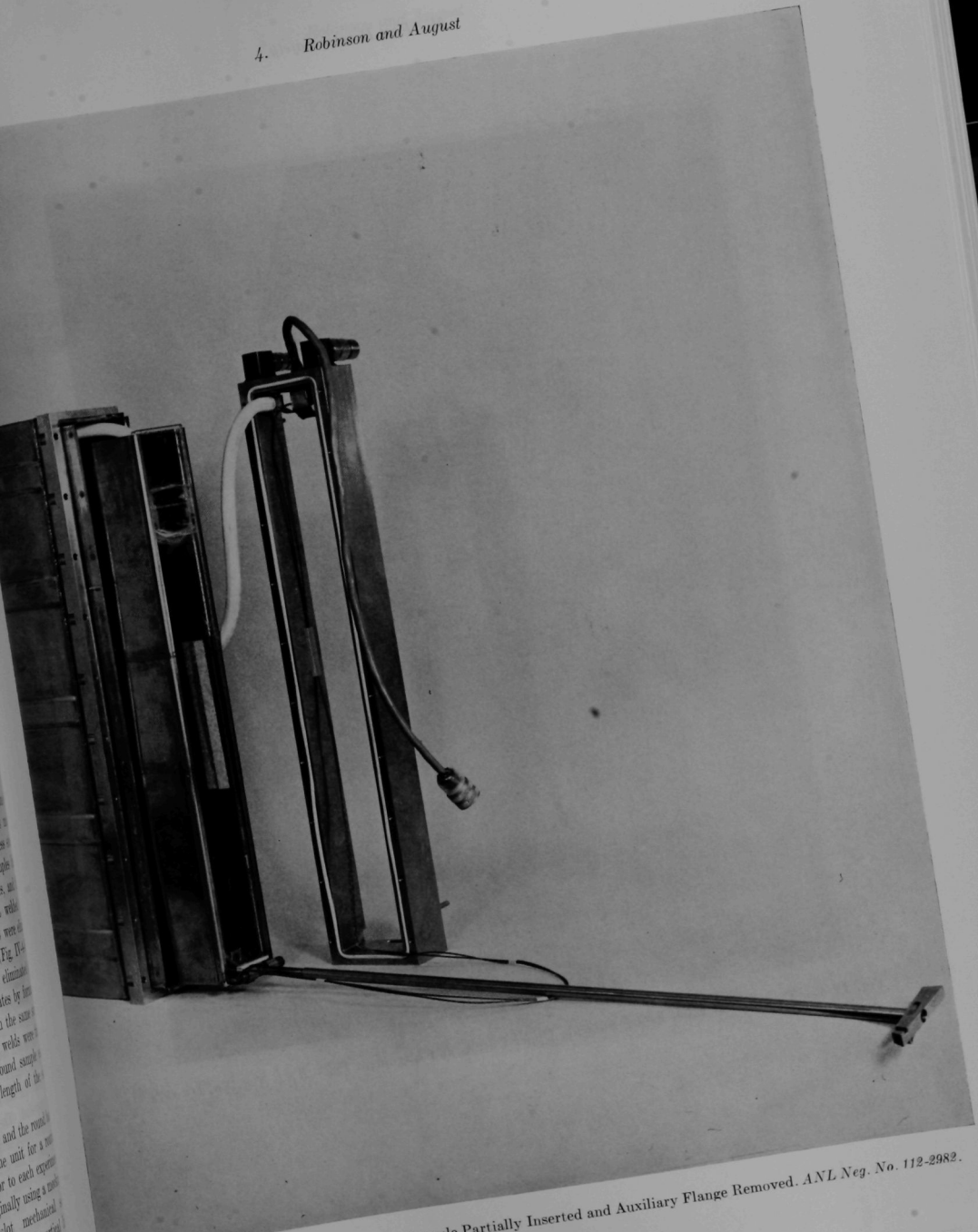

Liner with Capsule Partially Inserted and Auxiliary Flange Removed. *ANL Neg. No. 112-2982.*

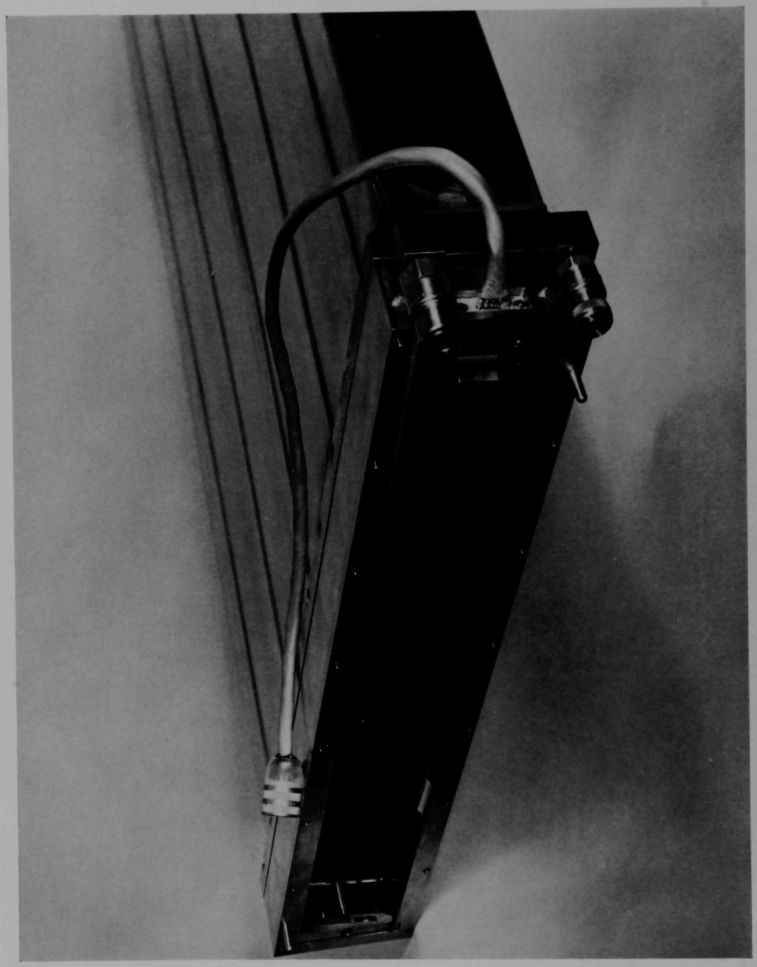

FIG. IV-4-6. View of Slot Liner Front, Showing Upper Details and Alignment Pegs. *ANL Neg. No. 112-2974.*

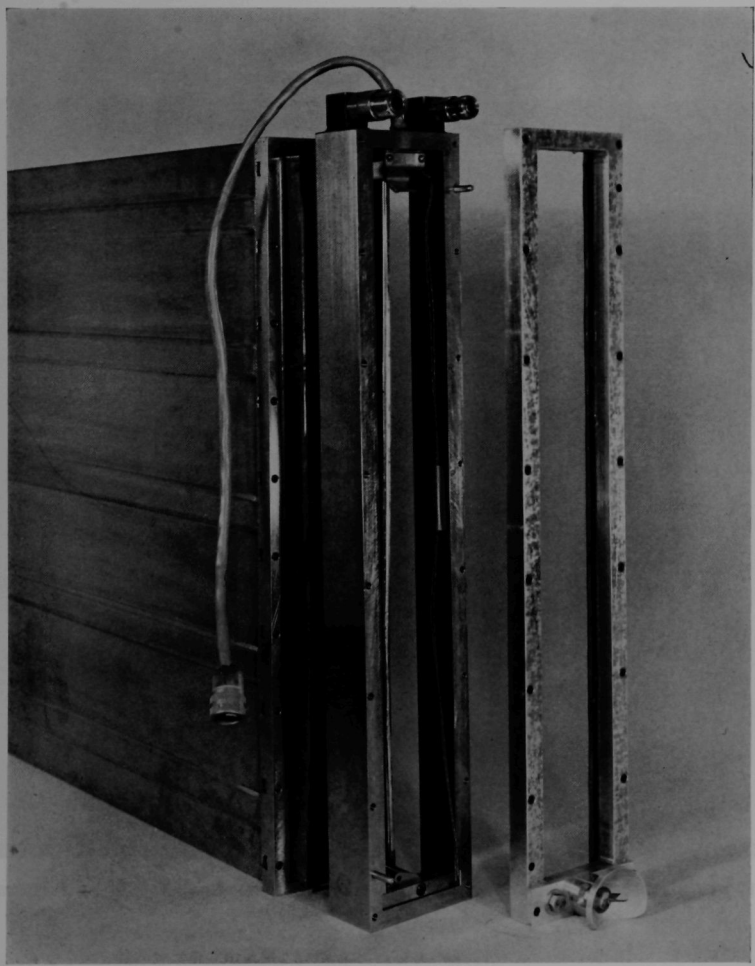

FIG. IV-4-7. View of Slot Liner Front End Showing Relationship of Main Flange, Auxiliary Flange, and Window Flange Subassembly. *ANL Neg. No. 112-2977.*

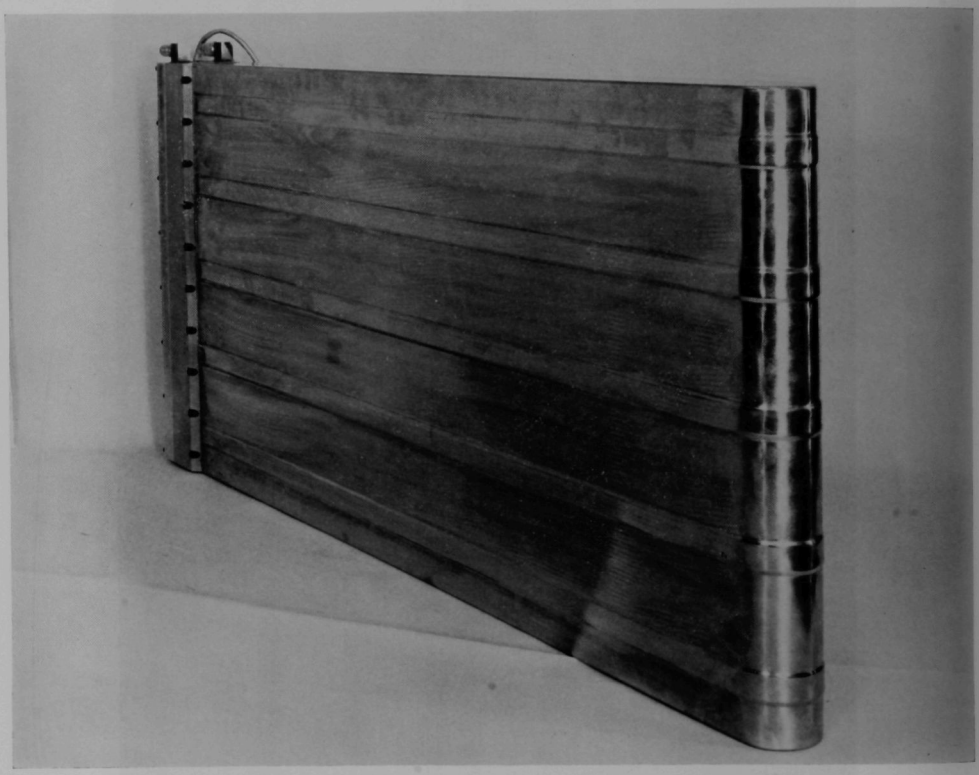

FIG. IV-4-8. Back View of Assembled Slot Liner, Showing Stiffening Bands. *ANL Neg. No. 112-2980.*

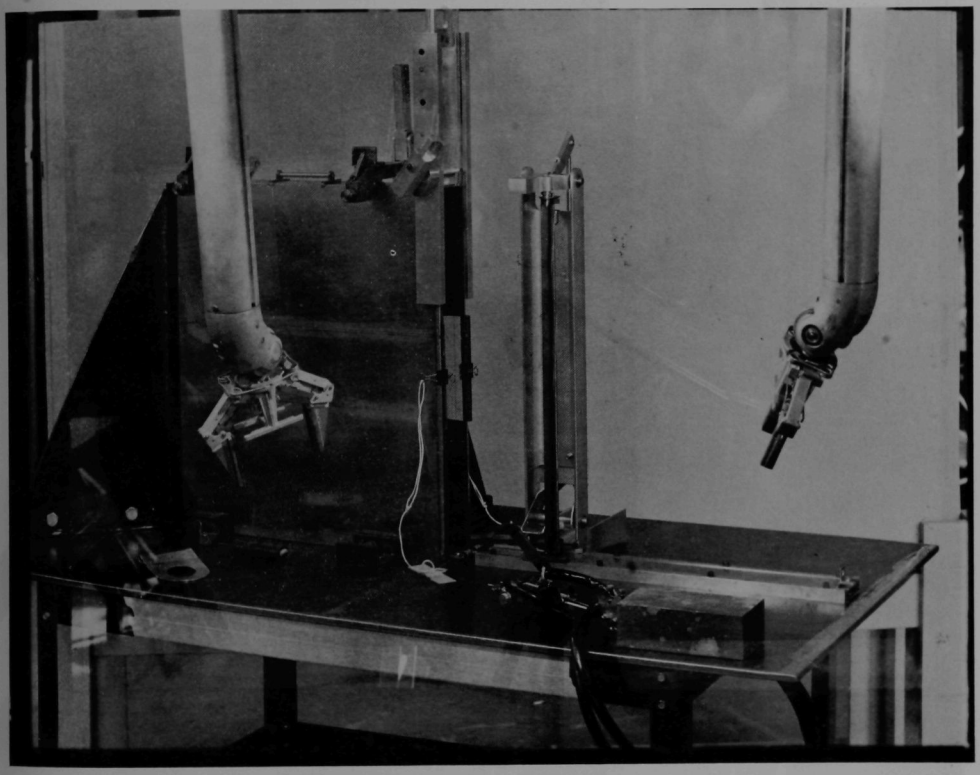

FIG. IV-4-9. View Through Cave Window of Remote Capsule Loading. *ANL Neg. No. 112-2433.*

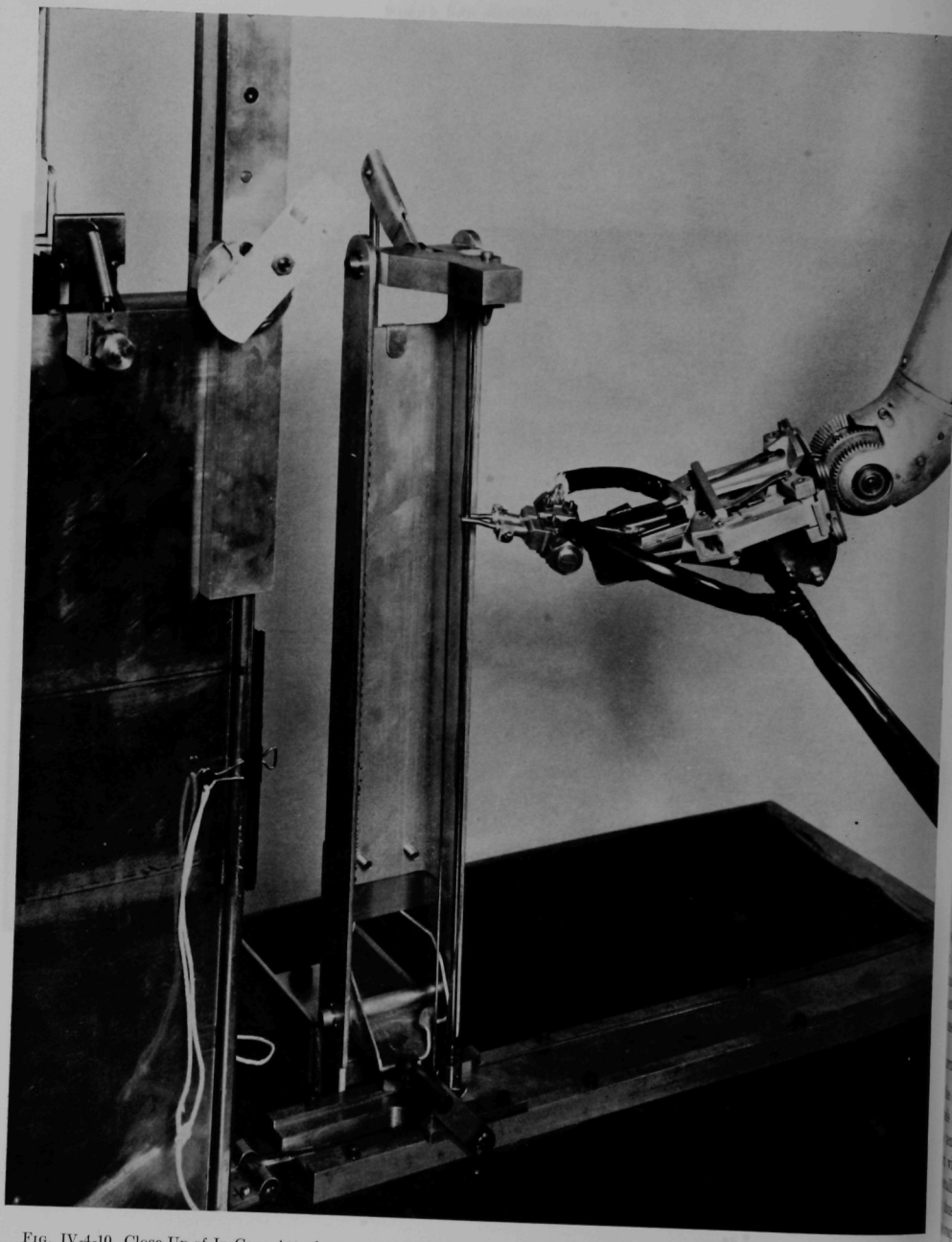

FIG. IV-4-10. Close-Up of In-Cave Attachment of Thermocouple to Cladding of Pre-Irradiated TREAT Sample. *ANL Neg. No. 112-2431.*

were made inside the handling coffin, using grid-like inserts on either side to mock up the slot environment. This pressure capability, coupled with the 52 liter liner internal volume was sufficient to accommodate experimental requirements for the capability to meet accidents including the following:

1. Air atmosphere in the slot liner caused by malfunction of the cover gas system, not detected on system instrumentation. This includes possible reactions with the fuels and with sodium released upon failure of sodium-bonded fuels.
2. Decomposition of paint inside zircaloy capsule.
3. Over-pressures caused by accidental excessive energy input to the sample.

The zircaloy capsules have functioned, as designed, to safely contain meltdown of the samples. In addition, the double-walled capsule construction provides a convenient method of loading cadmium neutron absorbers to shape sample neutron flux or to shield the entire sample. "Sandwiches" consisting of a layer of cadmium foil between two layers of fiberglass are held between the two zircaloy walls. Because of this multiple-layer construction, the low melting-point cadmium is thermally shielded from local overheating by spattered molten fuel or sodium.

USE OF APPARATUS

The apparatus for photographic experiments on fast reactor fuel failure has been in routine use during a period of approximately five years. It has functioned satisfactorily in experiments on metallic samples[2] and on oxide samples.[3,4] Slot linears have been reused routinely. The remote assembly zircaloy capsules were made to be interchangeable with the earlier bench assembly capsules,[1] and they have been routinely reused in experiments both on unirradiated and irradiated pins.

REFERENCES

1. G. H. Golden, C. E. Dickerman and L. E. Robinson, *Facility for Photographing In-Pile Meltdown Experiments in TREAT*, ANL-6457 (1962).
2. C. E. Dickerman, L. E. Robinson, E. S. Sowa, J. H. Monaweck and C. August, *TREAT Meltdown of Irradiated Metallic Fast Reactor Fuel in an Inert Atmosphere*, Nucl. Appl. **3**, 461 (1967).
3. C. E. Dickerman, L. E. Robinson and R. Stewart, *Photographic Fast Reactor Safety Experiments on Irradiated Oxide Pins at the Transient Reactor Test (TREAT) Facility*, Reactor Physics Division Annual Report, July 1, 1965 to June 30, 1966, ANL-7210, pp. 241–245.
4. C. E. Dickerman and R. Stewart, *Results from Transient Reactor Test (TREAT) Facility Fast Reactor Oxide Pin*, Reactor Physics Division Annual Report, July 1, 1966 to June 30, 1967, ANL-7310, pp. 276–280.

IV-5. Standards, Quality Control, Fabrication and Assembly of Mark II Integral Sodium TREAT Loops

L. E. ROBINSON

INTRODUCTION

A second generation of integral sodium loops is under development. These will contain much higher internal pressures and will provide more extensive instrumentation than the Mark I integral sodium loops previously used in the TREAT facility.

DESCRIPTION OF MARK II INTEGRAL SODIUM LOOP

In the destructive meltdown of ceramic Fast Reactor fuels in the presence of sodium coolant, the absolute temperatures of molten fuel ejected into the coolant will be about 2½ times as high as those of the metallic fuels examined in the Mark I integral loops; thus the pressures resulting from the near-explosive vaporization of sodium can be expected to be significantly higher, also. Because of gross uncertainties in the visualization of the mechanisms of such fuel failures and the actual amplitudes of pressures to be realized, the pressure containment capabilities of the Mark II integral loops were increased over those of the Mark I loops by more than an order of magnitude—from 30 to 340 atm—while the design operating loop temperature was kept about the same.

Doubling the in-pile cross section to be occupied by the integral loop and fitting the Mark II loop into the volume of two TREAT fuel elements, made possible a simplified closed circuit, direct flow, recirculating system, as shown in Fig. IV-5-1. The use of a single-walled loop geometry permits complete instrumentation of the test section at inlet and outlet, for pressure, temperature and sodium flow. At the same time, the direct flow system minimizes hydraulic losses in the sodium flow and permits the incorporation of a more versatile pumping system.

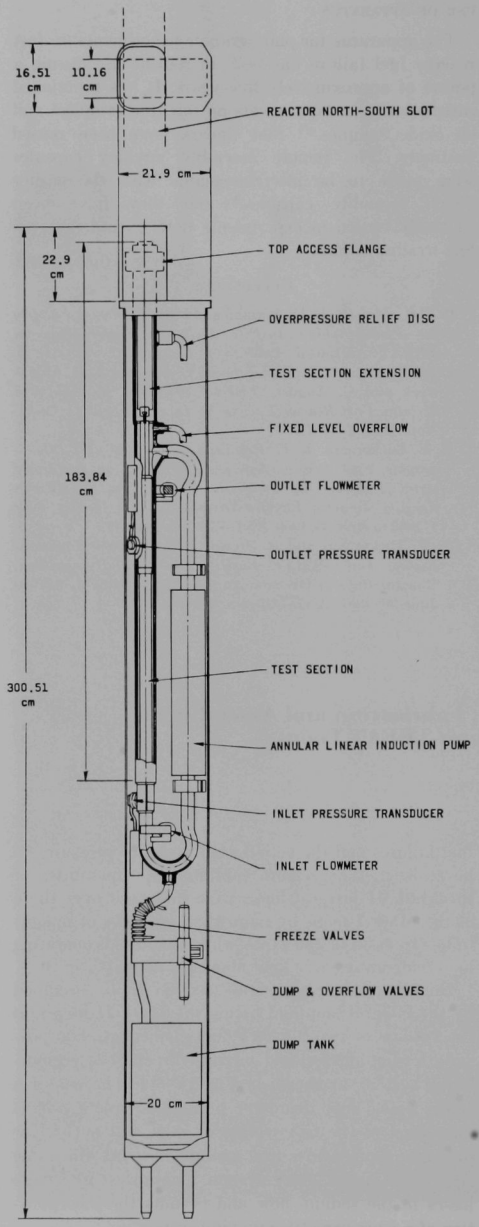

FIG. IV-5-1. Line Drawing of the Mark II Integral TREAT Sodium Loop. *ANL Neg. No. 112-6768.*

To meet the need for containment of sodium at elevated temperatures, plutonium-bearing reactor fuels, and the high amplitude pressure pulses to be expected from the meltdown of refractory materials in the presence of sodium, the Mark II integral loop was specified to meet material fabrication, and dimensional requirements for a steady state rating of 340 atm (5000 psi) at 532°C (1000°F) with a sizeable safety margin.

DESIGN PROCEDURES AND STANDARDS

As a basis for the detailed design of the Mark II integral loop, the ASME Boiler and Pressure Vessel Code[1] was selected from those available. The choice of this code stemmed from the realization that the Mark II loop should be considered to be equivalent to a Class A nuclear pressure vessel,[2] particularly since the loop is intended for use in the meltdown of plutonium-containing fast reactor fuel samples. Since the Mark II loop must be utilized in experimentation as a free-surface vessel with top penetration to load or remove test samples and closure to zero-leakage conditions prior to actual experiments in TREAT, as opposed to a permanently joined, fully-filled welded piping system, it was deemed particularly suitable to base the design upon the established standards and specification of the ASME Code.

The conservatism of the ASME Code, with its 4-to-1 margin of ultimate tensile stress to rated tensile stress was an added incentive for use of this design base.

Although the Mark II loop was designed in accordance with the standards and specifications of the ASME Code, the finished loops cannot be granted the Code stamp of approval, primarily because it does not meet thermal expansion criteria based on long term cycling service. The exceptions taken in the choice of materials, inspection procedures and criteria, and the specifications of heat treatments will be described briefly below. In most cases, the exceptions are refinements in the standards of assurance in the acceptance or rejection of materials, components, and the results of fabrication processes; the remainder are options taken from the Code to provide desired improvements in the metallurgical properties of the loop body material.

The major exception to the Code was the use of an unqualified material for a portion of the loop flow channel wall and primary containment. The flow tube of the Annular Linear Induction Pump (ALIP) was designed to be made of Inconel X-750, fully age-hardened, and clamped between mating flanges in the down-comer leg of the loop proper. The superalloy was required for its unusual high-temperature high-strength properties, which permitted thinning the

pump wall to minimize the magnetic gap between the ALIP stator and central core. The Inconel pump wall thickness of 0.25 4cm (0.100 in.) with a 2.67 cm bore exceeds the exact design thickness requirement by more than 16%.

While the Inconel X-750 is unqualified by the ASME Code for the prescribed use, the maximum design stress for the material was calculated according to the most conservative method used in the determination of such stresses for qualified materials. As a further conservatism, the physical properties of wrought bar Inconel at 1000°F was used, instead of the much higher strengths of the fully age-hardened metal, as the base property for the calculation of design stress value. The Code prescribes that the lesser value obtained by calculating 62½% of the yield strength at temperature, or determining 25% of the tensile strength, shall be taken to be the maximum allowable design stress of the subject material. The yield strength of Inconel X-750 is given as 84,000 psi and the tensile strength as 140,000 psi at the 1000°F design temperature of the Mark II loop. The maximum allowable design stress of the Inconel used in the loop was taken to be 25% of the tensile strength at temperature, i.e., 35,000 psi. Derating of the finished pump by 10%—to an efficiency of 0.90—to account for possible weld deficiencies, an effective maximum allowable stress of 31,500 psi was obtained and used in the design of Inconel components of the Mark II loop. Stresses are produced by the differential thermal expansion between the Inconel pump and the steel loop in excess of code specifications. Calculations[3] indicated these stresses to be acceptable for the loop service, with final confirmation to be made by proof tests.

Early in the construction of the Mark II loops, it became obvious that a major problem was involved in the procurement of the heavy-walled seamless tubing required, in the SA-312 Type 316 stainless steel specified, and with the necessary chemical composition. The minimum order (10,000 feet mill-run, in many cases) required by possible suppliers, made direct purchase of the tubing prohibitive in cost, and very long, indefinite lead times left no assurance as to when construction could begin. As a result, the only solution that was found was fabricating every component of the loop proper (the loop "body") from bar stock. This entailed gun drilling and boring the tubular parts from selected bar, forming the tubes into the small-radius bends, and sequentially joining the components to make the loop body.

Since the finished components were to meet requirements of Group A Finished Tubular Products, the bar stock was required to meet criteria more severe than the code requirements for bar stock. X-ray radiography and ultrasonic non-destructive test methods were specified as the inspection techniques to be used throughout material selection and fabrication, since these methods are the only Code-specified methods which are applicable to the Mark II loop. Bar selected from available stocks, of proper size and nominally correct chemical composition, was first examined by pulsed ultrasonics, to eliminate those specimens with unacceptable internal flaws. The reference defects prescribed by the Code for the ultrasonic examination of bars (Section III, Art. N-322)[1] are a ½ x 3 in. hole in a 2½ x 30 in. bar for the longitudinal wave technique, and a 1 x 0.075 in. groove in the same bar for the shear wave technique. These were considered as far too large in size to be meaningful in this case.

With the object of ultimately obtaining a Group A Finished Tubular Product from the bar stock, the ultrasonic reference defect was decreased in size to 1/32 in. diam x ½ in. depth for the initial selection of the bar. Following gun drilling of the round bar, the finished straight sections of tubing were examined by ultrasonic and radiographic methods, as prescribed by the ASME Code, with all pieces indicating *perceptible* flaws being rejected. After a mechanical forming process, as required, the finished product was again ultrasonically and radiographically examined, to conform to the Code requirements for Group A Finished Tubular Products.

Inspections of finished weld joints were performed, as far as possible according to the ASME Code, with the exception of the establishment of criteria for acceptance or rejection. The exception taken from the Code in the case of Tungsten Inert-Gas welds (TIG) consisted of the specification that all completed welds were to be totally clear of flaws detected by full radiographic examination, rather than to conform with the Code which allows detectable flaws below acceptable flaw size limits. Although the Code prescribes that finished welds be inspected by at least two of the several methods given, as applicable, and despite the desirability of using the ultrasonic and radiographic techniques throughout the system, the small scale and complexity of the loop system rendered the use of the ultrasonic method in the inspection of finished welds impractical. As a result, the welds were checked initially by the Zyglo dye-penetrant method to indicate gross subsurface and superficial surface flaws, and then they were thoroughly x-ray radiographed.

In certain cases (such as in the final weld of the Inconel pump flow tube) the alternate method of electron-beam welding was required as a means of

precisely controlling shrinking and to eliminate the necessity for adding extra metal during the welding process. It was recognized that no standards existed by which the weld could be inspected by either the ultrasonic or radiographic method, because of the extremely small size of the electron-beam weld zone. Since all welds were specified to be full-penetration and completely clear, it became necessary to establish some method by which the criteria for acceptance might be met. During the welding process a massive internal back-up ring of Inconel was used, with a minimum of 40% penetration of the electron beam into the ring specified. After welding, the penetration was determined by machining the ring out of the inner bore prior to full radiographic examination. While wholly empirical in method, this technique assured full penetration in welding, whereas neither radiography nor ultrasonic inspection was capable of detecting incomplete penetration.

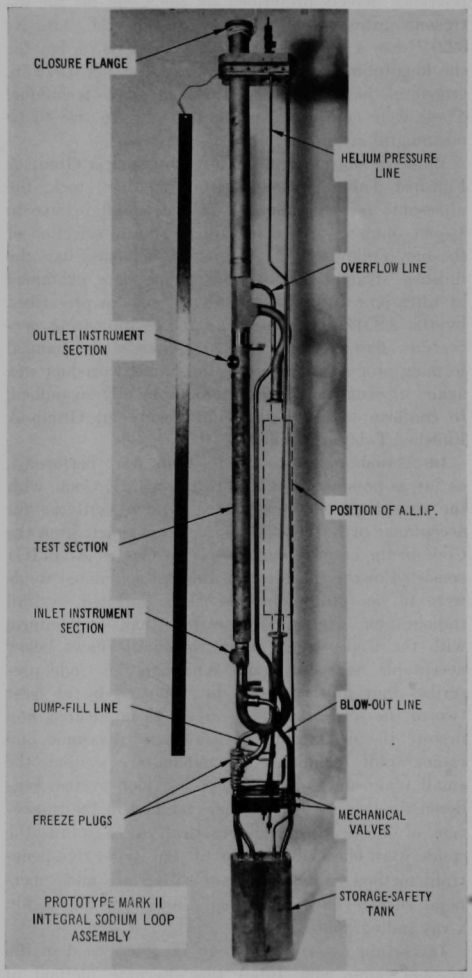

FIG. IV-5-2. Prototype Mark II Integral Sodium Loop Assembly. *ANL Neg. No. 112-9515 A.*

QUALITY CONTROL IN FABRICATION AND ASSEMBLY

Early in the procurement-fabrication process on the Mark II loops, it was found that vendor certifications of chemical composition and/or heat treatment history of purchased materials were unreliable. Errors in certifications of chemistries often arise from carelessness in transcription of data, as well as the vendor's insistence on using heat or batch chemistries, although wide variations can exist in the chemical compositions of particular pieces from a single heat or batch. Errors in heat treatment certification usually arise from the efforts of individuals to substitute "educated guesses" for complete knowledge of the past history of the material. In such certifications the fact that the statements are made under notarization is apparently immaterial.

As a means of obtaining assurance as to the chemical content of the material from which a particular component was to be made, it was found necessary to obtain certifications from independent testing laboratories, with re-tests or comparisons with secondary standards required in cases of repeated discrepancy. This procedure was followed in the fabrication of every component in the Mark II loops, including the additive metal wire used in the TIG weld. The SA-312 T-316 stainless steel parent metal was required to have a carbon content of 0.04 to 0.08%, without exception; chromium and nickel content was held within the usual specifications for normal T-316 SS. Weld wire was required to possess a carbon content of 0.05–0.07%, to minimize carbide precipitation; fusion ring material had the same chemistry as the parent metal.

During the fabrication of the primary portion of the loops (loop body), each component was individually inspected for dimensional accuracy within specified tolerances and surface condition. Fractional tolerances were specified wherever possible; high surface finishes were required only for interior surfaces, where the metal was to be in direct contact with high velocity liquid metal. Prior to joining, all components were subjected to ultrasonic and radiographic examination, with detection of a *perceptible* flaw giving sufficient reason for rejection.

Fabrication of the loop bodies was accomplished

by TIG welding, with each weld made in a fixed sequence. The rigid sequence of joining was necessary to permit clean-up of each weld interior, followed by full radiographic examination. Post-fabrication inspection was impractical because of the combination of thick wall and compact design of the facility.

The unusual geometry and great length of the Mark II loop bodies necessitated some development work before the optimum method of full austenization heat treatment was found. First efforts were made with a massively strong Inconel 600 fixture restraining the loop body; this was discovered to hamper the movement of the body during the heat cycle and to produce residual distortion. Finally, the most practical technique was found to be heat treatment with the 7-ft long device hanging in free suspension, completely without restraint throughout the heat-quench cycles.

Complete austenization of the T-316 stainless steel by solution heat treatment was deemed necessary to minimize the propensity of the high-carbon metal for precipitation of brittle carbides, and to optimize the physical properties of the steel. The ASME Code prescribes a minimum heat treatment for the material of 1800°F in order to realize the higher strength of the T-316; heat treatment of the entire loop body, after weld fabrication, became necessary because of the uncertainty in the heat treatment histories of the various components. Heat treatment was carried out in a radiant-tube pit furnace having a temperature variation of less than 10°F from top to bottom, purged with an argon atmosphere. After 2 h at 1950°F, the loop was withdrawn into an argon-purged shroud, from which it was lowered into a natural-water quench tank; surface scaling was minimized through use of the inert gas.

Test weld coupons were included with each loop during the heat-quench cycle, and metallographic examinations were made of each coupon's weld zone to verify the austenization of both the parent metal and weld and the elimination of precipitated carbides.

The flow tube of the sodium pump and the pump/pressure transducer clamps, composed of Inconel X-750, were heat treated to the fully age-hardened condition for maximum strength at elevated temperatures. Heat treatment was carried out in a vacuum furnace to minimize scaling oxidation.

The assembly of the loop bodies with the auxiliary connecting lines and the dump tank was accomplished through essentially the same operations as for the loop bodies. The exceptions were in the heat treatment of the relatively thin-walled smaller tubing of the overflow, fill/dump, and blowout lines prior to their assembly by TIG welding, and in the post-weld heat treatment. All connecting tubing was solution-treated and austenized before fitting. The finished assembly welds were not heat treated, since the thermal gradients in the region of the welds joining the smaller tubing were not sufficiently steep to cause carbide precipitation; in this case, the prescription of the Code, which "neither requires nor prohibits" post-weld heat treatment of a "P-8" material such as T-316 SS, was invoked. The certification of chemistries of all materials, full penetration, and full radiography of finished welds were as required for the loop body. The completed assembly is shown in Fig. IV-5-2.

Following complete assembly of the Mark II loops, each is given an overall dye penetrant examination to determine ageing or post welding surface flaws. Finally, the assembly is closed off and subjected to a vacuum leak check for helium tightness to the maximum sensitivity of the VEECO MS9AB mass spectrometer leak detector.

When the assembled loop has been outfitted with sodium pump, heaters, power leads, instruments, and thermal insulation, the Mark II facility is subjected to a proof test of performance, prior to its use for in-pile meltdown experiments. The proof test is carried out pneumatically, with the loop partially filled with sodium, to 125% of rated pressure while at temperature, as prescribed by the ASME Code. Although more dangerous than a simple hydrostatic test, the at-temperature test is required because of the indeterminacy of theoretical stress analyses in which even the choice of the Code to be used is arguable. The sodium presence in the loop during the proof tests is necessary to establish the temperature distributions to be realized during experimental operation in the TREAT facility, and to provide the actual thermal stresses which will affect the loop.

Only after each assembled and fully outfitted Mark II integral loop has survived the prescribed proof-test of performance (out-of-pile) will it be used for meltdown experiments.

References

1. American Society of Mechanical Engineers, Boiler and Pressure Vessel Code, 1965 Edition, with Winter Addendum of 1966.
2. ibid., Section III, Nuclear Vessels, Art. N-130, p. 2.
3. Memorandum, R. A. Valentin to C. E. Dickerman, *Estimate of Stresses in Mark II-B Loop Due to Differential Expansion of Inconel "X" and 316 Stainless Steel*, Argonne National Laboratory (February 16, 1968).

IV-6. Design of Advanced Shipping Cask for Transient Reactor Test (TREAT) Facility Experiments

C. E. Dickerman, A. P. Gavin,* R. Robertson,* F. L. Willis and J. Cizek

A shipping cask has been designed for transporting advanced loops and capsules between the TREAT Facility and the examination facilities in Illinois. The Mark II TREAT sodium loop was used as the reference for designing the cask package, although capability was provided to include other types of TREAT irradiation facilities sized to occupy the space, 10 x 20 x 240 cm, of two TREAT core elements. In addition, the new cask is designed to meet the stringent regulations for both "normal transport" and "hypothetical accident" specified by the Atomic Energy Commission in the Code of Federal Regulations Title 10, Part 71, "Packaging of Radioactive Material for Transport," and the applicable Department of Transportation regulations.

The basic cycle of operations used in design is as follows:

1. Use of the cask as auxiliary shielding at the hot laboratory contamination barrier when the test section is loaded and unloaded into the loop.
2. Shipping.
3. Compatibility with TREAT operations for transferring the loop to and from the reactor handling cask.

Activity to be contained consists of fission products in the sample, resulting both from transient TREAT irradiation and from prior irradiation at a total steady-state power level of 40 kW and six months of "cooling time" after removal from the steady state reactor. Total activity for the design is 320 curies. Because a TREAT "meltdown" experiment may cause the sample to change shape and move inside the main containment body of the loop or capsule, full shielding extends the length of the loop. Weight limitations and consideration of the fire criteria of the "hypothetical accident" specifications resulted in the selection of depleted uranium for shielding material. (The specified fire temperature is 1475°F, which is above the lead melting point but well below the uranium melting point. Consideration was taken in the design for potential difficulties due to attack of the steel cask structure by uranium-steel eutectic formation at the reference design temperature of 1475°F.) No credit in design analysis was taken for the experimental loop as a sealed secondary container. Loop and container structural steel was used in the shielding analysis.

Figure IV-6-1 is a drawing of the shipping cask design. Omitted for simplicity is the shipping skid, which also was specially designed to meet regulation specifications of "normal transport" criteria. The loop (or capsule) proper is shown, in dashed lines, inside a "special form" container, also in dashed lines. The "special form" container provides a secondary container, meeting requirements for impact and temperature capabilities. Outside the special form container is the cask proper. Stepped construction at the two ends of the loop and auxiliary uranium shielding inserts in the top and bottom of the cask provide shielding for a sample that is carried to the extreme ends of the loop during the TREAT excursion. The main (radial) shielding is a uranium sleeve 7.5 cm thick.

The main cask structure is a steel shell, 56 cm o.d. by 3.7 cm thick. (The figure, which is based on the construction drawings, gives basic dimensions in inches.) Steel trunnions are located at the bottom of the cask to provide a pivot for uprighting the cask. Two more lifting trunnions are at the top (flange) end. Both sets of trunnions are set into 2.5 cm thick steel sleeves and are designed to receive the load of a 9.15 m (30 ft) drop without rupturing the cask body. The cask flange is sealed by an Inconel-asbestos spiral-wound high-temperature gasket, located inside the 56 cm steel shell to protect the cask seal in case it is dropped in a handling or shipping accident. The cask structure is designed to meet a design criterion of a 9.15 m drop on top, bottom, side, or "corners" on an essentially unyielding surface.

The entire cask is designed to meet the fire "hypothetical accident" criterion of exposure to a 1475°F environment for 30 min. This includes a cask structure that will maintain adequate uranium shielding during and after the fire, have adequate strength, and maintain the compression on the high temperature cask gasket. Uranium side shielding is shown with steps in the figure. These are designed to prevent radiation streaming through the cask walls. The step dimensions are sized to maintain acceptable shielding during and after the hypothetical accident fire conditions.

Design of the cask has been coordinated with the development of handling and transfer design work for

* Reactor Engineering Division, Argonne National Laboratory.

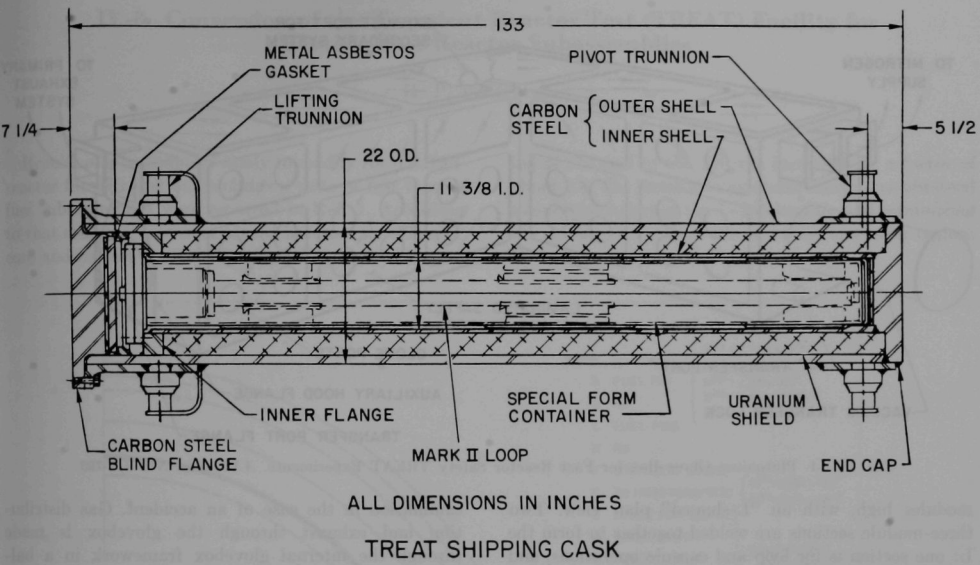

FIG. IV-6-1. Side View of Shipping Cask Package Showing Principal Components and Key Dimensions. *ANL Neg. No. 113-784 T-1.*

the Hot Fuels Examination Facility which is being designed by ANL for construction at the Idaho site in order to permit use of the cask for transportation between that future hot laboratory complex and TREAT.

REFERENCE

1. L. E. Robinson, *Design of the Mark II Integral Transient Reactor Test (TREAT) Facility Sodium Loop*, Reactor Physics Division Annual Report, July 1, 1965 to June 30, 1966, ANL-7210, pp. 245–250.

IV-7. Low Level Activity Plutonium Handling Facility for Transient Reactor Test (TREAT) Facility Experimental Apparatus

C. E. DICKERMAN, C. AUGUST, N. R. TUCKER and W. B. DOE*

The reference design specifications have been reported[1] for a nitrogen glovebox facility in building 301 which is to be used in operations on TREAT loops and capsules containing plutonium-bearing samples. Detailed review of operations with the facility has resulted in extensive design changes, and the glovebox as built differs significantly from the reference design. The basic requirement is that the facility be capable of servicing autoclaves from the Chemical Engineering Division TREAT program and the loops and capsules of the Reactor Physics Division TREAT experiments. Two principal design changes were made:

1. Glovebox size and configuration: Upon detailed review of glovebox operations, it was concluded that the two-level design[1] did not provide adequate handling space, necessary height above working levels, and separation of operations. The basic CENHAM glovebox design was retained, but the original layout of two three-module tiers was replaced by a single-working-level glovebox, one and one-half

* Remote Control Division, Argonne National Laboratory.

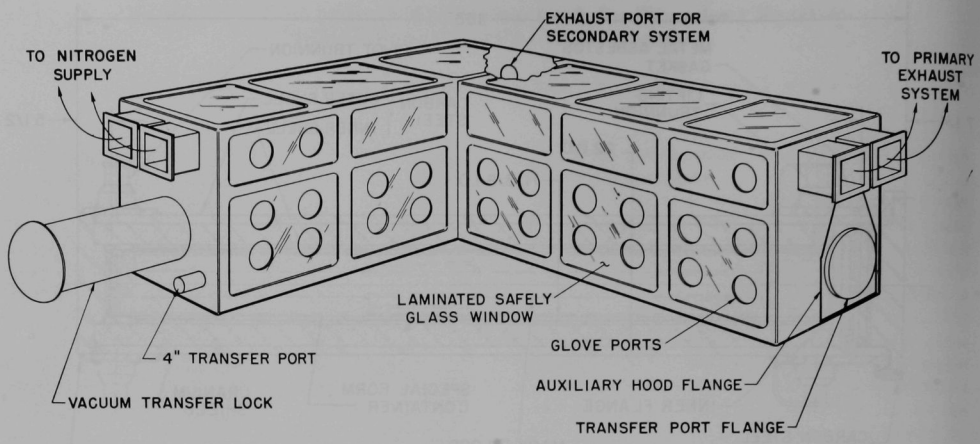

FIG. IV-7-1. Plutonium Glove Box for Fast Reactor Safety TREAT Experiments. *ANL Neg. No. 113-793.*

modules high, with an "L-shaped" plan view. Two three-module sections are welded together to form the L: one section is for loop and capsule operations, and the other is designed for autoclave disassembly. Samples can be transferred from one part of the glovebox to the other.

2. Gas System. After additional review of potential gas system malfunctions and the integration of glovebox operations into routine building operations, it was decided to change from a recirculating gas system with purification to a once-through system supplied by liquid nitrogen. The gas system can be fully converted to operation with argon if future needs require.

Figure IV-7-1 is an isometric view of the glovebox facility. Each module is a cube approximately 105 cm on a side. The full-size safety glass panels have four glove ports each, located on a square pitch of 45 cm. The top row of half modules has two glove ports located in each corner panel (see Fig. IV-7-1). Glovebox lighting is provided by fluorescent fixtures above blank (i.e., no ports) safety glass panels in the top of the glovebox. One end of the "L" is equipped with a 48 cm diam vacuum lock for bagging material into and out of the box and a small 10 cm diam (4 in.) entry port. The other end has a transfer port flange to hold transfer ports for attaching loops or capsules to the box by means of the split flange technique. An auxiliary loading hood (not shown) will be supplied as a permanent secondary containment area for the transfer port. The auxiliary hood flange is shown in Fig. IV-7-1.

Nitrogen gas is supplied to the glovebox through a pair of inlet filters above the vacuum lock. The filters are provided to protect the supply system from contamination in the case of an accident. Gas distribution and exhuast through the glovebox is made through the internal glovebox framework in a balanced duct system with dual primary exhaust ports at the other end of the L (see Fig. IV-7-1). Each exhaust port has two AEC filters in series to confine contamination to the box.

After the gas leaves the filters, it enters the primary gas exhaust system. Both the primary and secondary exhaust systems have two motor-exhaust fans in parallel. One exhauster is adequate for full design flow in its system; to assure continuous operation, automatic power transfer switches have been provided so that within each system a malfunction of the operating exhauster will activate the other as a standby unit. Automatic reserve power is available from the building 301 emergency power system. The primary exhaust system has a design capability of 25 cfm, adequate for normal supply and box gas purging. A high-capacity, secondary exhaust branch with design flow of 500 cfm is activated by a box pressure-operated relief valve to maintain the glovebox gas pressure negative with respect to atmospheric pressure in the event of an emergency. The secondary exhaust port is located near the intersection of the two three-module sections forming the L-shaped Box (see Fig. IV-7-1).

REFERENCE

1. C. E. Dickerman, L. E. Robinson and R. Ivins, *Design of the Glovebox Facility for the Transient Reactor Test (TREAT) Facility Loop and Capsule Operations with Plutonium-Bearing Samples*, Reactor Physics Division Annual Report, July 1, 1966 to June 30, 1967, ANL-7310, pp. 281–282.

IV-8. Conversion of the Transient Reactor Test (TREAT) Facility for Testing Fast Reactor Subassemblies

H. P. Iskenderian

Results of a preliminary study to modify the TREAT reactor for carrying out meltdown tests of fast reactor fuel subassemblies were reported in Ref. 1. According to that study, a converter placed between the TREAT core and its test section *TS*, (Fig. IV-8-1), could cause complete meltdown of a small cluster of fuel pins in the *TS* by neutrons with a spectrum typical of a fast reactor on the conditions that

(1) The core temperature does not exceed 400°C
(2) The converter temperature does not exceed 1800°C
(3) Maximum/minimum power ratio in a fuel pin of the *TS* is ≤ 1.01
(4) The loss of reactivity due to insertion of the converter assembly is $< 1\%$.

The Ref. 1 study has been extended by a reasonable relaxation of the above requirements: $T_{core} \rightarrow 600°C$, the maximum/minimum power ratio in the $TS < 1.10$, and the maximum available energy for complete melting of the fuel in the *TS* was increased by a factor of about 2.6. The increase in available energy was obtained mainly by reducing the U-235 loading and minimizing the density of U-238 in the two inner converter regions of the four-region converter.

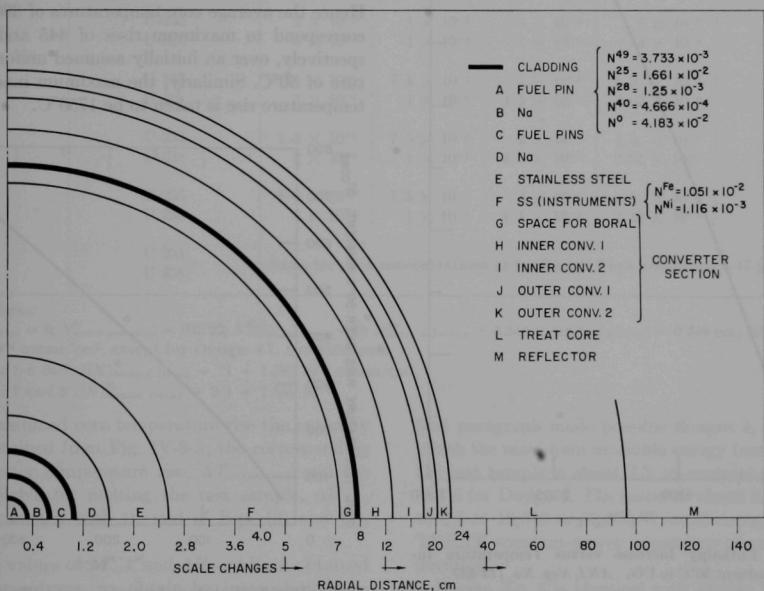

Fig. IV-8-1. Geometrical Configuration of TREAT Core, Converter, and Test Section in a Radial Direction. *ANL Neg. No 112-9102 Rev. 1.*

Nuclear calculations were made using the SNARG-1D[2] code in the S_4 approximation, with cross sections in the thermal group corrected for core temperatures; thermal calculations were based on single-pulse adiabatic heating, with (Fission density)$_\ell \propto (\Delta H)_\ell = (\bar{C}_p \Delta T)_\ell$, where ℓ refers to region. Graphs relating enthalpy ΔH to temperature rise ΔT for UO_2* and for the TREAT core are shown in Figs. IV-8-2 and IV-8-3, respectively.

Important parameters in our calculations are

* As noted in Table IV-8-II, the Inner Converter regions are essentially UO_2 ; hence Fig. IV-8-1 is used for converter enthalpy survey calculations.

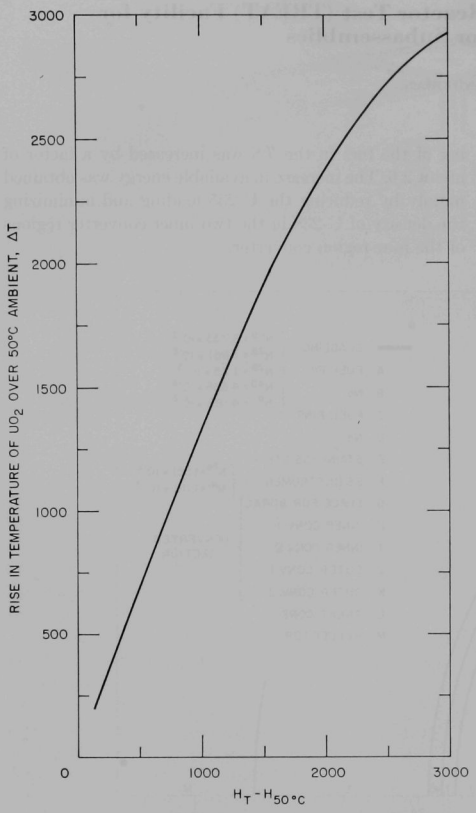

FIG. IV-8-2. Enthalpy Increase versus Temperature Increase above Ambient 50°C in UO_2. *ANL Neg. No. 113-837.*

$$\frac{\Delta H_{TS}^{center\ line}}{\Delta H_{core}^{maximum}} = b \tag{1}$$

$$\frac{\Delta H_{converter}^{maximum}}{\Delta H_{TS}^{center\ line}} = a_m \tag{2}$$

$$\frac{\Delta H_{converter}^{maximum}}{\Delta H_{core}^{maximum}} = a_m b \tag{3}$$

$$\frac{\Delta H_{TS}^{maximum}}{\Delta H_{TS}^{minimum}} = c. \tag{4}$$

Limiting values of converter and core peak temperatures were set at 1800°C and 600°C, respectively, with an initial temperature of 50°C. The corresponding ΔH values, $\Delta H_{converter}^{max}$ and ΔH_{core}^{max}, are obtained from Figs IV-8-2 and IV-8-3. These values of ΔH are listed in Table IV-8-I.

For any converter design, the maximum available energy change ΔH_{TS}^{max} at the test section, was determined as follows.

The core temperature dependent fission density ratios a_m, b, and $a_m b$ were obtained for assumed average core temperatures of 23, 390, and 600°C from SNARG-1D calculations. It is of interest to note that $a_m b$ varies nearly linearly with ΔT_{core} (see Table IV-8-III).

In the proposed arrangement (Fig. IV-8-1) of the TREAT core—not including the test section or converter—the maximum to average power ratio is 1.27. Hence the average core temperatures of 390 and 600°C correspond to maximum rises of 445 and 712°C, respectively, over an initially assumed uniform temperature of 50°C. Similarly, the maximum inner converter temperature rise is taken to be 1750°C.

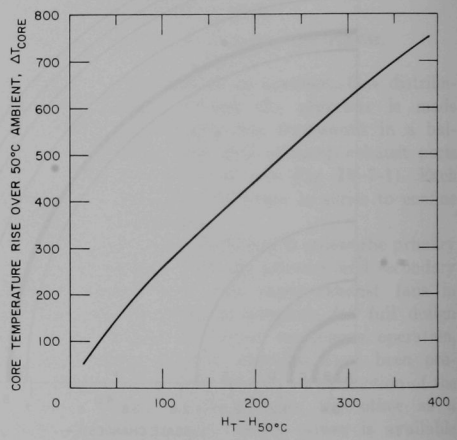

FIG. IV-8-3. Enthalpy Increase versus Temperature Increase in TREAT Core above Ambient 50°C. *ANL Neg. No. 113-834.*

TABLE IV-8-I. LIMITING TEMPERATURE AND ENTHALPY VALUES

	Case 1	Case 2
ΔT_{core}^{max}	350°C	550°C
ΔH_{core}^{max}	150 cal/cc	260 cal/cc
$\Delta T_{converter}^{max}$	1750°C	1750°C
$\Delta H_{converter}^{max}$	1345 cal/cc	1345 cal/cc
$\frac{\Delta H_{converter}^{max}}{\Delta H_{core}^{max}}$	8.97	5.17

TABLE IV-8-II. ISOTOPIC CONCENTRATIONS IN THE CONVERTER, $\times 10^{24}$

Design	Isotope	Inner Converter (1)	Inner Converter (2)	Outer Converter (1)	Outer Converter (2)	(N^B) borated lining, $\times 10^{-3}$
1	U-235	4×10^{-3}	2×10^{-3}	6×10^{-4}	3×10^{-4}	1
	U-238	0.0224	0.0240	6×10^{-5}	3×10^{-5}	
2	U-235	4×10^{-3}	2×10^{-3}	6×10^{-4}	3×10^{-4}	1
	U-238	0.0120	0.0120	6×10^{-5}	3×10^{-5}	
3	U-235	4×10^{-3}	2×10^{-3}	6×10^{-4}	3×10^{-4}	1
	U-238	3×10^{-4}	1×10^{-4}	6×10^{-5}	3×10^{-5}	
4	U-235	2×10^{-3}	1×10^{-3}	4×10^{-4}	2×10^{-4}	1
	U-238	3×10^{-4}	1×10^{-4}	6×10^{-5}	3×10^{-5}	
5	U-235	1.5×10^{-3}	7.5×10^{-4}	3×10^{-4}	1.5×10^{-4}	1
	U-238	3×10^{-4}	1×10^{-4}	4.5×10^{-5}	2.25×10^{-5}	
6	U-235	1.5×10^{-3}	7.5×10^{-4}	2×10^{-4}	1.5×10^{-4}	1
	U-238	3×10^{-4}	1×10^{-4}	4.5×10^{-5}	2.95×10^{-5}	
7	U-235	1.5×10^{-3}	7.5×10^{-4}	2×10^{-4}	1.5×10^{-4}	2
	U-238	3×10^{-4}	1×10^{-4}	4.5×10^{-5}	2.25×10^{-5}	
8	U-235, U-238	Same isotopic concentrations as for Design 7 but containing a 17 pin test section.				

For all designs:
$N^{C}_{inner\ converter} = 0$; $N^{C}_{outer\ converter} = 0.0722$; $N^{Fe}_{inner\ converter} = 0$; $N^{Fe}_{outer\ converter} = 3.343 \times 10^{-5}$. $(t_W)_{total} = 0.349$ cm; $(tN)^{B}_{borated\ lining} = (1 + 1.58)\ 10^{-4}$ atoms/cm², except for Design #7. $t \equiv$ thickness.
For designs 1–6 incl. $(tN)^{B}_{borated\ lining} = (1 + 1.58)\ 10^{-4}$ atoms/cm².
For designs 7 and 8 $(tN)^{B}_{borated\ lining} = 2(1 + 1.58)\ 10^{-4}$.

For any assumed core temperature rise the enthalpy ΔH_{core} is obtained from Fig. IV-8-3; the corresponding inner converter temperature rise, $\Delta T_{converter}$, and the energy available for melting the test sample, ΔH_{TS}, are then evaluated with the aid of Eqs. (3) and (1), respectively.

From the values of ΔT_{core} and $\Delta H_{TS}/\Delta H_{melt}$ obtained at two temperatures, we obtain by interpolation the maximum allowable ratio $\Delta H_{TS}/\Delta H_{melt}$; i.e., the ratio for which ΔT_{core} or $\Delta T_{converter}$ does not exceed their limiting values of 550 and 1750, respectively.

Tables IV-8-II and IV-8-III list the isotopic concentrations used in converter assembly calculations and the power distribution data for a number of converter designs. Designs 0–1 and a 7-pin mixed oxide sample cluster and loop identical with those described in Ref. 1.

Design 0 is similar to that of TREAT without a converter assembly. Design 1 has a hard neutron spectrum with a maximum-to-minimum power ratio of ~1.001 in a fuel pin of the test section, and maximum available energy at the center line of the test section of 1.5 times that required for total melting of a UO_2 specimen.

Relaxation of the initial requirements specified in the first paragraph made possible designs 4, 5, 6 and 7, in which the maximum available energy factor for melting the test sample is about 2.5, in contrast with the ratio of 1.5 for Design 2. The factor of about 2.5 corresponds to $2.5 \times 13{,}346 \approx 33{,}360$ W/cc of energy to carry out TREAT constant-power excursions of several seconds duration.

Design No. 8 is identical with Design 7, except that the test section contains 17 fuel pins rather than 7, in spite of the change in sample size. Both the maximum available energy and the variation of power across the cluster are acceptable.

Relaxation of the initial requirements referred to above has resulted in only a small amount of softening of the neutron spectrum in the test section, as indicated in Table IV-8-IV.

The effects of the converter assembly on the nuclear properties of TREAT are summarized below:

a) *Temperature coefficient of reactivity*—$(\delta k/°C) \times 10^4$

Temperature Range	Reference Design 0	#1	#7	#8
23–390°C	2.52	1.38	1.96	1.94
23–600°C	1.83	1.12	1.56	1.55
390–600°C	0.62	0.81	0.87	0.86

TABLE IV-8-III. POWER CHARACTERISTICS OF CONVERTER DESIGNS AND MAXIMUM AVAILABLE ENERGY FOR MELTING OF FUEL PINS IN THE TEST SECTION

Design	Assumed[a] Average Core Temp. T, °C	k	$-10^4\overline{\left(\frac{\partial k}{\partial T}\right)}$, Room to Temp. T	a_m[b]	b[c]	$a_m b$[d]	$\left(\frac{P_{max}}{P_{min}}\right)_{TS}$[e]	Converter[f] Temperature Rise above 50°C, °C	Corrected[g] Limiting Value of Converter Temperature above 50°C, °C	Corrected[h] Rise of Core Temperature above 50°C, °C	$\frac{\Delta H^{center\ line}_{TS}}{\Delta H^{(UO_2)}_{melt}}$
0[j]	23	1.1643	—	—	50.	—	3.71				
	390	1.0710	2.52	—	59.	—	4.50				
	600	1.0585	1.83	—	61.	—	4.96				
1	23	1.1627	—	0.302	21.1	6.36	1.002				
	390	1.1116	1.38	0.319	30.0	9.58	1.001	2340	1750	350	1.33
	600	1.0947	1.117	0.323	33.8	10.92	1.001				
2	390	1.1413		0.274	34.6	9.49	1.006	2330	1750	355	1.52
	600	1.1256		0.279	38.5	10.76	1.005				
3	390	1.1793		0.228	42.1	9.63	1.024	2220	1750	345	1.90
	600	1.1637		0.228	46.4	10.60	1.023	2370			
4	390	1.1116		0.154	40.9	6.3	1.070	1670	1610	422.5	2.50
	600	1.0941		0.155	45.4	7.04	1.068	2770			
5	390	1.0920		0.131	40.6	5.32	1.101	1430	1365	422.5	2.50
	600	1.0756		0.131	45.3	5.93	1.106	2510			
6	390	1.087		0.125	40.3	5.04	1.104	1360	1350	422.5	2.49
	600	1.071		0.131	44.9	5.88	1.108	2500			
7	23	1.1424	—	0.117	29.8	3.48	1.108				
	390	1.0703	1.95	0.121	38.2	4.62	1.103	1250	1230	422.5	2.36
	600	1.0520	1.56	0.126	42.5	5.35	1.105	2350			
8	23	1.1410	—	0.128	26.9	3.44	1.150				
	390	1.0695	1.94	0.132	34.9	4.60	1.140	1250	1220	422.5	2.16
	600	1.0514	1.55	0.135	39.1	5.30	1.138	2330			

[a] In the present TREAT core designs (max/average) power ≈1.29.
[b] $a_m \equiv \Delta H^{max}_{converter}/\Delta H^{center\ line}_{TS}$
[c] $b \equiv \Delta H^{center\ line}_{TS}/\Delta H^{max}_{core}$.
[d] $a_m b \equiv \Delta H^{max}_{converter}/\Delta H^{max}_{core}$.
[e] $(P_{max}/P_{min})_{TS} \equiv$ max/min ratio of power in a test pin in TS.
[f] Converter temperature rise obtained from Eq. (3) and graph of Fig. 1.
[g] Limiting value of converter temperature rise is 1750° for $\Delta T^{max}_{core} \leq 550$°C.
[h] Corrected core temperature rise is that value for which $\Delta T^{max}_{converter}$ or ΔT_{core} do not exceed time limiting values of 1750°C and 550°C, respectively.
[i] $\Delta H^{center\ line}_{TS}/\Delta H^{UO_2}_{melt} \equiv$ ratio of available energy per cc of test section at center line to energy required for complete meltdown of one cc of UO_2.
[j] Reference core.

TABLE IV-8-IV. AVERAGE ENERGY OF FISSION DENSITY,

$$\bar{E}_\ell \equiv \sum_i E_i \int_{E,V} \phi_\ell \Sigma_{f,\ell}\, dV dE \Big/ \sum_i \int_{E,V} \phi_\ell \Sigma_{f,\ell}\, dV dE, \text{ MeV}$$

Design	Center Pin	Ring	Inner Converter 1	Inner Converter 2	Outer Converter 1	Outer Converter 2
1	0.650	0.634	—	—	—	—
7	0.527	0.474	0.316	0.197	0.106	0.0267

The reduction in $(\delta k/\delta T)$ with increasing temperature is expected. This may be seen readily from the equation derived using Fermi Age theory[3] (neglecting the non-1/v correction in U-235):

$$\delta k_{eff} = \frac{\sqrt{\frac{\Sigma_2}{\Sigma_1}} - 1}{\sqrt{\frac{\Sigma_2}{\Sigma_1}} + \frac{1}{L^2B^2}},$$

where subscripts 1 and 2 refer to initial and final temperatures, respectively.

It is seen that there is a small reduction in the temperature coefficient of reactivity of the converted TREAT design over that of the reference core.

b) *Control rod worth of the central ring of 8 rods*

The presence of converter Design 7 was calculated to reduce the total rod worth about 4% Δk for an initial worth of 22% Δk.

c) *Neutron lifetime*

The effect of the converter assembly was to reduce the prompt neutron lifetime by about 2×10^{-5} sec below the original value of 9.0×10^{-4} sec.

Our SNARG-1D calculations refer to a core with infinite height. The results of fission density ratios apply to the actual TREAT reactor of finite height as well, since we have a uniform cosine variation of axial flux.

These calculations also refer to a converter having thermal properties of solid UO_2. In Designs 5–8, in which the amount of U-238 has been greatly reduced, use of a converter with a UO_2-ZrO_2-CaO core should yield a cooler converter than that indicated in Table IV-8-IV, by about 4%.

References

1. H. P. Iskenderian, *Conversion of the Transient Reactor Test (TREAT) Facility for Testing Fast Fuel Subassemblies*, Reactor Physics Division Annual Report, July 1, 1966 to June 30, 1967, ANL-7310, pp. 295–299.
2. G. J. Duffy, H. Greenspan, S. D. Sparck, J. V. Zapatka and M. K. Butler, *SNARG-1D, A One-Dimensional Discrete-Ordinate, Transport Theory Program for the CDC-3600*. ANL-7221 (1966).
3. H. P. Iskenderian, *Physics Analysis of the TREAT Reactor Design*, ANL-6025 (1959).
4. F. S. Kirn, J. F. Boland, H. Lawroski and R. D. Cook, *Reactor Physics Measurements in TREAT*, ANL-6173 (1960).

IV-9. Analytical Studies of Experiments on Transient Sodium Vaporization and Expulsion in Fast Reactor Coolant Channels[1]

N. W. Hough,* C. E. Dickerman and D. A. Daavettila†

An analytical study was conducted for the purpose of specifying experimental parameters for a first set of experiments in the Transient Reactor Test (TREAT) Facility to check D. MacFarlane's model[2] of transient sodium vaporization and expulsion from a fast reactor coolant channel. The SAS-I code was used to perform a parameter study which investigated the experimental uncertainties involved in specifying the TREAT experiments. The results of this parameter study were used to specify the experiments and predict how well the model could be checked.

The proposed experiments were planned to study the sodium hydrodynamics only, and therefore fuel failure could not occur during the experiment. For this reason, a limit of 40% fuel melted was set as the threshold of fuel failure for the calculations. The calculational model for the parameter study treated a single fuel pin and its associated coolant. Although the test equipment (Mark-II Integral Sodium Loop) had the capability of containing a fuel pin array, a single pin was decided upon as being simplest and did not assume anything beyond MacFarlane's model. To define the flow area to be associated with the fuel pin, a flow tube was designed which essentially consisted of two concentric pipes with an evacuated gap between them. The pipe dimensions were specified to give the correct coolant volume fraction for the fuel pin. The fuel type used in the calculations was initially chosen to be uranium-5 w/o fissium because of its good heat transfer properties. Preliminary calculations showed that this was not a good choice since too much fuel had melted by the time coolant boiling began for the transients studied in this work. Therefore uranium carbide gas-bonded fuel pins were specified. The fuel pins were 0.325 cm o.d., with type 304 stainless steel cladding 0.331 cm i.d. and 0.368 cm o.d. The fuel pins were 45 cm long, with the upper 5 cm being a zero heat generation region for expansion of fission and bond gases. The system pressure for all experiments was three atmospheres. This pressure corresponds to a saturation temperature of about 1016°C for liquid sodium and was a reasonable pressure for current fast power reactor designs. The initial temperature for the experiments was to be 400°C, since this was close to the inlet temperature of EBR-II and therefore represents an inlet temperature in the range of interest for fast power reactors. The inlet temperature of 400°C was also chosen because the sodium loop was rated at 538°C, and the 400°C inlet temperature gave a convenient margin.

* Student, Michigan Technological University, Houghton, Michigan.

† Michigan Technological University, Houghton, Michigan.

Three case studies were to be used in the initial TREAT experiments: a rapid rise to constant power, a short burst transient, and a constant power with a flow decay transient.

For each of the three cases the parameters which were varied were those thought to involve the greatest amount of uncertainty for the experimental conditions. The variable parameters were: bond conductance parameter, initial mass flow rate, superheat required to initiate boiling, constants for the convective heat transfer coefficient correlations, and the pump decay constant. For the fuel coefficient of expansion due to melting, no published data are available. The value used was that for uranium dioxide and had to represent an approximation to the actual value.

A flat axial power profile was used in the calculations since it was easier to achieve this in the experimental setup than a shaped profile. A number of calculational difficulties were encountered in using a flat power profile. In these calculations instabilities were noticed at the beginning of coolant boiling; this caused the calculation to fail to converge. The manner in which the instability occurred depended on the particular set of input parameters, but instability always occurred just at the start of boiling or shortly thereafter. MacFarlane's original ALGOL code was checked for instability and it was found that it too became unstable at the point of boiling for flat axial power profiles. G. Fischer and N. McNeal (Reactor Physics Division, Argonne National Laboratory) also encountered this problem in subsequent calculations for the Swimming Pool Research Reactor, Cadarache, France (CABRI) single-pin experiments. In both this work and the work of Fischer and McNeal it was found that a slight shaping of the power profile resulted in a stable calculation. Some calculations were run for pressures below the specified three atmospheres and it was noticed that some instabilities did occur for pressures $\leqslant 2$ atm.

In general, the calculations for the three case studies showed that uncertainties in the fuel bond conductance parameter affected the condition of the fuel fairly strongly, but not the time to boiling or the point of voiding in the channel. The coolant expulsion velocity was shown to be higher for low bond conductance parameters than for high bond conductance parameters. The mass flow rate was shown to affect quite strongly the time to boiling, point of channel voiding, and the condition of the fuel at incipient boiling. The effect of mass flow rate on the expulsion velocities was inconclusive since calculation instabilities obscured these data. As may be expected, the mass flow rate was shown to very strongly influence the time to boiling and the point of initial channel voiding for the flow coastdown cases. Variations in the convective heat transfer coefficient were shown to have very little effect on the time to boiling, point of initial channel voiding, and the fuel condition at the start of boiling. The amount of liquid superheat to initiate boiling strongly affected the time to boiling and the condition of the fuel at the start of coolant boiling, but the point of channel voiding showed no effect.

The above results are for calculations using a flat axial power profile. They are somewhat inconclusive due to the convergence difficulties mentioned above. Further work of this nature for slightly shaped power profiles is continuing.

These preliminary calculations have indicated that the flow coastdown transients may be the best source of data with which to check the model. Although considering the limited instrumentation currently available on the Mark II loop, it would be doubtful whether the experimental data would allow one to either accept or reject details of MacFarlane's model.[2]

References

1. N. W. Hough, *A Study of an Analytical Model for Transient Boiling of Sodium in Reactor Coolant Channels*, M. S. Thesis, Michigan Technological University, Houghton, Michigan (June 1968).
2. D. R. MacFarlane, *An Analytical Study of the Transient Boiling of Sodium in Reactor Coolant Channels*, ANL-7222 (1966).

IV-10. Modifications of the Transient Heat Transfer Code ARGUS

J. P. Regis

The ARGUS transient heat transfer code[1] is a highly flexible program for computing transient temperatures in a cylindrical geometry. Its features include provision for up to 25 regions, multiple coolant channels, and arbitrary time functions for heat input and coolant flow. As such, it is particularly well suited to analysis of Transient Reactor Test (TREAT) Facility experiments and is complementary to the more recent four-region code[2] developed as part of the Safety Analysis System code package.

As needs have arisen for special calculations in analysis of TREAT fast reactor safety experiments, minor modifications have been made in duplicates of the ARGUS code deck. These changes have included the specification of inlet coolant temperature as a function of time and a (non-reversible) change in fuel surface conductance keyed to the fuel "slumping temperature". In addition to these modifications, made for limited usage and restricted to special code decks, two changes have been made in the general ARGUS code and these have been made operational for routine use. They consist of additions of a flexible plotting package and a change in the heat transfer calculations for solid regions. The latter gives a more accurate calculation for materials with the low thermal conductivity k and large changes in k as a function of temperature which are characteristic of oxide fuels.

Plotting Option

The plotting option has been added to ARGUS in order to eliminate the need to plot the results by hand. The option will plot temperature as a function of time, as a function of radial position, or as a function of axial position.

The graph size is 15 cm (6 in.) high by 20 cm (eight in.) long. It is labeled with the title and problem number and a key to describe each curve. A curve may consist of an unbroken line, symbols marking each point connected by straight line segments, or unconnected symbols. Up to six curves of the same type and from the same problem can be plotted on one graph. Thus, for example, the user can plot on the same graph the fuel centerline temperature and the fuel surface temperature as functions of time. Such graphs are convenient for comparison purposes.

The problem to be plotted, the type of plot, the number of curves to be plotted on one graph, which curves to plot, and what type of curve (unbroken line, symbols, etc.) are determined by input cards. The set of input cards describing one graph is a plot data set. There are as many plot data sets as there are graphs to be plotted.

Modification of Solid Region Heat Transfer Calculations

The basic treatment of solid region heat transfer in the new version of ARGUS is that used in an "experimental" hybrid computer code developed earlier.[3]

In the original difference equations, the heat stored at a node point i is calculated by the relationship

$$\text{Heat stored} = \text{Heat conducted in} - \text{Heat conducted out} + \text{Heat generated.}$$

The heat conducted into node point i is defined as coming from node point $i - 1$.* The heat conducted from node point i goes to node point $i + 1$.* The heat generated is that generated at node point i. Originally, ARGUS[1] calculated heat transfer from node point i to node point $i + 1$, using the value of k for the temperature of node point i. However, when the heat stored at node point $i + 1$ was calculated according to the above relationship, the value of k for the temperature at node point $i + 1$ is used to calculate heat transfer from node point i to node point $i + 1$. Thus, for the high thermal gradients and large variations in k as a function of temperature typical of oxide fuel calculations, the calculation of heat storage in adjacent points may be inconsistent when the original ARGUS code[1] is used.

In the modified equations, one value of k is used for a given pair of node points, regardless of which node point is under consideration. This value of k is taken to be the linear average of the values of k at the temperatures at node points i and $i + 1$. Included in this modification is an interpolation routine for k. In the original (metal fuel-oriented) version of ARGUS, k has a constant value until a material phase change is reached. Then k acquires a new value which is constant until the next material phase change, and so on. In the modified version, the value of k is interpolated throughout each temperature range.

* These are general definitions. With this convention, the heat transferred can be either positive or negative, depending on the temperature gradient.

REFERENCES

1. D. F. Schoeberle, J. Heestand and L. B. Miller, *A Method of Calculating Transient Temperatures in a Multiregion, Axisymmetric, Cylindrical Configuration. The ARGUS Program, 1089/RE248, Written in Fortran II*, ANL-6654 (1963).
2. J. C. Carter, G. J. Fischer, T. Heames, D. R. MacFarlane, N. A. McNeal, C. K. Sanathanan, W. T. Sha and C. K. Youngdahl, *Fast Reactor Accident Analysis Through Computer Program Development*, Reactor Physics Division Annual Report, July 1, 1966 to June 30, 1967, ANL-7310, pp. 299–300.
3. L. T. Bryant, L. W. Amiot, C. E. Dickerman and W. P. Stephany, *A Hybrid-Computer Program for Transient Temperature Calculations on TREAT Fast Reactor Safety Experiments*, ANL-7374 (1967).

IV-11. Sodium Boiling Transients in Carbide-Fueled Fast Reactors

D. R. MacFarlane, N. A. McNeal, D. A. Meneley and C. K. Sanathanan

Introduction

The work described here is a continuation of previously reported calculations[1,2] on the behavior of large (1000 MWe) sodium cooled fast breeder reactors during sodium boiling accidents. The work described is part of Argonne National Laboratory's fast reactor safety program which has as one of its goals the development of a better understanding of coolant voiding effects in large fast power breeder reactors. The calculations reported previously were based on oxide fueled fast reactors, while the calculations reported here are for carbide fueled systems. Since the physical models and mathematical techniques used in the analysis have already been described in detail in Refs. 1 and 2, these descriptions will not be repeated—except for some changes which have been made to improve the calculation since the last annual report.

Basically the model and calculations are aimed toward analyzing transients which are slow enough so that there is time for heat transfer to the coolant before the threshold for fuel subassembly damage is reached. Accordingly, in both the power and flow coast-down transients we are concerned with cases in which the time to reach coolant boiling after a flow or power perturbation from the normal steady state operating conditions is in the range of 1–10 sec. Once the threshold for coolant boiling is reached, the expulsion of sodium due to boiling occurs fairly rapidly. Voiding times are typically less than several hundred milliseconds.

MODIFICATIONS OF CALCULATIONAL SCHEME

Since performing the calculations for the oxide fueled reactors reported in the last annual report, two significant modifications to the calculational method have been made. The first of these involves adjusting the Doppler coefficient for changes in the local sodium density due to void formation. This is done by linearly interpolating between Doppler values for zero void and a completely voided core. This value of Doppler reactivity is region weighted by the square of the power distribution function, as before, and the total Doppler feedback is obtained by summing the contributions of all the axial segments.

The second improvement involved including the reactivity effects due to heating of the single phase coolant before boiling starts. This is essentially an extension of the calculation of sodium void reactivity worths wherein the density change in the coolant prior to boiling is translated into an equivalent void fraction. Except for these changes the calculational scheme is essentially the same as that reported in Ref. 1.

NUMERICAL RESULTS

The present series of calculations for carbide fueled cores was aimed toward determining whether or not there are significant differences in the behavior of reactor cores, from a safety standpoint, which result from the heat transfer characteristics of the fuel. Accordingly calculations were performed in an attempt to determine the differences in dynamic response of carbide fueled fast reactor cores with unbonded (gas gap) and sodium bonded fuel. The calculations were performed for the large (10,000 MW thermal) annular carbide fueled core described in Ref. 3 which has inner and outer radii of 303 and 375 cm, respectively, and a core height of 110 cm (16,700 liters). The core has fuel rods 0.80 cm in diameter and a maximum fuel thermal rating of 1 kw/cm. The parameters for the reactor are summarized in Tables IV-11-I through IV-11-III. The fuel-to-cladding conductance is expressed in the heat transfer model as

$$bc = \frac{h_b}{\tau(z,t)} \qquad \text{for } bc \leq bc_{max} ,$$

TABLE IV-11-I. PARAMETERS FOR CARBIDE FUELED REACTOR

Core length, L, cm	110
Blanket thickness, R, cm	40
Core diameter (annular)	
Inner radius, cm	303
Outer radius, cm	375
Fuel rod o.d., cm	0.80
Coolant inlet temperature, °C	450
Coolant outlet temperature, at $t = 0$, °C	629
Coolant velocity, at $t = 0$, m/sec	9.8
Maximum fuel thermal rating, kw/cm	1
Maximum steady state heat flux, cal/cm²-sec	95
Channel exit plenum pressure, P_{ex}, atm	3.0
Number of core radial zones	1
Sodium volume fraction	0.494
Fuel volume fraction	0.283
Stainless steel volume fraction	0.168
Control volume fraction	0.055

TABLE IV-11-II. MIDLIFE ISOTOPIC COMPOSITION OF CORE FUEL FOR 110,000 MWd/Tonne BURN UP

(*Midlife fertile/fissile ratio = 5.3*)

U-238	0.737
Pu-239	0.140
Pu-240	0.054
Pu-241	0.009
Pu-242	0.003
F.P. pairs	0.057

TABLE IV-11-III. SODIUM REACTIVITY COEFFICIENT FOR 110 cm CARBIDE ANNULAR CORE[a]

	Length of Channel Segment, cm	$\rho_{Na}(z)$
Core	$z = 0$ (midplane)–11	3.81×10^{-3}
	11–22	3.09×10^{-3}
	22–33	1.79×10^{-3}
	33–44	2.20×10^{-4}
	44–55	-1.24×10^{-3}
Blanket	55–65	-1.07×10^{-3}
	65–75	-3.88×10^{-4}
	75–85	-1.36×10^{-4}
	85–95	-5.01×10^{-5}

[a] $\beta = 2.94 \times 10^{-3}$.
Prompt generation time, $\Lambda = 2.94 \times 10^{-7}$ sec.
A (Doppler), no void $= -2.76 \times 10^{-3}$
A (Doppler), voided $= -1.29 \times 10^{-3}$,
where A (Doppler) $= T(dk/dT)$.
Reactivity change upon voiding entire core plus axial blanket = +$4.10.

where

$bc \equiv$ bond conductance
$h_b \equiv$ bond conductance parameter
$\tau(z,t) \equiv$ variable gap width.

In addition, an explicit term for the radial component (usually small) is included when computing the heat flux across the gap. The bond gap parameters used for the two cases were

	Unbonded (gas gap)	Sodium Bonded
h_b	0.008 watts/cm-°C	0.05
bc_{max}	2.0 watts/cm²-°C	4.0

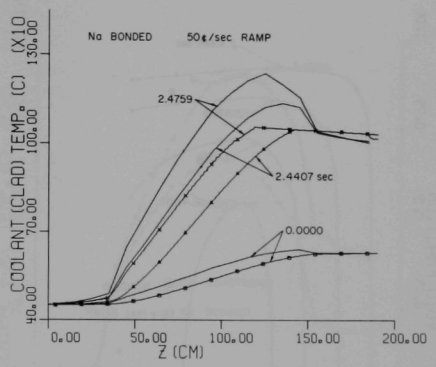

FIG. IV-11-1. Coolant Temperature Profiles at Various Times During Power Transient. *ANL Neg. No. 113-736.*

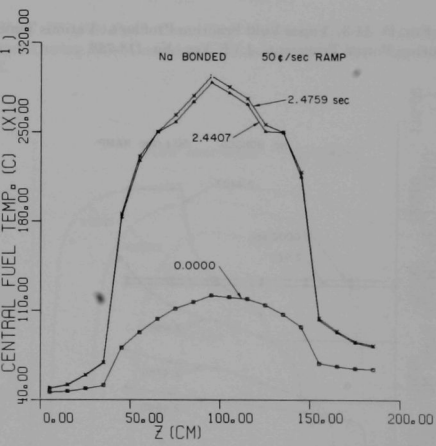

FIG. IV-11-2. Fuel Centerline Temperatures at Various Times During Power Transient. *ANL Neg. No. 113-725.*

The results of a 50¢/sec reactivity transient for the sodium bonded fuel are summarized in Figs. IV-11-1 through IV-11-7. The reactor starts from the steady state operating condition with a maximum fuel centerline temperature of 1219°C and a coolant outlet temperature of 629°C. As shown in Fig. IV-11-1, the time to coolant boiling is 2.42 sec at which point the maxi-

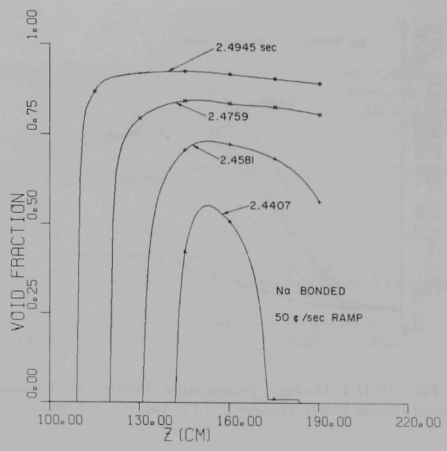

FIG. IV-11-3. Vapor Void Fraction Profiles at Various Times During Power Transient. *ANL Neg. No. 113-732.*

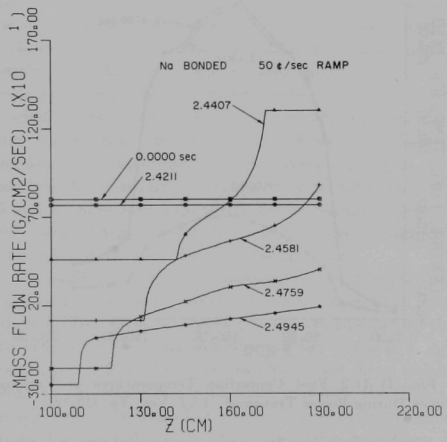

FIG. IV-11-4. Mass Flow Rate Profiles at Various Times During Power Transient. *ANL Neg. No. 113-726.*

mum fuel centerline temperature is 2847°C and the maximum clad surface temperature is 1107°C. The fraction of the fuel molten at the axial center point of the pin is 32%. The curves in Figs. IV-11-1 through IV-11-7 are qualitatively similar to those obtained previously for oxide fueled fast reactors. The reader is referred to Refs. 1 and 2 for a description of the prominent features of these curves.

The transient calculation is terminated due to high void fraction 74 msec after the start of boiling at which time the single phase entrance liquid leg is 109 cm (over 40% of channel in two phase flow). At this time the maximum fuel centerline temperature is 3000°C and the maximum clad surface temperature is 1275°C. The fraction of the fuel melted at the axial center point of the pin is 44%.

An identical calculation was run for the unbonded fuel (that is, 50¢/sec ramp) and all parameters are the same as those listed in Tables IV-11-I through IV-11-III. In this case the fuel centerline temperature at the start of the transient was 1638°C. Since the curves are qualitatively similar to the ones already presented for the sodium bonded case they have not been included

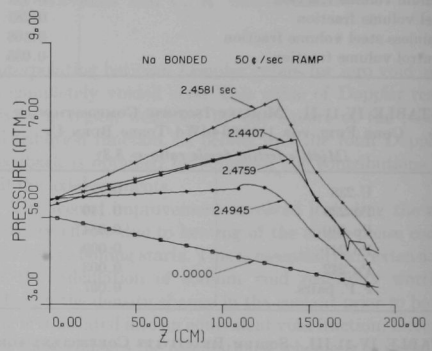

FIG. IV-11-5. Pressure Profiles at Various Times During Power Transient. *ANL Neg. No. 113-733.*

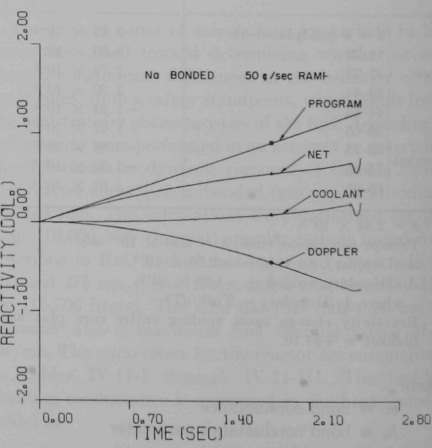

FIG. IV-11-6. Feedback Reactivities Versus Time During Power Transient. *ANL Neg. No. 113-728.*

here. The major differences were that the time to reach boiling is somewhat shorter, that is 2.21 sec, at which time the maximum fuel centerline temperature was 3314°C and the maximum clad surface temperature was 1132°C. The fraction of fuel molten at the axial center point of the pin was 58 %. The calculation in this case was terminated due to high void in the two phase region 75 msec after the start of boiling. At this time the maximum fuel centerline temperature was 3515°C and the maximum clad surface temperature was 1296°C, while the fraction of the fuel molten at the axial center point of the pin was 74 %. The power rise before boiling is somewhat less rapid in the case of the sodium bonded

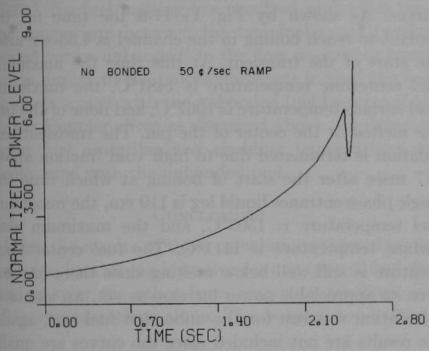

FIG. IV-11-7. Power Level Versus Time During Power Transient. *ANL Neg. No. 113-729.*

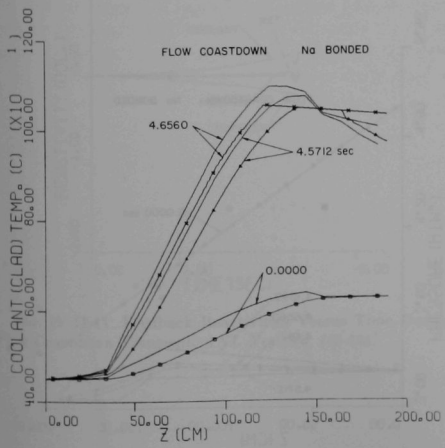

FIG. IV-11-8. Coolant Temperature Profiles at Various Times During Flow Coastdown Transient. *ANL Neg. No. 113-723.*

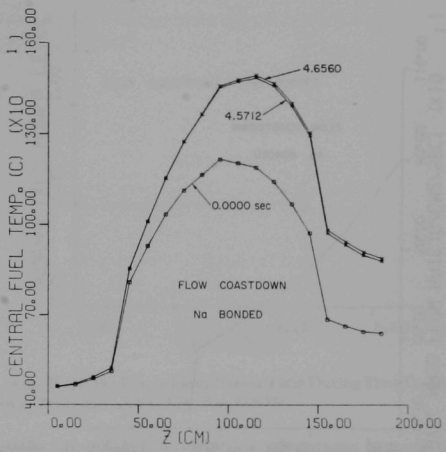

FIG. IV-11-9. Fuel Centerline Temperature at Various Times During Flow Coastdown Transient. *ANL Neg. No. 113-735.*

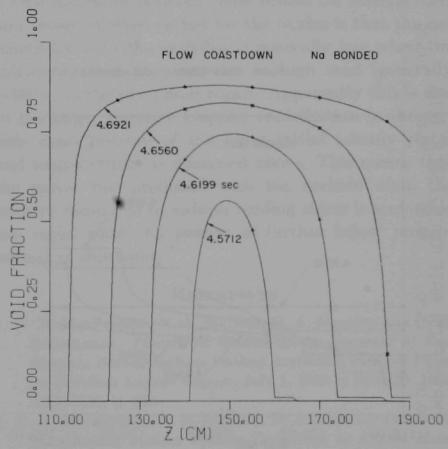

FIG. IV-11-10. Vapor Void Fraction Profiles at Various Times During Flow Coastdown Transient. *ANL Neg. No. 113-724.*

fuel. This is due to the fact that the Doppler feedback is initially larger in the sodium bonded case because of the lower initial fuel temperature and the $1/T$ dependence of the Doppler coefficient. This is shown by the fact that the Doppler reactivity feedbacks were $-74¢$ and $-58¢$, for the sodium bonded and unbonded fuels, respectively, at the time boiling started. Once boiling starts, however, the coolant expulsion behavior is

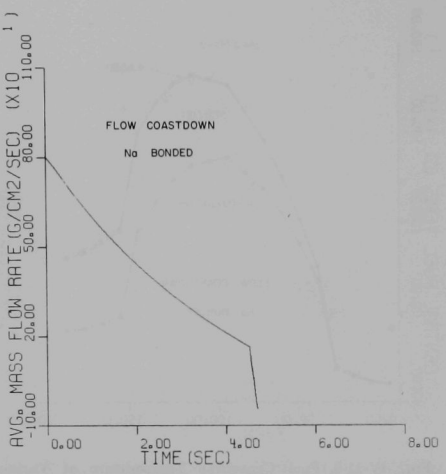

FIG. IV-11-11. Average Mass Flow Rate During Flow Coastdown Transient. *ANL Neg. No. 113-722.*

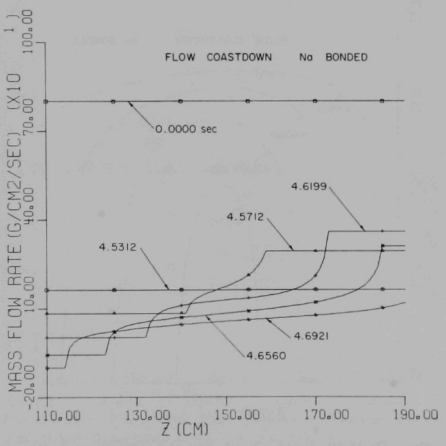

FIG. IV-11-12. Mass Flow Rate Profiles at Various Times During Flow Coastdown Transient. *ANL Neg. No. 113-727.*

similar with the two types of fuel. In general, the results with the unbonded fuel are qualitatively what one would expect—that is, fuel and cladding temperatures and fraction of fuel molten are higher than in the case of sodium bonded fuel.

Flow coastdown transients for the two carbide fuel types were run starting with the same steady state power condition as in the case of the power transients. In a pump coastdown transient the available pressure drop across the channel (the pressure difference between inlet and outlet coolant plenums) is assumed to decrease exponentially, that is

$$\Delta p(t) = \Delta p(0) \exp(-\lambda_p t).$$

A value of $\lambda_p = 0.50$ sec^{-1} was chosen since this gives about 50% of full flow in 2 sec. The results of the calculations for the sodium bonded fuel coastdown are summarized in Figs. IV-11-8 through IV-11-15. Since these curves are qualitatively similar to those obtained for a similar calculation on an oxide fueled reactor reported earlier, the reader is referred to Ref. 2 for detailed descriptions of some of the features of these curves. As shown by Fig. IV-11-8 the time for the coolant to reach boiling in the channel is 4.53 sec after the start of the transient. At this time the maximum fuel centerline temperature is 1481°C, the maximum clad surface temperature is 1067°C, and none of the fuel has melted at the center of the pin. The transient calculation is terminated due to high void fraction about 177 msec after the start of boiling at which time the single phase entrance liquid leg is 110 cm, the maximum fuel temperature is 1503°C, and the maximum clad surface temperature is 1111°C. The fuel center temperature is still well below melting since there has not been an appreciable power increase as yet. An identical calculation was run for the unbonded fuel and, again, the results are not included since the curves are qualitatively similar to those already presented for the sodium bonded case. As in the power transients, boiling

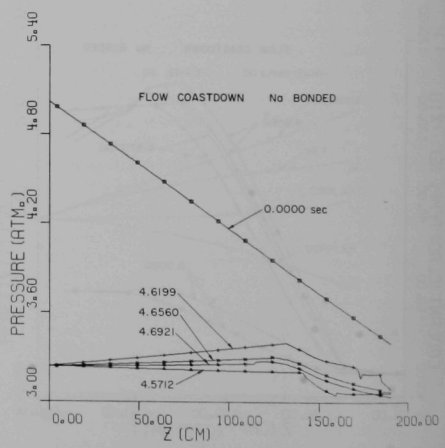

FIG. IV-11-13. Pressure Profiles at Various Times During Flow Coastdown Transient. *ANL Neg. No. 113-730.*

occurs sooner with the unbonded fuel than with the sodium bonded fuel because of the larger Doppler feedback due to the lower initial temperature with the sodium bonded fuel. The Doppler reactivity at the time boiling starts is $-20¢$ for the sodium bonded case versus $-16¢$ for the unbonded case. With the unbonded fuel, the time for the coolant to reach boiling is 4.38 sec after the start of the transient at which time the fuel centerline temperature maximum is 1905°C and the maximum clad surface temperature is 1069°C. The calculation is terminated due to high void fraction in the two phase region 164 msec after the start of boiling at which time the maximum fuel center temperature is 1925°C and the maximum clad surface temperature is 1102°C. No fuel melting has occurred up to this time. The comparison between the two fuel types (sodium bonded versus unbonded) in the flow coastdown transients is similar to the power transients in that the boiling starts sooner with the unbonded fuel because of the weaker Doppler effect as discussed above. As expected, higher fuel centerline and cladding temperatures are encountered with the unbonded fuel.

Conclusions

From the results of these calculations there does not appear to be a strong incentive for one type of fuel-clad bonding over the other from reactivity feedback and safety considerations alone. The sodium bonded fuel,

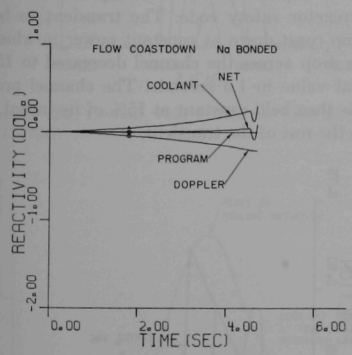

Fig. IV-11-14. Feedback Reactivities Versus Time During Flow Coastdown Transient. *ANL Neg. No. 113-734.*

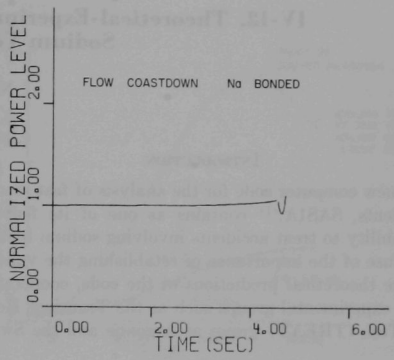

Fig. IV-11-15. Power Level Versus Time During Flow Coastdown Transient. *ANL Neg. No. 113-731.*

on the other hand, has obvious advantages because of the lower fuel center temperatures for a given set of conditions (assuming suitable means are provided for preventing boiling of the bond).

One difference between these results for carbide fuels and those reported earlier for the oxides is that the net reactivity with the carbides is generally less when the calculation is terminated due to high void (generally ~90%) in the two phase region. Apparently this is due to the larger negative Doppler contribution in the carbide cases because of the lower initial (steady state) fuel temperatures as discussed above. This means that the power rise produced with the carbide when the positive ramp due to sodium voiding starts is somewhat less rapid since the reactor is further below prompt critical at this time.

References

1. D. R. MacFarlane, N. A. McNeal, D. A. Meneley and C. K. Sanathanan, *Theoretical Studies of the Response of Fast Reactors During Sodium Boiling Accidents*, Reactor Physics Division Annual Report, July 1, 1966 to June 30, 1967, ANL-7310, p. 310.
2. D. R. MacFarlane, N. A. McNeal, D. A. Meneley and C. K. Sanathanan, *Sodium Boiling Transients in Liquid Metal Fueled Fast Breeder Reactors*, Nucl. Eng. & Design, **7**, No. 5 (1968), p. 411.
3. K. A. Hub, I. Charak, D. E. Lutz, D. H. Thompson, P. F. Gast, D. A. Meneley and I. M. Keyfitz, *Feasibility Study of Nuclear Steam Supply System Using 10,000 MW, Sodium Cooled Breeder Reactor*, ANL-7183 (1966), p. 34.

IV-12. Theoretical-Experimental Collaboration on Fast Reactor Sodium Void Safety Problems

N. A. McNeal

Introduction

A new computer code for the analysis of fast reactor accidents, SAS1A,[1] contains as one of its features the ability to treat accidents involving sodium boiling. Because of the importance of establishing the validity of the theoretical predictions of the code, cooperation with experimental groups such as the Transient Reactor Test (TREAT) group at Argonne and the Swimming Pool Research Reactor (CABRI) group in Cadarache, France, has been pursued.

TABLE IV-12-I. CABRI Experimental Data

Fuel	UO_2
Channel length	100 cm
Diameter of fuel pin	0.58 cm
Cladding thickness	0.045 cm
Coolant volume fraction	0.333
Initial coolant mass flow rate	338.5 g/cm²-sec
Coolant inlet temperature	410°C
Exit plenum pressure	1.5 atm
Total power in pin	1200 W

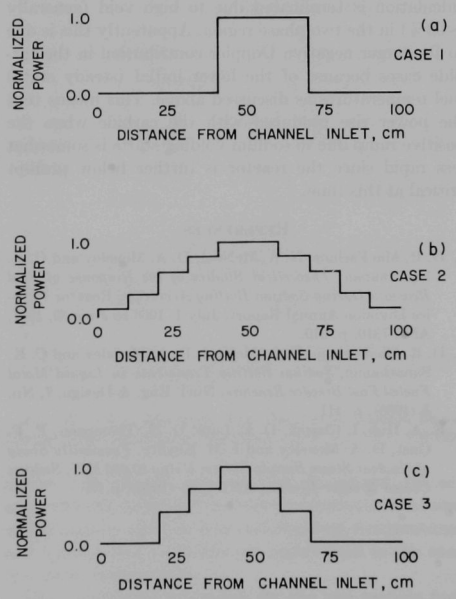

Fig. IV-12-1. Power Profiles for Three Test Cases. *ANL Neg. No. 113-1212.*

Since the reactivity worth of the coolant in large sodium-coolant fast reactors may be on the order of several dollars,[1] the rate of void growth in a coolant boiling accident is very important in determining the progress of the accident. Any mathematical model which attempts to predict the manner in which the void grows in a coolant boiling accident must be verified experimentally. Additionally, the experimental setup should generate void growth patterns which approximate as closely as possible those which occur in actual reactors.

This article discusses the result of computations using data from a proposed CABRI experiment to study sodium boiling accidents. A proposed change in the experiment will be shown to improve the approximation of the CABRI setup to the true fast reactor coast-down accident.

CABRI Experimental Setup

The data in Table IV-12-I and Fig. IV-12-1a was supplied by the people at the CABRI test facility for use as input to a preliminary version of the SAS1A reactor safety code. The transient to be run is a pump coast down at constant power in which the pressure drop across the channel decreased to 15% of its initial value in 1.5 seconds. The channel pressure drop was then held constant at 15% of its initial value through the rest of the transient.

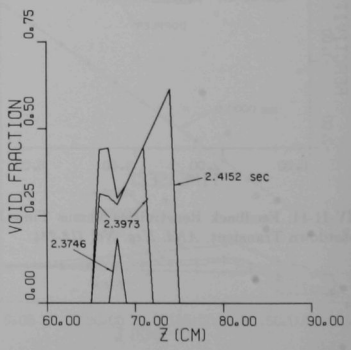

Fig. IV-12-2. Coolant Void Profile for Case 1. *ANL Neg. No. 113-1234.*

RESULTS

The coolant void profiles which were calculated by SAS1A for the above case are shown in Fig. IV-12-2. These profiles do not compare favorably with profiles obtained in previous power reactor calculations using SAS1A.[1, 2] In flow coast-down accidents, the coolant flow is so low when boiling starts that the void tends to grow symmetrically about the point of boiling initiation.[2]

For comparative purposes, a similar calculation was run using the "typical reactor" power shape shown in Fig. IV-12-1b. The resulting void profiles are shown in Fig. IV-12-3. These profiles exhibit a symmetry about the initial boiling point.

The movement of the down-channel interface between liquid and two-phase fluid is governed mostly by the dynamics of the exit liquid slug ejection. The

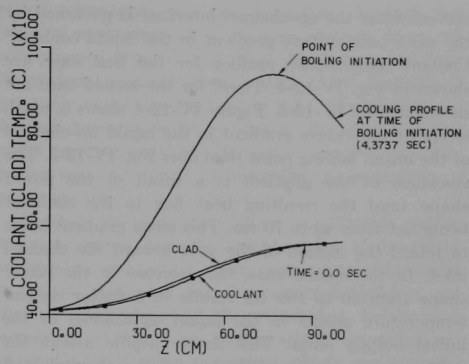

FIG. IV-12-5. Coolant Temperature Profile for Case 2. *ANL Neg. No. 113-1210.*

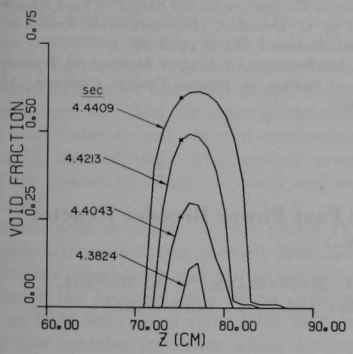

FIG. IV-12-3. Coolant Void Profile for Case 2. *ANL Neg. No. 113-1232.*

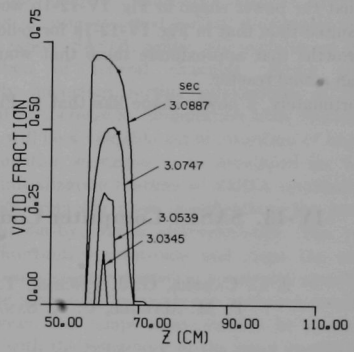

FIG. IV-12-6. Coolant Void Profile for Case 3. *ANL Neg. No. 113-1231.*

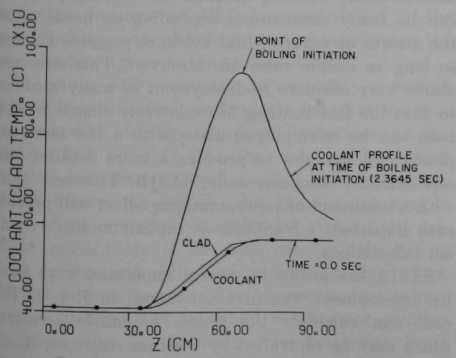

FIG. IV-12-4. Coolant Temperature Profile for Case 1. *ANL Neg. No. 113-1211.*

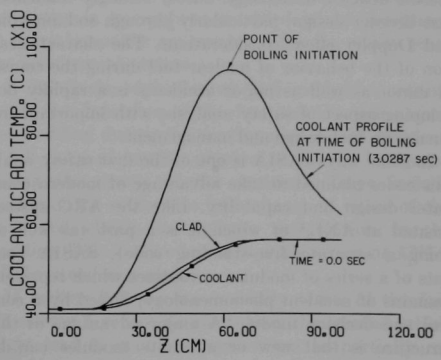

FIG. IV-12-7. Coolant Temperature Profile for Case 3. *ANL Neg. No. 113-1233.*

movement of the up-channel interface is governed by the axial temperature gradient in the liquid coolant.[3] Coolant temperature profiles for the first case are shown in Fig. IV-12-4. Those for the second case are shown in Fig. IV-12-5. Figure IV-12-4 shows a much steeper temperature gradient in the liquid up-channel of the initial boiling point than does Fig. IV-12-5. The steepness of the gradient is a result of the power shape (and the resulting heat flux to the coolant) being flat from 40 to 70 cm. This steep gradient tends to retard the motion of the void toward the channel inlet. In the second case, the decrease in the power shape from 50 to 100 cm results in a flatter coolant temperature profile in the liquid up-channel of the initial boiling point. This flatter profile allows the void to grow more rapidly toward the channel inlet than the profile in the first case.

The coolant voiding model used in SAS1A indicates that the power shape in Fig. IV-12-1b would be better suited than that in Fig. IV-12-1a for generating void growths that approximate those that would occur in an actual reactor.

Unfortunately, a power shape like that in Fig. IV-12-1b may be difficult to achieve. Therefore, a compromise power shape shown in Fig. IV-12-1c is suggested. The results of calculations using this power shape are shown in Figs. IV-12-6 and IV-12-7. The void growth patterns in Fig. IV-12-6 show the symmetry about the initial boiling point better than those in Fig. IV-12-2. These calculations indicate that a power shape similar to that in Fig. IV-12-1c is better suited than that in Fig. IV-12-1a for use in experiments designed to test coolant boiling models.

References

1. D. R. MacFarlane, N. A. McNeal, D. A. Menely and C. K. Sanathanan, *Theoretical Studies of the Response of Fast Reactors During Sodium Boiling Accidents*, Reactor Physics Division Annual Report, July 1, 1966 to June 30, 1967, ANL-7310, pp. 310–317.
2. D. R. MacFarlane, N. A. McNeal, D. A. Meneley and C. K. Sanathanan, *Theoretical Studies of the Response of Fast Reactors During Sodium Boiling Accidents*, Proc. International Conference on the Safety of Fast Reactors, Edited by G. Denielou, (Documentation Francaise, Paris, 1968). Section I, No. 5, pp. 1–26.
3. D. R. MacFarlane, *An Analytic Study of the Transient Boiling of Sodium in Reactor Coolant Channels*, ANL-7222 (1966).

IV-13. SAS1A Computer Code as a Tool for Fast Power Breeder Reactor Safety Analysis

J. C. Carter, G. J. Fischer, T. J. Heames, D. R. MacFarlane, N. A. McNeal, P. M. Margel, C. K. Sanathanan, W. T. Sha and C. K. Youngdahl*

The analysis of fast breeder reactors for their safety characteristics is a major element of fast breeder reactor technology. Safety strongly influences fast breeder design, particularly through sodium void and Doppler effect considerations. The characterization of the behavior of nuclear fuel during the course of minor as well as major accidents is a rapidly developing aspect of safety analysis, with important influence on fuel design and management.

In some ways SAS1A is one of the first safety analysis codes planned to take advantage of modern computer design and capability. Like the ARC system created at ANL,[1] of which it is a part (as well as being a separate free-standing code), SAS1A consists of a series of modules or routines which represent domains of accident phenomenology, linked by a control and decision module. A major advantage of this structure is that new or alternate modules can be created and used without reprogramming other portions of the code. Alternate more sophisticated modules or faster running modules for scoping purposes can be freely substituted, depending on needs or as the growth of experimental evidence suggests change, so long as simple rules are observed. This structure allows very effective re-deployment of many modules so that the fast running but relatively simple SAS1A code can be re-employed along with a few more sophisticated modules to produce a more detailed and sophisticated computer code, SAS1B. This new code, with a minimum of reprogramming effort will provide such important advantages as explicit multiple channel calculations.

SAS1A has grown in several important ways since its development was first announced in Ref. 2. The code can calculate the course of minor accidents which may be controlled by a scram response; it can compute both coast down and ramp type sodium void accidents, with explicit analysis of sodium void de-

* Reactor Engineering Division, Argonne National Laboratory.

velopment and with spatially dependent void feedback and space- and sodium void-dependent Doppler effect reactivity feedback calculation. If the course of the accident becomes severe, the consequent reactor disassembly is computed in SAS1A by means of a two-dimensional Bethe-Tait type of calculation. All of this is executed in a few minutes of IBM 360, Model 50/75 time at one operation, and without intermediate action by the user or machine operator. A major gain in the meaningfulness of accident analysis is that the input to the severe or "Design Basis Accident" is achieved as a logical product of the "initiating events" which lead to the disassembly accident. The Design Basis Accident need no longer be based upon the use of a hypothetically conceived $60/second ramp rate of reactivity addition whose source is poorly defined and for which the degree of conservatism is largely unknown.

SAS1A also contains a module of value to reactor designers and fuel cycle code users. This is an initial condition computing module which itself defines the initial pumping pressure required in order to achieve the required fuel center line temperature, sodium outlet temperature, etc., and for input parameters such as fuel rod diameter and thermal conductivity, as specified by the code user. This module avoids the cut and try procedures which are costly and wasteful of staff time.

The entire code is written in FORTRAN IV. It is undergoing active debugging through 1000 MWe reactor accident calculations and will be publicly available through the Argonne Code Center early in 1969 in both an IBM 360 version and a CDC 6600 version. Because new modules are under active development, improved versions of the code will be made available as significant improvements are achieved. The generous cooperation of other institutions (LASL, APDA), and other divisions of ANL has contributed to the quality of this code development and accelerated the rate of achievements to the present status.

The nature and computational capability of SAS1A are worth specification, particularly for what the code can do and to identify its present limitations. An important first point is that the code employs point kinetics, including delayed neutron accounting. As is well known, the use of point kinetics can lead to very serious errors in certain modes of reactivity addition, particularly if the code user is not alert to these dangers and skilled at minimizing their effect. For many cases however, this approximation is reasonable, and more so for many fast reactor accident conditions than for thermal reactor transients. Point kinetics is used in almost all currently available accident analysis codes, primarily because of computing speed advantages but also in default because fast running space-dependent kinetics routines have not existed until very recently (Ref. 3). A very fast two-dimensional space-dependent code (ARC Module) is presently under development at ANL. The current intention, however, is to use this in the more sophisticated accident code, SAS1B, and to preserve the computing speed of SAS1A by accepting the limitations of point kinetics.

Another speed-giving feature of SAS1A, which again somewhat detracts from the value of the safety information computed, is that only a single channel is explicitly calculated for the thermo-hydraulics, sodium voiding phases of the calculation. In the first version of SAS1A to be made available non-coherence of voiding and space dependent effects are approximated by partitioning reactivity changes for up to four reactor segments to follow the voiding pattern of the one explicitly calculated channel, after accumulation of user-specified further increments of total reactor power. SAS1B, again, will perform an explicit calculation of several channels, giving possibly critically important further information at the expense of an increase in computation time. Studies with SAS1B will be a valuable aid in invention of improved approximation strategies to be developed for SAS1A.

The initialization routines of SAS1A establish automatically from the users specifications the pre-accident thermo-hydraulics characteristics. The routine gives interpretive print-outs and stops the calculation if some reactor operating constraint specified by the code user, such as maximum pumping pressure or fuel center line temperature, cannot be made compatible with the remainder of the input specifications, which include such other parameters as pin diameter and core height. The change in fuel, gas bond, and cladding dimensions and sodium density spatial characteristics in going from specified initial conditions to operating power are computed for the steady state pre-accident calculation.

A relatively sophisticated fuel mechanics routine treats the expansion of the fuel and the stress upon the cladding during the development of the accident. A full range of possible physical states can be treated during the course of the accident. These include closing of the center line hole, change of phase of the fuel, and elastic and plastic deformation in the cladding. This routine has been made a part of ANL's ARC system[1] as a module.

If molten fuel can move axially inside of the fuel pin during a severe accident, then the stresses which might lead to cladding rupture can be partially relieved. A reduction in reactivity should most often accompany this axial fuel motion. A currently rela-

tively simple module of SAS1A, FUELDYN, calculates this motion. It also very carefully watches the state of the cladding, computing its distortion with temperature-dependent strain functions, so that the time during the accident at which cladding rupture occurs is calculated as accurately as possible under limitations of current understanding of the phenomena and of the simplifications of the routine. The axial height along the pin at which rupture occurs is another product of the calculation which is of great importance, since the next phase of the accident is most likely to be dominated by fuel-coolant interaction and extremely rapid reactivity changes due to sodium vapor pressures which might be several hundreds of atmospheres. A module to compute the source of the dynamics of fuel expulsion from the fuel pin and fuel-coolant interaction is a major objective of the SAS1A code. Very early work which seeks only to verify the ability of SAS1A to predict clad rupture for very simplified TREAT experiments has been remarkably successful, but a full module in this area is still unsatisfactorily remote.

An outstanding feature of SAS1A is that sodium voiding dynamics, for both coast-down type accidents and transient voiding accidents is explicitly calculated as a routine or module within the code. This means, particularly, that very accurate feedback response to the two-phase voiding pattern can communicate with the kinetics routine and very accurately describe the course of the accident dynamics during the critical accident interval when the reactor may be approaching prompt critical. The voiding pattern reactivity feedback operates from a table look up procedure of the code. The user supplies the space dependent voiding reactivity terms used in the table, which he has computed using cross sections and codes of his own selection. Another advantage is that since the important Doppler feedback coefficient depends strongly upon the degree of sodium void fraction (*falling* about a factor of two for full voiding) SAS1A requires space- and sodium-void fraction-dependent Doppler feedback data.

Another feedback calculation in SAS1A is that of radial expansion, primarily through expansion of the subassembly cans. This is especially important for slower accidents, such as coast-down accidents, where there is time for heat to diffuse into the subassembly can. Because the lower portion of the subassembly may expand relatively little, because of the constant temperature of the inlet sodium, while the temperature of the upper portion of the subassembly may increase many hundreds of degrees, this response produces a core-height dependent feedback. This is how it is treated in SAS1A. Bowing feedback calculations were explicitly excluded from the current version of SAS1A because investigations showed that bowing behavior is strongly associated with the design of each reactor in a complex way. Naive bowing calculations can be very deceptive. The outer zone, or zones, of enrichment of fast power breeders have strong power gradients which can be a source of vigorous bowing action, however. Therefore, a fully satisfactory safety code must be capable of accounting for this action.

There is a trend in current 1000 MWe fast power breeder designs to emphasize reactor design features which improve economic and engineering aspects of the reactor, often at the expense of some definite increase in sodium-void reactivity gain on voiding, and also at the expense of some loss in shutdown capability through Doppler effect response. This leads to an enhanced desire to reduce uncertainties in calculations of the course of a severe disassembly accident. A major fault of previous "Design Basis Accident" calculations has been that the quite important parameter, the rate of reactivity addition at the start of the severe accident, was usually estimated in a very crude manner. It was often simply postulated.

SAS1A contains as one of its sub-modules a version of the two-dimensional Bethe-Tait weak explosion code MARS,[4] produced by APDA and improved in some important respects at ANL. A major contribution of SAS1A to safety analysis of severe disassembly accidents is that the modules of SAS1A which describe the early stages (the "initiating mechanisms" stages described under Task 10-2.1 of Vol. 10 of the LMFBR Program Plan) generate, in a soundly based manner and within the accuracy of SAS1A analysis, the input terms required for the severe accident, if one comes about as a result of the course of the minor accident. Thus the severe accident (the "Hypothetical Accident" of Task 10-2.2 of the same Vol. 10) calculation no longer relies on the poorly justified initial conditions previously employed.

The particular improvements made in MARS consist of the substitution of a more effective kinetics routine, provision of a routine to solve a second order linear differential equation (which was not provided by APDA and which was essential for use of the code), and a treatment of reactivity changes associated with moving boundaries, as between core zones and between core and blanket.[5] A major advantage of the two-dimensional explosion code is that a pancake reactor can be represented in r-z geometry as a pancake for the first time. Previously pancake reactors have been represented in almost every case in a very awkward spherical approximation until the MARS code was developed.

The Bethe-Tait approximation, as in MARS, is

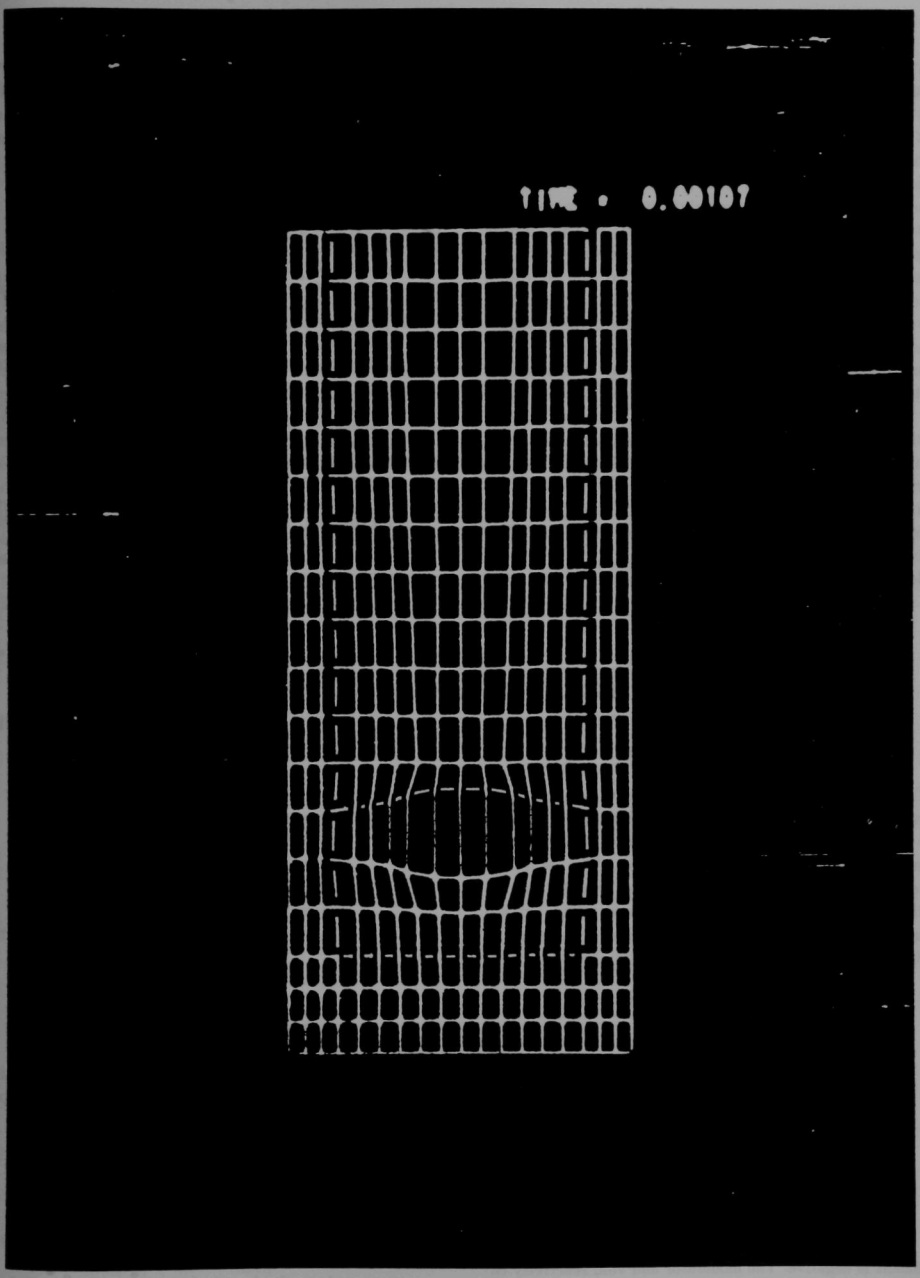

FIG. IV-13-1. Spatial Mesh Distortion of Sodium-voided 1000 MWe Oxide Core During Severe Disassembly Accident, as Calculated by ANL's VENUS Code. *ANL Neg. No. 113-1541.*

very ingenious but also imposes some severe constaints regarding which there may be major doubts for very large breeder accidents. The procedure assumes that events leading up to the disassembly accident are such that the analyst can claim that he knows such critical factors as power and material worth distributions from preliminary calculations. It also assumes that all displacements are very small, so that power shapes and worth distributions essentially do not change during the severe transient. Also, the complete validity of the point kinetics assumption is assumed.

In order to remove some of these doubtful assumptions for the SAS1B code, a two-dimensional hydrodynamics routine has been created by the Applied Mathematics Division of ANL, in cooperation with the Safety Analysis Section of the Reactor Physics Division. This module has been linked with the neutronics-related portion of MARS/SAS for early exploratory and debugging calculations. Figure IV-13-1 is an example of the physical distortions which are computed to occur in a 1000 MWe oxide pancake core in the course of a severe accident.

Because of the importance of the increased information available through employment of this improvement over MARS, this package will be made available to all users in the spring of 1969.[6] This code is entirely in FORTRAN IV language and will be available as IBM 360 and CDC 6600 computer versions.

References

1. B. J. Toppel, *The Argonne Reactor Computation (ARC) System*, ANL-7332, (1967).
2. J. C. Carter, G. J. Fischer, T. J. Heams, D. R. MacFarlane, N. A. McNeal, C. K. Sanathanan, W. T. Sha and C. K. Youngdahl, *Fast Reactor Accident Analysis Through Computer Program Development*, Reactor Physics Division Annual Report, July 1, 1966 to June 30, 1967, ANL-7310, p. 299.
3. K. O. Ott and D. A. Meneley, *Accuracy of the Quasistatic Treatment of Spatial Reactor Kinetics*, Nucl. Sci. Eng. (submitted for publication).
4. N. Hirakawa, *MARS, A Two-Dimensional Excursion Code*, APDA-198 (June 1967).
5. W. T. Sha and R. B. Nicholson, *Maximum Accident of Zoned Fast Reactors*, Trans. Am. Nucl. Soc., **11**, 696–697 (1968).
6. W. T. Sha and T. H. Hughes, *VENUS, A Two-Dimensional Severe Disassembly Code Employing Two-Dimensional Hydrodynamics*, ANL—(to be published).

IV-14. Stability in the Large of Reactor Systems

W. T. Sha

The reactor kinetics models without delayed neutrons, similar to those of H. Smets,[1,2] are employed in this study. The models include Doppler, coolant temperature, and coolant void feedbacks. The stability criteria in the sense of A. Liapounoff via A. Lur'e's method[3] for these systems are derived. The system equations expressed in terms of a critical point may be written as follows:

$$\begin{aligned}
\frac{dP}{dt} &= \frac{\delta k}{\ell}(P + n_0) \text{ for } n_0 > 0 \text{ and } \ell > 0 \\
\frac{dT_F}{dt} &= a_1 P - h_5(T_F - T_M) \\
\frac{dT_M}{dt} &= h_6(T_F - T_M) - (S - S_0) + h_7 v \qquad (1) \\
\frac{dv}{dt} &= h_4(T_F - T_M) - h_3 v \\
\delta k^* &= -\alpha_1 T_F + \alpha_2 T_M + \alpha_3 v - \gamma P,
\end{aligned}$$

where

$p = n - n_0$

$T_F = T_1 - T_{10}$

$T_M = T_2 - T_{20}$

$v = v_1 - v_{10}$

$n \equiv$ neutron density

T_1 and $T_2 \equiv$ fuel and moderator temperatures, respectively

$v_1 \equiv$ coolant void fraction

S is proportional to the rate of heat removal

$\ell \equiv$ the neutron lifetime

δk_0 and $\delta k \equiv$ excessive reactivity at initial time and at any subsequent time, respectively

$h_3 \equiv$ rate of bubble collapse constant

$h_4 = (1 - F)h_8$

$h_5 \equiv$ heat transfer coefficient

$h_6 = Fh_9$

$h_7 v \equiv$ rate of heat added to the liquid phase of coolant due to bubble collapse

$h_8 \equiv$ coolant bubble formation coefficient

$h_9 \equiv$ heat transfer coefficient

* It is explicitly assumed here that the Doppler reactivity coefficient is negative. The moderator and void reactivity coefficients are positive. The generalization of reactivity coefficients taking any arbitrary sign is trivial.

$F \equiv$ fraction of heat going to the liquid phase of coolant

$a_1 \equiv$ heat generation coefficient in the fuel rod

α_1, α_2, and $\alpha_3 \equiv$ magnitudes of reactivity coefficients of Doppler, coolant temperature, and void coefficients, respectively

$\gamma \equiv$ external reactivity control coefficient.

Any quantity with subscript 0 denotes the value at the critical point.

Two cases are considered here. Case 1 assumes that $S - S_0 = 0$, i.e., constant heat removal; Case 2 assumes that $S - S_0 \approx h_2 T_M$, i.e., the rate of heat loss is approximately proportional to the coolant temperature. Since the system Eq. (1) describes the dynamic behavior of the reactor core only, the inlet and outlet conditions of the coolant are regarded as external variables. The two cases considered above serve as upper and lower bounds of actual reactor operating conditions.

Let us make the following sequential transformations:

1) $u = T_F - T_M$.

2) For Case 1

$$u = \frac{a_1}{\lambda_1 - \lambda_3}[(h_3 + \lambda_1)z_1 - (h_3 + \lambda_3)z_3]$$

$$T_M = \frac{a_1[h_6(h_3 + \lambda_1) + h_4h_7]}{\lambda_1(\lambda_1 - \lambda_3)} z_1 + \frac{a_1(h_3h_6 + h_4h_7)}{\lambda_1\lambda_3} z_2 + \frac{a_1[h_6(h_3 + \lambda_3) + h_4h_7]}{\lambda_3(\lambda_3 - \lambda_1)} z_3$$

$$v = \frac{a_1h_4}{\lambda_1 - \lambda_3}(z_1 - z_3);$$

For Case 2

$$u = \frac{a_1(h_2 + \lambda_1)(h_3 + \lambda_1)}{(\lambda_1 - \lambda_2)(\lambda_1 - \lambda_3)} z_1 - \frac{a_1(h_2 + \lambda_2)(h_3 + \lambda_2)}{(\lambda_1 - \lambda_2)(\lambda_2 - \lambda_3)} z_2 + \frac{a_1[h_6(h_3 + \lambda_2) + h_4h_7]}{(\lambda_1 - \lambda_3)(\lambda_2 - \lambda_3)} z_3$$

$$T_M = \frac{a_1[h_6(h_3 + \lambda_1) + h_4h_7]}{(\lambda_1 - \lambda_2)(\lambda_1 - \lambda_3)} z_1 - \frac{a_1[h_6(h_3 + \lambda_2) + h_4h_7]}{(\lambda_1 - \lambda_2)(\lambda_2 - \lambda_3)} z_2 + \frac{a_1[h_6(h_3 + \lambda_2) + h_4h_7]}{(\lambda_1 - \lambda_3)(\lambda_2 - \lambda_3)} z_3$$

$$v = \frac{a_1h_4(h_2 + \lambda_1)}{(\lambda - \lambda_2)(\lambda_1 - \lambda_3)} z_1 - \frac{a_1h_4(h_2 + \lambda_2)}{(\lambda_1 - \lambda_2)(\lambda_2 - \lambda_3)} z_2 + \frac{a_1h_4(h_2 + \lambda_3)}{(\lambda_1 - \lambda_3)(\lambda_2 - \lambda_3)} z_3.$$

3) $$x = \log\left(\frac{P + n_0}{n_0}\right)$$

$$f(x) = n_0(e^x - 1)$$

$$h_1 = h_5 + h_6.$$

The system Eqs. (1) become

$$\begin{aligned} \frac{dx}{dt} &= [-\beta_1 z_1 - \beta_2 z_2 - \beta_3 z_3 - \gamma f(x)]/\ell \\ \frac{dz_1}{dt} &= \lambda_1 z_1 + f(x) \\ \frac{dz_2}{dt} &= \lambda_2 z_2 + f(x) \\ \frac{dz_3}{dt} &= \lambda_3 z_2 + f(x), \end{aligned} \tag{2}$$

where,

for Case 1

$$\lambda_1 + \lambda_3 = -(h_1 + h_3), \lambda_1\lambda_3 = h_1h_3 + h_4h_7,$$

$$\lambda_2 = 0, \operatorname{Re}\lambda_1 < 0, \operatorname{Re}\lambda_3 < 0$$

$$\beta_1 = \frac{\alpha_1 a_1}{\lambda_1 - \lambda_3}(h_3 + \lambda_1) + (\alpha_1 - \alpha_2) \cdot \frac{a_1[h_6(h_3 + \lambda_1) + h_4h_7]}{\lambda_1(\lambda_1 - \lambda_3)} - \frac{\alpha_3 a_1 h_4}{\lambda_1 - \lambda_3}$$

$$\beta_2 = (\alpha_1 - \alpha_2)\frac{a_1[h_3h_6 + h_4h_7]}{\lambda_1\lambda_3}$$

$$\beta_3 = \frac{\alpha_1 a_1}{\lambda_1 - \lambda_3}(h_3 + \lambda_3) - (\alpha_1 - \alpha_2) \cdot \frac{a_1[h_6(h_3 + \lambda_3) + h_4h_7]}{\lambda_3(\lambda_1 - \lambda_3)} + \alpha_3\frac{a_1h_4}{\lambda_1 - \lambda_3};$$

for Case 2

λ_1, λ_2 and λ_3 are the roots of $-\lambda^3 + f_1\lambda^2 - f_2\lambda + f_3 = 0$

$\operatorname{Re}\lambda_1 < 0$; $\operatorname{Re}\lambda_2 < 0$, $\operatorname{Re}\lambda_3 < 0$

$$f_1 = -(h_1 + h_2 + h_3);$$

$$f_2 = h_1h_2 + h_1h_3 + h_2h_3 - h_2h_6 + h_4h_7;$$

$$f_3 = h_2h_3(h_6 - h_1)$$

$$\beta_1 = \frac{a_1}{(\lambda_1 - \lambda_2)(\lambda_1 - \lambda_3)} \{\alpha_1(h_2 + \lambda_1)(h_3 + \lambda_1) + (\alpha_1 - \alpha_2)[h_6(h_3 + \lambda_1) + h_4 h_7] - \alpha_3 h_4(h_2 + \lambda_1)\}$$

$$\beta_2 = \frac{a_1}{(\lambda_1 - \lambda_2)(\lambda_2 - \lambda_3)} \{-\alpha_1(h_2 + \lambda_2) \cdot (h_3 + \lambda_2) - (\alpha_1 - \alpha_2) \cdot [h_6(h_3 + \lambda_2) + h_4 h_7] + \alpha_3 h_4(h_2 + \lambda_2)\}$$

$$\beta_3 = \frac{a_1}{(\lambda_1 - \lambda_3)(\lambda_2 - \lambda_3)} \{\alpha_1(h_2 + \lambda_3) \cdot (h_3 + \lambda_3) + (\alpha_1 - \alpha_2) \cdot [h_6(h_3 + \lambda_3) + h_4 h_7] - \alpha_3 h_4(h_2 + \lambda_3)\}.$$

For simplicity and without losing any generality, it is assumed that all the characteristic roots λ_i are real and negative. Following A. Lur'e's[3] formulation, Liapounoff's function corresponding to the system Eqs. (2) may be written as follows:

$$V = -\sum_{i=1}^{3}\sum_{j=1}^{3} \frac{C_i z_i C_j z_j}{\lambda_I + \lambda_j} + \ell \int_0^x f(x)dx + \frac{1}{2}\beta_2 z_2^2 \quad (3)$$

$$-\dot{V} = [\sqrt{\gamma}\, f(x) + (C_1 z_1 + C_2 z_2 + C_3 z_3)]^2 \quad (4)$$

$$2C_i\sqrt{\gamma} - 2C_i \sum_{j=1}^{3} \frac{C_j}{\lambda_i + \lambda_j} = \beta_i (i = 1, 2, \text{and } 3), \quad (5)$$

where

C_1, C_2, and C_3 must be real and $\beta_2 \geq 0$.

For Case 1 set $C_2 = 0$; for Case 2 discard the last term on the right hand side of Eq. (3).

The stability criteria in the large, based on Eq. (3) for the case of $\gamma = 0$, are:

Case 1	Case 2
1) $\beta_2 \geq 0$ or $\alpha_1 - \alpha_2 \geq 0$.	1) $A_{-1} \geq 0$.
For Case 1	For Case 2
2) $-\frac{\beta_1}{\lambda_1} - \frac{\beta_3}{\lambda_3} > 0$, if $\theta \geq 0$	2) $A_1 > 0$
3) $-\frac{\beta_1}{\lambda_1} - \frac{\beta_3}{\lambda_3} + 4\theta > 0$, if $-\infty < \theta < 0$,	3) $-f_3^2 A_{-3} - 2f_3\sqrt{A_1 A_{-1}} > 0$; [If (3) is not satisfied, then F must be greater than zero in order to maintain stability in the large],

(6)

where

$$\theta = \frac{(\beta_1 - \beta_3)(h_1 - h_3)}{4h_1 h_3}$$

$$A_1 = -\lambda_1\beta_1 - \lambda_2\beta_2 - \lambda_3\beta_3$$

$$A_{-1} = -\frac{\beta_1}{\lambda_1} - \frac{\beta_2}{\lambda_2} - \frac{\beta_3}{\lambda_3}$$

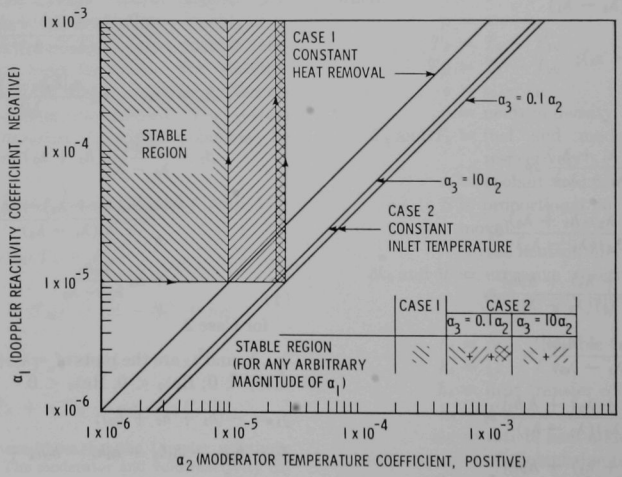

FIG. IV-14-1. α_2 As a Function of α_1 and α_3. *ANL Neg. No. 113-1245.*

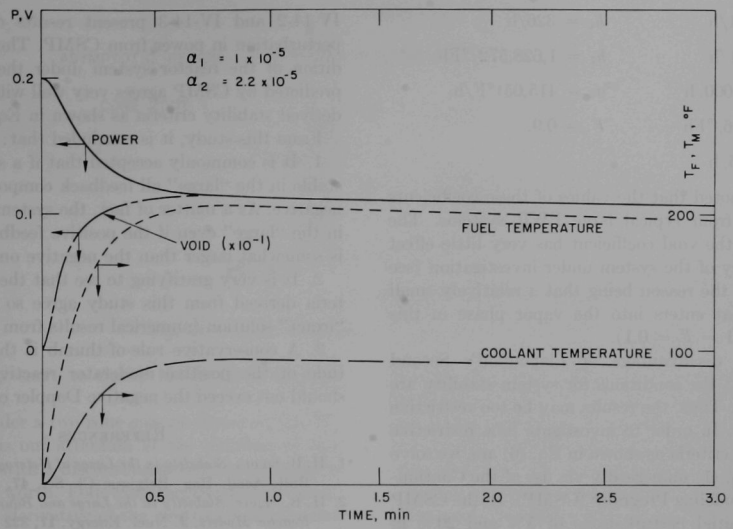

FIG. IV-14-2. System Response With $\alpha_2 = 2.2 \times 10^{-5}$. *ANL Neg. No. 113-1249.*

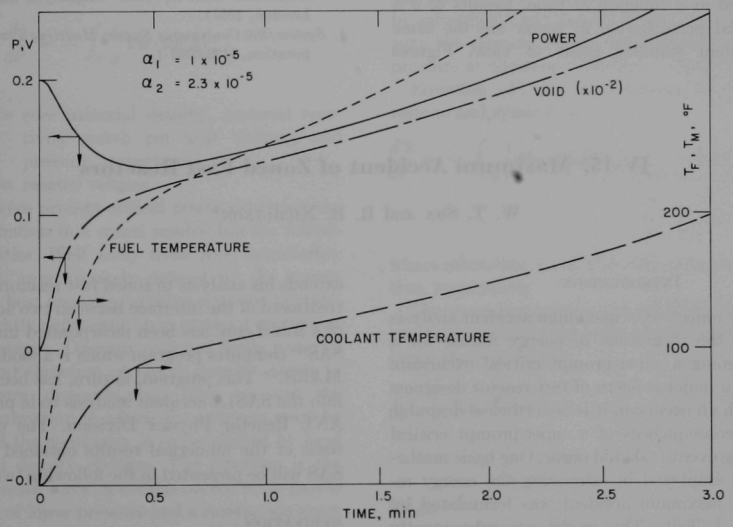

FIG. IV-14-3. System Response with $\alpha_2 = 2.3 \times 10^{-5}$. *ANL Neg. No. 113-1247.*

$$A_{-3} = -\frac{\beta_1}{\lambda_1^3} - \frac{\beta_2}{\lambda_2^3} - \frac{\beta_3}{\lambda_3^3}$$

$$F = [f_3^2 A_{-3} + A_{-1}(2f_1 f_3 - f_2^2)]^2 - 4f_3^2 A_1 A_{-1}.$$

The following numerical example will demonstrate the usefulness of these stability criteria as shown in Eq. (6). Figure IV-14-1 presents the maximum allowable magnitude of α_2 in the parametric space as a function of α_1 and α_3. The values of coefficients of the system Eq. (1) used in the numerical example are

$h_1 = 741/\text{h}$ $\quad h_6 = 326/\text{h}$

$h_2 = 591/\text{h}$ $\quad h_7 = 1{,}628{,}572/°\text{Fh}$

$h_3 = 36{,}000/\text{h}$ $\quad a_1 = 415{,}051°\text{F/h}$

$h_4 = 0.36/°\text{Fh}$ $\quad F = 0.9.$

$h_5 = 415/\text{h}$

It is to be noted that the values of these coefficients are obtained from typical large PWR systems. The magnitude of the void coefficient has very little effect on the stability of the system under investigation (see Fig. IV-14-1), the reason being that a relatively small amount of heat enters into the vapor phase in this example (i.e., $1 - F = 0.1$).

The major disadvantage of Liapounoff's Second Method is that the conditions for system stability are only sufficient. Thus, the results may be too restrictive or impractical. In order to investigate how restrictive these stability criteria as shown in Eq. (6) are, we solve the system Eq. (1) numerically via use of the Continuous System Modeling Program[4] (CSMP). In the CSMP calculation, initial perturbations of 5% and 20% in power were introduced, and the system-dependent variables calculated as a function of time. Results of 5% and 20% initial perturbation in power are the same from the system stability point of view. Figures IV-14-2 and IV-14-3 present results of 20% initial perturbation in power from CSMP. The stability condition of the reactor system under the consideration predicted by CSMP agrees very well with theoretically derived stability criteria as shown in Eq. (6).

From this study, it is concluded that:

1. It is commonly accepted that if a system is to be stable in the "large" all feedback components must be negative. As a matter of fact, the system can be stable in the "large" even if the positive feedback coefficient is somewhat larger than the negative one.

2. It is very gratifying to see that the solubility criteria derived from this study agree so well with the "exact" solution (numerical results from CSMP).

3. A conservative rule-of-thumb is that the magnitude of the positive moderator reactivity coefficient should not exceed the negative Doppler coefficient.

References

1. H. B. Smets, *Stability in the Large of Heterogeneous Reactors*, Bull. Acad. Rag. Belgique Cl. Sci. **47**, 382–405 (1961).
2. H. B. Smets, *Stability in the Large and Boundedness of Some Reactor Models*, J. Nucl. Energy, **17**, 322 (1963).
3. A. I. Lur'e, *Some Non-Linear Problems in the Theory of Automatic Control*, (Her Majesty's Stationery Office, London, 1957).
4. *System/360 Continuous System Modeling Program*, IBM Corporation, H20-0367-1.

IV-15. Maximum Accident of Zoned Fast Reactors

W. T. Sha and R. B. Nicholson*

Introduction

The primary objective of maximum accident analysis is to estimate the magnitude of energy release for a reactor undergoing a super-prompt critical excursion. Although it is a major concern of fast reactor designers to prevent such an excursion it is nevertheless desirable to study the consequences of a super-prompt critical excursion in the event it should occur. One basic mathematical model employed in estimating the energy release during a maximum accident was formulated by H. Bethe and J. Tait.[1] This model was subsequently modified by V. Jankus,[2] and R. Nicholson.[3] One of the modifications of Jankus[2] worth noting is the treatment of the interface between core and blanket with a discontinuous derivative of material reactivity worth. The present work is a generalization of Jankus'[(2)] work and extends his analysis to zoned fast reactors. The detailed treatment of the interface between two adjacent regions of a zoned core has been incorporated into the MARS/SAS[(4)] computer program which is a modified version of MARS.[(5)] This program, in turn, has been incorporated into the SAS1A accident analysis code produced by the ANL Reactor Physics Division. The derivation and some of the numerical results obtained from MARS/SAS will be presented in the following two sections.

* Idaho Division, Argonne National Laboratory.

Derivation

The following derivation is fairly straightforward and no originality is claimed. However, from the authors' knowledge, no detailed derivation of the treatment of interfaces in zoned cores with a discontinous derivative of material reactivity worth has yet appeared in the literature. Furthermore, it is felt that the detailed

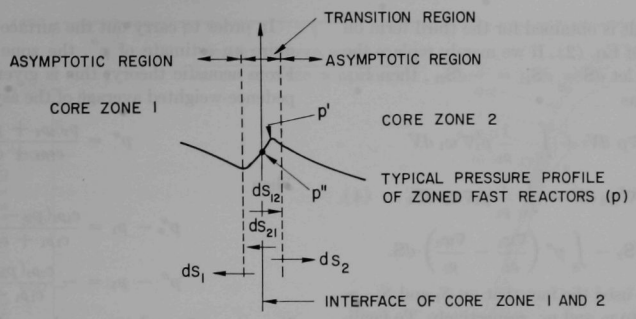

FIG. IV-15-1. Two-Zone Reactor. *ANL Neg. No. 113-1251.*

derivation may serve to clarify the problem involved in the analysis.

Let us consider a two-zone core as shown in Fig. IV-15-1, and focus our attention at the interface of core zones 1 and 2 with a discontinuous derivative of material reactivity worth. Following the Bethe-Tait analysis, the second derivative of the neutron mulitplication factor with respect to time, due to core material motion, can be expressed as

$$\frac{d^2k}{dt^2} = -\int_V \frac{1}{\rho} \nabla w \cdot \nabla p \, dV,$$

where

ρ, w, and p ≡ core material density, material reactivity worth per unit volume, and pressure, respectively

V ≡ reactor volume.

During a severe prompt-critical power excursion the pressure distribution in a zoned reactor has the following characteristics. Well away from zone boundaries, the pressure is approximately defined by the energy deposition, the heat capacity, and the equation of state, and is only slightly dependent upon material movement and density changes. Discontinuities of fissile material enrichment, and therefore of power density, tends to produce pressure discontinuities. But we use the acoustic approximation in which the pressure must be continuous and the continuity is accomplished by local movement and density changes. The interface is the source of a pressure wave. A compressional wave moves into the region of lower pressure and a rarefaction wave moves into the region of high pressure. If the time scale of the power excursion is short enough, then the wave can move only a short distance.

We can divide the reactor volume into two regions. One is a small region which brackets the interface (the transition region); the other is the remainder of the reactor (the asymptotic region). Our results are accurate only if the power excursion is sufficiently sharp so that the transition region is small and in fact the approximation is effected by taking the limit as the transition region thickness goes to zero. However, in practice it is usually the case that the errors are not very great even when the transition region becomes quite large.

Figure 1 shows the nature of the pressure distribution near a zone boundary and the division into transition and asymptotic regions. For convenience we also distinguish between the left and right side of the boundary by subscripts 1 and 2, respectively. The p' and p'' designate the pressure inside the transition region and the pressure at the zone boundary respectively.

Equation (1) can be rewritten in terms of these regions and symbols as

$$\frac{d^2k}{dt^2} = -\int_{V_A} \frac{1}{\rho} \nabla w \cdot \nabla p dV - \int_{V_{T1}} \frac{1}{\rho_1} \nabla w_1 \cdot \nabla p_1' dV - \int_{V_{T2}} \frac{1}{\rho_2} \nabla w_2 \cdot \nabla p_2' \, dV, \tag{2}$$

where subscripts A and T denote asymptotic and transition, respectively.

The second integral on the right hand side of Eq. (2) can be manipulated by a vector identity and the divergence theorem to give

$$\int_{V_{T1}} \frac{1}{\rho_1} \nabla w_1 \cdot \nabla p_1' \, dV = -\int_{V_{T1}} \frac{1}{\rho_1} p' \nabla^2 w \, dV + \int_{S_1} \frac{1}{\rho_1} p_1' \nabla w_1 \cdot d\mathbf{S}_1 + \int_S \frac{1}{\rho_1} p'' \nabla w_1 \cdot d\mathbf{S}_{12}, \tag{3}$$

where

S_1 ≡ surface between the transition and asymptotic regions on the left side of the zone boundary

S ≡ zone boundary surface

$d\mathbf{S}_1$ and $d\mathbf{S}_{12}$ ≡ vector surface elements as shown in Fig. IV-15-1, directed from the transition region to the asymptotic region and from core zone 1 to 2, respectively.

An analogous result is obtained for the third term on the right hand side of Eq. (2). If we merely replace the subscript 1 by 2 and let $d\mathbf{S} = d\mathbf{S}_{12} = -d\mathbf{S}_{21}$, then Eq. (2) may be written as

$$\frac{d^2k}{dt^2} = -\int_{V_A} \frac{1}{\rho} \nabla w \cdot \nabla p \, dV + \int_{V_{T1}} \frac{1}{\rho_1} p_1' \nabla^2 w_1 \, dV + \int_{V_{T2}} \frac{1}{\rho_2} p_2' \nabla^2 w_2 \, dV - \int_{S_1} \frac{1}{\rho_1} p_1 \nabla w_1 \cdot d\mathbf{S}_1 - \int_{S_2} \frac{1}{\rho_2} p_2 \nabla w_2 \cdot d\mathbf{S}_2 - \int_S p'' \left(\frac{\nabla w_1}{\rho_1} - \frac{\nabla w_2}{\rho_2} \right) \cdot d\mathbf{S}. \tag{4}$$

In Eq. (4), we have used the fact that on S_1 and S_2, p_1 and p_2' are identical to p_1 and p_2, respectively. To facilitate the calculation (since we do not know the function p') we approximate $\frac{d^2k}{dt^2}$ by taking its limit as V_{T1} and $V_{T2} \to 0$. In this limit the first term is integrated over the entire volume (excepting the discontinuity which is developed at the boundary by the limiting process). The second ant third terms go to zero as V_{T1} and V_{T2} go to zero. In the fourth and fifth terms S_1 and S_2 become the left and right sides of S; thus, $d\mathbf{S}_1 \to -d\mathbf{S}$ and $d\mathbf{S}_2 \to d\mathbf{S}$. It is then possible to combine the last three integrals of Eq. (4), giving

$$\frac{d^2k}{dt^2} \approx \lim_{\substack{V_{T1} \to 0 \\ V_{T2} \to 0}} \frac{d^2k}{dt^2} = -\int_V \frac{1}{\rho} \nabla w \cdot \nabla p dV - \int_S \left[(p'' - p_1) \frac{\nabla w_1}{\rho_1} - (p'' - p_2) \frac{\nabla w_2}{\rho_2} \right] \cdot d\mathbf{S}. \tag{5}$$

In order to carry out the surface integral, we still require an estimate of p'', the zone boundary pressure. From acoustic theory, this is given as an acoustic impedence-weighted average of the asymptotic pressures:

$$p'' = \frac{p_1 c_2 \rho_2 + p_2 c_1 \rho_1}{c_1 \rho_1 + c_2 \rho_2}. \tag{6}$$

Then

$$p'' - p_1 = \frac{c_1 \rho_1 (p_2 - p_1)}{c_1 \rho_1 + c_2 \rho_2} \tag{7}$$

$$p'' - p_2 = -\frac{c_2 \rho_2 (p_2 - p_1)}{c_1 \rho_1 + c_2 \rho_2}. \tag{8}$$

Equations (7) and (8) may be used to simplify Eq. (5):

$$\frac{d^2k}{dt^2} \approx -\int_V \frac{1}{\rho} \nabla w \cdot \nabla p dV + \int_S (p_1 - p_2) \frac{c_1 \nabla w_1 + c_2 \nabla w_2}{c_1 \rho_1 + c_2 \rho_2} \cdot d\mathbf{S}. \tag{9}$$

This result was also obtained by E. Hicks and D. Menzies[6] but presented without derivation. If we apply a vector identity and the Divergence Theorem to the first term on the right hand side of Eq. (9) and recombine terms and then further set $p_2 = 0$ to approximate a core-blanket interface, we obtain Jankus'[2] result:

$$\frac{d^2k}{dt^2} \approx \int_V \frac{1}{\rho_1} p_1 \nabla^2 w_1 \, dV_1 - \int_S p_1 \frac{c_2 \rho_2}{c_1 \rho_1 + c_2 \rho_2} \left(\frac{\nabla w_1}{\rho_1} - \frac{\nabla w_2}{\rho_2} \right) \cdot d\mathbf{S}. \tag{10}$$

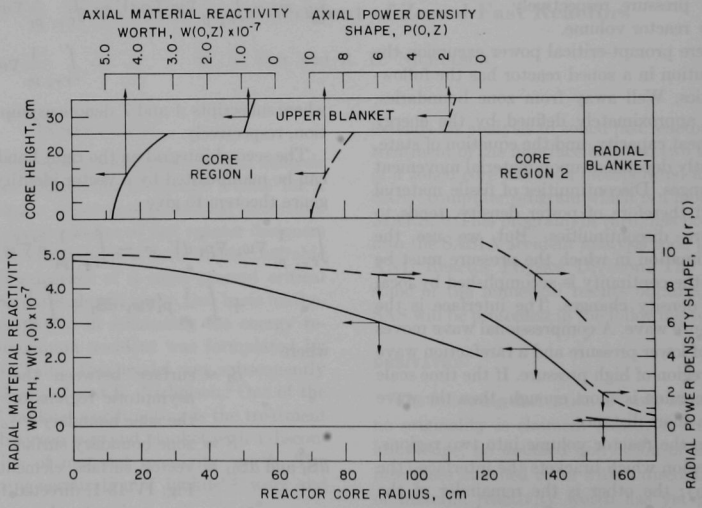

FIG. IV-15-2. Core Characteristics. *ANL Neg. No. 113-1244.*

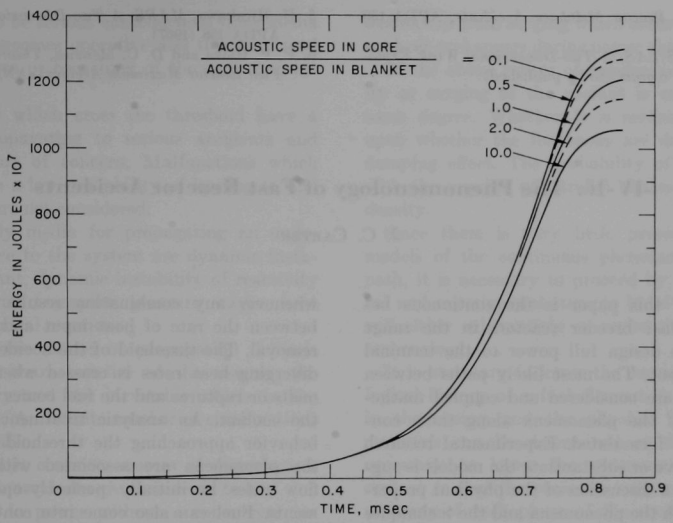

FIG. IV-15-3. Energy Release Versus Time. *ANL Neg. No. 113-1246.*

The derivation presented is quite general and the extension to more than two zones is straight forward.

NUMERICAL RESULTS

In most previous energy release calculations,[3,5] the derivative of reactivity worth at an interface is assumed to be continuous. Hicks and Menzies[6] pointed out that the approximation of the continuous derivative of material reactivity worth at zoned boundaries is not very accurate but often is conservative. Usually, it does not increase the energy yield by more than 20%.

In the present work, we have incorporated Eq. (9) into the computer program MARS/SAS. As an example, upon considering a large zoned pancake core with oxide fuel, it is found that there is a large difference in ∇w between core and blanket as well as between core regions 1 and 2, as shown in Fig. IV-15-2. Under these conditions it also becomes important to have the correct ratio of the acoustic speed, $C_{core}/C_{blanket}$. Figure IV-15-2 shows the core dimension, power density, and material reactivity worth distributions used in the sample calculations. Some of the additional core characteristics are presented below:

Prompt-neutron lifetime	$= 5 \times 10^{-7}$ sec
Initial core average power density	$= 4000$ W/cm^3
Rate of reactivity addition	= \$100/sec
Core mass (½ core) (does not include mass in both radial and axial blankets)	= 8800 kg
Volume fraction of U-238/volume of Pu-239 in region 1	≈ 5.0
Volume fraction of U-238/volume fraction of Pu-239 in region 2	≈ 3.0.

Figure IV-15-3 presents the energy release versus time as a function of various assumed ratios of acoustic speed of the reactor core and blanket. The same acoustic speed was assumed in both core zones 1 and 2 in this calculation.

CONCLUSION

The effect of a discontinuous derivative at interfaces of zoned fast reactors on the total energy release of a maximum accident with various ratios of $C_{core}/C_{blanket}$ has been investigated. From this study, it is concluded that for the current interest of zoned fast reactor designs, this effect on the total energy release is no more than 15%. Whether the total energy yield is increased or decreased depends upon the ratio of core to blanket acoustic speed as well as the material reactivity worth and power density distribution.

REFERENCES

1. H. A. Bethe and J. H. Tait, *An Estimate of the Order of Magnitude of the Explosion when the Core of a Fast Reactor Collapses*, UKAEA-RHM (56)/113 (1956).
2. V. Z. Jankus, *A Theoretical Study of Destructive Nuclear Bursts in Fast Power Reactors*, ANL-6512 (1962).
3. R. B. Nicholson, *Methods for Determining the Energy Release*

in Hypothetical Reactor Meltdown Accidents, APDA-150 (1962).
4. W. T. Sha, *MARS/SAS, A Two-Dimensional Weak Explosion Computer Program* (to be published).
5. H. Hirakawa, *MARS, A Two-Dimensional Excursion Code*, APDA-198 (1967).
6. E. P. Hicks and D. C. Menzies, *Theoretical Studies on the Fast Reactor Maximum Accident*, ANL-7120 (1965).

IV-16. The Phenomenology of Fast Reactor Accidents

J. C. Carter

The subject of this paper is the continuous behavior of large fast breeder reactors in the range of operation from design full power to the terminal point of an accident. The most likely paths between these two points are considered and coupled mathematical models of the phenomena along these continuous paths are formulated. Experimental research intended to disprove or substantiate the models is suggested along with a discussion of the physical properties associated with the phenomena and the techniques for determining these properties.

The large breeder reactor constitutes a closed loop dynamic system with feedbacks in which large amounts of energy can be transformed at a very rapid rate, and therefore it is very sensitive to disturbances to equilibrium. The phenomena of the system are considered to be understood and controllable up to and including full power operation. Above full power, across the accident threshold, and into the realm of irreversible behavior the phenomena are not well understood except for the calculations of maximum energy release based on assumed initial conditions. It is the intent to seek a mathematical representation of these continuous phenomena between full power operation and the terminal points of an accident which causes the reactor to cross the threshold.

The threshold of an accident is defined as a plane separating reversible phenomena from irreversible phenomena. Continuity is maintained by space, energy, and time dependent variables which are common to the phenomena on each side and pass through the plane. Continuity in phenomena is essential in safety analysis for without it the dynamic loop is not closed and the probability of certain events occurring cannot be estimated by analytical methods. Since there is very limited fast reactor operating experience in the range above full power, it is deemed necessary to seek an understanding of the consequences of doing so from concurrent analytical and experimental research.

The causes of accidents and their consequences can be postulated and combined in an infinite number of ways with the potential for an accident existing whenever any combination results in a divergence between the rate of heat input and the rate of heat removal. The threshold of the accident resulting from diverging heat rates is crossed when the fuel casing melts or ruptures and the fuel comes into contact with the coolant. An analytic treatment of the dynamic behavior approaching the threshold is possible when the phenomena are associated with diverging heat flow rates in initially perfectly-operating fuel elements. Fuel can also come into contact with coolant due to mechanical trouble or material defects which may be completely independent of thermal phenomena. When the threshold is crossed because of mechanical trouble and/or material defects it is predictable only by statistical and empirical techniques. Both the phenomena amenable to analytic techniques and the phenomena amenable to statistical techniques are considered.

Since there are also an infinite number of variations in fast reactor design it is necessary to select what is currently considered to be a typical fuel element in a typical core as the physical object upon which to postulate the phenomenology.

The typical fuel element consists of concentric cylinders of fuel (UO_2) bond, casing, and coolant. The overall length of the element's core section is about 100 cm and the casing outside diameter is about 0.63 cm. The axial blankets are about 60 cm long. The typical core is a right cylinder composed of hexagonal cans of fuel elements called subassemblies. The overall dimensions of a unit cylindrical core are those typical of 1000 MWe reactors.

While it is undesirable to operate in the area between design full power and the threshold of an accident it does not create irreversible conditions and no serious damage to the reactor. As the threshold is crossed conditions occur which are irreversible and an accident is considered to have occurred. It may have only minor economic implications or it may have economic plus disaster implications. If there is a continuing transformation of energy into undesirable forms (propagation) after the threshold is crossed

there are likely to be serious consequences since media for propagation becomes operative and this may lead to a core meltdown or breaching of the core containment.

Only accidents which cross the threshold have a possibility of propagating to serious accidents and these are therefore of concern. Malfunctions which are likely to have a low probability of leading to fuel element failures are not considered.

The most likely media for propagating an undesirable disturbance to the system are dynamic instability of the coolant, dynamic instability of reactivity feedbacks, material transport, pressure waves, heat transfer, and chemical reactions.

The rate and the extent of propagation depends upon the design characteristics of the reactor, the irradiation history and the inevitable effects in the fuel and structure. An infinite number of combinations are possible here also.

Some of the most common sources of disturbances which may lead to accidents are considered to be:

1. An increase in power without a concurrent increase in coolant velocity. An example is a reactor excursion to which the feedbacks and control system cannot respond.

2. A dynamic unbalance in the various reactivity feedbacks. The phase angles and amplitudes frequently shift during operation in a most inexplicable manner due to such things as dynamic unbalance in coolant flow, spectral shifts, and migration of fissionable material.

3. A restriction in the flow of coolant from any of a number of causes. This is particularly serious when only one or a few elements are involved since it is difficult to detect before the fuel element melts. This could occur as a result of material transport. Material which may comprise parts of the reactor system or which may be extraneous objects inadvertently left on the reactor may be carried into the filters or may clog flow passages.

4. Vapor formation to the extent that the heat transfer rate from casing to coolant is reduced to the point where the fuel element is vapor bound and melts down into the bottom of the subassembly. This situation could occur as the result of non-uniformity in the fuel, fuel swelling, or operating the reactor above full power. A serious condition is considered to occur if for any reason coolant has been vaporized and coolant returns to a hot fuel element. The rapid formation of coolant vapor is almost certain to result in strong pressure waves.

5. Dynamic instability of the coolant for which the control system and the auxiliary cooling system cannot compensate. This may result from pump troubles or from surging which occurs in parallel channel heat exchangers during power changes.

Of the above causes of accidents, dynamic instability or surging of the coolant is certain to occur in some degree. Whether it is serious or not depends upon whether the feedbacks are designed to have a damping effect. The probability of surging increases with the number of parallel channels and the power density.

Since there is very little precedent for creating models of the continuous phenomena along a given path, it is necessary to proceed by alternate analytical and experimental steps to build the models which will either substantiate or revise the postulated phenomenology.

It is necessary to know the continuous phenomenological history of a fuel element so that the pressure in the casing and the physical properties of the materials can be determined at the crossing. It is necessary to know the continuous history of the coolant so that the pressure, temperature and relative amounts of each phase of the coolant are known at the instant of crossing. When a fuel elements fails, the fuel bond, casing, and coolant come into contact. The amounts involved and the rates with which they come into contact will determine what, if any, mechanism and media exist for propagating the failure.

The result of this concurrent analytical and experimental effort to bridge the gap between design operating conditions and the terminal point of an uncontrollable operating condition hopefully will be a mathematical representation of the continuous phenomena substantiated by experimental research. The models are created in the following sequence: models of single fuel elements, models of fuel elements connected in parallel, models of subassemblies connected in parallel, and a model of the reactor system.

Phenomenological Paths

In an accident tree (now being prepared) it is shown that there can be a large number of phenomenological paths between a disturbance to the closed loop dynamic system representing a large ceramic fueled fast reactor and the terminal point of the continuous sequence of events set in motion by this disturbance.

There is considered to be a high probability that these paths wherever they originate converge toward a common path as they leave design operating conditions and approach the threshold of an accident and that this common path if it crosses the threshold diverges into paths leading to an infinite number of terminal points. (Fig. IV-16-1). The continuous

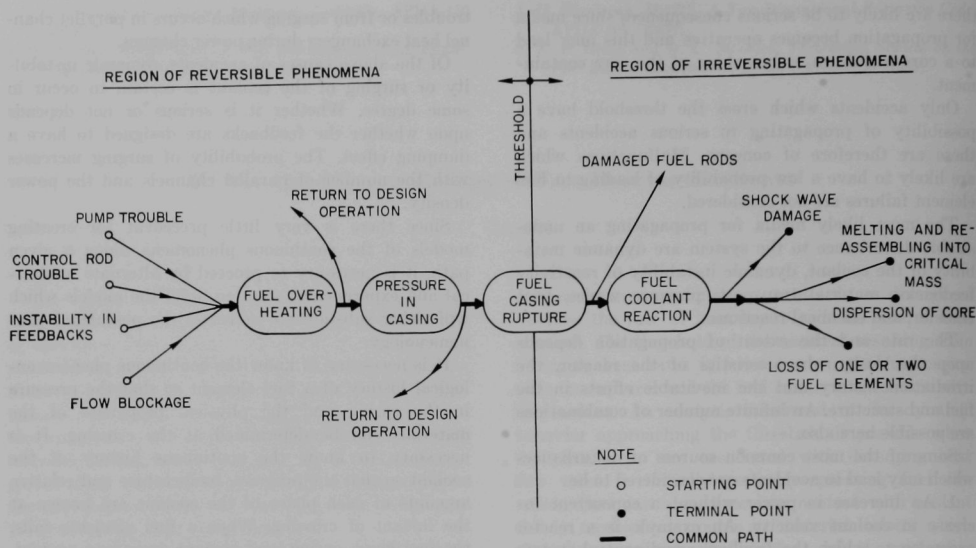

FIG. IV-16-1. Phenomenological Paths. *ANL Neg. No. 113-797.*

phenomena along this most likely common path approaching the threshold is that associated with the overheating of fuel, the structural integrity of the fuel element, the dynamics of the coolant and the dynamics of the reactivity feedbacks. If the disturbance to the system is such that the threshold is crossed, fuel and coolant come into contact and the phenomena continues into that associated with the fuel coolant energy transfer. From this point in the path there is the possibility of branching paths leading to an infinite number of terminal points. The least serious terminal point is considered to be the structural deterioration of a few fuel elements accompanied by the release of fission products and debris in the coolant. The most undesirable terminal point is reached by following a continuous phenomenological path to the consequences of a core meltdown and reassembly.

The probability of following either of these extreme paths or a path to any of the terminal points in between has not been determined.

The continuous phenomenological path from design operating conditions to the branching of the path beyond the threshold will be presented in terms of coupled mathematical models. Some of the models of phenomena from full power to the terminal points of an accident are:

1. Heat transfer within a fuel element.
2. Internal pressure within a fuel element casing.
3. Coolant flow in heated parallel channels.
4. Coolant vaporization.
5. The thermodynamic reaction of fuel and coolant coming into contact.
6. The energy transformation in melting cores.

These models can be adapted to fit into the closed loop of the present concepts of large power breeder reactors.

Experimental research which is required to substantiate the models and to determine the yet unknown physical properties associated with the phenomena is in the planning phase.

IV-17. Phenomena Leading to Fuel Casing Rupture During Transients

C. K. Sanathanan and J. C. Carter

This is an analysis of the thermo-mechanical phenomena associated with temperature transients in UO_2 fast reactor fuel elements in the operating range from normal power to the threshold of casing rupture. A mathematical model of space and time dependent temperature and metal phase transformation occurring with a fuel element over this operating range is presented. The phenomenological transition from the area of design operation across the accident threshold (usually manifest by casing rupture) into a region from which it is impossible to return to the area of normal operation is dynamic and is bound by the laws of conservation and continuity. It is necessary to understand how the accident threshold is approached and how it is crossed, since that which transpires after the crossing depends upon the physical conditions existing at the instant of casing rupture. There certainly will be contact between hot fuel and relatively cold sodium and a transition from thermo-mechanical to thermo-chemical phenomena with attendant pressure waves. This is believed to be one of the primary sources of accident propagation. The analytic work reported here is intended to complement future experiments planned at Argonne.

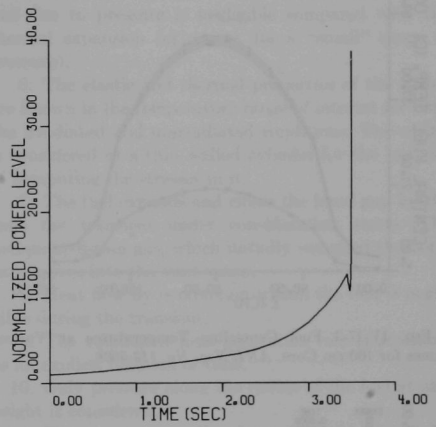

Fig. IV-17-2. Power Level Versus Time for 100 cm Core. *ANL Neg. No. 112-9051.*

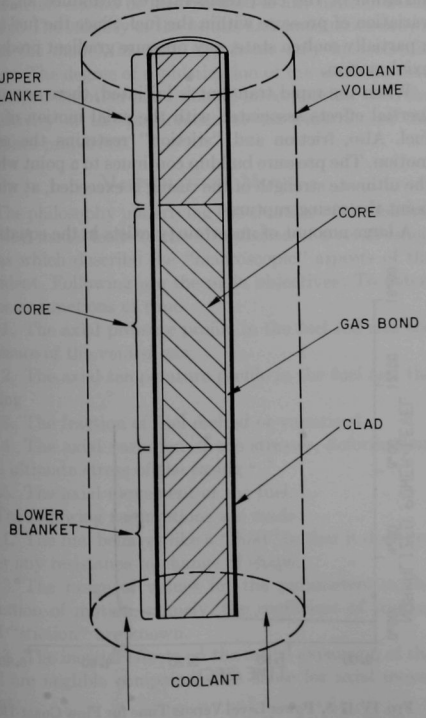

Fig. IV-17-1. Fuel Cell. *ANL Neg. No. 112-8544.*

A typical fuel cell is shown in Fig. IV-17-1. It consists of a stainless steel casing into which the fuel is placed either as small cylindrical pellets (about ½ in. long) or as vibrationally compacted powder. The fuel (at design temperature) is generally about 90% theoretical density. When the fuel is in the form of pellets there is usually a gas or sodium bond between the fuel and the casing. A space is provided at the top end of the casing for the fission gases.

The motivation for the present investigation arises from the recent analytical studies directed towards the sodium boiling accidents.[1] Some typical accidents are described to give some background for the quantitative approach used in this study.

AN ACCIDENT DUE TO A RAPID INCREASE IN REACTIVITY

A situation of this nature is conceivable when there is an accidental withdrawal of one or more control rods from the reactor. A detailed calculation model for such an accident is reported in Ref. 1. Some results from Ref. 1 are reproduced there to illustrate the consequent

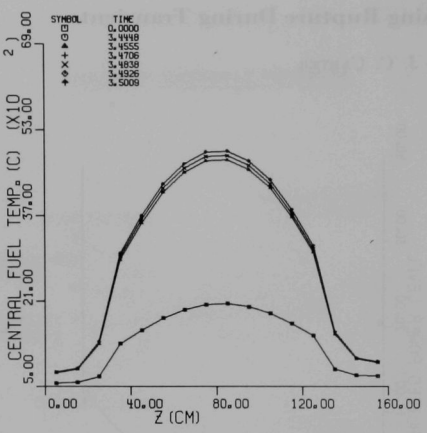

FIG. IV-17-3. Fuel Centerline Temperatures at Various Times for 100 cm Core. *ANL Neg. No. 112-9068.*

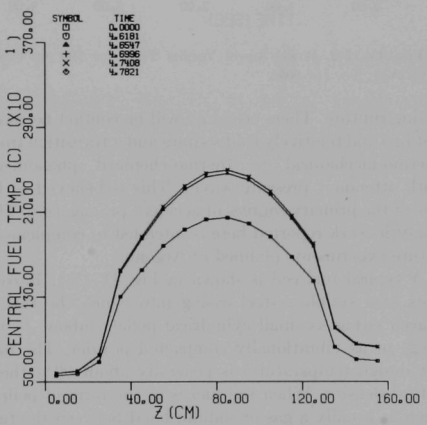

FIG. IV-17-4. Fuel Centerline Temperatures at Various Times for Flow Coast-Down. *ANL Neg. No. 112-9069.*

phenomena. The reactor fuel rods considered are those from Ref. 1.

From Figs. IV-17-2 and IV-17-3 several things are apparent. The power of the reactor increases rather slowly until boiling of sodium occurs at which time there is a rapid increase of reactivity resulting in periods of 2–100 msec. Figure IV-17-3 shows that the maximum fuel centerline temperature increased from 2000 to about 4000°C at the time boiling started. The fuel centerline temperature exceeded the melting point of 2800°C over the entire length of the core portion and the fuel is in the form of partially molten "slurry".

AN ACCIDENT DUE TO A LOSS OF COOLANT

An accident of this type may arise when there is an unexpected pump failure or rupture of the line between the pump and the reactor. Figures IV-17-4 and IV-17-5 are presented to show some typical temperature and power changes within fuel rods following such an accident. From Fig. IV-17-4 it is obvious that the temperatures are lower than those for the previously described accident. From Fig. IV-17-5 one observes that the reactor power rises slowly before boiling starts. However, when boiling starts, the reactor power rapidly increases as indicated in Fig. IV-17-2.

With the increase in power, the fuel undergoes thermal expansion and phase changes. Any radial expansion of the fuel is resisted by the stainless steel casing resulting in an increase of pressure in the fuel and stress in the casing.

The axial variations of the heat generation rate and the elastic properties of the casing (due to the axial variation of the clad temperature) introduce an axial variation of pressure within the fuel. Since the fuel is in a partially molten state, any pressure gradient produces axial motion.

When the rapid transient is initiated, there are some inertial effects associated with the axial motion of the fuel. Also, friction and "stiction" restrains the axial motion. The pressure buildup continues to a point where the ultimate strength of the casing is exceeded, at which point the casing ruptures.

A large amount of uncertainty exists in the equations

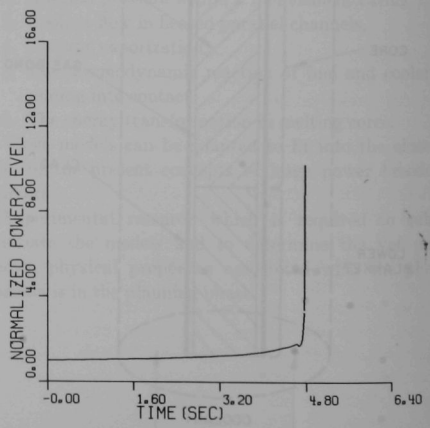

FIG. IV-17-5. Power Level Versus Time for Flow Coast-Down. *ANL Neg. No. 112-9053.*

of state of UO_2 in its liquid and vapor states. In particular, available vapor pressure equations[2-4] are all derived from experimental observations at very low pressures.

The elastic properties of steel change considerably with temperature, especially when the temperature approaches the melting point. Also, irradiation has an influence on these properties. Since the pressures and stresses calculated are strongly dependent on the elastic properties, the existing uncertainty in these properties directly affects the results.

The swelling and migration within the fuel affect its configuration in an indeterminate manner. In gas bonded fuel pins this frequently introduces hot spots which makes predictions about fuel failure less certain.

Axial motion of the fuel within the jacket has a strong influence upon the transient pressure profile. The parameters used in the equations of motion, namely the coefficient of friction and "stiction" therefore play an important role. These parameters are also not known to a high degree of exactitude.

In view of the above uncertainties, the facility to cover a reasonable spectrum of values for the various parameters should be incorporated in any mathematical model. The validity of the results and conclusions drawn from the model, in turn, also holds only in a certain range. The degree of sophistication of the mathematical model, on the other hand, should be compatible with the sensitivity of the phenomena to the variation of the physical properties.

Mathematical Model

The philosophy underlying the creation of the mathematical model leads to the formulation of a set of equations which describe the "macroscopic" aspects of the accident. Following are the main objectives: To determine as functions of time

1. The axial pressure profile in the fuel rod and the pressure of the vented gas
2. The axial temperature profile in the fuel and the casing
3. The fraction of fuel melted or vaporized
4. The axial variation of the stresses, deformation, and ultimate stress of the casing
5. The axial movement of the fuel.

The following assumptions are made:

1. The fuel behaves like a "fluid" in that it does not offer any resistance to change of shape.
2. The range of values for the parameters in the equation of motion, namely, the coefficient of friction and "stiction" are known.
3. The inertial effects on the radial expansion of the fuel are neglible compared with those for axial movement.
4. The equations of state for the fuel in its three phases and any of the possible combinations of these phases are available.
5. The internal energy of the fuel in its solid and liquid phases does not have explicit dependence on pressure. This is so because the volumetric change of the fuel due to pressure is negligible compared with the thermal expansion (of course, for a "small" range of pressure).
6. The elastic and thermal properties of the casing are known in the temperature range of interest for both the irradiated and unirradiated conditions. The casing is considered as a thin walled cylinder for the purpose of computing the stresses in it.
7. The fuel expands and closes the bond gap by the time the transient under consideration starts. The helium or fission gas, which initially occupied the bond gap, moves into the vent space.
8. Heat flow by conduction within the fuel is negligible during the transient.
9. The volumetric heat generation rate is available as an explicit function of time.
10. Only pressure along the radius of the fuel at any height is considered.
11. The pressure profile along the axis is initially taken as uniform since the fuel is at rest.

The mathematical model employed is a simultaneous representation of the space- and time-dependent thermomechanical phenomena in the fuel and the casing. It is found practical to solve the equations of the model numerically. For this, time and space are discretized.

The fuel is subdivided into several axial segments. The thermal expansion and the axial movements of these segments are determined through each increment of time. Consistency is achieved by conserving the mass, energy, and momentum of the system throughout all energy and phase transformations.

The computational procedure is as follows:

1. In the first time step all the heat generated is assumed to be used for increasing the internal energy of the fuel. This results in an increase in volume of the fuel. Since the fuel is at rest initially and any axial movement has to result from a pressure gradient, the thermal expansion in the first time increment is accommodated by a corresponding radial expansion. The radial expansion of the fuel is restrained by the casing. A force balance gives the corresponding pressure rise in the fuel along the axis.

2. After the first time step, a two-pass system is used. In the first pass, over a given heat addition, the previous values of acceleration and movement are used to find an approximate value of the pressure at the end of the time step. This pressure is then used to complete the acceleration over the time step. Acceleration of the interface

is based on the Lagrangian motion due to the pressure difference between the adjacent centers of mass.

3. The heights of the various segments (from item 2) and their respective radii (from item 1) give the respective volumes V_j available in the axial sections. The heat addition in the second time increment gives the thermal expansion for the fuel.

4. If the volume V_j just computed is smaller than the volume V_j resulting from thermal expansion, a suitable extension of the radius is computed to accommodate the thermal expansion. A corresponding increase in the stress of the casing and the pressure exerted by the fuel is also computed.

5. The movement of the fuel into the vent space compresses the fission gas in the vent. An adiabatic compression of the gas is considered and the corresponding pressure increase of the gas is computed. This restrains the fuel motion.

6. The above process is repeated for several time increments.

7. It is possible that the fuel may vaporize during the transient if the volume computed in item 3 is larger than the volume resulting from thermal expansion of the liquid fuel. The saturated vapor pressure corresponding to the temperature of the fuel is obtained from the vapor pressure equation due to R. Ackerman et al.[2] The corresponding extension of the casing gives the radius of the fuel. A new volume corresponding to this radius is computed. If this volume is still larger than the volume of the fuel at the above temperature then there is vaporization. Assuming this to be the volume, the amount of vapor present is determined by solving a set of thermodynamic equations.[5-6] The temperature and pressure which are given by the solution is compared with those used in the beginning of item 7. Some iteration may be necessary to obtain consistency.

8. The heat flow to the casing depends upon the difference between the fuel surface temperature and the average casing temperature. The temperature of the casing at the various axial locations affects the elastic properties and the ultimate strength of the casing.

9. If at any time the stress in the casing exceeds the ultimate stress (corresponding to the temperature) at any axial location, the computations are terminated.

Following are the various equations used in the computational procedure described above:

EQUATION OF MOTION AND CONSERVATION OF MASS

The equation of motion is written in one-dimensional space, namely, along the Z-axis of the fuel element[7]:

$$\frac{\partial^2 Z}{\partial t^2} = -\frac{1}{\rho}\frac{\partial P}{\partial Z} - F\frac{\partial Z}{\partial t} - g, \tag{1}$$

where $Z = 0$ is at the bottom of the element, P is the pressure in the fuel, F is a coefficient such that $F\frac{dZ}{dt}$ gives the frictional force per gram, g is the acceleration due to gravity, and t is the independent time variable. The equation of motion is discretized in space and time.

Consider first the discretization in Z (see Fig. IV-17-1). The axial motion of the various segments are obtained by associating each with a certain mass, velocity, pressure, and temperature. In other words, it is the motion of the interface of each segment which is described by the discretized form of Eq. (1):

$$M_j \frac{d^2 Z_j}{dt^2} = \frac{\pi(R_j^2 + R_{j+1}^2)}{2}(P_j - P_{j+1}) - M_j F \frac{dZ_j}{dt} - M_j g, \tag{2}$$

where M_j, the mass of the jth axial segment, is given by

$$M_j = \pi R_j^2 (\Delta Z_j)\rho_j . \tag{3}$$

R_j is the radius, ΔZ_j is the length, and ρ_j is the average density of the jth segment. M_j is held constant through the transient. This accounts for the conservation of mass.

Dividing Eq. (2) by M_j,

$$A_j = (P_j - P_{j+1})\left(\frac{R_j^2}{M_j} + \frac{R_{j+1}^2}{M_{j+1}}\right)\frac{\pi}{2} - F\frac{dZ_j}{dt} - g, \tag{4}$$

where

$$A_j = d^2 Z_j / dt^2.$$

Equation (4) is further discretized in time to convert it completely into a different equation. Considering the complexity of the problem, an explicit scheme, namely, the central differencing scheme was chosen. The limitations imposed on the size of the time increments by numerical stability consideration are discussed below. Let H_j^2 represent the position of the interface of the jth segment at some time t, H_j^1 at Δt earlier, and H_j^3 at Δt_1 later.

The time increments need not be uniform. The second derivative with respect to time is expressed as

$$\frac{d^2 H_j}{dt^2} \approx \frac{1}{(\Delta t + \Delta t_1)} \Big/ 2\left[\frac{H_j^3 - H_j^2}{\Delta t_1} - \frac{H_j^2 - H_j^1}{\Delta t}\right]. \tag{5}$$

In the case of uniform time increments Eq. (5) reduces to the familiar form

$$\frac{d^2 H_j}{dt^2} \approx \frac{H_j^3 - 2H_j^2 + H_j^1}{(\Delta t)^2}$$

and dH_j/dt is approximated as

$$\frac{dH_j}{dt} \approx \frac{H_j^2 - H_j^1}{\Delta t}. \tag{6}$$

The axial pressure profile and the velocity at a certain time are used in Eq. (4) to compute the accelerations A_j at that time. Using Eq. (5) one solves for the position H_j^3 at some time Δt later.

The rapid transient under consideration here is almost always initiated when there is still some solid fuel close to the casing. Therefore, in axial locations where the fuel has expanded and completely closed the bond gap, there would exist some initial resistance to axial motion.

Therefore, in the calculational procedure, the axial motion of any increment is delayed until a certain pressure gradient is built up. This may be expressed quantitatively as follows:

$$A_j = 0$$

if

$$|P_{j-1} - P_j| < \delta P_j,$$

when δP_j is a specified quantity. A_j is computed using Eq. (4) if

$$|P_{j-1} - P_j| \geq \delta P_j.$$

EQUATIONS OF THERMODYNAMICS

The computational method for obtaining the pressure profile along the axis is developed in the following.

The heat generation per gram of fuel is expressed as an explicit function of time multiplied by a shape function $S(z)$.

$$q = q_0 e^{at} S(z). \tag{7}$$

The internal energy U per gram is computed from

$$U = U_0 + q - W, \tag{8}$$

where U_0 is the initial internal energy; W is the sum of the kinetic energy, the work done in expanding the casing, and the work done in compressing the gas in the vent. Generally W is negligible.

The temperature of the liquid UO_2 and its internal energy are assumed to be related by*

$$U_\ell = T[a + bT], \tag{9}$$

where $a = 0.286$ and $b = 0.037 \times 10^{-3}$. Equation (9) implies a linearly varying specific heat (at constant volume) with temperature.[3]

The specific volume V_{s1} of the liquid UO_2 is given by[3]

$$V_{s1} = \frac{c + T}{d}, \tag{10}$$

where $c = 2000.0$ and $d = 40{,}000.0$.

The vapor pressure equation due to Ackerman[2] is

$$P_s = T^{a_1} e^{(a_2 + a_3 T)}, \tag{11}$$

where

$$a_1 = -4.026$$
$$a_2 = 59.45$$
$$a_3 = 74590.0.$$

The Clapeyron equation of the latent heat of vaporization L is

$$L = T \frac{dP_s}{dT} (V_{sg} - V_{s\ell})/J, \tag{12}$$

where V_{sg} is the specific volume of the gas; $\frac{dP_s}{dT}$ is the gradient of the vapor pressure relationship of Eq. (11); and J is the mechanical equivalent of heat.

Differentiating Eq. (11) with respect to T,

$$\frac{dP_s}{dT} = \frac{P_s}{T}\left[a_1 - \frac{a_3}{T}\right]. \tag{13}$$

V_{sg} is computed assuming the UO_2 vapor to be an ideal gas[8]:

$$V_{sg} = b_1 \frac{T}{P_s}, \tag{14}$$

where $b = 314.0$.

An iterative method is adopted to obtain simultaneously P_s, T, and the quality of the UO_2 vapor from the knowledge of the heat added per gram and the volume available per gram.

EQUATIONS FOR THE DEFORMATION OF THE CASING

The "membrane" theory[9] is adopted to relate the radial extension Δr of the casing with the pressure P developed in the fuel:

$$P = [\Delta r - r\alpha\, \Delta T] \frac{E_\tau}{r^2[1 - \nu/2]}, \tag{15}$$

where r is the inner radius, τ is the thickness of the casing, E is the modulus of elasticity, α is the coefficient of thermal expansion, and ν is Poisson's ratio. Both E and ν change with temperature.

For stainless steel ($T_0 = 500°K$) the following values are taken[10]:

$$E_0 = 1.90 \times 10^9 \text{ g/cm}^2$$
$$E_1 = -4.25 \times 10^5 \text{ g/cm}^2\text{-°K}$$
$$E_2 = -4.55 \times 10^2 \text{ g/cm}^2\text{-(°K)}^2$$
$$E_3 = -0.40 \text{ g/cm}^2\text{-(°K)}^3.$$

* All that is necessary here is a specific relation between U_ℓ and T.

The above values for the coefficients reduce E by roughly a factor of two in the temperature range from 800 to 1400°K. (The values for the coefficients are applicable at negligible irradiation levels. Irradiation generally reduces the value of E.) Similarly, the temperature dependence of the ultimate stress is expressed as[10]:

$$\sigma_{ult}(T) = \sigma_0 + \sigma_1(T - T_0) + \sigma_2(t - T_1)^2 + \sigma_3(t - T_0)^3 + \sigma_4(T - T_1)^4;$$

for $T_0 = 800°$,

$$\sigma_0 = 7.746 \times 10^6 \text{ g/cm}^2$$
$$\sigma_1 = -9.462 \times 10^3 \text{ g/cm}^2\text{-(°K)}^2$$
$$\sigma_2 = -5.692 \times 10^1 \text{ g/cm}^2\text{-(°K)}^2$$
$$\sigma_3 = 1.363 \times 10^{-1} \text{ g/cm}^2\text{-(°K)}^3$$
$$\sigma_4 = -8.200 \times 10^{-5} \text{ g/cm}^2\text{-(°K)}^4.$$

The above values for the coefficients reduce $\sigma_{ult}(T)$ by a factor of 20 in the temperature range from 800 to 1400°K.

CASING TEMPERATURE CALCULATION

Fuel surface temperature T_{fs} is obtained by integrating

$$C_p \frac{dT_{fs}}{dt} = q. \tag{16}$$

The casing temperature, T_{c1}, is obtained by solving

$$\frac{dT_c}{dt} = \frac{1}{\tau_{c1} C_{c1} \rho_{c1}} [h_f(T_{fs} - T_{c1}) - h_c(T_{c1} - T_c)]. \tag{17}$$

where C_{c1} and ρ_{c1} are the specific heat and density of the casing respectively, h_f is the heat transfer coefficient between the fuel and casing, h_c is the heat transfer coefficient between the casing and coolant, and T_c is the coolant temperature. T_c is assumed to be known. The heat transfer coefficient h_f is assumed to increase with internal pressure:

$$h_f = h_{f0}[1 + \beta(P - P_0)], \tag{18}$$

where h_{f0} is the initial heat transfer coefficient value when $P = P_0$, and β is a positive coefficient. In the calculations made in this study,

$$h_{f0} = 1.8 \text{ W/cm}^2\text{-°K}$$
$$\beta = 10^{-4}$$

Numerical Stability

The system of equations is much too complex to derive quantitative limits on the time and space increments in order to ascertain numerical stability of the solution. However, some comments are in order.

The assumption of constant acceleration during any time increment introduces inaccuracies in the determination of the axial motion of the fuel, especially when time increments are large. Any error in the axial movement introduces errors in the radial expansion, since the radial expansion of the casing is closely related to the axial movement (see Eq. (3)). Error in the radial expansion of the casing directly affects the pressure developed in the fuel which in turn affects the accelerations to be computed for the succeeding time increment. The magnitude of the error varies directly with the modulus of elasticity.

One way to prevent any "oscillations" in pressure is by choosing a value for Δt such that the pressure changes from time step to time step is kept within a certain limit, say 1 atm. About 10 axial segments were found to be adequate to describe the axial pressure profile. Time increments varied from 0.0001 to 0.00001 sec for the various transients considered.

Results and Discussions

The method of analysis developed is applied to some specific fuel elements to illustrate the effects of fuel motion quantitatively. To accomplish this, the simpler case in which there is no relative motion between the fuel and the casing is discussed. This then is compared with the more realistic case when there is relative motion between the fuel and the casing. In addition, the effect of casing thickness upon various quantities such as the internal pressure generation, fuel movement (with the consequent effects of friction and "stiction"), and the time taken to reach the instant of rupture are also discussed.

A fuel element 100 cm long and 0.3 cm i.d. for the casing, is considered. Two different casing thicknesses, namely 0.05 cm and 0.25 cm are chosen. A vent space of 0.5 cc (of length 1.67 cm) is situated on top of the fuel. The initial power distribution along the axis is that for which the power curve of Fig. IV-17-2 just begins to increase rapidly due to sodium boiling. The fuel along its entire length is partially molten at this time. The maximum temperature along the axis (slightly above the midpoint) is about 4000°K. The initial pressure in the can is taken as 2 atm. Vapor pressure equations (Eq. (11)) indicated that this pressure is well above the saturated vapor pressure corresponding to 4000°K, and there is no vapor present initially.

Three exponential power rises with periods of 20, 10 and 2 msec are considered. The heat generation rate is assumed to be uniform radially and has an axial distribution as shown in Fig. IV-17-6. This axial distribution (Fig. IV-17-6) is assumed not to change during

transients. The maximum heat generation rate initially is taken as 4000 W/gm. The initial coolant temperature profile is obtained from Ref. 1 and it is assumed not to change during the transients. In fact, there would be some changes in the coolant temperatures. However, for the purposes of the present sudy, the effects of these changes are unimportant.

CASE A: RESTRAINED AXIAL MOTION

The axial pressure profiles for the three rates of heat generation and for the two casing thicknesses are presented in Fig. IV-17-7. These profiles are those determined at the threshold of casing rupture. Consider first the three curves pertaining to the 0.05 cm thickness of the casing. If the temperature of the casing were uniform along the Z-axis, the modulus of elasticity and ultimate strength of the casing would have been nonuniform along the Z axis also; and consequently, the pressure profile would have had a shape similar to that of the heat generation rate. But since the coolant temperature varies along Z the temperature of the casing, and consequently its thermal and mechanical properties also vary along Z. Since the pressure is a result of both the heat generation rate and the mechanical properties of the casing, it is obvious that the pressure profile attains a peak below the midpoint of the axis. It is readily observed in Fig. IV-17-7 that there exist large gradients in the pressure profiles. This is a consequence of restraining the fuel from moving axially. From Fig. IV-17-7 it is further apparent that the effect of reduced casing thickness (0.025 cm) has only decreased the pressures developed, without significantly affecting the shape of the profiles. Also, slower rates of heat input seem to lower the internal pressures. This is explained as follows. The slower rates of heat input increase the time taken to rupture the casing. During the added interval, there is a corresponding increase in the temperature of

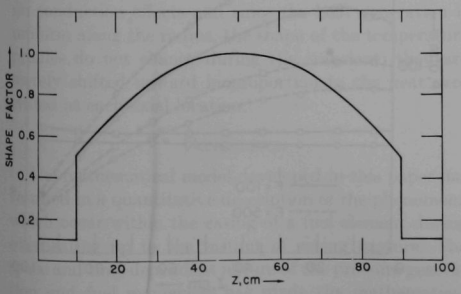

FIG. IV-17-6. Axial Distribution of Heat Generation. *ANL Neg. No. 113-1499.*

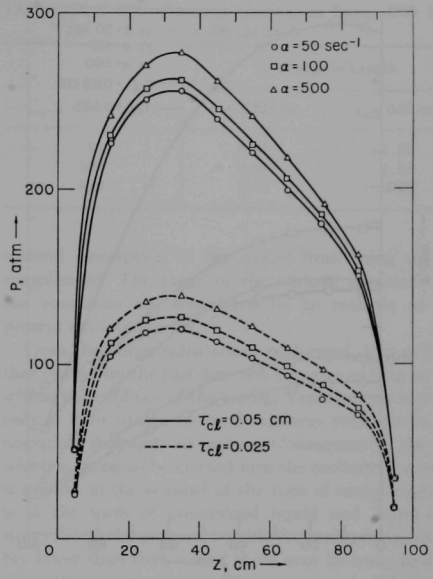

FIG. IV-17-7. Pressure Profiles for the Case of Restraint Axial Motion. *ANL Neg. No. 113-1503.*

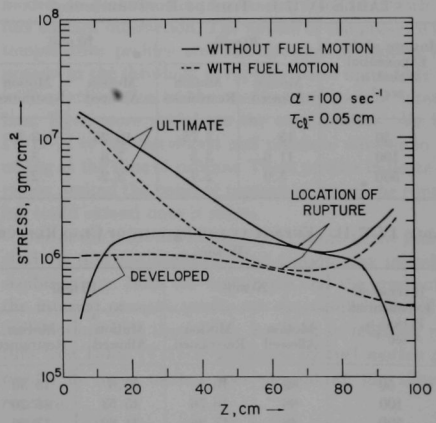

FIG. IV-17-8. Profiles of Developed and Ultimate Stresses. *ANL Neg. No. 113-1495.*

the casing and a consequent decrease in the modulus of elasticity.

The rupture point does not coincide with the location of the pressure peak. The location of rupture is at the point where the stress in the casing has exceeded the

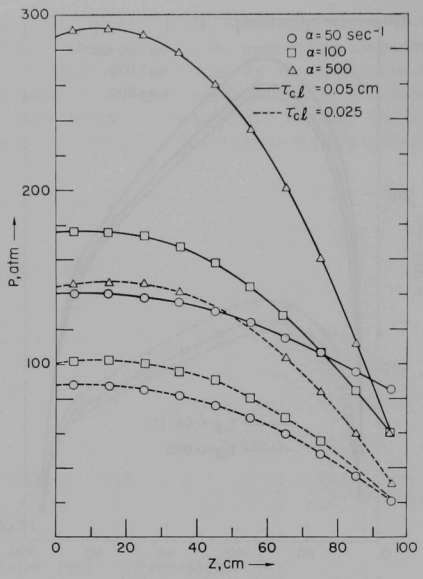

FIG. IV-17-9. Pressure Profiles for the Case of Unrestrained Axial Motion. *ANL Neg. No. 113-1504.*

TABLE IV-17-I. TIME OF RUPTURE (msec)

Inverse of the Exponential Period, α, sec^{-1}	20 mill		10 mill	
	Motion Allowed	Motion Restrained	Motion Allowed	Motion Restrained
50	15	3.75	10.25	3.5
100	11.6	3.5	7.6	3.4
500	3.9	2.4	3.2	2.3

TABLE IV-17-II. ENERGY AT THE INSTANT OF CLAD RUPTURE (W-sec)

Inverse of Exponential Period, α, sec^{-1}	20 mill		10 mill	
	Motion Allowed	Motion Restrained	Motion Allowed	Motion Restrained
50	89	16.5	53.6	15.30
100	86	16.76	45.53	16.20
500	48	17.26	31.62	17.26

ultimate stress. This point is usually somewhere between 60 and 80% of the height from the bottom. Figure IV-17-8 represents the developed and ultimate stress profiles along the axis at the time of rupture for the case of 0.05 cm thick casing, and for the heat generation rate

$$q(Z) = 4000\ (SZ)e^{100t}\text{W/gm}.$$

CASE B: UNRESTRAINED

One of the obvious effects of axial motion of the fuel is to reduce the internal pressures and their gradients. This is illustrated on Fig. IV-17-9. The pressure profiles no longer resemble the axial profile of heat generation rate. In particular, the movement of fuel toward the bottom of the can markedly raised the local pressures, thus reducing the steep gradient.

The increased time required to attain rupture and the corresponding increase in the total heat input before rupture are illustrated by Tables IV-17-I and IV-17-II. The additional heat input results in a higher percent of molten fuel before the casing rupture occurs; this in turn increases the amount of hot fuel that comes in contact with the coolant.

An inspection of Fig. IV-17-8 indicates that the location of rupture has moved toward the midpoint of the axis as a result of fuel movement. This figure also gives the difference made in the stress profiles along the axis.

In all of the above examples, the value of the coefficient of friction F of Eq. (4) has been taken to be 500 cgs units. This corresponds to a deceleration due to friction of approximately 10 g if the material were to move inside the casing at a constant speed of 1 ft/sec. This number for the friction factor, of course, is arbitrary at this time. Some laboratory tests have to be performed in order to ascertain a definite range of values for this coefficient.

The effect of decreasing this coefficient is to increase the rate of fuel movement and vice-a-versa. The value of

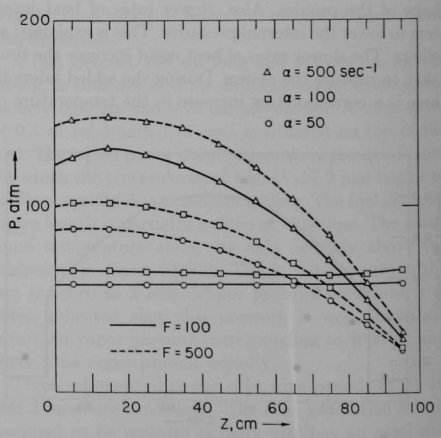

FIG. IV-17-10. Effect of Friction Upon Pressure Profiles. *ANL Neg. No. 113-1512.*

F is arbitrarily reduced to 100 cgs units for the case of 0.025 cm thick casing. The results are shown in Fig. IV-17-10. The increased motion has practically flattened out to pressure profiles for the lower rates of exponential increase in heat input, namely for $\alpha = 50$ and 100 sec^{-1}. However, for $\alpha = 500$ sec^{-1}, there are still large gradients in the internal pressure. This is due to the fact that at $\alpha = 500$ sec^{-1}, the heat generation rate far exceeds the rate of alleviation of internal pressure caused by the fuel movements.

"Stiction" (coulomb friction) affects only the fuel movement initially. Because of the rapid pressure buildup when the fuel is restrained from moving, any reasonable "stiction" would be overcome soon after the start of the transient. Even though this would affect the intermediate pressure profiles, it has practically no influence on the pressure profile existing at the time of rupture. In the examples considered above, the pressure difference between adjacent segments (δP_j) was varied along the axis, starting at 10 atm at the bottom, decreasing to 2 atm in the middle, and then increasing 10 atm to the top. This pattern of δP_j is to take into account in a semi-quantitative manner the effect of increased fuel melting in the middle portions of the can.

The actual extent of the fuel movement is influenced by four principal parameters, namely, the amount of vent space available, the thickness of the casing, the rate of heat generation, and the degree of restraint to motion. The movement has direct effect in terms of reactivity feedback. The value of this feedback depends upon the specific design of the reactor. Table IV-17-III gives the percent change in length of fuel during the transient up to the point when the casing ruptured for various transients.

Detailed radial and axial temperature profiles are computed throughout the transient. The amount of molten fuel is estimated at each axial section from the knowledge of the location of melting along the radius. Since computation of temperature is done by assuming no conduction effects and since the heat generation is uniform along the radius, the shape of the temperature profiles do not change during the transient; they are merely shifted upward in proportion to the heat generated at each axial location.

TABLE IV-17-III. PECENTR CHANGE IN LENGTH OF FUEL (F = *500 cgs units*)

α	% Change in Length	
	τ = 0.025 cm	τ = 0.05 cm
50	0.87	1.62
100	0.67	1.55
500	0.27	0.63

CONCLUSION

The mathematical model developed in this paper has resulted in a quantitative description of the phenomena which occur within the casing of a fuel element during overheating up to the instant of casing rupture. The space and time dependent nature of the pressure generation and fuel movement has made the mathematical formulation of the problem more complex. Some simplifying assumptions are made to prevent the mathematical description of the model from being unduly complicated. The range of the various parameters in the equations are considered to be realistic at the present state of the art.

From the many calculations performed, it is evident that ordinarily the fuel does not vaporize as long as it is within the confines of the casing. Vaporization is noted only in some situations involving large vent spaces and negligible restraints to motion. Consequently, the fuel which is going to be ejected into the coolant (if coolant is present in the channel at the time of casing rupture) is in the form of pressurized liquid and liquid-solid slurry. Since the pressure outside the casing is considerably lower than that inside, there may be some flashing when the rupture occurs. The net amount of fuel that may be ejected outside the casing cannot be estimated at the present time because of the lack of mathematical models to describe the phenomena associated with the fuel coolant interaction. The nature of the pressure and temperature profiles and the amount of molten fuel present at the threshold of rupture are of immediate use in the formulation of the ensuing fuel-coolant interaction. Even more useful are the axial profiles (see Fig. IV-17-9) of the developed and ultimate stresses in the casing at the time of rupture. These profiles indicate the region around the point of rupture to which the rupturing could extend once it starts.

One of the most important observations of the present study is that the neglect of fuel motion may introduce sizable errors. Both the magnitude and the gradient of the internal pressure profile are drastically affected by fuel motion. The time delay involved in reaching rupture (see Table IV-17-I) produced by fuel motion also results in more molten fuel present at the time of rupture.

The axial motion of the fuel during a transient could also result in a negative feedback of reactivity which in turn could limit the severity of the reactor transients. The actual magnitude of the reactivity coefficient would depend upon the specific reactor involved. A closed loop computation involving neutron kinetics and coolant dynamics is underway to study the overall effects of fuel motion.

Several experiments are being planned to further the understanding of the phenomena involved in the failure of fuel elements, fuel coolant interaction, and the propagation of these accidents to nearby fuel elements and subassemblies. It is hoped that the theoretical developments along these lines would influence the planning of the experiments, and the experiments in turn would substantiate the theoretical predictions. In particular, the various predictions of the present mathematical model such as when and how the casing rupture occurs and the pressures and temperatures involved are all experimentally verifiable.

References

1. D. R. MacFarlane, N. A. McNeal, D. A. Meneley and C. K. Sanathanan, *Sodium Boiling Transients in Mixed Oxide-Fueled Fast Reactors*, Nucl. Eng. and Design, **7**, (May 1968).
2. R. J. Ackerman, et al., *High Temperature Thermodynamic Properties of Uranium Oxide*, J. Chem. Phys. **25**, 1089 (1956).
3. J. Belle, ed., *Uranium Oxide: Properties and Nuclear Applications* (USAEC Division of Development, Washington, D.C., 1961).
4. D. C. Menzies, *The Equations of State of Uranium Dioxide at High Temperatures and Pressures*, TRG Report 1119(D) UKAEA (1966).
5. V. M. Fiares, *Thermodynamics* (The Macmillan Company, New York, 1962) p. 571.
6. M. W. Zemansky, *Heat and Thermodynamics* (McGraw-Hill Book Co., New York, 1943) p. 284.
7. A. Sommerfeld, *Mechanics of Deformable Bodies* (Academic Press Inc., New York, 1950) p. 94.
8. D. Miller, *A Critical Review of the Properies of Materials at the High Temperatures and Pressures Significant for Fast Reactor Safety*, Proc. Conference on Safety, Fuels and Core Design in Large Fast Power Reactors, October 11–14, 1965, ANL-7120, pp. 641–653.
9. S. Timoshenko, *Theory of Plates and Shells* (McGraw-Hill Book Co., New York, 1940) p. 383.
10. *Steels for Elevated Temperature Service*, Monograph United States Steel Corp., Pittsburgh (1965).

IV-18. Accelerated Creep in Fuel Cladding

J. C. Carter

The Fuel Failure Propagation Test Program requires simulation of pre-accident elastic conditions in a fuel element cladding. The metal cladding with an irradiation history of the time of the propagation test will have already progressed along the path to failure by virtue of creep which is a time dependent elastic phenomenon.

The elastic condition resulting from normal operation for a long period of time can be reproduced in a shorter period (hours instead of months) by the method described by S. S. Manson and A. M. Haferd,[1] thus permitting a realistic fuel failure propagation test to be performed.

A time-temperature parameter based on examination of the published stress-rupture data for a variety of materials, rather than on physical theory, is presented in the form $(T - T_a)/(\log t - \log t_a)$, where T is temperature in degrees Fahrenheit, t is rupture time in hours, and T_a and $\log t_a$ are material constants determinable from rupture data in the time range between 30 and 300 hours. S. S. Manson and A. M. Haferd[1] found that there is an approximately linear relationship between $\log t$ and T for a constant nominal stress in the rupture-time range above 10 hours. A plot of this parameter against stress for a given material results in a single curve with relatively little scatter for various combinations of time, temperature, and stress in the rupture-time range above approximately 10 hours. For the materials investigated, the use of data in the time range below 300 hours resulted in very good extrapolation to longer times (up to 10,000 h when data were available). This linear stress-temperature-time correlation enables a relationship to be established between heat generation rate, coolant flow and the lifetime of the cladding.

Accelerated creep tests of this sort, however, do involve some other changes from normal or slightly abnormal operating conditions. At higher temperatures more of the fuel is molten and subject to injection into the coolant by the higher pressure fission gas. This will probably increase the stress levels induced by pin failure above those to be expected under failure from slightly abnormal operation. Maximum clad and coolant temperatures, the amount of fuel melted, fission gas pressures, and clad stress (hoop stress only) are plotted against heat rate and flow rate in Figs. IV-18-1 and IV-18-2 for a UO_2 fuel pin of the following characteristics:

Length of fuel section—60.96 cm
Length of gas chamber—91.44 cm
O.D. of casing—0.635 cm

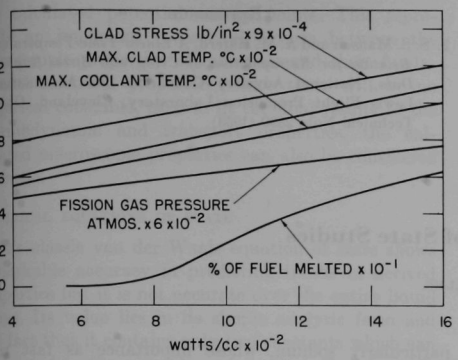

FIG. IV-18-1. Pressure Stress, Temperature and Percent Fuel Melted Versus Heat Rate. *ANL Neg. No. 113-855.*

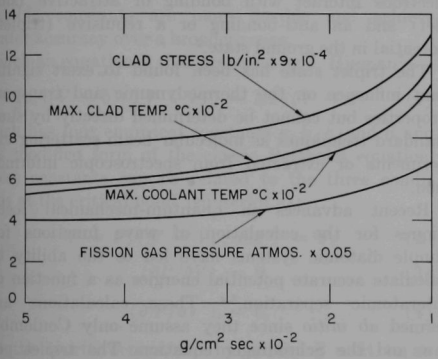

FIG. IV-18-2. Pressure Temperature and Stress Versus Flow Rate. *ANL Neg. No. 113-858.*

I.D. of cladding—0.557 cm
O.D. fuel rod—0.52837 cm
Cross section of fuel—0.219 cm^2
UO_2 density—10 g/cm^3
Casing material—18.8 S.S.

The lifetime of the cladding of a fuel pin which has sustained 100,000 MWD/T service is calculated and plotted on Figs. IV-18-3 and IV-18-4. Figure IV-18-3 shows the effect of increasing the heat rate while holding the flow rate constant and Fig. IV-18-4 shows the effect of decreasing the flow rate while holding the heat rate constant. The heating rate was varied from 2000 W/cc of UO_2 to 4500 W/cc for a flow rate of 400 g/cm^2-sec and then the flow rate was varied from 500 g/cm^2-sec to 100 g/cm^2-sec for a heat rate of 2000 W/cc of UO_2.

The maximum cladding temperature occurs at the end of the fuel section. The fission gas temperature is taken to be the same as the sodium temperature surrounding the fission gas reservoir section of the fuel pin.

It is concluded that flow blockage experiments with flow reduced to ~25–50% of normal can be conducted

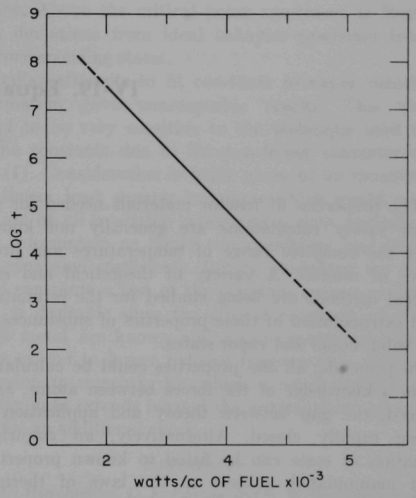

FIG. IV-18-3. Heat Rate Versus Log t. *ANL Neg. No. 113-888.*

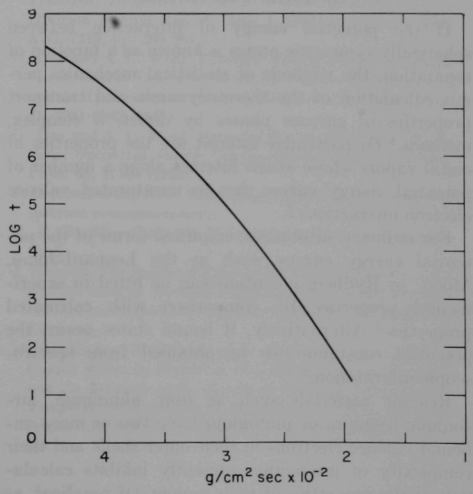

FIG. IV-18-4. Flow Rate Versus Log t. *ANL Neg. No. 113-890.*

in reasonable test times (~1 to 10 h) and can be expected to yield realistic estimates of damage. Fuel overheating experiments are more difficult to accelerate and can be expected to yield conservative damage estimates.

REFERENCE

1. S. S. Manson and A. M. Haferd, *A Linear Time-Temperature Relation for Extrapolation of Creep and Stress-Rupture Data*, National Advisory Committee for Aeronautics, Lewis Flight Propulsion Laboratory, Cleveland, Ohio, Technical Note 2890 (1953).

IV-19. Equation of State Studies

D. MILLER

The properties of reactor materials needed for reactor safety calculations are generally not known over the complete range of temperatures and pressures of interest. A variety of theoretical and empirical methods are being studied for the estimation and extrapolation of these properties of substances in the solid, liquid and vapor states.

In principle, all the properties could be calculated from a knowledge of the forces between atoms, and, indeed, the gap between theory and application is being rapidly closed. Alternatively, an empirical equation of state can be fitted to known properties and manipulated, subject to the laws of thermodynamics and other empirical relations among properties, to yield the desired information.

AB INITIO CALCULATIONS

If the potential energy of interaction between spherically symmetric atoms is known as a function of separation, the methods of statistical mechanics permit calculation of the thermodynamic and transport properties of gaseous phases by direct, if complex, methods.[1] Of particular interest are the properties of metal vapors whose atoms interact along a number of potential energy curves due to unsaturated valence electron interactions.[2]

For ordinary substances, empirical forms of the potential energy curves, such as the Lennard-Jones, Morse, or Rydberg potentials can be fitted to experimental properties by comparison with calculated properties.[1] Alternatively, if bound states occur, the potential constants can be obtained from spectroscopic information.[2]

Reactor materials such as iron, aluminum, zirconium, uranium or plutonium have two or more unbound valence electrons in their outer shells and their complexity of interaction presently inhibits calculation of the properties of their vapors. Of practical, as well as theoretical interest are the alkali metals, particularly sodium, whose importance as fast reactor coolants provides additional incentive for study. The alkali metal atoms, with their single valence electrons interact with bonding or attractive (singlet) and an anti-bonding or a repulsive (triplet) potential in the ground state.[2]

The triplet state has been found to exert significant influence on the thermodynamic and transport properties but cannot be determined directly by such standard techniques as molecular beam scattering experiments or extracted from spectroscopic information.

Recent advances in quantum-mechanical techniques for the calculation of wave functions for simple diatomic systems have led to the ability to calculate accurate potential energies as a function of interatomic separation.[3,4] These calculations are termed *ab initio* since they assume only Coulomb's law and the Schrödinger equation. The triplet potential can be calculated with accuracy comparable to that of the singlet.

Economic limitations on computing time prohibit the calculation of many points on these curves. Enough points have been calculated for systems involving lithium[4] and sodium[5] to indicate the accurate calculation of equilibrium internuclear separation and substantially correct dissociation energies for the singlet. Combining rules for interaction between unlike atoms have been shown to be adequate but not highly accurate.

Although additional points at small and large separations are needed, it was found that the triplet was lower than predicted by an "anti-Morse" potential previously used.[2] This is in the direction to produce closer agreement with limited experimental data.[6] Empirical potentials have given high accuracy in fitting singlet potential values only near the potential minimum coefficients, and transport integrals will be calculated from piecewise curve fits to

the calculated potential energy points. This represents an important theoretical closure between the macroscopic properties of materials and their fundamental electrical properties. Since there will be no empirical constants, used to fit the final results to the thermodynamic and transport properties, the calculated macroscopic properties can also be considered *ab initio*.

EMPIRICAL EQUATIONS OF STATE

The classic van der Waals equation of state shows remarkable accuracy in predicting trends in derived properties but it is not accurate over the entire liquid range. Its value lies in its simple analytic form and the fact that it contains only two constants which can be related to the properties of pressure P, volume V, and temperature T at the thermodynamic critical point. Other equations, with a larger number of variable constants are more flexible and achieve greater accuracy over a broader range.

Such an equation is that proposed by J. Himpan[7]:

$$P + \{a/[(V - b)(TV - c)]\} = RT/(V - d) \qquad (1)$$

which has four empirical constants a, b, c, and d and is a modified form of the classic Berthelot equation. These constants can be related to the three conditions at the critical point (subscript c):

$$P = P_c\,,\ V = V_c\,,\ \text{and}\ T = T_c \qquad (2)$$

$$(\partial P/\partial V)_c = 0 \qquad (3)$$

$$(\partial^2 P/\partial V^2)_c = 0, \qquad (4)$$

and the fourth determined by requiring a fit to an experimental point such as the melting or boiling point. For extrapolation purposes estimates of the critical properties and the highest temperature at which accurate volumetric data are available can be used.

Interest in the Himpan equation was generated by its use by M. Keilhacker[8] to fit sonic velocities in copper vapor generated from an exploding wire. If applicable to other metals, particularly sodium, it could be used to calculate thermodynamic properties off the saturation curve, and, by appropriate analytical manipulation, the deviations from ideal gas behavior of enthalpy, entropy and heat capacity. The ideal gas behavior is accurately known from spectroscopic information and therefore permits calculation of thermodynamic processes without relying exclusively on the law of corresponding states.

Constants fitted to the estimated critical properties of sodium and liquid density at the boiling point give a satisfactory description of the liquid properties but predict vapor properties, such as compressibility, to engineering accuracy (about 12 per cent). Differences between states are predicted to somewhat better accuracy. Above the critical point agreement is found with deviations from ideal behavior predicted from the corresponding states.

Similar attempts to fit constants to vapor density information gave unacceptable results. This was found to be very sensitive to the technique used to fit the constants due to the non-linear character of Eq. (1). Consideration is being given to an iterative, non-linear, least squares technique which would permit use of all available experimental data, including such information as liquid compressibility and thermal expansion coefficients. Before publishing the derived constants a test of the equation against cesium data is desirable since the critical constants of this alkali metal are known and measurements on properties extend to larger reduced temperatures. Similar extension to mercury, for which a small amount of density data extends beyond the critical point, should provide an additional check.

REFERENCES

1. J. O. Hirschfelder, C. F. Curtiss and R. B. Bird, *Molecular Theory of Gases and Liquids*, (John Wiley, New York, 1965).
2. D. Miller, *Theoretical Prediction of Thermodynamic and Transport Properties of Metal Vapors*, Reactor Physics Division Annual Report, July 1, 1965 to June 30, 1966, ANL-7210, pp. 280–284.
3. G. Das and A. C. Wahl, *Extended Hartree-Fock Wave Functions: General Theory of Optimized Valence Configurations and its Application to Diatomic Molecules*, J. Chem. Phys. **41**, 2934–2942 (1967).
4. G. Das and A. C. Wahl, *Extended Hartree-Fock Wave Functions: Optimized Double Configurations for F_2*, J. Chem. Phys. **44**, 87–96 (1966).
5. P. Bertoncini and A. C. Wahl, Argonne National Laboratory (private communication).
6. C. F. Bonilla, Columbia University (private communication).
7. J. Himpan, *The Definitive Form of the New Thermal Equation of State with its Material Constants for Over 100 Different Substances*, Monatshefte für Chemie **86**, 259–268 (1955), (in German).
8. M. Keilhacker, *Mechanism of the Explosive Vaporization of Copper Wires by Means of Very Strong Current Impulses and the Behavior of the Copper at the High Pressures and Temperatures which Occur*, Z. für angew. Phys. **12**, 49–59 (1959), (in German); English translation AERE Trans. 989.

IV-20. Calculation of Expansion of Super-critical Sodium Vapor Released in an Experimental-Loop Accident

D. Miller

As part of the experimental investigation of severe transients in sodium-cooled systems using the Transient Reactor Test Facility (TREAT), a problem arose in the prediction of the consequences of an accident in the Mark II TREAT loop. Intimate contact between molten fuel and cladding materials can raise sodium coolant to temperatures above its estimated critical temperature. Expansion of this vapor into inert gas in the outer can of the loop will raise its temperature and pressure and threaten the integrity of the loop and the reactor.

To estimate the consequences of such an expansion several phenomena must be considered, the principal one being the effect of condensation. In addition, since experimental data on the thermophysical properties of sodium are limited to temperatures below 2000°K, errors are introduced in the extrapolation and estimation of these properties. Most of the calculations rely on the differences between values and, if calculated in a self-consistent way, should minimize errors.

Because the assumed initial temperature of 4000°K was well above the estimated critical temperature of 2733°K for sodium,[1] the equation of state was used to completely define this initial condition and the calculated values of the deviation from the ideal gas entropy, enthalpy, and energy agreed with values from the modified corresponding states tabulations of O. Hougen, K. Watson and R. Ragatz.[2]

These tables used the critical compressibility $Z_c = P_cV_c/RT_c$ as an additional parameter, where P is the pressure, T is the absolute temperature, V is the molar volume, and the gas constant R and the subscript c indicate the critical condition; the table entries were independent of Z_c for values of $(P/P_c) > 2$ as was also the case of the initial condition. Within the accuracy of the modified corresponding states principle, the reduced properties of sodium would be expected to be similar to those of water since its estimated value of $Z_c = 0.2301$ is very close to that of water. However, vaporization behavior of metals is expected to be different since the sodium is fully ionized in the liquid state and is a dielectric in the vapor state—different from the behavior of most of the fluids on which the tables are based.

The equation of state chosen was that of J. Himpan[3] which was found to accurately predict the behavior of the liquid and vapor states for many materials as well as their derived thermodynamic properties. This equation will be discussed in greater detail below (see Paper IV-19).

In addition, several asymptotic solutions were calculated as recommended by Y. Zel'dovich and Y. Raizer.[4] These include the equilibrium temperature, vapor pressure, and volume along the saturation curve which should be an upper bound to the final temperature and pressure. Lower bounds were isentropic expansions which neglected the condensation of vapor and the associated heat of condensation. The isentropic expansions followed the relation

$$PV_0^{\gamma-1} = P_0V_0^{\gamma}\,, \tag{1}$$

where the subscript 0 indicates the initial conditions, and γ is the isentropic exponent which is generally related to the ratio of constant pressure and constant volume heat capacities. Substitution of the ideal gas relation and neglect of condensation related the temperature and volume by

$$TV^{\gamma-1} = T_0V_0^{\gamma-1}. \tag{2}$$

Two values of γ were used: the value of 5/3 for monatomic gases and the effective value of 1.35 determined for the flow of saturated sodium vapor through a nozzle.[5] The higher exponent produced lower final pressures and temperatures.

The actual expansion will follow the isentropic path until sufficient subcooling below the equilibrium temperature causes nucleation and subsequent condensation. The final condition for a rapid expansion into the two-phase region will be determined by the condition of no change in the internal energy or a Maxwell expansion.[2] This energy balance will determine the mass fraction of vapor x (or "quality") for a given final temperature. The final temperature is subject to the constraint that the final volume will be given by the sum of the liquid and vapor volumes. The total pressure in the system will be the sum of the partial pressure of the sodium vapor and that of the heated argon gas.

These relations can be expressed by the following energy, U, balance equations based on a mole of sodium and N_{Ar} moles of argon.

$$\begin{aligned}\Delta U = {} & (U_2 - U_2^*) + (U_2^* - U_1^*) \\ & + (U_1^* - U_1) + N_{Ar}(U_{2Ar} - U_{0Ar}).\end{aligned} \tag{3}$$

Here the subscripts 0, 1 and 2 refer to the initial argon condition, initial sodium condition, and final

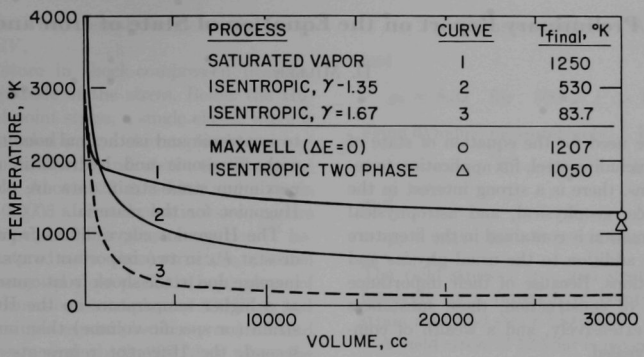

FIG. IV-20-1. Expansion of Two-phase Supercritical Sodium. *ANL Neg. No. 113-1538.*

sodium and argon temperatures. The subscript Ar corresponds to argon and the superscript * refers to the ideal gas state. If liquifaction occurs,

$$\begin{aligned} U_2^* - U_2 &= x(U_2^* - U_2)_G + (1 - x) \\ &\quad \cdot (U_2^* - U_2)_L \\ &= (U_2^* - U_2)_G + (1 - x) \\ &\quad \cdot [\Delta H_v - P_2(V_G - V_L)]. \end{aligned} \tag{4}$$

The subscripts G and L refer to the saturated vapor and liquid and ΔH_v is the heat of vaporization. Finally, the volume will be calculated from the temperature T_2 and quality x from the temperature dependent molal volumes:

$$V_F = xF_G + (1 - x)V_L\,. \tag{5}$$

The terms on the right side of Eq. (3) are calculated from the equation of state or corresponding states and the ideal gas heat capacity. The final pressure is calculated from

$$P_F(T_2) = P_{Na}(T_2) + \frac{T_2}{T_0}. \tag{6}$$

The second term on the right side of Eq. (6) is due to the heating of the argon gas, initially at one atmosphere, to the temperature T_2.

Results from the calculation of the expansion of 16.6 g of sodium initially at a temperature of 4000°K and a volume of 92 cm³ into 30 liters containing argon gas initially at 473°K are displayed in Fig. IV-20-1. The final temperature for the two-phase expansion is estimated to be 1207°K and the final total pressure is estimated to be 4.12 atm. Since this is higher than the estimated buckling pressure of the can, a rupture disc and relief line must be provided.

REFERENCES

1. D. Miller, A. B. Cohen and C. E. Dickerman, *Estimation of Vapor and Liquid Density and Heat of Vaporization of the Alkali Metals to the Critical Point*, Proc. International Conference on the Safety of Fast Breeder Reactors, 1967, Aix-en-Provence, sponsored by CEA, Paris, France.
2. O. A. Hougen, K. M. Watson and R. A. Ragatz, *Chemical Processing Principles* (John Wiley, New York, 1959), Vol. II, Thermodynamics.
3. J. Himpan, *The Definitive Form of the New Thermal Equation of State with its Material Constants for Over 100 Different Substances*, (in German) Monatshefte für Chemie **86**, 259–268 (1955). Also, *The Definitive Form of the New Thermal Equation of State: Practical Applications* (in German) Monatshefte für Chemie **86**, 491–501 (1951).
4. Ya. B. Zel'dovich and Yu. P. Raizer, *Physics of Shock Waves and High-Temperature Hydrodynamic Phenomena* (Academic Press, New York, 1967), Vol. II, p. 587.
5. L. J. Goldman, *Expansion and Flow Characteristics of Initially Saturated Sodium, Potassium and Cesium Vapors*, NASA-TN-D-3743, (November 1966).

IV-21. Preliminary Report on the Equation of State of Iron and Steel

D. Miller

In addition to the need for the equation of state of iron and its alloys, including steel, for application to reactor safety problems, there is a strong interest in the subject for ordnance, geophysical, and astrophysical studies. Much information is contained in the literature of these subjects in addition to the usual physics and engineering publications. Because of their importance as prime materials of construction, these substances have been studied extensively, and a wealth of complexity has been revealed.

Most of the information obtained for the pressure-volume relation for solid iron at high applied stresses has been obtained by dynamic studies,[1-13] although static[14-18] and dynamic results have been brought into good agreement in recent years by improved experimental technique, calibration, and understanding of the phenomena.

For the purpose of discussion, Fig. IV-21-1 gives an exaggerated description of some of the phenomena and the nomenclature generally used in their description. The dynamic stress-strain curve represents the average stress-strain path followed by materials as a wave front moves through it. This path is a function of

1. the strain rate and the wave shape
2. temperature
3. composition—alloying agents, porosity
4. previous history—residual strain, dislocations.

As the wave front moves through the solid, the strain rate reaches a maximum value and then decreases as the peak stress is reached.[19] This peak stress, σ_H, has been found to be very close to the quasistatic value, and it is the most useful point to serve as a basis for conversion to isentropic and isothermal conditions for comparison with ultrasonic and hydrostatic experiments. These maximum stress-strain data are plotted and form the Hugoniot for the material.

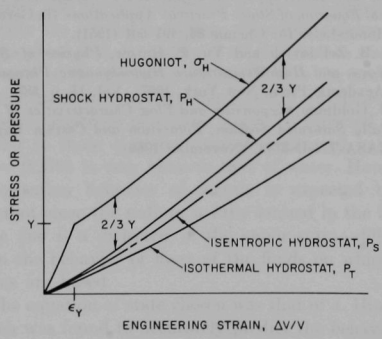

Fig. IV-21-1. Stress or Pressure Versus Strain. *ANL Neg. No. 113-951.*

The Hugoniot curve differs from the isentropic hydrostat P_S in two important ways. First, the entropy increase due to the shock front causes the material to be at a higher temperature on the Hugoniot for a given strain (or specific volume) than on the isentrope; and second, the Hugoniot represents the state of stress composed of the spherical component of the hydrostat plus a deviatoric component due to the material yield strength Y.

A simple relation between the quasistatic uniaxial-stress flow condition and the uniaxial-strain flow condition is used, although this flow condition may be strain-rate,[20-24] temperature,[12,16,25] composition,[26-34] and strain history dependent.[35-36] The spherical component, or pressure, on the shock hydrostat P_H is related to the Hugoniot stress σ_H and yield stress Y by

$$P_H = \sigma_H - \tfrac{2}{3}Y. \tag{1}$$

The strains ϵ_X along the Hugoniot are related to the uniaxial strain ϵ by

$$\epsilon_X = \tfrac{3}{2}\epsilon - Y/6K = 1 - V/V_0\,, \tag{2}$$

where K is the bulk modulus defined by

$$K = -V\left(\frac{\partial P}{\partial V}\right), \tag{3}$$

V is the volume, and V_0 is the volume at the initial pressure (usually taken as one atmosphere and equivalent to zero pressure on the scale of the phenomena considered here.)

Since the bulk modulus has been found to be linear[37-40] over a wide range of pressure,

$$K(V,T) = K_0(T) + K'(T)P(V) \tag{4}$$

where $K' = (\partial K/\partial P)_T$, Eq. (3) can be integrated to give the Murnahagn equation of state in the purely elastic region:

$$P = \frac{K_0}{K'}\left[\left(\frac{V_0}{V}\right)^{K'} - 1\right] \quad \text{for} \quad 0 \le \sigma_H \le Y. \tag{5}$$

This form of the pressure-volume relation fits experimental data for both isentropic and isothermal compression in the elastic region and can be made to fit the elastic-plastic[41] and purely plastic regions to be introduced below in spite of phase changes which take place

at higher pressures. The internal energy can be found from $E = -\int P\,dV$.

The wave structure in shock-compressed iron depends on the magnitude of the stress. Below the Hugoniot elastic yield-point stress, a single elastic wave is found. In pure annealed iron, a slower plastic wave of greater stress amplitude is found above the Hugoniot elastic limit (HEL). Above 129 ± 1 kbar and a strain ϵ_{trans} of 0.0640 ± 0.0005 a second plastic wave appears corresponding to a polymorphic phase transition[7,15] between the body centered cubic (bcc) structure of α-iron and the denser hexagonal close packed (hcp) phase of ϵ-iron. This transformation is complete at 330 kbar, and the elastic and the single second plastic waves are found between this pressure and about 660 kbar when the second plastic wave outruns the elastic wave and a single wave structure is observed at higher pressures. The regions are shown in Fig. IV-21-2.

These transitions are composition[26-34] and temperature[12,16,25] dependent, but only the behavior of pure iron will be described here.

While the linear shock velocity U_S and particle relation U_p in the form

$$U_S = C_0 + SU_p \tag{6}$$

is often convenient for describing the Hugoniot equation of state, the transitions make this convenient only in the purely plastic region. Murnahagn constants have been fitted to both the static[17] and dynamic[41] results in the regions of multiple waves.

Constants to be used are the ultrasonic isothermal values of M. Guinan and D. Beshers[40] at 300 ± 1°K for bcc iron up to 10 kbar,

$$K_0^T = 1635 \text{ kbar}$$

$$\rho_0 = 7.85 \text{ g/cc} = 1/V_0$$

and

$$K^{T'} = \frac{dK^T}{dP} = 5.20.$$

Isentropic values are similar:

$$K_0^S = 1664 \pm 17 \text{ kbar} \quad \text{and} \quad K^{S'} = 5.29 \pm 0.25,$$

where S and T refer to isentropic and isothermal values of the constants defined in Eq. 4. These values agree well with those of C. Rotter and C. Smith[39] and also agree well with the static measurements of H. Mao, W. Bassett, and T. Takahashi[17] who found

$$K_0^T \text{ bcc} = 1628, \qquad K^{T'} = 5.92$$

and

$$\rho_0 = 7.87 \text{ g/cc} \quad \text{for} \quad P < 130 \text{ kbar} \quad \text{at} \quad 23°\text{C};$$

and

$$K_0^T \text{ hcp} = 1658, \qquad K^{T'} = 5.10$$

and

$$\rho_0 = 8.32 \quad \text{for} \quad 300 > P > 130 \text{ kbar}.$$

From dynamic measurements, J. Erkman[42] recommends

$$K_0^S = 369, \qquad K^{S'} = 22.8,$$

and

$$\rho_0 = 8.38 \quad \text{for} \quad P > 131 \text{ kbar}.$$

The yield stress of iron and steel has been studied extensively as a function of composition, temperature, strain rate, and strain history.

A yield stress of 12 kbar is recommended for annealed pure iron and the strain rate dependence is

$$Y_{dynamic} = Y_{static}\left[\left\{\frac{d\epsilon}{dT}\Big/ 40.4\right\}^{1/5} + 1\right] \tag{7}$$

as fitted to the data of M. Manjoine[21] for mild steel. The temperature dependence suggested by J. Bell[25] for annealed fcc metals in plastic deformation is

$$Y_{static} = 5.47\left(1 - \frac{T°\text{K}}{T_m°\text{K}}\right)\epsilon^{1/2} \text{ kbar}, \tag{8}$$

where T_m is the absolute melting temperature. The effect of pressure on melting is given by the relation[43]

$$T_m(°\text{K}) = 1807 + 3.8P \text{ (kbar)}.$$

The heat of fusion is 64.9 cal/gm. The heat of vaporization is 1626 cal/g and the boiling temperature is 3340°K.

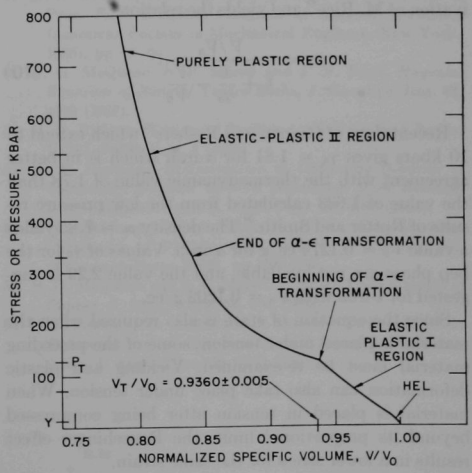

FIG. IV-21-2. The Hugoniot of Annealed Iron. *ANL Neg. No. 113-949.*

TABLE IV-21-I. SHOCK VELOCITY CONSTANTS FOR IRON AND STEEL[a]

Author	ρ_0, g/cc	C, mm/μsec	S	Pressure Range, kbar
Altschuler[9]	7.85	3.80	1.58	400–5000
Skidmore and Morris[13]	7.84	3.67	1.645	330–5000

[a] Other data can be found in the compilation of van Thiel.[6]

The heat capacity is characterized by a Debye temperature of 432°K.[18]

It should be noted that the yield-stress phenomena completely disappear in samples prepressurized to 10 kbar due to the reduction of dislocations.[35]

Above the elastic-plastic region, the constants for the linear shock velocity-particle velocity, Eq. (6), can be chosen from Table IV-21-I.

The shock hydrostats can be corrected to the isentropes and isotherms by using the Grüneisen equation

$$P - P_H = \frac{\gamma(V)}{V}(E - E_H). \tag{9}$$

The volume dependence of the Grüneisen coefficient γ is not well known, although the assumption of $\gamma/V = \gamma_0/V_0$ has been widely used[1] and agrees reasonably well with experiment.[44] Alder[47] has suggested $\gamma/\sqrt{V} = \gamma_0/\sqrt{V_0}$ is more nearly correct for iron. The volume dependence of γ is still under active study,[44-50] but the recent results of H. Richter[50] lend support to the derivation of M. Rice[45] and yields the relation

$$\gamma = \frac{V/V_0}{1 + \dfrac{1}{\gamma_0} - \dfrac{V}{V_0}}. \tag{10}$$

Recent data of Guinan and Beshers[40] which extend to 10 kbars gives $\gamma_0 = 1.81$ for α-iron which is in better agreement with the thermodynamic value of 1.78 than the value of 1.633 calculated from the low pressure results of Rotter and Smith.[39] The density $\rho_0 = 7.85$ yields a value $V_0 = 0.1274$ cc/g for α-iron. Values of γ_0 for the hcp phase are not available, and the value 2.29 is suggested for ϵ-iron with $V_0 = 0.1202$ g/cc.

Since the equation of state is also required when the material is placed under tension, some of the preceding material must be re-examined. Yielding and plastic deformation can also take place under tension. When material is placed in tension after being compressed beyond its proportional limit, the Bauschinger effect results in a lower stress for the same strain.[36,51]

Because of the two-wave structure in iron, a negative shock will always occur above the transition point.[52] Several models have been proposed[53] for the equation of state in the tensile region and have given reasonable descriptions of the fracture phenomena for copper and other materials, although the tensile strength is dependent on the stress gradient or stress rate.[54] The stress rate can be of the order of 1 Mbar/μsec and corresponds to strain rates of about 10^6 sec^{-1}.

REFERENCES

1. M. H. Rice, R. G. McQueen and J. M. Walsh, *Compression of Solids by Strong Shock Waves*, Solid State Phys. **6**, 1 (1958).
2. G. E. Duvall, *Some Properties and Applications of Shock Waves*, Response of Metals to High Velocity Deformations, P. G. Shewmon and V. F. Zackay, Eds. (Interscience Publishers, New York, 1961), pp. 165–202.
3. R. G. McQueen, *Laboratory Techniques for Very High Pressures and the Behavior of Metals Under Dynamic Loading*, Metallurgy at High Pressures and High Temperatures, K. A. Gschneider, Jr., M. T. Hepworth and N. A. D. Parlee, Eds. (Gordon and Breach Publishers, New York, 1964), pp. 44–132.
4. L. V. Altschuler, *Use of Shock Waves in High-Pressure Physics*, Sov. Phys.-Usp. **8**, 52 (1965).
5. D. G. Doran and R. K. Linde, *Shock Effects in Solids*, Solid State Phys. **19**, 229 (1966).
6. M. van Thiel, A. S. Kusubov, A. C. Mitchell and V. W. Davis, *Compendium of Shock Wave Data*, UCRL-50108 (1966).
7. D. Bancroft, E. L. Peterson and S. Minshall, *Polymorphism of Iron at High Pressure*, J. Appl. Phys. **27**, 291 (1956).
8. J. M. Walsh, M. H. Rice, R. G. McQueen and F. L. Yarger, *Shock-Wave Compression of Twenty-Seven Metals. Equations of State for Metals*, Phys. Rev. **108**, 196 (1957).
9. L. V. Altschuler, K. K. Krupnikov, B. N. Lebedev, V. I. Zhuchikhin and M. I. Brazhnik, *Dynamic Compressibility and Equation of State of Iron Under High Pressure*, Sov. Phys.-JETP. **7**, 606 (1958).
10. S. Katz, D. G. Doran and D. R. Curran, *Hugoniot Equation of State of Aluminum and Steel from Oblique Shock Measurements*, J. Appl. Phys. **30**, 568 (1959).
11. R. G. McQueen and S. P. Marsh, *Equations of State of Nineteen Metallic Elements from Shock Wave Measurements to Two Megabars*, J. Appl. Phys. **31**, 1253 (1960).
12. P. Johnson, B. Stein and R. S. Davis, *Temperature Dependence of the Shock Induced Transformation in Iron*, J. Appl. Phys. **33**, 557 (1962).
13. I. C. Skidmore and E. Morris, *Experimental Equation of State Data for Uranium and Its Interpretation in the Critical Region*, Thermodynamics of Nuclear Materials, International Atomic Energy Agency, Vienna, 1962 (STI/PUB/58) p. 173; see also E. Morris, *The Equation of State and Uranium in the Critical Region*, AWRE-0-61/62, (1962).
14. R. L. Clendenin and H. G. Drickamer, *The Effect of Pressure on the Lattice Parameters of Ruthenium and Iron*, J. Phys. Chem. Solids **25**, 865 (1964).
15. T. Takahashi and W. A. Bassett, *High-Pressure Polymorph of Iron*, Science **145**, 483 (1964).
16. F. P. Bundy, *Pressure-Temperature Phase Diagram of Iron to 200 kbar, 900°C*, J. Appl. Phys. **36**, 616 (1965).
17. H. K. Mao, W. A. Bassett and T. Takahashi, *Effect of Pressure on Crystal Structure and Lattice Parameters of Iron*

up to 300 kbar, J. Appl. Phys. **38**, 272 (1967). Erratum **38**, 2142 (1967).

18. G. L. Stepakoff and L. Kaufman, *Thermodynamic Properties of h.c.p. Iron and Iron-Ruthenium Alloys*, Acta. Met. **16**, 13 (1968).
19. D. E. Munson and L. M. Barker, *Dynamically Determined Pressure-Volume Relationships for Aluminum, Copper, and Lead*, J. Appl. Phys. **37**, 1652 (1966).
20. B. M. Butcher and C. H. Karnes, *Strain Rate Effects in Metals*, J. Appl. Phys. **37**, 402 (1966).
21. M. J. Manjoine, *Influence of Rate of Strain and Temperature on Yield Stresses of Mild Steel*, J. Appl. Mech. **11**, A211 (1944).
22. J. W. Taylor and M. H. Rice, *Elastic-Plastic Properties of Iron*, J. Appl. Phys. **34**, 364 (1963).
23. E. A. Ripperger, *Dynamic Plastic Behavior of Aluminum, Copper, and Iron*, Behavior of Materials Under Dynamic Loading, N. J. Huffington, Jr., Ed. (American Society of Mechanical Engineers, New York, 1965), p. 62.
24. S. R. Bodner and P. S. Symonds, *Plastic Deformation in Impact and Impulsive Loading of Beams*, Brown University, ONR Contract No.-562(10).
25. J. F. Bell, *Single, Temperature-Dependent Stress-Strain Law for Dynamic Plastic Deformation of Annealed Face-Centered Cubic Metals*, J. Appl. Phys. **34**, 134 (1963).
26. D. R. Curran, *On the Possibility of Detecting Shock-Induced Second-Order Phase Transitions in Solids. The Equation of State of Iron*, J. Appl. Phys. **32**, 1811 (1961).
27. F. S. Minshall, *The Dynamic Response of Iron and Iron Alloys to Shock Waves*, Response of Metals to High Velocity Deformation, P. G. Shewmon and V. F. Zackay, Eds. (Interscience Publishers, New York, 1961), p. 249.
28. C. M. Fowler, F. S. Minshall and E. G. Zukas, *A Metallurgical Method for Simplifying the Determination of Hugoniot Curves for Iron Alloys in the Two-Wave Region*, Response of Metals to High Velocity Deformation, P. G. Shewmon and V. F. Zackay, Eds. (Interscience Publishers, New York, 1961), p. 275.
29. A. S. Balchan and G. R. Cowan, *Shock Compression of Two-Iron-Silicon Alloys to 2.7 Megabars*, J. Geophys. Res. **71**, 3577 (1966).
30. S. B. Kormer and A. I. Funtikov, *A Study of Impact Compression of Ferrosilicon and a Possible Composition of Earth's Core*, Phys. Solid Earth **5**, 285 (1956).
31. T. R. Loree, C. M. Fowler, E. G. Zukas and F. S. Minshall, *Dynamic Polymorphism of Some Binary Iron Alloys*, J. Appl. Phys. **37**, 1918 (1966).
32. R. G. McQueen and S. P. Marsh, *Shock-Wave Compression of Iron-Nickel Alloys and the Earth's Core*, J. Geophys. Res. **71**, 1751 (1966).
33. R. A. Graham, D. H. Anderson and J. R. Holland, *Shock-Wave Compression of 30% Ni-70% Fe Alloys: The Pressure Induced Magnetic Transition*, J. Appl. Phys. **38**, 223 (1967).
34. F. P. Bundy, *Fe-Co and Fe-V Alloys for Pressure Calibration in the 130- to 300-kbar Region*, J. Appl. Phys. **38**, 2446 (1967).
35. F. P. Bullen, F. Henderson, M. M. Hutchison and H. L. Wain, *The Effect of Hydrostatic Pressure on Yielding in Iron*, Phil. Mag. **9**, 285 (1964).
36. O. E. Jones and J. R. Holland, *Bauschinger Effect in Explosively Loaded Mild Steel*, J. Appl. Phys. **35**, 1771 (1964).
37. O. L. Anderson, *The Use of Ultrasonic Measurements Under Modest Pressures to Estimate Compression at High Pressure*, J. Phys. Chem. Solids **27**, 547 (1966).
38. H. G. Drickamer, R. W. Lynch, R. L. Clendenin and E. A. Perez-Albuerne, *X-Ray Diffraction Studies of the Lattice Parameters of Solids Under Very High Pressure*, Solid State Phys. **19**, 135 (1966).
39. C. A. Rotter and C. S. Smith, *Ultrasonic Equation of State of Iron. I. Low Pressure, Room Temperature*, J. Phys. Chem. Solids **27**, 267 (1966).
40. M. W. Guinan and D. N. Beshers, *Pressure Derivatives of the Elastic Constants of α-Iron to 10 KBS*, J. Phys. Chem. Solids **29**, 541 (1968).
41. Y. K. Huang and N. Davids, *Shock Dynamics of Hypervelocity Impact of Metals*, J. Franklin Inst. **276**, 39 (1963).
42. J. O. Erkman, *Smooth Spalls and the Polymorphism of Iron*, J. Appl. Phys. **32**, 939 (1961).
43. K. F. Sterrett, W. Klement, Jr. and G. C. Kennedy, *Effect of Pressure on the Melting of Iron*, J. Geophys. Res. **70**, 1979 (1965).
44. J. W. Taylor, *Residual Temperature in Shocked Copper*, J. Appl. Phys. **34**, 2727 (1963).
45. M. H. Rice, *Pressure-Volume Relations for the Alkali Metals from Shock-Wave Measurements*, J. Phys. Chem. Solids **26**, 483 (1965).
46. D. T. Morgan, M. Rockowitz and A. L. Atkinson, *Measurement of the Grüneisen Parameter and the Internal Energy Dependence of the Solid Equation of State for Aluminum and Teflon*, AVCO Corp. Report AFWL-TR-65-117 (1965).
47. B. J. Alder, *Is the Mantle Soluble in the Core?* J. Geophys Res. **71**, 4973 (1966).
48. H. C. Rodean, *Thermodynamic Relations for Shock Waves*, Proc. Fifth National Congress of Applied Mechanics (American Society of Mechanical Enginers, New York, 1966), pp. 89–96.
49. R. G. McQueen, S. P. Marsh and J. N. Fritz, *Hugoniot Equation of State of Twelve Rocks*, J. Geophys. Res. **72**, 4999 (1967).
50. H. P. Richter, *Numerical Problems with Gürneisen Ratios*, UCRL-70670, Rev. 1 (1968).
51. W. F. Hartman, *Determination of Unloading Behavior of Uniaxially Strained 6061-T6 Aluminum from Residual Strain Measurements*, J. Appl. Phys. **35**, 2090 (1964).
52. I. C. Skidmore, *Shock Waves in Solids*, Encyclopaedic Dictionary of Physics, Sup., Vol. 1, J. Thewlis, Ed. (Pergamon Press, 1965), pp. 290–293.
53. R. G. McQueen and S. P. Marsh, *Ultimate Yield Strength of Copper*, J. Appl. Phys. **33**, 654 (1962).
54. B. R. Breed, C. L. Mader and D. Venable, *Technique for the Determination of Dynamic-Tensile-Strength Characteristics*, J. Appl. Phys. **38**, 3271 (1967).

IV-22. Surface Tension and Critical Points of Alkali Metals

D. Miller

The surface tensions of reactor materials are of interest for theoretical and practical applications. Alkali metals are of special theoretical importance because of the relative simplicity of their electronic structure and their plasma-like nature. Surface tension also provides a measure of the rate of decrease of inter-atomic forces in the vicinity of an interface. Practical application includes this property as a parameter in relations governing bubble growth and collapse rates, as in boiling heat transfer or cavitation; the size of drops and their adhesion to surfaces of solids; the determination of wave length in some hydrodynamic stability analyses of boiling and expulsion; and as a principal determinant in the performance of heat pipes under agravitic conditions.

At temperatures approaching the thermodynamic critical point, the surface tension decreases rapidly and can be used to estimate the critical temperature T_c, at which it vanishes, thus serving as a test of an extended principle of the law of corresponding states.[1]

Recent experimental data[2] extend to higher temperatures than previously available and are in good agreement with several other investigators at lower temperatures. Data[3] for sodium and potassium of lower purity are available to slightly higher temperatures but have been rejected because of the lack of agreement with other investigators. Curve fitting of the data was attempted in two forms. The first was a simple linear extrapolation

$$\sigma = \sigma_0 - bT, \tag{1}$$

where σ is the surface tension in dynes/cm, T is the absolute temperature in degrees K, σ_0 is the surface tension if the liquid metal existed at absolute zero, and b is the temperature coefficient $d\sigma/dT$.

The second form is called the Goldhammer-Guggenheim relation,[1,4] which can be derived from empirical relations between other physical properties and is

$$\sigma = \sigma_0[1 - (T/T_c)]^p. \tag{2}$$

Here the symbols have their previous meanings while p is supposedly a universal constant which is taken as 11/9 for normal liquids. Others[5] have found p to vary around this value, and theory[6] predicts $1.20 < p < 1.29$ if quantum and other effects can be neglected.

A. Grosse[7] examined the merits of these two equations and showed that linear extrapolation gave a slightly higher value of σ_0 except for sodium. Linear extrapolation also underestimates the critical temperature. The experimental data[2] may be slightly in error due to the density equations used in the reduction of their data. These equations are somewhat different from those recommended[8] after a study of recent experimental data. However, these data were used to determine the constants in Eqs. (1) and (2) by a least squares technique. In applying Eq. (2), two methods were used:

(a) The critical temperatures of D. Miller, A. Cohen, and C. Dickerman[8] were assumed from which σ_0 and p were determined; this is termed σ_0^a.

(b) The exponent 11/9 was assumed and γ_0 and T_c determined; here the value is termed σ_0^b.

The results are given in Table IV-22-I with the values for xenon given for comparison.

Values of σ_0 are not strongly dependent on the method of fitting the data, but the critical temperatures are lower than those estimated from density and heat of vaporization[8]—although the discrepancies are not large for those calculated from Eq. (2) by assuming $p = 11/9$. Slight increases in p to the value of 1.29 as predicted by theory bring the estimated critical temperatures into better agreement, although there are indications that the surface tension data for lithium and cesium are both on the low side.

The corresponding states parameter,[1,9] $\sigma_0 V_c^{2/3}/T_c$, where T_c is the critical volume in cc/gm-mol,[(8)] is roughly constant as expected but about half the value found by Guggenheim and others for normal fluids, such as organics and rare gases (cf. xenon). These values range from about 4.0 to 4.7 with the exception of the value for water which is 2.7. A quantum mechanical effect[9] should cause the value for lithium to be lower than those for the other alkali metals. The constants given in Table IV-22-I can be used in Eq. (2) to calculate the surface energy E from the relation

$$E = \sigma - T\frac{d\sigma}{dT}, \tag{3}$$

or to extrapolate to higher temperatures where data are unavailable.

Equation (2) can be substituted into Eq. (3) with the result

$$E = \sigma_0\left(1 - \frac{T}{T_c}\right)^{p-1}\left\{1 + \frac{T}{T_c}(p\sigma_0 - 1)\right\}. \tag{4}$$

If p were a universal constant, E would be a function of only σ_0 and the reduced temperature $T_R = T/T_c$. This relation predicts zero surface energy at the critical point as expected.

TABLE IV-22-I. CONSTANTS FITTED TO EXPERIMENTAL SURFACE TENSION DATA

Material	σ_0 (Eq. 1), dynes/cm	b, dynes/cm-°K	T_c (Eq. 1), °K	σ_0 (Eq. 2), Method a	p	T_c (Ref. 8)	σ_0 (Eq. 2), Method b	T_c, °K	$\frac{\sigma_0 V_c^{2/3}}{T_c}$
Lithium	473.8 ±2.1	0.163 ±0.5 $\times 10^{-5}$	2913	494±1.4	1.770	4310±100	482.2	3306	2.62
Sodium	227.5 ±0.97	0.0951±0.18$\times 10^{-4}$	2392	234±0.97	1.248	2733±40	233.1	2697	2.27
Potassium	138.8 ±1.3	0.0787±0.18$\times 10^{-5}$	1764	142.8 ±1.1	1.479	2287±40	141.2±1.19	2005	2.24
Rubidium	105.0 ±1.1	0.0657±0.17$\times 10^{-5}$	1598	108.7 ±1.0	1.582	2164±40	106.7±1.0	1800	2.02
Cesium	86.80±0.82	0.0569±0.87$\times 10^{-6}$	1524	90.24±0.73	1.586	2040±40	88.4±0.82	1720	2.10
Xenon	43.06±0.51	0.1537±0.15$\times 10^{-4}$	286.5	54.59±0.32	1.287	289.74	54.00	283.60	4.56

REFERENCES

1. E. A. Guggenheim, *The Principal of Corresponding States*, J. Chem. Phys. **13**, 253–261 (1945); Proc. Phys. Soc. (London) **85**, 811 (1965).
2. J. Bohdansky and H. E. J. Schins, *The Surface Tension of the Alkali Metals*, J. Inorg. & Nucl. Chem. **29**, 2173–2179 (1967).
3. A. N. Solov'ev and O. P. Markova, *Study of the Surface Tension of Liquid Sodium and Potassium*, High Temperature **4**, 187–192 (1965) [translated from Teplofizika Vysokikh Temperatur **4**, 189–195 (1965)].
4. D. A. Goldhammer, *Studien über die Theorie der übereinstimmenden Zustände*, Z. Phys. Chem. **71**, 577–624 (1910).
5. F. P. Sprow and J. M. Prausnitz, *Surface Tensions of Simple Liquids*, Trans. Faraday Soc. **62**, 1097–1104 (1966).
6. B. Widom, *Surface Tension and Molecular Correlations Near the Critical Point*, J. Chem. Phys. **43**, 3892–3897 (1965).
7. A. V. Grosse, *The Relationship Between the Surface Tensions and Energies of Liquid Metals and Their Critical Temperatures*, J. Inorg. & Nucl. Chem. **24**, 147–156 (1962).
8. D. Miller, A. B. Cohen and C. E. Dickerman, *Estimation of Vapor and Liquid Density and Heat of Vaporization of Alkali Metals to the Critical Point*, Proc. International Conference on the Safety of Fast Reactors, Commission A L'Energie Atomique, Sept. 19–22, 1967.
9. A. P. Watkinson and J. Lielmez, *Corresponding-States Principle and Surface Tension*, J. Chem. Phys. **47**, 1558–1559 (1967).

IV-23. Fast Reactor Fuel Testing in a Thermal Reactor

J. C. CARTER

The Fuel Failure Propagation Program requires that assemblies of fast fuel elements (7 or more) be placed in an environment similar to that existing in the core of a sodium-cooled fast reactor. This can only be accomplished by placing the fast fuel elements in the core of a nuclear reactor.

The reactor must be capable of producing and maintaining the required heat generating conditions in the fast fuel. In addition, the reactor complex must have adequate test loop handling facilities, facilities for removing the heat generated in the test assembly, hot cell facilities for disassembling the loop, and provision for instrumenting the reactor loop and test fuel elements. These essential requirements are evaluated and compared. The selection of the reactor is based on what is considered to be the best combination of these requirements in currently available facilities.

The lengths of fuel elements to be tested (90 cm) and the length of the integral loop (25 ft) preclude any existing fast reactor core and its associated loop handling facilities unless extensive modifications are made both to the loop and reactor facilities. The alternative is that of surrounding the assembly of fast fuel rods by a thermal neutron filter and/or a converter and placing this assembly in a thermal reactor of high thermal power, of low cadmium ratio and requiring a minimum amount of structural revision. The assembly of fast fuel elements is to be isolated from the reactor and its systems by virtue of the fact that the assembly would be totally enclosed in a self-sufficient test loop. The structural integrity of the loop is such that the fuel elements within it can disintegrate and cause no damage to the reactor.

Since many kinds of reactors might conceivably be used for the tests in this program, a survey was made by Argonne staff of all known reactors in the USA. The materials testing type of reactor appears to be the type best suited for the experiments of this program and a few of these meet most of the criteria for the test reactor. They are listed in Table IV-23-I. Some have sufficient power in the core but do

TABLE IV-23-I. REACTORS SUITABLE FOR TESTING FAST FUEL ELEMENTS

Reactor	Av Power Density		Test Hole		Flux Available in Test Hole, n/cm²-sec × 10^{14}	
	Fuel, kW/kg U^{235}	Core, kW/liter	Active Core Length, ft	Cross Section, in.	Thermal	Fast
ATR[a]	8500	670	4	5.25 dia.	>10	15
ETR[b]	7600	494	3	6 × 6	4	4
GETR[c]	6200[d]	625[d]	3	3 × 3	2	5
HFIR[e]	10,640	2000				
MTR[f]	9000	400	2	3 × 3	5	5
ORR[g]	4700	200	2	3 × 3	3	—

[a] Advanced Test Reactor, NRTS
[b] Engineering Test Reactor, NRTS
[c] General Electric Test Reactor, Pleasanton, California
[d] Estimate for 50 MW operation
[e] High Flux Isotope Reactor (ORNL)
[f] Materials Testing Reactor NRTS
[g] Oak Ridge Research Reactor, ORNL

TABLE IV-23-II. CHARACTERISTICS OF ETR CORE

Total reactor power	MWt	175
Thermal neutron flux	n/cm²-sec × 10^{14}	1.6 to 5
Epithermal neutron flux	n/cm²-sec × 10^{14}	5 to 15
Fuel-Uranium enriched to 93%	U-235	
Amount of U-235 in core	kg	23
Core diameter	cm	81.28
Core height	cm	91.44
Avg. specific power	kW/kgU	76.00
Power density	kW/liter of core	494
Metal-to-water ratio		0.67
Poison contents (natural boron)	g	150
Control rod worth		
(a) safety	%k	6 to 16.6
(b) shim	%k	1 to 4
Vertical max-to-av power ratio in fuel		2.4
Horizontal max-to-av power ratio in fuel		1.7
Initial excess reactivity	%k	8 to 11

not currently have either the availability or facilities required for the program, and would require extensive modifications to make them suitable. The research reactors of the pool type generally have very low power, such as the Babcock and Wilcox Nuclear Development Center Test Reactor (BAWTR) which has one of the highest fluxes available in a pool reactor. The power demonstration reactors are either shut down or are currently undergoing structural changes. Transient type reactors, such as the Transient Reactor Test Facility (TREAT), the Power Burst Reactor (PBR) and the Modification to Spert IV (CDC), represent another class in which some experiments in the program may be conducted.

From an evaluation of the reactors in the survey of existing reactors which may be available, the Engineering Test Reactor (ETR) is considered to be the most suitable for the fuel failure propagation program with assemblies of fast reactor fuel elements from a consideration of fast flux, loop handling facilities, licensing, and sodium/water safety assessment. The characteristics of the ETR reactor are given in Table IV-23-II.

The position in the core is the 6 x 6 in. J-13 hole (Fig. IV-23-1) for which the estimated fluxes are

thermal, 3.5 to 4 × 10^{14}
fast, 2 to 2.5 × 10^{14}
epithermal, 4 × 10^{14}
cadmium ratio, 8.

The required epithermal flux estimated for the fuel elements to be tested is on the order of 1 × 10^{14}. For most of the contemplated experiments a heat generation rate of at least 2000 W/cc of UO_2 fast reactor is required.

In this reactor all experimental facilities are vertical and are inside the reactor vessel. The reactor control rod drives are mounted below the reactor bottom head where the experimental facilities least interfere with them. The top of the reactor is near floor level because of the large clear-height needed to remove experimental apparatus. Such things as the depth of the vessel, position of the core, and size of the biological shield are set by allowable radiation level and biological considerations.

The ETR facility is a complete nuclear engineering test facility. The reactor is light-water cooled and moderated and has a thermal rating of 175 MW. It is housed in a gastight building 112 x 136 feet, extending 58 feet above and 38 feet below grade. The reactor vessel consists of the multidiameter vessel proper, removable elliptical dome with flat top flange, flat bottom head, a discharge chute, inlet water flow distributor, experimental hanger supports, experimental access nozzles, and outlet line connections. The vessel serves the functions of containing the reactor core and of providing radiation space and facilities to accommodate the in-pile tubes to be used for nuclear radiation experiments. Facilities are also provided for control rods, instrumentation, shielding of the vessel walls, directing coolant flow through the core, and support of all internal structure. The stainless steel clad carbon steel and stainless steel reactor vessel design pressures and temperatures are

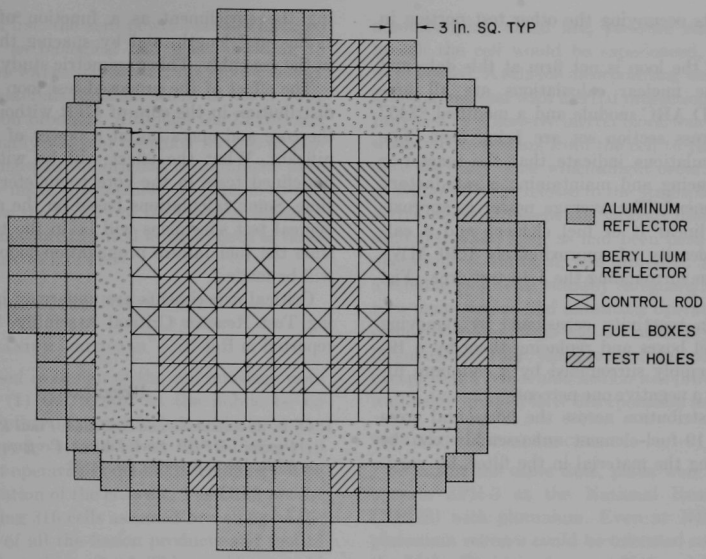

FIG. IV-23-1. ETR Core. *ANL Neg. No. 113-861.*

250 psig and 200°F. Operating pressures and temperatures are 200 psig at 110°F inlet and 150 psig at 133.5°F outlet.

The vessel internals consist of the inner tank, the internal thermal shields, reactor core, core support structure and the experiment upper support ring. The core support consists of six structural supports extending from the reactor bottom head up to and including the support plate and reactor grid plate. This structure supports the reactor core, beryllium reflector and aluminum reflector, serves as a guide for the experimental in-pile tubes and control rods, and transmits the pressure drop load across the core to the reactor bottom head.

The reactor core is a square configuration of 52 fuel elements, 12 shim control rods, 4 safety control rods, 4 corner filler pieces, and 9 experimental facilities and it is approximately 30.4 inches square.

The beryllium reflector is a 4½ inch thick layer of beryllium extending completely around the core. The two originally designed regulating rods were contained in holes on opposite sides in the beryllium reflector. Space also is provided in the beryllium for additional capsule-type experiments. The aluminum reflector pieces extend from the beryllium reflector out to the inner tank walls. Provision is made for eight experimental facilities in the aluminum reflector. Each aluminum reflector element is built with a hollow interior providing for additional irradiation space of the capsule type.

The reactor vessel is enclosed and supported by a high density concrete biological shield extending from the first floor to the basement ceiling. This shield is 8 feet thick at the core centerline. The 25-foot outside diameter of the shield is covered with a ¾-inch steel plate.

Material handling facilities include a 30/5-ton bridge crane, a 2-ton bridge crane, the 1½-ton GEEL bridge crane, a freight elevator, a passenger elevator, two hatchways, and associated equipment. Individual experiments use various types of handling facilities which, due to their specialized nature, are not discussed.

The objectives of the nuclear calculations are to determine the following:

1. The ability of the ETR core to produce and maintain a heating rate of at least 2000 W/cc-cm of the UO_2 fuel

2. The characteristics of the neutron filter and the enrichment distribution within the assembly of UO_2 fuel rods which most nearly produce the desired power distribution within the UO_2 fuel

3. The effect of the pressure of the test loop upon the ETR core without and with other as yet unde-

fined experiments occupying the other test portion in the core.

The design of the loop is not firm at this date and consequently the nuclear calculations are all preliminary. The 2D ARC module and a modified "345" sixteen group cross section set are being used. The preliminary calculations indicate that the reactor is capable of producing and maintaining a satisfactory nuclear environment. The average power is approximately 15 kW/linear ft of fuel element and a calculated power density of approximately 0.50 MW/liter in the region surrounding the J-13 test area (Fig. IV-23-1).

The change in reactivity occasioned by removing the standard fuel boxes and replacing them by a 19-fuel-element assembly surrounded by a cadmium filter was less than a negative one percent.

The power distribution across the horizontal cross section of the 19-fuel-element subassembly can be varied by varying the material in the filter, by varying the enrichment as a function of fuel assembly radius and length, and by spacing the fuel elements in the assembly. This parametric study is in progress.

The effect of the proposed test loop upon the power distribution in the core of ETR without other tests in the core and operating at a power of 175 W is insignificant. What the effect will be with other as yet undefined tests in the core is undeterminable at this time. Some calculations based on the assumption that typical test specimens will be in the test holes at the time the fuel failure propagation loop goes into J-13 will be made.

Critical experiments are underway in the Engineering Test Reactor Critical Assembly. The results are reported in Ref. 1.

Reference

1. D. R. de Boisblanc and S. Cohen, *Final Report—Conceptual Design LMFBR Fuel Failure Propagation Loop for the ETR*, IN-1208 (1968) pp. 24–31.

IV-24. Proposal on "Vented" Containment for a Liquid Metal Fast Breeder Reactor (LMFBR)

R. O. Brittan

This is a proposal for alleviating accident consequences by "venting" the secondary containment atmosphere through a heat sink filtering media to a standby control volume.

The LMFBR Containment Problem

It has become customary to provide mitigation and control of the consequences of a "design basis accident" (DBA) in design of a nuclear power plant. It is anticipated that this custom will persist beyond the design of future LMFBR's. The DBA arises as a result of a credible but unlikely series of events which cannot be clearly delineated until a particular design is conceived.

In general, however, the DBA will be characterized by either a rapid energy release leading to breaching of the primary system and burning of fuel and coolant or a massive break in the coolant system followed by core meltdown and burning of fuel and coolant. This applies only if the secondary atmosphere is not inert. If the energy release is "explosive", close-in structuring will attenuate the pressure wave and localize the damage. Hence, in either case successful control of the radioactive material will be contingent on the consequences of a metal fire.

In a constant volume housing, such as provided for the EBR-II and Fermi plants, such a metal fire can lead to overpressures of about 5 atm and temperatures of several thousand degrees, theoretically. Control of the radioactive material with such a system requires that an expensive pressure vessel housing be provided which does not leak materially at these pressures and temperatures.

The means provided in BWR and PWR plants to reduce the pressure and temperature cannot be employed with LMFBR's because burning metal and water are not compatible. Introduction of inactive gas following the accident to reduce the extent of burning is not very feasible because another pressure rise and/or displacement of the oxygenated atmosphere is necessary. No such displacement can occur in a constant volume system. Smothering with inactive solids is also difficult because of the unpredictable locations of the burning metal and the thickness of the smothering blanket required.

There are two other instances in which these types of DBA have been encountered for fast reactor systems. the ZPR-6 and -9 complex and the Zero Power Plutonium Reactor (ZPPR). They differ from the LMFBR

in two respects. First, the zero power reactors have no structuring such as biological and blast shielding to attenuate pressure waves and convert the kinetic energy of the reactor materials. Second, there is not a large inventory of fission products. Although the ZPR-6 and -9 complex originally was not designed for use of plutonium fuel, changes to the original containment were made which now make this possible. It is basic to this proposal to review the history of the problem solutions for the two systems noted. Initial work on both of these systems dates back to late 1955.

Background Experience

ZPR-6 and -9 Uranium Criticals

The criteria used in design of the cell housings were principally that (1) the hazard to the public be no greater than for other uranium fueled criticals at the site (i.e., ZPR-1, -2, -4, and -5 in the Building 316 cells) and (2) that operations outside the complex not be impaired by operation of the criticals. The DBA for the criticals in Building 316 cells assumed breaching of the cells and release of all the fission products and fuel to the atmosphere in a rising cloud. This would not yield doses of 25 rem beyond the control boundary. The DBA for the ZPR-6 and -9 criticals assumed that the maximum explosive energy release would not exceed in damage that due to a 100 lb. bare charge of TNT, followed by complete burning of the core materials, placing all the fission products and fuel air-borne in the cell. In order not to exceed the original hazards it is necessary to design a system which holds together sufficiently following the blast to ensure that the radioactivity released to the atmosphere would not result in doses greater than originally accepted. Since the U-235 in the fast criticals considerably exceeded that in the thermal and half-fast criticals, the cell structure would have to withstand the projected blast with only a small resultant leakage.

A design concept was proposed for the Building 316 cells in 1956 by the author which, by increasing somewhat (1 ft) the shielding wall and ceiling thickness (3 ft) required to meet the second criterion and adding reinforcing steel (¾%) to doubly reinforce the concrete slabs would allow meeting the first criterion. That is, sufficient blast protection would be afforded to make the radiological hazard to the public following the DBA no greater than for previous systems. After the design was complete, analysis and tests showed[1,2] that the cell would sustain no structural damage from detonation of a 100 lb bare charge of TNT, and only acceptable damage from a 250 lb bare charge blast. At the same time, it was pointed out that the minimal design did not provide complete containment because in the event of an accompanying metal fire, pressure rises sufficient to breach the cell would be experienced, unless the cell were vented. A scheme incorporating venting through a filtering medium with inertial protection of the medium provided by a massive inertia block was proposed.[3] This would allow venting from the cell to the filter medium only after any blast which might occur. Such a system could prevent the release to the atmosphere of all radioactive material except the gaseous fission products. A sand bed filter, such as had been used successfully in operations at Hanford, was proposed. This would give a reliable long term standby safeguard with essentially zero maintenance and automatic operation. Since such complete containment was not necessary for the installation at that time, this proposal was not incorporated, except that a removable section was provided in the cell wall below grade if later incorporation seemed desirable.

ZPPR Plutonium Criticals

At about the same time, plans were being made to operate ZPR-3 at the National Reactor Test Site (NRTS) with plutonium. Even at NRTS only small plutonium releases could be tolerated so G. Brunson of the Idaho Division, Argonne National Laboratory, began a searching investigation of experience with the behavior of volatilized and burnt plutonium preliminary to evaluating the hazards of the proposed experiment. Most of the experience had been in the weapons testing field. There he encountered a protection scheme which had been tested and shown to completely prevent escape and atmospheric dispersal of volatilized finely divided plutonium and PuO_2 following a sizable detonation of high explosives. This is now documented in the open literature.[4] Since this author was investigating containment problems generally, in connection with a review in preparation,[3] Mr. Brunson disclosed his findings in the hope that applications of the principle might be of some value. The author's evaluation was that application to fast power reactors was not valid since, although particulates were effectively contained, all gaseous fission products would be dispersed into the atmosphere. With the large inventory of such fission products present in a power reactor, the resulting radiological hazard would be intolerable.

However, shortly thereafter, when it became evident that a very large fast plutonium critical would be needed and would be built at NRTS, the author proposed that an adaptation of the "Gravel Gertie" principle would provide an ideal solution to the containment problem for the ZPPR. The criteria for ZPPR differed from those of the critical facilities at the Laboratory's Illinois site. The operational shielding criteria remained essentially the same, but the radiological hazard criteria had to be drastically altered because of the use of plutonium

rather than uranium fuel. The acceptable amount of plutonium fuel which may escape to the atmosphere became several orders of magnitude smaller than that of uranium fuel. The original DBA for ZPPR remained about the same. The cell design with the suspended gravel lens lid provided containment following an explosion of up to 500 lb of TNT bare charge equivalent and, with the addition of two sand layers, also acted as an adequate filter medium in case of metal fire alone. The DBA was altered later to exclude the possibility of an explosion. In addition, after completion of design the acceptable quantity of escaping plutonium was reduced three orders of magnitude by the AEC. This very small quantity (~1 g total) was below the limits of detection afforded in the full-scale "Gravel Gertie" test, so a "top-hat" plenum with high efficiency filter banks was added above the suspended gravel. This provided an additional attenuation by a factor of about a thousand on the passage of particulates. However, no radioactive gases were retained.[5] Although this "top hat" is considered superfluous, from the radiological hazard standpoint, it makes easier the assurance tests of the sand-gravel filter.

ZPR-6 AND -9 PLUTONIUM CRITICALS

Recently it became evident that the Illinois site critical facilities would have to incorporate plutonium fuel if they were to be useful in the projected civilian fast breeder program. This would require that means be provided to contain essentially all the plutonium following an accident. The modification of an existing leaky (~10%/day) facility to retain all but ~1 g of the plutonium required a different approach than design of a new system. The solution adapted[6] was to essentially (1) shroud the existing thick-walled concrete cells in a leakproof thin shell of steel and duct the air in the intermediate space through high efficiency filters to the atmosphere; and (2) duct the cell air through sand-bed filters and then through high efficiency filters to the atmosphere. Following an accident involving metal fires, contaminated air is forced through the sand filter and through leaks in the concrete cell wall. Both actions result in sufficient heat removal to protect the high efficiency filters against excessive temperatures. Item (2) of the design solution is an adaptation of the concept for a vented system proposed in Ref. 3, with a special valve replacing the inertia block to protect the filter system from blast. It should be noticed that the DBA finally used here does not include a blast. Furthermore, it should be pointed out that the noble gases and some volatile halogen fission products are allowed to escape to the atmosphere.

The Proposal for LMBFR Containment

Each time these vented containment schemes have been proposed for a critical facility, it has been suggested by some that the schemes might be suitable for fast power reactors. However, each time it was pointed out that whereas it is acceptable to release all the gaseous (e.g., krypton and xenon) and much of the volatile (e.g., bromine and iodine) fission products from the inventory and excursion fissions of a zero power reactor, such releases from a power reactor would be unacceptable.

The fission product gas release criterion then constitutes the first significant difference between critical facilities and power reactor facilities. The second principle difference encountered is that a power reactor has a large heating rate persisting after shutdown as a result of fission product decay, whereas a critical facility does not. The third significant difference is the presence of the metal coolant in the liquid state at high temperature and modest pressure in the power reactor and the stored heat in the solids of the core and blanket. The fourth significant difference is the persistent specific energy release in the power system as compared with the momentary release encountered in an excursion of the "zero" power reactor.

The author has devised a way to overcome the objection, based on the first difference noted above, to the utilization of his critical facility vented contaminant concepts for LMFBR containment. The proposal has been investigated with respect to the other consequential differences listed. It has been found that these differences influence the sizing and composition of components only, and do not obviate the basic principle.

Conceptually, the proposed system consists of: 1) a leak-tight normal containment building surrounding the primary system, including primary heat exchanger, fuel handling equipment, temporary fuel storage facility, and fuel transfer terminus; 2) a set of ducts connecting the building to a plenum containing a sand-gravel filter bed; 3) a second set of ducts connecting the filter bed to an auxillary variable volume closed to the atmosphere by a flexible membrane. This concept is shown schematically in Fig. IV-24-1.

If a pressure rise occurs in the normal containment building, the air passes through the filtering medium, giving up heat and depositing particulates and condensed volatiles. The "clean" gas continues into the auxillary volume where the membrane adjusts position to accommodate the "vented" gas. Thus the remaining noble gasses and volatile halogen fission-products are prevented from reaching the atmosphere except by leakage and by diffusion through the membrane.

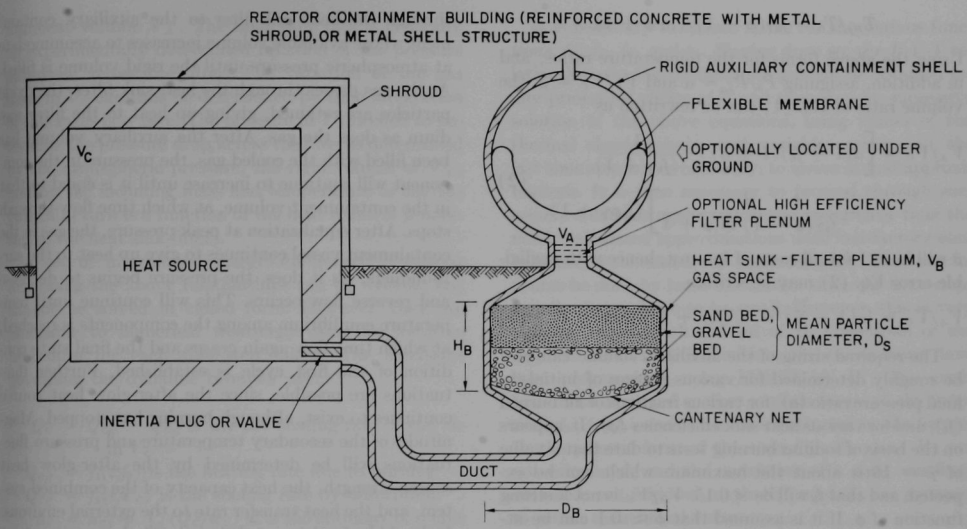

FIG. IV-24-1. "Vented" Containment Concept for LMFBR. *ANL Neg. No. 113-1537.*

STATIC ANALYSIS

A crude sizing study is possible by considering only initial and final states of the gas. Initially the gas system volume is composed of the containment vessel V_C and the void space in the heat sink-filter volume V_B. The gas temperature is initially uniform at T_0 and the pressure is uniform at P_0. Then the total initial weight of air is $w_0 = P_0(V_C + V_B)/RT$. During metal combustion, some fraction (f_b) of the air is burned, so that the final weight of air in the system

$$w_f = (1 - f_b)P_0(V_C + V_B)/RT_0 .$$

This final weight of air is distributed in three volume segments, V_C, V_B, and V_A, where V_A is the volume of the auxiliary containment beyond the heat sink-filter. Some heat is removed from the air by the heat sink-filter. Hence, the final temperature of the gas is different in each volume segment; T_{C_f} in the containment vessel, T_{A_f} in the auxiliary vessel, and a non-uniform T_{B_f} in the heat sink-filter varying from T_{C_f} at one end to T_{A_f} at the other. The final pressure P_f is uniform everywhere. Thus the weights of air in each of the segments are $w_{C_f} = P_f V_C/RT_{C_f}$, $w_{B_f} = P_f V_B/RT_{B_f}$, $w_{A_f} = P_f V_A/RT_B$. Here T_{B_f} is an "average" value. The sum of these three weights of air can be equated to w_f given above, assuming no leakage. Then with some manipulation the desired volume ratio is found to be

$$V_A/V_C = [(P_0/P_f)(T_{A_f}/T_0)(1 - f_b)(1 + V_B/V_C) - (T_{A_f}/T_{C_f}) - (V_B/V_C)(T_{A_f}/T_{B_f})]. \quad (1)$$

The temperature rise in V_C from initial to final state depends on the amount of burning and on the heat capacity of the air and combustion products if the assumption is made for this crude analysis that no heat is lost to the surroundings.

T_{C_f} can be related to the burning fraction f_b by introducing γ as the ratio of temperature rise that would occur if all the oxygen is burned to the initial temperature, all multiplied by the initial air-to-oxygen density ratio. Then

$$T_{C_f}/T_0 = f_b\gamma + 1.$$

T_{A_f} must be related to the heat removal ability of the heat sink-filter. The temperature state in such a system can be described by $(T_B - T_C)/(T_{C_f} - T_0)$ as a function of a position through the filter; i.e., $(T_B - T_0)/(T_{C_f} - T_0) = \phi^{x/L}$ where ϕ is the value of the function at the downstream end ($x = L$), namely

$$\phi = (T_{A_f} - T_0)/(T_{C_f} - T_0).$$

Hence

$$T_{A_f}/T_0 = \phi f_b\gamma + 1.$$

The average value of T_{B_f} is obtained by integrating the function given above over the filter length L, (from $x/L = 0$ to $x/L = 1$). The result is

$$T_{B_f}/T_0 = f_b\gamma(\phi - 1)/(\ln \phi + 1).$$

Using the above forms for the temperature ratios, and in addition, assigning $P_0/P_f = \alpha$ and $V_B/V_C = \beta$, the volume ratio of Eq. (1) can be rewritten as

$$V_A/V_C = \left[\alpha(1 - f_b)(1 + \beta) - \frac{1}{(f_b\gamma + 1)} - \frac{\beta}{f_b\gamma(\phi - 1)\ln \phi + 1}\right](f_b\phi\gamma + 1). \quad (2)$$

β will be $\ll 1$ for all cases of interest; hence with negligible error Eq. (2) may be written

$$V_A/V_C = [\alpha(1 - f_b) - 1/(f_b\gamma + 1)](f_b\phi\gamma + 1). \quad (3)$$

The required sizing of the auxiliary volume can now be roughly determined for various choices of initial-to-final pressure ratio (α), for various fractions of air burned (f_b), and for various heat sink efficiencies (ϕ). It appears on the basis of sodium burning tests to date that a value of $\gamma = 15$ is about the maximum which can be expected, and that f_b will be <0.15. V_A/V_C is not a strong function of ϕ. If it is assumed that $\phi \approx 0.1$ can be attained with a practical heat sink-filter, the required volume ratio can be listed as a function of acceptable overpressure:

Acceptable Overpressure, P_f/P_0 $(= 1/\alpha)$	Required, V_A/V_C
2.5	0.040
2	0.143
1.5	0.317
1.2	0.491

DYNAMIC BEHAVIOR ANALYSIS

The crude static analysis above may be used for rough sizing, but since the situation to which design is ultimately aimed is a dynamic one, it is necessary to explore the system behavior during the accident. To do this, the dynamic behavior of each component must be ascertained along with the interaction of each with the other. Pervading these interactions are thermodynamics, composition, and motion of the contaminated gas in the system.

The materials ejected from the primary system ignite and burn at a varying rate, depending on degree of dispersion, oxygen content of the air, and self blanketing, primarily. Of the heat released on burning, a portion remains with the oxide formed, a portion heats the air mass which is being depleted of oxygen. Some of the combustion products become airborne as smoke which along with the gas, transfers heat to other materials in the containment cell (walls, reactor shielding, other components, etc.) by convection, conduction, and radiation. As the gas heats up, the pressure increases so that some of the gas-bearing oxide particles are forced through the heat sink-filter to the auxiliary containment whose available volume increases to accommodate at atmospheric pressure until the rigid volume is filled. As the gas passes through the heat sink-filter, the oxide particles are retained, giving up heat to the filter medium as does the gas. After the auxiliary volume has been filled with the cooled gas, the pressure in the component will continue to increase until it is equal to that in the containment volume, at which time flow-through stops. After equalization at peak pressure, the gas in the containment vessel continues to give up heat to the surroundings. As it does, the pressure begins to decrease and reverse flow occurs. This will continue until temperature equilibrium among the components is reached, at which time flow again ceases and the final state condition of the first cycle is established. Further fluctuations are possible, since the after-glow heat source continues to exist, although burning has stopped. Magnitudes of the secondary temperature and pressure fluctuations will be determined by the after-glow heat source strength, the heat capacity of the combined system, and the heat transfer rate to the external environs. It should be further noted that the final quantity of gas will be decreased by the amount of oxygen consumed, so that at some time before ambient temperatures are attained, the internal pressure will decrease below atmospheric unless make-up gas is admitted. The dynamic behavior outlined above has been examined to the extent necessary to delineate the calculational analysis and experiments necessary to characterize the final system sufficiently for design purposes.

The analysis is presumed to begin with heat being added to the air in the containment volume V_C at a rate which varies arbitrarily with time. This bypsases temporarily the necessity of considering the mode of burning and heat transfer to the air and combustion products. In addition, it is assumed that all of the air in V_C heats or cools simultaneously. Thus all the air in V_C is characterized by a single temperature and pressure at any given time. In addition to the heat added, there is heat removed from the air in V_C through heat absorption by the materials in V_C exposed to the gas. This cooling rate is a function of time, but is determined by the gas temperature and by the temperature and thermal diffusivity of the materials (e.g., the containment wall).

The temperature of the air in V_C is determined from the heat content which in turn is determined by integration of the heating and cooling rates. The corresponding pressure is found from the perfect gas relationship among pressure, temperature, volume, and mass. However, the mass of gas is indeterminate because some passes out of V_C through the heat sink-filter as the pressure in V_C rises above the pressure in the auxilliary con-

tainment volume V_A. The mass flow rate is generally an experimentally determined function of the pressure difference across the filter. The variation of the gas mass in V_C can thus be determined by time integration of this mass flow rate. The pressure in V_A needed to determine the pressure drop across the filter is determined by the atmospheric pressure, the rigid volume of V_A, and by the incoming mass and temperature of the gas (which in turn is a function of the heat removal properties of the heat sink-filter).

A set of interrelated integro-differential equations describing the above relationships can be written, but cannot be solved in closed form. However, they are amenable to numerical treatment using an iterative procedure for each time-step taken. The equations governing the dynamic behavior are:

$Q_C = Q_{C_H} - Q_{C_C}$ is the net heating rate of the air in V_C

$Q_{C_H} = f_1(t, f_b)$ is the heating rate due to burning

$Q_{C_C} = f_2(t, T_C)$ is the cooling rate by absorption

$h_C = h_{C_0} + \int_0^t (Q_C/w_C)\, dt$ is the enthalpy of a unit mass of gas in V_C

$T_C = h_C/c_v$ is the temperature (absolute) of gas in V_C

$c_v = f_3(T_C)$ is specific heat at constant volume of gas in V_C

$w_C = w_{C_0} - \int_0^t (dw_C/dt)\, dt$ is total weight of gas in V_C

$dw_C/dt = f_4(P_C, P_A) + BQ_{C_H}$ is rate of gas mass flow through filter plus rate of oxygen consumption ($B \equiv$ mass of oxygen/unit enthalpy)

$P_C = P_{C_0} + (R/V_C)\left[\int_0^t (Q_C/c_v)\, dt - T_{C_0}\int_0^t (dw_C/dt)\, dt\right]$ is pressure (absolute) of gas in V_C

$w_A = \int_0^t (dw_C/dt)\, dt$ is weight of air in auxiliary containment

$T_A = f_5(T_C, P_C, P_A)$ is temperature of air in auxiliary containment

$V_A = (RT_A/P_A)\int_0^t (dw_C/dt)\, dt$ is variable volume of gas in auxiliary containment, constant after V_A equals rigid volume V_{A_R}

$P_A = P_0$ until V_A equals V_{A_R}; $= w_A R T_A / V_{A_R}$ after V_A equals V_{A_R} — is pressure in auxiliary containment.

In these equations

$t \equiv$ time after burning starts

$f_n \equiv$ function, $n = 1, 2, \cdots 5$

$f_b \equiv$ fraction of air burned

$R \equiv$ gas constant;

$_C$ denotes containment cell

$_A$ denotes auxiliary cell

$_0$ denotes initial value.

It is necessary to choose forms for the various functions, f_2, f_3, f_4, and f_5. Having done so, the P-V-T relationships for the containment gas can be obtained for any prescribed choice of f_1 and time step by successive solution of the above equations, using values of the thermal characteristics and variables existing at the last time step where necessary, to arrive at first approximations. It is then necessary to proceed through successive solutions again and again, using each time the newly calculated approximations until satisfactory convergence is obtained for each variable. This can of course be done by hand calculation since the time steps usually do not have to be small. However, this is very tedious. Hence, with the aid of H. Greenspan of the Applied Mathematics Division, the calculations have been programmed, using FORTRAN IV. The cards have been arranged so that various forms of the functions f_2, f_3, f_4, and f_5 can be substituted in the future. In the present form of the code P_A, T_A, and V_A are not calculated, and the restriction of a rigid auxiliary volume is not imposed, so that P_A and T_A are assumed to retain their initial values.

The initial selection of the functions f_n were as follows:

$$f_1 = A_1 + A_2 t + A_3 t^2;$$

this is the heat release rate due to burning with A_1, A_2, and A_3 as input data.

$$f_2 = (B_1 + B_2 T_C + B_3 T_C^2)(dT_C/dt) = Q_{C_C};$$

this form assumes only that a very thin layer of the concrete walls is heated uniformly to the gas temperature and that the specific heat of the wall is a quadratic function of the temperature.

$$f_3 = (C_1 + C_2 T_C + C_3 T_C^2) = C_V;$$

this is a reasonable form for the value of the specific heat of air at constant volume, and the constants C_1, C_2, and C_3 are available from handbooks.

$$f_4 = (D_1 + D_2\sqrt{P_C - P_A} + D_3(P_C - P_A) + D_4(P_C - P_A)^2;$$

this is the rate of air flow through a sand bed filter. The constants can be obtained from flow tests. Values used in present calculations were obtained from tests on a sand bed filter proposed for the cells of Building 316.[6]

$$f_5 = T_{C_0};$$

this is an assumed constant, which implies heat removal rates for the heat sink filter equal to Q_C.

Several sample problems were run to check the sensitivity to variations in assumptions on these functions. The results indicated that:

1) The inclusion of $Q_{C_C} = f_2$ strongly affects the re-

sultant temperature and pressure in V_C. The heat removal mechanism by absorption must be included, but it must always be conservative. This is not always true for the f_2 chosen. To ensure conservatism, it is necessary to utilize a more exact model for the heat absorption, including radiative transfer. The absorption is principally affected and governed by the thermal diffusivity of the absorber. A mathematical solution of the heat transfer problem for an arbitrarily varying source temperature is not available. A relative simple numerical solution based on the semi-graphical solution method of E. Schmidt[7] has been formulated. A quasi-conductivity of the gas was developed to include radiative transfer effects. Various starting schemes were examined to yield that one which would result in the least deviation from true values. Such a calculation could replace that originally chosen. However, this more sophisticated scheme has not as yet been programmed and coded.

2) It is important to leave $c_v = f_3$ variable because of the wide range of T_C encountered. Use of a selected mean c_v will generally result in a calculated temperature rise which is too small initially and too large in the later stages.

3) The detailed flow characteristics of the heat sink-filter strongly affect the peak pressure developed. A large amount of experimental data has been obtained on pressure drops experienced in flow through packed beds.[8] The pressure drop is assumed to be a function of superficial velocity, a friction factor, length of bed, particle size and shape, void fraction, and the mechanical properties of the fluid. The friction factor is correlated with a modified Reynolds number. The velocity may be obtained for a given set of properties and pressure drop by iterative calculation on the velocity-dependent friction factor. The correlation of experimental data on friction factor versus Reynolds number has been examined and it was found that the spread is sufficient to yield an uncertainty in friction factor of $\sim \pm 50\%$. Furthermore, there is a spread in shape factor for nonsphericity from 0.6 to 1.0. The combination of these uncertainties makes estimation of the velocity uncertain to $+60\%$ and -30%. Thus in practice it would be imperative to obtain the correct relationship between pressure drop and mass flow rate experimentally to ensure proper performance. If experimental data are not available, the function f_4 may be assumed to have a linear relationship between pressure drop and velocity for Reynolds numbers <5, using the area of the particle surface per unit of bed as the characteristic area in $N_{\mathrm{Re}} = v_0/\nu S$, where v_0 is the superficial fluid velocity and ν is the fluid kinematic viscosity.

4) It is unconservative to assume that the exit temperature of the gas from the heat sink-filter has been reduced to initial temperature, and that the rigid volume of the auxiliary containment is infinite. Many studies have been made of the heat absorption efficiency of the packed bed. However, both the experimental and theoretical analysis have assumed constant gas inlet temperatures. The heat transferred is a strong function of this temperature and of the thermal diffusivity of the packing particles. Realistic analyses with variable inlet temperature remain to be done. A variation of the same method used to determine heat soaked up by the wall could readily be applied to spherical particles and incorporated into the numerical calculation scheme. In the period before this is accomplished the following considerations can be used to relate exit temperature to inlet temperature, initial bed temperature velocity, and time using the mechanical characteristics of the bed and thermal characteristics of the gas and bed.

A correlation for the ratio of outlet to inlet gas temperature excesses of a hot gas moving through an initially cold pebble bed in a tube has been obtained experimentally by O. Saunders and H. Ford.[9] Specifically if $T_C - T_0 = \Theta_0$ and $T_A - T_0 = \Theta_L$, the experimenters have plotted Θ_L/Θ_0 against the dimensionless number $v_0 C_g t/C_s D_s = \Psi$, with H_B/D_s as the parameter. Their correlation holds for $D_B/D_s > 10$, at least. Here C_g and C_s are the volume specific heats of the gas and particles respectively, D_B and D_s are the diameters of the bed and particles respectively, and H_B is the bed height. This correlation has been used but Ψ versus H_B/D_s with Θ_L/Θ_0 as the parameter has been plotted. It is found that the relation is linear in the ranges $2[1 - \exp(H_B/D_s)] < \Psi < 1.2(H_B/D_s)$ and $0.10 < \Theta_L/\Theta_0 < 0.80$ so that $\Psi = \lambda + \xi(H_B/D_s)$ within. Also λ and ξ are linear with Θ_L/Θ_0. Hence within the limits of the above ranges, it was found that

$$\Psi = \{7(\Theta_L/\Theta_0) - 4.4 + 0.4[1.15 + (\Theta_L/\Theta_0)](H_B/D_s)\}$$

or

$$\Theta_L/\Theta_0 = [\Psi + 4.4 - 0.46(H_B/H_S)]/[7 + 0.4(H_B/H_S)].$$

It is recommended that this relation be used in developing f_5 until a more realistic solution is available. Furthermore, it is important to the design studies to know how long the hot gas can be passed through the bed before the exit temperature rises significantly. This information would have to be correlated with the amount and rate of burning to determine adequacy of the bed as a heat sink.

Concluding Remarks

Enough of a study has been made to assure that a reasonably practical design of heat sink-filter and auxil-

iary containment building can be obtained which will result in a significant reduction in design pressure for a whole containment system. Further detailed study of the two heat sinks which were assumed, coupled with refinements in the current numerical dynamic analysis, is necessary before a specific design can be realized and its performance proved. Experimental studies of behavior of sand-gravel beds with variable inlet gas temperatures are recommended.

It should be realized that the alternative to such a "vented" system would be to operate with an inert atmosphere. This inerting would eliminate the burning heat source, but not the after-glow heat source. It is possible that a combination scheme in which oxygen is limited and "venting" is resorted to may prove to yield the most practical and economical system. At any rate, the work program recommended herein needs to be done before the relative effect of these two measures in obtaining an optimal system can be studied.

References

1. S. H. Fistedis, A. H. Heineman and M. J. Janicke, *Testing of Containment Capabilities of Reinforced Concrete-Shielded Enclosures*, ANL-6664 (1963).
2. R. O. Brittan, *Failure Pressures of Doubly-Reinforced Concrete Cells*, Reactor Physics Division Annual Report, July 1, 1965 to June 30, 1966, ANL-7210, pp. 291–296.
3. R. O. Brittan, *Reactor Containment*, ANL-5948, 241 (1959).
4. M. Cowan, *Measurements from Gravel Gertie Tests—Revised*, SC-R-64-127 (July 1964).
5. H. Lawroski, R. Palmer, F. Thalgott and R. N. Curran, *ANL Zero Power Plutonium Reactor—Final Safety Analysis Report*, Argonne National Laboratory, July 1967.
6. W. Y. Kato, C. E. Till, G. K. Rusch, A. Ancarani and J. Haugsnes, *Preliminary Safety Analysis Report on use of Plutonium and U-233 in ZPR-6 and -9*, ANL-7211 (1966).
7. E. Schmidt, *Foeppls Festschrift*, (Julius Springer, Berlin, 1924).
8. *Chemical Engineer's Handbook*, (McGraw-Hill Book Company, Inc., New York, 1950, Third Edition).
9. O. A. Saunders and H. Ford, *Heat Transfer in the Flow of Gas Through a Bed of Solid Particles*, J. Iron Steel Inst. **141**, 291 (1940).

IV-25. Contribution to Formulation of Fuel Failure Propagation Program

R. O. Brittan

Introduction

During the course of preliminary planning for a program to be addressed to the fuel failure propagation problem a series of related studies was made and the results are reported here.

There appears first an assessment of the problem and an outline of a projected attack on it, utilizing in-pile experiments. This is followed by a survey of existing loop technology and by the set of criteria selected and annotated to study suitability of various test beds. The results of these surveys and suitability studies, made prior to February 1, 1968, are presented (except for privileged information) along with recommendations on directions to be followed in developing the program.

Much of the information and techniques should be of interest to those defining experiments needed for the Liquid Metal Fast Breeder Reactors (LMFBR) safety program and studying facility needs to handle the experiments.

The Problem and Program Aims

It would be economically unsatisfactory to build a large fast breeder reactor in which fuel pin failures due to expected abnormalities would cause failure in adjacent subassemblies. If physical damage is constrained to one subassembly, the core can be repaired with little loss of time and at reasonable cost. If adjacent subassemblies are damaged progressively, and the core generally is damaged beyond reuse (or beyond recovery) as a result of a minor pin failure, the economic burden would be unbearable.

Single or few pin failures will occur, and even damaged single subassemblies are highly likely during a long core life, especially since it is usually economically sound to operate a given core as long as possible, even following occurrence of several failures.

It must therefore be a principal aim to design a core in which pin failures in a subassembly due to expected abnormalities, or at the end of the pin life span, do not propagate to the extent that adjacent subassemblies are affected. In addition, it would be highly desirable to render a design in which failure of a single pin would not cause failure of adjacent pins so that operation can continue, even at somewhat reduced power.

To accomplish these aims, it is necessary to study "normal" operational failure propagation within a subassembly and throughout adjacent subassemblies,

both experimentally and analytically. The fruits of such a study must act as a guide to the fuel element and core designers, enabling them to accomplish their aims. This study must lean on and mesh with the transient fuel failure and fuels technology programs extant. "Steady state" failure thresholds may also be established to provide data for operational judgements regarding continued operation after minor failures. Tests will also be needed to substantiate predictive methods of analysis. Consequently, this failure propagation program becomes an inherent part of any sound fuel technology program which has as its principal aim the development of fuel which can be integrated into a core design for an economically successful and adequately safe reactor plant.

It may be that during the course of such a program, results could make it possible to suggest an integrated core system in which propagation will not occur as the consequence of any expected abnormalities. It would seem prudent then to set up the failure propagation study program so as to have such an integrated system as a specific aim.

EXPERIMENTAL PROGRAM OUTLINE

Because of difficulties involved in preparing analytical models of propagative failure, the basic assumption must be made in preparing the program plan that the useful information, from the fuel development standpoint, will come from experiments. Furthermore, because of difficulties in simulating normal operating conditions (principally thermal) in the laboratory, the program plan must center about experimental studies in-pile. Out-of-pile tests are considered principally in a supporting role, preparatory to and interpretive of the in-pile experiments. Similarly, analyses play a supporting role, and in addition relate experiment to actual operational behavior.

In planning the program it is significant that determination of modes of single pin failure is not considered within the scope of work. It is assumed that these modes will be determined under the Fuel Development Program and the Fuel Meltdown Program, or other related studies.

For each failure mode deemed significant and chosen for study, it will be necessary to determine propagation (or lack of it) in a primary cluster (7-pin). If failure propagation is noted and cannot be corrected by design, continued failure propagation must be studied in successively larger clusters (13-, 19-, 31-, and 37-pin) throughout a subassembly. Should propagation be found to continue throughout a complete subassembly and not be corrective, it will be necessary to determine if failure propagates radially to adjacent subassemblies. In addition, indirect failure propagation to adjacent subassemblies as a result of axial coolant ejection and accompanying hydrodynamic effects or material transport to adjacent subassembly coolant inlets must be studied. Significant portions of this latter investigation should lend themselves to out-of-pile experiments.

Preparatory to the failure propagation experiments, single pin in-pile tests must be planned. After selecting the particular failure mode to be used in a series, it will be necessary to devise means of inducing such a failure at the desired time during the in-pile tests. Such means will be developed out-of-pile, but an in-pile check on the method must be made on a single pin before such failure can be assured in a cluster test.

Furthermore, non-failure control tests must accompany each propagation test series. Such control tests would simulate all the conditions of the propagation test except actual pin failure. It is necessary to perform these control tests to check the inter-relationship between the test reactor and the test conditions, to check thermal and mechanical performance, and to check instrument response in relation to test conditions.

On the basis of the above requirements and assumptions, Fig. IV-25-1 outlines a basic test program (in-pile) which would be necessary and sufficient for each failure mode to be investigated.

It should be noted in connection with such a program that if in a given test the failure does not propagate, it is unnecessary to carry out the succeeding tests. Thus the minimum number of in-pile tests per failure mode would be six, and the maximum would be twenty-one. As a modification, the seven-pin tests might possibly be omitted. One might go directly to the thirteen-pin configuration which provides line-of-sight isolation for, and thus more uniform masking of, the central (failing) pin.

The general sequence of operations envisaged for one test in such a program (after the single pin failure inducement test has been conducted) is listed as follows:

(1) Assemble loop test section
(2) Conduct pre-loading check-out of test section
(3) Prepare pins and delineate their original physical condition
(4) Load the test section
(5) Check instrumentation performance
(6) Transport package loop or test section to reactor
(7) Load test section into reactor
(8) Run test and ascertain data aquisition
(9) Remove test section from reactor to cooling-down storage

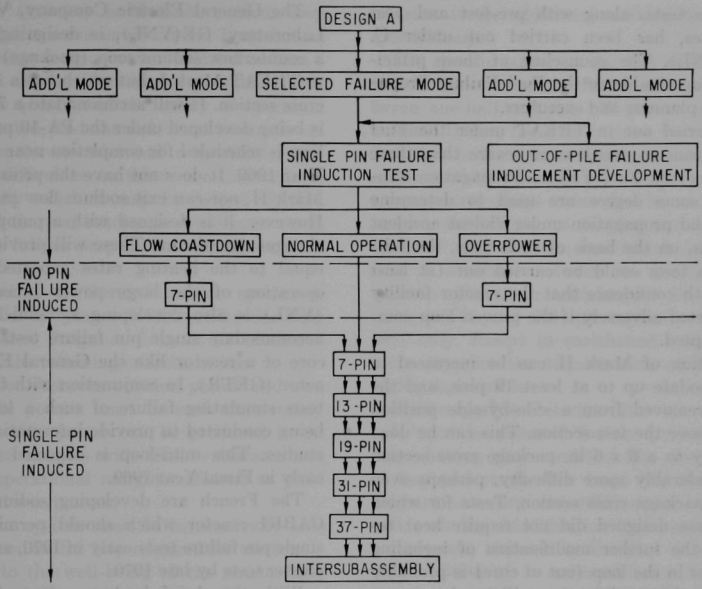

FIG. IV-25-1. Basic Test Program (In-Pile). *ANL Neg. No. 113-1507.*

(10) Transport test section to disassembly caves
(11) Conduct disassembly post mortem examination
(12) Bear the remains to final post mortem examination cave
(13) Perform detailed post mortem examination
(14) Ship remains to storage or burial
(15) Analyze and write up findings.

LOOP TECHNOLOGY AND TEST BEDS

The general nature of the program has been set forth above. It is necessary to consider next where the tests can be run, what loop technology is available, and how it can be adapted to the tests. These considerations must proceed together to some extent. For example, if two test reactors are found to be available, and one requires the development of a new test loop but the other can accommodate an existing loop (or modest rearrangement of one), the latter would be a superior choice from the standpoint of time and money.

Fortunately, flowing sodium loops have been developed and used to test seven-pin clusters under severe failure conditions (in-pile) for some time at ANL. Such loops, developed and used under the Fuel Meltdown Program in the Transient Reactor Test Facility (TREAT), are the so-called Mark-I loops (counter-flow package).

The experience with Mark I, and the need for testing ceramic fuel pins, has lead to the development and fabrication of a Mark II design. The modifications provide: 1) higher pressure capability (5000 psi); 2) much greater flow rates (about three times); 3) measurement of exit sodium flow rates. These were accomplished by incorporating the test section in one leg of a continuous loop (counter-flow eliminated), adapting a new pump concept, and increasing the wall thickness of the test section, principally. The loop is now an ASME Class A Nuclear Vessel rated for a steady state pressure of 340 atm at a temperature of 538°C. To accommodate the Mark II loop it was necessary to double the cross section of the test package from 4 x 4 in. to 4 x 8 in. (The TREAT modulus for holes is that of a fuel element cross section, 4 x 4 in.). The first Mark II loop has been fabricated and is being readied for initial tests. Nine more are being fabricated. Both Mark I and Mark II loops were designed and developed by L. Robinson (ANL). Preparation of loops for tests, plus loading, unloading, and post mortems have been carried out by a group of persons in the Reactor Physics Division, ANL, under K. Schmidt (ANL).

Planning of the tests, along with pre-test and post mortem analyses, has been carried out under C. Dickerman (ANL). The counseling of these principals should be invaluable to the Fuel Failure Propagation Program planners and executors.

The tests carried out in TREAT under the Fuel Meltdown Program are much more severe than those contemplated for the Fuel Failure Propagation Program, and to some degree are used to determine failure modes and propagation under violent accident conditions. Thus, on the basis of such tests, the failure propagation tests could be carried out (at least in TREAT) with confidence that the reactor facility will not be affected adversely if the proven loop components are adapted.

The test section of Mark II can be increased in size to accommodate up to at least 19 pins, and the pump can be removed from a side-by-side position to a position above the test section. This can be done easily to modify to a 6 x 6 in. package cross section and, with considerably more difficulty, perhaps even to a 3 x 3 in. package cross section. Tests for which the Mark II was designed did not require heat removal. Hence, the further modification of including a heat exchanger in the loop (out of core) is probably necessary. Since this modification will involve a new component, extensive testing and re-examination of safety considerations will be required.

In addition to the package loops, a "Large TREAT Loop" has been developed and installed at the TREAT facility. This loop was designed to study violent failure in a whole metal pin subassembly of the size found in EBR-II. The loop is of the counterflow type with only the test section in the reactor. The rest of the loop is permanently installed outside the reactor. Generally, the large amount of energy released on failure of ceramic pins at high rates can be expected to produce pressure pulses greater than the present loop can withstand. It may be possible to beef-up the test section and arrange a means of attenuating the pulse before it is seen by the rest of the loop. If so, failure propagation in 37-pin subassemblies, and radial propagation across such subassemblies, can be studied.

This large loop has a package cross section of 8 x 8 in. It is doubtful that re-arrangement and modification will permit squeezing down to a 6 x 6 in. cross section, principally because of projection of pressure sensors and the need for external heaters. However, experience gained during design and development of this large loop can be employed in designing a similar facility for reasons other than TREAT and which may be used in later stages of the Fuel Failure Propagation Program.

The General Electric Company, Valecitos Nuclear Laboratory, GE(VNL), is designing and developing a counterflow sodium loop (package) which is similar to TREAT Mark I, but which has a 3 x 3 in. package cross section. It will accommodate a 7-pin cluster, and is being developed under the PA-10 program. The first loop is scheduled for completion near the end of Fiscal Year 1969. It does not have the pressure capability of Mark II, nor can exit sodium flow rates be measured. However, it is designed with a pump and a heat exchanger out of core. These will provide a cooling rate equal to the heating rates expected during normal operation of the large power breeder reactor. GE (VNL) is also developing a "mini-loop" which will accommodate single pin failure tests adjacent to the core of a reactor like the General Electric Test Reactor (GETR). In conjunction with this development, tests simulating failure of such a loop in water are being conducted to provide information for the safety studies. This mini-loop is expected to be completed early in Fiscal Year 1969.

The French are developing sodium loops for the CABRI reactor which should permit conduction of single pin failure tests early in 1970, and possibly 7-pin cluster tests by late 1970.

With this brief background on loop technology, existing reactor facility(s) may be examined for suitability as test beds. Unfortunately, it appears now that no fast reactor (with the possible exception of SEFOR) will be available for tests under this program in the foreseeable future. SEFOR will be considered in the near future, but efforts in this study have been concentrated on existing thermal reactor systems.

The principal drawback of the thermal system is that the energy spectrum of the available neutrons is overbalanced in the thermal region. Since the thermal neutrons are absorbed principally in the outer layers of the outer pins of a cluster, fissions from these are distributed through the pins and cluster in a very non-uniform fashion. These slow neutrons then must be masked from the test section, so that only fissions by the neutrons from the higher end of the energy spectrum can occur. Thus, to yield adequate fission rates in the test pieces, the reactor must operate at substantially higher power levels than if thermal neutron fissions could be allowed. Also, additional means must be provided for removing heat from the mask. Variation of enrichment in and among test pins is not a very practical substitute for this masking procedure, although such variation may be required in conjunction with masking.

The other factor which makes the use of thermal systems for these contemplated tests difficult (with the exception of TREAT and in comparison with so-

dium-cooled fast systems) is that the sodium loop must be operated in a water environment. Loop failure would lead to intense sodium-water reactions so that a separate risk to the reactor integrity would exist. Hence, the entire question of the safety of operation must be re-evaluated, and the risk must be made acceptable to the reactor operator and to the AEC.

Having these difficulties in mind, a set of criteria was established by which it may be judged whether or not a selected thermal reactor is suitable as a test bed for fuel pin failure propagation experiments, as follows:

To judge whether a thermal reactor system is suitable for use in carrying out tests under the Fuel Failure Propagation Program, it must be examined against and meet the following criteria, at least:

(1) The relation between reactor power and test pin specific powers must be such that steady normal specific power can be produced in all of the test samples with little variation, and with an operational margin sufficient to yield substantial overpowers.

(2) The reactor system must be mechanically able to accommodate the loop required for the test.

(3) The risk to the well-being of the reactor and the safety of the public must be acceptable to the reactor operator and to the AEC.

It should be observed that with respect to Criterion (1):

To determine this relation it is necessary to assume that the neutron flux in the thermal energy region is masked, and that only fissions by epithermal neutrons can be counted in determining the fission rate in the sample. This requires knowledge of the fast spectrum shape and magnitude flux versus energy and of the relation of fast flux fission density to the reactor power level. The masking effect of the material of the test section on flux in the lower end of the spectrum can be neglected if the fast portion of the spectrum is reasonably hard, or if the calculational results are not borderline. However, fission rate distributions in the test section can be obtained readily in a 2-D calculation using a 16-group set of cross sections as was done by J. Madell for the Large TREAT Loop test section.[1]

Part of the criterion requires that a sufficiency test be applied to available excess reactivity. This can only be done by considering the reactor, the "thermal mask", and test section as a whole, then performing the calculations noted above. A portion of the test section, of course, must be considered a part of the "thermal mask". This requires that one calculation be done without added thermal masking to estimate the additional masking that must be provided, if any.

The specific power in the fuel of large fast power breeder reactors of the future is estimated to be between one-half and one kW per cc of test assembly volume. Hence, the reactor must be able to provide a fast flux in the test assembly capable of producing about 3×10^{13} fissions per cc of test volume on the average, or perhaps twice that as an upper limit. In judging the efficacy of varying enrichment it should be noted that uranium enrichment in the U-235 isotope is available between the limits 0.5 and 95%, whereas plutonium enrichments in the fissionable isotopes 239 and 241 are currently 65, 76, 88, and 96% only. Resort to enrichment variation of plutonium to meet the requirements of this criterion is highly undesirable.

With respect to Criterion (2):

It must be assumed for the present that package loops having characteristics like the TREAT Mark II loop and counterflow loops like the large TREAT loop are necessary and sufficient for all failure propagation studies. Modification by re-arrangement of the components, increase in diameter of the test section, and addition of an external heat exchanger are allowed in considering compatibility of the loop with the reactor being examined.

With respect to Criterion (3):

Three significant items introduced by testing under the Fuel Failure Propagation Program should be considered in re-evaluating the risks to the reactor system: the presence of sodium in a water-cooled reactor core, the presence of several kilograms of plutonium in the test samples, and the possibility of producing large pressure pulses in the sodium during pin failure. The reactor operator and the AEC will have to agree to accept those additional risks that may be determined to exist because of these three features before the reactor can be considered for use in the program.

Using these criteria, preliminary examinations were made with operator representatives of BAWTR, GETR, MTR, ETR, and TREAT. Following is an outline of the results of these preliminary examinations.

BAWTR (Babcock and Wilcox Nuclear Development Center Test Reactor)

This reactor, operating at 6 MW, fails to meet part of Criterion (1). Specifically, it would be capable of providing only a small fraction of the required power density (even with full sample enrichment) for reasonably uniform specific power density distributions through and among pins. This conclusion is based on a BAWTR analysis for a single ¼ in. pin in the center of

TABLE IV-25-I. FISSION RATE FRACTION PER ENERGY GROUP, PERCENT
(*Reactor Power: 6.5 MW*)

Power, kW/ft at core center (no masking)	U-235 Enrichment, %	Group Number and Energy Range			
		(1) 10 MeV–1.05 MeV	(2) 1.05 MeV–61 eV	(3) 61 eV–0.4 eV	(4) 0.4 eV–0.0 eV
11	0.72	2.8	2.2	4.1	90.9
14	20	2.7	2.9	10.6	83.8
18.5	93	3.3	5.1	23.0	68.6

TABLE IV-25-II. CENTRAL SPECIFIC POWER, kW/ft

U-235 Enrichment, %	Groups Masked Out		
	(4)	(3) and (4)	(2), (3), and (4)
0.72	1.00	0.55	0.31
20	2.27	0.78	0.38
93	5.81	1.55	0.61

the core, which yielded the data listed in Table IV-25-I. It can be seen that if Groups (4) and (3) are masked out, the specific powers are considerably reduced. From the data above, the specific power for various degrees of masking are seen to be approximately as indicated in Table IV-25-II. To realize a reasonably uniform distribution through a 7-pin cluster, Group (4) and part of Group (3) would have to be masked out. The central pin would be masked automatically by the outer ring in any event (for Groups (3) and (4)). Thus, with special masking efforts and varying enrichments, it may be possible to balance the central fission rates in the cluster so as to yield specific powers of 2 to 3 kW/ft, about 15% of normal operating specific power. It is estimated that the normal operating specific power is between 15 and 20 kW/ft, in the following manner:

For a 37-pin subassembly, the average specific power of a pin in kW/ft,

$$p_p = 4.6[2\sqrt{7}\,(d + s) + 2(s + h) + d]^2 p_R\,,$$

where

$d \equiv$ pin o.d., in.,
$s \equiv$ pin spacing, in.,
$h \equiv$ subassembly can wall thickness, in.,
$p_R \equiv$ average specific power of the reactor, MW/liter.

For a ¼ in. pin with $s = 0.043$ in. and $h = 0.083$ in., $p_p = 19.4\ p_R$ kW/ft. p_R is usually 0.6 to 0.75 MW/liter, and the max/ave specific power is about 1.35. Hence, $15 < p_p < 20$ kW/ft.

It would take a major redesign of the reactor, including pressurization, to raise the reactor power rating to 20 MW, at considerable cost, perhaps several million dollars. The attendant increase by a factor of about 3 in specific power would still be too little for the testing program in mind.

With respect to Criterion (2), it may be possible to accommodate a modified Mark II loop in a 6 x 6 in. hole in BAWTR, since there is a 4 in. hole in the lower grid plate and a 3 ft clearance below that. Considerable re-arrangement of the reactor control units would be necessary (and difficult). The test section itself in such a re-arrangement would probably be off-center by several inches. Such modification would result in essentially a new core, and considerable experimental and analytical physics and hazards analyses would have to be done.

Primarily, it is the restriction on specific power which makes BAWTR unsuitable for purposes of the Fuel Failure Propagation Program tests.

GETR (General Electric Test Reactor)

The GETR at VNL can produce much higher specific powers (8 to 10 times) in test samples than can BAWTR, with the required masking of the low energy neutron flux. Preliminary estimates made for a ¼ in. pin having fuel diameter = 0.22 in. and of composition 25% PuO_2-75% UO_2 indicate that the specific peak power generation rate obtainable with a flux filter varies from 12 kW/ft at 20% U-235 enrichment to about 20 kW/ft at 90% U-235 enrichment. Estimated average power ratios among pins in a seven pin cluster in a selected off-core center position run from 0.9 to 1.15 times average peak power for the optimum cluster orientation, and from 0.86 to 1.20 times average peak power for the most unfavorable orientation. These could be balanced by varying the enrichment among pins. Information is not available on variation within a pin, but it should not be more than about 3% with the flux filter.

A package loop having a test section holding a 7-pin cluster can be accommodated, but as in BAWTR the modular hole cross section is 3 x 3 in. A 9 x 9 in. central core section could be redesigned to provide a 4 x 8 in. hole with some effort. However, further study is needed to determine if the controls can be altered without increasing risks or sacrificing specific power. Such a redesign would result in the test section being off-center if the present Mark II loop is retained except for the dump-storage tank. The lower grid plate would have to be altered to accommodate the present Mark II design without change. The Mark II loop could be modified to sit in a 6 x 6 in. hole. Considerable redesign would be necessary to yield a loop of Mark II characteristics which would fit into a 3 x 6 in. hole.

GE (VNL) is developing (under another program) a loop of the Mark I type (counter-flow) to fit into a

3 x 3 in. hole. Further investigation should show that many of our tests on 7-pin clusters could be conducted in this so-called "Loopsule". Facilities exist at GE (VNL) such that test assembly and disassembly preparations and post mortems can be conducted either at VNL or at ANL. The Loopsule will not be able to measure coolant exit flow, and will be limited as to the number of information leads that can be installed. It should be possible to conduct tests with 50–100% overpower, either by altering reactor power or by removing special shielding during the test run.

The GE(VNL) schedule for completion of development and fabrication of the present Loopsule concept is about Spring of 1969. At this time a Loopsule could be made available for out-of-pile tests. Preparation of supplemental safety analyses and obtaining an operational change in the licensing precludes the possibility of actually performing tests with this loop in GETR until late Spring of 1970. To expand the facility for running tests using an adapted Mark II type loop for tests beyond 7-pin clusters and up to 19 pins would require a separate development by GE(VNL). Such a modified loop could be available some 18 months after development starts (still in time to operate by late Spring of 1970, say).

TREAT (Transient Reactor Test Facility)

TREAT was designed as a test bed for transient heating of fast reactor fuel pins to failure in flowing sodium. It has been utilized for this purpose successfully for several years.

In the Fuel Failure Propagation Program (In-Pile), it is required that the samples be operating initially at normal full power densities, temperature, and flow rates, and that the flow rate or power density then be perturbed. Such power-flow regimes and histories have not been available generally in TREAT, principally because of the upper limit imposed on total reactor energy release during a test, and secondarily because the package loops in use are not provided with the ability to remove heat at the rate at which it would be generated in normal operation.

However, modification of the TREAT operating limitations and controls are underway. The modification will permit a total reactor energy release during one test of 2000 MWsec. An automatic control system is planned which will allow attainment of full power densities in the samples for several tens of seconds, followed by a power increase or a reduction in loop coolant flow rate. Funds have been budgeted for this automatic control system in Fiscal Year 1968, and fabrication plus installation will procede so that this modification can be operational by the end of the 1969 calendar year.

It has already been demonstrated in the fuel meltdown program tests that with combinations of flux filters and variation in enrichments, TREAT can provide adequate fission rates at uniform or predetermined distribution (both radially and axially) for conduction of fuel failure tests.

It should be noted that since the coolant in a package loop cannot get rid of the heat it picks up during the test, both it and the test pieces will gradually heat up after normal operating specific power is attained. The temperature will rise at a rate approximately equal to the power generation rate in the test samples divided by the sum of the heat capacities of the coolant and the test pieces. Before simulation can be assumed, the attendant temperature changes after reaching normal power and until the end of the test must be reasonably small. Such a limitation may lead to requiring a modification of Mark II to include an external heat exchanger. This limitation may also be removed by bringing the loop sodium lines out to a large supply tank and dump tank arrangement, or by coupling with the existing external system which has been installed to handle the large TREAT loop.

Since the large TREAT loop is completed and operational, ostensibly failure propagation tests could be run in it on clusters up to a full-subassembly. By slight enlargement of the test section, inter-subassembly (simulated) tests could be run. A conceptual arrangement has been worked out for the full and partial subassemblies shown in Fig. IV-25-2 which can be placed in a test section enlarged from a flow separator diameter of 2.876 to 3.344 in. i.d., and a pressure tube diameter of 3.826 to 4.084 in. i.d. These changes would make the return flow area the same as the pin flow area. The pressure tube wall can be increased to give the same pressure pulse resistance as Mark II, if necessary. However, forthcoming tests under the Fuel Meltdown Program may prove that our tests can be run with the existing pressure limitations on the Large TREAT Loop.

MTR-ETR (Material Testing Reactor—Engineering Test Reactor)

Calculations have already been performed by Idaho-Nuclear Corporation (I-N) for a sodium loop with a seven-pin cluster in MTR. Essentially, MTR has the same physical limitations as GETR, except that it is somewhat less accessible. However, the criteria appear to be met for some portion of the failure propagation tests. Furthermore, much of the safety analysis work on such tests in MTR has been done. A modified Mark II loop could be adapted to MTR, and testing could begin in Fiscal Year 1969, perhaps in conjunction with TREAT tests. Since only

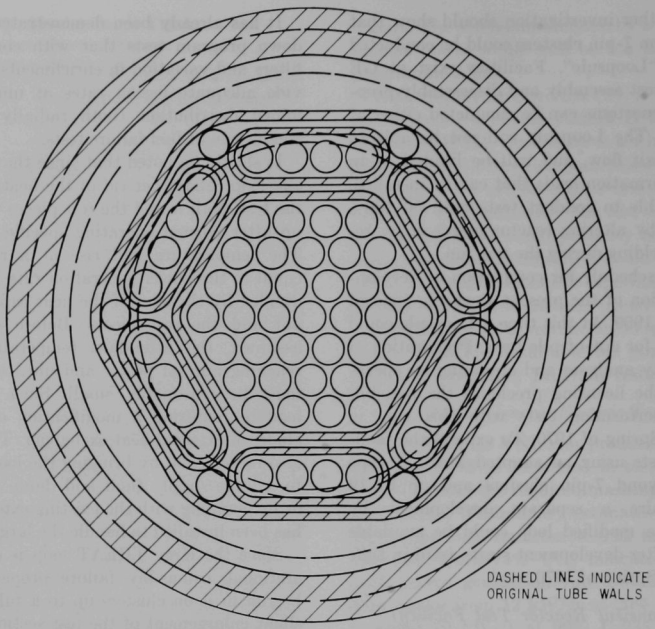

FIG. IV-25-2. Modified Large TREAT Loop Concept. *ANL Neg. No. 113-1506.*

a 3 x 6 in. test space could be made available, modifications probably would have to include moving the pump out of the core region and adding a heat exchanger. It appears possible to move the external portions of the Large TREAT Loop from TREAT to MTR if desired. With a special arrangement, it should be possible to run tests by the summer of 1969 in MTR.

ETR can easily accommodate all the contemplated tests under ANL's program. Early uniformity estimates by I-N indicate 3% variation in fission densities across pins, and 10% variation across a subassembly, with reasonable masking and enrichment. It would appear that if ATR is operational, testing of all types in ETR by late 1969 could be arranged if needed. A version of the Large TREAT Loop modified as in Fig. IV-25-2 could be adapted for use in FTR.

Other Reactors

The Experimental Organic Cooled Reactor (EOCR), Sodium Reactor Experiment (SRE) and Southwest Experimental Fast Oxide Reactor (SEFOR) were not examined in this study as possible test beds. Preliminary examinations by others indicate that EOCR is adequate up to 19 pins, and that SRE is inadequate for one pin with natural UO_2-20% PuO_2. Probably because of the soft spectrum of SRE, full U-235 enrichment would also yield substandard fission densities. SEFOR would probably be more suitable than any other system, since the spectrum is very hard, possibly more so than that of the LMFBR. This would lead one to expect that all tests could be run at below maximum reactor power capabilities, or at reduced enrichments. It seems possible that SEFOR could be made available for ANL's test program by 1970, since the results from the program are of interest to all those engaged in the LMFBR business. If this should prove to be true, plans could be laid to use SEFOR for tests on clusters larger than 19 pins.

ADVISORY

Until the question of using SEFOR is resolved, it was recommended that the near-term tests be planned for TREAT, MTR and ETR. To do this a team effort with I-N was recommended with initial stages carried out in the latter part of Fiscal Year 1968. This would allow ANL know-how on loops to be mated with I-N experience on test reactors and reactor tests. With sufficient escalation of effort in early Fiscal Year 1969, it should be possible to modify a TREAT Mark

II loop and run initial tests late in Fiscal Year 1969. This presupposes that work on inducing failure in single pins goes forward without a hitch. At least the loop operation could be checked out with the no-failure tests required.

Work should begin at once to determine what test modes can be utilized in TREAT and what modifications would be necessary. Calculations should begin to show whether the sodium temperature increases in the existing Mark II package loop during the test will allow a valid test, or whether heat removal must be arranged for. Plans should be studied for coupling the Mark II to a separate external portion of the Large Loop. Both flow-coastdown and power increase type tests should be checked out for adequacy of simulation. It should be assumed that the new integrated power limits and automatic control system will be available.

In addition, work should start to check the adequacy of the existing Large TREAT Loop for tests up to one subassembly. Modifications to "beef-up" the loop for handling larger pressure surges should be determined. Also modifications of the test section which would be required to handle the proposed special multi-subassembly test shown in Fig. IV-25-2 should be determined. Adequacy of the inlet sodium reservoir for extended time tests should also be checked.

It was recommended that work on TREAT tests begin at once, proceeding in parallel with, but separately from, the I-N–ANL team effort with respect to MTR-ETR utilization.

It is recommended that close liaison and consultation be arranged with Reactor Physics (ANL) personnel cited earlier, both by the investigators for TREAT tests and by the ETR-MTR team. It is essential to do this to get ANL know-how gained in the Fuel Meltdown Program on loops and TREAT tests into the projected Fuel Failure Propagation Program.

Reference

1. J. Madell, Argonne National Laboratory (private communication).

IV-26. Temperature Sensor Distribution Required for Gas Mass Determination in Leakage Tests

R. O. Brittan

This constitutes a study of errors made in determining true mean temperature differences in a large enclosed volume of gas by the use of distributed sensors when the gas temperature varies in space and time. A precision criterion is developed which indicates the number of sensors to be used to attain a desired minimum error. The study was made as an adjunct to a critical review by the author of some leakage test reports. This review has been published in Ref. 1.

Introduction

In the process of conducting leakage rate tests on large reactor containment structures it is necessary to determine a "true mean temperature" of the leaking gas at various times so that the weight of gas remaining in the vessel can be determined. The precision with which the true temperature value is approached must be such that the sum of the differences is smaller than the change in weight of gas divided by the initial weight of gas. If the latter is of the order of 10^{-3} and the absolute temperature about 500°R, the sum of the temperature differences must be $< \sim 5 \times 10^{-2}$°R to contribute less than 10% error in determining the leakage rate. To realize this precision the number and distribution of temperature sensors must be properly predetermined.

To assist the experimenter in such a determination, the author has studied the nature and magnitude of the errors associated with finding such "true" mean temperatures in systems where the temperature varies with space and time. The real "true" mean temperatures are determined analytically for widely varying temperature distributions in a cylindrical volume, and these are compared with indicated "true" mean temperatures obtained by various numbers of distributed sensors.

Consider an enclosed volume V of "perfect" gas. The state variables of the gas are related by

$$PV = wRT,$$

where

$P \equiv$ absolute pressure of the gas
$T \equiv$ absolute temperature of the gas
$w \equiv$ weight of the gas
$R \equiv$ constant
$V \equiv$ total volume.

The quantity to be determined in leakage rate tests is w, as a function of time t. In general, P varies with time

but is the same throughout the volume at a given time if the gas is still so that the dynamic pressure is zero; or still enough that the dynamic pressure is negligible. T varies in both space and time throughout the gas. For purposes of this study V can be considered invariant so that V/R is a constant. w, which represents the density, varies in space and time inversely as T and directly as P and the leakage. To develop the concept of a "true" mean temperature $T_M(t)$ the gas volume is divided into n segments ΔV_n so that $V = \sum_n \Delta V_n$. Each such volume segment has a weight of gas Δw_n at temperature T_n and pressure P. For this volume segment,

$$\Delta w_n = P\Delta V_n/RT_n .$$

Then

$$w(t) = \sum_n \Delta w_n(t) = \frac{P(t)}{R} \sum_n [\Delta V_n/T_n(t)];$$

but there is some mean value of the temperature $T_M(t)$ such that $w(t)$ is also equal to $P(t)V/RT_M(t)$, from which

$$T_M(t) = V/\sum_n [\Delta V_n/T_n(t)]. \tag{1}$$

This is the "true" mean temperature which must be established to enable $w(t)$ to be computed. If each T_n is uniform throughout ΔV_n and is exactly measured by a sensor, $T_M(t)$ can be computed exactly. In practice, however, n is usually a small number, so that ΔV_n is large, and T_n is not the same everywhere in ΔV_n. In such a situation the value of T_M which is computed will not be the required "true" value. Thus

$$(T_M)_c - T_M \neq 0,$$

but rather

$$(T_M)_c - T_m = \Delta T_m .$$

At the two points in time, t_1 and t_2, two values of $\Delta T_M(\Delta T_{M_1}$ and $\Delta T_{M_2})$ exist and

$$\Delta T_{M_2} - \Delta T_{M_1} = \delta_M .$$

Then the leakage rate determination will be in error by the fraction $\delta T_M/T_M$. Thus sufficient sensors must be distributed throughout the volume in such a way as to ensure that $\delta T_M/T_M < L$, the leakage rate fraction. If this is not accomplished, the error will be larger than the quantity L which is to be measured, and the test will be unsuccessful.

The condition $\delta T_M/T_M < L$ then becomes the central problem in planning and conducting a leakage rate test (after it is determined that the actual measurements of temperatures and pressures will be made with adequate precision, of course).

Analysis

To begin the study, the expression for $T_M(t)$ is put into integral form by letting $n \to \infty$:

$$T_{M_\infty}(t) = V \int_V dV/T(V,t).$$

Choosing an axisymmetric cylinder of cross sectional area A and height Z with the z-coordinate at the axis ($z = 0$ at the base),

$$\begin{aligned} dV &= Adz \\ V &= AZ. \end{aligned} \tag{2}$$

Next it is assumed that the temperature is uniform radially and has an axial distribution at time t_1 given by

$$T_1(z) = T_0[1 + az^2]. \tag{3}$$

At time t_2 it is assumed that the distribution has changed so that

$$T_2(z) = T_0[1 + b\sqrt{z}]. \tag{4}$$

Substituting Eq. (2) into Eq. (1a).

$$T_M(t) = Z \int_0^Z dz/T(z,t). \tag{5}$$

Now Eqs. (3) and (4) may be substituted successively into Eq. (5) and the integration can be performed to yield $T_{M_{\infty 1}}$ and $T_{M_{\infty 2}}$. The integration is possible since az^2 and $\sqrt{z}$ are both $\ll 1$, and $1/(1 + \epsilon) = 1 - \epsilon + \epsilon^2 - \epsilon^3 + \cdots$ for $\epsilon < 1$. (Actually, when Eq. (3) is used in Eq. (5), the value of the integral is known to be of a form containing $\tan^{-1}(az)$, but it is more convenient to use the series form.)

The two expressions to be evaluated (in integral form) are then

$$\begin{aligned} T_{M_{\infty 1}} &= AZ \Big/ \int_0^Z Adz/T(z) \\ &= T_0 Z \Big/ \int_0^Z [1 - (az^2) + (az^2)^2 - (az^2)^3 \cdots]\, dz \end{aligned} \tag{6}$$

and

$$\begin{aligned} T_{M_{\infty 2}} = T_0 Z \Big/ \int_0^Z [1 &- (b\sqrt{z}) \\ &+ (b\sqrt{z})^2 - (b\sqrt{z})^3 + (b\sqrt{z})^4 \cdots]\, dz. \end{aligned}$$

Performing the integrations and substituting the limits:

$$\begin{aligned} T_{M_{\infty 1}} = T_0/[1 &- \tfrac{1}{3}(aZ^2) + \tfrac{1}{5}(aZ^2)^2 \\ &- \tfrac{1}{7}(aZ^2)^3 + \tfrac{1}{9}(aZ^2)^4 \cdots] \end{aligned}$$

and (7)

$$\begin{aligned} T_{M_{\infty 2}} = T_0/2[\tfrac{1}{2} &- \tfrac{1}{3}(b\sqrt{Z}) + \tfrac{1}{4}(b\sqrt{Z})^2 \\ &- \tfrac{1}{5}(b\sqrt{Z})^3 + \tfrac{1}{6}(b\sqrt{Z})^4 \cdots]. \end{aligned}$$

These are the true mean temperatures, equivalent to those which would be obtained if an infinite number of sensors were distributed along the volume axis.

It is necessary next to arrive at expressions for the mean temperatures which would be obtained using a finite number of sensors. This is done by applying Eq. (1) to the case at hand. From Eqs. (1) and (2)

$$\begin{aligned} T_{M_n}(t) &= V/\sum_n [\Delta V_n/T_n(t)] \\ &= AZ/A\sum_n [\Delta z_n/T_n(t)] \qquad (8) \\ &= 1/\sum_n [\Delta z_n/Z)/T_n(t)]. \end{aligned}$$

Assuming that the cylindrical volume is uniformly segmented n times so that $n = Z/\Delta z$, Δz is constant for each n, and a temperature sensor measuring $T_n(t)$ is located at the centroid of each segment,

$$\begin{aligned} T_{M_n}(t) = n/[(1/T_1) &+ (1/T_2) \\ &+ (1/T_3) + \cdots + (1/T_n)]_t. \end{aligned} \qquad (9)$$

By substituting the two distributional forms for $T_n(t)$ given by Eqs. (3) and (4) into Eq. (9), the forms of T_{M_n} at times t_1 and t_2 are found to be

$$T_{M_n}(1) = nT_0 \Big/ \left[\frac{1}{1 + a/4n^2} + \frac{1}{1 + 9a/4n^2} + \frac{1}{1 + 25a/4n^2} + \cdots + \frac{1}{1 + (2n-1)^2 a/4n^2}\right]$$

or

$$T_{M_n}(1) = nT_0 \Big/ \sum_{j=1}^{j=(2n-1)^2} [1/(1 + ja/4n^2)],$$

for each $n, j = 1, 2, 3 \cdots (2n-1)^2$

and

$$T_{M_n}(2) = nT_0 \Big/ \left[\frac{1}{1 + (b/\sqrt{2n})} + \frac{1}{1 + \sqrt{3}(b/\sqrt{2n})} + \frac{1}{1 + \sqrt{5}(b/\sqrt{2n})} + \cdots + \frac{1}{1 + (\sqrt{2n-1})(b/\sqrt{2n})}\right]$$

or

$$T_{M_n}(2) = nT_0 \Big/ \sum_{k=1}^{k\sqrt{2n-1}} [1/(1 + kb/\sqrt{2n})],$$

for each $n, k = 1, 2, 3 \cdots \sqrt{2n-1}$.

It is assumed here that T_0 is the absolute temperature at $z = 0$ and that the absolute temperature at $z = Z$ is $T_0 + aT_0$ or $T_0 + bT_0$.

Eqs. (7) and (10) can now be evaluated for various n. It has been done for $n = 1, 2, 3, 5, 7, 10$ using Eq. (1) with $a = b = 0.005$, 0.01, and 0.02, assuming $T_0(1) = T_0(2)$. In addition Eqs. (7) (i.e., $n \to \infty$), for the same values of a and b, have been evaluated. Using the results, the following temperature differences were obtained for each b and a:

$$T_{M_{\infty 2}} - T_{M_{\infty 1}} = T_{M_\infty}$$

$$T_{M_{n2}} - T_{M_{n1}} = \Delta T_{M_n}$$

$$\Delta T_{M_\infty} - \Delta T_{M_n} = \delta T_M .$$

Here δT_M is the error in determining the mean temperature difference due to using n sampling positions.

It is found that

$$\log(\delta T_M) = \log(aT_0) + \log\lambda - \gamma\log n,$$

or (11)

$$\delta T_M = \lambda aT_0/n^\gamma.$$

To within a few percent accuracy, $\lambda = 1/8$ and $\gamma = 5/3$.

From the relationship given in Eq. (11), if δT_{M_a} represents the allowable error in temperature measurement due to sampling, the minimum required value of the integer n can be determined as

$$n_{min} \geqq [\lambda aT_0/\delta T_{M_a}]^{1/\gamma}.$$

Values of n_{min} are tabulated in Table IV-26-I for various aT_0 and δT_{M_a}.

TABLE IV-26-I. Minimum n Required

δT_{M_a}, °R	aT_0, °R		
	2.5	5	10
0.005	13	20	20
0.01	9	13	20
0.02	6	9	13
0.05	3	5	7
0.1	2	3	5
0.2	1	2	3
0.5	1	1	1
1.0	1	1	1

Conclusions

Evidently, use of a wire resistance thermometer with the wire stretched from top to bottom on the axis would be the equivalent of $n \to \infty$ and would yield zero sampling error, no matter how grossly the shape of the temperature distribution changes during the test. Such a measuring device has a conductance given by $G = 1/\sum_0^n (1/G_n)$, representing conductance of a number of segments in series where each segment has a conduct-

ance G_n. The conductance is thus analogous to the mean temperature. The number of wire segments of course approaches ∞. The precision of measurement with such a thermometer can easily be about 0.001°R.

This study has been made using the assumption that the temperature distribution is axisymmetric. This is not generally true. If the temperature distribution shape varies with azimuth a series of vertical sets of sensors would be needed. This evidently could best be accomplished by locating a wire resistance thermometer at at least four off-axis locations. If four locations are used, they should be at 0.6 of the radius from the axis, separated in azimuth by 90° of arc. Alternately, a set of wires could be strung in horizontal circles having $\frac{2}{3}$ the radius of the volume segment at as many vertical locations as would be dictated by the minimum n requirement given above. It would appear from these observations that a still air test is most desirable and the use of circulating fans should be avoided.

Reference

1. F. C. Zapp, *Testing of Containment Systems Used with Light-Water-Cooled Power Reactors*, ORNL-NSIC-26, (1968), Appendix E.

IV-27. Coherence Effects in Super-Prompt Critical Excursions

C. N. Kelber

The effects of the time distribution of reactivity additions in super-prompt critical excursions are frequently ignored in initial estimates of excursions in fast reactors. Instead, the total reactivity addition is usually assumed to be inserted at one time, or as a single ramp. As shown by D. Gopinath and C. Dickerman,[1] such estimates overlook a realistic spread in time of reactivity excursions expected in real systems. There are two questions to be resolved:

1. What is the estimated reduction in total energy release from a super-prompt critical excursion when the reactivity excess beyond prompt critical is introduced over a period of time instead of at a single instant?
2. How sensitive is the energy release estimate to variations in the times at which the reactivity increments are made?

To answer these questions we have used a highly idealized model which has the crucial features of excursion calculations. We use the Nordheim-Fuchs model and assume that reactivity over prompt critical is added in N steps of amount ρ_0 each, the value of ρ_0 being arbitrary. The mean time between steps is also arbitrary, and the actual time between steps is assumed to be normally distributed about this mean with a variance which is also arbitrary. Some care must be taken with this model since with a large ratio of variance to mean it is easy to encounter a negative time between steps.

Under these assumptions, the Nordheim-Fuchs equations during the nth time step, in dimensionless form, are

$$\frac{dP_n}{d\tau} = (n - W_n)P_n, \tag{1}$$

$$\frac{dW_n}{d\tau} = P_n \tag{2}$$

at

$$\tau = 0, \qquad W_n = W_n(0) = W_{n-1}(\tau_{n-1}), \tag{3}$$

$$P_n = P_n(0) = P_{n-1}(\tau_{n-1}); \tag{4}$$

also,

$$W_1(0) = 0$$

$$P_1(0) = p \ll 1.$$

The subscript n denotes the solution during the nth step; τ_{n-1} is the duration of the $(n - 1)$st time step.

The dimensionless variables are:

$$W = E/(\rho_0/\alpha)$$

$$P = \mathfrak{p}(\alpha\ell/\rho_0^2)$$

$$(\rho/\rho_0) = [n - (\alpha E/\rho_0)] \text{ (during the } n\text{th time step)}$$

$$\tau = t\rho_0/\ell,$$

where

$E \equiv$ energy content of the reactor, MW-sec

$\mathfrak{p} \equiv$ reactor power, MW

$\alpha \equiv$ reactor power coefficient, \$/MW-sec

$\ell \equiv$ reactor lifetime, sec/\$

$\rho_0 \equiv$ reactivity increment beyond prompt critical, \$

$t \equiv$ real time, sec.

These equations have the well-known solutions:

$$W_n = n + \sqrt{2C_{1,n} + n^2} \cdot \tanh\left\{\sqrt{2C_{1,n} + n^2}\left(\frac{\tau}{2} + C_{2,n}\right)\right\}$$

$$P_n = \frac{1}{2}(2C_{1,n} + n^2) \cdot \operatorname{sech}^2\left\{\sqrt{2C_{1,n} + n^2}\left(\frac{\tau}{2} + C_{2,n}\right)\right\},$$

where

$$C_{1,n} = \tfrac{1}{2}(W_n(0) - n)^2 + P_n(0) - \tfrac{1}{2}n^2$$

$$C_{2,n} = \frac{1}{\sqrt{2C_{1,n} + n^2}} \tanh^{-1}\left(\frac{W_n(0) - n}{\sqrt{2C_{1,n} + n^2}}\right).$$

As an example consider the case $N = 2$, and examine three cases: $\tau_1 \ll 1, \frac{\tau_1}{2} + C_{2,1} \approx 0$, and $\tau_1 \gg 2C_{2,1}$. Recall that $W_1(0) = 0$ and $P_1(0) = p \ll 1$. The solution constants are $C_{1,1} = p$ and $C_{2,1} \approx -2/p^2$.

Then, for the case $\tau_1 = \delta \ll 1$,

$$W_1(\tau_1) = W_2(0) \approx 2\delta$$

and

$$P_1(\tau_1) = p[1 + (2\delta/\sqrt{1 + 2p})].$$

Using these initial conditions, we find

$$C_{1,2} \approx p - 4\delta + (2p\delta/\sqrt{1 + 2p})$$

whence the final energy, $(2C_{1,2} + 4)^{1/2} + 2 = 4 - 2\delta + \frac{p}{2}$. If all reactivity were introduced at once the final energy would, of course, be $4 + \frac{p}{2}$. Hence the division into two steps decreases the final energy release by an amount corresponding to the small amount of reactivity compensation, 2δ, that occurred in the first step.

If

$$(\tau/2) + C_{2,1} \approx 0,$$

then

$$W_1(\tau) = W_2(0) = 1$$

and

$$P_1(\tau) = (1 + 2p)/2.$$

Thus, $C_{1,2} = 2p - \frac{1}{2}$ and the final energy release is $2 + \sqrt{3 + 4p}$, to be compared with $2 + \sqrt{4 + 2p}$.

Hence, the final energy release is smaller in this case by the factor $(1 + \sqrt{3/4})/2$ than the energy release obtained in a single step.

Finally, in the case $\tau/2 \gg |C_{2,1}|$, the final energy release is just $2 + \sqrt{p}$ corresponding to the complete reactivity compensation obtained during the first step.

TABLE IV-27-I. Effect of Random Variations in Length of Time Step on Final Energy Release

(*Note:* $\sigma \equiv$ *standard deviation*)

τ/τ_0	$\sigma(\tau)/\tau$	W/W_0	$\sigma(W)/W$
0.0234	0	1.0	0
0.0234	1.0	1.0	0
0.234	0.1	0.9999	0
0.234	1.0	0.9999	0
2.34	0.1	0.29	0.13 ± 0.4
2.34	1.0	0.57[a]	0.41 ± 0.04

[a] Many of the samples had a negative time selected and should have been discarded; this would increase the uncertainty in the variance.

The energy is reduced by a factor of $\frac{1}{2}$, corresponding to the fact that the reactivity after the first step is below prompt critical by just the amount added at the second step so that the system does not undergo any further excursion.

Therefore at this point we would conclude that a lack of coherence in reactivity calculations will reduce the total energy release, but the ratio of estimated energy releases will in general be close to one and certainly greater than $1/N$.

To investigate the effects of randomness the Eqs. (1) through (4) were programmed for the IBM 360/50-75 with τ_n chosen from a normal distribution with preassigned mean and variance. The results are given in Table IV-27-I for the case $N = 5$. The conclusion is that the variance in the time between additions is significant only when $\tau > 1$.

When $\tau \gg 1$, the dispersion of τ about its mean appears to be about the same as the dispersion of W about its mean. For the case of N very large, some care must be used in relating this study to particular cases. Although the Eqs. (1) through (4) are in dimensionless form, the amount of reactivity increment ρ_0 should be large compared with the delayed neutron fraction, β, for the equations to be useful; and, of course, the underlying assumption is that the system starts at prompt critical.

Reference

1. D. V. Gopinath and C. E. Dickerman, *Calculations of Coherence of Failure for Hypothetical Meltdown Accidents in an EBR-II-Like Reactor*, ANL-6844 (1964).

IV-28. Design Basis Accident Calculation for ZPR-6 and -9 Plutonium Safety Analysis Report

G. K. Rusch

A situation wherein a gross reactivity overload has been inadvertantly loaded into ZPR-6 or -9, and subsequently the movable table drives toward the stationary table until contact is made, is postulated along with a failure of all scram mechanisms, and the resulting excursion is analyzed. The movable half of the reactor is assumed to drive at its intermediate speed as described in Ref. 1 and is adding reactivity at a rate of $7.9 \times 10^{-4}\ \Delta k/k\ \text{sec}^{-1}$. The reactor involved is a plate type mockup of a 3500 liter plutonium-carbide core containing carbon, U-238, canned sodium, and a canned 28 w/o plutonium, 69.5 w/o U-238, 2.5 w/o molybdenum alloy. Table IV-28-I contains the reactor core and blanket material volume fractions and Fig. IV-28-1 the loading pattern assumed for heat transfer calculations within each drawer.

TABLE IV-28-I. Volume Fractions for 3500 Liter Plutonium Carbide Core

Material	Volume Fraction, %	
	Core	Blanket
Pu-239	2.05	—
Pu-240	0.29	—
Pu-241	0.05	—
U-235	0.02	—
U-238	16.40	83.0
Mo	0.24	—
C	10.95	—
Na	45.0	—
Stainless Steel	20.0	7.0
Void	5.0	10.0

The calculational model employed couples a point reactor kinetics code to a one dimensional heat transfer subroutine to obtain material temperatures, reactivity feedback, and k_{ex} as functions of time. For

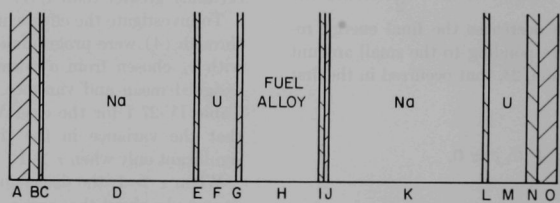

REGIONS	cm	INCHES
A = MATRIX TUBE	0.1524	0.060
B = DRAWER TUBE	0.0762	0.030
C = CLADDING Na CAN	0.0381	0.015
D = Na	1.2700	0.500
E = CLADDING Na CAN	0.0381	0.015
F = DEPLETED URANIUM	0.3175	0.125
G = CLADDING FUEL ALLOY	0.0381	0.015
H = Pu-U-Mo ALLOY	0.6350	0.250
I = CLADDING FUEL ALLOY	0.0381	0.015
J = CLADDING Na CAN	0.0381	0.015
K = Na	1.2700	0.500
L = CLADDING Na CAN	0.0381	0.015
M = DEPLETED URANIUM	0.3175	0.125
N = DRAWER TUBE	0.0762	0.030
O = MATRIX TUBE*	0.1524	0.060

14 REGIONS, 4 MATERIALS, 6 PROPERTY RANGES
*POSITION O REPRESENTS THE BEGINNING OF NEXT CELL

Fig. IV-28-1. Loading Pattern Assumed for Heat Transfer Calculations. *ANL Neg. No. 113-1540.*

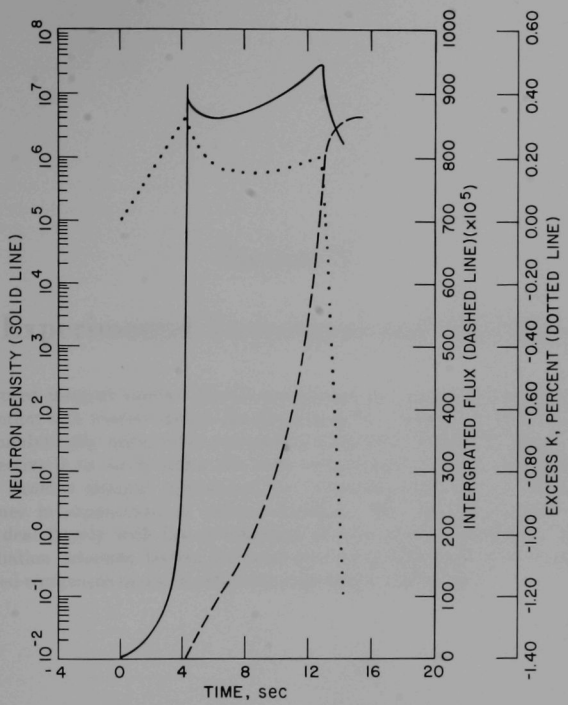

FIG. IV-28-2. Design Basis Accident Analysis for 3500 Liter Core. *ANL Neg. No. 113-1539.*

computational purposes the reactor was divided into five discrete zones and appropriate neutron flux, adjoint weightings and material worths were assigned to each zone. Heat was assumed to be generated only in the fuel; the remaining materials were heated by thermal conduction. Heat was assumed to be conducted only in the direction transverse to the vertical/axial planes formed by the material plates. (Details of the model, calculational procedures, and results are given in Ref. 1, and of the code in Ref. 2.)

The reactivity excursion was finally terminated by molten fuel flowing out of the core. Figure IV-28-2 shows the neutron density, integrated neutron density and reactivity as a function of time. A total of 2.7×10^{20} fissions occurred. Burning of vaporized sodium during the excursion and by afterheat in the core resulted in a peak reactor cell pressure of 20 psig—less than the 35 psig rating of the cell structure and thus the accident was contained. Pressure buildup during the excursion was relieved through a filter system consisting of sand and aggregate in series with HEPA filters. Approximately 6.2 mg of plutonium was calculated to be discharged through a 150 ft high stack to the air although a total of about 60 kg of plutonium was burned in the reactor cell. Detailed listings of released fission products and possible resultant radiation doses are given in Ref. 1.

In conclusion, a severe accident (2.7×10^{20} fissions) was found to be contained by the ZPR-6 and -9 containment system. Radiation levels and doses external to the containment cell were found to be tolerable even for this severe accident.

REFERENCES

1. W. Y. Kato, G. K. Rusch, L. R. Dates, C. E. Till, J. van Doorninck, and C. L. Cheever, *Final Safety Analysis Report on the Use of Plutonium in ZPR-6 and -9*, ANL-7442 (to be published).
2. G. K. Rusch and J. van Doorninck, *The Coupled One-Energy Group Point Reactor Kinetics Code/One Dimensional Heat Transfer Subroutine Used to Calculate the Design Basis Accident for the ZPR-6, -9 Plutonium Safety Analysis Report Addendum*, ANL-7508 (to be published).

Section V

Experimental Techniques and Facilities

Measured integral reactor physics parameters are necessary for either direct introduction into reactor design calculations or for comparison with values obtained analytically using basic microscopic cross section data. In the latter case the objective is to verify either the cross section data or the calculational techniques. Reactor integral parameters are obtained using special measurement techniques in exponential or critical facilities. The papers presented in this section deal largely with the development of such special techniques, facilities, and radiation detection devices. Included also are papers which describe specially developed equipment useful in obtaining microscopic nuclear data.

V-1. Basic Measurements Underlying Nuclear Reactor Data

A. De Volpi and K. G. Porges

Although a large number of cross sections and nuclear data are used in conjunction with other material characteristics to calculate the fuel requirements, safety characteristics, and conversion or breeding gain of reactors, constants associated directly with the neutron-induced fission stage play a major role in the design and extrapolation of reactor concepts. From a recent evaluation of the status of fundamental fission data,[1] we find that the absolute accuracy of many of the fission parameters can be traced to certain underlying basic measurements.

By virtue of their relationship to what are essentially relative (rather than absolute) measurements of some of the more difficult components of the experiment, the absorption cross section (σ_a) and the number of neutrons emitted per neutron absorbed (η) have the highest reliability. The reference energy is usually thermal, with most high energy data measured relative to thermal values; and the reference material is usually U-235 in view of its availability early in the atomic energy program. Thus, much of the basic fission data is connected with σ_a and η of U-235 at 2200 m/sec.

A second, partially redundant set of data, is derived from the product $\nu\sigma_f$. Both of these quantities turn out to be more difficult to measure with high accuracy because of intrinsic requirements for absolute measurements and because of angular correlation difficulties. For σ_f, frequently the B-10 absorption cross section is used as reference; for ν there is need to know (when measurements are made with the manganese bath) the ratio of the hydrogen/manganese cross sections.

There are a number of other cross sections connected primarily with the absorption or activation cross sections of hydrogen, boron, manganese, and gold. Consequently the values of these cross sections assume an importance which, in the past, has been obscured. In order to obtain accuracies in the order of ½% for some of the fission parameters, it becomes necessary to achieve accuracies of at least ¼% for these underlying cross sections.

As an integral part of our efforts to carry the measurements of ν to their logical level (approximately ½%), the derivation of all of these key cross sections has become both essential and consequential. In principle, the experiments are simple. By varying the concentration of manganese in an aqueous solution, the count rate (which is induced by a fixed neutron source) changes in a manner directly connected with the hydrogen/manganese cross-section ratio. In practice, a high degree of long-term stability is required before these numbers can be obtained with precision.

By poisoning the manganese bath with boric acid, two cross-section ratios can be independently determined: boron/manganese and hydrogen/manganese. Our value for the boron/manganese 2200 m/sec cross-section ratio can be used to generate a precise value for the manganese cross section based on the boron reference.

Additional experiments are scheduled to improve the precision of the boron/manganese ratio, while other experiments are planned to evaluate the hydrogen cross section independently. Since these techniques are relatively free from systematic error, their accuracy promises to be compatible with current requirements for cross-section standards.

Reference

1. A. De Volpi, *Current Values of Fundamental Fission Parameters*, Reactor Fuel-Processing Tech. **10**, No. 4, 271–288 (Fall 1967).

V-2. Absolute Fission Rate Measurements with Solid-State Track Recorders

R. Gold, R. J. Armani and J. H. Roberts*

The method of fission track counting has been placed on a precise absolute basis.[1] Sources of systematic error have been investigated and reduced or eliminated so that precise fission rate measurements can be conducted. Solid State Track Recorders (SSTR) of pre-etched mica and polycarbonate resin (Makrofol) were used. Experimental results depend critically on the quality of the fission sources employed. Consequently, different methods of fission source preparation have been examined. The efficiency and sensitivity of this method have been determined for both mica and Makrofol. An irradiation assembly providing uniform neutron flux exposures is used for relative measurements. Absolute calibrations have been carried out using Cm-244 spontaneous fission sources. A limiting accuracy of close to 1% for absolute uranium fission rate measurements has been achieved.

* Northwestern University, Evanston, Illinois.

Reference

1. R. Gold, R. J. Armani and J. H. Roberts, *Absolute Fission Rate Measurements with Solid-State Track Recorders*, Nucl. Sci. Eng. **34**, 13 (1968).

V-3. Fission Rate Measurements in Low Power Fast Critical Assemblies with Solid-State Track Recorders

J. H. Roberts*, S. T. Huang†, R. J. Armani and R. Gold

Solid-state track recorders (SSTR) have been used in the measurement of fission rates in ZPR-6 Assembly 5, which is a split-table, low power, fast critical assembly, the details of which may be found in Ref. 1. An extensive discussion of the SSTR method is given in Ref. 2. The experimental procedure for in-core critical assembly measurements is described in Ref. 3. Comparisons of SSTR data with radiochemical[4] and fission counter[5] measurements and with diffusion theory calculation[6] are presented below.

For the critical assembly experiments, thin U_3O_8 sources (approximately 93% enriched in U-235) and foils of uranium approximately 0.125 mm (depleted to approximately 0.2% U-235) were used. The SSTR fission source in-core configurations are illustrated in Fig. V-3-1. Selected pieces of mica were exposed to the fission sources. After exposure the mica was etched for approximately 90 min at room temperature in an HF concentration of 49%.

Axial and radial traverses were carried out in the movable half of the split-table assembly matrix core (Fig. V-3-2). Fine structure measurements in the fission rates were made in drawer 24-23. Additional measurements were made so that a complete fission rate profile could be obtained.

Results

Results of axial and radial fission rate traverses with U-235 are displayed in Figs. V-3-3 and V-3-4 respectively. The extrapolation length in the axial traverse was found to be 89 cm. A cosine distribution based on this length is given in Fig. V-3-3 and is in

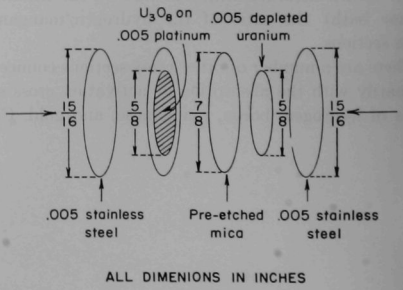

Fig. V-3-1. Geometrical Configuration of the SSTR and Fission Sources for the In-Core Critical Assembly Experiments. *ANL Neg. No. 112-9634.*

* Northwestern University, Evanston, Illinois.
† Student, Northwestern University, Evanston, Illinois.

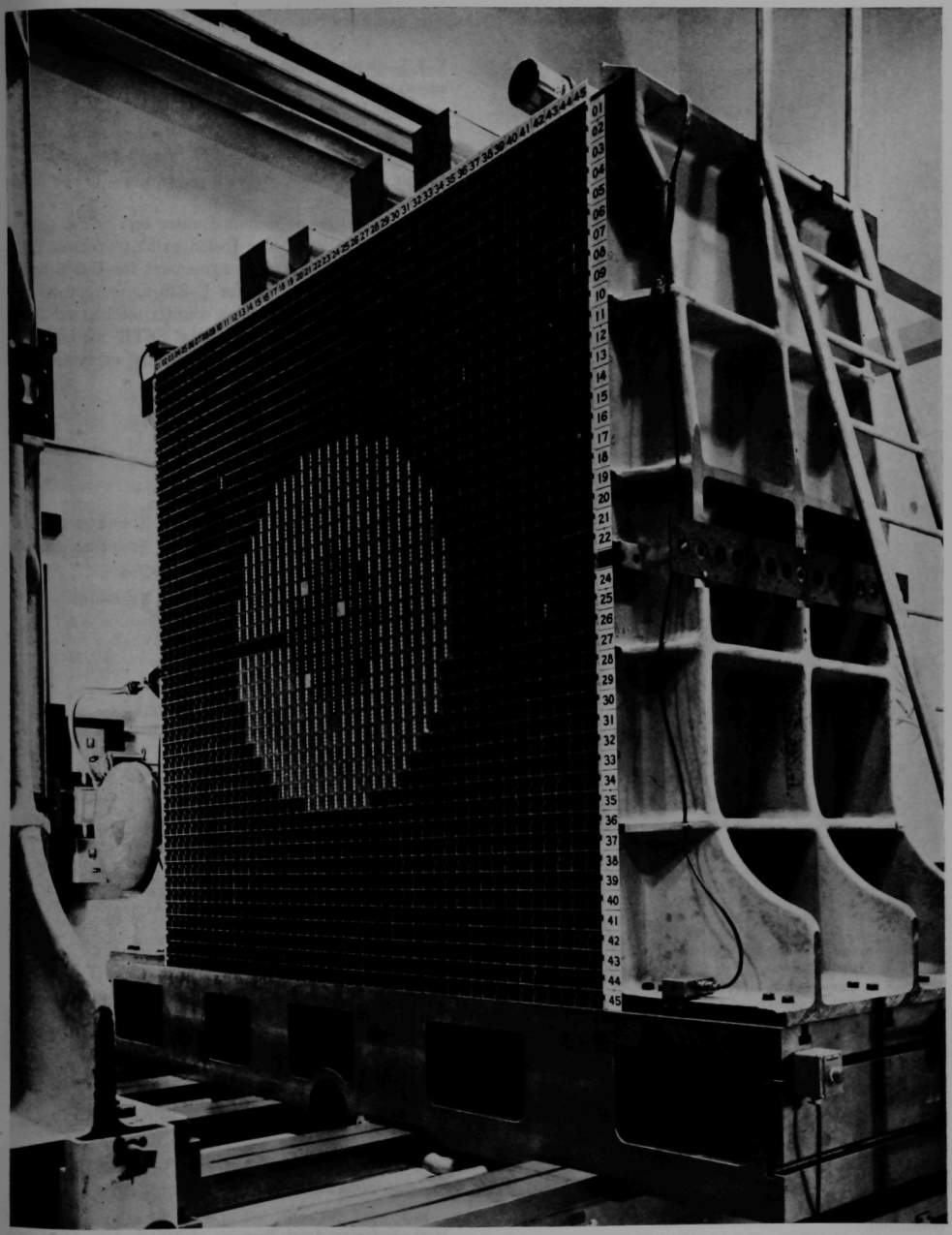

Fig. V-3-2. ZPR-6: Split-Table, Fast Critical Assembly Matrix Core. *ANL Neg. No. 112-3628.*

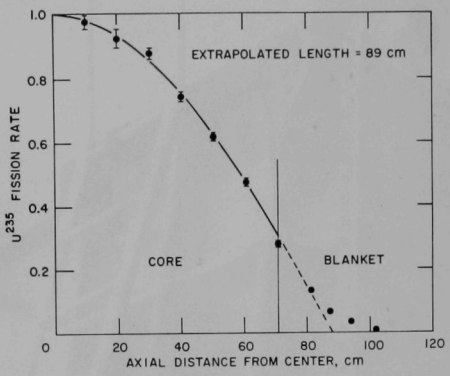

FIG. V-3-3. Comparison of Axial Fission Rate Measurements in ZPR-6, Assembly 5, with a Cosine Distribution Solution (smooth curve). Experimental Data Obtained with SSTR of Pre-Etched Mica and Sources of U-235. *ANL Neg. No. 113-1471.*

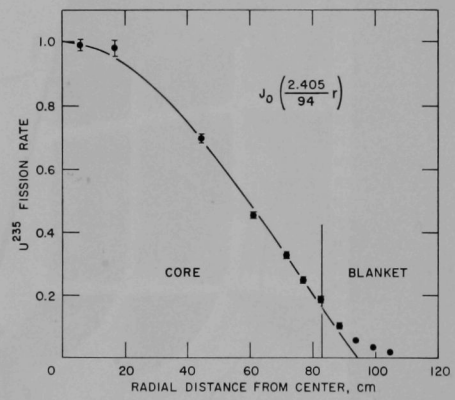

FIG. V-3-4. Comparison of Radial Fission Rate Measurements in ZPR-6, Assembly 5, with the Bessel Distribution Solution J_0 (smooth curve). Experimental Data Obtained with SSTR of Pre-Etched Mica and Sources of U-235, R = 94 cm. *ANL Neg. No. 113-1472.*

good agreement with the data. The radial traverse follows the diffusion theory solution $J_0[(2.405)/R]$ quite adequately. Here J_0 is the Bessel function of order zero and R is the extrapolation length. Both cosine and Bessel distributions are the well-known diffusion theory solutions for a finite cylindrical reactor that satisfy the extrapolated zero-flux boundary condition.[6]

As an example of fine-structure measurements, Fig. V-3-5 displays the U-238 fission rate distribution across drawer 24-23. The fission rate is seen to peak near the U-235 fuel layers. Similar fine-structure results have been obtained with the radiochemical method.[4] Much more detail in fine structure could be obtained because of the high space resolution available with SSTR.

A comparison of fission counter and SSTR data is given in Fig. V-3-6 for U-238 axial traverses. These two methods are in good agreement for U-235 fission rate measurements, but for U-238 measurements Fig. V-3-6 shows that the fission counter method exhibits a measurable deviation from the SSTR method. The source of this discrepancy is readily explained. The

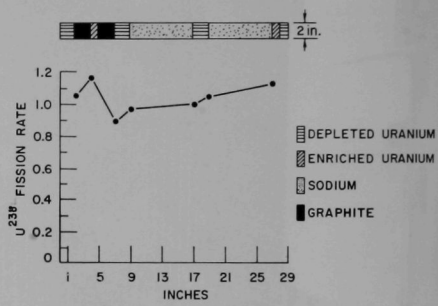

FIG. V-3-5. SSTR Measurements of Fine Structure in the U-238 Fission Rate Distribution Across Drawer 24-23. *ANL Neg No. 113-1475.*

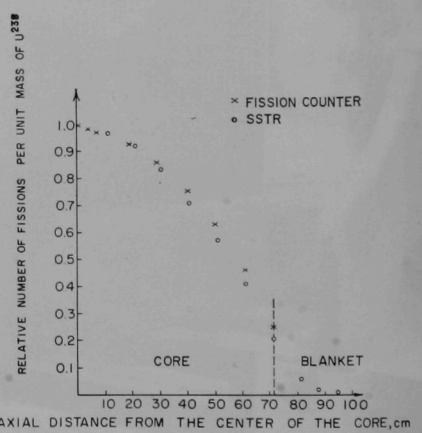

FIG. V-3-6. A Comparison of the SSTR and Fission Counter Methods for an Axial Traverse of ZPR-6, Assembly 5 with U-238. *ANL Neg. No. 112-9632.*

SSTR were placed between sodium and depleted uranium plates for these measurements. It follows from the fine structure data that the SSTR data are lower than the average fission rate observed by the fission counter. Sodium had to be removed to provide the necessary space to insert the fission counter. With sodium present more energy degradation of the fast spectrum occurs; this also implies that the SSTR method should yield lower values of U-238 fission rates in agreement with experiment.

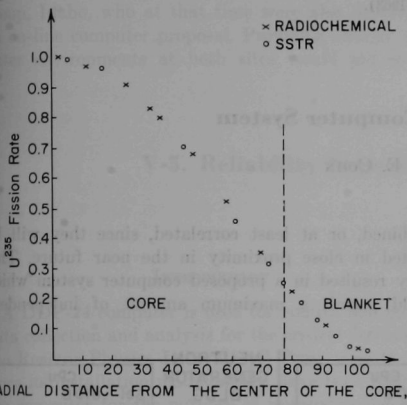

FIG. V-3-7. A Comparison of the SSTR and Radiochemical Methods for a Radial Traverse of ZPR-6, Assembly 5 with U-235. *ANL Neg. No. 112-9636.*

General agreement between SSTR and radiochemical methods is supported by a comparison of typical U-235 radial traverses given in Fig. V-3-7. However, the SSTR method does possess advantages over the radiochemical method. Since fission rates are measured directly, one need not be concerned with the problem of radioisotope fission yield varying with neutron energy, which is inherent in all radiochemical determinations.

Finally, Fig. V-3-8 displays a three-dimensional profile of the U-238 fission rate throughout the assembly. These data demonstrate the power of the SSTR method in obtaining fission rate measurements over large regions of a critical assembly from one or at most a few exposures.

References

1. R. A. Karam, L. R. Dates, E. Groh, W. Y. Kato, R. A. Lewis, G. Main, J. E. Marshall, G. K. Rusch and C. Till, *Measured Physics Parameters in a Large Uranium Carbide Fast Core, Assembly 5 ZPR-6*, Reactor Physics Division Annual Report, July 1, 1966 to June 30, 1967, ANL-7310, pp. 167–189.
2. R. Gold, R. J. Armani and J. H. Roberts, *Absolute Fission*

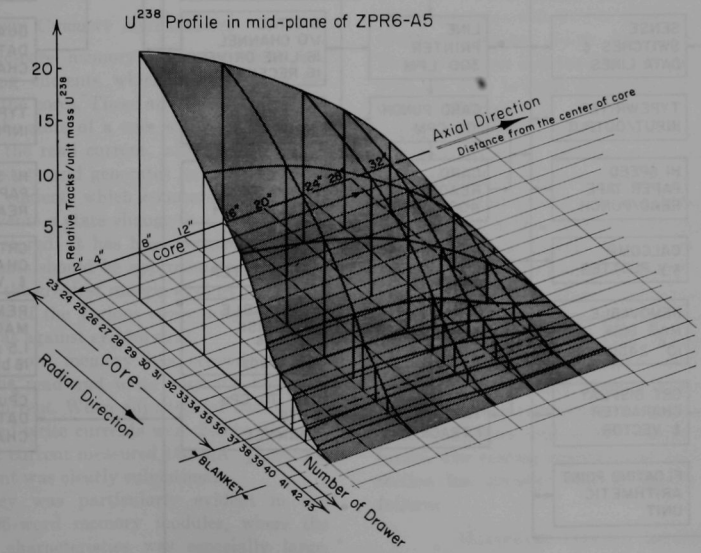

FIG. V-3-8. The Gross Volume U-238 Fission Rate Distribution in ZPR-6, Assembly 5 as Obtained from SSTR Measurements. *ANL Neg. No. 112-9641 T-1.*

Rate Measurements with Solid-State Track Recorders, Nucl. Sci. Eng. **34**, 13 (1968).
3. J. H. Roberts and S. T. Huang (Northwestern University), R. J. Armani and R. Gold (ANL), *Fission Rate Measurements in Low Power Fast Critical Assemblies with Solid-State Track Recorders*, Nucl. Appl. **5**(4), 247–252 (October 1968).
4. R. J. Armani, *Absolute Determination of Fission Rates in U-235 and U-238 and Capture Rates in U-238 by Radiochemical Techniques*, Proc. Symposium on Standardization of Radionuclides, Vienna, October 10–14, 1966 (IAEA, Vienna), pp. 621–627.
5. F. S. Kirn, *Neutron Detection with an Absolute Fission Counter*, Proc. Symposium on Neutron Dosimetry, Vienna, 1963, Vol. II (IAEA, Vienna), pp. 497–512.
6. S. Glasstone and M. C. Edlund, *The Elements of Nuclear Reactor Theory* (Reinhold Publishing Corp., New York, 1963).

V-4. A Shared Peripheral Computer System

J. F. Whalen and C. E. Cohn

A systems design study was made to determine if the on-line computer replacement requirements for the fast critical experiments sections and the Applied Nuclear Physcis section, Argonne site, could not be combined, or at least correlated, since they will be located in close proximity in the near future. This study resulted in a proposed computer system which would permit a maximum amount of independent

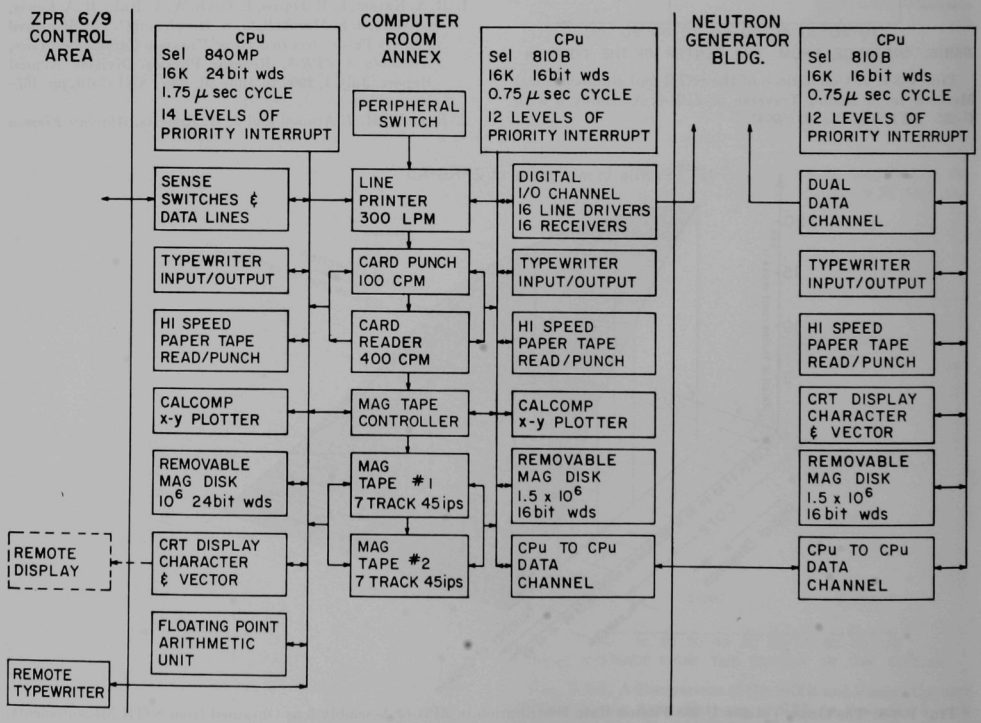

Fig. V-4-1. Unit Distribution and Data Paths for Reactor Physics Division On-line Computer System. *ANL Neg. No. 113-1442.*

usage by the individual sections and which at the same time would effect large savings by allowing the sharing of expensive peripheral equipment and providing semi-standardized interface entries. Another valuable aspect of compatability was accomplished by including in the design discussions representatives from the Zero Power Plutonium Reactor (ZPPR) group, Idaho, who at that time were also developing an on-line computer proposal. Providing similar computer environments at both sites would aid in the interchange of experimental setups, as well as software.

A request for proposal was submitted to 12 possible vendors together with detailed specifications. The resulting material was evaluated, a vendor was selected, and a contract negotiated. The complete system will be on-site by March 1, 1969 with partial deliveries up to that date. A work diagram showing the final configuration and item location is shown in Fig. V-4-1.

V-5. Reliability Improvements for the DDP-24 Computer

C. E. Cohn

Introduction

A DDP-24 computer is used for control and on-line data collection and analysis for the critical facilities in the Reactor Physics Laboratory.[1] From time to time since its installation modifications have been made on the computer for the purpose of improving the reliability of its operation. Earlier modifications are described in Ref. 2 and more recent modifications are discussed in the following paragraphs.

Memory Current Adjustments

In a magnetic-core memory there are three important operating currents which flow through the wires threading the cores. These are the write current, which changes the state of a core when a "one" is to be stored in it; the read current, which resets a core from the "one" state and generates an output signal; and the inhibit current, which counteracts the write current and prevents a state change in a core where a "zero" is to be stored. It has been pointed out[3] that these three currents should be approximately equal in order to provide the greatest margin against the spread in characteristics of the various cores throughout the memory as well as against system drift.

The DDP-24 core memory has screwdriver adjustments for the read and write currents, but none for the inhibit current. When adjusted for best operation, the read and write currents were 240 to 250 mA, while the inhibit current measured 160 mA. Therefore, the inhibit current was clearly suboptimal.

This deficiency was particularly evident in one of the two 4096-word memory modules, where the spread in core characteristics was especially large. In particular, there was one core whose threshold for state change was some 40 mA lower than all the rest. Possibly because of component aging, it became impossible to find an adjustment for this module at which all cores would function properly. Therefore, to restore proper operation it was imperative to increase the inhibit current.

There are twenty-four inhibit circuits, one for each bit, in each module. When a given bit is to be stored as a zero, the associated driver transistor conducts and draws a current through the inhibit wire as determined by a resistor network. (The resistor networks are contained on two inhibit component boards which are located inside the core-stack enclosure.) The current was increased by adding a resistor to each network. This brought the current through the inhibit wires to 255 mA.

This modification made it possible to obtain completely satisfactory adjustments in both modules. The write currents were now adjusted to around 260 mA, with margins of around ±20 mA in the difficult module and ±30 mA in the other one. The memory operations have since been highly satisfactory. Unfortunately, the increased inhibit current caused the failure of six driver transistors—three immediately after the modifications were completed and three subsequently. Since these failures are very readily localized and corrected, they are considered a small price to pay for the improved memory operation obtained. It is believed that they represent a sorting-out of particularly weak transistors, and so will become less likely in the future. The cooling improvement described in the next section has greatly reduced the likelihood of these failures.

Mainframe Cooling Improvements

From time to time throughout its life, the DDP-24 has been plagued with intermittent, evanescent main-

frame failures which were impossible to localize. Consideration of the causes for these failures pointed to inadequate cooling of the circuit boards from which the mainframe is constructed.

Adequate provisions for such cooling were not made in the design of the computer. The manufacturer did install a blower at the bottom of each of the three rack bays which contain the boards. However, he made no provisions to channel the air into the restricted spaces between the boards where the flow is really needed. As a consequence, most of the air bypassed the board enclosures and was ineffective for cooling.

In addition, it had become the practice to keep frequently-used program tapes on top of the computer. It appeared that an increase in the failure rate was correlated with an increase in such storage. This was confirmed by complete freedom from failures for two weeks after all tapes were removed from atop the ventilation openings. Since no more than one-third of the ventilation area had ever been covered, the existing cooling was evidently marginal.

An improved cooling arrangement was installed. The existing rack blowers were removed. In each bay, a standard 7 x 17 x 3-in. chassis base was mounted, inverted, snugly under the bottom row of boards. Under each chassis were mounted three 100-cfm axial-flow fans. The chassis serves as a plenum chamber to channel the air between the boards and provide even distribution. The design of the board enclosures then provides for air circulation upwards past all the boards in the bay.

Each memory module is equipped with fans which force air into the core-stack compartment and outwards between some additional boards. These fans were equipped with dust filters which seriously restricted the flow, even when clean. Therefore, the filters were removed. (Dust is not a major problem in this low-voltage, low-impedance circuitry.) The boards here include those containing the aforementioned inhibit-driver transistors. It is expected that the improved air flow will significantly lower the failure probability of these transistors.

The memory modules possess another stack of boards which is cooled by a 270-cfm axial-flow fan mounted under them. Here, again, no provision was made for channeling the air between the boards, so that most of the air again bypasses them. Although this area has not been troublesome in the past, a sheet metal shroud was installed over the fan to direct the air properly.

These cooling improvements have all but eliminated the mainframe failures and have completely eliminated intermittents. They have yielded improvement in reliability.

Typewriter Interface Improvements

The input-output typewriter has been one of the least reliable parts of the computer system. Although most of this unreliability must be charged directly to the typewriter, it appeared that some may be charged to the typewriter interface circuits in the computer, since the design of these departed in some respects from the typewriter manufacturer's recommendations. The areas of departure were:

(1) The contacts in the typewriter that determine timing are provided in break-before-make SPDT form, to allow for buffering against contact bounce using flip-flops. Advantage was not taken of this provision.

(2) As a consequence of the above, it was necessary to provide a 7-msec time delay in the timing circuits to allow the contacts to settle. This is contrary to a recommendation of the manufacturer that there should be no delay between the completion of one printing operation and the energizing of the selection magnets for the next operation. The recommendation was intended to insure maximum operating speed and minimum clutch wear.

(3) The voltages applied to the contacts and the current passed through them were below recommended minima. These recommendations were intended to insure against erratic contact operation under "dry-circuit" conditions. Some simple modifications were made on the interface circuits to correct these difficulties.

To eliminate the contact bounce problem, each SPDT contact set was buffered by a flip-flop. When a contact set is in its normal state, the dc set input of the flip-flop is grounded and the dc reset input is ungrounded. This places the flip-flop in the set state. When the contact changes state, the set input is ungrounded and the reset input is then grounded. The flip-flop immediately switches to the reset state. Once the flip-flop is latched in this state, further openings and closings of the normally open contact have no effect. Therefore, contact bounce has no effect unless the contacts bounce so badly as to reclose the normally closed contact. The contacts are specifically designed not to do this, and will not do it unless they are grossly misadjusted. On return to the normal state, the action is analogous.

In the original circuit, the feedback contacts were returned to −18 V through a 2.26-K resistor, and were clamped to −6 V through a diode. The contacts thus carried a current of 8 mA. Other typewriter contacts were connected in the same way, while still others were returned to −6 V though 5.1-K resistors, and would thus draw slightly over 1 mA. These operating conditions did not conform to recommendations that

the contacts should switch at least 40 mA and 10 V. The typewriter manufacturer feels that these currents and voltages are necessary to insure the breakdown of surface films and the establishment of reliable contact. If such currents were drawn from the normal computer power supplies, regulation problems could result, so a separate 12-V dc power supply was provided. All typewriter contacts were returned to the negative side of this supply through 240-Ω resistors, and thus draw 50 mA each.

Other Modifications

Various console control functions were handled by magnetic-core pulsers attached to pushbutton switches. These pulsers have been quite unreliable, and several have failed. In accord with the principle of not replacing an unreliable part with more of the same, the pulsers were replaced with simple resistor-capacitor-diode circuits.

Modifications to the paper-tape punch circuits have been reported previously.[2]

References

1. C. E. Cohn, *Use of a Small Digital Computer in Data Analysis and Control of Critical Facilities*, Reactor Physics Division Annual Report, July 1, 1965 to June 30, 1966, ANL-7210, pp. 330–337.
2. C. E. Cohn, *Further Development of the DDP-24 Computer System*, Reactor Physics Division Annual Report, July 1, 1966 to June 30, 1967, ANL-7310, pp. 402–407.
3. C. P. Womack, *Schmoo Plot Analysis of Coincident-Current Memory Systems*, IEEE Trans. Electron. Computers **EC-14**, 36–44 (1965).

V-6. Digital-Computer Processing of Sampling-Oscilloscope Data

C. E. Cohn

Introduction

A digital computer can process information from a sampling oscilloscope to average out noise and fluctuations on the observed waveform and estimate the true shape of that waveform.

The sampling oscilloscope is a useful instrument for observing signals that are too fast for other methods. However, it is best suited to a repetitive signal whose form is unvarying. Where the signal is subject to noise and fluctuations, as are pulses from nuclear detectors, the sampling-oscilloscope display becomes blurred, and the "true" shape of the pulse cannot readily be seen. The technique described here extracts that information.

This type of averaging has been done previously with a wired-program analyzer.[1] A stored-program computer provides more flexibility and allows more sophisticated information handling.

Hardware

The sampling-oscilloscope interface must digitize the time and voltage information produced by the oscilloscope at each sampling, and transmit the data to the computer, as controlled by the clock pulses generated by the oscilloscope. In addition, the interface must reject data produced during retrace of the oscilloscope staircase sweep.

The oscilloscope used here is a Tektronix 564, with a 3S3 sampling-probe unit and a 3T77 sampling-sweep unit. The dual analog-digital converters were built by the Electronics Division, and are as described in Ref. 2 except for having a 5-MHz clock frequency. The computer is the DDP-24.

A block diagram of the setup is shown in Fig. V-6-1. The analog X and Y information needed is available at the front panel of the oscilloscope with a calibration factor of one volt per scale division on the oscilloscope screen. These voltages are passed through signal conditioning amplifiers which invert the polarity and shift the zero to make the signals suitable for the analog-to-digital converters (ADC)'s. The outputs of the amplifiers go directly to the inputs of the linear gates.

The sampling-sweep unit generates a clock pulse to indicate that a sampling has occurred. This pulse is passed into a linear amplifier, single channel analyzer, and coincidence circuit on the ADC chassis. The latter strobes the linear gates, making the ADC's digitize the information from the sampling. The time (X) information is digitized to 512 channels, while the amplitude (Y) information is digitized to 1024 channels.

The address-advance pulses from the ADC's go to the computer's 24-stage binary input scaler. The Y information is accumulated in the higher-order 12 bits, while the X information is accumulated in the lower-order 12 bits. On completion of conversion, the termination of the width-modulated pulses from the

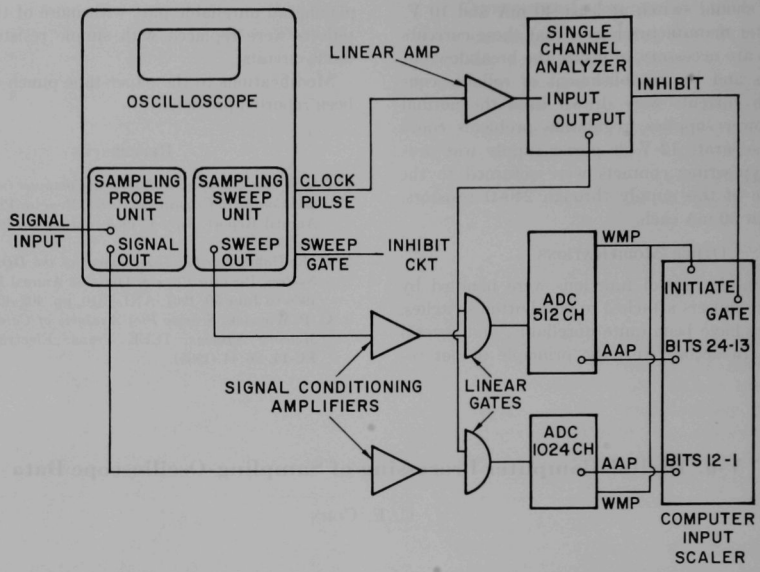

FIG. V-6-1. Block Diagram of Setup for Sampling-Oscilloscope Data Processing. *ANL Neg. No. 112-9984.*

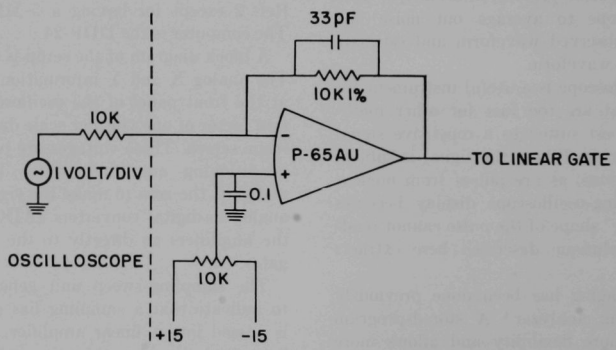

FIG. V-6-2. Signal-conditioning Amplifier. *ANL Neg. No. 112-9983.*

ADC's signals the computer to read the data. Conversion of subsequent samplings is inhibited until the input data transfer is complete and the scaler has been reset.

Figure V-6-2 shows one of the two identical signal-conditioning amplifiers. The oscilloscope signal outputs have an effective 10K series output resistance. The operational amplifier and its 10K feedback resistor, in conjunction with this output resistance, form a unity-gain inverter which transforms the positive oscilloscope output to the negative polarity required by the ADC. The 10K helipot allows the output voltage range of the amplifier to be set as required by the ADC (i.e. 0 to −10 V).

Conversion of data produced during staircase-sweep retrace is inhibited by the circuit shown in Fig. V-6-3. During retrace, the sampling-sweep unit blanks the cathode ray tube (CRT) beam so that samples taken then will not be displayed. A portion of the blanking voltage is made available as a "sweep gate". This

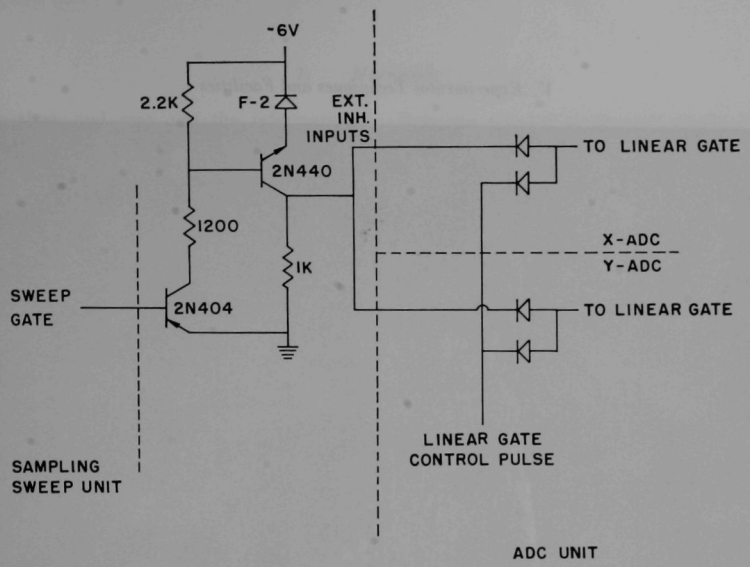

FIG. V-6-3. Circuit to Inhibit Data-taking During Sweep Retrace. *ANL Neg. No. 112-9982.*

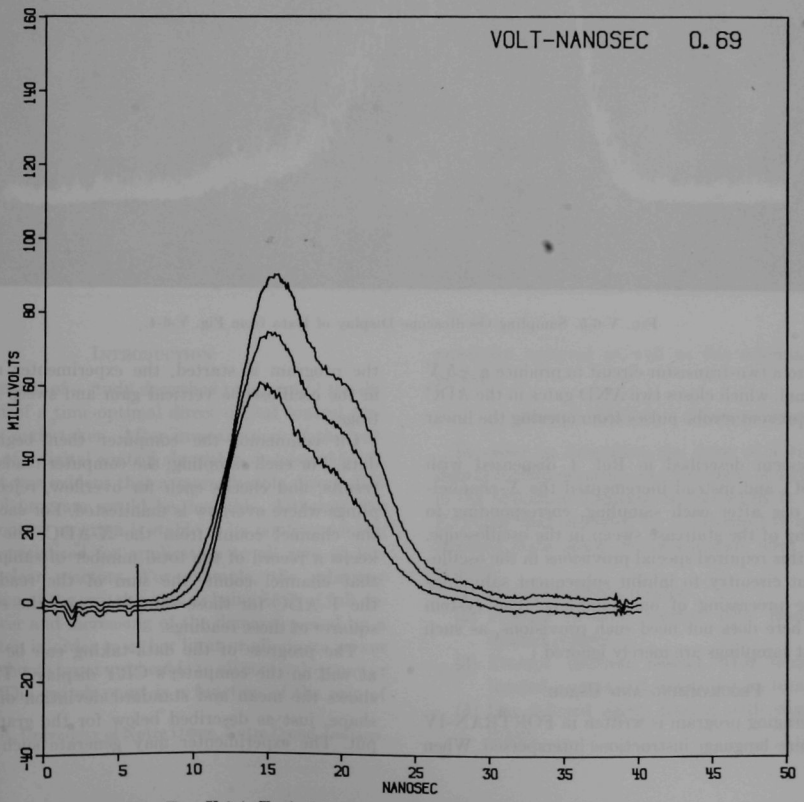

FIG. V-6-4. Typical Output Graph. *ANL Neg. No. 112-9259.*

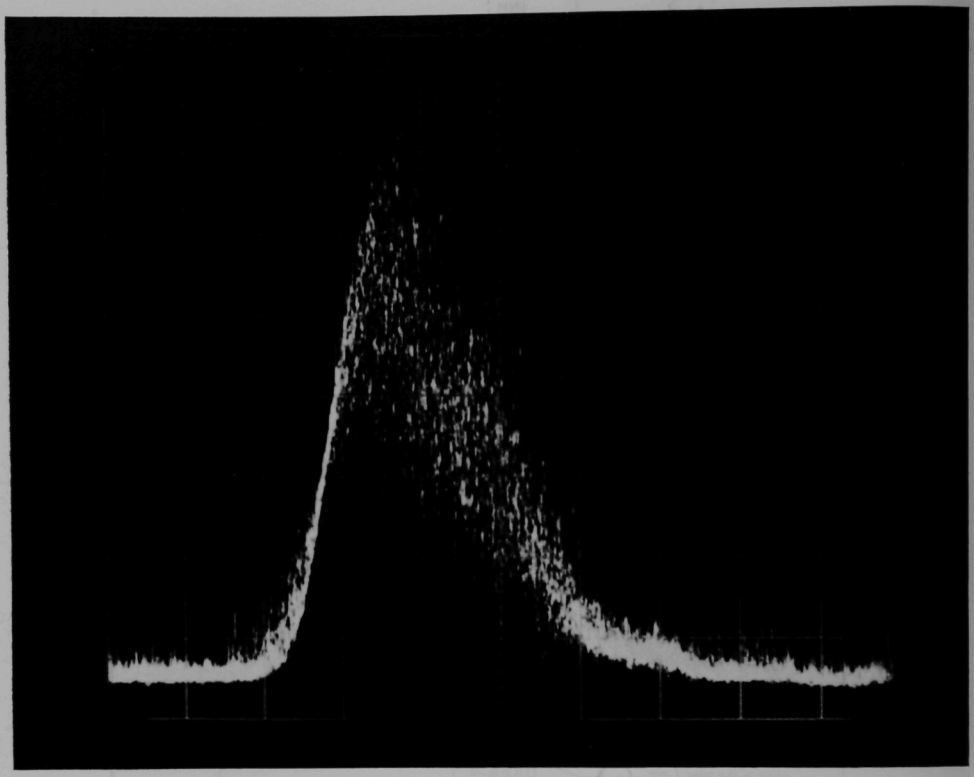

Fig. V-6-5. Sampling-Oscilloscope Display of Data from Fig. V-6-4.

is applied to a two-transistor circuit to produce a −5 V inhibit signal, which closes two AND gates in the ADC chassis to prevent strobe pulses from opening the linear gates.

(The system described in Ref. 1 dispensed with the X-ADC, and instead incremented the X-channel-count by one after each sampling, corresponding to the stepping of the staircase sweep in the oscilloscope. However, this required special provisions in the oscilloscope input circuitry to inhibit subsequent samplings during the processing of one sampling. The system described here does not need such provisions, as such subsequent samplings are merely ignored.)

Programming and Usage

The averaging program is written in FORTRAN-IV with machine language instructions interspersed. When the program is started, the experimenter must type in the oscilloscope vertical gain and sweep speed settings.

On command, the computer then begins taking data. For each sampling, the computer reads the ADC results, and checks each for overflow, rejecting samplings where overflow is manifested. For each value of the channel count from the X-ADC, the computer keeps a record of the total number of samplings with that channel count, the sum of the readings from the Y-ADC for those samplings and the sum of the squares of those readings.

The progress of the data-taking can be monitored at will on the computer's CRT display.[3] The display shows the mean and standard deviation of the pulse shape, just as described below for the graphical output. The experimenter may generate such a display

from time to time, and may use the information thereon as a basis for deciding when enough data have been accumulated.

After the experimenter terminates data taking, he must look at the CRT display and decide at what time the pulse began to rise from the baseline or zero level. He types in the time in terms of the horizontal divisions on the CRT graticule. The computer averages the amplitudes for all samplings preceding this time, and uses that average value as the baseline level. That level is subtracted from the average amplitude at all time points, and the difference is numerically integrated. The computer then plots the results.

Results

The output from the program is in the form of a graph. A typical one is shown in Fig. V-6-4. The pulse-shape information is in the form of three lines. The middle line gives the mean amplitude at each sampling time, while the two outer lines are displaced from the mean by an amount equal to the standard deviation of a single sampling. Thus, these lines indicate the dispersion of the data.

The time scale is referenced to the time of the earliest sampling recorded, while the voltage scale is referenced to the previously-described baseline. A vertical line crosses the pulse-shape traces at the time that was selected as the end of the baseline. Both time and voltage scaling are adjusted by the computer so that the pulse-shape trace will fill the graph area as much as possible and still have round-number scale markings. The time integral of the pulse shape is written in the upper right-hand corner in volt-nanoseconds. (For this to be correct, the pulse must return and settle to its baseline during the time span shown on the graph.)

Figure V-6-4 is taken from selected anode pulses from a photomultiplier viewing a plastic scintillator bombarded by alpha particles. Data were taken for about 15 min, with the ADC's operating at about 20% deadtime. For comparison, Fig. V-6-5 shows these same pulses as photographed from the screen of the sampling oscilloscope in a 15-sec exposure. The improvement in the definition of the pulse shape is evident.

References

1. O. J. Steingraber and I. B. Berlman, *Versatile Technique for Measuring Fluorescence Decay Times in the Nanosecond Region*, Rev. Sci. Instr. **34**, 524 (1963).
2. M. G. Strauss, *Solid-State Pulse-Height Encoding System with Pileup Reduction for Counting at High Input Rates*, Rev. Sci. Instr. **34**, 335 (1963).
3. C. E. Cohn, *Further Development of the DDP-24 Computer System*, Reactor Physics Division Annual Report, July 1, 1966 to June 30, 1967, ANL-7310, pp. 407–409.

V-7. Time-Optimal Direct Digital Control of Zero Power Nuclear Reactors

T. J. Marciniak*

Introduction

As the result of a study described previously,[1] the development of a time-optimal direct digital control program was undertaken. After investigation of the performance of a digital control algorithm developed by C. Cohn,[2,3] it was evident that a more flexible direct digital control program would be desirable. Although the original control program is stable in its nonlinear form, it is too specialized for application to all zero or low power nuclear reactors. For example, the arbitrary specification of the switch point as being 55% of full demand power and increasing of the demand period by a factor of ten in order to either limit or eliminate power level overshoots is not applicable to all zero or low power reactors. The switch point is a function of the rate of reactivity removal as well as the minimum allowed period.

Switch Equation Development

In order to determine the form of a time-optimal digital control sequence, use was made of a discrete form of the Maximum Principle developed by B. Jordan and E. Polak[4] and extended by K. Monta,[5] to include constrained state space. Several models were studied including:

(1) Prompt neutron reactor
(2) Prompt neutron reactor with reactivity rate limited control
(3) Prompt neutron reactor with reactivity rate limited control and constraint on total reactivity
(4) One-delayed group reactor with step reactivity input.

* Student, University of Notre Dame, Notre Dame, Indiana.

The main problem considered was to ensure that when the demand power level was reached that the reactivity insertion rate was sufficient to maintain the power level. If the reactor power is rising on a period τ, then in order to maintain the power level, the reactivity insertion rate is given as

$$\dot{\rho}(t) = -\sum_{i=1}^{6} \frac{\lambda_i \beta_i}{\tau\lambda_i + 1} e^{-\lambda_i(t-t_f)}, \qquad t \geq t_f, \quad (1)$$

where λ_i is the decay constant of the ith group and β_i is the delay fraction. As can be seen from Eq. (1), the maximum reactivity rate occurs when $t = t_f$, the time at which the demand power level is reached. For a one-delay-group reactor the reactivity insertion rate, as a function of time, is given as

$$\dot{\rho}(t) = -\frac{\lambda\beta}{\tau\lambda + 1} e^{-\lambda(t-t_f)}, \qquad t \geq t_f. \quad (2)$$

In the derivation of the switch equation, the one-delay-group equation was used since it was simpler and was not significantly different from the six-group equation for periods greater than 20 sec.

Suppose that the maximum reactivity insertion rate for a reactor is $\dot{\rho}_{max}$, corresponding to a period τ_f calculated using Eqs. (1) or (2), but that the reactor is rising on a period τ_0 where $\tau_0 < \tau_f$—a situation quite common in very low power reactors. The reactivities necessary to hold periods τ_f and τ_0 are ρ_f and ρ_0, respectively. Thus, in order for the insertion rate to hold the demand power level, the reactivity insertion must begin at time t_0. If the control rod worth is linear and the precursors are in equilibrium at the demand power level with respect to the period τ_f then the difference between the time that the reactivity insertion is begun and the demand power level is reached while the neutron density is increasing on period τ_f is given by

$$t_f - t_0 = \frac{\beta}{\dot{\rho}_{max}} \left(\frac{1}{\lambda\tau_f + 1} - \frac{1}{\lambda\tau_0 + 1} \right). \quad (3)$$

Using this time difference a switch equation based on power level or neutron density may be derived using the linearized, one-delay-group equations.[3]

The switch equation is

$$\frac{n_0}{n_f} = \left\{ \begin{aligned} & b + cd_f + b(1 - d_f)\frac{c_0}{n_0} \\ & + \left[\frac{c}{\ell a}(1 - d_f) + \frac{b}{\ell}(t_f - t_0) \right] \rho_0 \\ & + \dot{\rho}_{max} \left\{ \frac{c}{\ell a} \left[(t_f - t_0) - \frac{(1 - d_f)}{a} \right] \right. \\ & \left. + \frac{b}{2\ell}(t_f - t_0)^2 \right\} \end{aligned} \right\}^{-1}, \quad (4)$$

where

$$a = \lambda + \beta/\ell$$

$$b = \lambda/a$$

$$c = \beta/\ell a$$

$$d_f = \exp[-a(t_f - t_0)]$$

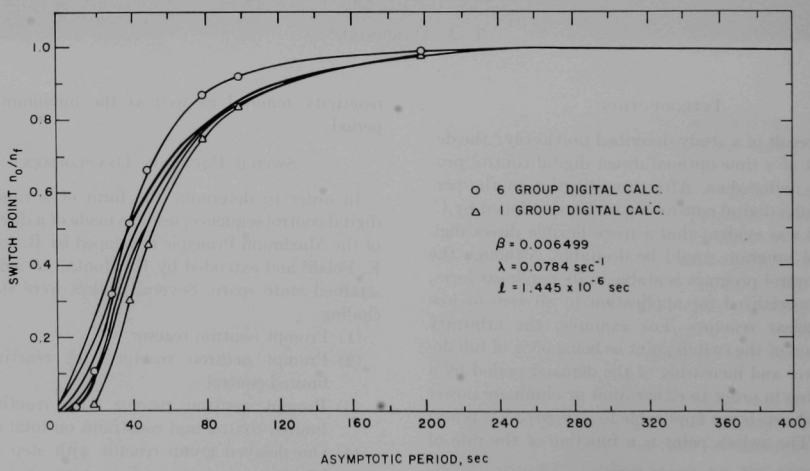

FIG. V-7-1. Switch Point Calculated Using One-Delay-Group Iteration, Normalized at n_0. $\dot{\rho} = -0.0000122$ $(\delta k/k)$/sec. *ANL Neg. No. 113-92.*

$$\frac{c_0}{n_0} = \frac{\beta}{\ell(\lambda + 1/\tau_0)}$$

$$\rho_0 = \frac{\beta}{\lambda\tau_0 + 1}$$

$\frac{n_0}{n_f} \equiv$ ratio of switch point power level to demand power level.

In order to minimize possible objections to the use of the linearized, one-delay-group equations when the ratio n_0/n_f is less than about 0.95, the switch point calculation is broken up into N intervals in the period, i.e. $\tau_0, \tau_1, \cdots, \tau_i, \cdots, \tau_{N-1}, \tau_N$. Denoting an incremental switch point to change from period τ_{i-1} to τ_i as

$$\frac{n_i}{n_{i-1}} = f_i(\tau_i, \tau_{i-1}) = f_i, \tag{5}$$

then a better approximation for the total switch point is

$$\frac{n_0}{n} = \prod_{i=1}^{N} f_i = f. \tag{6}$$

Another question is whether the equations should be normalized around n_0 or n_f, since these represent the extremes in the application of the equation. It was found that normalization around n_f causes a negative value of n_0/n_f for periods shorter than about 20 sec. Since this problem did not occur for a normalization about n_0, this was used in the program to calculate the switch point. A comparison between the iteration scheme described and one- and six-delay-group calculations for a ramp input of reactivity of $\dot{\rho} = -0.0000122$ $(\delta k/k)$/sec is shown in Fig. V-7-1. It may be noted that as the number of intervals is increased the curve approaches the one-delay-group from above, thus giving a somewhat less conservative switch point than the one-delay-group nonlinear kinetics equations. The points shown for the one- and six-group switch point were calculated using a standard kinetics code developed by J. Kaganove.[6]

The ideal control sequence for a power level increase

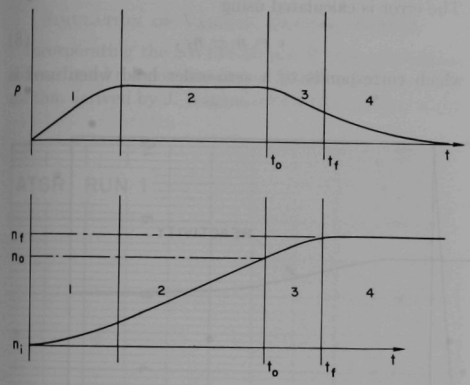

FIG. V-7-2. Ideal Variation of Reactivity and Neutron Density during a Time-Optimal Power Increase. *ANL Neg. No. 113-76.*

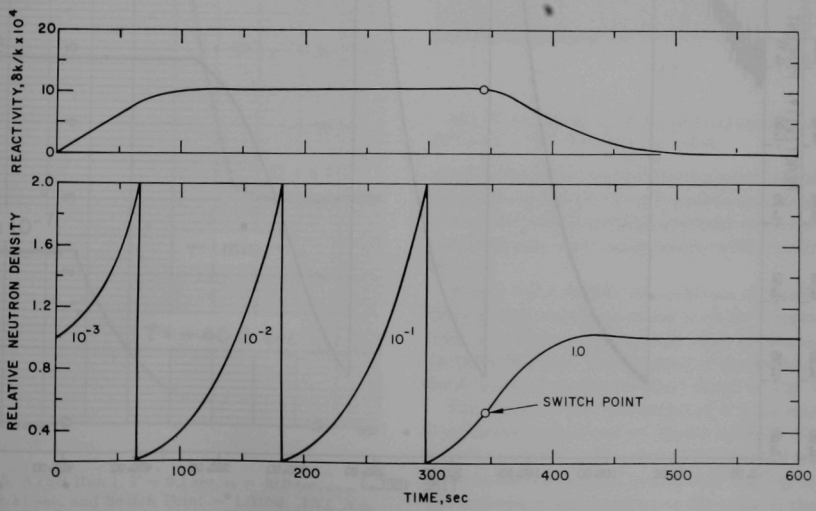

FIG. V-7-3. Reactivity and Relative Neutron Density Versus Time for Reactor with Linear Control Rod. *ANL Neg. No. 113-74.*

is shown in Fig. V-7-2. Section 1 of the upper curve indicates the reactivity insertion to reach the total reactivity necessary to maintain the minimum allowed period as shown in Section 2. Section 3 depicts the linear removal of reactivity until the demand power level is reached. In Section 4 the reactivity removal is exponential in order to maintain the demand power level while the precursor densities reach equilibrium. The lower curve depicts the corresponding neutron density variation.

Control Program

The control program used in the reactor simulation studies is divided into two main sections, namely subroutine SWITCH and subroutine RULE which couples the computer to the reactor to perform the actual control.

Subroutine RULE controls the period by varying the inverse period as a function of the power level according to the equation

$$\frac{1}{\tau} = \frac{1}{\tau_0} \min \left\{ 1, \left[\frac{n_f - n}{n_f} + \frac{\tau_0}{\tau_f} \cdot \left(\frac{n}{n_f} - f \right) \right] \Big/ 1 - f \right\} . \tag{7}$$

The error is calculated using

$$\epsilon = n - n_f , \tag{8}$$

which corresponds to a zero-order hold when used in

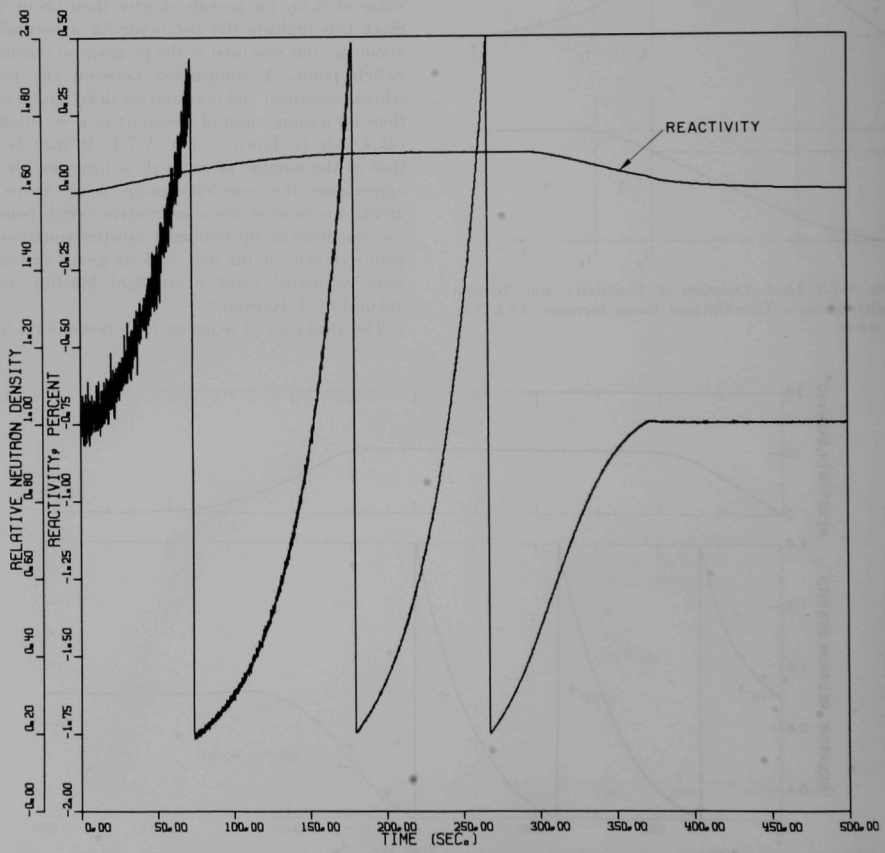

Fig. V-7-4. Reactivity and Relative Neutron Density for a Reactor with a Nonlinear Control Rod and Noise. *ANL Neg. No. 112-9979.*

conjunction with the computer. For a noise-free reactor simulation, the period is checked within subroutine RULE using simply

$$\tau = T/\ln (n_j/n_{j-1}), \tag{9}$$

where T is the sampling interval, n_j is the present neutron density, and n_{j-1} is the neutron density at the previous sampling time. For a noisy reactor an average period is used. Listings of subroutines RULE and SWITCH, as well as the reactor simulation codes may be found in Appendix D of Ref. 3.

Simulation of Various Reactor Models

Incorporating the SWITCH and RULE subroutines with a digital reactor simulation model based on an algorithm derived by J. Kaganove[8] for the solution of the space-independent reactor kinetics equations, the control program was tested. Reactor models simulated included zero power with linear and nonlinear control rods in the noise-free case, and a noisy reactor with a nonlinear control rod.

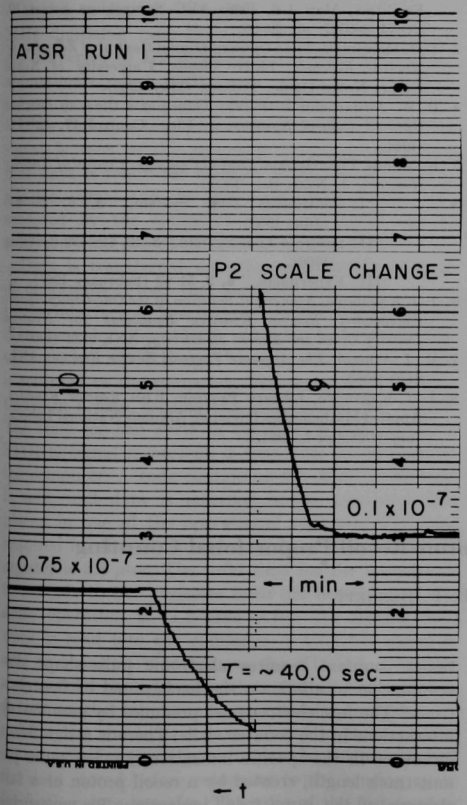

Fig. V-7-5. ATSR Run 1. $T = 0.1$ sec, $\tau_0 = 40.0$ sec, $\dot{\rho}_{max} = 0.0001704$ $(\delta k/k)$/sec, and Switch Point = 1.00283. *ANL Neg. No. 113-73.*

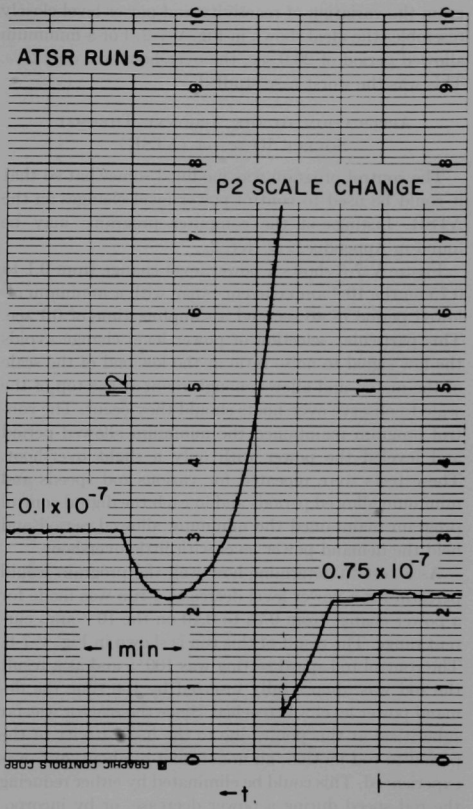

Fig. V-7-6. ATSR Run 5. Power Level Decrease from 0.75×10^{-7} to 0.1×10^{-7}. *ANL Neg. No. 113-90.*

Figure V-7-3 depicts the variation of reactivity for a three-decade change in power level for a reactor model with a nonlinear control rod. The minimum allowed period is 30.03 sec. The variation of reactivity and power level closely resemble the ideal shown in Fig. V-7-2.

The results of the simulation of a noisy reactor with a nonlinear control rod are shown in Fig. V-7-4. In this case the period is averaged over the past 2.0 sec in order to maintain the demand period while making the control rod movement less sensitive to the noise in the neutron level. Again, it can be seen that using the control pro-

gram the variation of reactivity and power level closely resembles the ideal shown in Fig. V-7-2. For a minimum allowed period of 20.0 sec, the overshoot was only 2%. This was the worst case studied.

Application to the Argonne Thermal Source Reactor (ATSR)

The control program was modified somewhat so that it could be used to control power level changes on the ATSR. Listings of the computer programs may be found in Appendix E of Ref. 2.

Figure V-7-5 shows a power level change from 0.1 to 0.75 on the 10^{-7} amp current range with a minimum allowed period of 40 sec and a sampling time of 0.1 sec. This particular selection of power level change avoids the low signal-to-noise ratio at the low end of the scale of the meter, and allows enough room at the top of the scale to observe overshoots should they occur. The control program maintained the minimum allowed period and leveled the power with only a slight overshoot. These tests were repeated for various rod speeds and minimum allowed periods and in each the digital control program maintained the minimum allowed period and held the demand power level with little overshoot.

As a test to determine how well the program would perform for a power level decrease, a run was made for a power change from 0.75 to 0.10 on the 10^{-7} amp current range. The result of this run is shown in Fig. V-7-6. The control rod speed setting was 100% and as a result the rod was almost fully inserted by the time the demand power level was reached. Since the reactor was far subcritical at this point, due to the insensitivity of the period to rod motion, an undershoot of about 26% was experienced. This could be eliminated by either reducing the rod speed during a power decrease, or by incorporating a test in the control program which would not permit rod movement if a corresponding period change does not occur during a power level decrease.

As evidenced from the various tests performed on the ATSR, it can be concluded that the control program performs well. It maintains the minimum allowed period and levels the reactor at the demand power with very little overshoot. The power rises found in both the simulations and applications on ATSR are all similar to the ideal case shown in Fig. V-7-2.

References

1. T. J. Marciniak, *Study of a Sampled-Data Control Algorithm for Zero-Power Reactors*, Reactor Physics Division Annual Report, July 1, 1966 to June 30, 1967, ANL-7310, pp. 410–415.
2. C. E. Cohn, *Automatic Data Analysis and Control for Critical Facilities*, Proc. Symposium on Use of Computers in Analysis of Experimental Data and Control of Nuclear Facilities, May 4–6, 1966. AEC Symposium Series 10, CONF-660527, pp. 49–66.
3. T. J. Marciniak, *Time-Optimal Digital Control of Zero-Power Nuclear Reactors*, Ph.D. Thesis, University of Notre Dame, Notre Dame, Indiana (May 1968).
4. B. W. Jordan and E. Polak, *Theory of a Class of Discrete Optimal Control Systems*, J. Elec. Control **17**, 697–711 (1964).
5. K. Monta, *Time Optimal Digital Computer Control of Nuclear Reactors*, J. Nucl. Sci. Tech.:
   "I: Continuous Time System," **3**, 6, 227–236 (June 1966).
   "II: Discrete Time System," **3**, 10, 418–429 (October 1966).
   "III: Experiment," **4**, 2, 51–62 (February 1967).
6. J. J. Kaganove, *Numerical Solution of the One-Group Space-Independent Reactor Kinetics Equations for Neutron Density Given the Excess Reactivity*, ANL-6132 (1960).
7. R. J. Armani, *The Argonne Thermal Source Reactor*, ANL-6440 (1962).
8. J. J. Kaganove, Library Program R101 *Reactor Kinetics*, Applied Mathematics Division, Argonne National Laboratory (October 7, 1964).

V-8. Use of a Small Computer for Proton-Recoil Proportional Counting

T. J. Yule and E. F. Bennett

The use of computers for data acquisition and preliminary processing has become increasingly popular in nuclear research.[1] An on-line computer increases significantly the flexibility of the experimenter for data handling operations. This paper describes the use of a small computer for fast neutron spectroscopy by proton-recoil proportional counting.

The technique currently used at Argonne for in-core measurements of neutron spectra with proportional counters requires electronic pulse-shape discrimination to eliminate the background of fast electrons.[2] The fast electrons are produced by gamma-ray interactions in the counter walls. There is a significant difference in the specific ionization, i.e. ion pairs per unit track length, created by a recoil proton or a fast electron of the same total ionization. By measuring the rise time of a pulse, one obtains a quantity which is proportional to the radial extension of the

track. The ratio of the radial extension to the ionization is large for a recoil-proton event and on the average considerably smaller for a gamma-induced electron event.

A block diagram of the electronics used for proportional counting is shown in Fig. V-8-1. Each pulse from the counter is analyzed by two separate systems. The fast system produces a pulse which is proportional to the rise time of the incident pulse. The slow system produces a pulse which is proportional to the ionization deposited in the counter by the event. Each slow pulse passes through a pulse selector which determines whether the pulse is distorted by other pulses occurring at approximately the same time. The pulse selector provides a gating pulse to the analog-to-digital converter, which allows only undistorted events to be analyzed.

Analog-to-digital conversion is performed at a 40 MHz digitizing rate. Both the fast and slow pulses are converted to 512 channels. Dead time per event is approximately $3 + 0.025N$ μsec, where N is the channel number of the larger analyzed input.

Once the encoding process is complete, a STORE signal is sent to the computer interface, indicating that data is ready for transfer to the computer. The STORE signal and the two 9-bit codes remain until accepted by the computer. No new signal can be analyzed while the STORE command is present.

Data is transferred into the computer in a series of operations. First, the computer transmits a code to the interface to test whether a STORE signal has been sent by the ADC's (Analog-to-Digital Converters). If a STORE signal is not present, a false code is returned to the computer. The computer then continues in a loop, sensing the condition of the ADC's. The time for one cycle in the loop is 7.8 μsec. If a STORE signal is present, a true code is returned to the computer. A code containing the ADC to be read is sent, and data is returned to the computer and placed in one of the operational registers. The time required for the transfer of data from each ADC to a register is 3.8 μsec. The total time for the transfer of two words to two registers from the beginning of the sense operation is 11.2 μsec. After the second data word is read into the computer, a CLEAR signal is sent to the ADC's to remove the STORE command and to reset the address scalers and all logic circuits so that another input can be accepted for analysis.

After the words have been placed in the registers, some preliminary data reduction is performed and the data stored before returning to the sensing cycle for further data transfer. The ratio of the fast-to-slow pulse height is formed, i.e. the radial specific ionization of the event. This ratio is scaled to 32 channels and

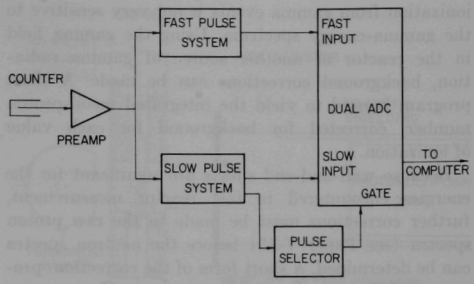

FIG. V-8-1. Block Diagram of the Electronics for Proton-Recoil Measurements. *ANL Neg. No. 113-863.*

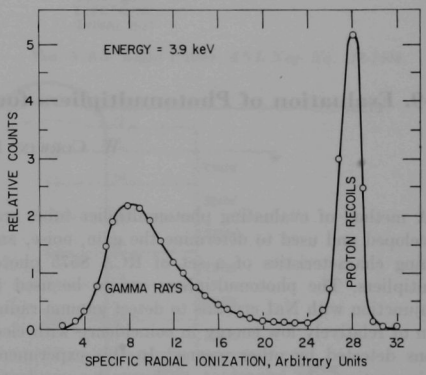

FIG. V-8-2. Distribution of Specific Radial Ionization Showing Both Neutron and Gamma-Induced Events. *ANL Neg. No. 113-848.*

the ionization data is scaled to 100 channels. Checks are made that the ratio and ionization are within preset bounds. The data are then stored in a 100 x 32 channel array. The time required for the preliminary data reduction and storage is approximately 110 μsec.

The stored array may be output from the computer in a number of ways. For a given ionization, one may display counts versus specific radial ionization on an oscilloscope. Figure V-8-2 contains a representation of such an output. The region at low values of the specific radial ionization corresponds to gamma-ray events, while the one at high values corresponds to recoil-proton events. The whole array may be punched on paper tape or printed on a teletype.

Some data reduction and analysis can also be performed with the computer. As is evident from Fig. V-8-2, the distribution of gamma-ray events is quite broad and thus some form of background subtraction is necessary. The shape of the spectrum of specific

ionization from gamma events is not very sensitive to the gamma-energy spectrum. Using the gamma field in the reactor or another source of gamma radiation, background corrections can be made. A short program is used to yield the integrated recoil-proton number, corrected for background for each value of ionization.

Because wall-and-end effects are significant for the energies encountered in fast reactor measurement, further corrections must be made to the raw proton spectra (see Paper V-13) before the neutron spectra can be determined. A short form of the correction program PSNS can be run on the computer. The program corrects for wall-and-end effects and uses the corrected distribution to determine the neutron spectra.

Although this paper considered only the use of a small computer for proton-recoil proportional counting, the application is rather typical of the uses of small computers in nuclear research and points out the flexibility that an on-line computer affords the experimenter.

References

1. B. I. Spinrad, Coordinator, *Use of Computers in Analysis of Experimental Data and the Control of Nuclear Facilities*, Proc. of a Symposium at Argonne National Laboratory, Argonne, Illinois, May 4–6, 1966, AEC Symposium Series 10, CONF-660527 (USAEC Division of Technical Information Extension, Oak Ridge, Tennessee, 1967).
2. E. F. Bennett, *Fast Neutron Spectroscopy by Proton-Recoil Proportional Counting*, Nucl. Sci. Eng. **27**, 16 (1967).

V-9. Evaluation of Photomultipliers for Optimum Noise and Timing Characteristics

W. Corwin, K. Porges and R. Gold

A method of evaluating photomultiplier tubes was developed and used to determine the gain, noise, and timing characteristics of a set of RCA 8575 photomultipliers. The photomultipliers are to be used in conjunction with NaI crystals to detect gamma radiation of relatively low energy in coincidence with electrons detected by other means.[1] In this experiment, it is particularly important to keep the accidental coincidence background rate low; this calls for coincidence gates of shortest possible length. The time jitter in the gamma channel imposes a lower limit on this length through the statistics of photoelectron release in response to NaI scintillation, as well as through time jitter in the photomultiplier. The effect of photoelectron statistics on timing is expressed by the well-known formula of R. Post and L. Schiff[2, 3] which gives the relative variance attached to the time of release of the kth out of R photoelectrons, where R is proportional to the gamma energy. The variance is roughly proportional to k and inversely proportional to R. For low energy gamma radiation, it is thus expedient to trigger on one of the first few photoelectrons; in practice, the pulses released by individual photoelectrons at the anode pile up such that the relative height of the trigger level determines, on the average, the order number k. Triggering on the very first photoelectron is, however, inadmissible since this would include all thermally emitted single electrons, the so-called "dark current".

The characteristics of a photomultiplier most suited for this experiment thus must include not only low dark current and accurate timing, but also a relatively sharply peaked single photoelectron pulse height distribution, allowing a trigger level which fires on the second or third photoelectron of a group, but not on singles. To select the best from an available sample of fifteen photomultipliers of type RCA 8575, single electron (SE) spectra, dark current spectra, total dark current, gain and timing characteristics were measured for each tube. The dependence of dark current and timing on anode to first dynode voltage was determined and the distribution of after-pulses investigated. Experimental SE spectra were compared with theoretically predicted curves given by J. Prescott.[4] A number of similar investigations, involving other types of photomultipliers, have been reported.[5-9] The information available from these reports was, however, insufficient for the purpose described above and thereby furnished the motivation for the measurements reported here.

Light Source Development

The dark current pulse height distribution can be measured in principle with a very fast amplifier and multichannel analyzer of commensurate bandwidth. As such analyzers are not presently available, it becomes necessary to select pulses in some way to avoid pileup; alternatively, one may hope to reduce thermal emission through cooling. Difficulties encountered in a preliminary attempt to cool tubes reliably to con-

stant temperature led to the development of a logic pulse selection system described below. The spectrum obtained with this system consists of a SE component, a strong component at small pulse heights due to dynode emission, and a weak component of relatively large mean height due to positive ions formed in the residual gas, and accelerated toward the photocathode, where their impact may release several photoelectrons at once. Other mechanisms for generating large pulses, such as intermittent discharges inside the tube structure, have been identified. For present purposes, we wish to determine the mean SE pulse height, which allows an unequivocal calibration of the trigger level used in the experiment described above. The presence of a strong dynode component makes this determination difficult from observed dark current spectra, particularly at relatively low tube voltages where the SE distribution is broad. Spectrum component subtraction can be effected in principle by making measurements with and without SE component enhancement through additional weak light incident on the photocathode. In practice, such additional light tends to activate the photocathode; as a result, several hours of rest are required to restore normal dark current emission. A more practical means of spectrum separation may be based on an associated channel and *short* light pulses. The latter are available, for instance, from an alpha source embedded in a small plastic or liquid scintillator, which is then attached to the photocathode of another tube. Signals from the associated channel are used to open a linear gate which locks out all pulses except those generated by alpha-induced scintillations. The geometry of this arrangement must be adjusted to make the number of photons per scintillation reaching the photocathode of the tube under test much smaller than unity. From the Poisson statistics of this process, one can calculate the ratio of events in which *two* photoelectrons are released to those in which a single photoelectron is released. This ratio must be kept within a certain acceptable limit by adjusting input light intensity.

Alpha-induced scintillation, while producing better results than irradiation by a DC light source and subsequent subtraction, still produces undesirable background due to slowly decaying components of available plastic or liquid scintillators, as well as gamma transitions with half-lives in the nanosecond region found in many readily fabricated alpha sources. These difficulties led to the development and construction of a number of coaxial spark light flashers, from which a fast-rising pulse was available at a 50 Ω output in coincidence with a spark of one nanosecond mean duration.

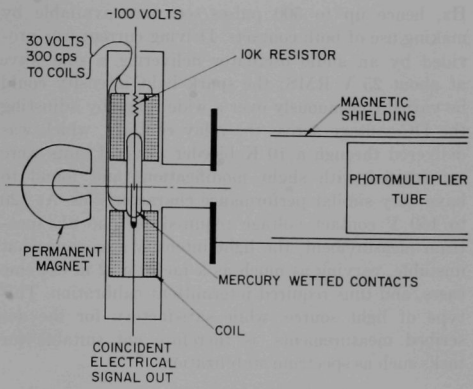

FIG. V-9-1. Light Pulser. *ANL Neg. No. 113-1508.*

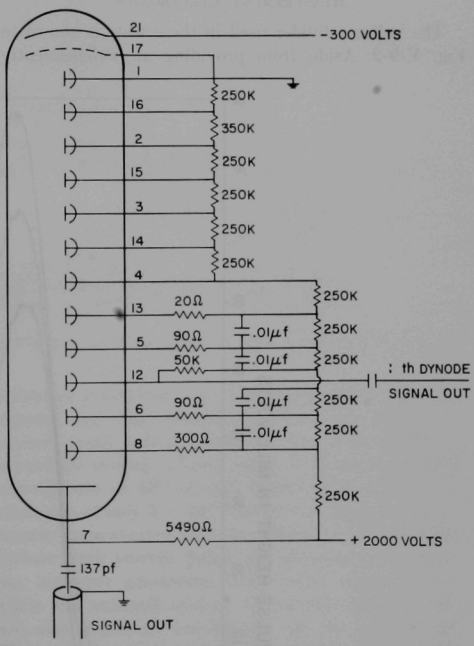

FIG. V-9-2. Photomultiplier Tube Voltage Dividing Network. *ANL Neg. No. 113-1470.*

To fabricate such a light source a mercury-wetted relay was carefully disassembled and rearranged as shown in Fig. V-9-1 to provide a direct optical path between the relay contacts and the photocathode. With an additional coil and biasing permanent magnet, the relay could be operated at rates up to 250

Hz, hence up to 500 pulses/sec were available by making use of both contacts. Driving current was provided by an audio oscillator delivering a sine wave at about 25 V RMS; the spark light intensity could be varied continuously over a wide range by adjusting the DC voltage across the relay contacts, which was delivered through a 10 K bleeder. Several units were constructed with slight modifications and found to have very similar performance characteristics. At 120 to 150 V contact voltage required for the SE spectrum measurement, the light intensity was somewhat unstable, varying as much as a factor of 2 in extreme cases, and thus required intermittent calibration. This type of light source, while satisfactory for the described measurements, is therefore not suitable for tasks such as spectrum stabilization.

Single Electron Spectrum Measurement Electronics

The voltage divider used in these tests is shown in Fig. V-9-2. Aside from providing an independently variable potential between photocathode and first dynode, this divider is dimensioned according to the manufacturer's recommendations; resistance values were, however, increased to reduce joule heating. Attempts to secure a faster output pulse rise by making use of the internal strip-line construction of the output section, as suggested by the manufacturer, were unsuccessful since this led to strong oscillations. For some of the tubes tested, such oscillations could be suppressed only by increasing the blocking series resistors to values up to 300 Ω. Typical pulse shapes, observed by means of a method described below, are shown in Fig. V-9-3.

The electronics used for SE spectrum acquisition are shown as a block diagram in Fig. V-9-4. Anode pulses are fed directly to an amplifier of 200 Mc bandwidth, into which a fast output splitter had been incorporated.[10] The light pulser trigger signal is delayed, shaped in a fast trigger and presented to one input of a fast coincidence. The other input to this coincidence stage is taken from one output of the signal splitter,

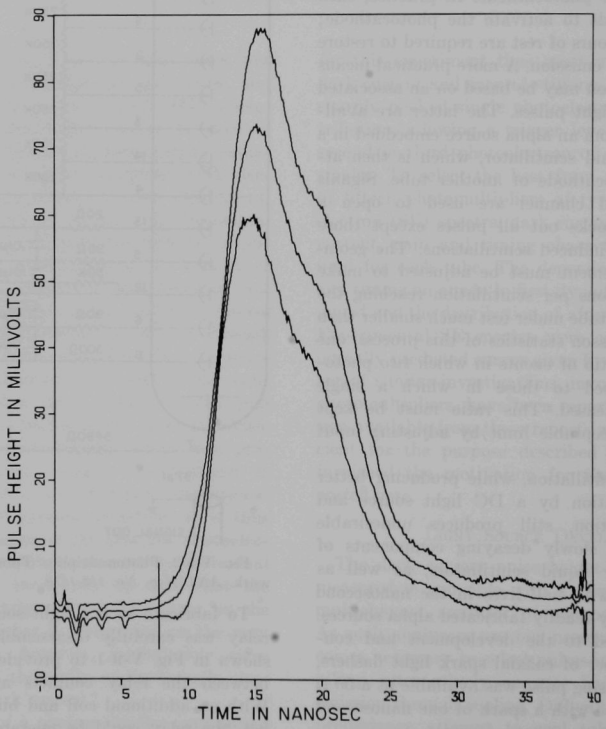

Fig. V-9-3. Computer Averaged Pulse Shape. *ANL Neg. No. 113-1514.*

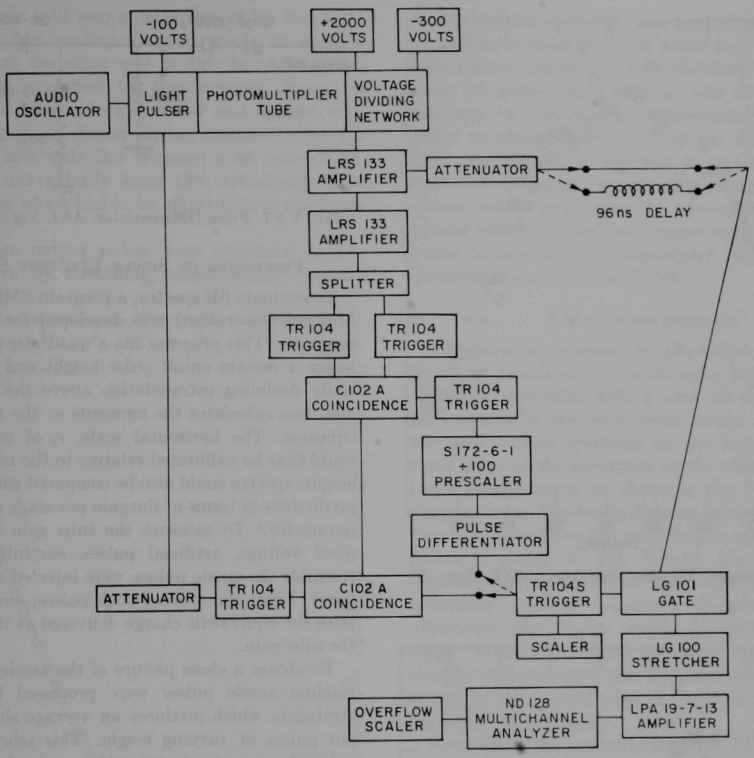

FIG. V-9-4. Block Diagram of Experimental Arrangement for Single Electron and Noise Spectrum Measurements. *ANL Neg. No 113-1481 Rev. 1.*

mentioned above, through an "antiwalk" discriminator[11] (formed by two fast discriminators, a coincidence and appropriate delay and clipping). The purpose of this arrangement was to obtain a sharply timed signal upon the arrival of every anode pulse derived from a light flash. The coincidence output is converted into a gate of exactly 30 nsec length and applied to the control input of a linear gate. The signal input of this linear gate is taken from another output of the anode signal splitter, through appropriate delay and possibly attenuation (for higher tube voltages, it is necessary to attenuate in order to keep signals within the linear range of the electronics; for this reason, the available two-stage gain of the amplifier was split as shown in Fig. V-9-4). Delay was adjusted to open the gate approximately 5 nsec ahead of the arrival of a pulse, and close it about 2 nsec after return to baseline.

The system locks out dark current entirely and admits all SE pulses generated by light flashes, with the following exceptions: (a) accidental overlap of dark current and light-generated pulses, (b) failure to process small light-generated pulses. With regard to accidental overlap, a gate width of 30 nsec and dark current rate of 10^5/sec still results in an accidental/true ratio of only 3×10^{-3}; moreover, these pulses are largely concentrated near the bottom of the spectrum (where dark current pulses are abundant). Concerning improper processing, very small pulses do not allow the antiwalk scheme to function properly and are also processed non-linearly by the gate circuit. These two factors tend to impose a lower limit on the spectra acquired by this method, much as noise limitation of ordinary pulse height analysis.

Pulses passed by the linear gate were stretched in a simple circuit built into the gate module.[12] Stretched pulses were further processed in one of two multichannel analyzers of conventional design used in this work; spectra were accumulated and periodically read out into paper tape.

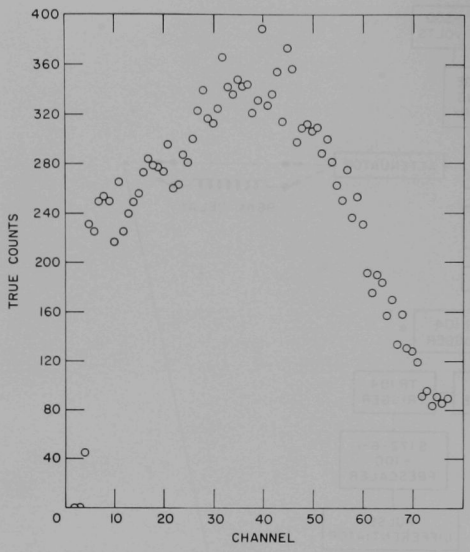

FIG. V-9-5. Single Electron Spectrum. *ANL Neg. No. 113-1482.*

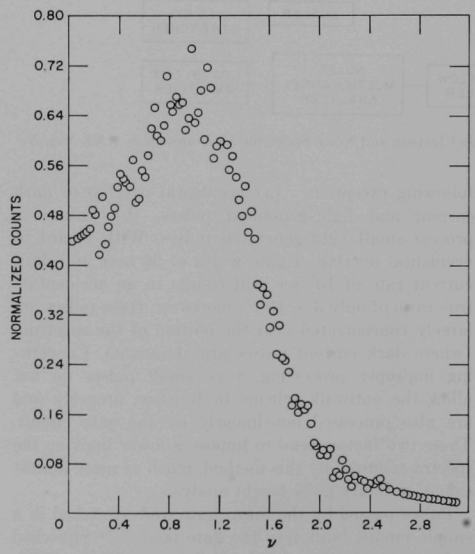

FIG. V-9-6. Normalized Single Electron Spectrum. *ANL Neg. No. 113-1479.*

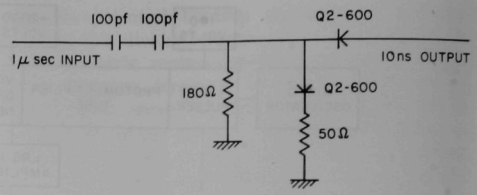

FIG. V-9-7. Pulse Differentiator. *ANL Neg. No. 113-1473.*

PROCESSING OF SINGLE ELECTRON SPECTRA

To evaluate SE spectra, a program SMOG (Spectral Moment Generation) was developed for the DDP-24 computer. This program fits a quadratic extrapolation below a certain cutoff pulse height and an exponentially declining extrapolation above the top channel, and then calculates the moments of the resultant distribution. The horizontal scale, ν, of resulting plots could thus be calibrated relative to the mean SE pulse height; spectra could also be compared with theoretical predictions in terms of the gain per stage and a quality parameter.[4] To measure the tube gain at given applied voltage, artificial pulses, carefully shaped to resemble the anode pulses, were injected at the system input. From the area of such pulses, one then calculates the equivalent charge delivered at the anode and the tube gain.

To obtain a clean picture of the anode pulse shape, random anode pulses were processed by a simple stratagem which produces an average shape from input pulses of varying height. This scheme, first developed as a wired system[13] was implemented as a computer program[14] in conjunction with a sampling scope. A typical averaged pulse shape is shown in Fig. V-9-3; calculated variances are indicated by lines at both sides of the average. A typical experimental spectrum is illustrated in Figs. V-9-5 and V-9-6 which give the raw SE data and the processed spectrum, respectively.

DARK CURRENT MEASUREMENTS

The dark current spectra and total dark current were measured for all tubes by means of sampling system also shown in Fig. V-9-4. The dark current spectrum reveals, among other factors, the possible presence of unusually large pulses, described above, which become important at higher trigger levels in any counting experiment where background must be kept low. As shown in Fig. V-9-4, anode pulses are sampled by scaling, which tends both to provide random selection and allow the slow components of the electronics (slow amplifiers and analyzer) time to recover. Anode pulses

are accordingly split into a delay line and a fast scale of 100; the last scaling stage is made to open a linear gate at the other end of the delay line. The scaler output is shaped for that purpose through a simple circuit, shown in Fig. V-9-7 and applied to a gate-forming stage. Scaler timing characteristics allowed a 30 nsec gate but required a 96 nsec delay, introducing unavoidably some 12% attenuation into the signal line which had to be allowed for in spectrum comparisons.

Linear gate output pulses were processed as described above by stretching, amplification, shaping in conventional circuitry, and final accumulation in a multichannel analyzer, with paper tape output. Total dark current above a certain threshold (measured in mean SE pulse heights, i.e., ν) was determined concurrently by accumulating the analyzer overflow in a scaler to obtain exactly 1% of the above threshold dark current rate. In addition to spectrum plots, the computer program also provided discriminator bias curves, which could then be compared with experimental curves to facilitate trigger level setting in the course of setting up an experiment. Such an integral spectrum is shown in Fig. V-9-8.

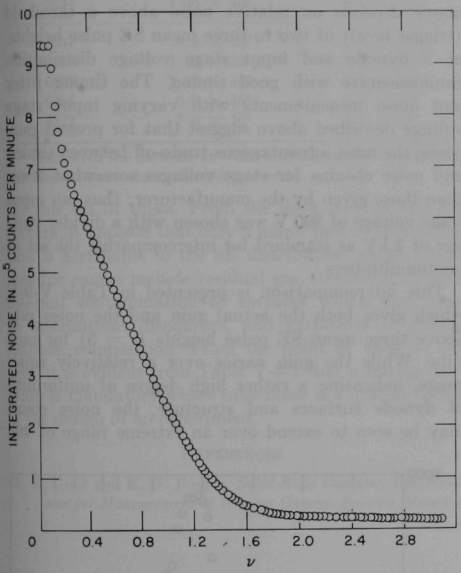

FIG. V-9-8. Integral Noise as a Function of Pulse Height in Terms of the Mean Single Electron Pulse Height. *ANL Neg. No. 113-1513.*

Timing Measurements

The possible presence of afterpulses was investigated by means of a time-to-pulse height converter (TPHC), especially with a view of correlating this phenomenon to the large pulse height component of the dark current spectrum on one hand, and to the input stage of the multiplier on the other hand. Electronic arrangements are shown in Fig. V-9-9, in block diagram form. The block diagram of the instrumentation used to observe the pulse height spectra of afterpulses is shown in Fig. V-9-10. The large delays required were furnished by using ANL D-63 fast discriminator circuits,[11] especially designed to provide adjustable and highly stable paralysis over wide range. When the output pulses of this circuit are sharply differentiated and inverted, the next unit is driven by the trailing edge of the pulse, thus converting paralysis into delay.

A random pulse is used to start the TPHC, with just enough delay to prevent the same pulse from also terminating the cycle, which is therefore stopped by the very next pulse. Given a Poisson time distribution, the TPHC spectrum is then expected to decrease exponentially with a time constant equal to the mean pulse interval. Observations bear out this prediction; in addition, they show a fairly narrow peak centered on a mean delay which varies inversely with photo-

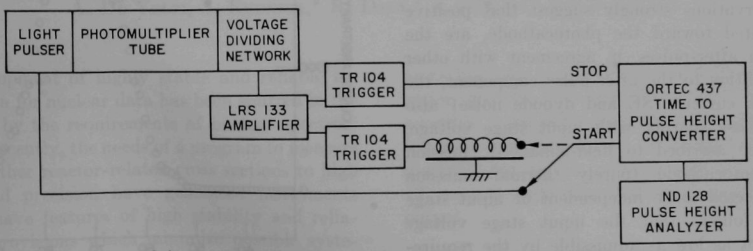

FIG. V-9-9. Experimental Arrangement for Observing Timing and Afterpulses. *ANL Neg. No. 113-1498 Rev. 2.*

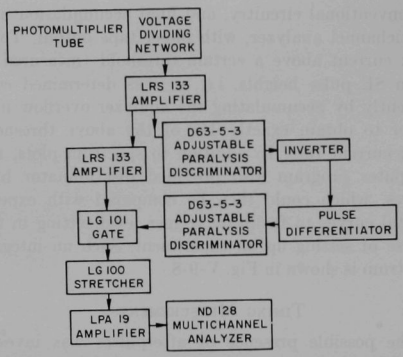

FIG. V-9-10. Instrumentation for Pulse Height Analysis of Afterpulses. *ANL Neg. No. 113-1505 Rev. 2.*

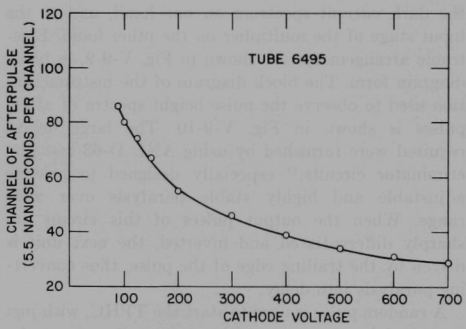

FIG. V-9-11. Time of Afterpulse Versus Cathode to First Dynode Potential. *ANL Neg. No. 113-1474.*

cathode to first dynode (input stage) voltage as shown in Fig. V-9-11. Note that only the first of a possible group of after-pulses can be observed with this arrangement, since the first after-pulse preempts shutdown of the TPHC. The mean after-pulse height came to about six mean SE pulses, i.e., $\nu = 6$.

These observations strongly suggest that positive ions, accelerated toward the photocathode, are the cause of such after-pulses, in agreement with other work.[6] In addition to the after-pulse component, the ordinary dark current (SE and dynode noise) also tends to increase sharply with input stage voltage, which may be ascribed to field-enhanced emission from the photocathode (purely thermal emission would be expected to be independent of input stage voltage). It follows that the input stage voltage should be kept as low as admissible by the requirements of low timing jitter (which increases as the electron velocity across the input stage decreases).

The effect of input stage voltage on time dispersion was observed by using the spark light source in conjunction with the TPHC system described above; spark source trigger pulses were fed to the start, and anode pulses to the stop, input of the TPHC. At a system resolution of better than 0.25 nsec, observed distribution widths showed somewhat surprisingly little change, from about 2 nsec (FWHM) for the lowest practical input stage voltages to 1.9 nsec for 700 V. A typical distribution is shown in Fig. V-9-12.

RESULTS

The quality of performance of a photomultiplier in connection with an experiment of the type described above depends on relative noise above a threshold (trigger level) of two to three mean SE pulse heights, at a dynode and input stage voltage distribution commensurate with good timing. The timing jitter and noise measurements with varying input stage voltage described above suggest that for present purposes, the most advantageous trade-off between timing and noise obtains for stage voltages somewhat lower than those given by the manufacturer; thus, an input stage voltage of 300 V was chosen with a divider voltage of 2 kV as standard for intercomparing the set of photomultipliers.

This intercomparison is presented in Table V-9-I, which gives both the actual gain and the noise rate above three mean SE pulse heights ($\nu = 3$) for each tube. While the gain varies over a relatively small range, indicating a rather high degree of uniformity of dynode surfaces and structure, the noise count may be seen to extend over an extreme range of 400

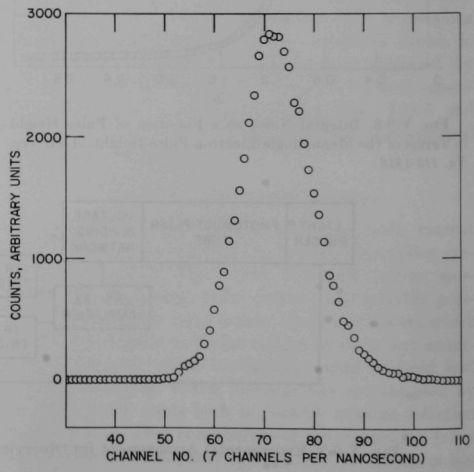

FIG. V-9-12. Time Distribution of Photomultiplier Tube Pulses. *ANL Neg. No. 113-1478.*

TABLE V-9-I. GAIN AND NOISE CHARACTERISTICS

Tube Number	Gain[a]	Noise in Counts per Minute[b]
8451	9.5×10^7	6×10^2
8416	7.8×10^7	4×10^2
4370	1.4×10^8	1.5×10^3
0768	1.0×10^8	1.6×10^3
3629	9.9×10^7	2.5×10^3
8419	11.8×10^7	5.3×10^3
0258	8.5×10^7	4.2×10^3
0321	1.32×10^8	5.3×10^3
0324	2.1×10^8	7.5×10^3
3524	1.96×10^8	9.5×10^3
7057	9.5×10^7	2.5×10^4
9568	1.48×10^8	3.5×10^4
0573	1.23×10^8	3.1×10^4
6495	6.9×10^7	1.8×10^5
4322	7.0×10^7	1.1×10^5

[a] Gain with the cathode at −300 and the anode at +2000 V.
[b] Noise above three electrons, $\nu = 3$.

for this set of tubes. From the dark current and SE spectra, it appears that only a minor part of this variation is ascribable to the SE distribution width. Other possible causes include residual gas, structural defects, internal contamination of surfaces which may lead to intermittent discharges, and variations in photocathode composition. From the point of view of the user, it is evident from Table V-9-I that a testing program is mandatory where tube noise is a crucial factor in the design of an experiment.

REFERENCES

1. R. Gold and K. G. Porges, *Solid-State Compton Spectrometer for Measurement of Reactor Gamma Spectra*, Reactor Physics Division Annual Report, July 1, 1965 to June 30, 1966, ANL-7210, pp. 306–308.
2. R. F. Post and L. I. Schiff, *Time Dispersion in Scintillation Detectors*, Phys. Rev. **80**, 1113 (1952).
3. F. T. Arecchi, A. DeMattecs and E. Gatti, *Statistical Limits in Timing with Slow Scintillators*, Energia Nucleare **7**, No. 10, 697 (October 1960).
4. J. R. Prescott, *A Statistical Model for Photomultiplier Single-Electron Statistics*, Nucl. Inst. Methods **39**, 173–179 (1966).
5. H. M. Smith, *Photomultiplier Investigation*, RCA Laboratories, Princeton, New Jersey, August 9, 1966.
6. G. A. Morton, H. M. Smith and R. Wasserman, *Afterpulses in Photomultipliers*, IEEE Trans. Nucl. Sci. (February 1967).
7. H. R. Krall, *Evaluation of New Photomultipliers for Scintillation Counting*, IEEE Trans. Nucl. Sci., Vol. NS-12, No. 1 (February 1965).
8. M. Duquesne, I. Tatischeff and M. N. Recouvreur, *Spectres D'impulsions A 'Un Photoelectron,'* Nucl. Inst. Methods **41**, 13–29 (1966).
9. D. Porter, J. McDonald and D. T. Stewart, *Photomultiplier Resolving Time Measurements Utilizing a Light Pulse Generator*, Nucl. Inst. Methods **44**, 309–313 (1966).
10. D. E. Trinko, *Three Fold Fanout, Modification to Bottom Half of LRS Dual Linear Amplifier*, Drawing No. EL A5531A, Electronics Division, Argonne National Laboratory.
11. A. De Volpi, J. J. English, A. J. Metz, K. Porges and S. J. Rudnick, *Versatile Gated Discriminator with Adjustable Paralysis Useful in Fast-Slow Coincidence Experiments*, Reactor Physics Division Annual Report, July 1, 1966, to June 30, 1967, ANL-7310, pp. 396–399.
12. R. Howard and J. English, *Pulse Integrator*, Drawing No. EL A5469Q, Electronics Division, Argonne National Laboratory.
13. O. J. Steingraber and I. B. Berlman, *Versatile Technique for Measuring Fluorescence Decay Times in the Nanosecond Region*, Rev. Sci. Inst. **34**, 524 (1963).
14. C. E. Cohn, *Computer Processing of Sampling-Oscilloscope Data*, Trans. Am. Nucl. Soc. **11**, 72 (1968).

V-10. Instrumentation for Processing Nuclear Detector Data

A. DE VOLPI, S. RUDNICK,* R. DALY,* J. ENGLISH* and R. PECINA*

The development of highly stable and reliable instrumentation for nuclear data has been spurred in the past mainly by the requirements of nuclear spectroscopy. More recently, the needs of a program to measure fission and other reactor-related cross sections to high accuracy and precision have generated instruments which also have features of high stability and reliability plus provisions which minimize possible systematic errors due to known causes.

Three such specialized instruments whose development has been supported by the Reactor Physics Division will be discussed. They are: (1) a charge-sensitive, low-input-impedance preamplifier with tailored output provisions; (2) a highly stable versatile discriminator having reliable deadtime features; and (3) an automatic data handling system with Teletype output.

* Electronics Division, Argonne National Laboratory.

PREAMPLIFIER

Frequently in radiation environments it is either necessary or desirable to separate the radiation detec-

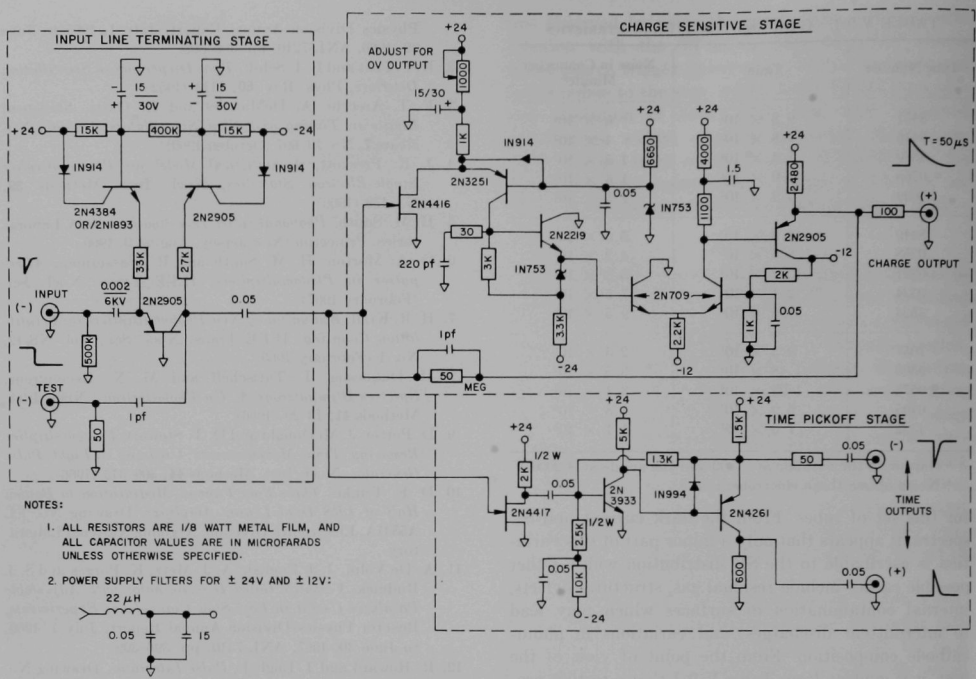

FIG. V-10-1. Preamplifier. The Input Stage Terminates a Coaxial Cable in its Characteristic Impedance and Two Output Stage Provide Pulses for Energy and Timing Applications. *ANL Neg. No. 113-1208.*

tion stage from the electronic processing components. When processing a signal from a detector separated from its preamplifier, cable reflections must be eliminated in order to determine precise timing of the detector signal. Also, the input stage of the preamplifier must be designed to minimize the noise component caused by the large value of input cable capacity.

In the preamplifier shown in Fig. V-10-1, the low-noise input stage is a common-base bipolar transistor biased to terminate the input cable without a series emitter resistor and to minimize 60 Hz on the output. The input stage drives both a low-noise field effect transistor (FET)-input charge sensitive amplifier and a low-noise FET-input fast amplifier. The output from the charge sensitive amplifier is a 50-μsec decay time constant pulse compatible with pole-zero cancellation main amplifiers, and the output from the fast amplifier is a narrow pulse with a rise-time less than 2 nsec suitable for timing applications.

Discriminator

The advent of integrated circuits has presented an opportunity to redesign level discriminators, thereby achieving low sensitivity to temperature drift and other disturbances. Such a discriminator has been built with operational features similar to the Adjustable Paralysis Discriminator previously described.[1] The input circuits of the new discriminator are shown in Fig. V-10-2. The dc restorer provides good baseline stability and allows operation at very high input rates without the usual threshold shift and threshold resolution degradation. The integrated differential comparator is used as a high gain biased amplifier to determine if the input signal exceeds the threshold level. The comparator takes advantage of the component matching properties associated with monolithic construction techniques. The resultant discrimination threshold stability is substantially better than that previously attained with discrete components. The 10-turn Helipot provides threshold adjustment from 0 to 4 V.

As indicated in Fig. V-10-3, the remaining processing is digital. The timing loop precisely establishes the width and paralysis time of the output pulse. Accurate timing characteristics are very important in absolute coincidence counting work. The delayed output is useful when a pair of these discriminators are

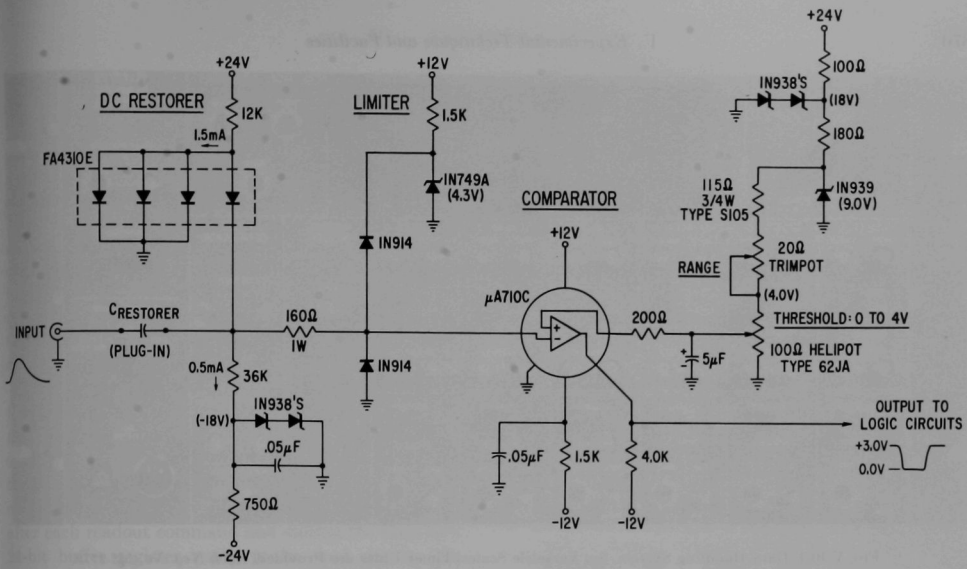

FIG. V-10-2. Discriminator Input Circuits. The d.c. Restorer Ensures Good Performance at High Input Rates and the Use of an Integrated Comparator as the Basic Threshold Element Substantially Reduces Sensitivity To Temperature Variations. *ANL Neg. No. 143-2744.*

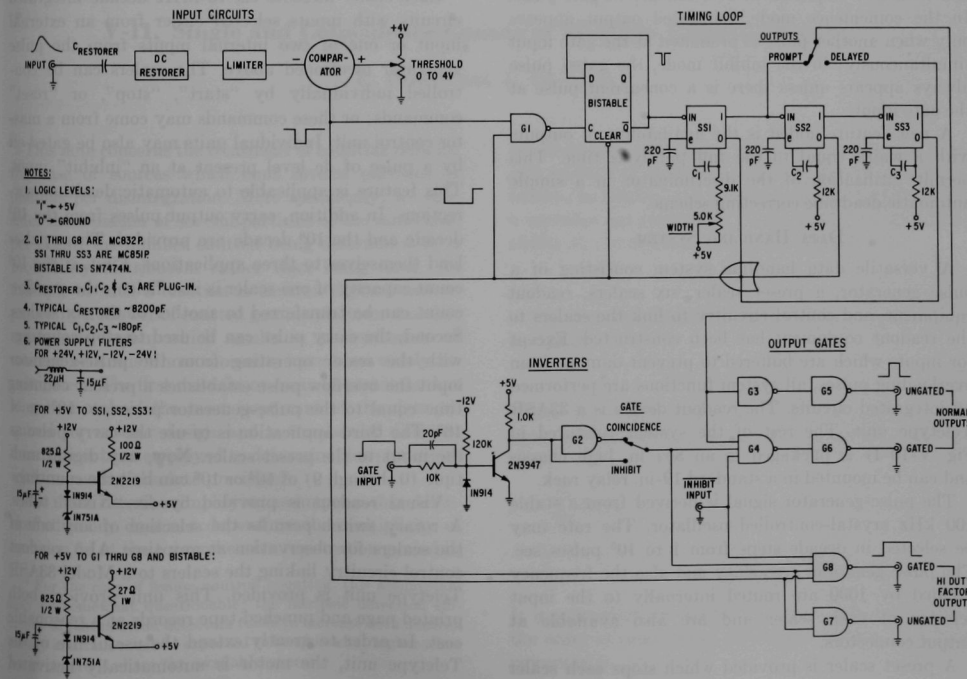

FIG. V-10-3. Complete Discriminator. The Timing Loop Precisely Determines the Output Pulse Widths and Paralyses While the Gates Provide Operational Versatility. *ANL Neg. No. 143-2745.*

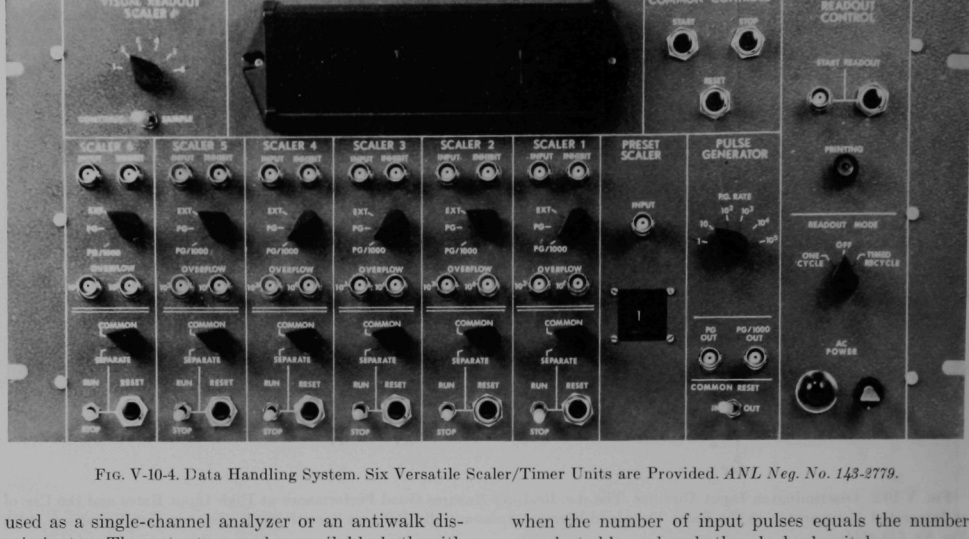

Fig. V-10-4. Data Handling System. Six Versatile Scaler/Timer Units are Provided. *ANL Neg. No. 143-2779.*

used as a single-channel analyzer or an antiwalk discriminator. The outputs are also available both with and without a requirement of a concurrent gate pulse. In the coincidence mode, the gated output appears only when another pulse is presented at the gate input simultaneously; in the inhibit mode, the gated pulse always appears unless there is a concurrent pulse at the gate input.

A new feature added is the availability of outputs with a width equal to the full paralysis time. This permits utilization of the discriminator in a simple automatic deadtime correcting scheme.

Data Handling System

A versatile data handling system consisting of a pulse generator, a preset scaler, six scalers, readout equipment, and control circuitry to link the scalers to the readout equipment has been constructed. Except for inputs which are buffered to prevent damage from overloading pulses, all system functions are performed by integrated circuits. The readout device is a 33ASR Teletype unit. The rest of the system (pictured in Fig. V-10-4) is packaged in an 8¾ in. high chassis and can be mounted in a standard 19-in. relay rack.

The pulse-generator signal is derived from a stable 100 kHz crystal-controlled oscillator. The rate may be selected in decade steps from 1 to 10^5 pulses/sec. The pulse generator frequency and also the frequency divided by 1000 are routed internally to the input selector of each scaler and are also available at output connectors.

A preset scaler is provided which stops each scaler when the number of input pulses equals the number preselected by a decade thumbwheel switch.

Each scaler includes six 10-MHz decade integrated circuits with inputs selected either from an external input or one of two internal inputs from the pulse generator mentioned above. The scalers can be controlled individually by "start", "stop", or "reset" commands; or these commands may come from a master control unit. Individual units may also be gated off by a pulse of dc level present at an "inhibit" input. This feature is applicable to automatic deadtime corrections. In addition, carry output pulses from the 10^3 decade and the 10^6 decade are provided. These pulses lend themselves to three applications. First, if the 10^6 count capacity of one scaler is insufficient, the overflow count can be transferred to another of the six scalers. Second, the carry pulse can be used to stop counting: with the scaler operating from the pulse-generator input the overflow pulse establishes a present counting time equal to the pulse-generator period $\times$ 10^3 or $\times$ 10^6. The third application is to use the carry pulse as the input to the preset scaler. Now, any digital multiple (0 through 9) of 10^3 or 10^6 can halt the counting.

Visual readout is provided by six "Nixie" tubes. A rotary switch permits the selection of any one of the scalers for observation at any time. Also, readout control circuitry linking the scalers to a Model 33ASR Teletype unit is provided. This unit provides both printed page and punched tape records at a reasonable cost. In order to greatly extend the useful life of the Teletype unit, the motor is automatically activated

before each readout and turned off after each readout.

Three modes of Teletype readout are available; manual, one-cycle, and continuous recycle. In the manual mode printout can only be initiated by the operator. In the one-cycle mode data is read out to the Teletype unit after a preset count (or time) is reached and no further data are required. The continuous recycle mode initiates readout when a preset count (or time) is reached. After the scalers are read out, they are reset, and precisely 10 sec after start of readout they are enabled in order to being the next data cycle.

Sometimes it is necessary to record the actual clock time at the start of each readout. By allowing the first scaler to count pulse generator pulses continuously without reset or interruption, the total elapsed time is accumulated. The clock time is accurately recorded by sampling the continuous timer immediately after each readout command and storing the data in a 24-bit buffer register ready to be read out by the relatively slow serial Teletype unit. When the system is operated with both a continuous timer and a preset timer, then four scalers are available for detector data. This is usually sufficient for most applications including coincidence work where normally three data channels are required.

The cost of this data handling system has been significantly reduced by incorporating integrated circuit decade chips available from another experimental system[2] into its design and also by sharing the readout between the six scalers. A high degree of reliability is anticipated in the use of these scaler systems.

References

1. A. De Volpi, J. J. English, A. J. Metz, K. Porges and S. J. Rudnick, *Versatile Gated Discriminator with Adjustable Paralysis Useful in Fast-Slow Coincidence Experiments*, Reactor Physics Division Annual Report, July 1, 1966 to June 30, 1967, ANL-7310, pp. 396–399.
2. A. De Volpi, R. Pecina, C. H. Freese, E. Rolnicki, D. Travis and G. Larsen, *Extended Capability for Fast Neutron Hodoscope Used at TREAT*, IEEE Trans. Nucl. Sci. NS-15, No. 1, 77–86 (1968).

V-11. Single and Coincidence Counts of Multiply Emitting Sources

K. Porges and A. De Volpi

This note concerns the treatment of counting data for the case of sources which emit several particles or photons per disintegration. More specifically, we consider the emission of several particles of the same kind per event, the number emitted being determined by a probability distribution rather than being fixed. An example of such a reaction is neutron capture accompanied by a shower of emitted gamma photons. Another example is fission, which results in a distribution of emitted neutrons whose moments have been widely investigated.[1] The first moment or mean in particular has long been one of the most important of the data required for reactor design and a number of different means have been employed to determine this parameter with increasing absolute precision.[2]

We make here the simplifying assumption that detection efficiency does not depend on the multiplicity of emission.* Let the comprehensive registration probability (including solid angle, intrinsic detection efficiency and fraction of delivered pulses accepted by the electronics) be labelled p. A specific event, in which exactly n particles are emitted, is detected with overall probability P_n, or not detected with probability P_{nu}:

$$P_n + P_{nu} = 1. \tag{1}$$

Non-detection requires that *all* of the n particles fail to register:

$$P_{nu} = (1 - p)^n. \tag{2}$$

If now $W_n \equiv$ probability of emission of exactly n particles, we may write the mean event detection efficiency e as

$$\begin{aligned} e &= \sum_{n=0}^{\infty} W_n[1 - (1 - p)^n] \\ &= \sum_{n=0}^{\infty} W_n \sum_{k=1}^{n} p^k \binom{n}{k} (-1)^{k+1}. \end{aligned} \tag{3}$$

It is convenient to expand the polynomial and reverse the order of summation, yielding a series in increasing powers of p:

* For the case of fission neutron counting, this assumption may be somewhat questionable: the intrinsic detection efficiency of fast neutron detectors tends to increase with neutron energy and thus must be expected to be somewhat higher when fewer neutrons share the available energy.

$$e = a_1 p - a_2 p^2 + a_3 p^3 \cdots . \qquad (3')$$

The coefficients a_k are given in Table V-11-I. Clearly, the use of a detector whose overall detection probability exceeds 10% or so requires the use of at least the first two terms of Eq. (3′) when high precision is required; this practically implies knowledge of the moments appearing in the second coefficient.

The above simple treatment can be readily extended to coincidences between several equivalent channels: for instance, two count channels with registration probabilities p_1 and p_2. The underlying assumption of this treatment is that angular correlations among emitted particles or photons are weak enough to be negligible. This is certainly not the case for fission neutrons (which tend to directional correlation with emitted fission fragments) but may be admissible for gamma cascades emitted in nuclear transformations which leave a residual nucleus with a closely spaced level structure in a highly excited state.

Let $P'_{n1} \equiv$ detection probability *exclusively* in channel 1 for an event in which exactly n particles are emitted,

TABLE V-11-I. Event Detection Efficiency Coefficients a_k

k	a_k
1	m_1
2	$(m_2 - m_1)/2!$
3	$(m_3 - 3m_2 + 2m_1)/3!$
4	$(m_4 - 6m_3 + 11m_2 - 6m_1)/4!$
5	$(m_5 - 10m_4 + 35m_3 - 50m_2 + 24m_1)/5!$
	$m_k \equiv k$th moment $= \sum_{n=1}^{\infty} n^k W_n$

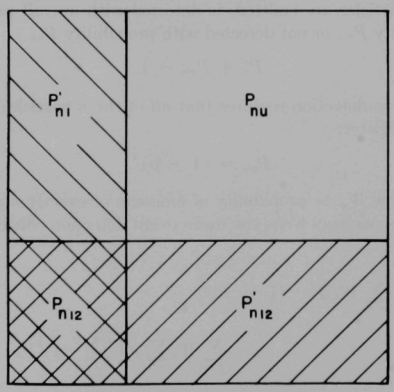

Fig. V-11-1. Borel Diagram for Detection in Two Channels. Shaded Areas are Proportional to Channel Count Rates. *ANL Neg. No. 113-1291.*

while $P_{n1} \equiv$ corresponding detection probability without regard to detection in the other channel, and $P_{n12} \equiv$ coincident detection probability:

$$P_{n1} = P'_{n1} + P_{n12} . \qquad (4)$$

If $P_{nu} \equiv$ probability of non-detection (either channel), then

$$P'_{n1} + P'_{n2} + P_{n12} + P_{nu} = 1 \qquad (5)$$

$$P_{n12} = P_{n1} + P_{n2} - (1 - P_{nu}). \qquad (6)$$

These relations may be illustrated by means of a Borel diagram, such as depicted in Fig. V-11-1, where a square of unit area has been divided into regions of areas proportional to channel detection probabilities for exactly n emitted particles.

Averaging again over all emission multiplicities, we may put the coincidence detection probability

$$e_{12} = \sum_{n=0}^{\infty} W_n \sum_{k=1}^{n} [(p_1 + p_2)^k - (p_1^k + p_2^k)] \binom{n}{k} (-1)^k, \qquad (7)$$

which yields the series

$$e_{12} = 2p_1p_2a_2 - 3p_1p_2(p_1 + p_2)a_3 \; [6p_1p_2 + 4(p_1^2 + p_2^2)]p_1p_2a_4 \cdots \qquad (7')$$

in terms of the same coefficients listed in Table V-11-I.

It is often possible to employ two detectors subtending the same solid angle at the source, having closely similar channel electronics; the channel efficiencies e_1 and e_2, rates R_1 and R_2, and particle registration probabilities p_1 and p_2 may thus be made equal. The coincidence event detection efficiency under these conditions becomes

$$e_{12} = 2p^2a_2 - 6p^3a_3 + 14p^4a_4 \cdots \qquad (7'')$$

and the coincidence ratio $R^2/R_{12} = Se^2/e_{12}$, from which one might hope to infer the source strength S, becomes

$$R^2/R_{12} = (Sa_1^2/2a_2)[1 + p(3a_3/a_2 - 2a_2/a_1) + p^2(a_2^2/a_1^2 - 4a_3/a_1 + 9a_3^2/a_2^2 - 7a_4/a_2)\cdots]. \qquad (8)$$

Evidently, the source strength can be precisely determined only for detectors with relatively low particle registration probabilities p; moreover, at least the first and second moment of the distribution must be known. Conversely, approximate values of these moments can be evaluated from measurements made with a known source. The evaluation of desired parameters may be made more precise by noting that

$$R - \tfrac{1}{2}R_{12} = Sa_1p(1 - 2a_3p^2/a_1\cdots). \qquad (9)$$

Dropping the small term in p^2 and inserting the value of p found from Eq. (9) into Eq. (8), one finds

$$S = \left(\frac{2a_2}{a_1^2}\right)\frac{R^2}{R_{12}} - \left(\frac{3a_3}{a_1a_2} - \frac{a_2}{a_1^2}\right)\left(R - \frac{1}{2}R_{12}\right) \quad (10)$$

as a better approximation, which however requires knowledge of the first three moments of the distribution. It is evidently also possible, in principle, to obtain distribution parameters from the measured count rates and known source strength; for instance, a series of counts at different solid angles should allow a polynomial fit of the above equations.

We note that cascades of many photons or particles naturally tend to the Poisson distribution. For the latter case,

$$W_n = e^{-m_1}(m_1)^n/n!. \quad (11)$$

The channel efficiencies are given by

$$e_1 = 1 - e^{-m_1p_1} \quad (12a)$$

$$e_2 = 1 - e^{-m_1p_2} \quad (12b)$$

$$e_{12} = e_1 + e_2 - [1 - e^{-m_1(p_1+p_2)}] \quad (12c)$$

as expected from Eq. (6). Thus, equal channel probabilities yield a coincidence rate

$$R_{12} = S(1 - e^{-m_1p})^2. \quad (13)$$

The coefficients a_k for the Poisson distribution Eq. (11) become, simply,

$$a_k = (m_1)^k/k!. \quad (14)$$

When these are inserted into Eq. (8), one finds that the coincidence ratio R^2/R_{12} just equals the source strength S. This may also be verified from Eqs. (12) and (13). Moreover, this holds true (as one must expect from the randomness of the process) for unequal channel registration probabilities p_1 and p_2.

The simple considerations developed here can be practically applied in precision measurements of distribution parameters. More specifically, they suggest that source strength measurements aiming at very high precision must be made with rather small registration probabilities p if coefficients a_k are not known; or else they must carefully account for the terms in higher orders of p.

References

1. E. K. Hyde, *Fission* (Prentice Hall, Englewood Cliffs, New Jersey, 1964).
2. C. H. Westcott, *A Survey of Values of 2200 m/s Constants for Four Fissile Nuclides*, Atomic Energy Review **3**, 2 (1965); see also, A. De Volpi and K. G. Porges, *Average Fission Neutron Yield from ^{235}U and ^{252}Cf*, Proc. Conference on Nuclear Data and Microscopic Cross Sections, Paris, October 1966.

V-12. Compton Recoil Continuum Measurements for In-Core Gamma-Ray Spectroscopy

R. Gold

Introduction

The in-core radiation environment of a reactor is not exclusively composed of neutrons, since an important component of the radiation field owes its existence to gamma rays. Reactors are, however, neutron multiplication systems. Consequently, the neutron population must play the dominant role. For this reason, it is understandable that in-core reactor physics experiments have concentrated almost exclusively upon reaction rate measurements with neutrons. Precise definition of in-core reactor radiation fields cannot, however, be realized without inclusion of the gamma-ray component. Aside from this more general motivation, the intensity and energy spectrum of in-core gamma rays is of practical interest in such areas as gamma-ray heating, shielding, and radiation damage.

The development of high-resolution (lithium-drifted) solid-state detectors for gamma-ray measurements is a significant experimental advance which has been widely applied in nuclear spectroscopy. Work with these detectors has focused on precise definition of nuclear energy levels by accurate gamma-ray energy measurements (of the photo-peak response). In such investigations, only a limited number of transitions can be successfully analyzed because of the dominance of the Compton response in these detectors. Hence, these detectors cannot be used in the same manner (i.e. as photo-peak detectors) for measurement of continuous gamma-ray spectra.

While the dominance of the Compton recoil continuum in these detectors is regarded as an unwanted and troublesome complication in nuclear (energy-level) spectroscopic studies, it is precisely this response which can be exploited for continuous gamma-ray spectroscopy.

Indeed, the Compton distribution and the continuous gamma-ray spectrum are directly related by a well-defined integral equation. Consequently, the continuous gamma-ray spectrum can be determined from an unfolding problem,[1] in terms of the measured electron-recoil spectrum. The definition and treatment of this specific unfolding problem has already been reported[2] and is given in sequel.

Some obvious advantages of this method can be cited at the outset. The response kernel (or response matrix) can be directly calculated from first principles. This assumption rests upon the dominance of the Compton response, by roughly one-to-two orders of magnitude, in the broad energy region from about 100 keV up to a few MeV. In comparison, all other photon interaction modes can be regarded as higher-order perturbations and as such will be neglected in the present treatment. Consequently, a geometry-independent formulation can be introduced, which is valid as long as effects of finite detector size are small (i.e. up to a few MeV). It follows that the required response function for these detection systems need not be determined experimentally. Only through higher-order effects can the specific type, geometry, or design of the solid-state detector have an influence. It is, therefore, interesting to contrast the present formulation and treatment with the work of M. Silk and S. Wright[3,4] who have independently recognized the merit of Compton continuum measurements.

There are additional advantages which automatically accrue from the use of solid-state detectors, namely sensitivity, resolution, and compactness, all of which should allow adequate in-core measurements with little perturbation of the environment. Finally, the well-established Compton scattering kernel should permit *absolute* measurement of continuous photon-energy spectra. In this regard, the relative error of this method can only be estimated, at present, to lie in the range of 10–20% and is dominated by the neglect of higher-order effects already mentioned.

Formulation of the Integral Equation

Let $\phi(\epsilon_0, \mathbf{\Omega}_p)$ be the (steady-state) angular photon flux at energy ϵ_0 in the direction $\mathbf{\Omega}_p$. Here ϕ possesses the customary units of an angular flux, namely photons per unit area per unit time per unit energy per steradian. (Note that the absence of any space-dependent argument in ϕ implies that the angular flux $\phi(\mathbf{r}, \epsilon_0, \mathbf{\Omega}_p)$ does not vary rapidly over the region of the detector.) Let $dN(\mathbf{\Omega}_e)$ be the number of electron recoils per unit time arising in the solid angle $d\mathbf{\Omega}_e$ at $\mathbf{\Omega}_e$. Introducing the Compton-scattering cross section per steradian (per free electron), $d\sigma_c/d\mathbf{\Omega}_e$, one has

$$dN(\mathbf{\Omega}_e) = N_e d\mathbf{\Omega}_e \int\int \frac{d\sigma_c}{d\mathbf{\Omega}_e}(\epsilon_0, \mathbf{\Omega}_p \cdot \mathbf{\Omega}_e) \cdot \phi(\epsilon_0, \mathbf{\Omega}_p)\, d\mathbf{\Omega}_p\, d\epsilon_0, \tag{1}$$

where N_e is the total number of electrons in the detector. As is well-known, the Compton cross section $d\sigma_c/d\mathbf{\Omega}_e$ can be expressed as a function of only the original photon energy ϵ_0 and the cosine of the scattering angle.[5,6] Here $\mathbf{\Omega}_p \cdot \mathbf{\Omega}_e$ is simply the cosine of the angle between the original photon direction and the electron recoil direction.

The observable reaction rate obtained from a solid-state detector is, however, the number of electrons per unit time arriving in a final state energy interval dE, at E. Consequently, it is necessary to transform from the variable $\mathbf{\Omega}_p \cdot \mathbf{\Omega}_e$ to the final state electron recoil energy E. In this event, Eq. (1) becomes

$$dN(E) = N_e\, dE \int\int \frac{d\sigma_c}{dE}(E, \epsilon_0)\phi(\epsilon_0, \mathbf{\Omega}_p)\, d\mathbf{\Omega}_p\, d\epsilon_0, \tag{2}$$

where

$$\frac{d\sigma_c}{dE}(E, \epsilon_0) = \frac{d\sigma_c}{d\mathbf{\Omega}_e}(\epsilon_0, \mathbf{\Omega}_p, \cdot \mathbf{\Omega}_e)\frac{\partial \mathbf{\Omega}_e}{\partial E} \tag{3}$$

is the Compton-scattering cross section for an initial state photon energy ϵ_0 and a final state electron recoil energy between E and $E + dE$. This representation of the Compton cross section can be obtained directly from the Klein-Nishina formula in the form[7]

$$\frac{d\sigma_c}{dE}(E, \epsilon_0) = \frac{\pi r_0^2}{(\epsilon_0 - E)^2}\left\{\left(\frac{E}{\epsilon_0^2}\right)^2 + 2\left(\frac{\epsilon_0 - E}{\epsilon_0}\right)^2 + \frac{(\epsilon_0 - E)}{\epsilon_0^3}[(E-1)^2 - 1]\right\}, \tag{4}$$

where $r_0^2 = e^2/mc^2$ is the classical electron radius, with e the electron charge, m the electron rest mass, and c the velocity of light in vacuum. In addition, the initial photon energy ϵ_0 and the final state electron energy E are expressed in mc^2 units.

Introducing the scalar photon flux

$$\Phi(\epsilon_0) = \int \phi(\epsilon_0, \mathbf{\Omega}_p)\, d\mathbf{\Omega}_p, \tag{5}$$

and the measured electron-recoil spectrum

$$W(E) = \frac{dN(E)}{dE}, \tag{6}$$

Eq. (2) becomes

$$W(E) = N_e \int \frac{d\sigma_c}{dE}(E, \epsilon_0)\Phi(\epsilon_0)\, d\epsilon_0. \tag{7}$$

Equation (7) is the desired integral equation relating

TABLE V-12-I. COMPTON RESPONSE MATRIX
($n = 71$, $A = 0.02$ MeV, $N_e = 1.4 \times 10^{24}$)

Row No.	Column No. 69	70	71	72	73	74	75
50	3.21083 − 003	3.09620 − 003	2.98999 − 003	2.89121 − 003	2.79900 − 003	2.71263 − 003	2.63150 − 003
51	3.28584 − 003	3.16321 − 003	3.05010 − 003	2.94533 − 003	2.84789 − 003	2.75696 − 003	2.67180 − 003
52	3.37021 − 003	3.23832 − 003	3.11727 − 003	3.00563 − 003	2.90223 − 003	2.80610 − 003	2.71639 − 003
53	3.46526 − 003	3.32266 − 003	3.19243 − 003	3.07291 − 003	2.96269 − 003	2.86063 − 003	2.76575 − 003
54	3.57262 − 003	3.41754 − 003	3.27670 − 003	3.14808 − 003	3.03004 − 003	2.92120 − 003	2.82043 − 003
55	3.69420 − 003	3.52455 − 003	3.37137 − 003	3.23224 − 003	3.10519 − 003	2.98859 − 003	2.88109 − 003
56	3.83235 − 003	3.64558 − 003	3.47800 − 003	3.32667 − 003	3.18922 − 003	3.06369 − 003	2.94848 − 003
57	3.98990 − 003	3.78292 − 003	3.59846 − 003	3.43290 − 003	3.28338 − 003	3.14755 − 003	3.02350 − 003
58	4.17031 − 003	3.93936 − 003	3.73497 − 003	3.55275 − 003	3.38917 − 003	3.24141 − 003	3.10716 − 003
59	4.37791 − 003	4.11828 − 003	3.89028 − 003	3.68842 − 003	3.50839 − 003	3.34674 − 003	3.20070 − 003
60	4.61806 − 003	4.32393 − 003	4.06772 − 003	3.84260 − 003	3.64321 − 003	3.46532 − 003	3.30556 − 003
61	4.89760 − 003	4.56157 − 003	4.27143 − 003	4.01856 − 003	3.79625 − 003	3.59927 − 003	3.42348 − 003
62	5.22523 − 003	4.83786 − 003	4.50658 − 003	4.22035 − 003	3.97073 − 003	3.75117 − 003	3.55655 − 003
63	5.61226 − 003	5.16134 − 003	4.77969 − 003	4.45304 − 003	4.17062 − 003	3.92417 − 003	3.70730 − 003
64	6.07357 − 003	5.54304 − 003	5.09910 − 003	4.72302 − 003	4.40088 − 003	4.12217 − 003	3.87883 − 003
65	6.62909 − 003	5.99752 − 003	5.47561 − 003	5.03844 − 003	4.66778 − 003	4.35005 − 003	4.07497 − 003
66	7.30598 − 003	6.54420 − 003	5.92343 − 003	5.40988 − 003	4.97931 − 003	4.61393 − 003	4.30049 − 003
67	8.14211 − 003	7.20960 − 003	6.46154 − 003	5.84122 − 003	5.34580 − 003	4.92164 − 003	4.56140 − 003
68	9.19153 − 003	8.03058 − 003	7.11578 − 003	6.38100 − 003	5.78082 − 003	5.28329 − 003	4.86537 − 003
69	1.05336 − 002	9.05978 − 003	7.92212 − 003	7.02444 − 003	6.30250 − 003	5.71217 − 003	5.22230 − 003
70	0.00000 + 000	1.03744 − 002	8.93180 − 003	7.81661 − 003	6.93547 − 003	6.22597 − 003	5.64519 − 003
71	0.00000 + 000	0.00000 + 000	1.02199 − 002	8.80744 − 003	7.71392 − 003	6.84877 − 003	6.15134 − 003
72	0.00000 + 000	0.00000 + 000	0.00000 + 000	1.00700 − 002	8.68653 − 003	7.61394 − 003	6.76426 − 003
73	0.00000 + 000	0.00000 + 000	0.00000 + 000	0.00000 + 000	9.92450 − 003	8.56894 − 003	7.51656 − 003
74	0.00000 + 000	0.00000 + 000	0.00000 + 000	0.00000 + 000	0.00000 + 000	9.78314 − 003	8.45452 − 003
75	0.00000 + 000	0.00000 + 000	0.00000 + 000	0.00000 + 000	0.00000 + 000	0.00000 + 000	9.64577 − 003

the measured Compton continuum, $W(E)$, with the scalar photon flux, $\Phi(\epsilon_0)$. The response kernel of this unfolding problem is simply the Compton cross section per free electron given in Eq. (4) scaled by N_e, the total number of electrons in the detector.

RESPONSE MATRIX CONSTRUCTION

In the numerical treatment of this type of integral equation,[1] it is customary to introduce the matrix approximation

$$\mathbf{W} = C\mathbf{\Phi}, \tag{8}$$

where $\mathbf{W}$ and $\mathbf{\Phi}$ are vector representations of the continuous electron and photon spectra, respectively. The response matrix C is defined in terms of the response kernel in the usual manner as

$$C_{ij} = \int_{(\epsilon_0)_j}^{(\epsilon_0)_{j+1}} \frac{d\sigma_c}{dE}(E_i, \epsilon_0)\, d\epsilon_0. \tag{9}$$

Using constraints imposed by the Compton-scattering process, one can obtain a particularly advantageous representation of the response matrix C. More specifically, given a recoil electron of energy E, the permissible range of initial photon energies is bounded from below by[5,6]

$$(\epsilon_0)_{min} = \frac{E}{2}\left[1 + \left(1 + \frac{2}{E}\right)^{1/2}\right]. \tag{10}$$

Thus, for this given recoil energy E, the response kernel $d\sigma_c/dE$ must vanish for all $\epsilon_0 \leq (\epsilon_0)_{min}$. This condition can be used to obtain an upper triangular representation for the C matrix. The advantages which accrue in iterative unfolding from triangular type response matrices are well established.[1]

To this end, let A be the energy mesh spacing (in MeV units) used for the measurement of the Compton recoil distribution $\mathbf{W}$. Hence, the mid-bin electron energy, E_i, corresponding to the component, W_i, is given by

$$E_i = \frac{A \cdot i}{\mathrm{mc}^2}, \qquad i = 1, 2 \cdots n. \tag{11}$$

Consequently the upper and lower energy values bounding the ith bin are just

$$E_i^{\ell} = E_i - \frac{A}{2\ \mathrm{mc}^2} \tag{12a}$$

and

$$E_i^u = E_i + \frac{A}{2\,mc^2}, \tag{12b}$$

respectively. This experimentally dictated mesh in E-space can be used in Eq. (10) to generate a corresponding decomposition of ϵ_0-space. One finds

$$(\epsilon_0)_i = \frac{E_i}{2}\left[1 + \left(1 + \frac{2}{E_i}\right)^{1/2}\right], \tag{13a}$$

$$(\epsilon_0)_i^\ell = \frac{E_i^\ell}{2}\left[1 + \left(1 + \frac{2}{E_i^\ell}\right)^{1/2}\right]. \tag{13b}$$

and

$$(\epsilon_0)_i^u = \frac{E_i^u}{2}\left[1 + \left(1 + \frac{2}{E_i^u}\right)^{1/2}\right]. \tag{13c}$$

For this specific decomposition of E-space and ϵ_0-space, the C matrix possesses the triangular form

$$C_{ij} = N_e \int_{(\epsilon_0)_j^\ell}^{(\epsilon_0)_j^u} \frac{d\sigma_c}{dE}(E_i, \epsilon_0)\, d\epsilon_0, \qquad i \le j \tag{14a}$$

and

$$C_{ij} = 0, \qquad i > j. \tag{14b}$$

A computer code, COMPSCAT, has been developed to generate Compton response matrices as defined in Eqs. (11) through (14). As an example of the response matrices produced by COMPSCAT, Table V-12-I presents the lower portion of a (71 × 71) C matrix. This response matrix covers the energy region 0.1–1.5 MeV in E-space. The values $N_e = 1.40 \times 10^{24}$ and $A = 0.02$ MeV used to generate this matrix correspond to a silicon solid-state detector of 200 mm^2 area by 5 mm depletion depth with a 20 keV electron resolution (298°C).

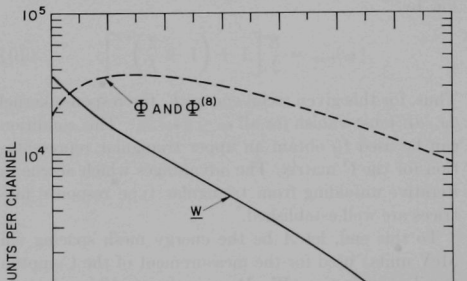

FIG. V-12-1. Comparison of the Assumed Test Vector $\mathbf{\Phi}$ in Eq. (15) with Both the $\mathbf{W}$ Vector Obtained from Eq. (8) and the Iterative Solution $\mathbf{\Phi}^{(8)}$. *ANL Neg. No. 113-840.*

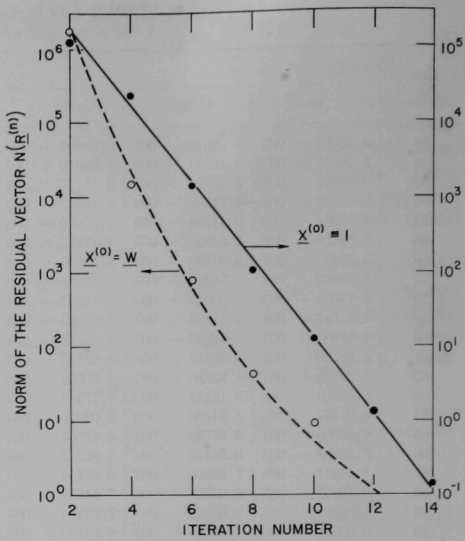

FIG. V-12-2. Norm of the Residual Vector $N(\mathbf{R}^{(n)})$ as a Function of Iteration Number n, for the $\mathbf{W}$ Vector Given in Fig. V-12-1 and the C-matrix of Table V-12-I. The Two Cases Depicted Correspond to Two Different Initial Vectors, $\mathbf{X}^{(0)} \equiv 1$ and $\mathbf{X}^{(0)} = \mathbf{W}$, used for initiating the iteration process. *ANL Neg. No. 113-841.*

Iterative Unfolding Convergence Properties

The applicability of iterative unfolding for this class of response matrices has already been established.[1] To illustrate convergence properties for this specific system, viz. Eqs. (8), (14a), and (14b), different test assumptions can be introduced to simulate the input photon vector, Φ, i.e. the continuous gamma-ray spectrum. This test vector is then placed in Eq. (8) to obtain a corresponding output electron vector $\mathbf{W}$. Using $\mathbf{W}$ and the response matrix, iterative unfolding is employed to examine convergence of the set of iterative approximations $\{\Phi^{(n)}\}$ to the assumed test vector Φ. The computer program ITERATE,[1] a general code for the iterative treatment of the unfolding problem, is used for these computations.

Figure V-12-1 exhibits a test vector of the form

$$\Phi_i = S(\epsilon_0)_i e^{-\alpha(\epsilon_0)_i}, \quad i = 1, 2 \cdots n, \quad (15)$$

where the constants S and α are approximately chosen for scaling purposes. The **W** vector generated from this test vector $\mathbf{\Phi}$, with the C matrix described in Table V-12-I is also depicted in Fig. V-12-1. For this test case, iterative convergence rates were quite rapid as can be inferred from the behavior of the norm of the residual vector, $\mathbf{R}^{(n)} = \mathbf{W} - \mathbf{W}^{(n)}$, which is displayed in Fig. V-12-2 for two choices of the initial vector $\mathbf{X}^{(0)}$. Adequate convergence was obtained with as few as eight iterations, as can be seen in Fig. V-12-1 wherein $\mathbf{\Phi}^{(8)}$ can be seen to coincide with the original test vector $\mathbf{\Phi}$. In general, appropriate solutions have been obtained for a variety of C matrices and test vectors in less than ten iterations.

REFERENCES

1. R. Gold, *An Iterative Unfolding Method for Response Matrices*, ANL-6984 (1964).
2. R. Gold, *Compton Continuum Measurements for Continuous Gamma-Ray Spectroscopy*, Bull. Am. Phys. Soc. **13**, 1405 (1968).
3. M. G. Silk, *Iterative Unfolding of Compton Spectra*, AERE-R5653 (1968).
4. M. G. Silk and S. B. Wright, UKAEA, Atomic Energy Establishment, Harwell, England (private communication).
5. W. Heitler, *The Quantum Theory of Radiation* (Oxford University Press, London, 1954).
6. R. D. Evans, *Compton Effect*, Handbuch der Physik (Springer, Berlin, 1958), Vol. XXXIV, pp. 218–297.
7. A. T. Nelms, *Graphs of the Compton Energy-Angle Relationship and the Klein-Nishina Formula from 10 keV to 500 MeV*, NBS Circular 542 (1953).

V-13. Analysis and Reduction of Proton-Recoil Data

R. GOLD, E. F. BENNETT and I. K. OLSON

The interpretation of neutron spectroscopy measurements using the proton-recoil method can be conveniently divided into two parts. First, one attempts to recreate, using experimental pulse-height data, the energy distribution of recoiling protons in an infinite hydrogenous medium. Second, one converts the idealized proton-energy distribution into a distribution of incident neutron energy by differentiation, with use of the well-known energy-dependence of the neutron-proton scattering cross section.

Unfolding methods may be used to correct observed (distorted) distributions to infinite (undistorted) values and the treatment can be extended to include a consistent estimate of errors.

A discussion of this data reduction procedure has been published,[1-3] including various relevant computer codes.

One particular figure serves to illustrate the main point developed in the aforementioned reports, namely that finite size effects are ordinarily significant at all energies of a spectral measurement and are not confined alone to the common wall-and-end type of response behavior. In order to illustrate the extent of finite size effects upon a representative fast neutron spectrum, Fig. V-13-1 presents a comparison of neutron spectra obtained from both raw and unfolded (for finite-size effects) proton-recoil spectra. The data in Fig. V-13-1 have been smoothed to eliminate statistical fluctuations so that the general nature of the correction can be more readily observed. The uncorrected neutron spectrum departs significantly from the true spectrum in that deviation is well in excess of experimental statistics over almost the entire region of the spectrum.

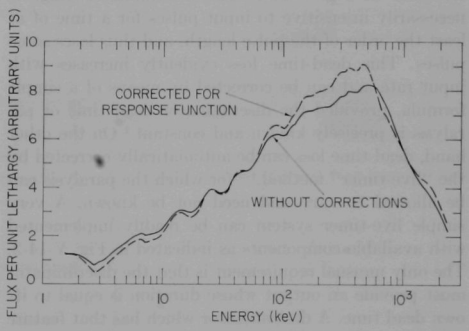

FIG. V-13-1. An Example of Spectral Distortion Due to Finite Size Effects in Proton-Recoil Proportional Counters. *ANL Neg. No. 112-8539 Rev. 1.*

REFERENCES

1. E. F. Bennett, R. Gold and I. K. Olson, *Analysis and Reduction of Proton-Recoil Data*, ANL-7394 (January 1968).
2. R. Gold and E. F. Bennett, *Effects of Finite Size in 4π-*

Recoil Proportional Counters, Nucl. Inst. Methods **63**, 285 (1968).

3. R. Gold and E. F. Bennett, *Error Estimates for Iterativ Unfolding*, J. Comp. Phys. 3, No. 2, 167 (1968).

V-14. Automatic Dead-Time Correction in Precision Counting Experiments

K. G. Porges and S. J. Rudnick*

The precision required of even routine counting tasks, in reactor physics measurements as well as many other applications, is steadily increasing. This demand is being met, on one hand, through improved radiation detectors and electronics; on the other hand, the published literature reflects a growing interest in the subject of count corrections for instrumental effects, or elimination of such effects by means of logic circuitry. Specifically, any nuclear detector channel delivers some unwanted pulses, either due to competing radiation or due to electronic noise, which can be eliminated only by imposing pulse-height discrimination. The digital portion of a conventional counting system is shown for reference in Fig. V-14-1. The discriminator stage is necessarily insensitive to input pulses for a time of at least the order of the pulse length, and thus loses some pulses. This dead-time loss evidently increases with input rate and can be corrected by means of a simple formula, provided the discriminator dead time or paralysis is precisely known and constant.[1] On the other hand, dead-time loss can be automatically corrected by the "live-timer" method,[1-5] for which the paralysis can be allowed to vary and need not be known. A very simple live-timer system can be readily implemented with available components as indicated in Fig. V-14-2. The only unusual requirement is that the discriminator must provide an output whose duration is equal to its own dead time. A discriminator which has that feature and also a very stable threshold was recently developed at ANL.[6]

In comparison with applied formula corrections the convenience of live-timer correction is evident; immediate availability of results and elimination of possible mistakes and errors are further advantages. As regards the precision of either approach, the inherent independence of paralysis stability should favor the live-timer method, provided no additional statistical error is introduced in the sampling process through which the live time is developed.

As considered in detail in Ref. 1, the statistics of live-timer correction can be developed by means of probability generating functions; the variance attached to each of a number of cyclically concatenated "games" can thus be compounded to yield the variance attached to the resultant count.[7] More particularly, the effect of the quantization of time in oscillator periods may be shown to be reducible to zero, if the ratio of paralysis and oscillator period is made an integer. A slight shift in the paralysis still results in a negligible effect. On the other hand, if the paralyses vary irregularly, as for example in multichannel analysis, the quantizing effects can be reduced to negligible proportions by selection of a sufficiently high oscillator frequency. The concatenated variance $\sigma^2(C)$ in a count C, with paralysis θ, count rate c, and oscillator frequency f can be shown to be

$$\sigma^2(C) = C\{1 + [(c\theta)^2(1 - f\theta)/f\theta(1 - c\theta)^2]\} \quad (1)$$

for the case where $f\theta \approx 1$. Similar expressions apply for other values of $f\theta$. The correction term is evidently very small even for $f\theta$ values differing somewhat from unity. The mean count C, accumulated in the live-time interval, can be compared with the count C_0 accumulated during the nominal (preset) time; this yields

$$C = C_0/(1 - c\theta). \quad (2)$$

Equation (2) is identical with the usual correction formula, whence C is equal to the *input* N accumulated over the *preset* time.

Neither calculated nor automatic corrections eliminate certain second-order effects which occur when the mean interval between pulses becomes comparable to the pulse length. For instance, a pulse may exist at the discriminator input at the moment the paralysis (due to a preceding count) is turned off. Such a pulse may then be counted, rendering the effective dead time somewhat smaller than the imposed paralysis. This effect can be prevented with simple logic circuitry provided in the equipment described in Ref. 6. Other effects, such as pulse pileup, cannot be readily eliminated or allowed for in applied corrections since they are strongly dependent on the input pulse-height distribution. Such effects therefore impose an upper limit on the input pulse duration to mean interval ratio for which high precision can be obtained. For medium pre-

* Electronics Division, Argonne National Laboratory.

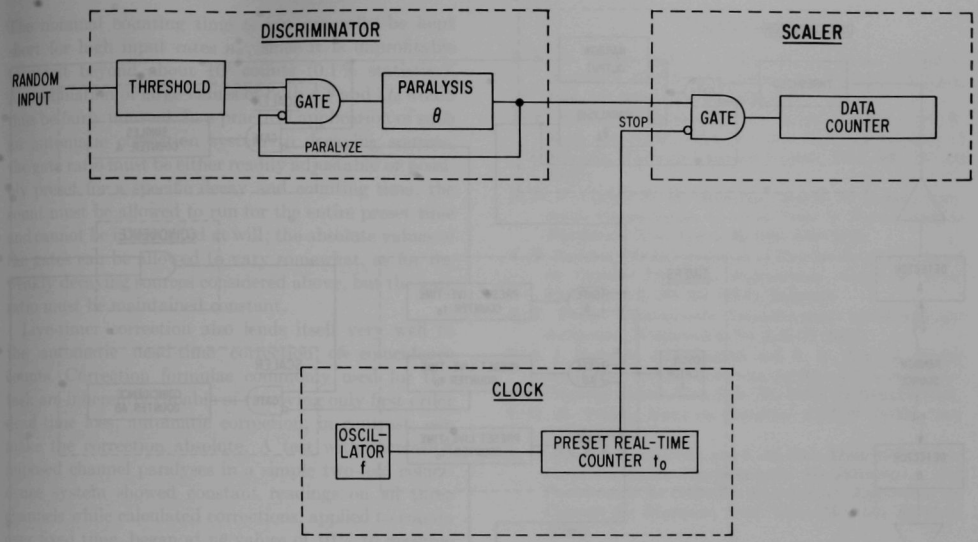

FIG. V-14-1. Conventional Counting System. *ANL Neg. No. 143-2742.*

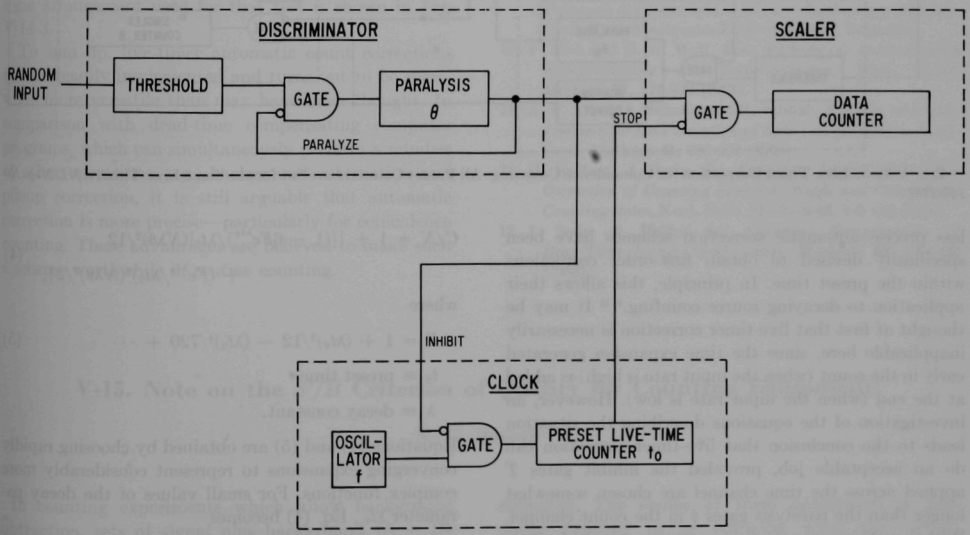

FIG. V-14-2. Live-Timer Method of Automatic Correction for a Single Counting Channel. *ANL Neg. No. 143-2743.*

cision applications, e.g., reactor flux monitoring through a counting channel, the appearance of additional pile-up pulses can be made use of to compensate for dead-time losses, thus extending the approximately linear range of the channel.[8]

In a number of counting chores, the decay of sources during the count is not negligible (e.g., in foil counting for reactor flux measurements). It is thus of interest to consider whether live-timer correction can be applied to such a case. A number of other more complex and

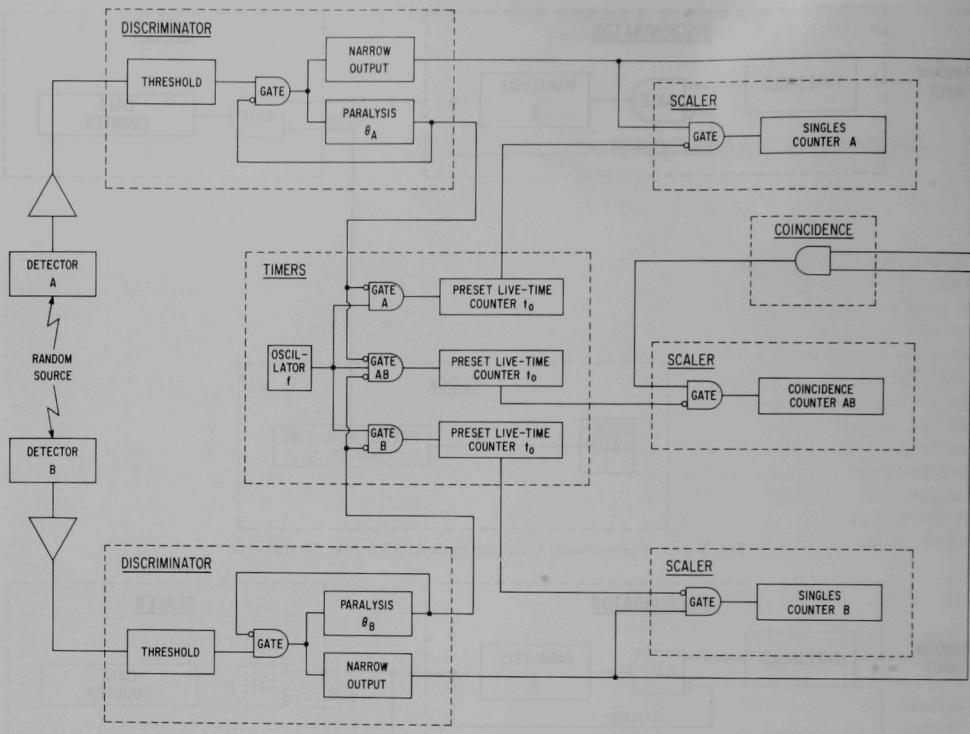

FIG. V-14-3. Live-Timer Correction for Coincidence Counting. All Preset Counters are Set for the Same Live-Time. *ANL Neg. No. 143-2737.*

less precise automatic correction schemes have been specifically devised to obtain first-order corrections within the preset time. In principle, this allows their application to decaying source counting.[9-13] It may be thought at first that live-timer correction is necessarily inapplicable here, since the time expansion generated early in the count (when the input rate is high) is added at the end (when the input rate is low). However, an investigation of the equations describing the situation leads to the conclusion that live-timer correction can do an acceptable job, provided the inhibit gates T applied across the time channel are chosen somewhat longer than the paralysis gates θ in the count channel. With a certain amount of computation, one finds that, if the gate ratio is set to

$$T/\theta = (1 + e^{\lambda t_0})/2,$$

then

$$C/N = 1 + \{[(1 - 6Fe^{\lambda t_0})/\lambda t_0](N\lambda\theta)^2/12 + (Fe^{\lambda t_0}/\lambda t_0)^2(N\lambda\theta)^3/2\}, \tag{4}$$

where

$$F = 1 + (\lambda t_0)^2/12 - (\lambda t_0)^4/720 + \cdots \tag{5}$$

$t_0 \equiv$ preset time

$\lambda \equiv$ decay constant.

Equations (4) and (5) are obtained by choosing rapidly converging expansions to represent considerably more complex functions. For small values of the decay parameter λt_0, Eq. (4) becomes

$$C/N = 1 - \tfrac{1}{2}(n_0\theta)^2 \lambda t_0[(1 - n_0\theta) - \tfrac{1}{6}(\lambda t_0) + (\tfrac{1}{12} - 2n_0\theta)(\lambda t_0)^2 + \cdots], \tag{6}$$

where

$n_0 \equiv$ input rate at the start of the count.

The nominal counting time t_0 can generally be kept short for high input rates n_0, since it is unprofitable to count beyond about 10^6 counts (0.1% statistics). A combination of large values of both $n_0\theta$ and λt_0 would thus be fairly unusual. In a practical application of such an automatic correction system to decaying sources, the gate ratio must be either readily adjustable or possibly preset for a specific decay and counting time; the count must be allowed to run for the entire preset time and cannot be interrupted at will; the absolute values of the gates can be allowed to vary somewhat, as for the weakly decaying sources considered above, but the gate ratio must be maintained constant.

Live-timer correction also lends itself very well to the automatic dead-time correction of coincidence counts. Correction formulae commonly used for this task are inherently capable of removing only first-order dead-time loss; automatic correction, in contrast, can make the correction absolute. A test with increasing imposed channel paralyses in a simple two-fold coincidence system showed constant readings on all three channels while calculated corrections, applied to counts over fixed time, began at $n\theta$ values of 10% to disagree with counts obtained at negligible short paralysis. The logic arrangement used for that test is shown in Fig. V-14-3.

To sum up, live-timer automatic count corrections can be readily implemented and turns out to be somewhat more versatile than may have been thought. In comparison with dead-time compensating computer programs, which can simultaneously perform a number of other operations, e.g., background subtraction and pileup correction, it is still arguable that automatic correction is more precise—particularly for coincidence counting. These advantages are believed to make such a scheme worthwhile in routine counting.

References

1. K. G. Porges and S. J. Rudnick, *Live-Timer Method of Automatic Dead-Time Correction for Precision Counting*, Rev. Sci. Instr. (to be published).
2. T. Emmer, *Multichannel Pulse Height Analyzers*, H. W. Koch and R. W. Johnston, eds., National Academy of Sciences, National Research Council, Publ. **467**, 182–184 (1957).
3. D. F. Covell, M. M. Sandomire and M. S. Eichen, *Automatic Compensation of Dead Time in Pulse Analysis Equipment*, Anal. Chem. **32**, 1086–1090 (1960).
4. V. Radeka, *The Determination of Random Event-Rate Based on Counter Live-Time Measurement*, Conf. on Nucl. Electronics **2**, 361–367 (1961), Belgrade.
5. T. Friese, *Automatische Totzeitkorrektur bei Strahlungsmeßgeräten*, Nukleonik **4**, No. 2, 67–71 (1961).
6. S. J. Rudnick, J. J. English and R. H. Howard, *Highly Stable High-Rate Discriminator for General Use in Nuclear Counting Applications*, Rev. Sci. Instr. (to be published).
7. O. R. Frisch, *Notes on Statistics*, CRL-57 (1959); also AECL-748 (1959).
8. G. Bonnet, V. Delcroix and V. Q. Mai, *Etude de Certaines Particularites de Fonctionnement des Detecteurs a Gaz Fonctionnant en Collection Electronique. Application au Controle des Reacteurs*, Nucl. Instr. Methods **45**, 87–92 (1966).
9. J. J. Point and A. Blave, *Méthodes Originales de Correction Continue des Pertes de Comptage dues Aux Temps de Paralysie des Détecteurs et de Leur Électronique Associée*, Conf. Nucl. Electronics **2**, 345–360 (1961), Belgrade.
10. F. Rau and G. H. Wolf, *Eine Methode zur automatischen Kompensierung von Totzeitverlusten*, Nucl. Instr. Methods **27**, 321–322 (1963).
11. A. F. Arbel, A. Suhami and B. Sabbah, *The Use of Derandomizers for the Prevention of Spectrum Distortion*, Nucl. Instr. Methods **41**, 286–292 (1966).
12. H. Seufert, *A Device for Automatic Digital Dead-Time Correction of Counting Losses of Single and Coincidence Counting Rates*, Nucl. Instr. Methods **44**, 335–340 (1966).
13. J. Seda, *A Method for Automatic Compensation of Dead-Time Losses*, Nucl. Instr. Methods **59**, 179–180 (1968).

V-15. Note on the S^2/B Criterion of Quality for Counting Equipment

K. G. Porges

In counting experiments which allow background subtraction, sets of signal plus background $(S + B)$ counts are obtained, and the pure background (B) count rate is established separately.[1] The design and adjustment of the counting equipment (detectors, shielding, and electronics) can often be arranged so as to produce different signal and background strengths. The choice of these parameters is generally believed to be optimum when the (S^2/B) ratio is highest. It is pointed out here that this criterion applies only to those experiments in which a very weak source is counted against a strong and unavoidable background. For experiments in which signal rates, possibly well above background, are to

be measured with the highest possible precision in the shortest possible time, it is appropriate to maximize the signal strength, as is demonstrated by simple statistical considerations. Such an example, in which signal and background result in different pulse-height distributions, is that of fission counts and gamma background in a fission chamber channel. The optimum position of an integral pulse-height discriminat then clearly depends on the maximum signal.

Reference

1. K. G. Porges, *Note on the S^2/B Criterion of Quality for Cou ing Equipment*, Intern. J. Appl. Rad. Isotopes **19**, 7 (1968).

V-16. Noise Studies on a Digital Reactor Control System

C. E. Cohn

The polarity-correlation algorithm previously developed for fast-reactor noise analysis[1] has been used to study the dynamic characteristics of a computerized reactor control system.[2] For these tests, the control system was applied to one of the control rods on the Argonne Thermal Source Reactor. The algorithm was set up to calculate the autocorrelation function of the motion of the control rod. During any one control interval, the control system commands the rod to withdraw (increasing reactivity), insert, or remain stationary. Thus, the sequence of rod motion commands forms a ternary (three-valued) time series, whose members have values of +1, −1, or 0, respectively.

For these tests, the reactor was in equilibrium at a steady power of 2.5W. The fluctuations observed were excited by inherent neutronic noise and dete tion noise. Each test was run for about 20 min with fixed deadband equal to the estimated standard d viation of one flux reading.

To obtain the necessary data, the computer pr gram doing the control was made to punch a cha acter onto paper tape, indicating the rod-moti command given during each sampling interval. Fo lowing the run, the data on the tape were processe When read back into the computer, each character the tape was translated to the appropriate data val in memory.

To make the algorithm handle the ternary seri it was necessary only to provide for the compil tion of a no-operation instruction to correspond a zero datum. For autocorrelation, of course, on

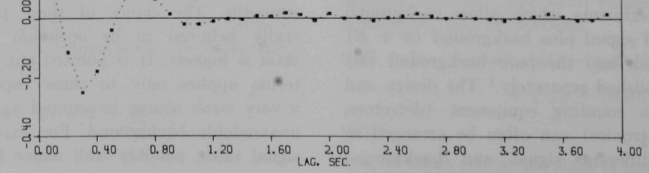

Fig. V-16-1. Autocorrelation Function of Rod Control Signal with 0.1-sec Sampling Interval and Actual Control Algorithm. A *Neg. No. 113-158.*

one string of instructions is compiled and that acts upon its own originating time series. The resulting code read 1000 data points from the tape and calculated the autocorrelation function for every value of lag from zero through 200 sampling intervals. Then the code read another thousand points from the tape and calculated the autocorrelation function for these, repeating the process until the end of the run. (If the last segment read did not contain a full thousand points, that segment was discarded.) The autocorrelation functions from each calculation were averaged to give the final results. These were plotted by the computer up to a selected maximum lag.

The correlogram for the normal control setup with 0.1-sec sampling interval is shown in Fig. V-16-1.

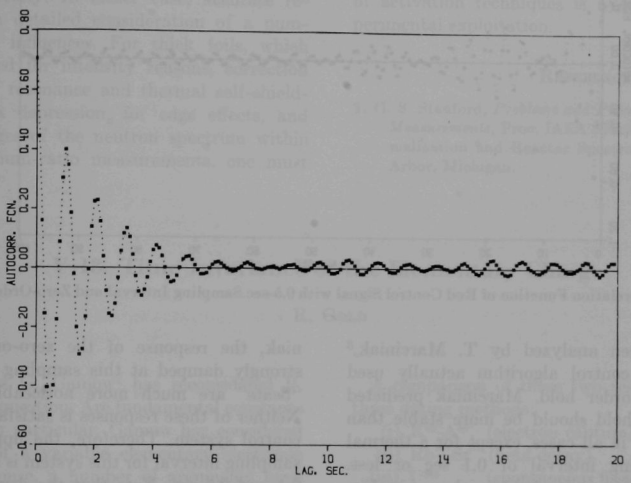

FIG. V-16-2. Autocorrelation Function of Rod Control Signal with 0.1-sec Sampling Interval and Zero-Order Hold. *ANL Neg. No. 113-159.*

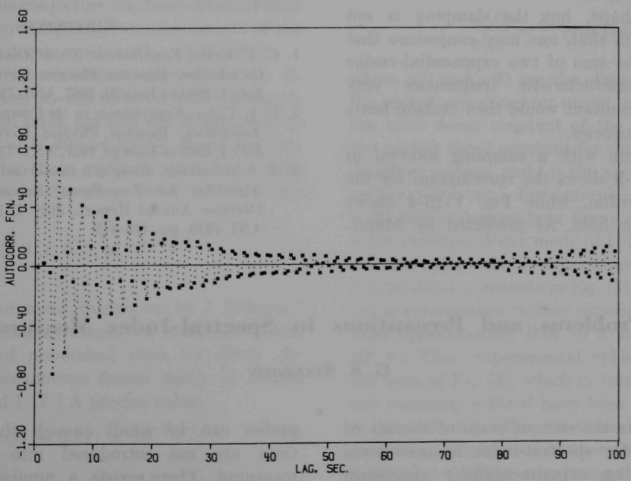

FIG. V-16-3. Autocorrelation Function of Rod Control Signal with 0.5-sec Sampling Interval and Actual Control Algorithm. *ANL Neg. No. 113-160.*

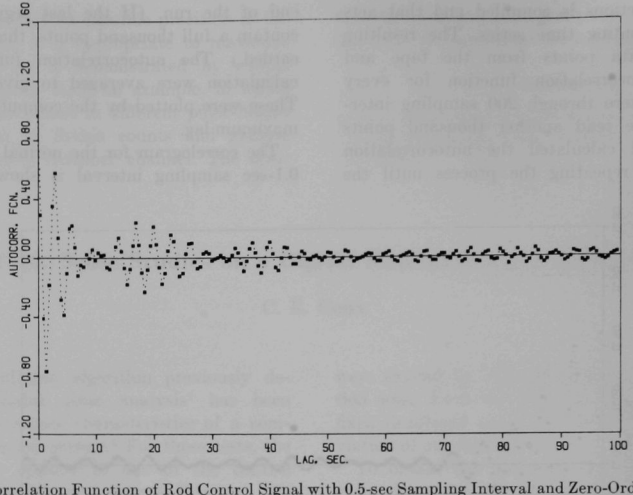

FIG. V-16-4. Autocorrelation Function of Rod Control Signal with 0.5-sec Sampling Interval and Zero-Order Hold. *ANL Neg. N 113-161.*

This system has been analyzed by T. Marciniak,[3] who compared the control algorithm actually used with a simple zero-order hold. Marciniak predicted that the zero-order hold should be more stable than the actual algorithm in all cases, except for a thermal reactor with sampling interval of 0.1 sec or less. The result for the zero-order hold is shown in Fig. V-16-2. As predicted, it is more underdamped.

This latter correlogram is close to the familiar exponential-cosine shape, but the damping is not monotonic. To explain that, one may conjecture that the correlogram is the sum of two exponential-cosine components with characteristic frequencies very close together. The resultant would then contain beats between the two frequencies.

Tests were also run with a sampling interval of 0.5 sec. Figure V-16-3 shows the correlogram for the acutal control algorithm, while Fig. V-16-4 shows that for a zero-order hold. As predicted by Marciniak, the response of the zero-order hold is mo strongly damped at this sampling interval. Also, tl "beats" are much more noticeable for these case Neither of these responses is satisfactory for an actu control system. Therefore, the upper limit of usab sampling interval for this system is somewhere betwe 0.1 and 0.5 sec. Note that the degree of damping, well as the "beats", are easier to see on the correl gram than they would be in a power-spectrum plot.

REFERENCES

1. C. E. Cohn, *Fast-Reactor Noise Analysis by Polarity Cro Correlation*, Reactor Physics Division Annual Repor July 1, 1966 to June 30, 1967, ANL-7310, pp. 415–423.
2. C. E. Cohn, *Experiments in the Computer Control of Critic Assemblies*, Reactor Physics Division Annual Repor July 1, 1966 to June 30, 1967, ANL-7310, pp. 408–410.
3. T. J. Marciniak, *Study of a Linearized Sampled-Data Contr Algorithm for Zero-Power Reactors*, Reactor Physi Division Annual Report, July 1, 1966 to June 30, 196 ANL-7310, pp. 410–415.

V-17. Problems and Precautions in Spectral-Index Measurements

G. S. STANFORD

Reference 1 reports the current state of the art of activation methods for spectral-index measurements as examined from an experimentalist's viewpoint. This type of measurement is appealing, because activation data are easy to obtain, and activation probes can be small enough that gross perturb tions are not introduced into the system bei measured. There exists a number of nuclides wi resonances at various energies $\lesssim$ 1 keV and wi other properties making them suitable for activati

experiments. Techniques that have been used include measurement of activation ratios, utilization of self-shielding in the foil-sandwich method, and the use of absorbing foil covers, notably cadmium. The data can be employed in two different ways: a) comparison of the observed activation data with the results of calculations; b) application of various mathematical techniques in an attempt to derive a spectral shape directly. In either case, accurate results depend upon detailed consideration of a number of perturbing influences. For thick foils, which often must be used for intensity reasons, correction must be made for resonance and thermal self-shielding, for outer flux depression, for edge effects, and possibly for changes of the neutron spectrum within the foil. In cadmium-ratio measurements, one must consider in some detail absorption and scattering of neutrons by the cadmium. Other activation ratios must be determined in carefully calibrated counting systems, or in conjunction with reference measurements in known spectra. While all these effects, and others, have been discussed in detail in the literature, it can be said that techniques have not yet been well enough standardized that the full potential of activation techniques is available for routine experimental exploitation.

Reference

1. G. S. Stanford, *Problems and Precautions in Spectral-Index Measurements*, Proc. IAEA Symposium on Neutron Thermalization and Reactor Spectra, July 17–21, 1967, Ann Arbor, Michigan.

V-18. Time Invariance of the Elementary Charge

R. Gold

In recent papers G. Gamow[1] has reconsidered P. Dirac's[2] intriguing question: Are fundamental constants really constant? In particular, Gamow has considered the implications of a variable elementary electronic charge, e. In response, a number of arguments have been given which support the time invariance of the elementary charge.[3-5] In particular, experimental evidence bearing on this conjecture has been obtained from a comparison of two independent measurements of the spontaneous fission decay constant, λ_F, of U-238.[(6)]

In one of these measurements, carried out by R. Fleischer and P. Price,[7] λ_F was inferred from a comparison of "fossil" fission track age and age determinations based on the decay of K-40 and Rb-87. Requiring that the ages obtained by these methods agree for a large number of minerals, in the range 10^7-2×10^9 y, the value

$$\lambda_F = (6.9 \pm 0.2) \times 10^{-17} \mathrm{y}^{-1} \tag{1}$$

was deduced.

The second measurement, carried out by J. Roberts,* R. Gold and R. Armani,† employed solid-state track recorders (SSTR) of pre-etched mica for direct observation of the spontaneous fission decay of U-238. (See Papers V-2 and I-17.) A precise value,

$$\lambda_F = (7.03 \pm 0.11) \times 10^{-17} \mathrm{y}^{-1}, \tag{2}$$

was obtained.

A comparison of these two results implies that the three dating methods:

(i) K^{40}-A^{40} (electron capture)
(ii) Rb^{87}-Sr^{87} (beta decay)
(iii) U^{238} (spontaneous fission)

are concordant. Consider, therefore, the form of the dating equation

$$\frac{\rho_i(t)}{\rho(t)} = \frac{\lambda_i}{\lambda} [\exp(\lambda t) - 1], \tag{3}$$

where $\rho(t)$ and $\rho_i(t)$ are the observed concentrations of the parent and daughter nuclei, respectively. Here λ is the total decay constant of the parent nucleus, λ_i is the partial decay constant for the formation of the ith daughter nucleus, and t is the age of the specimen (e.g. tektite, mica, etc.). For example, it is well known that K-40 also undergoes beta decay and that alpha decay is the principal decay mode of U-238.

Using independently determined experimental values for the decay constants in Eq. (3), these three methods are in concordance (within experimental error) for ages from approximately 0.01 to 2 eons ago. (One eon is 10^9 y.) Thus, experimental evidence clearly supports the form of Eq. (3), which in turn implies that the decay constants utilized have been time-independent for at least 2 eons. The existence of a time-dependent elementary charge would therefore contradict the experimental evidence supporting the constancy of these completely different decay constants.

The experimental error associated with these two in-

* Northwestern University, Evanston, Illinois.
† Argonne National Laboratory.

dependent measurements of λ_f [cf. Eqs. (1) and (2)] places a bound on the variability of the elementary charge, extending back to roughly 2 eons ago. Application of the liquid drop model by V. Viola and B. Wilkins[8] provides the following relations for heavy element (even-even nuclei) spontaneous fission:

$$\ln T_F = 6.884\, E_F - 21.50 \tag{4}$$

and

$$E_F = 22.57[1 - (Z^2/A)(a_c/2a_s)] + \cdots. \tag{5}$$

Here T_F is the spontaneous fission half-life (in years) and E_F is the fission barrier height (in MeV). In addition, a_s and a_c are the surface energy and Coulomb energy coefficients of the *semiempirical mass formula*, respectively. Consequently, a_c depends linearly on e^2. Additional terms that should be included in Eq. (5) have been omitted here, since these terms are independent of e. For e^2 increasing with time, spontaneous fission decay rates would increase with time in contrast to the exact opposite effect in alpha decay.[1] It is also important to note that the spontaneous fission decay constant is independent of g, the Fermi weak interaction constant. It therefore follows that a bound on the variation of e can be obtained without introducing any assumptions concerning g.[1,3]

Equations (4) and (5) yield

$$\frac{\delta T_F}{T_F} = -3.344(Z^2/A)[\delta(e^2)/e^2], \tag{6}$$

which for U-238 is approximately

$$\left(\frac{\delta\lambda_F}{\lambda_F}\right) \approx 120\left[\frac{\delta(e^2)}{e^2}\right]. \tag{7}$$

Assuming that the experimental error for each o these measurements is random and uncorrelated, th difference obtained from Eqs. (1) and (2) is $|\delta\lambda_F| = (0.13 \pm 0.23) \times 10^{-17}\text{y}^{-1}$. This numerical result i clearly consistent with a time-independent elementar charge and provides an upper limit,

$$|\delta\lambda_F/\lambda_F| \lesssim 5.1 \times 10^{-2}.$$

Consequently,

$$|\delta(e^2)/e^2| \lesssim 4.25 \times 10^{-4} \tag{8a}$$

or correspondingly

$$|\delta e/e| \lesssim 2.13 \times 10^{-4} \tag{8b}$$

is an approximate upper bound on the variation of th elementary charge within the last two eons.

References

1. G. Gamow, *Electricity, Gravity, and Cosmology*, Phys. Rev Letters **19**, 759 (1967); ibid. **19**, 913 (1967); Science **158** 766 (1967).
2. P. A. M. Dirac, *The Cosmological Constants*, Nature **139**, 32 (1937); *A New Basis for Cosmology*, Proc. Roy. Soc (London) **A165**, 198 (1938).
3. F. J. Dyson, *Time Variation of the Charge of the Proton* Phys. Rev. Letters **19**, 1291 (1967).
4. A. Peres, *Constancy of the Fundamental Electric Charge* Phys. Rev. Letters **19**, 1293 (1967).
5. J. N. Bahcall and M. Schmidt, *Does the Fine-Structure Constant Vary with Cosmic Time?* Phys. Rev. Letters **19** 1294 (1967).
6. R. Gold, *Time Invariance of the Elementary Charge*, Phys Rev. Letters **20**, 219 (1968).
7. R. L. Fleischer and P. B. Price, *Decay Constant for Spontaneous Fission of U^{238}*, Phys. Rev. **133**, B63 (1964).
8. V. E. Viola, Jr., and B. D. Wilkins, *Fission Barriers and Half-Lives of the Trans-Radium Elements*, Nucl. Phys. **82** 65 (1966).

Section VI

Reactor Computation Methods and Theory

To a large degree, the quality of reactor design and performance depends upon the quality of the conceptual models and their portrayal in accurate mathematical representation, and upon the quality and efficiency of computational methods. A priori, the continuous development and refinement of theory and computational methods leads to the design of more dependable, safer, and better performing reactors. It is with this intent that the studies described in this section were undertaken.

VI-1. The Argonne Reactor Computation (ARC) System

B. J. Toppel and L. Just*

The Laboratory has initiated and is vigorously pursuing the development of a unified and integrated code system for reactor computations (the ARC system) to fully utilize the growing capability afforded by the new generations of computers. The growth of computing has made computer utilization a much more complex operation. Also, the importance of standarization of computational algorithms and of minimization of programming duplication in the reactor community is obvious.

The ARC system is being developed to perform the many interrelated studies needed for fast reactor design. In the development of the ARC system, the areas of physics, safety, and fuel cycle have been initially emphasized, with core design and other engineering modules to follow. The development of this code system is an essential step in the full utilization of the growing sophistication of modern computers.

Some of the desirable features of an integrated computational system are listed below:

1. Simplicity and flexibility in regard to implementing algorithm linkages
2. Simplicity in regard to user input required to invoke a particular collection of algorithms
3. Flexibility and efficiency in regard to automated storage and recall of interface data required for algorithm linkages
4. Elimination of human manipulation of interface data when linking complementary algorithms
5. Standardization of user data input formats
6. Standardization of module generated interface data with regard to structure and organization
7. Facilitation of numerical experimentation and development, and extension into new algorithmic areas
8. Elimination of unnecessary algorithm duplication
9. Provision of an environment which encourages algorithm exchanges with other computer groups
10. Ease of replacement of part of a total computational package with improved algorithms.

Reference 1 presents extensive details regarding the current system configuration. This report is intended to provide other laboratories, interested in making use of ARC program modules, with information concerning the module interfaces and the purpose and scope of the various ARC modules. This document sets forward specifications and standards for the guidance of other laboratories in regard to organization of their local codes so as to facilitate their incorporation into the current ARC system.

The first use of the ARC system began early in calendar year 1968. The first paths being implemented provide a one-dimensional diffusion theory and S_n transport theory capability for slab, sphere, and cylinder geometries, for real, adjoint, or source calculations, and include criticality searches on composition, dimensions, or buckling.

The MC^2 cross-section code[2] which is currently operational on the CDC-3600 was also made available in the ARC system early in calendar year 1968 in a modularized form which provides the same calculational capability as the CDC-3600 version.

The 2D-diffusion theory capability was made available for user testing to gain operational experience late in FY 1968.

A general burnup and fuel management module has been completed and a 1D-diffusion theory capability is undergoing initial user testing. The modularity and interface standardization of the ARC system will permit flux calculations to be provided in either one or two dimensions by either diffusion or transport theory algorithms as the various modules become available. Testing of the 2D-burnup capability was also initated during the last half of FY 1968.

Operation of the ARC system is made possible through the use of the IBM System/360 Operating System and the ARC system-modules.[3] Some of the ARC system-modules occupy core for the entire ARC run and others are called in as required.

The ARC system-modules provide the following functions:

(1) Dynamic loading of programs
(2) Location of data sets
(3) Dynamic data storage allocation
(4) Production of BCD data sets from card input
(5) Maintenance of tables required during an ARC run.

The executable programs in the ARC system are stored in a partitioned data set whose members may be:

* Applied Mathematics Division, Argonne National Laboratory.

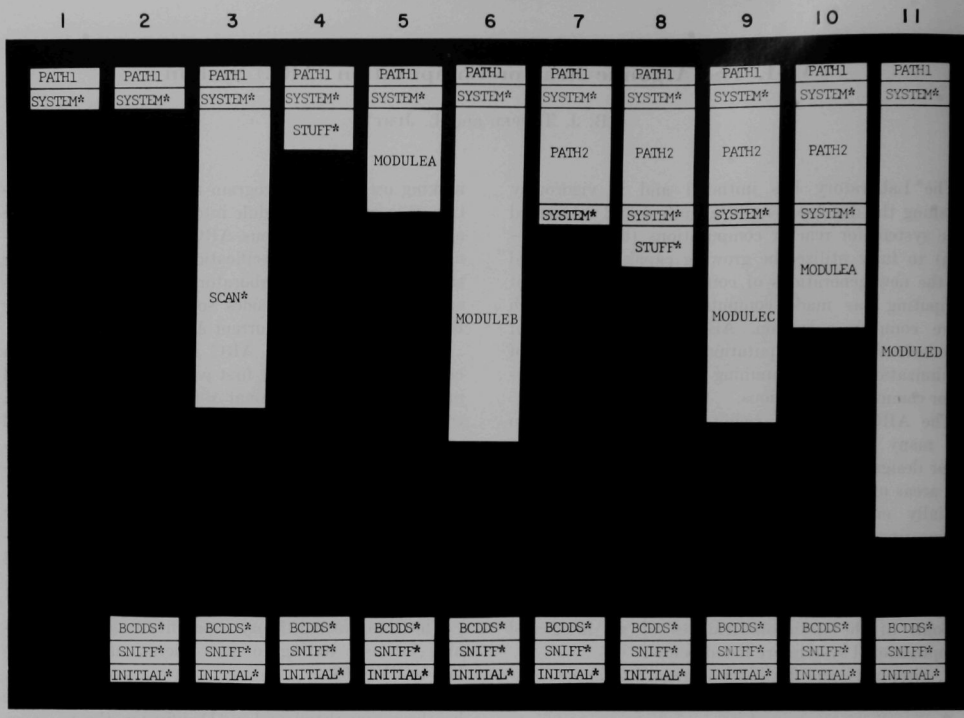

FIG. VI-1-1. Core Storage Allocation During an ARC Run. Modules Marked with an Asterisk are ARC System-Modules. *ANL Neg. No. 112-9376 Rev. 1.*

(1) Computational modules
(2) ARC system-modules
(3) Path drivers or executive modules
(4) Overlay structures containing (1), (2), and (3).

A revision of the ARC system-modules has been completed which increases the flexibility of module linkages and simplifies development and extension of standard paths. Under the earlier system, each path was a load module in the IBM sense and required construction by the Linkage Editor before use. This had the disadvantage of engendering module duplication in various standard paths and presented the problem of avoidance of control section duplication within the standard path load modules.

Under the revised system, the individual computational modules and standard path control programs are linkage edited to produce load modules. The construction of the standard paths is accomplished by linkages at run time using the new ARC system-modules.

Figure VI-1-1 is a dynamic picture of the core with time increasing from left to right. The ARC system-modules are marked with an asterisk. A description of events in each time interval follows:

Time Interval	Events
1	PATH1 is to be executed so it is in core. ARC system-module SYSTEM is part of this initial load module.
2	PATH1 called SYSTEM causing INITIAL, SNIFF and BCDDS to be loaded.
3	INITIAL, SNIFF and BCDDS are executed for the first time causing tables to be initialized and flags to be set so that a subsequent call to any of these modules will not re-initialize the tables. The first call to BCDDS loads SCAN to process all of the input data into one data set. This data set will be processes piecemeal by STUFF.
4	PATH1 needs BCD data so a call to BCDDS results in the loading of STUFF to process the input data for the first call from PATH1.
5	CALL LINK ('MODULEA') causes loading and execution of MODULEA.

TABLE VI-1-I. ARC SYSTEM-MODULE DESCRIPTIONS

Module	Language	Function
LOAD	ASSEMBLY	Locates a module in a library and loads it into core generally for the duration of the run.
LINK	ASSEMBLY	Causes execution of modules already loaded into core and loading and execution of those that are not in core.
SYSTEM	FORTRAN IV	The first executable statement in a path driver must be CALL SYSTEM. This causes the system to be initialized. This module also contains LINK and LOAD. SYSTEM must be part of every non-system-module in the library.
SNIFF	FORTRAN IV	Given a data set name, SNIFF returns the data set reference number and also maintains tables of data set usage.
BCDDS	FORTRAN IV	With modules SCAN and STUFF, BCDDS creates BCD data sets from card input.
SCAN	FORTRAN IV	This module is only called once to create a data set containing all of the card input.
STUFF	FORTRAN IV	Provides BCD data sets as they need to be created.
INITIAL	FORTRAN IV	Works with SYSTEM to initialize the system.

6 CALL LINK ('MODULEB') causes loading and execution of MODULEB.
7 PATH1 executed CALL LINK ('PATH2'). PATH2 is loaded and given control. PATH2 tries to initialize the system but cannot, so PATH1 is still in control of tables.
8 PATH2 needs BCD data so a call to BCDDS causes STUFF to be loaded and executed.
9 PATH2 executes CALL LINK ('MODULEC').
10 PATH2 executes CALL LINK ('MODULEA').
11 Control has passed back to PATH1 which has executed CALL LINK ('MODULED').

Table VI-1-I lists the system-modules with a brief description of the functions performed. With the exception of LOAD and LINK, all system-modules are written in FORTRAN IV.

The current ARC system configuration cannot as yet be thought of as being a truly automated computation system in the fullest sense. This is due to the rigidity of the module interfaces coupled with the inadequacy of the FORTRAN language with regard to flexible data managemennt capability. The approach being taken at the Laboratory should be thought of as representing a start toward achieving some of the objectives set forth earlier.

The key to fully achieving the objectives of an integrated computation system will be the development of a sophisticated data management capability together with a user oriented system management language. The specification of such a user-oriented operating system, to avoid user involvement in the highly specialized IBM job control language, has been completed and is described in an Applied Mathematics Division internal memorandum.

REFERENCES

1. B. J. Toppel, *The Argonne Reactor Computation System, ARC*, ANL-7332 (1968).
2. B. J. Toppel, A. L. Rago and D. M. O'Shea, *MC²*, *A Code to Calculate Multigroup Cross Sections*, ANL-7318 (1967).
3. B. J. Toppel, *The Argonne Reactor Computation (ARC) System*, Reactor Physics Division Annual Report, July 1, 1966 to June 30, 1967, ANL-7310, pp. 433–436.

VI-2. Accuracy of Factorizing Methods in Spatial Kinetics

K. O. OTT,* D. A. MENELEY and E. S. WIENER

INTRODUCTION

The need for careful analysis of the dynamics of large fast power reactors imposes severe demands on mathematical models of the various physical processes with regard to accuracy. This need exists because the complexity and cost of dynamics experiments in such systems limits these experiments in scope and number. Limited scope experiments must be designed to obtain a basic understanding of the processes on a microscopic scale, to provide physical parameters for mathematical models, and to verify these models in special cases so that they may be applied with confidence within their range of validity. It is obvious that the diversity of fast reactor designs and possible modes of abnormal behavior restricts the range of usefulness of data from integral dynamics experiments on prototypical reactors,

* Purdue University, Lafayette, Indiana.

in lieu of comprehensive mathematical modelling of the system behavior.

This comprehensive calculational model must include many parts. The work described here is concerned with the development of an adequate description of neutronic behavior. Basic requirements of the model are assumed to be: at least two space dimensions, detailed description of the energy spectrum, and ability to treat nonlinear problems with no fundamental approximation. Further, it has been assumed that multigroup diffusion theory is an adequate basis for the model (a nonessential limitation), and that a direct space-time differencing method applied to an equation set with the above-defined capabilities would result in an excessively expensive calculation tool.

The Quasistatic Model [1-4] is identified as one member of a sequence of methods classified as "factorizing" methods. All of these, to a greater or lesser degree, make use of the fact that the overall neutron population may grow or decay much more rapidly than the relative space-energy distribution of that population. This is because this rate of change in space-energy is determined primarily by the rate of movement of components of the system. These rates are strictly limited in a real reactor by inertia and momentum considerations. The overall neutron population growth rate above prompt critical is limited only by the value of excess multiplication relative to the neutron generation time. Thus, particularly in fast reactors, the space-energy distribution varies slowly relative to the total neutron population under these conditions. In the reactivity range below prompt critical the total neutron population, including its space-energy shape, is "slowly varying" within the context of this discussion.

From the point of view of a numerical solution, factorization of the flux into a slowly time-varying function in space-energy and a purely time dependent function which may vary rapidly provides the abilty to determine only a few of the expensive space-energy solutions, while the time dependent function may be determined on a fine time mesh when required in order to ensure accuracy.

The following section contains a brief comparative description of each member of a sequence of factorizing methods, some of which are in common use for dynamics analysis. The section entitled *Sample Problems* presents some illustrative cases for quantitative comparison of the methods.

Factorizing Methods

The general problem is to solve the time dependent multigroup diffusion equation

$$[-M + F_p]\Phi(\mathbf{r},E,t) + S_d[\Phi(\mathbf{r},E,t')] = \frac{1}{v}\frac{\partial}{\partial t}\Phi(\mathbf{r},E,t). \quad (1)$$

The operator $[-M + F_P]$, with M representing removal and scattering and F_P representing prompt fission, is applied to Φ at time t. However, the delayed neutron source $S_d[\Phi(\mathbf{r},E,t')]$ has the form of a convolution integral over the flux history. All operators depend implicitly on time—linearly from induced changes and non-linearly from feedback.

Following the derivation given in Ref. 5, factorize the total flux $\Phi(\mathbf{r},E,t)$ into an "amplitude" function $\phi(t)$ and a "shape" function $\psi(\mathbf{r},E,t)$:

$$\Phi(\mathbf{r},E,t) = \phi(t)\psi(\mathbf{r},E,t), \qquad \phi(0) = 1.0. \quad (2)$$

The factorization in Eq. (2) requires another separation condition for $t > 0$ in order to become a unique definition of $\phi(t)$ and $\psi(\mathbf{r},E,t)$. This splitting is to be made in such a way that $\phi(t)$ contains the main time dependence of the total flux, so that the time dependence of $\psi(\mathbf{r},E,t)$ has to account only for the relatively slow space-energy variations. There are many conditions which can be used, all of which involve constraining some space-energy integral of $\psi(\mathbf{r},E,t)$ to a constant value for all $t > 0$. The only basic requirement is that $\psi(\mathbf{r},E,t)$ remain positive and bounded at all points in space $(\mathbf{r},E)$ for all times.[6] According to A. Henry[5]:

$$\iint \frac{\psi^*(\mathbf{r},E,0)\psi(\mathbf{r},E,t)}{v}\, d\mathbf{r}\, dE = \text{constant} \quad (3)$$

fulfills the requirements for the constraint condition and has the added advantage that it simplifies the expression for the amplitude function. In Eq. (3) $\psi^*(\mathbf{r},E,0)$ is the adjoint function for the initial steady state of the system. It is obvious that any weighting function could be used without influencing the result for $\Phi(\mathbf{r},E,t)$, which is unique.

Splitting the total flux into two functions ϕ and ψ naturally implies a subsequent splitting of the basic Eq. (1) into two equations, one for the amplitude $\phi(t)$ and one for the shape $\psi(\mathbf{r},E,t)$. These equations are coupled. For numerical calculations it is desirable that the coupling be strong in one direction only. For the split chosen the space-energy shape of the ψ function depends only weakly on the value of $\phi(t)$, as is illustrated below.

Henry[5] showed that, using Eq. (3), the $\phi(t)$ equation reduces to the form of the point kinetics equation (with common notation):

$$\frac{d\phi(t)}{dt} = \frac{[\rho(t) - \bar{\beta}(t)]}{\Lambda(t)}\phi(t) + \sum_k \lambda_k\eta_k(t), \quad (4)$$

with the vital difference that the integral quantities

ρ, $\bar{\beta}$, etc., must be averaged with the time-dependent shape $\psi(\mathbf{r},E,t)$. Therefore

$$\rho = \frac{1}{\bar{F}} \iint \psi^*(\mathbf{r},E,0) \cdot [-M + F_p + F_d]\psi(\mathbf{r},E,t)\, d\mathbf{r}\, dE$$

$F_d \equiv$ delayed fission operator

$$\bar{\beta}_k = \frac{1}{\bar{F}} \iint \psi^*(\mathbf{r},E,0) F_{d,k}\psi(\mathbf{r},E,t)\, d\mathbf{r}\, dE$$

$$\bar{\beta} = \sum_k \bar{\beta}_k$$

$$\Lambda = \frac{1}{\bar{F}} \iint \psi^*(\mathbf{r},E,0)\, \frac{1}{v}\, \psi(\mathbf{r},E,t)\, d\mathbf{r}\, dE \tag{5}$$

$\lambda_k \equiv$ delayed neutron precursor decay constant

$$\bar{F} = \iint \psi^*(\mathbf{r},E,0)[F_p + F_d]\psi(\mathbf{r},E,t)\, d\mathbf{r}\, dE$$

$$\eta_k(t) = \int_{-\infty}^{t} \frac{\bar{\beta}_k(t')}{\Lambda(t')}\, \phi(t') e^{-\lambda_k(t-t')}\, dt'.$$

The shape equation is readily derived from Eq. (1) by insertion of Eq. (2). Division by $\phi(t)$ gives

$$[-M + F_p]\psi(\mathbf{r},E,t) + \frac{S_d[\phi(t')\psi(\mathbf{r},E,t')]}{\phi(t)} = \frac{1}{v}\left[\frac{\psi(\mathbf{r},E,t)}{\phi(t)}\frac{d\phi}{dt} + \frac{\partial}{\partial t}\psi(\mathbf{r},E,t)\right]. \tag{6}$$

In addition the constraint condition (3) must be fulfilled.

Equations (6) and (4) are coupled in three ways:

a. The delayed source term depends on $\phi(t')$ and also is divided by $\phi(t)$.

b. The right hand side of Eq. (6) contains the term $\frac{1}{\phi}\frac{d\phi}{dt}$.

c. The feedback results in a time-dependence in all cross sections; the cross sections are functions of the full flux at $t' \leq t$.

Up to this point the factorizing approach does not introduce any approximation. It has led, however, to a more complicated formulation than the original. The advantage is gained when one makes use of an assumption which is mostly fulfilled, namely: The time dependence of the shape function is of lesser importance than the time dependence of the amplitude function. This will be utilized in all factorizing methods in a characteristic way: One calculates *many* values of the *amplitude* along the time axis but only a *few shape functions*.

The specific approximations inherent in each method are described below. In addition to these fundamental approximations, in any numerical solution one must introduce discretization and linearization errors. Since these errors are dependent on the skill and ingenuity of the analyst who formulates the numerical solution they cannot be discussed independent of a specific formulation.

POINT REACTOR MODEL

This commonly used factorization method is based on the primary assumption that the shape function used in computing the integral quantities of Eq. (5) is time independent, and equal to the steady state solution of Eq. (6) at $t = 0$. This assumption removes all coupling between Eqs. (4) and (6), such that reactivity changes may be precomputed and inserted into Eq. (4). Feedback partial reactivities may be expressed as functions of $\phi(t)$ with precalculated coefficients. In principle, any given partial reactivity may be expressed as a function of several system parameters to account for the interdependence of the partial reactivities. This technique becomes laborious in practice.

The greatest weakness of this model lies in the $\rho(t)$ function in Eq. (5). This fact may be illustrated by considering the second order error terms which arise from use of this perturbation expression. If ΔA represents the total change in the diffusion operator since time $t = 0$ and $\Delta\psi$ represents the change in shape function, the error term relative to the computed perturbation reactivity may be written as

$$\frac{\iint \psi^*\Delta A\Delta\psi\, d\mathbf{r}\, dE}{\iint \psi^*\Delta A\psi_0\, d\mathbf{r}\, dE}. \tag{7}$$

ΔA may be localized in the $(\mathbf{r},E)$ space, and it is common in weakly coupled systems for this asymmetry in ΔA to result in a $\Delta\psi$ which is of the same order as ψ_0. Therefore the neglected term can be of the same order as the calculated $\rho(t)$. It is obvious that the error in $\rho(t)$ must be much smaller than this in the range $\rho \approx \beta$ if the computed $\phi(t)$ is to bear any relation to the true value. Note that the ΔA operator includes space-differential terms. If these terms are significant, one must also be concerned with the magnitude of the error $\Delta\frac{\partial\psi}{\partial\mathbf{r}}$ in the first spatial derivative of ψ.

The allowable error in $\rho(t)$ decreases with the neutron generation time $\Lambda(t)$ in this range due to the greater importance of super-prompt critical transients to the subsequent behavior of the system.

The point model is very rarely used in the form described here. Instead, it is common to precompute partial reactivity changes for the known system

changes (such as control rod removal), using the asymptotically correct ψ functions for those changes. This procedure in reality makes use of one form of the so-called adiabatic model.

ADIABATIC MODELS[5,7]

The *simplest type* of adiabatic model was introduced in the preceding paragraph. Three fundamental approximations are required. First, it does not distinguish the shape of the delayed neutron source from the shape of the prompt source, thus neglecting the time retardation in adjustment of the shape of the precursor distribution:

$$F_p\psi(\mathbf{r},E,t) + \frac{S_d[\phi(t')\psi(\mathbf{r},E,t')]}{\phi(t)} \rightarrow F\psi(\mathbf{r},E,t). \quad (8)$$

Secondly, it neglects both time derivative terms in Eq. (6). Instead, an eigenvalue is applied to get a stationary expression for the shape function

$$\left[-M + \frac{1}{k}F\right]\psi(\mathbf{r},E,t) = 0. \quad (9)$$

Thirdly, the explicit coupling between the shape equation, Eq. (9) and the amplitude Eq. (4) via feedback functions is neglected, making the two equations completely independent.

In this model, the static Eq. (9) is solved repeatedly to calculate the "time dependent" flux shape corresponding to a given set of compositions. These shape functions are then used prior to the calculation of the amplitude to compute the integral quantities from Eq. (5). Then, in a completely decoupled second step, these quantities are used as input to a point kinetics code which gives the flux amplitude $\phi(t)$.

This model has been shown[8] to describe the major part of the spatial effects in reactor kinetics. It is, however, restricted to problems in which the states that the system will assume during an excursion are known in advance.

The *second type* of adiabatic model also employs Eq. (9) for obtaining the shape function. The difference is that the equation is solved sequentially in parallel with Eq. (4). Thus the feedback reactivity coupling (which appears in operators M and F) may be accounted for. Also, due to the sequential nature of the ψ solutions, this method is not restricted in application as is the first type of adiabatic model.

QUASISTATIC APPROXIMATION[1-4]

This method contains only one fundamental approximation, namely, the time derivative of $\psi(\mathbf{r},E,t)$ in Eq. (6) is neglected. Equations (4) and (6) are solved sequentially, as in the second type of adiabatic model. The delayed neutron precursor distribution $S_d[\Phi(\mathbf{r},E,t$ is found directly from the flux history, and the curre ϕ and $d\phi/dt$ values from Eq. (4) are inserted into E (6).

The most important improvement over the adiabat method lies in the treatment of the delayed neutr precursor distribution. Some examples of the impo tance of this inclusion to very weakly coupled systen are given below.

IMPROVED QUASISTATIC (DIRECT FACTORIZATION) METHOD[9]

This method solves the full Eq. (6). It only replac the derivative of ψ by a backward difference of fir order:

$$\frac{\partial}{\partial t}\psi(\mathbf{r},E,t) = \frac{[\psi(\mathbf{r},E,t) - \psi(\mathbf{r},E,t-\Delta t)]}{\Delta t}, \quad (10$$

where $t - \Delta t$ is the time of the last shape calculatio With this we obtain an equation which is formall identical to that of the quasistatic approach. Since th shape function is slowly varying, this first order diffe ence form can be applied over a much larger Δt interv than would be possible for $\Phi(\mathbf{r},E,t)$.

In this approximation one actually computes ψ fro the equation

$$\left[-M + F_p - \frac{1}{v}\left(\frac{1}{\phi}\frac{d\phi}{dt} + \frac{1}{\Delta t}\right)\right]\psi(\mathbf{r},E,t) = -\left\{\frac{S_d[\phi(t')\psi(\mathbf{r},E,t')]}{\phi(t)} + \frac{\psi(\mathbf{r},E,t-\Delta t)}{v\Delta t}\right\}. \quad (11$$

On inspection of Eq. (11) it can be seen that, fo cases of practical interest, the space and energy shap of ψ is relatively insensitive to errors in ϕ and it derivative. This is due primarily to the fact that the multiplier on the time derivative terms makes ther very small in realistic cases. In addition, the first ter on the right hand side of Eq. (11) consists of a convolu tion integral over all $t' \leq t$, and so is relatively insensi tive to errors in $\phi(t')\psi(\mathbf{r},E,t')$, which accumulate onl over the interval Δt. Errors in the denominator of th term tend to scale the magnitude of $\psi(\mathbf{r},E,t)$ but do no greatly affect its space-energy distribution. The scalin error can be removed by application of the constrai condition, Eq. (3).

The effectiveness of this form of the shape-functio time-derivative in extreme cases is illustrated in th next section. A summary of the approximations applie in this sequence of models is given in Table VI-2-I.

SAMPLE PROBLEMS

For purposes of illustration one simple slab react was selected. The material constants for the initi

critical system are taken from Ref. 8; they are reproduced in Table VI-2-II. Two variants of this reactor, are presented and labelled "Thermal Core" and "Fast Core 2". The second case is identical to the thermal core with the exception of the inverse velocities, which are 9.97486×10^{-9} and 4.26076×10^{-8} (cm/sec)$^{-1}$ for groups 1 and 2, respectively.

With the exception of the different transverse bucklings in the three regions, the reactor is homogeneous. Region 1 extends from 0 to 60 cm, region 2 from 60 to 180 cm, and region 3 from 180 to 240 cm.

Transients are induced by a linear increase in ν in Region 1 according to $\nu(t) = (1 + 1.50832\ t)\nu(0)$. The ramp is terminated at 0.011 sec. One effective group is used for precursors and delayed neutrons, with $\beta = 0.0064$ and $\lambda = 0.08$ sec^{-1}. These values are held constant in order to simplify the comparison of thermal and fast core results.

The transients were computed using models: point, adiabatic, quasistatic (the QX1 program),[3] improved quasistatic (the modified QX1 code, FX1),[9] and direct numerical (WIGLE).[10]

The largest error arising from the adiabatic approximation is due to the assumption that the delayed neutron source density at any time is proportional to the total flux at that time. This neglect of the time delay of the adaption of the precursor spatial distribution to a distorted flux shape introduces an error in the computed shape and therefore an error in the growth or decay rate of the total flux. This error is removed in the quasistatic model by correct treatment of the delayed neutron source distribution; the remaining error is due to neglect of the delay in adaption of the flux shape due to the finite prompt neutron generation time. Figure VI-2-1 shows the true flux shape and precursor spatial distribution at the end of the ramp and the asymptotic flux shape, for the thermal core. The asymptotic shape is identical to that which is used in calculation of the adiabatic reactivity at the end of the ramp, with the exception of the small difference between the shapes of the λ-mode (adiabatic) and the ω-mode (correct).

TABLE VI-2-I. Sequence of Approximation in Factorizing Methods Showing Effects Treated by the Various Models

Term	Model					
	Direct Numerical	Improved Quasistatic	Quasistatic	Adiabatic	Adiabatic with Precalculated Shape Functions	Point Kinetics
$\frac{\partial\psi}{\partial t}$	yes	approx.	no	no	no	no
$\frac{1}{v}\frac{1}{\phi}\frac{d\phi}{dt}$	yes	yes	yes	no	no	no
$S_d[\phi\psi]$	yes	yes	yes	no	no	no
Implicit coupling via feedback	yes	yes	yes	yes	no	no
Decoupled shape distortion	yes	yes	yes	yes	yes	no
Initial shape	yes	yes	yes	yes	yes	yes

TABLE VI-2-II. Two Group Constants for Thermal Core

D_1, cm	1.69531
D_2, cm	0.409718
Σ_{a1}, cm^{-1}	0.0137513
Σ_{a2}, cm^{-1}	0.261361
Σ_{21}, cm^{-1}	0.0164444
$\nu\Sigma_{f1}$, cm^{-1}	0.0194962
$\nu\Sigma_{f2}$, cm^{-1}	0.497857
B^2, cm^{-2}	
Region 1	0.01090505
Region 2	0.01199452
Region 3	0.01088500
$1/v_1$, (cm/sec)$^{-1}$	0.
$1/v_2$, (cm/sec)$^{-1}$	4.5455×10^{-6}
χ_1	1.0
χ_2	0.

In Fig. VI-2-2 the reactivity versus time values are plotted for four models in the thermal core and in fast core 2. Note that the QX1 reactivity is higher than the true value (as derived from WIGLE calculations); however the error is much smaller than that arising from the adiabatic approximation. The dashed curve representing the reactivity function in the fast core is seen to rise essentially to the asymptotic value by the end of the ramp. This is due primarily to the more rapid increase of the flux amplitude relative to the delayed neutron source density in this range, which results in a smaller influence of delayed neutrons on the flux shape and hence on the system reactivity.

The errors in the total flux in the fast group at two points in the reactor for the adiabatic and quasistatic approximations are shown in Fig. VI-2-3 for both cases. The figure presents the ratio of the total flux in group 1 of the two group scheme as computed using each model, relative to the WIGLE flux at two points, $x = 45$ cm and $x = 195$ cm. These are approximately the points of maximum and minimum relative error. The group 2 relative errors are essentially the same. By comparison of the adiabatic and quasistatic results it can be seen that incorrect treatment of the delayed

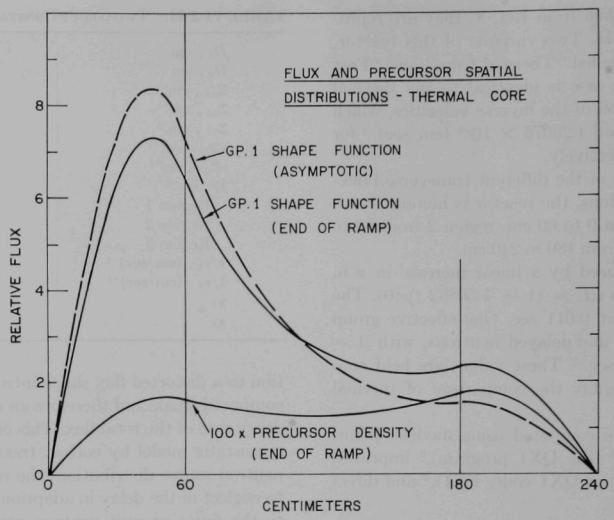

FIG. VI-2-1. Spatial Distribution of Fast Group Shape Function and Delayed Precursor Concentration in Thermal Core. *ANL Neg. No. 112-9832.*

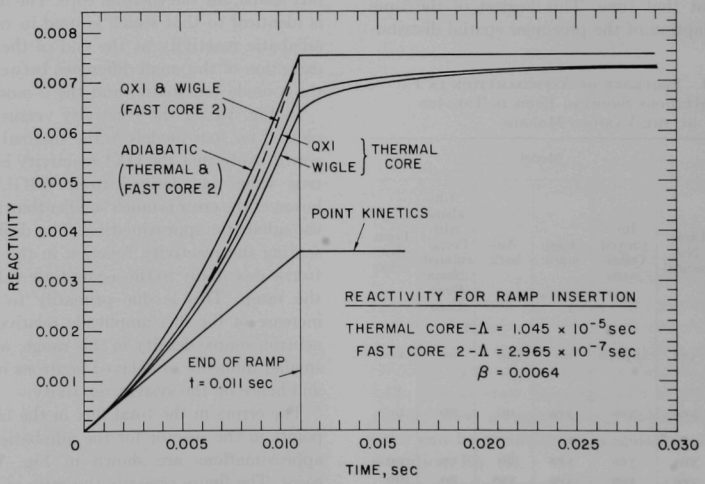

FIG. VI-2-2. Reactivity Versus Time for Limited Ramp Insertion in Thermal Core and Fast Core 2, for Point, Adiabatic, Quasistatic and WIGLE Models. *ANL Neg. No. 112-9835 Rev. 1.*

neutron distribution is the larger source of error in the adiabatic model. Note that the asymptotic relative error in the quasistatic model drops from 8.5% to 4.5% in going from the thermal to the fast core. In the latter case virtually all of the error is accumulated in the are of the prompt critical transition, which is reached a 0.01 seconds. The reason is that the effect of the delaye neutron source on the flux shape decreases rapidly i

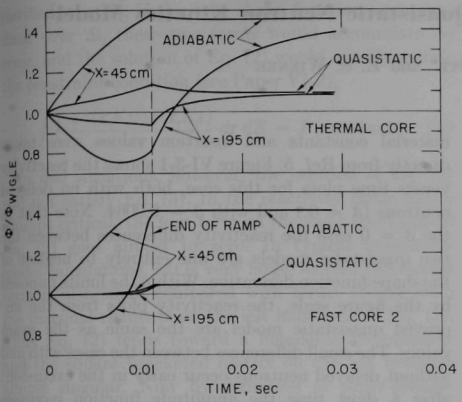

FIG. VI-2-3. Total Flux Relative to WIGLE Values at Positions $x = 45$ cm and $x = 195$ cm in 240 cm Slab Reactors. *ANL Neg. No. 113-664.*

this range, resulting in a large shape function time derivative term and hence an appreciable error due to its neglect in the quasistatic model. The improved quasistatic model, as described in Ref. 9, introduces no error relative to WIGLE, so that the corresponding total flux ratios are 1.0 for both cases at all times. The errors of the point kinetics model are not shown since they are unbounded in time.

SUMMARY

Four degrees of sophistication of factorizing methods have been listed and discussed: point, adiabatic, quasistatic, and improved quasistatic. For treatment of non-linear problems, each of these methods has an accuracy advantage over the next lower order approximation. They have in common the principle that only a few shape functions are computed, as required by the particular problem being solved. As a result of this feature very little additional effort either in programming or problem run time is required to improve accuracy and general applicability within the sequence. The logical conclusion is that one should choose the best approximation, namely the improved quasistatic method, in designing a neutronics calculation model for treatment of non-linear space-time problems. In general, this method is particularly well suited for non-linear problems, since it involves an iterative solution in successive time intervals. The multigroup program FX1 embodying the improved quasistatic model, has been developed from the QX1 program for the purpose of fast reactor dynamics analysis.

REFERENCES

1. K. Ott, *Quasistatic Treatment of Spatial Phenomena in Reactor Dynamics*, Nucl. Sci. Eng. **26,** 563 (1966). J. T. Madell, Appendix to: *Quasistatic Treatment of Spatial Phenomena in Reactor Dynamics*, Nucl. Sci. Eng. **26,** 564 (1966).
2. K. Ott, D. A. Meneley and E. S. Wiener, *Quasistatic Treatment of Fast Reactor Excursions*, Reactor Physics Division Annual Report, July 1, 1965 to June 30, 1966, ANL-7210, pp. 370–373.
3. D. A. Meneley, K. Ott and E. S. Wiener, *Space-Time Kinetics, the QX1 Code*, Reactor Physics Division Annual Report, July 1, 1966 to June 30, 1967, ANL-7310, pp. 471–476.
4. K. O. Ott and D. A. Meneley, *Accuracy of the Quasistatic Treatment of Spatial Reactor Kinetics*, Nucl. Sci. Eng. (submitted for publication).
5. A. F. Henry, *The Application of Reactor Kinetics to the Analysis of Experiments*, Nucl. Sci. Eng. **3,** 52 (1958).
6. E. P. Gyftopoulos, *The Technology of Nuclear Reactor Safety*, (MIT Press, Cambridge, Massachusetts, 1964) Vol. 1, p. 179.
7. A. F. Henry and N. J. Curlee, *Verification of a Method of Treating Neutron Space-Time Problems*, Nucl. Sci. Eng. **4,** 727 (1958).
8. J. B. Yasinsky and A. F. Henry, *Some Numerical Experiments Concerning Space-Time Reactor Kinetics Behavior*, Nucl. Sci. Eng. **22,** 171 (1965).
9. D. A. Meneley, K. O. Ott and E. S. Wiener, *Influence of the Shape Function Time Derivative on Spatial Kinetics Calculations in Fast Reactors*, Trans. Am. Nucl. Soc. **11,** 225 (1968).
10. W. R. Cadwell, A. F. Henry and A. J. Vigilotti, *WIGLE—A Program for the Solution of the Two-Group Space-Time Diffusion Equations in Slab Geometry*, WAPD-TM-416 (1964).

VI-3. Further Developments of the Quasistatic Neutron Kinetics Model

D. A. Meneley, K. O. Ott* and E. S. Wiener

Introduction

Development and testing of the QX1 program[1-3] has led to several changes in the model and calculation methods from those originally reported. The most important of these are inclusion of the time derivative of the flux shape function,[4] and an improved iteration procedure for evaluation of the shape function. In addition, the necessary modifications have been made to allow calculation of cases with external sources, according to the formulation reported in Ref. 3.

Shape Function Derivative

The basic quasistatic model neglects the time partial derivative of the shape function which appears in the factorized equations (see Eq. (9), Ref. 3). This neglect is justified by the fact that the shape function varies slowly in realistic cases, since its variation is determined largely by the rate of change of system parameters. These parameters are certainly slowly varying (at least in fast reactors) on the scale of a few neutron generation times, which is the time scale on which the shape function responds to changed system conditions. This basic model probably gives adequate precision for the great majority of fast reactor dynamics problems.

It has been found[4] that the range of applicability of the model can be extended even to extreme cases in reactors with long generation times. This is accomplished by replacing the time derivative by a backward linear difference form

$$\left.\frac{\partial\psi}{\partial t}\right|_t \approx [\psi(t) - \psi(t - \Delta t)]\frac{1}{\Delta t}, \tag{1}$$

where t is the time at which ψ is being evaluated and Δt is the time interval since the last calculation of the shape function, $\psi(t - \Delta t)$. Since the time Δt may be large compared with the generation time, this is not a very accurate form; however, since the term is small in realistic cases, great precision is not required. In any event, since the interval Δt can be reduced as desired by reduction of convergence limits the model can be made to yield essentially exact results for any type of excursion.

As an example of the behavior of the improved quasistatic model in an extreme case, the super-prompt critical excursion in the 240 cm thermal core of Ref. 5 was run with both the basic and improved models. The material constants and insertion values were taken directly from Ref. 5. Figure VI-3-1 shows the reactivity versus time plots for this case, both with no delayed neutrons ($\beta = 0.$) and with $\beta = 0.0064$. Note that in the $\beta = 0$ case the reactivity differences between the two quasistatic models are due entirely to neglect of the shape function derivative. Within the limits imposed by the figure scale, the reactivity plots from the improved quasistatic model are the same as the exact values. The small differences between the cases with and without delayed neutrons occur early in the excursion; after a short time the amplitude function increases rapidly, thus reducing the influence of the delayed neutrons to essentially zero.

The reactivity plots from the improved quasistatic model contain some small discrepancies relative to WIGLE,[6] due to the fact that the shape function time intervals were relatively large in the first one or two milliseconds. The approximation to the shape derivative term thus introduces a noticeable truncation error in this extreme case. The resultant amplitude error has a maximum value of about 3% relative to WIGLE, as shown in Fig. VI-3-2.

Shape Function Iteration Procedure

A new method for calculation of the shape function has been found, which greatly reduces the total number of inner iterations required to obtain a solution when the system reactivity is above prompt critical. This is particularly useful in the multigroup (20–30 groups) problems which are typical of fast reactor excursion analysis.

The shape equation in the improved quasistatic model may be written (see Paper VI-2)

$$\left[-M + F_p - \frac{1}{v}\left(\frac{1}{\phi}\frac{d\phi}{dt} + \frac{1}{\Delta t}\right)\right]\psi(\mathbf{r},E,t) = -\left\{\frac{S_d[\phi(t')\psi(\mathbf{r},E,t')]}{\phi(t)} + \frac{\psi(\mathbf{r},E,t-\Delta t)}{v\Delta t}\right\}. \tag{2}$$

This is seen to be an inhomogeneous, ordinary differential equation. Note that the $\frac{1}{\phi}\frac{d\phi}{dt}$ and $S_d[\phi(t')\psi(\mathbf{r},E,t')]/\phi(t)$ terms are the result of the approximate solution of the amplitude and precursor equations over the range Δt, under the assumption of constant shape function in this interval; therefore they contain errors accumulated over Δt. If the assumption were fully

* Purdue University, Lafayette, Indiana.

justified, that is, if the true shape function were constant over Δt, these two terms would accumulate no error, and the solution of Eq. (2) would exactly satisfy the constraint condition (see Paper VI-2),

$$\iint \frac{\psi^*(\mathbf{r},E,0)\psi(\mathbf{r},E,t)}{v}\, d\mathbf{r}\, dE = P(\text{constant}). \quad (3)$$

In real situations, however, the solution of Eq. (2) will not satisfy Eq. (3). In the reactivity range above prompt critical, the first term on the right hand side of Eq. (2) goes almost to zero. In typical quasistatic model calculations, $v\Delta t$ is very large, so that the second term is also small compared with terms arising from the diagonal elements on the left hand side of Eq. (2). Thus Eq. (2) tends toward a homogeneous equation and the square bracketed matrix on the left becomes almost singular. Now by definition of super-prompt criticality, the largest eigenvalue of the matrix $-M + F_P$ is greater than zero, and it is the term $-\frac{1}{v}\left(\frac{1}{\phi}\frac{d\phi}{dt} + \frac{1}{\Delta t}\right)$ which holds the largest eigenvalue of the square bracketed matrix to a value slightly less than zero. It follows that a small error in $\frac{1}{\phi}\frac{d\phi}{dt}$ may have a large effect on this eigenvalue and hence a large effect on the *magnitude* of the resultant ψ solution. This leads to the usual problems of slow convergence and poor acceleration associated with this type of equation.

The technique which has been developed to avoid this problem involves a modification of Eq. (1) and addition of an iteration between the ψ solution at t and

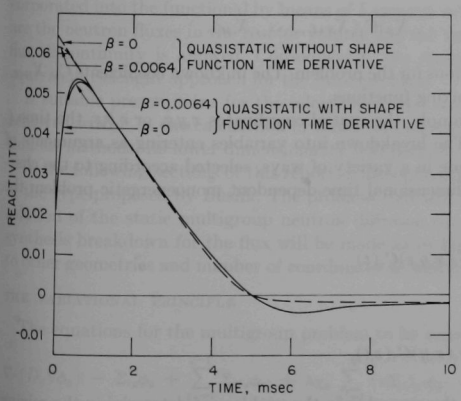

FIG. VI-3-1. Reactivity Versus Time Given by the Quasistatic Model for the Super-Prompt Critical Excursion in the 240 cm Thermal Core as Described in Ref. 5. *ANL Neg. No. 113-795.*

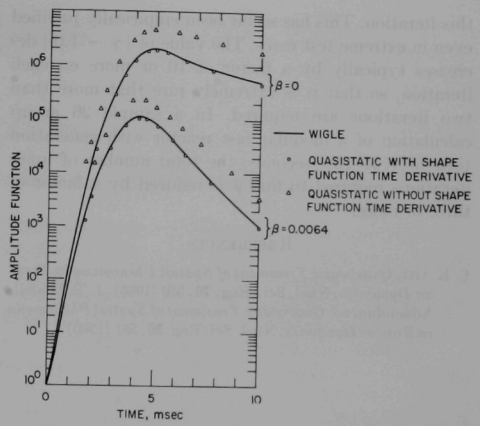

FIG. VI-3-2. Amplitude Functions Corresponding to the Reactivity Insertions of Fig. VI-3-1. *ANL Neg. No. 113-796.*

the amplitude solution over the range Δt. Eq. (2) becomes

$$\left[-M - \frac{1}{v}\left(\frac{1}{\phi}\frac{d\phi}{dt}\right)\right]\psi'(\mathbf{r},E,t) = -\frac{1}{\gamma}F_p\psi'(\mathbf{r},E,t) - \left\{\frac{S_d[\phi(t')\psi(\mathbf{r},E,t')]}{\phi(t)} + \frac{\psi(\mathbf{r},E,t-\Delta t)}{v\Delta t}\right\}, \quad (4)$$

where

$$\gamma = \frac{1}{P}\iint \frac{\psi^*(\mathbf{r},E,0)\psi'(\mathbf{r},E,t)}{v}\, d\mathbf{r}\, dE.$$

The γ factor is recomputed after each mesh sweep during the inner iterations; thus the solution procedure resembles a standard power iteration technique, with the exception of inclusion of the small inhomogeneous term. The ψ' solution will satisfy Eq. (3) within the factor $\gamma \approx 1.0$.

After the ψ' solution is obtained the γ factor is examined. If it is significantly different from 1.0, the amplitude solution is recalculated over the Δt range, with coefficients determined using a linear interpolation of $\psi(\mathbf{r},E,t-\Delta t)$ and $\psi'(\mathbf{r},E,t)$ for the shape function within the range. Equation (4) is then solved again with the updated values from the amplitude solution, and the iteration proceeds. Since the linear interpolation is consistent with the assumption (Eq. (1)) on the shape function time derivative, this iteration procedure will converge to $\gamma \equiv 1.0$ and $\psi'(\mathbf{r},E,t) \equiv \psi(\mathbf{r},E,t)$ provided the $\psi'(\mathbf{r},E,t)$ solution is closer to $\psi(\mathbf{r},E,t)$ than is $\psi(\mathbf{r},E,t-\Delta t)$, which is the first estimate of $\psi(\mathbf{r},E,t)$ in

this iteration. This has so far been empirically justified even in extreme test cases. The value of $|\gamma - 1.0|$ decreases typically by a factor of 10 or more on each iteration, so that it is extremely rare that more than two iterations are required. In a sample 26 group calculation of a modular fast reactor with generation time of 4×10^{-7} seconds, the total number of inner iterations required to find ψ is reduced by a factor of three or more.

References

1. K. Ott, *Quasistatic Treatment of Spatial Phenomena in Reactor Dynamics*, Nucl. Sci. Eng. **26**, 559 (1966). J. T. Madell, Addendum to: *Quasistatic Treatment of Spatial Phenomena in Reactor Dynamics*, Nucl. Sci. Eng. **26**, 561 (1966).
2. K. Ott, D. A. Meneley and E. S. Wiener, *Quasistatic Treatment of Fast Reactor Excursions*, Reactor Physics Division Annual Report, July 1, 1965 to June 30, 1966, ANL-7210.
3. D. A. Meneley, K. O. Ott and E. S. Wiener, *Space-Time Kinetics, The QX1 Code*, Reactor Physics Division Annual Report, July 1, 1966 to June 30, 1967, ANL-7310.
4. D. A. Meneley, K. O. Ott and E. S. Wiener, *Influence of the Shape Function Time Derivative on Spatial Kinetics Calculations in Fast Reactors*, Trans. Am. Nucl. Soc. **11**, 225 (June 1968).
5. J. B. Yasinsky and A. F. Henry, *Some Numerical Experiments Concerning Space-Time Reactor Kinetics Behavior*, Nucl. Sci. Eng. **22**, 171 (1965).
6. W. R. Cadwell, A. F. Henry and A. J. Vigilotti, *WIGLE—A Program for the Solution of the Two-Group Space-Time Diffusion Equations in Slab Geometry*, WAPD-TM-416 (1964).

VI-4. Variational Flux Synthesis With Discontinuous Trial Functions

V. Luco and G. K. Leaf*

Introduction

The continuously increasing demand for more accurate descriptions of the neutron flux distribution in complex reactor systems has been the driving force behind the development of approximate flux synthesis techniques to calculate those neutron flux distributions. Using these techniques a reasonably accurate picture of the neutron flux distribution is obtained at a substantially lower cost than a comparable "exact" calculation using straight finite difference approximations to the equations of the problem.

The idea of flux synthesis in reactor physics consists of the assumption that the multi-dimensional neutron fluxes in the reactor, let us say $\phi(X_1,X_2, \cdots, X_M)$, can be represented with reasonable accuracy by a linear combination of a finite (and usually small) number of known functions $\psi_i(X_1, \cdots, X_S)$ of lower dimensionality $(S \leq M)$:

$$\phi(X_1, X_2, \cdots, X_M) \approx \sum_{i=1}^{M} \psi_i(X_1, \cdots, X_S) C_i(X_{S+1}, \cdots, X_M).$$

The functions of $\psi_i(X_1, \cdots, X_S)$ are known as the trial functions for the problem. The unknown coefficients $C_i(X_{S+1}, \cdots, X_M)$ of the linear combination are usually called the mixing functions.

The variables of the problem can be quite diverse: for example, the spatial coordinates x,y,z, or r,θ,z, the time t, the neutron energy E, the angle Ω of the neutron motion. The breakdown into variables entering as arguments of the trial functions or of the mixing functions can also be made in a variety of ways, selected according to the characteristics of the problem at hand. For example in a three-dimensional time-dependent monoenergetic problem the synthesis assumption could be

$$\phi(x,y,z,t) \approx \sum_{i=1}^{M} \psi_i(x,y,z) C_i(t)$$

or

$$\phi(x,y,z,t) \approx \sum_{i=1}^{M} \psi_i(x,y) C_i(z,t).$$

In the first case the mixing functions are time functions; in the second case the problem of determining the mixing functions is two-dimensional. Another example: The two-dimensional flux $\phi(r,z)$ can be synthesized as follows:

* Applied Mathematics Division, Argonne National Laboratory.

$$\phi(r,z) \approx \sum_{i=1}^{M} \psi_i(r) C_i(z)$$

or

$$\phi(r,z) \approx \sum_{i=1}^{M} \psi_i(z) C_i(r), \tag{1}$$

and the choice between these two options will depend on which one of the expressions is more convenient in the particular reactor configuration being considered.

The object of a flux synthesis calculational method is to specify some way of obtaining the mixing functions. As the synthesis expansions are essentially approximations, the determination of the coefficient functions is done not with the idea of actually obtaining the exact solution, but aiming at an optimum choice as judged with some arbitrarily chosen criterion. The goodness of approximation to the real fluxes of these synthesis solutions depends largely on how good a choice of trial functions ψ_i has been made. There are a number of flux synthesis methods, depending both on the type of trial functions used and on the techniques prescribed to determine the mixing functions.

The most successful and commonly used synthesis techniques are the variational synthesis methods. In the variational method, once the trial functions have been selected, the determination of the mixing functions is done in such a way as to produce second order errors in some reactor parameter of interest, usually k_{eff}. The earliest developments of these techniques were done using continuous sets of trial functions. This means that the same set of trial functions $\psi_i(X_1, \cdots, X_S)$ are used throughout the whole range of the variables $X_1, \cdots, X_M$. In some cases though it is clear that some of the trial functions $\psi_i(X_1, \cdots, X_S)$ used are important only over certain ranges of the variables and could be ignored at other locations in the reactor.

A synthesis method that allows one to do precisely this, that is, to expand the flux in different sets of trial functions at different locations in the reactor, is known as a discontinuous trial function synthesis. Variational synthesis techniques have been developed that synthesize fluxes using discontinuous trial functions and achieve accuracy in the approximation of fluxes and eigenvalues comparable to those obtained by the continuous methods and at a lower computational cost.[1,2] The functional used in these variational techniques is a special functional proposed by D. Selengut (Knolls Atomic Power Laboratory), which avoids the mathematical difficulties encountered when the usual functional is used together with discontinuous trial functions. It uses both the neutron fluxes and neutron currents in the reactor volume as independent-variable functions—that is, as functions that admit arbitrary variations.

Recently A. Buslik[3] has proposed another functional that can be used as the basis for a discontinuous trial function synthesis method. In it the continuity conditions for flux and adjoint are treated as subsidiary conditions and incorporated into the functional by means of Lagrange multipliers. The independent-variable functions in his functional are the neutron fluxes in the reactor volume and the normal neutron current at those inside reactor surfaces where a flux discontinuity is allowed. Consequently, the dimensionality of the synthesis problem posed is lower than the equivalent Selengut approach for the same problem.

If suitable prescriptions for the selection of trial functions are developed for Buslik's approach and the accuracy achieved with it in the calculation of fluxes and eigenvalues is comparable to that of the presently available discontinuous methods, its lower dimensionality will perhaps result in a more economic calculation.

In the following sections of this report, a discontinuous flux synthesis technique is presented, based on a functional of the type proposed by Buslik. The problem that will be used to illustrate the method proposed is the approximate solution of the static multigroup neutron diffusion equations in two-dimensional (r,z) cylindrical coordinates. The synthesis breakdown for the flux will be made as in Eq. (1). The method proposed can of course be easily adapted to other geometries and number of coordinates as well as to other synthesis expansions.

THE VARIATIONAL PRINCIPLE

The equations for the multigroup problem to be considered are

$$\nabla\cdot(D_g\nabla\phi_g) - \Sigma_{rg}\phi_g + \sum_{g'=1}^{g-1} \Sigma_{g'g}\phi_{g'} + \lambda\chi_g \sum_{g'=1}^{G} (\nu\Sigma_f)_{g'}\phi_{g'} = 0, \qquad g = 1, \cdots, G, \text{ the number of energy groups,} \tag{2}$$

and the adjoint set

$$\nabla\cdot(D_g\nabla\phi_g^*) - \Sigma_{rg}\phi_g^* + \sum_{g'=g+1}^{G} \Sigma_{gg'}\phi_{g'}^* + \lambda(\nu\Sigma_f)_g \sum_{g'=1}^{G} \chi_{g'}\phi_{g'}^* = 0 \qquad g = 1, \cdots, G, \tag{3}$$

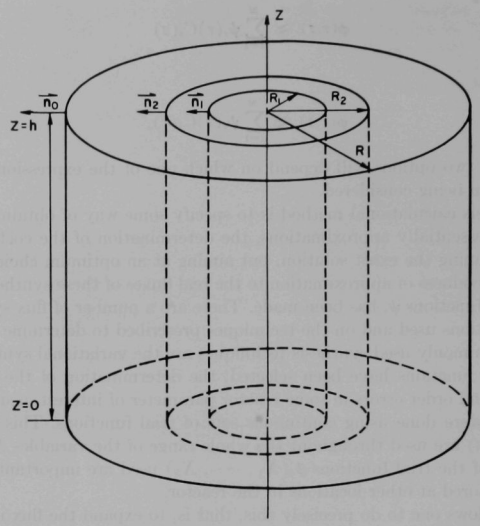

FIG. VI-4-1. Schematic Representation of the Reactor. *ANL Neg. No. 113-666 T-1.*

with conditions

$$\left.\begin{aligned} \frac{\phi_g}{2} &= -D_g \frac{\partial \phi_g}{\partial n} \\ \frac{\phi_g^*}{2} &= -D_g \frac{\partial \phi_g^*}{\partial n} \end{aligned}\right\} g = 1, \cdots, G \text{ at the outside reactor boundary } S_0 \tag{4}$$

with the usual meanings for the constants. $\partial/\partial n$ indicates derivative with respect to the positive (meaning *out-going*) normal vector at the outside reactor surfaces.

The reactor geometry is represented in Fig. VI-4-1. The regions shown, limited by the radii $R_1, R_2, \cdots R_i, \cdots$, are synthesis regions where different sets of trial functions will be assumed. There may be quite a few of these regions for a practical calculation. The trial functions used will be functions of the z coordinate, one set in each region, for both flux and adjoint. The cylindrical surfaces of radii R_i are the surfaces at which the trial function discontinuities occur. θ symmetry is assumed throughout.

The variational functional to be used is

$$\begin{aligned} J[u_g^k(r,z), u_g^{k*}(r,z), \alpha_g^k(z), \beta_g^k(z)] \equiv \sum_{k=1}^{K} \Bigg\langle 2\pi \int_{V_k} \sum_{g=1}^{G} \Bigg\{ \nabla u_g^{k*} \cdot D_g \nabla u_g^k + u_g^{k*} \Bigg[\Sigma_{rg} u_g^k - \sum_{g'=1}^{G-1} \Sigma_{g'g} u_{g'}^k \\ - \lambda \chi_g \sum_{g'=1}^{G} (\nu\Sigma_f)_{g'} u_{g'}^k \Bigg] \Bigg\} r dr dz \Bigg\rangle - \sum_{k=1}^{K-1} \Bigg\langle 2\pi R_k \int_0^h \sum_{g=1}^{G} \{ \alpha_g^k [u_g^{(k+1)}(R_k,z) - u_g^k(R_k,z)] \\ + [u^{(k+1)*}(R_k,z) - u_g^{k*}(R_k,z)] \beta_g^k \} dz \Bigg\rangle + \sum_{g=1}^{G} \Bigg\langle \sum_{k=1}^{K} \Bigg\{ \pi \int_{R_{(k-1)}}^{R_k} [u_g^{k*}(r,h) u_g^k(r,h) + u_g^{k*}(r,0) u_g^k(r,0)] r dr \Bigg\} \\ + 2\pi R \int_0^h \Bigg[u_g^{K*}(R,z) \frac{u_g^K(R,z)}{2} + \frac{\partial u_g^{1*}}{\partial r}\bigg|_{r=0} \cdot \frac{\partial u_g^1}{\partial r}\bigg|_{r=0} \Bigg] dz \Bigg\rangle, \end{aligned} \tag{5}$$

where

V_k is the volume between $R_{k-1} \le r \le R_k$, $0 \le z \le h$.

$u_g^{k*}(r,z)$, $u_g^k(r,z)$ are independent-variable functions defined in region K.

These will be identified later with $\phi_g^{k*}(r,z)$ and $\phi_g^k(r,z)$ when at their stationarv values.

$\alpha_g^k(z)$, $\beta_g^k(z)$ are functions of z only, defined at the cylindrical surfaces with radius R_k.
There are K synthesis regions:

$$R_0 = 0$$

$$R_K \equiv R, \text{ the outside reactor radius.}$$

The k-dependence of the parameters in the functional has not been emphasized since the k boundaries may not be boundaries between different material compositions.

Which among the family of functions $u_g^k(r,z)$, $u_g^{k*}(r,z)$, $\alpha_g^k(z)$ and $\beta_g^k(z)$ will make the functional J stationary? To find out the conditions to be satisfied by the $u_g^k(r,z)$ and $\beta_g^k(z)$, the first term in the volume integrals in Eq. (5) is transformed in the following way, using Green's theorem:

$$\begin{aligned}\sum_{=1}^{K}\sum_{g=1}^{G} 2\pi \int_{V_k} \nabla u_g^{k*}\cdot D_g \nabla u_g^k r dr dz &= -\sum_{k=1}^{K}\sum_{g=1}^{G} 2\pi \int_{V_k} u_g^{k*}\nabla\cdot(D_g\nabla u_g^k) r dr dz \\ &+ \sum_{k=1}^{K-1}\sum_{g=1}^{G}\left\{2\pi R_k \int_0^h \left[u_g^{k*}(R_k,z) D_g \left.\frac{\partial u_g^k}{\partial r}\right|_{r=R_k} - u_g^{(k+1)*}(R_k,z) D_g \left.\frac{\partial u_g^{(k+1)}}{\partial r}\right|_{r=R_k}\right] dz\right\} \qquad (6)\\ + \sum_{k=1}^{K}\sum_{g=1}^{G}\left\{2\pi \int_{R_{(k-1)}}^{R_k}\left[u_g^{k*}(r,h) D_g \left.\frac{\partial u_g^k}{\partial z}\right|_{z=h} - u_g^{k*}(r,0) D_g \left.\frac{\partial u_g^k}{\partial z}\right|_{z=0}\right] r dr\right\} &+ 2\pi R \sum_{g=1}^{G}\int_0^h \left[u_g^{K*}(R,z) D_g \left.\frac{\partial u_g^K}{\partial r}\right|_{r=R}\right] dz.\end{aligned}$$

Introducing this result into Eq. (5):

$$\begin{aligned} J \equiv \sum_{k=1}^{K} 2\pi \sum_{g=1}^{G}\int_{V_k}\Bigg\{ & u_g^{k*}\Bigg[-\nabla\cdot(D_g\nabla u_g^k) + \Sigma_{rg}u_g^k - \sum_{g'=1}^{g-1}\Sigma_{g'g}u_{g'}^k - \lambda\chi_g\sum_{g'=1}^{G}(\nu\Sigma_f)_{g'}u_{g'}^k\Bigg] r dr dz\Bigg\} \\ &+ \sum_{k=1}^{K-1}\sum_{g=1}^{G} 2\pi R_k \int_0^h \Bigg\{\alpha_g^k[u_g^{(k+1)}(R_k,z) - u_g^k(R_k,z)] - u_g^{(k+1)*}(R_k,z)\left[\beta_g^k(z) + D_g\left.\frac{\partial u_g^{(k+1)}}{\partial n}\right|_{r=R_k}\right] \\ &+ u_g^{k*}(R_k,z)\left[D_g\left.\frac{\partial u_g^k}{\partial r}\right|_{r=R_k} + \beta_g^k(z)\right]\Bigg\} dz + \sum_{k=1}^{K}\sum_{g=1}^{G} 2\pi \int_{R_{(k-1)}}^{R_k}\Bigg\{u_g^{k*}(r,h)\left[\frac{u_g^k(r,h)}{2} + D_g\left.\frac{\partial u_g^k}{\partial z}\right|_{z=h}\right] \qquad (7)\\ &+ u_g^{k*}(r,0)\left[\frac{u_g^k(r,0)}{2} - D_g\left.\frac{\partial u_g^k}{\partial z}\right|_{z=0}\right]\Bigg\} r dr + \sum_{g=1}^{G} 2\pi R\int_0^h\Bigg\{u_g^{K*}\left[\frac{u_g^K(R,z)}{2} + D_g\left.\frac{\partial u_g^K}{\partial r}\right|_{r=R}\right] + \left.\frac{\partial u_g^{1*}}{\partial r}\right|_{r=0}\cdot\left.\frac{\partial u_g^1}{\partial r}\right|_{r=0}\Bigg\} dz. \end{aligned}$$

Varying $u_g^{k*}(r,z)$ and $\alpha_g^k(z)$ arbitrarily in Eq. (7), the following necessary conditions for stationariness are obtained. Writing ϕ_g^k and j_g^k for the stationary values of u_g^k and β_g^k:

$$-\nabla\cdot(D_g\nabla\phi_g^k) + \Sigma_{rg}\phi_g^k - \sum_{g'=1}^{g-1}\Sigma_{g'g}\phi_{g'}^k - \lambda\chi_g\sum_{g'=1}^{G}(\nu\Sigma_f)_{g'}\phi_{g'}^k = 0, \qquad k = 1, \cdots, K \qquad (8)$$

$$\left.\begin{aligned} \phi_g^{(k+1)}(R_k,z) &= \phi_g^k(R_k,z) \qquad (9)\\ j_g^k(z) = -D_g\left.\frac{\partial\phi_g^k}{\partial r}\right|_{r=R_k} &= -D_g\left.\frac{\partial\phi_g^{(k+1)}}{\partial r}\right|_{r=R_k} \qquad (10)\end{aligned}\right\}, \qquad k = 1, \cdots, K-1$$

$$\left.\begin{aligned} \frac{\phi_g^k(r,h)}{2} &= -D_g\left.\frac{\partial\phi_g^k}{\partial z}\right|_{z=h} \qquad (11)\\ \frac{\phi_g^k(r,0)}{2} &= +D_g\left.\frac{\partial\phi_g^k}{\partial z}\right|_{z=0} \qquad (12)\end{aligned}\right\} \qquad k = 1, \cdots, K$$

$$\frac{\phi_g^K(R,z)}{2} = -D_g\left.\frac{\partial\phi_g^k}{\partial r}\right|_{r=R} \qquad (13)$$

$$\left.\frac{\partial\phi_g^1}{\partial r}\right|_{r=0} = 0, \qquad (14)$$

with $g = 1, \cdots, G$ in all of these equations. The functions ϕ_g^k and j_g^k thus determined provide the solution to the variational problem posed and at the same time clearly are the functions that give the solution to the neutron diffusion problem formulated in Eqs. (2) and (4).

It should be noted that even though the functional J admits discontinuous functions u_g^k, with finite jumps at the surfaces with radius R_k, the stationary "point" occurs for functions which are continuous across those boundaries. The Lagrange-multiplier functions $\beta_g^k(z)$ turn out to be [see Eq. (10)] the values of the normal neutron currents at the boundaries between synthesis regions. Conditions (11), (12), and (13) are the usual conditions of zero incoming current at the reactor boundaries. Condition (14) is a natural condition to require when the flux is symmetric in θ.

To find out the necessary conditions for $u_g^{k*}(r,z)$ and $\alpha_g^k(z)$ the sums in energy in the first summation of Eq. (5) are rearranged in order to take u_g^k as a common factor of the g' sums; the following transformation, the symmetric of Eq. (6), is then introduced, giving

$$\sum_{k=1}^{K}\sum_{g=1}^{G}\int_{V_k}\nabla u_g^{k*}\cdot D_g\nabla u_g^k rdrdz = -\sum_{k=1}^{K}\sum_{g=1}^{G}\int_{V_k}u_g^k\nabla\cdot(D_g\nabla u_g^{k*})rdrdz + \sum_{k=1}^{K-1}\sum_{g=1}^{G}\left\{2\pi R_k\int_0^h\left[u_g^k(R_k,z)D_g\frac{\partial u_g^{k*}}{\partial r}\bigg|_{r=R_k}\right.\right.$$
$$\left.\left.-u_g^{(k+1)}(R_k,z)D_g\frac{\partial u_g^{(k+1)*}}{\partial r}\bigg|_{r=R_k}\right]dz\right\} + \sum_{k=1}^{K}\sum_{g=1}^{G}\left\{2\pi\int_{R_{(k-1)}}^{R_k}\left[u_g^k(r,h)D_g\frac{\partial u_g^{k*}}{\partial z}\bigg|_{z=h} - u_g^k(r,0)D_g\frac{\partial u_g^{k*}}{\partial z}\bigg|_{z=0}\right]rdr\right\}$$
$$+ 2\pi R\int_0^h\left[u_g^k(R,z)D_g\frac{\partial u_g^{k*}}{\partial r}\bigg|_{r=R}\right]dz.$$

The new form of the functional J is

$$\begin{aligned}
J \equiv & \sum_{k=1}^{K}\sum_{g=1}^{G}2\pi\int_{V_k}\left\{u_g^k\left[-\nabla\cdot(D_g\nabla u_g^{k*}) + \Sigma_{rg}u_g^{k*} - \sum_{g'=g+1}^{G}\Sigma_{gg'}u_{g'}^{k*} - \lambda(\nu\Sigma_f)_g\sum_{g'=1}^{G}\chi_{g'}u_{g'}^{k*}\right]rdrdz\right\} \\
& + \sum_{k=1}^{K-1}\sum_{g=1}^{G}2\pi R_k\int_0^h\left\{[u_g^{(k+1)*}(R_k,z) - u_g^{k*}(R_k,z)]\beta_g^k\right. \\
& \left. - u_g^{(k+1)}(R_k,z)\left[\alpha_g^k(z) + D_g\frac{\partial u_g^{(k+1)*}}{\partial r}\bigg|_{r=R_k}\right] + u_g^k(R_k,z)\left[\alpha_g^k(z) + D_g\frac{\partial u_g^{k*}}{\partial r}\bigg|_{r=R_k}\right]\right\}dz \\
& + \sum_{k=1}^{K}\sum_{g=1}^{G}2\pi\int_{R_{(k-1)}}^{R_k}\left\{u_g^k(r,h)\left[\frac{u_g^{k*}(r,h)}{2} + D_g\frac{\partial u_g^{k*}}{\partial z}\bigg|_{z=h}\right]\right. \\
& \left. + u_g^k(r,0)\left[\frac{u_g^{k*}(r,0)}{2} - D_g\frac{\partial u_g^{k*}}{\partial z}\bigg|_{z=0}\right]\right\}rdr \\
& + \sum_{g=1}^{G}2\pi R\int_0^h\left\{u_g^K(R,z)\left[\frac{u_g^{K*}(R,z)}{2} + D_g\frac{\partial u_g^{K*}}{\partial r}\bigg|_{r=R}\right] + \frac{\partial u_g^1}{\partial r}\bigg|_{r=0}\cdot\frac{\partial u_g^{1*}}{\partial r}\bigg|_{r=0}\right\}dr.
\end{aligned} \tag{15}$$

Varying arbitrarily $u_g^k(r,z)$ and $\beta_g^k(z)$ in Eq. (15) the following necessary conditions for stationariness follow:

$$-\nabla\cdot(D_g\nabla\phi_g^{k*}) + \Sigma_{rg}\phi_g^{k*} - \sum_{g'=g+1}^{G}\Sigma_{gg'}\phi_{g'}^{k*} - \lambda(\nu\Sigma_f)_g\sum_{g'=1}^{G}\chi_{g'}\phi_{g'}^{k*} = 0, \qquad k = 1, \cdots, K \tag{16}$$

$$\left.\begin{aligned}
\phi_g^{(k+1)*}(R_k,z) &= \phi_g^{k*}(R_k,z) \qquad (17)\\
J_g^{k*}(z) = -D_g\frac{\partial\phi_g^{(k+1)*}}{\partial r}\bigg|_{r=R_k} &= -D_g\frac{\partial\phi_g^{k*}}{\partial r}\bigg|_{r=R_k} \qquad (18)
\end{aligned}\right\}, k = 1, \cdots, K-1$$

$$\left.\begin{aligned}
\frac{\phi_g^{k*}(r,h)}{2} &= -D_g\frac{\partial\phi_g^{k*}}{\partial z}\bigg|_{z=h} \qquad (19)\\
\frac{\phi_g^{k*}(r,0)}{2} &= +D_g\frac{\partial\phi_g^{k*}}{\partial z}\bigg|_{z=0} \qquad (20)
\end{aligned}\right\}, k = 1, \cdots, K$$

$$\frac{\phi_g^{K*}(R,z)}{2} = -D_g\frac{\partial\phi_g^{K*}}{\partial r}\bigg|_{r=R} \tag{21}$$

$$\frac{\partial\phi_g^{1*}}{\partial r}\bigg|_{r=0} = 0, \tag{22}$$

with $g = 1, \cdots, G$ in all these equations.

These sets of equations and conditions satisfy both the variational condition required and the adjoint diffusion Eqs. (3) and (4).

THE SYNTHESIS ASSUMPTION AND THE SYNTHESIS EQUATIONS

The following synthesis assumptions are now introduced:

$$\left.\begin{aligned} u_g^k(r,z) &= \sum_{n=1}^{N_g^k} H_{gn}^k(z)T_{gn}^k(r) \qquad (23)\\ u_g^{k*}(r,z) &= \sum_{n=1}^{N_g^k} H_{gn}^{k*}(z)T_{gn}^{k*}(r), \qquad (24)\end{aligned}\right\} \quad k = 1, \cdots, K, \; g = 1, \cdots, G.$$

Here $H_{gn}^k(z)$ and $H_{gn}^{k*}(z)$, usually referred to as the trial functions, are known functions. The functions $T_{gn}^k(r)$ and $T_{gn}^{k*}(r)$ are unknown functions to be determined. The numbers N_g^k of trial functions at each group and region do not have intrinsic limitations except the obvious one $N_g^k \geq 1$. The functions $\beta_g^k(z)$ and $\alpha_g^{k*}(z)$ are also expanded:

$$\left.\begin{aligned} \beta_g^k(z) &= \sum_{n=1}^{M_g^k} B_{gn}^k(z)b_{gn}^k \qquad (25)\\ \alpha_g^k(z) &= \sum_{n=1}^{M_g^k} A_{gn}^k(z)a_{gn}^k \qquad (26)\end{aligned}\right\} \quad k = 1, \cdots, K-1, \; g = 1, \cdots, G.$$

Here the mixing coefficients a_{gn}^k and b_{gn}^k are pure numbers. The numbers M_g^k of trial functions for the normal currents at the interfaces have upper and lower bounds as will be shown later.

The selection of trial functions $H_{gn}^k(z)$, $H_{gn}^{k*}(z)$ and $B_{gn}^k(z)$, $A_{gn}^k(z)$ has to be guided by whatever knowledge or intuition that the user of the method has about the system to be calculated. The variational method, or any other similar method, can only combine these preselected flux shapes in some optimum way, but it will never achieve a good approximation to the actual fluxes of the system with a poor selection of trial functions.

From the variational point of view the assumptions (23)–(26) mean that the freedom of choice of independent-variable functions for the functional (5) is now restricted to functions of the form given in those expansions. The problem is now restricted to finding functions with the forms of (23), (24), (25) and (26) that will make stationary the value of the functional (5).

A variational problem like the one posed in connection with the functional in (5) is defined both by the functional used and by the set of admissible functions used with it. We are thus now treating a different variational problem from the initial one because the set of admissible functions is severely restricted by the synthesis assumption.

The functional J' obtained by substituting the synthesis assumptions [Eqs. (23)–(26)] into Eq. (5) is called the "reduced" functional. Its independent variable functions are now the $T_{gn}^k(r)$, $T_{gn}^{k*}(r)$, a_{gn}^k, b_{gn}^k. The corresponding necessary conditions for a stationary value, its Euler equations, are also of a lower dimensionality.

The functional J' is

$$\begin{aligned} J'[T_{gn}^k(r), T_{gm}^{k*}(r), b_{gn}^k, a_{gm}^k] \equiv \sum_{g=1}^{G} \Bigg\langle \sum_{k=1}^{K} \int_{R_{(k-1)}}^{R_k} 2\pi r dr \Bigg\{ \frac{d\bar{T}_g^{k*}}{dr}[D_g^k]\frac{d\bar{T}_g^k}{dr} + \bar{T}_g^{k*}\{[L_g^k] + [\Sigma_g^k] + [C_g^k]\}\bar{T}_g^k \\ - \sum_{g'=1}^{g-1} \bar{T}_g^{k*}[\Sigma_{g'g}^k]\bar{T}_{g'}^k + \lambda \sum_{g'=1}^{G} \bar{T}_g^{k*}[(\chi_g(\nu\Sigma_f)_{g'})^k]\bar{T}_{g'}^k \Bigg\} \Bigg\rangle \\ + \sum_{g=1}^{G} \Bigg\langle \sum_{k=1}^{K-1} [2\pi R_k \, \bar{a}_g^k\{[A_g^k]\bar{T}_g^k(R_k) - [A_g^{(k+1)}]\bar{T}_g^{(k+1)}(R_k)\} \\ + \{\bar{T}_g^{k*}(R_k)[B_g^k] - \bar{T}_g^{(k+1)*}(R_k)[B_g^{(k+1)}]\bar{b}_g^k\}] \\ + \pi R\bar{T}_g^{K*}(R)[W_g^K]\bar{T}_g^K(R) + \frac{d\bar{T}_g^{1*}}{dr}\bigg|_{r=0}[W_g^K]\frac{d\bar{T}_g^1}{dr}\bigg|_{r=0} \Bigg\rangle, \end{aligned} \qquad (27)$$

where the following nomenclature has been adopted: $\bar{T}_g^k$ and $\bar{b}_g^k$ are column vectors with components $T_{gn}^k(r)$ and b_{gn}^k. $\bar{T}_g^{k*}$ and $\bar{a}_g^k$ are row vectors with components $T_{gm}^{k*}(r)$ and a_{gm}^k. Left multiplication on a matrix implies a row vector, right multiplication a column vector.

$[D_g^k]$ is an N_g^k by N_g^k square matrix with elements defined by

$$\int_0^h D_g(r,z)H_{gm}^{k*}(z)H_{gn}^k(z)\,dz = D_{gk}^{mn}(r); \qquad (28)$$

$[\mathrm{I}_g^k]$ is an N_g^k by N_g^k square matrix with elements defined by

$$-\int_0^h H_{gm}^{k*}(z)\,\frac{d}{dz}\left[D_g(r,z)\,\frac{dH_{gn}^k(z)}{dz}\right]dz = L_{gk}^{mn}(r); \tag{29}$$

$[\Sigma_g^k]$ is an N_g^k by N_g^k square matrix with elements defined by

$$\int_0^h \Sigma_{rg}(r,z)H_{gm}^{k*}(z)H_{gn}^k(z)\,dz = \Sigma_{gk}^{mn}(r); \tag{30}$$

$[C_g^k]$ is an N_g^k by N_g^k square matrix with elements defined by

$$H_{gm}^{k*}(h)\left[\frac{H_{gn}^k(h)}{2} - D_g(r,h)\,\frac{dH_{gn}^k}{dz}\bigg|_{z=h}\right] + H_{gm}^{k*}(0)\left[\frac{H_{gn}^k(0)}{2} + D_g(r,0)\,\frac{dH_{gn}^k}{dz}\bigg|_{z=0}\right] = C_{gk}^{mn}(r); \tag{31}$$

$[\Sigma_{g'g}^k]$ is an N_g^k by $N_{g'}^k$ matrix with elements defined by

$$\int_0^h \Sigma_{g'g}(r,z)H_{gm}^{k*}(z)H_{gn}^k(z)\,dz = \Sigma_{g'g,k}^{mn}(r); \tag{32}$$

$[(\chi_g(\nu\Sigma_f)_{g'})^k]$ is an N_g^k by $N_{g'}^k$ matrix with elements defined by

$$\int_0^h (\chi_g\nu_{g'}\Sigma_{fg'})(r,z)H_{gm}^{k*}(z)H_{g'n}^k(z)\,dz = (\chi_g\nu_{g'}\Sigma_{fg'})_k^{mn}(r); \tag{33}$$

$[W_g^k]$ is an N_g^k by N_g^k square matrix with elements defined by

$$\int_0^h H_{gm}^{k*}(z)H_{gn}^k(z)\,dz = W_{gk}^{mn}. \tag{34}$$

$[A_g^k]$ is an M_g^k by N_g^k rectangular matrix
and
$[A_g^{(k+1)}]$ is an M_g^k by $N_g^{(k+1)}$ rectangular matrix with elements defined by

$$\int_0^h A_{gm}^k(z)H_{gn}^k(z)\,dz = A_{gk}^{mn} \tag{35}$$

and

$$\int_0^h A_{gm}^k(z)H_{gn}^{(k+1)}(z)\,dz = A_{g(k+1)}^{mn}, \text{ respectively;} \tag{36}$$

$[B_g^k]$ is an N_g^k by M_g^k rectangular matrix
and
$[B_g^{(k+1)}]$ is an $N_g^{(k+1)}$ by M_g^k rectangular matrix with elements defined by

$$\int_0^h H_{gm}^{k*}(z)B_{gn}^k(z)\,dz = B_{gk}^{mn} \tag{37}$$

and

$$\int_0^h H_{gm}^{(k+1)*}(z)B_{gn}^k(z)\,dz = B_{g(k+1)}^{mn}, \text{ respectively.} \tag{38}$$

In order to obtain the Euler equations in $\bar{T}_{gn}^k(r)$ and β_{gn}^k for this functional it is convenient to transform Eq. (27) by integrating the double gradient term by parts:

$$\begin{aligned}\sum_{g=1}^{G}\sum_{k=1}^{K}\int_{R_{(k-1)}}^{R_k} 2\pi r dr\,\frac{d\bar{T}_g^{k*}}{dr}\,[D_g^k]\,\frac{d\bar{T}_g^k}{dr} = \sum_{g=1}^{G}\Bigg\langle\sum_{k=1}^{K}\int_{R_{(k-1)}}^{R_k} &- 2\pi\bar{T}_g^{k*}\,\frac{d}{dr}\left\{r[D_g^k]\,\frac{d\bar{T}_g}{dr}\right\}dr \\ &+ \sum_{k=1}^{K-1} 2\pi R_k\left\{\bar{T}_g^{k*}(R_k)[D_g^k]\,\frac{d\bar{T}_g^k}{dr}\bigg|_{r=R_k} - \bar{T}_g^{(k+1)*}(R_k)[D_g^{(k+1)}]\,\frac{d\bar{T}_g^{(k+1)}}{dr}\bigg|_{r=R_k}\right\} + 2\pi R\bar{T}_g^{K*}(R)[D_g^K]\,\frac{d\bar{T}_g^K}{dr}\bigg|_{r=R}\Bigg\rangle.\end{aligned} \tag{39}$$

Introducing Eq. (39) into Eq. (27):

$$
\begin{aligned}
j' \equiv \sum_{g=1}^{G} \Bigg[\sum_{k=1}^{K} \Bigg\langle \int_{R_{(k-1)}}^{R_k} & 2\pi r dr \bar{T}_g^{k*} \left\{ -\frac{1}{r}\frac{d}{dr}\left(r[D_g^k]\frac{d\bar{T}_g^k}{dr} \right) + \{[L_g^k] + [\Sigma_g^k] + [C_g^k]\}\bar{T}_g^k - \sum_{g'=1}^{g-1} [\Sigma_{g'g}^k]\bar{T}_{g'}^k \right. \\
& \left. + \lambda \sum_{g'=1}^{G} [(\chi_g(\nu\Sigma_f)_{g'})^k]\bar{T}_g^k \right\} \Bigg] + \sum_{k=1}^{K-1} \Big\langle 2\pi R_k \bar{a}_g^k \{[A_g^k]\bar{T}_g^k(R_k) - [A_g^{(k+1)}]\bar{T}_g^{(k+1)}(R_k)\} \\
& + 2\pi R_k \bar{T}_g^{k*}(R_k) \left\{ [D_g^k]\frac{d\bar{T}_g^k}{dr}\bigg|_{r=R_k} + [B_g^k]\bar{b}_g^k \right\} - 2\pi R_k \bar{T}_g^{(k+1)*}(R_k) \left\{ [D_g^{(k+1)}]\frac{d\bar{T}_g^{(k+1)}}{dr}\bigg|_{r=R_k} + [B_g^{(k+1)}]\bar{b}_g^k \right\} \Big\rangle \\
& + 2\pi R \bar{T}_g^{K*}(R) \left\{ [W_g^K]\frac{\bar{T}_g^K(R)}{2} + [D_g^K]\frac{d\bar{T}_g^K}{dr}\bigg|_{r=R} \right\} + \frac{d\bar{T}_g^{1*}}{dr}\bigg|_{r=0} \cdot [W_g^1]\frac{d\bar{T}_g^1}{dr}\bigg|_{r=0} \Bigg].
\end{aligned}
\tag{40}
$$

And now an arbitrary variation in the independent variable-functions $T_{gm}^{k*}(r)$ and a_{gm}^k yields immediately the following conditions for stationariness for $T_{gn}^k(r)$ and b_{gn}^k, now named $\psi_{gn}^k(r)$ and j_{gn}^k. In the volumes V_k:

$$
\begin{aligned}
\sum_{n=1}^{N_g^k} & \left\{ -\frac{d}{dr}\left(rD_{gk}^{mn}\frac{d\psi_{gn}^k}{dr} \right) + r\,(L_{gk}^{mn} + \Sigma_{gk}^{mn} + C_{gk}^{mn})\psi_{gn}^k \right\} \\
& - \sum_{n=1}^{N_{g'}^k} \left\{ \sum_{g'=1}^{g-1} r\Sigma_{g'gk}^{mn}\psi_{g'n}^k + \lambda \sum_{g'=1}^{G} r[(\chi_g(\nu\Sigma_f)_{g'})_k^{mn}]\psi_{g'n}^k \right\} 0, \qquad m = 1, 2, \cdots, N_g^k, \qquad k = 1, 2, \cdots, K;
\end{aligned}
\tag{41}
$$

at the cylindrical surfaces with radii R_k:

$$
\sum_{n=1}^{N_g^k} A_{gk}^{mn}\psi_{gn}^k(R_k) = \sum_{n=1}^{N_g^{(k+1)}} A_{g(k+1)}^{mn}\psi_{gn}^{(k+1)}(R_k), \qquad m = 1, 2, \cdots, M_g^k \tag{42}
$$

$$
\sum_{n=1}^{N_g^k} D_{gk}^{mn}(R_k)\frac{d\psi_{gn}^k}{dr}\bigg|_{r=R_k} + \sum_{n=1}^{M_g^k} B_{gk}^{mn} j_{gn}^k = 0, \qquad m = 1, 2, \cdots, N_g^k \tag{43}
$$

$$
\sum_{n=1}^{N_g^{(k+1)}} D_{g(k+1)}^{mn}(R_k)\frac{d\psi_{gn}^{(k+1)}}{dr}\bigg|_{r=R_k} + \sum_{n=1}^{M_g^k} B_{g(k+1)}^{mn} j_{gn}^k = 0, \qquad m = 1, 2, \cdots, N_g^{(k+1)}; \tag{44}
$$

at the outer surface of the reactor:

$$
\sum_{n=1}^{N_g^K} \left\{ D_{gK}^{mn}(R)\frac{d\psi_{gn}^K}{dr}\bigg|_{r=R} + \frac{1}{2}W_{gK}^{mn}\psi_{gn}^K(R) \right\} = 0, \qquad m = 1, \cdots, N_g^k; \tag{45}
$$

at $r = 0$:

$$
\sum_{n=1}^{N_g^1} \left\{ W_{g1}^{mn}\frac{d\psi_{gn}^1}{dr}\bigg|_{r=0} \right\} = 0, \qquad m = 1, 2, \cdots, N_g^1, \tag{46}
$$

and $g = 1, 2, \cdots, G$ in Eqs. (41) through (46).

To obtain the Euler equations in $T_{gn}^{k*}(r)$ and a_{gn}^k, the following transformation which is symmetric to Eq. (39) is made:

$$
\begin{aligned}
\sum_{g=1}^{G}\sum_{k=1}^{K} \int_{R_{(k-1)}}^{R_k} 2\pi r dr \frac{d\bar{T}_g^{k*}}{dr}[D_g^k]\frac{d\bar{T}_g^k}{dr} = \sum_{g=1}^{G} \Bigg\langle & 2\pi \int_{R_{(k-1)}}^{R_k} - \frac{d}{dr}\left\{ r\frac{d\bar{T}_g^{k*}}{dr}[D_g^k] \right\} \bar{T}_g^k\, dr \\
& + \sum_{k=1}^{K-1} 2\pi R_k \left\{ \frac{d\bar{T}_g^{k*}}{dr}\bigg|_{r=R_k} [D_g^k]\bar{T}_g^k(R_k) \right. \\
& \left. - \frac{d\bar{T}_g^{(k+1)*}}{dr}\bigg|_{r=R_k} [D_g^{(k+1)}]\bar{T}_g^{(k+1)}(R_k) \right\} \\
& + 2\pi R \frac{d\bar{T}_g^{k*}}{dr}\bigg|_{r=R} [D_g^K]\bar{T}_g^K(R) \Bigg\rangle,
\end{aligned}
$$

and introduced into Eq. (27). After this substitution, an arbitrary variation in $T_{gn}^k(r)$ and b_{gn}^k results in the following conditions for stationariness for $T_{gm}^{k*}(r)$ and a_{gm}^k, now called $\psi_{gm}^{k*}(r)$ and j_{gm}^{k*} respectively. In the volumes V_k:

$$\sum_{m=1}^{N_g^k}\left\{-\frac{d}{dr}\left(rD_{gk}^{mn}\frac{d\psi_{gm}^{k*}}{dr}\right)+r\,(L_{gk}^{mn}+\Sigma_{kg}^{mn}+C_{gk}^{mn})\psi_{gm}^{k*}\right\}$$
$$-\sum_{m=1}^{N_{g'}^k}\left\{\sum_{g'=g+1}^{G}r\Sigma_{gg'k}^{mn}\psi_{g'm}^{k*}+\lambda\sum_{g'=1}^{G}r[(\chi_{g'}(\nu\Sigma_f)_g)_k^{mn}]\psi_{g'm}^{k*}\right\}=0,\ n=1,2,\cdots,N_g^k,\ k=1,2,\cdots,K; \tag{47}$$

at the cylindrical surfaces with radii R_k :

$$\sum_{m=1}^{N_g^k}B_{gk}^{mn}\psi_{gm}^{k*}(R_k)=\sum_{m=1}^{N_g^{(k+1)}}B_{g(k+1)}^{mn}\psi_{gm}^{(k+1)}(R_k),\quad n=1,2,\cdots,M_g^k, \tag{48}$$

$$\sum_{m=1}^{N_g^k}D_{gk}^{mn}\frac{d\psi_{gm}^{k*}}{dr}\bigg|_{r=R_k}+\sum_{m=1}^{M_g^k}A_{gk}^{mn}j_{gm}^{k*}=0,\qquad n=1,2,\cdots,N_g^k, \tag{49}$$

$$\sum_{m=1}^{N_g^{(k+1)}}D_{g(k+1)}^{mn}\frac{d\psi_{gm}^{(k+1)*}}{dr}\bigg|_{r=R_k}+\sum_{m=1}^{M_g^k}A_{g(k+1)}^{mn}j_{gm}^{k*}=0,\quad n=1,2,\cdots,N_g^{(k+1)}; \tag{50}$$

at the outer surface of the reactor:

$$\sum_{m=1}^{N_g^K}\left\{D_{gK}^{mn}(R)\frac{d\psi_{gm}^{K*}}{dr}\bigg|_{r=R}+\frac{1}{2}W_{gK}^{mn}\psi_{gm}^{K*}(R)\right\}=0,\qquad n=1,2,\cdots,N_g^K; \tag{51}$$

at $r=0$:

$$\sum_{m=1}^{N_g^1}\left\{W_{g1}^{mn}\frac{d\psi_{gm}^{1*}}{dr}\bigg|_{r=0}\right\}=0,\qquad n=1,2,\cdots,N_g^1, \tag{52}$$

and $g=1,2,\cdots,G$ in Eqs. (47) through (52).

The systems of Eqs. (41) through (46) and (47) through (52) form well-determined systems of equations with an equal number of unknowns and conditions. From the physical point of view though, it is necessary to impose bounds on the numbers M_g^k of trial functions B_{gn}^k and A_{gn}^k. From the structure of the conditions, Eqs. (42) through (46), it is clearly necessary that

$$1\le M_g^k\le N_g^k+N_g^{k+1} \tag{53}$$

if one is to avoid zero values for the fluxes and adjoints at the interface.

Finally, the approximate values of fluxes and adjoints are obtained by substituting the solutions $\psi_{gn}^k(r)$, $\psi_{gm}^{k*}(r)$, j_{gn}^k and j_{gm}^{k*} of this system of differential equations into Eqs. (23) and (24).

DISCRETE APPROXIMATIONS AND METHOD OF SOLUTION

Rewriting the synthesis equations (41) through (46) in matrix form, using definitions (28) through (38), we obtain:

$$-\frac{1}{r}\frac{d}{dr}r[D_g^k]\frac{d\bar{\psi}_g^k}{dr}+[\Sigma_{Rg}^k]\bar{\psi}_g^k=\sum_{g'=1}^{g-1}[\Sigma_{g'g}^k]\bar{\psi}_{g'}^k+\lambda\sum_{g'=1}^{G}[(\chi_g(\nu\Sigma_f)_{g'})^k]\bar{\psi}_{g'}^k \tag{54}$$

with interface and boundary conditions

$$[A_g^k]\bar{\psi}_g^k(R_k)=[A_g^{(k+1)}]\bar{\psi}_g^{(k+1)}(R_k) \tag{55}$$

$$[D_g^k(R_k)]\frac{d\bar{\psi}_g^k}{dr}\bigg|_{r=R_k}+[B_g^k]\bar{j}_g^k=0 \tag{56}$$

$$[D_g^{(k+1)}(R_k)]\frac{d\bar{\psi}_g^{(k+1)}}{dr}\bigg|_{r=R_k}+[B_g^{(k+1)}]\bar{j}_g^k=0 \tag{57}$$

$$[D_g^K(R)]\frac{d\bar{\psi}_g^K}{dr}\bigg|_{r=R}+\frac{1}{2}[W_g^K]\bar{\psi}_g^K(R)=0, \tag{58}$$

with $k=1,2,\cdots,K$ and $g=1,2,\cdots,G$. $\bar{\psi}_g^k$ and $\bar{j}_g^k$ are column vectors with components ψ_{gn}^k and j_{gn}^k respectively and

$$[\Sigma_{Rg}^k] \equiv [L_g^k] + [\Sigma_g^k] + [C_g^k]. \tag{59}$$

With this notation it is seen that the system has the form of the usual one dimensional multigroup equation where matrices now replace the usual scalar coefficients. This observation forms the basis for the derivation of a finite difference approximation to the given system. Since most of the derivation is involved with the Laplacian term, it will suffice to consider the case of one group. Thus the group index is dropped.

Let the reactor domain be the interval $[0,R]$, and impose a mesh $0 = \rho_0 < \rho_1 < \cdots < \rho_I = R$ on this interval in such a manner that

(i) any synthesis interface coincides with some mesh point ρ_i,

(ii) any region interface coincides with some mesh point ρ_i. Then in any interval $[\rho_{i-1}, \rho_i]$ we can assume that we have a differential system of the form

$$-\frac{1}{r}\frac{d}{dr}\left(rD_i\frac{d\psi}{dr}\right) + (\Sigma_R)_i\psi = f_i(r) \tag{60}$$

with interface conditions

$$\begin{aligned}
A_{i-1}\psi(\rho_{i-1}^-) &= \hat{A}_{i-1}\psi(\rho_{i-1}^+)\\
A_i\psi(\rho_i^-) &= \hat{A}_i\psi(\rho_i^+)\\
D_{i-1}\psi'(\rho_{i-1}^-) + B_{i-1}j_{i-1} &= 0\\
\hat{D}_{i-1}\psi'(\rho_{i-1}^+) + \hat{B}_{i-1}j_{i-1} &= 0\\
D_i\psi'(\rho_i^-) + B_ij_i &= 0\\
\hat{D}_i\psi'(\rho_i^+) + \hat{B}_ij_i &= 0,
\end{aligned}$$

where the vector and matrix notation has been dropped, for simplicity. The relation between A_i and $\hat{A}_i$, B_i and $\hat{B}_i$, D_i and $\hat{D}_i$ is the same as that which exists between $[A_g^k]$ and $[A_g^{k+1}]$, $[B_g^k]$ and $[B_g^{k+1}]$, and $[D_g^k(R_k)]$ and $[D_g^{(k+1)}(R_k)]$ where now i indicates mesh point ρ_i. ρ_i^- and ρ_i^+ indicate evaluation at point ρ_i using functions defined to the left or right of the point respectively. ψ' indicates derivative with respect to r. The dimension of $\psi(r)$ is N_i, where $N_i = N_k$ when the interval $[\rho_{i-1}, \rho_i]$ lies in the kth synthesis region. Since each interval lies entirely within a region of constant composition, the coefficient matrices are constant over each interval. If ρ_i is a regular interface point in the sense that it does not separate two synthesis regions, then the dimension of $\psi(r)$ does not change when passing from $[\rho_{i-1}, \rho_i]$ to $[\rho_i, \rho_{i+1}]$. In this case the interface conditions are defined by the matrix relationships

$$\begin{aligned}
A_i &= \hat{A}_i = I; \qquad N_i \times N_i\\
B_i &= \hat{B}_i = I; \qquad N_i \times N_i.
\end{aligned}$$

On the other hand if R_i separates the kth synthesis region from the $(k+1)$st, then the interface matrices are defined by

$$\begin{aligned}
A_i &= A_k; \quad M_i \times N_i, \quad M_i = M_k, \quad N_i = N_k\\
\hat{A}_i &= A_{k+1}; \quad M_i \times N_{i+1}, \quad N_{i+1} = N_{k+1}\\
B_i &= B_k; \quad N_i \times M_i\\
\hat{B}_i &= B_{k+1}; \quad N_{i+1} \times M_i.
\end{aligned}$$

In order to derive a finite difference approximation, consider the following class of functions defined on the interval $[r_i, r_{i+1}]$, where r_i is the mid-point of the interval $[\rho_{i-1}, \rho_i]$:

$$\psi(r) = \begin{cases}\psi(r_i) + (r - r_i)\zeta, & r_i \le r \le \rho_i\\ \psi(r_{i+1}) - (r_{i+1} - r)\xi, & \rho_i \le r \le r_{i+1}\end{cases}$$

which satisfy the conditions

$$\begin{aligned}
A_i\psi(\rho_i^-) &= \hat{A}_i\psi(\rho_i^+)\\
D_i\psi'(\rho_i^-) + B_ij_i &= 0\\
\hat{D}_i\psi'(\rho_i^+) + \hat{B}_ij_i &= 0.
\end{aligned}$$

Here ζ, ξ, and j_i are assumed to be given vectors having dimensions N_i, N_{i+1}, and M_i respectively.

Applying the interface conditions to this class of functions, it is seen that ζ, ξ, and j_i must satisfy the following system of equations:

$$\begin{aligned} \tfrac{1}{2}\delta_i A_i\zeta + \tfrac{1}{2}\delta_{i+1}\hat{A}_i\xi &= \hat{A}_i\psi(r_{i+1}) - A_i\psi(r_i) \\ D_i\zeta + B_i j_i &= 0 \\ \hat{D}_i\xi + \hat{B}_i j_i &= 0. \end{aligned}$$

Here δ_i denotes the length of the interval $[\rho_{i-1}, \rho_i]$.

Up to this point no assumptions have been made concerning the nature or structure of the matrices A_i, $\hat{A}_i$, D_i, $\hat{D}_i$, B_i and $\hat{B}_i$; thus the question of existence of a solution to the above system is still open. In fact, the matter is not trivial even in the case of a regular interface. In this case the system reduces to the following system by eliminating the vector j_i:

$$\begin{aligned} \tfrac{1}{2}\delta_i\zeta + \tfrac{1}{2}\delta_{i+1}\xi &= \psi(r_{i+1}) - \psi(r_i) \\ -D_i\zeta + \hat{D}_i\xi &= 0. \end{aligned}$$

This leads to the equation

$$[\tfrac{1}{2}\delta_i\hat{D}_i + \tfrac{1}{2}\delta_{i+1}D_i]\xi = D_i[\psi(r_{i+1}) - \psi(r_i)].$$

The question now arises whether the matrix

$$\Delta_i = \tfrac{1}{2}\delta_i\hat{D}_i + \tfrac{1}{2}\delta_{i+1}D_i$$

is invertible. If it is, then

$$D_i\zeta = \hat{D}_i\xi = \hat{D}_i\Delta_i^{-1}D_i[\psi(r_{i+1}) - \psi(r_i)].$$

At this point it is not clear that D_i is non-singular unless certain assumptions are made on the weighting functions. For example, suppose $D_i x = 0$; then

$$(D_i x)_m = \int_0^T D_i(t)\left(\sum_{n=1}^{N_i} x_n F_i^n(t)\right)F^{*m}(t)\,dt = 0 \text{ for } m = 1, 2, \cdots, N_i.$$

Thus there exists a function

$$C(t) = \sum_{n=1}^{N} x_n F_i^n(t)$$

in the span of the set $\{F_i^n\}_{n=1}^{N_i}$ which is orthogonal to the subspace generated by $\{F_i^{*m}\}$, $m = 1, \cdots, N_i$. In the same way, the question of the existence of Δ_i^{-1} for the regular interface case leads to a similar conclusion with the measure

$$d\hat{\mu}(t) = [\tfrac{1}{2}\delta_i\hat{D}_i(t) + \tfrac{1}{2}\delta_{i+1}D_i(t)]\,dt.$$

Returning to the general system for ξ, ζ, and j_i, we find that if D_i and $\hat{D}_i$ are non-singular, then

$$\begin{aligned} \zeta &= D_i^{-1}B_i j_i, \\ \xi &= \hat{D}_i^{-1}\hat{B}_i j_i, \end{aligned}$$

and

$$(\tfrac{1}{2}\delta_i A_i D_i^{-1}B_i + \tfrac{1}{2}\delta_{i+1}\hat{A}_i\hat{D}_i^{-1}\hat{B}_i)j_i = \hat{A}_i\psi(r_{i+1}) - A_i\psi(r_i).$$

If the $M_i \times N_i$ dimensional matrix

$$\Omega_i = \tfrac{1}{2}\delta_i A_i D_i^{-1}B_i + \tfrac{1}{2}\delta_{i+1}\hat{A}_i\hat{D}_i^{-1}\hat{B}_i$$

has an inverse, then

$$\begin{aligned} D_i\zeta &= B_i\Omega_i^{-1}[\hat{A}_i\psi(r_{i+1}) - A_i\psi(r_i)] \\ \hat{D}_i\xi &= \hat{B}_i\Omega_i^{-1}[\hat{A}_i\psi(r_{i+1}) - A_i\psi(r_i)]. \end{aligned}$$

With the assumption of invertibility, $\psi(r)$ has now been determined as a class of piecewise linear vector-valued functions which satisfy the given interface conditions.

Returning to the differential Eq. (60) and integrating it with respect to r over the interval $[\rho_{i-1}, \rho_i]$ leads to the following equation:

$$-[\rho_i D_i \psi'(\rho_i^-) - \rho_{i-1} D_i \psi'(\rho_{i-1}^+)] + (\Sigma_R)_i \int_{\rho_{i-1}}^{\rho_i} \psi(r) r dr = \int_{\rho_{i-1}}^{\rho_i} f_i(r) r dr, \qquad 1 \le i \le I. \tag{61}$$

The solution to this system within the class of functions just constructed is required. Using the expressions for $D_i\psi'(\rho_i^-)$ and $D_i\psi'(\rho_{i-1}^+)$ just derived, the following system is obtained:

$$\begin{aligned} -\{\rho_i B_i \Omega_i^{-1}[\hat{A}_i \psi(r_{i+1}) - A_i \psi(r_i)] - \rho_{i-1} \hat{B}_{i-1} \Omega_{i-1}^{-1}[\hat{A}_{i-1}\psi(r_i) - A_{i-1}\psi(r_{i-1})]\} + (\Sigma_R)_i \int_{\rho_{i-1}}^{\rho_i} \psi(r) r dr \\ = \int_{\rho_{i-1}}^{\rho_i} f_i(r) r dr. \end{aligned} \tag{62}$$

Integrating the functions in this class would result in a quadrature formula linking $\psi(r_{i-1})$, $\psi(r_1)$, and $\psi(r_{i+1})$. However, the truncation error is of a higher order than that which results from the derivative terms. In addition such a quadrature formula leads to non-symmetric matrices even in the case of regular interface conditions. For these reasons, the following quadrature formulas will be used:

$$\int_{\rho_{i-1}}^{\rho_i} \psi(r) r\, dr \approx \tfrac{1}{2}(\rho_i^2 - \rho_{i-1}^2)\psi(r_i) = V_i \psi(r_i)$$

$$\int_{\rho_{i-1}}^{\rho_i} f_i(r) r\, dr \approx V_i f_i(r_i).$$

With these approximations, the following matrices can be defined:

$$\begin{aligned} G_i &= \rho_i B_i \Omega_i^{-1} \hat{A}_i\,; & N_i \times N_{i+1} \\ H_i &= \rho_{i-1} \hat{B}_{i-1} \Omega_{i-1}^{-1} A_{i-1}\,; & N_i \times N_{i-1} \\ E_i &= \rho_i B_i \Omega_i^{-1} A_i + \rho_{i-1} B_{i-1} \Omega_{i-1}^{-1} \hat{A}_{i-1} + V_i \Sigma_{Ri}\,, \end{aligned} \tag{63}$$

for $i = 1, 2, \cdots, I$ with $H_1 = 0$, $G_I = 0$ and

$$E_I = \rho_I D_I [D_I + \tfrac{1}{2} W_I \tfrac{1}{2} \delta_I]^{-1} \tfrac{1}{2} W_I + \rho_{I-1} \hat{B}_{I-1} \Omega_{I-1}^{-1} \hat{A}_{I-1} + V_I \Sigma_{RI}$$

where

$$\delta_I = \rho_I - \rho_{I-1}\,,$$

and

$$W_I = [W_g^K].$$

At a regular interface $N_i = N_{i+1}$ and $A_i = \hat{A}_i = B_i = \hat{B}_i = I$; thus $H_{i+1} = G_i$. However, in general $H_{i+1} \neq G_i$; therefore the matrices are not symmetric.

With the above matrices the differential system has been approximated by the following algebraic system:

$$\begin{bmatrix} E_1 & -G_1 & 0 & \cdots & 0 \\ -H_2 & E_2 & -G_2 & \cdots & 0 \\ & \ddots & \ddots & \ddots & \\ 0 & -H_3 & \cdots & \cdots & \\ \vdots & \ddots & \ddots & \ddots & -G_{I-1} \\ \vdots & & \ddots & \ddots & \\ 0 & & & -H_I & E_1 \end{bmatrix} \psi = f, \tag{64}$$

where $\psi = [\psi_1, \psi_2, \cdots, \psi_I]$ and $\psi_i = \psi(r_i)$.

In the multigroup case there are G matrices of the above form which will be denoted by P_g. Letting

$$\Sigma^{g'g} = \operatorname{diag}\{V_i\Sigma_i^{g'g}\}_{i=1}^{I},$$

$$F^{g'g} = \operatorname{diag}\{V_iF_i^{g'g}\}_{i=1}^{I}$$

for $g' \geq 1$, $g \leq G$ and defining $\psi_g \equiv [\psi_{g1}, \psi_{g2}, \cdots, \psi_{gI}]$, the discrete approximation to the original differential equation system takes the form

$$P_g\psi_g = \sum_{g'=1}^{g-1} \Sigma^{g'g}\psi_{g'} + \lambda \sum_{g'=1}^{G} F^{g'g}\psi_{g'}, \qquad 1 \leq g \leq G. \tag{65}$$

Since $M_g^{-1} > 0$ and the matrices $\Sigma^{g'g}$ and $F^{g'g}$ are non-negative, this system is solved for the dominant eigenvalue and eigenvector by the power iteration technique. Thus, given any guess $\psi^{(0)} > 0$ and $\lambda^{(0)}$ for the dominant eigenvector and eigenvalue, the successive approximations are generated by the following scheme:

$$P_g\psi_g^{(n+1)} = \sum_{g'=1}^{g-1} \Sigma^{g'g}\psi_{g'}^{(n+1)} + \lambda^{(n)} \sum_{g'=1}^{G} F^{g'g}\psi_{g'}^{(n)} \tag{66}$$

$$\lambda^{(n)} = \lambda^{(n-1)} \frac{(\phi^{(n)}, \phi^{(n-1)})}{(\phi^{(n)}, \phi^{(n)})}, \tag{67}$$

where

$$(\phi,\psi) = \sum_{g=1}^{G} \sum_{i=1}^{I} \sum_{\ell=1}^{N_i} \phi_{li g}\psi_{li g}.$$

The generation of $\psi_g^{(n+1)}$ thus involves the solution of the system

$$P_g\psi_g = f_g \quad \text{for} \quad g = 1, 2, \cdots, G. \tag{68}$$

Since each matrix P_g is block tridiagonal, each system can be solved directly by factoring the matrix P_g using a variant of Choleski's method. For simplicity the group index is dropped. Then $P = LU$, where L and U have the forms

$$L = \begin{bmatrix} U_1 & 0 & \cdots & 0 \\ -H_2 & U_2 & \cdots & 0 \\ \vdots & \ddots & \ddots & \\ 0 & & -H_I & U_1 \end{bmatrix},$$

$$U = \begin{bmatrix} I & -V_1 & 0 & \cdots & 0 \\ 0 & I & -V_2 & \cdots & 0 \\ \vdots & & \ddots & \ddots & \\ 0 & & & & -V_{I-1} \\ 0 & & & & I \end{bmatrix}. \tag{69}$$

This factorization leads to the following recursive relations for the matrices U_i and V_i.

$$U_1 = E_1\,, \qquad U_1V_1 = G_1$$

$$H_iV_{i-1} + U_i = E_i\,, \qquad U_iV_i = G_i\,, \qquad 2 \le i \le I,\ (G_I = 0). \tag{70}$$

With this factorization, the single system $M\psi = f$ is equivalent to the pair of equations

$$L\omega = f$$

$$U\phi = \omega.$$

Hence

$$\begin{aligned} \omega_1 &= U_1^{-1}f_1 \\ \omega_i &= U_1^{-1}[f_i + H_i\omega_{i-1}], \qquad 2 \le i \le I \\ \Phi_I &= \omega_I \\ \Phi_j &= \omega_j + U_j^{-1}G_j\Phi_{j+1}\,, \qquad I - 1 \ge j \ge 1. \end{aligned} \tag{71}$$

The method requires the creation and storage of the matrices $\{U_i^{-1}\}_{i=1}^{I}$. However, these matrices can replace the matrices E_i which are not needed in the actual solution.

References

1. J. B. Yasinsky and S. Kaplan, *Synthesis of Three-Dimensional Flux Shapes Using Discontinuous Sets of Trial Functions*, Nucl. Sci. Eng., **28**, 426–437 (1967).
2. E. L. Wachspress and M. Becker, *Variational Multichannel Synthesis with Discontinuous Trial Functions*, KAPL-3095, (1965).
3. A. L. Buslik, *A Variational Principle for the Neutron Diffusion Equation Using Discontinuous Trial Functions*, WAPD-TM-610 (1966).

VI-5. A New Formulation of Multigroup Microscopic Cross Sections[1]

A. Travelli

Introduction

The multigroup cross-section sets used in fast reactor analyses are usually calculated on the basis of a fundamental mode spectrum, as is done, for instance, in the ELMØE[2] and in the MC²[3] codes. Within a given definition of the Boltzmann equation, the neutron spectrum is calculated for a bare reactor with a very large number of groups (from 600 to 2,000 groups, in current calculations), and then used to collapse the macroscopic multigroup cross sections for the material under study.

The fluxes and the cross sections used in the ultrafine calculation are also multigroup fluxes and cross sections, but the discrete points are so close to each other that the ultrafine calculation may be considered to be continuous in energy for the purpose of this work. For instance, in the diffusion approximation the ultrafine flux and current may be considered to follow from

$$\left[\frac{B^2}{3\Sigma_{tr}(E)} + \Sigma_t(E)\right]\phi(E) = \int_0^\infty \left[\Sigma_{s0}(E' \to E) + \frac{1}{k}\,\chi(E)\nu\Sigma_f(E')\right]\phi(E')\,dE' \tag{1}$$

$$J(E) = \frac{B}{3\Sigma_{tr}(E)}\,\phi(E)\,, \tag{2}$$

where $\phi(E)$ and $J(E)$ are the neutron flux and current, $\Sigma_t(E)$ and $\Sigma_{tr}(E)$ are the total and transport macroscopic cross-sections, $\Sigma_{s0}(E' \to E)$ is the zeroth Legendre component of the macroscopic scattering cross section, $\chi(E)$ is the fission spectrum and $\nu\Sigma_f(E)$ is the product of the average number of neutrons emitted per fission times the macroscopic fission cross-section. The effective multiplication constant k is usually set equal to unity and the buckling B^2 is found as the eigenvalue of Eq. (1).

The multigroup macroscopic cross sections are then collapsed to produce a cross-section set with N groups so that a set of $2N$ equations can be written in the form

$$\left[\frac{B^2}{3\bar{\Sigma}_{tr_I}} + \bar{\Sigma}_{t_I}\right]\bar{\phi}_I = \sum_{J=1}^{N}\left[\bar{\Sigma}_{s0_{J\to I}} + \frac{1}{k}\,\bar{\chi}_I\overline{\nu\Sigma_{f_J}}\right]\phi_J \tag{3}$$

$$\bar{J}_I = \frac{B}{3\bar{\Sigma}_{tr_I}}\,\bar{\phi}_I, \qquad (I = 1, 2, \cdots, N) \tag{4}$$

with the same values for k and for B as in Eqs. (1) and (2), and with

$$\phi_I = \int_I \phi(E)\,dE \tag{5}$$

$$J_I = \int_I J(E)\,dE. \tag{6}$$

By integrating Eqs. (1) and (2) over the energy width of the I-th group, a convenient definition of the multigroup cross sections that appear in Eqs. (3) and (4) is found to be[4]

$$\bar{\chi}_I = \int_I \chi(E)\,dE \tag{7}$$

$$\bar{\Sigma}_{tr_I} = \frac{\bar{\phi}_I}{\displaystyle\int_I \frac{\phi(E)}{\Sigma_{tr}(E)}\,dE} \tag{8}$$

$$\bar{\Sigma}_{t_I} = \frac{1}{\bar{\phi}_I}\int_I \Sigma_t(E)\phi(E)\,dE \tag{9}$$

$$\overline{\nu\Sigma}_{f_I} = \frac{1}{\bar{\phi}_I}\int_I \nu\Sigma_f(E)\phi(E)\,dE \tag{10}$$

$$\Sigma_{s0_{J\to I}} = \frac{1}{\bar{\phi}_J}\int_I dE'\int_J \Sigma_{s0}(E\to E')\phi(E)\,dE. \tag{11}$$

Equations (7–11) are used by most cross-section reduction codes, including ELMØE and MC², for the definition of the macroscopic multigroup cross-sections.

In principle, the procedure outlined here is needed for every composition whose macroscopic multigroup cross-sections are desired. The practical application may turn out to be very expensive, however, because a typical MC² problem takes approximately one hour of computer time when it is run on the CDC-3600. In order to avoid some of the calculations, many of the group-collapsing codes calculate microscopic multigroup cross sections for the individual isotopes, in addition to the macroscopic multigroup cross sections for the composition at hand. The microscopic cross sections may be used in a number of ways: for instance, they can be used in calculations of reaction rates or of material worths. One of the most interesting applications, however, is based on the assumption that the microscopic multigroup cross sections, when multiplied by the corresponding isotopic concentrations and added, provide fairly accurate macroscopic multigroup cross sections not only for the composition for which the calculation was run, but also for compositions which are not too different from it. This means that if a reactor contains M isotopes, and if we indicate by N_0^m the concentration of the m-th isotope in the standard composition for which the calculation of the ultrafine spectrum was run, and by N^m the concentration of the same isotope in some other composition, we would like the relation

$$\bar{\Sigma}_I[N^{(1)}, N^{(2)}, \cdots, N^M] \approx \sum_{m=1}^{M} \bar{\sigma}_I^m N^m \tag{12}$$

to hold approximately in the $[N^{(1)}, N^{(2)}, \cdots, N^M]$ region which is close to the $[N_0^{(1)}, N_0^{(2)}, \cdots, N_0^M]$ point where the calculation of the ultrafine spectrum was run. By expanding Eq. (12) in a first-order Taylor series of the isotopic concentrations around the standard composition, it is found that the following equations should be satisfied by the microscopic multigroup cross-sections:

$$\left.\begin{aligned}\sum_{m=1}^{M} \bar{\sigma}_I^m N_0^m &= \bar{\Sigma}_I[N_0^{(1)}, N_0^{(2)}, \cdots, N_0^M] && (13)\\ \bar{\sigma}_I^m &= \frac{\partial \bar{\Sigma}_I}{\partial N^m}[N_0^{(1)}, N_0^{(2)}, \cdots, N_0^M], && (14)\end{aligned}\right\} m = 1, 2, \cdots, M.$$

The current definitions of the microscopic multigroup cross-sections, and the way in which they are calculated, are usually in very poor agreement with the requirements stated by Eqs. (13) and (14). The most notable example is provided by the microscopic multigroup transport cross section, for which most current codes use one of the three following definitions:

$$\bar{\sigma}_{tr}^m = \frac{\bar{\sigma}_I}{\displaystyle\int_I \frac{\phi(E)}{\sigma_{tr}^m(E)}\, dE} \qquad \text{(definition A)} \tag{15}$$

$$\bar{\sigma}_{tr_I}^m = \frac{1}{\bar{\phi}_I}\int_I \sigma_{tr}^m(E)\phi(E)\, dE \qquad \text{(definition B)} \tag{16}$$

$$\bar{\sigma}_{tr_I}^m = \frac{1}{\bar{\phi}_I}\int_I \left[\frac{\bar{\Sigma}_{tr_I}}{\Sigma_{tr}(E)}\right]\sigma_{tr}^m(E)\phi(E)\, dE \qquad \text{(definition C)}. \tag{17}$$

Definition A is the most widely used definition. It was used, for instance, in the preparation of the Yiftah-Okrent-Moldauer cross-section set,[5] and it is a standard option of the GALAXY code.[6] Its justification lies on the similarity that it bears to the definition of the macroscopic multigroup transport cross section, as given by Eq. (8). Definition B has been used less frequently, but it is mentioned in Ref. 7 and is also an option of the GALAXY code; it is supported by its similarity with the definition of the macroscopic multigroup total cross section, as given by Eq. (9). Neither definition satisfies Eq. (14); the two definitions do not even satisfy Eq. (13), that is, they do not add up to the macroscopic multigroup transport cross-section even for the standard composition. The latter weakness of the first two definitions of $\bar{\sigma}_{tr_I}^m$ was stressed by P. Zweifel and G. Ball,[8] who were able to prove that use of definition A leads always to an underestimate of $\bar{\Sigma}_{tr_I}$, while use of definition B leads always to an overestimate of it. Definition C was introduced only recently by J. Ferziger and P. Zweifel[9] and by B. Toppel et al.[3] This definition is a vast improvement over definitions A and B, because it has the advantage of satisfying Eq. (13); however, no claim can be made directly about the way in which the defintion satisfies Eq. (14).

The definitions that are universally accepted for the other multigroup microscopic cross-sections within the framework of real-flux weighting are

$$\bar{\sigma}_{t_I}^m = \frac{1}{\bar{\phi}_I}\int_I \sigma_t(E)\phi(E)\, dE \tag{18}$$

$$\overline{\nu\sigma_{f_I}^m} = \frac{1}{\bar{\phi}_I}\int_I \nu\sigma_f^m(E)\phi(E)\, dE \tag{19}$$

$$\bar{\sigma}_{s0_{J\to I}}^m = \frac{1}{\bar{\phi}_J}\int_I dE' \int_J \sigma_{s0}^m\,(E \to E')\phi(E)\, dE. \tag{20}$$

These definitions are seen immediately to satisfy Eq. (13). However, as in the case of Eq. (17), no claim can be made about the way in which they satisfy Eq. (14).

It is the purpose of this work to introduce new definitions of the microscopic multigroup cross sections which are superior to definitions (17–20), in that they satisfy identically both equations (13) and (14) within the framework of acceptable physical assumptions.

Discussion

It is not possible to claim a priori the existence of a definition of the microscopic transport cross sections that satisfies identically both Eqs. (13) and (14). Equation (14) may be written for any of the M isotopes, and the two equations combined provide therefore a homogeneous system of $(M + 1)$ equations in the M unknowns ($\bar{\sigma}_{tr_I}^m$; $m = 1, 2, \cdots, M$). Thus, the system is overdetermined and, in general, the existence of a solution satisfying all the conditions cannot be assumed. However, it is possible to start by imposing that the definitions satisfy the M equations represented by Eq. (14). For the various cross sections, we get

$$\bar{\sigma}^m_{tr_I} \equiv \frac{\partial}{\partial N^m}\left\{\frac{\int_I \phi(E)\,dE}{\int_I \frac{\phi(E)}{\Sigma_{tr}(E)}\,dE}\right\} = \frac{1}{\bar{\phi}_I}\int_I \left\{\frac{\bar{\Sigma}_{tr_I}}{\Sigma_{tr}(E)}\,\sigma^m_{tr}(E) - [\bar{\Sigma}_{tr_I} - \Sigma_{tr}(E)]\left[\frac{1}{\phi(E)}\frac{\partial\phi(E)}{\partial N^m}\right]\right\}\frac{\bar{\Sigma}_{tr_I}}{\Sigma_{tr}(E)}\,\phi(E)\,dE \tag{21}$$

$$\bar{\sigma}^m_{t_I} \equiv \frac{\partial}{\partial N^m}\left\{\frac{\int_I \Sigma_t(E)\phi(E)\,dE}{\int_I \phi(E)\,dE}\right\} = \frac{1}{\bar{\phi}_I}\int_I \left\{\sigma^m_t(E) - [\bar{\Sigma}_{t_I} - \Sigma_t(E)]\left[\frac{1}{\phi(E)}\frac{\partial\phi(t)}{\partial N^m}\right]\right\}\phi(E)\,dE \tag{22}$$

$$\overline{\nu\sigma}^m_{f_I} \equiv \frac{\partial}{\partial N^m}\left\{\frac{\int_I \nu\Sigma_t(E)\phi(E)\,dE}{\int_I \phi(E)\,dE}\right\} = \frac{1}{\bar{\phi}_I}\int_I \left\{\nu\sigma^m_f(E) - [\overline{\nu\Sigma}_{f_I} - \nu\Sigma_f(E)]\left[\frac{1}{\phi(E)}\frac{\partial\phi(E)}{\partial N^m}\right]\right\}\phi(E)\,dE \tag{23}$$

$$\bar{\sigma}^m_{s0_{F\to I}} \equiv \frac{\partial}{\partial N^M}\left\{\frac{\int_I dE' \int_J \Sigma_{s0}(E\to E')\phi(E)\,dE}{\int_J \phi(E)\,dE}\right\} = \frac{1}{\phi_J}\int_I dE' \int_J \left\{\sigma^m_{s0}(E\to E') - \left[\frac{\Sigma_{s0_{J\to I}}}{\Delta E_I} - \Sigma_{s0}(E\to E')\right]\right.$$
$$\left.\cdot\left[\frac{1}{\phi(E)}\frac{\partial\phi(E)}{\partial N^m}\right]\right\}\phi(E)\,dE. \tag{24}$$

An approximate expression for the term $\left[\frac{1}{\phi(E)}\frac{\partial\phi(E)}{\partial N^m}\right]$, which appears in Eqs. (21–24), may be found by assuming that

$$\frac{1}{\phi(E)\Sigma^K_{tr}(E)}\frac{\partial[\phi(E)\Sigma^K_{tr}(E)]}{\partial N^m} = C^m_I, \qquad \text{for } E \text{ in group } I, \tag{25}$$

where C^m_I is an arbitrary constant which may be different for any isotope m and group I, and where K is an arbitrary integer which defines the type of approximation to be introduced. We shall consider three possible choices for K which correspond to assumptions having a clear physical meaning: (-1), (0), and (1). The various choices of K correspond to the three following assumptions:

$$(K = -1): \qquad \frac{1}{J}\frac{\partial J}{\partial N^m} = C^m_I \tag{26}$$

$$(K = 0): \qquad \frac{1}{\phi}\frac{\partial\phi}{\partial N^m} = C^m_I \tag{27}$$

$$(K = 1): \qquad \frac{1}{[\phi\Sigma_{tr}]}\frac{\partial[\phi\Sigma_{tr}]}{\partial N^m} = C^m_I, \tag{28}$$

which are physically equivalent to assuming that the relative change of the current, the flux, or the transport collision density, respectively, is constant over each group following an infinitesimal addition of the m-th isotope to the standard composition. Only the third of these approximations has a sound physical foundation, which follows from the fact that the transport collision density is a relatively smooth function of energy, and that its relative change can also be expected to be smooth. Therefore, the accuracy of the approximation expressed by Eq. (25) can be expected to improve as K changes from (-1) to (0), and from (0) to (1).

The expression for the logarithmic derivative of the flux can be obtained directly from Eq. (25):

$$\frac{1}{\phi(E)}\frac{\partial\phi(E)}{\partial N^m} = C^m_I - K\frac{\sigma^m_{tr}(E)}{\Sigma_{tr}(E)}, \tag{29}$$

and can be substituted into Eqs. (21–24). When the substitution is performed, all terms containing the C^m_I constant cancel each other, and the result is given by the following equations:

$$\bar{\sigma}^m_{tr} = \frac{1}{\bar{\phi}_I}\int_I \left\{(K+1)\left[\frac{\Sigma_{tr_I}}{\Sigma_{tr}(E)}\right]^2 - K\left[\frac{\Sigma_{tr_I}}{\Sigma_{tr}(E)}\right]\right\}\sigma^m_{tr}(E)\phi(E)\,dE \tag{30}$$

$$\bar{\sigma}^m_{t_I} = \frac{1}{\bar{\phi}_I}\int_I \left\{\sigma^m_t(E) + K[\bar{\Sigma}_{t_I} - \Sigma_t(E)]\frac{\sigma^m_{tr}(E)}{\Sigma_{tr}(E)}\right\}\phi(E)\,dE \tag{31}$$

$$\overline{\nu\sigma}_{f_I} = \frac{1}{\bar{\phi}_I}\int_I \left\{\nu\sigma^m_f(E) + K\,[\overline{\nu\Sigma}_{f_I} - \nu\Sigma_f(E)]\frac{\sigma^m_{tr}(E)}{\Sigma_{tr}(E)}\right\}\phi(E)\,dE \tag{32}$$

$$\bar{\sigma}^m_{s0_{J\to I}} = \frac{1}{\bar{\sigma}_J}\int_I dE'\int_J \left\{\sigma^m_{s0}(E\to E') + K\left[\frac{\Sigma_{s0_{J\to I}}}{\Delta E_I} - \Sigma_{s0}(E\to E')\right]\frac{\sigma^m_{tr}(E)}{\Sigma_{tr}(E)}\right\}\sigma(E)\,dE\,. \tag{33}$$

These equations satisfy the M conditions expressed by Eq. (14) with an accuracy that depends only on the validity of Eq. (25) for the chosen value of K. Furthermore, for any value of K, they satisfy identically also Eq. (13), as can be verified by direct substitution. Therefore, the problem of overdetermination has disappeared.

For the three choices of K that are being considered, the definitions reduce to the following expressions:

$(K = -1)$:

$$\bar{\sigma}^m_{tr_I} = \frac{1}{\bar{\phi}_I}\int_I \left[\frac{\Sigma_{tr_I}}{\Sigma_{tr}(E)}\right]\sigma^m_{tr}(E)\phi(E)\,dE \tag{34}$$

$$\bar{\sigma}^m_{t_I} = \frac{1}{\bar{\phi}_I}\int_I \left\{\sigma^m_t(E) - [\bar{\Sigma}_{t_I} - \Sigma_t(E)]\frac{\sigma^m_{tr}(E)}{\Sigma_{tr}(E)}\right\}\phi(E)\,dE \tag{35}$$

$$\overline{\nu\sigma}^m_{f_I} = \frac{1}{\bar{\phi}_I}\int_I \left\{\nu\sigma^m_f(E) - [\overline{\nu\Sigma}_{f_I} - \nu\Sigma_f(E)]\frac{\sigma^m_{tr}(E)}{\Sigma_{tr}(E)}\right\}\phi(E)\,dE \tag{36}$$

$$\bar{\sigma}_{s0_{J\to I}} = \frac{1}{\bar{\phi}_j}\int_I dE'\int_J \left\{\sigma^m_{s0}(E\to E') - \left[\frac{\bar{\Sigma}_{s0_{J\to I}}}{\Delta E_I} - \Sigma_{s0}(E\to E')\right]\frac{\sigma^m_{tr}(E)}{\Sigma_{tr}(E)}\right\}\phi(E)\,dE\,; \tag{37}$$

$(K = 0)$:

$$\bar{\sigma}^m_{tr_I} = \frac{1}{\bar{\phi}_I}\int_I \left[\frac{\Sigma_{tr_I}}{\Sigma_{tr}(E)}\right]^2\sigma^m_{tr}(E)\phi(E)\,dE \tag{38}$$

$$\bar{\sigma}^m_{t_I} = \frac{1}{\bar{\phi}_I}\int_I \sigma^m_t(E)\phi(E)\,dE \tag{39}$$

$$\overline{\nu\sigma}^m_{f_I} = \frac{1}{\bar{\phi}_I}\int_I \nu\sigma^m_f(E)\phi(E)\,dE \tag{40}$$

$$\bar{\sigma}^m_{s0_{J\to I}} = \frac{1}{\bar{\phi}_J}\int_I dE'\int_J \sigma^m_{s0}(E\to E')\phi(E)dE; \tag{41}$$

$(K = 1)$:

$$\bar{\sigma}^m_{tr_I} = \frac{1}{\bar{\phi}_I}\int_I \left\{2\left[\frac{\Sigma_{tr_I}}{\Sigma_{tr}(E)}\right]^2 - \left[\frac{\Sigma_{tr_I}}{\Sigma_{tr}(E)}\right]\right\}\sigma^m_{tr}(E)\phi(E)\,dE \qquad \text{(definition D)} \tag{42}$$

$$\bar{\sigma}^m_{t_I} = \frac{1}{\bar{\phi}_I}\int_I \left\{\sigma^m_t(E) + [\bar{\Sigma}_{t_I} - \Sigma_t(E)]\frac{\sigma^m_{tr}(E)}{\Sigma_{tr}(E)}\right\}\phi(E)\,dE \tag{43}$$

$$\overline{\nu\sigma}^m_{f_I} = \frac{1}{\bar{\phi}_I}\int_I \left\{\nu\sigma^m_f(E) + [\overline{\nu\Sigma}_{f_I} - \nu\Sigma_f(E)]\frac{\sigma^m_{tr}(E)}{\Sigma_{tr}(E)}\right\}\phi(E)\,dE \tag{44}$$

$$\bar{\sigma}^m_{s0_{J\to I}} = \frac{1}{\bar{\phi}_J}\int_I dE'\int_J \left\{\sigma^m_{s0(E\to E')} + \left[\frac{\bar{\Sigma}_{s0_{J\to I}}}{\Delta E_I} - \Sigma_{s0}(E\to E')\right]\frac{\sigma^m_{tr}(E)}{\Sigma_{tr}(E)}\right\}\phi(E)\,dE. \tag{45}$$

Equations (42–45) correspond to the choice of K that has the best physical meaning, and they provide the new definitions proposed in this work. It is interesting to note, however, that Eq. (34) is the definition currently used in MC² for the microscopic transport cross section, while Eqs. (39–41) are the definitions that MC² uses for the other microscopic cross-sections. Thus, the MC² definition of the microscopic transport cross section implicitly assumes that the logarithmic derivative of the current is constant over every group, while the other MC² definitions imply the same assumption about the flux. Both assumption may be valid if the width of the group is very small, but as the group increases in width the first assumption grows progressively worse than the second, and both of them become

TABLE VI-5-I. Core Composition of ZPR-3 Assembly No. 48

Isotope	Concentration, $\times 10^{22}$ atoms/cm³
Pu-239	0.1645
Pu-240	0.0106
Pu-241	0.0011
U-235	0.0016
U-238	0.7427
C	2.0767
Na	0.6231
Fe	0.9985
Cr	0.2681
Ni	0.1330
Mo	0.0206
Al	0.0109

TABLE VI-5-II. Comparison of Various Definitions of the Sodium Transport Cross Section in Assembly No. 48

Group Number	Lower Energy, eV	$\bar{\sigma}_{tr}^{Na}$, b				$\frac{\partial \bar{\Sigma}_{tr}}{\partial N^{Na}}$
		A	B	C	D	
2[a]	2.222×10^6	1.687	1.721	1.720	1.728	1.723
3	1.342×10^6	1.634	1.667	1.662	1.658	1.657
4	8.244×10^5	2.715	2.786	2.770	2.751	2.756
5	4.977×10^5	4.043	4.448	4.408	4.340	4.340
6	3.003×10^5	3.202	3.306	3.289	3.272	3.264
7	1.844×10^5	3.481	3.857	3.763	3.657	3.664
8	1.094×10^5	3.204	3.205	3.206	3.278	3.300
9	6.721×10^4	3.415	3.437	3.440	3.537	3.583
10	4.056×10^4	4.409	5.254	4.982	4.654	4.606
11	2.491×10^4	3.891	3.895	3.885	4.290	4.481
12	1.503×10^4	4.110	4.112	4.102	4.182	4.191
13	9.077×10^3	4.998	5.052	5.050	5.050	5.053
14	4.293×10^3	8.332	9.002	9.040	9.242	9.234
15	2.591×10^3	31.716	64.211	43.084	30.357	31.288
16	2.031×10^3	8.211	9.718	9.413	8.940	8.691
17	1.225×10^3	3.813	3.921	3.920	3.917	3.917
18	9.608×10^2	3.035	3.036	3.036	3.036	3.037
19	5.799×10^2	3.016	3.016	3.016	3.017	3.022
20	2.743×10^2	3.017	3.017	3.017	3.017	3.023
21	1.016×10^2	3.019	3.019	3.019	3.019	3.021
Mean square deviation over lethargy, b		0.047	0.235	0.091	0.012	—
Na-void effect,[b] $\%\delta k$		−3.97	−4.21	−4.15	−4.11	−4.09[c]

[a] The upper energy of Group 2 is 3.684 MeV.

[b] Diffusion-theory perturbation calculations for a bare sphere.

[c] From a calculation using 605 groups.

worse than the assumption concerning the transport collision density. Thus, in general, definitions (42–45) should be more satisfactory than definitions (17–20), and the difference should be particularly relevant for the microscopic transport cross section.

Numerical Results

The validity of the new definitions was checked by means of a modification of the ELMØE code, which could collapse the microscopic transport cross sections according to the various definitions. The code could also calculate the exact derivatives of the macroscopic transport cross sections, with which the results of the various definitions are to be compared.

The cross sections used in the test were taken from the 22-group Argonne Set 224 and from the EOMØE Legendre library. The ultrafine spectrum was calculated by the code over an ultrafine group structure including 605 groups, and then used to collapse the cross sections over the group structure of Set 224. Since the first and the last group of the ultrafine calculation were undivided, the corresponding cross sections are identical to the cross sections obtained after collapsing. Therefore, only the twenty intermediate groups of Set 224 need to be considered in the comparison, and their cross sections were obtained by collapsing 603 ultrafine groups.

The calculations were run for the composition of ZPR-3 Assembly No. 48, which is shown in Table VI-5-I. This composition is typical of a large carbide fast breeder reactor, and the results and conclusions obtained from it are in excellent agreement with those derived for other fast breeder reactors.

The ultrafine current, flux and transport collision density are shown in logarithmic scale in Fig. VI-5-1. An arbitrary constant was subtracted and added, respectively, to the first and to the third curve for graphical reasons.

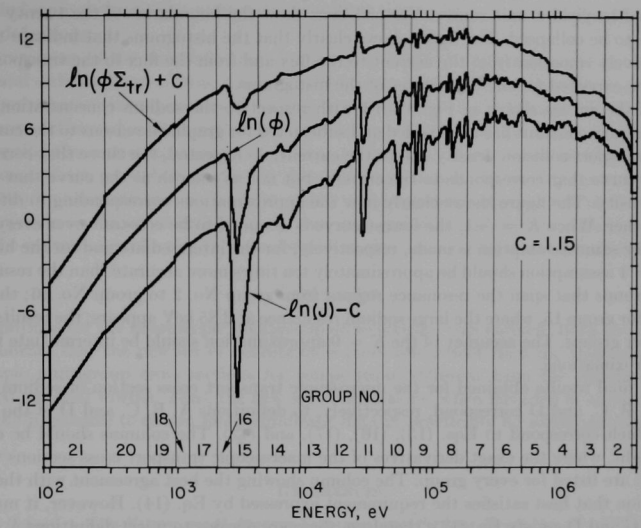

FIG. VI-5-1. The Energy Dependence of the Logarithm of the Current, of the Flux, and of the Transport Collision Density in ZPR-3, Assembly No. 48. Vertical Lines Indicate the Group Boundaries of Argonne Set 224. *ANL Neg. No. 113-1304.*

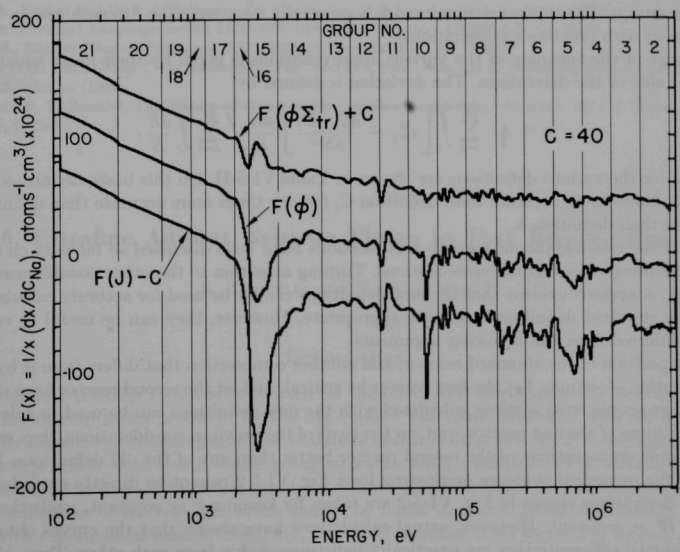

FIG. VI-5-2. The Energy Dependence of the Logarithmic Derivative of the Current, of the Flux, and of the Transport Collision Density by Respect to the Sodium Concentration in ZPR-3, Assembly No. 48. Vertical Lines Indicate the Group Boundaries of Argonne Set 224. *ANL Neg. No. 113-1305.*

The flux is normalized to yield a unit source. Vertical lines show the boundaries of the twenty groups over which the cross sections are to be collapsed. The figure shows clearly that the histograms that indicate the ultrafine calculations grow progressively smoother from the current to the flux and from the flux to the transport collision density. A similar trend can be expected for the derivatives of the histograms.

The derivatives of the curves shown in Fig. VI-5-1 with respect to the sodium concentration are shown in Fig. VI-5-2. Again, an arbitrary constant has been added and subtracted for graphical reasons to the curves corresponding, respectively, to the transport collision density and to the current. As expected, the curve that corresponds to the flux is smoother than the curve that corresponds to the current, but not as smooth as the curve that corresponds to the transport collision density. The figure shows clearly how the approximations corresponding to different choices of K compare with each other. When $K = -1$, the lowest curve is assumed to be constant over every fine group. When $K = 0$ and $K = 1$, the same assumption is made, respectively, for the intermediate and for the highest curve. Thus, the results of the $K = 1$ assumption should be approximately ten times more accurate than the results of the $K = -1$ assumption for the groups that span the resonance region, from group No. 2 to group No. 16; the difference should be particularly large for group 15, where the large sodium resonance at 2.85 keV appears; the results should be roughly equivalent in the other groups. The accuracy of the $K = 0$ approximation should be intermediate between the results of the other two approximations.

A summary of the final results obtained for the microscopic transport cross section of sodium is shown in Table VI-5-II. Columns A, B, C, and D correspond, respectively, to definitions A, B, C, and D of the microscopic transport cross-section, which correspond to Eqs. (15), (16), (17), and (42). The columns should be compared with the last column on the right, where the exact derivatives of the macroscopic transport cross sections with respect to the sodium concentration are listed for every group. The column showing the best agreement with the derivatives corresponds to the definition that best satisfies the requirement expressed by Eq. (14). However, it must be remembered that only definitions C and D satisfy Eq. (13); therefore, there are reasons to reject definitions A and B even though they were to compare favorably in Table VI-5-II.

From the results shown in the table, definition D appears to be consistently more accurate than any of the other definitions, the only exception occurring in the first group. The accuracy of definition D is approximately ten times greater than the accuracy of definition C over the first sixteen groups, while the two definitions are practically equivalent over the other groups. The difference in accuracy is especially large over the fifteenth group. These results are in excellent agreement with previous considerations.

An overall measure of the accuracy of the various approximations is given by their mean square deviation over lethargy from the value of the derivatives. The deviation is defined by

$$\mu = \sqrt{\sum_{I=2}^{21} \int_I \left[\sigma_{trI}^{m} - \frac{\partial \Sigma_{tr}(E)}{\partial N^m} \right]^2 \frac{dE}{E} \Big/ \sum_{J=2}^{21} \int_J \frac{dE}{E}}, \tag{46}$$

and the values of μ for the various definitions are shown in Table VI-5-II. On this basis, definition D appears to be approximately eight times more accurate than definition C, twenty times more accurate than definition B, and four times more accurate than definition A.

The definitions of the microscopic multigroup cross-sections have been discussed so far only on the basis of their use to calculate macroscopic multigroup cross-sections. Turning attention to the other possible uses that have been mentioned for them, it appears evident that the new definitions cannot be used for accurate calculations of reaction rates, for which the standard definitions are more appropriate. However, they can be useful to calculate material worths, as can be inferred from the following arguments.

Consider the composition of the standard reactor, and another composition that differs from it by an infinitesimal additional concentration of sodium. Let the first reactor be critical, and let the second reactor have the same buckling as the first. The microscopic cross sections calculated with the new definitions can be used to calculate exactly the macroscopic cross sections of the first reactor, and, on the basis of the previous considerations, they can be used to calculate the macroscopic cross-sections of the second reactor better than any of the old definitions. It may be noted, at this point, that the numerical evidence originating from Fig. VI-5-2 cannot be directly extended to support this point. The partial derivatives shown in Fig. VI-5-2 are taken by keeping k = constant, while they should now be taken by keeping B^2 = constant. However, actual calculations have shown that the curves obtained by the two different types of partial differentiation are practically indistinguishable from each other. Thus, also the difference between the effective multiplication constants of the reactors should be better calculated by using the new definitions. For an infinitesimal addition of material, the difference between the effective multiplication constants is given exactly by first-order perturbation theory, and it follows from this that the total material worths for uniform addi-

tion can be calculated more accurately in perturbation theory by using the new definitions given in this paper rather than the standard definitions.

A test of the convenience of the new definitions for material-worth computations was run by calculating the reactivity effect of total sodium removal from a bare spherical core having the same composition as ZPR-3 Assembly No. 48. Diffusion perturbation theory was used with the cross-sections of the Argonne Set 224 and with the microscopic transport cross-sections of sodium replaced by the values obtained by the various definitions. The standard definitions for collapsing the scattering cross-sections were used in all cases, but their effect can be neglected because the leakage component of the perturbation effect is strongly predominant. An ultrafine perturbation calculation for the same case was run by using 605 groups, and the results are compared in the last row of Table VI-5-II. Definition D appears to be superior to the other definitions in this test, and this confirms the validity of the considerations given above, and the convenience of using the new definitions also for material worth calculations.

Conclusion

A new set of definitions for the microscopic multigroup cross-sections was derived. Both the derivation and actual test calculations indicate that the new set of definitions is more convenient than the traditional sets when used to calculate macroscopic multigroup cross sections for compositions different from the standard composition, or to calculate distributed material worths. Thus, the new set of definitions, when included in current cross-section reduction codes, will make it possible to obtain more significant data at practically no additional computational expenditure.

References

1. A. Travelli, *A New Definition of the Microscopic Multigroup Transport Cross Sections*, Trans. Am. Nucl. Soc., **11** (2), 532–533 (1968).
2. A. L. Rago and H. H. Hummel, *ELMØE: An IBM-704 Program Treating Elastic Scattering Resonances in Fast Reactors*, ANL-6805 (1964).
3. B. J. Toppel, A. L. Rago and D. M. O'Shea, *MC²*, *A Code to Calculate Multigroup Cross Sections*, ANL-7318 (1967).
4. R. V. Meghreblian and D. K. Holmes, *Reactor Analysis*, (McGraw-Hill Book Company, New York, 1960), p. 522.
5. S. Yiftah, D. Okrent and P. A. Moldauer, *Fast Reactor Cross Sections*, (Pergamon Press, New York, 1960), p. 102.
6. W. M. M. Kerr, K. Parker and D. V. J. Williams, *The Calculation of Group Averaged Neutron Cross Sections: GALAXY 3 Facilities Available in S2 (Fortran) Language for the IBM-7030 (Stretch) Computer*, AWRE-0-97/64 (1965).
7. L. J. Templin, Ed., *Reactor Physics Constants*, ANL-5800, Second Edition, 557 (1963).
8. P. F. Zweifel and G. L. Ball, *Group Cross Sections for Fast Reactors*, Proc. Seminar of Physics of Fast and Intermediate Reactors, Paper SM-18/65, Vienna (1962).
9. J. H. Ferziger and P. F. Zweifel, *The Theory of Neutron Slowing Down in Nuclear Reactors* (M.I.T. Press, Cambridge, Massachusetts, 1966), p. 239.

VI-6. Ultrafine Adjoint Neutron Fluxes in Fast Breeder Reactors

A. Travelli and J. D. Eckard*

Introduction

A computer program (ADJØINT) has been written for the CDC-3600 to calculate the multigroup quantities adjoint to the real multigroup fluxes produced by the MC² code.[1] The basic difference between this type of calculation and most other adjoint calculations performed to date is that it is done over an ultrafine group structure including up to 2,100 groups rather than over a coarse group structure using a collapsed cross section set.

It is known from previous studies[2,3] that the use of an ultrafine group structure in real computations of fast breeder reactors reveals oscillations of the real flux which cannot be found in coarse group calculations, and which are in good agreement with experimental results.[4] Similarly, the use of ultrafine cross sections in adjoint calculations shows oscillations that could not be detected by coarse-group methods and which may affect the results of material worth computations.

* Student, Massachusetts Institute of Technology, Cambridge, Massachusetts.

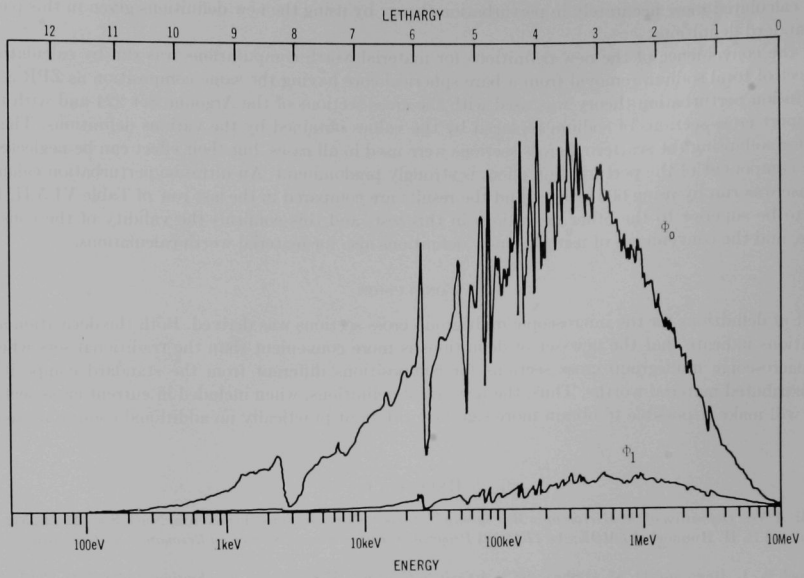

FIG. VI-6-1. Ultrafine Real Neutron Flux and Current in ZPR-3, Assembly No. 48. *ANL Neg. No. 113-1302.*

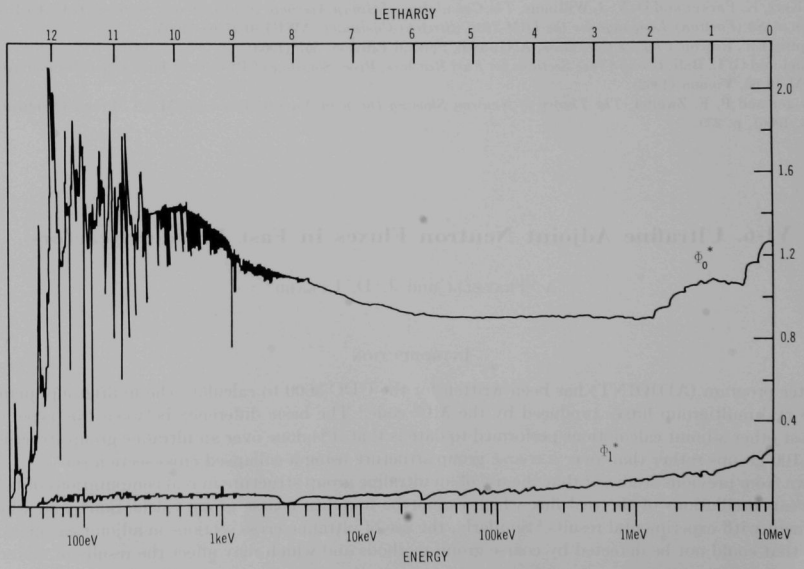

FIG. VI-6-2. Ultrafine Adjoint Neutron Flux and Current in ZPR-3, Assembly No. 48. *Anl Neg. No. 113-1306.*

Method

Schematically, and in the same notation used in Ref. 1, the equations used to determine the adjoint flux in the ordinary P_1 approximation are:

$$\phi_k^{+ufg} = \frac{S_k^{+ufg}}{L_k} \tag{1}$$

$$S_k^{+ufg} = \langle\nu\rangle_K^{fg}\langle\Sigma_f\rangle_K^{fg} + \nu_k^{ufg}\Sigma_{fk}^{ufg} + \sum_{j\neq k}\Sigma_{el_{k\to j}}^{ufg}\phi_j^{+ufg} + \sum_{J\neq K}\sum_j^J\left\{\left[\Sigma_{inel_k}^{ufg}\frac{\langle\Sigma_{inel}\rangle_{K\to j}^{fg}}{\langle\Sigma_{inel}\rangle_K^{fg}} + 2\Sigma_{n,2n_k}^{ufg}\frac{\langle\Sigma_{n,2n}\rangle_{K\to J}^{fg}}{\langle\Sigma_{n,2n}\rangle_K^{fg}}\right]\frac{\Delta e_j^{ufg}}{\Delta e_J^{fg}}\phi_j^{+ufg}\right\} \tag{2}$$

$$L_k = \frac{B^2}{3\Sigma_{tr_k}} + \langle\Sigma_c\rangle_K^{fg} + \Sigma_{c_k}^{ufg} + \langle\Sigma_f\rangle_K^{fg} + \Sigma_{f_k}^{ufg} + \langle\Sigma_{el}\rangle_{K\to K+1}^{fg} + \Sigma_{el_{r_k}}^{ufg} + \Sigma_{inel_k}^{ufg}\left(1 - \frac{\langle\Sigma_{inel}\rangle_{K\to K}^{fg}}{\langle\Sigma_{inel}\rangle_K^{fg}}\right) + \Sigma_{n,2n_k}^{ufg}\left(1 - \frac{2\langle\Sigma_{n,2n}\rangle_{K\to K}^{fg}}{\langle\Sigma_{n,2n}\rangle_K^{fg}}\right) + \langle\Sigma_{np}\rangle_K^{fg} + \langle\Sigma_{n\alpha}\rangle_K^{fg}. \tag{3}$$

In the consistent P_1 and B_1 approximations, Eq. (1) is replaced by the following expressions:

$$\phi_k^{+ufg} = \frac{S_k^{+ufg} + \dfrac{B}{\lambda_k\Sigma_{tot_k}}\sum_{j\neq k}\Sigma_{el_{k\to j}}^{1,ufg}J_j^{+ufg}}{L_k} \tag{4}$$

$$J_k^{+ufg} = \frac{1}{\gamma_k\Sigma_{tot_k}}\sum_{j\neq k}\Sigma_{el_{k\to j}}^{1,ufg}J_j^{+ufg} - \frac{\phi_k^{+ufgB}}{3\gamma_k\Sigma_{tot_k}}. \tag{5}$$

Minor modifications of these equations are used to take into account the eventual presence of hydrogen and of thermal neutrons.

Results

Both real and adjoint calculations for the neutron flux and the neutron current of ZPR-3 Assembly No. 48[5] were run on the CDC-3600 by using the ADJØINT program coupled to the MC² code. Figures VI-6-1 and VI-6-2 show, respectively, the real and adjoint fluxes obtained in the consistent B_1 approximation with 2,100 groups. The eigenvalues obtained in the two calculations agreed exactly with each other.

The oscillations of the adjoint flux at energies higher than 1 MeV are almost entirely due to the coarseness of the fine fission cross sections, and have little physical meaning; however, they indicate that some improvement in the calculations could be obtained by a more detailed handling of these cross sections. The wide oscillations of the adjoint flux at energies lower than 1 keV, on the other hand, have a clear physical meaning because they correspond to capture and fission resonances.

References

1. B. J. Toppel, A. L. Rago and D. M. O'Shea, *MC², A Code to Calculate Multigroup Cross Sections*, ANL-7318 (1967).
2. A. Travelli, *A Comment on the Comparison of Theoretical with Experimental Neutron Spectra in Fast Critical Assemblies*, ANL-7320, Proc. International Conference on Fast Critical Experiments and Their Analysis, Argonne, Illinois, October 10–13, 1966, pp. 481–485.
3. B. J. Toppel and H. H. Hummel, *Comparative Physics Analysis of Fast Reactors as a Function of Refinement in Multigroup Cross Section Preparation*, Proc. International Conference on Research Reactor Utilization and Reactor Mathematics, Mexico City, May 2–4, 1967.
4. E. F. Bennett, *Neutron Spectrum Measurement in a Fast Critical Assembly*, Nucl. Sci. Eng. **27**, 28–33 (1967).
5. A. M. Broomfield, P. I. Amundson, W. G. Davey, J. G. Gasidlo, A. L. Hess, W. P. Kenney and J. K. Long, *ZPR-3 Assembly 48: Studies of a Dilute Plutonium-Fueled Assembly*, ANL-7320, Proc. International Conference on Fast Critical Experiments and Their Analysis, Argonne, Illinois, October 10–13, 1966, pp. 205–215.

VI-7. A Modification of the Bell Approximation for Slab Geometries

A. Travelli

Introduction

The MC² code[1] makes use of the Bell approximation[2] to calculate Dancoff factors with a modification introduced by H. Hummel.[3] The modification, however, applies only to cylindrical geometries. Since many MC² calculations concern slab geometries, it is desirable to extend the modification so that it includes this particular case with reasonable accuracy, and to evaluate the difference between calculations for the two types of geometry.

Discussion

If we define, according to the MC² notation,

$C \equiv$ Dancoff coefficient

$\gamma = 1 - C \equiv$ Surface correction factor

$\gamma_B = (1 + \Sigma_{e1}/\Sigma_1)^{-1} \equiv$ Bell approximation of γ

$\Sigma_{e1} \equiv$ Inverse average chord of the coolant region,

then the surface correction factor is calculated by MC² according to the relation

$$\gamma = \gamma_B + \gamma_B^4 (1 - \gamma_B), \tag{1}$$

where the term $\gamma_B^4(1 - \gamma_B)$ corresponds to the Hummel modification of the Bell approximation.

The value of the surface correction factor that corresponds to the Dancoff-Ginsburg formulation for slab geometry is given by

$$\gamma = 2E_3[0.5\gamma_B/(1 - \gamma_B]), \tag{2}$$

where the function $E_3(x)$ is defined by

$$E_3(x) = \int_1^\infty e^{-xt} t^{-3}\, dt.$$

Equation (2) can be derived from Ref. 4 by using the definitions that have been introduced above.

Several expansions are known for the E_3 function,[5] and they could be used to introduce Eq. (2) into the MC² slab calculations. The expansions are somewhat complicated, however, and it is desirable to replace them with some approximation combining accuracy with speed of calculation.

A convenient solution is to replace Eq. (1) with

$$\gamma = \gamma_B + \gamma_B^4(1 - \gamma)b, \tag{3}$$

where the constant b is 1.0 in cylindrical geometries and 1.7 in slab geometries. Equation (3) reduces obviously to Eq. (1) in cylindrical geometry; in slab geometry it agrees with Eq. (2) within 1% over the γ_B range that spans from 0.0 to 0.875. This range corresponds to a Σ_1/Σ_{e1} range from 0.0 to 7.0 and covers most practical applications. Even for larger values of γ_B, the discrepancy between the two equations is never larger than 2%. A graphical comparison of Eq. (2) with the values obtained from Eq. (3) with $b = 0, 1$, and 1.7 is shown in Fig. VI-7-1 over the whole γ_B range. The fairly large deviations of the Bell approximation from the Dancoff-Ginsburg calculations for slab geometry and for large values of γ_B is in good agreement with the comments of C. Kelber and P. Kier on the subject.[6]

Results

A test was run for a slab lattice corresponding to the fourth experiment described in Ref. 6. The cell is comprised of a metallic plutonium slab (1.13792 cm thick, with 3.98212×10^{22} atoms/cm³) and of a graphite slab (5.08008 cm thick, with 8.82846×10^{22} atoms/cm³) at 300°K. This is a fairly extreme case, because the scattering cross section of carbon is close to 5 b over most of the energy range; thus, $\Sigma_1/\Sigma_{e1} \approx 4.5$, $\gamma_B \approx 0.82$. The ENDF/B data file was used for the cross-sections and the calculations were run with the ultrafine group structure in the consistent B-1 approximation. The constant a in MC² was chosen to be unity.

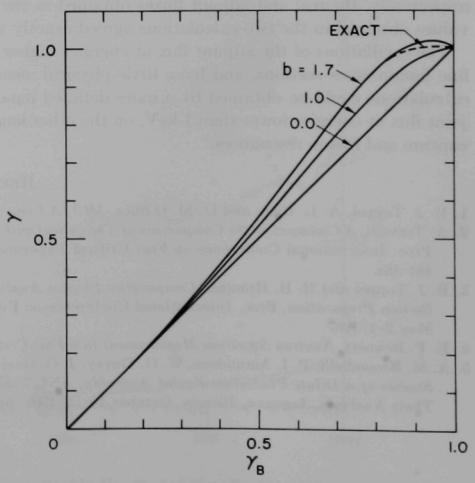

Fig. VI-7-1. Comparison of Various Approximations of the Surface Correction Factor with the Exact Solution for Plane Geometry. *ANL Neg. No. 113-860.*

TABLE VI-7-I. Pu-239 Cross Sections and Fluxes with $b = 1.0$

Group	Lower Energy, eV	σ_c, b	σ_f, b	ϕ	ϕ^*
1	0.6065×10^7	0.1000×10^{-9}	2.167	0.2544	0.9097
2	0.3678×10^7	0.1000×10^{-9}	1.900	1.109	0.9012
3	0.2231×10^7	0.1000×10^{-9}	2.013	2.417	0.9627
4	0.1353×10^7	0.4879×10^{-2}	1.924	3.476	0.9719
5	0.8208×10^6	0.4484×10^{-1}	1.757	3.382	1.012
6	0.4978×10^6	0.8876×10^{-1}	1.624	3.043	1.067
7	0.3019×10^6	0.1348	1.501	2.602	1.114
8	0.1831×10^6	0.1800	1.481	2.133	1.158
9	0.1110×10^6	0.2090	1.516	1.713	1.193
10	0.6737×10^5	0.2220	1.527	1.364	1.217
11	0.4086×10^5	0.2971	1.493	1.084	1.236
12	0.2478×10^5	0.5098	1.638	0.8480	1.263
13	0.1503×10^5	0.7349	1.838	0.6481	1.296
14	0.9118×10^4	0.9564	2.060	0.4848	1.332
15	0.5530×10^4	0.1154×10^1	2.301	0.3558	1.373
16	0.3354×10^4	0.1350×10^1	2.514	0.2557	1.423
17	0.2034×10^4	0.1609×10^1	2.886	0.1783	1.480
18	0.1234×10^4	0.1851×10^1	3.345	0.1199	1.552
19	0.7485×10^3	0.1982×10^1	3.833	0.07739	1.637
20	0.4540×10^3	0.2796×10^1	5.447	0.04851	1.733
21	0.2753×10^3	0.1485×10^1	4.612	0.02843	1.857
22	0.1670×10^3	0.2889×10^1	9.870	0.01347	1.954
23	0.1013×10^3	0.4006×10^1	9.057	0.006475	1.924
24	0.6144×10^2	0.2209×10^1	15.23	0.002564	2.103
25	0.3726×10^2	0.8769×10^1	21.63	0.0006154	1.730
26	0.2260×10^2	0.2922×10^1	32.25	0.0004034	1.167

TABLE VI-7-II. Pu-239 Cross Sections and Fluxes with $b = 1.7$

Group	Lower Energy, eV	σ_c, b	σ_f, b	ϕ	ϕ^*
1	0.6065×10^7	0.1000×10^{-9}	2.167	0.2544	0.9097
2	0.3678×10^7	0.1000×10^{-9}	1.900	1.109	0.9012
3	0.2231×10^7	0.1000×10^{-9}	2.013	2.417	0.9627
4	0.1358×10^7	0.4879×10^{-2}	1.924	3.476	0.9719
5	0.8208×10^6	0.4484×10^{-1}	1.757	3.382	1.012
6	0.4978×10^6	0.8876×10^{-1}	1.624	3.043	1.067
7	0.3019×10^6	0.1348	1.501	2.602	1.114
8	0.1831×10^6	0.1800	1.481	2.133	1.158
9	0.1110×10^6	0.2090	1.516	1.713	1.193
10	0.6737×10^5	0.2219	1.526	1.364	1.218
11	0.4086×10^5	0.2968	1.492	1.084	1.236
12	0.2478×10^5	0.5095	1.637	0.8481	1.264
13	0.1503×10^5	0.7345	1.838	0.6482	1.296
14	0.9118×10^4	0.9562	2.061	0.4849	1.332
15	0.5530×10^4	0.1155×10^1	2.303	0.3558	1.373
16	0.3354×10^4	0.1354×10^1	2.519	0.2556	1.420
17	0.2034×10^4	0.1616×10^1	2.897	0.1781	1.480
18	0.1234×10^4	0.1864×10^1	3.362	0.1196	1.551
19	0.7485×10^3	0.2003×10^1	3.858	0.07703	1.636
20	0.4540×10^3	0.2822×10^1	5.476	0.04815	1.732
21	0.2753×10^3	0.1518×10^1	4.648	0.02812	1.856
22	0.1670×10^3	0.2922×10^1	9.936	0.01326	1.954
23	0.1013×10^3	0.4051×10^1	9.129	0.006346	1.925
24	0.6144×10^2	0.2228×10^1	15.32	0.002503	2.105
25	0.3726×10^2	0.8865×10^1	21.92	0.0005956	1.734
26	0.2260×10^2	0.2962×10^1	32.58	0.0003889	1.168

TABLE VI-7-III. Relative Percent Changes from $b = 1.0$ to $b = 1.7$

Group	Lower Energy, eV	$100 \times \left(\frac{\delta\sigma}{\sigma}\right)_{cap}$	$100 \times \left(\frac{\delta\sigma}{\sigma}\right)_{fis}$	$100 \times \left(\frac{\delta\phi}{\phi}\right)$	$100 \times \left(\frac{\delta\phi^*}{\phi^*}\right)$
1	0.6065×10^7	0.00	0.00	0.00	0.00
2	0.3678×10^7	0.00	0.00	0.00	0.00
3	0.2231×10^7	0.00	0.00	0.00	0.00
4	0.1353×10^7	0.00	0.00	0.00	0.00
5	0.8208×10^6	0.00	0.00	0.00	0.00
6	0.4978×10^6	0.00	0.00	0.00	0.00
7	0.3019×10^6	0.00	0.00	0.00	0.00
8	0.1831×10^6	0.00	0.00	0.00	0.00
9	0.1110×10^6	0.00	0.00	0.00	0.00
10	0.6737×10^5	−0.04	−0.02	0.00	0.00
11	0.4086×10^5	−0.07	−0.04	0.00	0.00
12	0.2478×10^5	−0.06	−0.03	0.01	0.01
13	0.1503×10^5	−0.05	−0.01	0.01	0.01
14	0.9118×10^4	−0.01	0.03	0.01	0.01
15	0.5530×10^4	0.07	0.10	0.00	0.01
16	0.3354×10^4	0.23	0.22	−0.03	−0.19
17	0.2034×10^4	0.46	0.36	−0.11	0.00
18	0.1234×10^4	0.72	0.50	−0.25	−0.02
19	0.7485×10^3	1.05	0.63	−0.46	−0.04
20	0.4540×10^3	0.93	0.53	−0.73	−0.05
21	0.2753×10^3	2.17	0.78	−1.07	−0.05
22	0.1670×10^3	1.14	0.57	−1.51	0.00
23	0.1013×10^3	1.14	0.79	−1.98	0.01
24	0.6144×10^2	0.85	0.58	−2.38	0.11
25	0.3726×10^2	1.10	1.32	−3.23	0.22
26	0.2260×10^2	1.37	1.02	−3.60	0.10

The main results for a 26-group set with constant 0.5 lethargy width and with $b = 1.0$ and $b = 1.7$ are given, respectively, in Tables VI-7-I and VI-7-II. Table VI-7-III shows the percent changes found in Table VI-7-II with respect to Table VI-7-I.

Both the capture and the fission effective cross-sections of Pu-239 are found to be slightly larger at low energies with $b = 1.7$. The maximum increase in σ_{cap} is 2.17% around 0.3 keV, and the increase is already 1% at 1.0 keV. By contrast, the increase of σ_f is larger than 1% only at energies lower than 50 eV. The combined effect of the changes in the two types of cross sections is such that, in the case considered, no change was found in the critical buckling (0.0184076 cm^{-2}). The increase of σ_{cap} causes a slight hardening of the real flux: the population of the last group decreases by 3.6%. The combined and balancing changes of σ_{cap} and σ_f cause some very minor oscillations in the adjoint flux.

Conclusion

No major cross section changes are expected to result when the Dancoff coefficient is calculated in slab geometry rather than in cylindrical geometry. The results of the test, however, appear to warrant the inclusion of the modification in the MC^2 calculations. The effect is

bound to be felt only in calculations very sensitive to the shape of the flux in the low-energy range, such as Doppler and sodium-void calculations.

References

1. B. J. Toppel, A. L. Rago and D. M. O'Shea, *MC²*, *A Code to Calculate Multigroup Cross Sections*, ANL-7318 (1967).
2. G. I. Bell, *A Simple Treatment for Effective Resonance Integrals in Dense Lattices*, Nucl. Sci. Eng. **5**, 138 (1959).
3. H. H. Hummel, *Equivalence Between Homogeneous and Heterogeneous Resonance Integrals in Cylindrical Geometry*, Reactor Physics Division Annual Report, July 1, 1964 to June 30, 1965, ANL-7110, pp. 319–320.
4. S. M. Dancoff and M. Ginsburg, *Surface Resonance Absorption in a Close Packed Lattice*, CP-2157 (1944).
5. K. M. Case, F. De Hoffmann and G. Placzek, *Introduction to the Theory of Neutron Diffusion*, (Superintendent of Documents, U. S. Government Printing Office, Washington, D. C.) p. 154 (1953).
6. C. N. Kelber and P. H. Kier, *Comments on Bell's Approximation to the Resonance Integral*, Nucl. Sci. Eng. **6**, 251 (1959).
7. A. Goodwin and C. L. Shuske, *Plutonium Graphite Assemblies, Part II*, RFP-158 (1959).

VI-8. Multigroup Transport Analysis of Neutron Wave Propagation in Fast Multiplying Media[1]

A. Travelli

Introduction

The study of neutron wave propagation in fast multiplying media in multigroup transport theory presents two main difficulties which are not encountered in the study of neutron wave propagation in moderators,[2] and which make it necessary to change the analytical and computational procedures.

The first difficulty is caused by the presence of delayed multiplication which, even though it may be found also in thermal systems, requires methods of calculation which have not been previously developed.

The second difficulty is caused by the great irregularity with which the cross sections depend on energy over the energy range of interest in fast systems; this behavior of the cross sections makes it necessary to use a very large number of groups which cannot be handled by present computers if codes are used that require the calculation of complex determinants including the scattering matrices.

Discussion

The delayed multiplication problem

The Boltzmann equation in plane geometry may be written to include the effect of delayed multiplication as follows:

$$\left[\mu \frac{\partial}{\partial x} + \frac{1}{v}\frac{\partial}{\partial t} + \Sigma_t(E)\right]\Phi(\mu,E,t,x) = \sum_{\ell=0}^{\infty} \frac{2\ell+1}{2} P_\ell(\mu) \int_0^\infty \Sigma_s^\ell(E' \to E) \cdot \Phi_\ell(E',t,x)\, dE' + \frac{1-\beta}{2}\chi_p(E) \cdot \int_0^\infty \nu\Sigma_f(E')\Phi_0(E',t,x)dE' + \frac{1}{2}\sum_{m=1}^{M} \lambda_m \chi_m(E) C_m(t,x) \tag{1}$$

$$\frac{\partial}{\partial t} C_m(t,x) = \beta_m \int_0^\infty \nu\Sigma_f(E')\Phi_0(E',t,x)dE' - \lambda_m C_m(t,x); \qquad m = 1, 2, \cdots, M, \tag{2}$$

where

$\mu \equiv$ angle cosine
$x \equiv$ spatial coordinate
$t \equiv$ time
$E \equiv$ energy
$v \equiv$ neutron speed
$\Phi(\mu,E,t,x) \equiv$ neutron flux
$P_\ell(\mu) \equiv \ell$th Legendre polynomial
$\Phi_\ell(E,t,x) \equiv \ell$th Legendre component of the neutron flux
$\Sigma_s^\ell(E' \to E) \equiv \ell$th Legendre component of the scattering kernel
$\Sigma_t(E) \equiv$ total cross-section
$\nu\Sigma_f(E) \equiv$ average number of neutrons emitted per fission times the fission cross-section
$\chi_p(E) \equiv$ fission spectrum of prompt neutrons
$M \equiv$ number of families of delayed neutrons
$C_m(t,x) \equiv$ precursor concentration of the mth family of delayed neutrons
$\chi_m(E) \equiv$ fission spectrum of the mth family of delayed neutrons
$\lambda_m \equiv$ decay constant of the mth family of delayed neutrons
$\beta_m \equiv$ fraction of fission neutrons in the mth family of delayed neutrons
$\beta \equiv$ fraction of fission neutrons in all families of delayed neutrons.

We assume for the neutron flux a solution of the type:

$$\Phi(\mu,E,t,x) = \mathrm{Re}\,[\phi(\mu,E)e^{i\omega t - px}], \tag{3}$$

which leads immediately to similar expressions for the various Legendre components of the neutron flux:

$$\Phi_\ell(E,t,x) = \mathrm{Re}\,[\phi_\ell(E)e^{i\omega t-\rho x}]. \tag{4}$$

The variables ω and ρ, which appear in Eqs. (3) and (4), correspond respectively to the angular frequency of the neutron wave under study and to its complex inverse relaxation length.

Substitution of Eq. (4) into Eq. (2) yields

$$\frac{\partial}{\partial t} C_m(t,x) = F_m(x)e^{i\omega t} - \lambda_m C_m(t,x)\,, \tag{5}$$

with

$$F_m(x) = \beta_m e^{-\rho x}\int_0^\infty \nu\Sigma_f(E')\phi_0(E')\,dE', \quad \text{for} \quad m = 1, 2, \cdots, M. \tag{6}$$

The general solution of the homogeneous equation associated with Eq. (5) is

$$C_m^h(t,x) = C_{m0}(x)\exp(-\lambda_m t),$$

and a particular solution is

$$C_m^p(t,x) = \frac{F(x)}{i\omega t + \lambda_m}\,e^{i\omega t}.$$

If the initial transients are not of special interest and the attention is focused only on the behavior of the neutron wave at steady state, only very large values of time need be considered. As the variable t tends to infinity, the contribution of $C_m^h(t,x)$ to the general solution tends to zero, so that only the contribution of the particular solution must be taken into account. Thus, the expression of the concentration of the mth precursor that corresponds to the neutron wave represented by Eq. (3) is found to be

$$C_m(t,x) = \frac{\beta_m}{i\omega + \lambda_m}\,e^{i\omega t-\rho x}\int_0^\infty \nu\Sigma_f(E')\phi_0(E')\,dE'. \tag{7}$$

Equations (3) and (7) may now be substituted into Eq. (1) to give

$$\begin{aligned}\left[-\mu\rho + \frac{i\omega}{v} + \Sigma_t(E)\right]\phi(E,\mu) &= \sum_{\ell=0}^{\infty}\frac{2\ell+1}{2}P_\ell(\mu)\int_0^\infty \Sigma_s^\ell(E'\to E)\phi_\ell(E')\,dE' \\ &+ \frac{1}{2}\left[(1-\beta)\chi_p(E) + \sum_{m=1}^{M}\frac{\lambda_m\beta_m}{i\omega+\lambda_m}\chi_m(E)\right] \\ &\cdot\int_0^\infty \nu\Sigma_f(E')\phi_0(E')\,dE'.\end{aligned} \tag{8}$$

Within the framework of multigroup theory Eq. (8) may be rewritten in the following matrix form:

$$\begin{aligned}[-\mu\rho\underline{I} + i\omega\underline{v}^{-1} + \underline{\Sigma}_t]\phi(\mu) &= \sum_{\ell=0}^{\infty}\frac{2\ell+1}{2}P_\ell(\mu)\underline{\Sigma}_{s\ell}\phi_\ell + \frac{1}{2}(\boldsymbol{\nu\Sigma}_f\cdot\phi_0) \\ &\cdot\left[(1-\beta)\chi_p + \sum_{m=1}^{M}\frac{\lambda_m\beta_m}{i\omega+\lambda_m}\chi_m\right],\end{aligned} \tag{9}$$

where underlining is used to indicate matrices, and the bold-face symbols indicate vectors.

With the introduction of two new definitions, in which the symbol $\delta_{m,n}$ indicates the Kronecker's delta function,

$$\underline{\Sigma}_t^* = \underline{\Sigma}_t + i\omega\underline{v}^{-1} \tag{10}$$

$$\underline{\Sigma}_{s\ell}^* = \underline{\Sigma}_{s\ell} + \left\{(1-\beta)\chi_p + \sum_{m=1}^{M}\frac{\lambda_m\beta_m}{i\omega+\lambda_m}\chi_m\right\}\cdot\boldsymbol{\nu\Sigma}_f\delta_{\ell,0}\,, \tag{11}$$

Equation (9) can be written in a simpler form:

$$(-\mu\rho\underline{I} + \underline{\Sigma}_t^*)\phi(\mu) = \sum_{\ell=0}^{\infty}\frac{2\ell+1}{2}\underline{\Sigma}_{s\ell}^*\phi_\ell. \tag{12}$$

Equation (10) is of particular interest because it is exactly the same equation that is found in the analysis of the propagation of neutron waves in moderators,[2] with the only difference that the matrix $\underline{\Sigma}_{s\ell}$ is now replaced by the matrix $\underline{\Sigma}_{s\ell}^*$. Thus, the same method used in Ref. 2 can be applied to find the solution of Eq. (12). The result is given by the following equations:

$$\left\{\sum_{n=0}^{\infty}\frac{2n+1}{\rho}\underline{Q}_n(\rho^{-1}\underline{\Sigma}_t^*)\underline{\Sigma}_{sn}^*\underline{H}_n - \underline{I}\right\}\phi_0 = 0, \tag{13}$$

where $Q_n(x)$ indicates the Legendre functions of the second kind and of nth order, and the matrices $\underline{H}_n$ are defined by

$$\begin{aligned}&\underline{H}_{-1} = 0;\quad \underline{H}_0 = \underline{I}; \\ &\underline{H}_n = \frac{2n-1}{\rho n}[\underline{\Sigma}_t^* - \underline{\Sigma}_{s(n-1)}^*]\underline{H}_{n-1} - \frac{n-1}{n}\underline{H}_{n-2}, \qquad n \geq 1.\end{aligned} \tag{14}$$

The complex eigenvalue ($\rho = \alpha + i\xi$) and the complex eigenfunction ($\phi_0 = \phi_{0R} + i\phi_{0I}$) of Eq. (13) provide, respectively, the complex inverse relaxation length and the spectral properties of the scalar flux of the neutron wave propagating with angular frequency ω. The spectra of the higher Legendre components of the neutron flux are obtained from

$$\phi_n = \underline{H}_n\phi_0\,. \tag{15}$$

THE ENERGY PROBLEM

As pointed out in the introduction, a rather large number of energy groups is needed to take accurately

into account the sharp variation of the cross sections with energy in the energy range which is of interest in most fast systems. Calculations performed by the ELMØE[3] and MC² [4] codes may use from 600 to 2,100 groups to calculate accurately the stationary spectrum in fast reactors. The same number of groups should be used in the analysis of neutron waves if a comparable accuracy is desired. The size of the matrix which appears in Eq. (13) is given by the number of the groups, and if the eigenvalue ρ is sought by imposing that the determinant of the matrix vanish,[2] two rather difficult problems arise; most computers do not have a prompt storage large enough to accommodate the entire matrix, and the time needed to calculate the determinant by the same method used in Ref. 2 is excessively long. Since the time needed to compute a determinant is approximately proportional to the third power of the matrix size, the calculation of a determinant for a problem of this type on the CDC-3600, which takes approximately 10 seconds with 30 groups, may be estimated to require 20 and 1000 hours of computing time when run, respectively, with 600 and with 2100 groups. The difficulty may be resolved by taking advantage of the absence of upscattering in fast systems in a way which is similar to the methods used in the ELMØE and MC² codes.

The matrix that premultiplies $\boldsymbol{\phi}_0$ in Eq. (13) may be decomposed into the difference between a lower-triangular matrix (because of the absence of upscattering) and the product of a column vector (χ) times a row vector ($\nu\boldsymbol{\Sigma}_f$). If the complex scalar flux is normalized so that the real part of the scalar product ($\nu\boldsymbol{\Sigma}_f \cdot \boldsymbol{\phi}_0$) is unity and the imaginary part vanishes, Eq. (13) assumes the form of an inhomogeneous equation in which the matrix is lower-triangular and depends on the value assumed for the eigenvalue ρ. The eigenfunction of the problem can then be obtained directly by starting from first group and by solving the problem progressively for all successive groups. The eigenvector $\boldsymbol{\phi}_0$ obtained in this way satisfies the imposed normalizing condition only if the proper value is assumed for the eigenvalue ρ. Thus, it is possible to proceed according to a Newton-Raphson iteration scheme that leads simultaneously to the determination of the eigenvector ρ and of the corresponding eigenvector $\boldsymbol{\phi}_0$.

This process requires storage only of the non-zero elements of the lower-triangular matrix, and reduces the computing time so that only 15 seconds per iteration are needed on the CDC-3600 with 600 energy groups. Thus, the computing time for this type of problem is reduced by a factor of approximately 5,000 from the time needed by the method described in Ref. 2; furthermore, the computing time required by this method is approximately proportional to the square of the number of groups, rather than to their cube.

Results

Some calculations were run to test the method in a particular case. The material chosen for the study of the dispersion law was the core of ZPR-6 Assembly No. 5,[5] whose composition is shown in Table VI-8-I. Table VI-8-II lists the main parameters used for the six families of delayed neutrons considered in the test. The parameters were taken from Ref. 6, from which also the energy-dependent emission spectra of the delayed families were adapted. The elastic scattering cross sections of the light elements were prepared from the ELMØE library over a 605 group structure; the other cross sections were prepared over a coarser group structure (22 groups) from the Argonne Set 224.[7]

The value of k_∞ in Assembly No. 5 is very close to 1.2. This value was changed in various calculations by modifying the value of $\bar{\nu}$, the average number of neutrons emitted per fission. The change made it possible to investigate numerically the dependence of the dispersion law of neutron waves on the reactivity of the material.

Figure VI-8-1 shows the dispersion laws obtained from the calculations for various values of the reactivity. Some basic properties of the curves may be inferred directly from the form of Eq. (13), which was used to derive them. For instance, if the eigenvalues α and ξ are expanded in a Maclaurin series of the angular frequency ω, it can be shown that for $k_\infty < 1$ all even terms of the α-expansion vanish with all odd terms of the ξ-expansion. For $k_\infty > 1$ the situation is reversed. Thus, for zero frequency, all curves shown in Fig. VI-8-1 intersect the α axis at right angles when $k_\infty < 1$, and

TABLE VI-8-I. Core Composition of ZPR-6 Assembly No. 5

($atoms\ cm^{-3} \times 10^{22}$)

U-235	0.153
U-238	1.060
Na	0.920
C	1.290
Fe	0.904
Ni	0.113
Cr	0.239

TABLE VI-8-II. Delayed Neutron Data

m	γ_m, sec^{-1}	$\beta_m \times 10^3$
1	0.0130	0.240
2	0.0314	0.137
3	0.1360	1.210
4	0.3400	2.600
5	1.3200	0.820
6	3.5000	0.170

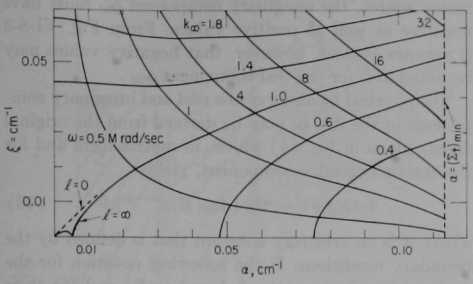

FIG. VI-8-1. The Dispersion Law in ZPR-6, Assembly No. 5 for Various Values of k_∞. *ANL Neg. No. 113-1298 T-1.*

the ξ axis when $k_\infty > 1$. When $k_\infty = 1$, it can be shown that they intersect the origin at 45 deg. As the frequency increases, the curves move away from the axes, but very high frequencies are needed to achieve any significant change in the constants. The curves eventually merge in the continuum[2] at extremely high frequency; this merging is not shown in Fig. VI-8-1, where the curves are shown only within the area $\alpha \leq (\Sigma_f)_{min}$, where no continuum exists.

The presence of delayed neutrons affects the dispersion law at very low frequency ($\omega \leq 80$ rad/sec), when they cause a deviation which is particularly appreciable for $k_\infty = 1$. The effect of the delayed neutrons for this case is shown in Fig. VI-8-1 by comparing the actual dispersion law, indicated by a solid curve, with the dotted curves that are obtained when all decay constants of the delayed neutron precursors are divided by a constant ℓ which may assume the values zero or infinity. These two choices of the constant ℓ correspond, respectively, to the case when all delayed neutrons are considered to behave as prompt neutrons and to the case when their presence is entirely neglected. The solid curve may be considered to correspond to a third value of ℓ, chosen to be unity.

The effect of delayed neutrons on the dispersion law in the case $k_\infty = 1$ and at low frequency is shown in greater detail in Fig. VI-8-2. The solid curve that corresponds to $\ell = 1$, and which takes correctly into account the presence of delayed neutrons, tends to the $x = y$ line at very low frequency, as expected. The same behavior is found for the $\ell = 0$ curve, which corresponds to considering the delayed neutrons as if they were prompt; the similarity is due to the fact that the approximation introduced does not affect the value of k_∞. It may be noted, however, that even though the two curves tend to become tangent to the same straight line, the distance between points corresponding to the same frequency on the two curves is always finite; in the limit, as the frequency tends to zero, it may be shown that this distance is related to the reactor period. The third curve, which corresponds to $\ell = \infty$ and, therefore, to the case when the existence of delayed neutrons is neglected, intersects the α-axis at a finite point $\alpha = \alpha^*$, rather than the origin, because the neglect of delayed neutrons reduces k_∞ to a value smaller than unity.

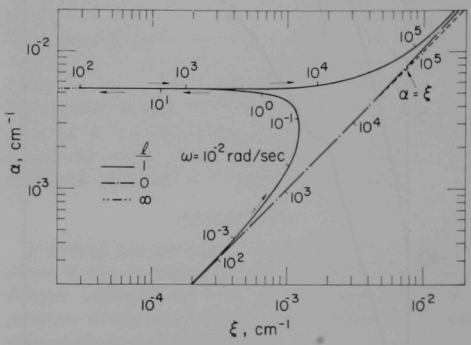

FIG. VI-8-2. The Dispersion Law in ZPR-6, Assembly No. 5 for $k_\infty = 1$. *ANL Neg. No. 113-1301 T-1.*

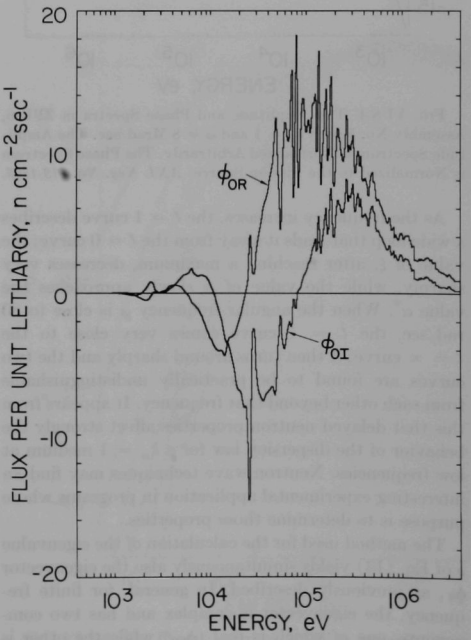

FIG. VI-8-3. The Real and Imaginary Components of the Scalar Flux in ZPR-6, Assembly No. 5 with $k_\infty = 1$ and $\omega = 8$ Mrad/sec. The Flux is Normalized to Give a Unit Fission Source. *ANL Neg. No. 113-1299 T-1 Rev. 1.*

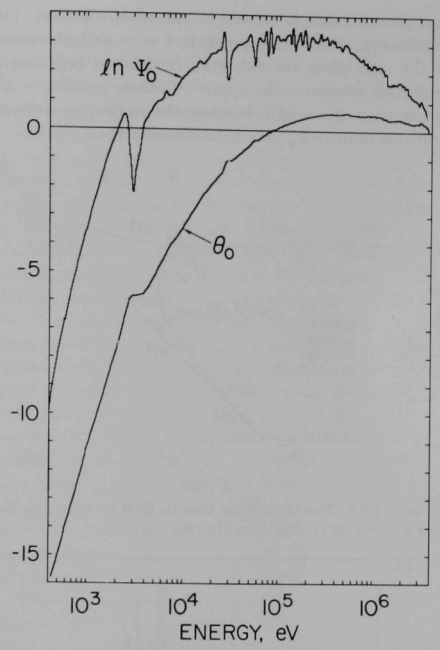

FIG. VI-8-4. The Amplitude and Phase Spectra in ZPR-6, Assembly No. 5 with $k_\infty = 1$ and $\omega = 8$ Mrad/sec. The Amplitude Spectrum is Normalized Arbitrarily. The Phase Spectrum is Normalized to the Fission Source. *ANL Neg. No. 113-1303.*

As the frequency increases, the $\ell = 1$ curve describes a wide loop that leads it away from the $\ell = 0$ curve; the value of ξ, after reaching a maximum, decreases very sharply, while the value of α slowly approaches the value α^*. When the angular frequency ω is close to 80 rad/sec, the $\ell = 1$ curve comes very close to the $\ell = \infty$ curve; it then turns around sharply and the two curves are found to be practically undistinguishable from each other beyond that frequency. It appears from this that delayed neutron properties affect strongly the behavior of the dispersion law for a $k_\infty = 1$ medium at low frequencies. Neutron wave techniques may find an interesting experimental application in programs whose purpose is to determine those properties.

The method used for the calculation of the eigenvalue ρ of Eq. (13) yields simultaneously also the eigenvector ϕ_0, as previously described. In general, for finite frequency, the eigenvector is complex and has two components, one of which is real (ϕ_{0R}) while the other is complex (ϕ_{0I}). The two components are shown in Fig. VI-8-3 for the case $k_\infty = 1$ and $\omega = 8$ Mrad/sec. Since the complex eigenvector is normalized to a unit real fission source, the imaginary component ϕ_{0I} must have negative as well as positive values. From Fig. VI-8-3 it appears evident, however, that negative values may be found also for the real component ϕ_{0R}.

The physical meaning of the real and imaginary components of the flux ϕ_0 may be derived from the original ansatz given in Eq. (4) which, in matrix form and for the zeroth Legendre component, yields

$$\Phi_0(E,t,x) = \mathrm{Re}\,[A\phi_0(E)e^{i\omega t-\rho x}], \tag{16}$$

where A is an arbitrary constant that is defined by the boundary conditions. If the following notation for the real and imaginary parts of A and $\phi_0(E)$ and for their moduli and arguments is introduced:

$$A = A_R + iA_I \tag{17}$$

$$\phi_0(E) = \phi_{0R}(E) + \phi_{0I}(E) \tag{18}$$

$$A_1 = \sqrt{A_R^2 + A_I^2} \tag{19}$$

$$A_2 = \tan^{-1}\frac{A_I}{A_R} \tag{20}$$

$$\psi_0(E) = \sqrt{\phi_{0R}^2(E) + \phi_{0I}^2(E)} \tag{21}$$

$$\theta(E) = \tan^{-1}\frac{\phi_{0I}(E)}{\phi_{0R}(E)}, \tag{22}$$

Eq. (16) may be rewritten in any of the two following equivalent forms:

$$\begin{aligned}\Phi_0(E,t,x) = A_1e^{-\alpha x}\{&\phi_{0R}(E)\cos(\omega t - \xi x + A_2)\\ &+ \phi_{0I}(E)\sin(\omega t - \xi x - A_2)\}\end{aligned} \tag{23}$$

$$\begin{aligned}\Phi_0(E,t,x) = A_1e^{-\alpha x}\psi_0(E)\cos[&\omega t - \xi x\\ &+ \theta_0(E) + A_2].\end{aligned} \tag{24}$$

Equation (23) shows that the initial ansatz for the scalar flux, as introduced by Eq. (4), implies that the flux may be written as the superposition of two waves, one of which has a spectrum equal to $\phi_{0R}(E)$, while the spectrum of the other is $\phi_{0I}(E)$. The two waves propagate with the same amplitude and phase constants, but have a phase shift of $\pi/2$ with respect to each other. Therefore, at any given point in space the total scalar flux caused by the wave, which is made up of the superposition of the two component waves, has a spectrum which is not constant with time and oscillates sinusoidally between $\phi_{0R}(E)$ and $\phi_{0I}(E)$.

Equation (24) shows the same phenomenon from a different point of view. Here the two component waves have been combined in a single wave having a neutron spectrum $\psi(E)$ in which, however, the phase depends on energy through the function $\theta_0(E)$. Thus, the neutrons of all energy groups propagate as waves which all have the same attenuation and phase constants; however, waves corresponding to different energy groups are in

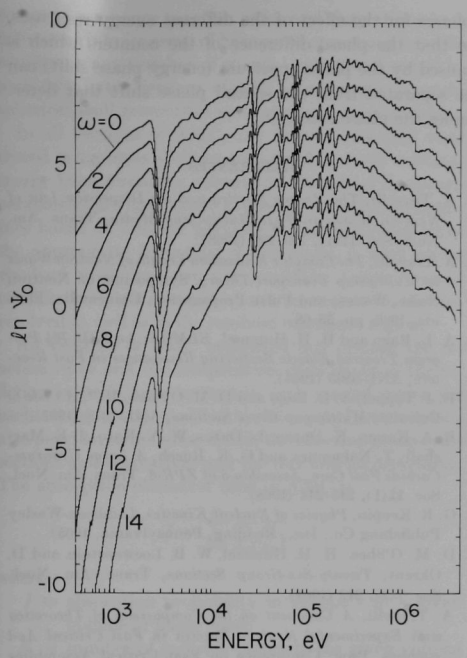

FIG. VI-8-5. The Amplitude Spectrum in ZPR-6, Assembly No. 5 with $k_\infty = 1$ at Various Frequencies. The Angular Frequency ω is Expressed in Mrad/sec. The Spectra are Normalized Arbitrarily with an e Ratio Between the Normalization Constants of Adjacent Curves. *ANL Neg. No. 113-1297.*

general not in phase with each other, and their difference in phase is given by the difference between the values that the function $\theta_0(E)$ assumes at the various energies. We shall name $\psi_0(E)$ and $\theta_0(E)$, respectively, the amplitude spectrum and the phase spectrum of the neutron wave.

Physically, the function $-\theta_0(E)/\omega$ corresponds to the time needed by the neutrons to reach the energy E starting from the various fission and leakage sources. The amplitude and phase spectra of the same neutron wave considered in Fig. VI-8-3 are shown in Fig. VI-8-4. The amplitude spectrum of the neutron wave is always positive by definition (see Eq. (21)), and the phase spectrum behaves very regularly and with an energy dependence close to the reciprocal of the neutron speed, which is in agreement with the physical interpretation mentioned for it. The function $\theta_0(E)$ shows plateaus over the elastic scattering resonances that cause fluctuations in $\psi(E)$, because such resonances cause instantaneous energy losses for the neutrons, which may reduce greatly the time delay between the neutron populations of the initial and final groups between which the scattering occurs.

The amplitude spectrum and the phase spectrum of a neutron wave may be expanded in a power series of the angular frequency ω after normalization. It can be shown that all the odd terms of the $\psi_0(E)$ expansion vanish, and that the same happens to all the even terms of the $\theta_0(E)$ expansion. Thus, to a first approximation, the amplitude spectrum and the phase spectrum have a dependence on the angular frequency which is, respectively, quadratic and linear. This is confirmed by the curves shown in Figs. VI-8-5 and VI-8-6, which show the behavior at various frequencies of the same spectra considered in Fig. VI-8-4. The $\psi_0(E)$ curve for $\omega = 0$ is in good agreement with experimental results.[8]

Conclusion

A method was developed for the analysis of neutron waves in fast multiplying media, taking into account delayed multiplication and the ultrafine energy dependence of the cross sections. The method was tested successfully in a particular case.

Extremely high frequencies were found to be needed

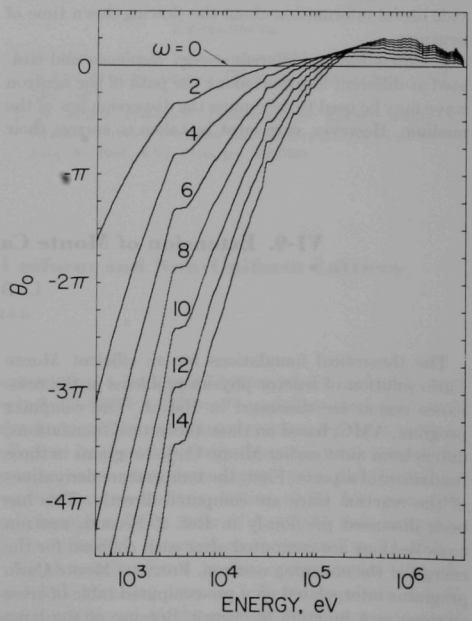

FIG. VI-8-6. The Phase Spectrum in ZPR-6, Assembly No. 5 with $k_\infty = 1$ at Various Frequencies. The Angular Frequency ω is expressed in Mrad/sec. The Spectra are Normalized to the Fission Source. *ANL Neg. No. 113-1300.*

to achieve large values of both the attenuation constant and the phase constant of the waves. However, it was found that the dispersion law of a medium with unit infinite multiplication constant could provide useful information on delayed neutron properties at relatively low frequency.

The neutron wave was found to have different phases at different energies; this phenomenon has some important experimental implications. Since the neutron populations in every energy group propagate as waves all having the same attenuation and phase constants, the correct values for the constants will be determined if counters having identical energy responses are used to detect the wave at different locations. However, waves at various energies may be opposite in phase and their effects may tend to cancel each other if the counters are sensitive to all of them. Thus, the choice of the energy response of the counters may affect considerably the intensity of the signal and the accuracy of the results; the effect may be different at different frequencies.

Two counters having different energy responses and situated at the same location would yield signals whose difference in phase depends simply on $\psi_0(E)$, $\theta_0(E)$, and counter responses. This type of experiment could provide useful information about the slowing-down time of neutrons.

Counters having different energy responses and situated at different locations along the path of the neutron wave may be used to determine the dispersion law of the medium. However, care must be taken to correct their phases for the effect of the different energy responses, so that the phase difference of the counters which is caused by the phase spectrum (energy phase shift) can be separated from the spatial phase shift that determines the phase constant.

References

1. A. Travelli, *The Energy Spectra and the Dispersion Law of Neutron Waves in Fast Multiplying Media*, Trans. Am. Nucl. Soc. **11**(1), 189–190 (1968).
2. A. Travelli, *The Complex Relaxation Length of Neutron Waves in Multigroup Transport Theory*, Symposium on Neutron Noise, Waves, and Pulse Propagation, Gainesville, Florida, 1966, pp. 55–68.
3. A. L. Rago and H. H. Hummel, *ELMOE: An IBM-704 Program Treating Elastic Scattering Resonances in Fast Reactors*, ANL-6805 (1964).
4. B. J. Toppel, A. L. Rago and D. M. O'Shea, *MC²*, *A Code to Calculate Multigroup Cross Sections*, ANL-7318 (1967).
5. R. A. Karam, K. Dance, L. Dates, W. Y. Kato, J. E. Marshall, T. Nakamura and G. K. Rusch, *A Large Uranium-Carbide Fast Core, Assembly-5 of ZPR-6*, Trans. Am. Nucl. Soc. **11**(1), 243–244 (1968).
6. G. R. Keepin, *Physics of Nuclear Kinetics*, (Addison-Wesley Publishing Co., Inc., Reading, Pennsylvania, 1965).
7. D. M. O'Shea, H. H. Hummel, W. B. Loewenstein and D. Okrent, *Twenty-Six-Group Sections*, Trans. Am. Nucl. Soc. **7**(2), 242 (1964).
8. A. Travelli, *A Comment on the Comparison of Theoretica with Experimental Neutron Spectra in Fast Critical As-l semblies*, Proc. Conference on Fast Critical Assemblies and Their Analyses, October 10–13, 1966, ANL-7320, pp. 681–685.

VI-9. Extension of Monte Carlo Methods of Reactor Analysis

L. B. Miller

The theoretical foundations for an efficient Monte Carlo solution of reactor physics problems in the resonance region are discussed in Ref. 1. The computer program, AMC, based on these theoretical foundations, differs from most earlier Monte Carlo programs in three fundamental aspects. First, the temperature derivatives of the reaction rates are computed directly. This has been discussed previously in Ref. 2. Second, neutron cross sections are computed after each collision for the energy of the emerging neutron. Previous Monte Carlo programs interpolated on a pre-computed table of cross sections as a function of energy. Because of the large number of energy points required to describe cross sections in the resonance region, it was necessary to use auxillary storage for the cross section table. Execution was slowed by the need to transfer cross section data from auxiliary storage to fast memory during the calculation. By computing the cross sections at each neutron energy, the AMC code not only avoids errors which may result from tabulation of resonance cross sections at an insufficient number of energy points, but also achieves faster execution by storing all data in fast memory. The third significantly different aspect of AMC is the utilization of the fractional interaction model for space transport. This eliminates the need for complex geometrical calculations to determine the optical path length of neutron trajectories in each region. The validity of this technique is proved with mathematical rigor in Ref. 1.

The original version of the AMC code was written to

compute resonance reaction rates and derivatives in a finite or an infinite array of hexagonal or rectangular cells containing any number of co-axial cylindrical annuli in each cell. Later versions of AMC also treat concentric spherical shell geometries and infinite slab geometries.

In all versions of AMC, the neutron histories were traced using cross sections computed at every neutron energy from resonance parameters. Resolved resonance parameters are used where available. A resonance structure based on average parameters and generated from the appropriate statistical distributions is used where resolved resonances are not available. Later versions consider both p-wave and s-wave resonances in the unresolved as well as in the resolved resonance region.

All versions of AMC computed and printed the reaction rates and the temperature derivatives of the reaction rates in each isotope in each spacial region for each energy group specified in the input. Later versions also provide, in the same detail, the effective group cross sections and derivatives and the flux and its derivative. The absorption estimator used in AMC is

$$I = \sum_{i=1}^{N} \frac{\Sigma_a^z(\chi_i)}{\Sigma_t(\chi_i)},$$

where

$I \equiv$ absorption probability in isotope z in a given volume of phase space

$N \equiv$ number of collision points in the given volume of phase space

$\Sigma_a^z \equiv$ macroscopic absorption cross section of isotope z at space and energy phase point χ_i

$\Sigma_t \equiv$ macroscopic total cross section at phase point χ_i.

The corresponding integrated flux estimator is

$$\phi = \sum_{i=1}^{N} \frac{1}{\Sigma_t(\chi_i)}.$$

Effective macroscopic cross sections for each isotope and for each composition are obtained in each subdivision of phase space by dividing the reaction rate in each region of phase space by the corresponding integrated flux. The cross sections are an order of magnitude more accurate than either the reaction rate or the flux, due to the obvious statistical correlation between the latter two quantities.

Despite the continuing increase in computer speeds, the Monte Carlo method remains appropriate primarily for problems that cannot be satisfactorily or conveniently solved by other methods. The AMC code is written with sufficient flexibility to solve many of the problems in this category. But it is perhaps more important that the code is divided into modules (subroutines) in such a way that modifications can be made expeditiously to solve special problems as they arise in the future.

References

1. L. B. Miller, *Monte Carlo Analysis of Reactivity Coefficients in Fast Reactors: General Theory and Applications*, ANL-7307 (1967).
2. L. B. Miller, *Stochastic Techniques for Reactor Analysis*, Reactor Physics Division Annual Report July 1, 1964 to June 30, 1965, ANL-7110, pp. 357–359.

VI-10. Comparison of Reaction Rates in Uniform and Non-Uniform Lattices

L. B. Miller

The execution of various zero power experiments involving clusters or lattices of fuel rods will be greatly simplified if the desired uniform enrichment can be satisfactorily represented by mixing fuel elements of two different enrichments. Before this procedure is adopted, it is necessary to investigate the possibility that it might distort the experimental results. Therefore, the AMC code[1] was used to determine the total reaction rates and temperature derivatives of reaction rates for each isotope in two lattices containing the same amount of each isotope, but with the isotopes distributed differently.

In one array the isotopes were distributed uniformly; that is, all cells in the lattice were identical, representing a hexagonal lattice of 73 uniformly enriched (U-238/Pu-239 = 7) stainless steel clad fuel pins immersed in sodium and surrounded by a perfect reflector. In the other array the same total number of uranium and plutonium atoms were distributed to represent a non-uniform lattice of 73 fuel rods—36 rods having a U/Pu ratio of 5 and 37 rods having a U/Pu ratio of 9, arranged as shown in Fig. VI-10-1.

Total reaction rates in the energy region 100 eV to 4 keV resulting from a $1/E$ source above 4 keV and proportional to the slowing down power in each spatial region were determined with a statistical error of 0.3%. Simultaneously, the temperature derivatives of the reaction rates were determined with a statisti-

cal error of 5%. The results are shown in Tables VI-10-I and VI-10-II.

The difference between the results for the uniform and the non-uniform lattices differ by less than the statistical error in the calculation. Therefore, it can be concluded that the effect of using fuel pins of two different enrichments in a non-uniform lattice to represent a uniform lattice of intermediate enrichment is insignificant.

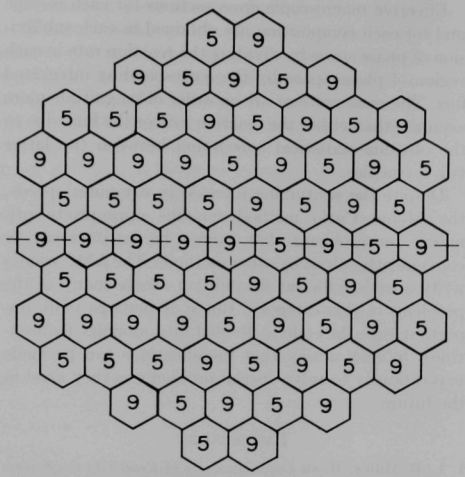

Fig. VI-10-1. Arrangement of Fuel Pins in Non-Uniform Lattice. *ANL Neg. No. 113-1252.*

TABLE VI-10-I. Fission and Capture Rates in Uniform and Non-Uniform Lattices

	Non-Uniform Lattice	Uniform Lattice
Pu-239 fission	0.4214 ± 0.0010	0.4218 ± 0.0010
Pu-239 capture	0.3107 ± 0.0010	0.3114 ± 0.0010
U-238 capture	0.2502 ± 0.0010	0.2495 ± 0.0010
Cladding capture	0.00617 ± 0.00002	0.00613 ± 0.00002
Coolant capture	0.00122 ± 0.00001	0.00121 ± 0.00001

TABLE VI-10-II. Derivatives of Fission and Catpure Rates

	Non-Uniform Lattice, $\times 10^{-4}$	Uniform Lattice, $\times 10^{-4}$
Pu-239 fission	−0.362 ± 0.020	−0.397 ± 0.020
Pu-239 capture	−0.172 ± 0.010	−0.160 ± 0.010
U-238 capture	0.644 ± 0.020	0.665 ± 0.020
Cladding capture	−0.0144 ± 0.0003	−0.0139 ± 0.0003
Coolant capture	−0.0028 ± 0.0001	−0.0026 ± 0.0001

Reference

1. L. B. Miller, *Monte Carlo Analysis of Reactivity Coefficients in Fast Reactors; General Theory and Applications*, ANL-7307 (1967).

VI-11. An Equivalence-Theory Capture Cross Section Code for Plate-Type Cells

K. D. Dance

A code, SIGP, has been written to calculate the potential scattering cross section σ_p as well as the resonance range capture or fission cross sections for typical ZPR lattice cells. The code provides a convenient means of obtaining both the resonance range in-plate cross sections for use in cell calculations, and the cell-averaged cross sections for use in homogenized-cell calculations. Further, calculations have shown that cross sections generated by the SIGP code are in good agreement with the results of the more detailed, and much more time consuming, MC² code.

The basic capture and fission cross sections in the resonance region for each absorber plate are shielded through the usual σ_p formulation after finding the Dancoff shielded σ_p of each individual absorber plate using the two sided E_3 formulation of D. Meneghetti.[1] (E_3 is the standard exponential integral of order three.) The group capture and fission parameters as a function of σ_p were calculated by R. Lewis[2] using conventional isolated-resonance theory with approximate corrections applied to account for same-sequence and inter-sequence resonance overlap. The calculations were performed using ENDF/B resonance parameters. In order to determine the cell-averaged cross sections, a simple relation for the flux shape in the diluent was developed using the usual narrow resonance, flat-source assumptions. With these assumptions, the flux shape between two black absorber plates separated by distance d is given as

$$\phi(x) = \frac{1}{2}\left\{\int_0^x E_1(x - x')\,dx' + \int_0^{d-x} E_1(x')\,dx'\right\}, \tag{1}$$

where $E_1(x)$ is the standard exponential integral of order one and all distances are measured in units of mean free paths. The code calculates the cell-averaged cross section by using Eq. (1) for the flux shape in the diluent region at resonant energies and by assuming a flat flux in the diluent region at nonresonant energies.

Calculations for ZPR-6 Assemblies 5 and 6 showed excellent agreement between the final resonance range cell-averaged cross section obtained using the SIGP code and cell-averaged cross sections obtained from an MC² run in conjunction with a linear flux cross section weighting using SNARG fluxes. Further, a RABZPR calculation of the cell-averaged, broad-group cross section for one broad energy group in the resonance range showed good agreement with the broad-group cell-averaged cross section determined from the SIGP code.

References

1. D. Meneghetti, *Calculational Studies of Sodium-Void Reactivity Variations Due to Thin Slab Heterogeneities in Fast Critical Assemblies*, ANL-7320, pp. 377–386.
2. R. Lewis, Argonne National Laboratory, (private communication).

VI-12. Use of Group-Space-Dependent Bucklings to Simulate a Transformation of the Coordinate System in Neutron Diffusion Calculations

A. J. Ulrich

Introduction

The r, θ, z coordinate system is the one naturally chosen for solution of neutronic problems for the right circular cylindrical reactor. But if a slab-like zone of differing material properties splits the cylinder along a plane containing the axis, as in the split-core concept for the Fast Flux Test Facility (FFTF),[1] it is usually more convenient to use a two-dimensional x, y computation. The material properties can then be a function of the distance x from the plane. It would be highly desirable, however, to use one dimension in the direction perpendicular to the split and to reserve a dimension to adequately treat variations in the z-direction, as in the FFTF concept. In order to proceed, then, within the framework of a two-dimensional calculation it is necessary to simplify the cylindrical part.

Description of Method

Consider a finite cylindrical reactor of uniform composition with a reflector. For simplicity use only one group of neutrons. The radial portion of the diffusion equation in any region is

$$\frac{1}{\phi^c}\frac{d^2\phi^c}{dr^2} + \frac{1}{r\phi^c}\frac{d\phi^c}{dr} - B_z^2 + \frac{k-1}{D}\Sigma = 0. \qquad (1)$$

The slab diffusion equation with x as the coordinate is

$$\frac{1}{\phi}\frac{d^2\phi}{dx^2} - B_y^2 - B_z^2 + \frac{k-1}{D}\Sigma_a = 0. \qquad (2)$$

It is apparent that the two equations are of the same form if

$$B_y^2 = \frac{1}{r\phi^c}\frac{d\phi^c}{dr}. \qquad (3)$$

When the two equations are of the same form and have the same boundary conditions, they also have the same solution. Thus the flux ϕ^c of the cylindrical solution may be used to compute an effective transformation buckling B_y^2 for each region of a multiregion slab problem, Fig. VI-12-1, causing the solution of the slab problem to approach the cylindrical solution with increasing number of elementary slab regions. In effect, the solution of Eq. (2) is the same as the solution of Eq. (1) except that the converged value of the second term is used starting with the first iteration.

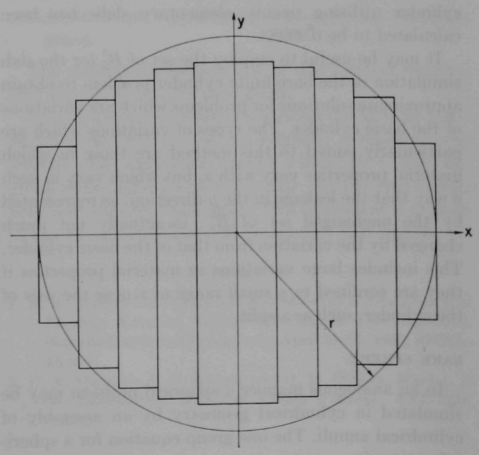

Fig. VI-12-1. Cylinder Conceived As An Assembly of Slabs. *ANL Neg. No. 113-1207.*

TABLE VI-12-I. RATIO OF EFFECTIVE TRANSFORMATION BUCKLING TO RADIAL BUCKLING OF A CYLINDER

x/R_c	B_y^2/B_r^2	x/R_c	B_y^2/B_r^2
0.025	0.5002	0.525	0.6361
0.075	0.5020	0.575	0.6763
0.125	0.5057	0.625	0.7282
0.175	0.5114	0.675	0.7971
0.225	0.5192	0.725	0.8922
0.275	0.5295	0.775	1.0305
0.325	0.5425	0.825	1.2489
0.375	0.5588	0.875	1.6433
0.425	0.5791	0.925	2.5648
0.475	0.6044	0.975	7.1731

In another sense the set of B_y^2 may be viewed as introducing a fictitious group-dependent leakage absorber or source in each elementary slab region which simulates the dilution or concentration of the neutron population in the circumferential direction as it diffuses outward or inward radially.

BARE CYLINDER IN ONE GROUP

For the case of a bare finite cylinder of critical radius R_c the flux is $\phi^c = \phi_0 J_0(2.405r/R_c)$, and the radial buckling is $B_r^2 = (2.405/R_c)^2$. The value of B_y^2 for each elementary slab is then given analytically as a function of r, which is now identified with x of the slab simulation by

$$B_y^2 = B_r^2 J_1(2.405\, x/R_c)/(2.405\, x/R_c) J_0(2.405\, x/R_c).$$

Values of ratio B_y^2/B_r^2 are listed in Table VI-12-I for the case of twenty elementary slab divisions between $x = 0$ and $x = R_c$. The k_{eff} of a simulated critical finite cylinder utilizing twenty elementary slabs has been calculated to be 0.99983.

It may be useful to employ the set of B_y^2 for the slab simulation of the bare finite cylinder problem to obtain approximate solutions for problems which are variations of the basic cylinder. The types of variations which are particularly suited to this method are those in which material properties vary with x, but which vary in such a way that the leakage in the y-direction, as represented by the unchanged set of B_y^2, is actually not much changed by the variation from that of the basic cylinder. This includes large variations in material properties if they are confined to a small range of x near the axis of the cylinder, such as a split.

BARE SPHERE

In an analogous manner a spherical problem may be simulated in cylindrical geometry by an assembly of cylindrical annuli. The one group equation for a spherical reactor is

$$\frac{1}{\phi}\frac{d^2\phi}{d\rho^2} + \frac{2}{\rho\phi}\frac{d\phi}{d\rho} + \frac{k-1}{D}\Sigma_a = 0. \tag{4}$$

It is apparent that this equation is of the same form as Eq. (1), which is for cylindrical geometry, if the cylindrical axial buckling B_z^2 is $B_z^2 = (-1/\rho\phi)d\phi/d\rho$, where ρ is the radius of the sphere. For the bare sphere the ratio of B_z^2 to the buckling B_s^2 of a sphere is given as a function of the radius r of the cylinder by

$$\frac{B_z^2}{B_s^2} = \left[\frac{\frac{1}{\pi^2}\left(\frac{R_s}{r}\right)\sin\left(\frac{\pi r}{R_s}\right) - \pi\cos\left(\frac{\pi r}{R_s}\right)}{\left(\frac{r}{R_s}\right)\sin\left(\frac{\pi r}{R_s}\right)}\right],$$

where R_s is the radius of the sphere.

This simulation allows an approximate solution when variations in material properties vary with r, the distance from a particular diameter of the sphere.

Similarly, if variations in material properties of a spherical assembly depend on the distance z from a given plane which passes through the center, the sphere may be simulated by an assembly of elementary disks. The basic radial buckling B_r^2 of the elementary disks is given by $B_r^2 = (-2/\rho\phi)d\phi/d\rho$, since this transforms Eq. (4) into the slab form,

$$\frac{1}{\phi}\frac{d^2\phi}{dz^2} - B_r^2 + \frac{k-1}{D}\Sigma_a = 0.$$

For a bare sphere we then have

$$\frac{B_r^2}{B_s^2} = \frac{\frac{2}{\pi^2}\left(\frac{R_s}{z}\right)\sin\left(\frac{\pi z}{R_s}\right) - \pi\cos\left(\frac{\pi z}{R_s}\right)}{\frac{z}{R_s}\sin\left(\frac{\pi z}{R_s}\right)}.$$

This method can also be adapted to other cases where the basic solution is obtained in one coordinate system and the variations in material properties are imposed in another coordinate system in which an approximate solution is obtained.

REFLECTED CYLINDER

Equations (1), (2) and (3) apply to the reflector of a reflected cylinder as well as to the core. The transformation buckling in the reflector, $B_{y2}^2(x)$, of a reflected cylinder, considering only one group of neutrons, is

$$B_{y2}^2(x) = B_{y1}^2(x_1)\frac{D_1}{D_2}\frac{x_1}{x}\frac{K_0\left(\frac{ax_1}{R_c}\right)K_1\left(\frac{ax}{R_c}\right)}{K_0\left(\frac{ax}{R_c}\right)K_1\left(\frac{ax_1}{R_c}\right)}, \tag{5}$$

where $B_{y1}^2(x_1)$ is the transformation buckling for this core evaluated at the core-reflector interface at x_1, D_1 and D_2 are the core and reflector diffusion constants, respectively, K_0 and K_1 are Bessel functions, and R_c is

the extrapolated bare core radius. The quantities x_1, a and R_c are related by the transcendental criticality equation. Equation (5) shows that the transformation buckling has a discontinuous jump in value at the core-reflector interface. This jump, present in multigroup problems as well, results in continuity in the value of $DB_y^2(x)$ at the boundary.

DISTRIBUTION OF NEUTRON FLUX ALONG A CHORD OF A BARE CYLINDER

In the previous discussion a method is described by which a cylindrical reactor in coordinates r and z may be viewed as a slab reactor in coordinates x, y, and z, making use of a buckling $B_y^2(x)$ which forces $\phi(x)$ to be of the same form as the known cylindrical solution $\phi(r)$. In this description x is identified with r. It is possible to define another transformation buckling $B_y^2(x)$ such that $\phi(x)$ is of the same form as $\phi(u)$, where $\phi(u)$ gives the distribution of neutron flux along a chord rather than along a radius.

If the distance from the center of the cylindrical geometry to the chord is y_0,

$$u = \sqrt{r^2 - y_0^2}.$$

In analogy with the previous derivation it may be shown that

$$B_y^2 = -\frac{1}{\phi}\left[\frac{y_0^2}{r^2}\frac{d^2\phi}{dr^2} + \frac{r^2 - y_0^2}{r^3}\frac{d\phi}{dr}\right],$$

where

$$r^2 = y_0^2 + u^2.$$

This reduces to the previously obtained expression when the chord coincides with the diameter, i.e., when $y_0 = 0$.

For the case of a bare cylinder of critical radius r_c, the radial distribution is $\phi = \phi_0 J_0(2.405\ r/r_c)$, and the radial buckling is $B_r^2 = (2.405/r_c)^2$. The value of B_y^2 is then given analytically as a function of u by

$$B_y^2 = B_r^2 \frac{y_0^2}{u^2 + y_0^2} + \left(\frac{u^2 - y_0^2}{u^2 + y_0^2}\right) \cdot \frac{J_1\left(\dfrac{2.405\sqrt{u^2 + y_0^2}}{r_c}\right)}{\left(\dfrac{2.405\sqrt{u^2 + y_0^2}}{r_c}\right) J_0\left(\dfrac{2.405\sqrt{u^2 + y_0^2}}{r_c}\right)},$$

where the range of u is $0 \le u \le \sqrt{r_c^2 - y_0^2}$.

In Tables VI-12-II and VI-12-III the values of B_y^2/B_r^2 are listed for $y_0/r_c = 1/3$ and $y_0/r_c = 2/3$, respectively, as a function of $u/\sqrt{r_c^2 - y_0^2}$.

When these region-dependent bucklings are used in the appropriate slab problems, k_{eff} is 0.9998 and 0.9999 for the cases $y_0/\sqrt{c} = 1/3$ and $y_0/\sqrt{c} = 2/3$, respectively.

TABLE VI-12-II. RATIO OF EFFECTIVE TRANSFORMATION BUCKLING TO RADIAL BUCKLING OF A CYLINDER FOR $y_0/r_c = 1/3$

$u/\sqrt{r_c^2 - y_0^2}$	B_y^2/B_r^2	$u/\sqrt{r_c^2 - y_0^2}$	B_y^2/B_r^2
0.025	0.4552	0.525	0.5741
0.075	0.4568	0.575	0.6093
0.125	0.4600	0.625	0.6547
0.175	0.4650	0.675	0.7150
0.225	0.4718	0.725	0.7982
0.275	0.4808	0.775	0.9192
0.325	0.4922	0.825	1.1104
0.375	0.5065	0.875	1.4554
0.425	0.5243	0.925	2.2617
0.475	0.5464	0.975	6.2936

TABLE VI-12-III. RATIO OF EFFECTIVE TRANSFORMATION BUCKLING TO RADIAL BUCKLING OF A CYLINDER FOR $y_0/r_c = 2/3$

$u/\sqrt{r_c^2 - y_0^2}$	B_y^2/B_r^2	$u/\sqrt{r_c^2 - y_0^2}$	B_y^2/B_r^2
0.025	0.2159	0.525	0.2446
0.075	0.2163	0.575	0.2530
0.125	0.2171	0.625	0.2637
0.175	0.2183	0.675	0.2779
0.225	0.2200	0.725	0.2973
0.275	0.2222	0.775	0.3254
0.325	0.2249	0.825	0.3696
0.375	0.2284	0.875	0.4490
0.425	0.2327	0.925	0.6338
0.475	0.2380	0.975	1.5557

APPLICATION TO MULTIGROUP CYLINDRICAL CALCULATIONS

The multigroup formulation of this method requires that Eq. (3) be true for each group.

In a six-group test comparison using the MACH-1 diffusion code,[2] the k_{eff} of the reflected cylindrical core and its slab simulation agreed within 10^{-4}. The six-group fluxes agreed within less than one per cent except very near the outer boundary. This agreement is as good as can be expected using 20 elementary slab regions.

REFERENCES

1. E. R. Astley, *The Conceptual Evaluation of A Fast Flux Test Facility*, National Topical Meeting on Fast Reactors, Battelle Northwest Laboratory, April 10–12, 1967, BNWL-SA-978.
2. D. A. Meneley, L. C. Kvitek and D. M. O'Shea, *Mach-1, A One-Dimensional Diffusion Theory Package*, ANL-7223, (1966).

VI-13. Efficient Programming in FORTRAN[1]

C. E. Cohn

A number of techniques can be used to decrease the running-time and memory-space requirements for FORTRAN programs. The usage of these depends upon the characteristics of a particular compiler and system. Normally, they save both running time and memory space. The discussion applies in general to any problem-oriented language.

Arithmetic expressions and replacement statements can be optimized by eliminating the repeated calculation of redundant subexpressions. If a loop contains an expression whose variables do not change value during the course of the loop, time (but not space) may be saved by evaluating the expression once, outside the loop, and holding the result until needed. Arithmetic operations on whole numbers are best done in integer mode, with the results converted to real where needed. Where mixed-mode arithmetic is allowed, it is best to write constants in the dominant mode of the expression to avoid needless conversions. Arithmetic operations on constants should be performed by the programmer before writing an expression. Constants should be written to as many significant figures as the computer handles in its arithmetic, so that full advantage is taken of the computer's precision.

In many compilers, the use of the "**" notation calls upon a special subroutine in the library. If only small whole-number powers are to be calculated, the time and space required for this subroutine can be saved by avoiding that notation.

Ordinarily, there is no penalty for attaching a number to a statement even when not needed for reference by another statement, except for two special circumstances. Some small-machine compilers have limited memory space for assignment tables. Elimination of unneeded statement numbers reduces the burden on the available space. Also, some compilers perform limited optimization on sequences of arithmetic replacement statements. This optimization is done only if none of the statements has a number, indicating that the sequence is never entered in the middle.

Where the quantity calculated in the expression imbedded in an IF statement, or any part of it, is also used earlier or later in the program, the unnecessary repeated calculations of that quantity should be avoided as described for redundant subexpressions. The FORTRAN-IV logical IF statement is not handled efficiently by some compilers. In such cases it is efficient to replace logical IF statements with one or more three-branch IF statements as required.

Retrieval or storage of subscripted variables always requires more work than the retrieval or storage of unsubscripted variables, because the address of the datum must be calculated from the subscript combination. Where the same subscripted variable is referenced in two or more statements, these references may be handled as redundant subexpressions, provided the values of the subscripts do not change through the sequence. Where the value of a subscripted variable is formed in one statement and used in a subsequent statement, the extra reference may be eliminated similarly. For subscripted-variable references with constant subscripts, most compilers will perform the address arithmetic during compilation. Otherwise, an unsubscripted variable name may be made equivalent to the element in question and used in all references. Sometimes a two- or three-dimensional array may be handled more efficiently by making it equivalent to a one-dimensional array.

The input or output of an entire array may be specified either by a DO-implying loop over the array or by mention of the name of the array with no qualification. Often, the latter saves central-processor time. Sometimes there is a space penalty for specifying additional input-output modes, since each mode requires its own subroutine from the library.

Use of subprogram organization incurs a time and space penalty because of the linkage instructions. The space penalty is more than made up, however, if the subprogram is called from more than one place in the main program. If, instead, a subprogram is called from only one place in the main program, it is most efficient to eliminate its separate identity as a subprogram and incorporate it directly into the main program. There are two ways of linking variables between a main program and a subprogram—through argument lists and through COMMON statements—and each has its proper role. There is a time and space penalty associated with the use of argument lists. With COMMON linkage, on the other hand, there is no penalty.

Where a variable in the subprogram always corresponds to the same variable in the main program at every call of the subprogram, then the linkage should be through COMMON. Where a variable in the subprogram may correspond to different variables in the main program at different calls of the subpro-

gram, then the linkage should be through the argument list. Normally, COMMON storage is assigned to the memory area occupied by the loader. A program that taxes memory can thus obtain some relief by use of COMMON storage.

There is a penalty associated with each additional reference to an argument within a subprogram. If an unsubscripted variable is referenced more than once in a subprogram, it could be worthwhile to use a local variable made equal to the argument or vice versa at the beginning or end of the subprogram, depending upon whether the argument is an input or output variable. Some compilers handle arithmetic statement functions like open subroutines or macroinstructions. This saves a little time at the cost of much space. If such a program is space-limited, the arithmetic statement functions should be replaced with function subprograms.

Reference

1. C. E. Cohn, *Efficient Programming in FORTRAN*, Software Age **2**, No. 5, 22–31 (1968).

VI-14. Error Analysis of Linked Difference Equations

N. F. Morehouse* and J. C. Carter

The creation of large computational systems for the purpose of simulating the performance of nuclear reactors involves the automatic linking of computational modules of the various categories of physical phenomena occurring simultaneously in a reactor.

Since the equations in these modules are difference equations and since the linkage of modules creates a dynamic system, it is considered that the error analysis of any programmed path through the linked modules may be facilitated by a merger of the technologies of system analysis and numerical analysis. A system of linked groups of difference equations represent a dynamic system which may be analyzed with the same techniques as are used on other dynamic systems. The transfer function or describing function of the difference equations is determined and compared with those of the differential equations which the difference equations simulate. A further development of the Fourier series method of system analysis may be applied to linked difference equations for which the conventional methods of error analysis are inadequate. The Fourier method also gives insight into the relationship between the wave lengths of the harmonics and the mesh spacing.

As far as is known, error analysis of linked codes, particularly those involving partial differential equations, has not been attempted for any but very simple cases. It is recognized that such an analysis for the large computational systems associated with safety analysis, although difficult, has considerable significance in determining whether instability is due to numerical instability or reactor feedbacks.

* Applied Mathematics Division, Argonne National Laboratory.

An error analysis of individual and linked sets of difference equations involve two principal sources of error, the truncation and round-off errors.

In order to solve a system of differential equations on a digital computer the differential equations must be replaced by difference equations. The difference between the analytic solution of difference equations and the analytic solution of the differential equations is called the truncation error. The difference between the analytic solution of the system of difference equations and the actual computer calculation solution is called the "round-off" error since it is due to the arithmetic involved in computing the solution.

Historically three different approaches have been used to estimate truncation errors. The first and most generally used is to compare the first few terms of the Taylor series of expansions of the solutions of the differential equations and the difference equations. Almost all of the literature of numerical analysis uses this approach. The second approach considers the system of difference equations as matrix equations in a finite dimensional vector space. Truncation error estimates are then obtained by comparing the eigenvalues of the matrices with the eigenvalues of the infinitesimal operators in the differential equations.

In the third method, which is attributed to J. Von Neumann, the Fourier series or integral expansion of the solution of the differential equations is compared with the Fourier series or integral expansion of the solution of the difference equations. The comparison of the first few terms of the Taylor series expansions does not provide much information about the truncation error which, of course, depends frequently on the higher terms of the Taylor series expansion and always

on the overall behavior of the solution rather than the behavior in just the neighborhood of a finite set of points.

The second approach offers a considerable improvement in that it puts finite difference methods in operator form thereby permitting many of the global properties of the solution to be determined. In particular the numerical stability of many systems of difference equations whose steady state solution was to approximate the steady state solution of a system of differential equations has been investigated by these methods.

Although the third method has seldom been used it is felt that it offers considerable promise. It puts the solution of difference equations in the same form as the solution of the differential equations. From an operator standpoint, finite difference operators may be directly compared with infinitesimal operators. In particular, most of the theory which has been developed concerning the stability of systems of differential equations can be applied to systems of difference equations. In other words, the truncation error is expressed in the language of present day systems analysis, thus permitting the direct application of highly developed techniques in this branch of science. In particular, it provides the only way in which the overall truncation error can be estimated when several codes are combined to simulate a system, since the techniques of systems analysis may be used to give the overall truncation error from the individual truncation errors. The following example serves to illustrate the general approach.

Consider the time-dependent heat transfer equation

$$\frac{\partial u}{\partial t} = \sigma \frac{\partial^2 u}{\partial x^2}. \tag{1}$$

If one considers the case of a temperature distribution which is initially distributed sinusoidally about a mean temperature T_m, one has

$$u = T - T_m, \tag{2}$$

$$u(0,x) = e^{i\omega x}. \tag{3}$$

One difference scheme for solving Eq. (1) would be to replace the derivatives by divided differences

$$\frac{u(t + \Delta t,x) - u(t,x)}{\Delta t} = \sigma \frac{u(t,x + \Delta x) - 2u(x,t) + u(t,x - \Delta x)}{\Delta x^2}. \tag{4}$$

The analytic solution of Eq. (1) is obtained by letting

$$u = e^{\beta t + i\omega x}. \tag{5}$$

Substituting Eq. (5) into Eq. (1) gives

$$\beta = -\sigma\omega^2. \tag{6}$$

Therefore, $u(t,x)$ approaches zero exponentially with time, which means that T approaches T_m.

If one now considers Eq. (4) to be a continuous difference equation,[1] substituting Eq. (5) into Eq. (4) gives

$$e^{\beta \Delta t} = 1 - \frac{2\sigma \Delta t}{\Delta x^2}(1 - \cos \omega \Delta x) \tag{7}$$

or

$$\beta = \frac{1}{\Delta t} \ln \left[1 - \frac{2\sigma \Delta t}{\Delta x^2}(1 - \cos \omega \Delta x) \right]. \tag{8}$$

In order for the solution to go exponentially to zero one must have

$$\left| 1 - \frac{2\sigma \Delta t}{\Delta x^2}(1 - \cos \omega \Delta x) \right| \leq 1 \tag{9}$$

or

$$\frac{2\sigma \Delta t}{\Delta x^2} \leq 1. \tag{10}$$

Equation (10) is just the Courant-Levy criterion[2] which states that if Eq. (10) is fulfilled, then as Δt and Δx tend to zero, the solution of the difference equation (4) approaches the solution of the differential equation (1) as a limit. The Courant-Levy condition gives no information about the truncation error for finite Δx and Δt but Eq. (8) does. In particular if one notes that $\omega \Delta x = 2\pi/n$ where n is the number of x mesh points per cycle of $e^{i\omega x}$, then Eq. (8) becomes

$$\beta = \frac{1}{\Delta_t} \ln \left[1 - 2\frac{\sigma \Delta t}{\Delta x^2}\left(1 - \cos \frac{2\pi}{n}\right) \right]. \tag{11}$$

If Eq. (10) is fulfilled and if $\frac{2\pi}{n} \leq \frac{\pi}{2}$ or $n \geq 4$ then β is a negative real number. On the other hand, if $n < 4$, β is a complex number with a negative real part. This shows that spurious spatial oscillations are introduced, although in the limit the correct solution is approached.

In many cases, the rate at which the temperature approaches equilibrium is important. For such problems Δt and Δx must be chosen to give a sufficiently accurate β, since merely satisfying the Courant condition is not sufficient.

If Eq. (4) is just one of a large system of equations, the Courant condition no longer holds. In order to find suitable stability criteria for such systems each subsystem must be analyzed in terms of its response. The overall system can then be analyzed by combining the responses of the subsystems.

Consider the wave equation

$$\frac{\partial^2 y}{\partial t^2} = c^2 \frac{\partial^2 y}{\partial x^2}. \tag{12}$$

Upon substituting differences for the derivatives in

Eq. (12),

$$\frac{y(t+\Delta t,x) - 2y(t,x) + y(t-\Delta t,x)}{(\Delta t)^2} = c^2\,\frac{y(t,x+\Delta x) - 2y(t,x) + y(t,x-\Delta x)}{(\Delta x)^2}. \tag{13}$$

Let

$$y(t,x) = e^{i\omega x}$$
$$y(t,x) = e^{\beta t + i\omega x}. \tag{14}$$

Equation (14) then becomes

$$\frac{e^{\beta\Delta t} - 2 + e^{-\beta\Delta t}}{(\Delta t)^2} = c^2\,\frac{e^{i\omega\Delta x} - 2 + e^{-i\omega\Delta x}}{(\Delta x)^2}$$

or

$$\cos\beta\Delta t - 1 = \frac{c^2(\Delta t)^2}{(\Delta x)^2}(\cos\omega\Delta x - 1)$$

or

$$\cos n\beta\Delta t = 1 - \frac{c^2(\Delta t)^2}{(\Delta x)^2}(1 - \cos\omega\Delta x). \tag{15}$$

If

$$\frac{c^2(\Delta t)^2}{(\Delta x)^2} \leq 1 \tag{16}$$

then β is imaginary and

$$y(t,x) = e^{\beta t + i\omega x}.$$

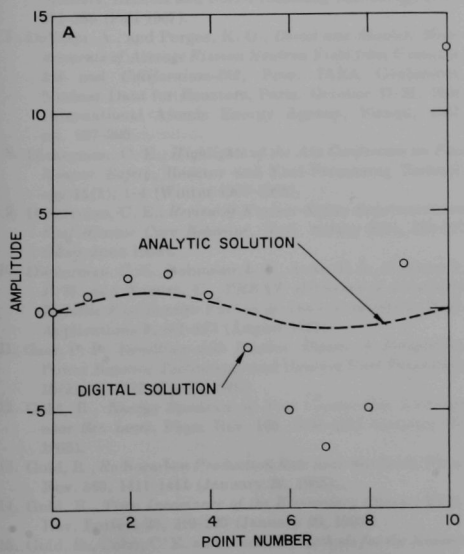

FIG. VI-14-1a. 10 Points per Cycle. *ANL Neg. No. 113-889.*

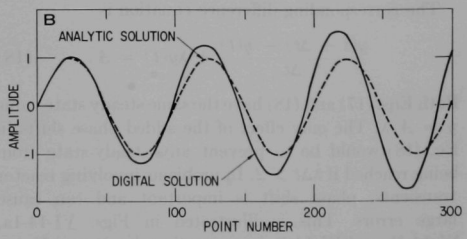

FIG. VI-14-1b. 100 Points per Cycle. *ANL Neg. No. 113-865 Rev. 1.*

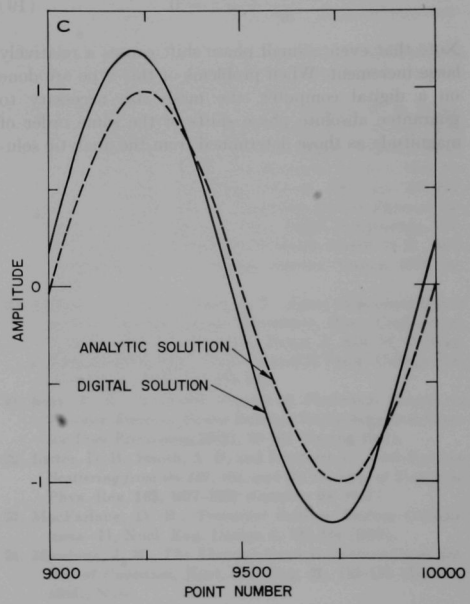

FIG. IV-14-1c. 1000 Points per Cycle. Ninth Cycle is Plotted. *ANL Neg. No. 113-862.*

If Eq. (16) is not satisfied then β is positive and real for some ω and the solution fails. Eq. (16) is the Courant condition.

How much truncation error can be tolerated while still yielding a satisfactory solution varies considerably and depends on the system and whether transience is involved. When only final steady-state solutions are to be computed the phase shift is relatively unimportant. An illustration is given by the simple equation:

$$\frac{dx}{dt} + \lambda x = A. \tag{17}$$

The corresponding difference equation is

$$\frac{y(t + \Delta t) - y(t)}{\Delta t} + \lambda y(t) = A. \qquad (18)$$

Both Eqs. (17) and (18) have the same steady state value $y = A/\lambda$. The only effect of the added phase shifts in Eq. (18) would be to prevent any steady-state from being reached if $\lambda\Delta t > 2$. In problems involving reactor transients, phase shift is important and can cause large errors. This is illustrated in Figs. VI-14-1a, VI-14-1b and VI-14-1c by a fourth-order Runge-Kutta integration of the simple equation

$$\frac{d^2x}{dt^2} + \omega^2 x = 0. \qquad (19)$$

Note that even a small phase shift causes a relatively large increment. When problems of this type are done on a digital computer, the mesh size necessary to guarantee absolute phase shifts of the same order of magnitude as those determined from the analytic solution almost always requires an excessive number of mesh points to allow the computation to be performed. Consequently, digital methods which rely on the cancelling of two large phase shifts must be used. There is as yet no known general technique for doing this and a great deal of skill and some luck is needed for even small systems. It is believed that the merger of technologies of system and numerical analysis will result in the much needed means of analyzing the dynamic characteristics of large computation systems.

The intent is to develop a concise and relatively simple method of analyzing the errors associated with linking many diverse digital codes into a large closed loop computational system.

References

1. N. F. Morehouse and A. L. Winiecki, *A Comparison of Computors For the Solution of Differential Equations*, (to be published).
2. R. D. Richtmyer, *Difference Methods for Initial Value Problems*, (Interscience Publishers, Inc., N. Y., 1967), 2nd Ed

Section VII

Publications

July 1, 1967 to June 30, 1968

Open Literature

1. Avery, R., Dickerman, C. E., Kato, W. Y., Long, J. K., Smith, A. B., Wall, I. B. and Wolfe, B., *The U. S. Experimental Program for Fast Reactor Physics*, Proc. Conference on Fast Breeder Reactors, London, May 17–19, 1966. (Pergamon Press, Oxford, 1967) pp. 403–420.
2. Cohn, C. E., *Automated Data Analysis and Control for Critical Facilities*, Proc. Symposium, Use of Computers in Analysis of Experimental Data and the Control of Nuclear Facilities, Argonne National Laboratory, May 4–6, 1966. USAEC Symposium Ser. 10, CONF-660527 (May 1967), pp. 49–66.
3. Cohn, C. E., *Simple Storage-Oscilloscope Displays for Small Laboratory Computers*, Rev. Sci. Instr. **38**, 984–985 (July 1967).
4. Cohn, C. E., *Solid-State Drive Circuit Considerations for Paper-Tape Punches*, Rev. Sci. Instr. **38**, 1662 (November 1967), Note.
5. Cox, S. A., *Multiple Scattering Correction Using a Combination of Monte Carlo and Analytical Methods*, Nucl. Instr. Methods **56**(2), 245–253 (1967).
6. DeVolpi, A., *Current Values for Fundamental Fission Parameters*, Reactor and Fuel-Processing Technology **10**(4), 271–288 (Fall 1967).
7. DeVolpi, A., and Porges, K. G., *Direct and Absolute Measurements of Average Fission Neutron Yield from Uranium-235 and Californium-252*, Proc. IAEA Conference, Nuclear Data for Reactors, Paris, October 17–21, 1966. International Atomic Energy Agency, Vienna, 1967, pp. 297–306.
8. Dickerman, C. E., *Highlights of the Aix Conference on Fast Reactor Safety*, Reactor and Fuel-Processing Technology **11**(1), 1–4 (Winter 1967–1968).
9. Dickerman, C. E., *Review of Nuclear Safety Experiments on Fast Reactor Core Behavior*, Nucl. Safety **9**(3), 210–217 (May–June 1968).
10. Dickerman, C. E., Robinson, L. E., Sowa, E. S., Monaweck, J. H. and August, C., *TREAT Meltdown of Irradiated Metallic Fast-Reactor Fuel in an Inert Atmosphere*, Nucl. Applications **3**, 461–473 (August 1967).
11. Gast, P. F., *Desalting with Nuclear Power: A Perspective*, Power Reactor Technology and Reactor Fuel Processing **10**(2), 111–117 (Spring 1967).
12. Gold, R., *Energy Spectrum of Fast Cosmic-Ray Neutrons near Sea Level*, Phys. Rev. **165**, 1406–1411 (January 25, 1968).
13. Gold, R., *Radiocarbon Production Rate near Sea Level*, Phys. Rev. **165**, 1411–1414 (January 25, 1965).
14. Gold, R., *Time Invariance of the Elementary Charge*, Phys. Rev. Letters **20**, 219–220 (January 29, 1969).
15. Gold, R., Cohn, C. E. and Olson, I., *Methods for the Numerical Evaluation of Fourier Integrals*, J. Comput. Phys. **1**(4), 536–540 (June 1967).
16. Golden, G. H., Tokar, J. V. and Miller, D., *Thermophysical Properties of Sodium—Recommended Values*, Reactor and Fuel-Processing Technol. **11**(1), 27–48 (Winter 1967–1968).
17. Havens, W. W., Kolstad, G. A., Smith, A. B. and Taschek, R. F., *The European-American Nuclear-Data Committee*, Phys. Today **20**, 35–42 (May 1967).
18. Hummel, H. H., Greebler, P., Loewenstein, W. B., Nims, J. B., Reynolds, A. B. and Pitterle, T. A., *Recent Theoretical Work in the U.S. on Fast Reactor Physics*, Proc. Conference on Fast Breeder Reactors, London, May 17–19, 1966. (Pergamon Press, Oxford, 1967) pp. 493–511.
19. Kelber, C. N., *Physics of Plutonium-Fuelled Thermal Research and Test Reactors*, Proc. IAEA Symposium, Plutonium as a Research Fuel, Brussels, March 13–17, 1967. International Atomic Energy Agency, Vienna, 1967, pp. 43–49.
20. Kelber, C. N. and Madell, J. T., *Space Dependent Effects on Fast Thermal System Parameters*, Proc. Conference, Coupled Reactor Kinetics, Texas A and M College, January 23–24, 1967. (Texas A and M Press, College Station, Texas, 1967) pp. 379–384.
21. Kier, P. H., *Neutronic Aspects of Plutonium Recycle in Thermal Reactors*, Power Reactor Technology and Reactor Fuel Processing **10**(2), 93–101 (Spring 1967).
22. Lister, D. B., Smith, A. B. and Dunford, C., *Fast-Neutron Scattering from the 182, 184, and 186 Isotopes of Tungsten*, Phys. Rev. **162**, 1077–1087 (October 20, 1967).
23. MacFarlane, D. R., *Transient Sodium Boiling Calculations*—II, Nucl. Eng. Design **6**, 103–114 (1967).
24. Meadows, J. W., *The Thermal-Neutron Capture Cross Section of Cadmium*, Nucl. Sci. Eng. **31**, 152–153 (January 1968), Note.
25. Meneghetti, D. and Azzoni, P. M., *Calculational Study of Pu^{239}, U, U^{233}-Th Metal, Carbide, and Oxide Fast Breeder Systems*, I Reatorri Veloci. 1967 Publication of the Italian Atomic Energy Commission Comprising the Papers Presented at the 1963 Nuclear Symposium in Rome, pp. 215–229.
26. Miller, D., *Discussion of Papers 27, 30, 86, 87, 88, 131, 135; Reports on Papers 31, 37, 38, 39, 40*, Proc. Third International Heat Transfer Conference AIChE, New York, 1967, Vol. 6, pp. 100–101, 107–108, 198, 290, 301, 109, 114.
27. Moldauer, P. A., *Unitary Models of Nuclear Resonance Reactions*, Phys. Rev. **157**, 907–921 (May 20, 1967).
28. Moldauer, P. A., *Effects of T Violation in Nuclear Reactions*, Phys. Rev. **165**, 1136–1146 (January 20, 1968).
29. Moldauer, P. A., *Flux Conversion in Resonance Reactions*, Proc. International Nuclear Physics Conference, Gatlin-

burg, Tenn., September 12–17, 1966, Eds., R. L. Becker and A. Zucker; (Academic Press, New York, 1967) pp. 815–818.

30. Moldauer, P. A., *Sum Role for Resonance Reactions*, Phys. Rev. Letters **19**, 1047–1048 (October 30, 1967).
31. Moldauer, P. A., *T-Violation and Detailed Balance in Direct Reactions*, Phys. Letters **26B**(12), 713–715 (1968).
32. Nelson, P. A., Butler, D. K., Chasanov, M. G. and Meneghetti, D., *Fuel Properties and Nuclear Performance of Fast Reactors Fueled with Molten Chlorides*, Nucl. Appl. **3**, 540–547 (September 1967).
33. Redman, W. C. and Bretscher, M. M., *Low-Flux Measurement of ^{235}U Epicadmium Capture-to-Fission Ratio*, Nucl. Sci. Eng. **31**, 247–253 (February 1968).
34. Shaftman, D. H. and Savio, R. P., *The Argonne Advanced Research Reactor (AARR)*, Proc. AEC-ENEA Seminar, Intense Neutron Sources, Santa Fe, New Mexico, September 19–23, 1966. USAEC Report CONF-660925, pp. 215–259.
35. Smith, A. B., Guenther, P. T. and Whalen, J. F., *Fast-Neutron Scattering from Ta, Re, and Pt*, Phys. Rev. **168**, 1344–1355 (April 20, 1968).
36. Smith, A. B. and Whalen, J. F., *Computers on Line with Experimental Facilities*, Nucl. News **11**(4), 31 (1968).
37. Spinrad, B. I., *Fuel Burn-up Predicitions in Thermal Reactors: A Review of Recent Work in the United States of America*, Proc. IAEA Panel, Fuel Burn-up Predictions in Thermal Reactors, Vienna, April 10–14, 1967. International Atomic Energy Agency, Vienna, 1968, pp. 65–80.
38. Spinrad, B. I., *Burnup Predictions for Thermal Reactors—A Synthesis of Approximations*, Reactor and Fuel-Processing Technology **10**(3), 190–198 (Summer 1967).
39. Spinrad, B. I., *Limitations of Steady State, High Flux Reactors, Current and Future*, Proc. AEC-ENEA Seminar, Intense Neutron Sources, Santa Fe, New Mexico, September 19–23, 1966. USAEC Report CONF-660925, pp. 319–359.
40. Stanford, G. S., *Problems and Precautions in Spectral-Index Measurements*, Proc. IAEA Symposium, Neutron Thermalization and Reactor Spectra, Ann Arbor, July 17–21, 1967. International Atomic Energy Agency, Vienna, 1968, pp. 37–47.
41. Whalen, J. F., *A Completely Automated Van de Graaff Accelerator*, Proc. Symposium, Use of Computers in Analysis of Experimental Data and the Control of Nuclear Facilities, Argonne National Laboratory, May 4–6, 1966. USAEC Symposium Ser. 10, CONF-660527 (May 1967), pp. 37–41.

Reports

1. Bryant, L. T., Amiot, L. W., Dickerman, C. E. and Stephany, W. P., *A Hybrid-Computer Program for Transient Temperature Calculations on TREAT Fast Reactor Safety Experiments*, ANL-7374 (1967).
2. Doerner, R. C., Knapp, W. G., Karam, R. A. and Butler, D. K., *ZPR-9 Assemblies No. 6–9 Critical Experiments*, ANL-7208 (1967).
3. Fromm, L. W., Matousek, J. F., Rohde, R. R., Shaftman, D. H., Tessier, J. H., Levenson, M. and Charak, I., *Preliminary Safety Analysis Report on the Argonne Advanced Research Reactor*, ANL-7448 (1968).
4. Iskenderian, H. P., *The Effectiveness of Control-Rod Materials*, ANL-7303 (1967).
5. Kier, P. H., *Analysis of the Initial Critical Experiments of the EBWR Plutonium Recycle Program*, ANL-7368 (1967).
6. Kier, P. H. and Robba, A. A., *RABBLE, A Program for Computation of Resonance Absorption in Multiregion Reactor Cells*, ANL-7326 (1967).
7. Miller, D., *Thermal Expansion Coefficient, Compressibility, and Sonic Velocity for Liquid Sodium*, Thermophysical Properties of Sodium. ANL-7323, 63–75 (1967).
8. Miller, L. B., *Monte Carlo Analysis of Reactivity Coefficients in Fast Reactors. General Theory and Applications*, ANL-7307 (1967).
9. Pennington, E. M., *Analysis of High Conversion Critical Experiments*, ANL-7270 (1967).
10. Pennington, E. M., Gajniak, J. C. and Mewaldt, R. A., *Programs for Analysis of Scattering Angular Distributions*, ANL-7306 (1967).
11. Plumlee, K. E., Craig, D. S., Dates, L. R., Juliano, J. O., Kelber, C. N. and Lennox, D. H., *Addenda to the Hazards Summary Report on the Oxide Critical Experiments*, ANL-5715 Addenda (1967).
12. Richards, H. K., *Experimental Investigation of Low-Pressure Alkali-Metal Thermionic Converters for DC and RF Power*, ANL-7377 (1967).
13. Smith, A. B., Guenther, P. T., Hayes, R. and Whalen, J. F., *Fast-Neutron Scattering from Tantalum, Rhenium, and Platinum*, ANL-7363 (1967).
14. Stanford, G. S., *The Codes NURF, COMBO, and TWOSORCE for Processing Foil Counting Data*, ANL-7356 (1967).
15. Toppel. B., J., Rago, A. L. and O'Shea, D. M., *MC^2, a Code to Calculate Multigroup Cross Sections*, ANL-7318 (1967).

Abstracts

1. Bennett, E. F. and Gold, R., *Neutron Spectrum Measurements in ZPR-3, -6, and -9 Using Hydrogen-Recoil Proportional Counters*, Trans. Am. Nucl. Soc. **10**(2), 577 (November 1967).
2. Cohn, C. E., *Computer Processing of Sampling Oscilloscope Data*, Trans. Am. Nucl. Soc. **11**(1), 72 (June 1968).
3. Cox, S. A., *Polarization of Neutrons Elastically Scattered from Silicon and Magnesium*, Bull. Am. Phys. Soc. **12**, 1186 (December 1967).
4. Cox, S. A., *Multiple Angle Detector System for Neutron Elastic Scattering and Polarization Measurements*, Bull. Am. Phys. Soc. **12**, 652 (June 1967).
5. Cox, S. A. and Whiting, E. E. D., *Polarization in the Elastic Scattering of Neutrons from Intermediate Weight Elements*, Bull. Am. Phys. Soc. **13**, 116 (January 1968).
6. Dawson, F. G., Kier, P. H. Goldsmith, S., and Liikala, R. C., *The EBWR Plutonium Demonstration Experiment*, Trans. Am. Nucl. Soc. **10**(2), 500 (November 1967).

6a. DeVolpi, A., Pecina, R. J., Freese, C. H., Rolnicki, E. W., Travis, D. J. and Larsen, G. R., *Extended Capability for Fast Neutron Hodoscope Used at TREAT*, IEEE Trans. **NS-15**(1), 77–86 (February 1968).

7. Dickerman, C. E., Purviance, R. T. and Cohen, A. B., *Analyses and Significance of Initial EBR-II Mark I Cluster Fast-Reactor Safety Integral Loop Experiments in TREAT*, Trans. Am. Nucl. Soc. **10**(2), 698 (November 1967).
8. Gold, R., Armani, R. J. and Roberts, J. H., *Accurate Fission-Rate Measurements by Fission Track Counting*, Trans. Am. Nucl. Soc. **11**(1), 322 (June 1968).
9. Jankus, V. Z., *A Qualitative Consideration of Nuclear Excur-*

sion Initiated by a Shock Wave, Trans. Am. Nucl. Soc. **10**(2), 695 (November 1967).

10. Karam, R. A., *Analysis of the Die-Away of Prompt Neutrons with Two-Group Time-Dependent Solution of the Diffusion Equations in Reflected Reactors*, Trans. Am. Nucl. Soc. **10**(2), 593 (November 1967).
11. Karam, R. A. Dance, K. D., Dates, L. R., Kato, W. Y., Marshall, J. E., Nakamura, T. and Rusch, G. K., *A Large Uranium-Carbide Fast Core, Assembly-5 of ZPR-6*, Trans. Am. Nucl. Soc. **11**(1), 243 (June 1968).
12. Karam, R. A., Dance, K. D., Dates, L. R., Kato, W. Y., Marshall, J. E. and Rusch, G. K., *Heterogeneity Effects in a Large Uranium-Carbide Fast Reactor*. Trans. Am. Nucl. Soc. **11**(1), 245 (June 1968).
13. Karam, R. A., Dates, L. R., Kato, W. Y., Marshall, J. E. and Rusch, G. K., *Sodium-Void Effects in a Large Uranium-Carbide Fast Reactor*, Trans. Am. Nucl. Soc. **11**(1), 244 (June 1968).
14. Lewis, R. A. and Johnson, T. W., *Sensitivity of Small-Sample Doppler Effect Measurements to Environment*, Trans. Am. Nucl. Soc. **11**(1), 242 (June 1968).
15. Lister, D. B. and Smith, A. B., *Fast Neutron Scattering from Germanium*, Bull. Am. Phys. Soc. **12**, 1042 (November 1967).
16. MacFarlane, D. R., McNeal, N. A., Meneley, D. A. and Sanathanan, C. K., *Theoretical Studies of the Response of Fast Reactors during Sodium Boiling Accidents*, Trans. Am. Nucl. Soc. **10**(2), 694 (November 1967).
17. Madell, J. T., *Importance of the Weighting Spectrum in Reactivity Calculations*, Trans. Am. Nucl. Soc. **11**(1), 246 (June 1968).
18. Meneghetti, D. and Phillips, K. E., *Fine-Spectral Interface Effects of Resonance Scattering upon Multigroup Cross-Section Averaging*, Trans. Am. Nucl. Soc. **11**(1), 205 (June 1968).
19. Meneley, D. A., Ott, K. O. and Wiener, E. S., *Influence of the Shape-Function Time Derivative on Spatial Kinetics Calculations in Fast Reactors*, Trans. Am. Nucl. Soc. **11**(1), 225 (June 1968).
20. Miller, L. B. and Hwang, R. N., *Recent Studies of the Doppler Effect in Heterogeneous Systems*, Trans. Am. Nucl. Soc. **11**(1), 206 (June 1968).
21. Moldauer, P. A., *Measurement, Memory and Classical States*, Bull. Am. Phys. Soc. **13**, 180 (February 1968).
22. Moldauer, P. A., *Strong Absorption and Direct Effects in Compound Reactions*, International Conference on Nuclear Structure, Tokyo, September 7–13, 1967, p. 339.
23. Moldauer, P. A., *T-Violation Effects in Nuclear Reactions*, Bull. Am. Phys. Soc. **12**, 1173 (December 1967).
24. Persiani, P. J., Bump, T. R., Cushman, R. A., Long, J. K. and Kucera, D. A., *Analysis of the Variation in the EBR-II Power Coefficient due to Blanket Change*, Trans. Am. Nucl. Soc. **11**(1), 282 (June 1968).
25. Persiani, P. J., Kallfelz, J. M., Kirn, F. S., Long, J. K. and Smith, R. R., *EBR-II Power Coefficient Variations during Operational Run 26*, Trans. Am. Nucl. Soc. **11**(1), 281 (June 1968).
26. Roberts, J. H., Gold, R. and Armani, R. J., *Decay Constant for the Spontaneous Fission of U^{238}*, Bull. Am. Phys. Soc. **12**, 922 (August 1967).
27. Robinson, L. E., Dickerman, C. E. and Willis, F. L., *Initial (7-Pin) EBR-II Mark I Scale-Up Cluster Fast-Reactor Safety Integral Loop Experiments in TREAT*, Trans. Am. Nucl. Soc. **10**(2), 697 (November 1967).
28. Smith, A. B., *Intermediate Structure in Fast Neutron Processes: Fact, Fantasy, and Maybe*, Bull. Am. Phys. Soc. **12**, 1168 (December 1967).
29. Travelli, A., *The Energy Spectra and the Dispersion Law of Neutron Waves in Fast Multiplying Media*, Trans. Am. Nucl. Soc. **11**(1), 189 (June 1968).
30. Whiting, E. E. D. and Cox, S. A., *Polarization and Differential Cross Section Measurements for Neutrons Elastically Scattered from Intermediate Weight Elements*, Bull. Am. Phys. Soc. **13**, 681 (April 1968).

B